

Lecture Notes in Mechanical Engineering

Mukul Kumar
R. K. Pandey
Vikas Kumar *Editors*

Advances in Interdisciplinary Engineering

Select Proceedings of FLAME 2018

 Springer

Lecture Notes in Mechanical Engineering

Lecture Notes in Mechanical Engineering (LNME) publishes the latest developments in Mechanical Engineering - quickly, informally and with high quality. Original research reported in proceedings and post-proceedings represents the core of LNME. Volumes published in LNME embrace all aspects, subfields and new challenges of mechanical engineering. Topics in the series include:

- Engineering Design
- Machinery and Machine Elements
- Mechanical Structures and Stress Analysis
- Automotive Engineering
- Engine Technology
- Aerospace Technology and Astronautics
- Nanotechnology and Microengineering
- Control, Robotics, Mechatronics
- MEMS
- Theoretical and Applied Mechanics
- Dynamical Systems, Control
- Fluid Mechanics
- Engineering Thermodynamics, Heat and Mass Transfer
- Manufacturing
- Precision Engineering, Instrumentation, Measurement
- Materials Engineering
- Tribology and Surface Technology

To submit a proposal or request further information, please contact the Springer Editor in your country:

China: Li Shen at li.shen@springer.com

India: Dr. Akash Chakraborty at akash.chakraborty@springernature.com

Rest of Asia, Australia, New Zealand: Swati Meherishi at swati.meherishi@springer.com

All other countries: Dr. Leontina Di Cecco at Leontina.dicecco@springer.com

To submit a proposal for a monograph, please check our Springer Tracts in Mechanical Engineering at <http://www.springer.com/series/11693> or contact Leontina.dicecco@springer.com

Indexed by SCOPUS. The books of the series are submitted for indexing to Web of Science.

More information about this series at <http://www.springer.com/series/11236>

Mukul Kumar · R. K. Pandey ·
Vikas Kumar
Editors

Advances in Interdisciplinary Engineering

Select Proceedings of FLAME 2018

 Springer

Editors

Mukul Kumar
R&D Center
HEG Ltd.
Bhopal, Madhya Pradesh, India

R. K. Pandey
Department of Mechanical Engineering
Indian Institute of Technology Delhi
New Delhi, Delhi, India

Vikas Kumar
Department of Mechanical Engineering
Amity University
Noida, Uttar Pradesh, India

ISSN 2195-4356 ISSN 2195-4364 (electronic)
Lecture Notes in Mechanical Engineering
ISBN 978-981-13-6576-8 ISBN 978-981-13-6577-5 (eBook)
<https://doi.org/10.1007/978-981-13-6577-5>

Library of Congress Control Number: 2019931858

© Springer Nature Singapore Pte Ltd. 2019

This work is subject to copyright. All rights are reserved by the Publisher, whether the whole or part of the material is concerned, specifically the rights of translation, reprinting, reuse of illustrations, recitation, broadcasting, reproduction on microfilms or in any other physical way, and transmission or information storage and retrieval, electronic adaptation, computer software, or by similar or dissimilar methodology now known or hereafter developed.

The use of general descriptive names, registered names, trademarks, service marks, etc. in this publication does not imply, even in the absence of a specific statement, that such names are exempt from the relevant protective laws and regulations and therefore free for general use.

The publisher, the authors and the editors are safe to assume that the advice and information in this book are believed to be true and accurate at the date of publication. Neither the publisher nor the authors or the editors give a warranty, expressed or implied, with respect to the material contained herein or for any errors or omissions that may have been made. The publisher remains neutral with regard to jurisdictional claims in published maps and institutional affiliations.

This Springer imprint is published by the registered company Springer Nature Singapore Pte Ltd. The registered company address is: 152 Beach Road, #21-01/04 Gateway East, Singapore 189721, Singapore

Preface

This book brings together the collection of cutting-edge research articles on Interdisciplinary Engineering from the First International Conference on Future Learning Aspects for Mechanical Engineering (FLAME), which was organized by Amity University, Uttar Pradesh, Noida, India, from October 3 to 5, 2018.

The primary mission of the conference was to lay a platform that brings together academicians, scientists, and researchers across the globe to share their scientific ideas and vision in the areas of thermal, design, industrial, production, and interdisciplinary areas of mechanical engineering. FLAME 2018 played a key role to set up a bridge between academician and industry.

The conference hosted almost 550 participants to exchange scientific ideas. During three days of the conference, researchers from academics and industries presented the most recent cutting-edge discoveries, went through various scientific brainstorm sessions, and exchanged ideas on practical socioeconomic problems. This conference also provided a scope to establish a network for joint collaboration between academia and industry. Major emphasis was focused on the recent developments and innovations in various fields of mechanical engineering through plenary lectures.

This book covers the interdisciplinary engineering areas such as automobile engineering, mechatronics, applied and structural mechanics, biomechanics, biomedical instrumentation, ergonomics, biodynamic modeling, nuclear engineering, agriculture engineering, and farm machineries. This book caters to the interdisciplinary aspects, will mainly serve as a reference guide for researchers and practitioners, and is expected to foster better communication and closer cooperation between academia and industry partners.

The editors would like to acknowledge all the participants who have contributed to this volume. We also deeply express our gratitude to the generous support provided by Amity University Uttar Pradesh (AUUP), Noida; Science Engineering and Research Board (SERB), an enterprise of Department of Science and Technology (DST), Government of India; Siemens; ISME; and Begell house. We also thank the publishers, faculty, and staff members of the department and institute who have directly or indirectly helped to accomplish this goal. Finally, we would

also like to express their gratitude to respected Founder President, Amity University, Dr. Ashok K. Chauhan, for providing all kinds of support, and this book is not complete without his blessings.

In spite of sincere care, there might be typos and always a space for improvement. We would appreciate any suggestions from the reader for further improvements in this book.

Noida, India
New Delhi, India
Bhopal, India
January 2019

Dr. Vikas Kumar
Prof. (Dr.) R. K. Pandey
Dr. Mukul Kumar

Contents

NO_x Emission Reduction in Diesel Engine Through Developed Cooled EGR Setup	1
Jaspreet Hira, Rohit Sharma, Kushal Kamboj, Vikas Kumar and Prakhar Sharma	
Artificial Neural Networks Methodologies to Optimize Engine Performance Parameters Using MATLAB	15
N. Balaji Ganesh and P. V. Srihari	
Intelligent Analysis of Refrigeration System Using Fuzzy Logic	27
Sanjeev Kumar, Syed Mujahid Azam and Ravindra Kannojiya	
A Study on Gaming Engines Accessibility	33
Mayank Tyagi, Chetna Choudhary and Rana Majumdar	
Study of Enablers and Attributes for Effective SCM of FMEG: A Review	43
Ravinder Kumar, Ravi Singh and Srilekh kalas	
Reactivity Effects of In-Pin Fuel Motion in Modern Fast Breeder Reactors	49
Anuj Dubey, T. Sathiyasheela and Anil Kumar Sharma	
Assessment, Modeling, and Optimization During Nd:YAG Laser Microgrooving of Titanium Alloy	59
D. Dhupal, S. R. Dixit, S. Pattanayak, R. R. Routray, A. K. Behura and Sudhansu Ranjan Das	
Mechanical Behavior of Stir-Casted Al + ZrB₂ + Al₂O₃ Metal Matrix Composites	71
B. P. Sharma, Mohd. Junaid, D. Akhil, G. S. Rao and Umesh Kumar Vates	
Impact Strength of Silver Date Palm Leaf Reinforced Polyester Composites	79
B. P. Sharma, S. Sareen, D. Tokas, G. S. Rao and Umesh Kumar Vates	

Onsite Technical and Economic Performance Evaluation of PWT (Pipeline Welding Technology): A Comparative Analysis with CRC-Evans Welding Technology	85
Anubhav Rawat and Bhagwat Singh Shishodia	
Fuzzy Logic Modeling of Explanatory Variables of Catalytic Converter of an Automobile for Prediction of CO₂ Emission	97
Rajesh P. Verma, Ayush Kumar, P. K. Chauhan and Ankit Dimri	
Improved Fourier Polynomial Based Phase Modeling for Estimating Instantaneous Frequency from a Noisy FM Signal	107
Sankar Kumar Roy	
Combustion Event Detection in a Single Cylinder Diesel Engine by Analysis of Sound Signal Recorded by Android Mobile	121
Sankar Kumar Roy	
Separation of Nitrogen from Combustion Using Pressure Swing Adsorption (PSA) Technique and Incorporating Zeolites	131
Yogya Khanna, Shivam Puri, Prakhar Verma, Dasaradhi Putta and Preeti Joshi	
Reduction in Exhaust Emission Using Constantan Catalyst in the Diesel Engine	141
Vivek Kumar Banerjee, Tanmay Agrawal, Basant Singh Sikarwar and Mohit Bhandwal	
CFD Modeling of Commercial Slurry Flow Through Horizontal Pipeline	153
Om Parkash, Arvind Kumar and Basant Singh Sikarwar	
Real-Time Vibration Analysis of a Robotic Arm Designed for CT Image Guided Diagnostic Procedures	163
Mohapatro Gourishankar, Mishra Ruby, Shah Shubham and Ghosh Taniya	
Development of Low-Cost Wind Power Estimation System in Enggano Island Indonesia	173
Novalio Daratha, Indra Agustian, Dedi Suryadi, Agus Suandi and Neeraj Gupta	
Performance Investigation of a Nanofluid-Based Parabolic Trough Solar Collector	183
Devander Kumar and Sheela Kumari	
A Novel System Based on the Principle of Electrochemical Treatment to Reduce Exhaust Emission from Gasoline-Operated Engine	199
Prem Pal, Priyanka Sharma, Ajay Sharma and Mohit Bhandwal	

The Importance of Methanol–Gasoline Blend in Spark Ignition Engine—A Review 207
 Keshav Jangid, Vivek Verma, Velpula Surya, Rohit Gupta and Devendra Vashist

Review on Dental Implant with Special Reference to Tooth Abutment Implant 217
 Shailja Awasthi, Vinay Pratap Singh and S. K. S. Yadav

Performance and Emission Analysis of a C.I. Engine Using Ethanol and Its Blends with Jojoba Biodiesel and Diesel as a Fuel 229
 Amanpreet Singh, Sandeep Singh, Varun Singla and Varinder Singh

Solar Distiller Unit Loaded with Nanofluid—A Short Review 241
 Dharamveer, Samsheer, Desh Bandhu Singh, Ashok Kumar Singh and Navneet Kumar

Computational Investigation of Various Transition Stages in the Drop Formation Process 249
 Bishnoi Pardeep and M. K. Sinha

An Arduino Micro-controller Operated Automobile Air Conditioning System 263
 Hiren Shah, Aftab Maniar, Kushal Tailor, Dhruv Patel and Harsh Patel

Experimental Investigation of Bio-Oil Based Nanofluid Spray Cooling During AISI 316 SS Turning 277
 Ukamanal Manoj, P. C. Mishra, A. K. Sahoo and Panigrahi Subhashree

Biodynamic Responses of Human Body in Standing and Seated Position 287
 Rajesh Govindan and Suraj Prakash Harsha

Simulation and Modeling of Solar Trough Collector 301
 Mukundjee Pandey, Biranchi Narayana Padhi and Ipsita Mishra

Accepting Renewable Technologies for Waste Management Promoting Sustainable Living Among Rural Habitats 319
 F. Rajemahadik Chandrasen and A. Ghaste Akash

Optimizing the Performance of Catalytic Convertor Using Turbulence Devices in the Exhaust System 333
 Tanmay Agrawal, Vivek Kumar Banerjee, Basant Singh Sikarwar and Mohit Bhandwal

A Comprehensive Review on LiBr–H₂O Based Solar-Powered Vapour Absorption Refrigeration System 343
 S. Somesh, Sumit Kumar Shaw and Piyush Mahendru

Multi-objective Process Optimization of Biodiesel Synthesis from <i>Acacia concinna</i> Seed Oil Using TOPSIS and GRA Approach	353
Vishal Saxena, Niraj Kumar and Vinod Kumar Saxena	
Comparative Analysis of Wavelet Encoder and Hybrid Wavelet-Based Fractal Encoder for Image	363
Richa Gupta, Deepti Mehrotra and Rajesh Kumar Tyagi	
Automation of Business Cards	371
Shreya Srivastava, Suryanshu Sahay, Deepti Mehrotra and Vikas Deep	
Fractional Order Sliding-Mode Controller for Quadcopter	381
Om Veer Dhakad and Vivek Kumar	
An Investigation of the Impact of Injection Profile Shaping on the Performance-Emission Characteristics of an Existing CI Engine: A CFD Approach	393
Sudharani Panda and Rahul Banerjee	
Effect of AR Coating Properties on Diffused Reflectance and Overall Efficiency of mc-Si Silicon Solar Cells	407
Shivangi, A. K. Saxena and M. Shadab Siddiqui	
Comparative Study of Sheet Metal and Carbon Fibre Reinforced Composites Ceiling Fan Blade	413
Himanshu Garg, Joginder Singh, M. R. Tyagi, Kunal Singh, K. Aditya and Himanshu Gupta	
Kinematics of Sit-to-Stand Task for Knee Osteoarthritis Patients	421
Siddharth Bhardwaj, Abid Ali Khan and Mohammad Muzammil	
A Critical Assessment of J-Integral and CTOD as Fracture Parameters	429
R. Harihara Subramanian, Subbaiah Arunkumar, Sreekumar Jithin and Ravi Kiran Bollineni	
Financial Performance Evaluation Using MADM Approaches in Indian Banks	439
Neeraj Saini and Dinesh Khanduja	
Performance Analysis of Free Air Cooling Conditioning Chamber (FACCC) to Develop Improved Cold Chain During Transportation of Agricultural Crops in India	451
Vardan Parashar, Abid Haleem and J. A. Usmani	
Nanoparticles Reinforcement Effect on the MMC's Characteristics	459
Siddhartha Kosti, Jitender Kundu and Chandra S. Malvi	

Nonlinear Finite Element Analysis of a Gecko Spatula Adhesion on a Rigid Substrate	471
Saipraneeth Gouravaraju and Sachin S. Gautam	
Effect of Oxygen Enrichment on the Performance of a Rotary Furnace: A Harbinger to Ecological Sustenance and Pollution-Free Castings	481
Dilip Kumar, Ranjit Singh and Ashok Yadav	
Modeling and Analysis for Barriers in Healthcare Services by ISM and MICMAC Analysis	501
Kanishka Kumar, Vardeep S. Dhillon, Punj Lata Singh and Rahul Sindhvani	
Pothole Detection and Warning System for Indian Roads	511
Sunil Kumar Sharma and Rakesh Chandmal Sharma	
Self-Driving Car Using Artificial Intelligence	521
Sahil Gupta, Divya Upadhyay and Ashwani Kumar Dubey	
Mitigation of Risk in CNG Station Using Fuzzy-Integrated Technique	535
Priyank Srivastava, Mohit Agarwal, Aditya Narayanan, Manik Tandon and Mridul Tulsian	
Role of Additives in Enhancing the Performance Characteristics and Stability of Biodiesel—A Review	543
Akshay Rasal, Sarthak Saxena, Naveen Nair, Mohit Vikal, Khushbu Yadav and Gaurav Dwivedi	
Investigation of Leakage Sources in Gasoline Muffler Using RCFA, CFD, and Experimental Validation	553
Mritunjay Upreti and Sumit Sharma	
Technology Entrepreneurship Capability Development in Indian Automotive Industry	561
Mohd Talha Khan and Niraj Kumar	
Green Energy: A Building Block for Smart City in India	569
Mugdha Mishra, Mohd. Talha Khan and Niraj Kumar	
Modification of Two-Load Method for Measuring Acoustic Properties with Mean Flow	579
Deepankar Das, Utkarsh Chhibber and R. N. Hota	
BSA Detection on Polymeric Nanocantilever	589
Aviru Kumar Basu, Amar Nath Sah, Asima Pradhan and Shantanu Bhattacharya	

Modeling and Control of Underactuated System Using LQR Controller Based on GA	595
Vishal Dhiman, Gurminder Singh and Munish Kumar	
Analysis of Higher Alcohol Fuel Blends for IC Engine—A Review	605
Rahul Sharma, Dilip Kumar, Mayank Chhabra and Gaurav Dwivedi	
Hydrogen Vehicle—Opportunities and Challenges	613
Prabhakar Alok Ravi, Verma Vivek and A. K. Jouhari	
A Neural Network-Based Comparative Analysis of BR, LM, and SCG Algorithms for the Detection of Particulate Matter	619
Monika Arora, Farhan Ashraf, Vipul Saxena, Garima Mahendru, Monica Kaushik and Pritish Shubham	
Performance Testing of Biodiesel in CI Engine	635
Kunal Bhatt, Om Prakash Chaudhary, Fahad Khan and Dev Kumar Gautam	
Modelling of Photovoltaic Losses from Available Meteorological Data	645
Rachit Gada, Ishan Doshi and Kashinath Patil	
Bio-Tribological Study of Synovial Fluid in the Orthopedic Implants	657
Shariq Ahmad Bhat and M. S. Charoo	
Design and Implementation of Obfuscating Tool for Software Code Protection	665
Akshay Kumar and Seema Sharma	
A Critical Review on Calibration of Robots	677
Tanvi Verma and Nathi Ram Chauhan	
Castor Biofuel a Renewable Energy Source in India—Status and Overview	685
Satyam Vatsa and Madhuranjan Vatsa	
Renewable Energy-Based Hybrid System	695
Yaduvir Singh and Nitai Pal	
Performance and Combustion Analysis of a PPCCI Engine with Diesel as a Premixed Fuel to Reduce Soot Emission	703
S. Sendilvelan, K. Bhaskar, M. Kiani Deh Kiani, Satishkumar Subendran, M. Thrinadh, P. Santheep Pandian and L. R. Sassykova	
Theoretical Study of Solar Air Heater Using MATLAB	715
Vijay Singh Bisht, Ankit Singh Bisht and Pooja Joshi	

Path Planning of Multiple Unmanned Aerial Vehicles Based on RRT Algorithm	725
Arleen Kaur and Mani Shankar Prasad	
Coal Mine Rescue Robot Simulation Using V-Rep and Python	733
Preeti Rani and Nathi Ram Chauhan	
Characterisation and Zeta Potential Measurements of CuO–Water Nanofluids	741
Vinay Singh and Munish Gupta	
Analytical Model to Predict the Dislocation at Different Interfaces in Thin-Film Multilayer: Application to LED Multi-quantum Well (MQW)	749
Mishra Dhaneshwar, Seo Youjeong and Pak Y. Eugene	
Surface Modified Carbon Fibre Reinforced PA6 and its Blend-Based Composites	759
Anurag R. Patil, S. Aparna and D. Purnima	
Study of Bubble Dynamics and Free Liquid Surface Mixing in a Rectangular Container Having Ullage Area with Double Gas Inlets	769
Sarath Raj and J. S. Jayakumar	
Performance Enhancement of Induction Motor Using PID Controller with PID Tuner	783
Megha Yadav and Vijay Kumar Tayal	
IoT (Internet of Things) Based Emergency Push-Button System	795
Jasmeen Kaur Ahluwalia and Misha Kakkar	
Investigative Analysis of Thumba Biodiesel Blends in a Single Cylinder Four Stroke IDI CI Engine at Varying Loads	807
Rabisankar Debnath, G. R. K. Sastry, R. N. Rai and Jibitesh Kumar Panda	
Breast Cancer Detection Using Image Processing Techniques	813
Poorti Sahni and Neetu Mittal	
Reduction of Noise of Cloud Medical Images Using Image Enhancement Technique	825
Ayushi Chauhan, Neetu Mittal and Sunil Kumar Khatri	
Segmentation of Skin Lesion Images Using Fudge Factor Based Techniques	837
Sudhriti Sengupta, Neetu Mittal and Megha Modi	
Nanomaterial in Lubricants—A Real Approach	847
Neha Deepak Saxena and Nathi Ram Chauhan	

Emission Control System Using Lambda Sensors and Application in Soil Respiration	855
Sharad Chandra and Sheelam Misra	
Renewable Energy Sources and Development in Their Use	865
Mohit Misra, Vijay Kumar Tayal and H. P. Singh	
Performance Analysis of PV System Integrated with Boost Converter for Low Power Applications	879
Ruchira, R. N. Patel and Sanjay Kumar Sinha	
Modal Analysis of 132 kV Double Circuit Electric Power Transmission Tower Made up with Composite Material Thermoplastic Long Carbon Fiber Nylon 66	891
Chiranjit Bhowmik, Prasun Chakraborti, Shankar Swarup Das and Ram Singh	
Decision-Making for Selection of Most Suitable Materials for Biomedical Applications	901
Shankar Swarup Das, Prasun Chakraborti, Chiranjit Bhowmik and Ram Singh	

About the Editors

Dr. Mukul Kumar obtained his Ph.D. in physics jointly from Bihar University and IIT Bombay, India. His research areas include electroless synthesis of photoactive semiconductor thin films for solar energy conversion, electrochemical studies of metals and alloys of group II-VI materials, chemical vapor deposition and catalysis, synthesis, characterization and application of carbon nanotubes. He has published over 60 research articles in peer-reviewed international journals, and contributed chapters in three books on carbon nanomaterials. He also holds seven patents on synthesis of glassy carbon, carbon nanotubes and their applications. Currently, he is Associate Vice President (Head of the R&D Center), HEG Ltd., Mandideep, India.

Dr. R. K. Pandey is a professor in the department of Mechanical Engineering, IIT Delhi, India. He received his Ph.D. from the department of Mechanical Engineering, IIT Delhi. His research interest includes bearing lubrication, tribological elements design, engine tribology, and lubrication in metal forming. He has published several research papers in international journals and conferences.

Dr. Vikas Kumar is Assistant Professor in the department of Mechanical Engineering, Amity School of Engineering and Technology, Amity University, Noida, India. He obtained his Ph.D. in mechanical engineering from IIT Roorkee. He has published several articles in the field of vibration and ergonomics in reputed journals, and he is also a reviewer for many of them. He has recently filed for two patents to the Indian patent office.

NO_x Emission Reduction in Diesel Engine Through Developed Cooled EGR Setup



Jaspreet Hira, Rohit Sharma, Kushal Kamboj, Vikas Kumar
and Prakhar Sharma

Abstract In the present research work, an experimental investigation is performed on single-cylinder air-cooled direct injection diesel engine by incorporating cooled EGR into the intake manifold for reducing NO_x emission. A surge tank is designed, fabricated, and utilized for the flow of cooled EGR into the intake manifold as it dampens the fluctuations caused by exhaust gases during engine running. A 20% blend of karanja biodiesel and diesel fuel B20 is utilized for the experimental investigation. The combined effect of varying the percentage of cooled EGR and karanja B20 biodiesel fuel on engine performance and emission characteristics such as brake thermal efficiency, brake specific fuel consumption, cylinder pressure, and exhaust emission has been investigated. From the results, it has been concluded that at 100% of engine load, the NO_x emission reduced substantially from 662 to 503 ppm with 15% of EGR. Also for all operating conditions, a better trade-off between HC, CO, and NO_x emissions is attained within a limited EGR rate of 5–15% with a little economy penalty.

Keywords EGR · Emissions · Biodiesel · Surge tank

1 Introduction

The increasing trends in the automobile manufacturing sector have led to an increase in the number of petro-diesel vehicles and this increasing trend is escalating in the last number of years. The emissions on road caused by these vehicles and manufacturing industries have caused havoc in the environment and diesel engine vehicles are the most polluter vehicles as they emit greater amount of NO_x, with unburned hydrocarbons and particulate matter in the environment. Alternative fuel and emission reduction technologies have come to rescue in reducing the emissions. Using biodiesel, the exhaust emissions of the particulate matter (PM) were 30% lower than the overall PM emissions using petro-diesel [1]. With a 20% blend of biodiesel with

J. Hira (✉) · R. Sharma · K. Kamboj · V. Kumar · P. Sharma
Amity University, Noida, Uttar Pradesh, India
e-mail: jhira@amity.edu

© Springer Nature Singapore Pte Ltd. 2019
M. Kumar et al. (eds.), *Advances in Interdisciplinary Engineering*, Lecture Notes in
Mechanical Engineering, https://doi.org/10.1007/978-981-13-6577-5_1

mineral diesel, the cetane number of the diesel improved which also improved the thermal efficiency by 2.5% and also the combustion duration was slightly longer for biodiesel compared to petro-diesel [2]. The diesel biodiesel blend showed lower carbon monoxide and smoke emission with increase in the oxides of nitrogen but using exhaust gas recirculation (EGR) the NO_x emission were reduced [3]. The diesel soybean blend reduced carbon monoxide, hydrocarbons, and sulfur dioxide emissions by the desired values [4]. The blend of diesel and karanja esterified biodiesel oil helps in reducing the air pollution and also the brake specific fuel consumption [5]. The performance, emission, and combustion characteristics can be enhanced by optimizing the injector pressure, injector timing, and injection rate when the diesel engine is to be operated with jatropa oil [6]. A 2.6% jatropha fuel blended with diesel fuel produced maximum value of brake power and brake thermal efficiency with minimum value of specific fuel consumption and jatropha fuel acts as ignition accelerator for diesel fuel [7]. The blend of diesel and refined bran oil reduced the emissions such as CO, CO_2 , and HC by 60, 86, and 91%, respectively. But however, the NO_x emission increased by 23.48% [8]. With the addition of EGR to engine inlet air flow appeared to be beneficial in reducing the NO_x emission in the diesel engine [9]. By incorporating either the hot EGR or cooled EGR, cooled EGR performs lower thermal efficiency than hot EGR but gives a lower NO_x emission values as compared to hot EGR [10]. The excess amount of EGR leads to unstable combustion and even misfires in the engine intake manifold [11]. Diesel engine working on 100% liquefied petroleum gas (LPG) with diethyl ether (DEE) added for ignition enhancer using the EGR at part load increased the thermal efficiency by 2.5%, the higher EGR affected the combustion rate and the peak pressure at maximum load [12]. By using Jojoba methyl ester as renewable fuel in diesel engine and working at all operating conditions, the oxides of nitrogen yield higher values but while incorporating cooled EGR the NO_x emission reduced substantially [13]. 15% of EGR is the optimum value for maximum η_{bth} (Brake thermal efficiency) and minimum BSFC (brake specific fuel consumption) [14]. EGR with 5–25% reduces the NO_x emission through controlling the oxygen content and peak combustion temperature [15]. EGR is one of the most promising technology to improve the control of NO_x emissions by reducing the combustion temperature [16]. The incorporation of higher percentage of biodiesel reduces the NO_x emission significantly [17].

From the above literature review, it is found that a lot of research work has been published on the emission reduction technologies and thereby EGR is the most prominent way of reducing NO_x . So, in this research work, our main aim was to design and develop a cooled EGR surge tank setup and incorporating into diesel engine using blend of diesel and biodiesel B20 (20% of Karanja oil) for reducing the inlet temperature thereby reducing NO_x . The effect of EGR flow and biodiesel fuel is analyzed through the experimentation.

2 Experimental Setup

In this research work, air-cooled single cylinder Kirloskar diesel engine has been used at a constant speed of 1500 rpm. The setup used in this work is shown in Fig. 1 consisting of EGR surge tank, water inlet, rotameter, thermocouple arrangements, control valves, and EGR flow line. The purpose of using surge tank was to dampen the vibrations and fluctuations of recirculated hot gases. The performance parameters such as A/F ratio, BSFC (brake specific fuel consumption), η_{bth} (brake thermal efficiency) were investigated with the engine system equipped with AVL437 EPOSTM (Engine Performance & Optimization system) and Table 1 shows the engine specifications.

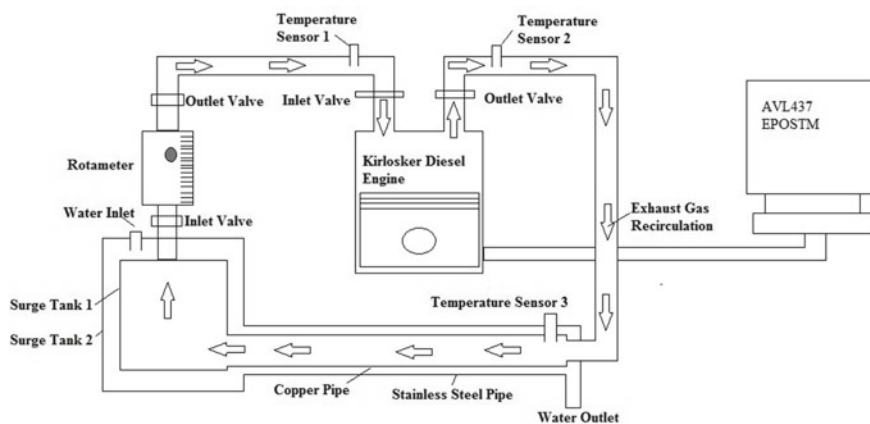


Fig. 1 Layout of diesel engine with cooled EGR setup

Table 1 Engine specifications

S. No.	Description	Data
1.	Name of the engine	Kirloskar oil engine limited
2.	Type of engine	Vertical single acting 4 stroke, high-speed total enclosed, CI diesel engine
3.	No. of cylinders	Single cylinder
4.	Bore	87.5 mm
5.	Stroke	110 mm
6.	Cubic capacity	0.991 L
7.	Nominal compression ratio	17.5:1
8.	IS Rating at 1500 rpm	7.4 kW (10 bhp)
9.	Fuel timing by spill	23°
10.	Governing class	A2

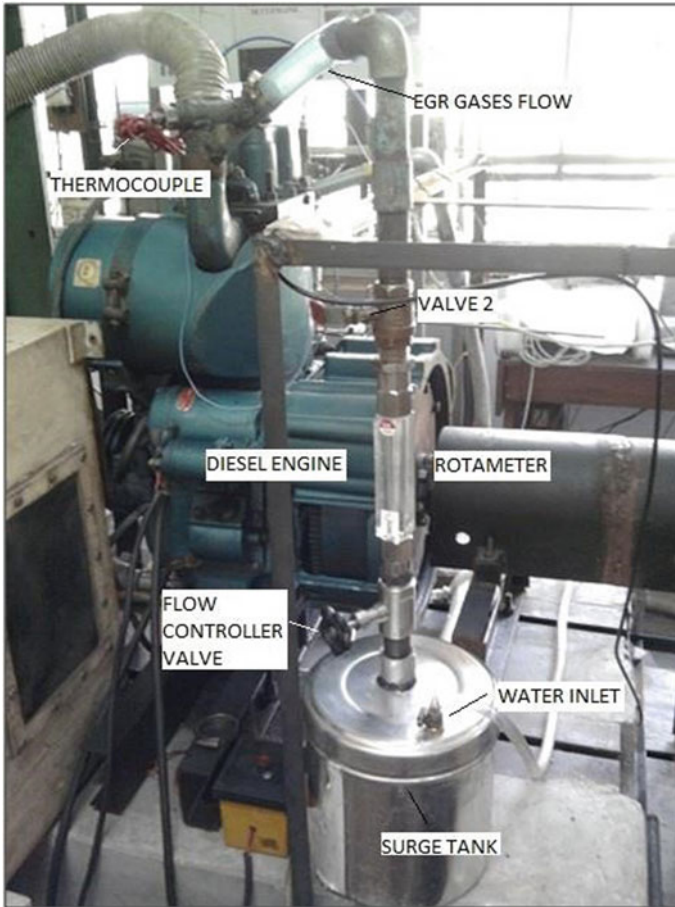


Fig. 2 Developed EGR setup

A rotameter was installed in the EGR line after the surge tank in order to measure the flow rate of recirculated exhaust gases. The load on the engine was applied with dynamometer attached with engine o/p shaft. The inlet airflow was measured by using a digital manometer. Thermocouples were installed at the two ends of the pipeline to measure the hot gas temperature at the exhaust and cold gas temperature at the inlet of the engine manifold. The blended Karanja biodiesel fuel was fed to the injector pump and the volumetric flow rate was measured using burette and stopwatch. The AVL437 was also used to calibrate the engine speed and the exhaust gases emissions such as CO, HC, and CO₂ by the nondispersive infrared analyzer and NO_x by electrochemical method. The smoke opacity meter measured the exhaust gas opacity. The EGR system installed with controller valves was used to regulate the quantity of EGR. The following steps were used for performing the experiment:

1. The engine was run with a blend of diesel and biodiesel B20 without EGR to generate baseline data.
2. To evaluate the performance and emission characteristics, the load on the engine was varied from no load to 100% load.
3. The exhaust gases were cooled with the water circulated inside the surge tank and hollow cylindrical section fabricated with copper as the material.
4. The temperature of the cooled exhaust gases was observed in the range of 46–57 °C, which varied with load and EGR percentage.

Figure 2 shows the developed EGR setup. This developed cooled EGR setup was utilized for experimentation, which includes the engine performance characteristics (viz., volumetric efficiency, BSFC, and η_{bth}), emission parameters (viz., HC, CO₂, CO and NO_x), and combustion characteristics (viz., ignition delay and heat release rate).

3 Design of Intercooler Surge Tank

Figure 3 shows the schematic diagram of the designed surge tank. It consists of a copper pipe for the flow of hot EGR, which is also enclosed with a steel pipe with cooled water flow. The exhaust gases come out from the copper pipe then enters into the aluminum surge tank where the fluctuations of the exhaust gases are dampedened

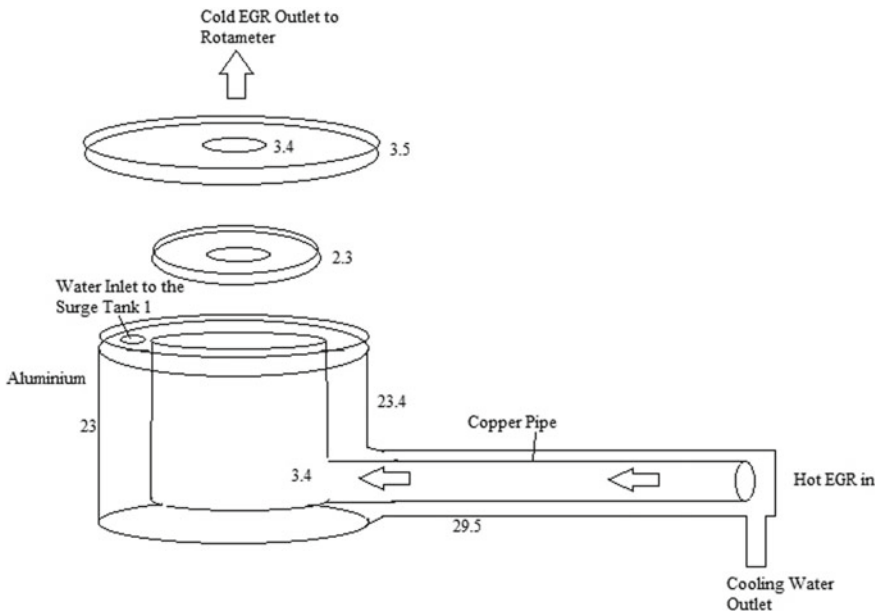


Fig. 3 Schematic diagram of designed surge tank

Table 2 Dimensions of intercooler

L	Length of the pipe	0.295 m
h_1	Convective heat transfer of water	100 W/m ² K
r1	Inner radius of copper rod	0.034 m
r2	Outer radius of copper rod	0.036 m
r3	Inner radius of aluminum rod	0.056 m
r4	Outer radius of aluminum rod	0.058 m
h_2	Convective heat transfer of gases	300 W/m ² K
k_1	Thermal conductivity of copper	401 W/m °C
k_2	Thermal conductivity of aluminum	250 W/m °C
T_1	Temperature inlet	500 °C
T_2	Temperature outlet	47 °C

due to enlarge in the area. The amount of exhaust gases are then controlled though the rota meter. The temperature of the exhaust gases obtained at the upper end of the surge tank 1 was 43–49 °C, which reduces effectively.

Table 2 shows the dimensions of the intercooler and by substituting these values in Eq. (1), the following heat transfer coefficient is calculated:

$$Q = m_h C_{p,h} (T_{h,i} - T_{h,o}) = m_c C_{p,c} (T_{c,o} - T_{c,i}) \quad (1)$$

Further, Eq. 1 consists of the heat transfer calculated in the design intercooler. After calculating, the amount of heat transfer from the surge tank is 2.37 kW.

4 Results and Discussion

A number of experiments were performed on the engine at constant RPM. The various engine performance parameters, viz., BSFC, η_{bth} , volumetric efficiency were investigated at different loadings ranging from 50 to 100% of engine load. The emission characteristics were investigated at different loading such as HC, CO, CO₂, NO_x, and smoke with opacity. The various combustion characteristics such as inline pressure, ignition delay, and heat release rate were investigated at a different weight percent of EGR. The present research work will be helpful for reduction in engine emission and the technology will be fruitful for overall diesel engine performances.

4.1 Engine Performance for Biodiesel with Different Percentage of Exhaust Gas Recirculation (EGR)

4.1.1 Brake Thermal Efficiency (η_{bth})

Figure 4 indicates the variation of brake thermal efficiency (η_{bth}) at different levels of EGR from 0 to 15.5% and at different loading conditions. It has been observed from the Fig. 4 that η_{bth} is maximum at 75% loading condition then followed by 100 and 50% loading conditions, respectively. At 100% of engine loading, the η_{bth} increased with the increase of EGR percentage from 5 to 10. This is due to the higher inlet temperature of air in the EGR operated engine which helps in improving the in-cylinder charge mass which led to complete combustion at higher loading. In addition, EGR is being at slightly higher pressure than the atmospheric which might have reduced pumping losses and results in an increase of η_{bth} . The chemical effect associated with dissociation of carbon monoxide to form free radical can also improve efficiency.

Figure 5 shows the comparison of η_{bth} between Karanja B20 and Diesel fuel and found a higher value of η_{bth} for diesel fuel in comparison of Karanja B20. And this was due to an increase of turbulence caused by EGR and higher cetane number of diesel fuel.

4.1.2 Brake Specific Fuel Consumption (BSFC)

Figure 6 shows the variation of BSFC with the percentage of EGR at different loading conditions. It is found that the BSFC increases with an increase in the percentage of EGR and reaches a minimum value at no EGR and then increases to a maximum at

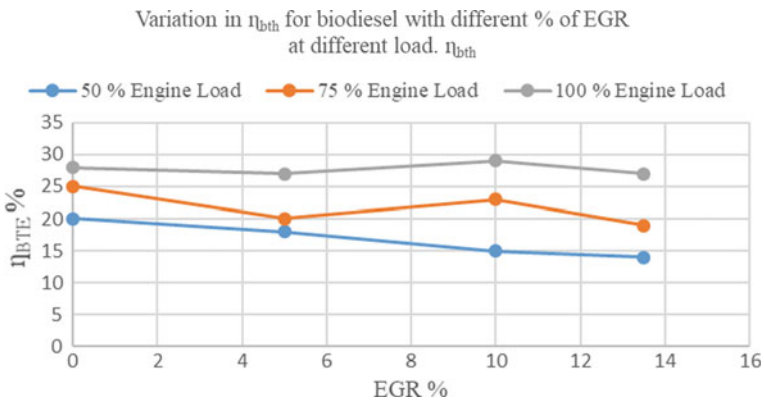


Fig. 4 Variation in η_{bth} for biodiesel with different % of EGR at different load. η_{bth}

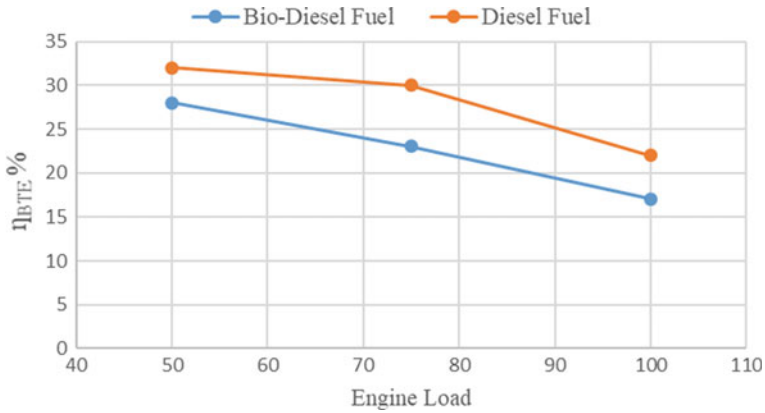


Fig. 5 Comparison of η_{ITE} between Karanja B20 and diesel fuel

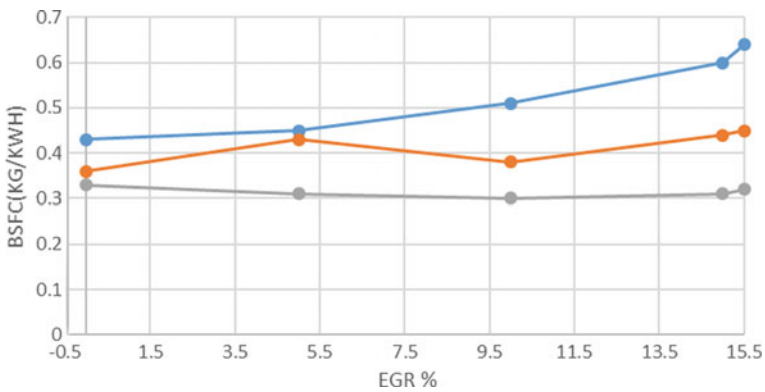


Fig. 6 Variation in BSFC for biodiesel with different % of EGR at different load

15.5% EGR. The increase of BSFC is due to the addition of exhaust gases into the intake manifold resulting in a reduction of indicated power and brake power.

4.1.3 Volumetric Efficiency

Figure 7 shows the variation of volumetric efficiency with EGR percentage. The volumetric efficiency decreases with an increase in EGR%. The air flow into the intake manifold is decreased because the amount of air has been replaced by cooled exhaust gas recirculation. The diesel fuel has high volumetric efficiency as compared to Karanja B20 Fuel as shown in Fig. 7.

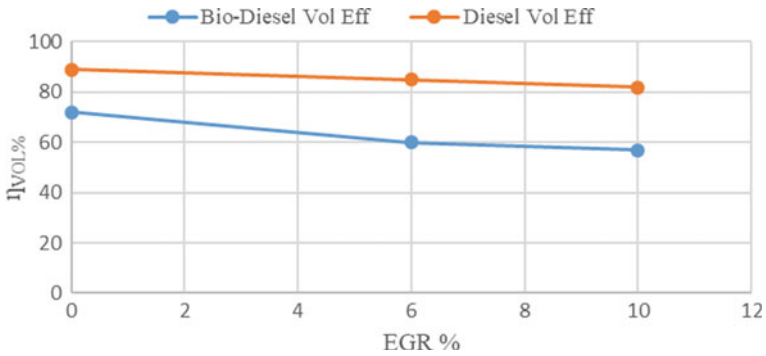


Fig. 7 Comparison of volumetric efficiency between Karanja B20 and Diesel

4.2 Engine Emission for Biodiesel with Different Percentage of Exhaust Gas Recirculation (EGR)

4.2.1 Carbon Monoxide (CO)

Figure 8 indicates the CO variation with various EGR levels and engine loadings. It has been observed from figure that at 100% engine loading, the CO emission is maximum for 13% of EGR. This is due to lower excess oxygen available for complete combustion. Oxygen concentration resulted in rich air–fuel mixtures at a different location inside the combustion chamber. This heterogeneous mixture of cooled EGR and biodiesel fuel did not burn properly in the engine which has resulted in higher CO emissions.

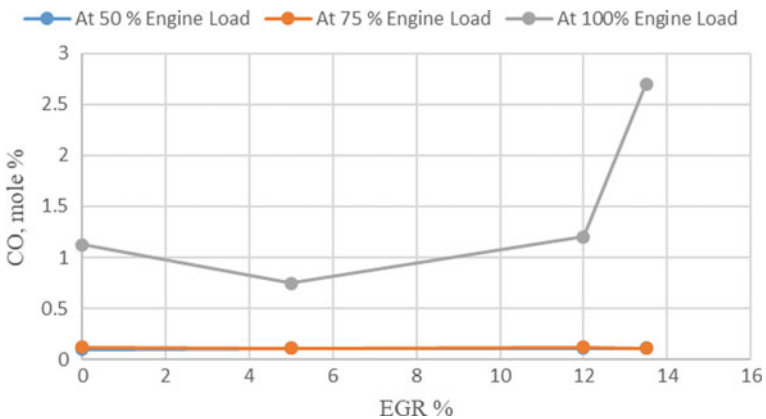


Fig. 8 Variation in CO emission for biodiesel with different % of EGR at different load

4.2.2 Hydrocarbon (HC)

Figure 9 shows the variation of HC emission with EGR% at different loading conditions. The HC increase sharply from 420 ppm without EGR to 535 ppm with 15.68% EGR at full load. This high increase in emission may be because of the reduced availability of oxygen, which makes the mixture heterogeneous inside the cylinder. This heterogeneous mixture may not have burnt properly inside the engine, thereby resulting in a higher value of hydrocarbon.

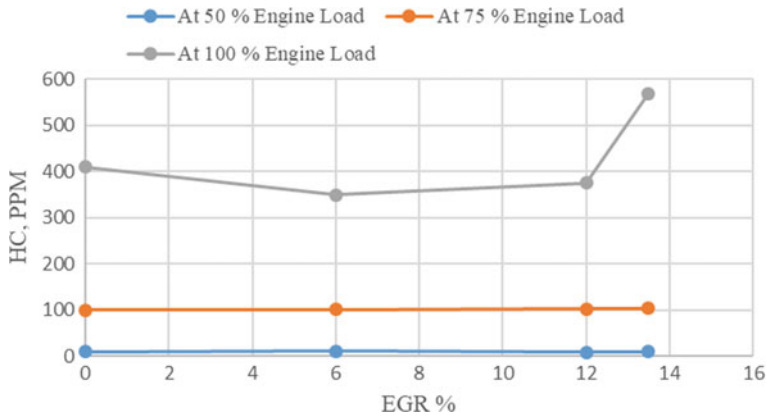


Fig. 9 Variation in HC emission for biodiesel with different % of EGR at different load

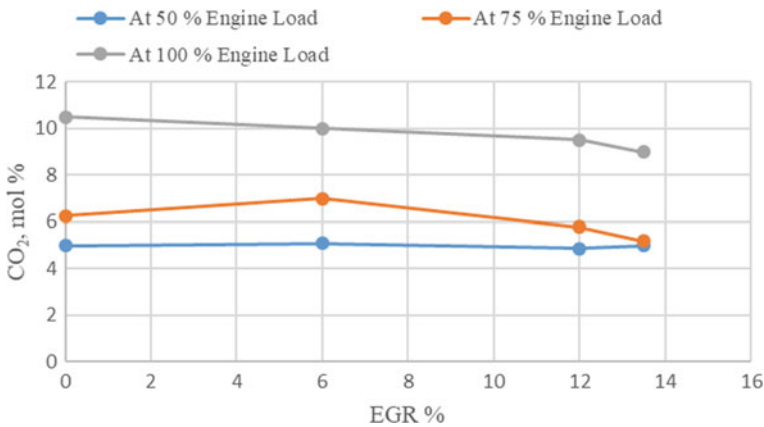


Fig. 10 Variation in CO₂ emission for biodiesel with different % of EGR at different load

4.2.3 Carbon Dioxide (CO₂)

Figure 10 shows the variation of CO₂ with EGR% at different loading conditions. It has been observed from Fig. 9 that for 75% load and 100% load, the CO₂ emissions decrease after 5% EGR. At 100% loading and 13% of EGR, the decline rate is fast as compared to other engine loading conditions.

4.2.4 Oxide of Nitrogen (NO_x)

Figure 11 shows the variation of NO_x emission with EGR% at different loading conditions. The EGR reduces the oxygen concentration in the charge and consequently, the combustion pressure and temperature were also reduced. The temperature of the exhaust gas with biodiesel was found to be lower in the case of EGR operated engine which indicates lower cylinder gas temperature. As cylinder gas temperature decreases due to the high specific heat of EGR, the formation of NO_x also reduces. The high rate of EGR is found to be effective at lower loads as inert gases are low in concentration and oxygen rate is higher in the exhaust. At full load, NO_x reduces to 503 ppm with 15.86% EGR from 662 ppm. At lower loads, 50% and 75% with 15.86% EGR, NO_x emission for biodiesel reduce to 409 and 443 from 435 and 613 ppm, respectively.

Figure 12 shows the comparison of NO_x (PPM) between Karanja B20 and diesel fuel and it has been observed that diesel fuel has lower NO_x at 10% EGR as compared to Karanja B20.

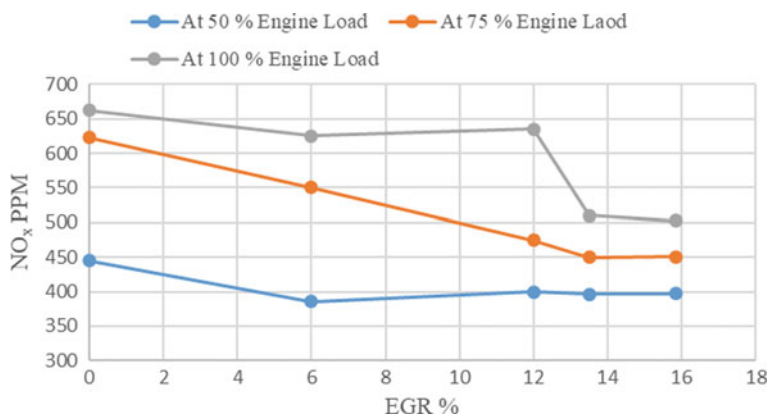


Fig. 11 Variation in NO_x emission for biodiesel with different % of EGR at different load

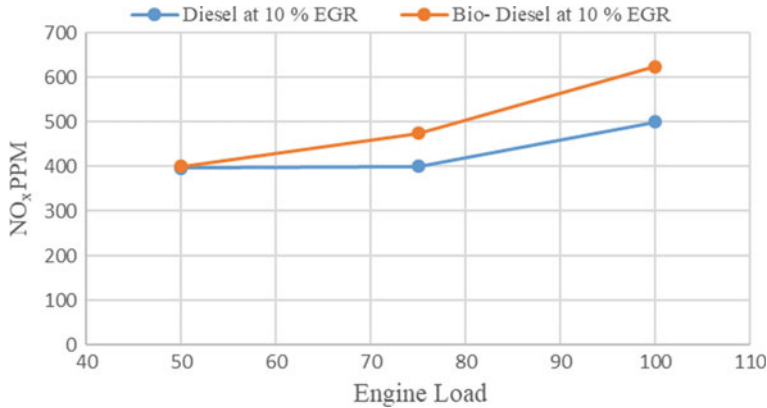


Fig. 12 Comparison of NO_x (PPM) between Karanja B20 and diesel

5 Conclusions

1. The designed and developed surge tank can be effectively utilized for cooling the exhaust gases from the air-cooled Kirloskar diesel engine.
2. The fluctuations caused by the exhaust gases can be dampened by the designed cylindrical surge tank.
3. The overall heat transfer from the surge tank setup has been evaluated with a value of 2.3786 kW.
4. The performance parameters such as the brake thermal efficiency (η_{bth}) and the volumetric efficiency both decreased with an increase in the percentage of EGR.
5. The brake specific fuel consumption BSFC increase with an increase in the percentage of EGR, and the indicated power (ip) is being reduced by the replacement of exhaust gases into the inlet manifold.
6. The emissions such as CO, CO₂, and HC increase with an increase in the EGR percentage.
7. At 100% engine load, there is 24% reduction of NO_x emission, i.e., 662–503 ppm and this decrease is at 15% EGR.
8. The experimental study on cooled EGR can be effectively utilized for stationary power generation diesel engine reducing NO_x for eco-friendly environment.
9. For all operating conditions, a better trade-off between HC, CO, and NO_x emissions can be attained within a limited EGR rate of 5–15% with a little economy penalty.
10. The developed setup can be effectively utilized for circulating cooled EGR into the inlet manifold thereby reducing NO_x at all inlet temperature and pressure.

Acknowledgements This research was supported by Dr. K. A. Subramanian Associate Professor at Centre for Energy Studies, Indian Institute of Technology Delhi. We would also like to show our

gratitude to (Prof. M. K. G. Babu) for sharing their pearls of wisdom with us during the research work and supportive team including lab staff of Laboratory IC Engine, Centre for Energy Studies IIT Delhi.

References

1. Demirbas A (2007) Importance of biodiesel as transportation fuel. *Energy Policy* 35:233–271
2. Agrawal A (2007) Biofuels (Alcohols and Biodiesel) applications as fuels for internal combustion engine. *Prog Energy Combust Sci* 33:233–271
3. Nabi MN, Akhtar MS, Shahadat MMZ (2007) Improvement of engine emissions with conventional diesel fuel and diesel-biodiesel blends. *Bioresour Technol* 97:372–378
4. Pereira RG, Oliveria CD, Fellows CE (2007) Exhaust emissions and electric energy generation in a stationary engine using blends of diesel and soyabean biodiesel. *Renew Energy* 32:2453–5460
5. Raheman H, Phadatare AG (2004) Diesel engine emissions and performance from blends of Karanja methyl ester and diesel. *Biomass Bioenergy* 27:393–397
6. Reddy NJ, Ramesh A (2004) Parametric studies for improving the performance of jatropha oil fuelled compression engine. *Renew Energy* 29:1994–2016
7. Forsan FK, Oduro EK (2004) Performance of jatropha oil blends in a diesel engine. *Renew Energy* 29:1135–1145
8. Singh RN, Singh SP, Pathak BK (2005) Investigation on operation of CI engine using producer gas and rice bran oil in mixed fuel mode. *Renew Energy* 32:1565–1580
9. Ganeshan V (2012) *Internal Combustion Engine*, 4th edn. Tata McGraw-Hill
10. Abd-Alla GH (2002) Using exhaust gas recirculation in internal combustion engine: a review. *Energy Conserv Manag* 43:1027–1042
11. Haiyong PYC, Lei S, Kangyo D (2008) Effects of exhaust gas recirculation (EGR) on combustion and emission during cold start of direct injection (DI) diesel engine. *Energy* 33:471–479
12. Miller NK, Nagarajan G, Renganarayanan S (2008) LPG fueled diesel engine using diethyl ether with exhaust gas recirculation. *Int J Therm Sci* 47:450–457
13. Saleh HE (2009) Effect of exhaust gas recirculation on diesel engine nitrogen oxide reduction operating with jojoba methyl ester. *Renew Energy* 34:2178–2186
14. Venkateswarlu K, Murthy BSRC, Subbarao VV (2013) The effect of exhaust gas recirculation and di-tertiary butyl peroxide on diesel-biodiesel blends for performance and emission studies. *Int J Adv Sci Technol* 54:49–60
15. Palash SM, Kalam MA, Masum BM, Fattah IM, Mofijur M (2013) Impacts of biodiesel combustion on NOx emissions and their reduction approaches. *Renew Sustain Energy Rev* 23:473–490
16. Babu MKG, Subramanian KA (2013) *Alternative transportation fuels. Utilization in Combustion Engines*, 1st edn. CRC Press, Taylor & Francis
17. Sinay J, Puskar M, Kopas M (2018) Reduction of the NOx emissions in vehicle diesel engine in order to fulfill future rules concerning emissions released into air. *Sci Total Environ* 624:1421–1428

Artificial Neural Networks Methodologies to Optimize Engine Performance Parameters Using MATLAB



N. Balaji Ganesh and P. V. Srihari

Abstract This work is concerned with the use of artificial neural network as a simulation tool for optimizing the performance of four-stroke single-cylinder diesel engine, operating at various conditions for this performance, test on a four-stroke diesel engines is conducted and the performance parameters are calculated with standard formulae. The output values obtained from the conventional method are used as input for training artificial neural networks in combination with backpropagation algorithm has been performed using MATLAB. The results obtained from the practical networks are compared with the conventional values and the errors are estimated for each parameter. The error deviation obtained against each parameter indicates the net variation of engine output, and accordingly the corrective actions may be initiated with the engine for the improvement of performance parameters.

Keywords Artificial neural network · Backpropagation algorithm · MATLAB · CI Engine

1 Introduction

ANN is an efficient approach amid the black-box design approach that is extensively used in different engineering applications in recent years [1]. This craft aims to greatly decrease dynamometer analysis, thereby developing scientific models of the engine outputs using a smaller subset of experimental data. Once the scientific models have been refined, the errors can be minimized using techniques such as gradient procedures [2], different approaches are included for using ANN to boost up modeling and graduate of engines [3]. The capability of ANN as a system testimony tool is pre-owned to represent the nonlinear performance of engine operations. Many analysts used ANN for predicting twisting moment, brake power, total fuel consumption, and

N. Balaji Ganesh (✉)

Department of Mechanical Engineering, Aditya College of Engineering, Madanapalli, India
e-mail: balajiganeshn@gmail.com

P. V. Srihari

Department of Mechanical Engineering, RV College of Engineering, Bangalore, India

© Springer Nature Singapore Pte Ltd. 2019

M. Kumar et al. (eds.), *Advances in Interdisciplinary Engineering*, Lecture Notes in Mechanical Engineering, https://doi.org/10.1007/978-981-13-6577-5_2

smoke formation including engine speed and diesel injection pressure [1, 4, 5, 6, 7, 8] found the ANN adds accuracy and ease in the inquiry of the engine performance. GISCA and WU described how effectively ANN is used for deciding the operating parameters of the compression ignition engine, being internal pressure in cylinders or the fuel–air ratio [9, 10]. But in ANN design draft of network topology, the trigger function, learning rule, and the permissible error for stopping the training phase is crucial and done by the engineer. So, it is tough to frame the size of the network as there is no fixed method to do it. Even though the neural networks based results is very dynamic in terms of evolution, time, and resources. By practicing and being employed on different planning, weights, and designs, we can afford actual solutions. By conducting accurate research by using various innovations and selected the best one that gives efficient output by considering input details. Depending upon the experimental data, ANN correlates various engine operating parameters with the input data. Garg explained a broad literature review and different utilizations of ANN [11]. Thus, actual-time activity and averaging of complex, nonlinear, and dynamic patterns in engine operations are challenges to be met in today’s engine advancement. Neural networks architectures, combinations of networks, and different algorithms play an important role in the execution. There is a need to use ANN as an execution critical tool that optimizes cost and time in advancing new models and techniques for overall engine performance. Further, it will support in achieving which algorithm is perfect for the appropriate situation.

2 Experimental Setup and Engine Specifications

The below line diagram represents the engine along with various parts incorporated in it (Fig. 1).

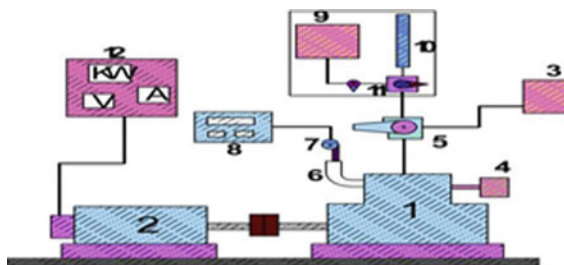


Fig. 1 Experimental setup of engine. 1. Almgir engine, 2. T alternators, 3. Diesel tank, 4. Air filter, 5. Three-way valve, 6. Exhaust pipe, 7. Probe, 8. Exhaust gas analyzer, 9. Fuel tank, 10. Burette, 11. Three-way valve, 12. Control panel

2.1 Engine Specifications

See Table 1.

Table 1 Specifications of engine

Make	Alamgir Industries Ltd.
Ignition system	Compression ignition
Arrangement of cylinder	Vertical
Cooling	Air cooled
Bore	0.102 m
Stroke	0.116 m
Compression ratio	19.5
Speed	1500 rpm
Rated power	9 HP
Fuel	Diesel
Lubricant	SAE 20/SAE 40

Table 2 Standard formulae to calculate performance parameters

1. Brake power (B.P)	$VI \cos \phi / \eta_{tran} \times \eta_{gen} \times 1000$ (units kW)
Where V	Voltage, volts
I	Current, amp
η_{tran}	Transmission Efficiency = 0.8
η_{gen}	Generator Efficiency = 0.9
$\cos \phi$	Power factor = 1
2. Total fuel consumption (TFC)	$20 * 0.85 * 3600 / t * 1000$ (units kg/h)
3. Brake-specific fuel consumption	TFC/BP (units kg/kW-h)
4. Heat input	TFC* calorific value of fuel (units kJ/kg)
5. Frictional power (F.P)	From Williams line method
6. Indicated power (I.P)	B.P + F.P (units kW)
7. Mechanical efficiency (η_{mech})	B.P/I.P
8. Indicated thermal efficiency ($\eta_{I,Th}$)	I.P/Heat input
9. Brake thermal efficiency ($\eta_{B,Th}$)	B.P/Heat Input
10. Brake mean effective pressure (BMEP)	$B.P * 60 / LANK$ (units kN/m ²)
11. Indicated mean effective pressure (IMEP)	$I.P * 60 / LANK$ (units kN/m ²)
12. Volumetric efficiency	Actual air intake/Theoretical air intake

Table 3 Experimental values for diesel

S. No.	Item	Units	Trail-1	Trail-2	Trail-3	Trail-4	Trail-5	Trail-6
1	Load	W	0	1000	2000	3000	4000	5000
2	Speed	Rpm	1500	1500	1500	1500	1500	1500
3	Voltage	Volts	270	260	250	230	215	200
4	Current	Amp	2.5	5.2	8.5	12	15.5	18
5	Time taken for 20 c.c fuel consumption	Sec	80	58	47	40	35	32
6	Exhaust gas temperature	°C	87	124	167	201	243	275
7	Air velocity	m/s	7.2	8.2	8.2	8.2	8.2	8.2
8	Brake power	kW	0.765	1.53	2.4	3.12	3.77	4.08
9	Total fuel consumption	Kg/h	0.76	1.05	1.3	1.53	1.74	1.91
10	BSFC	Kg/kW.h	0.993	0.686	0.5416	0.49	0.461	0.468
11	Heat input	kW	8.86	12.2	15.16	17.85	20.28	22.26
12	Friction power	kW	1.6	1.6	1.6	1.6	1.6	1.6
13	Indicated power	kW	2.365	3.13	4	4.72	5.37	5.68
14	Mechanical efficiency	%	32.34	48.88	60	66.1	70.2	71.8
15	Brake thermal efficiency ($\eta_{B.Th}$)	%	8.63	12.54	15.83	17.47	18.58	18.32
16	Indicated thermal efficiency ($\eta_{I.Th}$)	%	26.69	25.65	26.38	26.44	26.47	25.5
17	Volumetric efficiency	%	58.46	66.58	66.58	66.58	66.58	66.58
18	Brake mean effective pressure	kN/m ²	64.56	129.13	202.56	263.32	318.18	344.35
19	Indicated mean effective pressure	kN/m ²	199.6	264.17	337.6	398.36	453.22	479.39

2.2 *Formulae*

See Table 2.

2.3 *Experimental Values for Diesel*

See Table 3.

3 Working with MATLAB

MATLAB is widely used in scientific estimations. It integrates computation, perception, and programming in a simple manner in which questions and answers are revealed in simple mathematical notation.

3.1 *Feeding Inputs and Outputs in MATLAB*

The input values are entered in command window, which is scaled in between 0 and 1 for minimizing the error.

Speed	= [0.1500 0.1500 0.1500 0.1500 0.1500 0.1500]
Voltage	= [0.270 0.260 0.250 0.230 0.215 0.200]
Input	= [Speed; Voltage]
Bp	= [0.0765 0.153 0.240 0.312 0.377 0.408]
Tfc	= [0.076 0.105 0.13 0.153 0.174 0.191]

The output is entered in the same form of input data by varying the neurons according to the preference of the user.

For example, if the user prefers 2 neurons, then the output should be assigned as
 Output1 = [Bp; Tfc]

Likewise, all other individual output parameters are grouped as 2 rows and initialized in the MATLAB command window. Similarly, for the same individual output variable, various neurons are selected and initialized in the same manner as shown above. As soon as they entered, they are recorded as a matrix in the workspace and it is saved with the file extension MAT.

3.2 Working with Neural Network

To invoke the neural network toolbox, a command, tool is entered in the command window. The following window pops up as shown in Fig. 2.

The input values are given by clicking the import button in this window. The following window pops up (Fig. 3).

All initialized data are automatically stored in the data manager scroll box and for giving the input the variable input1 is selected and is to be imported as inputs. Similarly, variables output 1 and output 2 are selected as target values which have to be optimized depending upon the neurons.

Now all the selected data are imported in neural network toolbox, next a network is to be formed. For this, new network icon in the neural network manager is clicked.

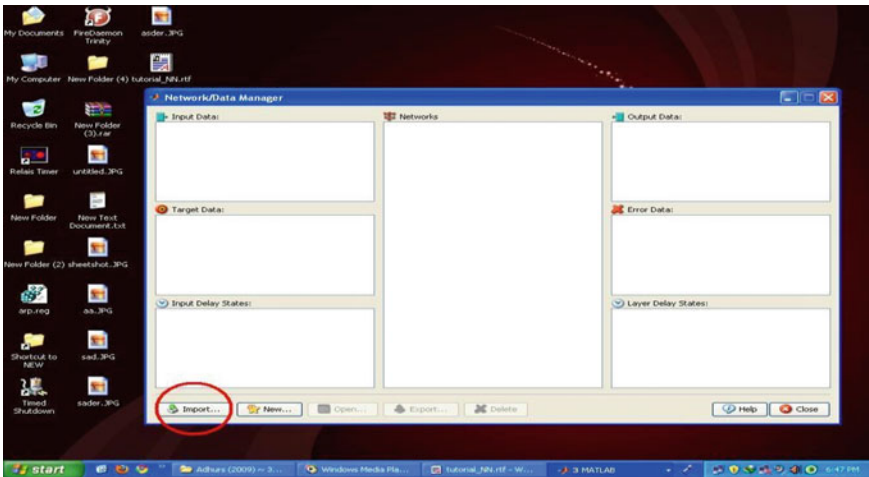


Fig. 2 Network data manager

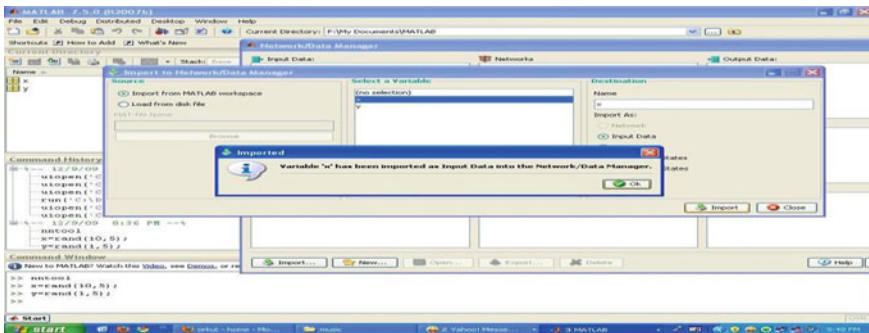


Fig. 3 Data manager

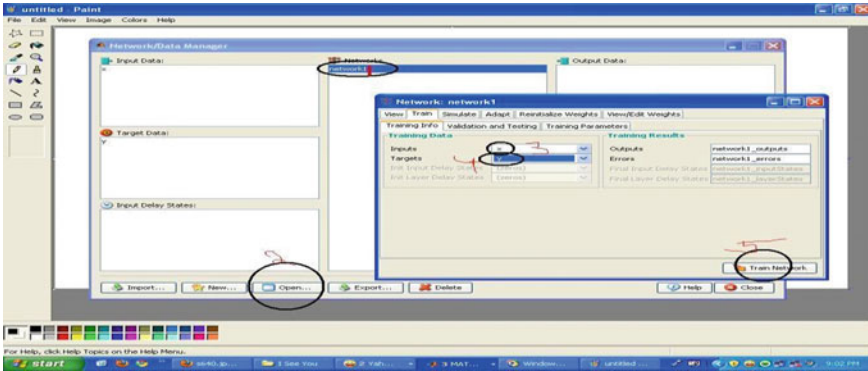


Fig. 4 Training a network

In that dialog box, various networks types are available in that we have selected “FEED FORWARD BACK PROPAGATION” network type with the training function as trained. The ranges for the input can be taken from the variable input1. The number of layers to be specified here is the total number of hidden layers and neurons for output data’s. For each layer, the number of neurons is specified and the suitable transfer function of purelin is chosen and by clicking create button in the dialog box, new network is created, next, the network has to be trained. There is an icon available in the network manager. The following window pops up (Fig. 4).

The training data are taken from input 1 and output 1, by scrolling down the pull-down menu. The training parameters specify the numbers of epochs, goal, etc., are also given. The network is then trained. A window with the training graph appears. The training stops if the goal is reached or if the number of epochs exceeds or if one intentionally stops the training. Confirmatory values are simulated and it is displayed in the network output dialog box of network manager toolbox and similarly the trained error values are displayed in network error of network manager toolbox. The network error and output values are in scaled form.

3.3 Trained Values for Diesel with Network 2 Hidden Layers 2 Neurons

See Table 4.

3.4 Error Values for Diesel

See Table 5.

Table 4 Trained values for diesel

S. No.	Parameters	Trail 1	Trail 2	Trail 3	Trail 4	Trail 5	Trail 6
1	B.P	0.076755	0.153521	0.216788	0.312402	0.3771	0.397027
2	I.P	0.236848	0.313689	0.341977	0.472522	0.53712	0.559671
3	T.F.C	0.085204	0.123424	0.132431	0.149023	0.171052	0.181499
4	S.F.C	0.992878	0.741593	0.543347	0.503409	0.475381	0.469018
5	B.Th	0.0863	0.128712	0.154048	0.178341	0.183833	0.18525
6	I.Th	0.265759	0.255004	0.255005	0.255004	0.255003	0.255002
7	Vol Eff	0.604222	0.664712	0.665765	0.665796	0.6658	0.6658
8	Mech Eff	0.34087	0.499495	0.604254	0.645813	0.675763	0.685874
9	BMEP	0.008587	0.136874	0.207421	0.285753	0.321876	0.334208
10	IMEP	0.203629	0.252193	0.314663	0.421597	0.464949	0.475287

Table 5 Error values for diesel

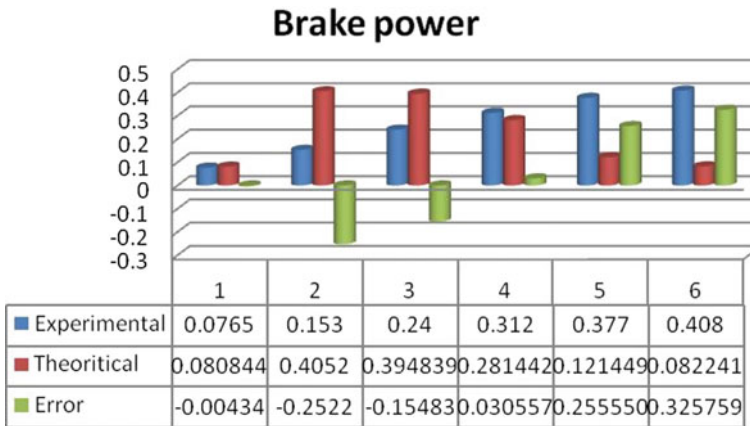
S. No.	Parameters	Trail 1	Trail 2	Trail 3	Trail 4	Trail 5	Trail 6
1	B.P	-2.55E-04	-5.21E-04	0.023212	-4.02E-04	-1.00E-04	0.010973
2	I.P	-3.48E-04	-6.89E-04	0.058023	-5.22E-04	-1.20E-04	0.008329
3	T.F.C	-9.20E-03	-0.01842	-0.00243	0.003977	0.002948	9.50E-03
4	S.F.C	1.22E-04	-0.05559	-0.00175	-0.01341	-1.44E-02	-0.00102
5	B.Th	-8.29E-09	-3.31E-03	0.004252	-0.00364	0.001967	-2.05E-03
6	I.Th	0.001141	1.50E-03	0.008795	0.009396	0.009697	-2.40E-06
7	Vol Eff	-0.01962	0.001088	3.49E-05	3.50E-06	3.48E-07	8.33E-08
8	Mech Eff	-1.75E-02	-0.0107	-0.00425	0.015187	0.026237	3.21E-02
9	BMEP	-0.00246	-0.00774	-0.00486	-0.02243	-0.0037	1.01E-02
10	IMEP	-4.02E-03	0.011979	0.022937	-0.02323	-0.01173	4.10E-03

4 Results and Discussion

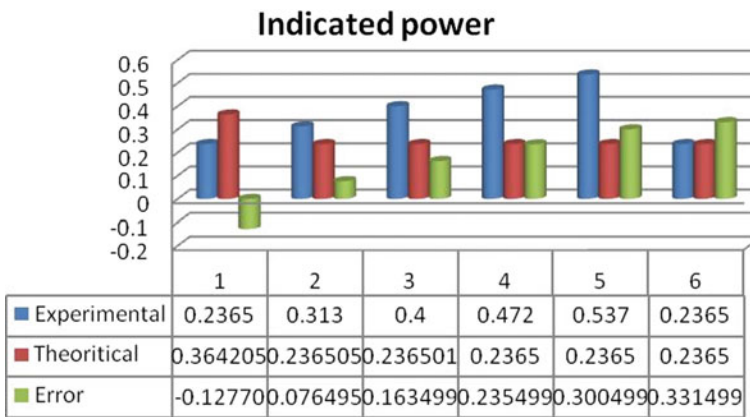
Graph between Experimental Values and Theoretical values:

From Graph 1 brake power values obtained from experimental and theoretical results are compared, error is calculated, and the error is minimum for trail 4 and maximum for trail 6, the maximum value of brake power by theoretical method is 0.4052 for trail 2 and by experimental method is 0.408 for trail 6, so in order to reduce the error the number of hidden layers has to be increased.

From Graph 2 indicated power values obtained from experimental and theoretical results are compared, error is calculated and the error is minimum for trail 2 and maximum for trail 6, the maximum value of indicated power by theoretical method is 0.364 for trail 1 and by experimental method is 0.537 for trail 5, so in order to reduce the error the number of hidden layers has to be increased.



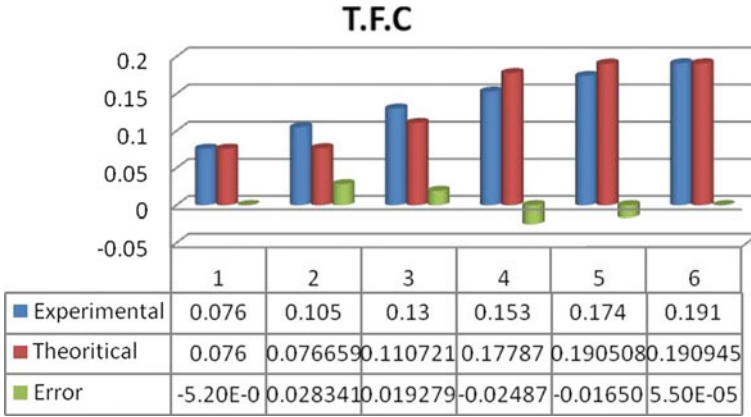
Graph 1 Error for brake power



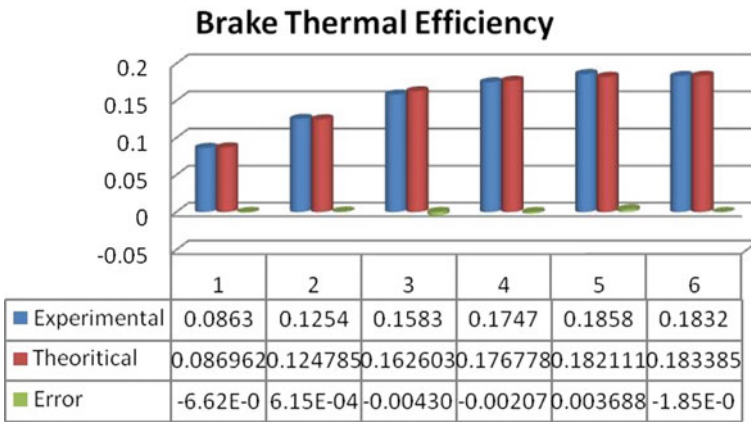
Graph 2 Error for indicated power

From Graph 3 total fuel consumption obtained from experimental and theoretical results are compared, error is calculated and the error is minimum for trail 1 and maximum for trail 2, the maximum fuel consumption by theoretical method is 0.1909 for trail 6 and by experimental method is 0.191 for trail 5, error is minimum in this case and no need to change the hidden layers.

From Graph 4, brake thermal efficiency values obtained from experimental and theoretical results are compared, the error is calculated and the error is minimum all the trails, the maximum efficiency is obtained for trail 6 in both the cases and no need to change the hidden layers.



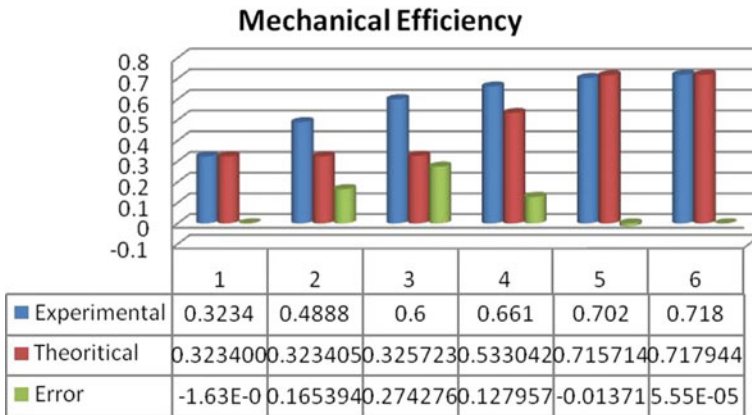
Graph 3 Error for total fuel consumption



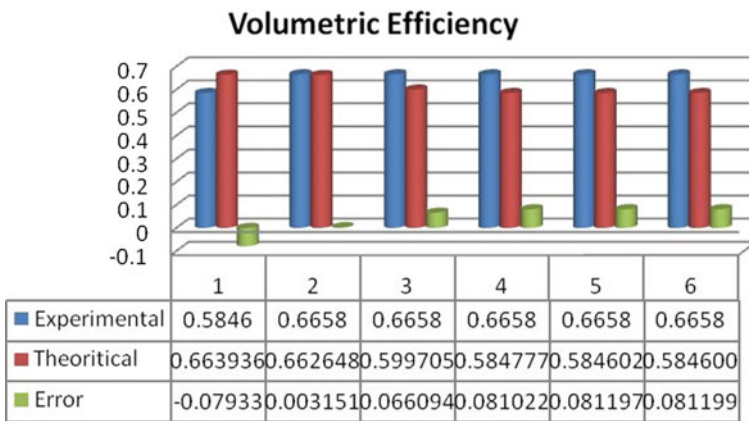
Graph 4 Error for brake thermal efficiency

From Graph 5, mechanical efficiency values obtained from experimental and theoretical results are compared, error is calculated, and the error is minimum for trail 1 and maximum for trail 3, the maximum value of mechanical efficiency by theoretical method is 0.717 for trail 6 and by experimental method is 0.718 for trail 6, so in order to reduce the error the number of hidden layers has to be increased.

From Graph 6, volumetric efficiency values obtained from experimental and theoretical results are compared, error is calculated and the error is minimum for trail 2 and maximum for trail 5, the maximum value of volumetric efficiency by theoretical method is 0.663 for trail 1 and by experimental method is 0.665 for trail 6, so in order to reduce the error the number of hidden layers has to be increased.



Graph 5 Error for mechanical efficiency



Graph 6 Error for volumetric efficiency

5 Conclusions

The experimental data is trained in MATLAB using neural networks by backpropagation algorithm and all the error values are measured. By measuring the error deviation between experimental values and trained values engine performance parameters are optimized and required changes are suggested in the experimental setup which can improve the performance of engine so that error values are minimized further. ANN will be a very good tool to optimize the engines in the future.

References

1. Zweiri YH (2006) Diesel engine indicated torque estimation based on artificial neural networks. *Int J Intell Technol* 2(2):233–239. <https://doi.org/10.1109/AICCSA.2007.370723>
2. Vossoughi GR, Rezazdeh S (2005) Optimization of the calibration for an internal combustion engine management system using multi-objective genetic algorithms. *Int J Comput Intell* 2(5):151–161. <https://doi.org/10.1109/CEC.2005.1554834>
3. Desantes JM, Lopez JJ, Garcia JM, Hernandez L (2002) Application of neural networks for prediction and optimization of exhaust emissions in a H.D. diesel engine. SAE Technical Paper No. 01-1144. <https://doi.org/10.4271/2002-01-1144>
4. Akcayoli MA, Can CR, Bulbul H, Kilicarsalan A (2004) Artificial neural network based modeling of injection pressure in diesel engines. www.wseas.us/elibRARY/conferences/miami2004/papers/484-222.pdf
5. Sekmen Y, Gölcü M, Erduranlı P, Pancar Y (2006) Prediction of performance and smoke emission using artificial neural network in a diesel engine. *Math Comput Appl* 11, 3:205–214. Association for Scientific Research. <https://doi.org/10.3390/mca11020205>
6. Gholamhassan N, Barat G, Talal Y, Hadi R (2007) Combustion analysis of a CI engine performance using waste cooking biodiesel fuel with an artificial neural network aid. *Am J Appl Sci* 4(10):756–764. <https://doi.org/10.3844/ajassp.2007.759.767>
7. Ghobadian B, Rahimi H, Nikbakht AM, Najafi G, Yusaf TF (2009) Diesel engine performance and exhaust emission analysis using waste cooking biodiesel fuel with an artificial neural network. *Renew Energy* 34(4):976–982. <https://doi.org/10.1016/j.renene.2008.08.008>
8. Tutuncu K, Allahverdi N (2009) Modeling the performance and emission characteristics of diesel engine and petrol-driven engine by ANN. In: International conference on computer systems and technologies, *CompSysTech'09*. <https://doi.org/10.1145/1731740.1731803>
9. Gisca V, Mereacre A, Pisarenco M (2004) Utilization of neural networks for observing the internal combustion engine's function. In: 7th International conference on development and application systems, Suceava, Romania, 27–29 May 2004
10. Wu B, Zoran F, Denise MK, Ohl GL, Prucka MJ, DiValentin E (2004) Using artificial neural networks for representing the air flow rate through a 2.4 liter VVT engine. In: SAE international 2004-01-3054, Powertrain and fluid systems conference and exhibition Tampa, Florida, USA, 25–28 October 2004. <https://doi.org/10.4271/2004-01-3054>
11. Garg AB, Diwan P, Saxena M (2012) Artificial neural networks based methodologies for optimization of engine operations. *Int J Sci Eng Res* 3(5)

Intelligent Analysis of Refrigeration System Using Fuzzy Logic



Sanjeev Kumar, Syed Mujahid Azam and Ravindra Kannojiya

Abstract This paper deals with the working properties of R22 refrigerant to scrutinize the performance of refrigeration system and mathematical modelling through MATLAB tools such as fuzzy logic and using algorithms based on fuzzy logic to calculate the efficiency of the vapour-compressor refrigeration system while comparing it with real-world results. It is through the literature of various researchers, we are aware that dependency of COP on temperature and pressure of system components, is vital in the thermal applications. In the present paper, COP values are calculated depending upon the temperature and pressure.

1 Introduction

Heat transfer occurs because of the temperature gradient (high to low temperature) in nature, but it occurs in opposite in refrigeration system. Refrigeration is a system which maintains a temperature difference from surrounding and removes heat in the environment. In this particular, thermal system process takes place in the reverse direction. It is achieved through substances known as refrigerant that absorbs heat which vanishes or boils at evaporator pressure in the gaseous state. Then takes place compression by applying high pressure so that it transfers the heat and absorbing liquid and water comes back using condense process [1]. Two different types of refrigeration cycles are generally used that we have focused on namely vapour-compression refrigeration cycle (VCRS) and vapour-absorption refrigeration cycle (VARC). Both of these are used for refrigeration. But they entirely differ from each other and the main difference between them is as follows. In few research works, mathematical modelling and characteristics of variable speed experimentation on thermal systems by using various algorithms satisfying the criteria and by applying concepts of neural network are being investigated [2]. The data used for the input and output values are taken from the experimentation of thermal system. We have applied a few techniques

S. Kumar (✉) · S. Mujahid Azam · R. Kannojiya
Department of Mechanical Engineering, Amity School of Engineering and Technology,
Amity University, Noida, India
e-mail: sanjeevkuma1997@gmail.com

of fuzzy logic for refrigeration system at selected temperatures and pressure. The usage of modelling tactics in anticipation of the characteristics while using cooling tower in the refrigeration system has been observed. There are three input and five output data used in the fuzzy logic for controlling refrigerator [3]. The coefficient of performance value of 'Vapour-Compression Refrigeration System' is dependent on few essential parameters such as cooling condition, component temperatures, superheating and subcooling temperatures. The design operation of refrigeration system are evaluated by using the heat rejection to the environment from refrigeration. It required a number of geometrical parameters for defining mathematical analyses of refrigeration system. The mathematical design of cooling system required experimental data points and prediction of this not so easy. So this can be done using MATLAB and fuzzy logic. Performance evaluation in 'variable speed refrigeration system', with artificial data network, was carried out with the help of experimental data mentioned as 'ice box'. The system performance can be evaluated using compressor functions. This study leads to highlight the energy utilization by finding the combinations of optimum network of compressor. The working method provides homogeneity in thermodynamic interpretation of refrigeration systems. The data set for input and output values consisted of data sequence obtained through set up in experiment. We developed a fuzzy logic for refrigeration system at different temperature and pressure. There are three input and five output data used in the fuzzy logic for controlling refrigerator.

2 Literature Survey

Fuzzy logic's linguistic terminology gives a suitable method for defining the operational characteristics of thermal systems. Data input for the experimental outcome is received by performing it in the climatic conditions of 'Ankara in Turkey'. Performance analysis between analytical equations and by using fuzzy logic gives deviations in the COP values and circulation factor, in the range of working temperature which is below 2, 5 and 0.2% [4]. The fuzzy logic methodology converts the fuzzy variables into crisp data set so that the actual system can utilize the variables. This process is known as de-fuzzification. This operation can be performed in many ways. The simplest way is implementing the height method [5]. Some inputs and outputs are entered and logic is given on basis of taking uses by machine. The refrigeration system is designed by logic of fuzzy and easily controlled by applying logic. Four vital components in 'Vapour-Compression Refrigeration Cycle' are compressor unit, condenser process, expansion valve part, evaporator function. The functions and working of all the components are described below. Fuzzy logic is generated from one to another as vapour compression, condenser expansion valve, evaporator are linked. In this paper, refrigeration are designed to control variation of temperature in different compartments.

3 Methodology

There are two different types of refrigeration cycles that we have focused on namely vapour-compression refrigeration cycle (VCRC) and vapour-absorption refrigeration cycle (VARC). Both of these are used for refrigeration. But they entirely differ from each other and the main difference between them are as follows. Compressor is the only movement part in VCRC, whereas pump is the movement part in VARC. The consumption for the movement of piston VCRC is higher whereas the energy consumption unit is lesser in VCAC. The performance of VCRC is good whereas the performance of VCAC is poor. For refrigeration system.

4 Vapour-Compression Refrigeration Unit

The functions and working of all the components are described below. Starting from the compressor, it has two main functions. First, it has to create the flow of refrigerant and second creates the pressure difference. The main components present inside the compressor are crankshaft, piston, cylinder bore, suction valve, discharge valve, etc. When the crankshaft moves then the piston moves from up to down this is called suction stroke and through suction stroke vacuum is created inside the cylinder bore. By creating a vacuum inside the cylinder bore, the lower pressure and temperature vapour refrigerant, inside evaporator pushes the suction valve and enters into the cylinder bore. When piston comes from down to up then it is called compression stroke and the refrigerant gets compressed and its pressure gets increased and discharge valve gets opened. This refrigerant gets discharged, and in this way the compressor compresses the refrigerants. There are two main functions of condenser. First, it removes the heat from the refrigerant and second converts the vapour refrigerant into liquid refrigerant. When high-pressure and high-temperature vapour refrigerant comes from compressor to the condenser, an exchange of heat will take place as in condenser, refrigerants temperature is high with respect to the external environment due to which condenser removes its heat from to the external environment, this is because heat flows from higher temperature to lower temperature and converts vapour refrigerants to liquid refrigerants. Now comes the expansion device, whose function is to decrease the pressure of refrigerant. To decrease the pressure of the refrigerant, there is a small hole in the expansion device through which, when the refrigerant passes it offers restriction, due to which pressure gets decreased and hence, low pressure and temperature liquid refrigerant moves to the evaporator. Evaporator also has got two functions. First, to absorb the heat of the external environment and second converts the liquid refrigerant to vapour refrigerant. When the low pressure and temperature liquid refrigerant enters into the evaporator, refrigerant temperature is less than the surrounding temperature, due to which external heat gets into the evaporator coil and make the evaporator boil. And in this way, liquid refrigerant is converted into the vapour refrigerant. And hence the vapour-compression refrigeration cycles get completed. The Fig. 1 shows all the components present in the vapour-compression refrigeration cycle.

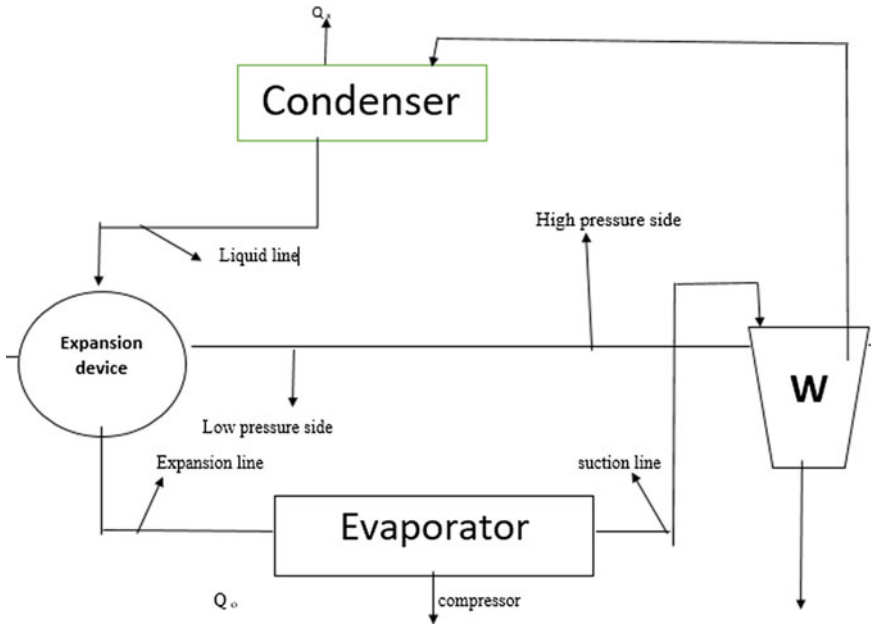


Fig. 1 Vapour-compression refrigeration cycle

5 Result and Discussion

Figure 2 shows the map of input values and set of membership functions for input and output determination.

Following Figs. 3, 4 and 5 show the variation in COP with changes in temperature of evaporator, temperature of condenser, pressure of compressor simultaneously.

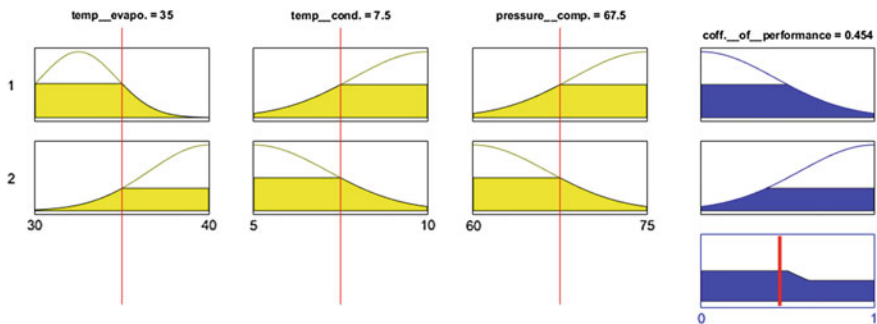


Fig. 2 Membership function

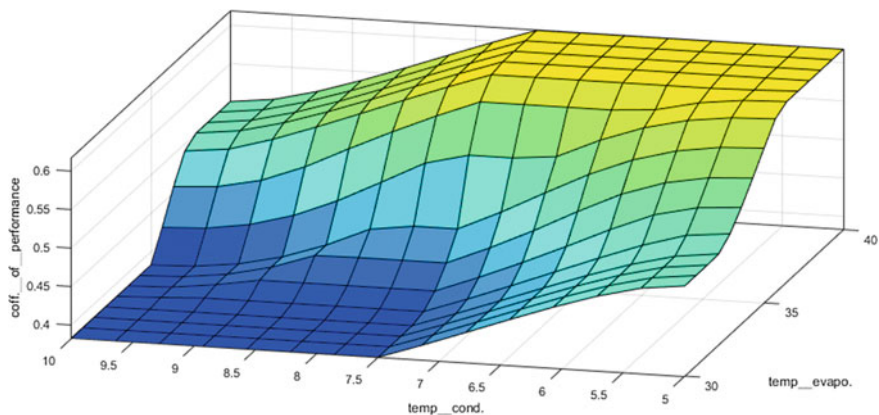


Fig. 3 Input temperature of evaporator and condenser

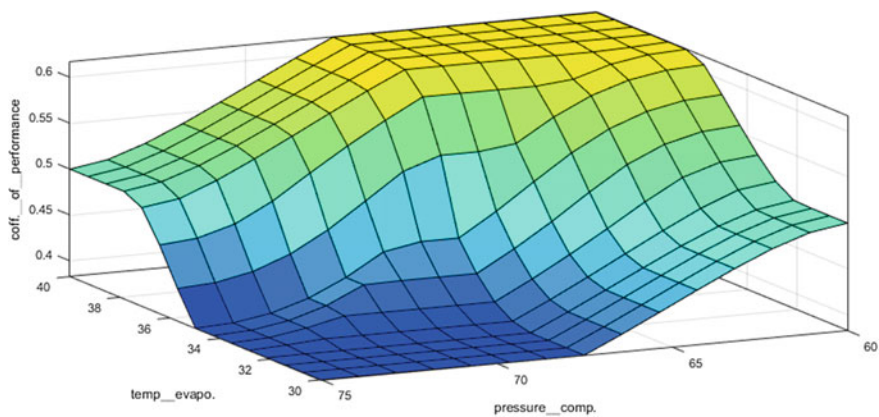


Fig. 4 Input temperature of evaporator and pressure compressor

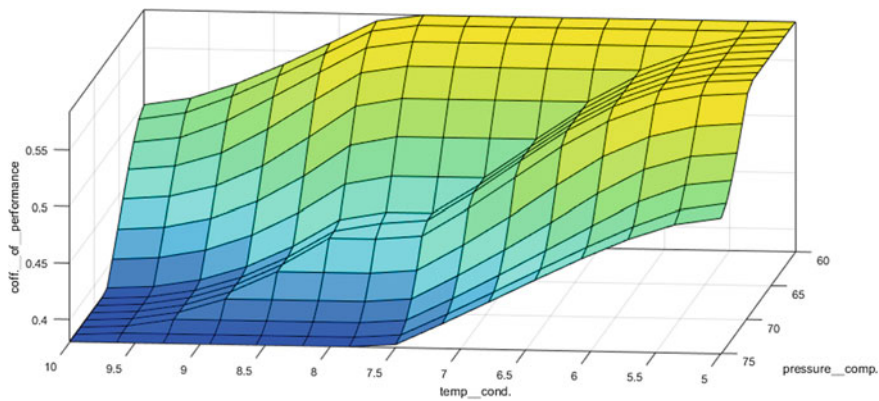


Fig. 5 Input temperature of condenser and pressure compressor

Figure 3 is between temperature of evaporator, temperature of condenser and coefficient of performance. Here, we can observe that with low temperature of condenser and high temperature of evaporator, coefficient of performance is maximum and with high temperature of condenser and low temperature of evaporator, coefficient of performance is minimum.

Figure 4 is between temperature of evaporator, pressure of compressor and coefficient of performance. Here, we can clearly observe that with low pressure of compressor and high evaporator temperature coefficient of performance is maximum and with high pressure of compressor and low evaporator temperature coefficient of performance is minimum.

Figure 5 is between temperature of condenser, pressure of compressor and coefficient of performance. Here, we can clearly observe that with low pressure of compressor and low condenser temperature coefficient of performance is maximum and with high pressure of compressor and high condenser temperature coefficient of performance is minimum.

6 Conclusion

Heat transfers from hot body to cold body in nature, but in refrigeration system it occurs vice versa. Refrigeration is a system which maintains a temperature difference from surrounding and remove heat in the environment. In this system, heat flows in reverse direction. Two different types of refrigeration cycle are generally used that we have focused on namely vapour-compression refrigeration cycle (VCRS) and vapour-absorption refrigeration cycle (VARC). The advances in thermal systems are improved by the intelligent techniques introduced in it. The applications of intelligent techniques are vital in today's world for thermal systems.

References

1. Sencan A (2007) Performance of ammonia–water refrigeration systems using artificial neural networks. *Renew Energy* 32:314–328
2. Hosoz M, Ertunc HM, Bulgurcu H (2011) An adaptive neuro-fuzzy inference system model for predicting the performance of a refrigeration system with a cooling tower. *Expert Syst Appl* 38:14148–14155
3. Metin Ertunc H, Hosoz M (2008) Comparative analysis of an evaporative condenser using artificial neural network and adaptive neuro-fuzzy inference system. *Int J Refrig* 31:1426–1436
4. Sözen A, Kurt M, Ali Akçayol M, Özalp M (2004) Performance prediction of a solar driven ejector-absorption cycle using fuzzy logic. *Renew Energy* 29:53–71
5. Aprea C, Mastrullo R, Renno C (2004) Fuzzy control of the compressor speed in a refrigeration plant. *Int J Refrig* 27:639–648

A Study on Gaming Engines Accessibility



Mayank Tyagi, Chetna Choudhary and Rana Majumdar

Abstract From the past few decades, video games had changed from a leisure time into a perspective of the evolution of new changes in human beings that is changing the way people think, behave, learn, and interact with other people all around the world. In compliment to this, games are also used in the sectors of education and health. Even after all the advancement in the recent gaming engines development, many people all around the world are still facing a lot of problem in the accessibility of the games due to their disability. These problems are: (1) Don't receive feedbacks; (2) No identification of in game responses; (3) No way to provide the input from the various input devices used. This paper surveys various gaming engines and their accessibility with the advancement in technology of the gaming engines being used. Majority of games are surveyed for different types of problems faced by people and how the gaming engines have evolved during the last few decades to match the emotions and intensity felt by people playing their respective games with full involvement.

Keywords Evolution · Disability · Identification · Gaming · Engines

1 Introduction

Over the past few decades, games have become a part of many individuals across this whole world. The worldwide sales of various games over the whole globe are even surpassing the sales of Hollywood movies; such is the craze for playing video games. This whole concept of this huge popularity can be explained by the fact that the movies, books, and music cannot provide interaction with the real-time user.

M. Tyagi (✉) · C. Choudhary · R. Majumdar
Amity University, Noida, Uttar Pradesh, India
e-mail: mayank18tyagi@gmail.com

C. Choudhary
e-mail: cchoudhary@amity.edu

R. Majumdar
e-mail: rmajumdar@amity.edu

© Springer Nature Singapore Pte Ltd. 2019

M. Kumar et al. (eds.), *Advances in Interdisciplinary Engineering*, Lecture Notes in Mechanical Engineering, https://doi.org/10.1007/978-981-13-6577-5_4

Software technology is difficult to provide access for players who are suffering from different types of disabilities. In the previous years, a lot of efforts have been taken to improve the state of accessibility of software to the disabled people. Due to this, various operating systems have accessibility features inbuilt, such as screen readers and support for keyboard shortcuts. During the 1990s, introduction of new technologies helps everyone to access World Wide Web such as Internet and use of email, which led to the definition of the W3C Web Content Accessibility Guidelines (WCAG).

Games are different from software, as their main use is for entertainment. The whole purpose is for entertaining the people playing games in their leisure time. There were two efforts made for the set of game accessibility guidelines similar to the W3C web content guidelines [1]. The Independent Game Developers Association (IGDA) Special Interest Group (SIG) on Game Accessibility published in a white paper [2] in 2004 that uses the 19 accessibility guidelines derived from a survey from 20 accessible games. Most of these games do include games for the visual disability and support motor and hearing impaired. Guidelines are that they assume an absolute validity, but in are only applicable in specific contexts [3, 4, 5]. For example, “provide subtitles” [2] is not applicable to a game without audio dialogs. “Allow for variable game speed” [6] is not appropriate for the games which are based on turns such as chess. One more problem with the guidelines was that they did not explain what type of disability to work on and because of all these problems the game developers face the problems of what type of guidelines they should follow to make a game more accessible for the users all around the world. The gaming guidelines which still exist were made way back in 2004 for a small number of genres and video games. Since then various gaming engines have been developed over the span of 13 years with more complex models and less genres being included in their guidelines.

This paper provides a detailed theory on how the people are using the games as a platform to express themselves, the research sectors and practicing the accessibility of these games. The goals of this surveys are as follows: (1) To check how a person is able to play a game is affected by his disability; (2) To make models and advanced techniques to make the games more accessible for the people; and (3) to identify various sectors for the future research work. The remainder of this paper identifies the techniques and the discussion over various accessibility issues faced by people.

The paper also explains to us about few gaming engines and how the real-life experience while playing those games have changed the perception of different societies. This survey will also show us about the latest gaming engines which are helping the game developers to put more real-life experiences into the game and provide more in-depth analysis of different types of languages used in developing these types of gaming engines.

Serious games and their applications in industry, organizations and other “genuine” territories is a quickly developing inclination. An accomplishment of genuine amusement or genuine gamified application’s usage and use in industry altogether relies upon nature of outer specialized gamification stage to be utilized, or, genuine amusement motor (SGE). The objectives of the current SGE Research Group venture at Bradley University (Peoria, IL) incorporate an investigation of 100 + genuine

diversions and genuine gamified applications in industry, improvement of an extensive SGE Near Analysis Framework, and order of SGE and positioning of nature of SGE highlights, and age of an arrangement of suggestions on choice and use of SGE. This paper presents the primary discoveries and results of the SGE inquire about venture [7].

2 Natures of Disabilities

Before introducing various gaming models, this section provides background information on disabilities and video games, as well as a consistent reference. Video games are of different genres and more than 20 genres had been identified [6, 8–10]. In reference to the players with impairments or disabilities, the survey is using the classification of impairments as defined by the World Health Organization's (WHO) manual: International Classification of Impairments, Disabilities and Handicaps (ICIDH). This classification is in accordance with the writing guidelines for technology and people with disabilities:

- (1) **Visual Disability**—It is because of a specific degree of vision loss with respect to low vision and partial sightedness, legal, and complete blindness. Color blindness comes under visual impairment or disability.
- (2) **Hearing Disability**—It refers to the partial or complete loss of hearing ability. The impairment level can be from mild to chronic. Deafness is the term which refers to the completely losing of hearing ability from both the ears.
- (3) **Motor Disability**—It is the limiting the muscle movement or complete loss in mobility of a functional muscle of a body. The common issues include paralysis, arthritis, and repetition of a strain injury. This type of impairment may also include hindrances in speech control and the urgency to use input devices other than a mouse or a keyboard.
- (4) **Cognitive Disability**—causes a slight but noticeable and measurable **decline** in **cognitive** abilities, including memory and thinking skills. A person with MCI is at an increased risk of developing Alzheimer's or another dementia.

3 Interactive Gaming Models

Due to various types of impairments and disabilities, a person is not able to play games. To improve this situation, a different type of generic gaming model is made based upon what type of disability a person is bearing. These models were based on how a person interacts with various types of gaming genres, play, and provide input for its respective actions and then finding similarities between the next steps that will be performed when playing any type of a game. An example of this analysis and in order to illustrate how the model was derived, the next portion shows the interaction

of a player with three different game types of games (First-person shooter, puzzles and racing games) divided into different number of steps. The gaming interaction model consists of the following three steps:

3.1 Receiving the Stimuli

Games do provide a stimulus in the following forms: Haptic, visual and auditory. It depends on the types of games; stimuli can also be divided into furthermore two categories:

- (a) Stimuli (Primary)—It must be perceived by the player to play any game. All games follow stimuli to play various games by using visuals. For example, in a first-person shooter (FPS) game, visuals are used as an primary stimuli and without providing any feedback which is based on visuals the games cannot be played. Even though sound and haptic feedbacks are being provided but this doesn't guarantee that the game can be played properly with any hindrances. Taking an example is that a person may be able to identify his enemy's presence and hear them too but they won't be able to identify where his enemy is located. The problem of this location identification makes it very tough for the person suffering from the visual disability. Thus, many games such as which are based upon dance and music they heavily rely upon music to such an extent that both the audio and visuals are primary stimuli.
- (b) Stimuli (Secondary)—It is defined as an additional supplement to the stimulus which are primary. Although the ability to play a game doesn't depend upon the secondary stimuli. In a first-person shooting game, a person can still play a game without having the audio and haptic feedbacks whereas they might suffer from a decreased gaming experience which will reduce the user review about that particular game, but the person can still play that game to a very large extent without interrupting the gameplay.

3.2 Response Time Determination

Based on responses and stimuli, the player must give or choose which in game responses he should use from the available playing actions and these actions are specifically present in the game and are well defined by the game genre. For an example, an RTS type of game engine will only allow the player to regroup its units whereas an FPS type of game will allow the player to navigate his or her character which is defined by the game genre.

3.3 *Providing Inputs*

The player must use the input action physically while playing a game in response to a specific action which is based on various responses already present in the game. Generally, games do require a physical device to map the actions provided by the game from keyboards, mouse, joysticks, controllers, and other input devices. Many games also use voice recognition to play games.

Input devices are differentiated into two different types:

- **Discrete inputs**

It is a device which measures inputs which are discrete and has an on-off switch function. Examples are keyboards and buttons of a controller.

- **Analog inputs**

It is a device that calculates the input which is continuous for example inputs coming from a mouse or a controller. It is all because the intensity of interaction needed for controlling an analog input device is much higher than that of a discrete device, more precise motor skills are a must. If the input is small, then the discrete inputs are easy to handle and control in games. In various cases when the number of outputs is very high that is when a multi-key game is played on a keyboard to perform various actions in the game, then it becomes very difficult for a gamer or a person to play a game more efficiently. For improving such problems, we use controllers which have a combination of both analog and discrete inputs which are being used by the gamer. Most of the controllers are having two analog sticks used as inputs and various numbers of discrete buttons or triggers as an input. These input controllers can also come in the form of wheel controllers more specifically used in playing racing games thus also provide a real-life experience for the gamers or the person playing that specific game. These controllers thus provide the user to play a game more efficiently.

4 **Gaming Engines of Varying Types**

Unreal Engine—It is one of the older games in terms of development; this engine is best suited for FPS like (the Unreal tournament). Well like many other gaming engines, this unreal engine not only provides tools for game building but also provide the C++ source code. With the passage of time and years, the developers all across the globe have put this engine to a more innovative use and are using it to make more complex games for the gamers. This engine operates based on subscription, if we talk about the game development world; Double-edged is the term which defines the functioning of Unreal gaming engine.

Unity Engine—This engine was first introduced more than a decade ago as a game development platform for Apple' operating system X, the Unity game engine

Table 1 Tabular formation

First-person shooter (Counter Strike)	Puzzle games (Candy block mania)	Racing games (Split Second)	Player
Enemy is visible. Explosions can be heard	Music is available and a block is falling	The road and car's opponent is available. Music is available with feedbacks	The player receives the stimuli
Player can decide to fire	The player decides to change the shape of the block and the way it falls	An opponent is overtaken by speeding up the car and using additional nitro	The player determines the response
The gun is fired once the player presses his button on the controller	With the help of arrow keys player changes the path of the block before dropping it down using space bar	The player uses the wheel to tilt it against other opponents	Input is provided
The enemy has been killed and a new enemy will be reborn	When the whole line is cleared then a new block will appear	The opponent is overtaken and the racer can lead	All the steps from 1, 2, 3 are repeated

now supports and give platform to a variety of gaming engines which works in Xbox, PlayStation, Windows and mobile OS such as iOS and Android. The Developers use Boo (similar to python) and C# to develop the Unity engine. Like the Unreal engine, Unity is offered on the basis of a subscription (Table 1).

Cry Engine—Talking about the above discussion, in the comparison of Lumberyard by Amazon, this engine is favored more by the developers the rendering qualities provided by this engine. It is also based on the basis of subscription, and then it also provides full licensing by adding support from its platform creator known as Crytek along with the access to the source code. The Crytek is not free and it also sells its software with some cost and moreover unlike its other competitors it doesn't demand a number of developer royalties being offered. Majority of the games under this engine includes the Everybody Gone to Rapture and Homefront.

Corona SDK—It is a platform which features a large library made up of API and also provides various tools for the development which supports a lot of platforms such as Android, iOS, and further Windows phone also. The Corona SDK is mainly based on OpenGL 2.0. This version is not on free subscription basis in fact it is having a high cost depending upon the range of \$78 or \$198 a month per seat.

5 Problem Conceptualisation and Strategies Identified

There is a very small amount of games that need to fix the needs of individuals with different types of disabilities and after the important work done there are few strategies which are being provided on the basis of similarities between all these games. These strategies include various factors as below

- **Reducing time factors**—These games are hardly depending on time and thus are way too time sensitive and as a result, there is no external or extra pressure on the player for making a decision to respond within a specific frame of time period. There are games that stops so frequently that the overall user experience is so bad the user end up neglecting the game completely at times.
- **Reduce the features of various stimuli**—The games which consist of various coinciding features do provide with some amount of visual features too. All the game objects are limited on the screen and whatever the information is required by the gamer to play a certain type of game is available on the main screen without any interruption.
- **Reducing the inputs**—This technique is very much similar to the techniques in which the games are used for making more games more accessible for the impaired people who are mostly impaired. If we talk about almost every game that is cognitive then these games give very less or limited controls that are intuition based for impaired people by using various actions such as touch screen controls. Hence thereby reducing the various inputs we can achieve our desired automatic input through these strategies.

6 Conclusions

A very large number of games that are accessible were surveyed for different types of problems related to disabilities and impairments and thus many strategies were discussed for the development phase. Very limited types of genres of games are discussed in this survey. After applying various accessibility techniques, the changes were observed in terms of gameplay alteration and one thing that the developers need to understand about the games that they need to make games which are more relevant and are fun to play because in the end if the game is not fun to play then how can a developer expect the game to be launched successfully in the market among different sets of people with disabilities and no disabilities. This study also pointed out how the future work can be carried out in the research sector. Many popular games are based on strategies and first-person role-playing games do lack a lot of accessible options for many disabled people thus very few games have been developed for the cognitive players who are suffering from various impairments. Thus, the developers should be investing their time in carrying out strategies to make the games more accessible for the disabled people so as to increase their game sales. The development sector can

improvise on these strategies and bank on them for future purposes of helping the disabled in playing the games.

7 Future Scope

Various genres in games—As previously discussed in the above portions, we got to know that many disabled people can only play games in very limited ways and a very specific type of games are playable. Many new popular games which are made by using various gaming engines such as Unreal, Unity, Cry Engine and corona SDK which do make games in the categories of sports, strategies and first-person role-playing games genres are still not available for these disabled people. While for those people who are disabled by hearing, they are still able to play games more efficiently in comparison to several motor and visually disabled people who are not able to play these games at all. But still in the case of first-person shooter games, these games are made accessible for all the types of disabilities and impairment [11–13]. First-person shooter games are different from rest of the games because they are based on open sources and these games also allow to make modifications to the respective games by using various software development tools and kits [14]. By reusing an already existing game also reduce the costs of further developing an already accessible game.

Cognitive disabilities—These disabilities are very variable and change a lot and thus are very complex to understand. The hindrances faced during the research work. The hindrances mainly were the effects that needed to be understood on how to combat these challenges. There are only five games which were identified to have been accommodating the players with different cognitive disabilities and impairments. Through various different studies, it is indicated that many people with cognitive impairments do play various games, but it is very less known of the fact about what types of problems they are facing.

Metric—The accessibility of the games after being measured is known as to be very complex because of various factors. A possible way to enhance this problem would be to make games accessibility ratings for the games that are very likely the same as the Entertainment Software Rating Board [15] ratings. Then after these ratings, it would generally help all the disabled people with a sense that which game they can actually play with less number of hindrances and enjoy the gaming experience. In this way, they can buy various games and give their own opinions to enhance the credibility of the games. The accessibility ratings on the top of the gaming boxes will give rise to the potential and enhance the awareness needed for the need of accessibility in games for different types of disabled people and in fact for normal people also. This is all because the low-level techniques are context dependent and also depend a lot on the genre type of the game and following this many game can accessed for various genre types and thus new games can be developed over the course of time. These types of referencing games should be the most accessible game for all the types of disabilities and it should also allow how the accessibility of these

games can be measured. Well these accessibility ratings do provide an indication for each category of disabled people on a specific type of scale and thus it will act as the highest and most efficient rating for that genre type of a gaming series.

COST—Many people around the globe don't understand that people with disabilities also like to play the games that normal people play. The reasons behind this type of no awareness are that various schools do not include the development of games in their school curriculum because of the high cost of very good game development kits. Many schools term them as not a resource of an income as not every person can code. Many books are being published but only one book that talked about the game accessibility was this. Another reason for such a type of lack of awareness is that within the gaming world or industries the people think that they won't get enough profit out of the selling of games.

References

1. WAI (2008) Web accessibility initiative. <http://web-game.co.uk/accessible-games/>. Accessed October 2008
2. IGDA-SIG (2004) IGDA game accessibility white paper. Technical report. Accessed December 2008
3. van Welie M., van der Veer GC, Eliëns A (2000) Patterns as tools for user interface design. In: International workshop on tools for working with guidelines, Biarritz, France, pp 313–324
4. Folmer E (2006) Usability patterns in games. In: Future Play'06: proceedings of the 2006 conference
5. Frutos-Pascual M, Zapirain BG, Zorrilla AM (2014) Adaptive tele-therapies based on serious games for health for people with time-management and organisational problems: preliminary results. *Int J Environ Res Public Health* 11(1):749–772
6. Djaouti D, Alvarez J, Jessel J-P (2011) Classifying serious games: the G/P/S model. *Handbook of research on improving learning and motivation through educational games: multidisciplinary approaches*, pp 118–136
7. Vasudevamurt VB, Uskov A (2015) Serious game engines: analysis and applications. In: 2015 IEEE international conference on electro/information technology (EIT). IEEE, pp 440–445
8. Wikipedia (2008) Video game genres. <http://en.wikipedia.org/wiki/video>. Accessed August 2008
9. ESA (2008) Essential facts about the computer and video game industry. <http://www.theesa.com/facts/pdfs/esaef2008.pdf>. Accessed March 2009
10. Hussaan AM, Sehaba K, Mille A (2011) Helping children with cognitive disabilities through serious games: project CLES. In: Proceedings of the 13th international ACM SIGACCESS conference on computers and accessibility, pp 251–252
11. Kimball R (2008) Doom3 cc. <http://gamescc.rbkdesign.com/>. Accessed August 2008
12. GMA (2008) Shades of doom. <http://www.gmagames.com/sod.html>. Accessed September 2008
13. Cai W et al (2016) The future of gaming. *Proc IEEE* 104(4):687–691
14. Valve (2006) Source SDK, valve developer community. <http://developer.valvesoftware.com>. Accessed March 2009
15. ESRB (2008) The entertainment software rating board. <http://www.esrb.org/ratings/index.jsp>. Accessed September 2008
16. Saunders K, Novak J (2006) *Game development essentials: game interface design*. Thomson Delmar Learning

Study of Enablers and Attributes for Effective SCM of FMEG: A Review



Ravinder Kumar, Ravi Singh and Srilekh kalas

Abstract Globalization of the world economy has forced global supply chains to become more innovative to sustain in this highly competitive global market. With growth in infrastructure project all around the world have given rise to fast-moving electric goods industry making it a bustling industrial sector. In this paper, authors have studied issues related to FMEG industries. For literature review, 70 research papers from referred journals have been studied and research gaps found out. Literature review has indicated that FMEG industries face a frequent change in consumption pattern due to brief product life cycle. The organizations involved in FMEG industry face difficulty in determining and forecasting the demand. The point of sale being highly unorganized in India makes it difficult for the industry to match up with customer satisfaction by integration of customer and product development activity. Adding to the adversity is the raw material scarcity in India and delay in transportation from foreign countries. Indian FMEG industries are facing the challenges of intricate supply chains, fast changing market with tighter margins, production better quality products at a cheaper price for customer satisfaction. Government taxation and regulation in all energy efficient products along with introduction of e-commerce marketing affect the dynamics of industry.

Keywords Supply Chain Management (SCM) · Fast-Moving Electrical Goods (FMEG) · Enablers

1 Introduction

Fast-Moving Electric Goods (FMEG) is an emerging sector in the present market scenario in Indian industry. With the growth in infrastructure in areas of residential, commercial and industrial the consumption of electric goods have increased in exponential ratio. This has fueled the rise of FMEG industry in India featuring domestic players with greater and intense involvement in the market, in order to grab their

R. Kumar (✉) · R. Singh · S. kalas
Amity University, Noida Sec-125, Noida, UP, India
e-mail: ravinderkumar.ap@amity.edu

© Springer Nature Singapore Pte Ltd. 2019
M. Kumar et al. (eds.), *Advances in Interdisciplinary Engineering*, Lecture Notes in Mechanical Engineering, https://doi.org/10.1007/978-981-13-6577-5_5

market share. To increase the share of profit, every enterprise has started innovating their supply chain practice thus evolving the whole way of doing business. The supply chain includes the manufacturers, the suppliers, the transporters, the warehouses, the retailers, the distributors, and the customers themselves also [1].

Sila et al. [2] stated that SCM involves the planning of what to produce and how to produce and distribution of produced products. Supply chain connects raw material suppliers, manufacturer with customers through retailers and wholesalers [3].

2 Literature Review

Raw materials stocking is necessary to ensure continuous production, as high volume production requires a high inventory level [4]. The cost of procurement and inventory carrying cost makes a major share of total logistic costs of an organization [5]. According to Bottani and Montanari [6], the number of supply chain members, reorder policy formulation, demand forecast information sharing mechanisms, and demand behavior are some of the critical primary factors of concern. Top management commitment towards formulation of policy with long-term vision for enterprise helps to create better relationships among supply chain and efficient information sharing among its members.

Simpson [7] observed that top management commitment is essential for supply chain members' relationship which provides a significant driver for enhancing organization's know-how of material value, recycling opportunity, new customers, or markets for their product and for combining existing and new resources and thus improving the process of recycling. Cooperation and coordination between enterprises can bring-in great benefits in supply chains [4]. Frequent regulatory changes affect channel and structure of marketing and distribution strategy and as a result, it becomes a challenge to adapt challenges according to market scenario [8]. Companies with common goals can get into equally profitable long-term business partnerships by improving standards and thereby reducing risks [9]. The market share of the product significantly depends on the brand knowledge and awareness of consumers on brand [10].

In general, the main purpose of maintaining high inventory is the uncertain pattern of flow of goods in supply chain. Customer-oriented strategies and planning by keeping core capabilities of organization in mind ultimately helps [11]. In FMEG industry, variability of supply chain of each type of product is very high. The product life cycle of modern retail FMEG products is much shorter than previous retail products in case of retail consumers whereas for industrial use products product life cycle does not affect [12].

FMEG sector being exposed to products with short product life cycle is prone to stiff competition. It is essential for organization to innovate continuously to maintain market share and sustain product line. Learning and planning based on current market scenario lead to innovation and increases in market share [13].

Top management commitment for formulation of policy and long-term vision helps to create better relationships and efficient information sharing among supply chain members. Chaturvedi [14] observed that energy efficient lighting and use of low energy consuming materials decrease the carbon emission indirectly.

3 Findings from Literature Review

Following are critical enablers and challenging factors of the FMEG sector found from literature (Table 1).

After thorough study of literature, it is found that companies of FMEG sector consistently stagger in managing the product life cycle and maintain market share of product line. With longer lead times for procurement of raw material and pressure to maintain high inventory at warehouses and stiff competition from other brands at the end results in lower profit margins.

Moreover, FMEG being a sector related to electrical appliances or components requires to follow stringent regulatory obligations in order to maintain higher quality and safety standards for which continuous research and development activity by organizations' have become a necessity.

Though the sector faces barriers in terms of challenging factors but effect of those factors can be compensated with streamlining the supply chain with better management of information flow within members of supply chain by using modern IT tools.

Collaborating with global companies and partnering for technology sharing will further help to introduce new technology in the market giving an edge. Efficient

Table 1 Critical enablers and challenging factors of FMEG sector

S. No.	Challenging factors	Enablers
1	Energy efficient products	Top management commitment
2	Profit margin	Long-term vision for sustainability
3	Demand forecasting	Cost-efficient logistic management
4	Product life cycle management	Partnership with global companies
5	Longer lead times for procurement of raw material	Information sharing between SC members
6	Higher quality standards	Strategic geographical location of SC members
7	High-quality Research and Development (R&D)	Efficient networking of warehouse with market
8	Competition from other brands	Agility of SC to market fluctuations
9	Taxation and regulatory obligations	Use of modern IT tools
10	High inventory maintenance	Better marketing strategy

networking of warehouses with members of supply chain will further make the process streamlined and balanced. Long-term vision for sustainability along with top management commitment for the growth of organization will drive the organization in a positive dimension.

4 Research Gaps and Concluding Remarks

Authors have revied the literature from different sources such as Science Direct, Emerald Insight, Springer, etc. Different enablers and challenges for FMEG supply chain have been identified from review of seventy research papers.

Most of the studies have studied issues such as quality management, inventory management, leadership issues, constraints and challenges related to top management but not holistically. From literature review authors have observed following research gaps:

- The sector being new and emerging in market have very less detailed research content on strategy development for successful management of critical factors.
- Study on strategies formation for development of FMEG organizations is missing.
- Use of modern IT tools as success element is not done by FMEGs for improving management of supply chain.
- Authors have found that there are very few studies which focused on issues related to satisfaction of customers and qualities of services.
- Very few studies have discussed enablers and challenges taking performance and strategy formation under consideration for FMEGs.
- Most of the frameworks have focused on only few areas rather considering the sector as whole.

Literature on companies of FMEG sector and supply chain members of FMEG sectors were analyzed, where role of inventory, logistics and profit margin were found to crucial. Current paper has tried to identify different important factors of the FMEG sector which as a whole define it. On the basis of challenging factors and enablers identified for the FMEG sector further detailed study can be done in different economies. The sector is just experiencing its growth in new emerging markets such as India and will give highly useful insight into future research.

References

1. Chopra S, Meindl P (2007) Supply chain management strategy, planning & operation. In: Das summa summarum des management. Gabler, pp. 265–275
2. Sila I, Ebrahimpour M, Birkholz C (2006) Quality in supply chains: an empirical analysis. *Supply Chain Manage Int J* 11(6):491–502
3. Mungan D, Yu J, Sarker BR (2010) Manufacturing lot-sizing, procurement and delivery schedules over a finite planning horizon. *Int J Prod Res* 48(12):3619–3636

4. Oláh J, Lakner Z, Hollósi D, Popp J (2017) Inventory methods in order to minimize raw materials at the inventory level in the supply chain. *LogForum* 13(4)
5. Burnson P (2012) Major growth predicted for US manufacturing. *Supply Chain Manag. Rev.* 16(6)
6. Bottani E, Montanari R (2010) Supply chain design and cost analysis through simulation. *Int J Prod Res* 48(10):2859–2886
7. Simpson D (2010) Use of supply relationships to recycle secondary materials. *Int J Prod Res* 48(1):227–249
8. Mishra DP (2008) FMCG distribution channels in India: challenges and opportunities for manufacturers and retailers. *J Global Business Issues* 2(2):175
9. Khan S (2009) Corporate social performance of Indian FMCG companies. *Issues Soc Environ Account* 3(2):180–201
10. Ramakrishnan L, Shaban M (2016) Advertising media efficiency of FMCG firms in India: an empirical investigation using data envelopment analysis. *IUP J Manage Res* 15(1):37
11. Kaže V, Škapars R (2011) Paradigm shift in consumer segmentation to gain competitive advantages in post-crisis FMCG markets: lifestyle or social values? *Econom Manage* 16
12. Karim MA, Smith AJR, Halgamuge SK, Islam MM (2008) A comparative study of manufacturing practices and performance variables. *Int J Prod Econ* 112(2):841–859
13. Chindhuru R, Hamlin R (2007) Future of the brand management structure in FMCG. *J Brand Manage* 14(3):232–239
14. Chaturvedi S (2008) Energy efficiency and sustainability in buildings. In: *AEI 2008: Building Integration Solutions*, pp. 1–8

Reactivity Effects of In-Pin Fuel Motion in Modern Fast Breeder Reactors



Anuj Dubey, T. Sathiyasheela and Anil Kumar Sharma

Abstract The dynamic behaviour of a fast breeder reactor core during an unprotected transient-overpower accident (hereafter UTOPA) is a function of various thermomechanical mechanisms. These impact the neutron flux in the core which in turn may affect the reactivity of the reactor. These phenomena are often quantified in the form of reactivity feedbacks. In-pin fuel motion, also known as fuel squirting, is a hydrodynamic phenomenon which can potentially create a negative reactivity feedback during the accident. The estimation of this negative reactivity feedback is essential for predicting the reactor behaviour and power excursion during UTOPA. In this work, a multiphase thermal hydraulic model for in-pin fuel motion is dynamically coupled with an in-house reactor dynamics code 'PREDIS' to predict in-pin fuel motion based reactivity feedback and estimate the outcome of UTOPA. Simulations of the reactor core are carried out with parallel processing to determine the melt propagation in different core subassemblies. It is found that in-pin fuel motion positively assists in the mitigation of a UTOPA event during severe accidents.

Keywords In-pin fuel motion · Multiphase flow · Nuclear fuel melting

1 Introduction

Fast breeder reactor safety studies involve experimental and numerical simulation of various thermomechanical and neutronic phenomena that take place inside the reactor vessel during accident conditions. Integration of these phenomena gives an overall picture of the evolution and possible outcome of the accident. The primary

A. Dubey (✉)

Homi Bhabha National Institute Mumbai, Kalpakkam 603102, Tamil Nadu, India

e-mail: anuj@igcar.gov.in

T. Sathiyasheela

Indira Gandhi Centre for Atomic Research, Kalpakkam 603102, India

A. K. Sharma

Fast Reactor Technology Group, Indira Gandhi Centre for Atomic Research, HBNI, Kalpakkam 603102, India

© Springer Nature Singapore Pte Ltd. 2019

M. Kumar et al. (eds.), *Advances in Interdisciplinary Engineering*, Lecture Notes in Mechanical Engineering, https://doi.org/10.1007/978-981-13-6577-5_6

objective of such analyses is to ensure confinement of radioactivity to the greatest possible extent for a given design. Within the various severe accident scenarios, UTOPA involves a situation where an accidental control rod withdrawal leads to positive reactivity insertion inside the reactor core. This may lead to fuel heat-up and melting.

In-pin fuel motion is a peculiar phenomenon observed in transient overpower accident experiments [1, 2]. Upon melting, molten fuel travels axially along the length of the pin to regions of lower neutron density, where it solidifies, thereby effectively altering the reactivity configuration of the reactor core. This alteration is expected to give a decreasing influence on the reactivity, given the relocation occurs from where melting occurs (high flux region) to lower flux regions. This influence is quantified in the form of a reactivity feedback for the purpose of reactor dynamics calculations.

It is in this regard that a multiphase thermal hydraulic model has been developed by the authors for simulating this phenomenon [3]. The model employs enthalpy formulation to track the melting and solidification of fuel. A two-phase flow model with separate conservation equations for both liquid fuel and fission gases is employed to track the flow. The mathematical model deterministically predicts in-pin fuel motion and resultant relocation. In this work, the model is further validated against the CABRI-E9 (bis) experiment for the purpose of fluid flow comparison [4]. The model is implemented over the fuel region of a typical 500 MWe fast reactor core. The relocation feedbacks are evaluated based on the first order perturbation fuel removal worth. A dynamic coupling with PREDIS, an in-house fast reactor dynamics code is used to gauge the influence of these feedbacks on reactivity during slow transients [5]. Other feedbacks considered in power calculations are the Doppler feedback and fuel axial expansion feedback.

2 Mathematical Modelling

2.1 Reactor Core Configuration

Fuel, blanket, safety and other utility-based subassemblies in a typical 500 MWe fast breeder reactor core are arranged in a hexagonal geometry. These subassemblies can be grouped in zones or hexagonal rings, depending upon the neutron density experienced collectively by each subassembly. The subassemblies closest to the centre of the reactor core have the highest neutron density and therefore the highest power generation. This also implies that relocation in these subassemblies results in greater reactivity changes. Table 1 displays the number of fuel subassemblies, radial power factor and the fuel removal worth percentage for each zone in the reactor core. The second zone, with thirty subassemblies and closest to the centre of the core, has the largest fuel removal worth.

Table 1 Configuration of a typical 500 MWe reactor core

Zone	No. of fuel subassemblies	Fuel removal worth (%)	Radial power factor (%)
1	1	0.8	100
2	30	21.3	94.8
3	24	14.0	86.6
4	30	15.4	79.9
5	30	19.8	90.2
6	42	20.6	72.7
7	24	8.1	55.3

2.2 Solution Methodology

The model consists of two solvers coupled within the solution domain; the heat conduction and phase change module and the multiphase flow module. The 2-D heat conduction module employs enthalpy formulation to evaluate heat conduction, melting and solidification inside the fuel pin. The 1-D multiphase flow module works in conjunction with the heat conduction module [3]. Separate governing equations are solved for each of the constituent flow phases, i.e. liquid fuel and fission gases in space and time. The model utilizes a fully explicit finite difference scheme for numerical solution.

3 Results and Discussion

3.1 Validation Study

A validation exercise of the model has been carried out against the experimental data of the CABRI-E9 (bis) test [4]. Since a major objective of this work is the evaluation of reactivity changes in the reactor due to in-pin fuel motion, it is important to ensure that the developed mathematical model is generating accurate fuel relocation data. This experiment provides a unique opportunity in this regard. An annular type fast reactor fuel rod (OPHELIE-6) was subjected to slow overpower and flow coast down conditions. An important aspect was the presence of fractured pellets in the upper blanket column. This led to the recognition of a large spike in the hodoscope signal upon penetration of molten fuel inside these fractured blanket pellets. As a result, the time for this penetration was observed to be between 65 and 69 s in the transient. This time of penetration of liquid fuel into the upper blanket is a unique fluid flow parameter as far as slow transient experiments over modern fast reactor fuel pins are concerned. It was reported that the velocity of flow of liquid fuel towards the upper blanket was slow, which was in contrast with previous experimental data.

Table 2 Comparison of simulated versus experimental test parameters

Parameter	Model	Experiment
Power to melt (kW/m)	72.5	72.7
Final radial melt limits at peak power location (% Ro)	80.8	82 ± 2
Pin averaged mass melt fraction (%)	43	40–50
Time of penetration of upper blanket (s)	69	65–69

With this background, the mathematical model was further developed and validated against the experimental parameters available in literature. The results of the study are tabulated in Table 2. The model thermal parameters are in good conformance with the experimental data. Time of penetration in the model (69 s) is a clear indication that the predicted fluid flow is in line with the experimental results.

3.2 Fast Reactor Conditions: Case Study

The behaviour of fuel pins under UTOPA conditions in fast reactors differs from the behaviour observed in transient overpower tests. A major reason for this deviation is the presence of a fast neutron flux, which is not available in experimental environments, since experimental test reactors employ thermal neutron flux. The result is that while in experimental test reactors, there is an attenuation of neutron flux from the outer to the inner radius of the fuel pellets, there is virtually zero attenuation in fast reactors. This causes heat-up and melting at L.H.R values lower than in experimental reactors.

A nominal case study with transient parameters described in Table 3 (Case 1) is carried out on a Zone 1 fuel pin to illustrate the flow behaviour in fast reactor conditions. The resultant fuel column states are displayed in Fig. 1. From steady state ($t = 0$ s), the fuel pin heat-up causes initiation of melting ($t = 59.5$ s). Further heat-up increases the mass melt fraction. The molten fuel initially relocates towards the lower region and chokes the cavity ($t = 68$ s). Further heat-up causes evolution of a column of liquid fuel. This trend continues until the end of the transient ($t = 100$ s).

In order to correlate the effect of such relocation on the reactivity, mass worth modifications (pcm/mass of element) are evaluated for each time step of the transient. The net sum of these modifications gives the total negative reactivity feedback due to relocation within the fuel pin. Taking into consideration the central zone, the

Table 3 Transient parameters for various case studies (steady state L.H.R. is indicated)

Case	Time (s)	Insertion unit	Insertion rate	Max. insertion
1	100	(%) L.H.R.	1	100
2	750	pcm	1	500

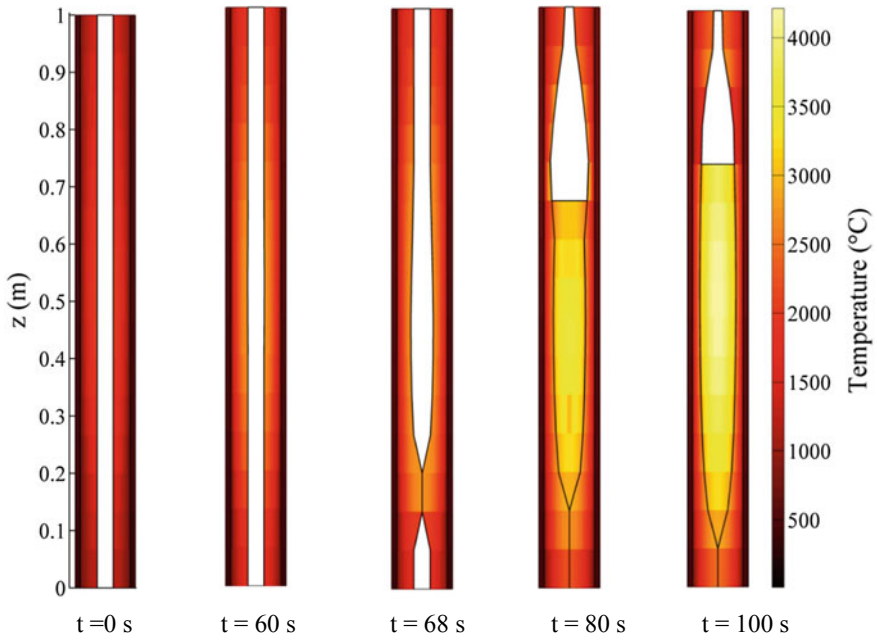


Fig. 1 Melting and fuel relocation behaviour in fast reactor conditions (Maximum temperature in all plots = 4213 $^{\circ}\text{C}$; axial position is from the bottom of fuel column)

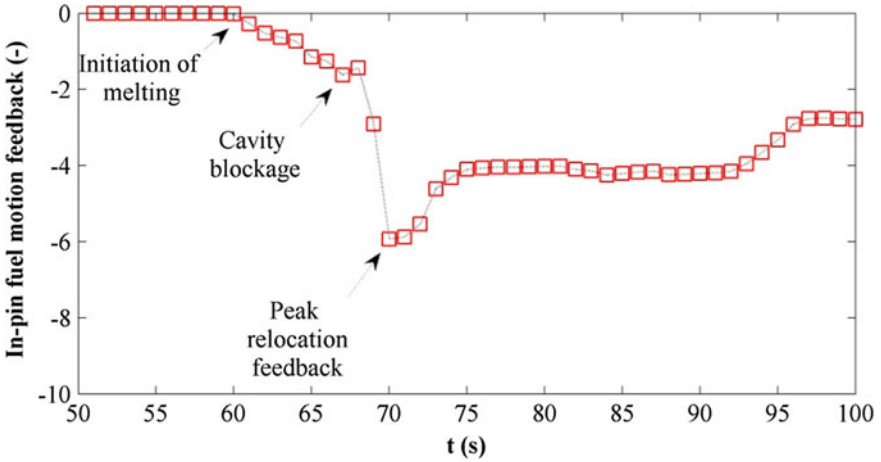


Fig. 2 Relocation reactivity feedback for ZONE 1 (CASE 1)

evolution of the relocation reactivity feedback is presented in Fig. 2. Initially, molten fuel at the centre of the fuel pin relocates downwards, thus initiating a negative feedback. Eventual cavity blockage ($t = 68$ s) prohibits further relocation, and the curve exhibits a slight perturbation. Opening of cavity restarts relocation and results in a peak magnitude ($t = 70$ s). Beyond this point, relocation to the lowest flux regions is no longer possible as the cavity fills up with molten fuel. Hereafter, the combined influence of filling of the central cavity regions and thermal expansion of liquid fuel guides the relocation feedback.

3.3 Whole Core Simulation

To evaluate the response of the entire core to a transient overpower scenario, the mathematical model has been implemented over all seven fuel zones, taking into account the respective fuel mass worth and thermal parameters of each zone, as illustrated in Table 1. Using the transient parameters described in Table 3 (Case 1), melting and fuel relocation in a single pin of each zone is simulated. The state of the fuel columns at the end of the transient ($t = 100$ s) is displayed in Fig. 3. The resultant relocation feedback time history is plotted in Fig. 4.

The results indicate that melting and fuel relocation in each zone initiates at a different time. The maximum magnitude occurs in Zone 2, whereas Zone 6 and

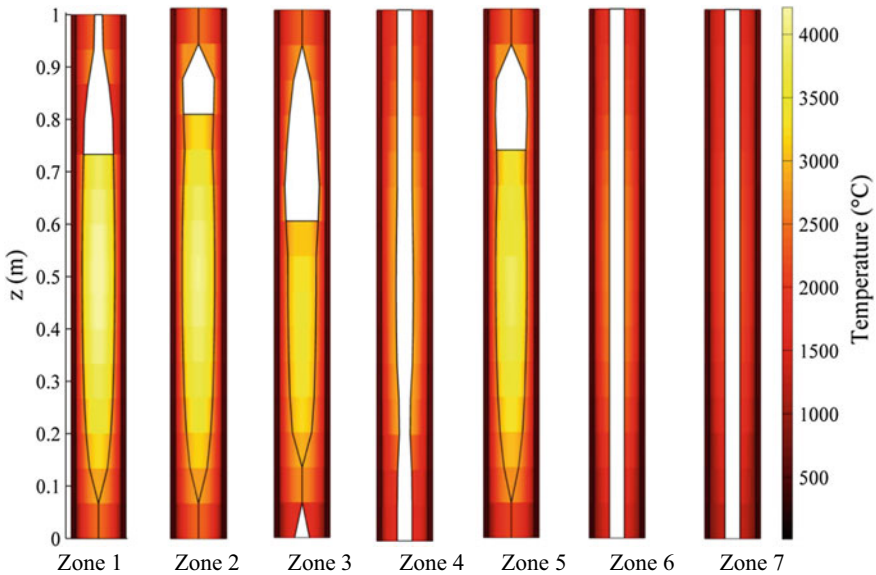


Fig. 3 Melting and fuel relocation behaviour in fast reactor conditions. (Maximum temperature in all plots = 4213 °C; Axial position is from the bottom of fuel column)

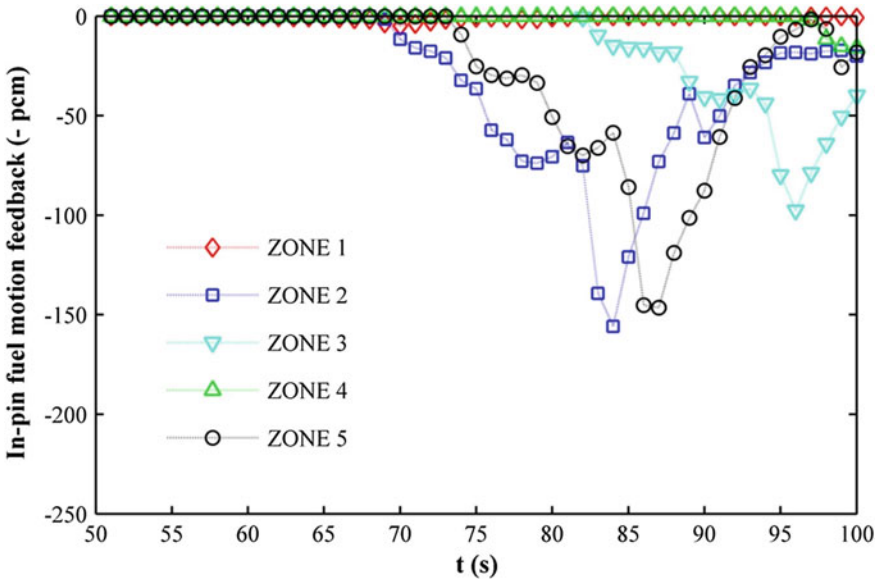


Fig. 4 Relocation reactivity feedbacks for all fuel zones (Case 1; sixth and seventh zone fuel pins did not undergo melting)

Zone 7 do not undergo melting. It is expected that during a transient overpower accident, as power rise continues in time, in-pin fuel motion in different zones will provide negative reactivity feedback at different stages.

3.4 Coupling with Reactor Neutronics

As part of this work, the developed mathematical framework has been coupled with a reactor dynamics code ‘PREDIS’. Seven modules for each of the fuel zones are run in parallel with PREDIS. Upon melting, the reactor neutronics code extracts relocation feedback from each zone dynamically and returns the resultant reactor power for the next time step. The melting and fuel relocation modules for each zone receive power data and evaluate fuel relocation for the next time step. The relocation feedbacks for this time step are again extracted by PREDIS. This coupling integrates in-pin fuel motion and reactor neutronics into the evaluation of a given UTOPIA scenario.

The transient parameters used for coupled simulation are presented in Table 3 (Case 2). The external power insertion is in the form of reactivity insertion (500 pcm max), which corresponds to a conservative core removal worth of a single control safety rod from the reactor core. Beyond 500 s, the reactivity insertion rate is zero. This signifies a complete withdrawal of the control rod. Results of simulation are plotted in Fig. 5. Fuel melting first starts in Zone 1 (t = 269 s). Further into

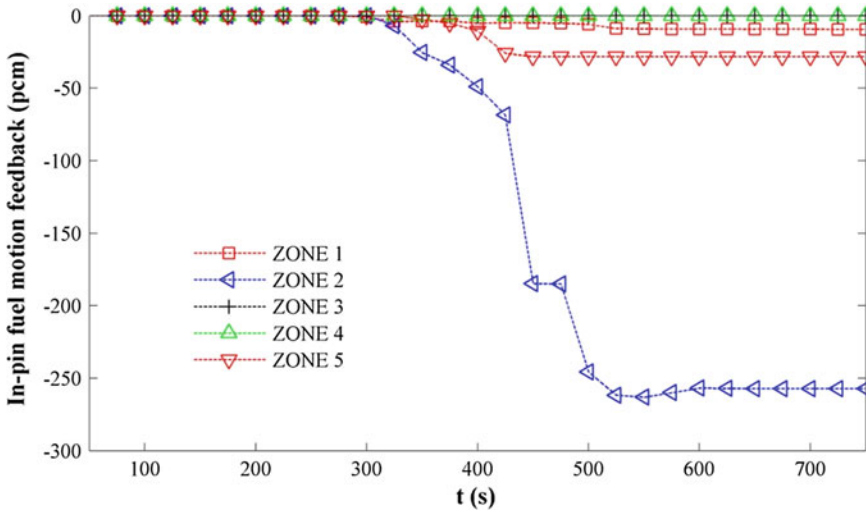


Fig. 5 Relocation reactivity feedbacks for all zones (Case 2; fourth, sixth and seventh zone fuel pins did not undergo melting)

the transient, melting initiates in the second and fifth zones. Relocation in Zone 2 causes a large negative feedback. This results in reduced reactivity in the core. The power level peaks up to 1.89 times steady power at peak reactivity insertion ($t = 500$ pcm). Beyond this point, the reactivity feedbacks stabilize, indicating arrest of further power increase and melting. Reactor power stabilizes at 1.52 times steady-state power towards the end of the transient. Melting remains limited to Zones 1, 2 and 5. The combined influence of fuel Doppler (-250 pcm), fuel axial expansion (-141 pcm) and in-pin fuel motion (-284.5 pcm) reduces the core reactivity sufficiently, thus mitigating the accident. It is evident that in-pin fuel motion acts in combination with fuel Doppler and other reactivity feedbacks and provides a significant mitigating effect. The relative magnitude of the feedbacks shows the significance of in-pin fuel motion.

4 Conclusions

The work is focused towards investigation of in-pin fuel motion in fast breeder reactor core and the resultant influence on the evolution of slow UTOPA events. A mathematical model developed for evaluating in-pin fuel motion is validated against experimental data to examine the predicted fluid flow behaviour. The model is implemented over all the fuel zones of a typical 500 MWe reactor core. The model is dynamically coupled with a reactor dynamics code 'PREDIS' to integrate relocation effects in the reactor power calculations. The results of the study indicate that melting and fuel relocation initiates at different stages in the transient in individual zones of the

core. Relocation in Zone 2 generates maximum negative reactivity feedback. Further, melting initiates fuel relocation and related feedback in outer zones. Simulation of a typical localized control rod withdrawal accident indicates that relocation related feedback sufficiently retards fuel melting and contains it within the first, second and fifth zones, thereby demonstrating its potential as a mitigating mechanism for slow UTOPIA events. In future, the developed computational system will be implemented for the study of medium and fast transients, which are postulated to occur during an unprotected loss of flow accident.

Acknowledgements The authors would like to express their gratitude to Shri P. Puthiyavinayagam, Director, Reactor Design Group, IGCAR for his constant motivation and support. The authors would also like to thank Dr. G. S. Srinivasan, Head of Safety Analysis Section, Reactor Design Group, IGCAR for his guidance and encouragement.

References

1. Porten DR, Padilla A, Baars RE (1979) Concept verification of an inherent shutdown mechanism for HCDA's. In: International meeting on fast reactor safety technology, pp 991–1000. HEDL, Richland (1979)
2. Sato I, Lemoine F (2004) Transient fuel behaviour and failure condition in the CABRI-2 experiments. *Nucl Technol* 145:115–137
3. Dubey A, Sharma AK (2018) Melting and multi-phase flow modelling of nuclear fuel in fast reactor fuel rod. *Int J Therm Sci* 125:256–272
4. Charpenel J, Sato I, Struwe D, Pfrang W (2000) Fuel pin behaviour under the slow power ramp transients in the CABRI-2 experiments. *Nucl Technol* 130:252–271
5. Sathiyasheela T, Natesan K, Srinivasan GS, Devan K, Puthiyavinayagam P (2015) Analysis of unprotected transients with control and safety rod drive mechanism expansion feedback in a medium sized oxide fuelled fast breeder reactor. *Nucl Eng Des* 291:1–9

Assessment, Modeling, and Optimization During Nd:YAG Laser Microgrooving of Titanium Alloy



D. Dhupal, S. R. Dixit, S. Pattanayak, R. R. Routray, A. K. Behura and Sudhansu Ranjan Das

Abstract This study focuses on experimental investigation, predictive modeling, and process optimization in Nd-YAG laser microgrooving operation of titanium alloy (Ti_6Al_4V) by considering diode current, pulse frequency, scan speed, and the number of passes as process parameters. The technological response characteristics in the laser microgrooving process such as upper width, depth, and heat-affected zone have been considered to assess the machining performances. Thirty-one sets of laser microgrooving trials based on the design of experiment (DOEs) are performed along with analysis of variance (ANOVA), response surface methodology (RSM), and particle swarm optimization (PSO) that are subsequently applied for parametric influence study, mathematical modeling and multi-response optimization, respectively. Results indicated that groove width and HAZ decrease with a lower magnitude of diode current but opposite trend occurs with scan speed and the groove depth increases with the increase of pulse frequency. From the pre-cited parameters, the number of passes is found to be the most significant parameter that affects almost all quality characteristics. By solving the optimization problem with PSO, corresponds to the optimal setting of process parameters (diode current = 24.5 amp, pulse frequency = 29.36 kHz, scan speed = 40 mm/s, number of passes = 9) with estimated upper width 0.0596 mm, heat-affected zone 0.1303 mm, and depth 0.3966 mm.

Keywords Laser microgrooving · Ti_6Al_4V · ANOVA · RSM · PSO

1 Introduction

Nowadays, titanium alloys have renewed attention because of their biochemical and electrochemical compatibility. Application of titanium alloys in the marine and aerospace industry is increasing due to its compatibility with composite materials.

D. Dhupal · S. R. Dixit · S. Pattanayak · R. R. Routray · S. R. Das (✉)
Department of Production Engineering, VSS University of Technology, Burla 768018, India
e-mail: das.sudhansu83@gmail.com

A. K. Behura
School of Mechanical Engineering, VIT University, Vellore 632014, India

© Springer Nature Singapore Pte Ltd. 2019
M. Kumar et al. (eds.), *Advances in Interdisciplinary Engineering*, Lecture Notes in Mechanical Engineering, https://doi.org/10.1007/978-981-13-6577-5_7

However, titanium alloys are one of the most difficult materials to machine because of their low thermal conductivity, which leads to high cutting temperatures, and low elastic modulus, which leads to tool vibrations and poor surface finish. Owing to these complexities, the task to machine a component with deterministic precision becomes challenging. In the recent past, laser beam machining (LBM) has been explored as an effective and emerging process for shaping titanium alloy materials, which generally uses a pulsed laser of low pulse width with high peak power is efficient for micromachining.

When the metal cutting industries are dealing with multiple conflicting objectives, modeling as well as optimization techniques help in enhancing the efficacy of the machining process. For sure, it offers the most prominent measure of data with a specific end goal to settle on a choice on selecting process parameters in machining. Researchers have employed various methods MRA [2, 3] and ANN [4, 5] for mathematical modeling in order to predict the responses and RSM [6, 7], GA [8], PSO [9, 10] for multi-response optimization in order to control the process parameters during laser micromachining process, which have been explored as effective and reliable tool in advanced computing technology for the outline of high-quality frameworks since it gives a straightforward, proficient, and well-organized way to optimize output, for example, performance, cost, and quality. The appropriate combination and utilization, along with proper adjustment of machining parameters are of prime importance for acquiring good grade of microgrooves, which generally consumes precious time and effort due to the dynamic behavior of the laser micromachining process. Thus, the present study focuses on the development of empirical models and multi-response parametric optimization in microgrooving of titanium alloy (Ti_6Al_4V) through Nd:YAG laser treatment. Particularly, the design of experiments, response surface methodology, and particle swarm optimization have been applied for process improvement.

2 Experimental Procedure

A 75 W diode-pumped Nd:YAG laser (model: SPRIGO LD) was used to conduct the experiments which have assisted gas supply unit. For experimentation, the laser beam (focused by the lens with focal length of 77 mm) was set at workpiece surface as the focal plane which resulted in the laser beam spot size of nearly 21 μm . Titanium alloy (Ti_6Al_4V) flat workpiece was subjected to microgrooving by multiple laser pulses using DPSS Nd:YAG laser treatment with actual peak power moving between 0.7 and 5 kW.

In the current investigation diode current, pulse frequency, scan speed, and the number of passes are considered to be the process parameters which affect the response of interest in laser microgrooving process namely groove upper width, heat-affected zone, and groove depth. The identified process parameters and their levels are presented in Table 1. Using the selected factors (4) and parameters levels (5), a design matrix was formulated in conformance with central composite design

Table 1 Process parameters and levels

Parameters	Symbols	Units	Levels				
			-2	-1	0	1	2
Diode current	X ₁	amp	18.5	20	21.5	23	24.5
Pulse frequency	X ₂	kHz	28	31	34	37	40
Scan speed	X ₃	mm/sec	40	50	60	70	80
Number of passes	X ₄		9	10	11	12	13

(CCD) design of experiments (DOEs) associated with 31 experimental runs. Design of experimental plan with an actual value of process parameters, measured responses are presented in Table 2. The different responses (GUW, HAZ, GD) of machined microgroove were measured by utilizing a scanning electron microscope (model: STM6, make: Olympus). Figure 1 shows the schematic layout of the methodology followed in the current study.

3 Results and Discussion

3.1 Development of Response Model

After conducting the tests using CCD-based response surface methodology (RSM), a second-order regression equation was developed to analyze the parametric influences on each response quality characteristic. RSM approach forms a mathematical linkup between response parameter and the various input process parameters. The regression equations corresponding to upper width, HAZ thickness and depth for laser engraving are given by

$$\begin{aligned}
 Y_{\text{GWD}} = & 43 + 84.5X_1 - 125.8X_2 - 30.46X_3 + 387X_4 \\
 & - 5.76X_1^2 + 0.448X_2^2 + 0.0303X_3^2 - 14.84X_4^2 \\
 & + 3.056X_1X_2 + 1.617X_1X_3 - 33X_1X_4 \\
 & + 0.150X_2X_3 + 2.83X_2X_4 - 1.175X_3X_4
 \end{aligned} \tag{1}$$

$$\begin{aligned}
 Y_{\text{HAZ}} = & 113 + 7.5X_1 + 24.32X_2 - 3.75X_3 - 82.3X_4 \\
 & + 0.489X_1^2 + 0.3716X_2^2 + 0.00289X_3^2 + 3.264X_4^2 \\
 & - 1.306X_1X_2 + 0.3350X_1X_3 - 0.233X_1X_4 \\
 & - 0.2771X_2X_3 - 0.471X_2X_4 + 0.5638X_3X_4
 \end{aligned} \tag{2}$$

$$\begin{aligned}
 Y_{\text{GD}} = & 25450 - 1080X_1 - 236.1X_2 + 29.7X_3 - 1861X_4 \\
 & + 27.70X_1^2 + 1.146X_2^2 + 0.1095X_3^2 + 32.20X_4^2
 \end{aligned}$$

Table 2 Design of experimental plan and experimental results

Run	Coded values				Actual settings				Responses			
	X ₁	X ₂	X ₃	X ₄	Diode current (amp)	Frequency (kHz)	Scan speed (mm/Sec)	No. of passes	GUW (μm)	HAZ (μm)	GD (μm)	
1	1	1	-1	-1	23	37	50	10	259.906	93.115	433	
2	0	0	0	-2	21.5	34	60	9	218.937	93.614	545.843	
3	-1	-1	1	1	20	31	70	12	231.531	104.507	409.5	
4	-1	1	-1	-1	20	37	50	10	262.531	107.938	406.906	
5	0	0	0	0	21.5	34	60	11	279.464	88.087	352.178	
6	0	0	0	2	21.5	34	60	13	261.437	102.839	426.468	
7	0	-2	0	0	21.5	28	60	11	247.687	102.839	426.468	
8	-1	1	1	-1	20	37	70	10	253.156	81.959	520.875	
9	-1	1	1	1	20	37	70	12	275.281	98.384	518.656	
10	-1	-1	-1	-1	20	31	50	10	255.281	80.061	587.375	
11	0	0	0	0	21.5	34	60	11	282.464	85.875	348.678	
12	0	0	0	0	21.5	34	60	11	278.964	85.637	409.678	
13	2	0	0	0	24.5	34	60	11	241.187	94.091	705.968	
14	-1	-1	1	-1	20	31	70	10	230.906	85.863	612.656	
15	1	-1	-1	-1	23	31	50	10	210.906	85.238	701.531	
16	1	-1	-1	1	23	31	50	12	228.281	81.963	573.625	
17	0	0	0	0	21.5	34	60	11	280.464	88.587	407.178	
18	1	-1	1	-1	23	31	70	10	252.281	112.328	500	
19	0	0	2	0	21.5	34	80	11	316.937	96.622	404.968	

(continued)

Table 2 (continued)

Run	Coded values				Actual settings				Responses			
	X ₁	X ₂	X ₃	X ₄	Diode current (amp)	Frequency (kHz)	Scan speed (mm/Sec)	No. of passes	GUW (μm)	HAZ (μm)	GD (μm)	
20	-1	1	-1	1	20	37	50	12	362.156	100.694	375.5	
21	0	0	0	0	21.5	34	60	11	319.714	87.837	342.928	
22	-1	-1	-1	1	20	31	50	12	302.406	73.111	336.531	
23	0	0	0	0	21.5	34	60	11	319.714	82.475	368.178	
24	0	0	-2	0	21.5	34	40	11	306.437	76.031	397.343	
25	1	1	-1	1	23	37	50	12	319.281	83.559	559.531	
26	1	-1	1	1	23	31	70	12	248.656	133.284	448.281	
27	0	2	0	0	21.5	40	60	11	383.687	94.260	370.718	
28	1	1	1	1	23	37	70	12	365.156	97.361	469.125	
29	0	0	0	0	21.5	34	60	11	320.214	83.2	344.178	
30	1	1	1	-1	23	37	70	10	348.781	90.211	362.656	
31	-2	0	0	0	18.5	34	60	11	254.187	85.062	507.343	

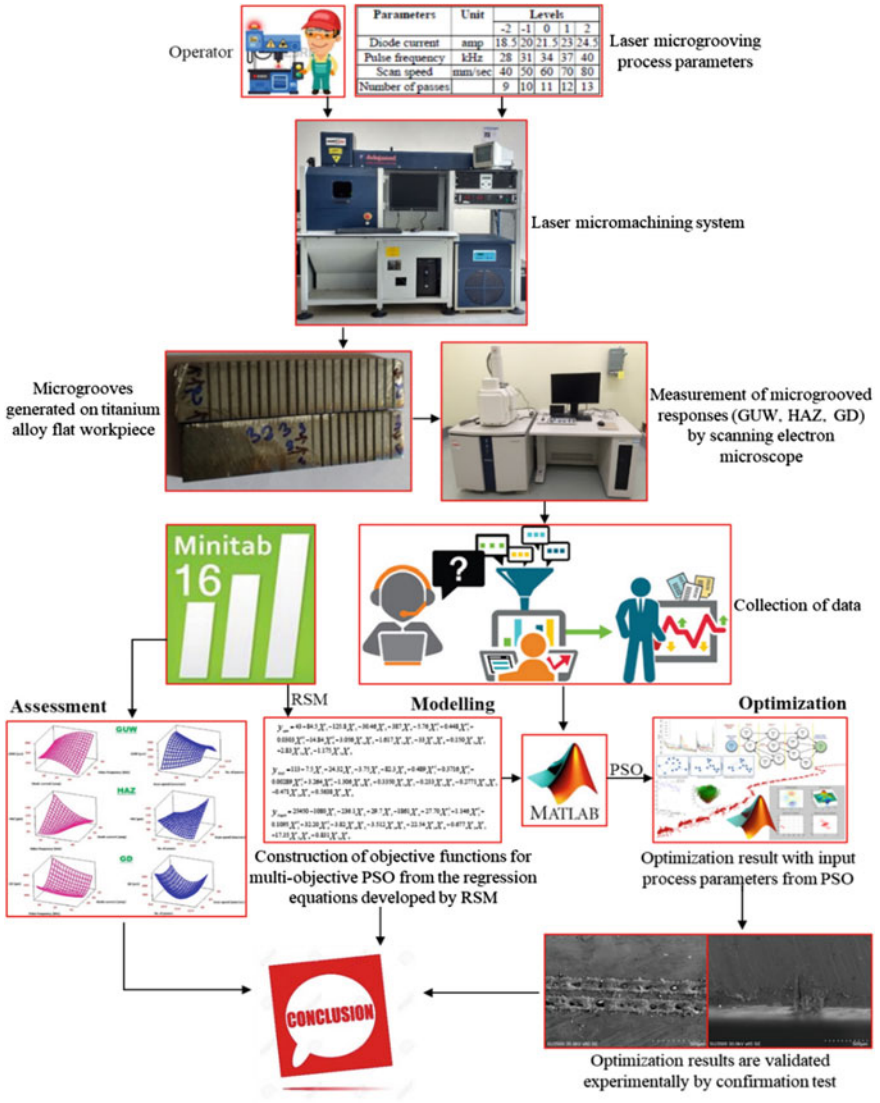


Fig. 1 Schematic layout of experimental setup and methodology proposed

$$\begin{aligned}
 & - 3.82X_1X_2 - 3.512X_1X_3 + 22.54X_1X_4 + 0.677X_2X_3 \\
 & + 17.35X_2X_4 + 0.831X_3X_4
 \end{aligned}
 \tag{3}$$

For keeping away from the misleading conclusion, the statistical validity as well as adequacy of developed quadratic model for the responses (GUW, HAZ, and GD) are checked by ANOVA analysis, shown in Table 3 followed by normal probability plot associated with Anderson–Darling test, as shown in Fig. 2. From the analysis,

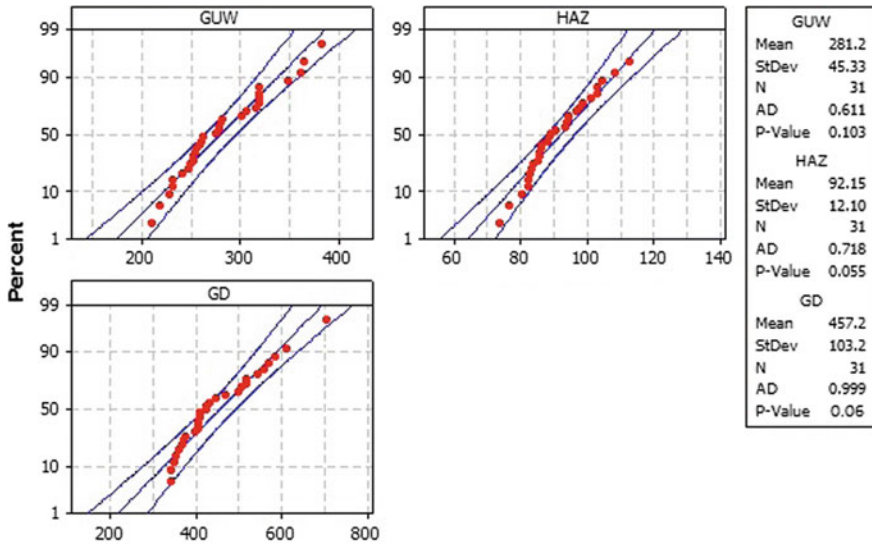


Fig. 2 Normal probability plot for technological response characteristics of laser microgroove

it has been observed that pulse frequency, number of passes, square effect of diode current and number of passes along with interaction effect between pulse frequency and number of passes influences the groove width most significantly. Since their P-value is less than 0.05. Correspondingly, the diode current, scan speed, number of passes, square effect of diode current, and the interaction effect between pulse frequency and scan speed have statistical as well as significant impact on the HAZ thickness. Also, current, frequency, square effect of scan speed, the interaction effect of diode current and pulse frequency; and between pulse frequency and scan speed affects the groove depth. It is clearly visible from Table 3 that, values of R^2 and $R^2(\text{adj.})$ are much higher. So it has been concluded that the measured values of each response characteristics were well fitted in the developed model. Moreover, the P-values of the regression model are found to be lower than 0.05 for groove width, depth, and HAZ, which revealed that the second-order regression model developed for these responses are significant.

3.2 Response Optimization Using PSO

PSO is a soft computing approach which relies on some programming commands to generate the global optimal result. The regression Eqs. (1)–(3) developed by RSM approach for groove width, heat-affected zone thickness, and groove depth are utilized in the generation of the objective function for PSO. The minimum and maximum values of the process parameters were used as constraints for the objective function.

Table 3 Results of ANOVA analysis

Terms	Symbol	P-value of responses			
		GWD	HAZ	GD	
Constant	-	0.000	0.000	0.000	
Diode current	X ₁	0.668	0.000	0.000	
Pulse frequency	X ₂	0.000	0.138	0.000	
Scan speed	X ₃	0.742	0.000	0.433	
No. of passes	X ₄	0.000	0.000	0.000	
(Diode current) ²	X ₁ ²	0.000	0.029	0.000	
(Pulse frequency) ²	X ₂ ²	0.193	0.000	0.035	
(Scan speed) ²	X ₃ ²	0.322	0.524	0.078	
(No. of passes) ²	X ₄ ²	0.000	0.000	0.000	
Diode current × Pulse frequency	X ₁ X ₂	0.003	0.000	0.034	
Diode current × Scan speed	X ₁ X ₃	0.000	0.000	0.000	
Diode current × No. of passes	X ₁ X ₄	0.226	0.580	0.000	
Pulse frequency × Scan speed	X ₂ X ₃	0.274	0.000	0.015	
Pulse frequency × No. of passes	X ₂ X ₄	0.048	0.037	0.000	
Scan speed × No. of passes	X ₃ X ₄	0.009	0.000	0.279	
Regression	Groove width (GWD)		Groove depth (GD)		
	F	P	F	P	F
		R ²		R ²	R ²
	16.33	0.000	48.75	0.000	95.71%
				(adj)	
				97.71%	
				95.71%	
				90.86%	

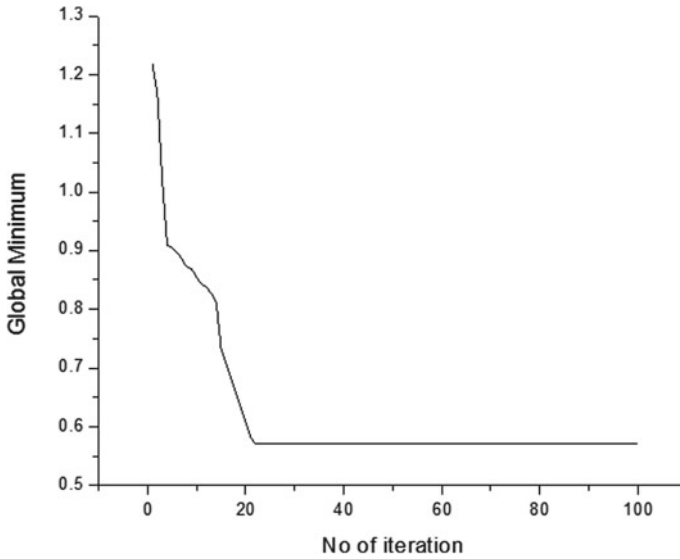


Fig. 3 Optimal convergence curve for multi-objective PSO

Multi-objective particle swarm optimization (MOPSO) for multi-response optimization, the following equation is developed considering all the responses, simultaneously optimized and optimal parameter setting can be found out by the objective function:

$$Z_{GLOBALMIN} = W_1 * \frac{Y_{GWD}}{Y_{GWDMIN}} + W_2 * \frac{Y_{HAZ}}{Y_{HAZMIN}} + W_3 * \frac{Y_{GD}}{Y_{GDMIN}} \quad (4)$$

Figure 3 presents the convergence plot, which aims to optimize the abovementioned three laser microgrooving responses in the presence of PSO specific parameters. By solving the optimization problem with PSO, it was found that the Z_{MIN} value is 0.5708, occurring at a weightage of 0.80 to upper width. Also 10% (i.e. weightage of 0.1) equal importance has been given to the other two responses. Moreover, it can be concluded that the optimal solution occurs at a sudden decrease in global minimum with a less processing time due to lesser complexity as well as significant improvement in computational efficiency of the PSO algorithm. The optimal process parameters setting for microgrooving variables in laser machining of titanium alloy (Ti_6Al_4V) are diode current 24.5 amp, pulse frequency 29.3645 kHz, scan speed 40 mm/s, no. of passes 9, with estimated groove width (GWD) of 0.0596 mm, heat-affected zone (HAZ) of 0.1303 mm, and groove depth (GD) of 0.3966 mm.

3.3 Parametric Effect on Technological Responses of Microgroove

High diode current excites the lasing material rigorously. Thus, more photon (energy packets) will be accumulated in the active medium. So heat energy on the material surface increases, as a result of which groove width increase (see Fig. 4a). Scan speed refers to the meeting time between laser beam and workpiece. When it increases, the beam will remain on the material surface for a long period of time, as a result, groove width increases (see, Fig. 4b). A number of passes appreciably affects the groove width. The heat-affected zone thickness (HAZ) increases with the higher magnitude of diode current (refer, Fig. 4c), because of increased thermal energy on the material surface. The interaction time between laser beam and workpiece is cut down when scan speed reduces. So the material absorbs lesser amount of energy from the laser beam, that shortening the HAZ thickness. HAZ increases with increase in the number of passes (refer, Fig. 4d), because of more thermal energy on the material surface. High pulse frequency delivers a large number of pulses onto the material surface that

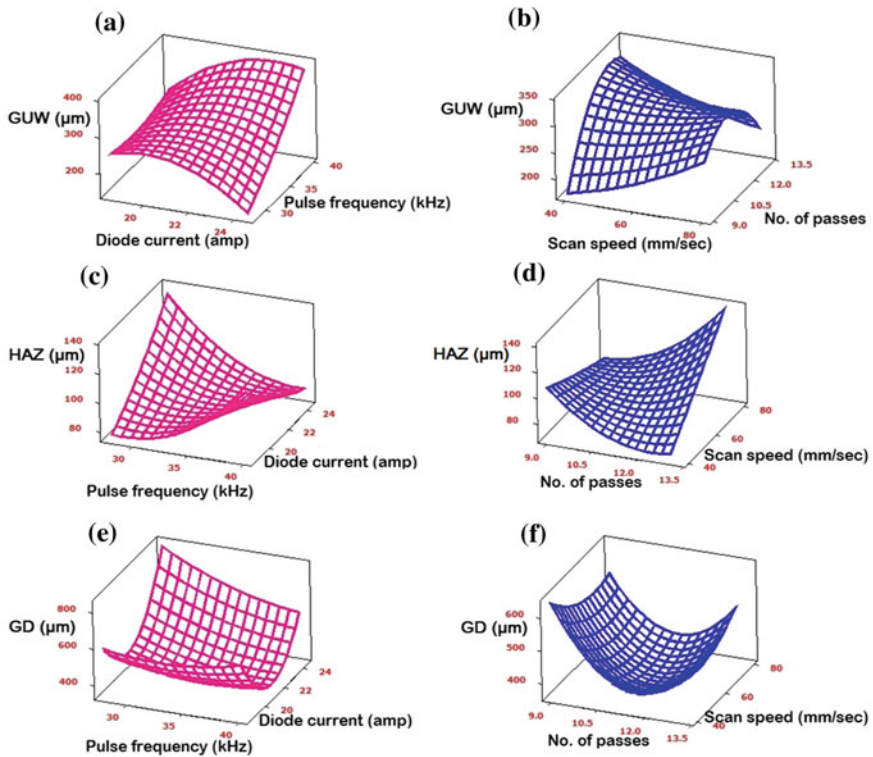


Fig. 4 Parameters effect 3D surface plots for responses (GUV, HAZ, and GD)

helps in evacuation of molten metal from the grooves. So the groove depth decreases with higher values of pulse frequency (see, Fig. 4e).

4 Conclusions

In the present work, laser engraving has been carried out on Ti_6Al_4V substrate. The experiments were modeled using a CCD-based RSM approach. The P-values of the models are under 0.05. Thus, all the developed models are exceptionally significant and adequate. The regression equations developed in RSM approach were used to generate the objective function for the PSO approach, which demonstrated the ability to optimize and to accurately model the technological response characteristics of microgroove through advances in computer technology. Results indicated that groove width and HAZ decrease with a lower magnitude of diode current but opposite trend occurs with scan speed and the groove depth increases with the increase of pulse frequency. The number of passes is found to be the most significant parameter that affects almost all quality characteristics. By solving the optimization problem with PSO, corresponds to the optimal setting of process parameters (diode current = 24.5 amp, pulse frequency = 29.36 kHz, scan speed = 40 mm/s, number of passes = 9) with estimated upper width 0.0596 mm, heat-affected zone 0.1303 mm, and depth 0.3966 mm.

References

1. Das SR, Dhupal D, Kumar A (2015) Study of surface roughness and flank wear in hard turning of AISI 4140 steel with coated ceramic inserts. *J Mech Sci Technol* 29:4329–4340
2. Dhupal D, Doloi B, Bhattacharyya B (2008) Parametric analysis and optimization of Nd:YAG laser micro-grooving of aluminum titanate (Al_2TiO_5) ceramics. *Int J Adv Manuf Technol* 36:883–893
3. Biswas R, Kuar AS, Mitra S (2015) Process optimization in Nd:YAG laser micro drilling of alumina–aluminium interpenetrating phase composite. *J Mater Res Technol* 4:323–332
4. Kibria G, Doloi B, Bhattacharyya B (2014) Modelling and optimization of Nd:YAG laser micro-turning process during machining of aluminum oxide (Al_2O_3) ceramics using response surface methodology and artificial neural network. *Manuf Rev* 1:1–12
5. Teixidor D, Grzenda M, Bustillo A, Ciurana J (2015) Modeling pulsed laser micromachining of micro geometries using machine-learning techniques. *J Intell Manuf* 26:801–814
6. Biswas R, Kuar AS, Mitra S (2015) Process optimization in Nd:YAG laser microdrilling of alumina–aluminium interpenetrating phase composite. *J Mater Res Technol* 4:323–332
7. Wang T, Liu J, Yang B, Chen X, Wang X, Yang C Optimization of micropipette fabrication by laser micromachining for application in an ultrafine atmospheric pressure plasma jet using response surface methodology. *J Micromech Microeng* <https://doi.org/10.1088/0960-1317/26/6/065001>
8. Mohammed MK, Umer U, Ahmari AA (2017) Optimization of laser micro milling of alumina ceramic using radial basis functions and MOGA-II. *Int J Adv Manuf Technol* 91:2017–2029

9. Bessmeltsev VP, Bulushev ED (2014) Optimization of laser micromachining regimes. *Opto-electron Instrum Data Proc* 50:533–548
10. Wang W, Chen J, Li D, Feng D, Tu Y (2016) Modelling and optimization of a femtosecond laser micro-machining process for micro-hole array products. *Int J Adv Manuf Technol* 82:1293–1303

Mechanical Behavior of Stir-Casted Al + ZrB₂ + Al₂O₃ Metal Matrix Composites



B. P. Sharma, Mohd. Junaid, D. Akhil, G. S. Rao and Umesh Kumar Vates

Abstract In recent years, many experiments have been devoted to additive technologies and their applications. In the present manufacturing scenario, aluminum-based metal matrix composites are widely used in various industrial divisions especially in automobiles, aircraft, marine, and mineral processing divisions due to its high tensile, impact, and hardness values. Although, several compositions are still remaining to research for enhancing the mechanical behavior of aluminum-based hybrid composites. In this direction, present research is based on the development of pure aluminum (Al-1100) based composites through stir-casting process with different mass fractions of zirconium diboride and alumina reinforcement such as 7% Al₂O₃–3%ZrB₂, 6%Al₂O₃–9%ZrB₂, 5%Al₂O₃–5%ZrB₂, 7.5%Al₂O₃–7.5%ZrB₂. Further, obtained performs were converted into specimens as per ASTM standards and Brinell hardness numbers, as well as impact strengths, were investigated. Increase in the percentage contents of ZrB₂ results improved shining nature and reduced ductility of composites at the initial investigation. Also, improved corrosion resistance and mechanical behavior noted from newly developed performs.

Keywords Composite · Stir-casting · Hardness test · Impact strength

1 Introduction

In the present manufacturing scenario, aluminum has become one of the most important metals for every precise application such as aerospace and automobile. Due to its lower density, good corrosion resistance, better mechanical and recycling properties, aluminum, and its alloys are recommended to use for such a tedious application. Only due to this fact, many researchers are working for the development of aluminum-based metal matrix composites (MMC) with different types and particle sizes of reinforcements. In general, such MMC can be prepared by liquid state, semisolid,

B. P. Sharma (✉) · Mohd. Junaid · D. Akhil · G. S. Rao · U. K. Vates
Department of Mechanical Engineering, Amity University, Noida, India
e-mail: bpsharma15482@gmail.com

© Springer Nature Singapore Pte Ltd. 2019
M. Kumar et al. (eds.), *Advances in Interdisciplinary Engineering*, Lecture Notes in Mechanical Engineering, https://doi.org/10.1007/978-981-13-6577-5_8

and powder metallurgy methods. Stir-casting technique is a method of liquid state for the preparation of MMC in which reinforcement particulates are mixed in molten base metal uniformly through a stirrer at the temperature above the melting point of the base metal. The only condition for the selection of base metal and reinforcement in liquid state method is that the melting point of reinforcement particulates should be three times that of base metal so that reinforcement particulates does not even recrystallize on melting of base metal [1]. Aluminum-based MMC reinforced with nanoparticles and microparticles of different ceramics that are attaining wide status among high-performance material due to its enriched strength, better elastic modulus, and improved wear resistance. Such newly developed MMC exhibit superior strength-to-weight and strength-to-stiffness ratio as well as strength-to-cost ratio over conventional base alloys [2]. Al alloy-based MMC are presently used in several applications such as pistons, cylinder liners, brake discs, and pushrods.

In recent years, nitrides, borides, and carbides as newly advanced ceramics have been used MMC as reinforcements [3]. Zirconium diboride (ZrB_2) has been reported to ensure the best performance as reinforcements develop new MMC [4]. This material falls under the category of ultrahigh temperature ceramics (UHTCs) [5]. This family is characterized by high-melting points (3245°C for ZrB_2 and 3225°C for TiB_2), high hardness, and good chemical inertness [6]. Therefore, in the present research work, ZrB_2 is identified as reinforcement with almost pure aluminum and alumina is also added as an antioxidant to improve corrosion resistance. In this direction, present research is based on the development of pure aluminum (Al-1100) based composites through stir-casting process with different mass fractions of zirconium diboride and alumina reinforcement such as $7\%Al_2O_3-3\%ZrB_2$, $6\%Al_2O_3-9\%ZrB_2$, $5\%Al_2O_3-5\%ZrB_2$, $7.5\%Al_2O_3-7.5\%ZrB_2$. Further, obtained performs were converted into specimens as per ASTM standards and Brinell hardness numbers were investigated. Also, the microstructural study was carried out using scanning electron microscopy with dispersive energy conjugation in X-ray spectroscopy to characterize the composite phase. This paper is divided into five parts in which the first part introduction explores aluminum-based MMC and reason for the selection of reinforcements in the present research. The second part is dedicated to a detailed literature review of MMC and its development processes. The third part is based on experimental investigation and microstructural studies towards development of present hybrid MMC. Forth part claims the results, discussion, applications, and future scope of the present research along with considerable limitations.

2 Literature Review

Use of composite materials may be considered before human civilization since birds have started construction of their castles using different natural fibers. Also, in the fourteenth chapter of Bhagavad Gita, the three modes of material nature were mentioned by Lord Krishna as goodness, passion, and ignorance and what these modes are, how they act upon us, how one transcends them, and the symptoms of one who

has attained the transcendental state. In the present scenario, the constant need of strength-to-weight ratio as well as stiffness-to-weight ratio conflict with the fact that other properties such as wear resistance, machinability, electrical and thermal conductivity, and corrosion resistance are of significant technological importance for the research in the area of materials to meet the demand for improved road, rail, and air transport systems and infrastructure industries. To furnish this requirement, MMC has emerged as qualified candidates and can be tailored to offer improved properties in a wide variety of applications [7].

Schwartz (1984) has defined composites as a system of materials which is a combination of two or more macro constituents differing in composition and that they are essentially insoluble in each other [8]. The reinforcements are usually a ceramics, although refractory metals have occasionally been used. A less restrictive MMC definition could also include materials such as oxide dispersion strengthened alloys or Al–Si eutectic alloys [Miracle 2005]. Based on the type and nature of the reinforcement, MMCs can be broadly classified into three basic types.

Dasgupta and Meenai (2005) have already proven that aluminum and its alloy based MMC are having greater wear resistance for sliding applications [7]. Over the past two decades, there has been a consistent interest in developing advanced materials like aluminum metal matrix composites for their attractive mechanical and corrosion properties [6–8]. Though, they have attractive mechanical and corrosion properties the usage of the aluminum metal matrix composites is restricted because of the problems that are related to the joining of these metals by fusion welding processes [7, 9]. It has been clearly established in the literature that AMCs are generally not recommended for welding using fusion welding processes due to incomplete mixing between filler and BM, the formation of excess eutectic, the presence of large size porosity of more than 100 μm in the fusion zone, and reaction between molten metals and reinforcements resulting in undesirable phases such as Al_4C_3 [5]. Nevertheless, a sound welded joint of AMC's with no significant change in reinforcement volume fraction was achieved by Friction stir welding (FSW). However, the maturity of using this joining process to weld AMCs is still at an early stage in research and has not yet been fully implemented in industry. There is a clear need for more efforts to understand the effect of FSW on these materials in adequate depth to meet design and production requirements. For instance, there is a need for systematic studies which take into account the effects of reinforcement percentage and types of reinforcement on joint efficiency. More work is needed to understand the performance of FSW joints. It has been proven by many researchers that high joint efficiency with low distortion and partial dissolution of reinforcement particles could be accomplished using a friction stir welding process (FSW) for very few aluminum matrix composites. There have been a number of studies [10] on various aspects of friction stir welding process. Thomas et al. [10], Rai et al. [11], and Zhang et al. [12] have thoroughly investigated the friction stir welding tools and its development.

3 Experimental Investigations

In the present investigation, adopted stir-casting process set up to prepare required composite specimens is shown in Fig. 1. In a stir-casting process, powdered form of the reinforcing phases at the macro level is distributed into molten aluminum ingots by mechanical stirring. First of all, surfaces of base metal and reinforcing particles

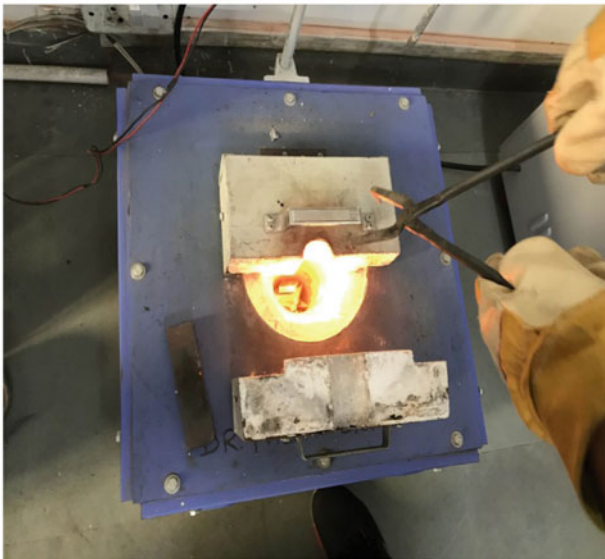
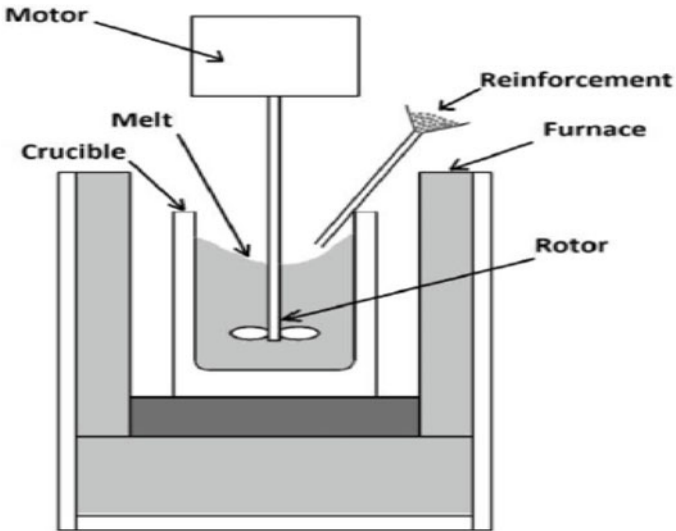


Fig. 1 Stir-casting setup

are properly cleaned to minimize the reaction between them. During the addition of reinforcement particles to the stirred molten matrix, chances of other impurities entrapment such as metal oxide and slag increases which are formed on the surface of the melt. Arresting air envelopes between particles is also important while pouring which can cause several defects in the specimens. Distribution of the reinforcing particles in the molten matrix depends upon several factors such as the geometry of the mechanical stirrer, stirring parameters, placement of the mechanical stirrer in the melt, melting temperature, and the characteristics of the particles added.

In the present fabrication procedure, Al-1100 ingots were heated in the electric furnace above its melting point then decrease of temperature till melting point, stirring and the addition of reinforcement of particles takes place simultaneously. After holding this process for ten minutes at the melting point, mixed material is poured carefully in suitable molds. After cooling, performs were machined to convert in specimen size as per ASTM standards for mechanical testing as shown in Fig. 2. The process is repeated for different compositions and specimens were tested.

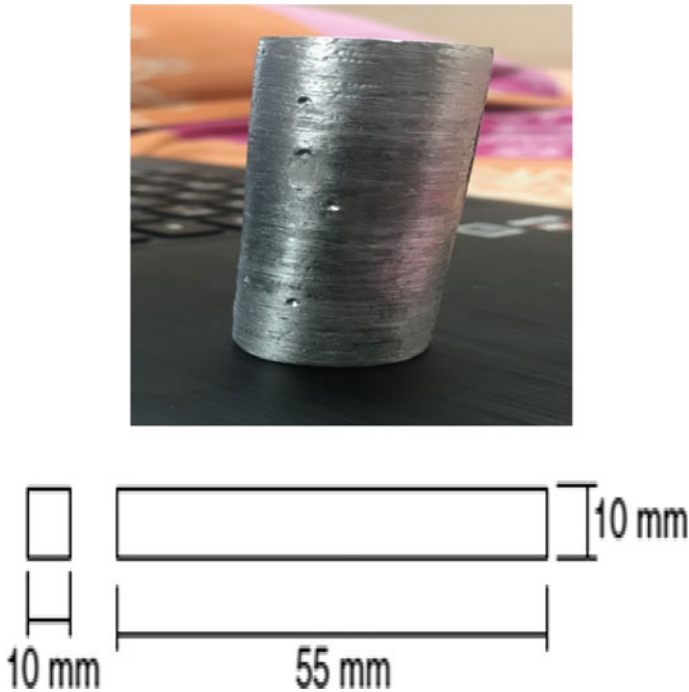



Fig. 2 Specimen for testing

4 Mechanical Characterization

Mechanical characterization is the identification of mechanical properties of composite materials which provide the basis for preventing failure of materials during service. These properties are influenced by the dispersion of reinforcements in the composite and also by the wettability between matrix and reinforcement particles. After getting two suitable specimens, Charpy impact tests were performed in the inspection and testing Engineers Lab Greater Noida and hardness tests were performed in the mechanics of solids lab Amity University Noida as shown in Fig. 3. Following readings were achieved as shown in Table 1.


INSPECTION & TESTING ENGINEERS



F-22423, Site-C, Surajpur Industrial Area, UPSIDC, Greater Noida, Gautam Budh Nagar (U.P.)
 Mobile : +91 9810059715, +91 9891174696, Phone : +91 120 4310675
 E-mail : ite.noida@hotmail.com, Website: http://www.itenoida.com, http://www.inspectionandtestingengineers.com

TEST REPORT

Test Report No.	ITE/JA/2018/04/18/03	Date	18/04/2018
Customer's Name	Junaid, Akhil.		
Address	Amity University, Sec-125 Noida (U.P.)		
Sample(s) Received on	18/04/2018	Sample(s) Tested on	18/04/2018
Description of Sample	Al Base MMC Samples		
Test Method Used	Tested at Calibrated impact tester		

TEST RESULTS

Impact Test:-			
Test Id	S1	S2	
Charpy Impact Value (J)	22	44	
Sample Dimension :	10.0*10.0*55.0		
Remarks:	NA.		

*** END OF REPORT ***

Fig. 3 Impact test report

Table 1 Hardness and impact test results

Sample	Composition	Hardness value (HB)	Impact result (Joule)
1	Al-1100	8	10
2	5%Al ₂ O ₃ -10%ZrB ₂	31	43
3	10%Al ₂ O ₃ -5%ZrB ₂	28	24
4	5%Al ₂ O ₃ -5%ZrB ₂	27	22
5	10%Al ₂ O ₃ -10%ZrB ₂	32	44
6	7.5%Al ₂ O ₃ -7.5%ZrB ₂	29	39

5 Conclusion

From the above research work, it is concluded that the following:

- The hybrid metal matrix composite can be developed effectively using the stir-casting technique.
- Hardness and impact values found to increase with increase zirconium diboride particles in the composites.
- The shining nature of the performs increases with the increase of zirconium diboride in comparison to alumina.
- By analyzing all the values hardness number and impact result, it can be concluded that aluminum metal matrix composite is having higher strength when 10% of zirconium diboride and aluminum oxide is added to aluminum 1100.

References

1. Looney LA, Monaghan JM, Reilly PO, Taplin TMR (1992) The turning of an Al/SiC metal-matrix composite. *J. Mater. Process. Technol.* 33:453–468
2. Natarajan S, Naraynasamy R, Kumaresh Babu SP, Dinesh G, Anil kumar B, Sivaprasad K (2009) Sliding wear behavior of Al 6063/TiB₂ in situ composites at elevated temperatures. *Mater Design* 30(7):2521–2531
3. Hong E, Kaplin B, You T et al (2011) Tribological properties of copper based composites reinforced with tungsten carbide particles. *Wear* 270:591–597
4. Dinaharan I, Murugan N (2012) Dry sliding wear behavior of AA6061/ZrB₂ in situ composite. *Trans Nonferrous Metals Soc China* 22:810–818
5. Farhadinia F, Sedghi S (2014) Fabrication of Al₂O₃/(ZrB₂ + TiB₂) composite using MACS and microwaves. *Metall Mater Trans A* 45:3125–3129
6. Bansal NP (2005) Handbook of ceramic composites. Norwell (Kluwer), pp 198–203
7. Hunt WH Jr (2009) Metal matrix composites: applications. In: Buschow KHJ, Cahn R, Flemings MC, Ilshner B, Kramer EJ, Mahajan S, Veysiere P (Eds.), *Encyclopedia of materials: science and technology*, pp 5442–5446
8. Schwartz MM (1984) Composite materials handbook. McGraw-Hill Book Company, USA
9. Dasgupta R, Meenai H (2005) SiC particulate dispersed composites of an Al–Zn–Mg–Cu alloy: property comparison with parent alloy. *Mater Charact* 54:438–445
10. Thomas WM, Staines DG, Norris IM, de Frias R (2003) Friction stir welding tools and developments. *Weld World* 47:10–17
11. Rai R, De A, Bhadeshia HKDH, DebRoy T (2011) Review: friction stir welding tools. *Sci Technol Weld Join* 16(4):325–342
12. Zhang YN, Cao X, Larose S, Wanjara P (2012) Review of tools for friction stir welding and processing. *Can Metall Q* 51(3):250–261

Impact Strength of Silver Date Palm Leaf Reinforced Polyester Composites



B. P. Sharma, S. Sareen, D. Tokas, G. S. Rao and Umesh Kumar Vates

Abstract In the present research work, a new composite material has been fabricated using silver date palm fiber as reinforcement in the plain polyester resin. The composites have been fabricated up to a maximum volume fraction of fiber about 0.434. The impact strength of fabricated composites was investigated as a function of fiber content. It has been observed that the impact strength of the composite material increases with an increase in fiber content. It is found that the maximum impact strength of the composite is 290 J for the highest volume fraction 0.434. These results show that at high volume of fiber, the silver date palm fibers are capable of preventing the growth of propagating cracks from a surface of the notch, thus reducing the crack by delamination. It has been concluded that using silver date palm fiber as reinforcement in plain polyester resin plays a major role in terms of high impact strength of a new fabricated composite material.

1 Introduction

The natural fibers extracted from plants such as vakka, sisal, banana, and bamboo have many attractive benefits over synthetic fibers. These fibers are cheaper, easily available, low density and they are also recyclable and eco-friendly. Therefore, the natural fiber reinforced composites are emerging as realistic alternatives to replace the synthetic fiber reinforced composites in many applications. These composites exhibit high tensile, flexural strength and resistance to fracture when the suitable coupling agents are used for making the bond between the hydrophilic natural fibers and hydrophobic matrix.

The mechanical behavior of sisal, hemp, and banana fiber reinforced composites using novolac resin, with and without maleic anhydride treatment was investigated [1]. It has been observed that the maleic anhydride treatment when applied on the fibers increases mechanical properties like the modulus of elasticity, flexural mod-

B. P. Sharma (✉) · S. Sareen · D. Tokas · G. S. Rao · U. K. Vates
Department of Mechanical Engineering, Amity University Uttar Pradesh,
Noida, Uttar Pradesh, India
e-mail: bpsharma15482@gmail.com

ulus, and impact strength. The tensile behavior of elephant grass fiber reinforced composites fabricated from retting, chemical extraction and treated by KMnO_4 was reported [2]. It is found that the fibers treated by KMnO_4 have shown significant improvement in tensile strength and modulus compared to that of the fibers extracted by retting and manual process. The fabrication and testing of thermoplastics and thermosetting composites reinforced with commonly used natural fibers like coir, banana, hemp, and sisal with or without chemical treatment by different methods were studied by many researchers [3–7]. The effect of moisture content on mechanical properties of natural fibers such as jute, coir, sisal, flax, kenaf, and abaca was investigated by Symington et al. [8]. It has been observed that the jute fiber showed superior mechanical properties than other fibers. An attempt was made by Ratna Prasad et al. [9] to study mechanical properties of sisal, bamboo and jowar fiber reinforced composites. It has been observed that the tensile modulus of jowar fiber reinforced composite is better than sisal and bamboo fiber reinforced composites. The tensile properties of different natural fiber reinforced composites made from jute, kenaf, hemp, coir, and sisal were reported by Wambua Paul et al. [10] and found that hemp fiber reinforced composite exhibited highest tensile strength values whereas coir showed the lowest. The tensile strength and impact behavior of rice straw polyester composites have been investigated by Ratna Prasad et al. [11]. It has been found that the rice straw fiber reinforced composites exhibited higher tensile and impact strength compared to that of pure polyester resin.

Though a huge amount of research work has been reported on various natural fibers and its composites but no work has been reported on impact behavior of a silver date palm leaf fiber reinforced polyester composites. Thus, the aim of this work is to introduce a newly identified natural fiber, i.e., silver date palm leaf as reinforcement in the development of new composite materials for lightweight vehicle applications and to investigate the impact properties of a silver date palm leaf fiber reinforced polyester composites.

2 Experimental Procedure

2.1 Materials

The source of this fiber is leaves of silver date palm tree, which grows in all parts of India is shown in Fig. 1. Unsaturated polyester resin, methyl ethyl ketone peroxide (catalyst), and cobalt naphthanate (accelerator) were procured from ICA (Pvt) Ltd. (Delhi, India). Rubber molds are prepared according to ASTM standards (63.5 mm long, 12.7 mm deep and 10 mm wide). Thin transparent plastic sheets are used to cover the molds from one side for arresting the air. Five sets of bend specimens of each volume fraction (0.18, 0.24, 0.33, 0.37 and 0.43) have been fabricated as per ASTM D 256 M.



Fig. 1 Silver date palm tree

2.2 Preparation of Fiber

Initially, leaves were separated from the stems of the silver date palm tree and kept in water for about 2–3 h and followed by washing with normal water, so as to clean dust that might have presented on the leaves owing to their exposure to the environment. The wet fibers were dried under the sun for few hours and subsequently dried in the furnace at 70 °C for 1 h. After that the fibers have been cut to the required length.

2.3 Composite Preparation

In the current research work, the composites have been prepared using hand lay-up method. For 100 ml of the polyester resin 1.5% of catalyst and accelerator were added. The composites were fabricated, gradually by filling the mixture of resin into the mold and unidirectional fibers, starting and ending with alternative layers of resin. Subsequently, a thin transparent plastic sheet has been placed on the mold from one side to arrest the air by pressing the sheet gently with the steel rule and instantly followed by applying a compressive pressure of 0.05 MPa on the mold. Then the specimens were allowed to cure for one day. Nevertheless, the movement of the fiber in the mold should be minimized for yielding sound quality fiber reinforced composites. Then, the specimens were also post-cured at 70 °C for 1 h after being removed from the mold.

2.4 Impact Testing of Composites

The dimensions of the flexural test specimens are 62.5 mm in length, 12.7 mm deep and 10 mm wide. Three-point bend tests were conducted on five identical specimens of each volume fraction as per ASTM D 790 M for measuring flexural properties. All the specimens were tested in an impact testing machine at Amity University, Noida, and Uttar Pradesh.

3 Results and Discussions

3.1 Impact Properties of Silver Date Palm Fiber Reinforced Composites

The fractured impact specimens for various volume fractions (0.18, 0.24, 0.33, 0.37, and 0.43) are shown in Fig. 2. It is found that the impact strength increases with an increase in volume fraction of the fiber and the maximum impact strength of the composite are found to be 290 J for the highest volume fraction 0.43. It has been also observed that the impact strength of silver date palm fiber reinforced composite increases with an increase in volume fraction of fiber content. It clearly indicates that reinforcing small amount of the fiber in resin improves significant impact strength of the composite. These results show that at high volume of fiber the silver date palm fibers are capable of preventing the growth of propagating cracks from a surface of the notch, thus reducing the crack by delamination. It has been concluded that using silver date palm fiber as reinforcement in plain polyester resin plays a major role in terms of high impact strength of a new fabricated composite material.

4 Conclusions

A lightweight composite material has been fabricated using silver date palm tree leaf fiber as reinforcement in polyester resin matrix. The density of the fiber is found to be 500 kg/m³. It has been observed that the impact strength of the composite increases with an increase in fiber content. It clearly indicates that reinforcing small amount of the fiber in resin improves significant impact strength of the composite. These results show that at high volume of fiber, the silver date palm fibers are capable of preventing the growth of propagating cracks from a surface of the notch, thus reducing the crack by delamination. It has been concluded that using silver date palm fiber as reinforcement in plain polyester resin plays a major role in terms of high impact strength of a new fabricated composite material.

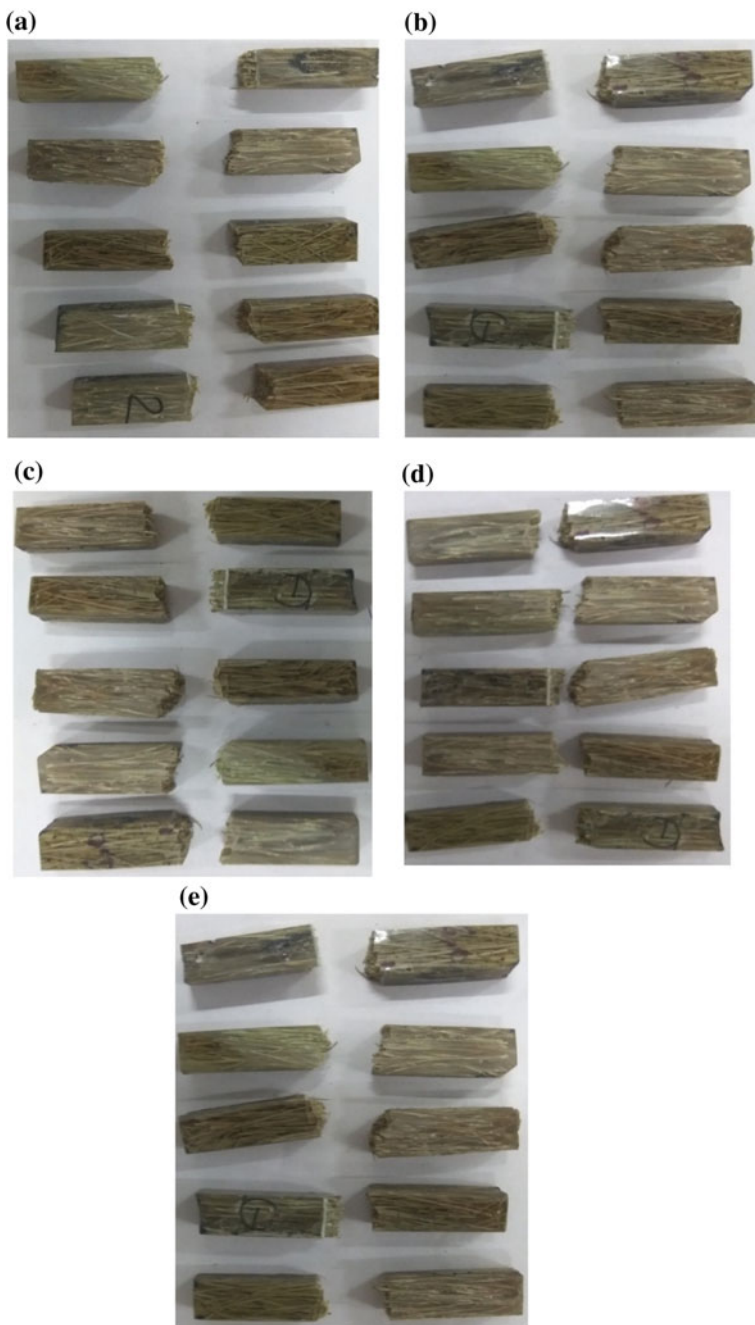


Fig. 2 Impact test specimens after failure for various volume fractions **a** 0.18 **b** 0.24 **c** 0.33 **d** 0.37 and **e** 0.43

References

1. Mishra S, Naik JB, Patil YP (2000) *Compos Sci Tech* 60:1729
2. Murali Mohan Rao K, Ratna Prasad AV, Ranga Babu MNV, Mohan Rao K, Gupta AVSSKS (2007) The tensile behavior of elephant grass fiber reinforced composites fabricated from retting, chemical extraction and treated by KMnO_4 . *J Mater Sci* 42:3266–3272. <https://doi.org/10.1007/s10853-006-0657-8>
3. Li Y, Mai YW, Lin Y (2000) Sisal fibre and its composites: a review of recent developments. *Compos Sci Tech* 60:2037–2055
4. Singh B, Gupta M, Verma A (1996) Influence of fiber surface treatment on the properties of sisal–polyester composites. *Polym Compos* 17:910–918
5. Manikandan Nair KC, Diwan SM, Thomas S (1996) Tensile properties of short sisal fiber reinforced polystyrene composites. *J Appl Polym Sci* 60:1483–1497
6. Geethamma VG, Joseph R, Thomas S (1995) Short coir fibre-reinforced natural rubber composites: effects of fibre length, orientation and alkali treatment. *J Appl Polym Sci* 55:583–594
7. Mishra S, Naik JB, Patel YP (2000) The compatibilising effect of maleic anhydride on swelling and mechanical properties of plant-fibre-reinforced novolac composites. *Compos Sci Tech* 60:1729–1735
8. Symington MC, Banks WM, West Opukuro David, Pethrick RA (2009) Tensile testing of cellulose based natural fibers for structural composite applications. *J Compos Mater* 43:1083–1086
9. Ratna Prasad AV, Mohan Rao K (2011) Mechanical properties of natural fiber reinforced polyester composites: jowar, sisal, and bamboo. *Mater Des* 32(8–9):508–513
10. Paul Wambua, Jan Ivens, Ignaas Verpoest (2003) Natural fibers: can they replace glass in fibre reinforced plastics? *Compos Sci Technol* 63:1259–1264
11. Ratna Prasad AV, Mohan Rao K, Gupta AVSSKS (2007) Tensile and impact behavior of rice straw-polyester composites. *Indian J Fiber Text Res* 32:399–403

Onsite Technical and Economic Performance Evaluation of PWT (Pipeline Welding Technology): A Comparative Analysis with CRC-Evans Welding Technology



Anubhav Rawat and Bhagwat Singh Shishodia

Abstract During cross-country underground pipeline construction welding is one of the major construction activity. At various parts of the world, many pipeline welding machines are in use to produce defect-free economic pipeline joints. Every weld machine manufacturer claims its own advantages and other's drawbacks. Two famous welding machine manufacturing companies for pipelines are PWT (Italy) and CRC-Evans (USA). Thus, the current work at the cross-country gas pipeline construction site from Vijaypur (MP, India) to Dadri (UP, India) (VDPL) is taken up to determine which of the above two mentioned machines are technically better and relatively cheaper while determining weld joint cost and overall pipeline construction cost. Data of two construction sites of VDPL namely Guna and Mathura are collected for weld joint construction and repair. The sites were constructed by ESSAR and EIL for GAIL. The carbon steel pipeline being laid was of 48" nominal size. A detailed cost analysis of the machines is estimated by considering all the related man, machine and material cost, both for mainline weld and weld joint repair. Technical performance of the weld machines is evaluated by comparing various weld parameters for pipeline weld joints. Performance of both of the machines is found to be comparable and almost equal in terms of total cost involved but the repair cost of PWT is less than CRC. Both PWT and CRC are found to produce weld defects with defect of incomplete fusion (IF) more frequently. Suitable remedies are suggested for improvement.

Keywords Pipeline · Construction · Pipeline welding technology · Weld defects · Incomplete fusion (IF) · Weld construction cost

A. Rawat (✉)

Department of Mechanical Engineering, Ben Gurion University of the Negev, Beersheba, Israel
e-mail: rawat@post.bgu.ac.il

B. S. Shishodia

Department of Mechanical Engineering, JIET, Jodhpur, India

© Springer Nature Singapore Pte Ltd. 2019

M. Kumar et al. (eds.), *Advances in Interdisciplinary Engineering*, Lecture Notes in Mechanical Engineering, https://doi.org/10.1007/978-981-13-6577-5_10

1 Introduction

On-site costing of a pipeline project is a very cumbersome task as it involves many components. The actual on-site costing many a time is far different from the planned budget for a particular activity. Pipeline welding is the most important part of pipeline construction and control of the onsite incurred cost on this aspect is a very tedious task as it involves many technicalities. At previous occasions, many kinds of limited studies [1–8] on welding cost and performance determinations have been performed. Also for cross-country pipelines use of the same kind of welding machines is not feasible hence more than one kind of welding machines like PWT, CRC-Evans, and Lincoln etc are used for the same project. Thus, current works have been taken up, not only to determine overall welding cost incurred onsite but also to establish a technical and economical comparison between two famous automatic welding machines available worldwide, i.e., PWT (Italy make) and CRC-Evans (USA make). This kind of study may be useful for future pipeline designers and construction companies.

2 Details of Pipeline Construction Site Considered in the Study

Details of the pipeline construction site have been explained in the subsequent sections.

2.1 Introduction to VDPL Project

VijaypurDadri Pipeline (VDPL) project was an LNG pipeline project for transferring LNG specially to meet the energy requirements of the 2010 Delhi Common Wealth Games from Vijaypur (M.P.) to Dadri (U.P.) [9]. Here, GAIL was a client and Essar Construction India Ltd (ECIL)-STG consortium was a contractor for its two of the three sections.

M/s GAIL (India) Ltd was implementing an approximately 592 km long pipeline project for transportation and distribution of Re-gasified LNG from Vijaipur to Bawana via Dadri as part of capacity augmentation of existing Gas Rehabilitation and Expansion Project (GREP) pipeline to cater to the demand of consumers in Uttar Pradesh, Haryana, and Delhi state. The proposed pipeline from Vijaipur (M.P.) to Dadri (U.P.) comprised of 48" OD and approx. 498 km long pipeline. The complete work from Vijaipur to Dadri had been divided into three sections (Section-A, B & C) as indicated below.

Section-A: Section-A covered approx. 169.500 km long 48” OD pipeline and pipeline facilities from Vijaipur dispatch terminal (Chainage 0.000 km) up to Ch. 169.500 km. This section included works at dispatch terminal (DT) at Vijaipur and various intermediate facilities such as six (6) sectionalizing valve (SV) stations and one intermediate pigging station.

Section-B: Section-B covered approx. 165.500 km long 48” OD pipeline and pipeline facilities from Chainage 169.500 km to Ch. 335.00 km. This section included works at various intermediate facilities such as five (5) sectionalizing valve (SV) stations, one intermediate pigging station and one no. intermediate pigging cum future compressor station.

Section-C: Section-C covered approx. 163.000 km long 48” OD pipeline and pipeline facilities from Ch. 335.000 km to receipt terminal at Dadri (Ch. 497.79 km). This section included works at various intermediate facilities such as five (5) sectionalizing valve (SV) stations, one no. intermediate pigging cum future compressor station and hook up at receipt terminal at Dadri.

2.2 Construction Activities for Pipeline Laying

For laying the above pipeline many construction activities [9, 10] viz. Permits, Pre-Construction Survey, ROU Clearing and Grading, Trenching, Blasting, Stringing, Bending, Welding including Weld Repair, Non Destructive Testing (NDT), Joint Coating, Concrete Coating, Lowering (including OFC Laying), All Crossings and Horizontal Directional Drilling (HDD), Temporary Cathodic Protection (TCP) and Permanent Cathodic Protection (PCP), Back Filling & Tie-in, OFC Jointing, Hydrotest etc. took place. Out of these, the current work is focused on the welding related activities only.

2.3 Parametric Details of Welding Machines Considered in the Study

For the current work, two welding machines were considered: PWT and CRC-Evans. For the work taken up by Essar Constructions India Ltd., PWT was used at Guna area and CRC-Evans was used in Mathura Area. For technical comparison, the parameters shown in Table 1 are considered and for economic comparison, parameters are shown in Table 2 are considered.

Table 1 Weld parameters considered for technical comparison in the study

S. no.	Parameter	S. no.	Parameter
1	Filler material	8	Weld joint design
2	Shielding gas type	9	Run sequence
3	Weld material Flow rate	10	Travel and wire speed
4	AWS weld type	11	Stick out
5	Number of runs	12	Time lapse between the end of root pass and start of hot pass
6	Direction of weld	13	Time lapse between the end of hot pass and start of subsequent pass
7	Welding position		

Table 2 Parameters considered for economic comparison in the study

S. no.	Parameter	S. no.	Parameter
1	Manpower cost for mainline	4	Manpower cost for repair of weld
2	Machine power cost for mainline	5	Machine power cost for repair of weld
3	Material cost for mainline	6	Material cost for repair of weld joints

3 Technical Comparison of PWT and CRC-Evans

Based on the parameters as described above, the data for technical comparison has been collected and summarized in Figs. 1 and 2, and Tables 3, 4, 5 and 6 separately for both of the welding machines for the pipe thickness of 20.7 mm.

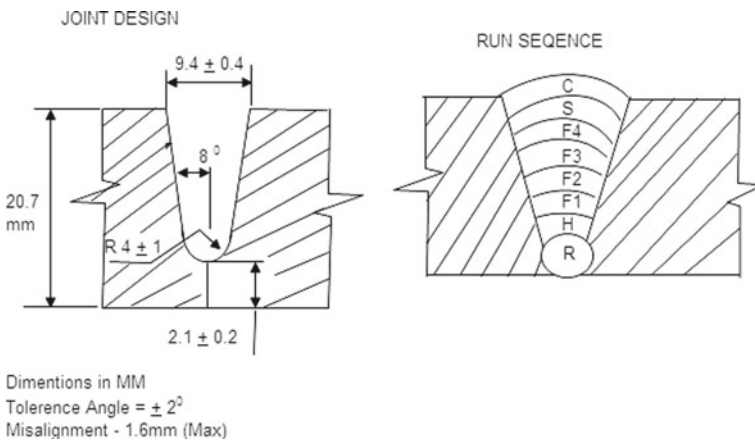


Fig. 1 Weld joint design for PWT weld machine

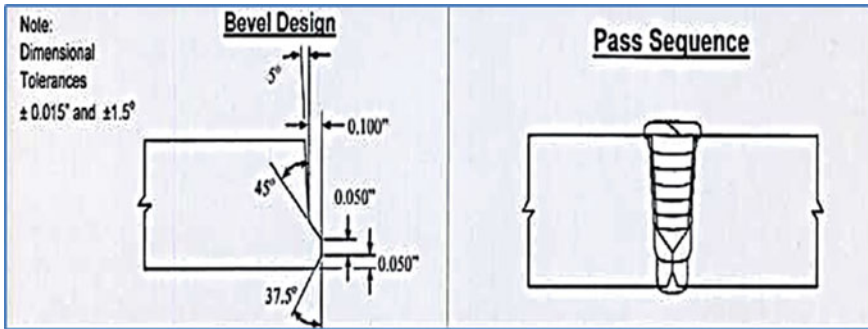


Fig. 2 Weld joint for CRC-Evans weld machine

Table 3 Torch features and fillers for PWT

Pass no.	Diam. (mm)	Filler metal type	Shielding gas type	Flow rate L/min.	AWS classification
Root	1.2	REDAELLI RMS/T	CO ₂	100%26-30	AWS 5.28-ER 80S-G
Hot	1.2	REDAELLI RMS/T	CO ₂	100%26-30	AWS 5.28-ER 80S-G
Fills (1-5)	1.2	REDAELLI RMS/T	CO ₂	50%/ARG 50%26-30	AWS 5.28-ER 80S-G
Cap	1.2	REDAELLI RMS/T	CO ₂	50%/ARG 50%26-30	AWS 5.28-ER 80S-G
Minimum run number: 8			Minimum welders number for a joint: 2		
Direction of welding: all passes downhill			Welding position: 5G (horizontal axis)		

4 Economical Comparison of PWT and CRC-Evans

The cost incurred (man, machine and materials) in the welding and repair of defected welds have been accumulated for both mainline and repair crew. The costs have been drawn in the form of pi charts separately both for PWT and CRC-Evans in Figs. 3 and 4, respectively.

Table 4 Weld parameters for PWT

Pass No.	Cur AC-DC	Pol.	Volts	Amps	H.T. kJ/mm	Travel speed cm/min.	Wire speed m/min.	Stick out mm.	Oscillation	
									Width mm	Speed cm/min.
Root	DC	+	19-22	260-320	0.48	60-90	6.5-9	10-15	0-1.5	300
Hot	DC	+	20-23	260-320	0.70	40-60	6.5-9	12-15	2.5-4.5	250-300
Fill1	DC	+	19-22	250-310	0.69	40-60	6.5-9	12-15	3.5-5.5	250-300
Fill 2	DC	+	19-22	240-300	0.74	35-55	6-8.5	12-15	4.5-6.5	250-300
Fill 3	DC	+	19-22	240-300	0.74	35-55	6-8.5	12-15	5-7	250-300
Fill 4	DC	+	19-22	220-280	0.65	35-55	5.5-8	12-15	5.5-7.5	250-300
Strip	DC	+	18-21	180-250	0.56	35-55	4.5-7.5	12-15	6.5-8	250-300
C/AP	DC	+	17-20	150-210	0.89	15-30	3-5.5	10-12	8-10	150-230
Time lapse between the end of root pass and start of hot pass:										
Maximum 5 min										
Time lapse between the end of hot pass and start of subsequent pass:										
Maximum 10 min										

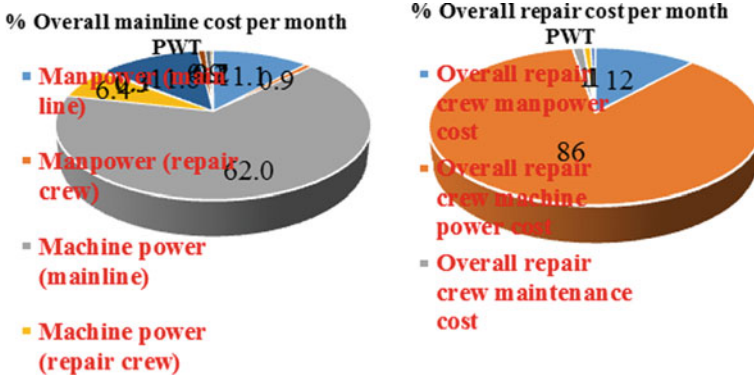


Fig. 3 Cost analysis of PWT welding machine

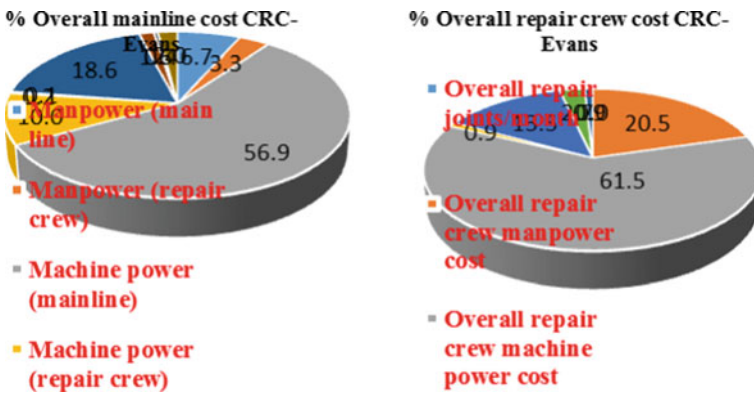


Fig. 4 Cost analysis of CRC-EVANS welding machine

5 Overall Comparison

Based on the analysis of the technical and economic data collected from construction sites mentioned in Sects. 3 and 4, a detailed technical and economical comparison of the two welding machines is done and is presented in Table 7.

From Table 7, it is clearly seen that the performance of both of the machines is comparable and almost equal in terms of total cost involved but the repair cost of PWT is less than CRC. Both PWT and CRC are found to produce weld defects with defect of incomplete fusion (IF) more frequently (Table 8).

Table 5 Torch features and filler materials for CRC-Evans

Pass No.	Diam. (inch)	Filler metal type (Tade name)	Shielding gas Type + 10%	Flow rate CFH (cubic feet per h)	AWS classification
Root	0.035	Thyssen ^a	Ar 80%/CO ₂ 20%	65–100	Aws5.18–ER70S-G
Hot	0.035	Thyssen ^a	CO ₂ 100%	60–90	Aws5.18–ER70S-G
Fill(1–6)	0.040	Thyssen ^a	Ar 80%/CO ₂ 20%	45–60	Aws5.18-ER70S-6
Cap(1-2)	0.040	Thyssen ^a	Ar 80%/CO ₂ 20%	45–60	Aws5.18-ER70S-6
Backing: no backing			Minimum welder number for a joint: 2		
Direction of welding: all passes downhill			Welding position: 5G (horizontal axis)		

^a(TS-6) Germany Make

6 Conclusions and Suggestions

Based on the above data collected, performance lacking areas are observed and suggestion for their mitigation for PWT have been given.

From Table 8, it is obvious that incomplete fusion (IF) is a serious weld defect generated by both of the weld machine. In 90% of the cases for PWT weld joints, IF was the weld defect. From the site data causes have been identified for IF and suitable remedies have been suggested in Table 8.

As far as weld cost reduction is concerned, simultaneous weld testing can result in fewer defects and thus reducing the cost of the weld. Omni scan is recommended for this kind of simultaneous tests.

Some financial powers must be given to ESD persons to avoid break downs of mainline equipment. To avoid hindrance to regular work, ESD working hour may be shifted to night.

It is also found that utility percent of the equipment is very less. The overall cost can be reduced by increasing utility of mainline equipment.

Less skills of PWT technicians should be mitigated by proper training from time to time.

Preventive maintenance schedules of the equipment must be more efficiently planned.

More number of health and safety personals and measure should be managed to avoid accidents to maintain manpower and morale of employees.

Acknowledgements The authors are thankful to Essar Construction India Limited (ECIL), for allowing to work on their construction sites and providing access to all the necessary documents and information.

Table 7 Overall comparison between the two welding machines

S. no	Comparison property	PWT	CRC-Evans
1	Welding type	Less automatic	More automatic
2	Welding speed	Less	More
3	Wire feed rate	Less	More
4	Wire consumption	Same	Same
5	Technology	Less advanced	More advanced
6	Number of torches in root pass	One	One
7	Number of torches in hot pass	One	Two
8	Number of torches in fill pass	One	Two
9	Number of torches in cap	One	One
10	Number of welders	More	Less
11	Number grinders	More	Less
12	Complexity of system	Less	More
13	Energy consumption	Less	More
14	Break down rate	Less	More
15	Freedom to welders	More	Less
16	Welding defects	Less	More
17	Joints produced per day	Less	More
18	Quantity of Ar gas consumed	Less	More
19	Quantity of CO ₂ gas consumed	More	Less
20	Type of defect	IF&porosity	Lack of cross penetration &IF
21	Visual defects	More	Less
22	Porosity	Less	More
23	Gas mixing problem in hot pass	More	Less
24	Working in bad weather	Good ‘	Less
25	Quantity of IF	More	Less
26	Quantity of LCP	Less	More
27	Repair rate	20%of total joints	25%of total joints
28	Repair length per month	Less	More
29	Preheat temperature	Same	Same
30	Type of root pass	External	Internal
31	Type of hot and other passes	External	External

(continued)

Table 7 (continued)

S. no	Comparison property	PWT	CRC-Evans
32	Hiring cost	Less	High
33	Maintenance cost	Less	High
34	Per joint production cost	More	Less
35	Mainline equipment cost	High	Low
36	Mainline manpower cost	High	Low
37	Repair crew manpower cost	Less	High
38	Repair crew equipment cost	Less	High
39	Repair cost per joint	Less	More
40	Breakdown cost	Less	More

Table 8 Causes and remedies for IF

Causes for IF	Remedy
Insufficient heat input, wrong type or size of electrode, improper joint design	Follow correct welding procedure
Incorrect electrode position	Maintain proper electrode position
Weld metal running ahead of the arc	Reposition work, lower current or increase weld travel speed
Trapped oxides or slag on weld groove or face	Clean weld surface prior to cleaning
Welders less skilled	Welder training programme may be another option and will be cheaper than repair cost incurred
Welder's negligence	More inspection needed thus more number of engineer's deployment is recommended

References

1. Kim IS, Jeong YJ, Lee CW, Yarlagadda PK (2003) Prediction of welding parameters for pipeline welding using an intelligent system. *Int J Advanc Manufact Technol* 22(9–10):713–719
2. Yapp D, Blackman SA (2004) Recent developments in high productivity pipeline welding. *J Brazilian Soc Mech Sci Eng* 26(1):89–97
3. McAllister EW (2013) Pipeline rules of thumb handbook: a manual of quick, accurate solutions to everyday pipeline engineering problems. Gulf Professional Publishing
4. Vaidya V, Viwek V, Christopher C, Chasse L (2000) Methods and apparatus for welding performance measurement. U.S. Patent 6,051,805, issued April 18, 2000
5. Geisler R (2012) 'Estimating total welding costs'
6. Gordon R, Holdren R, Johnson M, Lozev M (2003) Reducing pipeline construction costs: New technologies. *Welding World* 47(5–6):7–14
7. Marco B 'Technical calculation and estimators man hour manual'
8. Costing of pipelines. <http://www.pipingguide.net/2009/04/costing-of-pipelines-1.html>
9. Essar projects, construction manuals
10. Anubhav R (2010) 'Welding stress and defect analysis of oil and gas pipelines' M. Tech. Thesis, University of Petroleum and Energy Studies, Dehradun, India

Fuzzy Logic Modeling of Explanatory Variables of Catalytic Converter of an Automobile for Prediction of CO₂ Emission



Rajesh P. Verma, Ayush Kumar, P. K. Chauhan and Ankit Dimri

Abstract The emission of CO₂ gases from catalytic converter demands attention to control for stability of climate system. In the present work, the explanatory parameters (exhaust gas flow rate, washcoat surface area and exhaust temperature) of catalytic converter of an automobile were modeled to predict the CO₂ emission using fuzzy logic approach. The effect of explanatory parameters on CO₂ emission was also studied and optimum ranges of the parameters were investigated to minimize the CO₂ emission. The result showed the greater dependency of CO₂ emission on engine exhaust gas flow rate followed by the washcoat surface area and exhaust gas temperature. 3D surface plots were also generated to study the interaction effects of the parameters on CO₂ emission. The optimum range of explanatory parameters of catalytic converter for reduced CO₂ emission was obtained as: exhaust gas flow rate: 300–550 cm³/min, washcoat surface area: 100–130 m²/g, exhaust temperature: 450–750 °C.

Keywords Automobile exhaust · CO₂ emission · Catalytic converter · Mamdani fuzzy logic

1 Introduction

Carbon dioxide (CO₂) gas plays a vital role in the stability of climate system and greenhouse effect. The concentration of CO₂ in atmosphere is increasing exponentially, which could not be taken lightly. The major sources of air pollution are the flue gases, emission from refineries and factories, exhaust emissions from vehicles. CO₂ emissions from vehicles significantly pollute air, therefore significant attention is required to reduce the amount of emission. A number of methods and technologies

R. P. Verma (✉) · A. Kumar · P. K. Chauhan
Department of Mechanical Engineering, Graphic Era (Deemed to Be University),
Dehradun, Uttarakhand, India
e-mail: rajesh_dival@yahoo.in

A. Dimri
Fedders Lloyd Corp. Ltd., New Delhi, India

© Springer Nature Singapore Pte Ltd. 2019
M. Kumar et al. (eds.), *Advances in Interdisciplinary Engineering*, Lecture Notes in
Mechanical Engineering, https://doi.org/10.1007/978-981-13-6577-5_11

are developed to control the vehicle emission. Some popular technological controls based on fuel treatment, combustion tuning, and exhaust treatment were proposed by many investigators [1–5] to reduce the CO₂ emission of an engine. Apart from it, a catalytic converter popularly used to control automobile exhaust for petrol driven vehicles. The catalytic converter (CC) is placed inside the tailpipe and it is used to convert automobile exhaust gases into CO₂, water, N₂, and O₂. The catalytic converter definitely controls the harmful effect of CO and other toxic exhausts, but it cannot control significantly the emission of CO₂. Among the number of parameters, air to fuel ratio, mass flow rate of exhaust gases, flue gas temperature, and surface area of catalyst play vital role to control the output of catalytic converter (emissions) [6]. Many researchers have attempted to control the catalytic converter emission of an automobile for green environment [7, 8].

Linear regression analysis is a powerful method to analyze the linear relationships between input and output parameters of a system. The linear regression method has been used by many researchers in prediction of CO₂ emission related research [9, 10]. In spite of the widespread use of the linear regression models in real-life applications, the existence of uncertainty in variables limits the application of this method [11]. Fuzzy linear regression method handles the uncertainty in qualitative variables very effectively and is used in estimating the relationships among variables where the available data are very limited and imprecise. A considerable amount of literature has been published on fuzzy application and optimization of CO₂ emissions, but hardly anyone has tried to model the catalytic converter input parameters for minimizing the CO₂ emissions in automobiles. In the present work, an attempt is made to model the catalytic converter input parameters (exhaust gas flow rate, washcoat surface area, and exhaust temperature) by fuzzy logic approach to predict the CO₂ emission from catalytic converter.

2 Methodology

Fuzzy logic model was developed to model the input parameters (exhaust gas temperature, exhaust gas flow rate and surface area of catalyst) of catalytic converter (Fig. 1) of an automobile based on Mamdani method using fuzzy logic tool in MATLAB. Optimal ranges of input parameters of catalytic converter were also investigated for minimum CO₂ emission. Fuzzy logic is used to represent, interpret, and compute vague and subjective information. Fuzzy reasoning provides an inference procedure that derives conclusions from known facts and a set of fuzzy IF-THEN rules. The structure of fuzzy logic system is shown in Fig. 2.

The “fuzzifier” translates input parameters into fuzzy values. The “inference engine” is the part that controls the process of deriving conclusions. It applies a fuzzy reasoning mechanism to obtain a fuzzy output using rules. The fuzzy inference system follows Mamdani fuzzy model. The “knowledge base” contains a set of fuzzy IF-THEN rules and a set of membership functions of fuzzy sets. The “defuzzifier” converts the fuzzy output into a crisp value that best represents the out fuzzy set

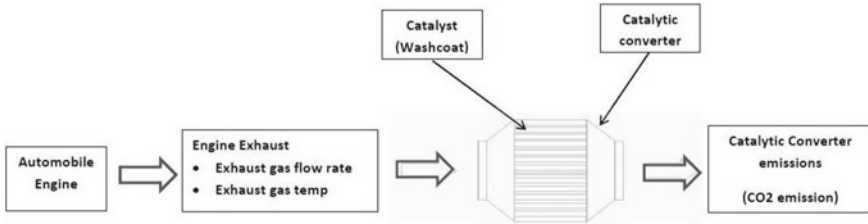


Fig. 1 Layout of input and output of a catalytic converter

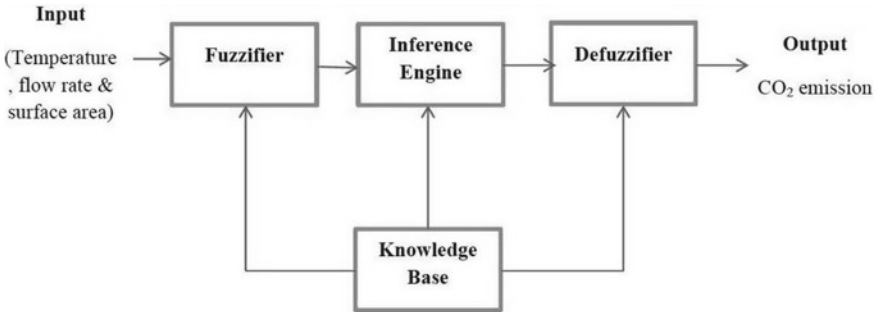


Fig. 2 Block structure of the fuzzy logic system

[12]. Development of fuzzy logic model for the prediction of CO₂ emission from catalytic converter was carried out in several phases:

1. Identification of the type of fuzzy system.
2. Identification of inputs and outputs and its ranges.
3. Selection of membership functions for inputs and outputs.
4. Generation of fuzzy rules.
5. Determination of the appropriate fuzzy inference functions and defuzzification method.

2.1 Identification of the Type of Fuzzy System

Mamdani fuzzy method and Tagaki-Sugeno (T-S) fuzzy method are two popular fuzzy rule based inference system. The T-S fuzzy inference system is best suited with linear techniques and generates continuity of the output surface. But the multi-parameter synthetic evaluation, assignment of weight to each input and fuzzy rules make the application of the T-S method complex and difficult. Whereas the legibility and easy understandability make the Mamdani model widely applicable [13]. The Mamdani fuzzy inference system also shows its advantage in output expression. Therefore, Mamdani fuzzy approach was used in the present work.

Table 1 The ranges of input and output parameters of catalytic converter and fuzzy linguistic variables

<i>Input parameters</i>		
Parameters	Ranges	Linguistic variables
Engine exhaust gas flow rate	50–800 cm ³ /min	Low, medium, high
Washcoat surface area	100–200 m ² /g	
Exhaust gas temperature	200–1000 °C	
<i>Output parameter</i>		
CO ₂ emission	120–150 g/km	Low, medium, high

2.2 Identification of Inputs/Outputs and Its Ranges

The fuzzy sets used in fuzzifying the input variables were exhaust gas temperature, exhaust gas flow rate and surface area of catalyst. Here, “exhaust gas” implies the exhaust from engine and input to the catalytic converter (Fig. 1). The fuzzy set used in fuzzifying the output variable was CO₂ exhaust emission. Figure 1 shows the selected inputs and output. In the study, three fuzzy sets were selected for inputs and output (low, medium and high). The ranges of inputs and output with fuzzy linguistic variables are presented in Table 1. The ranges of input parameters are surveyed from literature for motor gasoline. The levels of input parameters were low, medium and high as the minimum, central, and maximum value of the respective parameter.

2.3 Selection of Membership Functions for Inputs and Output

The membership function of a fuzzy set is a generalization of the indicator function in classical sets. Membership functions represent fuzzy subsets of variables. There are many membership functions available like triangular, trapezoidal, Gaussian, etc. The choice of membership function is subjective and problem dependent [10]. In the present work, combination of trapezoidal–Gaussian membership function and triangular membership function were selected for inputs and output respectively. Figure 3 shows the membership functions of temperature, flow rate, and surface area.

2.4 Generation of Fuzzy Rules

A set of 27 fuzzy IF-THEN rules with three inputs (temperature, flow rate, and surface area) and one output (CO₂ emission) was constructed. The fuzzy rules were obtained with the help of experts.

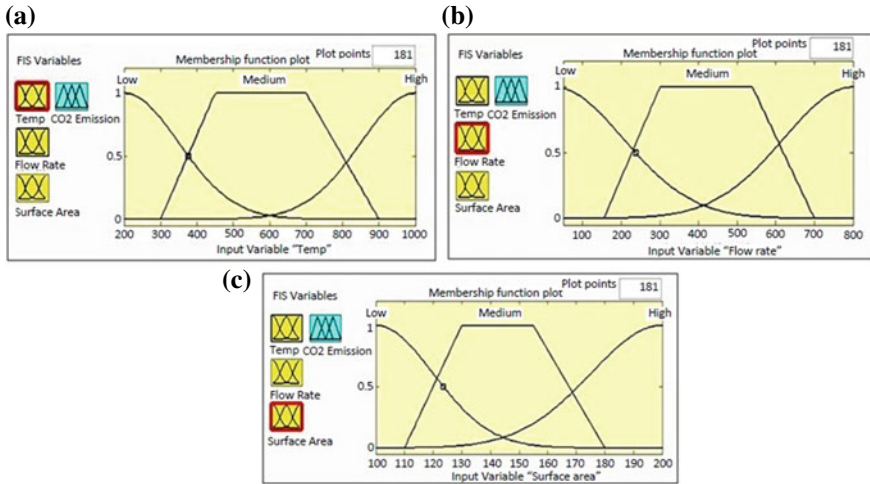


Fig. 3 Membership functions of temperature, flow rate and surface area

2.5 Determination of the Appropriate Fuzzy Inference Functions and Defuzzification Method

Fuzzy inference process was defined as:

“and method = min; or method = max; implication = min; aggregation = max and defuzzification method = centroid”.

3 Confirmation Test to Check Adequacy of the Developed Fuzzy Logic Model

In order to assess the prediction accuracy of the developed model, the prediction and real data were compared based on linguistic variables. The CO₂ emission was calculated by activity-based method (CO₂ emissions = fuel consumption × fuel emission conversion factor). The fuel emission conversion factor was taken as 2.8 for motor gasoline. The exhaust gas temperature was controlled by different types of cooling of tail pipe and flow rate was controlled by varying the diameter of pipe. Exhaust gas flow rate is decided by mathematical calculation depending on speed of the engine. Different catalytic converters were used for different washcoat areas. Experiments were performed at five combinations of parameters with for the comparison of output values (average of three similar tests) and predicted by fuzzy logic model as presented in Table 2 and it shows a good fit agreement. Low, medium, and high level of input parameters of catalytic converter in these experiments was taken as the minimum, central, and maximum value of the respective parameter. CO₂

Table 2 Comparison of CO₂ emission experimental data with results obtained from fuzzy logic model

S. No.	Temperature	Flow rate	Surface area	CO ₂ emission	
				Real	Fuzzy logic predicted
1	Low	Low	Medium	126 g/km (Low)	123.22 g/km (Low)
2	Low	High	Medium	132 g/km (Medium)	130.14 g/km (Medium)
3	Medium	Low	Medium	138 g/km (Medium)	131.41 g/km (Medium)
4	High	Low	Medium	135 g/km (Medium)	135.72 g/km (Medium)
5	High	High	Medium	146 g/km (High)	146.75 g/km (High)

emission between 120 and 130 g/km is taken “low”, between 130 and 140 g/km is taken as “medium” and between 140 and 150 g/km as “high”.

4 Results and Discussion

Initially, the effect of the explanatory variables of catalytic converter on the CO₂ emission was analyzed by changing one variable at a time, while keeping the other two variables constant at center level. The effects of the catalytic converter input parameters on the CO₂ emission are given in Fig. 4.

Figure 4a shows the variation of CO₂ emission with exhaust flow rate and there is minimum CO₂ emission between 300 and 500 cm³/min. By increasing the surface area of catalyst, CO₂ emission increases (Fig. 4b). The CO₂ emission increases exponentially between 160 and 180 cm³/min. After 180 cm³/min exhaust flow rate, the CO₂ emission is constant but at elevated level. As can be seen from Fig. 4c, an increase in the temperature increases the CO₂ emission, but there is a tendency of decreasing of CO₂ emission at temperature greater than 800 °C. The optimum range of surface area of catalyst is observed between 100 and 140 m²/g.

Engine exhaust gas flow rate has significant effect on CO₂ emission from catalytic converter. One major effect of gas flow rate is deterioration of the hydrocarbon sensor due to prolonged exposure to exhaust gases [13]. On the other hand, sufficient temperature is required for activation of catalytic converter, so trade-off of gas flow rate and exhaust temperature is required. Washcoat, a thin layer of inorganic oxide, is used for dispersion of active catalyst. It increases effective surface area and hence greater contact is achieved with reacting gases. The washcoat components support the catalyst function and to improve resistance of catalyst to thermal deactivation processes [14]. Hence sufficient surface area is required for functioning of

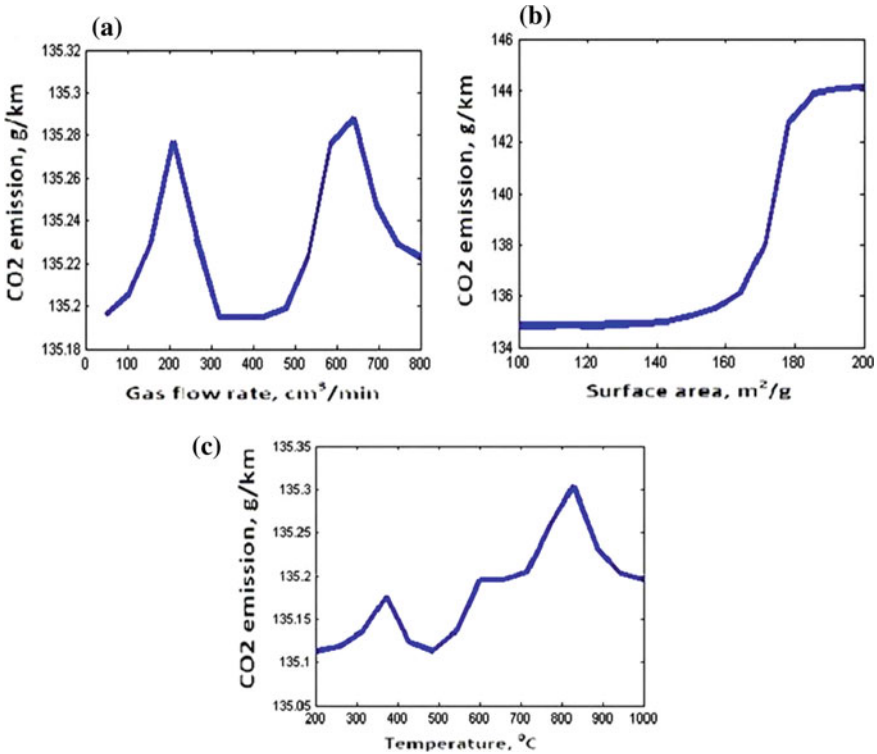


Fig. 4 Effect of **a** Engine exhaust gas flow rate **b** Washcoat surface area **c** Engine exhaust gas temperature on the CO₂ emission from catalytic converter

catalytic converter, but the increased surface area increases the CO₂ emission; hence optimization is required to achieve both goal.

The interaction effects of the parameters on the CO₂ emission were also investigated, which are presented in Fig. 5. Figure 5 shows 3-D surface plots, which were generated considering two parameters at a time, while the third parameter was kept constant at center level. Since there are three possible two-way interactions between the explanatory variables of catalytic converter, three 3-D surface plots were generated using the developed fuzzy logic model.

Figure 5a shows the CO₂ emission as a function of temperature and flow rate. The interaction is expressed by the difference between the relatively smaller influence of the temperature when using higher flow rate, and the greater influence of the temperature when using smaller flow rate. It could be observed that both combinations of “low temperature and high gas flow rate” and “high temperature and low gas flow rate” result in excessive CO₂ emission. Clearly, there exists a region of optimal temperature to gas flow rate by which the CO₂ emission is reduced. From Fig. 5b, it could be observed that high flow rate and moderate surface area is preferable to obtain reduced CO₂ emission. As shown in Fig. 5c, an increment in the temperature

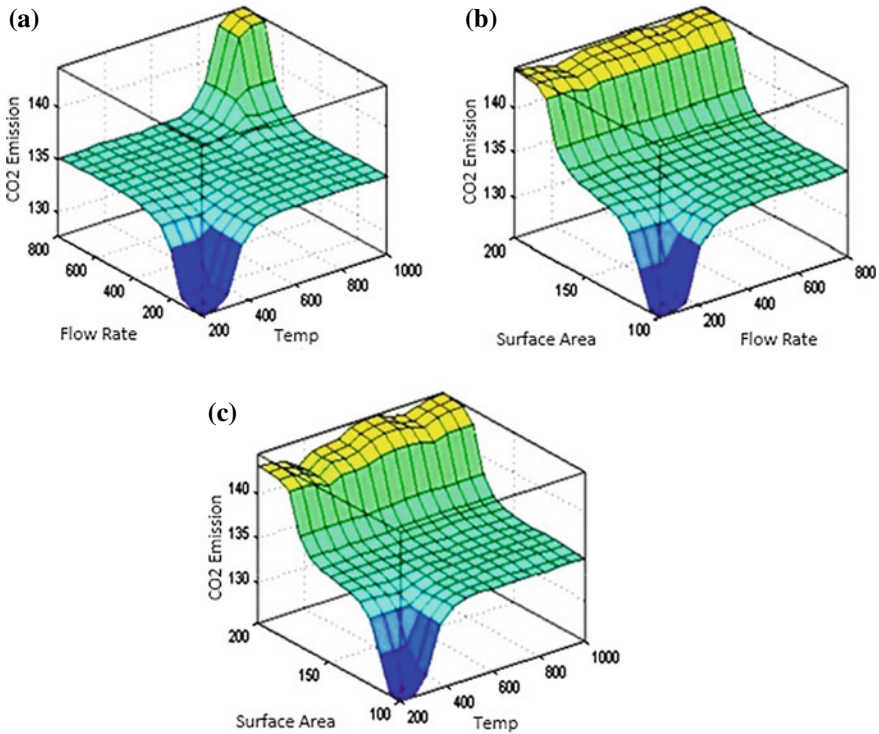


Fig. 5 3-D surface plots for interactions **a** flow rate \times temperature **b** surface area \times flow rate **c** temperature \times flow rate

efficiently reduces the CO₂ emission while using lower surface area, while increased CO₂ emission is observed if combination of high levels of temperature and surface area is used. From the analysis of the Figs. 4 and 5, it could be concluded that the exhaust gas flow rate has maximum influence on the CO₂ emission followed by the washcoat surface area and exhaust temperature.

5 Conclusions

From the analysis of the development and application of the fuzzy logic model within the covered ranges, the following can be concluded.

The selection of combination of trapezoidal-Gaussian membership function for inputs and triangular membership functions for output, Mamdani inference system, and centroid defuzzification method are suited in good agreement for prediction of CO₂ emission from catalytic converter. CO₂ emission is highly sensitive to the engine exhaust gas flow rate and their interactions. Nonlinear relationships are observed

between the CO₂ emission and the explanatory variables of catalytic converter as well as their interactions. Engine exhaust gas flow rate has maximum influence on the CO₂ emission followed by the washcoat surface area and exhaust temperature. The optimum range of input parameters to catalytic converter for minimum CO₂ emission is observed as: exhaust gas flow rate: 300–550 cm³/min, washcoat surface area: 100–130 m²/g, exhaust temperature: 450–750 °C.

References

1. Ahn K, Rakha H, Trani A, Van Aerde M (2002) Estimating vehicle fuel consumption and emissions based on instantaneous speed and acceleration levels. *J Trans Eng* 128(2):182–190
2. Riegel J, Neumann H (2002) Exhaust gas sensors for automotive emission control. *Germany Solid State Ionics* 152–153:783–800
3. Wua C, Chen R, Pu J, Lina T (2004) The influence of air–fuel ratio on engine performance and pollutant emission of an SI engine using ethanol–gasoline-blended fuels. *Atmos Environ* 38:7093–7100
4. Hsieha W, Chen R, Wub T, Lina T (2002) Engine performance and pollutant emission of an SI engine using ethanol–gasoline blended fuels. *Atmos Environ* 36(3):403–410 (2002)
5. Chen R, Chiang L, Chen C, Lin T (2011) Cold-Start Emissions of an SI engine using ethanol gasoline blended fuel. *Appl Therm Eng* 31(8–9):1463–1467
6. Marek W, Mitianiec W (2002) Modeling and research analysis of catalytic converter in a small SI two-stroke engine. *J KONES Int Combust Eng ISSN1231–4005*, 3–4, 176–184
7. Cenk S, Necait OA, Mustafa C (2010) The influence of operating parameters on the performance and emissions of a DI-diesel engine using methanol-blended-diesel fuel. 89, 1407–1414
8. Durairajan A, Kavitha T, Rajendran A, Kumaraswamidhas LA (2012) Design and manufacturing of nano catalytic converter for pollution control in automobiles for green environment. *Int J Innov Dev* 1(5):314–319
9. Heshmaty B, Kande A (1985) Fuzzy linear regression and its applications to forecasting in uncertain environment. *Fuzzy Set Syst* 15(2):159–191
10. Lee HT, Chen SH (2001) Fuzzy regression model with fuzzy input and output data for manpower forecasting. *Fuzzy Set Syst* 119(2):205–213
11. Takagi T, Sugeno M (1985) Fuzzy identification of systems and its applications to modeling and control. *IEEE Trans Syst* 15(1):116–132
12. Tapia JFD, Tan RR (2014) Fuzzy optimization of multi-period carbon capture and storage systems with parametric uncertainties. *Proc Safety Environ Protect* 92(6):545–554
13. Brondfield MN, Hutyra LR, Gately CK, Racit SM, Peterson SA (2012) Modeling and validation of on-road CO₂ emissions inventories at the urban regional scale. *Environ Pollut* 170, 113–123
14. Chen C, Park D, Ahn W (2014) CO₂ capture using zeolite 13× prepared from bentonite. *Appl Surf Sci* 292:63–67

Improved Fourier Polynomial Based Phase Modeling for Estimating Instantaneous Frequency from a Noisy FM Signal



Sankar Kumar Roy

Abstract Instantaneous frequency (IF) from a frequency modulated (FM) signal has number of applications in engineering disciplines such as telecommunication, analysis of radar signal, music signal, electrocardiogram signal, speed estimation from encoder signal, etc. There are many IF estimation techniques and these are divided into various groups, namely, zero crossing detection technique, time domain technique, frequency domain technique, time frequency domain technique. Among the various IF estimation techniques, Phase modeling by Fourier polynomial can estimate IF from a FM signal by fitting the Fourier polynomial to the zero crossing points. However, in a noisy FM signal, pseudo zero crossing points appear in place of actual zero crossing point. Therefore, a simple Fourier polynomial based phase modeling technique encounters some difficulties while it is applied in a signal of lower signal-to-noise ratio (SNR). Hence, improved Fourier polynomial based phase modeling technique has been developed for estimating IF from FM signal with low SNR. This improved technique is superior to simple Fourier polynomial based phase modeling technique and estimates better IF.

Keywords Frequency modulated signal · Noise · Instantaneous frequency

1 Introduction

Instantaneous frequency (IF) has achieved great importance in the area of signal processing since long over a decade. Starting from telecommunication application, the application of IF has been extended to sonar, radar, music, speech, cardiogram signal, etc. [1, 2]. The concept of IF generally comes into play when the frequency of a signal varies over time. In other words, IF is used for the analyses of nonstationary signal in practice. In real time, none of the signals show stationary behavior. Moreover, the signal is amalgamated with various types of noise. This noise could be

S. K. Roy (✉)
Mechanical Engineering Department, National Institute Technology Patna, Patna 800005,
Bihar, India
e-mail: sankar.roy@nitp.ac.in

white noise or colored noise. Therefore, estimation of true IF from the noisy signal is a challenging task for all the researchers. The researchers have developed various techniques to achieve the IF from a noisy signal. These techniques are divided into four major groups: zero crossing technique, time domain technique, frequency domain technique, time-frequency domain technique [1–3]. Zero crossing technique is an old technique to estimate the IF, where IF is measured between three zero crossings. Hence, achieved IF by this technique is constant over three zero crossings [4]. The frequency domain technique is based on analytical representation of a signal in time domain. The representation is achieved by Hilbert transform [2]. The literature review has revealed that estimated IF by frequency domain technique is better than zero crossing and time domain technique [5]. Further, literature review has also reported that specifically for noisy frequency modulated (FM) signal, band pass filtering in frequency domain can achieve better IF [6, 7]. Therefore, one should have prior information about the signal. On the other hand, time frequency domain technique can achieve better IF but the main set back of this technique is that it requires higher computation time. Therefore, in many cases, the application of this technique becomes unsuitable. In time-frequency domain techniques, the energy of a signal concentrated around the IF in time-frequency plane. Hence, peak detection in time-frequency plane can estimate the IF. The time-frequency domain techniques are short time Fourier transform (STFT), Wigner Ville distribution (WVD), continuous wavelet transform (CWT), S transform, etc. [1, 2, 8–15]. Besides the huge computation time, each time-frequency domain technique has its own drawback. The resolution of estimated IF by STFT technique depends on optimum window length. Again, the optimum window length is function signal phase differentiation [2]. Hence, prior guess of signal phase is quite difficult. Further, a cross term appears in time-frequency plane in Wigner Ville distribution, which generates an error in estimated IF [8, 9]. Various techniques have been developed to reduce this cross terms [14]. Still, the technique is somewhat deficient. Further, CWT-based IF estimation technique achieves better IF than STFT and WVD as it is variable windowed Fourier transform [12]. However, CWT faces the problem of nonadaptability. One time the wavelet function is selected then that function will be used for whole wavelet transform. On the other hand, S transform is a combination of STFT and WT [13–15]. Therefore, it takes both the advantages of STFT and WT. Still, the performance of this technique depends on window parameters [15]. Recently, researcher [16] has estimated IF from a sinusoidal FM signal submerged in Gaussian noise. Sinusoidal FM signal is a common model of radar signal. While radar signal reflects back from a vibrating or rotating object, then the signal becomes frequency modulated due to the Doppler effect [17]. High noise attenuation in this reflected radar signal is very common in military and civil applications [16]. Therefore, number of researches [16, 18–23] have been done on IF estimation from FM signal with different types of noise. Recently, researchers [24] have estimated the IF from a FM pulse signal by Fourier phase modeling. Hence, the phase modeling is achieved using zero crossing points.

In FM signal, the zero crossing points generally shift from its true one due to noise contamination. While the noise contamination is higher, then the noise con-

tamination creates some more zero crossing points in place of actual one, which incorporates more noise in estimated IF. Therefore, the aim of this paper is to develop better polynomial phase modeling technique to achieve better IF from a noisy signal. Besides this improved technique, a comparative study has been performed among frequency domain technique, Fourier polynomial representation of zero crossing points technique and improved Fourier polynomial representation of zero crossing points technique for single and multi-tone FM signal for different SNR.

The structure of the paper is as follows: Sect. 2 demonstrates background of FM signal, frequency domain IF estimation technique, and the Fourier polynomial representation of zero crossing points for IF estimation. As well as, it also discusses the improvement of abovementioned technique, while a FM signal poses high signal to noise ratio (SNR) and mean square error. The Sect. 3 illustrates the applicability of Fourier polynomial based IF estimation from a FM signal under different SNR. It also covers a comparative study between frequency domain technique and Fourier polynomial representation of zero crossing points technique. Further section covers a comparative study between Fourier polynomial representation of zero crossing points technique based IF estimation and improved one. Finally, a conclusion has been drawn based on the above study.

2 Theory

The general form of a FM signal is

$$s(t) = A \sin[\omega_c t + \sum_{i=1}^n a_i \sin(\omega_i t + \phi_i) + \phi_c] \tag{1}$$

where A is amplitude of the signal, ω_c is carrier frequency of the signal and ϕ_c is initial phase of the FM signal. Similarly, a_i, ω_i, ϕ_i are amplitude, frequency, and initial phase of i th modulating signal.

Further, the above signal can be written as

$$s(t) = A \sin[\phi(t)] \text{ where } \phi(t) = \omega_c t + \sum_{i=1}^n a_i \sin(\omega_i t + \phi_i) + \phi_c \tag{2}$$

Instantaneous frequency (IF) of a signal can be defined as [1]

$$IF = \frac{1}{2\pi} \frac{d\phi}{dt} \tag{3}$$

2.1 Fourier Polynomial Representation of Zero Crossing Points and IF Estimation

Time duration between three zero crossings of a single frequency signal is constant. While the signal becomes a FM signal, then the time duration between zero crossings will vary. In a sinusoidal signal, phase change that occurs between three zero crossings is 2π radian. Therefore, varying zero crossing time point is a function of phase angle. The varying zero crossing time points for a FM signal are shown in Fig. 1. Further, this time function can be modeled as summation of linear time-varying part and Fourier series [24]. Based on this modeling, the time function can be written as

$$t(\phi) = c_l\phi + \sum_{k=1}^m \left(c_k \cos\left(\frac{2\pi k\phi}{L}\right) + d_k \sin\left(\frac{2\pi k\phi}{L}\right) \right) \quad (4)$$

where, $k = 1, 2, \dots, 2m + 1$, $L = 2m\pi$. c_l is slope of linear time-varying part. c_k and d_k are Fourier coefficients.

Further,

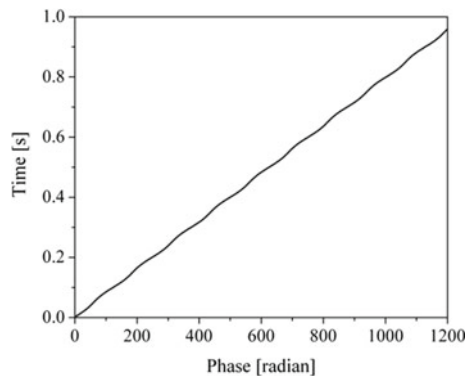
$$\frac{1}{\phi'(t)} = \frac{dt}{d\phi} = c_l + \sum_{k=1}^m \frac{2\pi k}{L} \left(-c_k \sin\left(\frac{2\pi k\phi}{L}\right) + d_k \cos\left(\frac{2\pi k\phi}{L}\right) \right) \quad (5)$$

Furthermore,

$$\omega = \frac{d\phi}{dt} = \left[c_l + \sum_{k=1}^m \frac{2\pi k}{L} \left(-c_k \sin\left(\frac{2\pi k\phi}{L}\right) + d_k \cos\left(\frac{2\pi k\phi}{L}\right) \right) \right]^{-1} \quad (6)$$

$$IF = \frac{1}{2\pi} \left[c_l + \sum_{k=1}^m \frac{2\pi k}{L} \left(-c_k \sin\left(\frac{2\pi k\phi}{L}\right) + d_k \cos\left(\frac{2\pi k\phi}{L}\right) \right) \right]^{-1} \quad (7)$$

Fig. 1 Varying zero crossing time points with respect to time



where

$$c_l = \frac{t_{end} - t_{initial}}{\phi_{end} - \phi_{initial}}$$

2.2 Improvement of Zero Crossing Point

Adding of noise with a FM signal shifts the zero crossing points and adding of more noise sometimes creates few extra zero crossings in place of its actual one. Figure 2a, b show shifting of zero crossing point and formation of new extra zero crossings, respectively. In Fig. 2a, it is observed that the zero crossing points are shifted from true point due to noise addition. However, in Fig. 2b, there are newly formed zero crossing points due to heavier noise addition.

Tese excessive zero crossings incorporate huge error in the estimated IF. Therefore, groups of zero crossing points that have much lesser time gap are averaged to achieve a single zero crossing point which is shown in Fig. 2c.

2.3 Frequency Domain Technique and IF Estimation

The frequency domain technique is based on Hilbert transform of a signal. Hilbert transform [1, 2] of a signal $x(t)$ is defined as

$$H[x(t)] = x(t) * \frac{1}{\pi t} = \frac{1}{\pi} \int_{-\infty}^{\infty} \frac{x(\tau)}{t - \tau} d\tau \quad (8)$$

The transform is basically a convolution of two signals $x(t)$ and $1/\pi t$, respectively. Thus, it shifts the phase of the signal $x(t)$ by 90° . Therefore, the signal $x(t)$ can be represented analytically using Hilbert transform as

$$\begin{aligned} z(t) &= x(t) + jH[x(t)] \\ &= A(t)e^{j\phi(t)} \end{aligned} \quad (9)$$

where $\phi(t)$ is instantaneous phase. Further, differentiation of instantaneous phase generates the IF.

$$\begin{aligned} \ln z(t) &= \ln[A(t)e^{j\phi(t)}] \\ \frac{\dot{z}(t)}{z(t)} &= \frac{\dot{A}(t)}{A(t)} + j \frac{d\phi}{dt} \end{aligned} \quad (10)$$

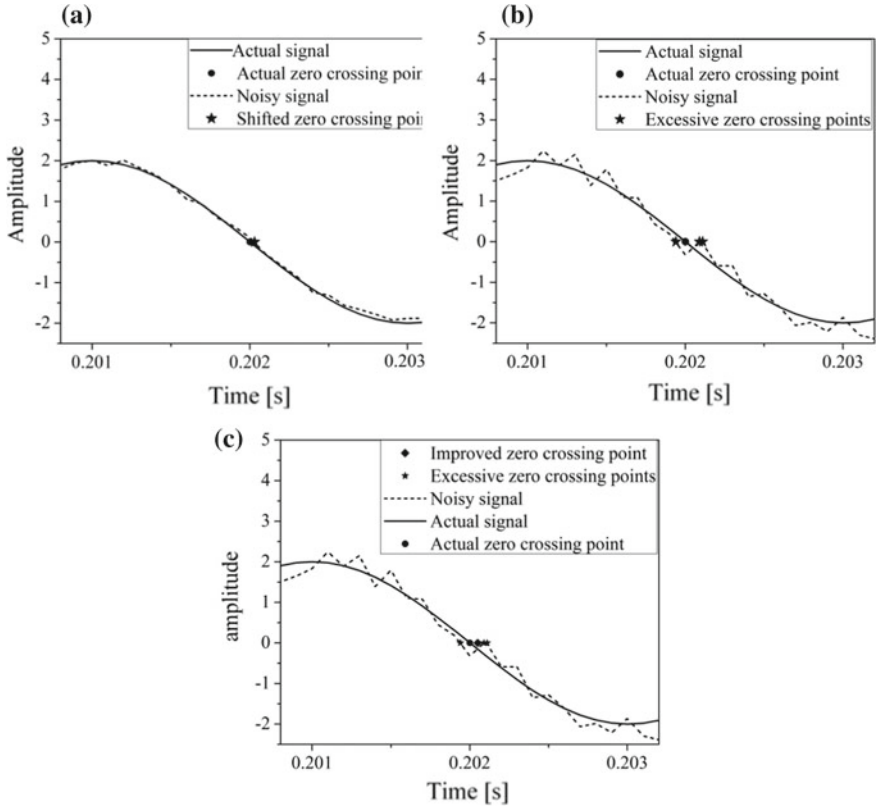


Fig. 2 **a** Shifting of actual zero crossing point due to addition of noise, **b** formation of extra zero crossings due to addition of heavier noise, **c** improved zero crossing point by adding extra zero crossing points

$$IF = \frac{1}{2\pi} \text{Imag} \left[\frac{\dot{z}(t)}{z(t)} \right] \tag{11}$$

Further,

$$A(t) = \text{Re}[z(t)]$$

Therefore,

$$\frac{\dot{A}(t)}{A(t)} = \text{Re} \left[\frac{\dot{z}(t)}{z(t)} \right]$$

$$\frac{\dot{z}(t)}{z(t)} = \text{Re} \left[\frac{\dot{z}(t)}{z(t)} \right] + j \frac{d\phi}{dt}$$

$$IF = \frac{1}{2\pi} \text{Imag} \left[\frac{\dot{z}(t)}{z(t)} \right] \quad (12)$$

2.4 Mean Square Error

Mean square error (MSE) is a variance of an estimated quantity. MSE is measured by averaging the square of the error between estimated quantity and true quantity. Hence, MSE can be mathematically represented as

$$MSE = \frac{1}{N} \sum_{i=1}^N (\hat{f}_i - f_i)^2 \quad (13)$$

where \hat{f}_i and f_i are estimated and true quantity, respectively. N is total number of discrete points of a quantity.

3 Simulation Results and Discussions

The Fourier polynomial representation of zero crossing points technique has been applied to simulated FM signals to estimate the IF while the signal is adulterated with additive white noise. Two FM signals are used for the simulation process. The first signal is modulated with single sine wave and the second one is modulated by multiple sine waves. Hence, the first signal is

$$y_1 = 2 \sin[200\pi t + 3 \sin(18\pi t)] \quad (14)$$

Corresponding IF

$$IF_1 = 100 + 27 \cos(18\pi t) \quad (15)$$

Second signal is

$$y_2 = \sin[400\pi t + 2 \sin(100\pi t) + 12 \sin(25\pi t)] \quad (16)$$

Corresponding IF

$$IF_2 = 200 + 100 \cos(100\pi t) + 150 \cos(25\pi t) \quad (17)$$

These signals are made to signals of different SNR by adding white noise.

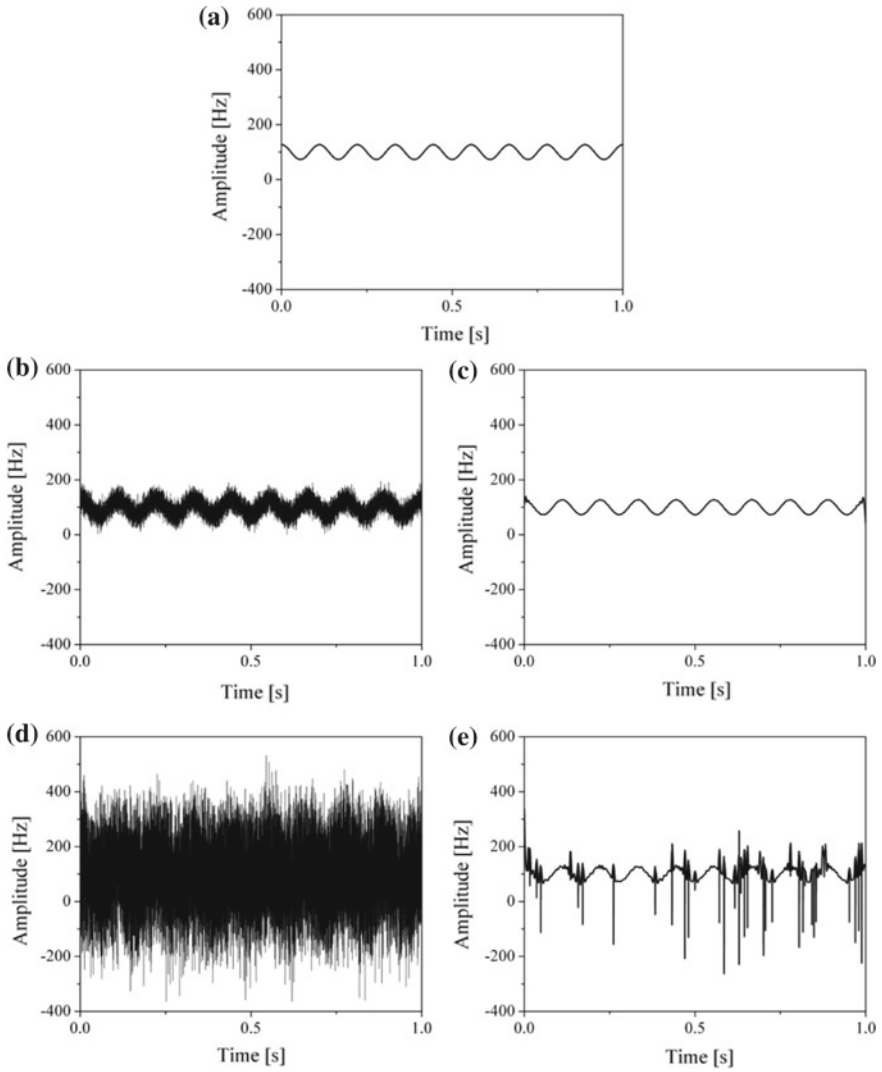


Fig. 3 **a** True IF from a FM signal, y_I , **b** estimated IF by frequency domain technique, **c** estimated IF by Fourier polynomial representation of zero crossing points technique, while SNR is 30 dB, **d** estimated IF by frequency domain technique, **e** estimated IF by Fourier polynomial representation of zero crossing points technique, while SNR is 15 dB

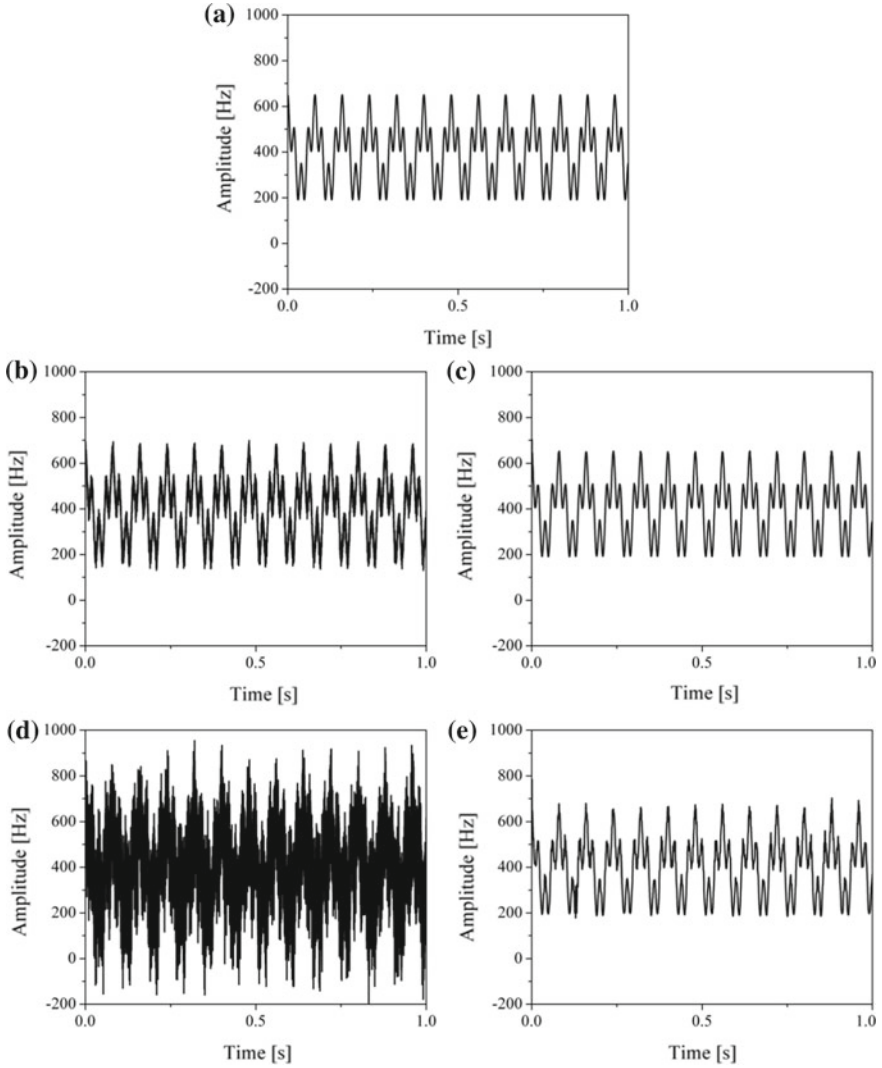


Fig. 4 **a** True IF from a FM signal, y_2 , **b** estimated IF by frequency domain technique, **c** estimated IF by Fourier polynomial representation of zero crossing points technique, while SNR is 30 dB, **d** estimated IF by frequency domain technique, **e** estimated IF by Fourier polynomial representation of zero crossing points technique, while SNR is 15 dB

3.1 Comparative Study of Frequency Domain Technique and Fourier Polynomial Representation of Zero Crossing Points Technique

A comparative study has been performed between frequency domain technique and Fourier polynomial representation of zero crossing points method which is shown in Figs. 3 and 4. The result reveals that Fourier polynomial representation of zero crossing points based technique estimates better IF than frequency domain technique while the signal is submerged in 30 dB and 15 dB white noise. Further, the result also reveals that the error incorporation in the estimated IF is less while signal-to-noise ratio becomes high. The reason behind it is that less noise contamination does not shift the zero crossing point very much. However, in case of low SNR signal, the estimated IF poses a large amount of noise, which occurs due to the formation of more number of zero crossing points than actual one. Basically, shifting of zero crossing points and more number of zero crossing form entirely new Fourier polynomial than its actual one. Thus, the coefficients of Fourier polynomial alter. This alteration in Fourier coefficients added the error in the estimated IF.

3.2 Comparative Study of Existing and Improved Fourier Polynomial Representation of Zero Crossing Points Technique

It is already shown how more number of zero crossing points are formed. Therefore, noise generation in the estimated IF is also shown in previous section. That is why an improved technique has been developed where the extra zero crossing points are averaged to form only one zero crossing point. The extra zero crossings are selected in this way while the time gap between two crossings is less than 25% of mean time gap of all zero crossings. Then those zero crossings are selected in one group and

Table 1 Comparison of MSE of estimated IF between Fourier polynomial representation of zero crossing points modeling and improved Fourier polynomial representation of zero crossing points modeling for different SNR

		$20\log_{10}(\sigma/\epsilon)$					
		15 dB		10 dB		5 dB	
		Fourier phase modeling	Improved Fourier phase modeling	Fourier phase modeling	Improved Fourier phase modeling	Fourier phase modeling	Improved Fourier phase modeling
MSE	y ₁	692.06	5.45	2724.20	9.83	7569.40	19.26
	y ₂	151.69	122.30	1431.80	352.09	15235	960.75

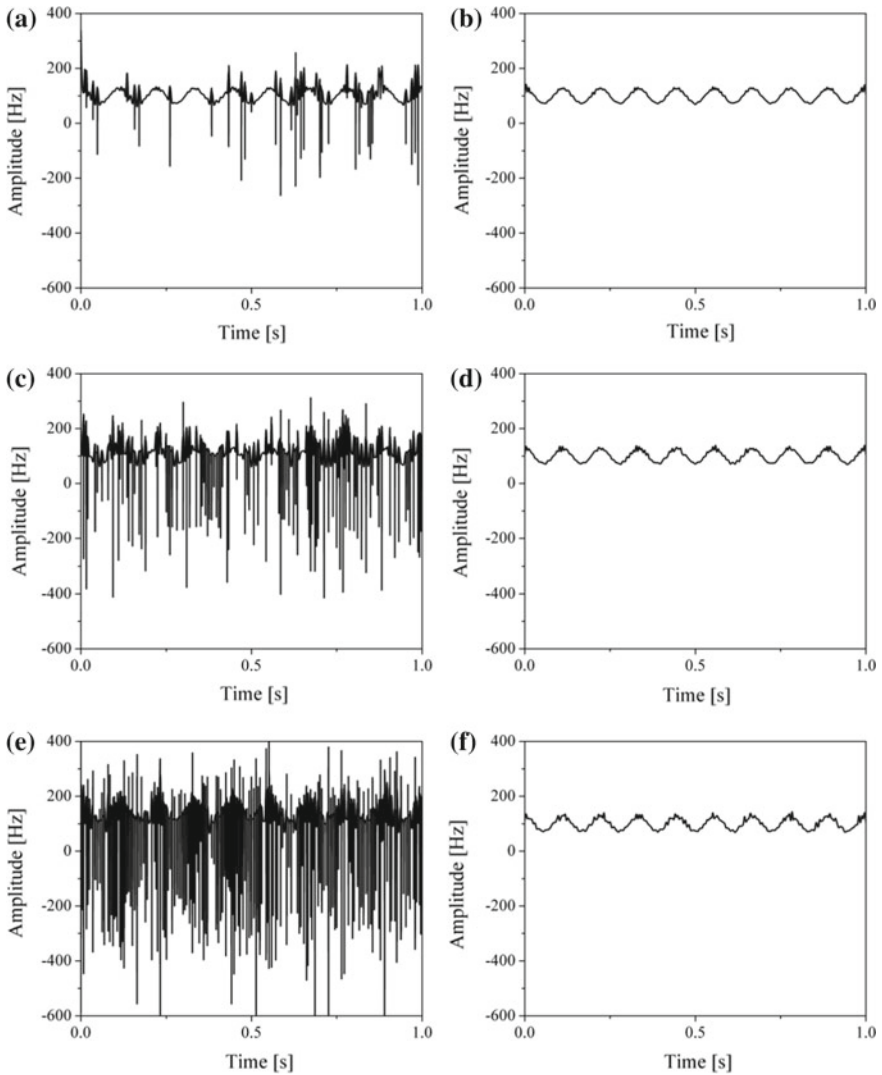


Fig. 5 Estimated IF from FM signal, y_1 based on **a** Fourier polynomial representation of zero crossing points technique, **b** improved Fourier polynomial representation of zero crossing points technique, while SNR is 15 dB; estimated IF from FM signal, y_1 based on **c** Fourier polynomial representation of zero crossing points technique, **d** improved Fourier polynomial representation of zero crossing points technique, while SNR is 10 dB; estimated IF from FM signal, y_1 based on **e** Fourier polynomial representation of zero crossing points technique, **f** improved Fourier polynomial representation of zero crossing points technique, while SNR is 5 dB

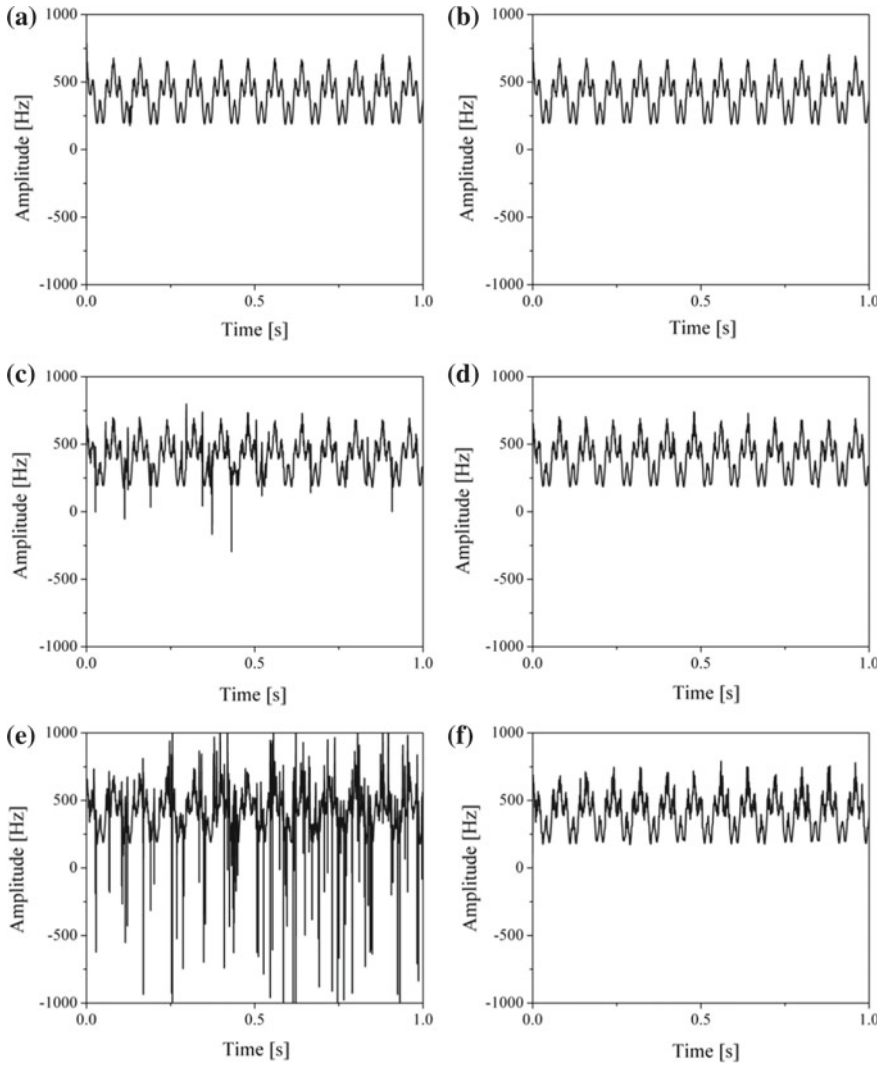


Fig. 6 Estimated IF from FM signal, y_2 based on **a** Fourier polynomial representation of zero crossing points technique, **b** improved Fourier polynomial representation of zero crossing points technique, while SNR is 15 dB; estimated IF from FM signal, y_2 based on **c** Fourier polynomial representation of zero crossing points technique, **d** improved Fourier polynomial representation of zero crossing points technique, while SNR is 10 dB; estimated IF from FM signal, y_2 based on **e** Fourier polynomial representation of zero crossing points technique, **f** improved Fourier polynomial representation of zero crossing points technique, while SNR is 5 dB

averaging has been done on that group. Using the improved zero crossing points, the IF is estimated and a comparative study has been performed on

$$t_{threshold} < 0.25t_{mean} \quad (18)$$

both the signals (y_1 and y_2) for three different noisy conditions (15, 10, and 5 dB) which are shown in Figs. 5 and 6. Further, MSE is calculated between estimated IF and true IF. Hence, the result shows that improved zero crossing points can reduce large amount of noise incorporation in the estimated IF. The fact is that averaging of the group of zero crossing points incorporates the effect of low pass filter in the estimated IF. Although the technique reduces large amount of noise, the estimated IF poses little amount of high-frequency noise due to small shifting of average point from its actual one. The Fourier polynomial representation of zero crossing points technique based estimated IF has another limitation. It creates end perturbation in the estimated IF due to Fourier series truncation error and extrapolation at the ends (Table 1).

4 Conclusions

An improved Fourier polynomial representation of zero crossing points technique has been applied to the noisy single and multi-tone FM signal to estimate the IF. The technique estimates better IF than actual Fourier polynomial representation of zero crossing points technique and frequency domain technique. The limitation of actual Fourier polynomial representation of zero crossing points technique is that it estimates noisy IF from a FM signal of low SNR. Hence, the improved technique has removed this limitation effectively and can be applied to estimate IF from a noisy signal of low SNR.

References

1. Boashash B (1992) Estimating and interpreting the instantaneous frequency of signal, parts 1 and 2. Proc IEEE 80(4):520–568
2. Cohen L (1995) Time-frequency analysis. Prentice Hall. Englewood Clis, New Jersey
3. Li Y, Gu F, Harris G et al (2005) The measurement of instantaneous angular speed. Mech Syst Signal Process 19(4):786–805
4. Yang J, Pu L, Wang Z et al (2001) Fault detection in a diesel engine by analyzing the instantaneous angular speed. Mech Syst Signal Proc 15(3):549–564
5. Girolami G, Vakman D (2002) Instantaneous frequency estimation and measurement: a quasi-local method. Meas Sci Technol 13(6):909–917
6. Lathi BP (1998) Modern digital and analog communication systems. Oxford University Press, New York

7. Gu F, Yesilyurt I, Li Y, Harris G, Ball A (2006) An investigation of the effects of measurement noise in the use of instantaneous angular speed for machine diagnosis. *Mech Syst Signal Process* 20(6):1444–1460
8. Cohen L (1989) Time-frequency distributions-a review. *Proc IEEE* 77(7):941–981
9. Kadambe S, Fave G, Bartels B (1992) A comparison of the existence of ‘cross terms’ in the Wigner distribution and the squared magnitude of the wavelet transform and the short time Fourier transform. *IEEE Trans Signal Process* 40(10):2498–2517
10. Rankine L, Mesbah M (2007) IF estimation for multi component signals using image processing techniques in the time–frequency domain. *Sig Process* 87(6):1234–1250
11. Todorovsk MI (2001) Estimation of instantaneous frequency of signals using the continuous wavelet transform. Report CE 01–07, Department of Civil Engineering, University of Southern California
12. Sejdic E, Djurovic I, Stankovic L (2008) Quantitative performance analysis of scalogram as instantaneous frequency estimator. *IEEE Trans Signal Process* 56(8):3837–3845
13. Sejdic E, Stancovic L, Dakovic M, Jiang J (2008) Instantaneous frequency estimation using the S-transform. *IEEE Trans Signal Process Lett* 15:309–312
14. Sejdic E, Djurovic I, Jiang J (2009) Time–frequency feature representation using energy concentration: an overview of recent advances. *Digit Signal Proc* 19(1):153–183
15. Lin W, Xiaofeng M (2011) An adaptative generalized S-transform for instantaneous frequency estimation. *Sig Process* 91(8):1876–1886
16. Djurovic I (2017) Estimation of sinusoidal frequency modulated signal parameters in high noise environment. *SIViP* 11:1537–1541
17. Chen VC, Li F, Ho S-S, Wechsler H (2006) Micro-Doppler effect in radar: phenomenon, model, and simulation study. *IEEE Trans Aerosp Electron Syst* 42(1):2–21
18. Barkat B, Boashash B (2003) IF estimation of FM signals in multiplicative noise. In: Boashash B (ed) *Time frequency signal analysis and processing: A comprehensive reference*. Elsevier, Amsterdam, The Netherlands, Boston, U.S, pp 457–463
19. Boudraa A (2011) Instantaneous frequency estimation of FM signals by Psi_B-energy operator. *Electron Lett* 47(10):623–624
20. Kazlauskas K, Pupeikis R (2012) A forward-backward approach for instantaneous frequency estimation of frequency modulated signals in noisy environment. *Informatica* 23(1):65–76
21. Stankovi´c L, Djurovi´c I, Stankovi´c S, Simeunovi´c M, Djukanovi´c S, Dakovi´c M (2014) Instantaneous frequency in time–frequency analysis: Enhanced concepts and performance of estimation algorithms. *Digit Signal Process* 35:1–13
22. Zhang H, Bi G, Yang W, Razul SG, See CMS (2015) IF estimation of FM signals based on time frequency image. *IEEE Trans Aerosp Electron Syst* 51(1):326–343
23. Khan NA, Boashash B (2016) Multi-component instantaneous frequency estimation using locally adaptive directional time frequency distributions. *Int J Adapt Control Signal Process* 30:429–442
24. Yu S, Zhang X (2010) A data processing method for determining instantaneous angular speed and acceleration of crankshaft in an aircraft engine-propeller system using a magnetic encoder. *Mech Syst Signal Process* 24(4):1032–1048

Combustion Event Detection in a Single Cylinder Diesel Engine by Analysis of Sound Signal Recorded by Android Mobile



Sankar Kumar Roy

Abstract Combustion event detection is an important issue in internal combustion engine. The combustion is mostly detected by measurement of pressure by a pressure sensor which is mounted in cylinder head. However, the cost of pressure sensor is very high. Therefore, an effort has been made to detect the combustion event in a diesel engine by analysis of sound signal recorded by android mobile. The sound signal carries various frequencies. Therefore, an algorithm based on wavelet packet transform (WPT) has been developed to detect the combustion event in a single cylinder diesel engine.

Keywords Diesel engine · Sound signal · Android mobile phone

1 Introduction

Combustion and combustion-related parameters detection in an internal combustion (IC) engine is always an important concern as the power output relies on it [1]. Detection of combustion is mainly done by measuring the in-cylinder pressure by a pressure sensor [2, 3]. However, the cost of pressure sensor is very high and its installation on the cylinder head is a complicated exercise. Therefore, researchers are using alternate signals such as vibration signal [4–6], speed signal [7–15], acoustic signal [16–18] for detecting the combustion event. Based on these signals, standard monitoring systems have already been developed for detection and analysis of combustion event. These signals are mainly measured by standard sensors like accelerometer, optical encoder, hall effect sensor, microphone, etc. However, all of these sensors requires special mounting system for monitoring the in-cylinder combustion or pressure. Researchers have tried to reconstruct in-cylinder pressure by applying different techniques such as cepstral de-convolution technique [3], time domain smoothing technique [4], cyclostationary approach [5], inverse filtering tech-

S. K. Roy (✉)

Mechanical Engineering Department, National Institute Technology Patna, Patna 800005, Bihar, India

e-mail: sankar.roy@nitp.ac.in

© Springer Nature Singapore Pte Ltd. 2019

M. Kumar et al. (eds.), *Advances in Interdisciplinary Engineering*, Lecture Notes in Mechanical Engineering, https://doi.org/10.1007/978-981-13-6577-5_13

121

nique [6] on the vibration signal. Apart from vibration signal, researchers have also used speed fluctuations [7–9] to estimate the in-cylinder pressure. Besides pressure reconstruction, vibration signal and speed signal are also used for monitoring the in-cylinder combustion [3, 10–18]. Author [15] has earlier used instantaneous angular speed for combustion detection in four-stroke single cylinder gasoline engine. Recently, acoustic signal analysis has got tremendous application in monitoring purposes. The idea of acoustic signal analysis is that any change in the system will directly reflect on the intensity of sound signal. Researchers have used acoustic signal to find out combustion in IC engine [16–18]. Kaminsky et al. [16] have predicted the in-cylinder pressure variation through the analysis of sound signal by nonlinear multidimensional method. Recently, Delvecchio et al. [18] have detailed various ways of condition monitoring using acoustic signal. In their paper, they have mentioned that the sound signal captured from the IC engine is a combination of combustion, mechanical, and aerodynamic noise signals. Hence, acoustic signal needs rigorous signal processing technique to detect the combustion.

Recently, due to technological development, Android mobile phone becomes less costly and is used for multiple applications. Nowadays, it is also carried by most of the people and it can record the sound with sampling frequency 44.1 kHz. This sampling frequency allows to retain combustion frequency, rotational frequency, and its harmonics of an IC engine in the recorded sound signal. Recently, few researchers have found potentiality of the sound signal recorded by the Android mobile and used to detect fault in rolling element bearing [19, 20]. Siegel et al. [21] have used mobile-recorded sound signal to detect misfire in four-cylinder engine by applying machine learning technique. Hence, this sound signal has a lot of scope for monitoring various machineries. Therefore, the objective of the paper is to detect each combustion event in a four-stroke single cylinder diesel engine by analysis of sound signal recorded by an Android mobile. In the paper, the hypothesis is that the sound intensity will be higher during combustion rather than suction, compression, and exhaust strokes. Therefore, successive sound ratios of recorded sound signal has been measured and analyzed to execute the objective effectively.

2 Theory

2.1 Hilbert Transform

Hilbert transform [22] is a mathematical technique where a signal $x(t)$ is transformed as

$$H[x(t)] = x(t) * \frac{1}{\pi t} = \frac{1}{\pi} \int_{-\infty}^{\infty} \frac{x(\tau)}{t - \tau} d\tau \quad (1)$$

The technique is mainly a convolution of two signals $x(t)$ and $1/\pi t$, respectively. As a result, the signal is shifted by a phase of 90° . Hence, the signal $x(t)$ can be further analytically represented as

$$z(t) = x(t) + jH[x(t)] = A(t)e^{j\phi(t)} \tag{2}$$

where $A(t)$ and $\phi(t)$ are amplitude and phase modulated part, respectively. Further amplitude demodulation is done to find out amplitude modulated part $A(t)$

$$A(t) = \sqrt{\{x(t)\}^2 + \{H[x(t)]\}^2} \tag{3}$$

$A(t)$ is also called envelope of the signal.

2.2 Wavelet Packet Transform

Wavelet packet transform (WPT) [23, 24] is an extension of discrete wavelet transform (DWT), where a signal is decomposed into sub-signals of different frequency band. In WPT, the wavelet function can be written as

$$W_{j,k}^n(t) = 2^{j/2} W^n(2^j t - k) \tag{4}$$

where j, k are two integers denoting scale and translation parameters. While, j and k are zero then scaling function $\phi(t)$ and mother wavelet $\psi(t)$ can be defined as

$$W_{0,0}^0(t) = \phi(t) \tag{5}$$

$$W_{0,0}^1(t) = \psi(t) \tag{6}$$

while, $n = 2, 3, \dots$, the wavelet packet functions are defined as

$$W^{2n}(t) = \sqrt{2} \sum_{k=1}^N h(k) W_{1,k}^n(2t - k) \tag{7}$$

$$W^{2n+1}(t) = \sqrt{2} \sum_{k=1}^N g(k) W_{1,k}^n(2t - k) \tag{8}$$

k is varying by $\{k = 1, 2, \dots, 2^n, N = 2^n\}$ and N is the length of the signal, where $h(k)$ and $g(k)$ are high-pass and low-pass filter defined in terms of inner product as

$$h(k) = 1/\sqrt{2} \langle \phi(t), \phi(2t - k) \rangle \tag{9}$$

$$g(k) = 1/\sqrt{2}\langle\psi(t), \psi(2t - k)\rangle \quad (10)$$

where $\langle \cdot, \cdot \rangle$ are addressing the inner product. Further, $h(k)$ and $g(k)$ are orthogonal and expressed through this relationship as

$$g(k) = (-1)^k h(1 - k) \quad (11)$$

The wavelet packet coefficients are achieved by the inner product of signal $x(t)$ and wavelet packet function.

$$C_{i,j}^n = \langle x, W_{j,k}^n \rangle = \int_{-\infty}^{\infty} x(t) W_{i,j}^n(t) dt \quad (12)$$

Hence, at j th level, a signal $x(t)$ will be decomposed into 2^j packets. The wavelet packet tree has been formed with the binary order $n = 1, 2, \dots, 2^j$. Hence, each level, the sampling frequency decreases by 2. At j th level, p th packet coefficients will be of the frequency band from $(p - 1)*Fs/2^{j+1}$ to $p*Fs/2^{j+1}$. Hence, a different passband signal can be reconstructed by making the coefficients of undesired nodes to zero. Thus, the WPT has been utilized for signal filtering [24, 25].

3 Experimental Setup

The sound signal is captured from a four-stroke, single cylinder, horizontal Diesel engine with rated power 10 HP at 500 RPM, which is located in internal combustion engine laboratory at NIT Patna. The engine is made by UNI-INSTAS. The engine is water cooled, where loading on the engine can be applied through rope brake dynamometer. An Android mobile with specification (Samsung J5, Android 5.1 with quad-core 1.2 GHz cortex-A53) is used to record the sound by its in-built sound recorder from 30 cm distance from the engine (Fig. 1).

4 Result and Discussion

Sound signal has been acquired by the Android mobile phone in Wma format. Further, this has been converted into WAV format and it has been analyzed in MatLab environment. Figure 2a shows the sound signal recorded by the Android mobile phone during no load and 500 RPM running speed. Therefore, the combustion frequency and running frequency of the diesel engine are 4.16 Hz and 8.32 Hz, respectively. Figure 2b shows frequency spectrum of the recorded sound signal. The frequency spectrum shows harmonics of rotational frequency and combustion frequency. However, amplitude of 1st combustion frequency and rotational frequency are very much



Fig. 1 Single cylinder diesel engine

low. Therefore, the signal needs alternative signal processing technique to extract combustion frequency rather than direct fast Fourier transform.

Hence, envelope of the sound signal has been extracted, which is shown in Fig. 3a. Further, frequency spectrum of envelope shows the combustion, rotational frequency, and its harmonics, which is shown in Fig. 3b.

Although the combustion frequency is detected, yet the detection of each combustion event is an important issue for online monitoring. Therefore, the envelope is low pass filtered using WPT. Daubechies10 wavelet has been used for the decomposition as it creates no redundancies [24]. The filtered envelope signal is shown in Fig. 4. However, the filtered signal was found not able to detect the occurrence of each combustion. As the envelope is unable to detect each combustion, the sound signal is analyzed by another methodology. Hypothesis utilized in the paper is that the amplitude variation of sound signal during combustion is generally higher as compared to other strokes like suction, expansion, and exhaust. Therefore, successive sound ratios will be higher during combustion stroke as compared to other strokes. Hence, the sound signal is already with zero mean. Therefore, an absolute value (slightly more than the minimum value of the signal) has been added with this signal to obtain

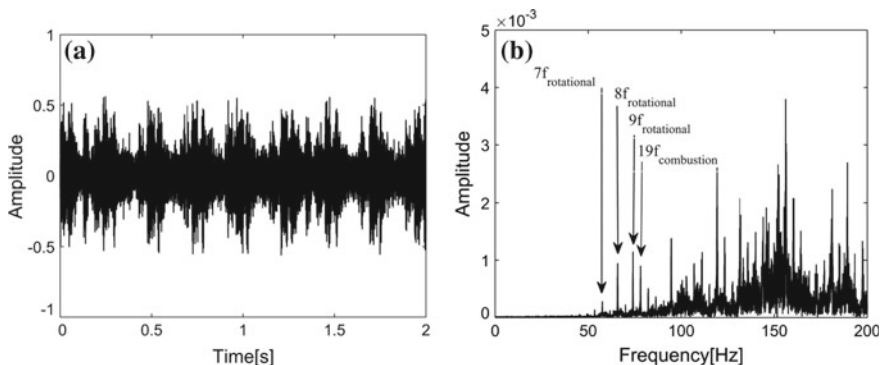


Fig. 2 **a** Recorded sound signal by Android mobile phone; **b** Frequency spectrum of the sound signal

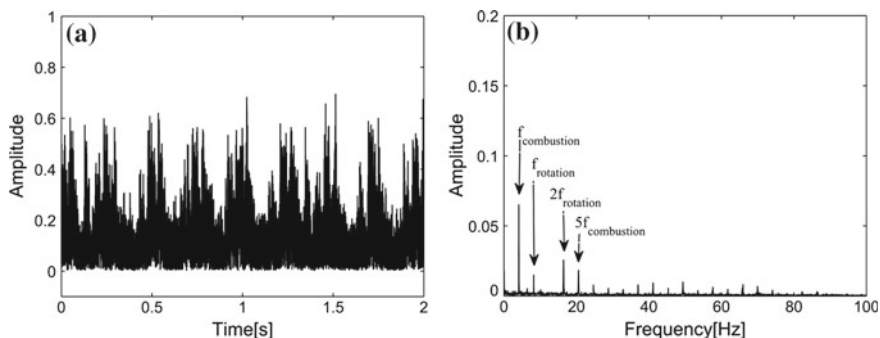


Fig. 3 **a** Envelope of the recorded sound signal; **b** Frequency spectrum of envelope signal

the sound signal with positive mean. Further, ratio of two successive points of the entire sound signal are calculated as successive sound ratios. The reason for making the sound signal with positive mean is that the calculated successive sound ratios become real. The i th successive sound ratio (SSR) for recorded sound signal (S) can be written as

$$SSR = \frac{S_{i+1}}{S_i} \tag{12}$$

The successive sound ratios measured from recorded sound signal are low pass filtered by WPT. The filtered successive sound ratios have been shown in Fig. 5. It shows that the peaks in the filtered successive sound ratios are appeared with around 0.243 s time gap. This time gap is an inverse of combustion frequency 4.16 Hz. Thus, the filtered successive sound ratios can detect the occurrence of each combustion effectively. Hence, WPT based low pass filtering of envelope and successive sound ratios have been performed through few steps. First, envelope and successive sound

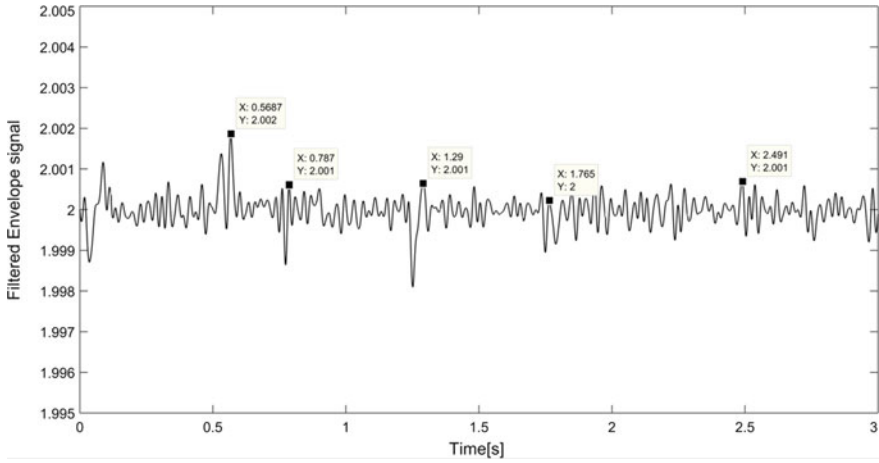


Fig. 4 Filtered envelope of sound signal

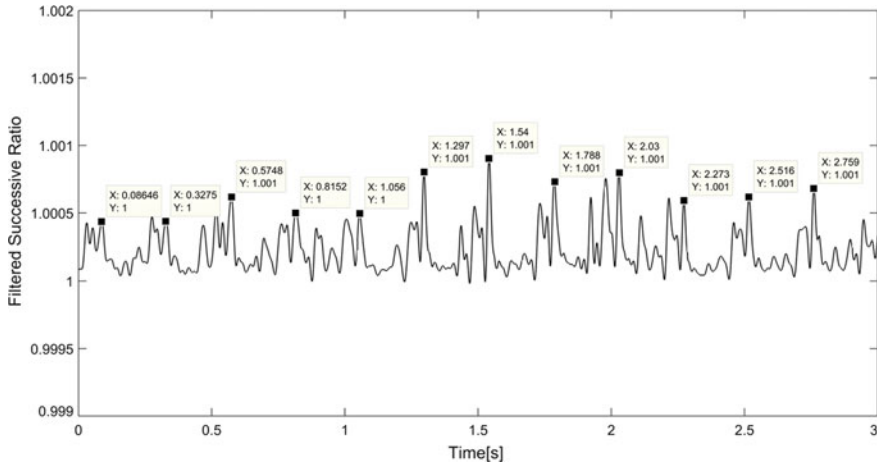


Fig. 5 Filtered successive ratio of sound signal

ratios are decomposed up to ninth level using WPT. Thus, p th node at ninth level of WPT tree contains the frequency band from $(p - 1) * 44100/2^{9+1}$ Hz to $p * 44100/29+1$ Hz. Hence, the frequency content of the first node is 0–43 Hz. As the first node contains less harmonics. Both the signals (envelope and successive sound ratios) have been reconstructed by setting the node’s coefficients to zero except first node. Thus, the frequency content of filtered signals (envelope and successive sound ratios) become 0–43 Hz.

5 Conclusion

This paper has detected the combustion event in a single cylinder diesel engine by analysis of sound signal recorded by Android mobile. Hence, the sound signal has been utilized to detect the combustion quantitatively. WPT-based filtering of sound signal's envelope is unable to detect each combustion event. Therefore, successive sound ratios have been combined with WPT to detect each combustion event efficiently.

References

1. Heywood JB (1988) Internal combustion engine fundamentals. McGraw-Hill, New York
2. Mobley C (1999) Non-intrusive in-cylinder pressure measurement of internal combustion engines. SAE Paper, 1999-01-0544
3. Lyon RH, DeJong RG (1984) Design of a high-level diagnostic system. *J Vib Acoust* 106:17–21
4. Gao Y, Randall RB (1999) Reconstruction of diesel engine cylinder pressure using a time domain smoothing technique. *Mech Syst Signal Process* 13:709–722
5. Antoni J, Daniere J, Guillet F (2002) Effective vibration analysis of IC engines using cyclostationarity; A methodology for condition monitoring—part 1. *J Sound Vib* 257:815–837
6. Antoni J, Daniere J, Guillet F (2002) Effective vibration analysis of IC engines using cyclostationarity; A methodology for condition monitoring—Part 2. *J Sound Vib* 257:839–856
7. Connolly FT, Yagle AE (1992) Modeling and identification of the combustion pressure process in internal combustion engines using engine speed fluctuations. In: American society of mechanical engineers, dynamic systems and control division, vol 44. Anaheim, CA, pp 191–206
8. Brand D, Onder C, Guzzella L (2005) Estimation of the instantaneous in-cylinder pressure for control purposes using crankshaft angular velocity. In Proceedings: SAE world congress paper 2005-01-0228, (2005)
9. Moro D, Cavina N, Ponti F (2002) In-cylinder pressure reconstruction based on instantaneous engine speed signal. *J Eng Gas Turbines Power* 124:220–225
10. Yang J, Pu L, Wang Z, Zhou Y, Yan X (2001) Fault detection in a diesel engine by analysing the instantaneous angular speed. *Mech Syst Signal Process* 15:549–564
11. Rizzoni G (1989) Diagnosis-of individual cylinder misfires by signature analysis of crankshaft speed fluctuations. SAE Paper No. 890884
12. Ponti F (2008) Instantaneous engine speed time-frequency analysis for onboard misfire detection and cylinder isolation in a V12 high-performance engine. *J Eng Gas Turbines Power* 130:1–9
13. Charles P, Sinha JK, Gu F, Lidstone L, Ball AD (2009) Detecting the crankshaft torsional vibration of diesel engines for combustion related diagnosis. *J Sound Vib* 321:1171–1185
14. Charles P, Sinha JK, Gu F, Ball AD (2010) Application of novel polar representation method for monitoring minor engine condition variations. *Mech Syst Signal Process* 24:841–843
15. Roy SK, Mohanty AR (2017) Use of rotary optical encoder for firing detection in a spark ignition engine. *Measurement* 98:60–67
16. Kamin'ski T, Wendeker M, Urbanowicz K, Litak G (2004) Combustion process in a spark ignition engine: Dynam. Noise level estimation. *Chaos*, 14, 401–406 (2004)
17. Jeong-Guon I, Kim HJ, Lee SH, Shinoda K (2009) Prediction of intake noise of an automotive engine in run-up condition. *Appl Acoust* 70(2):347–355
18. Delvecchio S, Bonfiglio P, Pompoli F (2018) Vibro-acoustic condition monitoring of internal combustion engines: a critical review of existing techniques. *Mech Syst Signal Process* 99:661–683

19. Irawan YS, Suyono H (2014) Bearing damage detection based on sound signal. *Appl Mech Mater* 548–549:698–702
20. Orman, M., Rzeszucinski, P., Tkaczyk, A., Krishnamoorthi, K., Pinto, C., Sulowicz, M.: Bearing fault detection with the use of acoustic signals recorded by a hand held mobile phone. In: second international conference on condition assessment techniques in electrical systems, IEEE CATCON 2015, pp. 252–256, Bangaluru (2015)
21. Siegel J, Kumar S, Ehrenberg I, Sarma S (2016) Engine misfire detection with pervasive mobile audio. In: Berendt B, Bringmann B, Fromont E, Garringa G, Miettinen P, Tatti N, Tresp V (eds) *Machine learning and knowledge discovery in databases. ECML PKDD 2016*. Springer, Riva Del Garda, Italy, pp 226–241
22. Mohanty, A.R.: *Machinery Condition Monitoring: Principles and Practices*, 1st edn, CRC Press (2014)
23. Coifman RR, Meyer Y, Quake S, Wickerhauser MV (1994) Signal processing and compression with wavelet packets. In: Byrnes JS, Byrnes JL, Hargreaves KA, Berry K (Eds.), *Wavelets and their applications*, pp 363–379
24. Fan X, Zuo MJ (2006) Gearbox fault detection using Hilbert and wavelet packet transform. *Mech Syst Signal Process* 20(4):966–982
25. Vong CM, Wong PK (2011) Engine ignition signal diagnosis with wavelet packet transform and multi-class least squares support vector machines. *Expert Syst Appl* 38(7):8563–8570

Separation of Nitrogen from Combustion Using Pressure Swing Adsorption (PSA) Technique and Incorporating Zeolites



Yogya Khanna, Shivam Puri, Prakhar Verma, Dasaradhi Putta and Preeti Joshi

Abstract The main problem nowadays for industries to handle is the large amount of emissions that come out of the large chimneys from their boiler plants. Though it is an important part of combustion to emit exhaust, this causes the environment to be polluted and thus also causes harm to not only the life of people present in the industry but also to the water bodies around the industry. The pollution level in New Delhi 2015 was a record-breaking 989 ppm; about 600 ppm above the danger limit. Delhi in the year 2016 was named as one of the most polluted city on the planet. These industries not only cause the air to pollute but also the water also which is a needful form of food for many creatures. Keeping all this in mind the main aim of the project that we put forward is the reduction of nitrogen constituent in the air present around us by the use of pressure swing adsorption method. In this method, we would adsorb nitrogen present in the air which comes in from an inlet hose and adsorbed in the first chamber with the help of zeolites. For the adsorption of other harmful gases such as carbon monoxide and SO_x , we have also incorporated two types of zeolites (5A and 13X); one which adsorbs the light particles of NO_x and other which adsorbs the heavy particles of sulfur and some other harmful gases. The main aim of the project is to produce a model that adsorbs nitrogen separating it out from the oxygen so that it can be sent in for better combustion in boilers.

Keywords SO_x · NO_x · Zeolite 5A · Zeolite 13X · Adsorption · Pressure swing adsorption

1 Introduction

Any combustion process needs oxygen to burn fuel and produce thermal energy in the form of steam in a boiler. This thermal energy is then converted to electrical energy through steam turbines in thermal power plants. The ambient air is generally used after preheating to provide required quantity of oxygen for combustion. As we know,

Y. Khanna (✉) · S. Puri · P. Verma · D. Putta · P. Joshi
Amity School of Engineering and Technology, Amity University, Noida, Uttar Pradesh, India
e-mail: yogyakhanna@gmail.com

© Springer Nature Singapore Pte Ltd. 2019
M. Kumar et al. (eds.), *Advances in Interdisciplinary Engineering*, Lecture Notes in Mechanical Engineering, https://doi.org/10.1007/978-981-13-6577-5_14

air consists of more than 70% of nitrogen which does not take part in combustion. Rather presence of nitrogen has several adverse effects like producing toxic gaseous pollutant in the form of nitrogen oxides besides causing appreciable heat losses in the boiler furnace.

1.1 Pressure Swing Adsorption

Pressure swing adsorption (PSA) is an innovation used to isolate a few gas animal types from a blend of gases under strain as indicated by the species' atomic qualities and liking for an adsorbent material. It works at close surrounding temperatures and contrasts fundamentally from cryogenic refining systems of gas detachment. Particular adsorptive materials (e.g., zeolites, initiated carbon, atomic strainers, and so forth) are utilized as a trap, specially adsorbing the objective gas species at high weight. The procedure at that point swings to low strain to desorb the adsorbed material [1].

Besides their capacity to separate various gases, adsorbents for PSA frameworks are normally exceptionally permeable materials picked on account of their huge particular surface regions. Normal adsorbents are actuated carbon, silica gel, alumina, sap, and zeolite. In spite of the fact that the gas adsorbed on these surfaces may comprise a layer just as a single or at most a couple of particles thick, surface territories of a few hundred square meters for each gram give power to the adsorption of a critical bit of the adsorbent's weight in gas. Notwithstanding their selectivity for various gases, zeolites and a few sorts of actuated carbon called carbon atomic sifters may use their subatomic strainer qualities to avoid a few gas particles from their structure in light of the extent of the atoms, along these lines limiting the capacity of the bigger atoms to be adsorbed.

Rege et al. concluded in his study that it is important to pretreat the zeolites before going in for any process such as pressure swing or vacuum swing adsorption so that

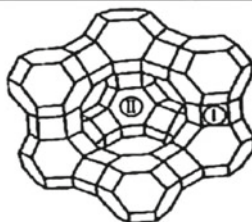
Fig. 1 Zeolite properties of zeolite 5A

Chemical Name	$\text{Na}_{12}[(\text{AlO}_2)_{12}(\text{SiO}_2)_{12}] \cdot 27\text{H}_2\text{O}$
Pore Diameter	5Å
Mesopore Volume	0.062 cm ³ /g
Micropore Volume	0.176 cm ³ /g
Surface Area	571 m ² /g
Mass of Crushed Sample	2.046 g



Fig. 2 Zeolite properties of zeolite 13X

Chemical Name	$\text{Na}_{56}[(\text{AlO}_2)_{56}(\text{SiO}_2)_{106}] \cdot \text{H}_2\text{O}$
Pore Diameter	~8Å
Mesopore Volume	0.165 cm^3/g
Micropore Volume	0.17 cm^3/g
Langmuir Surface Area	571 m^2/g
Mass of Pellet Sample	2.37 g
Mass of Crushed Sample	2.49 g



these contaminants do not affect their functionality and also give the best results that are desired [2] (Figs. 1 and 2).

2 Methodology

The main zeolites used for our project are zeolite 5A and 13X [3]. We have a cylinder which is made up of mild steel with two perforated sheet pairs in it. These sheets are put in equal distances and at a gap of 50 mm. Zeolites would be poured between these two sheets. The compressor is switched on and air is passed through via a ball valve. This air then passes through the first zeolite layer of zeolite 5A and then zeolite 13X. The layers of zeolites are arranged between two perforated sheets placed at a distance of 50 mm and used in two pairs. The air is then passed through the O_2 sensor which then gives the amount of oxygen present and thus helps us to know the decrease in nitrogen in the air [4]. We calculated the amount of zeolites that should be enough to be adsorbed by 1 kg of zeolites and then we calculated the total volume that could be filled by the zeolites between the perforated sheets. We observed that the volume that could be filled by the area of the perforated sheets is more than what we needed which was a plus point. We filled the volume with 5 kg zeolites for both 5A and 13X and observed the increase in amount of oxygen at the outlet.

According to Karimi Abolfazl et al., vacuum swing adsorption method is developed to be used for separating the components unnecessary and also components that need to be purified [5]. The VSA method is known to be producing 15 ton/day oxygen at a time as compared to PSA apparatus and is also much more economical to its counterpart as for 40 ton/day to the cryogenic distillation method [6]. According to Ehsan Javadi Shokroo et al., there is likewise temperature swing adsorption strategy that can be utilized for air cleansing, and as a result of their expectation in

adsorption motor. Zeolites 5A and 13X are the most generally utilized adsorbents in air partition for oxygen creation [7].

The novel properties of zeolites are begun from this reality that their surfaces are shaped with contrarily charged oxides. Also, the nearness of confined cations over their surface structure is another explanation behind their uniqueness. Regardless of knowing the selectivity of O_2/N_2 by zeolite, there was no advance on account of air detachment by adsorption process until 1960 [8], even after the innovation of synthetic zeolites 5A and 13X and PSA cycles. The main problem outlined for VSA system not to be used in spite of its economical outputs is that it operates at near ambient pressure and temperature which is easy to achieve but the output is fairly inaccurate [9–13]. This method differs from pressure swing adsorption as in PSA zeolites to be used need to adsorb at a minimum temperature of 6 bar or above.

Important efforts have been given to the development of technologies that specifically address carbon capture, that is, to the separation of carbon dioxide from flue gas to avoid its release into the atmosphere [14–16]. The utilization of absorption via alkanolamines has been one solution offered to deal with this problem. Absorption via alkanolamines is well known and a commercially established technology in the industry of natural gas sweetening.

3 Calculations

See Fig. 3.

1. Thickness of the Shell

$$T_s = \frac{P * R}{(2 * S * E) + (0.4 * P)}$$

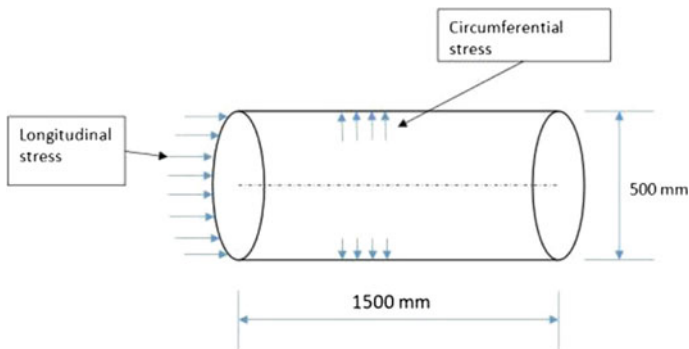


Fig. 3 Diagram for calculations of thickness

Parameters are as follows:

Shell side pressure	$P = 20 \text{ bar} = 2 \text{ MPa}$
Inside radius of shell	$R = 250 \text{ mm}$
Max. allowable stresses of shell material E250	$S = \text{yield stress/FOS}$
Yield stress of E250 is 250, FOS is 3–5	$250/4 = 62.5 \text{ MPa}$
Consideration, joint efficiency of shell	$E = 1$

2. For Longitudinal Stress

$$\begin{aligned}
 T_s &= \frac{P * R}{(2 * S * E) + (0.4 * P)} \\
 &= 2 * 250 / ((2 * 62.5 * 1) \\
 &\quad + (0.4 * 2)) t_s = 3.97 \text{ mm or } 4 \text{ mm}
 \end{aligned}$$

3. For Circumferential Stresses

$$\begin{aligned}
 T_s &= \frac{P * R}{(2 * S * E) + (0.6 * P)} \\
 &= 2 * 250 / ((62.5 * 1) \\
 &\quad + (0.6 * 2)) t_s = 8.16 \text{ mm}
 \end{aligned}$$

Therefore, the thickness of the shell was assumed to be 10 mm including all the tolerances for the pressure vessel.

4 Design Report and Fabrication

This is the schematic figure of the final design that we have made for our project. Basically, we had to fabricate a pressure vessel that could take up to a pressure of 25 bar and also hold the pressure for us to accurately find out the readings. We had to fabricate the pressure shell or the main shell separately and machine the dish ends separately [17]. We first fabricated the dish ends using dish end formers and using material 6013 mild steel of thickness 10 mm. We then fabricated the cylindrical shell according to our requirement from Enviropol engineering factory where they provided us with the metal and filler material for the welding procedure [18]. We then welded the perforated sheets inside the shell at equal distances. There were two sheets welded for each zeolite. These sheets were cut first on a standard cutter and

then the 2 mm thick sheets were welded. We then finally welded the whole section together and checked for any leakage that may have been caused (Figs. 4, 5 and 6).

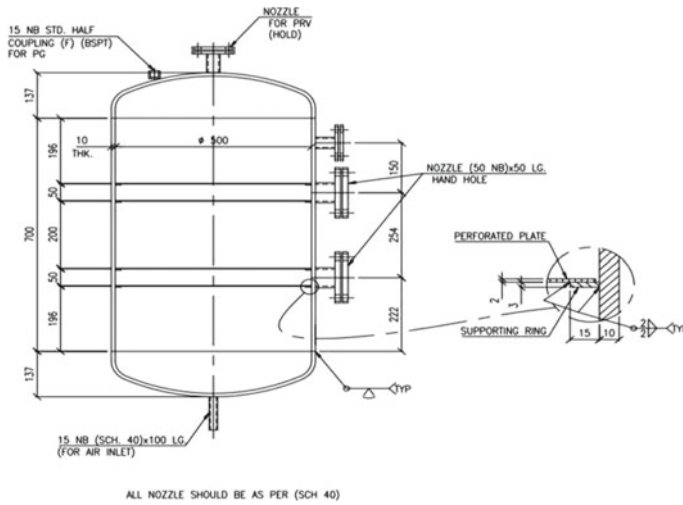


Fig. 4 Schematic diagram of the design



Fig. 5 Machined cylindrical vessel



Fig. 6 Cylindrical pressure vessel with color-coded paint

5 Testing and Results

We were successful in machining and also finding out the observations which help us prove the increase in oxygen is possible in such a cheaper way without much of expensive machinery.

At 3 kg zeolites (Fig. 7).

These are the readings for 3 kg of zeolites filled inside the perforated trays for adsorption. As you can see when we increase the pressure, the adsorption rate of zeolites increases, and hence it adsorbs more nitrogen and gives out more oxygen. We can see that when we added 3 kg zeolites, the amount of oxygen increased would be about 29%. This increase in oxygen is followed by the decrease in nitrogen as well.

At 5 kg zeolites (Fig. 8).

When we increased the concentration of zeolites, the adsorption rate increased even further and we can see by the graph that an amount of 40% increase in oxygen

At 3 Kg Zeolites

S.no	Pressure (In bars)	Level of oxygen at start	Level after adsorption	% increase in oxygen
1	6	17.9	21.7	21.22905028
2	7	17.9	22.6	26.25698324
3	8	17.9	23.1	29.05027933

Fig. 7 Readings with 3 kg zeolites in the vessel

At 5kg zeolites

S.no	Pressure (In bars)	Level of oxygen at start	Level after adsorption	% increase in oxygen
1	6	17.9	22.8	27.37
2	7	17.9	23.7	32.40
3	8	17.9	25.2	40.78

Fig. 8 Readings with 5 kg zeolites in the vessel

concentration. Clearly, by the above graphs, we can say that a higher amount of oxygen can be sent into the combustion chamber for better and a much cleaner combustion. The CO₂ emissions from major industries, such as power generation and steel and cement industries, cause serious global environment problems and their mitigation is urgently needed. Several technologies are being evaluated to capture CO₂ from flue gases, among which absorption and adsorption are the leading candidates [19]. It should be noted, however, that zeolites are very sensitive to water present in flue gas which is very strongly adsorbed and difficult to remove. Zeolite 13X has a higher working mass capacity for CO₂ than zeolite 5A [20, 21]. By these results, we are hoping that the boiler plants and thermal power plants will have reduced emissions which would also decrease the amount of pollutants emitted after combustion.

6 Conclusions

In this project, we have chosen a lot of acronyms and the biggest decision for us was to select the use of zeolites for the adsorption of nitrogen gas onto it. This step was taken after researching the various properties of the zeolites and how it would perform under various temperature readings and other environmental factors. Another mechanical aspect that we had to choose was the use of which type of weld that would be suitable for the design and fabrication of the model. We ended up manufacturing the model by using arc welding using the filler material as 6021 and the whole body to be IS 2061 material grade of mild steel [18] (Figs. 9 and 10).

The increase in oxygen has been monitored with the help of oxygen sensors [18]. The PSA method is a little expensive and thus we decided to use the adsorption power of zeolites for a better adsorption rate and cheaper method. This method is helpful for us and has given the results which we wanted to reduce NO_x production. We machined a shell of IS: 2061 Grade using arc welding and using 6021 filler material. The readings were taken in three different pressures and the initial content of oxygen is taken as measured.

We see a 40% increase in the oxygen level of the compressed air passed and also the design of the apparatus was successfully made as it could withstand all the pressure that was given in the chamber.

As a future prospect, we have two vital aims:

Fig. 9 Graph for increase in oxygen for 3 kg zeolites

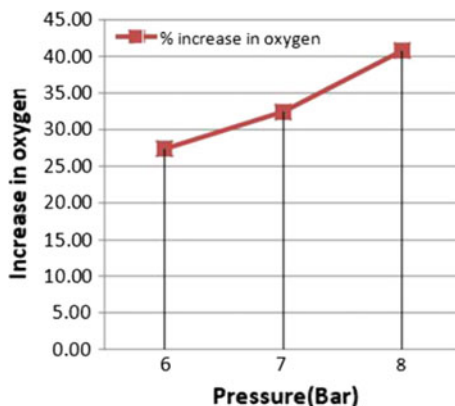
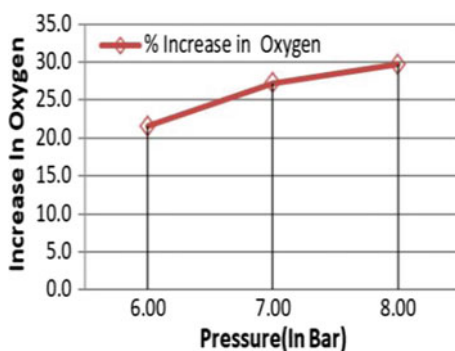


Fig. 10 Graph for increase in oxygen for 5 kg zeolites



To make the project much more compact: The current model weighs approximately 190 kg which is a lot considering the amount of pressure that has to be absorbed by the vessel. We plan to search alternate materials that could work at pressures as high as 6 bar and not flex [22].

To study the various properties of fuels used in boilers and to use that knowledge to make the vessel more efficient in its working.

References

1. University of Romania (2004) Study of sulphur adsorption on γ zeolite
2. Chou CT, Chen CY (2004) Carbon dioxide recovery by vacuum swing adsorption. *Sep Purif Technol* 39:51–65
3. Hamed HH, The use of zeolite 5A for adsorption of nitrogen
4. Grande CA (2012) Advances in pressure swing adsorption for gas separation. *ISRN Chem Eng* 2012:13 (Article ID 982934). <https://doi.org/10.5402/2012/982934>
5. Jee JG, Jung JH, Lee JW, Suh SH, Lee CH (2006) Comparison of vacuum swing adsorption process for air separation using zeolite 10x and 13x. *J Revue Roumaine de Chimie* 51(11):1095–1108

6. Ruthven DM, Farooq S, Knaebel KS (1994) Pressure swing adsorption. VCH Publications, Inc, New York
7. Santos JC, Magalhaes FD, Mendes A (2008) Contamination of zeolites used in oxygen production by PSA: effects of water and carbon dioxide. *Ind Eng Chem Res* 47:6197–6203
8. Rege SU, Yang RT, Qian KY, Buzanowski MA (2001) Air-prepurification by pressure swing adsorption using single/layered beds. *Chem Eng Sci* 56:2745
9. Xiao P, Zhang J, Webley P, Li G, Singh R, Todd R (2008) Capture of CO₂ from flue gas streams with zeolite 13X by vacuum-pressure swing adsorption. *Adsorption* 14:575–582
10. Cavenati S, Grande CA, Rodrigues AE (2004) Adsorption equilibrium of methane, carbon dioxide, and nitrogen on zeolite 13X at high pressures. *J Chem Eng Data* 49(4):1095–1101
11. Rutherford SW, Do DD (2000) Adsorption dynamics of carbon dioxide on a carbon molecular sieve 5A. *Carbon* 38:1339–1350
12. Koltsakis GC, Stamatelos AM Catalytic automotive exhaust aftertreatment; PH: S0360-1285(97)00003-8: Laboratory of Applied Thermodynamics, Aristotle University Thessaloniki, Thessaloniki, Greece
13. Koltsakis GC, Stamatelos AM (1995) Detection of automotive catalyst failure by use of on-board diagnostics. *Proc Inst Mech Eng Part D J Autom Eng* 209:171–182
14. Melissa Magee H, Nitrogen gas adsorption in zeolites 13X and 5A, Walla Walla University, College Place, WA
15. Enviropol Engineers, Cylinder machining and welding equipment providers for our project
16. Liu Z, Grande CA, Li P, Yu J, Rodriguez AE (2011) Adsorption and desorption of carbon dioxide and nitrogen on zeolite 5A. *Separation Sci Technol* 46:434–451. Copyright # Taylor & Francis Group, LLC ISSN: 0149-6395 Print = 1520-5754 Online <https://doi.org/10.1080/01496395.2010.513360>
17. Abolfazl K, Maryam K, Masoumeh M (2016) Study of nitrogen adsorption in modified 13X zeolite with acid and alcohol wash. *Sci Technol* 6(2):36–44. <https://doi.org/10.5923/j.scit.20160602.02>
18. Kumar P, and Sons, Machinery for manufacturing the dish ends and finishing
19. Gomes VG, Yee KWK (2002) Pressure swing adsorption for carbon dioxide sequestration from exhaust gases. *Sep Purif* 161–171
20. Milton RM (1959) Molecular sieve adsorbents, US Patent, 2,882,243
21. Na BK, Lee H, Koo KK, Song HK (2002) Effect of rinse and recycle methods on the pressure swing adsorption process to recover CO₂ from power plant flue gas using activated carbon. *Ind Eng Chem Res* 41:5498–5503
22. Fairchild P (2014) Adsorption reversibility of SO₂, NO₂, and NO on 13X and 5A zeolites. Bachelor of Science University of South Carolina

Reduction in Exhaust Emission Using Constantan Catalyst in the Diesel Engine



Vivek Kumar Banerjee, Tanmay Agrawal, Basant Singh Sikarwar and Mohit Bhandwal

Abstract Catalytic convertor plays an important role in reducing harmful emissions in the form of NO_x , HC, and CO. Various technologies have been developed to reduce vehicular emissions; however, it comes with the expense of engine performance and cost. In this research, harmful emissions from the exhaust gases of diesel engines are reduced without compromising the engine efficiency and cost-effectiveness. In this context, a new monolith is designed and fabricated with copper–nickel alloy (constantan wire) as catalyst enclosed by an aluminum casing. This device is tested on a single cylinder diesel engine at 1500 rpm and it shows 60% NO_x , 60% CO, and 35% HC conversion efficiency. This research is helpful for partial replacement of the platinum-grade material used in the present catalytic converter.

Keywords Catalytic converter · Constantan · Exhaust emissions · Diesel engine

1 Introduction

The biggest challenge of the twenty-first century is the increasing amount of pollution in the atmosphere. The major sources of air pollution from the combustion of fossil fuels are NO_x , CO, CO_2 [1, 2]. These harmful emissions are disrupting the complex, dynamic natural gaseous system of our atmosphere that supports life. Oxides of nitrogen and carbon cause severe environmental problems like acid rain, ozone layer depletion, global warming, etc. [3]. But, among all these oxides NO_x is the biggest concern. One study reported that the contribution of automobile in NO_x emission is 49% and from power plant is 46% [4]. Report also claims that as the NO_x level gets doubled into the atmosphere the ozone layer is depleted by 12% and atmospheric temperature rises by 0.3 [5, 6]. Government has imposed stringent norms on automobile industries to reduce the amount of exhaust emissions. In India, Bharat Stage 6 is on the verge of getting applied. So, several researches are going on for

V. K. Banerjee (✉) · T. Agrawal · B. S. Sikarwar · M. Bhandwal
Department of Mechanical Engineering, Amity University Uttar Pradesh, Noida, Uttar Pradesh, India
e-mail: vivekbanerjee@gmail.com

purification of auto exhaust by using catalytic devices. In NO_x catalyst research, two reaction procedures have been proposed; direct decomposition reaction and reduction [7–10]. The reaction rate of direct decomposition is very slow, so application of this scheme is hardly considered. Whereas reduction reaction is comparatively fast and it takes place in presence of CO , H_2 , and hydrocarbons as reducing agent which are present in exhaust gases [11]. Many technologies have been developed to use these simple reaction schemes for auto exhaust reduction. Catalytic convertor is one of the technologies that are presently working in this context. It is a device used to reduce vehicular emissions by conducting two simple chemical reaction processes, i.e., reduction of NO_x and the oxidation of hydrocarbons and carbon monoxide, by using the catalyst platinum, palladium, and rhodium [12, 13]. The basic reactions that occur inside the catalytic converters are [14]



The use of these platinum-grade material has dominated in reducing the vehicular pollution, but they all are very rare and therefore costly [15–17]. Thus, it leads to the development of technologies that can explore other cheap sources and methods to reduce the vehicular emission. Some of the promising researches have been observed in the development of the catalytic materials, which includes ammonia-based catalysts, carbon-supported catalysts, silica catalysts, zeolite-based catalysts like ruthenium zeolite catalyst [18–22]. Of late split injection strategy has drawn the attention of the researcher due to its effective NO_x reduction capacity along with reduction in soot formation and piston work trade-offs [23]. Studies show that oxides like cerium oxide (CeO_2) and titanium oxide (TiO_2) have good redox properties. M. S. Hedge in 2010 proposed preparative method to form catalysts of different combinations of CeO_2 and TiO_2 with the noble metals like platinum, palladium, and rhodium [24]. In 2006, Nitin Labhsetwar studied the application of perovskite-type catalysts with ABO_3 -type structure which posses very good thermal stability characteristics [25]. Clearly, the efforts were made to reduce the cost of catalytic converter without compromising with the catalytic activity. However, in the year 2010, S. Chauhan expressed his views on the noble metals like platinum, palladium, and rhodium which are the best option available for reducing the exhaust emissions, although they are very expensive and in a limited supply [26]. He also studied the different catalysts like iridium, copper, ruthenium, zeolite, and nickel. N. Nedunchizehian in his paper shows the effects of nickel–copper alloy in the reduction of the oxides of nitrogen in the diesel engine exhaust [27–29]. The alloy used was Monel which includes 65% nickel, 33% copper, and 2% other elements. Their study shows 70% reduction in

oxides of nitrogen and it has been concluded that the efficiency of the conversion is dependent upon the bed temperature.

In this paper, a similar study has been conducted with the sole purpose of reducing the consumption of expensive platinum-grade material. Thus, it reduces the cost of the catalytic converters without compromising with its conversion efficiency. For this purpose, the study is strictly based on the material to be used in the monolith substrate. Here, we are using the nickel–copper alloy, i.e., constantan as a catalyst which includes 45% nickel, 55% copper, and no other alloying elements. A device has been fabricated using constantan wire as a newly developed monolith. Experimental study is done to check the percentage conversion of oxides of nitrogen, carbon monoxide, and hydrocarbon.

2 Materials and Methods

The exhaust reducing device is fabricated in two parts; inner monolith of constantan wire mesh and outer casing made of aluminum. The monolith is made of galvanized iron wire net structure of dimension (500 × 160) mm in which constantan wire of 0.5 mm thickness (See Fig. 1a) is weaved throughout. Constantan wire of 200 and 150 mm length is cut and weaved through every alternate hole of the GI wire mesh. The mesh density is kept high to offer maximum surface area for reaction to take place. The monolith is coated with a layer of calcium sulfate hemihydrate to hold the mesh in structure and to enable maximum heating inside the monolith. A 3 mm layer of rubber coating is given over the surface of the monolith to absorb maximum shocks in operating condition.

The outer casing is made of aluminum sheet metal of thickness 2 mm (See Fig. 1b). The structure of the outer casing is kept similar to the presently used catalytic converter. The dimensions of the fabricated device are shown in Fig. 2. The total length

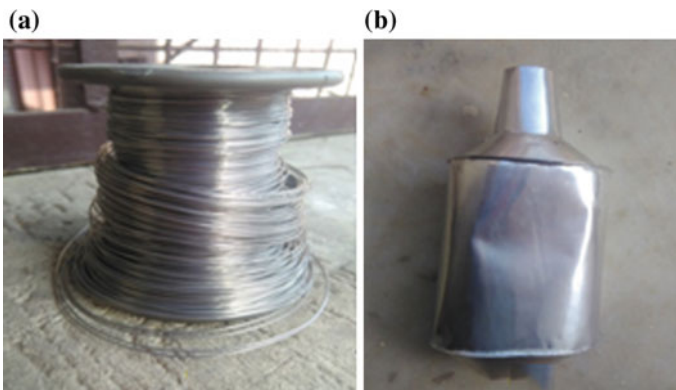


Fig. 1 Image of **a** constantan wire **b** fabricated device

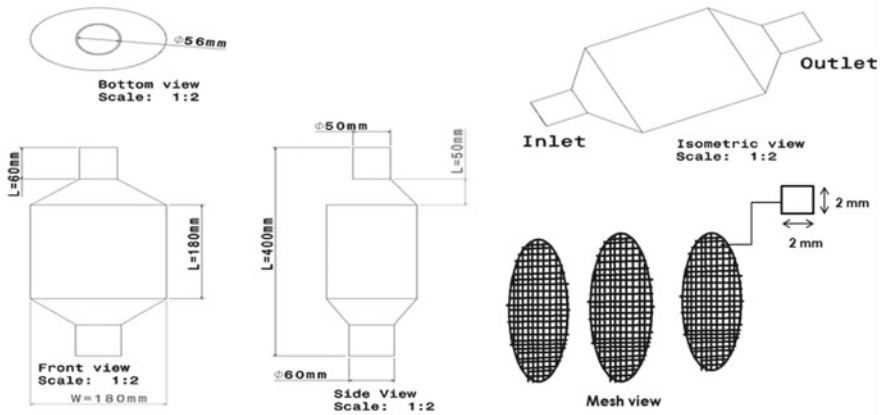
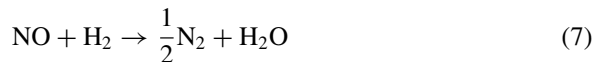
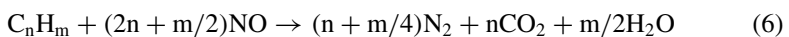
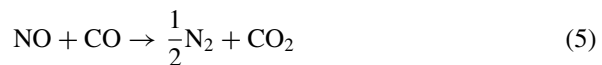


Fig. 2 Drafting of the device showing dimensions

of the device is 400 mm with the inlet and outlet diameters of 56 mm. The mesh view of Fig. 1 shows the arrangement of the constantan wire such that the cross-link arrangement of the wires forms very fine square with the sides of 2 mm.

Here in Fig. 3 point 1 shows the inlet section of the device, and this section is attached to the exhaust pipe of the engine. Point 2 shows the outer aluminum casing of the device. This metal covering supports the inner components and protects the device from any mechanical damage. Point 3 shows the layer of rubber cladding applied below the metallic casing to damp mechanical vibrations. Also, it seals exhaust gases from escaping the wire mesh inside the device. Point 4 shows the layer of calcium sulfate hemihydrate enclosing the wire mesh. This layer provides thermal insulation to the device. Point 5 shows the dense copper–nickel alloy (constantan) wire mesh. This mesh acts as the catalyst for the reaction to occur. Following reaction take place in presence of constantan as catalyst:



Point 6 shows the outlet section of the device. This section can either be exposed to the atmosphere or can be attached to the catalytic converter as per the requirements of the user.

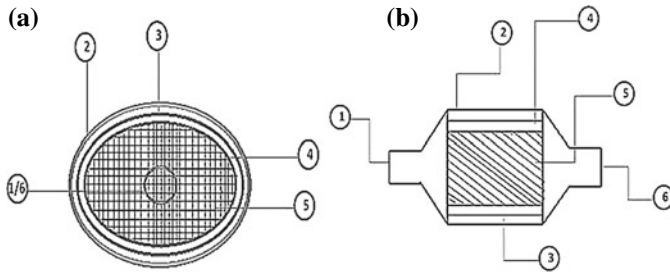


Fig. 3 Schematic diagram of **a** front view **b** side view of the device

3 Experimental Procedure

In order to measure the reduction efficiency of the newly fabricated device with constantan as a monolith, the device is fitted to the exhaust tailpipe of a water-cooled single cylinder direct injection engine. The specifications of the engine are given in Table 1. The experimental schematics are shown in Fig. 4. The NO_x, CO, and HC emissions are measured by AVL DGAS 444 analyzer. The fuel flow is measured with the help of the burette and stopwatch. The device is fitted to the exhaust system and no leakage is verified. The engine is run at a constant 1500 rpm at no load condition for 1 h. At the initial stage, the engine and the device are allowed to get heated up to avoid any cold starting problem. The AVL DGAS 444 analyzer is used first to record the emissions of NO_x, CO, and HC without the device and then the same is recorded with the device attached. All the readings are recorded for 15 min duration and the same is tabulated and compared graphically.

Table 1 Engine specifications

Make	Apex Innovation 240 Pe
No. of cylinder	1
No. of strokes	4
Bore diameter	87.5 mm
Stroke length	110 mm
Connecting rod length	234 mm
Orifice diameter	20 mm
Dynamometer arm length	185 mm
Fuel	Diesel
Power	3.5 kW
Speed	1500 rpm
Compression ratio range	12:1 to 18:1
Injection point variation	0–25 (in degree) BTDC

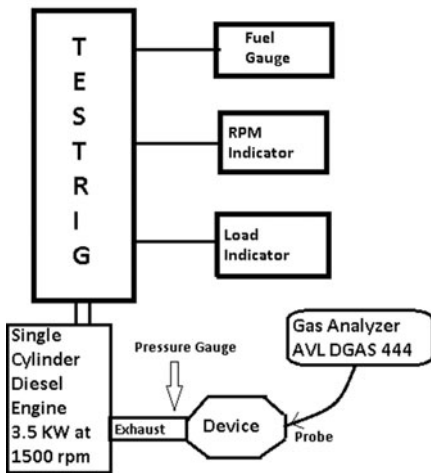


Fig. 4 Schematic diagram of the experimental setup and photograph of the experiment

AVL DGAS 444 Gas Analyzer Calibration. Before performing the emission testing, the gas analyzer is run through several testing procedures to ensure correct functioning. These tests are a prerequisite to its working.

Leak test. The gas in port is covered by the thumb and leak test is run. After 30 s, the leak test confirmation is achieved. In case of any anomaly, the error message is shown on the screen.

Residual Test. Soon after the leak test, residual test is checked. This test is done to ensure complete evacuation of any residual exhaust particles inside the channel of the analyzer. After positive residual test, calibration of the analyzer is required.

IRO Sensor Calibration Test. This test is run to calibrate various sensors in the analyzer like oxygen sensor, etc. with the ambient condition.

Hydrocarbon Residual Test. This test is run to ensure the complete absence of any particulate matter of any hydrocarbon residue inside the analyzer system.

After performing the entire abovementioned test, the AVL DGAS 444 gas analyzer is ready to be used for emission testing. All the parameters are set with respect to ambient conditions.

4 Results and Discussions

Experimental investigations are carried out and variations of exhaust emissions in the form of NO_x, CO, and HC are graphically represented with respect to time factor at a constant 1500 rpm at no load condition.

The conversion efficiency of the device is calculated by the following formula:

$$\frac{\text{Emissions without device} - \text{Emissions with device}}{\text{Emissions without device}} \times 100\%$$

4.1 Effect of Device on NO_x Reduction

Emission testing shows a significant reduction in NO_x with the use of the device. All the emissions are recorded with respect to time. At time t = 1 min, the conversion efficiency of the device for NO_x is 76%, which fluctuates till 60% at the end of 15 min and then get stabilized. The increase in conversion efficiency is because with time the device also gets heated up. For the reaction to take place, the device needs to reach its light-off temperature. So as the device reaches its maximum efficiency it gets stabilized. The emissions of NO_x with and without device with respect to time are plotted in Fig. 5.

4.2 Effect of Device on Hydrocarbon Conversion

The device shows a significant reduction in emissions of hydrocarbon. The reduction of NO_x starts from 57.45% at time t = 1 min and get stabilized at 35% at the end of 15 min. The emissions of HC with and without device with respect to time are plotted on Fig. 6.

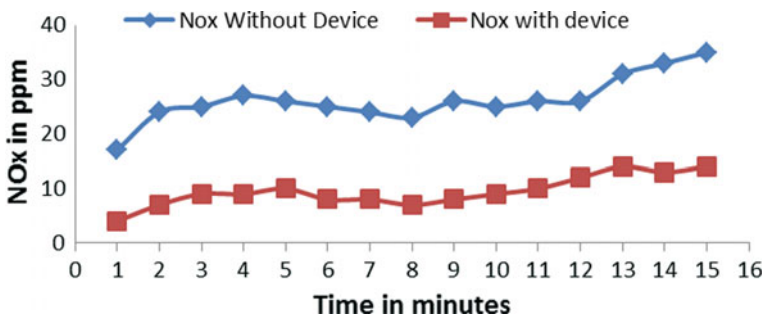


Fig. 5 Variation in NO_x emissions with and without device w.r.t. time in minutes

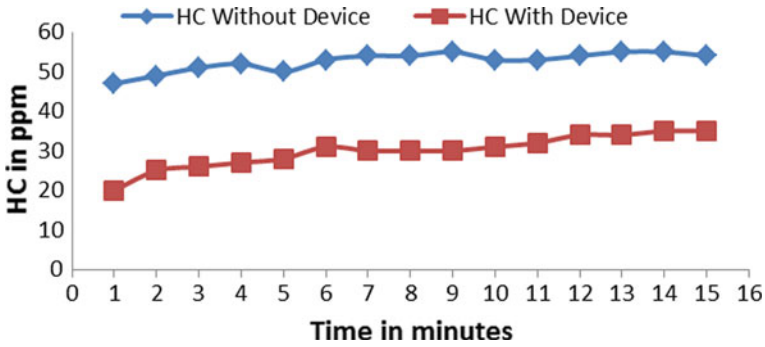


Fig. 6 Variation in HC emissions with and without device w.r.t. time in minute

4.3 Effect of Device for Carbon Monoxide Conversion

The device shows a remarkable reduction in emissions of CO. At the beginning of emissions testing, the oxidation of CO was recorded as 63.33% which undergoes slight fluctuation with time and get stabilized at 60.11% at the end of time $t = 15$ min. The emissions of HC with and without device with respect to time are plotted in Fig. 7.

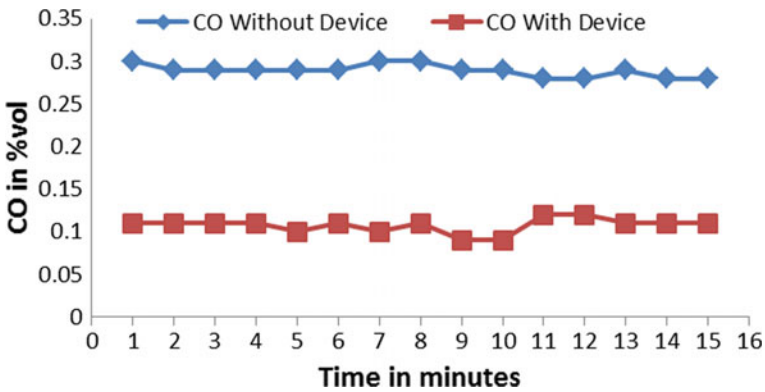


Fig. 7 Variation in CO emissions with and without device w.r.t. time in minutes

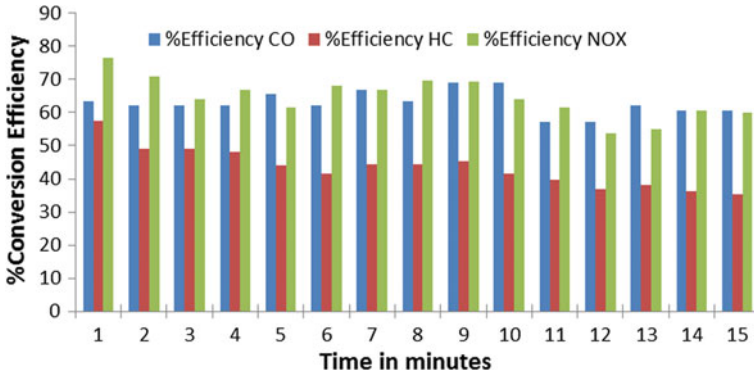


Fig. 8 Comparison of conversion efficiency of CO, HC, and NO_x w.r.t. time

4.4 Comparison of Percentage Conversion Efficiency of the Device

The device shows significant results for NO_x, CO, and HC conversion. Results also show evident fluctuation of emissions with time. Figure 8 represents the percentage conversion efficiency variation for CO, HC, and NO_x, respectively, with time.

5 Conclusion

Based on the results it can be inferred that the device shows significant reduction in exhaust emissions when tested on a single cylinder diesel engine. NO_x, CO, and HC emissions are reduced by 60, 60, and 35% approx, respectively. During experimental investigation, the device generates no back pressure, so the loss in engine efficiency does not come into existence. Further, the cost analysis of the device shows that the manufacturing of the device is cheap. This device can be utilized as a partial replacement or as an add-on with the presently used three-way catalytic convertor. This will ensure less use of the platinum-grade materials like platinum, palladium, and rhodium in the present catalytic convertor with its improved efficiency. Also, this device can be used in other standalone power generating IC engine units where no catalytic converters are used. The above study tries to work on a noble cause of pollution reduction from auto exhausts and shows promising results for future application of it in the automobile market.

References

1. Perry R, Gee IL (1994) Vehicle emissions and effects on air quality : indoors and outdoors, pp 224–236
2. Sharma RC, Sharma N (2014) Environmental impact of automobiles in India, pp 46–49
3. Briggs D (2018) Environmental pollution and the global burden of disease, pp 1–24
4. Guttikunda SK, Jawahar P (2014) Atmospheric emissions and pollution from the coal- Fi red thermal power plants in India. *Atmos Environ*, e11–e11
5. Ramanathan V, Feng Y (2009) Air pollution, greenhouse gases and climate change: global and regional perspectives. *Atmos Environ*, 37–50
6. Dasch JM (1992) Nitrous oxide emissions from vehicles 3289
7. Trout BL, Chakraborty AK, Bell AT (2012) Analysis of the thermochemistry of NO_x decomposition over CuZSM-5 based on quantum chemical and statistical mechanical calculations, pp 17582–17592
8. Huang T, Chiang D, Shih C, Lee C, Mao C, Wang B (2015) Promoted decomposition of NO_x. *Environ Sci Technol*, 3711–3717
9. Miwa K, Mohammadi A, Kidoguchi Y (2001) A study on thermal decomposition of fuels and NO_x formation in diesel combustion using a total gas sampling technique. *Int J Engine Res*, pp 189–198
10. Klimisch RL, Larson JG (eds) (1975) *The catalytic chemistry of nitrogen oxides*. Springer US, Boston, MA
11. Yu Y, Li Y, Zhang X, Deng H, He H, Li Y (2015) Promotion effect of H₂ on ethanol oxidation and NO_x reduction with ethanol over Ag/Al₂O₃ catalyst. *Environ Sci Technol* 49:481–488
12. Chalapathi KS, Murthy CB, Kumar BSP (2014) Development of automobile catalytic converter during last four decades. *Int J Res Appl Sci Eng Techn* 2(XI):321–333
13. Farrauto RJ, Heck RM (1999) Catalytic converters: state of the art and perspectives. *Catal Today*, 351–360
14. Mohiuddin AKM, Rahman A (2012) Investigation using simulations for the development of low cost catalytic converter from non-precious metals. *Adv Mater Res* 445(X):899–904
15. Kalam A, Hassan MH (2011) Design, modification and testing of a catalytic converter for natural gas fueled engines, pp 677–688
16. Kalam MA, Masjuki HH, Redzuan M, Mahlia TMI, Fuad MA, Mohibah M, Halim KH (2009) Development and test of a new catalytic converter for natural gas fuelled engine, pp 467–481
17. Ghodrati M, Shara P, Samali B (2018) Recovery of platinum group metals out of automotive catalytic converters scrap : a review on Australian trends and challenges
18. Teng H, Hsu L, Lai Y, Kung NC (2001) Catalytic reduction of NO with NH₃ over carbons impregnated with Cu and Fe, pp 2369–2374
19. Taylor KC (1984) *Automobile catalytic converters*
20. Huuhtanen M (2006) Zeolite catalysts in the reduction of NO_x in lean automotive exhaust gas conditions. *Behaviour of Catalysts in Activity, DRIFT and TPD Studies*
21. Andreas M (2016) Zeolite catalysis. *Catalysts* 6–118
22. Paramadayan T, Pant A (2013) Selective catalytic reduction converter design : the effect of ammonia nonuniformity at inlet 30(12):2170–2177
23. Sindhu R, Rao GAP, Murthy KM (2017) Effective reduction of NO_x emissions from diesel engine using split injections. *Alexandria Eng J*
24. Bera P, Hegde MS (2010) Recent advances in auto exhaust catalysis. *J Indian Inst Sci* 90:299–395
25. Labhsetwar N, Biniwale RB, Kumar R, Rayalu S, Devotta S (2006) Application of supported Perovskite-type catalysts for vehicular emission control, pp 55–64

26. Chauhan S (2010) *J Chem Pharm Res*, 602–611
27. Balagurunathanb K, Ganesanc V (1995) Reduction of Nitrogen Oxide emissions using Nickel-Copper alloy catalyst in diesel engines, pp 167–171
28. Leman AM, Afiqah J, Fakhrurrazi R, Dafit F, Supa Z, Rahmad R (2016) Catalytic converter developed by Washcoat of γ -Alumina on Nickel Oxide (Nio) catalyst in FeCrAl substrate for exhaust emission control : a review 1045:1–7
29. Amin CM, Goswami JJ, Rathod PPP (2012) Copper based catalytic converter, pp 1–7

CFD Modeling of Commercial Slurry Flow Through Horizontal Pipeline



Om Parkash, Arvind Kumar and Basant Singh Sikarwar

Abstract In this paper, slurry flow characteristics of glass beads–water slurry has been studied in a pipe of 0.0549 m diameter using commercial software FLUENT. The study was carried out using Eulerian–Eulerian two-phase model with RNG K-epsilon model turbulence closure. The simulation was carried out for a glass bead particle of size 440 μm having efflux concentration ranging from 10 to 30% by volume with Prandtl fluid ($\text{Pr} = 5.83$) at different Reynolds number. The results of solid concentration contour, velocity contour, and pressure drop were predicted at different Reynolds numbers to analyze the slurry flow characteristics. The plot between pressure drop versus Reynolds number was plotted at different solid concentrations. The simulation results of the present study show good results with the experimental results of the literature. The present model shows the enhancement of suspension suitability of glass bead particles at a larger distance. Post-validation, parametric studies are carried out to study the effect of parameters.

Keywords Slurry flow · Horizontal pipeline · Eulerian two-phase model · Pressure drop

1 Introduction

Slurry is a mixture of liquid and solids flowing through the pipeline. Transportation of solids and wastes with water or some other fluids as a carrier in the form of slurry through pipeline system has wide applications such as mines, chemical, energy, metallurgical, food, power generation, and other industrial enterprises. Water is the most commonly used fluid as a carrier for solid transportation. Transportation of slurry

O. Parkash (✉)
Amity University Gurgaon, Gurgaon, Haryana, India
e-mail: om.mech8@gmail.com

A. Kumar
YMCA University of Science and Technology, Faridabad, India

B. S. Sikarwar
Amity University Uttar Pradesh, Noida, Uttar Pradesh, India

© Springer Nature Singapore Pte Ltd. 2019

M. Kumar et al. (eds.), *Advances in Interdisciplinary Engineering*, Lecture Notes in Mechanical Engineering, https://doi.org/10.1007/978-981-13-6577-5_16

through this mode is attractive when compared with the conventional modes of transportation such as road, rail, shipping, and air because it reduces traffic, air pollution, noise, man power, accidents, energy consumption, maintenance, and ecological disturbances. Pressure drop is the key parameter for designing the pipeline system of slurry flow. Many researchers have carried out the experimental and numerical study on fly ash, bottom ash, glass beads, and sand for their easier transportation at high concentration to the pipeline. Literature has been reviewed in this field which reflects the experimental and numerical study by various researchers. Toda et al. [1] performed an experimental investigation of solid materials hydraulic transport over horizontal and vertical pipe bends and pressure drops were measured in the pipe bends. Solid particles used in their experiments were glass beads (0.5–2.0 mm in dia.) and polystyrene (1 mm in dia.) particles. They concluded that the additional pressure drop in case of glass particles increases with the increase in concentration in vertical pipe bend and both glass bead particles. The polystyrene particles show an additional pressure drop, which is the same as that of in horizontal bend and almost remains constant irrespective of the fluid flow. Turian and Yuan [2] developed a correlation for the pressure drop considering the different cases of slurry flow such as stationary bed formation, and homogeneous and heterogeneous flows. In their study, they concluded that empirical correlation is possible for prediction of pressure drop. Gillis et al. [3] proposed a two-layer model for the coarse particle slurry flow in a horizontal pipeline. In their model, they have predicted the head losses and pressure drop for coarse particle slurry. Gillies et al. [4], Gillies and Shook [5] focused their study on the concentration distribution of solid particles in slurry flow. Matousek [6] performed an experiment for sand slurry in different pipes viz. horizontal, vertical, and 35° descending pipes. In their experimental study, they determine the pressure drop and flow patterns for small- and large-sized particles. It was found that the pressure drop for small-sized sand particle is lower than the large-sized sand particle. The pressure drop in the vertical pipe is found to be less than horizontal pipe. Kaushal and Tomita [7] performed experimental study in a slurry pipeline for coarser particles to study the effect for near wall lifts. The pressure drop for finer particles is compared with equivalent fluid. In their study, they presented the slip velocity effect on pressure drop and the effect is high at higher slip velocities and low at lower slip velocities. Chandel et al. [8] performed an experiment in a pipeline for highly concentrated slurry of fly ash and bottom ash. They measured the pressure drop at different concentrations using a pilot plant test loop. They also developed a rheological model and by using this model, they predicted the pressure drop behavior. Their predicted results are also compared with the measured results and have shown good agreement. Melorie et al. [9] experimentally studied the impact of chemical additives on rheological characteristics in iron ore slurry having concentration range of 18.8–25.8%. They found that the addition of hydrated lime increases yield stress at different solid concentrations. Singh et al. [10] predicted the flow characteristics of bottom ash–water slurry flow in a 0.050 m diameter horizontal pipe. The study was carried out at different bottom ash concentrations for wide velocity ranges using Eulerian–Lagrangian two-phase approach with SST $K-\omega$ turbulence closure. The simulated results are also compared with the experimental results of Chandel et al.

[8]. It is very difficult to evaluate the pressure, velocity, and concentration distribution at different locations in a pipeline. So experimental analysis to evaluate various results of a slurry pipeline is difficult and time-consuming. However, computational fluid dynamics has sufficient capability to predict all these parameters at any section of the pipeline. In present study, RNG K- ϵ turbulence model was used for simulation of slurry flow at different Reynolds numbers, i.e., Re_1 —64017, Re_2 —128035, and Re_3 —192054. Post-validation and parametric study were carried out to analyze the flow characteristics of the slurry flow. The aim of this work is to check the capability of CFD to predict the slurry flow characteristics for Prandtl fluid ($Pr = 5.83$) at different Reynolds numbers. The finding of the paper shows the pressure drop variation with Reynolds number and suitable turbulence model for research and industrial design purposes.

2 Mathematical Model

In this paper, the Eulerian–Eulerian two-phase model was adopted for numerical simulation. As the Eulerian model has been reported as an efficient multiphase model for the simulation, the following governing equations are used for the turbulent flow of glass bead particles in Newtonian fluid.

2.1 Eulerian Model

In Eulerian model, the slurry is assumed to be comprised of solid and fluid phases. The concentrations of the two phases are assumed to be α_s and α_f for $\alpha_s + \alpha_f = 1$. The forces acting on a single particle in the slurry are as follows:

1. Static/solid pressure gradients, $\nabla P / \nabla P_s$.
2. Forces due to the difference in velocities of two phases, $K_{sf}(\vec{v}_s - \vec{v}_f)$
3. Viscous and body forces, $\nabla \cdot \overline{\tau}_f$ and $\rho \vec{g}$, where $\overline{\tau}_f$ represents the stress tensor of fluid, ρ denotes the mass density, and g is gravitational acceleration.
4. Lift and virtual mass forces. The coefficient of virtual mass/lift forces, C_L/C_{vm} are assumed to be 0.5.

The continuity and momentum equations for each phase are defined as follows:

Continuity Equation

$$\nabla \cdot (\alpha_t \rho_t \vec{v}_t) = 0 \quad (1)$$

where t is either s or f .

Momentum Equations

For fluid phase:

$$\begin{aligned} \nabla \cdot (\alpha_f \rho_f \vec{v}_f \vec{v}_f) = & -\alpha_f \nabla P + \nabla \cdot (\overline{\tau}_f + \overline{\tau}_{i,f}) + \alpha_f \rho_f \vec{g} + K_{sf}(\vec{v}_s - \vec{v}_f) \\ & + C_{vm} \alpha_s \rho_f (\vec{v}_s \cdot \nabla \vec{v}_s - \vec{v}_f \cdot \nabla \vec{v}_f) \\ & + C_L \alpha_s \rho_f (\vec{v}_f - \vec{v}_s) \times (\nabla \times \vec{v}_f) \end{aligned} \quad (2)$$

For solid phase:

$$\begin{aligned} \nabla \cdot (\alpha_s \rho_s \vec{v}_s \vec{v}_s) = & -\alpha_s \nabla P - \nabla P_s + \nabla \cdot (\overline{\tau}_s + \overline{\tau}_{i,f}) + \alpha_s \rho_s \vec{g} + K_{fs}(\vec{v}_f - \vec{v}_s) \\ & + C_{vm} \alpha_s \rho_f (\vec{v}_f \cdot \nabla \vec{v}_f - \vec{v}_s \cdot \nabla \vec{v}_s) \\ & + C_L \alpha_s \rho_f (\vec{v}_s - \vec{v}_f) \times (\nabla \times \vec{v}_f) \end{aligned} \quad (3)$$

Here, $\overline{\tau}_{i,f}$ is the Reynolds stress tensor and $\overline{\tau}_s$ and $\overline{\tau}_f$ are viscous stress tensor for solid and fluid phases as given below.

Wall function

The standard wall function proposed by Launder and Spalding has been employed in the present study. The chosen wall function provides more precise and meticulous results for both fluid and liquid phases using Eulerian two-phase model.

3 Numerical Solution for Simulation

3.1 Geometry and Mesh Generation

The uniform hexahedral structured grid has been created for a straight horizontal pipe of length 3.8 m and 54.9 mm diameter in ANSYS 16 as shown in Fig. 1. The length of the pipeline in the present study is more than 50 diameters, which is sufficiently long for fully developed flow. The grid independent test is performed for geometry containing 1.0, 2.43, 3.82, 4.62, and 5.22 lakh elements at the highest Reynolds number. The solid phase velocity profile for different grid geometries is shown in Fig. 2. It is seen that the identical results are obtained for the pipe geometry containing 4.62 and 5.22 lakh cells. Hence, a grid with 4.62 lakh cells is chosen in the present study to carry out the simulation of slurry flow.

3.2 Boundary Conditions

The pipeline geometry comprises three bounded faces viz. inlet, outlet, and wall boundaries to accomplish fluid domain calculations. The velocity inlet, pressure outlet, and no-slip conditions are considered for the fluid flow domain computations.

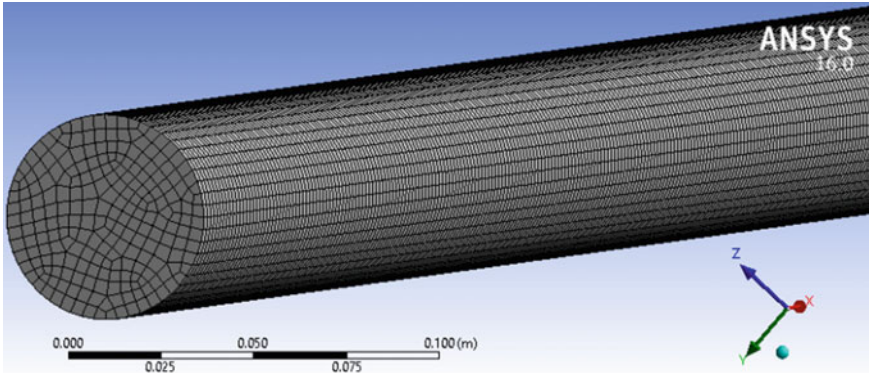
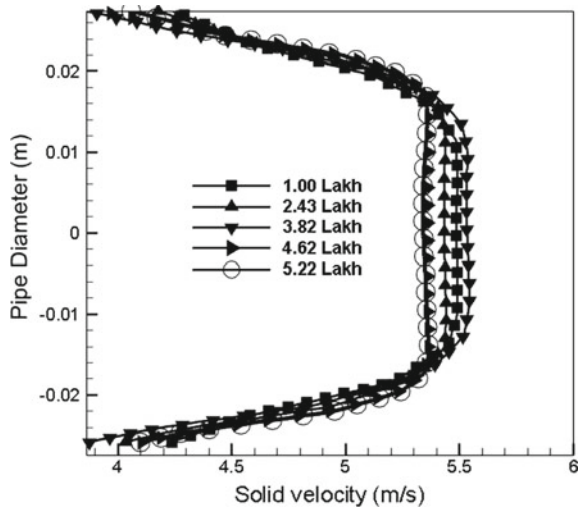


Fig. 1 Mesh geometry

Fig. 2 Grid independent test (solid phase velocity profile at $Re = 192054$ and $C_{vf} = 10\%$)



The inlet and outlet boundary conditions are applied to the fluid domain at particular velocity and volume fractions. The assumption of no-slip conditions has been considered at the wall. Additionally, the roughness constant of the wall is assumed as 0.5.

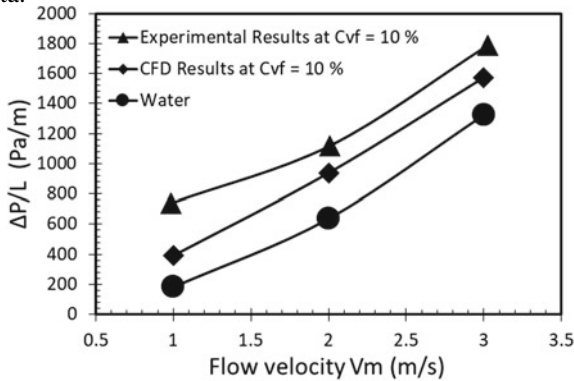
3.3 Solution Strategy and Convergence

In order to simplify momentum, turbulence kinetic energy, and fluid flow dissipation rate equations, a second-order upwind structure is used. The scheme offers high accuracy, stability, and convergence of the solutions. In the present study, the values

are preset to 0.001 times the initial residual value for each variable. In order to couple the pressure and velocity of the fluid flow, SIMPLE algorithm has been adopted. The other solution strategies include the under-relaxation factor of pressure—0.3, momentum—0.5, volume fraction—0.2, turbulent viscosity—0.8, turbulent kinetic energy, and dissipation energy as 0.8. This converges the nonlinear equations into linear ones.

4 Validation

The simulation results of the present study for pressure drop at $C_{vf} = 10\%$ are validated with the available experimental results from the literature Kaushal et al. [7]. It has been found that the present study gives good results with the experimental data.



5 CFD Modeling Results

5.1 Concentration Distribution

The solid concentration distribution ranging from 10 to 30% by volume is shown in Figs. 3a–c, 4a–c, and 5a–c at different Reynolds number. It has been found that the suspension stability of the glass bead particles increases with an increase in Reynolds number. The glass bead particles in Figs. 3c, 4c, and 5c have high suspension stability as compared to Figs. 3b, a, 4b, a, and 5b, a. However, as the concentration increases the glass bead particles at low Reynolds number try to settle down at the bottom of the pipe as the increase in concentration of glass beads in water results in the increase of mixture density, which decreases the suspension stability of the particle.

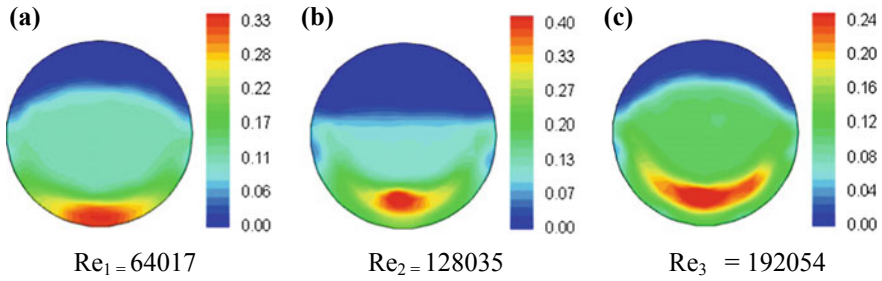


Fig. 3 Solid concentration distribution predicted at $C_{vf} = 10\%$

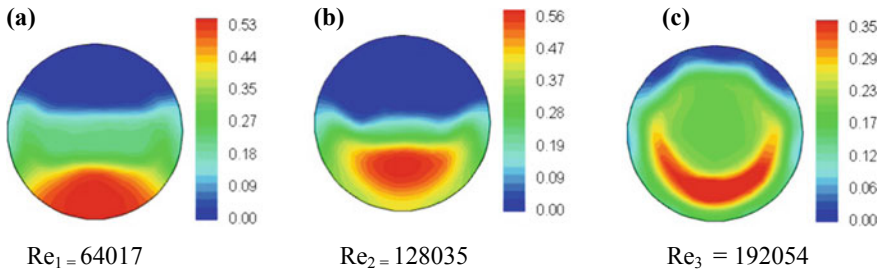


Fig. 4 Solid concentration distribution predicted at $C_{vf} = 20\%$

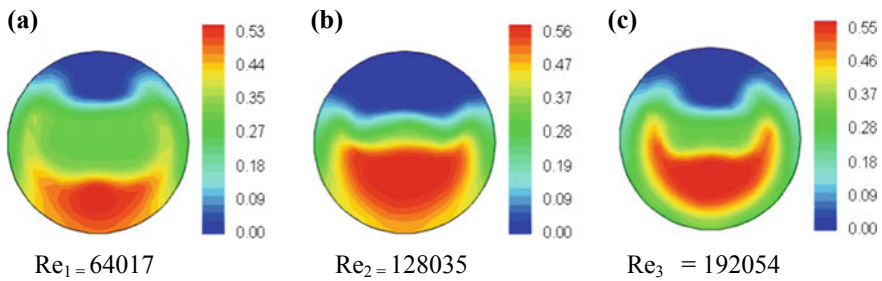


Fig. 5 Solid concentration distribution predicted at $C_{vf} = 30\%$

5.2 Velocity Distribution of Solid Phase

The velocity distribution contours for the concentration ranging from 10 to 30% by volume as shown in Figs. 6a–c, 7a–c, and 8a–c at different Reynolds number. The velocity profile is symmetrical (as shown in Fig. 6a–c) in nature for low concentration of glass beads in water but as the glass bead concentration increases, the velocity profile becomes asymmetrical (as shown in Figs. 7a–c and 8a–c) in nature. This

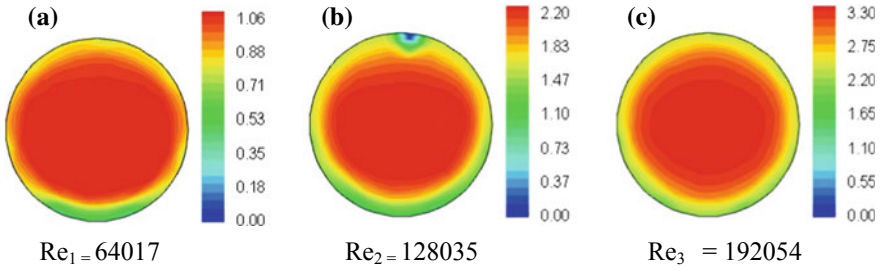


Fig. 6 Velocity distribution predicted at $C_{vf} = 10\%$

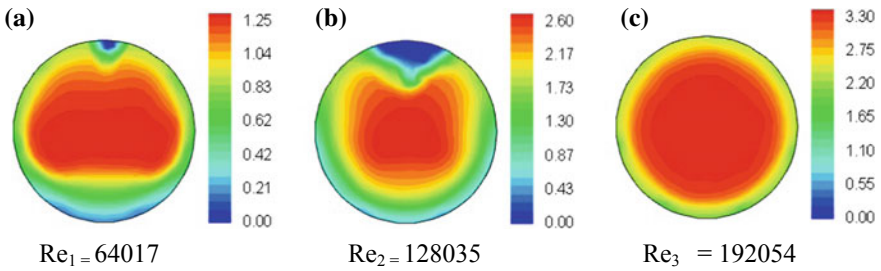


Fig. 7 Velocity distribution predicted at $C_{vf} = 20\%$

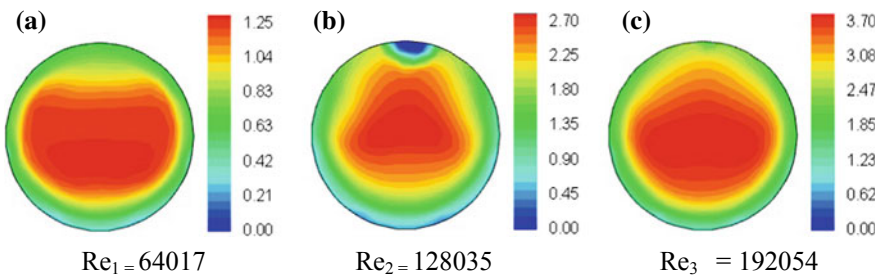
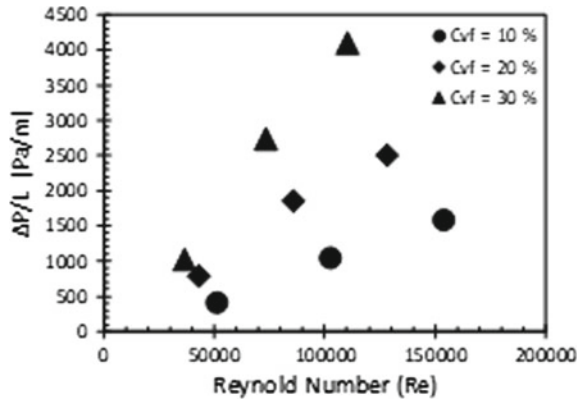


Fig. 8 Velocity distribution predicted at $C_{vf} = 30\%$

happens because increase in concentration of solids in the water increases the mixture density and turbulence mixing, which results in the decrease in value of the Reynolds number. The velocity contours in Fig. 8a–c are highly asymmetrical as compared to the velocity contour in Fig. 7a–c.

Fig. 9 Pressure drop versus Reynolds number



5.3 Pressure Gradient

The pressure drop results at different concentrations ranging from 10 to 30% for the glass beads have been plotted in Fig. 9. It has been found that the pressure gradient is small at low Reynolds number but it increases sharply at high Reynolds number at all efflux concentration of the glass bead particles.

6 Conclusions

The following conclusions have been drawn based on present study of glass beads–water slurry flow.

1. It is observed that Eulerian–Eulerian two-phase model with RNG k- ϵ turbulence closure is more appropriate and meticulous for the predictions of the pressure drop, solid concentration, and velocity distribution.
2. The glass bead concentration is more at the bottom of the pipe at low value of the Reynolds number and their suspension stability increases at high Reynolds number.
3. The velocity distribution is symmetrical at lower concentration of glass bead particles and it became asymmetrical at high concentration.
4. The pressure drop increases linearly with increase in Reynolds numbers at different solid concentrations.
5. The suspension stability of the glass bead particles increases at Prandtl fluid ($Pr = 5.83$), which results in transportation of slurry at a longer distance.
6. The present study gives satisfactory results with the available experimental results of the literature.

References

1. Toda M, Komori N, Saito S, Maeda S (1972) Hydraulic conveying of solids through pipe bends. *J Chem Eng Jpn* 5(1):4–13
2. Turian RM, Yuan TF (1977) Flow of slurries in pipelines. *AIChE J* 23(3):232–243
3. Gillies RG, Shook CA, Wilson KC (1991) An improved two-layer model for horizontal slurry pipeline flow. *Can J Chem Eng* 69(1):173–178
4. Gillies RG, Hill KB, Mckibben MJ, Shook CA (1999) Solids transport by laminar Newtonian flows. *Powder Technol* 104:269–277
5. Gillies RG, Shook CA (2000) Modelling high concentration settling slurry flows. *Can J Chem Eng* 78:709–716
6. Matousek V (2002) Pressure drops and flow patterns in sand-mixture pipes. *Exp Thermal Fluid Sci* 26(6–7):693–702
7. Kaushal DR, Tomita Y (2007) Experimental investigation for near-wall lift of coarser particles in slurry pipeline using γ -ray densitometer. *Powder Technol* 172(3):177–187
8. Chandel S, Singh SN, Seshadri V (2010) Transportation of high concentration coal ash slurries through pipelines. *Int Arch Appl Sci Technol* 1:1–9
9. Melorie AK, Kaushal DR (2017) Experimental investigations of the effect of chemical additives on the rheological properties of highly concentrated iron ore slurries. *KONA Powder Part J* 2018001
10. Singh JP, Kumar S, Mohapatra SK (2017) Modelling of two-phase solid-liquid flow in horizontal pipe using computational fluid dynamics technique. *Int J Hydrogen Energy* 42(31):20133–20137

Real-Time Vibration Analysis of a Robotic Arm Designed for CT Image Guided Diagnostic Procedures



Mohapatro Gourishankar, Mishra Ruby, Shah Shubham  and Ghosh Taniya

Abstract Robots are used in many fields like medicine, agriculture, industries, etc. A robotic arm is designed so that it can be used in the field of medicine for diagnostic purposes in radiology department. Accuracy, precision, and space efficiency play an important role specifically while dealing with biopsies of tumors and cancer tissues. The robotic arm designed here takes the coordinates from the CT image as input and reaches the target point with precision. In this research paper, the main focus is on reducing the vibration of the end needle to increase the accuracy during operation of the robot. LabVIEW has been used for programming to measure the axial vibrations of the links. Accelerometer connected with MyRio controller was used for measuring vibrations caused due to the functioning of actuators. Structure of the robot was optimized by adding a support structure to reduce vibrations. Vibration analysis was done again using same setup. Amplitude of vibrations of Link 4 where the needle will be attached is analyzed using GRAPH software by generating a moving average which acts as a baseline. From graphical method, it was found that on an average the amplitude of vibration was reduced in the range of 62.5–66.67%.

Keywords Real-time vibration analysis · 5-axis robot · Structural optimization

1 Introduction

The field of medicine and technology are working to provide better care and facilities to the patients worldwide. Many research works are being carried out in the field of engineering to provide better guidance and supervision to the medical professionals. Technologies such as robots are extensively being used in the field of medicine for performing surgical operations. Robots are highly favored since they are quite precise and accurate along with being space efficient. In this research, a robotic

M. Gourishankar · M. Ruby (✉) · S. Shubham · G. Taniya
KIIT Deemed to be University, Bhubaneswar, India
e-mail: rubymishrafme@kiit.ac.in

S. Shubham
e-mail: shubham.prasad1@gmail.com

© Springer Nature Singapore Pte Ltd. 2019
M. Kumar et al. (eds.), *Advances in Interdisciplinary Engineering*, Lecture Notes in Mechanical Engineering, https://doi.org/10.1007/978-981-13-6577-5_17

arm has been experimentally modeled that can be used in the field of radiology for retrieval of tissue samples. The robotic arm is programmed in such a way that it can take coordinates from CT image and reach the target point. While functioning of the robotic arm, vibrations due to the motion of actuators and structural constraint cause deviation of the end effector. In this research paper, the main focus is on minimizing the vibration of the links so that there is minimal deflection of the end needle while reaching the target point. An accelerometer was used to measure the vibration in the links generated during functioning of the robotic arm by using the LabVIEW software. The robotic arm was then structurally modified. It was analyzed again with the help of an accelerometer to find the vibrations generated in the links. The structural optimization of the robotic arm reduced the vibrations in the links.

In the research by Supriya et al., experimental design of an industrial robotic was done in CATIA V5. It was then analyzed for various modes of frequency with the help of ANSYS. The analysis gave them the weak parts and then optimization was done accordingly [1]. In the paper by Marco et al., an analysis was carried out to find the cutting ability of industrial robots. Static and dynamic analyses were carried out on the robot for different poses. They came to a conclusion that dynamic behavior of IR needs to be accounted for when vibration is considered as a performance factor [2]. In the paper by Patil et al., experimental test by using Gear Dynamic Stress Test Rig was carried out for testing and analyzing a helical gear for the frictional forces. The results were compared with the help of finite element frictional contact analysis [3]. In the research paper by Jakob et al., a design of an end effector was given that would divert the reaction forces away from the end effector. They gave a design approach for a self-supporting robotic tool [4].

Structural optimization to reduce vibration in a 5-axis robotic arm has not been extensively researched. Vibration has a very negative impact on the accuracy of end effector of robots. Hence, this paper makes an attempt to reduce this research gap.

2 Methodology

2.1 Unoptimized Design and Vibration Analysis

A robotic manipulator is designed and fabricated with a 5-axis robotic system. Each joint consists of a stepper motor which act as actuators for the robot. The links of the robot are made from aluminum for its lightweight and rigidity. The design of this robot is based on inverse kinematics and it requires coordinate points as input to calculate the joint parameters from the transformation matrix. This robotic arm is designed to work by the guidance of a CT scan images and perform biopsy procedure on a patient by retrieving a tissue sample from the suspected region in a patient's body. The fabricated model is a preliminary test model. The governing equations for the robotic arm with respect to X-, Y-, and Z- axes coordinates are shown in Eqs. (1), (2), and (3). These equations are derived from transformation matrix of the robotic

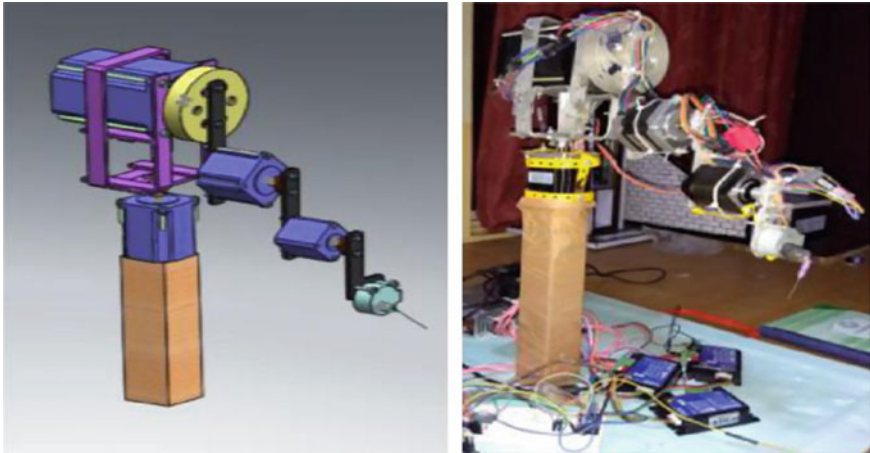


Fig. 1 3D CAD model of the robotic arm and fabricated experimental model of the robotic arm

arm according to DH parameters. Here, $C\theta$ is cosine θ and $S\theta$ is sine θ . θ_i , where i is 1, 2, 3, 4, or 5 is the angle between two consecutive links. Similarly, a_i or l_i is the length of each link and d_i is the displacement of one link with respect to the other and α_i is the link twist angle.

$$\begin{aligned}
 X = & (\cos(\theta_1) \times l_2 \times \cos(\theta_2)) - (\sin \theta_1 (d_2 + d_3 + d_4 + d_5)) + (l_3 \times \cos(\theta_1) \\
 & \times \cos(\theta_2 + \theta_3)) + (l_4 \times \cos(\theta_1) \times \cos(\theta_2 + \theta_3 + \theta_4)) + (l_5 \times \cos(\theta_1) \\
 & \times \cos(\theta_2 + \theta_3 + \theta_4 + \theta_5))
 \end{aligned} \tag{1}$$

$$\begin{aligned}
 Y = & \cos \theta_1 (d_2 + d_3 + d_4 + d_5) + (\sin(\theta_1) \times l_2 \times \cos(\theta_2)) \\
 & + (l_3 \times \sin(\theta_1) \times \cos(\theta_2 + \theta_3)) \\
 & + (l_4 \times \sin(\theta_1) \times \cos(\theta_2 + \theta_3 + \theta_4)) \\
 & + (l_5 \times \sin(\theta_1) \times \cos(\theta_2 + \theta_3 + \theta_4 + \theta_5))
 \end{aligned} \tag{2}$$

$$\begin{aligned}
 Z = & (l_1) - (l_2 \times \sin(\theta_2)) - (l_3 \times \sin(\theta_2 + \theta_3)) - (l_4 \times \sin(\theta_2 + \theta_3 + \theta_4)) + (l_5 \\
 & \times \sin(\theta_2 + \theta_3 + \theta_4 + \theta_5))
 \end{aligned} \tag{3}$$

In Fig. 1a, 3D CAD model of the robotic arm designed in SolidWorks is shown beside an experimental model of the robotic arm which was fabricated.

As the application is intended to be medical based any amount of vibrations in the system can cause deviation from the desired target point. Hence, measuring vibrational amplitudes in a robotic system and optimizing the amplitudes are of utmost importance.

Here, an accelerometer PMOD ACL sensor is connected with a MyRio controller of National instruments programmed using LabVIEW. Vibrational amplitude data

was recorded directly from MyRio in real time. Each link was given a feed of 90° and the accelerometer sensor was attached to the end of each link to measure the maximum vibration due to the motion of all the joints. Figure 2 shows the VI and graphical programming for accelerometer integration.

Vibrational amplitude graph was formed from the data acquired in Figs. 2, 3, and 4 which show the graphs of vibration of each link in X-axis, Y-axis, and Z-axis (Fig. 5).

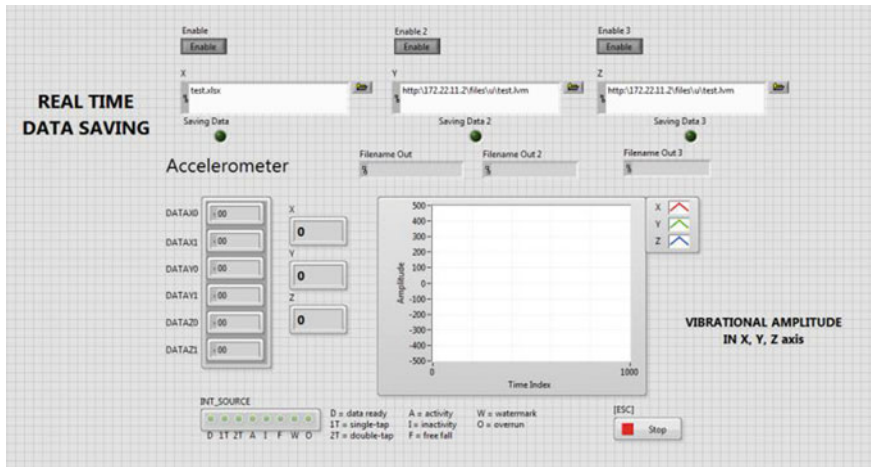


Fig. 2 Virtual interface and programming for accelerometer integration for vibration measurement

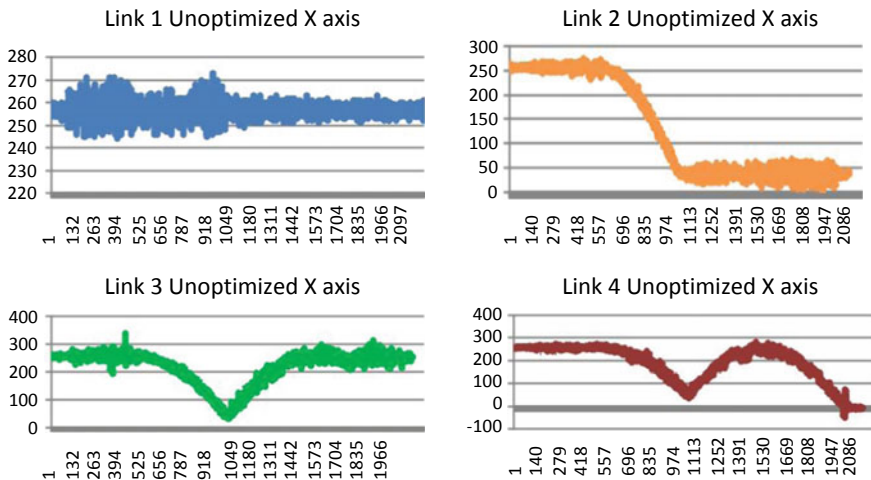


Fig. 3 Vibrational amplitude of all links in X-axis

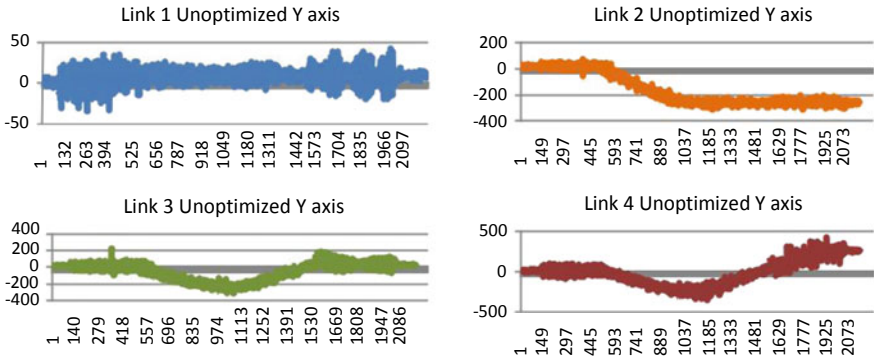


Fig. 4 Vibrational amplitude of all links in Y-axis

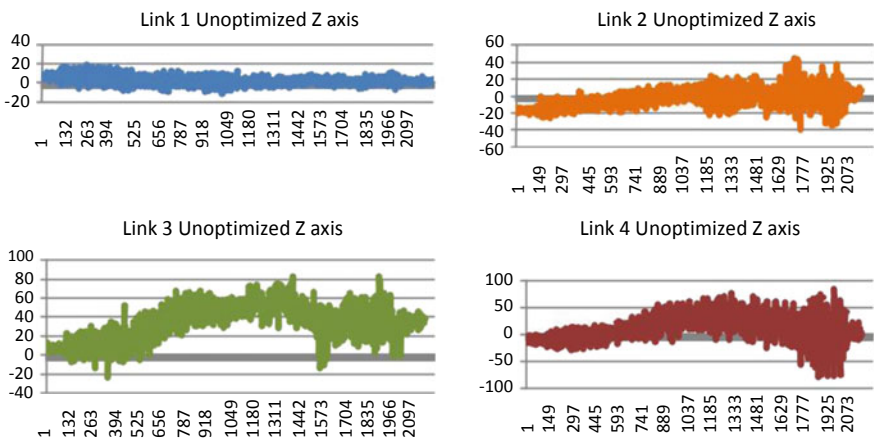


Fig. 5 Vibrational amplitude of all links in Z-axis

2.2 Optimized Design and Vibration Analysis

Vibration was found to be in the level of 150–200 $\hat{A}\mu\text{m}$ and in order to reduce the amplitudes of vibration the structure was optimized. A link was added to Link 2 in between joint 2 and joint 3 forming a triangular structure in kinematic sense. Figure 6 shows a 3D CAD model of structurally optimized robotic arm along with optimized experimental model.

Vibrational analysis was again done in the same manner using accelerometer attached with MyRio controller programmed with LabVIEW. Vibrational amplitude graph for each link in X-axis, Y-axis, and Z-axis is shown in Figs. 7, 8, and 9.

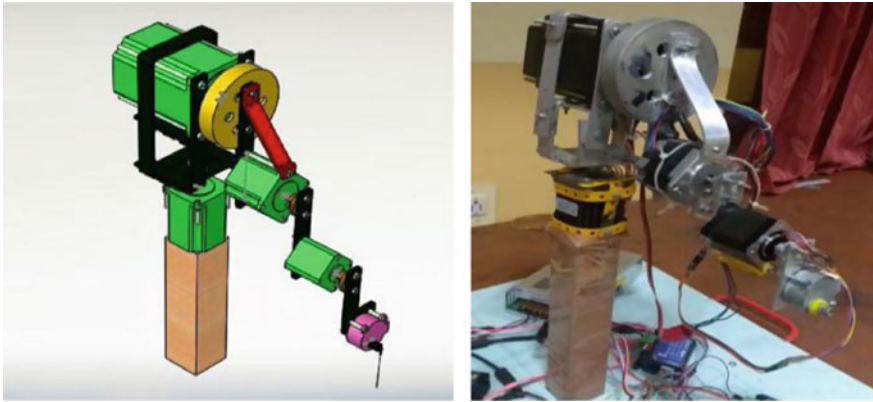


Fig. 6 Optimized 3D CAD model and optimized experimental model

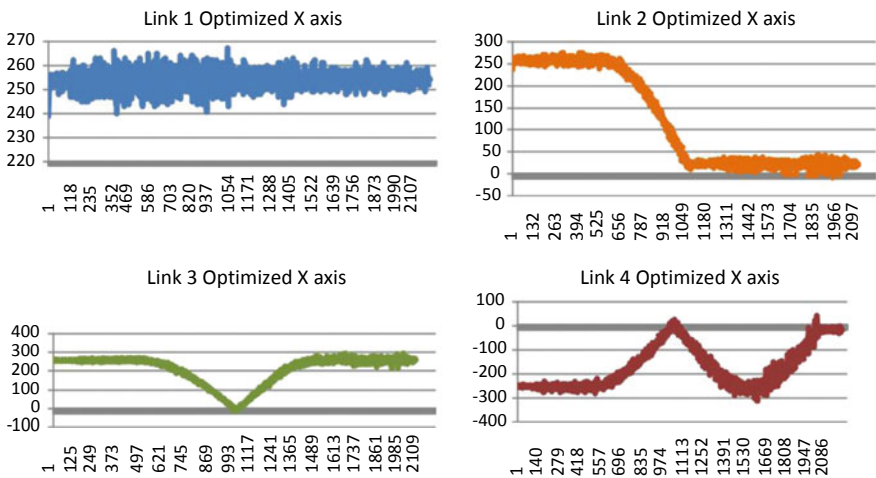


Fig. 7 Vibrational amplitude of all links in X-axis after optimization

3 Results

Vibration on Link 4 was analyzed by comparing the amplitude graph of unoptimized and optimized model. Figure 10 shows the comparison graph. GRAPH software was used to analyze this amplitude graph.

Using the graphical method it was found that the amplitude of vibration at the end of Link 4 where the needle will be kept was reduced from the range of 150–200 μm to range of 50–75 μm . A moving average line was generated in graph software by taking 35 interval points for getting a baseline for both unoptimized and optimized

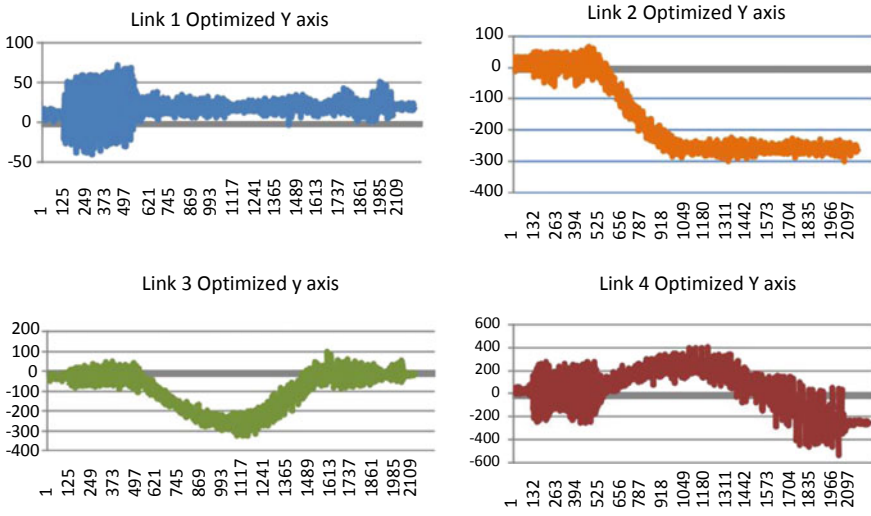


Fig. 8 Vibrational amplitude of all links in Y-axis after optimization

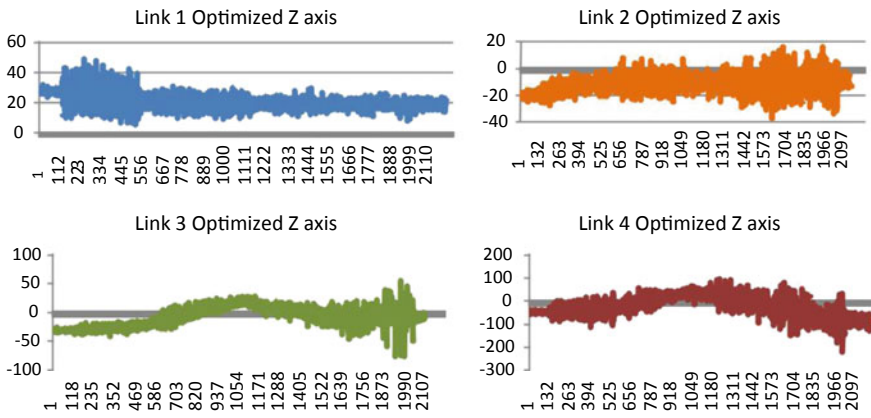


Fig. 9 Vibrational amplitude of all links in Z-axis after optimization

amplitude. Maximum reduction of $55 \mu\text{m}$ was also found in the moving average line which suggests reduction in overall vibration of the robotic arm. On an average, the amplitude of vibration was reduced by 62.5–66.67%.

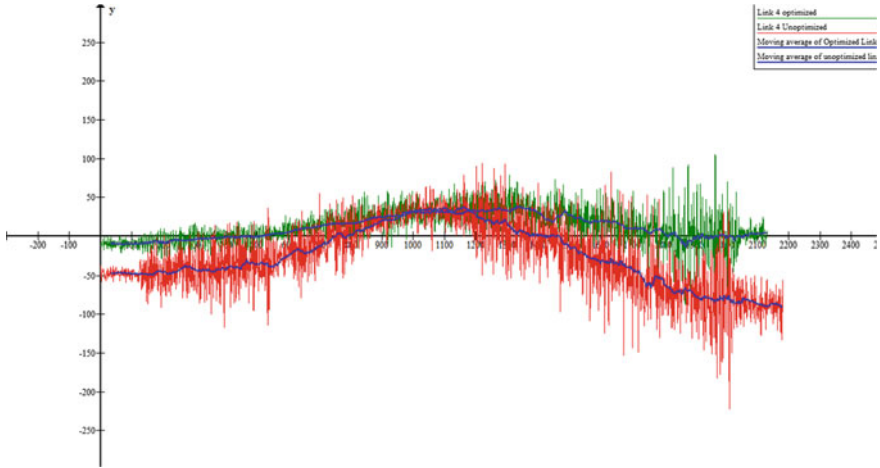


Fig. 10 Amplitude comparison graph of Link 4

4 Conclusion

In the above research, a vibration analysis is performed on a 5-axis robotic manipulator designed and fabricated for CT-guided biopsy interventions. Vibrational analysis was performed using an accelerometer connected with NI MyRio which was programmed using LabVIEW. The accelerometer sensor was placed at the end of each link of the experimental model to acquire maximum vibrational amplitude data.

Amplitudes of vibration in *X*-, *Y*-, and *Z*-axes were found for every joint. Structure of the robotic arm was optimized by attaching an aluminum bar in between joint 2 and joint 3 making a triangular structure with Link 2. Amplitudes of the vibration were again measured using accelerometer. To understand actual reduction of vibration GRAPH software was used to analyze the amplitude graph. A moving average with 35 interval points was taken to form a baseline for the amplitudes.

On an average vibration of Link 4 where the needle for biopsy will be attached was reduced by 62.5–66.67%. More optimization is needed to reduce the vibration even further as well as the design of the robot could be optimized even further, and Taguchi method could also be used to optimize the angular velocity of the actuators to reduce vibration as it is one of the important parameters contributing to vibration. More attempts will be made to make this design more optimized.

References

1. Supriya S (2017) A vibration analysis of a 6 axis industrial robot using FEA. *Mater Today Proc* 4:2403–2410
2. Marco L (2018) Vibration analysis of robotic milling tasks. *Proc CIRP* 67:262–267
3. Patil SS (2016) Experimental measurement of strain and stress state at the containing helical gear pairs. *Measurement* 82:313–322
4. Jakob KH, Raphael S (2016) Franz: self-supporting end effectors towards low powered robots for high power tasks. *Proc CIRP* 44:418–423
5. Alexandre CL, Martin O, Pierre LB (2016) A time-domain vibration observer and controller for physical human-robot interaction. *Mechatronics* 36:45–53
6. Sammali F, Xu L, Rabottia C (2018) Effects of vibration-induced fatigue on the H-reflex. *J Electromyogr Kinesiol* 39:134–141
7. Han Y, Eric C, Marc G (2017) Vibration analysis of cable-driven parallel robots based on the dynamic stiffness matrix method. *J Sound Vib* 394:527–544
8. Abd El Khalick M (2018) Design of a force-controlled end-effector with low inertia effect for robotic polishing using macro-mini robot approach. *Robot Comput Integr Manuf* 49:54–65
9. Karim H, Subhash R (2017) Fingers vibration transmission performance of vibration reducing gloves. *Int J Ind Ergon* 62:55–69
10. Yingjie G (2016) Vibration analysis and suppression in robotic boring process. *Int J Mach Tools Manuf* 101:102–110

Development of Low-Cost Wind Power Estimation System in Enggano Island Indonesia



Novalio Daratha, Indra Agustian, Dedi Suryadi, Agus Suandi and Neeraj Gupta

Abstract This paper describes an investigation of the wind potential in Enggano Island, Indonesia. A low-cost wind power estimation system was developed. The device is able to log the time series of the measurement data. Nonparametric estimation is used to calculate the power density function of wind power density. The device is portable and has low power consumption. Hence, it can also be used elsewhere in the world where wind power probabilistic characteristics are needed.

Keywords Wind power estimation · Low-cost measurement · Wind speed · Time series analysis · Probability density function · Energy analysis · Remote island

1 Introduction

Indonesia is an archipelago with many islands. Most of the small islands are not connected electrically to the big islands. In these islands, diesel generators provide electricity to their people. Hence, electricity is more expensive and certainly not environmentally friendly.

Enggano is an example of such island. It is connected to the power grid in Sumatra, the nearest big island. Its major source of electricity is now from diesel generator. While there has been effort to use photo voltaic to generate electricity, its portion is still low. Hence, Enggano's source of electricity is not environmentally friendly.

On the other hand, wind power has not been used to generate electricity in Enggano and many other similar islands in Indonesia. One of the many reasons is the unavailability of low-speed wind generator. In order to design and develop such system, information about the available wind power is required. Unfortunately, such infor-

N. Daratha · I. Agustian · D. Suryadi · A. Suandi
University of Bengkulu, Bengkulu, Indonesia
e-mail: ndaratha@unib.ac.id

N. Gupta (✉)
National Institute of Technology, Srinagar, Jammu and Kashmir, India
e-mail: neeraj5822@gmail.com

mation is mostly unavailable due to lack of measurements data. This work reports a low-cost wind power estimator device which can be used to measure the wind potential.

A popular indicator of wind power potential is wind power density, i.e., its probability density function (PDF). The density is calculated based on wind speed, air pressure, and temperature at a location [1]. Hence, the calculation requires long-term measurements data to reveal the wind characteristics. Therefore, the measurement device must have data logging capability and off-grid power supply.

Furthermore, some works assume that the PDF belong to certain class [2, 3, 8, 10]. The wind speed in Enggano is relatively slow [6, 7]. Hence, Weibull [13] and Rayleigh distribution are not suitable to describe the wind in Enggano [5]. This work assumes that the PDF in Enggano do not follow any popular class of distribution. Therefore, this work uses kernel density estimation in calculation of the PDF of the wind power.

This work differs from majority of previous works in the following way:

1. It uses nonparametric density estimation [11, 12] which does not assume any class of PDF of the wind speed.
2. It consider surface wind speed.

The rest of this paper is organized as follows. Section 2 describes general methodology and reviews the method of estimation of wind power density and the design of the measurement device. Section 3 discusses some initial results. Finally, Sect. 4 concludes this paper.

2 Methodology

Estimation of wind power potential in Enggano includes the following steps:

1. Measurement of wind speed.
2. Estimation of wind power density.
3. Estimation of wind probability density function.

The following subsections describe those three steps briefly.

2.1 *Measurement of Wind Speed*

Wind speed data on most of islands in Indonesia are not available. A measurement device was designed and developed for this project. Its wiring diagram of is shown in Fig. 1. All components can be bought online comparatively in low price as shown in Table 1.

The device is made of many subcomponents: microcontroller, speed sensor, and data logger. The arduino uno includes an ATmega328P as a microcontroller. The

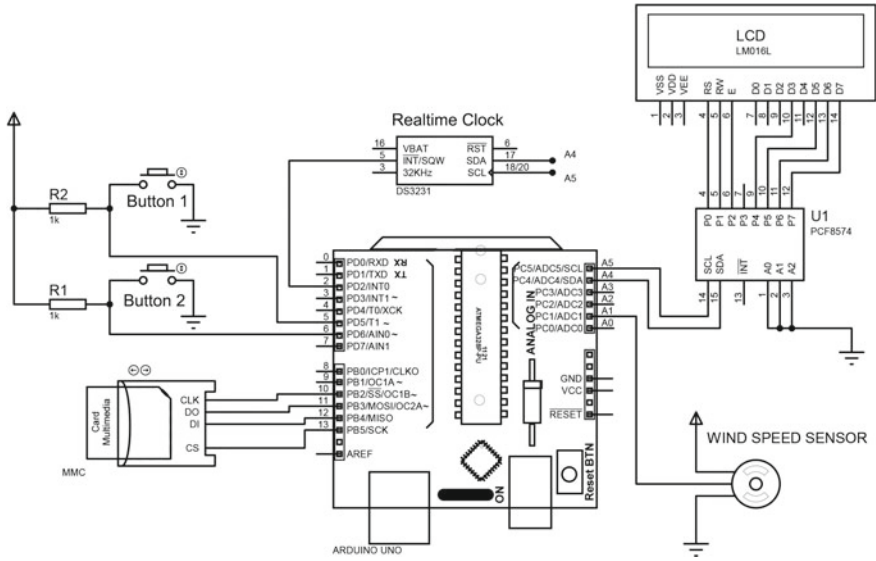


Fig. 1 Wiring diagram of the wind power measurement system

Table 1 Price list of components

No.	Component	Price (IDR)
1	Arduino Uno	88000
2	Battery clock	50000
3	LCD 16 × 2 + I2C	75000
4	Push button with cup B3F button 12 * 12 * 7.3 @ 1.200 × 2	2400
5	Accumulator	200000
6	Anemometer	750000
7	UBEC (Current Indicator and battery)	50000
8	Thinwall 1500 ml food container box	15000
9	Arduino data logger w DS1307 RTC	74600
10	Jumper wire @20 × 1000	20000
11	Memory card 4 GB SDHC	100000
	Total	775000

wind speed sensor is a cup anemometer. It has four hemispherical cups mounted on horizontal arms, all of which is mounted on a vertical shaft. However, the sensor does not have to be vertical during measurements. In addition, the sensor cannot give any information about the direction of the wind. The rotation of the anemometer is converted into electrical voltage. The voltage will range from 0.0 V (0m/s wind) up to 5.0 V (for 32.4 m/s wind speed). The voltage is then converted into a digital signal

by analog to digital converter (ADC). Arduino uno already includes an ADC for this purpose.

The interval of the voltage is 0–5 V with 10 bit bandwidth. Hence, the ADC maps voltages between 0 and 5 V into integer values between 0 and 1024. The sensor is linear in this interval and, hence, the wind speed is

$$v = V \frac{32.4}{1024} \quad (1)$$

where V is the output voltage of the anemometer in Volt and v is the wind speed in m/s. The calculated wind speed is displayed in the 16×2 LCD matrix and logged into an SD Card using DS3231. DS3231 is a Real Time Clock module. It adds data logging capability into the arduino uno.

Figure 1 shows that the device can have more sensors such as temperature and air pressure. Section 2.2 discusses how the addition of those sensors may improve the quality of wind power estimation. Hence, in the future works, those sensors can be integrated into the measurement device.

2.2 Wind Power Density Estimation

At a certain location where wind blows with speed v (m/s) and the air density is ρ (kg/m^3), power content per unit of area P (W/m^2) is given by

$$P = \frac{1}{2} \rho v^3 \quad (2)$$

In order to calculate (2), the air density can be estimated using

$$\rho = \frac{P_a}{R_s T} \quad (3)$$

where

P_a is the air pressure in Pascal,

R_s is the specific gas constant for dry air in $\text{J}/(\text{kgK})$,

T is the air temperature in Kelvin.

If the available power P is used to rotate a turbine, maximum attainable power is $\frac{16}{17}P$. This number also represent the upper limit of electricity power that can be generated for the wind.

In many studies, the air pressure and temperature are assumed to be constant. This certainly introduce some error in the results of calculations.

Furthermore, as air temperature and pressure and wind speed vary continuously over time, the power content of the wind also varies. This intermittent behavior leads to uncertainty in the estimation of power from wind in a location. Hence, the uncertainty of potential of the wind power is a natural phenomenon.

2.3 Wind Probability Density Function

From the measurements, we get time series of wind speed v

$$v = [v_1, v_2, v_3, \dots, v_n]. \quad (4)$$

we assume that the samples in v have the same probability density function (PDF) $f(x)$ at the interval of measurements. However, we do not assume the type of the PDF $f(x)$. In this kind of situation, kernel density estimation is suitable approach to estimate $f(x)$. Equation (5) of describes the estimate $f(\hat{x})$.

$$\hat{f}_n(v) = \frac{1}{nh^d} \sum_{i=1}^n K\left(\frac{v - V_i}{h}\right) \quad (5)$$

where $K : \mathbb{R}^d \rightarrow \mathbb{R}$ is the kernel function and $h > 0$ is the bandwidth. In this work, Gaussian kernel is used.

$$K(v) = \frac{\exp(-\|v\|^2/2)}{x_{1,d}}, \quad x_{1,d} = \int \exp(-\|v\|^2)dv. \quad (6)$$

3 Result and Discussion

The measurement was done in November 2018 at Bak Blaw and Kahyapu, both are in Enggano Island, Bengkulu, Indonesia (See Fig. 2). Bak Blaw is the mouth of a small river and Kahyapu is a port. Since, it was an initial survey, the height of measurement is around 30 cm from the ground at the beach of each location. Hence, speed was surface speed. Due to weather condition, the duration of measurement in Bak Blaw was longer than that in Kahyapu.

Wind power density as function of time of sampling are given in Figs. 3 and 4 for Kahyapu and Bak Blaw, respectively. The power density all below 100 W/m^2 . However, the wind at Bak Blaw was stronger in Kahyapu because Bak Blaw is facing toward the Indian Ocean while Kahyapu is not.

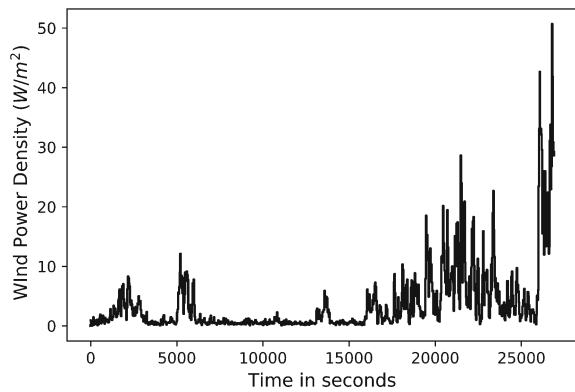
In addition, the fluctuations in those figures are also significant. Thus, it is better to describe the characteristics of the wind power using probabilistic indices. The wind probability density functions are shown in Figs. 5 and 6 for Kahyapu and Bak Blaw, respectively. These figures also show that the wind in Bak Blaw is stronger than the wind in Kahyapu.

It is important to remember that the measurements were done in few hours only wind four samples per second. Hence, the results given in Figs. 3, 4, 5 and 6 should not be used to judge the wind potential at Enggano Island. However, the results indicate that the device developed for this work is effective.



Fig. 2 Location of measurements

Fig. 3 Wind power density in Kahyapu



The results in this section were computed on a laptop with Intel Core i5-62000U at 2.30 GHz with 8 GB RAM running windows 10. The estimation of PDF was done using Python [4], Pandas [9].

Fig. 4 Wind power density in Bak Blaw

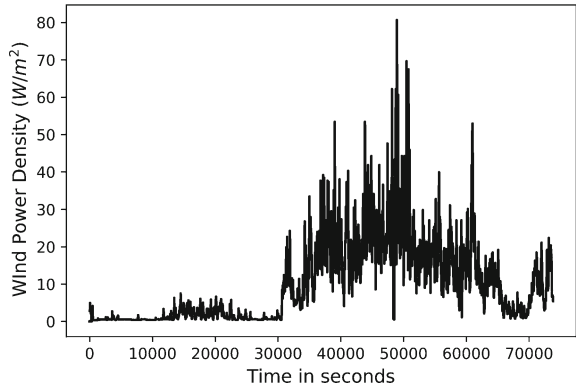


Fig. 5 PDF of wind speed in Kahyapu

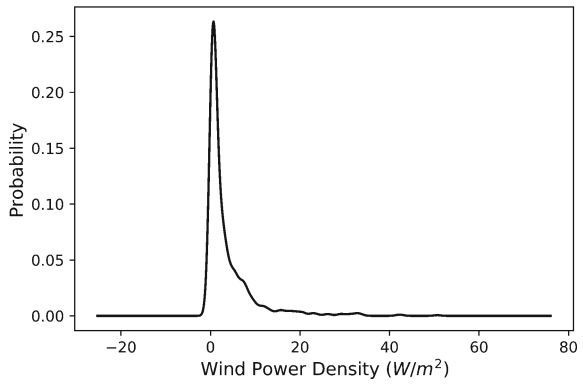
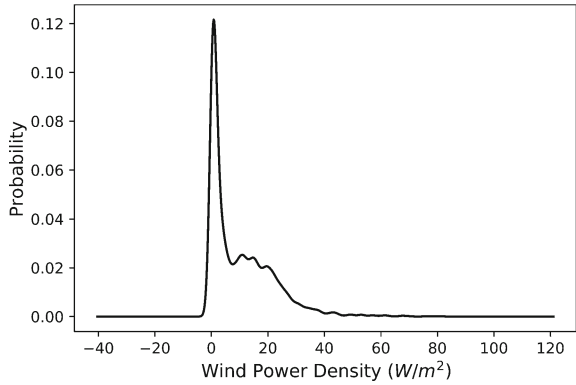


Fig. 6 PDF of wind power density at Bak Blaw



4 Conclusion

This paper presents an effort to estimate the potential of wind power in a remote location. First, this paper reports a low-cost wind speed measurements system. The system is portable since it can be powered by battery. The data is logged into a storage system. Second, this paper describes how wind power density can be calculated using time series of wind speed, temperature and air pressure. Third, this paper demonstrates how nonparametric approach can be used to estimate the PDFs of wind potential in those locations.

The forms of those PDFs are similar. It is also visible that there is more power in Bak Blaw than in Kahyapu. These results indicate that PDF is a good representative of the data. Thus, the size of storage in saving the original time series (Figs. 3 and 4) is bigger than that of PDFs. If period of measurement are long, such as one year or more, the size of the time series will be large. However, the size of the corresponding PDF will be much smaller.

However, the work described in this paper has some weaknesses. First, the period of measurements is very short. Second, the altitude of the measurements is also low (surface level). Third, air temperature and pressure are not measured.

Future works will be aimed at solving those weaknesses. In particular, when the period of measurement is long enough the forms of the PDFs of wind power potential will be compared with standard PDF such as Rayleigh and Weibull distributions.

In addition, we have found that this project has good pedagogical characteristics which can be integrated into undergraduate curriculum in Electrical Engineering. In the process of understanding the working principles of the measurement device, a student will integrate his/her knowledge in sensors and transducers, microcontroller, electronics, physics, and scientific computation.

References

1. Carta JA, Mentado D (2007) A continuous bivariate model for wind power density and wind turbine energy output estimations. *Energy Convers Manag* 48(2):420–432
2. Carta JA, Ramirez P, Velzquez S (2008) Influence of the level of fit of a density probability function to wind-speed data on the WECS mean power output estimation. *Energy Convers Manag* 49(10):2647–2655
3. Celik AN (2004) A statistical analysis of wind power density based on the Weibull and Rayleigh models at the southern region of Turkey. *Renew Energy* 29(4):593–604
4. Foundation PS (2018) Python language reference, version 3.6.0. www.python.org. Accessed 01 Jan 2018
5. Jamil M, Parsa S, Majidi M (1995) Wind power statistics and an evaluation of wind energy density. *Renew Energy* 6(5):623–628
6. Jung C, Schindler D, Laible J, Buchholz A (2017) Introducing a system of wind speed distributions for modeling properties of wind speed regimes around the world. *Energy Convers Manag* 144:181–192
7. Martosaputro S, Murti N (2014) Blowing the wind energy in Indonesia. *Energy Procedia* 47:273–282

8. Mazzeo D, Oliveti G, Labonia E (2018) Estimation of wind speed probability density function using a mixture of two truncated normal distributions. *Renew Energy* 115:1260–1280
9. McKinney W (2010) Data structures for statistical computing in python. In: van der Walt S, Millman J (eds) *Proceedings of the 9th python in science conference*, pp 51–56
10. Mohammadi K, Alavi O, Mostafaeipour A, Goudarzi N, Jalilvand M (2016) Assessing different parameters estimation methods of Weibull distribution to compute wind power density. *Energy Convers Manag* 108:322–335
11. Parzen E (1962) On estimation of a probability density function and mode. *Ann Math Stat* 33(3):1065–1076
12. Rosenblatt M (1956) Remarks on some nonparametric estimates of a density function. *Ann Math Stat* 27(3):832–837
13. Wais P (2017) Two and three-parameter Weibull distribution in available wind power analysis. *Renew Energy* 103:15–29

Performance Investigation of a Nanofluid-Based Parabolic Trough Solar Collector



Devander Kumar and Sheela Kumari

Abstract The present study is performed with the aim to investigate the simple methods of performance enhancement of parabolic trough collector (PTC). Nanofluid proposes exclusive advantages over conventional fluids due to their unique physical properties. In this manuscript, the thermal performance of PTC integrated with the storage tank is investigated experimentally using 0.0 and 0.1 wt% nanofluids based on the multi-walled carbon nanotube (MWCNT) particles. A nanofluid based on the MWCNT particles using triple deionized water as a base fluid is prepared and used as the working fluid in addition to the water for performance investigation. The performance has been evaluated in terms of useful heat gain, collector thermal efficiency, rise in water temperature within the storage tank, charging, and overall efficiency of system. Experimental results showed that the performance of the collector is improved using nanofluid as a working fluid in comparison to the water and average gain in thermal efficiency is achieved to be about 3% higher with nanofluid. The maximum charging efficiency of the system is found to be 62 and 59% with MWCNT nanofluid and water, respectively.

Keywords MWCNT nanofluid · Parabolic trough collector · Thermal efficiency · Charging and overall efficiency

Nomenclature

A_a Aperture area (m^2)
 $C_{p, pf}$ Specific heat of flowing fluid at mean temperature (J/kg K)
 $C_{p, bf}$ Specific heat of base fluid (J/kg K)
 $C_{p, nf}$ Specific heat of nanofluid (J/kg K)

D. Kumar (✉)
Oil and Natural Gas Corporation Ltd., Ahmedabad, India
e-mail: lambadev1@rediffmail.com

S. Kumari
Indian Institute of Technology, Roorkee, India
e-mail: sheelalamba@gmail.com

$C_{p,np}$	Specific heat of nanoparticles (J/kg K)
$C_{p,st}$	Specific heat of stored fluid (J/kg K)
D_{ai}	Inner diameter of absorber (m)
D_{ao}	Outer diameter of absorber (m)
D_{ci}	Inner diameter of glass cover (m)
D_{co}	Outer diameter of glass cover (m)
E_{co}	Collected energy (J)
E_{st}	Stored energy (J)
F	Focal length (m)
H	Height of inner storage tank (m)
I	Solar beam radiation on aperture plane of PTC (W/m ²)
L	Collector length (m)
L_{sr}	Supporting rod length (m)
\dot{m}	Mass flow rate of working fluid (kg/s)
m	Stored mass of fluid within the storage tank (kg)
\dot{Q}_u	Useful energy extracted (W)
S_a	Arc length of parabola (m)
T_{fi}	Inlet temperature of fluid (°C)
T_{fo}	Exit temperature of fluid (°C)
ΔT	Temperature difference between exit and inlet of receiver (°C)
T_{st}	Fluid temperature in storage tank (°C)
w_I	Error in solar beam irradiance (%)
w_m	Error in mass flow rate (%)
$w_{\Delta T}$	Error in temperature rise in the receiver (%)
w_η	Error in thermal efficiency of collector (%)
W_a	Aperture width (m)
x	Half of aperture width (m)
X	Height of thermocouples from base of inner storage tank (m)
Y	Depth of parabola from focal axis (m)

Subscripts

k	At any instant time
$k + 1$	One hour period after k th time
I	Inner
O	Outer

Greek Symbols

ϕ_r	Rim angle (°) chosen as 90°
η_I	Instantaneous thermal efficiency

η_{ch}	Charging efficiency
η_{ov}	Overall efficiency
Φ_{br}	Ball bearing diameter (m)
Φ_{ic}	Inner collar diameter (m)
Φ_{oc}	Outer collar diameter (m)
Φ_{sr}	Supporting rod diameter (m)
φ	Volume fraction of nanoparticles in nanofluid

1 Introduction

Over the last few decades, global demand for the energy consumption has been increasing at an alarming pace. Currently, fossil fuels like natural gas, oil, and coal have been fulfilling more than 90% energy requirements of the world [1]. Such fuels are non-renewable and limited in delivering the energy for infinite period of time. These resources of energy are depleting continuously. For fulfilling the increasing demand of energy and achieving global justice throughout the world, existing solar energy around the globe can be considered as one of the largest and sustainable renewable resources of energy. For higher temperature applications, PTC among the various type of concentrating collectors is the most popular system and experienced technology. PTCs are typically providing thermal energy over the wide range of temperatures, i.e., up to 450 °C. These are successfully utilized for numbers of applications like in steam generation, space heating and cooling, electricity production by utilizing generated steam, distillation of water, hot water production, industrial process heating, cooking, refrigeration, and air conditioning [2, 3]. In 2007, a fiber-glass reinforced PTC having 90° rim angle for generation of hot water was designed and constructed by Arasu and Sornakumar [4]. Although, expenditure is one of the key features making limitation on the growth of trough-type solar collectors system. Enhancing the thermal efficiency of PTC system can partly reduce such difficulty. In order to increase the efficiency of such systems, nanofluids have exhibited a remarkable potential.

Nanofluids are novel types of working fluids which have shown the superior thermal and physical properties like viscosity, thermal conductivity, and heat transfer coefficient due to the dispersion of metallic and non-metallic nano-sized particles in a base fluid [5]. In 1995, the term nanofluid was first used by Choi and Eastman [6] and later experimented by many researchers. For instance, thermal conductivity of copper is around 3000 times larger than the engine oil and around 700 times larger than the water at room temperature. Metallic liquids have the thermal conductivity much larger than the non-metallic liquids. So, the fluids having dispersed metallic particles are projected to have increased thermal conductivities in comparison to pure liquids [7]. Masuda et al. [8] mixed nanoparticles oxide (TiO₂ and Al₂O₃ with 4.3 wt%) in liquid and found improvement in the thermal conductivity as 11 and 32%, respectively.

Among the various nanoparticles, carbon nanotubes have exhibited superior properties. Choi and Eastman [9] reported that the CNT–water nanofluids have greater thermal conductivity in comparison to pure liquids. Lotfi et al. in 2012 [10] studied experimentally that there is an improvement in the heat transfer of multi-walled carbon nanotube (MWCNT)/water nanofluid when it is used inside the horizontal shell and tube type heat exchanger. It shows that heat transfer of working fluid is improved due to the presence of MWCNT as compared to the base fluid.

Recently, not much studies have been carried out about the utilization of nanoparticles for the thermal performance evaluation of PTC. Taylor et al. [11] offered a proposal for heat transfer enhancement of working fluid flowing inside the PTC receiver by using the nanofluid. Khullar et al. [12] investigated the applications of nanofluid into the PTC theoretically and made the comparison of theoretical results with the experimental results of PTC. Their results showed that 5–10% greater efficiency is found with nanofluid in comparison to the conventional fluid. Kasaeian et al. [13] estimated the performance of PTC using 0.2 and 0.3% carbon nanotube/mineral oil nanofluids as per the ASHRAE Standard 93 (2010). Around 4–5% and 5–7% of global efficiency is increased when 0.2 and 0.3% carbon nanotube/oil nanofluids are utilized in place of pure oil.

The preceding studies of the literatures showed that very few investigations have been carried out on the thermal behavior assessment of PTC using nanofluids experimentally. The purpose of current research is to estimate the thermal performance of PTC integrated with storage tank experimentally utilizing (MWCNT)-based nanofluid and water as working fluid. The objective of the present study is to enhance PTC output and accounting construction easiness.

2 Nanofluid Material and Preparation Method

In the present studies, the MWCNTs powders (United Nanotech Innovation Pvt. Ltd., Bangalore, India) with 98% of purity having mean size of particles as 500 nm at magnification of 100,000 \times were used. Figure 1 displays the scanning electron microscope (SEM) image of MWCNT particles. Sodium dodecyl benzene sulphonate from Sigma-Aldrich was utilized as a surfactant in order to disperse the MWCNT and triple deionized water as the base fluid.

For nanofluid preparation, initially, solid and liquid phases were weighted with the electronic balance having the resolution of 0.0001 g. In order to enhance dispersion behavior and reduce nanotube aggregation, 0.1 wt% MWCNTs and a suitable quantity of sodium dodecyl benzene sulphonate were blended to the triple deionized water to acquire a homogenous dispersed solution. Sonication time (chosen as 30 min) is an important factor for the dispersion of collective nanoparticles [14]. For getting nanofluid dispersion, vibration in the suspension was carried out by a bath sonicator from PCI, Mumbai, India, model 3.5 l 1004, with 40 W power and for 5 h. Figure 2 shows the nanofluid solution. MWCNTs seem to be harmful for humans and animals. But, the environmental effects of MWCNT are a part of research. The

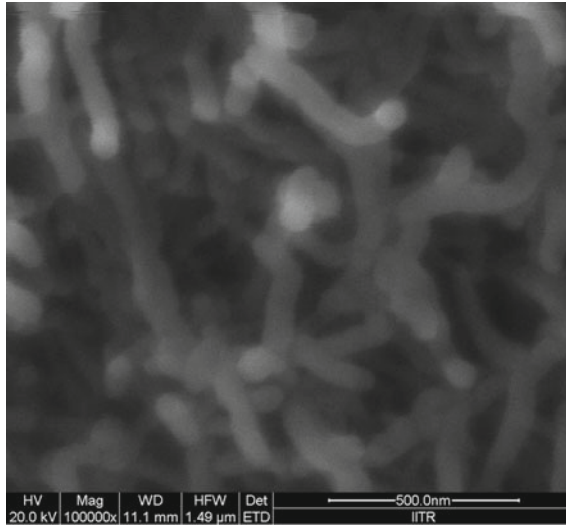


Fig. 1 SEM micrograph of MWCNT

cost of MWCNT powder and triple deionized water is around Rs. 600 g and Rs. 100 l respectively.

3 Experimental Setup Description and Procedure

3.1 Experimental Setup

Figure 3 displays an experimental setup of PTC with the storage tank. The description of the main components as follows.

Parabolic trough collector: The PTC consists of a concentrating parabolic surface which is situated on the reflector supporting frame having the parabolic shape. The reflector of PTC is made up of anodized aluminum sheet with specular reflectivity of 86% whose initial dimensions are 1.22 m length, 1.255 m width. The supporting structure of collector is made up of Mild Steel (MS) square pipe and MS flat plates. These plates and aluminum sheet are shaped into the form of parabola with the help of the following Eq. (1) [15].

$$x^2 = 4 \times F \times y \tag{1}$$

$$S_a = 2 \times F \times \left[\left(\sec \frac{\phi_r}{2} \times \tan \frac{\phi_r}{2} \right) + \left(\ln \left(\sec \frac{\phi_r}{2} + \tan \frac{\phi_r}{2} \right) \right) \right] \tag{2}$$

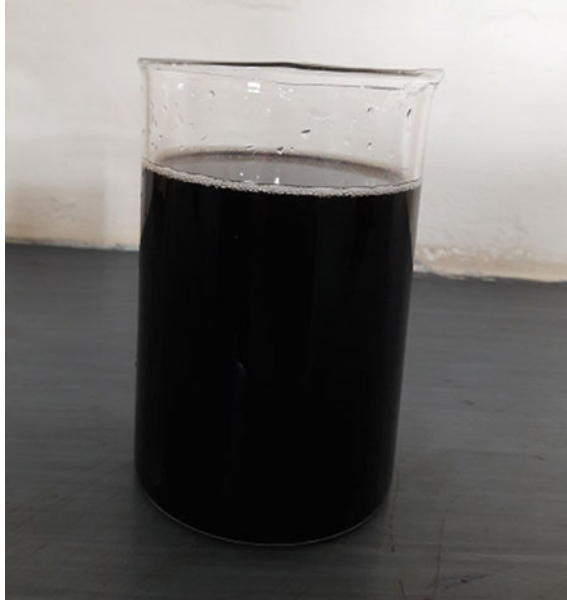


Fig. 2 The nanofluid having surfactant with appropriate sonication

Upon substituting the value of rim angle and arc length $S_a = 1.255$ m, F is found to be 0.273 m and obtained by the Eq. (2) [4]. It gives the value of half of aperture width ($x = 0.546$ m) of parabola upon substituting in Eq. (1). The value of the depth of parabola (y) is same as that of F for 90° rim angle. Hence, the value for aperture area of PTC is come out to be 1.33 m². The fabrication of the supporting structure

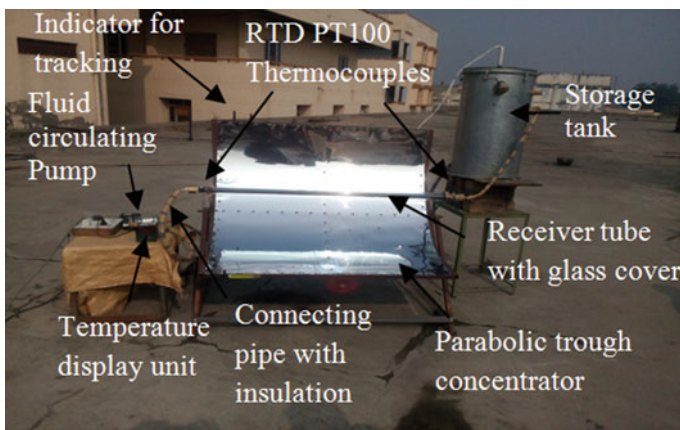


Fig. 3 Photograph of parabolic trough collector with storage tank

Table 1 Specifications of the parabolic trough collector

Design parameters of PTC	Value
Receiver external diameter	0.0318 m
Receiver internal diameter	0.0284 m
Glass cover external diameter	0.0556 m
Glass cover internal diameter	0.0506 m
Concentration ratio	10.60

of collector is carried out in two parts. In the first upper part, square pipe is marked, cut, and welded as per aperture area required for PTC. The straight MS flat plates are converted into a shape of parabola which is consistent with parabola drawn on a piece of paper manually. The second part is the legs-part which supports the upper part of the supporting structure and is placed on the floor.

The reflector of PTC reflects and concentrates the falling solar irradiance into the receiver, which is placed at the focal line of the reflector. The receiver assembly comprises of a copper receiver tube, which is coated by PU-matt black paint and is enclosed in a concentric borosilicate glass cover. The concentrated solar irradiance is absorbed by the receiver and afterward transmitted in the form of heat to the heat carrier fluid, which is circulating through the receiver. The detail specifications of PTC are given in Table 1.

Thermal storage tank and circulating pump: A thermal storage tank of 52 l capacity consists of two cylindrical tanks which are fabricated by the sheets of galvanized iron. The inner tank is placed inside the outer tank. Glass wool is filled in the gap between the two tanks in order to well insulate the inner tank in which liquid (water) is filled. A copper pipe acts as a heat exchanger which is located in at the base of the inner tank. Heat exchanger is joined to the receiver through the circulating pump, valve, and pipe fittings. The HTF is circulated by the pump in the closed circuit of receiver tube, plastic pipe, and copper pipe during the whole working of PTC system in order to transfer the heat of absorber tube to the stored water inside the storage tank. Approximately, 1 l of working fluid is sucked initially to fill the receiver tube, plastic, and copper pipes by the pump in open circuit. During working, the circuit is closed.

The top end of storage tank is covered by a GI sheet insulated cover to prevent heat loss from water at top side. A small hole is provided in the middle of cover through which a hollow PVC pipe with five small holes at different heights along its length is passed and kept inside the storage tank vertically. At these five holes, the thermocouples are inserted to know the temperature of water at different heights in the tank. For continuous monitoring, each thermocouple is connected to the temperature indicator kit. The detailed specifications of the storage tank are shown in Table 2.

Table 2 Specifications of the storage tank

Construction parameters	Value
Height of inner and outer tank	0.615 m, 0.655 m
Diameter of inner and outer tank	0.33 m, 0.41 m
Copper pipe outer and inner diameter in tank	0.0055 m, 0.0045 m
Length of copper pipe in tank	12 m
Insulation thickness	0.04 m

3.2 Measuring Instruments and Devices

RTD PT-100 thermocouples are placed at the outlet and inlet of the absorber for showing HTF temperature. These thermocouples are connected to the digital indicator which indicates the temperature with an error of $\pm 0.3\%$ and resolution of $0.1\text{ }^{\circ}\text{C}$. A mercury-in-glass thermometer is utilized for recording the temperature of ambient air with a resolution of $\pm 1\text{ }^{\circ}\text{C}$. The measurement for HTF flow rate is performed initially with the help of stopwatch (least count 1 s) and the volume measuring beaker (least count 10 ml) before closing the circuit. Solar intensity is measured by using calibrated solar power meter (TENMARS TM-207) with accuracy $\pm 5\%$ and resolution 1 W/m^2 [16].

3.3 PTC System Operation

Testing of PTC system is carried out at TIT&S, Bhiwani ($28^{\circ} 78'$ latitude North and $76^{\circ} 13'$ longitude East), a city situated in the northern region of India. Aperture plane of the collector is tilted an angle around 8° with respect to horizontal surface of place and facing due south with an orientation of collector axis in E-W direction. At this angle, highest solar energy would be concentrated on to the receiver of collector in the month of May of summer season. The schematic layout of testing apparatus is shown in Fig. 4.

3.4 Testing Procedure

First, fresh water is filled in the storage tank. At least 30 min before, PTC is positioned in south facing mode and exposed to the sun for starting the experiment. The pump is started at 8:30 a.m. In each experiment, the initial measured flow rate of HTF remains constant. The testing has been performed in the month of May by circulating working fluid through the collector. In north India, April and May are the months of summer season during which the highest solar irradiance is obtained in a year generally. The

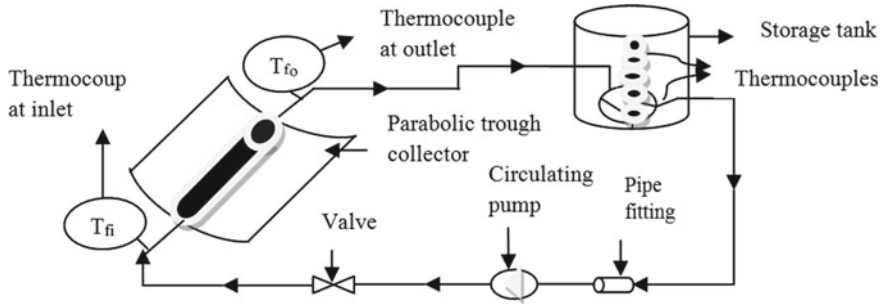


Fig. 4 Schematic layout of experimental setup

readings are noted down every hour in a table shape from 9:00 to 17:00 h. The pump is switched off at 5:00 p.m. because after that, the thermal losses of working fluid during circulation are considerable than the energy collected by collector in the circuit.

3.5 Parametric Performance

Useful heat gain (\dot{Q}_u)

$$\dot{Q}_u = \dot{m} \times C_{pf} \times (T_{fo} - T_{fi}) \quad (3)$$

$$C_{p,nf} = (1 - \varphi)(C_{p,bf}) + \varphi(C_{p,np}) \quad (4)$$

$C_{p,nf}$ is estimated as per [17]. $C_{p,bf}$ and $C_{p,np}$ are equal to 4182 and 710 J/kg K [18], respectively.

Instantaneous thermal efficiency (η_l)

$$\eta_l = \frac{\dot{m} \times C_{pf} \times (T_{fo} - T_{fi})}{I \times A_a} = \frac{\dot{Q}_u}{I \times A_a} \quad (5)$$

Collected energy (E_{co}) and stored energy (E_{st})

$$E_{co} = \frac{\dot{m} \times C_{pf} \times [(T_{fo} - T_{fi})_{k+1} + (T_{fo} - T_{fi})_k] \times 3600}{2} \quad (6)$$

where $(T_{fo} - T_{fi})_k$ and $(T_{fo} - T_{fi})_{k+1}$ indicate the difference in temperature of working fluid between exit and entrance of receiver tube at any instant of time k and after 1 h time period from the time k th, respectively.

$$E_{st} = m \times C_{p,st} \times (T_{st,k+1} - T_{st,k}) \quad (7)$$

Table 3 Uncertainties of measuring instruments

Parameters	Uncertainties (%)
Temperature (RTD PT-100 thermocouples)	± 0.3
Mass flow rate	± 5
Solar irradiance	± 5

where $T_{st,k}$ and $T_{st,k+1}$ indicate the mean temperature of water stored in storage container at k th time and after a gap of 1 h from the time k th.

Charging (η_{ch}) and overall efficiency (η_{ov})

$$\eta_{ch} = \frac{E_{st}}{E_{co}}; \quad \eta_{ov} = \frac{E_{st}}{I \times A_a} \quad (8)$$

Uncertainty analysis

An uncertainty analysis has been performed based on root square method on account of error propagation with experimental measurements like temperature, solar radiation intensity, and mass flow rate (assumed error $\leq 5\%$ on least count basis of stopwatch and volume measuring container). Table 3 shows the uncertainty of different measuring instrument. The uncertainty w_η of collector efficiency on the basis of Eq. (4) can be found by using the equation as follows [19]:

$$w_\eta = \sqrt{w_m^2 + w_I^2 + w_{\Delta T}^2} \quad (9)$$

The errors in C_{pf} and A_a are considered to be negligible. The uncertainty in collector efficiency is obtained to be approximately 7.08% and it is around 5% in the useful heat extraction and instantaneous stored energy.

4 Results and Discussion

For investigating the effect of nanofluid on thermal performance of PTC, a study has been carried out experimentally for 2 days. During the first day (May 16, 2016) and second day (May 18, 2016), water and MWCNT nanofluid solution is utilized as the heat exchanging medium, respectively. The measurements are carried out for a constant mass flow rate of 0.0325 kg/s. The detailed discussions of the obtained results are as follows.

The variation in the solar beam irradiance, ambient temperature, and temperature of heat exchange medium with time is shown in Fig. 5. The highest beam irradiance is obtained around noon time as 654 and 685 W/m² using water and MWCNT nanofluid, respectively. The value of solar beam irradiance is found to be 291 W/m² in the morning at 9:00 h and 55 W/m² in the evening at 17:00 h with water. Using

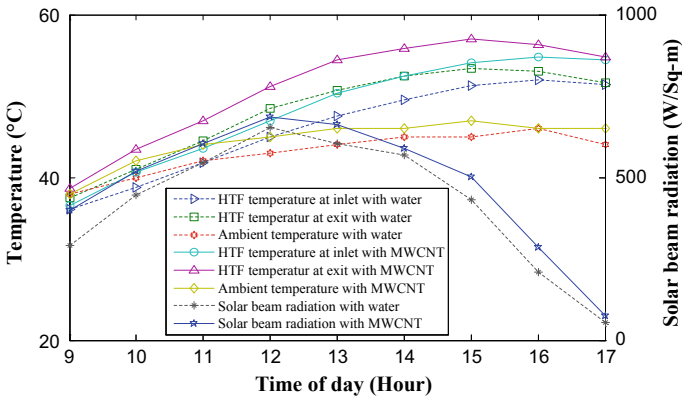


Fig. 5 Variation of heat transfer fluid temperature, ambient temperature, and solar beam radiation with time

MWCNT nanofluid, these values are 398 and 76 W/m². The effect of variation of solar irradiance during morning and evening time is less accounted reason being that of higher incidence angle which is in turn less focused radiation are absorbed on the receiver tube. The above discussion shows that input in the form of solar beam irradiance is almost equal for both cases of the working fluid. From Fig. 5, it is observed that the average ambient temperature is around 43 and 44 °C with water and MWCNT nanofluid, respectively. The highest exit temperature of working fluid attained by the collector is 57 °C with MWCNT nanofluid and 53.4 °C with water. The peak temperature difference of HTF attains to be 4.2 and 3.5 °C with MWCNT nanofluid and water, respectively. The temperature of working fluid at inlet and exit of receiver follow the same trend of variation for both cases of working fluid but higher values are obtained with MWCNT nanofluid in comparison to water. The reason being that nanofluid has improved thermophysical properties.

Figure 6 illustrates the variation of useful heat extraction and instantaneous thermal efficiency with time. The rise in the thermal efficiency and useful heat gain increases from morning to noon for both cases of the working fluid. Noontime after, the sun starts its retreating and beam irradiance starts to go down that leads to decrease in the thermal efficiency as well as useful heat gain. The thermal efficiency and useful heat gain attain a maximum value of 62% and 525.7 W for MWCNT nanofluid around noon. For water, these values are 58% and 477.75 W. This is because that the thermal efficiency and useful heat extraction are affected by the use of HTF and therefore, the difference in their values is found. An average 3% of higher thermal efficiency is obtained with MWCNT nanofluid in comparison to water as an HTF on account of improved heat transfer coefficient and thermal conductivity of MWCNT nanofluid. The obtained thermal efficiencies are comparable as reported by other investigators in their previous works [12, 13].

During the charging process, the variation of temperature of stored water with time inside the storage container is illustrated in Fig. 7. $X/H = 0$ shows the inner

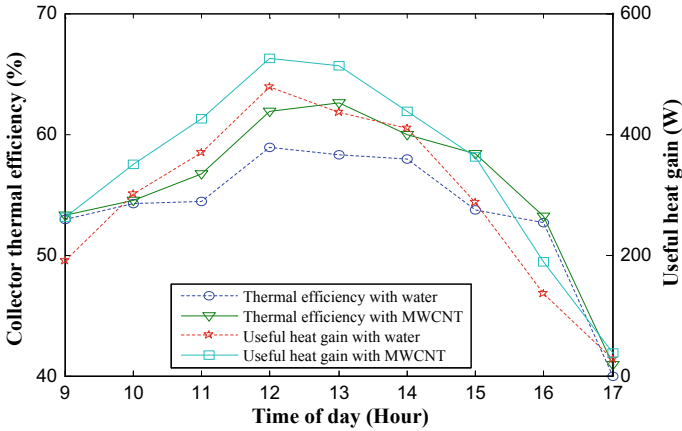


Fig. 6 Variation of collector instantaneous thermal efficiency and useful heat gain with time

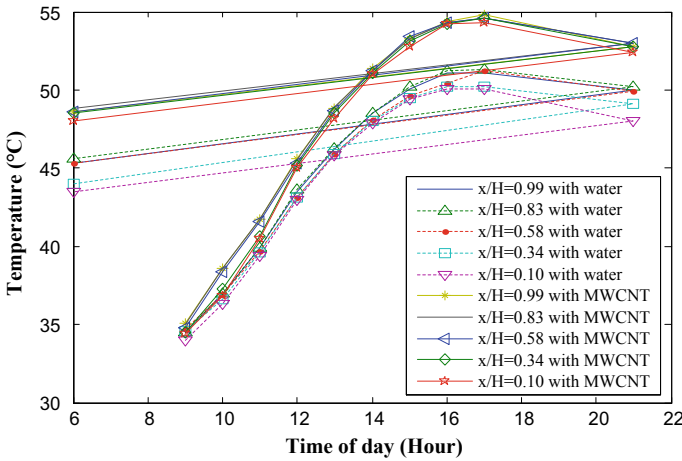


Fig. 7 Variation of average temperature within the storage tank with time

tank base of storage system. The positions of five thermocouples from the base of inner storage tank are $X/H = 0.10, 0.34, 0.58, 0.83,$ and 0.99 . Temperature variation depends upon the heat transferred to storage tank water and its heat loss. Further, heat transferred depends upon the amount of solar irradiance is obtained. The average highest water temperature in storage tank is recorded as 54.6 and 51.3 °C at 17:00 h using MWCNT nanofluid and water respectively. In order to utilization of storage water during late hours or next day, its temperature is further recorded. At 21:00 h and at 6:00 h (on next day), storage water temperature is recorded to be 52.8 and 48.5 °C with MWCNT nanofluid and 49.5 and 44.7 °C with water, respectively. It

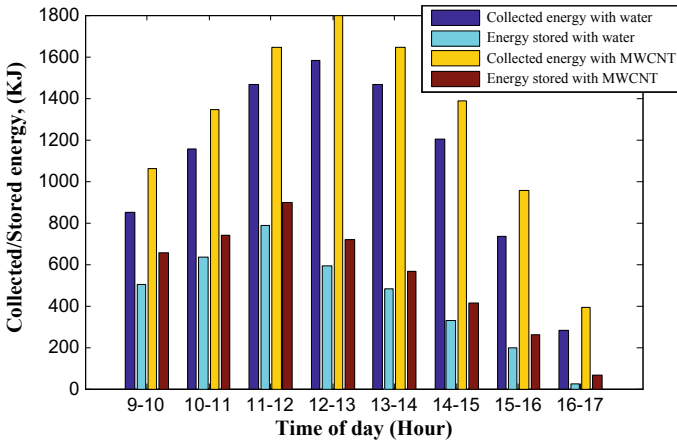


Fig. 8 Variation of hourly collected and stored energy with time

also shows that higher values of water temperature are achieved from the PTC in tank with MWCNT nanofluid.

As observed from Fig. 8 that the highest hourly collected and stored energy are found to be 1583 and 786 kJ using water as working fluid during noon. Whereas, this energy are 1798 and 895.5 kJ using MWCNT nanofluid. The hourly total collected and storage energy is obtained as 8.7 and 3.67 MJ with water, 10.23 and 4.32 MJ with MWCNT nanofluid, respectively, during the system operation from 9:00 to 17:00 h. These results again show that higher performance is achieved from the PTC with MWCNT nanofluid.

From Fig. 9, it is noticed that charging and overall efficiencies are slightly reduced up to 12:00 h with both of the working fluids. After then, the reducing trend is continued for these efficiencies up to the end of the experiment with both of the working fluids. Maximum charging and overall efficiencies are obtained to be 59 and 30.5% (at 9:00–10:00 h) when water is used as HTF. These efficiencies are 62 and 32.1% with MWCNT nanofluid. This decreasing trend in both efficiencies is due to variation of energy collected and storage, solar beam irradiance, and heat losses from the PTC system during the concerned time of operation.

It is observed from the above results that such collectors are capable to heat the stored water with higher performance using MWCNT nanofluid. These collectors can ideally suit for utilization in remote areas of the developing nations where either the technical knowledge of operation and sustain the collector tracking continuously may be lacking or they may not be viable economically.

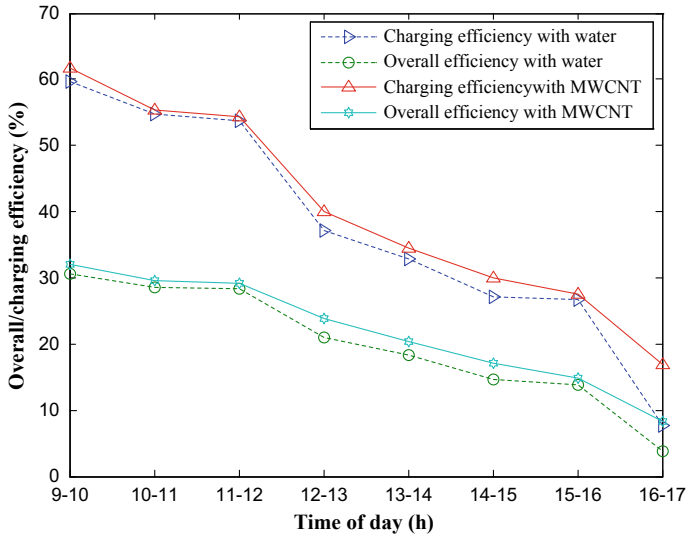


Fig. 9 Variation of system overall and charging efficiency with time

5 Conclusions

The peak thermal efficiency and useful heat gain achieved by the PTC are 58% and 477.75 W with 0.0 wt% MWCNT nanofluid and 62% and 525.7 W with 0.1 wt% MWCNT nanofluid with surfactant, respectively, in the month of May (summer season). The highest hourly collected and stored energy are achieved as 1583 and 786 kJ using water as working fluid. Whereas, this energy are 1798 and 895.5 kJ using MWCNT nanofluid.

The highest charging and overall efficiency of PTC system are found to be 59 and 30.5% with water. Whereas, these efficiency are 62 and 32.1% using MWCNT nanofluid. The use of MWCNT nanofluid in PTC system is one of the simple and proficient options to enhance its thermal performance.

References

1. Sokhansefat T, Kasaeian AB, Kowsary F (2014) Heat transfer enhancement in parabolic trough collector tube using Al_2O_3 /synthetic oil nanofluid. *Renew Sustain Energy Rev* 33:636–644
2. Kalogirou S, Lloyd S (1992) Use of solar parabolic trough collectors for hot water production in Cyprus—a feasibility study. *Renewable Energy* 2:117–124
3. Fernandez-Garcia A, Zarza E, Valenzuela L, Perez M (2010) Parabolic-trough solar collectors and their applications. *Renew Sustain Energy Rev* 14:1695–1721
4. Arasu AV, Sornakumar T (2007) Design, manufacture and testing of fiberglass reinforced parabola trough for parabolic trough solar collectors. *Sol Energy* 81:1273–1279

5. Zhu QZ, Cui Y, Mu LJ, Tang LQ (2013) Characterization of thermal radiative properties of nanofluids for selective absorption of solar radiation. *Int J Thermophys* 34:2307–2321
6. Choi SUS, Eastman JA (1995) Enhancing thermal conductivity of fluids with nanoparticles. ASME international mechanical engineering congress & exposition, November 12–17, San Francisco, CA
7. Choi SUS (1998) Nanofluid technology: current status and future research. US: Korea-U.S. Technical conference on strategic technologies. Vienna, VA
8. Masuda H, Ebata A, Teramae K, Hishinuma N (1993) Alteration of thermal conductivity and viscosity of liquid by dispersing ultra-fine particles (dispersion of g-Al₂O₃, SiO₂ and TiO₂ ultra-fine particles). *Netsu Bussei (Japan)* 7:227–233
9. Choi SUS, Eastman JA (2001) Enhanced heat transfer using nanofluids. 6221, 275, U.S. Patent
10. Lotfi R, Rashidi AM, Amrollahi A (2012) Experimental study on the transfer enhancement of MWNT-water nanofluid in a shell and tube heat exchanger. *Int Commun Heat Mass Transf* 39:108–111
11. Taylor RA et al (2011) Applicability of nanofluids in high flux solar collectors. *J Renew Sustain Energy* 3:023104
12. Khullar V, Tyagi H, Patrick E, Phelan PE, Otanicar T, Singh H et al (2012) Solar energy harvesting using nanofluids-based concentrating solar collector. *J Nanotechnol Eng Med* 3:031003–2
13. Kasaiean A, Daviran S, Azarian RD, Rashidi A (2015) Performance evaluation and nanofluid using capability study of a solar parabolic trough collector. *Energy Convers Manag* 89:368–375
14. Li XF, Zhu DS, Wang XJ (2007) Evaluation on dispersion behavior of the aqueous copper nano-suspensions. *J Colloid Interface Sci* 310:456–463
15. Heiti RV, Thodos G (1983) An experimental parabolic cylindrical concentrator: its construction and thermal performance. *Sol Energy* 30(5):483–485
16. Kumar D, Kumar S (2017) Thermal performance of the solar parabolic trough collector at different flow rates: an experimental study. *Int J Ambient Energy*. <http://dx.doi.org/10.1080/01430750.2016.1269673>
17. Zhang X, Gu H, Fujii M (2006) Effective thermal conductivity and thermal diffusivity of nanofluids containing spherical and cylindrical nanoparticles. *J Appl Phys* 100:044325
18. Touloukian YS, Kirby RK, Taylor RE et al (1970) Thermophysical properties of matters: specific heat, nonmetallic solids. Plenum, New York
19. Kumar DS (2000) Mechanical measurements and control, 3rd ed. Metropolitan Book Co. Pvt. Ltd., New Delhi

A Novel System Based on the Principle of Electrochemical Treatment to Reduce Exhaust Emission from Gasoline-Operated Engine



Prem Pal, Priyanka Sharma, Ajay Sharma and Mohit Bhandwal

Abstract The rising population is closely related to the improvement and importance of transportation. Moreover, the rapid increasing Indian economy also entangles manufactures in enhancing the performance of internal combustion engine. The increasing number of vehicles with speedy advancement of technology is leading world to have around 2 billion vehicles by 2020. The exhaust emission from these vehicles is also contributing to myriad problems. The exhaust contains harmful gases like carbon monoxide (CO), hydrocarbon (HC), sulfur oxides (SO_x), nitrogen oxides (NO_x), and particulate matters PM2.5 and PM10. Keeping in mind the Environment Act, 1986 of India and The Air (prevention and control of pollution) Act, 1981 of India, this paper is prepared for the betterment of our environment, and related to this is an idea to introduce an exhaust system in addition to three-way catalytic convertor for reducing the gases such as sulfur dioxide (SO₂), carbon dioxide (CO₂), and particulate matter emitted from vehicles comprising a heat absorbing freezer gel pack chamber which would be immediately preceded by the catalytic converter. A chamber containing graphite electrodes in aqueous electrolyte water to absorb sulfur dioxide (SO₂) and a chamber for absorbing carbon dioxides (CO₂) in alkali solution and for trapping particulate emitted in exhaust by catalytic convertor filter layer is being used.

Keywords Catalytic convertor · Nitrogen oxides · Carbon dioxide gas · Sulfur dioxide gas

1 Introduction

A rapid increasing pollution is becoming a matter of concern worldwide. In India, due to its large population, air pollution is becoming a serious matter of thinking. Air pollution in the capital of India, Delhi is a serious threat. The amount of foreign

P. Pal (✉) · P. Sharma · A. Sharma · M. Bhandwal
Department of Mechanical & Automation Engineering, Amity School of Engineering & Technology, Noida, Uttar Pradesh, India
e-mail: enggprenal@gmail.com

© Springer Nature Singapore Pte Ltd. 2019
M. Kumar et al. (eds.), *Advances in Interdisciplinary Engineering*, Lecture Notes in Mechanical Engineering, https://doi.org/10.1007/978-981-13-6577-5_20

particles in air, such as carbon dioxide, Sulfur dioxide, oxides of nitrogen, PM2.5, and PM10, is considerably very high and excessive intake of these may lead to severe diseases [1–7].

To overcome and to stop, mitigate such unavoidable issues in our ambience manufactures are doing great efforts. Nowadays in automobiles an anti-pollution device is installed known as catalytic convertor [6, 8, 9], which reduces the toxicity of emission coming out from internal combustion engine. The three main tasks of a catalytic convertor are to convert oxide of nitrogen, carbon monoxide, and unburnt hydrocarbon into nitrogen gas, carbon dioxide, and water vapor, respectively [10–13].

These reactions are



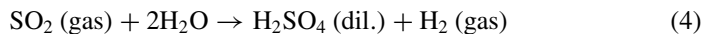
Catalytic convertor has various catalysts. They have certain efficiency to reduce harmful emissions from petrol-operated exhaust system of engines. Platinum and rhodium act as reduction catalyst while platinum and palladium act as oxidation catalyst.

This present idea is a small step in order to mitigate the problem discussed so far. Owing to the affinity toward certain chemicals and chemical reaction, pollutants like CO_2 , SO_2 , NO_x , and CO [10, 14–17] could be absorbed. In present work, it would be tried to absorb as maximum as it would be possible for a particular pollutant. Various pollutants are discussed below.

1.1 Concept of Working

The temperature of the exhaust coming out from the engine is nearly about 750°C and when it gets passed through catalytic convertor, the temperature of the same reaches to nearly about 350°C . In order to mitigate this temperature, we are using two layers of freezer gel pack on exhaust outlet pipe of catalytic convertor. A freezer gel pack is made up of sodium carboxymethyl cellulose and propylene glycol. These layers of freezer gel pack will absorb the heat of the exhaust gases.

After cooling down the temperature of exhaust, it will pass through electrolytic solution (aqueous water) with two graphite electrodes in aluminum alloy chamber as it is corrosion resistance. The two electrodes will be energized by a 12 V battery for carrying out electrochemical reactions. In this reaction, it is expected that SO_2 with desirable amount at anode can form a dil. solution of H_2SO_4 and H_2 in trace which is harmless. Chemical reaction is shown below:



These treated exhausts then pass through another aluminum alloy chamber without getting any exposure to environment. One layer of freezer gel is also used for further reduction in temperature of the exhaust. The layer of freezer gel pack will reduce the temperature up to 50–70 °C. Now, the second container contains ammonium hydroxide solution (NH_4OH) (3:1 concentration). This NH_4OH solution will have affinity toward CO_2 . The NH_4OH solution will absorb CO_2 and form ammonium carbonate. The by-product of ammonium carbonate will not further decompose to ammonia and carbon dioxide gas at low temperature. Now this exhaust gas will pass through a very fine mesh with charcoal powder to absorb carbon dioxide gas and other fine particles.

2 Material and Methodology

In order to perform experiment, fabrication of device is a must for us. An iron pipe of bore 152 mm and length 400 mm is taken, and this pipe is acting as the housing for aluminum container tightly screwed on the base on the pipe shell. For the fitting and placing of these two aluminum alloy containers, two cubic (101.6×101.6 mm) cuts are done. Two iron plates for coving the shell from both the ends are cut down of 152 mm diameter. A hole of 50.2 mm in diameter is made on each covering plate for exhaust pipe fitting. The two aluminum alloy containers are joined by an iron pipe having 25.4 mm diameter. At the outlet of exhaust, fine mesh is installed for trapping particulate matter. Figure 1a is representing the graphite electrodes used and Fig. 1b represents freezer gel pack used. Figure 2 shows the device.

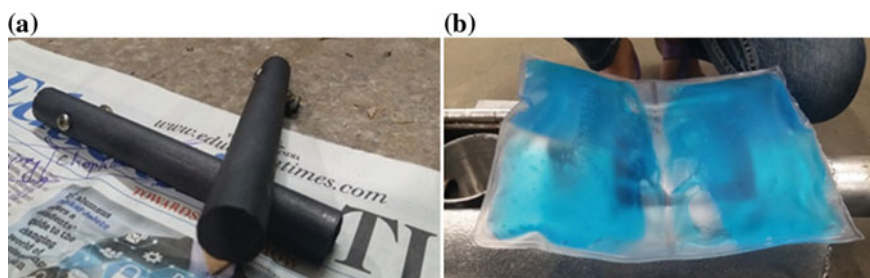


Fig. 1 a Carbon–graphite electrodes, b freezer gel pack

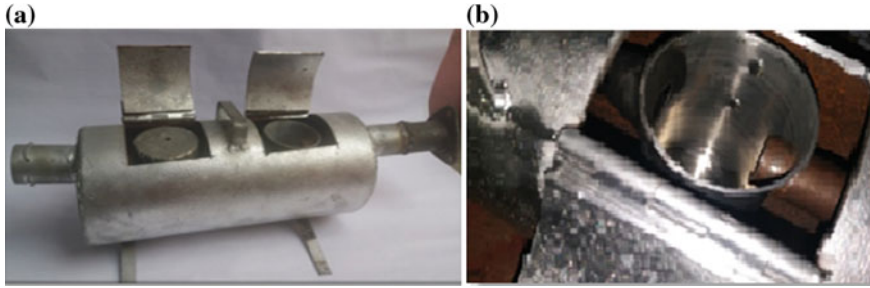


Fig. 2 **a** Image of the fabricated device, **b** image of the aluminum alloy container

2.1 Experimental Procedures

In order to check the performance and efficiency of the device, containing electrolytic solution with two graphite electrodes in one of aluminum alloy containers and NH_4OH dilute solution (1:3) in another container of the same material, it is connected to the exhaust tailpipe of the water-cooled four-cylinder spark ignition engine.

An air flow analyzer AVL-DGAS-444 is employed for analysis of emission coming out from the engine. The AVL-DGAS-444 has given the reading on hydrocarbon (HC), carbon monoxide (CO), carbon dioxide gas (CO_2), oxide of nitrogen (NO_x), and oxygen gas (O_2). Though we have concentrated our study on the emission and control of NO_x and CO_2 only, in the beginning, the experiment engine is operated at 1500 rpm at no-load condition for 1 h in order to avoid cold starting problems [8, 17, 18] and any glitch. Readings are taken at 1500, 2000, 2500, and 3000 rpm at no-load condition (load due to friction is only considered).

3 Result and Discussion

Experiment is performed and readings are taken out on nitrogen oxide (NO) and carbon dioxide gas (CO_2). Engine had run at different rpm with no-load condition (only load due to friction is shown here). Readings are shown in Table 1.

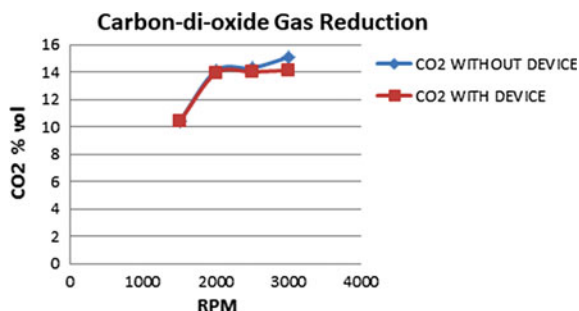
Mathematically, the % efficiency of the device is defined as

$$\frac{\text{Amount of pollutant (without device)} - \text{Amount of pollutant (with device)}}{\text{Amount of pollutant (without device)}} \times 100\%$$

Table 1 Experimental readings on NO₂ and CO₂ at different rpm and % efficiency on NO₂ and CO₂

Load (load due to friction)	3.2	11.6	12.5	14
RPM	1500	2000	2500	3000
NO _x (without device) ppm	26	735	945	1180
CO ₂ (without device) % vol.	10.40	14.10	14.13	15.1
NO _x (with device) ppm	46	296	823	1054
CO ₂ (with device) % vol.	10.40	13.92	14.01	14.12
% Efficiency NO _x	NA	59.72	12.91	10.677
% Efficiency CO ₂	0	0.56	2.027	6.49

Fig. 3 Variation of CO₂ with and without device



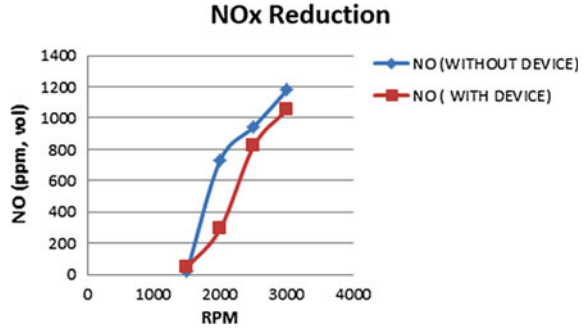
3.1 Effect on CO₂ (Carbon dioxide Gas) Emission

Experimental reading shows a continuous decrease in the amount of CO₂. Initially, there is no significant reduction in the amount of CO₂, but later on as the experiment is carried out at higher rpm reduction in amount of CO₂ is observed. Experimental reading on the emission of CO₂ is shown in Table 1 with device and without device. Graphically, the reduction in amount of CO₂ emission is also represented in Fig. 3.

3.2 Effect on NO_x (Oxide of Nitrogen) Emission

Experimental reading shows a continuous decrease in NO emission. Initially, there is a rapid increase in the amount of NO, but later on as the experiment is carried out at higher rpm it reduces. Experimental reading of the emission of NO is shown in Table 1 with device and without device. Graphical representation is shown in Fig. 4.

Fig. 4 Variation of NO_x with and without device



4 Conclusion

From the above experiments and readings, it can be seen and said that there is affinity and influence of chemicals (used) on pollutants like NO and CO₂ in the exhaust of engine and can be reduced. In future, use of such chemicals can enable us to reduce considerably the amount of emission of harmful gas from the exhaust of petrol-operated engine. This idea needs more R&D with its present condition for better results. Such devices can be used as a complementary to the present system of exhaust. The present idea and work is carried out for the noble cause of the society. Gradually increasing pollution in the capital and its territory is affecting our ecosystem and health of living organism.

References

1. Industries MH (2004) Environmental friendly diesel engine. *UEC Eco-Engine* 41(1):2–4
2. Elliott MA, Nebel GJ, Rounds FG (1955) The composition of exhaust gases from diesel, gasoline and propane powered motor coaches. *J Air Pollut Control Assoc* 5(2):103–108
3. Sharaf J (2013) Exhaust emissions and its control technology for an internal combustion engine. *Int J Eng Res Appl* 3(4):947–960. www.ijera.com
4. Saini B, Verma R, Himanshu SK, Gupta S (2013) Analysis of exhaust emissions from gasoline powered vehicles in a sub-urban Indian town. *Environment* 2(1):37–42
5. Roupail NM, Frey HC, Colyar JD, Unal A (2000) Vehicle emissions and traffic measures: exploratory analysis of field observations at signalized arterials. In: TRB annual meeting, Nov 2000
6. Tong HY, Hung WT, Cheung CS (2000) On-road motor vehicle emissions and fuel consumption in urban driving conditions. *J Air Waste Manag Assoc* 50(4):543–554
7. Shiva Nagendra S, Khare M (2003) Principal component analysis of urban traffic characteristics and meteorological data. *Transp Res Part D Transp Environ* 8(4):285–297
8. Leman AM, Rahman F, Jajuli A, Zakaria S, Feriyanto D (2017) Emission treatment towards cold start and back pressure in internal combustion engine against performance of catalytic converter : a review. In: 9th International UNIMAS STEM Engineering Conference (ENCON 2016), 02021, p 7
9. Pesansky JD, Majiros NA, Sorensen CM, Thomas DL (2009) The effect of three-way catalyst selection on component pressure drop and system performance

10. Marsh P, Acke F, Konieczny R, Brück R (2001) Application guideline to define a catalyst layout for maximum catalytic efficiency. Society of Automotive Engineers
11. Amirnordin SH, Seri SM, Salim WSW, Rahman HA, Hasnan K (2011) Pressure drop analysis of square and hexagonal cells and its effects on the performance of catalytic converters. *Int J Environ Sci Dev* 2(3):239–247
12. Korin E, Reshef R, Tshernichovesky D, Sher E (1999) Reducing cold-start emission from internal combustion engines by means of a catalytic converter embedded in a phase-change material. *Proc Inst Mech Eng Part D J Automob Eng* 213(6):575–583
13. Soumelldis MI, Stobart RK, Jackson RA (2007) A chemically informed, control-oriented model of a three-way catalytic converter. *Proc Inst Mech Eng Part D J Automob Eng* 221(9):1169–1182
14. Subramani T (2012) Study of air pollution due to vehicle emission in tourism centre. *Int J Eng Res Appl* 2(3):1753–1763
15. Farrauto RJ, Heck RM (1999) Catalytic converters: state of the art and perspectives. *Catal Today* 51(3–4):351–360
16. Greenstone M, Hanna R (2014) Environmental regulations, air and water pollution, and infant mortality in India
17. Karkanis AN, Botsaris PN, Sparis PD (2004) Emission reduction during cold start via catalyst surface control. *Proc Inst Mech Eng Part D J Automob Eng* 218(11):1333–1340
18. Zhang J, Song C, Zhang J, Baker R, Zhang L (2013) Understanding the effects of backpressure on PEM fuel cell reactions and performance. *J Electroanal Chem* 688:130–136

The Importance of Methanol–Gasoline Blend in Spark Ignition Engine—A Review



Keshav Jangid , Vivek Verma , Velpula Surya , Rohit Gupta 
and Devendra Vashist 

Abstract The air pollution produced by motor vehicles is getting worse day by day especially in major cities in the world. A very high density of motor vehicle traffic on road and change in lifestyles of the people contributed largely to the increase of pollution. The emission produced by the vehicles must be reduced and controlled to prevent or minimize the air pollution problem. It is also essential to meet the particular country emission standards. The principal polluting agents in gasoline emissions are CO, NO_x, hydrocarbons, etc. It was observed by various researchers that the fuel efficiency was improved by using a blend of methanol–gasoline in the gasoline engine. The methanol blend in gasoline was varied, and the performance of the engine regarding maximum output power and braking power was studied in several papers. The chemical and physical properties of the blend were also checked and reported. The present study aims to summarize the performance of methanol–gasoline blend used in spark ignition engine. The review is mainly focused on fuel properties, output power/torque, braking efficiency, emissions, etc. It was observed that the CO, NO_x, smoke, and particulate matter (PM) concentration in exhaust gas reduced significantly, whereas the CO₂ and unburnt hydrocarbons emissions were increased after using the blended gasoline in the engine.

Keywords Gasoline · Methanol · Engine · Emissions

Nomenclature

LHV	Lower heating value
RON	Research octane number
MON	Motor octane number
BSFC	Brake specific fuel consumption
BTE	Brake thermal efficiency

K. Jangid (✉) · V. Verma · V. Surya · R. Gupta · D. Vashist
Department of Automobile Engineering, Manav Rachna International Institute
of Research and Studies, Faridabad, Haryana, India
e-mail: keshujangid4@gmail.com

TWC	Three-way catalytic converters
M10/M20/M85 etc.	10%/20%/85% etc. methanol blend
BSEC	Brake specific energy consumption
CH ₃ OH	Methanol
HCHO	Formaldehyde
SI	Spark ignition
CO	Carbon monoxide
NO _x	Nitrogen oxides
PM	Particulate matter
GDI	Gasoline direct injected
PFI	Port fuel injected

1 Introduction

Limited reserves of fossil fuel, increased crude oil price, and stringent environmental norms prompted automakers and researchers to think about the alternative energy resources. The newly developed energy resources should meet the expectations like cost-effectiveness, reduced pollution, and improved efficiency. Several renewable energy resources are worked upon worldwide as an alternative to the petroleum products. The concept of blending gasoline with alcohol came in the late 1970s when the world had faced the scarcity of oil supply [1]. Predominantly, methanol or ethanol is used for the blending purpose in petroleum products [2]. The production of alcohol is based on the natural or waste products, unlike petroleum. Therefore, it is an alternative source of energy which is economical and abundantly available [3]. Among several, methanol is used as a blending product more frequently. The availability of methanol-blended gasoline was first marked in the early period of the 1980s. Methanol is miscible in water as well as in hydrocarbons. It has advantages like clean burning, high octane value, easy manufacturing process, low boiling temperature, high hydrogen-to-carbon ratio, and no sulfur contamination. A clean burning of methanol-blended gasoline in SI engine assisted in reducing the carbon footprint effectively [3]. The usage of methanol-blended gasoline in vehicles not only diminished the greenhouse gas emissions but also depreciate the incorporation of particulate matter (PM) in the environment. An efficient blending is able to provide premium quality gasoline at a lower cost. Therefore, the purpose of the present study is to provide a detailed review on the importance and performance of methanol-blended gasoline in spark ignition engine considering essential parameters.

2 Fuel Properties of Methanol–Gasoline Blend

The critical parameters related to fuel properties of methanol and gasoline is presented in Table 1. The methanol possesses fairly high auto-ignition temperature which assured its suitability for storage and utilization as fuel in the automobile

Table 1 Fuel-like properties of methanol and gasoline [4–7]

Properties	Methanol	Gasoline	M10 blend
Chemical formula	CH ₃ OH	C ₄ –C ₁₂	C _{6.37} –H _{13.02} –O _{0.1}
Molecular weight	32	95–120	
Carbon (wt%)	37.5	85.5	
Oxygen (wt%)	12.5	0	3.97
Hydrogen (wt%)	50	14.5	
Sulfur (wt%)	0	0.0042	
Density (kg/m ³)	0.795	0.700–750	773.7
Boiling point (°C)	64.7	30–225	43–206
Latent heat of evaporation (kJ/kg)	1100	310–320	
Lower heating value (LHV) (MJ/kg)	20.26	44.3	41.8
Calorific value (MJ/kg)	23	45.5–45.8	
Research octane number (RON)	110	90	88
Motor octane number (MON)	92	81–89	84.4
Cetane number	8	8.14	
Auto-ignition temperature (°C)	465	228–470	
Stoichiometric air fuel ratio	6.47	14.8	13.9
Stoichiometric mixture heating value (kJ/m ³ atm at 20 °C)	3557	3750	

sector. The volumetric efficiency of methanol is greater than gasoline owing to the higher latent heat of evaporation resulted in a lower temperature of the intake manifold. Also, the low stoichiometric air–fuel ratio of methanol prompted that small amount of oxygen is needed for complete burning. Nevertheless, the volume of methanol is almost double than gasoline to achieve similar energy output due to meager LHV. Therefore, despite having several advantages the utilization of bare methanol as a fuel is questionable. On the other hand, the positive properties of methanol could be fetched if it has been blended with gasoline [4].

3 Type of Methanol–Gasoline Blends

Two types of methanol–gasoline blends are generally considered as fuel, i.e., high-level and low-level blends. In case of a high-level blend, the blend consists more than or equal to 85 vol% methanol. On the other hand, if the methanol is less than or equal to 15 vol%, it is named as a low-level blend. The fundamental problem in employing high-level proportion as a fuel is materials compatibility. All the fuel delivery and storage parts fabricated from the conventional material with strong reaction tendency with methanol required to change for better longevity and efficient

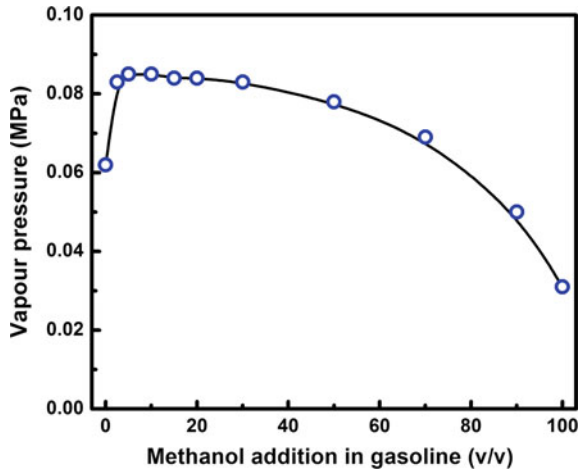


Fig. 1 Change in vapor pressure in low- and high-level methanol blending in gasoline [11]

performance. Another major issue is fuel volatility in some proportions. The change in vapor pressure of the gasoline with methanol addition is depicted in Fig. 1. It was noticed that the vapor pressure of the fuel is lowered with higher methanol addition. The low vapor pressure of high methanol-blended gasoline fuel reduced not only the evaporative emission but also the vapor lock possibility in the engine. On the contrary, the cold starting efficiency of the engine is significantly deterred by the lower vapor pressure fuels [8, 9]. A significant reduction in Reid vapor pressure of the methanol–gasoline blends was observed by Schifter et al. [10] when they added isopropyl alcohol in it.

4 Engine Performance on Methanol-Blended Gasoline

Eyidogan et al. [12] studied the effect of alcohol–gasoline fuel blends regarding the performance of an SI engine. They observed higher brake specific fuel consumption (BSFC) in the methanol–gasoline fuel blend than pure gasoline. As the energy content of the methanol–gasoline fuel blends is lower than the bare gasoline, the slight increase in fuel combustion for similar output is justified. The BSFC is lowered for both blended as well as pure gasoline with the increase in wheel power. At higher speed and higher wheel power, the brake thermal efficiency (BTE) of blended gasoline is better than the bare gasoline. The release of heat is started earlier in gasoline than the blended one. On the other hand, the heat release span is wider for blended gasoline. Liu et al. [13] examined the performance of engine fueled with methanol–gasoline blends. As per their findings, the low-level methanol gasoline blend could be used as a fuel without any modification in the engine. A slight reduction in engine

power and torque was observed by them, whereas BTE was improved significantly. Yanju et al. [14] investigated the engine power, thermal efficiency, and emissions of an engine fueled by M10 (10% methanol blend), M20 (20% methanol blend), and M85 (85% methanol blend) fuel. The best power, torque, and BTE were observed with M85 fuel. Abu-Zaid et al. [15] found best power output along with minimum BSFC when 15% methanol was blended with gasoline. As blended gasoline has higher octane number, the engine could operate at higher compression ratios. Agarwal et al. [16] noticed high BTE in a medium duty SI engine with M10 and M20 fuel. Heat release has started earlier in gasoline, whereas the combustion duration is higher in blended gasoline. Bilgin and Sezer [17] observed the best brake mean effective pressure with the M5 (5% methanol blend) blend, but best BTE was reported with M20 blend. Qi et al. [4] observed that the ethanol addition could solve the phase separation problem of methanol–gasoline blend. A reduction in power and torque was perceived when M10 or M25 (25% methanol blend) blend was used instead of pure gasoline. Fuel consumption is higher in case of blended gasoline than pure gasoline, whereas reverse is true when energy consumption was considered. Sayin et al. [18] studied the effect of methanol concentration, injection pressures, and injection timings of blended fuel in engine performance. They noticed higher BSFC, higher brake specific energy consumption (BSEC), and lower BTE with increased methanol concentration in diesel. Canakci et al. [19] examined the effect of fuel injection pressure in one-cylinder four-stroke engine. With the increased methanol concentration in the blend, the engine exhibited not only lower BTE, heat release rate, and peak cylinder pressure but also increased BSFC and BSEC. When injection pressure is lower than the original, the peak cylinder pressure and heat release rate decreased. Sapre [20] found that addition of methanol in gasoline improved octane number, lean limit, antiknocking tendency, compression ratio, and BTE remarkably. The methanol-blended gasoline has higher flame speed which assisted in a clean and faster burning of the fuel inside the engine cylinder. It also contributed to the overall BTE improvement of the engine [16]. Liao et al. [21] observed higher flame front speed for methanol–gasoline blends (till 30% methanol blend) with respect to pure methanol or pure gasoline at equal fuel/air ratio. Elfasakhany [22] observed improved engine performance when ethanol or methanol-blended gasoline was used as a fuel with respect to pure gasoline, n-butanol–gasoline blend, isobutanol–gasoline blend, and acetone–gasoline blend.

5 Possible Issues of Blending Methanol with Gasoline

The main problem arose by using methanol–gasoline blend was the exhaust gas mixed with unregulated emission mainly methanol (CH_3OH) and formaldehyde (HCHO). This situation was even worse when low-level methanol blend was used. It was reported in the literature that the HCHO is a carcinogenic product and the concentration of the same is increased in the exhaust gas with the increase of CH_3OH in gasoline [23]. Wei et al. [24] studied the HCHO and CH_3OH emissions from SI engine

fueled with methanol–gasoline blend. The HCHO emission is directly proportional to the engine speed, but the reverse was true for CH₃OH emission from the engine. Also, simultaneous increase of HCHO and CH₃OH emission was reported with the enhanced methanol concentration in gasoline. Similar results were also obtained by [25]. Wei et al. [26] examined the emanations of unregulated HCHO, acetaldehyde (CH₃CHO), and CH₃OH emissions from SI engine fueled with M10 blend. The HCHO emission increased while CH₃CHO emission decreased with M10 fuel than gasoline. The engine speed also contributed to the increased HCHO than CH₃OH emission. Zhang et al. [27] did numerical simulations and developed a model to study the methanol oxidation mechanism using CHEMKIN-based programs. The obtained results were very consistent with the experimental results. Additionally, the higher methanol concentration in gasoline prompted the higher CO₂ emission in the atmosphere [28]. The compatibility of the materials with the methanol-blended gasoline is a big issue. Methanol has potential to degrade plastic or rubber components and able to corrode metals like Al, Zn, and Mg [29]. Methanol-blended gasoline fuel required proper storage and distribution system which can prevent the leakage or miscibility of the methanol to the ambient. There must be a stringent norm for the same as the methanol is toxic and hazardous to human health [30]. Another major issue with the utilization of alcohol–gasoline blend as a fuel is to keep it in a stable and homogeneous liquid phase. The conventional method to overcome this problem is to adopt modified and new carburetor designs [31]. There is sufficient miscibility of methanol in gasoline at or above room temperature, but it has a poor solubility at zero and subzero temperatures. However, the addition of some volatile constituents is required for providing support to start the ignition in the winter season [3].

6 Materials Compatibility

As already mentioned in the previous section, the miscibility of alcohol into the water is very high in all proportions. On the other hand, gasoline cannot mix with water completely [32]. Therefore, the probability of finding water content in alcohol-blended gasoline is relatively high. The mechanical components made up of metals are more likely susceptible to corrosion. The most affected metals are Al, Mg, Zn, and their alloys [33]. Again, some elastomers also tend to react with alcohol more vigorously which can create an obstruction in the fuel transportation line by melting the rubber gaskets. The rubber made up of fluorocarbon has a lower chemical affinity toward methanol and could be considered as an alternative [34]. The commonly preferred and non-preferred materials are listed in Table 2. This is a tentative list because the materials selection for a particular application is primarily based on active service environment, fuel exposure duration, failure consequences, etc.

Table 2 The preferred and non-preferred materials list for methanol–gasoline blend [33, 35]

S. No.	Material type	Preferred materials	Non-preferred materials
1.	Metals	Carbon steel	Aluminum
		Stainless steel	Magnesium
		Bronze	Zinc
		–	Galvanized metals
2.	Elastomers	Fluoroelastomer	Nitrile rubber
		Fluorosilicone	Neoprene
		Polysulfide rubber	–
3.	Polymers	Acetal	Polyurethane
		Nylon	–
		Polyethylene	–
		Teflon	–
		Fiberglass-reinforced	–

7 Emissions

El-Emam and Desoky [36] studied the combustion properties of methanol, ethanol, and gasoline in SI engine. They noticed lowest CO and NO concentrations in the exhaust gas from methanol than ethanol and gasoline fuel. As per the study of Gabele [37], the share of non-methane organic gases in exhaust emission was lowest when M85 fuel was utilized. After using methanol gasoline blend as a fuel, the emission of CO and unburned hydrocarbons was reduced significantly. The implementation of the three-way catalytic converter further reduced the emissions (especially NO_x). On the contrary, higher methanol content in gasoline increased the unburned CH_3OH , HCHO, and unregulated emissions. Similar results were also obtained by Yao et al. [38] for four-stroke PFI SI engine fueled with different concentration of methanol–gasoline blends. The use of M30 blend also reduced the emission significantly during cold start and warming up process in winter [13]. The higher methanol–gasoline ratio reduced the concentration of CO and NO_x in the exhaust gas but increased the proportion of unburnt CH_3OH emission in it. There was no effect noticed on non-methanol hydrocarbons emissions after methanol addition [14]. In Sapre [20] investigation, although the addition of methanol (30–70 vol%) in gasoline reduced the NO_x emission, unwanted phase separation along with higher unburnt CH_3OH and HCHO was also noticed. Gong et al. [39] iterated that if the ambient temperature simultaneously raised, the emission of HCHO increased, whereas CH_3OH decreased considerably. Wei et al. [26] studied the effect of engine speed and tailpipe temperature on unregulated emissions when M10 blend was employed as fuel. They noticed higher HCHO emission from M10 blend with respect to pure gasoline. On the contrary, the CH_3CHO and CH_3OH emissions were decreased. The emissions of benzene, toluene, ethylbenzene, xylene, and volatile organic contents were decreased using methanol-blended

gasoline as fuel. The maximum reduction was observed with high-level methanol blend (M85) than low-level blend (M15). Besides, the HCHO emission increased with low to medium-level blend. A significant reduction in the emission of CO, NO_x, HCHO, and total HC was noticed for methanol-blended gasoline when new three-way catalytic converters (TWC) was employed [40]. The carbonyl compound emission is higher with M15 and M100 blend than pure gasoline. The use of newly designed TWC not only reduced HCHO emission but also reduced carbonyl compound efficiently [5]. Liang et al. [41] studied particulate matter (PM) emission from gasoline direct injected (GDI) and port fuel injected (PFI) engines fueled by gasoline or M15. They found that the PM emission was lower for M15 than gasoline.

8 Conclusions

In this article, the performance and emission characteristics of SI engine powered by methanol–gasoline blend were reviewed. It was observed that methanol has better fuel properties than pure gasoline in some aspects. In terms of performance, the engine fueled with blended gasoline exhibited significant improvement in brake thermal efficiency, octane number, heat release span, etc. Some studies claimed that utilization of methanol–gasoline blend slightly improved the engine power and torque with respect to pure gasoline. It was also claimed that the modification in engine is not required if low-level methanol blend is used in gasoline engine. The brake specific fuel consumption (BSFC) and brake specific energy consumption (BSEC) are mainly dependent on critical process and parameter variation. It has varied results in different situations. For high-level methanol blend, the engine needs to refurbish using methanol friendly materials. The presence of water content in methanol–gasoline blend has strong tendency to corrode or chemically degrade the existing engine components. In terms of exhaust emission, the blended gasoline emits fewer amounts of CO and NO_x than pure gasoline. On the other hand, the emissions of CO₂ and unregulated hydrocarbon are increased. In most of the situations, the HCHO emission increased, whereas CH₃OH and CH₃CHO emissions decreased after blended gasoline was employed. To control the unburnt and unregulated hydrocarbons, a three-way catalytic converter with varied design was suggested in several literature. The blended gasoline minimizes the fine pollutant particles commonly known as particulate matter (PM) in the atmosphere. Overall conclusion from the study is methanol–gasoline blend has potential to replace the pure gasoline in near future. As it has antiknock properties, the high compression ratio could be achieved. Therefore, methanol–gasoline fuel might be a fuel for automobile in near future with some modifications.

Acknowledgements Authors wish to thank Dr. Anil from Accendere Knowledge Management Services, CL Educate for his valuable contribution in manuscript preparation.

References

1. Huang P, Ju H, Tan S, Wang H, Zhao T (2015) The future of methanol fuel: an analysis on the feasibility of methanol as an alternative fuel. *Chile*
2. Bata RM, Elrod AC, Rice RW (1989) Emissions from IC engines fueled with alcohol–gasoline blends: a literature review. *J Eng Gas Turbines Power* 111:424–431
3. Reed TB, Lerner RM (1973) Methanol: a versatile fuel for immediate use. *Science* 182:1299–1304
4. Qi DH, Liu SQ, Zhang, CH, Bian YZ (2005) Properties, performance, and emissions of methanol–gasoline blends in a spark ignition engine. In: *Proceedings of the institution of mechanical engineers, Part D: journal of automobile engineering*, vol 219, pp 405–412
5. Zhao H, Ge Y, Hao C, Han X, Fu M, Yu L, Shah AN (2010) Carbonyl compound emissions from passenger cars fueled with methanol/gasoline blends. *Sci Total Environ* 408:3607–3613
6. Canakci M, Ozsezen AN, Alptekin E, Eyidogan M (2013) Impact of alcohol–gasoline fuel blends on the exhaust emission of an SI engine. *Renew Energy* 52:111–117
7. Shayan SB, Seyedpour SM, Ommi F, Moosavy SH, Alizadeh M (2011) Impact of methanol–gasoline fuel blends on the performance and exhaust emissions of a SI engine. *Int J Automot Eng* 1:219–227
8. Siwale L, Kristóf L, Bereczky A, Mbarawa M, Kolesnikov A (2014) Performance, combustion and emission characteristics of n-butanol additive in methanol–gasoline blend fired in a naturally-aspirated spark ignition engine. *Fuel Process Technol* 118:318–326
9. Awad OI, Mamat R, Ali OM, Sidik NAC, Yusaf T, Kadirgama K, Kettner M (2018) Alcohol and ether as alternative fuels in spark ignition engine: a review. *Renew Sustain Energy Rev* 82:2586–2605
10. Schifter I, Diaz L, Gonzalez U, Gonzalez-Macias C, Mejía-Centeno I (2018) The effects of addition of co-solvents on the physicochemical properties of gasoline–methanol blended fuels. *Int J Engine Res*. <https://doi.org/10.1177/1468087418757855>
11. Jackson MD, Ward PF (2013) Demonstrating the feasibility of methanol gasoline blends to reduce petroleum use in the United States. Fuel Freedom Foundation, Irvine, California
12. Eyidogan M, Ozsezen AN, Canakci M, Turkcan A (2010) Impact of alcohol–gasoline fuel blends on the performance and combustion characteristics of an SI engine. *Fuel* 89:2713–2720
13. Liu S, Clemente ERC, Hu T, Wei Y (2007) Study of spark ignition engine fueled with methanol/gasoline fuel blends. *Appl Therm Eng* 27:1904–1910
14. Yanju W, Shenghua L, Hongsong L, Rui Y, Jie L, Ying W (2008) Effects of methanol/gasoline blends on a spark ignition engine performance and emissions. *Energy Fuels* 22:1254–1259
15. Abu-Zaid M, Badran O, Yamin J (2004) Effect of methanol addition on the performance of spark ignition engines. *Energy Fuels* 18:312–315
16. Agarwal AK, Karare H, Dhar A (2014) Combustion, performance, emissions and particulate characterization of a methanol–gasoline blend (gasohol) fuelled medium duty spark ignition transportation engine. *Fuel Process Technol* 121:16–24
17. Bilgin A, Sezer I (2008) Effects of methanol addition to gasoline on the performance and fuel cost of a spark ignition engine. *Energy Fuels* 22:2782–2788
18. Sayin C, Ozsezen AN, Canakci M (2010) The influence of operating parameters on the performance and emissions of a DI diesel engine using methanol-blended-diesel fuel. *Fuel* 89:1407–1414
19. Canakci M, Sayin C, Ozsezen AN, Turkcan A (2009) Effect of injection pressure on the combustion, performance, and emission characteristics of a diesel engine fueled with methanol-blended diesel fuel. *Energy Fuels* 23:2908–2920
20. Sapre AR (1988) Properties, performance and emissions of medium concentration methanol–gasoline blends in a single-cylinder, spark-ignition engine. *SAE Trans*, 1105–1126
21. Liao SY, Jiang DM, Cheng Q, Huang ZH, Zeng K (2006) Effect of methanol addition into gasoline on the combustion characteristics at relatively low temperatures. *Energy Fuels* 20:84–90

22. Elfasakhany A (2017) Investigations on performance and pollutant emissions of spark-ignition engines fueled with n-butanol-, isobutanol-, ethanol-, methanol-, and acetone-gasoline blends: a comparative study. *Renew Sustain Energy Rev* 71:404–413
23. Fan Z, Xia Z, Shijin S, Jianhua X, Jianxin W (2009) Unregulated emissions and combustion characteristics of low-content methanol-gasoline blended fuels. *Energy Fuels* 24:1283–1292
24. Wei Y, Liu S, Liu F, Liu J, Zhu Z, Li G (2009) Formaldehyde and methanol emissions from a methanol/gasoline-fueled spark-ignition (SI) engine. *Energy Fuels* 23:3313–3318
25. Chen H, Yanga L, Zhanga P, Li J, Geng L, Ma Z (2014) Formaldehyde emissions of gasoline mixed with alcohol fuels and influence factors. *Jordan J Mech Ind Eng* 8
26. Wei Y, Liu S, Liu F, Liu J, Zhu Z, Li G (2010) Direct measurement of formaldehyde and methanol emissions from gasohol engine via pulsed discharge helium ionization detector. *Fuel* 89:2179–2184
27. Zhang F, Shuai S, Wang Z, Zhang X, Wang J (2011) A detailed oxidation mechanism for the prediction of formaldehyde emission from methanol-gasoline SI engines. *Proc Combust Inst* 33:3151–3158
28. Yang C-J, Jackson RB (2012) China's growing methanol economy and its implications for energy and the environment. *Energy Policy* 41:878–884
29. Olah GA (2005) Beyond oil and gas: the methanol economy. *Angew Chem Int Ed* 44:2636–2639
30. Vale A (2007) Methanol. *Medicine (Baltimore)* 35:633–634
31. Yüksel F, Yüksel B (2004) The use of ethanol-gasoline blend as a fuel in an SI engine. *Renew Energy* 29:1181–1191
32. Furey RL, Perry KL (1991) Composition and reactivity of fuel vapor emissions from gasoline-oxygenate blends. *J Fuels Lubr* 100:1257–1271
33. Coelho EP, Moles CW, dos Santos MA, Barwick M, Chiarelli PM (1996) Fuel injection components developed for Brazilian fuels. In: Presented at the SAE Brasil 96 V international mobility technology conference and exhibit
34. Naegeli DW, Lacey PI, Alger MJ, Endicott DL (1997) Surface corrosion in ethanol fuel pumps. In: Presented at the international spring fuels and lubricants meeting and exposition
35. Methanol use in gasoline-blending, storage and handling of gasoline containing methanol. Methanol Institute
36. El-Emam SH, Desoky AA (1985) A study on the combustion of alternative fuels in spark-ignition engines. *Int J Hydrog Energy* 10:497–504
37. Gabele P (1995) Exhaust emissions from in-use alternative fuel vehicles. *J Air Waste Manag Assoc* 45:770–777
38. Yao D, Ling X, Wu F (2016) Experimental investigation on the emissions of a port fuel injection spark ignition engine fueled with methanol-gasoline blends. *Energy Fuels* 30:7428–7434
39. Gong C-M, Li J, Li J-K, Li W-X, Gao Q, Liu X-J (2011) Effects of ambient temperature on firing behavior and unregulated emissions of spark-ignition methanol and liquefied petroleum gas/methanol engines during cold start. *Fuel* 90:19–25
40. Zhao H, Ge Y, Tan J, Yin H, Guo J, Zhao W, Dai P (2011) Effects of different mixing ratios on emissions from passenger cars fueled with methanol/gasoline blends. *J Environ Sci* 23:1831–1838
41. Liang B, Ge Y, Tan J, Han X, Gao L, Hao L, Ye W, Dai P (2013) Comparison of PM emissions from a gasoline direct injected (GDI) vehicle and a port fuel injected (PFI) vehicle measured by electrical low pressure impactor (ELPI) with two fuels: Gasoline and M15 methanol gasoline. *J Aerosol Sci* 57:22–31

Review on Dental Implant with Special Reference to Tooth Abutment Implant



Shailja Awasthi , Vinay Pratap Singh  and S. K. S. Yadav 

Abstract In human beings, tooth loss is a common problem which may be due to various diseases and trauma. Dental implants are used to provide support for replacement of missing teeth. At the present time, research is focused on implant design, materials, and techniques for fabrication of the dental implant. There is still a lot of work involved in the use of better material, implant design, surface modification, and functionalization of surfaces to improve the long-term benefits of implant treatment. This paper provides a brief history of dental implant and its classification, success, and failure rate of a dental implant, parameters such as length, diameter, geometry, and thread used for the current tooth abutment implant. It also discusses the various complexities associated with the dental implant such as complex design and machining of the screw, its cost, failure due to the motion of implant in the transverse direction, idea to remove complexities, and current technologies.

Keywords Tooth · Dental implant · Endosteal root form

1 Introduction

The teeth are a very important part of the human body which we used to break down food ingredients by cutting and crushing them in preparation for swallowing and digesting. There are four types of teeth in humans: incisors, canines, premolars, and molars, and each tooth has some special function. The incisors teeth cut the food, the canines teeth tear the food, and the molars and premolars teeth crush the food. The roots of teeth are embedded in the upper jaw or in the lower jaw and are covered by gums. Teeth are made of multiple tissues of varying density and hardness. Figure 1 shows various types of teeth.

Tooth abutment implant plays an important role in prosthodontics and restorative dentistry since the early 1970s. Tooth abutment implant is a type of endosteal dental implant which is classified on the basis of implant design. When some problem

S. Awasthi · V. P. Singh (✉) · S. K. S. Yadav
HBTU, Kanpur, India
e-mail: vinayforus@gmail.com

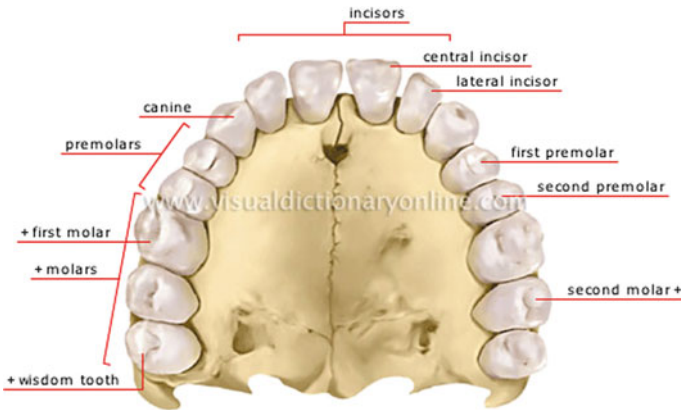


Fig. 1 Types of human teeth in lower jaw. *Source* [1]

occurs in the second premolar tooth of the human being and replacement is required then we use the tooth abutment implant as a root and place crown above it. There are three parts of this dental implant which are abutment, implant, and screw. Here, we use a screw for combining the remaining two parts (abutment and implant). Crown is mounted on the abutment and implant remain is fixed in the jaw bone. The success and failure of the implant mainly depend on the osseointegration but there are some other factors which also affect the success of the implant such as bone loss, implant design, implant parameter, surface properties, etc.

2 Dental Implant and Its Types

A dental implant is a surgical component that interfaces with jawbone to support a dental prosthesis such as a crown, bridge, denture, etc. [2].

2.1 Classification Based on Implant Design

There are four types of the dental implant on the basis of implant design (Figs. 2, 3)

1. Endosteal Implant—This type of implant is surgically implanted into the jawbone directly [3]. Endosteal implant is placed into the alveolar bone and or basal bone. Endosteal is divided into three types as given below:

Blade implant—There is a thin plate in the form of a blade which is embedded in the bone.

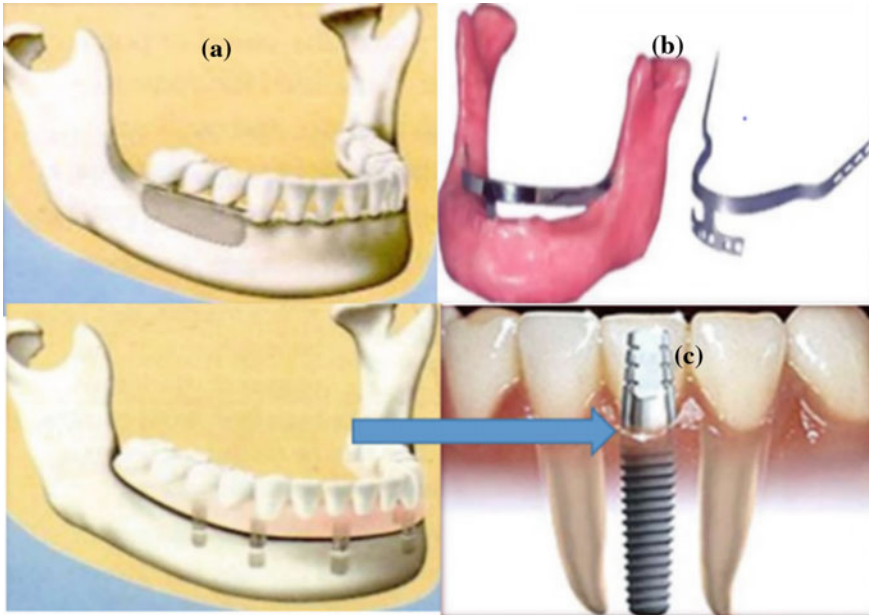


Fig. 2 Endosteal implant and its parts **a** blade implant, **b** ramus frame implant, **c** root form implant. *Source* [4]

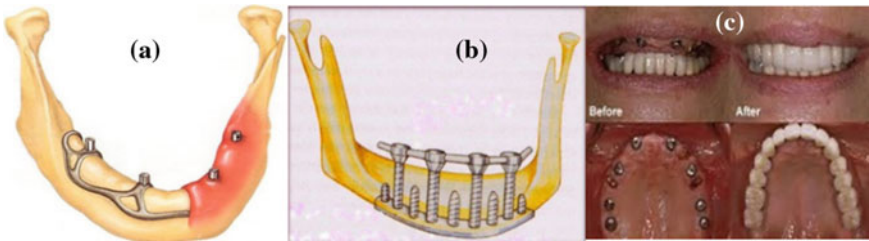


Fig. 3 Pictures of **a** subperiosteal implant, **b** transosteal implant, **c** intramucosal implant. *Source* [4]

Ramus frame implant—It is a horseshoe-shaped device which is made of stainless steel, and is inserted into the mandible from one retromolar pad to the other.

Root form implant—This type of implant is designed to mimic the shape of the tooth and also for directional load distribution [3].

2. Subperiosteal implant—We can use this type of implant when all teeth are absent in the mouth or when due to lack of enough jawbone width and height. The weight of this implant is very light and this is made from metal framework, and it provides roots for multiple teeth.

3. Transosteal implant—This is also called staple bone implant or mandibular staple implant or transmandibular implant. This type of implant is used only for the lower jaw and it is made from pure titanium and its alloy.
4. Intramucosal implant—This implant is inserted into the oral mucosa. This implant is used with the removable dentures. They have a mushroom-shaped design which is fit on the upper side of the mouth.

2.2 Classification Based on Attachment Mechanism of the Implant

There are two types of dental implant (Fig. 4)

1. Osseointegration—In the osseointegration, the jawbone attaches to dental implants directly and bone grows up to the implant surface without inverting soft tissue. It takes 4 to 6 months to complete the restorations [5].
2. Fibrointegration—This process is same as osseointegration but it needs soft tissues such as fibers or cells between implant and bone to completely attach and to heal. The fiber collagen formed around the implant makes the healing process faster than actual osseointegration process. The dentist can attach the abutment and crown at the time of implant surgery itself [6].

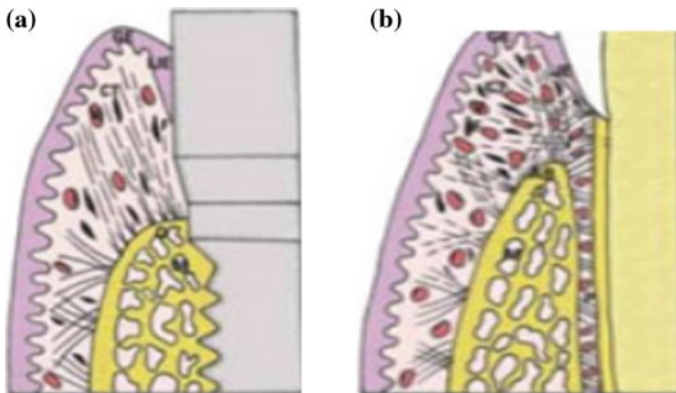


Fig. 4 Pictures of **a** osseointegration, **b** fibrointegration. Source [6]

2.3 Classification Based on Macroscopic Body Design of the Implant

There are six types of the dental implant on the basis of macroscopic body design of the implant. These are (Fig. 5) given as follows:

1. Cylindrical dental implants—These are cylindrical as the name suggest without screw threads and can be placed easily in the jawbone.
2. Threaded dental implants—We make the thread on the surface to increase its surface area and thread help in distribution of force in large peri-implant bone volume.
3. Plateau dental implants—These are plateau in shape with the sloping shoulder.
4. Perforated dental implants—These implants are of inert microporous membrane material in intimate contact with and supported by the layer of perforated metallic sheet material.
5. Solid dental implant—These type of implants of the circular cross section without any kind of hole in the body.

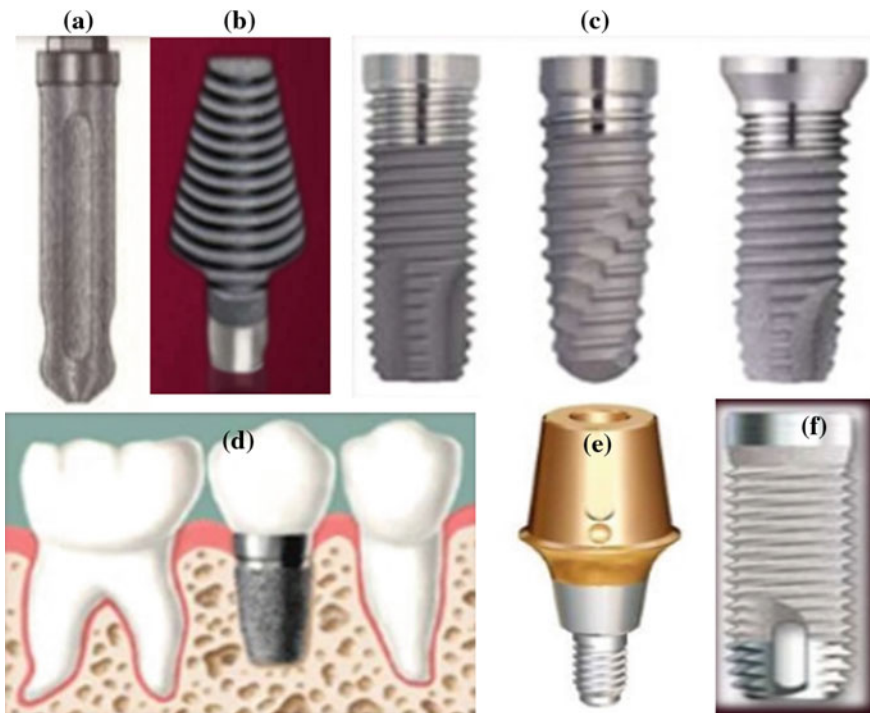


Fig. 5 Pictures of **a** cylindrical dental implant, **b** threaded dental implant, **c** plateau dental implants, **d** perforated dental implant, **e** solid dental implant, **f** hollow or vented dental implant. *Source [7]*

6. Hollow dental implants—These implants are hollow screw type and there are multiple holes in its lateral surface. These holes are used by the bone tissue for penetration into the implant, the contact area with the bone is increased, and therefore a high bonding force can be obtained.

2.4 Classification Based on the Implant Material

There are four types of dental implant on the basis of implant material (Fig. 6) which are given as follows:

1. Metallic implant—Stainless steel, cobalt chromium, molybdenum alloy, vitalium, and titanium material are used for implant.
2. Ceramic and ceramic-Coated Implant—Ceramic implants are fabricated by powder compaction or as a ceramic-coated metallic implant. The ceramic coating preferably contains a titanium oxide ceramic, zirconium oxide, etc.
3. Polymeric implant—Polymeric compounds adapted to be implanted at the external layer are those that known to be biocompatible and they have the ability to be drugged impregnated.
4. Carbon implants—Its modulus of elasticity is equivalent to the modulus of elasticity of bone and dentine.

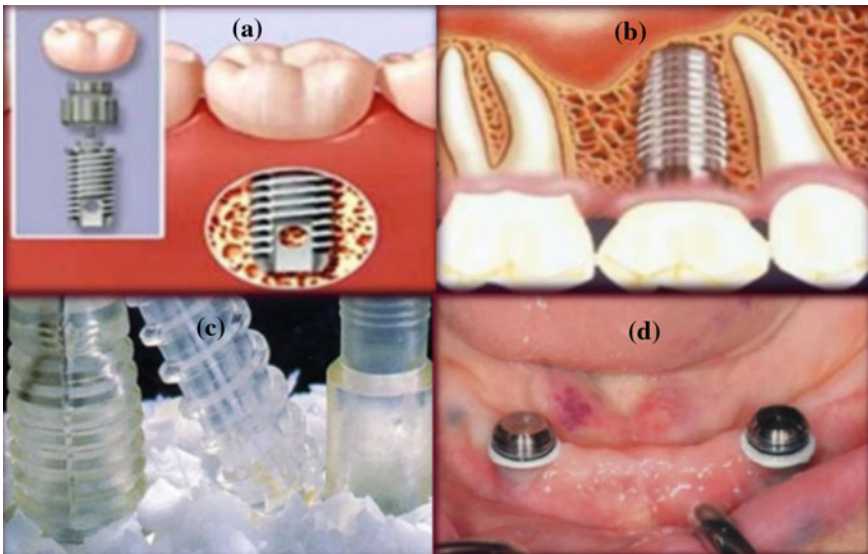


Fig. 6 Pictures of **a** metallic implant, **b** ceramic and ceramic-coated implant, **c** polymeric implant, **d** carbon implants. Source [8]

2.5 Classification on the Basis of the Surface of Implant

There are four types of the dental implant on the basis of the surface of the implant (Fig. 7) as given below:

1. Smooth surface implant—This type of implant has a very smooth surface as the name suggest. Smooth surface provides microbial plaque retention property.
2. Machined surface implant—Machined surface implants provide better anchorage of the implant to the bone.
3. Textured surface implant—We make the surface of the implant textured since surface roughness plays an important role in cell adhesion to surfaces of orthopedic prostheses and dental implants.
4. Coated surface implant—We generally use coated surface of the implant to improve the surface properties like hardness, the corrosion resistance of the substrate without changing the bulk materials.

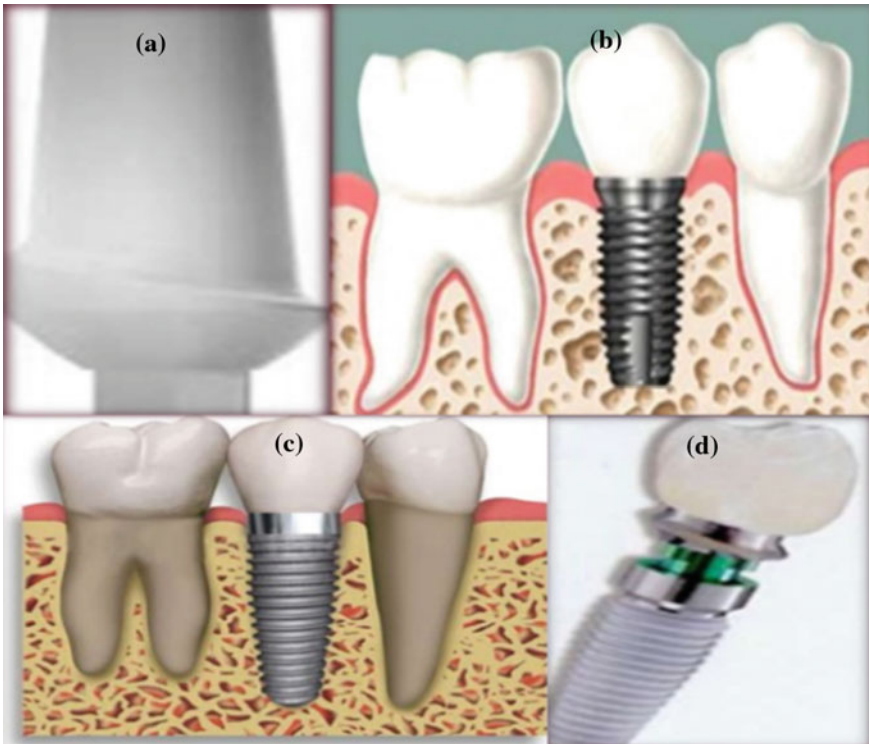


Fig. 7 Pictures of **a** smooth surface implant, **b** machined surface implant, **c** textured surface implant, **d** coated surface implant. *Source* [9]

3 Success and Failure Rates of Implant

After the missing tooth is replaced, the success of the implant is the only most important factor in treatment. Osseointegration is a key factor in implant success. We can place the implant below a denture or partial denture for stabilization and bone retention. We can use different types of the materials to make implants which include cobalt and chromium, aluminum stainless steel, titanium, etc [10]. Smeets et al. suggested that successful implants are based on the direct bone anchorage with the implant body. If we modified the surface texture up to more porous state then we will get best osseointegration. Osseointegration is an important factor in implant survival, without osseointegration it can lead to peri-implantitis and ultimately implant will fail. Periodontitis is the leading cause of tooth loss across the nation. Cho et al. state that periodontitis, a common periodontal disease, is an inflammatory disease that damages soft tissue and induces periodontium destruction. Giri and Saini, discovered peri-implantitis, like periodontitis, occurs primarily as a result of an overwhelming bacterial insult and subsequent host immune response. This can raise the risk of implant failure and bone loss in the region [11].

According to several researchers, various parameters which are related to the implant success are as follows:

- (i) Immobile implant, when tested clinically,
- (ii) No evidence of peri-implant radiolucency, and
- (iii) Bone loss that is less than 0.2 mm annually after the implant's first year of service.

According to Esposito, following were to be considered success criteria for osseointegration implants:

- (i) The absence of mobility,
- (ii) Less than 0.2 mm annually thereafter, and
- (iii) Absence of paresthesia.

There are many views for implant failures. According to Rosenberg et al., implant failures can be classified as infectious failures and traumatic failures. Esposito et al. classified the implant failures as biological failures, mechanical failures, iatrogenic failures, and inadequate patient education failures and Truhlar [12] classified failures as early failures and late failures. Finally, dental implant become successful when bone is comprised of homogeneous, compact bone throughout the entire jaw and bone has a core of dense trabecular bone surrounded by a thick layer of compact bone, high bone volume, clinician experience, mandibular placement, single tooth implant, implant length should be greater than 8 mm, axial loading of the implant, good oral hygiene, etc. and implant fail when bone has only a thin layer of cortical bone surrounding a core of dense trabecular bone, bone has a core of low-density trabecular bone of poor strength encased in thin cortical bone, low volume of bone, limited clinician experience, diseases like uncontrolled diabetes, HIV, etc., maxillary placement, particularly posterior region, short implant, due to acentric loading, etc.

4 Design Parameter of Endosseous (Tooth Abutment) Implant

Length

Implant length affects the stress distribution at the bone–implant interface and it also affects the success rate of the implant. There are various views about implant length [13], it can vary from 8–15 mm. If we take implant length of more than 10 mm, then it will not reduce so much the stress distribution [14, 15]. And the length of the abutment may be varied from 6 to 10 mm.

Diameter

We can vary the implant diameter from 3 to 7 mm and abutment diameter from 3 to 5 mm. Ivanoff et al. [16] concluded that larger diameter implants are more stable. Using various techniques, we find that implant diameter gives more effect on stress distribution than implant length in cortical bone but in cancellous bone implant length is predominant [17].

Geometry

Geometry is a very important factor which affects the interaction between the bone and implant, surface area, force distribution, and the implant stability [18]. There are various types of implant in the form of cylinder, conic, stepped, screw shaped, and hollow cylinder. After several studies, we found that conical implant with geometric discontinuities is best compared to smooth cylindrical or screw shaped because it provide more stress distribution.

Threads

We make the thread on the implant surface so that we can increase its surface area, improve its initial stability, and distribute stress favorably [19]. We make various threads on implant body like micro-thread on its neck part, macro-thread on its middle part and variety of altered pitch threads on its lower part [15].

4.1 Composition of Dental Implant

Titanium and its alloy is the main metallic material which is used for manufacturing of dental implant. Nowadays, we mostly make the implant of pure titanium and its alloy mainly because it is a light metal with the best biocompatibility, relatively high stiffness, and corrosion resistance [20]. Various other materials like ceramic, polymer, etc. are also being used for dental implant.

4.2 Complexities Associated with the Endosseous Implant and Its Removal

There is one major reason for implant failure which is microgap. If microgap is left after fixation, then it results in disease surrounding the implant. Microgap is the first stage of disease and due to this bone may lose or implant may fail. Sometimes this microgap occurs at the lower position of internal hexagonal connection leads to produce stress of dental implant so it increases the possibilities to be failure dental implant [21]. According to several studies, bone loss may be the reason for implant failures [22]. Implant parameters such as diameter, shape, length, and abutment type are not only the reason for bone loss but also external hex implant body abutment generated the maximum stress under vertical loading condition of forces than internal hex generated. Bone quality also affects the implant and produces more stress-like spongy bone [23]. There are some other problems occur in the implant which is related to the implant complex design. There are three parts in the tooth abutment dental implant. These are abutment, implant, and screw (Fig. 8).

For combining abutment and implant, we use a costly screw which has a very complex geometry and its machining process is very difficult so if we make a design which combine the abutment and the implant without using a screw and which make a better locking system between them then we can resolve this problem. FEA-based analysis, functionally graded materials, nanotechnology, etc. are various recent approaches used for the design of dental implants.



Fig. 8 Different parts of tooth abutment implant. *Source* [24]

5 Conclusions

A successful effort was made to review the details of various dental implants. It was observed that

1. The major classifications of dental implants are based on implant design, an attachment mechanism, macroscopic body design, implant material, and on the basis of surface of the dental implant.
2. The success of the dental implant mainly depends upon better osseointegration, the absence of mobility, surface characteristic of the dental implant, homogeneity of bone, higher volume and density of bone, clinician experience, implant parameter especially length, good oral hygiene, etc.
3. Implant failures occur mainly when there is no osseointegration, less volume and low density of bone, poor strength of the bone, less clinician experience, etc.

References

1. Bruinsma B, Rudebrush (2016) English composition IV, 16 Dec 2016
2. Dental implant and its type. <https://www.slideshare.net/desaghanavi/types-and-classification-of-dental-implants> (20-03-2018)
3. Dental implant. <https://www.google.co.in/search?q=endosteal+implant&oq=endosteal&aqs=chrome.3.69i57j0l5.31332j0j8&sourceid=chrome&ie=UTF-8> (22-03-2018)
4. Carranza FA, Newan MG, Takei HH (2002) *CliPerio*, 9th edn. Saunders, Philadelphia
5. Dental implant and its type. <https://tamardental.wordpress.com/2013/05/03/classification-of-dental-implants-based-on-attachment/> (22-03-2018)
6. Martin M, Haigh T, Lamar Institute of Technology Dental Hygiene program
7. Ullen G, Short implant: reality and predictability. A peer RPub. Heidari B, Bisadi H, Heidari Be, Kakhodazadeh M (2009) Influence of different tapered implants on stress and strain distribution in bone and implant: a FEA. *J Adv Periodontal Implant Dent* 1(1):11–19
8. Cimdins R, Riga Biomaterials Innovations and Development Centre of RTU, Institute of General Chemical Engineering, Faculty of MS and Applied Chemistry, Riga Technical University, Pulka 3, LV-1007 Riga, Latvia
9. Pye AD, Lockhart DEA, Dawson MP, Murray CA, Smith AJ, Glasgow Dental Hospital and School, Faculty of Medicine, Glasgow University, Glasgow, UK IRG
10. Dental implant and its type. <https://tamardental.wordpress.com/2013/04/26/design-based-classification-of-dental-implants/> (23-03-2018)
11. Saini R, Giri PA, Cho et al., Saini S, Saini SR (2014) Peri-implantitis: a review. *Pravara Med Rev*
12. Prashanti E, Sajjan S, Reddy JM (2011) Failures in implants. *Indian J Dent Res* 2:446–453
13. Atieh MA, Atieh AH, Payne AG, Duncan WJ (2009) Immediate loading with single implant crowns: a systematic review and meta-analysis. *Int J Prosthodont*, 378–387
14. Mijiritsky E, Mazor Z, Lorean A, Levin L (2013) Implant diameter and length influence on survival: interim results during the first 2 years of function of implants by a single manufacture. *Implant Dent* 22:394–398
15. Mandhane SS, More AP (2014) A review evaluation of design parameters of dental implant abutment. *Int J Emerg Sci Eng* 2:64–67
16. Ivanoff CJ, Sennerby L, Johansson C, Rangert B, Lekholm U (1997) Influence of implant diameters on the integration of screw implants. *Int J Oral Maxillofac Surg* 26:141–148

17. Baggi L, Cappelloni I, Di Girolamo M, Maceri F, Vairo G (2008) The influence of implant diameter and length on stress distribution of osseointegrated implants related to crestal bone geometry: a three-dimensional finite element analysis. *J Prosthet Dent* 100:422–431
18. Elias CN, Factors affecting the success of dental implant. InTech, Rijeka. Available from <http://www.intechopen.com/books/implant-dentistry-a-rapidly-evolving-practice/factors-affecting-the-success-of-dental-implants> (cited 2014 Apr 22)
19. Vidyasagar L, Apse P (2004) Dental implant design and biological effects on bone-implant interface. *Stomatologija* 6:51–54
20. Triplett RG, Frohberg U, Sykaras N, Woody RD (2003) Implant materials, design, and surface topographies: their influence on osseointegration of dental implants. *J Long Term Eff Med Implants* 13:485–501
21. Karunagaran S, Paprocki GJ, Wicks R, Markose S, A review of implant abutments—abutment classification to aid prosthetic selection. *J Tennessee Dent Assoc/pubmed.gov US National Library of Medicine National Institutes of Health*
22. Saidin S, Kadir MRA, Sulaiman E, Kassim NA (2010) Finite element analysis on Internal hexagonal and internal conical abutment. In: 2010 IEEE EMBS conference on biomedical engineering and sciences (IECBES 2010), Malaysia
23. Johnson NW, Meredith N, Stress distribution characteristics in dental implant influenced by its wall thickness (online article)
24. IOSR J Dent Med Sci (IOSR-JDMS) 11. e-ISSN: 2279-0853, p-ISSN: 2279-0861

Performance and Emission Analysis of a C.I. Engine Using Ethanol and Its Blends with Jojoba Biodiesel and Diesel as a Fuel



Amanpreet Singh, Sandeep Singh, Varun Singla and Varinder Singh

Abstract An experimental study is conducted to determine the influence of ethanol to the blends of Jojoba biodiesel and diesel on the performance and emissions characteristics of a C.I. engine. The fuel blends used are denoted as D80–JME10–E10 (80% Diesel, 10% Jojoba Methyl Ester and 10% Ethanol) and D60–JME20–E20 (60% Diesel, 20% Jojoba Methyl Ester and 20% Ethanol). In this study, Jojoba Methyl Ester was prepared from the transesterification process. The properties of Jojoba methyl ester were evaluated and compared with the latest biodiesel standards. Also, performance and emissions characteristics were measured on a C.I. engine. The investigation shows that fuel blend D80–JME10–E10 gave an increment in BTE of 2.91% and reduction in BSFC of 3.61% than that of D60–JME20–E20 at full load respectively. Reduction in CO emissions of 9.3% and 12.2% was observed for fuel blends D80–JME10–E10 and D60–JME20–E20 as compared to diesel, at full load. Also, NO_x emissions were reduced for the fuel blends D80–JME10–E10 and D60–JME20–E20 of about 40.2 and 28.6% as compared to diesel.

Keywords Ethanol · Compression ignition · Jojoba biodiesel · Transesterification · Brake thermal efficiency · Carbon monoxide

1 Introduction

Due to higher efficiency and easy adaptability, the diesel engines have wide applications in several domains. Diesel engines exhibits various exhaust emissions consists

A. Singh (✉) · S. Singh
Department of Mechanical Engineering, Punjabi University, Patiala, Punjab, India
e-mail: preetaman70@gmail.com

V. Singla
Department of Mechanical Engineering, I.K. Gujral Punjab Technical University, Jalandhar, Punjab, India

V. Singh
Department of Mechanical Engineering, Thapar Institute of Engineering and Technology, Patiala, Punjab, India

of unburned hydrocarbons (UHC), particulate matters (PM), nitrogen oxides (NO_x) and carbon oxides (CO) [1]. Therefore, the whole world is in the search for an alternative fuel due to global warming, environmental and public health issues [2]. So, biodiesel can be an alternative fuel due to the properties similar to the diesel [3]. Biodiesel is prepared from transesterification process consisting of a reaction of vegetable oil with methanol or ethanol which gives methyl ester or ethyl ester and glycerine as by products [4]. Due to similar properties, biodiesel prepared from vegetable oils can be easily used in present diesel engines after very little modifications. Also, biodiesels made from vegetable/edible oils are non-toxic and biodegradable in nature [5, 6]. Fatty acid content of the edible oils and production method has a great influence on the properties of the biodiesel. These properties can be improved by addition of biodiesel with another biodiesel or with diesel [6]. Biodiesel used in the diesel engines always should be in the blended form not neat biodiesel because neat biodiesel may create some problems in the engine [7]. Literature indicates that the addition of ethanol or methanol in the biodiesels decreases the HC, PM and CO emissions while little increment in NO_x emissions [8].

1.1 *Jojoba Liquid Fuel*

Jojoba oil has a great uniqueness in nature. Jojoba is like a perennial shrub that grows in deserts naturally. Jojoba is found in many countries like United States, Central America and South America etc. The seeds of jojoba contains about 45–55 wt% of oil-wax golden liquid which can be separated by a solvent extraction or cool pressing. Jojoba oil is a combination of long straight chain esters of fatty alcohols and fatty acids as shown in Fig. 1. It has wide applications in the different domains like cosmetics, pharmaceuticals and lubricants [9, 10].

Jojoba oil can be used as an alternative fuel in automobile sector and also as a lubricant [12]. Jojoba oil has high energy potential in its seeds as well as exhausts negligible SO_x emissions and relatively lesser NO_x emissions when burned. Therefore, these factors make jojoba oil as an alternative fuel [13]. Several investigators

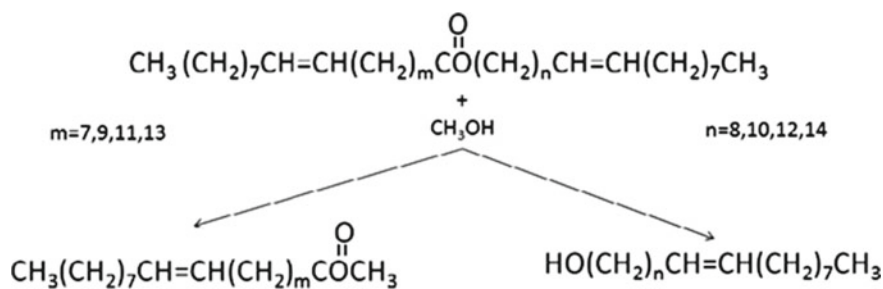


Fig. 1 Transesterification process of Jojoba oil [10, 11]

have conducted experimental study on the C.I. engine fuelled with Jojoba oil and its blends. Some of them are summarized the explanation in the following section.

Huzayyin et al. [14] investigated the performance and emissions parameters of a diesel engine run with jojoba and diesel blends and studied that with increase in amount of jojoba oil in the blended fuel, soot number decreased. Shah et al. [15] studied the various properties of jojoba oil and found that cloud and pour point of jojoba oil were high. Also, it showed high viscosity which is a major disadvantage of jojoba oil. Zayed et al. [16] investigated the various properties of jojoba oil and its blends with diesel fuel and sun flower biodiesel. They found that these properties were very close to diesel, so that, the jojoba oil and its blended form with diesel and sun flower biodiesel might be used as an alternate fuel. Shehata et al. [17] reported an experiment on diesel engine fuelled with B20 blend (20% jojoba oil + 80% diesel) and with sunflower oil (S100) and results were compared to the diesel at different speeds of engine. The results depicted that S100 or B20 has a potential of alternative fuel with high viscosity.

Saleh et al. [18] studied an experiment on diesel engine with jojoba methyl ester as main fuel and found the reduction in nitrogen oxide with exhaust gas recirculation (EGR). Selim et al. [19] investigated the combustion pressure and rate of its rise and other operating factors on a Ricardo E6 compression swirl diesel engine fuelled with JME and its blended fuel with gas oil. With the similar test rig, Hamdon et al. [20] investigated the performance of dual fuel diesel engine fuelled with JME as pilot fuel and hydrogen as a gaseous fuel and found the improved performance as compared to diesel fuel. Radwan et al. [21] studied the preparation and characterization of JME as a diesel fuel alternate. It was found that JME liquid fuel was safe and has zero sulphur content and reduced the engine wear as well as increases the life of lubricating oil. Shah et al. [22] investigated the catalytic conversion of pure jojoba oil into biodiesel by various catalysts. The optimization of different parameters was established to obtain the maximum yield of the biodiesel by using catalyst of dibutyltin diacetate ($(C_4H_9)_2Sn(OOCCH_3)_2$). The various physical and fuel properties of jojoba methyl ester were determined by ASTM methods and were obtained to be comparable to ASTM standards for diesels.

Awad et al. [23] reported the Jojoba biodiesel production and different properties of ethanol blends. The jojoba biodiesel and ethanol in its blends with different ratios (5, 10, 15 and 20% ethanol) have been taken. It has been found that 7% addition of ethanol in the blend gives the highest yield of biodiesel, taking the cost factor. More addition of ethanol in JEE resulted in the decrease of various properties like density, pour point, and low calorific value. El-Boulifi et al. [24] studied the transesterification method by using the pure jojoba oil (JO) with four different short-chain alcohols to formation of jojobyl alcohols (JA) as main product and fatty acid alkyl esters (FAAE) as co-product in biorefinery.

1.2 Ethanol as an Oxygenated Additive—A Review

Due to insufficient cold flow properties of biodiesel, it causes a resistance in the application of biodiesel-diesel blends in cold conditions. Therefore, ethanol may be used as an oxygenated additive in the engine operation to improve low cold flow properties of biodiesel [25]. Ethanol is used as one of the renewable and eco-friendly oxygenated additive for I.C. engine. In addition, ethanol has oxygen content, higher heat of vaporization and higher flame temperature and therefore has a reliable and positive effect on engine performance and emission characteristics [26]. Several investigators have executed experimental investigation on the C.I. fuelled with ethanol blended and concluded that ethanol is a significant additive.

2 Materials and Methods

In this present study, Jojoba Methyl Ester (JME) is prepared by transesterification process. Two biodiesel blends were prepared: Blend A—Diesel 80%, JME 10% and Ethanol 10% (by volume basis) designated as D80-JME10-E10 and Blend B—Diesel 60%, JME 20% and Ethanol 20% (by volume basis) designated as D60-JME20-E20. The various properties like density, flash point temperature, kinematic viscosity, calorific value and cetane number of diesel, biodiesel and ethanol were determined by using ASTM methods. The properties of various fuels used in the experimentation are shown in Table 1.

2.1 Experimental Setup and Testing

In the present study, the experiments were conducted on a single cylinder four stroke air cooled C.I. engine with electrical loading as shown in Fig. 2. The performance and emission characteristics of engine were compared with the diesel fuel. Experimental tests were conducted at a constant speed of 1500 rpm and at varying loads for all biodiesel blends. All the experimental tests were conducted at the fuel injection

Table 1 Properties of various fuels used

Property	Units	JME	Diesel	Ethanol	ASTM D6751
Kinematic viscosity at 40 °C	cSt	15.1	3.11	0.795	1.9–6
Flash point	°C	106	78	14	93 (min.)
Calorific value	MJ/kg	39.10	42.5	29.7	33 (min.)
Cetane number	–	53	55	8	47 (min.)

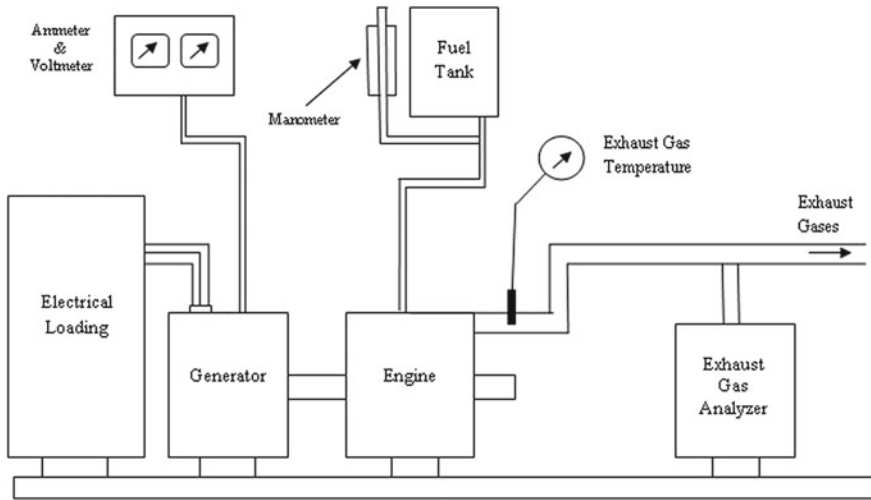


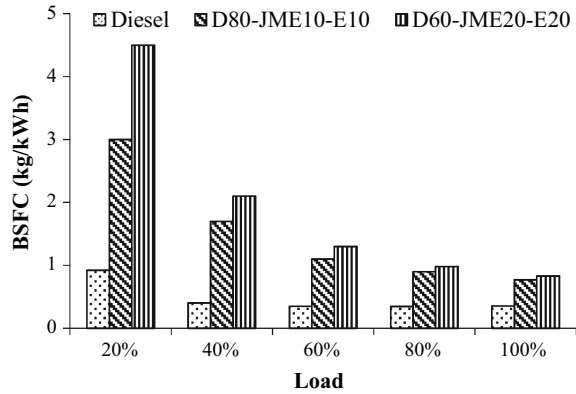
Fig. 2 Test engine setup

Table 2 Specifications of the test engine

Engine parameter	Specification
Engine model	FCD Ltd.
Number of cylinders	1
Cylinder bore/stroke	102/110 mm
Displacement volume	898.84 cc
Compression ratio	17.5: 1
Maximum power	6 KW
Rated speed	1500 rpm
Fuel injection pressure	210 Bars
Fuel injection system	Direct injection
Cooling system	Forced air cooled

pressure of 210 bars and static injection timing of 26° BTDC. AVL 4000 Di-Gas Analyzer was used to estimate the emissions such as unburned hydrocarbons (HC), carbon monoxide (CO) and nitrogen oxides (NO_x). The detailed specifications of the engine are given in Table 2.

Fig. 3 Variation of brake specific fuel consumption with the load



3 Results and Discussions

3.1 Performance Analysis

3.1.1 Brake Specific Fuel Consumption (BSFC)

It can be studied from Fig. 3 that, when the load on the engine increases, BSFC decreases for the all test fuels. This may be due to the higher fuel atomization and combustion quality which increases with increase in engine load.

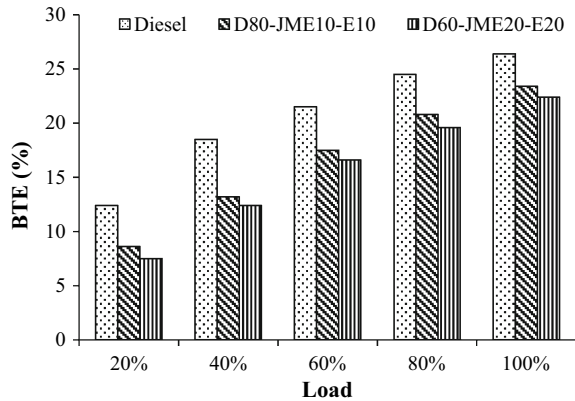
We know that, ethanol has low heating value, so the heating value of the diesel–JME–ethanol blends is comparatively low as to diesel fuel. This low heating value of blends of diesel–JME–ethanol increased the BSFC of the engine. This increase in BSFC mainly depends upon the amount of ethanol and JME in the blended fuel.

As the amount of JME and ethanol in the blended fuel increases, the BSFC of the engine also increases [27]. The BSFC of diesel, D80–JME10–E10 and D60–JME20–E20 are found to be approximate 0.38 kg/kWh, 0.80 kg/kWh and 0.83 kg/kWh respectively, at full load. D80–JME10–E10 gives a decrement in BSFC than that of D60–JME20–E20 at full load. The blended fuel D80–JME10–E10 gives a lower BSFC of about 3.61% than that of fuel blend D60–JME20–E20 at full load. Thus the amount of biodiesel JME and ethanol in the fuel blends should be low as possible because the BSFC depends upon these two factors also [27].

3.1.2 Brake Thermal Efficiency (BTE)

The BTE for all test fuels increases with the increase in the engine load as shown in the Fig. 4.

Fig. 4 Variation of brake thermal efficiency with the load



This increment in the BTE occurs due to the higher temperature of engine cylinder at relatively higher loads. Diesel fuel produces the highest BTE throughout the engine load as compared to blended fuels used. Higher calorific value of diesel is responsible for the higher BTE [27]. The BTE of diesel fuel is maximum, found to be of 26.5%, which is 3.28% more than that of fuel blend D80–JME10–E10 and 5.47% more than that of fuel blend D60–JME20–E20 respectively, at full load. The fuel blend D80–JME10–E10 shows an increment in BTE of 2.19% than that of fuel blend D60–B20–E20, at full load.

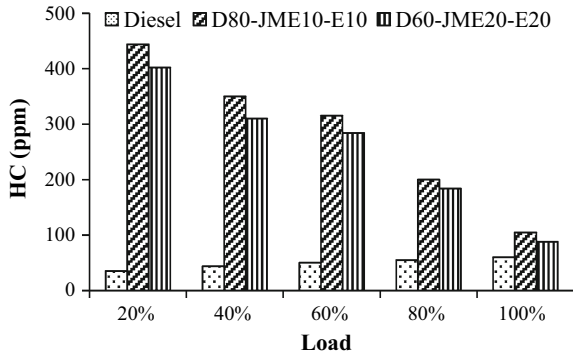
3.2 Emission Analysis

3.2.1 Hydrocarbon (HC) Emissions

Figure 5 illustrates the variations of HC emissions with respect to the load. Hydrocarbon emission is the residue of unburned hydrocarbons and is an indication of completeness of combustion [28]. As the load increases on the engine, an unburned HC emission decreases for the diesel–JME–ethanol blends as well as increase for diesel fuel. Both the diesel–JME operations with ethanol addition gave a higher HC emission as compared to diesel. This might be occur due to the presence of ethanol in the fuel blends which enhances the ignition delay for the fuel blends, resulting the incomplete combustion of fuel blends which in results increases the HC emission [29].

Higher HC emissions are to be found in diesel–JME–ethanol blends as comparable to the diesel throughout the whole engine load. This could be due to the slow vaporization rate of ethanol which produced an inhomogeneous blend with diesel, thus helps in the lean mixtures formation in some parts of the combustion chamber [30]. D80–JME10–E10 and D60–JME20–E20 gives HC emissions of about 42.1 and 32.5% higher than that of diesel respectively, at full load of engine. Also, fuel blend

Fig. 5 Variations of HC emissions with the load



D60-JME20-E20 gave lower HC emissions of about 10.2% than that of fuel blend D80-JME10-E10 at full load.

3.2.2 Carbon Monoxide (CO) Emission

The variations of CO emissions with the load are depicted in Fig. 6.

Concentration of higher CO emissions in the fuel blends may be due to the low temperature of the blend, lack of reactants (oxidants) and unsteady time for complete combustion. As the load on the engine increases, the CO emissions of the engine decreases. It may be occur due to the higher temperature in the cylinder which enhances the combustion rate [31, 32]. The blend D80-JME10-E10 and D60-JME20-E20 gave a reduction of 9.3 and 12.2% in CO emissions with respect to diesel respectively, at full load. The reduction in CO emissions may be possible due to the addition of ethanol, which improves the ignition process and decreases the period of ignition delay and gives additional time for oxidation of the blended fuel [33].

Fig. 6 Variations of CO emissions with the load

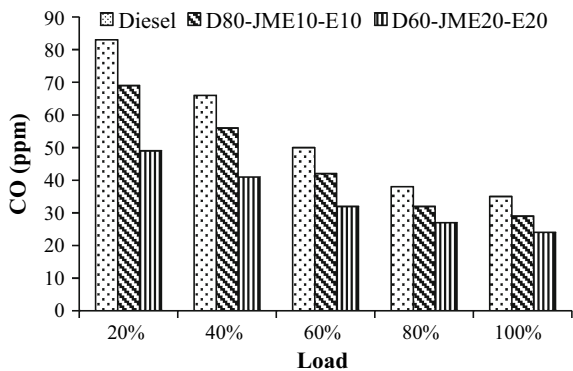
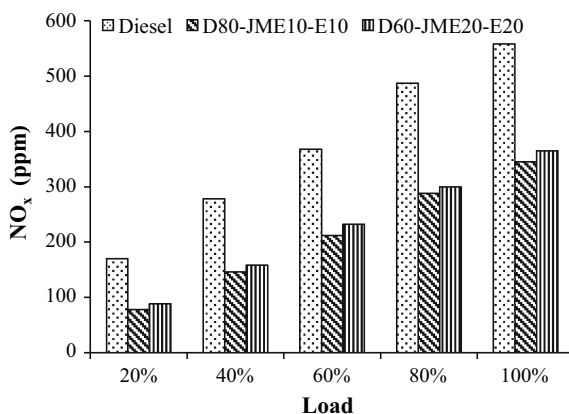


Fig. 7 Variations of CO emissions with the load
Variation of NO_x emissions with the load



3.2.3 Nitrogen Oxides (NO_x) Emissions

The variation of NO_x emissions with the load is depicted in Fig. 7. The amount of NO_x emissions increases as the load on the engine increases. Main reasons of NO_x formation are the high temperature inside the engine cylinder, the amount of oxygen, the reaction time for the combustion to take place and the equivalence ratio [34]. Another reason of lower amount of NO_x emissions from ethanol was cooling effect of evaporation of ethanol, due to which a reduced flame temperature is obtained. As the amount of ethanol increases in the blend, NO_x emissions slightly increases at all engine loads.

It is also clear from the figure that NO_x emissions of fuel blend D60–JME20–E20 are slightly higher than that of fuel blend D80–JME10–E10. This might be due to the increase in amount of oxygen contents in the diesel–JME–ethanol blended fuel. D80–JME10–E10 and D60–JME20–E20 gave a reduction of 40.2% and 28.6% in NO_x emissions with respect to diesel respectively, at full load.

4 Conclusion

The effect of 10 and 20% of Ethanol addition as an additive in a C.I. engine fuelled with diesel–JME blends was investigated. The ethanol quantity was varied and used with varied quantities of JME and diesel to obtain the feasible results in terms of performance and emission characteristics of the engine. In this study, the results of diesel–JME operation along with ethanol addition were compared with the diesel fuel. The results showed that blend D80–JME10–E10 gave an increment in BTE of 2.91% and reduction in BSFC of 3.61% than that of D60–JME20–E20 at full load respectively. Reduction in CO emissions of 9.3 and 12.2% was observed for D80–JME10–E10 and D60–JME20–E20 as compared to diesel respectively, at full

load. Also, NO_x emissions of 40.2 and 28.6% were reduced for the D80–JME10–E10 and D60–JME20–E20 as compared to diesel, at full load respectively. Also, fuel blend D60–JME20–E20 gave lower HC emissions of about 10.2% than that of fuel blend D80–JME10–E10 at full load.

References

1. Fayyazbakhsh A, Pirouzfard V (2016) Investigating the influence of additives-fuel on diesel engine performance and emissions: analytical modeling and experimental validation. *Fuel* 171:167–177
2. Ruiz FA, Cadrazco M, López AF, Sanchez-Valdepeñas J, Agudelo JR (2015) Impact of dual-fuel combustion with n-butanol or hydrous ethanol on the oxidation reactivity and nanostructure of diesel particulate matter. *Fuel* 161:18–25
3. Nalgundwar A, Paul B, Sharma SK (2016) Comparison of performance and emissions characteristics of DI CI engine fueled with dual biodiesel blends of palm and jatropha. *Fuel* 173:172–179
4. Krishnan PN, Vasudevan D (2015) Performance, combustion and emission characteristics of variable compression ratio engine fuelled with biodiesel. *Int J ChemTech Res* 7(1):234–245
5. Abu-Hamdeh NH, Alnefaie KA (2015) A comparative study of almond and palm oils as two bio-diesel fuels for diesel engine in terms of emissions and performance. *Fuel* 150:318–324
6. Ozturk Erkan (2015) Performance, emissions, combustion and injection characteristics of a diesel engine fuelled with canola oil–hazelnut soapstock biodiesel mixture. *Fuel Process Technol* 129:183–191
7. Kumar P, Sharma MP, Dwivedi G (2016) Impact of ternary blends of biodiesel on diesel engine performance. *Egyptian J Petroleum* 25(2):255–261
8. Yilmaz N, Vigil FM, Benalil K, Davis SM, Calva A (2014) Effect of biodiesel–butanol fuel blends on emissions and performance characteristics of a diesel engine. *Fuel* 135:46–50
9. Saleh HE, Selim MY (2017) Improving the performance and emission characteristics of a diesel engine fueled by jojoba methyl ester–diesel–ethanol ternary blends. *Fuel* 207:690–701
10. Canoira L, Alcantara R, García-Martínez MJ, Carrasco J (2006) Biodiesel from Jojoba oil–wax: Transesterification with methanol and properties as a fuel. *Biomass Bioenergy* 30(1):76–81
11. Sánchez M, Marchetti JM, El Boulifi N, Aracil J, Martínez M (2015) Kinetics of Jojoba oil methanolysis using a waste from fish industry as catalyst. *Chem Eng J* 262:640–647
12. Al-Widyan MI, Mu'taz A (2010) Experimental investigation of jojoba as a renewable energy source. *Energy Convers Manage* 51(8):1702–1707
13. Selim MY, Radwan MS, Saleh HE (2008) Improving the performance of dual fuel engines running on natural gas/LPG by using pilot fuel derived from jojoba seeds. *Renewable Energy* 33(6):1173–1185
14. Huzayyin AS, Bawady AH, Rady MA, Dawood A (2004) Experimental evaluation of diesel engine performance and emission using blends of jojoba oil and diesel fuel. *Energy Convers Manage* 45:203–212
15. Shah NS, Sharma BK, Moser BR, Erhan SZ (2010) Preparation and evaluation of jojoba oil methyl esters as biodiesel and as blend components in ultra low sulphur diesel fuel. *Bioenergy Res* 3:214–223
16. Al-Hamamre Z, Al-Salaymeh A (2014) Physical properties of (jojoba oil + biodiesel), (jojoba oil + diesel) and (biodiesel + diesel) blends. *Fuel* 123:175–188
17. Shehata MS, Abdel Razeq SM (2011) Experimental investigation of diesel engine performance and emission characteristics using jojoba/diesel blend and sunflower oil. *Fuel* 90:886–897
18. Saleh HE (2009) Experimental study on diesel engine nitrogen oxide reduction running with jojoba methyl ester by exhaust gas recirculation. *Fuel* 88:1357–1364

19. Selim MYE, Radwan MS, Elfeky SM (2003) Combustion of jojoba methyl ester in an indirect injection diesel engine. *Renewable Energy* 28:1401–1420
20. Hamdan MO, Selim MY (2016) Performance of CI engine operating with hydrogen supplement co-combustion with jojoba methyl ester. *Int J Hydrogen Energy* 41(24):10255–10264
21. Radwan MS, Ismail MA, Elfeky SMS, Abu-Elyazeed OSM (2007) Jojoba methyl ester as a diesel fuel substitute: preparation and characterization. *Appl Thermal Eng* 27(2–3):314–322
22. Shah M, Ali S, Tariq M, Khalid N, Ahmad F, Khan MA (2014) Catalytic conversion of jojoba oil into biodiesel by organotin catalysts, spectroscopic and chromatographic characterization. *Fuel* 118:392–397
23. Al Awad AS, Selim MY, Zeibak AF, Moussa R (2014) Jojoba ethyl ester production and properties of ethanol blends. *Fuel* 124:73–75
24. El-Boulifi N, Sánchez M, Martínez M, Aracil J (2015) Fatty acid alkyl esters and monounsaturated alcohols production from jojoba oil using short-chain alcohols for biorefinery concepts. *Industrial Crops Products* 69:244–250
25. Gorski K, Smigins R (2014) Impact of ether/ethanol and biodiesel blends on combustion process of compression ignition engine. *Energy* 72:760–771
26. Banapurmath NR, Khandal SV, Swamy RL, Chandrashekar TK (2015) Alcohol (ethanol and diethyl ethyl ether)-diesel blended fuels for diesel engine applications-a feasible solution. *Adv Automobile Eng* 4(1):1
27. Shahir SA, Masjuki HH, Kalam MA, Imran A, Ashraful AM (2015) Performance and emission assessment of diesel-biodiesel-ethanol/bioethanol blend as a fuel in diesel engines: a review. *Renew Sustain Energy Rev* 48:62–78
28. Cheenkachorn K, Fungtammasan B (2009) Biodiesel as an additive for diesohol. *Int J Green Energy* 6:57–72
29. Randazzo ML, Sodré JR (2011) Exhaust emissions from a diesel powered vehicle fuelled by soybean biodiesel blends (B3–B20) with ethanol as an additive (B20E2–B20E5). *Fuel* 90(1):98–103
30. He BQ, Shuai SJ, Wang JX, He H (2003) The effect of ethanol blended diesel fuels on emissions from a diesel engine. *Atmospheric Environment* 37:4965–4971
31. Hossain ABMS, Mekheld MA (2010) Biodiesel fuel production from waste canola cooking oil as sustainable energy and environmental recycling process. *Aust J Crop Sci* 4(7):543–549
32. Prakash R, Singh RK, Murugan S (2013) Experimental investigation on a diesel engine fueled with bio-oil derived from waste wood-biodiesel emulsions. *Energy* 55:610–618
33. Qi DH, Chen H, Geng LM, Bian YZ (2011) Effect of diethyl ether and ethanol additives on the combustion and emission characteristics of biodiesel-diesel blended fuel engine. *Renew Energy* 36:1252–1258
34. Ajav EA, Singh B, Bhattacharya TK (1998) Performance of a stationary diesel engine using vapourized ethanol as supplementary fuel. *Biomass Bioenergy* 15(6):493–502

Solar Distiller Unit Loaded with Nanofluid—A Short Review



Dharamveer, Samsher, Desh Bandhu Singh, Ashok Kumar Singh and Navneet Kumar

Abstract The contemporary issue of potable water shortage can be addressed by providing fresh water from a solar distiller unit, which solely works on solar energy. This method of solar water desalination is the most economical and user friendly. The daily yield of passive solar still varies from 1 to 3 kg/m² and the issue of low potable water production of passive solar still can be overcome by active solar still. The daily yield of active solar still varies from 4 to 15 kg/m². The production of potable water for active solar still can further be improved by using nanofluid. In recent years, the use of nanofluid in solar desalination unit has become popular due to enhanced thermophysical characteristic of nanofluid as compared to the base fluid such as water, oil, etc. The use of nanofluid in active solar still reduces the pumping power requirement due to reduced viscosity. The production of potable water for solar still has been found to increase if nanofluid is used due to improved thermal conductivity and absorptivity of nanofluid. In this work, nanofluid-loaded solar desalination units have been reviewed and the future scope has been presented.

Keywords Nanofluid · Solar still · Potable water production

1 Introduction

In view of higher demand of fresh water in the industrial and domestic application, it is quite obvious to find out better options of potable water production which will be economical, self-sustainable and efficient and solar distiller unit possesses all conditions up to certain level. Solar distiller unit uses abundantly available solar energy but to improve its efficiency and productivity some other embryonic fluids needs to be used like nanofluids. The current review highlights the application and

Dharamveer · Samsher
Department of Mechanical Engineering, Delhi Technological University, Delhi, India

D. B. Singh · A. K. Singh (✉) · N. Kumar
Mechanical Engineering Department, Galgotias College of Engineering and Technology,
Greater Noida 201306, UP, India
e-mail: agashok26@gmail.com

performance of nanofluids in solar distiller units for potable water production along with future scope recommendations.

Many researchers are continuously utilizing the nanotechnology (nanoparticles, nanopowder, nanotubes, nanocatalysts, nanoabsorbents, etc.) in a theoretical and practical way for desalting water. As nanofluids have extraordinary thermodynamic properties, they are treated as next-generation fluids. Nanofluid properties are further improved by tailoring the shape and size against the base fluid. In this way, the system can work more efficiently by providing precise nanofluid in appropriate proportion. Many researchers have done studies and experimental validation for optical properties, thermophysical properties of water-based TiO_2 nanofluid, experimented on flat plate collectors, reviewed for thermophysical properties, heat transfer coefficients, etc. [1–5]. Also, various works have been done by many researchers on the performance of various solar distiller units like investigation of convective heat transfer of water-based Al_2O_3 nanofluids, effect of temperature and concentration of nanofluids, heat transfer through heat exchanger using nanofluids, entropy generation, effect of tube roughness and nanoparticle size, etc. [6–9].

2 Solar Distiller Unit

Solar distiller unit is one of the simplest, environment-friendly, economic and self-sustainable system for producing water distillate using solar energy. It is broadly classified into two types as active and passive solar distiller unit and both can utilize nanofluids for enhancing its productivity, efficiency, exergoeconomic parameter, enviro-economic parameter, and energy metrics.

3 Nanofluid

Nanofluids are the next-generation fluid, which has extraordinary thermophysical and optical properties. Choi [10] coined the name nanofluid for the first time. Nanofluid is formed by the uniform mixture of 1–100 nm sized nanoparticles to liquid. In the case of water-based nanofluid, nanoparticles are mixed with water.

4 Solar Distiller Unit Loaded with Nanofluids

Sahota and Tiwari [11] investigated active double-slope solar still having N-photovoltaic thermal module- flat plate collectors (N-PVT-FPC) with nanofluids (water-based CuO , Al_2O_3 , and TiO_2) with and without a heat exchanger. Figure 1 represents the schematic diagram of active double-slope solar still having N-PVT-FPC with nanofluids and without a heat exchanger. It has been found that solar

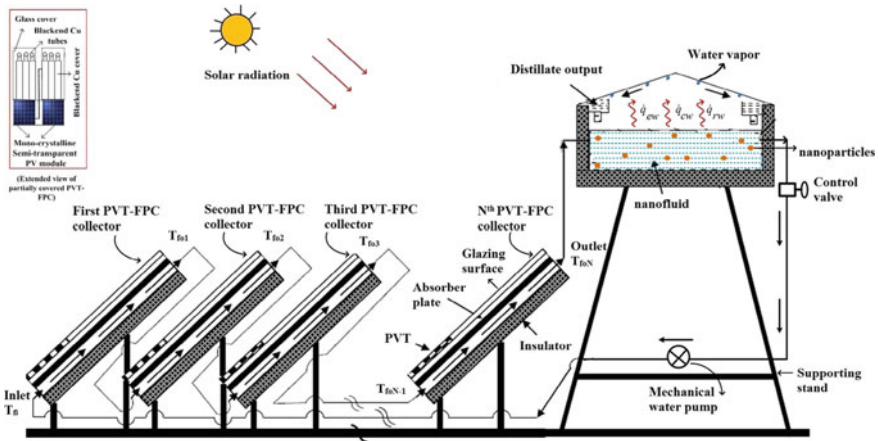


Fig. 1 Schematic diagram of active double slope still having N-PVT-FPC with nanofluids without heat exchanger [11]

still with heat exchanger and CuO–water-based nanofluids perform best among all combinations with daily productivity of 5.97 kg/m^2 .

Kabeel et al. [12] performed an experiment on passive single slope solar still having black paint inside the basin and nanofluids (water-based CuO). Nanofluid was utilized up to 40% and corresponding result of performance was improved by 25% that means distillate output found 4.25 and 3.65 kg/m^2 for 40% concentration of nanofluid with and without black paint inside the solar still basin because black paint increases the overall solar heat gain inside the still basin and increases temperature difference which causes to lead more evaporation.

Sahota and Tiwari [13] presented a study for passive double-slope solar still with nanofluids (water-based CuO, Al_2O_3 , and TiO_2) as shown in Fig. 2 and revealed the analytical expression for the characteristic equation. This theoretical model shows better performance with the combination of water-based Al_2O_3 of 50.34% maximum efficiency.

Kabeel et al. [14] experimented on active single slope solar still with water-based nanofluid (water-based Al_2O_3) associated with an external condenser as shown in Fig. 3. Result found 53.2% increment in distillate output with nanofluids only but 116% increment showed in distillate output with external condenser association because of the more condensing area and better condensation process which result in more distillate production.

Sharshir [15] performed an experiment with different combination of film cooling flow rates to single basin solar still associated with graphite and CuO micro-flakes nanoparticles as shown in Fig. 4. The result was found with better performance as 57.60% improved productivity with the appropriate variation in nanofluid concentration and film cooling low rate and efficiency was improved up to 49% as thin film cooling causes better condensation inside the still basin. Rashidi et al. [16] performed

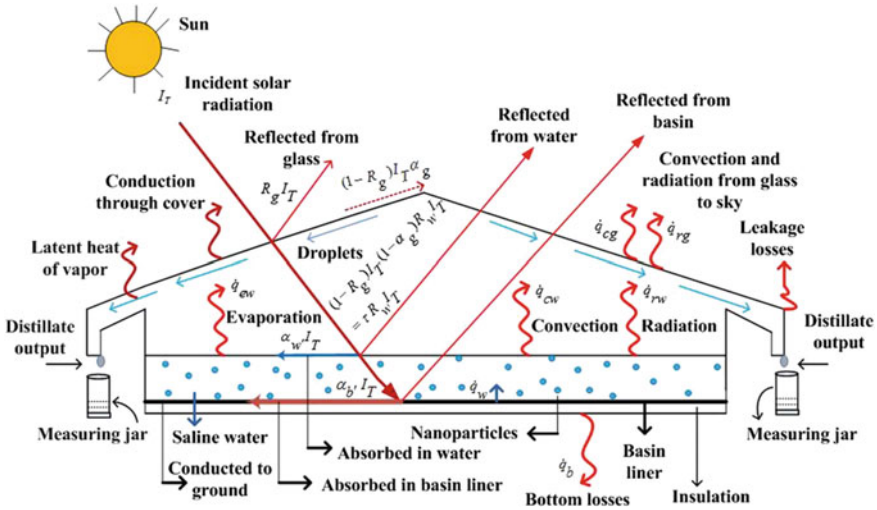


Fig. 2 Schematic view of passive double-slope solar still with nanofluids [13]

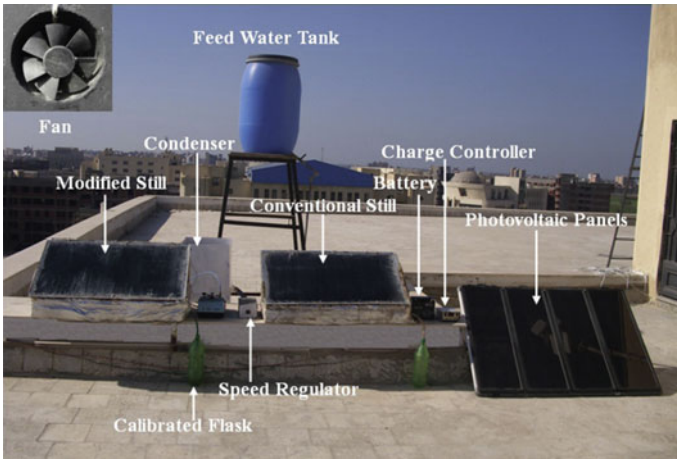


Fig. 3 Photographic image of active single-slope solar still with nanofluid and external condenser [14]

a sensitivity analysis on a single basin single slope stepped solar still with nanofluids as shown in Fig. 5 and optimized the dimensions of steps and concentration ratio of nanofluids (0–5%) ultimately results increased by 22% in hourly distillate production rate as stepped basin maintains the minimum basin water depth which leads better solar radiation absorption and causes more evaporation so more chance to condensation. The maximum rate of distillate output was 0.293 kg/m²/day.

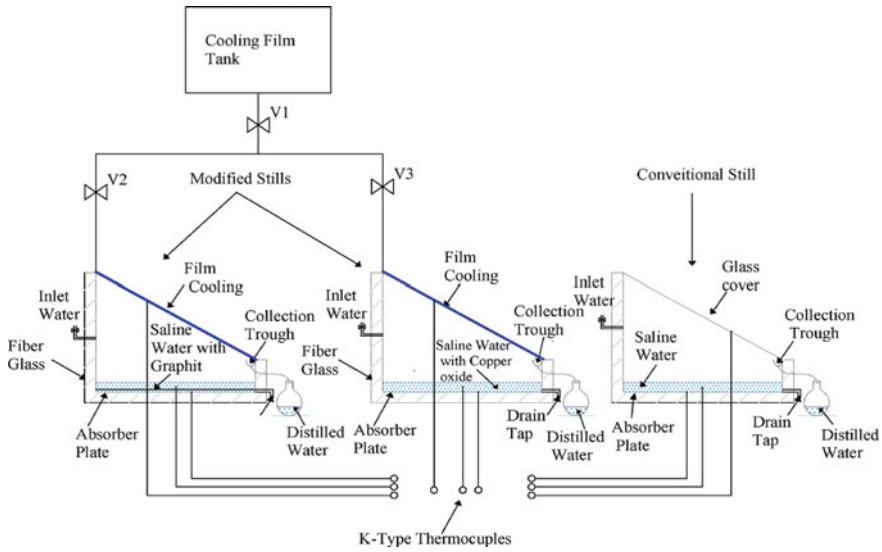


Fig. 4 Schematic diagram of the film-cooled single-slope solar still with nanofluid (graphite and CuO micro-flakes) [15]

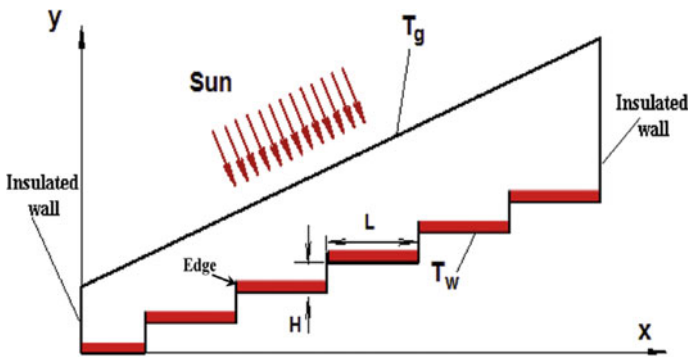


Fig. 5 Schematic view of the stepped solar still [16]

Elango et al. [17] presented a comparative study of single slope solar still with and without nanofluids (water-based Al_2O_3 , ZnO , Fe_2O_3 , and SnO_2) at varying concentration ratio and result found 29.95% maximum production for Al_2O_3 nanofluid combination because of the best possible concentration ratio of nanofluid which maintains the better working environment into the basin medium and nanoparticles utilizes its full potential while receiving and releasing solar radiation.

Kabeel et al. [18] presented a modified version of single basin solar still having nanofluids (water-based CuO and Al_2O_3) with external condenser by utilizing vacuum and low presser fan. The result was found by 46.23% of daily efficiency with

the possible modifications, whereas conventional still showed 34% daily efficiency only. The maximum distillate output was found 2.88 kg/m²/day with modified solar distiller unit. Related reviews with different types of solar distillation systems have also been presented by other researchers [19–21].

5 Conclusions

In the present study, a short review has been made over active and passive solar distiller units associated with nanofluids and found the following conclusions:

The overall performance of solar distiller units along with nanofluids always found higher than conventional solar distillation systems.

Active double solar distillation system with nanofluid (CuO) and heat exchanger performs better than active single slope solar distillation systems with the external condenser.

Internal paint color affects solar heat absorption and ultimately improves the solar still performance.

Film cooling is always better than flood cooling, in this way single slope solar still with film cooling shows a better result than conventional still.

As a variety of results has been appeared for the different combinations of solar distiller units so it is difficult to identify best and economical solar still because of variations in manufacturing processes, materials, and nanofluids.

References

1. Taylor RA, Phelan PE, Otanicar TE, Adrian R, Prasher R (2011) Nanofluid optical property characterization: towards efficient direct absorption solar collectors. *Nanoscale Res Lett* 6:225
2. Colangelo G, Favale E, Miglietta P, de-Risi A, Laforgia D (2013) A new solution for reduced sedimentation flat panel solar thermal collector using nanofluids. *Appl Energy* 111:80–93
3. Said Z, Saidur R, Hepbasli A, Rahim NA (2014) New thermo-physical properties of waterbased TiO₂ nanofluid-the hysteresis phenomenon revisited. *Int Commun Heat Mass Transf* 58:85–95
4. Solangi KH, Kazi SN, Luhur MR, Badarudin A, Amiri A, Sadri R, Zubir MNM, Gharehkhani S, Teng KH (2015) A comprehensive review of thermo-physical properties and convective heat transfer to nanofluids. *Energy* 89:1065–1086
5. Hussien AA, Abdullah MZ, Al-Nimr MA (2016) Single-phase heat transfer enhancement in micro/minichannels using nanofluids: theory and applications. *Appl Energy* 164:733–755
6. Heris SZ, Esfahany MN, Etemad SG (2007) Experimental investigation of convective heat transfer of Al₂O₃-water nanofluid in circular tube. *Int J Heat Fluid Flow* 28:203–210
7. Vajjha RS, Das DK (2012) A review and analysis on influence of temperature and concentration of nanofluids on thermophysical properties, heat transfer and pumping power. *Int J Heat Mass Transf* 55:4063–4078
8. Albadr J, Tayal S, Alasadi M (2013) Heat transfer through heat exchanger using Al₂O₃ nanofluid at different concentrations. *Case Stud Thermal Eng* 1:38–44
9. Mahian O, Kianifar A, Sahin AZ, Wongwises S (2014) Entropy generation during Al₂O₃-water nanofluid flow in a solar collector: effects of tube roughness, NP size, and different thermophysical models. *Int J Heat Mass Transf* 78:64–75

10. Choi SUS (1995) Enhancing thermal conductivity of fluids with nanoparticles. *ASME Publ.-Fed* 23, pp 99–106
11. Sahota L, Tiwari GN (2017) Analytical characteristic equation of nanofluid loaded active double slope solar still coupled with helically coiled heat exchanger. *Energy Convers Manage* 135:308–326
12. Kabeel AE, Omara ZM, Essa FA, Abdullah AS, Arunkumar T (2017) Augmentation of a solar still distillate yield via absorber plate coated with black nanoparticles. *Alexandria Eng J*
13. Sahota L, Tiwari GN (2016) Effect of nanofluids on the performance of passive double slope solar still: a comparative study using characteristic curve. *Desalination* 388:9–21
14. Kabeel AE, Omara ZM, Essa FA (2014) Enhancement of modified solar still integrated with external condenser using nanofluids: an experimental approach. *Energy Convers Manage* 78:493–498
15. Sharshir SW (2017) Enhancing the solar still performance using nanofluids and glass cover cooling: experimental study. *Appl Therm Eng* 113:684–693
16. Rashidi S, Bovand M, Rahbar N, Abolfazli J (2018) Steps optimization and productivity enhancement in a nano fluid cascade solar still. *Renew Energy* 118:536–545
17. Elango T, Kannan A, Murugavel KK (2015) Performance study on single basin single slope solar still with different water nanofluids. *Desalination* 360:45–51
18. Kabeel AE, Omara ZM, Essa FA (2017) Theoretical and experimental validation of modified solar still using nanofluids and external condenser. *J. Taiwan Inst Chem Eng* 0:1–10
19. Singh AK, Chattopadhyaya S, Singh DB, Kumar N (2017) Performance study for active solar stills based on energy metrics: a short review. *J Refrig Air Cond Heating Vent* 4(3):21–26
20. Singh AK, Singh DB, Mallick A, Kumar N (2018) Energy matrices and efficiency analyses of solar distiller units: a review. *Solar Energy* 173:53–75
21. Singh DB, Singh AK, Kumar N, Dwivedi VK, Yadav JK, Singh G (2019) Performance analysis of special design single basin passive solar distillation systems: a comprehensive review. https://doi.org/10.1007/978-981-13-6469-3_27

Computational Investigation of Various Transition Stages in the Drop Formation Process



Bishnoi Pardeep and M. K. Sinha

Abstract The aim of this paper to study the various transition stages of drop formation with the help of computational techniques. These regimes are being observed by varying capillary tube dimension and flow velocity. Two different drop formation mechanisms are famed: Either the drops are formed close to the capillary tip—dripping—or they break up from an extended liquid jet—jetting. Dripping faucet regime develops during the transition of the periodic regime to the jetting regime. We use glycerin as disperse phase liquid. We found that for low Weber number, the periodic dripping regimes are obtained whereas, for the high Weber number, jetting regimes are developed. We also study the variation in thread length and size of the breakoff drops and found that the variation of the thread length and the drop's size in periodic dripping is nearly constant while these properties change in dripping faucet regime as well as in jetting regimes.

Keywords Transition stages · Drop formation · Periodic dripping · Dripping faucet · Jetting regimes · Volume of fluid

1 Introduction

Study of Drop generation process has been carried out for more than a century now. The phenomenon of drop formation from a nozzle is a very complex process. The development of drop fascinates a lot of researchers due to its wide applications. It has applications in multiple domains like ink-jet technologies, spray painting, distillation, and mixing processes. In all these domains, drops of precise sizes are very needful. Understanding the various factors contributing to the breakup of the pendant drop is of major importance since it will allow control of those parameters to attain the desired goals. The transition stage of dripping to jetting has fundamental in industrial applications that involve droplets. Recently some novel systems having

B. Pardeep (✉) · M. K. Sinha
Department of Mechanical Engineering, NIT Jamshedpur, Jamshedpur, India
e-mail: pardeepbishnoi@yahoo.in

© Springer Nature Singapore Pte Ltd. 2019
M. Kumar et al. (eds.), *Advances in Interdisciplinary Engineering*, Lecture Notes in Mechanical Engineering, https://doi.org/10.1007/978-981-13-6577-5_25

249

low interfacial tension are used to generate droplets and have a great application in making biocompatible droplets [1–3].

Research is being carried out all over the world to study the formation of drops from a capillary tube experimentally and computationally. In case of drop formation through the capillary tube, three regimes are detected. To observe these different regimes, the velocity of the fluid at the tube inlet plays a vital role. For low velocity or we can also say that, for low flow rates, the periodic dripping regimes are observed in which drops are formed at a regular interval of time and of the same size in every drop. When we increase flow rate slightly, the drops developed have different diameters and are somewhat periodically developed and this regime of drop formation is the dripping faucet. Clanet and Lasheras [4] investigate the development of the three regimes both experimentally and computationally by varying the Weber number. They performed a number of experiments on the capillary tube of different diameters and increase the flow rate gradually until the different regimes were seen.

In dripping regime, the formation of satellite droplet is also observed. Basically, the satellite droplet is a very small size drop as compared to the primary drop. Notz et al. [5] investigated the shape of the satellite droplet by performing certain experiments using ultra-high-speed digital imaging technique. They studied the complex shape and advancement of the liquid thread linking the main drop to the liquid source and its disintegration in the satellite droplets under the effect of capillary forces. Henderson et al. [6] observed the breakup of the liquid ligament near its end and at interior points. After the primary drop's break off, due to some unbalanced forces, undulation developed in the liquid ligament, which was further responsible for generating the secondary droplets. The location of the secondary breakup depends on the most unstable wave for if the wavelength of the most unstable wave is shorter than the length of the ligament, it breaks up at interior points; otherwise, it pinches off near its ends. The same type of instability that affects the liquid thread is the same that disturbs the uniform liquid jet, as in the case studied by Rayleigh [7]. Savart [8] examined that the breakup of a jet is not controlled by the gravity forces, but it was generally due to the growth of undulations in the liquid column. Later, Plateau [9] revealed that surface tension is responsible for the development of undulations in the liquid threads. He also, developed an empirical relation, according to which the jet of water falling vertically will break off into droplets if its thread length is greater than about 3.13 times its diameter. Rayleigh [7] confirms the results of Plateau. For the experimental analysis of the drop formation, the setup must be accurate; the image captured from the high-speed camera must be on time. So, this type of analysis is quite difficult to undertake. In the Numerical analysis, the Navier–Stokes equation and Continuity equation are solved by implementing the boundary conditions. Zhang [10] used RIPPLE to simulate the mechanism of drop formation and study the effect of inertial, viscous, and gravitational forces. His conclusions agreed with the experiment results. Pardeep et al. [11] also validate the results obtained through the computation with the experimental results of Wilkes et al. [12]. Much research has

been done on the topic of drop formation from a capillary tube; some of those readings focused on the pendant drop in the periodic dripping regime while others focused on the formation of drop from a continuous long jet. Till date, dripping faucet regime is not studied thoroughly. Subramani et al. [13] were one of the few researchers who studied the dripping faucet regime and explained the mechanism of drop formation in that regime. Mak et al. [14] investigate the dripping to transition for low interfacial tension aqueous solution. The low jet velocity at the dripping-to-jetting transition represents an exceptionally small inertial force, and hence a relatively important viscous force for aqueous two-phase systems with low interfacial tension ($g < 1 \text{ mN m}^{-1}$). The dripping-to-jetting transition is more properly characterized by the force balance between the interfacial force and the sum of downstream forces that does not neglect the viscous effect of the jet phase. Nunes et al. [15] reviewed extensively about the dripping and jetting regimes in microfluidic multiphase flows. The observation is summarized for three main geometries, i.e., coaxial, flow focusing, and T -junction.

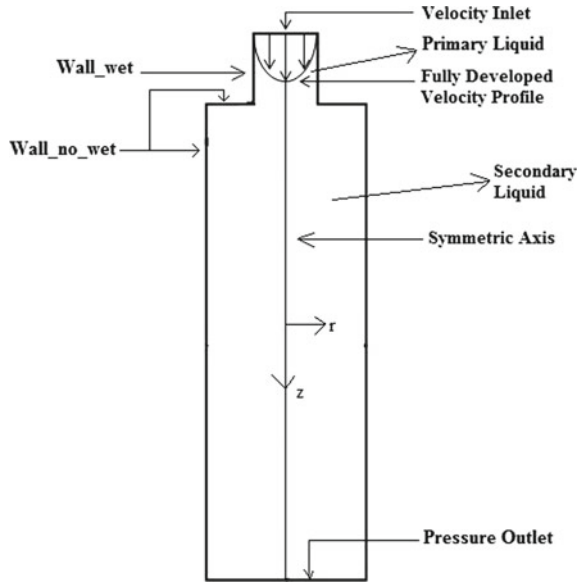
The focus of this article is to determine the various transition stages that occur in the development process of the drop from a capillary tube. Most researches deal with the breakup mechanism in either the dripping or jetting mode, but few have covered in great details on the full range of drop formation from dripping to jetting, and even fewer have acknowledged the chaotic behavior during the transition from the dripping regime to the jetting regime.

2 Computational Analysis of Drop Formation

2.1 Computational Domain with Boundary Conditions

The computational domain represents a basic form of the physical domain showing both the geometrical representation and imposed boundary conditions. The computational domain as shown in Fig. 1 consists of two regions. The upper zone consists of primary liquid, whereas the lower zone consists of air as a secondary liquid. The surface of the capillary tube is considered as a wettable zone, whereas the surface surrounding the capillary orifice is considered as non-wettable zone. To investigate the dynamics, process of the drop development, we use the “Volume of Fluid” method in computational process. At the initial time, $t = 0 \text{ s}$, primary liquid fills the capillary tube zone, whereas air captures the remaining zone. Initially, both fluids are considered at rest. To initiate the ejection process, a User-Defined Function (UDF) is attached with the initial boundary conditions. The liquid moves as a fully developed profile in the capillary tube and gravity forces also act towards z -direction as shown in Fig. 1.

Fig. 1 Computational domain model



2.2 Mathematical Modeling

In free surface flow analysis, the dynamics of drop formation depends upon a lot of factors, which include flow rate, viscosity, and density of the liquid. Following are the assumptions on which the governing Equations are developed.

- The fluid flows are laminar and Newtonian.
- The model is axisymmetric.
- The surrounding air can be considered as incompressible.
- The liquid properties are known and constant.
- The evaporation of the liquid is neglected.
- At the inlet of the capillary tube, fluid flow is assumed to be fully developed flow.
- The thickness of the nozzle is neglected.

After applying the assumptions, Navier–Stokes Equation in nondimensional form for the liquid’s transient motion is given as:

$$\nabla \cdot \mathbf{v} = 0, \tag{1}$$

$$Re \left(\frac{\partial \mathbf{v}}{\partial t} + \mathbf{v} \cdot \nabla \mathbf{v} \right) = \nabla \cdot \boldsymbol{\tau} + \left(\frac{G}{Ca} \right) \mathbf{j} \tag{2}$$

$$\boldsymbol{\tau} = -p\mathbf{I} + [\nabla \mathbf{v} + (\nabla \mathbf{v})^T] \tag{3}$$

The variables in Eq. (1) are ∇ as the gradient operator and \mathbf{v} as the resultant velocity vector. Similarly, in Eq. (2), $\boldsymbol{\tau}$ is the stress tensor; \mathbf{j} is the unit vector in the

z -direction. In Eq. (3), p represents the dimensionless pressure and \mathbf{I} is the identity tensor.

Also, during the nondimensionalization process, three dimensionless numbers are introduced in Eq. (2),

Reynolds number, $Re = \rho UD/\mu$,

Gravitational Bond number, $G = \rho g R^2/\sigma$,

Capillary number, $Ca = \mu U/\sigma$,

Since the flow is considered as fully developed, its velocity profile can be written as,

$$v_z = \frac{2Q}{\pi R^2} \left\{ 1 - \left(\frac{r}{R} \right)^2 \right\}, 0 \leq r \leq R \quad (4)$$

where r is the radial coordinate of drop phase and v_z is the flow velocity in z -direction.

The maximum velocity of liquid phase flow for the fully developed flow is given as

$$U = \frac{2Q}{\pi R^2} \quad (5)$$

Tracking of the interface between the two phases (i.e., p th and q th phases) is done by solving the mass conservation Equation. The mass conservation Equation is given as follows for the q th fluid:

$$\frac{1}{\rho_q} \left[\frac{\partial}{\partial t} (\alpha_q \rho_q) + \nabla \cdot (\alpha_q \rho_q \vec{v}_q) \right] = S_{\alpha_q} + \sum_{p=1}^n (\dot{m}_{pq} - \dot{m}_{qp}) \quad (6)$$

where, \dot{m}_{pq} the mass transfer from phase p to phase q is, \dot{m}_{qp} is the mass transfer from phase q to phase p . Generally, the source term, S_{α_q} on the right-hand side is zero. Only the volume fraction for the secondary phase fluid is solved. And the volume fraction of the primary phase fluid can be calculated by the following Equation:

$$\sum_{p=1}^n \alpha_q = 1 \quad (7)$$

The boundary conditions for the solution of Eqs. (1) and (2) which are also shown in Fig. 1 stated as

- Inlet of the domain is velocity inlet.
- Axis is considered as an axisymmetric axis.
- Free slip velocity condition near the wall because the fluid near the wall is air.
- Outlet of the computational domain is atmospheric pressure outlet.

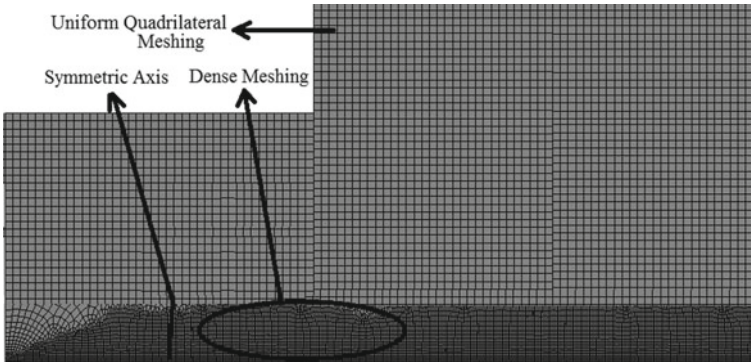


Fig. 2 Meshing of the computational domain

2.3 Grid Generation

Meshing plays an important role in finding the numerical solutions of the physical problem through computational methods. For precise results, grid size should be small, or one can say that the number of the cells must be more. This improves the accuracy of drop generation and its transport profile. Meshed cells are quadrilateral in shape and a total of 100,000 meshing cells are used for the computation process. The meshed geometry is shown in Fig. 2. Quadrilateral meshing is done throughout the computational domain.

3 Result and Discussion

In the present study, the focus was not on the jetting regime with very high velocity, and because of the limit on the length of the computational domain, the formation of drops very far from the tip of the nozzle was not studied. One objective of this study is to observe the drop formation in the different regimes; this goal was reached by running the cases and providing qualitative and quantitative descriptions. To generate the different regimes, the inlet velocity is gradually increased until the limits between the regimes are reached. The velocity limit is dependent on the nozzle diameter. The working fluid used in the present study is glycerin at 20 °C and its physical properties are as follows:

Dynamics Viscosity (μ) : 6.1×10^{-3} kg/ms

Density (ρ) : 1272 kg/m³

Surface tension Coefficient (σ) : 0.07 N/m

The computational analysis is done with four different diameters of the nozzle, along with a gradual increase in flow rate for each case. Table 1 shows the summary of the complete transition process, extracted from the computational simulation. For each set of analysis, the diameter of the capillary nozzle and the velocity is increased gradually. Due to these variations, we initially deal with the periodic dripping, then the dripping faucet, and finally the jetting regimes develop.

The Weber Number is a dimensionless value useful for analyzing fluid flows where there is an interface between two different fluids. The Weber Number is the ratio between the inertial force and the surface tension force and it indicates whether the kinetic or the surface tension energy is dominant. It can be expressed as

$$We = \rho v^2 D / \sigma, \quad (8)$$

where ρ is the fluid density, D is the inner diameter of the tube, v is the fluid velocity, and σ is the fluid surface tension.

The first regime has developed at the lowest velocity and is known as periodic dripping. The Weber number for these periodic dripping regimes is low. The various stages of drop formation in the periodic regime are shown in Fig. 3. In this regime, the drop develops by the steady flow of fluid through the capillary nozzle. Also, the drop is under quasi-equilibrium. When this equilibrium is lost, the detachment of the drop starts from the main region of the liquid. The primary droplet detaches from the liquid ligament (Neck). After the detachment of primary droplet, there is recoil movement in the neck or the liquid ligament. In this regime, Viscous and surface forces dominate over the recoil force. Due to this reason, the thread length of the successive drops is to be the same. Also, in the Periodic dripping regime, the phenomenon of satellite drop formation does not exist. The formation of satellite drops is closely related to the velocity. When the inlet velocity of the fluid in the nozzle increases, more fluid comes into the necking region connecting the pendant mass to the main part. As a result, the neck is thicker and does not break into satellite drops. The liquid drops of same sizes are produced during the periodic regimes, also, break off at the regular interval of time at the same detachment location.

The second regime which develops at slightly higher velocity is known as a dripping faucet. In general, in this regime, the secondary (small) droplet follows a primary droplet. The Weber number for this case is more than that of periodic dripping. Figure 4 shows the transition stage of the dripping faucet regime. A dripping faucet regime is the changeover state between the dripping and jetting regimes. With the increase in the Weber number, the periodic dripping regimes shift into the dripping faucet regime. The thread length for the successive drop is always more than its antecedent drop. In dripping faucet regimes, the growth of two periodic necking (162 ms in Fig. 4) and three periodic necking (229.5 ms in Fig. 4) develops. Due to the undulation created by initial drop, the liquid ligament having two necking period breaks into two different drops at the same instant of time. In this regime, multiple bifurcations may occur. In this regime, successive drops have different sizes, but it depends on the number of periods, there is a repetition of the drop sizes. Consider

Table 1 Summary of various transitions stage during drop formation

Diameter	Weber no.	Thread length (mm)			Volume of drop (mm ³)			Regimes
		L1	L2	L3	V1	V2	V3	
<i>Case 1</i>								
1.27	2.83	7.45	6.89	7.38	20.87	11.77	14.42	Periodic dripping (no satellite drops)
1.27	3.88	7.88	10.14	11.3	20.58	17.81	14.77	Periodic dripping (satellite drop)
1.27	4.27	13.03	13.03	15.14	12.55	10.04	8.87	Periodic Dripping (satellite drop)
1.27	4.67	7.313	6.47	6.12	24.72	15.72	15.57	Periodic Dripping (no satellite drops)
<i>Case 2</i>								
1.65	1.86	5.97	5.97	5.84	28.6	30.8	28.19	Periodic Dripping (no satellite drops)
1.65	2.7	10.31	7.28	8.52	30.87	18.92	33.31	Periodic Dripping (no satellite drops)
1.65	3.07	10.92	7.62	11.75	31.54	17.91	30.92	Dripping (no satellite drops)
1.65	3.466	10.98	7.97	14.5	33.21	17.45	31.3	Dripping Faucet (multiple drop sizes)
1.65	3.886	10.57	8.39	16.29	33.35	16.78	31.3	Jetting
<i>Case 3</i>								
2.11	0.862	7.03	6.64	6.70	43.22	42.82	39.41	Periodic dripping (no satellite drops)
2.11	2.39	6.92	7.19	7.26	47.28	22.76	28.69	Periodic dripping (no satellite drops)
2.11	2.79	6.98	7.36	8.94	36.09	21.09	23.7	Periodic dripping (no satellite drops)
2.11	3.68	9.078	9.67	17.51	29.28	19.9	40.26	Dripping faucet (multiple drop sizes)
2.11	4.43	8.616	11.05	19.76	29	23.7	50.51	Jetting (no pattern, detachment point moves downwards)

(continued)

Table 1 (continued)

Diameter	Weber no.	Thread length (mm)			Volume of drop (mm ³)			Regimes
		L1	L2	L3	V1	V2	V3	
<i>Case 4</i>								
2.77	0.32	8.47	8.73	9.219	40.24	59.73	59.66	Periodic dripping (no satellite drops)
2.77	1.132	9.426	7.972	8.041	54.71	33.91	41.51	Periodic dripping (satellite drop)
2.77	2.01	9.47	9.36	17.11	59.51	33.95	38.64	Dripping faucet (multiple drop sizes)
2.77	2.89	9.66	14.90	12.90	59.73	34.6	41.46	Dripping faucet (three periods)
2.77	3.67	10.33	19.40	16.07	54.78	65.21	54.78	Jetting (no pattern, detachment point moves downward)

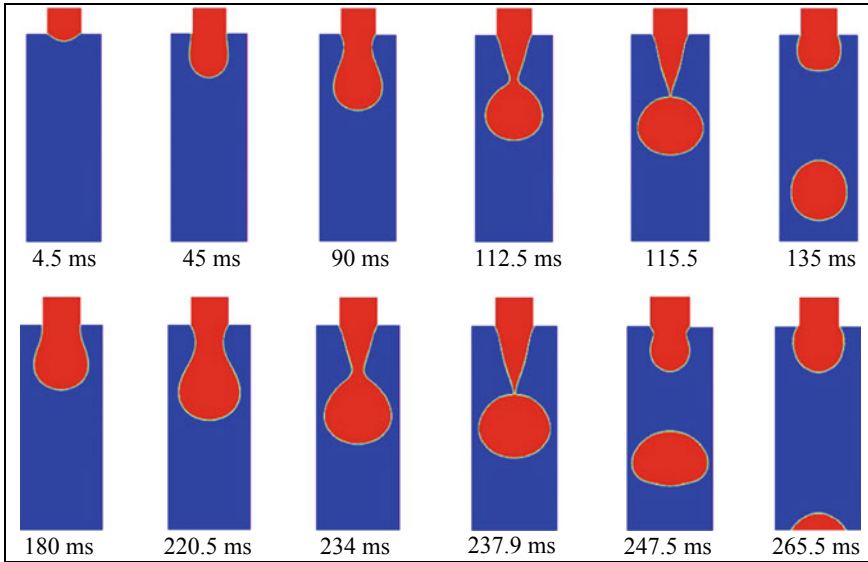


Fig. 3 Evolution of a pendant drop from a capillary tube of diameter of $D = 2.77$ mm for $We = 0.32$ (periodic dripping regime)

a case of drop formation at a particular velocity, the dripping faucet has the double periodic bifurcation, which means the first and the third drops have the same size. We can also notice that the dripping faucet is not periodic in time while the periodic dripping has periodic nature in detachment time as well as droplet's size. Also, due to undulation, development of satellite drops happens in this regime (243 ms in Fig. 4). The generation of satellite drop depends on the thread length of the ligament produced which generally occurs in the dripping faucet regimes and in jetting regimes. Also, just after the drop formation, the upper surface of the drop flattens (at 243 ms in Fig. 4), the inertial forces are the main reason behind this. The instant when the drop breaks, the inertial force dominates over the all other forces, i.e., viscous forces, surface forces. The upper surface of the drop has more inertia as compared to the lower part because of the development of recoil forces after the drops detachment, so it compresses the drop and makes its surface flattens.

The last regime which develops during the drop formation is jetting. In jetting regime, the flow rate of the liquid that flows through the capillary is high as compared to the other regimes. Also, the position of the detachment point continuously moves away from the nozzle and at last a long liquid column forms as shown in Fig. 5. Because of the high flow rates in the jetting regime, there is not wetting boundary condition and the exterior diameter of the tube is no longer the governing geometrical parameter. The mechanics of drop formation in the jetting regime is very complex. When the drops are formed close to the nozzle, the process of formation is due to the loss of equilibrium between the inertial, capillary, surface tension, and gravitational

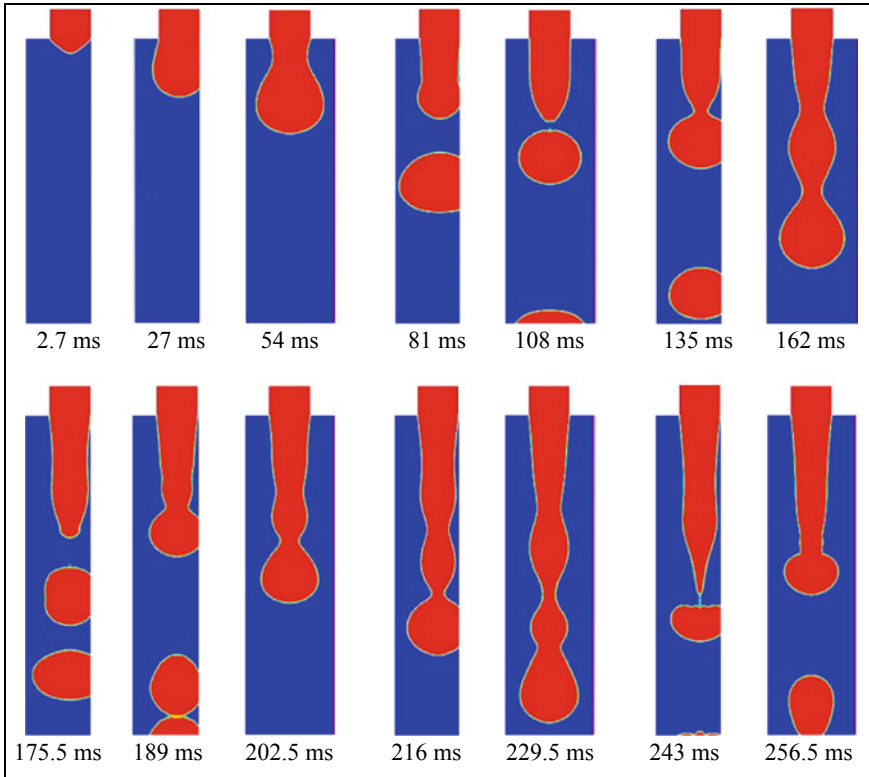


Fig. 4 Evolution of a pendant drop from a capillary tube of diameter of $D = 2.77$ mm for $We = 2.01$ (dripping faucet regime)

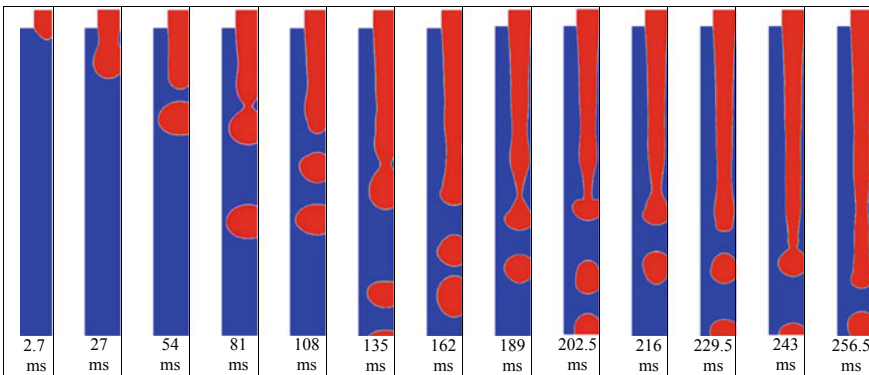


Fig. 5 Evolution of a pendant drop from a capillary tube of diameter of $D = 2.77$ mm for $We = 3.67$ (jetting regime)

forces. When the length of the liquid column is long, the drops are formed due to the Plateau–Rayleigh instability [16]. The Plateau–Rayleigh instability explains why a column of liquid decomposes into drops after it reaches a certain length.

4 Conclusions

In this study, flow regimes obtained as a consequence of two immiscible fluids interacting in a capillary tube of different diameters and at different flow rates of the continuous and dispersed phases have been presented. Volume of Fluid method-based simulation is used for perceiving the variations of the transition stages that develop during the drop formation. Weber number is used to differentiate the transition stages from dripping-to-jetting regimes. For example, at $We = 0.32$, this leads to the periodic dripping regimes. In this regime, the position of the thread length for the successive drops are always same. Also, the volume of the successive drops is nearly equivalent. For $We = 2.01$, the transition from periodic dripping-to-dripping faucet regimes takes place. Now the breakoff thread length of the successive drops is more than that of the antecedent droplet. In dripping faucet regime, multiple necking regions develop. The undulations caused by the break off of the antecedent drops help in the break up of the successive drops. For $We = 3.67$, drops are molded from a stretched liquid column and the detachment point of the drop is much away from the nozzle tip or close to the exit point. When the detachment position is far from the nozzle tip, the drops are mostly formed by the growth of perturbations or the action of the Plateau–Rayleigh instability.

References

1. Ziemecka I, Van Steijn V, Koper GJM, Kreutzer MT, Van Esch JH (2011) All-aqueous core-shell droplets produced in a microfluidic device. *Soft Matter* 7:9878–9880
2. Geschiere SD, Ziemecka I, Van Steijn V, Koper GJM, Van Esch JH, Kreutzer MT (2012) Slow growth of the Rayleigh-Plateau instability in aqueous two-phase systems. *Biomicrofluidics* 6:022007
3. Bishnoi P, Sinha MK (2018) A new approach to determine the diabetic level in patients. *U.P.B. Sci Bull, Series D* 80(1):71–84
4. Clanet C, Lasheras JC (1999) Transition from dripping to jetting. *J Fluid Mech* 383:307–326
5. Notz PK, Chen AU, Basaran OA (2001) Satellite drops: unexpected dynamics and change of scaling during pinch-off. *Phys Fluids* 13(3):549–552
6. Henderson D, Segur H, Smolka LB, Wadati M (2000) The motion of a falling liquid filament. *Phys Fluids* 12(3):550–565
7. Rayleigh L (1899) Investigations in capillarity: the size of drops—the liberation of gas from supersaturated solutions—colliding jets—the tension of contaminated water-surfaces—a curious observation. *Phil Mag* 48:321–337
8. Savart E (1833) Memoire sur la constitution des veines liquides lancees par des orifices circulaires en mince paroi. *Ann Chim* 53:337–386
9. Plateau J (1873) *Statique Experimentale et Theorique des Liquides*. Gauthier- Villars et Cie

10. Zhang X (1999) Dynamics of growth and breakup of viscous pendant drops into air. *J Colloid Interface Sci* 212:107–122
11. Srivastava M, Sinha MK (2018) Numerical simulation of dynamics of the drop formation at a vertical capillary tube. In: Singh MK et al. (eds) *Applications of fluid dynamics*, LNME, Springer, Singapore, pp 371–381. https://doi.org/10.1007/978-981-10-5329-0_27
12. Wilkes ED, Phillips SD, Basaran OA (1999) Computational and experimental analysis of dynamics of drop formation. *Phys Fluids* 11(12):3577–3598
13. Subramani JH, Yeoh HK, Xu Q, Ambravaneswaran B, Basaran OA (2006) Simplicity and complexity in a dripping faucet. *Phys Fluids* 18:1–13
14. Mak SY, Chao Y, Shum HC (2017) The dripping-to-jetting transition in a co-axial flow of aqueous two-phase systems with low interfacial tension. *RSC Adv* 7:3287
15. Nunes JK, Tsai SSH, Wan J, Stone HA (2013) Dripping and jetting in microfluidic multiphase flows applied to particle and fiber synthesis. *J Phys D Appl Phys* 46(11):114002
16. Rayleigh L (1879) On the instability of jets. *Proc London Math Soc* 10:4–13

An Arduino Micro-controller Operated Automobile Air Conditioning System



Hiren Shah , Aftab Maniar , Kushal Tailor , Dhruv Patel 
and Harsh Patel 

Abstract This paper describes the operation of the air conditioning system of Maruti Suzuki Wagon-R car which comprises a condenser, compressor, evaporator, receiver, drier, and expansion valve. It works on VCR system with refrigerant R600A + R290. As automation is becoming the pioneer in technology, it is important to step in its vicinity. The air conditioning model is connected to the computer system through Arduino UNO circuit. Arduino is a single board micro-controller that can sense and control physical parameters. The purpose of establishing this connection is to perform the automatic turning on/off the system and to obtain the temperature readings from the sensors attached to the components of the model. These readings are then transferred to MS Excel software with the help of PLX-DAQ software, where various thermodynamic calculations are performed. From the obtained results, it is found that the theoretical value of cop is twice that of actual values of COP. Also originate that, the theoretical second law efficiency is about 36% more than its actual value.

Keywords Arduino · Relay · 18B20 temperature sensor · MS Excel · PLX-DAQ

Nomenclature

VCR	Vapor Compression Refrigeration
SMPS	Switch Mode Power Supply
A.C	Alternating Current
D.C	Direct Current
COP	Coefficient of Performance
COP_{rev}	COP of Reverse Carnot Cycle
COP_{th}	Theoretical COP
COP_{act}	Actual COP

H. Shah (✉) · A. Maniar · K. Tailor · D. Patel · H. Patel
Chhotubhai Gopalbhai Patel Institute of Technology, Uka Tarsadia University,
Gopal-Vidyanagar, Maliba Campus, Surat Gujarat 394350, India
e-mail: hiren.shah@utu.ac.in

T_e	Evaporator outlet temperature in °C
T_c	Compressor outlet temperature in °C
T_d	Condenser outlet temperature in °C
H_1	Enthalpy of after evaporator (kJ/kg)
H_2	Enthalpy of after compressor (kJ/kg)
H_4	Enthalpy of after expansion (kJ/kg)

Greek Symbols

η_m	Mechanical Efficiency of the system
η_{ad}	Actual Efficiency of the system
η_{II}	Second Law Efficiency

1 Introduction

The world is drastically changing in terms of technology. Researches and innovations have already set a new trend of substituting manual operations with automation. This is driving the world at a much greater pace. Manpower and time are being immensely conserved. Majorly computer and electronics technologies together have brought this revolution. In the midst of such growth, optimization is playing a key role in developing efficient systems. This paper describes the application of automation to an automobile air conditioning system and obtaining its performance characteristics using software. For automation, Arduino UNO microcontroller and relay are used [1]. Digital temperature sensors 18B20 are used to fetch the temperature readings from the system components [2–4]. Arduino microcontroller acts as a medium for the connectivity of the relay and the temperature sensors with the computer system [5]. The programming of Arduino UNO is done in Arduino IDE software with C++ as a coding language. Relay is used as a switch for automatic turning on/off the system. The system is programmed for automatic starting and stopping the system in prescribed sets of time intervals. This is done to obtain the temperatures for different weather conditions throughout the day. Graphs are generated in MS Excel for the performance characteristics that provide clear visibility to the variations according to the different input parameters. Thus comparing the various results, the performance characteristics of the system is obtained.

1.1 System Layout

The refrigerant R600 + R290 is used. Its properties are described in Table 1. Temperature sensors are attached at the inlet and outlet of the respective components.

Table 1 The properties of the refrigerant R600A + R290 [10]

Molecular weight (kg/Kmol)	44.10	Critical density (kg/m ³)	459
Melting point (°C)	-187.7	GWP	3
Boiling point (1 atm) (K)	231	Power consumption(W)	1355
Liquid density (kg/m ³)	1040	COP (Cooling)	5.8
Vapor pressure (bar) (at 21°C)	7.7	Mass flow rate (kg/s)	0.0658
Critical pressure (Mpa)	4.90	Pressure ratio	3.39

The compressor is driven by a motor instead of an automobile engine [6]. The motor is A.C power supply driven and condenser fan is used to blow atmospheric air to the condenser to remove the heat from the flowing high-temperature refrigerant. SMPS converts A.C supply to D.C and also reduces the voltage for the condenser fan [7, 8]. It also operates blower [9]. For the automatic turning on and off of the system, a relay is connected in the power supply line to the motor. This relay is connected to the Arduino UNO board. Also, the temperature sensors are connected to other Arduino UNO board. Further, these two boards are connected to the computer system. A schematic diagram for this is shown in Fig. 1, where T_1-T_7 is the positions of temperature sensors placed at inlet and outlet of concerned system components as shown in Fig. 2.

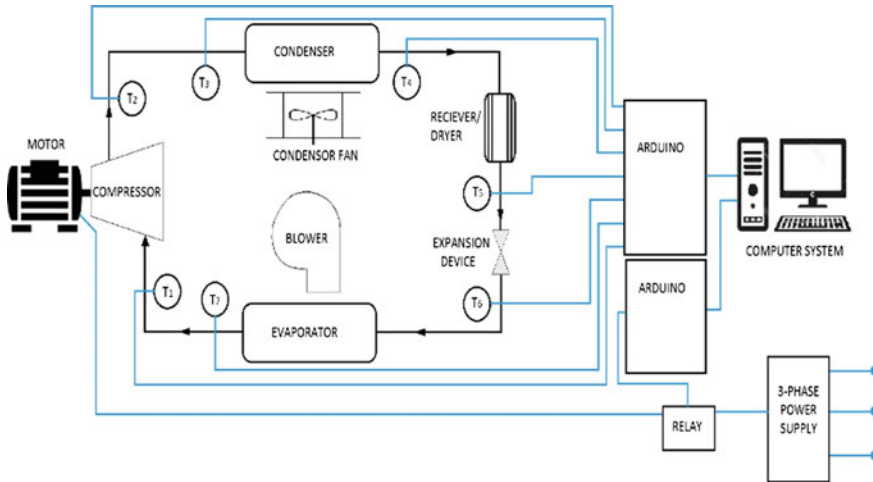


Fig. 1 Layout of Arduino microcontroller automobile air conditioning system

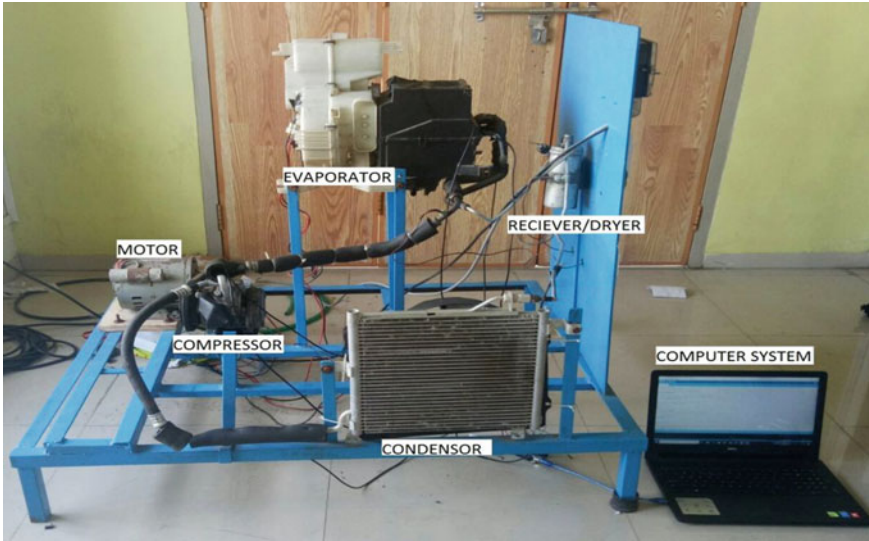


Fig. 2 Experimental setup

2 Automation Hardware Equipage

2.1 Arduino UNO

Arduino is an open-source prototyping platform based on easy-to-use hardware and software. Arduino board designs use a variety of microprocessors and controllers. The boards are equipped with sets of digital and analog input and output pins that may be interfaced to various expansion boards (shields) and other circuits. The board features serial communications interfaces, including Universal Serial Bus (USB), Bluetooth, and Wi-Fi, which are also used for loading programs from computers [11]. The actual Arduino board’s specifications are listed in Table 2.

Table 2 Specifications of Arduino UNO [12, 13]

Microcontroller	ATmega328P	PWM digital I/O pins	6
Operating voltage in V	5	Analog input pins	6
Digital I/O pins	14	SRAM in kb	2
DC current per I/O pin in mA	20	EEPROM in kb	1
DC current for 3.3 V pin in mA	50	Clock speed in MHz	16
Flash memory in kb	32 of which 0.5 issued by boot loader	Input voltage (Limit) in V	6–20
		Input voltage in V (Recommended)	7–12

2.2 Relay and Digital Sensors 18B20

The relay is an electrically operated switch that allows turning on and off the circuit using voltage and/or current much higher than the criteria the microcontroller could. There is no connection between the low voltage circuit operated by the microcontroller and the high power circuit [14, 15]. In the experimental setup, the relay is connected in the midst of power supply line to the motor. An Arduino board is connected to the relay. This is done for the automatic starting and stopping of the system.

The circuit diagram for relay and Arduino board connection is shown in Fig. 3. The DS18B20 digital sensor provides 9–12-bit Celsius temperature measurements. The DS18B20 can communicate over a 1-Wire bus. That means it requires only one data line (and ground) for communication with a central microprocessor. Each DS18B20 has a unique 64-bit serial code, which allows multiple sensors to function on the same 1-Wire bus. Thus, one microprocessor can control many DS18B20s [16, 17]. Using this advantage of DS18B20, all the sensors are connected to the input of the Arduino board. Absolute maximum ratings for the sensor are shown in Fig. 4:

- Voltage range on any pin relative to Ground is from -0.5 to $+6.0$ V.
- Operating temperature range is from -55 to $+125^{\circ}\text{C}$.
- Storage temperature range is from -55 to $+125^{\circ}\text{C}$.

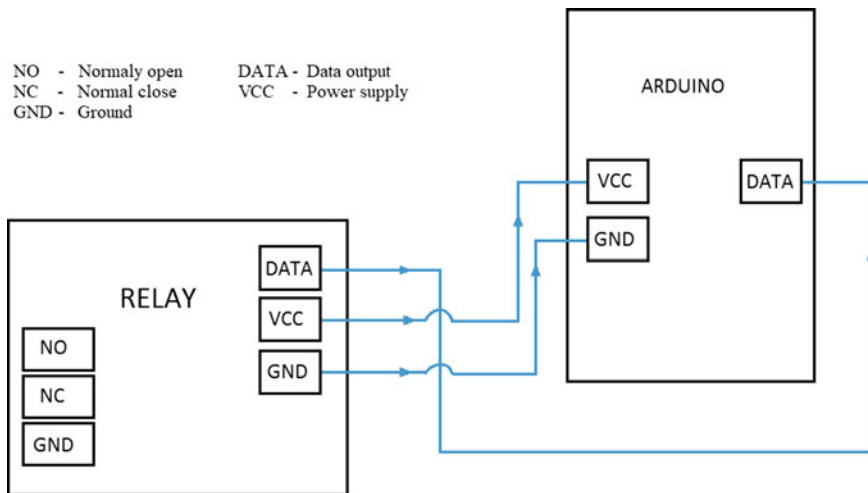


Fig. 3 Relay-Arduino UNO circuit

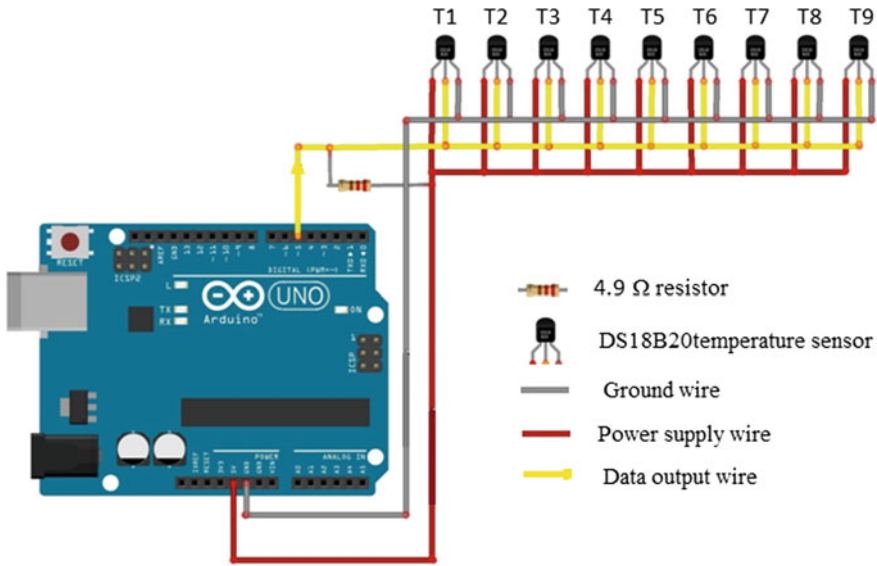


Fig. 4 DS 18B20-Arduino UNO connection circuit

3 Utility Software: Arduino IDE and PLX-DAQ

In automation industry, software is something what a soul is to a living body. It brings life to hardware. It plays an important role in both, pre-processing and post-processing part while implementation and execution of automation to any system.

Arduino provides its own Integrated Development Environment (IDE). Here the programming can be done using C/C++ coding language. The output of the program is displayed in the serial monitor section of the IDE. The coding for the automatic turning on and off the system in prescribed time interval (here for 10 min) and for the transfer of temperature reading from sensors to MS Excel through Arduino board (here for every 2 min interval) respectively, is as follows in Tables 3 and 4.

The temperature readings obtained on the serial monitor of Arduino IDE are transferred to the MS Excel sheet through PLX-DAQ software. PLX-DAQ is a Parallax microcontroller data acquisition add-on tool for Microsoft Excel. With any microcontroller connected with any sensor, the data can be directly transferred to Excel through the serial port of a computer [18]. Also, graphs for the real-time data from the Excel can be generated. 26 columns of data can be recorded with it.

Table 3 Coding for relay on and off

Program	Description
<code>int relay = 13;</code>	Integer for pin 13 slot in Arduino board
<code>void setup() {</code>	Start serial port
<code>Serial.begin(9600);</code>	Baud rate
<code>pinMode(relay, OUTPUT);</code> <code>}</code>	Initialise the Arduino data pin 13 for OUTPUT
<code>void loop() {</code> <code>while (Serial.available() == 0);</code> <code>int val = Serial.read()-'0';</code> <code>Serial.println(val);</code>	Start loop
<code>if (val ==1) {</code> <code>Serial.println("relay on");</code> <code>digitalWrite(relay, HIGH);</code>	Turn on relay on press "1" in serial monitor
<code>delay(600000);</code> <code>Serial.println("relay off");</code> <code>digitalWrite(relay, LOW);</code> <code>}</code>	Wait for 10 min Turn off relay
<code>else if (val ==0)</code> <code>{</code> <code>Serial.println("relay off");</code> <code>digitalWrite(relay, LOW);</code> <code>}</code>	Turn off relay on press "0" in between 10 min

4 Thermodynamic Equations

The mathematical calculations for obtaining the COP and Second Law Efficiency of the system are programmed in the Excel sheet. The lists of equations are presented below [19].

COP of Reversible Carnot cycle is given by,

$$COP_{re} = T_c / (T_c - T_e) \tag{1}$$

Theoretical work done by compressor is given by,

$$W_c = H_2 - H_1 \text{ kJ/kg} \tag{2}$$

Theoretical refrigerating effect is given by,

$$Q_e = H_1 - H_4 \text{ kJ/kg} \tag{3}$$

Theoretical COP of VCERS is given by,

$$COP_{th} = Q_e / W_c \tag{4}$$

Table 4 Coding for obtaining temperatures of required components of the system

Program	Description
#include <OneWire.h>	Include the libraries
#include <DallasTemperature.h>	Setup a oneWire instance to communicate with any OneWire devices
OneWire(5);	
DallasTemperature sensors(&oneWire);	
float COMPI;	Variable for temperature of components
float COMPO;	
float CONDI;	
float CONDO;	
float EXPI;	
float EXPO;	
float EVAPO;	
float Tcool;	
void setup() {	Start serial port
Serial.begin(56000);	Baud rate
Serial.println("CLEARDATA");	This string is defined as a command for the Excel VBA to clear all the rows and column
Serial.println("LABEL, Computer	LABEL command creates label for columns in the first row with bold font
time, COMPI, COMPO, CONDI, CONDO, EXPI, EXPO, EVAPO, Tcool");	
sensors.begin();	Start up the library
}	
void loop(){	Start loop
for(int a = 0; a < 5; a ++)	Defines that 5 readings taken
sensors.requestTemperatures();	Send command to get temperature readings

(continued)

Table 4 (continued)

Program	Description
<pre> COMPI = sensors.getTempCByIndex (0) ; COMPO = sensors.getTempCByIndex (1) ; CONDI = sensors.getTempCByIndex (2) ; CONDO = sensors.getTempCByIndex (3) ; EXPI = sensors.getTempCByIndex (4) ; EXPO = sensors.getTempCByIndex (5) ; EVAPO = sensors.getTempCByIndex (6) ; Tcool = sensors.getTempCByIndex (7) ; Serial.print ("DATA, TIME, ") ; </pre>	<p>One can add more than one temperature sensors on the same bus. Here for 8 components, 8 temperature sensors are used.</p>
<pre> Serial.print (COMPI) ; Serial.print (",") ; Serial.print (COMPO) ; Serial.print (",") ; Serial.print (CONDI) ; Serial.print (",") ; Serial.print (CONDO) ; Serial.print (",") ; Serial.print (EXPI) ; Serial.print (",") ; Serial.print (EXPO) ; Serial.print (",") ; Serial.print (EVAPO) ; Serial.println (Tcool) ; </pre>	<p>Print system time Take data from sensors and print</p>
<pre> delay (120000) ; } for (int b = 0 ; b >= 0 ; b++) { delay (1000) ; } } </pre>	<p>Take readings after every 2 min</p>

Theoretical Second Law Efficiency is given by,

$$\eta_{IIth} = COP_{th}/COP_{rev} \quad (5)$$

Flow rate of refrigerant is given by,

$$Mr = TR/Q_e \text{ kg/min} \quad (6)$$

Actual Power consumption is given by,

$$W_{act} = Mr * W_c/\eta_m * \eta_{ad} \quad (7)$$

Actual COP of VCRS is given by,

$$COP_{act} = 3.517/W_{act} \quad (8)$$

Actual Second Law Efficiency is given by,

$$\eta_{IIact} = COP_{act}/COP_{rev} \quad (9)$$

5 Result

Figure 5 describes that by commanding “1” as input it will start the relay. It results in starting of the project setup. Figure 6 describes the automatic transfer of temperature reading for different component to excel sheet with the help of PLX-DAQ as shown in Figs. 7 and 8.

Graphs for the obtained output data depicts the variations in the theoretical and actual performance parameters with respect to the specific time interval for the specific temperature range. Here the system is programmed to operate for 10 min, where temperature readings for every 2 min intervals are obtained. This process is repeated after every successive hours for a total operation of 720 min (12 h).

At constant compressor temperature, the actual and theoretical values of COP constantly increase with small variations with respect to increase in evaporator outlet temperature and condenser outlet temperature. The actual value of COP is about 50% less than theoretical value. The theoretical and actual value of second law



Fig. 5 Serial monitor screen of on/off program

	A	B	C	D	E	F	G	H	I	J	K	L
1	Computer time	COMPI	COMPo	CONDi	CONDo	EXPI	EXPo	EVAPo	Tcool			
2	11:26:30	28.06	38.75	39.88	35	34	27.56	25.75	24.69			
3	11:28:31	22.75	41.06	43.25	36.56	35.5	26.44	22.94	22.75			
4	11:30:33	21.12	41.56	43.94	36.88	35.69	25.94	22.12	22.62			
5	11:32:34	20.69	41.75	44.19	36.88	35.81	25.75	22	22.69			
6	11:34:36	20.62	41.81	44.38	36.94	35.75	25.94	22	22.62			

Fig. 6 Temperature readings appearing in 2 min interval

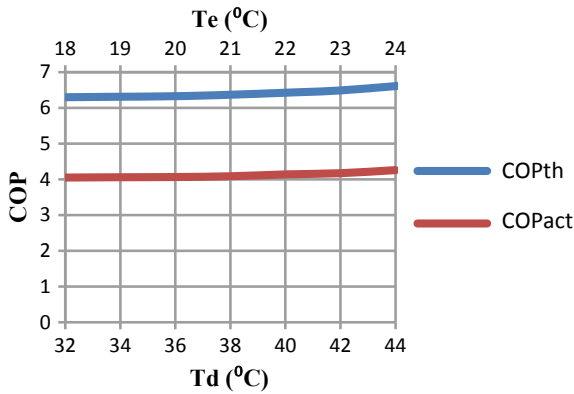


Fig. 7 COP versus condenser and evaporator outlet temperature

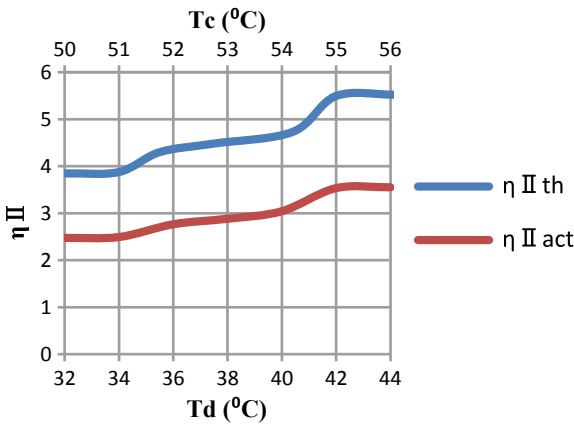


Fig. 8 COP versus condenser and compressor outlet temperature

efficiency increases with the rise in evaporator outlet temperature and condenser outlet temperature. The actual value of second law efficiency is about 36.84% less than theoretical value.

6 Conclusion

This paper describes the methodology to introduce automation in a mechanical system by considering a VCR system of automobile. The interconnection of hardware and software to make a system automatic is explained by showing the role and importance of microcontroller. The flexibility and interlinking of software used, such as Arduino IDE, MS Excel, and PLX-DAQ are emphasized here. Where the Arduino IDE provides the flexibility to impart modifications to the program/code according to the changes in input parameters from the system. MS Excel provides the flexibility to modify the equations and variable parameters. PLX-DAQ provides the flexibility to transfer data from Arduino IDE serial monitor to MS Excel automatically. The significance of coding is presented here as the key factor in imparting automation. Any possible desired output for the system can be obtained by modifying the relative input parameters in the program. Pertaining to this experiment, the time interval for starting and stopping the system and for the fetching of temperature readings from the sensors can be adjusted by simply replacing the time in the programming. The graphs obtained for the thermodynamic calculations show the variations in the actual and theoretical COP and second law efficiency respectively, for a 720 min of operation, by a set of 10 min for every successive hours. It is found that, for the system, theoretical value of cop is twice that of actual values of COP and theoretical Second Law Efficiency is about 36% more than its actual value.

References

1. Hari Sudhani R, Ganesh Kumar M, Udhaya Prakash A, Anu Roopa Devi S, Sathiya P (2015) Arduino ATMEGA-328 microcontroller. *Int J Innovative Res Electr Electron Instrum Control Eng* 3(4)
2. Louis L (2016) Working principle of Arduino and using it as a tool for study and research. *Int J Control, Autom Commun Syst (IJCACS)* 1(2)
3. David N, Chima A, Ugochukwu A, Obinna E (2015) Design of a home automation system using Arduino. *Int J Sci Eng Res* 6(6)
4. Shrikant S Malipatil (2016) Simulation of automatic air conditioning and heating control with RF arduino-melody by using LM35 temperature sensor in Proteus software. *Int J Emerg Res Manage Technol* 5(5)
5. Mahmood SN, Hasan FF (2017) Design of weather monitoring system using Arduino based database implementation. *J Mult Eng Sci Technol (JMEST)* 4(4)
6. Rahul D, Kathiwala, Shah HA, Joshi K (2017) Study on various geometries of automobile micro channel condenser: A review. In *PRIME 2017 National Conference on Progress, Research and Innovation in Mechanical Engineering* March, SCET, Surat, India
7. Maruti Suzuki WagonR car manual 2016 edition

8. Maruti 800 2004 car manual and Alto 2014 car manual
9. Parallax Inc. Rocklin, USA
10. Sumeru Kashni (2016) Comparative performance between R134a and R152 in air conditioning system of passenger car. *Jurnal Teknologi* 78:10–20
11. Smith AG (2011) Introduction to Arduino. create space independent publishing platform
12. Halvorsen H-P (2016) Introduction to Arduino. University College of Southeast Norway
13. Arduino—Introduction. www.arduino.cc
14. Specification for low voltage switchgear and control gear for industrial use. Terminal marking and distinctive number. General rules. BSI as BS 5472:1977 UK (1976)
15. Donghai Tongling Electric Appliance Co., Ltd. Address: Industrial Zone, Shuangdian Town, Donghai County, Lianyungang City
16. Bhalla S, Bhateja V, Chandavale AA, Hiwale AS, Satapathy SC (2017) Intelligent computing and information and communication. In *Proceedings of 2nd international conferences ICICC*
17. Maxim integrated. Rio Robles, San Jose, USA
18. PLX-DAQ v2.11
19. Lemmon EW, Huber ML, McClendon MO (2013) Reference fluid thermodynamic and transport properties (REFPROP), NIST Standard Reference Database 23, vol 9.1. National Institute of Standards 2013, Gaithersburg MD, USA

Experimental Investigation of Bio-Oil Based Nanofluid Spray Cooling During AISI 316 SS Turning



Ukamanal Manoj , P. C. Mishra, A. K. Sahoo and Panigrahi Subhashree

Abstract Nanofluid Spray Impingement Cooling (NSIC) has a huge potential of being used as lubricant and coolant in machining processes due to its excellent lubricating properties and high heat removal capacity. The current study was carried out to improve the machining performance along with heat transfer rate during turning of AISI 316 SS using uncoated carbide inserts under bio-oil based NSIC environment. Different volume concentrations of Karanja oil- based TiO_2 nanofluid were applied during turning operation using the spray setup. Tool and chip temperatures, surface finish, and tool flank wear were measured and analyzed. The heat transfer coefficient of the bio-oil was also determined. Linear regression models were developed to predict the machining responses, i.e., tool temperature, chip temperature, average surface roughness, and tool flank wear. Taguchi based gray relational analysis was used for optimization of the machining process parameters to obtain multiple performance quality characteristics of the AISI 316 steel during turning in the SIC environment. Results indicate that the application of bio-oil based TiO_2 NSIC during turning decreased the peak tool temperatures by 52% as compared to dry turning environment, i.e., 220–105 °C. There was a noticeable increase in surface finish quality by examination of the average roughness by of about 50.7%.

Keywords Spray impingement cooling · Nanofluid · TiO_2 · Bio-oil · AISI 316 SS

1 Introduction

Present-day standards have led the manufacturing industries to meet high precision and accurate alignment demands, which have made it completely necessary to use lubricants and coolants during the machining operation. Heat generated in the cutting zone due to shear stress, is a function of the cutting parameters such as depth of cut, feed rate, and cutting speed [1–6]. Abhang et al. [7] reported that heat is generated

U. Manoj (✉) · P. C. Mishra · A. K. Sahoo · P. Subhashree
School of Mechanical Engineering, KIIT, Deemed to Be University, Bhubaneswar 024,
Odisha, India
e-mail: manoj.ukamanalfme@kiit.ac.in

© Springer Nature Singapore Pte Ltd. 2019
M. Kumar et al. (eds.), *Advances in Interdisciplinary Engineering*, Lecture Notes in
Mechanical Engineering, https://doi.org/10.1007/978-981-13-6577-5_27

277

from the energy required to generate chips during cutting metals and alloys. This heat affects the tool life, surface roughness, cutting forces, dimensional accuracy, and other performance characteristics [1, 4–6]. Measurement of the cutting temperature is extremely difficult as the cutting zone involves complex events. Coolants are an essential part of a machining process which carried away the heat generated in the cutting zone. Conventionally mineral oils are used as coolants which are environmentally hazardous and as a replacement natural ester oils are being used due to their high cooling performance, biodegradability, better oxidation stability [8]. Limited data is available on the performance of nanoparticles added as an additive in a vegetable oil being used as a coolant/cutting fluid while machining. Padmini et al. [2] conducted an experimental investigation to determine the performance of vegetable oil based $n\text{MoS}_2$ (nano molybdenum disulfide) nanofluids while turning AISI 1040 steel in order to find its potential as cutting fluid/coolant during machining. They performed a comparison study of vegetable oil based $n\text{MoS}_2$ with dry machining and machining with pure oil and reported that vegetable oil based $n\text{MoS}_2$ provided much better performance. It was observed from the results that a reduction in cutting forces by 37%, reduction in cutting temperature by 21 and 44% reduction in tool wear was obtained compared to dry machining. Kus et al. [1] and Padmini et al. [2], used a thermocouple embedding technique to measure the temperature at the cutting zone. Khandekar et al. [3] observed that by using conventional cutting fluid based Al_2O_3 nanofluid, a reduction of 50% in cutting forces and 54.5% reduction in surface roughness when compared with dry machining of AISI 4340 using uncoated carbide inserts. Sharma et al. [9] obtained an increase of 8.5% thermal conductivity of vegetable oil–water emulsion based TiO_2 compared to the base fluid at 3% concentration by volume, 58% reduction in tool wear and 63% reduction in cutting force was observed during turning AISI 1040 steel using MQL technique. The aim of this study is to investigate the effects of Karanja oil based TiO_2 nanofluid on machining performance.

2 Experimental Design and Selection of Parameters

Cutting speed (N), depth of cut (t), feed rate (s), and air pressure (P_a) were the parameters selected as input cutting parameters. In the current study, Taguchi-based L16 design of experiments was used for optimizing the cutting parameters. Orthogonal array obtained from MINITAB software for spray experimentation is given in Table 1. Here A, B, C, and D are the depth of cut, feed rate cutting speed, and air pressure, respectively. Karanja oil based TiO_2 nanofluid pressure is set at 1 bar. Cutting temperature (T_t), surface roughness (R_a), and tool wear (VB_c) are the responses measured to obtain the machining performance.

Table 1 L16 orthogonal array for oil–air spray experiments

A	B	C	D
1	1	1	1
1	2	2	2
1	3	3	3
1	4	4	4
2	1	2	3
2	2	1	4
2	3	4	1
2	4	3	2
3	1	3	4
3	2	4	3
3	3	1	2
3	4	2	1
4	1	4	2
4	2	3	1
4	3	2	4
4	4	1	3

3 Experimental Setup

All the turning experiments were performed on HMT NH-22 high-speed lathe. The nanofluid spray was generated using an internally mixing 1/8 J type nozzle. Figure 1 shows the experimental setup used for turning. Tungsten carbide (uncoated), SNMG-120408, TTS-grade cutting inserts were used for turning AISI 316. A k-type thermocouple was embedded in the cutting tool 1 mm behind and 0.5 mm below the cutting tip as shown in Fig. 2. Thermocouple reading was measured and recorded at an interval of 0.1 s and redundant entries are eliminated using CHINO data acquisition system.

3.1 Nanofluid Preparation

Pure Karanja oil is a thick yellow-orange to brown oil is extracted from seed and the scientific name is *Millettia Pinnata* having a boiling point of 316 °C, density is 924 kg/m³ at 15 °C and a viscosity of 4.77 mm²/s at 40 °C. Karanja oil based TiO₂ nanofluid was prepared using the two-step method as shown in Fig. 3. TiO₂ nanoparticles are first produced by high energy ball milling machine and then 0.03% by weight of TiO₂ powders were manually dispersed into the base oil of 100 ml. The mixture was then stirred using a mechanical stirrer for 8 h. The stirred mixture was

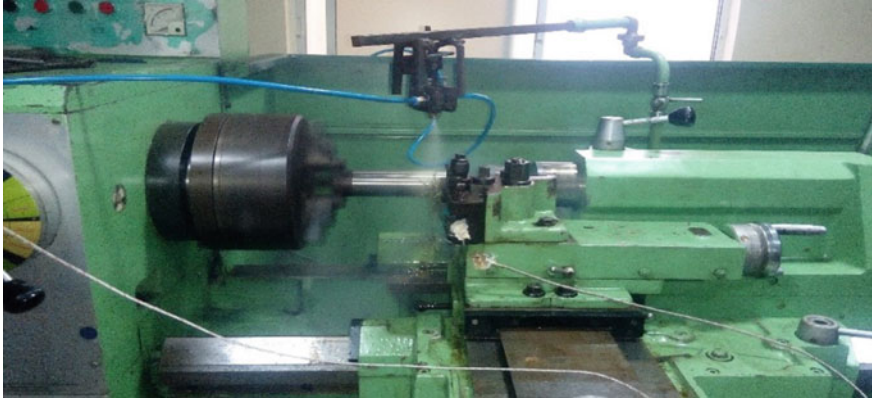


Fig. 1 Spray impingement cooling of AISI 316 SS

Fig. 2 Schematic diagram of thermocouple embedding in cutting insert

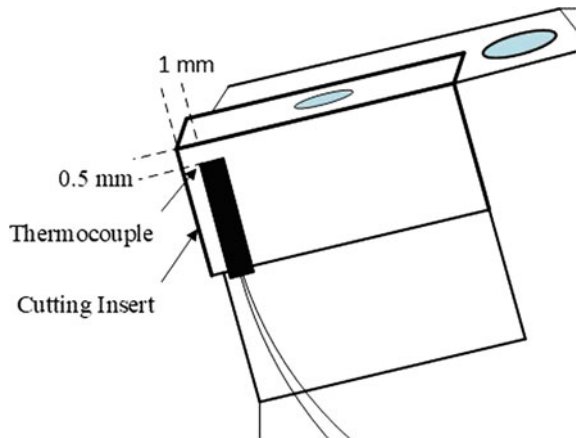
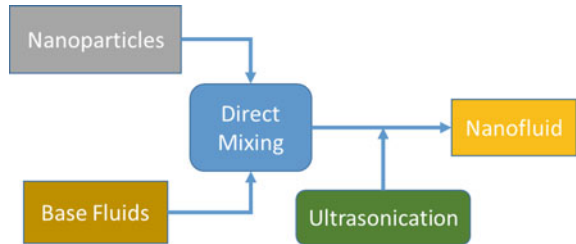


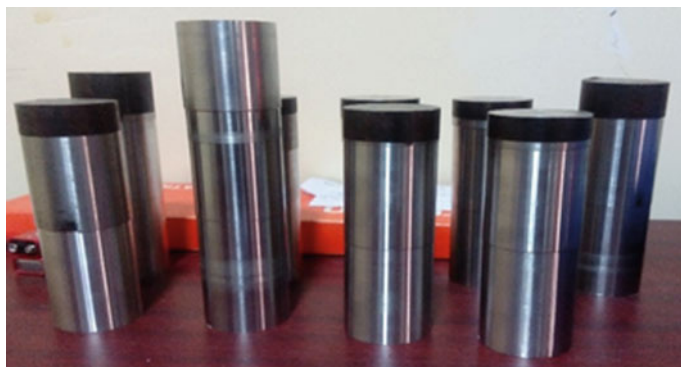
Fig. 3 Two-step method for nanofluid preparation



then subjected to sonication for 4 h. using ultra-sonication technique and then the mixture was stirred with the remaining oil to feed in the spraying system.

Table 2 Physical properties of AISI 316 stainless steel

Property	Value
Density	8.0 g/cm ³
Melting point	1375–1400 °C
Modulus of elasticity	193 GPa
Electrical resistivity	$0.074 \times 10^{-6} \Omega \text{ m}$
Thermal conductivity	16.3 W/m K at 100 °C
Thermal expansion	$15.9 \times 10^{-6}/\text{K}$ at 100 °C

**Fig. 4** Workpiece material—AISI 316 SS

3.2 Material

Due to high nickel and chromium content, stainless steel having high machinability characteristics and it generate high temperature and we apply more force to machining. Chemical composition, mechanical and physical properties of AISI 316 as shown in Table 2. Figure 4 shows the workpiece prepared.

4 Results and Discussion

Results reveal that the tool temperature was sufficiently lower than those in dry machining condition. It may be due to evaporative heat transfer to the mist formed by the compressed air–Karanja oil based TiO₂ nanofluid spray in the spray cooled environment. The temperatures increased with the increase in spindle speed, feed, or depth of cut as more heat is generated in the machining zone at higher levels of machining parameters. Main effects plots (Fig. 7) for the means of T_t in spray cooled environment reveal that the mean tool temperature increased with the increase of either depth of cut, feed and spindle speed. However, the tool temperature reduced on increasing air pressure. Feed had the highest contribution to the tool temperature.

Table 3 Grey relational coefficient (with $\zeta = 0.5$), grey relational grade and their order sequencing

Run No.	Gray relational coefficient			Grey relational coefficient	Order
	T_t	R_a	VB_c		
1	55	0.07	0.593	0.886	2
2	78	0.098	0.713	0.655	5
3	86	0.1	0.786	0.606	6
4	99	0.168	1.093	0.432	15
5	58	0.068	0.56	0.894	1
6	71	0.076	0.78	0.71	4
7	114	0.202	1.113	0.388	16
8	72	0.14	1.126	0.514	9
9	104	0.139	1.08	0.453	13
10	95	0.178	1	0.448	14
11	48	0.061	1.566	0.782	3
12	95	0.071	1.626	0.543	8
13	100	0.111	1.13	0.488	11
14	116	0.126	0.66	0.565	7
15	105	0.098	1.193	0.496	10
16	97	0.096	1.413	0.487	12

Main effects plot (Fig. 6) for the means of R_a reveal that the surface roughness reduced on increasing N , P_w , or P_a , but it increased on increasing either feed or depth of cut. The tool flank wear increased with the increase of either of the machining process parameters (t , s , or N). It may be due to the more heat generation at the machining zone that accelerated the tool wear. However, on increasing air pressure the tool temperature reduced and hence less tool wear was observed.

4.1 Multiple Response Optimization of Machining Process Parameters

Taguchi-based grey relational analysis was used to optimize the machining process parameters (N , s , t , and P_a) for the multiple performance quality characteristics (i.e., T_t , R_a , and VB_c) of the AISI 316 steel during turning in the spray cooled environment. The grey relational coefficients (with $\zeta = 0.5$) and the grey relational grades of the responses were calculated and are presented in Table 3. Strongest relational degree between ideal sequence and compatibility sequence was achieved for run no. 5, as it generated the highest value of grey relational grade, i.e., 1. But for run no. 7, the grey relational grade was 16, which imply the weakest relational degree between ideal and compatibility sequences for this experimental run (Figs. 5, 6 and 7).

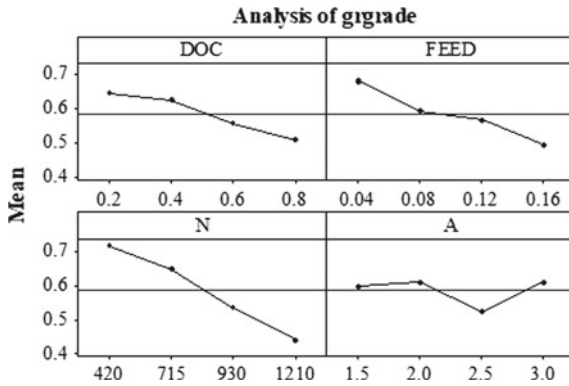


Fig. 5 Main effects plot for the means of grey relational grade

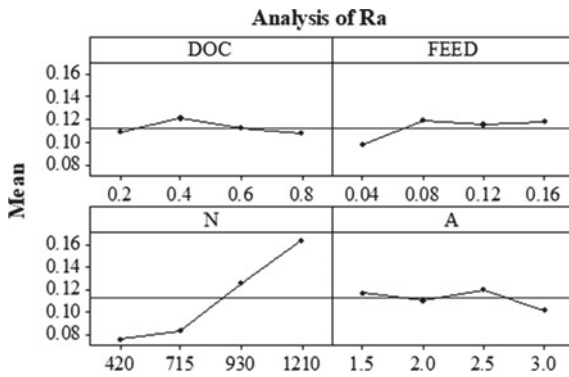


Fig. 6 Main effects plot for mean of R_a with t, s, N, P_a

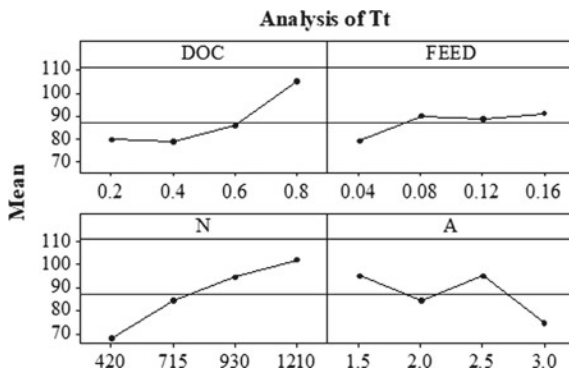


Fig. 7 Main effects plot for mean of tool temperature with the depth of cut, feed, cutting speed and air pressure

Table 4 Means of grey relational grade response table

Parameters	Level 1	Level 2	Level 3	Level 4
D	0.644	0.633	0.556	0.509
F	0.68	0.594	0.568	0.494
N	0.716	0.647	0.534	0.439
A	0.595	0.608	0.523	0.609

The combination of $N_2-s_2-t_2-P_{a2}$ provided maximum grey relational grade value of 0.894. This combination of parametric levels, i.e., 715 rpm of spindle speed, 0.04 mm/rev of feed, 0.4 mm of the depth of cut, 1 bar of oil pressure and 2 bar of air pressure is the optimal combination of process parameters for the multiple performance characteristics. The main effects plot for the means of the grey relational grade is shown in Fig. 5. The central horizontal line in this plot represents the total mean grey relational grade, i.e., 0.5689. Table 4 provides the response for the means. The predicted value of grey relational grade is exactly the same as its experimental value for the optimal process parameters. Grey relational grade for optimal process parameters was improved by 0.472, i.e., 74.52%.

5 Conclusion

1. During AISI 316 SS turning with uncoated carbide inserts in dry machining condition, tool temperature increased with the increase of either t , s , and N with a maximum temperature of 220 °C. Spindle speed was the most contributing parameter for the temperatures. Average surface roughness increased with the increase of depth of cut or feed, but it reduced on increasing the spindle speed.
2. In the spray environment, lower values of tool temperatures were observed as compared to those in a dry machining environment. The temperatures increased with the increase in the spindle speed, feed, or depth of cut. The average surface roughness reduced on increasing spindle speed, air pressure, but it increased on increasing either feed or depth of cut.
3. Grey relational analysis for machining the steel in air–oil spray cutting environment revealed that 715 rpm of spindle speed, 0.04 mm/rev of feed, 0.4 mm of the depth of cut, and 2 bar of air pressure was the optimal combination of process parameters for the multiple performance characteristics under consideration.
4. During spray cooled machining exhibit steep drop in tool temperatures compared to dry machining with the maximum temperature recorded at 105 °C.
5. The heat transfer rate increased for spray impingement cooling with only water as a coolant as compared to dry whereas for bio-oil cooling environment it was obtained highest.

References

1. Kus A, Isik Y, Cemal Cakir M, Coşkun S, Özdemir K (2015) Thermocouple and infrared sensor-based measurement of temperature distribution in metal cutting. *Sensors (Switzerland)* 15:1274–1291
2. Padmini R, Vamsi Krishna P, Krishna Mohana Rao G (2016) Effectiveness of vegetable oil based nanofluids as potential cutting fluids in turning AISI 1040 steel. *Tribol Int* 94:490–501
3. Khandekar S, Sankar MR, Agnihotri V, Ramkumar J (2012) Nano-cutting fluid for enhancement of metal cutting performance. *Mater Manuf Processes* 27:963–967
4. Sharma AK, Tiwari AK, Dixit AR (2016) Effects of Minimum Quantity Lubrication (MQL) in machining processes using conventional and nanofluid based cutting fluids: a comprehensive review. *J Clean Prod* 127:1–18
5. Mishra PC, Das DK, Ukamanal M, Routara BC, Sahoo AK (2015) Multi-response optimization of process parameters using Taguchi method and grey relational analysis during turning AA 7075/SiC composite in dry and spray cooling environments. *Int J Ind Eng Comput* 6:445–456
6. Sahoo AK, Mishra PC (2014) A response surface methodology and desirability approach for predictive modeling and optimization of cutting temperature in machining hardened steel. *Int J Ind Eng Comput* 5:407–416
7. Abhang LB, Hameedullah M (2010) The measurement of chip-tool interface temperature in the turning of steel. *Int J Comput Commun Inf Syst (IJCCIS)* 2:1–5
8. Mohamad MS, Zainuddin H, Ghani SA, Chairul IS (2017) AC breakdown voltage and viscosity of palm fatty acid ester (PFAE) oil-based nanofluids. *J Electr Eng Technol* 12:2333–2341
9. Sharma AK, Tiwari AK, Singh RK, Dixit AR (2016) Tribological investigation of TiO₂ nanoparticle based cutting fluid in machining under Minimum Quantity Lubrication (MQL). *Mater Today: Proc* 3:2155–2162

Biodynamic Responses of Human Body in Standing and Seated Position



Rajesh Govindan  and Suraj Prakash Harsha 

Abstract The paper presents the comparative study of the biodynamic response of human body in standing and seated position. A 3D model of the human body in standing and seated position are generated based on anthropometric data for Indian male subject in *SolidWorks*. The finite element tool, *ANSYS-Mechanical* was used to perform modal analysis and to obtain natural frequencies and associated mode shapes for both positions. The principal resonance in both standing and seated position occurred at 5–6 Hz. Further, the responses of the models to seat/floor excitation are derived through harmonic analysis. The frequency response of the human body to low-frequency vibration in both positions was determined in terms of normalized apparent mass and acceleration ratio. Both FE model was able to predict the response of human body that matches with data reported in the published literature. The model will be useful to predict the vibration response of human body under various vibration environments encountered in daily life.

Keywords Whole body vibration · Standing position · Seated position · Modal analysis · Harmonic analysis

1 Introduction

The human body is often exposed to vibration environment on a daily basis either while transit, working on giant earth movers or operating power tools, etc. Vibration exposure may cause discomfort, interferes to perform activities and health and safety issues. The human body is more sensitive to low-frequency vibration. In order to reduce the harmful effect of vibration on the human body, it is necessary to understand its dynamic behavior under such environment. The study of dynamic response to

R. Govindan (✉) · S. P. Harsha
Vibration & Noise Control Lab, Mechanical & Industrial Engineering Department,
IIT Roorkee, Roorkee, India
e-mail: raajgovindan@gmail.com

S. P. Harsha
e-mail: surajfme@iitr.ac.in

vibration and its effect on human body comes under the area of whole body vibration. Since last many decades, both experimental and analytical approaches are being used to investigate the dynamic responses of human body subjected to vertical whole body vibration. With the increase in computational power and efficiency, researchers now often employing finite element (FE) method to simulate such vibration environment and predict its effects on human body.

People more often are in a seated position while exposed to any form of vibration, e.g., in a car or driving a vehicle. Therefore, most of the studies are focused to investigate the responses of the human body to vibratory stimulus in a seated position. However, people also experience a vibration in standing position, e.g., passenger in public transits, a crew member of aircraft and trains, workers of the ship. Knowledge of similarity of dynamic responses of the human body in seated and standing position would enhance the understanding of human body responses and also suggest the extent to which responses of the human body in one position may be assumed for the other position [1].

There have been many previous studies in which human responses to vibration were determined either for seated or standing position but the comparative investigations are quite a few. Coermann [2] investigated the effect of three postures: “standing erect”, “sitting erect” and “sitting relaxed” on mechanical impedance and transmissibility. The principal resonance frequencies for three postures were obtained at 5.9, 6.3, and 5.2 Hz, respectively. The transmissibility of vertical vibration to head at resonance for one subject was found to be greater in a “sitting relaxed” posture while in “sitting erect” posture transmissibility is slightly higher than in “standing erect” postures. The modulus of mechanical impedance at resonance frequency was greater for “sitting erect” as compared to “standing erect” posture.

Miwa [3] measured the mechanical impedance of human body in various standing, sitting and working postures. The resonance peak for standing subject was observed at 7 Hz along minor peak at 20 Hz. In sitting posture, the main peak was found at 6–8 Hz and a minor peak in the frequency between 16 and 20 Hz. Kobayashi et al. [4] measured the vibration transmissibility to head for subjects in standing and sitting posture. It was found that at around 5 Hz, the vertical transmissibility was greater for the subject in sitting posture than in standing posture.

Matsumoto and Griffin [1] compared the dynamic response of the human body in sitting and standing position expose to vertical whole body vibration. The transmissibility and apparent mass of eight male subjects were measured at the head, along with the spine and the pelvis. The resonance peak was observed in the frequency range 5–6 Hz for both postures, with slightly lower frequency and higher apparent mass in the sitting posture. The vertical transmissibility at the head and in the thoracic region was found to have a similar magnitude for both standing and sitting postures.

The present study is aimed to develop FE model of the human body in standing and seated position based on anthropometric data and to obtain their natural frequencies and mode shapes. Further, acceleration responses of human body exposed to vertical whole body vibration were obtained to compare the apparent mass and transmissibility for standing and seated position.

2 Model and Method

The biodynamic responses of standing and seated human body subjected to vertical excitation were studied by developing a 3D CAD models for both postures in SolidWorks and subsequent modal and harmonic analysis were performed in ANSYS Workbench.

2.1 Model Geometry

A three-dimensional finite element (FE) model of the human body in standing and seated position were developed based on 50th percentile anthropometric data of 54 kg Indian male subject. The models consist of 15 body segments: head, neck, upper torso, central torso, lower torso, upper and lower arm (left and right), upper and lower leg (left and right), and foot (left and right). The shape of each body segment is assumed as ellipsoidal, which represents the volume and hence the mass of each body segment [5]. The ellipsoidal segments were created five percent truncation using anthropometric data from Chakrabarti [6]. The geometric dimensions of semiaxes of the truncated ellipsoidal segment were determined from formulae in Nigam and Malik [5] and are shown in Table 1.

2.2 Material Property

Though human body is a complex system with varying material properties, a linear and isotropic material model were assumed. Also, distribution of mass in the human body is not homogeneous, but different body segments have almost same average density [7]. Hence, an average density of human body as 1195.89 kg/m^3 is assigned to each body segment of the model to represent the inertia property [5]. The composition of the human body consists of muscles/tissues, bones, organs, etc. These constitutes have varying mechanical properties and volume fraction in different body segment. Therefore, model's stiffness property was assumed to attribute due to bones (E_b) and tissues (E_t) only and the effects of other constituents were ignored. For the human body model in the standing position, Young's modulus is taken equivalent to an optimized value obtained by Gupta and Gupta [8]. The Young's modulus for the seated human body was initially set equivalent to that employed for standing position model and adjusted after calibration. The damping ratio for both standing and seated position models were initially derived from previously reported literature [9, 10] and then adjusted manually during the calibration, as listed in Table 1. During calibration, Young's modulus of individual ellipsoidal segments was adjusted manually to obtain the apparent mass and body transmissibility for the seated human body as reported previously. Poisson's ratio was taken as 0.3 based on an experimental study of Mukherjee et al. [11].

Table 1 Geometric and material property of body segments [5, 6, 9, 10]

Body segment	a_i (mm)	b_i (mm)	c_i (mm)	Mass (kg)	Elastic modulus (as a fraction of $E_G = \sqrt{E_b \times E_t}$)		Damping ratio	
					Standing	Seated	Standing	Seated
Head (H)	73.50	73.50	93.50	2.3233	0.104	0.062	0.0092	0.0092
Neck (N)	53.64	53.64	40.00	0.52935	0.409	0.245	0.00958	0.00958
Upper Torso (UT)	149.00	107.00	156.00	5.7507	1.072	0.643	0.6339	0.6339
Central Torso (CT)	129.50	96.00	138.75	7.9853	0.518	0.311	0.0686	0.0686
Lower Torso (LT)	165.50	145.50	105.75	15.073	0.102	0.061	0.5	0.5
Upper Arm (UA)	38.83	38.83	156.00	1.0844	0.014	0.600	0.2668	0.2668
Lower Arm (LA)	36.29	36.29	122.00	0.73606	2.407	1.444	0.2668	0.2668
Upper Leg (UL)	67.48	67.48	275.00	5.7607	4.131	2.478	0.2939	0.47024
Lower Leg (LL)	50.77	50.77	229.00	2.7149	9.990	5.994	0.2939	0.47024
Foot (F)	47.00	124.00	30.50	0.87356	0.143	0.085	0.2939	0.47024

2.3 Boundary Conditions

The contacts between body segments for both standing and the seated model was assigned as bonded thus constraining relative motion at the interface. For standing model, the contact between the lower arm and lower torso was considered as no separation. The feet in case standing model and both feet and lower torso in case of the seated model are assumed as rigidly fixed to floor and seat respectively and thus relative motion between them is constrained by considering fixed boundary condition.

2.4 Mesh Study

The human body segments in the present study are represented by the ellipsoidal segment, which is geometrically simple. Also, as hexahedral elements are economical in terms of a number of elements. Therefore, both models were meshed using hexahedral elements with mid-side node set as program controlled. The grid dependency analysis was carried with varying element size to obtain mesh independent solution. The statistics of mesh independent model is listed in Table 2.

2.5 Methodology

Firstly, the modal analysis was executed to determine the natural frequencies and mode shapes. The natural frequencies were calculated to the frequency limit of 40 Hz in order to incorporate the full range of low-frequency vibration to which human body is highly sensitive. The natural frequencies and mode shapes were obtained by solving a linear equation of motion for free undamped vibration (Eq. 1). The mass, damping and stiffness matrices are calculated from the geometric and material property (Table 1) provided during preprocessing stage.

$$[M]\{\ddot{x}\} + [K]\{x\} = \{0\} \tag{1}$$

Thereafter, harmonic response analysis with mode superposition method was conducted to obtain frequency response of each body segment by solving a linear equation of motion for forced damped vibration (Eq. 2). The mode superposition

Table 2 Mesh statistics

Model	Nodes	Elements
Standing position	185,645	82,284
Seated position	249,330	122,668

method is computationally economical as the dynamic response of the model is approximated by a superposition of a small number of its eigenmodes.

$$[M]\{\ddot{x}\} + [C]\{\dot{x}\} + [K]\{x\} = \{F\} \quad (2)$$

In the harmonic response analysis, the vertical acceleration was applied as base excitation to the fixed support, i.e., bottom of feet (standing position) and; foot and lower torso (seated position). The exciting acceleration has a frequency ranging from 0.1 to 30 Hz. The response of different body segment as average acceleration amplitude and phase angle were obtained. The acceleration responses were further employed to calculate apparent mass and floor/seat to head acceleration ratio.

3 Results

The modal analysis of standing and seated FE model provided natural frequencies and associated mode shapes. Since a three-dimensional continuous structure have numerous natural frequencies and modes, therefore based on effective mass participation factor, modes were identified that will contribute to excitation in the vertical direction. Figure 1 shows the first and second mode shapes for the human body in standing and seated position in the vertical direction. For standing position, at first mode (5.379 Hz) the whole body moves axially in phase while the out-of-phase motion of upper and lower body is observed at second mode (15.2683 Hz). The first mode for the human body in a seated position at 5.4573 Hz shows the in-phase motion of lower arms about the elbow and upper body, whereas the second mode at 6.8359 Hz shows the out-of-phase motion of the lower arm and upper body. In both modes in a seated position, the lower body remained almost stationary.

The normalized apparent mass in the standing positions is computed from the responses obtained through harmonic analysis. The estimated values of the parameter: Young's modulus, density and damping coefficient were validated by comparing the results with those available in the literature. Figure 2 compares the normalized apparent mass of standing position with that presented in Rakheja et al. [12] and Matsumoto et al. [13]. The principal resonance frequency predicted by the FE model (5.023 Hz) is slightly towards the lower frequency side as compared to Rakheja et al. (5.638 Hz) and Matsumoto et al. (5.56 Hz). The normalized apparent mass for the model was greater than both Rakheja et al. and Matsumoto et al. up to principal resonance frequency and thereafter the trend matches with them.

The parameters of FE model of the seated subject were validated by comparing normalized apparent mass with the experimental data synthesized by Rakheja et al. [12] as shown in Fig. 3. The principal resonance frequency for the seated FE model is obtained at 5.457 Hz, which lies towards higher frequency side as compared to the experimental envelope. The response curve of seated FE model lies within the envelop up to the principal resonance frequency while afterward, the difference is

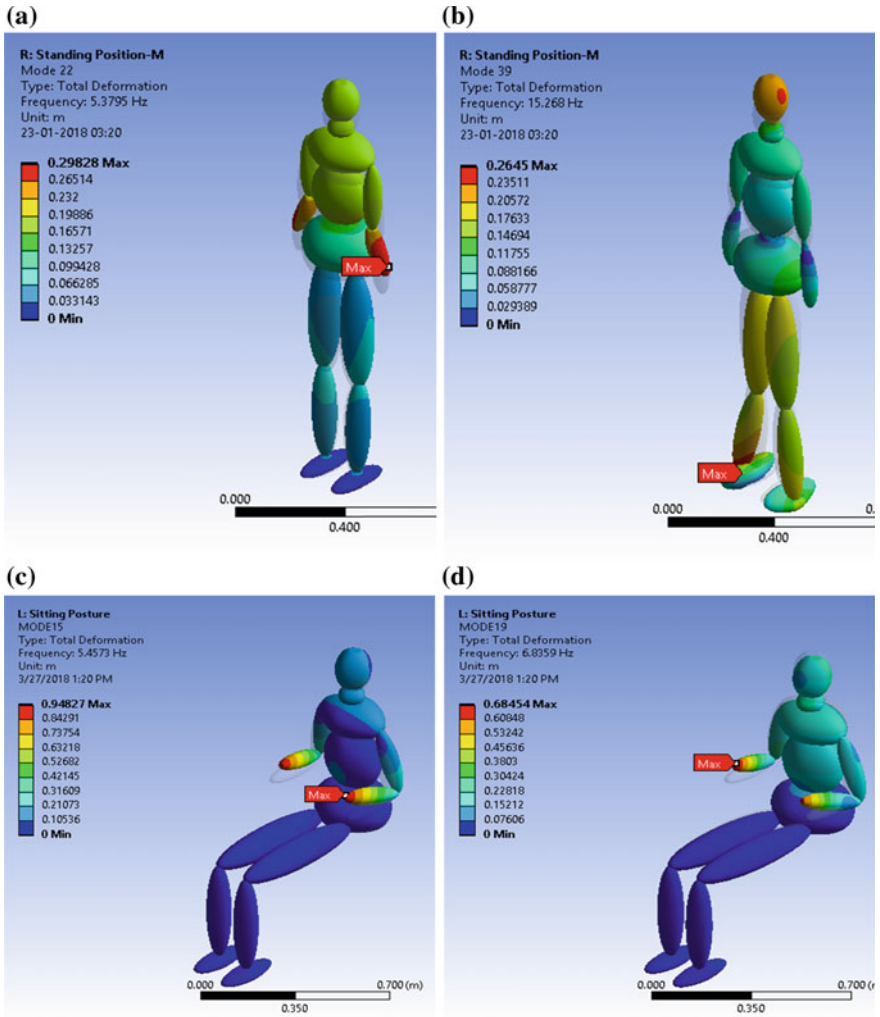


Fig. 1 Vibration modes of the FE model of human body in vertical direction. **a** First mode for standing position, 5.3795 Hz, **b** second mode for standing position, 15.268 Hz, **c** first mode for seated position, 5.4573 Hz, **d** second mode for seated position, 6.8359 Hz

quite significant. The higher value of apparent mass at excitation frequency greater than principal resonance may be attributed to varied mass distribution and anthropometric measurements of the human subjects involved in experimental studies.

The FE model of standing and seated position is further validated by comparing the response curve of the foot to head acceleration ratio with synthesized experimental data envelope. The foot-to-head acceleration ratio for standing position was calculated using the results obtained through harmonic analysis and compared with

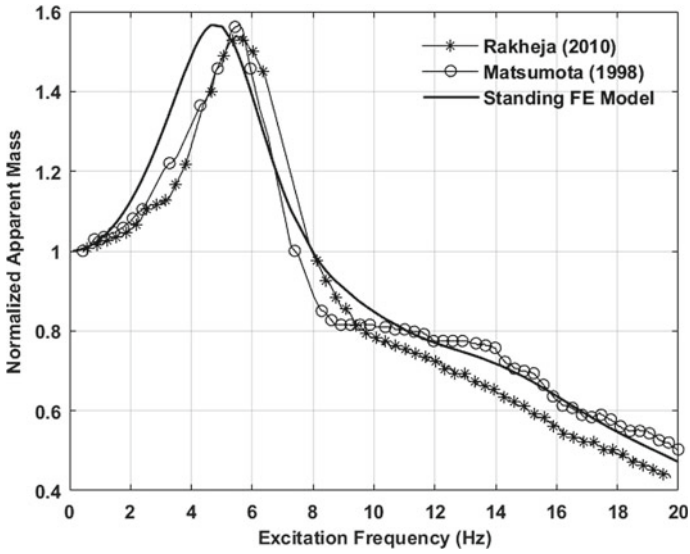


Fig. 2 Comparison of normalized apparent mass for standing position

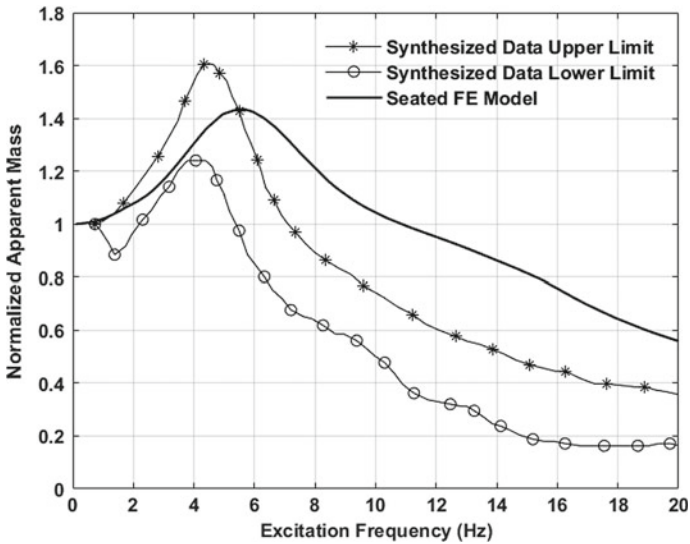


Fig. 3 Comparison of normalized apparent mass for seated position

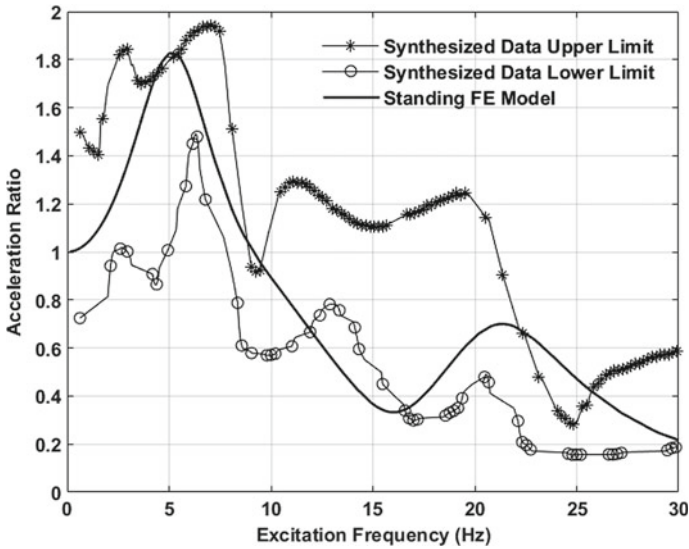


Fig. 4 Comparison of acceleration ratio for standing position

the envelope of synthesized experimental results of Gupta [10] and is shown in Fig. 4. For the standing position FE model, the values of elastic moduli and damping coefficients were based on the optimized results obtained by Gupta et al. [8], who also compared the response of its vibratory model with Gupta [10]. The response curve of the foot to head acceleration ratio obtained by FE model shows two peaks; at 5.02 and 21.44 Hz, similar results were obtained by Gupta et al. [8] through lumped parameter vibratory model. From Fig. 4, it is seen that the response of the model lies well within the experimental envelope. Therefore, it is ascertained that parameters used to develop FE model to simulate the response of standing human being subjected to vertical excitation is able to predict the response to a great extent.

Figure 5 shows the response of seat to head acceleration ratio against low-frequency excitation for seated position and the predicted response of FE model is compared with the envelope of experimental data synthesized by Rakheja et al. [12]. In the present study, a 54 kg human body model in a seated position without backrest is subjected to vertical sinusoidal excitation of magnitude 1 m/s^2 . The range of seat to head transmissibility (STHT) depicted by Rakheja et al. is valid for the seated position without the backrest subjected to vertical sinusoidal or random vibration with the magnitude of $1\text{--}2.75 \text{ m/s}^2$. The mass of body involved in the database selection to define the limits ranges between 58 and 99 kg but the effect of body mass on STHT is reported negligible. The principal resonance frequency for the seated position is observed at 5.933 Hz, which is slightly higher than the experimental envelope. The response matches quite well with the upper limit till the principal resonance frequency and a small divergence are observed thereafter for a small range of excitation frequency.

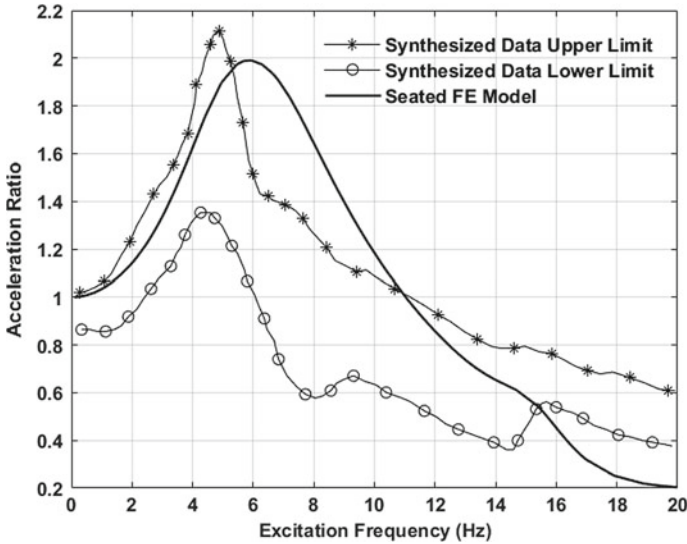


Fig. 5 Comparison of acceleration ratio for a seated position

The normalized apparent masses in standing and seated position were calculated from the responses of the FE model and their comparison is shown in Fig. 6. The principal resonance frequency in a seated position was slightly higher than those in the standing position. The magnitude of normalized apparent mass at the principal resonance frequency in the seated position is lesser than those in the standing position. The normalized apparent masses in the standing position were greater than those in the seated position at excitation frequencies lower than principal resonance frequency and thereafter the trend reverses.

The vertical acceleration ratio due to vertical excitation measured at the head for standing and seated position was compared in Fig. 7. The principal peak for standing and seated positions were observed at 5.02 and 5.933 Hz, respectively. The responses for both standing and sitting positions exactly match each other prior to the resonance frequency. The acceleration ratios for seated position tends to be higher than those for standing position for excitation frequencies greater than the principal resonance frequency. The response for the standing position again increases in the magnitude of acceleration ratio after 16.67 Hz and a secondary peak also observed at 21.22 Hz.

The vertical acceleration response to vertical excitation of each body segment for standing and seated position is compared in Fig. 8. Resonance peak in vertical acceleration response of most body segments was observed between 5 and 6 Hz for both standing and seated position. The vertical acceleration response for standing and seated position show similar magnitude to a frequency of 3 Hz for most of the body segment. The acceleration response of head, neck upper torso, central torso, and upper arms were greater for the standing position before resonance peak, thereafter acceleration response for the seated position becomes greater. In the entire low-

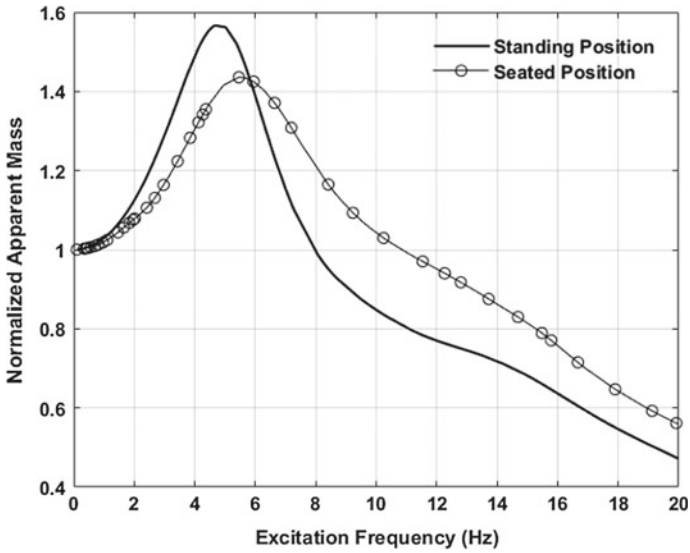


Fig. 6 Comparison of normalized apparent mass in standing and seated position

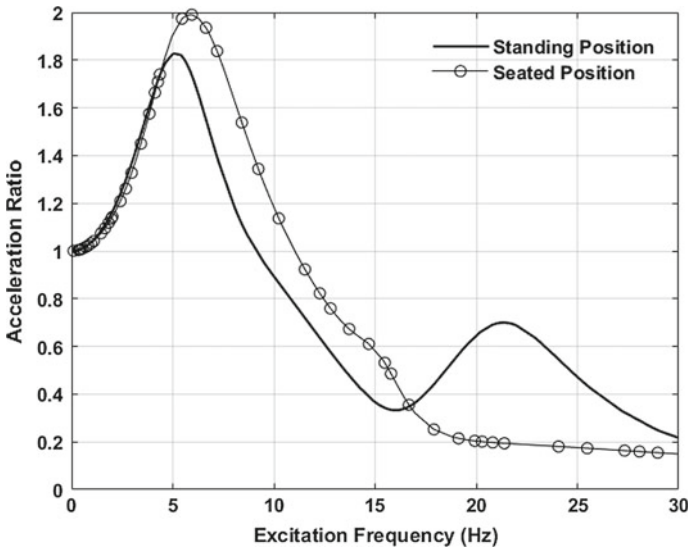


Fig. 7 Comparison of acceleration ratio in standing and seated position

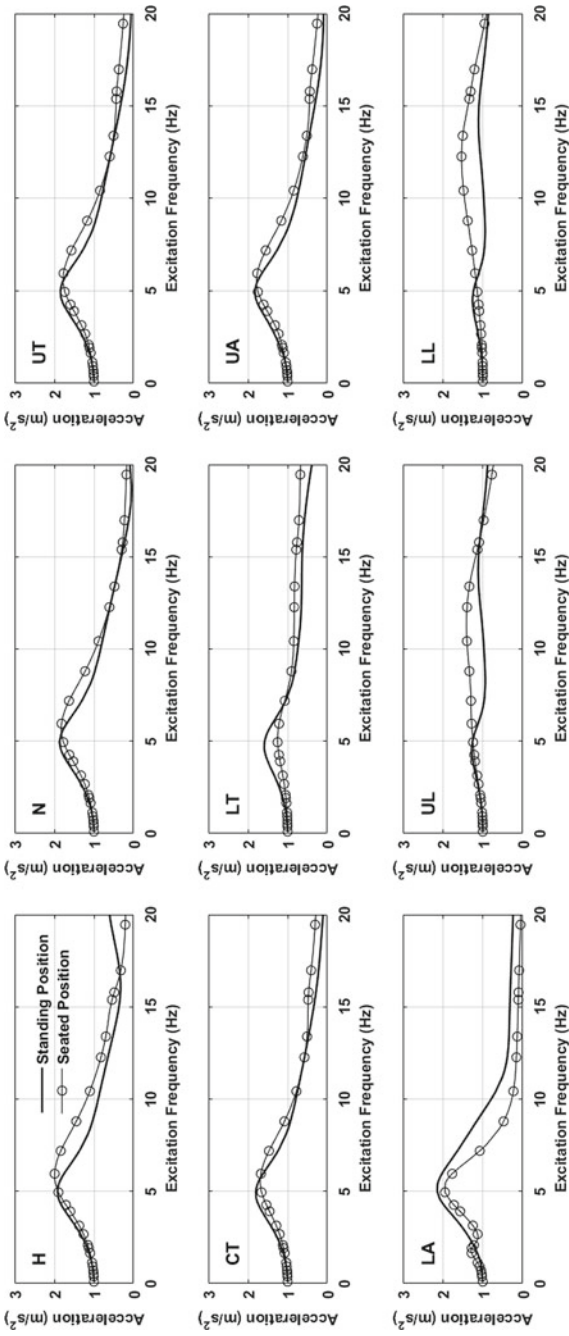


Fig. 8 Average acceleration response of each body segment for standing and seated position

frequency range, the acceleration response at lower arms was greater for standing position. The relative motion between central torso (CT) and lower torso (LT) was found to be greatest as compared to any other adjacent body segments for both standing and seated position.

4 Discussion

The principal resonance frequency of the normalized apparent mass was found between 5 and 6 Hz for the human body model in standing and seated position. The seated position model has slightly higher frequency than standing position model at resonance. Although, the difference between the resonance frequency between the two model is less than 1 Hz. Coermann [2] reported the similar difference between the main resonance frequency of mechanical impedance for “standing erect” and “sitting erect” posture.

The normalized apparent mass at resonance frequency was higher for the seated position than for standing position. At excitation frequency higher than 6 Hz, the normalized apparent mass for the seated position was greater than for standing position. Therefore, it can be discerned that the seated body has more damping than the standing one.

The principal resonance frequency of the vertical foot/seat to head acceleration ratio for both standing and the seated position was in the range of 5–6 Hz as it is obtained in the normalized apparent mass. The vertical acceleration ratio for seated posture was found to be greater than for standing position, which is consistent with the results reported by Coermann [2], Kobayashi et al. [4]. The attenuation above resonance frequency is more remarkable in the standing position than that for a seated position.

5 Conclusion

A three-dimensional FE model of the human body in standing and seated position based on anthropometric data was developed and used to extract the resonance frequencies and mode shapes. In both standing and seated posture, the principal resonance frequency was found at 5–6 Hz. The results obtained through harmonic analysis show that at principal resonance, the normalized apparent mass was greater for standing position whereas vertical vibration transmission to the head was observed higher for a seated position. Also, the relative motion between central torso and lower torso was greater than for any other adjacent body segment for both standing and seated position.

References

1. Matsumoto Y, Griffin MJ (2000) Comparison of biodynamic responses in standing and seated human bodies. *J Sound Vib* 238:691–704
2. Coermann RR (1962) The mechanical impedance of the human body in sitting and standing position at low frequencies. *Hum Factor* 4:227–253
3. Miwa T (1975) Postures, mechanical impedance of human body in various. *Ind Heal* 13:1–22
4. Kobayashi F, Katsumi H, Miyao S, Health P, June R (1981) Measurement of human head vibration. *Ind Heal* 19:191–201
5. Nigam SP, Malik I (1987) A study on a vibratory model of a human body. *J Biomech Eng* 109:143–153
6. Chakrabarti D (1997) Indian anthropometric dimensions for ergonomic design practice. National Institute of Design
7. Garg DP, Ross MA (1976) Vertical mode human body vibration transmissibility. *IEEE Trans Syst Man Cybern SMC-6*:102–112
8. Gupta TC (2007) Identification and experimental validation of damping ratios of different human body segments through anthropometric vibratory model in standing posture. *J Biomech Eng* 129:566
9. Bartz JA, Gianotti GR (1975) Computer program to generate dimensional and inertial properties of the human body. *ASME J. Eng Ind* 1:49–57
10. Gupta M, Gupta TC (2017) Modal damping ratio and optimal elastic moduli of human body segments for anthropometric vibratory model of standing subjects. *J Biomech Eng* 139:101006
11. Chawla A, Mukherjee S, Karthikeyan B (2006) Mechanical properties of soft tissues in the human chest, abdomen and upper extremities
12. Rakheja S, Dong RG, Patra S, Boileau PÉ, Marcotte P, Warren C (2010) Biodynamics of the human body under whole-body vibration: synthesis of the reported data. *Int J Ind Ergon* 40:710–732
13. Matsumoto Y, Griffin MJ (1998) Dynamic response of the standing human body exposed to vertical vibration: influence of posture and vibration magnitude. *J Sound Vib* 212:85–107

Simulation and Modeling of Solar Trough Collector



Mukundjee Pandey , Biranchi Narayana Padhi  and Ipsita Mishra 

Abstract Computational fluid dynamics (CFD) simulations are widely used; as these are cost effective in a manner that it saves finance for the preparation of experimental setups, and time involved in experimentation. This paper presents the CFD validation of L2S2 parabolic trough collector, which was determined by Sandia Laboratory USA in 1994. In this paper temperature variation of HTF (heat transfer fluid) with the variation of mass flow rates are investigated. Further the effects of receiver length and its diameter upon the temperature of HTF and glass cover are also studied. The HTF used here in the CFD model is same as that used in L2S2 parabolic trough collector (PTC) via Dudley, and this fluid is Syltherm-800. The novelty of this paper lies in the fact that it provides a CFD method to optimize a parabolic collector; that is, for a prescribed value of inlet temperature and solar flux with a particular fluid, what will be the optimized value of its geometrical dimensions and mass flow rate.

Keywords L2S2 PTC · HTF · Solar heat flux assignment · Receiver and cover tube diameter · Annular pressure

1 Introduction

Solar thermal energy is abundantly available which can be harnessed for all our civilization needs. In today's world, we are facing a lot of problems due to scarcity and availability of costlier energy. Solar energy is the solution to these problems; as it is inexhaustibly available and hence has received more and more attention as a promising candidate in place of fossil fuels. Out of the various solar collectors, PTC has high heat carrying capacity with respect to the area it acquires. The dimensioning of the receiver and determination of an optimized value of flow rate to extract maximum possible energy for a prescribed value of solar flux is one of the

M. Pandey (✉) · B. N. Padhi
International Institute of Information Technology, Bhubaneswar, India
e-mail: mukundjee27@gmail.com

I. Mishra
Centurion University, Bhubaneswar, India

© Springer Nature Singapore Pte Ltd. 2019
M. Kumar et al. (eds.), *Advances in Interdisciplinary Engineering*, Lecture Notes in Mechanical Engineering, https://doi.org/10.1007/978-981-13-6577-5_29

major thrust areas of research. Guo et al. [1] investigated the performance of PTC with respect to different parameters. Convective heat losses are greatest of all other forms of heat losses from the glass envelop. Also, the exergy loss due bellows are the highest as compared to exergy lost due to receiver at high temperatures. There exists an optimal value of mass flow rate for a prescribed value of exergy efficiency; also, both exergy and thermal efficiency have opposing tendencies with rise in inlet and ambient temperature. Therefore, the selection of different criteria for the optimization of PTC is crucial. Wang et al. [2] investigated that with increase in inlet temperature and velocity of HTF, the circumferential temperature difference (CTD) decreases whereas with the increase in solar flux (DNI) the circumferential temperature difference increases. Also, when compared to glass cover the thermal stresses and deformations are greater at the absorber.

Tzivanidis et al. [3] did a simulation based on Solidworks and validated with numerical model developed in the lab. Moreover, the temperature and heat flux distribution over the receiver were analyzed; also, convective heat transfer coefficient was predicted by this model and was compared with the theoretical model. Angle efficiency modifier was determined to predict optical and thermal efficiencies for different operating conditions. Tang et al. [4] investigated about the various effects on the temperature of different components of PTC with nonuniform heat flux distribution on glass cover. The effects of wind, annular pressure, and glass cover diameter upon the performance of PTC were studied. Fuqiang et al. [5] investigated that cylindrical glass envelop is much more effective as compared to elliptical glass cover. The strength and distribution of heat flux was found to be 32% reduced in case of elliptical glass cover. García-Valladares et al. [6] investigated numerically that the performance of PTC for double pass is more as compared to single pass. Alberti et al. [7] investigated numerically that the performance of coaxial receiver tube is more than that of a single pass cylindrical receiver tube. Sadaghiyani et al. [8] examined the performance of PTC by varying the dimension and position of a plug. The plug was placed in between the flow and within the absorber tube. Ghomrassi et al. [9] investigated the performance of PTC for different dimensions of the receiver tube. Bellos and Tzivanidis [10] investigated the enhancement of thermal efficiency with a star-shaped insert, also they had optimized the performance for different geometrical characteristics. It has been found that increase in dimensional parameters leads to increase in thermal efficiency but there occurs a decrease in pressure drop across the receiver. The thermal efficiency increases by 1% with increase in inlet temperature. Tang et al. [4] examined that decrease in annular gas pressure between glass and receiver tube beyond 0.1 Pa does not lead to further decrease in any heat loss. The effects on the performance of PTC with peripheral heat flux distribution, emissivity of material coating, envelop diameter as well as with inlet velocity of HTF on PTC were investigated. Yılmaz and Aggrey [11] reviewed and have presented the various modifications to PTC; like twisted tape, corrugated receiver, dimpled absorber, wavy tape inserts and unilateral longitudinal vortices which has led to significant increase in the performance of PTC. Thus, in the present study it has been tried to evaluate the performance of the solar parabolic collector with respect to different geometrical parameters and mass flow rate.

2 CAD Model and Numerical Analysis Method

2.1 CAD Model Definition and Meshing

In a sequence of evaluating the emanated data from the simulated outputs, this paper first validates the simulation from the experimental setup. Setup is named as SEGS LS-2 PTC and owned by Sandia National Laboratories (SNL); it was developed by Dudley et al. [12] with Syltherm-800 fluid as the HTF. A 3-D CAD model of the parabolic trough collector is illustrated in Fig. 1.

For the simplification of numerical analysis, the following assumptions are made:

- The heat transfer phenomenon is assumed to be in steady state.
- The optical errors associated by the parabolic reflector are neglected, and there is only convection heat transfer between HTF and the receiver tube. The fully developed condition was presumed within the region bounded by the HTF.

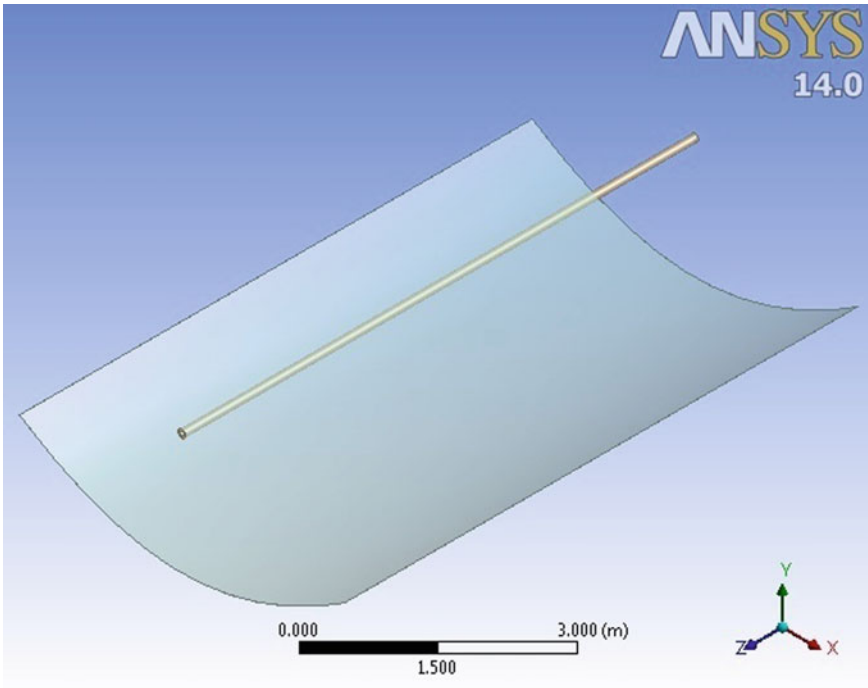


Fig. 1 Parabolic trough collector

- (c) The mode of heat transfer within the annular region of inner surface of glass cover and outer surface of receiver is radiation heat transfer. Heat conduction within tubes and bellows (supporting brackets) is insignificant.
- (d) The HFT is considered to be incompressible and turbulent.
- (e) The working fluid's (Syltherm-800) physical properties are supposed to be dependent upon temperature, and therefore the physical properties are considered to be a polynomial function of temperature.
- (f) The creation of vacuum in the annular region is very difficult, as in fluent there is no way to create vacuum. So, air is considered to be in the annular space provided its physical properties are reduced to 10^{-20} except for the value of specific heat (C_p) whose value is increased by 10^{-20} times.

Figures 1 and 2 shows that the PTC composed of a receiver tube and a concentrating reflector. The concentrating reflector is a curved in the horizontal axis in the form of parabolic geometric which is used for the concentration solar radiation in linear-axis fashion. The receiver tube comprises of a rounded glass cover consisting of a concentric metallic absorber tube coaxial with it; with maintained vacuum in annular space. This metallic absorber tube is painted with a selective material coating so that it can absorb the maximum amount of solar infrared radiations while emitting

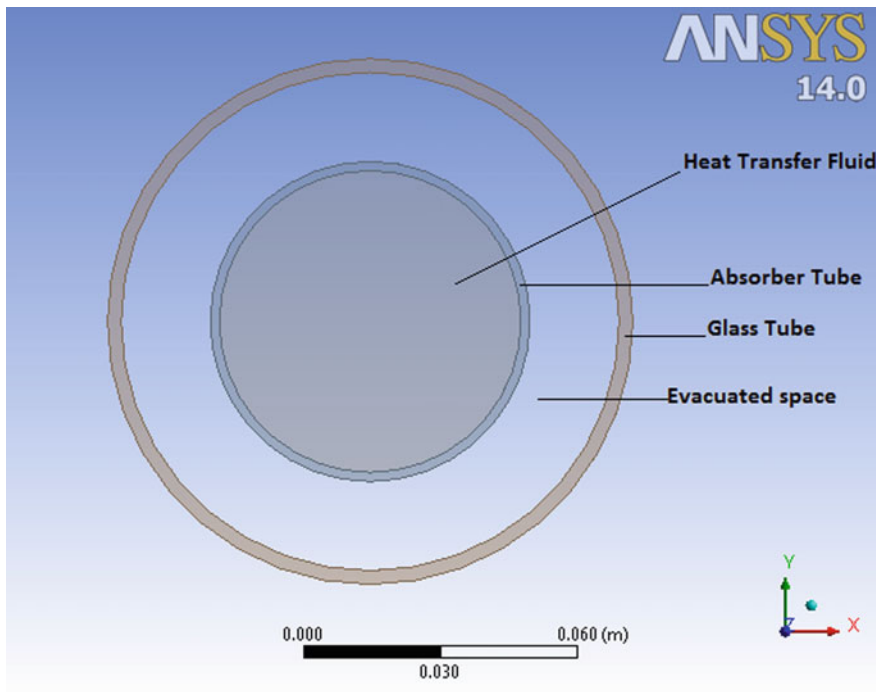


Fig. 2 Collector tube cross section

Table 1 Physical and geometrical parameters of LS-2 PTC collector by SNL

Parameters	Values
Focal length of concentrator	1.84 m
Aperture width of concentrator	5 m
Length of receiver tube	7.8 m
Concentration ratio of PTC	71
Outer diameter of receiver tube	70 mm
Inner diameter of receiver tube	66 mm
Outer diameter of glass cover	115 mm
Inner diameter of glass cover	109 mm
Reflectivity of concentrator	0.93
Transmittance of glass cover	0.95
Absorptivity of receiver	0.96

Table 2 Material specification

Materials	Thermal conductivity (W/m °C)	Specific heat capacity (kJ/kg K)	Density (kg/m ³)
Steel	46	0.25	8030
Glass	1.2	670	2500

a negligible amount of it. All the parameters of LS-2 PTC are entered in Table 1 along with the main material properties in Table 2. In computational fluid dynamics simulation, the ways of generating the meshes are incontrovertible. Meshes are generated by employing an Ansys software mesh generator, a preprocessor associated with the FLUENT. This preprocessor is used only after the creation of geometry in design modular. In fact, the quality of meshing is one of the most important tasks that affect the accuracy of the result to a good extent. The mesh initiated from this system composed of tetrahedral cells. The meshes generated are presented on Fig. 3. This initiated mesh composed of 422,501 cells. The grid sensitivity test was done and three types of meshing grids were applied to check the responsiveness of FLUENT solution. Refinement of grid that was employed during the meshing of the system, which constituted respectively, of 385,001 cells, 422,501 cells, and 712,071 cells as seen in the statistics section of “Details of mesh” window. But the results obtained from second and third meshing give a difference less than 1%, while the profiles obtained with the first meshing were unsatisfactory. Therefore second mesh was chosen as it had less number of elements in comparison to third meshing with the same level of accuracy. The enhanced wall treatment approach is applied in order to create a high resolution in adjacent wall’s interfaces.

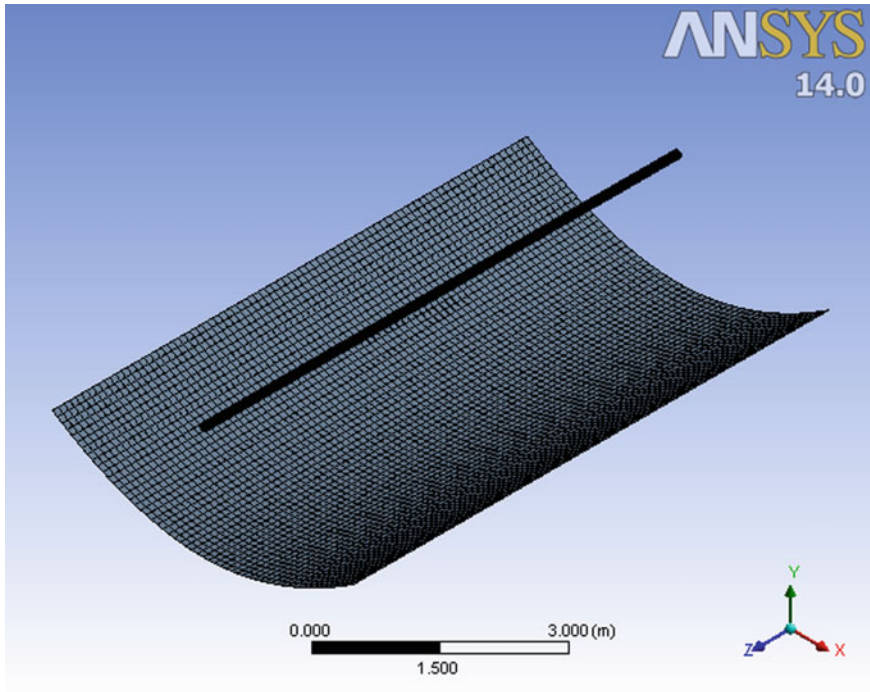


Fig. 3 Mesh generation of solar trough collector

2.2 Boundary Conditions

The boundary conditions are interpreted as below

The subsequent boundary conditions for HTF were considered for inlet and outlet openings of the receiver tube.

Inlet: $\dot{m}_{in} = \dot{m}_z = 0.6782 \text{ kg/s}$ and $\dot{m}_x = \dot{m}_y = 0 \text{ kg/s}$, and $T_{in} = 375.5 \text{ K}$. Outlet: fully developed assumption: $\partial u/\partial x = \partial v/\partial x = \partial w/\partial x = \partial k/\partial x = \partial \varepsilon/\partial x = \partial p/\partial x = \partial T/\partial x = 0$.

Lateral surfaces of the receiver tube and glass envelope were examined as “wall”. The condition “pressure outlet” was applied to the outlet of the receiver tube with both sides annular region was applied as “wall” of adiabatic nature. The operating pressure was chosen as 101,325 Pa, and hence all pressures that were asked in the inlet and outlet boundary conditions were treated as gauge pressure. Here we had applied 101,325 Pa pressures both for inlet and outlet boundary conditions. The outer wall of the receiver tube is applied to solar load condition from Ansys software; “surface to surface” condition was selected. Solar ray tracing option was selected with longitude -117.017281 and latitude 34.895798 of Barstow, CA, USA was entered. The value of total radiation (beam radiation + diffuse radiation) that was used to simulate the sunrise was assumed to be 933 W/m^2 . The HTF used is syltherm-800

and its temperature-dependent physical properties in terms of polynomial functions are listed below.

$$C_p = 0.00178T + 1.107798 \text{ (kJ/kg K)} \quad (1)$$

$$\rho = -0.4153495T + 1105.702 \text{ (kg/m}^3\text{)} \quad (2)$$

$$k = -5.753496 \times 10^{-10} - 1.875266 \times 10^{-4} + 0.1900210 \text{ (W/mK)} \quad (3)$$

$$\mu = 6.672 \times 10^{-13} - 1.566 \times 10^{-3} + 1388 \times 10^{-6} - 5.541 \times 10^{-14} + 8.487 \times 10^{-12} \text{ (Ns/m)} \quad (4)$$

2.3 The Governing Differential Equations

CFD analysis of a particular system necessitates the discretization of distinct conservation laws. For the discretization of the equations, different assumptions were made, that is, flow is static, incompressible, and Boussinesq approach are considered.

Continuity equation

$$\frac{\partial(\bar{\rho}\tilde{u}_i)}{\partial x_i} = 0 \quad (5)$$

$$\frac{\partial(\bar{\rho}\tilde{u}_i\tilde{u}_j)}{\partial x_i} = -\frac{\partial\bar{p}}{\partial x_i} + \frac{\partial}{\partial x_j} \left[\mu \left(\frac{\partial\tilde{u}_i}{\partial x_j} + \frac{\partial\tilde{u}_j}{\partial x_i} - \frac{2}{3}\delta_{ij} \frac{\partial\tilde{u}_k}{\partial x_k} \right) \right] \quad (6)$$

Convective transport expression

$$\left(\frac{\partial y}{\partial x} \right) (\tilde{u}_i\tilde{u}_j) \quad (7)$$

Energy conservation expression

$$\frac{\partial(\bar{\rho}\tilde{u}_j\tilde{T})}{\partial x_j} = \frac{\partial}{\partial x_j} \left[\frac{\lambda}{C_p} \frac{\partial\tilde{T}}{\partial x_j} - \overline{\rho u'_j T''} \right] + S_h \quad (8)$$

Boussinesq approximations, for various types of natural convection flow problems we can get faster solutions by using this approximation. This implies density as constant function in each of solved equations excluding for buoyancy terms in the momentum expression. But here in this paper, the solution deals with a value of density which is a function of temperature.

$$(\rho - \rho_0)g \simeq -\rho_0\beta(T - T_0)g \quad (9)$$

$$\rho = \rho_0(1 - \beta\Delta T) \quad (10)$$

$$\text{Re} = \frac{UD}{\nu} \quad (11)$$

where the constant value of density of HTF is ρ_0 , thermal expansion coefficient of HTF is β , and temperature of the HTF is T_0 . Using Boussinesq consideration the following expression is obtained

$$\rho = \rho_0(1 - \beta\Delta T) \quad (12)$$

Anyhow the density (ρ) is to be eliminated from buoyancy expression, and this assumption is authentic provided that the change in real density is insignificant, remarkably the Boussinesq assumption is justifiable when $\beta(T - T_0) \ll 1$.

But it was determined numerically that considering density as a polynomial function of temperature yields the simulated results in more accurate form as compared to Boussinesq approximation.

2.4 Numerical Simulation Setup

After meshing was done in the preprocessing unit of Ansys-FLUENT, then post-processing requirements had to be completed to get accurate results in solution step. Under the “set-up” section there is the first section named “General”, in which pressure-based solver with the steady-state condition was selected. The velocity under this subsection was chosen as absolute. Then, under the section of “Models”, energy equation was selected as one. Under the sub-section of the viscous model k-epsilon was selected, and then standard condition was selected under k-epsilon. Enhanced wall treatment was chosen under the sub-section of near-wall treatment; then thermal effects and viscous heating were selected. Then different materials are selected and created with the help of a material library. Then, under cell zone conditions, zones are specified either in terms of solid or in terms of fluid and that is based upon its physical state. After that boundary conditions are adjusted as discussed in Sect. 2.2; like inlet, outlet, and walls with a prescribed value of solar flux. After that in the mesh interfaces section, proper interfaces were created by selecting two consecutive interfaces at a time. Then in the reference section, the commute from was chosen as inlet fluent and under the reference zone fluent was selected. Then, under solution methods, second-order upwind was selected within the kinetic and momentum terms. Before going to run a calculation, standard initialization was selected by choosing all zones.

Table 3 Result validation and authentication Ref. [12]

Case study	DNI (W/m ²)	Mass flow rate (kg/s)	Inlet temperature (K) experimental	Outlet temperature (K) experimental	Outlet temperature (K) simulation	Efficiency % experimental	Efficiency % numerical	ΔT %
1	933.7	0.6782	375.5	397.5	403.2025	73.09	73.026	1.434
2	928.3	0.7205	471	493	487.33	73.09	73.15	1.15
3	909.5	0.81	524.2	542.9	538.304	73.12	73.17	0.846

3 CFD Simulation and Authentication

The purpose of this analysis is to framework a CFD simulation in a step-wise manner. Ansys-FLUENT is used for allocation of heat flux as one of the boundary conditions around the glass envelope. Surface-to-surface method is used under the solar load method, and the tracing of solar radiations is generated by Ansys-FLUENT software. The outcome of CFD simulation is compared with Dudley et al. experimental conclusions. Table 3 shows the comparison between numerical results and experimental values. $\Delta T\%$ was chosen as a criterion of comparison and is defined as below.

$$\Delta T\% = \frac{T_{ex} - T_{nu}}{T_{ex}} \times 100\% \quad (13)$$

4 Results and Discussion

4.1 Variation of Temperature with Mass Flow Rate

Figure 4 specifies that the outlet temperature of HTF decreases with an increase in mass flow rate, but the increase in mass flow rate leads to increase in convective heat transfer coefficient and it can be seen from Fig. 5. As it is clear that the increase in mass flow rate leads to increase in velocity; the HTF will get less time for interacting with the metallic absorber tube. Hence, here there are two factors which play an important role in the prediction of outlet temperature; one is the convective heat transfer coefficient and other is the velocity of HTF. With increased value of convective heat transfer coefficient and less time of interaction with the receiver tube; the temperature of HTF decreases from 0.2 to 0.6 kg/s of mass flow rate. As from 2 to 0.6 kg/s of mass flow rate the time-interaction factor supersedes the convective heat transfer factor. But from 0.6 to 0.7 kg/s of mass flow rate the temperature of HTF increases, and this happens only due to reason that convective heat transfer plays an important role in it. Figures 4 and 5 shows that increase in mass flow rate

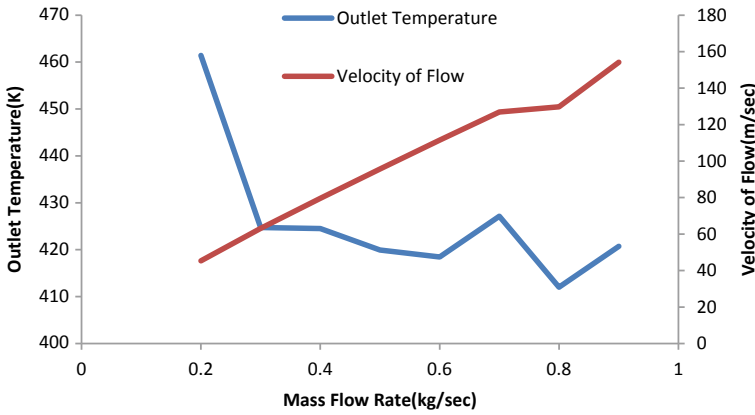


Fig. 4 Outlet temperature and velocity versus mass flow rate

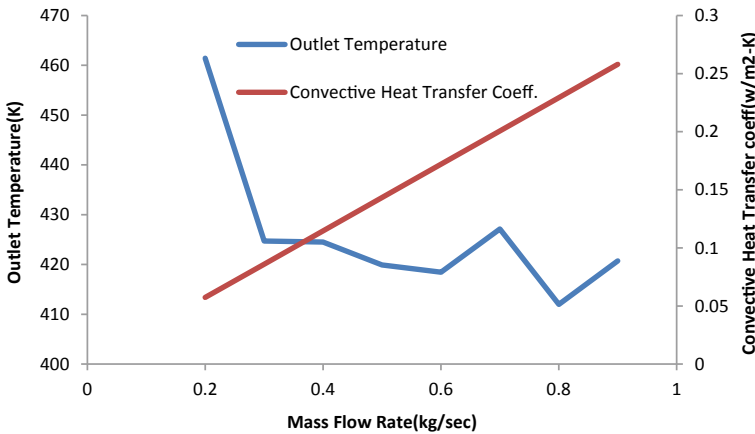


Fig. 5 Outlet temperature and convective heat transfer coefficient versus mass flow rate

also leads to increase in velocity of the HTF but increase in velocity have a negative effect upon temperature increment of HTF. Increase in velocity tends to decrease the time of contact between the absorber and the HTF; and due to this after a mass flow rate of 0.7 kg/s the velocity factor surpasses the effect of convective heat transfer coefficient to the mass flow rate of 0.81 kg/s, as convective heat transfer coefficient remains almost constant from the mass flow rate of 0.7 kg/s to a value of 0.81 kg/s.

Therefore, the mass flow rate of 0.7 kg/s was chosen as the optimum value because beyond it the outlet temperature again decreases. Figure 6 shows that with the flow of fluid through the receiver the temperature of the fluid increases up to certain maximum value and then gradually decreases till outlet is reached; this happens only due to reason that with travel of the HTF into receiver length the fluid gains the temperature which in turn increases the velocity and heat transfer coefficient of

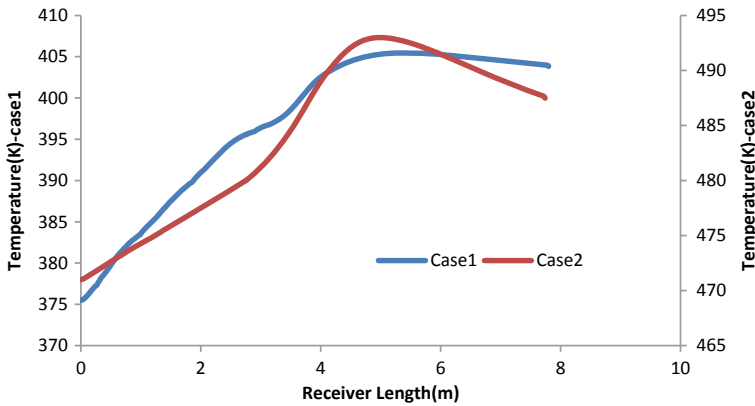


Fig. 6 Variation of temperature with receiver length

the fluid. But increase in velocity leads to decrease in outlet temperature whereas increase in heat transfer coefficient leads to an increase in outlet temperature; and here up to 4.3 m the HTF has gained the heat then due to increased heat transfer coefficient it starts losing heat to the absorber, and thus heat is lost from absorber to the glass cover as well as to ambient through radiation. This leads to a decrease in the temperature of HTF from 4.3 m length onwards. Here case 1 represents for syltherm-800 and case 2 for therminol-vp.

4.2 Effects of Internal Diameter

The convective heat transfer coefficient and velocity both decrease with an increase in the diameter of the receiver as shown in Fig. 7, but still the outlet temperature of the HTF increases with increase in diameter; this is only due to reason that the lateral surface area of the tube increases and due to this there occurs in an increase of the concentrated heat flux on the lower side and direct solar heat flux on the upper side. Thus, it is favoring the increase of outlet temperature of the fluid.

With an increase in diameter, there is an increase in temperature of the HTF as shown in Fig. 8, at critical radius there will be maximum heat transfer and therefore at a diameter of 0.071 m the temperature of HTF is 418.5465 K which is maximum of the temperature ranges. As from diameter range of 0.066–0.07 m the temperature of HTF increases; this is only due to reason that with an increase in diameter leads to an increase in lateral surface area. Due to this, there will also be an increase in the radiation losses to glass through the steel receiver. But after an increase in radius from 0.071 there is a decrease in temperature of HTF, this is only due to the critical radius factor; that is as the radius increases beyond the critical radius there will be decrease in heat transfer through the receiver to HTF, and due this there will be radiation heat

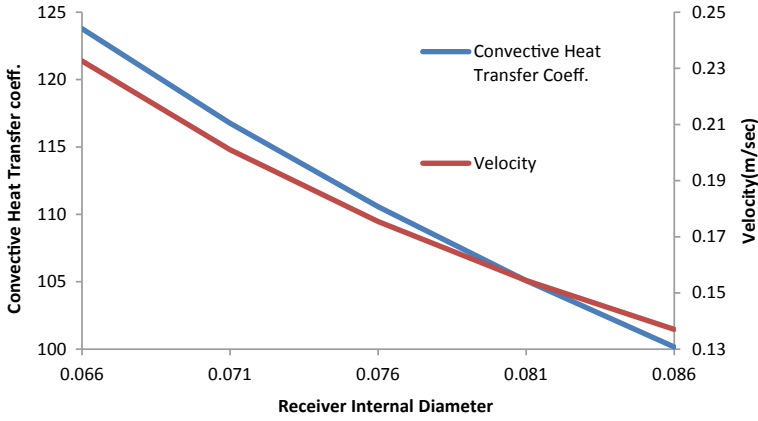


Fig. 7 Convective heat transfer coefficient and velocity versus receiver internal diameter

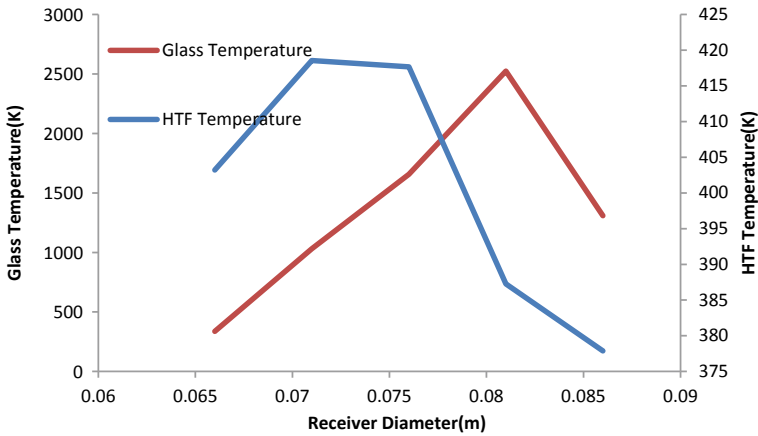


Fig. 8 Glass temperature and velocity versus receiver internal diameter

losses from receiver to the glass. Therefore, the temperature of the glass rises up from the receiver diameter of 0.071 m onwards to a diameter of 0.081 m, and then beyond a receiver diameter of 0.81 m it decreases because as the receiver diameter increases the lateral surface of the receiver shifts from the focus of the parabola. Due to the low concentration of solar radiation, the HTF temperature reduced as compared with values at other diameters; therefore, as the heat gain is reduced due to shifting from the focus, the radiation losses to the glass is also reduced.

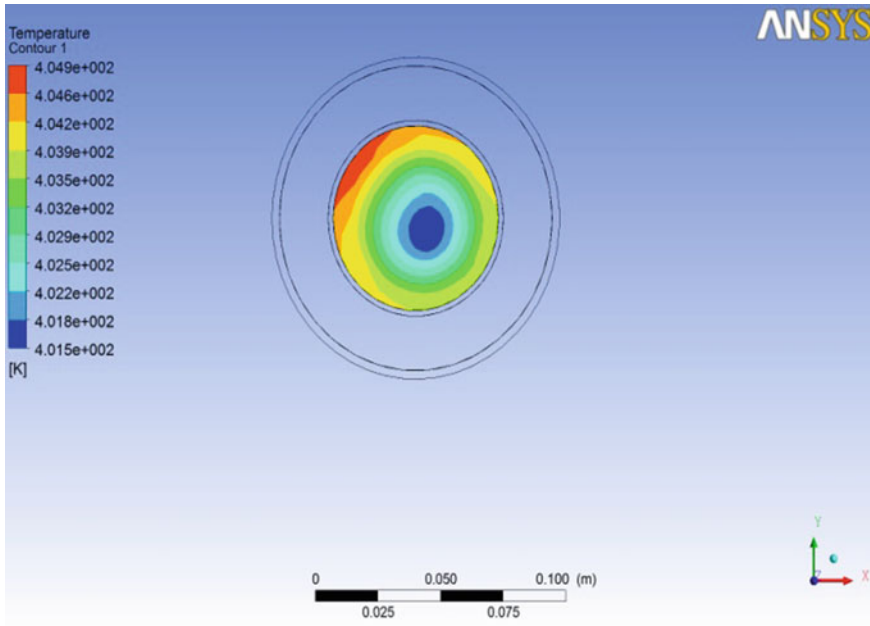


Fig. 9 Temperature contour of HTF at outlet

4.3 Temperature Variation in Cross Section

Figure 9 shows the variability in temperature at outlet along the cross section, it can be seen that the temperature is maximum at the outer circumference and is decreasing towards the center. However, there is an abnormal increase in temperature which is shown by a red patch, this is only due to natural convection and density difference; as hot less viscous fluids go upwards while the cold viscous fluid comes down. This happens because the high concentration of solar flux impinges on the bottom side of the receiver tube, due to focusing of parabolic rays towards the line focus of the parabolic concentrator; therefore, higher solar flux is available at the bottom part of the receiver tube as compared to the top part it; and therefore, it is the main cause of natural convection currents in the z -direction along the cross section.

Here in Fig. 10 it can be seen that the temperature of the glass is maximum at the bottom than at the top of the glass tube, this is only due to a higher concentration of solar flux in the lower half of the receiver than at the top. As the temperature of the vacuum cannot be defined therefore the temperature in Fig. 11 is shown by 1 K.

From Fig. 12 it can be seen that with a rise in inlet temperature of HTF there will be a decrease in temperature difference ($\Delta T = \text{outlet temperature of HTF} - \text{inlet temperature of HTF}$) of the fluid. This happens only because with low HTF temperature there will be more heat transfer from the absorber to HTF and therefore this causes an increase in the temperature difference of HTF.

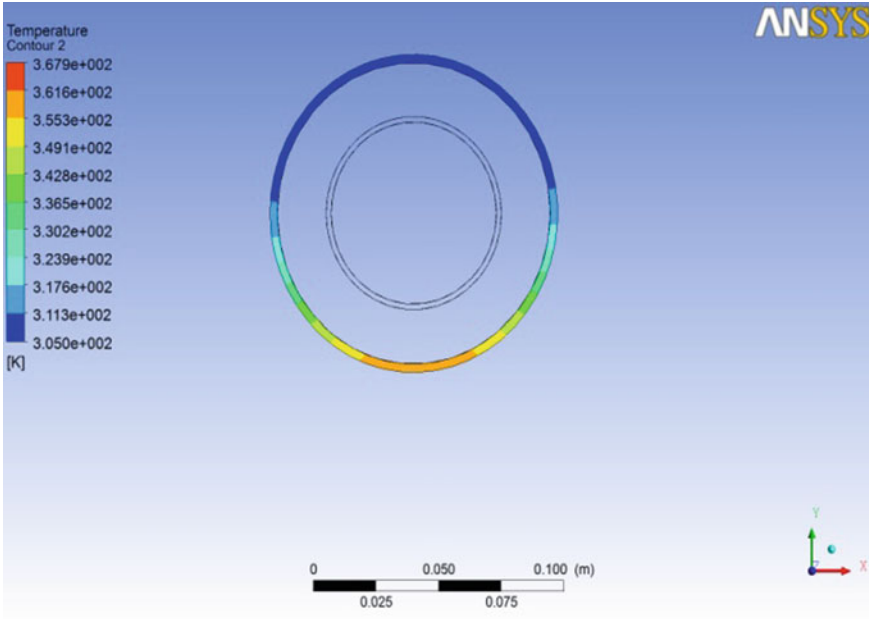


Fig. 10 Temperature contour of glass

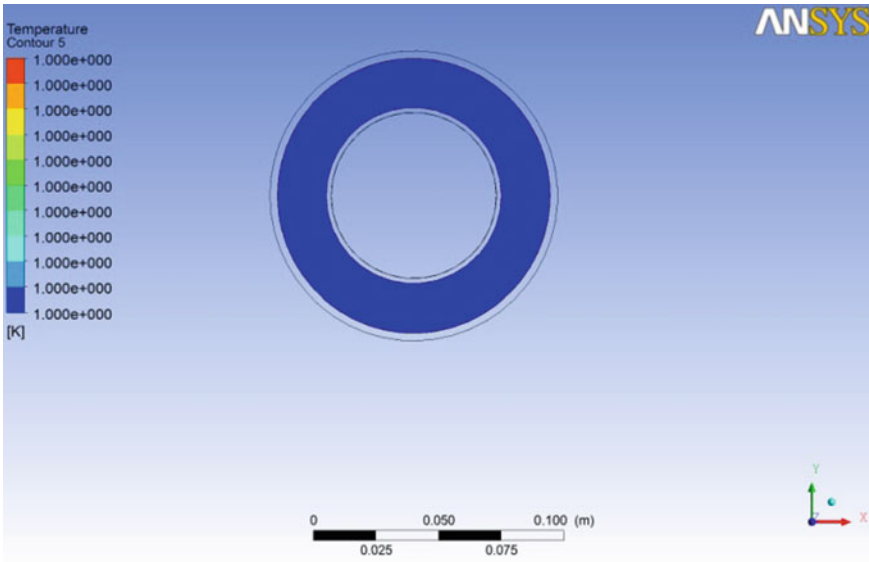


Fig. 11 Temperature contour of vacuum

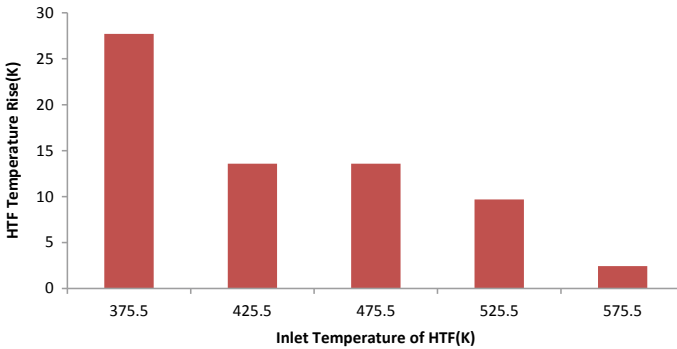


Fig. 12 Variation in difference of outlet and inlet temperature with inlet HTF temperature

5 Conclusion

Both velocity and convective heat transfer play a crucial role in the determination of outlet temperature of HTF. Here the optimum value of mass flow rate for a prescribed value of inlet temperature (375.5 K) and solar heat flux (933.7 W/m^2) was 0.6782 kg/s . With an increase in mass flow rate; velocity of flow and convective heat transfer coefficient both increases. But the convective heat transfer coefficient has positive while velocity has a negative effect on the outlet temperature of HTF. Thus, at a particular value of mass flow rate, there will be the occurrence of the maximum value of HTF temperature. The temperature of HTF increases with receiver length, but for a particular value of mass flow rate there will be a certain value of receiver length up to which the temperature of HTF increases; this happens only due to reason that with travel to receiver length the fluid gains the temperature which in turn increases the velocity and heat transfer coefficient of the fluid. But increase in velocity leads to decrease in outlet temperature whereas an increase in heat transfer coefficient leads to increase in outlet temperature; and here up to 4.3 m the HTF has gained the heat and then due to increased heat transfer coefficient it started losing heat to the absorber. With increase in diameter both velocity and heat transfer coefficient decrease but there will be an increase in the outlet temperature of HTF; this is only due to reason that the lateral surface area of the tube increases and due to this there occurs an increase of the concentrated heat flux on the lower side and direct solar heat flux on the upper side. Thus, it is favoring the rise in temperature of the HTF. The temperature contour of the cross section of HTF-outlet is having different variations of temperature region, this happens only due to density variation as a result of natural convection in the z -direction. With an increase in HTF inlet temperature, there will be a decrease in the temperature difference between outlet and inlet HTF.

This happens because of the decrease in heat transfer rate with an increase in inlet temperature of HTF as the temperature difference between the inlet and absorber of receiver decreases. Further research may be to develop receivers of different geometrical cross sections and to study its effect upon the performance of the PTC.

Appendix

Nomenclature		Greek symbols	
A_c	Aperture area of collector	ρ	Density (kg/m^3)
d	Differential	μ	Dynamic viscosity (Pa s)
D	Diameter	ε	Turbulent dissipation rate or emissivity
I	Direct normal irradiance (W/m^2)	β	Thermal expansion coefficient (K^{-1})
k	Thermal conductivity of HTF ($\text{W/m}^2\text{K}$)	Subscripts	
C_p	Specific heat capacity of HTF (kJ/kg K)	in	Inlet parameters
\dot{m}	Mass flow rate (kg/s)	o	Outlet parameters
x, y, z	Cartesian coordinates	HTF	Heat transfer fluid

References

- Guo J, Huai X, Liu Z (2016) Performance investigation of parabolic trough solar receiver. *Appl Therm Eng* 95:357–364. <https://doi.org/10.1016/j.applthermaleng.2015.11.035>
- Wang Y, Liu Q, Lei J, Jin H (2015) Performance analysis of a parabolic trough solar collector with non-uniform solar flux conditions. *Int J Heat Mass Transf* 82:236–249. <https://doi.org/10.1016/j.ijheatmasstransfer.2014.11.055>
- Tzivanidis C, Bellos E, Korres D, Antonopoulos KA, Mitsopoulos G (2015) Thermal and optical efficiency investigation of a parabolic trough collector. *C Stud Therm Eng* 6:226–237. <https://doi.org/10.1016/j.csite.2015.10.005>
- Tang Z, Zhao XP, Li ZY, Tao WQ (2017) Multi-scale numerical analysis of flow and heat transfer for a parabolic trough collector. *Int J Heat Mass Transf* 106:526–538. <https://doi.org/10.1016/j.ijheatmasstransfer.2016.09.002>
- Fuqiang W, Jianyu T, Lanxin M, Chengchao W (2015) Effects of glass cover on heat flux distribution for tube receiver with parabolic trough collector system. *Energy Convers Manag* 90:47–52. <https://doi.org/10.1016/j.enconman.2014.11.004>
- García-Valladares O, Velázquez N (2009) Numerical simulation of parabolic trough solar collector: improvement using counter flow concentric circular heat exchangers. *Int J Heat Mass Transf* 52:597–609. <https://doi.org/10.1016/j.ijheatmasstransfer.2008.08.004>
- Alberti F, Crema L, Bozzoli A (2012) Heat transfer analysis for a small-size direct-flow coaxial concentrating collector. *J Sol Energy Eng* 134:041009–041009-7. <https://doi.org/10.1115/1.4007297>
- Sadaghiani OK, Pourmahmoud N, Mirzaee I (2013) Numerical simulation coupled with MCRT method to study the effect of plug diameter and its position on outlet temperature and the efficiency of LS-2 parabolic trough collector. *J Sol Energy Eng* 135(4):041001–041001-7. <https://doi.org/10.1115/1.4024475>

9. Ghomrassi A, Mhiri H, Bournot P (2015) Numerical study and optimization of parabolic trough solar collector receiver tube. *J Sol Energy Eng* 137(4):051003-051003-10. <https://doi.org/10.1115/1.4030849>
10. Bellos E, Tzivanidis C (2018) Investigation of star flow inserts in a parabolic trough collector. *Appl Energy* 224:86–102. <https://doi.org/10.1016/j.apenergy.2018.04.099>
11. Yılmaz IH, Aggrey M (2018) Modeling simulation and performance analysis of parabolic trough solar collectors: a comprehensive review. *Appl Energy* 225:135–174. <https://doi.org/10.1016/j.apenergy.2018.05.014>
12. Dudley V, Kolb G, Sloan M, Kearney, D (1994) SEGS LS2 solar collector—test results. Report of Sandia National Laboratories. Report no. SANDIA94-1884

Accepting Renewable Technologies for Waste Management Promoting Sustainable Living Among Rural Habitats



F. Rajemahadik Chandrasen and A. Ghaste Akash

Abstract This paper elaborates on need of improvement in rural settings and its benefits after use of anaerobic digestion as renewable energy. The five villages under investigation have a human population of 12,217 and livestock of 8,141, which includes buffalo, goats, and hen. Among, livestock total waste discharged by buffalos is around 33 tonnes, goats discharge 3.5 tonnes, and hens per day discharge 400 kg of waste. Similarly, human population discharges near to 4 tonnes of excreta daily. This paper proposes a perspective for rural habitats reducing excess burden of sanitation, energy, fertilizers, and on health impacts. From the estimation of human excreta and livestock, both can generate biogas of 2060 m³ daily using renewable techniques. Similarly, accepting improved sanitation may reduce the risk of human health after excretion and emission of air pollutant, lowering premature deaths. Practicing anaerobic digestion, accounts to fulfill fertilizer requirement of N, P and K of approximately 74 ha of land per year. Furthermore, air pollutants such as carbon monoxide (CO), sulfur dioxide (SO₂), oxides of nitrogen (NO_x), carbon dioxide (CO₂), methane (CH₄), and particulate matter (PM_{2.5} and PM₁₀) could reduce to a greater extent. Biogas a renewable form can gain additional carbon credits to the rural community. Paper tries to present an overall positive viewpoint of such study in rural habitats of developing countries.

Keywords Biogas · Sanitation · Human health · Fertilizer · Economics

1 Introduction

In India, rural settings are still underdeveloped. Among 1,028,610,328 of total population of India, 72.18% reside in rural [1]. In addition, the population growth rate for India was 1.148% during the year 2016, suggests a decrease [2]. A scarcity of

F. Rajemahadik Chandrasen (✉)

Department of Civil Engineering, Sanjay Ghodawat Polytechnic, Kolhapur, India
e-mail: crajemahadik@gmail.com

A. Ghaste Akash

Department of Mechanical Engineering, Sanjay Ghodawat Polytechnic, Kolhapur, India

© Springer Nature Singapore Pte Ltd. 2019

M. Kumar et al. (eds.), *Advances in Interdisciplinary Engineering*, Lecture Notes in Mechanical Engineering, https://doi.org/10.1007/978-981-13-6577-5_30

319

primary needs of inhabits in rural is still a challenge. Among all amenities, energy proves as the most confirmatory requirement, which directly connects with the economy and growth of country [3]. Recently in the year 2005 around 412 million of the Indian population was not having accesses to electricity [3]. Consequently, in villages, biomass is a primary source of fuel for day to day activities [4]. Apart from electricity, kerosene as a major fuel source is used for lightening in around 43.3% of rural habitats of India [5]. Rural and urban household both depend on fuel sources like kerosene and similar products to satisfy daily needs [6]. The use of alternative fuel to overcome household needs demonstrate after insufficient quality and electricity supply [7]. Studies suggest more than seven hundred million of the population in rural India consume biomass for cooking [8], along with kerosene [9]. Eventually, firewood of around 64%, 13% of crop residue and a similar quantity of dung are used as cooking fuel [10]. In addition, only 9% of economically stable households of rural India use commercially available fuels [9]. Apart from energy, open discharge of human feces is prominent in rural, people are still unaware of the risks of exposed excretion on their health [11]. In addition, appropriate sanitation facilities encompass good hygiene, safe water, good health and economic development [12]. Due to improper sanitation, surface water bodies get polluted, where fecal coliform count can reach up to 20,000 MPN/100 mL of the sample [11]. This may be cause for oral and communal diseases outbreak. Moreover, biomass burning can also cause health impact among rural. The major cause is deprived quality of indoor air (IAQ) in the kitchen and near vicinity depends on ventilation [13]. Poor quality of indoor air is the fourth major cause in the world for premature deaths [14] and respiratory diseases, caused after the release of harmful air pollutant by burning of solid fuel in the traditional stove or chulas [15]. Such crude practices increase the economic burden and reduce life expectancy [16]. Presently, active thinking on sustainable development using human excreta and livestock waste is in promotion [17]. The anaerobic treatment process can prove a better alternative in rural with upright technology [18]. This study demonstrates the potential of waste to energy, impacts of waste generated and its extension toward economy and health.

2 Materials and Methods

2.1 Study Area

Villages located are within 50 km toward south of major city Kolhapur and around 30 km distance from national highway (NH-4). These five villages share common boundaries and are closely grouped with each other. The rural settings selected for the study are as follows Benikre, Haladi, Haldvade Karanjivane, and Doulatwadi. Figure 1, shows the location ($16^{\circ} 37'N$ Latitude and $74^{\circ} 27'E$ Longitude) of the selected study site.

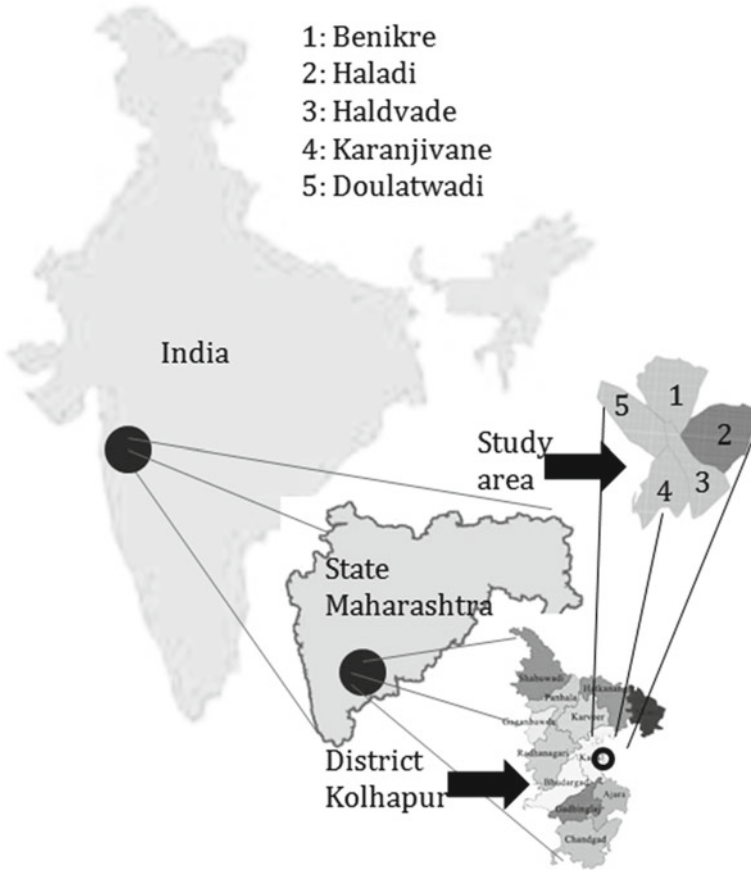


Fig. 1 Location of the study area

2.2 Data Collection

After identification of site, data was collected on the population and livestock of villages for study. The population of five villages is 12,217 among 1,432 households. The livestock of 2,214 buffalos, 1,927 of goats and 4,000 of hens were noted. Table 1, shows data on human, habitat, and livestock. Data required for calculations and assumptions scripted in this paper are from the literature survey.

Table 1 Details of village population and livestock

Name of village	Population	Households	Buffalo	Goats	Hens
Haldwade	2019	212	408	321	1000
Haladi	3952	413	650	421	1000
Benikre	2099	227	396	310	0500
Karanjivane	3044	431	443	451	1000
Doulatwadi	1103	149	317	424	0500
Total	12,217	1432	2214	1927	4000

2.3 Calculations

Biogas from human excreta:

$$Q_{WP} = P \times F_P \quad (1)$$

where Q_{WP} is Quantity of Waste (kg/C/day), P is human population (capita) and F_P is considered as 0.4 factor for waste/head day [19].

$$G_{YP} = Q_{WP} \times F_{PG} \quad (2)$$

where G_{YP} is Gas Yield (m^3 /day) and F_{PG} is considered as 0.028, factor for gas evolution/head day [19, 20].

Biogas from Buffalo waste:

$$Q_{WB} = P_B \times F_B \quad (3)$$

where Q_{WB} is Quantity of Waste (kg/Buffalo/day), P_B is Buffalo population (capita), and F_B is considered as 15, factor for waste generation/head day [19].

$$G_{YB} = Q_{WB} \times F_{BG} \quad (4)$$

where G_{YB} is Gas Yield (m^3 /day), Q_{WB} is Quantity of Waste (kg/Buffalo/day), and F_{BG} is considered as 0.04 (factor for gas evolution/head day) [21].

Biogas from Goat waste:

$$Q_{WWG} = P_G \times F_G \quad (5)$$

Whereas Q_{WWG} is Quantity of Wet Waste (kg/Goat/day), P_G is Goat population (capita) $\times F_G$ is considered as 1.8 (factor for wet waste generation head day) [19].

$$Q_{DWG} = Q_{WWG} \times F_{GG} \quad (6)$$

where Q_{DWG} is Quantity of Dry Waste (kg/Goat/day) and F_{GG} is considered as 0.4 (factor for dry waste generation/head day) [22].

$$G_{YG} = Q_{DWG} \times F_{GGY} \quad (7)$$

where G_{YG} is Gas Yield (m^3/kg of dry mass day) and F_{GGY} is considered as 0.35–0.61 (factor for gas evolution/head day) [23].

Biogas from Hen waste:

$$Q_{WH} = P_H \times F_H \quad (8)$$

where Q_{WH} is Quantity of Waste (kg/Hen/day), P_H is Hen population (capita) and F_H is considered as 0.18 (factor for waste/head day) [19].

$$G_{YH} = Q_{WH} \times F_{HG} \quad (9)$$

where G_{YH} is Gas Yield (m^3/kg day) and F_{HG} is considered as 0.011 (factor for gas evolution/head day) [19].

Calculation for air pollutant emissions:

$$E_P = Q_F \times F_E \quad (10)$$

where E_P is Emission of Pollutants, Q_F is the quantity of fuel consumed and F_E is the emission factor.

3 Results and Discussion

3.1 Biogas Generation from Human Excreta

Biogas generated from five villages sharing common boundaries is $136.82 m^3/day$ (Eqs. 1 and 2). Furthermore, Table 2 estimates population discharging wet waste, dry waste, and yield for biogas. The methane (CH_4) fraction in biogas is assumed as 60, and 40% of CO_2 [24]. Whereas, gas has the potential to generate $82.1 m^3$ of methane (CH_4) fraction. Where, density of methane is $0.75 kg/m^3$, which equals to 61 kg of CH_4 . This is equivalent of either 907.93 kWh of electricity or 22,447.5 kg of LPG annually. Moreover, proper maintenance and adoptions of modern technology can increase the yield of biogas for future needs [16].

Table 2 Details of gas yield generated from human waste

Name of village	Haldvade	Haladi	Benikre	Karanjivane	Doulatwadi
Population (C)	2019	3952	2099	3044	1103
Gas yield (m ³ /kg day)	22.61	44.26	23.51	34.09	12.35

Table 3 Details of biogas from buffalo waste

Name of village	Halawade	Haladi	Benikre	Karanjivane	Doulatwadi
Buffalo (C)	408	650	396	443	317
Gas yield (m ³ /kg day)	244.8	390	237.6	265.8	190.2

Table 4 Details of biogas from goat waste

Name of village	Halawade	Haladi	Benikre	Karanjivane	Doulatwadi
Goats (C)	321	421	310	451	424
Gas yield (m ³ /kg day)	100.1	132.62	97.65	142.1	131.27

Table 5 Details of biogas from hen waste

Name of village	Halawade	Haladi	Benikre	Karanjivane	Doulatwadi
Hens (C)	1000	1000	500	1000	5000
Gas yield (m ³ /kg day)	1.98	1.98	0.99	1.98	0.99

3.2 Biogas Generation from Livestock

Livestock such as buffalo, goat, and hens assessed for energy are according to Tables 3, 4 and 5. These Tables 3, 4, and 5 provide data of the quantity of livestock, wet waste, dry waste, and biogas yield produced daily among five villages. Biogas from five rural livestock shows that buffalo can generate 1,328.4 m³, goat's about 603.74 m³ and hens estimates about 8 m³ of biogas daily. This totals to 1,940.14 m³ of biogas daily or 7,08,151.1 m³ annually (Eqs. 3–9). Where methane fraction in biogas can be estimated up to 1,377.5 m³/day or 502787.28 m³ annually [23].

3.3 Impact of Crude Practices in Rural

Air pollution:

During day-to-day activities kerosene, dung cake, agricultural residues, and firewood which are burnt, emits air pollutants [carbon monoxide (CO), oxide of nitrogen (NO_x), Sulfur dioxide (SO₂), volatile organic compounds (VOC), and particulates (PM)] [25–27] including greenhouse gases such as CO₂ and CH₄ leading to human health issues [28]. During the 1990s, a total of 59% of fuelwood, dung cakes around

18%, and crop residue of 23%, was burnt in rural [29]. Majorly, kerosene as sources of fuel is consumed about 5 L/Household/month or 4.1 kg/Household/month [30], also 340 kg of firewood/Household/months [31]. Similarly, 113 kg/household/month of dung cakes and 69 kg/household/month of crop residue is consumed [32] in rural. The burning of fuels emit pollutants depending on the rate of consumption and type of fuel sources used. Five of villages which are under investigation have estimated potential to emit 1.77% of NO_x, 0.62% of SO₂, 82.80% of CO, 5.84% of VOC, 2.50% of PM₁₀ and 1.97% of PM_{2.5}, respectively; 1.44% of CO₂ and 3.06% of CH₄ of total weight percent of emission per year (Eq. 10) (Tables 6 and 7). These estimated values of pollutants are based on the consideration that, out of 1432 rural households, 6.5% use kerosene, 52.5% use firewood, and 9.8% use dung cake in their daily activities [5].

From Tables 6 and 7, a monthly requirement of fuel source and emissions after usage of estimated fuel source from rural houses, is calculated based on previous assumptions. Furthermore, carbon monoxide (CO) emission has the highest share of 82.80%, after methane (CH₄) and the lowest is sulfur dioxide (SO₂) emissions. In addition, greenhouse gases such as carbon dioxide (CO₂) and methane (CH₄) liberated with concentrations of 5.62×10^3 tonnes/year and 11.96×10^3 tonnes/year, respectively.

Health impacts: excretion and biomass burning

Human and animal waste discharge are responsible to introduce pathogens in the surrounding environment [36]. Impacts of these pathogens on humans and animals are caused either from drinking water, food [37, 38] or through carriers (e.g. flies). Nath (2003) reported, around 60–80% of diseases caused by fecal contamination and unhealthy sanitation. Health impact and deaths are prominent in undeveloped habitats around rural because of improper sanitation [39]. Therefore, proper sanitation can minimize health hazards in cost-effective way of promoting sustainable development [40, 41]. The possibility of risk count may decrease to 1.63 billion because of improved sanitation [42] from 2.5 billion of causalities suffering from diarrhea, help elevating economic growth [43]. In addition, most of the Indian rural communities use kerosene and biomass for cooking on low efficient stoves [44]. Such practices are a reason for 0.6 million of premature death per year in India [45]. From studies, rural population leads to a risk of respiratory and cardiovascular problems because of the high concentration of PM₁₀, PM_{2.5}, and CO [46]. Furthermore, emission of SO₂, CO₂, CH₄, VOC, NO_x, PM₁₀, and PM_{2.5} creates an unhealthy environment for the individual within the vicinity for a maximum duration of emitted pollutants [47]. Moreover, women in India have chronic lung disease, asthma, and bronchitis, who cooked food on biomass fuel in homemade mud stove [48]. These above considerations may lead to a reduction in life expectancy of adults and children's, enforcing economic crunch on the rural population. Thus, biogas can mitigate lower emissions environment compared to the burning of biomass.

Table 6 Type of fuel burnt and emission factors

Fuel source	Total consumption (kg/month)	NO _x	SO ₂	CO	VOC	PM ₁₀	PM _{2.5}	CO ₂	CH ₄
Kerosene	381.63	2.3 [33]	4 [33]	1.8 [33]	0.5 [33]	0.3 [33]	0.3 [35]	2.41 [18]	NA
Fierwood	255,612	2.2 [25]	0.7 [25]	99.3 [34]	7 [33]	3 [33]	2.1 [35]	1.83 [18]	3.9 [18]
Dung cakes	15857.96	0.8 [25]	1.4 [25]	99.3 [18]	7 [18]	3 [18]	6.5 [35]	NA	NA

NA not available

Table 7 Form of fuel burning and emissions concentrations

Fuel source	Total consumption (kg/month)	NO _x	SO ₂	CO	VOC	PM ₁₀	PM _{2.5}	CO ₂	CH ₄
Kerosene	381.63	877.75	1526.5	686.93	190.815	114.5	114.5	919.7	NA
Fierwood	255612	562,346	178928.4	25,382,272	1,789,284	766,836	536,785	467,770	996,887
Dung cakes	15857.96	12,686	22201.14	1574695.5	111,006	47573.88	103,077	NA	NA
Emissions (kg/month)		575,911	202656.04	26,957,654	1900480.82	814524.38	639,977	468,690	996,887
Emission (10 ³ tonne/year)		6.91	2.43	323.49	22.81	9.77	7.68	5.62	11.96

NA not available

Fertilizer usage

Biogas slurry is considered equal to dung added in a biogas plant, having nutrients such as 1.4–1.8% of Nitrogen (N), 1.1–1.7 of Phosphorous (P), and 0.8–1.3% of Potassium (K) on dry weight basis [49, 50]. Consumption of such nutrient is widely practiced in agriculture as fertilizer. In India, $N = 58.7 \times 10^3$ tonnes and $P = 6.9 \times 10^3$ tonnes was consumed in the year 1950–51, whereas in year 2013–14 it increased the usage to $N = 16750.1 \times 10^3$ tonnes, $P = 5633.5 \times 10^3$ tonnes and $K = 2098.9 \times 10^3$ tonnes [51]. The dry matter to the weight of slurry is assumed as 7% and rest of 93% is water [52]. A single biogas unit of 1 m^3 requires 25 kg dung and an equal amount of slurry is discharged [53, 54]. Therefore, 1 m^3 biogas digester estimates to produce a slurry of 25 L/day. Furthermore, 24.5 of N g, 19.25 g of P and 14 g of K nutrients are generated from 1 m^3 of biogas unit per day [18]. Therefore, 1923.27 m^3 of biogas is generated daily from five villages, achieves a potential to produce 47.12 kg of N, 37.02 kg of P, and 27 kg of K. This accounts to 17.19 tonnes of N, 13.5 tonnes of P and nearly 10.0 tonnes of K, annually.

3.4 Economic Benefits

Fertilizer

The fertilizer demand increased from 100.33 kg/ha/year in 2002 to 170.98 kg/ha/year in 2014 in India [55]. This consumption will rise in near future for maximum production of food. This may mitigate the requirement of fertilizer from slurry of biogas. Based on the literature, nutrient available in form of fertilizer can be utilized for approximately 74 ha of land per year among five villages [56]. This practice can give an economic benefit of the amount of \$10,782 USD/year, mitigating 22,347 kg of CO_2 equivalent per kg of N produced and 4,680 kg of CO_2 equivalent per kg of P and K produced [18]. Similarly, for the production of fertilizer from biogas slurry of livestock can gain US\$270/year as carbon credits among five villages.

Biogas:

In concern to liquid waste generated and disposed within rural requires major attention. Moreover, accepting sustainable technologies such as anaerobic digesters for treatment of liquid waste, estimates 1923.27 and 136.82 m^3 of biogas daily from livestock and human excreta, respectively. If the collection efficiency of dung is considered as 50% for livestock, it can generate 961.63 m^3 of biogas per day. This totals to 1098.45 m^3 of biogas per day from five villages investigated. From scenario, 1432 households required 381.63 kg of kerosene, 25,5612 kg of firewood, and 15,857.96 kg of dung cakes per month (Table 6). A 1 m^3 of biogas may replace 14.17 kg of kerosene, 105 kg of firewood, and nearly 370 kg of dung cakes of their monthly requirement [57]. The study estimates around 26.57 m^3 of biogas could substitute, demand for kerosene among 6.5% of total household in rural for a month. Similarly, demand for firewood exchanged with 683.45 m^3 of biogas for 52.5% of total households

depending on wood as fuel per month. A monthly dung cake requirement may fulfill by replacing 44 m³ of biogas for the remaining 9.8% of rural households. Therefore, the total demand for month accounts to 754.02 m³ of biogas. The fact is energy demand estimated is just 2.28% of biogas generated per month from five rural habitats. The overall calculation seems to have the potential to generate daily 2350.68 kWh of electricity from 97.71% of remaining biogas [58]. Biogas can save around US\$160/month on kerosene [59] and prevent from burning of 255.612 tonnes of firewood and 15.85 tonnes/month of dung cakes. In addition, biogas mitigates indoor and outdoor air pollution reducing the emission of greenhouse gases. In this case study, NO_x can be reduced by 575.91 tonnes/month, SO₂ by 202.65 tonnes/month, CO by 26957.65 tonnes/month, VOC by 814.6 tonnes/month, PM₁₀ by 814.6 tonnes/month and PM_{2.5} by 573.37 tonnes/month. An opportunity to gain carbon credits by mitigating CO₂ and CH₄ of 468.68 tonnes/month and 996.88 tonnes/month, respectively. This sustainable process can gain up to US\$4686.8/month from CO₂ and US\$209334.8/month from CH₄ as carbon credits for rural settings [18].

Health:

Accepting biogas in the backyard can improve the health of family by reducing the risk of diseases such as worms, bacterial, and viral infections caused after daily excretion [60]. Furthermore, biogas can decrease the risk of health caused by burning of primary fuels, of women's, children's and adults at habitats [61]. Among family members in rural, who spend a maximum of their time in the kitchen are females between 16 and 60 years spend 5 h, children's below 15 years spend 1.4 h and male spend 2.4 h in the vicinity of the cooking area [62]. Use of primary fuel can cost US\$1.5 to US\$10 per month per family for breathing and eye-related diseases [63]. Besides, economic impact due to illness in 1982 was around US\$34/head/year [64]. Sustainable thinking can help improve losses (economic, health and death) occurred after improper sanitation and erroneous in the usage of fuels in rural habitat. Total cost could reduce to 60% after accepting biogas technology [63].

4 Conclusions

Five villages investigated can gain major profits by accepting biogas. Active thinking and expression of interest in initial investment in a rural setting can develop a better model for future crisis. From the above studies, it is clear; if such models are developed in developing countries, it may reduce environmental, economic and health impacts. This will also reduce individual investment in fertilizer and energy. Initial investment to start a model can benefit everyone including climate change. From the above investigation, it concludes that a total of 1098.45 m³ of biogas per day is generated among five villages. The overall energy demand of five villages, which is satisfied using kerosene, wood, and/or cow dung is just 2.28% of total biogas generated per month. Similarly, around 2350.68 kWh of electricity can be generated daily from remaining 97.91% of biogas. This has the potential to reduce Tonne of

gas released from primitive practices. Such practice of accepting advance technology can reduce the burden on the health of family and economy. Furthermore, from biogas units among five villages can produce fertilizer to satisfy the demand of 74 ha per year. The overall analysis of such a model can give a win-win situation for rural India.

References

1. Census homepage (2011) http://www.censusindia.gov.in/vital_statistics/SRS_Reports.html. Last accessed on 16 Mar 2018
2. WHO Homepage (2017) <http://data.worldbank.org/indicator/SP.POP.GROW?end=2016&locations=IN&start=1960>. Last accessed on 29 Aug 2017
3. Frauke U, René B, Henri M (2009) Energy for rural India. *Appl Energy* 86:S47–S57
4. Kumar V, Aggarwal R, Baweja P, Sharma R, Gupta R (2016) A study on energy consumption pattern in fatehpur block of western himalayan state. *Br J Renew Energy* 01(02):0001–0004
5. Census homepage (2018) <http://censusindia.gov.in/Metadata/Metada.htm>. Last accessed on 16 Mar 2018
6. Bhattacharyya C (2006) Energy access problem of the poor in India: is rural electrification a remedy? *Energy Policy* 34(18):3387–3397
7. Sadhan M, Chanakya H, Dasappa S (2009) Evaluation of various energy devices for domestic lighting in India: technology, economics and CO₂ emissions. *Energy Sustain Dev* 13:271–279
8. Antonette D, Narasimha M (2004) LPG as a cooking fuel option for India. *Energy Sustain Dev* 1(8):31
9. Bhatt B, Sachan M (2004) Firewood consumption pattern of different tribal communities in Northeast India. *Energy Policy* 32:1–6
10. Tupkari S, Satish K, Thakre G, Shukla B, Aryan P (2016) DME blended LPG as a cooking fuel option for Indian household: a review. *Renew Sustain Energy Rev* 53:1591–1601
11. Nath K (2003) Home hygiene and environmental sanitation: a country situation analysis for India. *Int J Environ Health Res* 13:S19–S28
12. Mara D, Lane J, Scott B, Trouba D (2010) Sanitation and Health. *PLoS Med* 7(11):e1000363. <https://doi.org/10.1371/journal.pmed.1000363>
13. Chaya C, Rufus E, Rajesh B, Kyra S, Kirk S (2007) Impact of improved cook stoves on indoor air quality in the Bundelkhand region in India. *Energy Sustain Dev* 11(2):33–44
14. Johannes G, Chris G, Simon S, Paul L (2017) Producing a CO₂-neutral clean cooking fuel in India- Where and at what cost? *Int J Hydrogen Energy* 42(30):19067–19078
15. Agustin A, Jan B, Bjørn L, Fernanda N (2010) The economic costs of indoor air pollution: new results for Indonesia, the Philippines, and Timor-Leste. *J Nat Resour Policy Res* 2(1):75–93
16. Roshan M, Man-Hoe K (2017) Experimental study of power generation utilizing human excreta. *Energy Convers Manag* 147:86–99
17. Antonio Z, Marcos R, Cesar D, Norberto F (2010) Potential and cost of electricity generation from human and animal waste in Spain. *Renew Energy* 35:498–505
18. Pathak H, Jain N, Bhatia A, Mohanty S, Navindu G (2009) Global warming mitigation potential of biogas plants in India. *Environ Monit Assess* 157:407–418
19. Nagamani Ramasawamy K (1999) Biogas production technology: An Indian perspective. *Curr Sci* 77(1):44–56
20. Arunaachalam M (2017) Feasibility, health and economic impact of generating biogas from human excreta for the state of Tamil Nadu, India. *Renew Sustain Energy Rev* 69:59–64
21. Satish D, Vijaykumar P, Rajeshwar M (2013) Performance evaluation of fixed dome type biogas plant for solid state digestion of cattle dung. *Karnataka J Agric Sci* 26(1):103–106

22. Hemstock L, Hall D (1995) Biomass energy flows in Zimbabwe. *Biomass Bioenerg* 8(3):151–173
23. Tauseef S, Premalatha M, Tasneem A, Abbasi S (2013) Methane capture from livestock manure. *J Environ Manage* 117:187–207
24. Joan C, Aaron A, Forbis S, Marc D (2015) Anaerobic digestion of undiluted stimulant human excreta for sanitation and energy recovery in less-developed countries. *Energy Sustain Dev* 29:57–64
25. Gadi R, Kulshrestha UC, Sarkar AK, Garg SC, Parashar DC (2003) Emissions of SO₂ and NO_x from biofuels in India. *Tellus. Series B, Chem Phys Meteorol* 55:787–795. <https://doi.org/10.1034/j.1600-0889.2003.00065.x>
26. Parashar C, Gadi R, Mandal K, Mitra P (2005) Carbonaceous aerosol emissions from India. *Atmos Environ* 39:7861–7871. <https://doi.org/10.1016/j.atmosenv.2005.08.034>
27. Venkataraman C, Habib G, Eiguren-Fernandez A, Miguel H, Friedlander K (2005) Residential bio-fuels in South Asia: carbonaceous aerosols emissions and climate impacts. *Science* 307:1454–1456. <https://doi.org/10.1126/science.1104359>
28. Pathak H, Singh R, Bhatia A, Jain N (2006) Recycling of rice straw to improve crop yield and soil fertility and reduce atmospheric pollution. *Paddy Water Environ* 4(2):111–117. <https://doi.org/10.1007/s10333-006-0038-6>
29. Reddy M, Venkataraman C (2002) Inventory of aerosol and sulphur dioxide emissions from India: part II-biomass combustion. *Atmos Environ* 36:699–712
30. Ibrahim R, Preeti M, Ram P, Phool S (2005) Availability of kerosene to rural households: a case study from India. *Energy Policy* 33:2165–2174
31. Amulya R (1982) Rural energy consumption patterns—a field study. *Biomass* 2:255–280
32. Akash J, Prodyut B (2013) Fuelwood dependence around protected areas: a case of Suhelwa Wildlife Sanctuary, Uttar Pradesh. *J Human Ecol* 42(2):177–186
33. Hobson M, Thistlethwaite G (2003) Emission factors programme task 7, review of residential and small scale commercial combustion sources. Department for Environment, Food and Rural Affairs (DEFRA), United Kingdom
34. Houghton J, Ding Y, Griggs D, Noguer M, Van Der Linden P, Dai X, Maskell K, Johnson C (2001) Climate change 2001—the scientific basis: 3rd assessment report, Cambridge University Press, New York
35. Shekar R, Venkataraman C (2000) Atmospheric optical and radiative effects of anthropogenic aerosol constituents from India. *Atmos Environ* 34:4511–4523. [https://doi.org/10.1016/S1352-2310\(00\)00105-9](https://doi.org/10.1016/S1352-2310(00)00105-9)
36. Dadswell V (1993) Microbiological quality of coastal waters and its health effects. *Int J Environ Health Res* 3:32–46
37. Tat G, Richard H (2003) Pathogen survival in swine manure environments and transmission of human enteric illness—a review. *J Environ Qual* 32:383–392
38. Shannon M, Troy S, Valerie H, Samuel F, Jerzy L (2006) Detection of human-derived fecal pollution in environmental waters by use of a PCR-based human polyomavirus assay. *Appl Environ Microbiol* 72(12):7567–7574
39. Montgomery M, Elimelech M (2007) Water and sanitation in developing countries: including health in the equation. *Environ Sci Technol* 41(1):17–24
40. Dellström E (2005) A psychosocial analysis of the human–sanitation nexus. *J Environ Psychol* 25(3):335–346
41. Mara D (2013) Pits, pipes, ponds—and me. *Water Res* 47(7):2105–2117
42. Fewtrell L, Kaufmann B, Kay D, Enanoria W, Haller L (2005) Water, sanitation, and hygiene interventions to reduce diarrhoea in less developed countries: a systematic review and meta-analysis. *Lancet Infect Dis* 5:42–52
43. Bill and Milinda gates foundation homepage (2018) <https://docs.gatesfoundation.org/Documents/wsh-strategy-overview.pdf>. Last accessed on 16 Mar 2018
44. Singh D, Ranu G, Mandal T, Saud T, Saxena M, Sharma S (2013) Emissions estimates of PAH from biomass fuels used in rural sector of indo-gangetic plains of India. *Atmos Environ* 68:120–126

45. Smith R (2002) Indoor air pollution in developing countries: recommendations for research. *Indoor Air* 12:198–207
46. Sean S, Andrew A, Adamu W, Jo S (2014) Commentary: switching to biogas—what effect could it have on indoor air quality and human health? *Biomass Bioenerg* 70:125–129
47. Aaron C, Ross A, Bart O, Kiran P, Michal K, Nino K, Kersten G, Arden P, Isabelle R, Jonathan S, Kirk S (2005) The global burden of disease due to outdoor air pollution. *J Toxicol Environ Health, Part A* 68:1–7
48. Bhargava A, Khanna N, Bhargava K (2004) Exposure risk to carcinogenic PAHs in indoor-air during biomass combustion whilst cooking in rural India. *Atmos Environ* 38:4761–4767
49. Subrian P, Annadurai K, Palaniappan P (2000) *Agriculture: facts and figures*. Kalyani publisher, New Delhi
50. Roy N, Finck A, Blair G, Tandon S (2006) *Plant nutrition for food security a guide for integrated nutrient management*. Food and Agriculture Organization (FAO) of the United Nations, Rome
51. Government of India (Ministry of Agriculture) (2015) *Agricultural statistics at a glance 2014*, 1st edn. Oxford University Press, New Delhi
52. Sandeep K, Lal M, Mahesh M, Shakeel K (2015) Biogas slurry: source of nutrients for eco-friendly agriculture. *Int J Extens Res* 2(42–46):1–5
53. Jatinder S, Sooch S (2004) Comparative study of economics of different models of family size biogas plants for state of Punjab, India. *Energy Convers Manag* 45:1329–1341
54. Bhattacharya S, Jana C (2009) Renewable energy in India: historical developments and prospects. *Energy* 34:981–991
55. Datamarket homepage (2018) <https://datamarket.com/data/set/13d3/fertilizer-consumption-kilograms-per-hectare-of-arable-land#!ds=13d3!fe9=j.4v&display=line>. Last assessed 26 Apr 2018
56. Aladakatti Y, Palled Y, Chetti M, Halikatti S, Alagundagi S, Patil P, Patil V, Janawade A (2012) Effect of nitrogen, phosphorus and potassium levels on growth and yield of stevia (*Stevia rebaudiana* Bertoni). *Karnataka J Agric Sci* 25(1):25–29
57. Ramachandra T (2008) Geographical information system approach for regional biogas assessment. *Res J Environ Sci* 2(3):170–180
58. Kibaara S, Chowdhury S, Chowdhury SP (2012) A thermal analysis of parabolic trough CSP and biomass hybrid power system. In: *IEEE PES, 2012 transmission and distribution conference and exposition (T&D) on 2012*, pp 1–6. Orlando, FL, USA. (2012). <https://doi.org/10.1109/tdc.2012.6281660>
59. IOCL Homepage (2017) <https://www.iocl.com/TotalProductList.aspx>. Last assessed on 11 Sep 2017
60. Tom B, Michael T (2011) History and future of domestic biogas plants in the developing world. *Energy Sustain Dev* 15:347–354
61. Hari K, Alok B (2009) Biogas: a promising renewable technology and its impact on rural households in Nepal. *Renew Sustain Energy Rev* 13:2668–2674
62. Vinod J, Chandra A, Bhattacharya M (2009) Household energy consumption pattern and socio-cultural dimensions associated with it: a case study of rural Haryana, India. *Biomass Bioenerg* 33:509–512
63. Krishna P (2012) Cheaper fuel and higher health costs among the poor in rural Nepal. *Ambio* 41:271–283
64. Verma B, Srivastava R (1990) Measurement of the personal cost of illness due to some major water related diseases in an Indian rural population. *Int J Epidemiol* 19(1):169–176

Optimizing the Performance of Catalytic Converter Using Turbulence Devices in the Exhaust System



Tanmay Agrawal, Vivek Kumar Banerjee, Basant Singh Sikarwar and Mohit Bhandwal

Abstract Turbulence flow of exhaust gases improves the efficiency of the catalytic converter in the exhaust system of vehicle. In literature, additional devices are used for creating the turbulence. However, they reduce the engine performance by inducing additional backpressure. In this work, various configurations of turbulence generating device are considered for optimizing the performance of the exhaust system of vehicle such as maximum conversion efficiency of the catalytic converter with minimum back pressure at engine exhaust system. In this context, various configuration device for generating turbulence is attached before the catalytic converter for measuring back pressure and analysing the exhaust of four-cylinder 1400-cc diesel engine. The flow of exhaust is visualized using commercial software Fluent for knowing effect of device configuration on the flow pattern. It has been found that the turbulence device with swirl blade configuration is more effective in improving the conversion efficiency of the catalytic converter at low back pressure as compared to other configuration of devices. Therefore, the swirl blade turbulent device is effective and efficient.

Keywords Catalytic converter · Turbulence · CFD · Emissions

1 Introduction

The automobile industry grows rapidly every year and so is the need for technology that can help in reducing the harmful emissions of gases from the vehicles [1–5]. Among the various methods of reducing the harmful emission, the catalytic conversion is one of the methods which are used in the automobile exhaust system [6]. In this method, emissions of engine pass through two simple chemical reaction process to reduce NO_x and the oxidation of hydrocarbons and carbon monoxide in the presence of platinum, palladium, and rhodium as catalysts [7]. The chemical reactions used in catalytic converter device are

T. Agrawal (✉) · V. K. Banerjee · B. S. Sikarwar · M. Bhandwal
Department of Mechanical Engineering, Amity University Uttar Pradesh,
Noida, Uttar Pradesh, India
e-mail: tanmayag1993@gmail.com



Its construction is such that it uses the crystalline ceramic and metal monolith substrate which also carries a wash-coat. This helps to improve the conversion efficiency, more surface area for reaction to occur, and excellent thermal shock resistance capability. Carrier metal is made up of $\gamma\text{Al}_2\text{O}_3$, but it also has been developed tactically with stabilizers like La, Si, BA, etc. And for improvement in the catalytic activity by providing high surface area [8].

As far as the technology of catalytic converter seems a great deal for controlling emissions, it also comes with a few drawbacks like cold starting and pressure loss. The problem of cold starting is basically the time required by the catalytic converter to achieve its light-off temperature which is around 500 °C. However, the exhaust gas temperature of the diesel is 600–700 °C, still it takes few minutes to warm-up for its 50% effectiveness [9]. This warm-up time is crucial for upcoming government norms because in this warm-up window alone the catalytic converter fails to pass the emission test. The other major problem with the catalytic converters is the pressure loss which affects the engine performance by reducing the engine horsepower and increasing the fuel usage, the research shows that with the pressure loss of around 1000 Pa the power loss is about 300 W which itself is a great deal to overcome [10]. Hence, there should be the trade-off between the total pressure loss and the geometry of the substrate. It has been found that the pressure loss is associated with the two major components which are the substrate itself and the inlet and outlet manifolds, i.e., The inlet diffuser, thus the engineers have to optimize the geometry such that it could provide the high surface area with minimum pressure drop [11]. The current geometry of the catalytic converter includes the honeycomb structure and the cell wall thickness and the cell density, which is expressed in cells per square inch has been optimized, there is no way the catalytic converters can have very high cell densities because it may lead to the high surface area but also it may cause a high pressure drop and also increase in the manufacturing cost. Researchers have also employed performance evaluation criteria (PEC) to perform comparative analysis on different cell shapes and densities [12]. It has been found after emission testing that the square shape cell, however, provides more surface area is better than a hexagonal shape cell, but with slightly more pressure drop, but the square shape cell dominates the hexagonal structure in case if the surface area made equivalent for both. So if the trend between the different geometries is to be seen, it can be seen as square > hexagonal > sinusoidal > triangular [13–16]. Another type of research has been taken is related to a reduction in the pressure drop by using the different type of diffusers, Wenland produces the enhance diffuser heads

that show the reduction pressure drop and with that Hirata had reported that the 22% reduction in the backpressure can be successfully achieved by putting the flow deflector inside the diffuser head and this is better than the reduction provided by the enhance diffuser head [17]. In this study, the objective is to develop an alternate method to increase the surface area covered by the gas. This is done by virtue of providing turbulence in the exhaust gas at the inlet of the catalytic converter with the help of uniquely designed device that can be easily fit in the exhaust pipe and creates swirl in the flow, therefore, increasing the overall efficiency of the system. The three different turbulence generating configuration, i.e., Swirl contour, swirl venture, and swirl blade have been studied on a four-cylinder diesel engine and Computational Fluid Dynamics (CFD) solver Ansys fluent, for optimizing the device to maximize the efficiency of the catalytic converter with minimum back pressure. This comparative analysis is based on the back pressure developed by each of the devices and the effect of its geometry on the incoming flow. The pressure contour and vector plots have been generated to visualize the effect of different geometrical configurations in the flow pattern through the device. It was found that the swirl contour configuration yields maximum back pressure and have minimal effect in the performance of the catalytic converter, whereas the swirl blade induces minimum backpressure and have maximum effect on the conversion efficiency of the catalytic converter.

2 Methodology and Methods

To understand the effects of each configuration on the catalytic converter and the engine performance such as brake power and fuel consumption, the experiment is performed on a four-cylinder 1400 cc, 47.5 BHP TATA Indica V2 LS diesel engine. Figure 1 shows the schematic diagram of the experimental setup and the photograph of the setup. The setup has digital pressure gauge PG801C to measure the back pressure of the engine exhaust system. The pressure gauge is tightly fixed at the inlet of the device and sealed with the epoxy resin adhesive compound. The experiment is performed at the full throttle of engine and the readings of the gauge are noted for each of the configurations of device. In addition, the experiment is also performed at the constant 5000 RPM for measuring the emissions of hydrocarbons, carbon monoxide and oxides of nitrogen. A gas analyzer AVL DGAS 444 is used for these measurements. All the experiments are carried out at the same environmental conditions (room temperature = 30 °C and relative humidity is 50%).

The flow pattern of exhaust gases through the various configuration device is simulated using commercial software Ansys Fluent. Figure 2 shows the CAD model of each configuration of the turbulence generating device which is developed in Catia V5 software. It shows that the geometry of each device has its own tendency of generating swirl in flow by creating an obstruction in the flow path. Therefore, each of them generates some pressure loss. In order to simulate and calculate the pressure loss by each device, the turbulence modelling was done in ANSYS Fluent. The software ICEM CFD is used for generating the mesh. Reynolds Average Navier

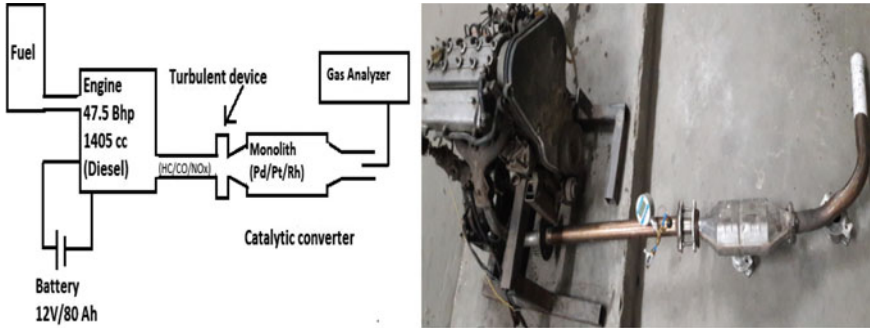


Fig. 1 Schematics diagram and image of the experimental setup

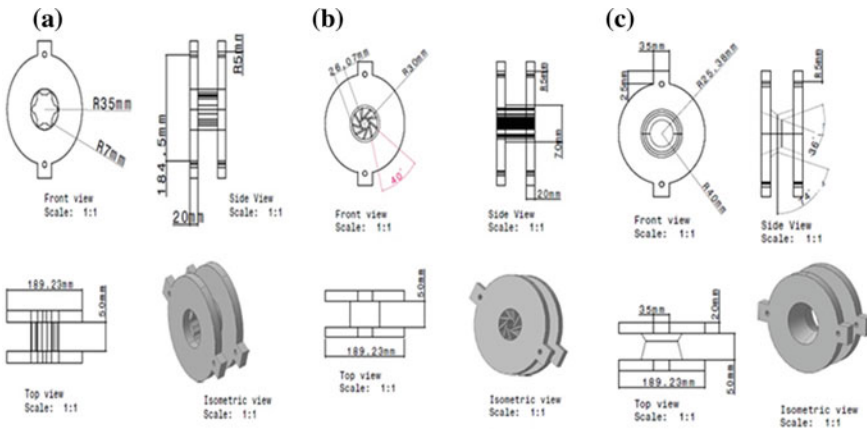


Fig. 2 The schematics of a swirl contour, b swirl blade and c swirl venturi respectively

Stokes Equations (RANS) and Renormalization Group (RNG) based K-ε is used with standard wall treatments to capture the effect of the geometry near the flow path [18, 19]. The air assumes as work fluid in place of exhaust gases. Flow is considered as incompressible since the Mach number is very small and acoustic waves has a negligible impact; also the temperature change of the system is not significant, hence, fluid properties will remain constant. The governing equations are as follows:

$$\nabla \cdot u = 0 \tag{5}$$

$$\rho \left(\frac{\partial u}{\partial t} + u \cdot \nabla \cdot u \right) = -\nabla p + \mu \nabla^2 u + S \tag{6}$$

Here in this equation t is time, u is the velocity, ρ is the density, p is the pressure, μ is the viscosity and S is the momentum source term. The transport equations for RNG K-ε model is

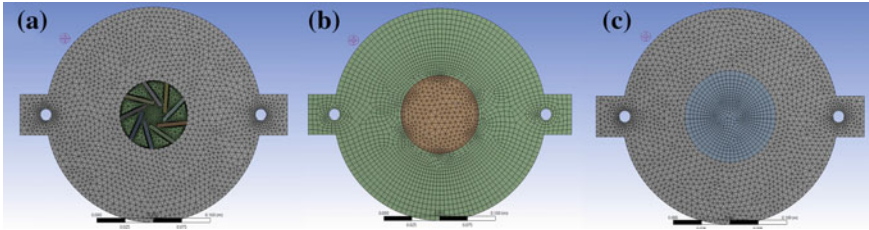


Fig. 3 Meshed structure of a swirl blade, b swirl contour and c swirl venturi

$$\frac{\partial}{\partial t}(\rho k) + \frac{\partial}{\partial x_i}(\rho k u_i) = \frac{\partial}{\partial x_j} \left(\alpha_k \mu_{\text{eff}} \frac{\partial k}{\partial x_j} \right) + G_k + G_b - \rho \varepsilon - Y_m + S_k \tag{7}$$

$$\frac{\partial}{\partial t}(\rho \varepsilon) + \frac{\partial}{\partial x_i}(\rho \varepsilon u_i) = \frac{\partial}{\partial x_j} \left(\alpha_\varepsilon \mu_{\text{eff}} \frac{\partial \varepsilon}{\partial x_j} \right) + C_{1\varepsilon} \frac{\varepsilon}{k} (G_k + C_{3\varepsilon} G_b) - C_{2\varepsilon} \rho \frac{\varepsilon^2}{k} - R_\varepsilon + S_\varepsilon \tag{8}$$

$$R_\varepsilon = \frac{C_\mu \rho \eta^3 \left(1 - \frac{\eta}{\eta_0} \right) \varepsilon^2}{1 + \beta \eta^3} \tag{9}$$

where, $\eta = \frac{S_k}{\varepsilon}$, $\eta_0 = 4.38$, $\beta = 0.01$.

Here, in Eqs. (7)–(9) ‘ k ’ is turbulent kinetic energy, ‘ ε ’ is kinetic energy dissipation rate, ‘ G_k ’ is generation of kinetic energy due to mean velocity gradient, ‘ G_b ’ is generation of kinetic energy due to buoyancy, ‘ Y_m ’ is fluctuation dilation incompressible turbulence to overall dissipation rate, ‘ σ_k ’ and ‘ σ_ε ’ are the Prandtl numbers for ‘ k ’ and ‘ ε ’ respectively, ‘ S_k ’ and ‘ S_ε ’ are the user source terms and ‘ $C_{1\varepsilon}$ ’, ‘ $C_{2\varepsilon}$ ’, ‘ $C_{3\varepsilon}$ ’ are the constants. Equations (7)–(9) are solved numerically using Finite Volume Method (FVM). In this method, the entire flow is discretized into tetrahedral elements in unstructured form as shown in Fig. 3. This method stores the solved variable in the centre of the grid cells, i.e. Control volume, therefore, to know the values of the variables at the faces of the grid cells the interpolation scheme of second-order upwind is used. For calculating the diffusive fluxes or velocity derivatives the gradient of solution variables is calculated by the least square cell-based method. Pressure-Based Coupled Solver (PBCS) algorithm is used for pressure–velocity coupling. This algorithm solves the pressure and momentum simultaneously for most of the single-phase flows and considerably reduces the computational time with high accuracy. The details of the algorithm are given in FLUENT document [20].

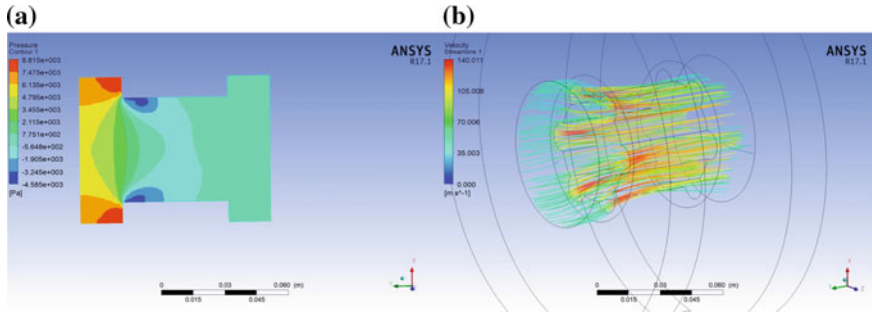


Fig. 4 a Pressure contour of the swirl contour device, b velocity vector of swirl contour device

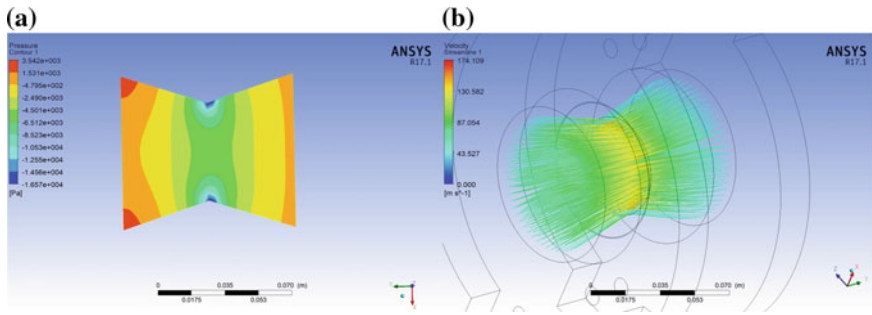


Fig. 5 a Pressure contour of swirl venture device, b velocity contour of the swirl venture device

3 Results

The flow pattern of the exhaust gases is analysed through the turbulent device using the commercial solver FLUENT and the result is represented in the form of the pressure contour and velocity vector plots. It has been found that the pressure contour shows significant development of the back pressure, i.e. 8.851 kPa at the inlet of the device as shown in Fig. 4a, because the geometric configuration of the device is causing great hindrance in the flow path of the gas and forcing it to move through the narrower region. Hence, generating backflow of the gases as shown in Fig. 4b. A similar event has been captured by the swirl venture device as shown in Fig. 5a, b. Therefore, it also generates heavy back pressure of 3.352 kPa in the exhaust system. Whereas, the case of the swirl blade configuration turbulent device shows least developed in the back pressure, i.e. 1.327 kPa as shown in Fig. 5a. This is due to the fact that the path of the gasses is not changed significantly due to the device configuration as shown in the vector plot in Fig. 5b thus, allowing the gases to move through the device freely.

The analysis of the back pressure is performed on the four-cylinder diesel engine exhaust system and the results are obtained from the readings on the digital pressure gauge with the engine running at full throttle at room temperature and pressure. The

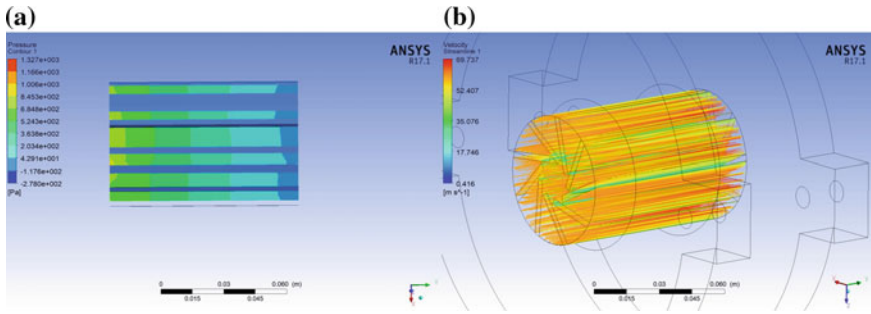


Fig. 6 **a** Pressure contour of swirl blade device, **b** velocity vector of swirl blade device

results show that the least back pressure is experienced by the swirl blade configuration, i.e. 1.4449 kPa, while the other configurations, i.e. swirl contour and the swirl venture experienced 9.307 and 3.723 kPa respectively. The graphical comparison of the back pressure due to each of the configuration is shown in Fig. 6.

The data obtained from the back pressure analysis of the diesel engine is then used to obtain the effect on the brake power of the engine using the equations

$$\text{Brake Power, BP} = \frac{PLAnK}{60,000} \tag{10}$$

$$P = P_{\text{eff}} - P' \tag{11}$$

where ‘ P_{eff} ’ is the mean effective pressure, ‘ P' ’ is the back pressure and ‘ L ’ is the stroke length, ‘ A ’ is area of cylinder, ‘ n ’ is strokes and ‘ K ’ is number of cylinders. It has been found that the BHP of the engine is dropped from 47.5.2 to 46.9 HP in the case of the swirl blade type device while there is a significant reduction in BHP due to the swirl contour device and the swirl venture device as shown in Fig. 7, this will have the greatest impact on the performance of the engine as well as the increase in the specific fuel consumption of the engine. The specific fuel consumption is given as

$$\text{Specific fuel consumption, Sfc} = \frac{m_f}{BP} \tag{12}$$

Here m_f is the mass flow rate of the fuel, the Eq. (12) shows that with the reduction in the brake power the brake specific fuel consumption will increase and this will decrease the mileage of the vehicle.

The effect of the turbulent device on the conversion efficiency of the catalytic converter is done by using the gas analyzer to measure the harmful emissions of the engine running with the constant 5000 RPM. The results of the gas analyzer are obtained in the form of the percentage conversion of the harmful gases by the catalytic converter and the graphical comparison of each pollutant is plotted with respect to each of the device. From Fig. 8 graphical comparisons show that the percentage

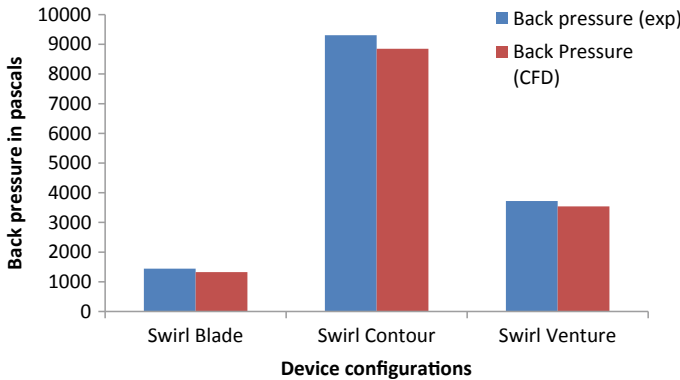


Fig. 7 CFD and experimental data of the back pressure

reduction in the carbon monoxide was only 16% without using any hypothetical devices, but it rises up to 33.86% with the application of the swirl blade device and 20.2 and 28.8% in the case of the swirl contour and swirl venture devices, respectively. Similarly, the percentage reduction in the hydrocarbons which are nothing but the unburnt charge in the exhaust gases was only 19.3% without using any hypothetical devices, now it rises up to 30.56% in the case of the swirl blade device and up to 22.55 and 27.57% in the case of the swirl contour and swirl venture devices respectively. However, the reduction in the oxides of nitrogen, which was only 27.5% without using any hypothetical devices, now reduces up to 25.7% in the case of the swirl blade device and 20.5 and 26.17% in the case of the swirl contour and swirl venture devices respectively. From the comparative study of each of the configuration, it has been found that the swirl blade geometry induces minimum back pressure at the engine exhaust system and also it is helpful in improving the conversion efficiency of the catalytic converter. Whereas, the swirl contour geometry induces the maximum back pressure in the catalytic converter and shows the least improvement in the conversion efficiency of the catalytic converter (Fig. 9).

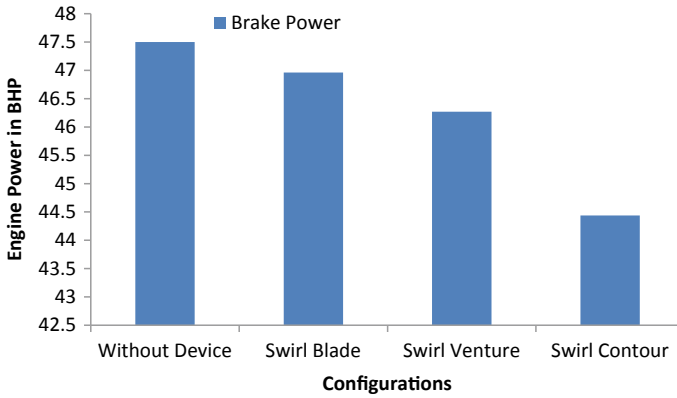


Fig. 8 Effect of back pressure on engine power

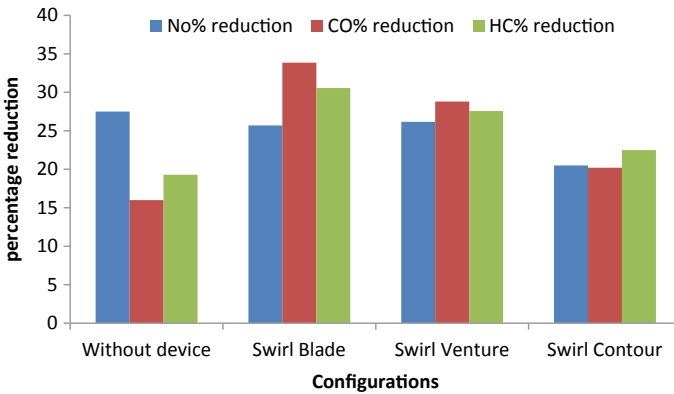


Fig. 9 Percentage reduction of emissions w.r.t each configurations

4 Conclusion

From the several attempts to improve the conversion efficiency of the catalytic converter, creating turbulence in the catalytic converter by the virtue of this turbulent device shows enhancement in the conversion efficiency without compromising the engine performance. However, this device creates turbulence only at the inlet of the catalytic converter, thereby increasing the surface area for the first contact of the gases only, also in the case of the swirl blade geometric configuration, it was found that there is decrement if the conversion efficiency of the oxides of nitrogen. Hence, the other methods can be developed to create the turbulence inside the pores of the monolith to further increase the efficiency of the system. The optimized turbulent device studied in this paper can be easily used in conjugation with the catalytic con-

verter without making any modification in the system and improves the conversion efficiency of the catalytic converter.

References

1. Leman AM, Rahman F, Jajuli A, Zakaria S, Feriyanto D (2017) Emission treatment towards cold start and back pressure in internal combustion engine against performance of catalytic converter: a review. In: 9th international UNIMAS STEM engineering conference (ENCON 2016), p 7
2. Subramani T (2012) Study of air pollution due to vehicle emission in tourism centre. *Int J Eng Res Appl* 2(3):1753–1763
3. Wang Y, Zhao T (2018) Impacts of urbanization-related factors on CO₂ emissions: evidence from China's three regions with varied urbanization levels. *Atmos Pollut Res* 9(1):15–26
4. Giovanis E (2018) The relationship between teleworking, traffic and air pollution. *Atmos Pollut Res* 9(1):1–14
5. Zalakeviciute R, Rybarczyk Y, López-Villada J, Diaz Suarez MV (2018) Quantifying decade-long effects of fuel and traffic regulations on urban ambient PM_{2.5} pollution in a mid-size south American city. *Atmos Pollut Res* 9(1):66–75
6. Taylor KC (1987) Automobile catalytic converters. *Stud Surf Sci Catal* 30:97–116
7. Mohiuddin AKM, Rahman A (2012) Investigation using simulations for the development of low cost catalytic converter from non-precious metals. *Adv Mater Res* 445:899–904
8. Farrauto RJ, Heck RM (1999) Catalytic converters: state of the art and perspectives. *Catal Today* 51(3–4):351–360
9. Korin E, Reshef R, Tshernichovesky D, Sher E (1999) Reducing cold-start emission from internal combustion engines by means of a catalytic converter embedded in a phase-change material. *Proc Inst Mech Eng Part D J Automob Eng* 213(6):575–583
10. Amirnordin SH, Seri SM, Salim WSW, Rahman HA, Hasnan K (2011) Pressure drop analysis of square and hexagonal cells and its effects on the performance of catalytic converters. *Int J Environ Sci Dev* 2(3):239–247
11. Brück R, Diewald R, Hirth P, Kaiser F (1995) Design criteria for metallic substrates for catalytic converters. *SAE Eng Soc Adv Mobil L Sea Air Sp*, p 12
12. Santos H, Costa M (2014) Influence of the three way catalytic converter substrate cell density on the mass transfer and reaction resistances. *Chem Eng Sci* 107:181–191
13. Santos H, Costa M (2008) Analysis of the mass transfer controlled regime in automotive catalytic converters. *Int J Heat Mass Transf* 51(1–2):41–51
14. Joshi SY, Harold MP, Balakotaiah V (2010) Overall mass transfer coefficients and controlling regimes in catalytic monoliths. *Chem Eng Sci* 65(5):1729–1747
15. Tsinoglou DN, Koltsakis GC, Missirlis DK, Yakinthos KJ (2004) Transient modelling of flow distribution in automotive catalytic converters. *Appl Math Model* 28(9):775–794
16. Arrighetti C, Cordiner S, Mulone V (2007) Heat and mass transfer evaluation in the channels of an automotive catalytic converter by detailed fluid-dynamic and chemical simulation. *J Heat Transfer* 129(4):536–547
17. Hirata K, Oda R, Tanaka S, Tanigawa H, Funaki J (2008) Pressure-loss reduction and velocity-profile improvement in a catalytic converter by a flow deflector. *Proc Inst Mech Eng Part D J Automob Eng* 222(3):455–467
18. Soumelldis MI, Stobart RK, Jackson RA (2007) A chemically informed, control-oriented model of a three-way catalytic converter. *Proc Inst Mech Eng Part D J Automob Eng* 221(9):1169–1182
19. Eghlimi A, Kouzoubov A, Fletcher CAJ (1997) A new RNG-based two-equation model for predicting turbulent gas-particle flows. In: Proceedings of the first international conference on CFD in mineral & metal processing and power generation industries, CSIRO, pp 279–284
20. ANSYS FLUENT theory guide, “Turbulence”, pp 46–137

A Comprehensive Review on LiBr–H₂O Based Solar-Powered Vapour Absorption Refrigeration System



S. Somesh , Sumit Kumar Shaw  and Piyush Mahendru 

Abstract Solar energy is used for refrigeration cycle in solar-powered vapour absorption refrigeration (SVAR) systems. The significance and explanation of eco-friendly SVAR system based on LiBr–H₂O are available in the literature. The use of solar power improves the coefficient of performance (COP) of the cycle, and it lies in between 0.27 and 1.20. The improvement in COP makes it suitable for industrial and commercial purposes. It was claimed that, this system is also worthy for the applications operated at or above 0 °C. The use of LiBr as absorbent allows the system to run without expansion valve. Use of water as refrigerant is helpful to keep the operating pressure low in condenser and evaporator. Even if the system works on lower pressure, the COP is not affected. The machine-driven parts are installed in pump housings only. Therefore, the complete operation is smooth, and the system is maintenance-free. This system might not produce any greenhouse gas and considered as a green technology for future. The load variation does not affect the performance of the system too. The use of LiBr provides the flexibility to replace the volatile liquid from the absorbent refrigerant pair. Also, the liquid exiting the generator does not contain absorbent mixed with refrigerant. Therefore, the analyzer and rectifier are absent which simplifies the design and reduce the production cost. The main limitations of this system are crystallization and reduction in efficiency at very low temperatures. In this article, the recent developments in the field of LiBr–H₂O-based SVAR system are reviewed.

Keywords Solar energy · Absorption · Refrigeration · LiBr–H₂O · Vapour absorption refrigeration systems

1 Introduction

The vapour absorption refrigeration (VAR) system comprises of the processes like absorption, condensation, expansion and evaporation. The main refrigerant used in

S. Somesh (✉) · S. K. Shaw · P. Mahendru
Department of Mechanical Engineering, Manav Rachna University, Faridabad, Haryana, India
e-mail: somesh.01.03@gmail.com

© Springer Nature Singapore Pte Ltd. 2019
M. Kumar et al. (eds.), *Advances in Interdisciplinary Engineering*, Lecture Notes in Mechanical Engineering, https://doi.org/10.1007/978-981-13-6577-5_32

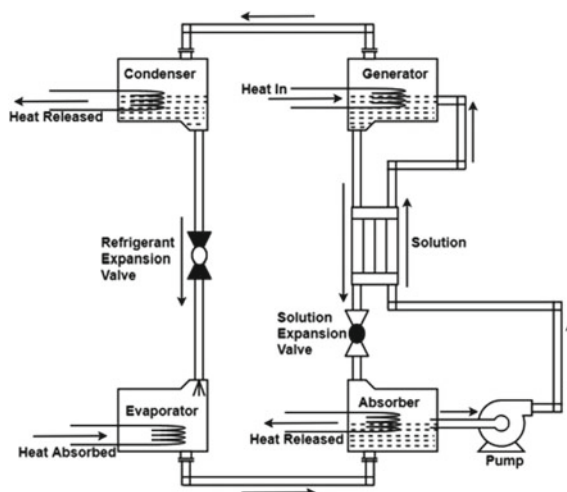
343

vapour absorption system is NH_3 (ammonia), H_2O (water) or LiBr (lithium bromide). The refrigerant gets condensed and evaporated simultaneously in the condenser and evaporator, respectively. In the evaporator, the evaporation of refrigerant produces the cooling effect by discharging the heat to the surroundings. Vapour compression and absorption are two leading techniques used in the refrigeration systems with varied suction and compression processes of refrigerant. The suction, compression and flow of the refrigerant during refrigeration cycle are carried out by the compressor in the vapour compression system. On the contrary, two devices, i.e. absorber and generator are employed to suck and compress the refrigerant in the vapour absorption system. Also, the flow of the refrigerant was managed by the absorbent in the cycle. Furthermore, the energy input is furnished to the vapour compression and vapour absorption systems is in the form of mechanical work and heat energy, respectively [1]. The use of solar energy for powering the air-conditioning and refrigeration units not only saves the limited fossil fuel reserves but also preserves the environment which is excessively deteriorating due to global warming. Solar energy in the form of sunlight is abundantly available yet a very small percent of that is utilized for the betterment of the human race. Challenges associated with solar energy need to be addressed properly before utilizing it as a primary source of energy in various engineering applications. A thorough literature review indicated that solar power can be employed in absorption refrigeration systems. The present article aims to provide a comprehensive analysis of the progress of solar-powered absorption refrigeration systems.

2 H_2O –LiBr VAR System

In H_2O –LiBr pair, H_2O is used as a refrigerant and LiBr as an absorbent. The main limitation of this system is that it cannot be employed for refrigeration process below 0°C . However, this system is primarily suitable for air-conditioning purpose only. A schematic representation of H_2O –LiBr VAR system is shown in Fig. 1. At extremely low temperatures, i.e. below 0°C , the refrigerant used in this system turns into solid. Additionally, the crystallization of LiBr at moderate concentrations is another major issue with the system. This problem mainly arises when the absorber unit is cooled with air cooling system. The absorbent with a blend of salts is used to overcome this issue. Another difficulty with this system is related to the flow because the viscosity of the solution increases at low pressure. A proper design of the equipment might solve this issue to some extent. Apart from the problems, this system provides the advantages like high safety, large volatility ratio, high affinity, excellent stability and tremendous latent heat [2, 3]. Most of H_2O –LiBr VAR machines are at risk of atmospheric air leakage if the unit is improperly maintained or mishandled owing to their low operating pressure. Trouble-free operation of the H_2O –LiBr system is ensured if the crystallization of LiBr is prevented using efficient

Fig. 1 Schematic of a H₂O–LiBr system



concentration control system. The COP of the H₂O–LiBr system is good, although the crystallization problem limits it. The increased mass flow rate of refrigerant in the generator due to high generator temperature resulted in enhanced COP followed by high cooling rate [2, 3].

3 Thermodynamic Analysis of VAR System

The optimization of the first and second law of thermodynamics maximizes the COP and exergy efficiency, respectively. In exergy method, the exergy loss due to irreversibility, and the useful work produced by a substance is calculated. Thermodynamic study of the energy transformation systems is carried out using this powerful tool. Aphornratana and Eames [4] described the second law analysis of VAR cycle. As per their investigation, the solution circulation ratio has a decisive role in determining the COP of the system. It is required to pay more attention to the performance of evaporator than absorber to improve the overall cycle performance. As crystallization temperature of a solution is fixed, the maximum efficiency can be fetched when it is being operated from low-grade heat instead of high-temperature heat sources. Berlitz et al. [5] discussed the economic aspects of absorption heat pumping equipment operating on H₂O–LiBr. Arora and Kaushik [6] developed a computational model for the parametric analysis of H₂O–LiBr VAR system. The study specified that COP and exergy efficiency increased with higher generator temperatures. An increase in temperature associated with absorber, condenser and evaporator increases the irreversibility of the system. Also, highest irreversibility was proclaimed for the absorber. Asdrubali and Grignaffini [7] simulated and verified the performance of a single-stage H₂O–LiBr absorption machine. Their results indicated that acceptable

efficiency could be achieved from the device in 65–70 °C temperature range. Thus, as per findings, solar energy could be used as an energy source for the machine in future. Domínguez-Inzunza et al. [8] examined the performance of various absorption cooling arrangements working with H₂O–LiBr fusion. They observed maximum COP with double effect systems. However, this type of systems is complex. Anand et al. [9] analysed the energy and exergy of H₂O–LiBr VAR plant. They observed maximum exergy loss in the generator. Also, COP of the system increased with higher evaporator temperature. The areas of energy wastage in the system are pointed out in the study as well. Samanta and Basu [10] developed a theoretical model for H₂O–LiBr-based single-stage VAR system and it has been optimized for minimum entropy and maximum COP. They reported that the entropy generation is minimum when the generator temperature is low. Therefore, the absorber has a significant role in enhanced irreversibility in the system. A thermoeconomic analysis based on exergy analysis for H₂O–LiBr VAR system was carried out by Misra et al. [11] and Bereche et al. [12]. This optimization technique assisted in achieving a cost-effective design of VAR system for optimum performance. Further, a higher exergetic cost of the main product is reported for a direct-fired VAR system.

4 Solar-Powered VAR System

Engineering sectors like food processing, air-conditioning, pharmaceutical, etc. require a cooling environment for multiple purposes. The vapour compression systems are largely catering the demands in such type of applications. The focus of the research in the recent time has shifted to develop technologies offering low power consumption, renewable and clean energy resources without compromising the level of comfort [13]. The use of solar power in refrigeration technologies eliminates most of the harmful effect produced by conventional refrigeration machines. On the other hand, the performance of such type of system is mainly dependent on the availability of the solar radiation. Also, it is required to convert solar energy into electricity or heat for powering a refrigeration system. Currently, research is focused on the development and improvement of vapour absorption system driven by solar power. The efficiency of solar photovoltaic (PV) collectors increased marginally (i.e. 10–15%) than solar thermal collectors in the recent past. Also, solar PV collectors bear fairly high initial cost [14, 15]. Therefore, refrigeration technologies are mainly focusing on absorption or adsorption systems utilizing solar temperature. Dieng and Wang [16] presented a review on solar adsorption systems based on fundamental understandings, design parameters and applicability in air-conditioning and refrigeration. This system is able to serve basic cooling requirements in remote locations. Additionally, systems powered by solar energy are noiseless, non-corrosive and environmental friendly. However, this type of system is useful for air-conditioning in vehicles, ice making, medical and food preservation/transportation. Still, this field requires a lot of advancements for competing with the already established vapour compression system. Low specific power and high cost need attention for the development of

solar absorption systems. Sumathy et al. [17] proposed a solar cooling system driven at low temperature. The proposed model is a two-stage LiBr absorption chiller. Their results exhibited that the system can run at 60–75 °C, which could be achieved easily by portable solar hot water plant. This type of system is not only efficient but also cost-effective. As per their results, the COP of a two-stage chiller is almost similar to well established single-stage chiller with an approximately 50% cost cutting. Apart from H₂O–LiBr absorption system, a solar-driven carbon (C)–NH₃ refrigeration system with claimed power densities of almost 1 kW cooling for 1 kg carbon is also gaining importance [18]. Renewable and clean energy sources (i.e. solar, wind, biomass, etc.) and their combinations are power packed alternatives for all the energy needs in the refrigeration and air-conditioning industries.

5 Progress of Solar-Powered H₂O–LiBr VAR System

Many researchers have explained theoretically and experimentally the significance of SVAR system using H₂O–LiBr. They have claimed that using solar energy makes the whole process eco-friendly. Additionally, there is no recharging cost of refrigerant which is inevitable in vapour compression system. Arunkumar and Ragavendran [19] stated that through solar energy, the working fluid is able to achieve COP of refrigeration up to 0.7–0.8, and due to considerable COP this can be used not only for domestic purposes but also for industrial purposes. They claimed that this system is useful for those applications where the required temperature is more than 0 °C. Some studies claimed that the expansion valve is not needed in the cycle when LiBr is used as an absorbent. As water is used as refrigerant, the operating pressure in the condenser and evaporator is low. Even if the system works on lower pressure, COP is not affected. The cycle operation is smooth, noiseless, maintenance free and cost-effective. One of the main advantages of the H₂O–LiBr system is that the absorbent is non-volatile. There is no absorbent mixed refrigerant (water) pair leaving generator, and so the analyzer and rectifier can be removed from the system thereby simplifying the design and reducing the cost of production [20].

The year-wise progress of the SVAR system is presented in Table 1. The effect of different type of collectors used to collect solar energy on the efficiency of the system is fetched from the literature and plotted in Fig. 2. From Fig. 2, it could be concluded that the maximum COP of the system is obtained when evacuated tube type collectors were used.

Table 1 Year wise work on solar vapour absorption system based on H₂O–LiBr pair reported in the various literatures

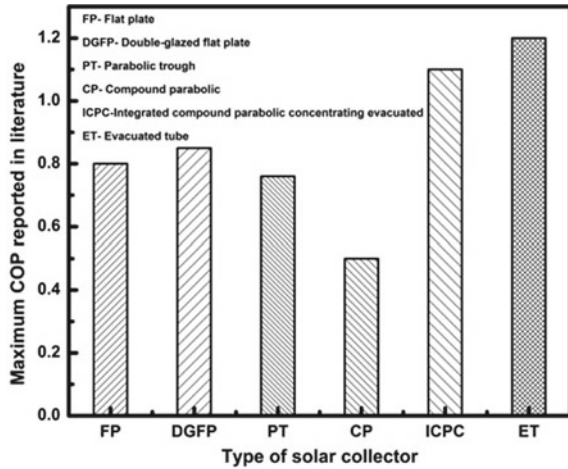
S. No.	Solar thermal technologies	Cooling technologies	Chillers types	COP	Remarks	Ref.	Year
1	Flat-plate collector	Continuous absorption	–	0.07	Storage tank size used is 2.75 m ³ (partitioned into two parts) for 4.7 kW cooling capacity	[21]	2001
2	Flat-plate collector	Continuous absorption	Single-effect	–	Optimized storage tank size is 1 m ³	[22]	2002
	Compound parabolic collector	Continuous absorption	Single-effect	–	Optimized storage tank size is 0.6 m ³		
	Evacuated tube collector	Continuous absorption	Single-effect	–	Optimized tank size is 0.6 m ³		
3	Tube type collectors	Continuous absorption	Double effect	1.2	Additional gas fired heating arrangement used	[23]	2004
4	Integrated compound parabolic concentrating reflector evacuated solar collector (ICPC)		Double effect	1.1	Daily collection efficiencies are 50–55%	[24]	2004
5	Parabolic trough solar collector	Continuous absorption	Single-effect	0.67–0.76	Minimum required collector area is 57.6 m ³ Storage tank capacity should be in between 0.68 and 1.23 m ³	[25]	2008
6	Flat-plate collector	Continuous absorption	Single-effect	0.74	The storage tank size used is 0.8 m ³	[26]	2008
7	Vacuum tubes solar collector	Continuous absorption	Single-effect	0.37–0.81	Absorption chiller with 35.17 kW cooling capacity. Hot and cold water storage tank capacity is 6.8 and 1.5 m ³ , respectively.	[27]	2008

(continued)

Table 1 (continued)

S. No.	Solar thermal technologies	Cooling technologies	Chillers types	COP	Remarks	Ref.	Year
8	Flat plate collector	–	Single-effect	0.41–0.66	Absorption chiller cooling capacity is 35 kW	[28]	2008
9	Evacuated tube solar collector	Continuous absorption	Single-effect	0.7	19% energy is provided to the chiller using a LPG-fired backup heating unit	[29]	2008
10	Flat-plate collector	Continuous absorption	Single-effect	0.8	Cooling water temperature should be below 40 °C	[30]	2014
11	Double-glazed flat plate collector	Continuous absorption	Single-effect	0.27–0.85	Required storage tank size is 0.68–1.23 m ³ for 10.39 kW of cooling loads	[31]	2014
12	Compound parabolic concentrators	Continuous	Double effect	0.4–0.5	No cooling tower employed	[32]	2014
13	Flat-plate collector	Continuous		0.77	Design with refrigerant storage is the best suited design for 24 h AC operation	[33]	2015
14	Evacuated tube array	Continuous	Single/double effect	0.69–1.08	The maximum COP was obtained when generator temperature was 120 °C	[34]	2016
15	Evacuated selective surface collector	Continuous	Single-effect	0.7–0.8	Evacuated selective surface collectors are better than single and double-glazed collector	[35]	2017
16	Parabolic trough collectors	Continuous	Single-effect	0.65	Optimal heat source temperature is 95.5 °C	[36]	2018

Fig. 2 Reported values of COPs of H₂O–LiBr based VAR system with various solar collectors



6 Conclusions

In this article, a review of the research state on the SVAR systems is presented. From the report, it can be concluded that the SVAR systems could be utilized for generating a broad range of temperatures for refrigeration and air-conditioning by the adoption of renewable energy source. It is an attractive technology that not only able to serve the demands for refrigeration/air-conditioning applications but also meet the requirement for energy conservation and climate protection. As per the review, evacuated tube collectors are able to extract high COP from the system. Absorption systems are more suitable for air-conditioning. Many areas related to SVAR technology is not fully investigated yet. Poor COP and low solar collector efficiency are mainly obstructing the commercialization of SVAR systems from demonstration/prototyping to the final product. However, a lot of research work is still needed for enhancing the heat and mass transfer to improve performances of SVAR systems. Incorporation of more advanced solar energy collectors, innovative optimization/simulation models and use of micro-exchangers could achieve required efficiency from the system.

Acknowledgements Authors wish to thank Dr. Anil from Accendere Knowledge Management Service, CL Educate, for his helpful suggestions during manuscript preparation.

References

1. Roy JD (1991) Principles of refrigeration. Prentice Hall, New Jersey
2. Horuz I (1998) A comparison between ammonia-water and water-lithium bromide solutions in vapor absorption refrigeration systems. *Int Commun Heat Mass Transf* 25:711–721
3. Totla NB, Arote SS, Gaikwad SV, Jodh SP, Kattimani SK (2016) Comparison of the performances of NH₃-H₂O and LiBr-H₂O vapour absorption refrigeration cycles. *Int J Eng Res Appl*

6:08–13

4. Aprhornratana S, Eames IW (1995) Thermodynamic analysis of absorption refrigeration cycles using the second law of thermodynamics method. *Int J Refrig* 18:244–252
5. Berlitz T, Satzger P, Summerer F, Ziegler F, Alefeld G (1999) A contribution to the evaluation of the economic perspectives of absorption chillers. *Int J Refrig* 22:67–76
6. Arora A, Kaushik SC (2009) Theoretical analysis of LiBr/H₂O absorption refrigeration systems. *Int J Energy Res* 33:1321–1340
7. Asdrubali F, Grignaffini S (2005) Experimental evaluation of the performances of a H₂O–LiBr absorption refrigerator under different service conditions. *Int J Refrig* 28:489–497
8. Domínguez-Inzunza LA, Sandoval-Reyes M, Hernández-Magallanes JA, Rivera W (2014) Comparison of the performance of single effect, half effect, double effect in series and inverse absorption cooling systems operating with the mixture H₂O–LiBr. *Energy Proc* 57:2534–2543
9. Anand S, Gupta A, Tyagi SK (2014) Exergy analysis of a LiBr–H₂O vapor absorption refrigeration plant: a case study. *Int J Air-Cond Refrig* 22:1450010–1450018
10. Samanta S, Basu DN (2016) Energy and entropy-based optimization of a single-stage water–lithium bromide absorption refrigeration system. *Heat Transf Eng* 37:232–241
11. Misra RD, Sahoo PK, Sahoo S, Gupta A (2003) Thermoeconomic optimization of a single effect water/LiBr vapour absorption refrigeration system. *Int J Refrig* 26:158–169
12. Bereche RP, Palomino RG, Nebra SA (2009) Thermoeconomic analysis of a single and double-effect LiBr/H₂O absorption refrigeration system. *Int J Thermodyn* 12:89–96
13. Florides GA, Tassou SA, Kalogirou SA, Wrobel LC (2002) Review of solar and low energy cooling technologies for buildings. *Renew Sustain Energy Rev* 6:557–572
14. Papadopoulos AM, Oxizidis S, Kyriakis N (2003) Perspectives of solar cooling in view of the developments in the air-conditioning sector. *Renew Sustain Energy Rev* 7:419–438
15. Fan Y, Luo L, Souyri B (2007) Review of solar sorption refrigeration technologies: development and applications. *Renew Sustain Energy Rev* 11:1758–1775
16. Dieng AO, Wang RZ (2001) Literature review on solar adsorption technologies for ice-making and air-conditioning purposes and recent developments in solar technology. *Renew Sustain Energy Rev* 5:313–342
17. Sumathy K, Huang ZC, Li ZF (2002) Solar absorption cooling with low grade heat source—a strategy of development in South China. *Sol Energy* 72:155–165
18. Critoph RE (1999) Rapid cycling solar/biomass powered adsorption refrigeration system. *Renew Energy* 16:673–678
19. Arunkumar S, Ragavendran R (2016) Design and fabrication of solar powered lithium bromide vapour absorption refrigeration system. *IOSR J Mech Civ Eng IOSR-JMCE* 13:57–62
20. Horuz I, Callander TMS (2004) Experimental investigation of a vapor absorption refrigeration system. *Int J Refrig* 27:10–16
21. Li ZF, Sumathy K (2001) Experimental studies on a solar powered air conditioning system with partitioned hot water storage tank. *Sol Energy* 71:285–297
22. Florides GA, Kalogirou SA, Tassou SA, Wrobel LC (2002) Modelling and simulation of an absorption solar cooling system for Cyprus. *Sol Energy* 72:43–51
23. Liu YL, Wang RZ (2004) Performance prediction of a solar/gas driving double effect LiBr–H₂O absorption system. *Renew Energy* 29:1677–1695
24. Duff WS, Winston R, O’Gallagher JJ, Bergquam J, Henkel T (2004) Performance of the Sacramento demonstration ICPC collector and double effect chiller. *Sol Energy* 76:175–180
25. Mazloumi M, Naghashzadegan M, Javaherdeh K (2008) Simulation of solar lithium bromide–water absorption cooling system with parabolic trough collector. *Energy Convers Manag* 49:2820–2832
26. Balghouthi M, Chahbani MH, Guizani A (2008) Feasibility of solar absorption air conditioning in Tunisia. *Build Environ* 43:1459–1470
27. Ali AHH, Noeres P, Pollerberg C (2008) Performance assessment of an integrated free cooling and solar powered single-effect lithium bromide-water absorption chiller. *Sol Energy* 82:1021–1030

28. Zambrano D, Bordons C, Garcia-Gabin W, Camacho EF (2008) Model development and validation of a solar cooling plant. *Int J Refrig* 31:315–327
29. Pongtornkulpanich A, Thepa S, Amornkitbamrung M, Butcher C (2008) Experience with fully operational solar-driven 10-ton LiBr/H₂O single-effect absorption cooling system in Thailand. *Renew Energy* 33:943–949
30. Saleh A, Mosa M (2014) Optimization study of a single-effect water–lithium bromide absorption refrigeration system powered by flat-plate collector in hot regions. *Energy Convers Manag* 87:29–36
31. Chougui ML, Said ZID (2014) Simulation of solar lithium bromide–water absorption cooling system with double glazed flat plate collector for Adrar. *Sci Technol A* 59–64
32. Li Z, Ye X, Liu J (2014) Performance analysis of solar air cooled double effect LiBr/H₂O absorption cooling system in subtropical city. *Energy Convers Manag* 85:302–312
33. Al-Ugla AA, El-Shaarawi MAI, Said SAM (2015) Alternative designs for a 24-hours operating solar-powered LiBr–water absorption air-conditioning technology. *Int J Refrig* 53:90–100
34. Wang RZ, Xu ZY, Pan QW, Du S, Xia ZZ (2016) Solar driven air conditioning and refrigeration systems corresponding to various heating source temperatures. *Appl Energy* 169:846–856
35. Kerme ED, Chafidz A, Agboola OP, Orfi J, Fakeeha AH, Al-Fatesh AS (2017) Energetic and exergetic analysis of solar-powered lithium bromide-water absorption cooling system. *J Clean Prod* 151:60–73
36. Kumar V, Pandya B, Patel J, Matawala V (2018) Vapor absorption system powered by different solar collectors types: cooling performance, optimization, and economic comparison. *Sci Technol Built Environ* 1–14

Multi-objective Process Optimization of Biodiesel Synthesis from *Acacia concinna* Seed Oil Using TOPSIS and GRA Approach



Vishal Saxena, Niraj Kumar and Vinod Kumar Saxena

Abstract The present study reports the potential of *Acacia concinna* (wild crop) non-edible seed oil as prospective feedstock for biodiesel production. Since *A. concinna* seed contains 21.0 wt% crude oil, with high acid value of 17.8 mg KOH/g therefore biodiesel synthesis was carried out in two-stage esterification process. The obtained biodiesel was characterized for different fatty acid esters and fuel properties strictly according to ASTM/IS standards. Further analysis presents an experimental design methodology integrated with TOPSIS and GRA approach for the selection of most optimal set of process variables for biodiesel production with multi-objective optimization of both quantity (biodiesel yield) and fuel properties. At optimum condition, the process variables methanol/oil molar ratio 8:1, catalyst concentration 1.0 wt% KOH, reaction temperature 60 °C and reaction time 60.0 min results in a maximum biodiesel yield and calorific value of 98.7%, 37.950 MJ/kg with lowest viscosity and FFA of 5.72 mm²/s, 0.33 respectively. Further analysis provides an overall augmentation of 0.88713 (TOPSIS) and 0.58976 (GRA) in the preferred values of output responses. However, Catalyst concentration was found to be most significant process variable among all. Finally as a conclusion, this comprehensive study indicates the viability of producing *A. concinna* biodiesel which makes it a suitable alternative fuel for existing diesel engine technology.

Keywords *A. concinna* biodiesel · Esterification · Optimization · TOPSIS · GRA

V. Saxena

Department of Fuel Engineering, IIT (ISM), Dhanbad, Jharkhand, India
e-mail: vishal.saxena@mjpru.ac.in

N. Kumar (✉)

Department of Mechanical Engineering, Amity University, Noida, Uttar Pradesh, India
e-mail: kniraj2006@gmail.com

V. K. Saxena

Department of Chemical Engineering, IIT (ISM), Dhanbad, Jharkhand, India
e-mail: vksaxenaism@hotmail.com

© Springer Nature Singapore Pte Ltd. 2019

M. Kumar et al. (eds.), *Advances in Interdisciplinary Engineering*, Lecture Notes in Mechanical Engineering, https://doi.org/10.1007/978-981-13-6577-5_33

1 Introduction

India, a fastest growing nation is facing energy deficiency in every sector of economy. Though, the high population burden of 1.3 billion [1] food, fuel security, sustainability and environment preservation are the main focus area of policy makers of the nation. However, to fulfil the energy needs our dependency on import of crude petroleum oil from other countries, further poses the financial burden. To cope up with above issues, energy cultivation seems to be the viable option for near future, thereby, cultivating more and more petro crops/ searching new non-edible feedstocks for the production of bio-derived fuels such as biomass, biodiesels and biogas etc [2]. Furthermore, with the increasing demand of these fuels and for its commercialization, it is very essential that the production protocol and its process variables should be optimized which could ensure high productivity in terms of yield and product quality. In recent years, sincere and systematic efforts have been made by researches to develop efficient protocol for the conversion of various vegetable derived oils to biodiesel. Out of various non-edible feedstocks, *Jatropha* and *karanja* have been exhaustively studied for this purpose. Though some new forest origin feedstock's such as *Calitropis gigantea*, *Thevetia poruviana*, *Schleichera triguga* and *Sapindus mukorossi*, etc. [3] have also been considered for biodiesel production, however still there exist a huge gap between requirement and availability of alternative fuels.

In an effort, to search new non-edible, economical and sustainable source for biofuel production, having apposite fuel characteristics, *Acacia concinna* (wild crop) seed oil has been first time investigated for biodiesel synthesis including optimization of production process variables giving equal weights to yield and other important fuel properties such as viscosity (ν), free fatty acid content (FFA), and calorific value (Cv). The present study employed TOPSIS and GRA multi-objective optimization techniques for the estimation of relative significance of various process variables on product quantity and quality. Therefore, the present study mainly focuses on to investigate the viability of *A. concinna* seed oil for biodiesel production and to quantify the number of different monoesters present in it using gas chromatography along with its physiochemical properties. Besides this, a significant work on multi-objective optimization of prominent process variables, and their output responses are performed in order to produce low cost, eco-friendly alternative fuel which can lend a hand to meet the ever ending energy needs of our modern civilization.

2 Material and Methodology

The *A. concinna* tree (Mimosidaeae family) is available in nearly all parts of India [4]. The pods of *A. concinna* are collected from the local market of Bareilly (U.P) and seeds are separated from pod manually which are ground in the blender. The ground seeds are then used for extraction of oil, which has an average oil content of 21.0 wt% after filtration. The GC results of extracted oil comprise triglycerides in a

Table 1 Fatty acid composition (% by weight) of *Acacia concinna* seed oil and produced biodiesel

S. No.	Fatty acid composition	<i>A. concinna</i> seed oil	<i>A. concinna</i> methyl ester oil
1	Palmitic acid (C16:0)	12.8	8.6
2	Stearic acid (C18:0)	7.3	4.9
3	Oleic acid (C18:1)	21.0	17.2
4	Linoleic acid (C18:2)	41.6	52.4
5	Linolenic acid (C18:3)	15.5	10.8

Table 2 Selection of input process variables for acid catalyzed esterification and alkaline transesterification process and their level of variability

S. No.	Input process Variables	Symbols and unit	Level of variability (L)						
			Esterification				Transesterification		
			L1	L2	L3	L4	L1	L2	L3
1	Methanol to oil molar ratio	Mo	6:1	7:1	8:1	9:1	6:1	8:1	10:1
2	Catalyst con.	Cc (wt%)	0.25	0.5	0.75	1.0	0.5	1.0	1.5
3	Reaction temperature	R_{tem} (°C)	50	55	60	65	30	60	90
4	Reaction time	R_t (min)	45	60	75	90	45	60	75

composition of long chain fatty acids with esters accounting high amount (78.1%) of unsaturated fatty acids (Linoleic, Oleic and Linolenic) predominate in triglycerides with remaining (20.1%) saturated acids (Palmitic and Stearic) and 1.8% of unidentified amount as shown in Table 1. The production is carried out on a laboratory scale of 5.0 kg reactor. All chemicals (methanol (CH₃OH), potassium hydroxide flakes, phenolphthalein, sulphuric acid used in the experiment are analytical grade (99.0% pure).

Due to very high acid value of *A. concinna* crude oil (17.8 mg KOH/g), the biodiesel production is carried out in two-step process i.e. acid esterification followed by transesterification. The selection of process variables and there level of variability as shown in Table 2 are based on their relative significance in the chemical reaction process, along with the flexibility of experimental setup.

2.1 Optimization Methodology

Technique for order of preference by similarity to ideal solution (TOPSIS Approach) and Grey relational Analysis (GRA Approach)

TOPSIS and GRA is a numerical technique that considers both multiple alternatives with multiple criteria in order to evaluate the performance of finite set of alternatives though similarity to ideal solution. This approach aims to determine the best suitable

alternative that maximizes output responses (quantity and quality) of the chosen attributes. However, GRA approach analyses the complicated interrelation between multi-variant and multi-response/attribute problems. The numerical method used in TOPSIS and GRA approach is explained elsewhere [5, 6]. However, both approaches when integrated together determine the optimal setting of process variables that would augment the biodiesel production process quantitatively and qualitatively. The output data/response parameters of produced biodiesel were measured in terms of biodiesel yield, viscosity, free fatty acid (FFA) value and Calorific value.

3 Results and Discussion

In order to optimize the biodiesel production process variables initially, acid esterification process is optimized with the sole requisite to reduce the total FFA content of *A. concinna* crude oil by less than 2%. From the experimental results, the most preferred set of process variables are found to be $M_o = 9:1$, $C_c = 1 \text{ wt\% H}_2\text{SO}_4$, $R_{tem} = 65 \text{ }^\circ\text{C}$, $R_t = 90 \text{ min}$ which provides the lowest FFA value of 0.7%. Further, in second-step alkaline transesterification process using methanol and catalyst potassium hydroxide (KOH), the heavy molecules fatty acid are broken down in monoalkyl methyl ester and glycerol, which after separation and purification produces biodiesel. The experimental and optimization results both are presented here and discussions are made on associated aspects of biodiesel production in the following section. A total of 27 experiments were performed for both acid and alkaline Trans (esterification) for optimization study.

3.1 Effect of Process Variables on Output Responses

All output parameters of produced biodiesel are influenced by the process variables used in the reactions. These variations are depicted in Fig. 1a–d.

The variation in output responses at selected levels of process variables M_o , C_c , R_{tem} , R_t are plotted as shown in Fig. 1a–d. It can be seen that in all cases the optimal value of output responses was found at a molar ratio of 8:1. This condition implies that the molar ratio was sufficient to precede the transesterification reactions towards completion and subsequent phase separation of glycerol from esters. However, catalyst concentration (KOH) showed more dominant effect than other variables, as it catalyzes and governs the reaction rate. As can we see from Fig. 1c that, $C_c = (0.5 \text{ and } 1.5 \text{ wt\%})$ led to poor output responses compared to KOH concentration of 1.0 wt%. The can be explained as when $C_c = 1.0 \text{ wt\%}$, the sufficient quantity of methoxide ion (CH_3O^-) in the reaction accelerate the catalyzes of heavy molecule of fatty esters with less emulsion effect which suppress the saponification reactions (loss of triglycerides) and augments the biodiesel quantity and quality. Another production process variable which has a significant effect on output responses is the reaction tempera-

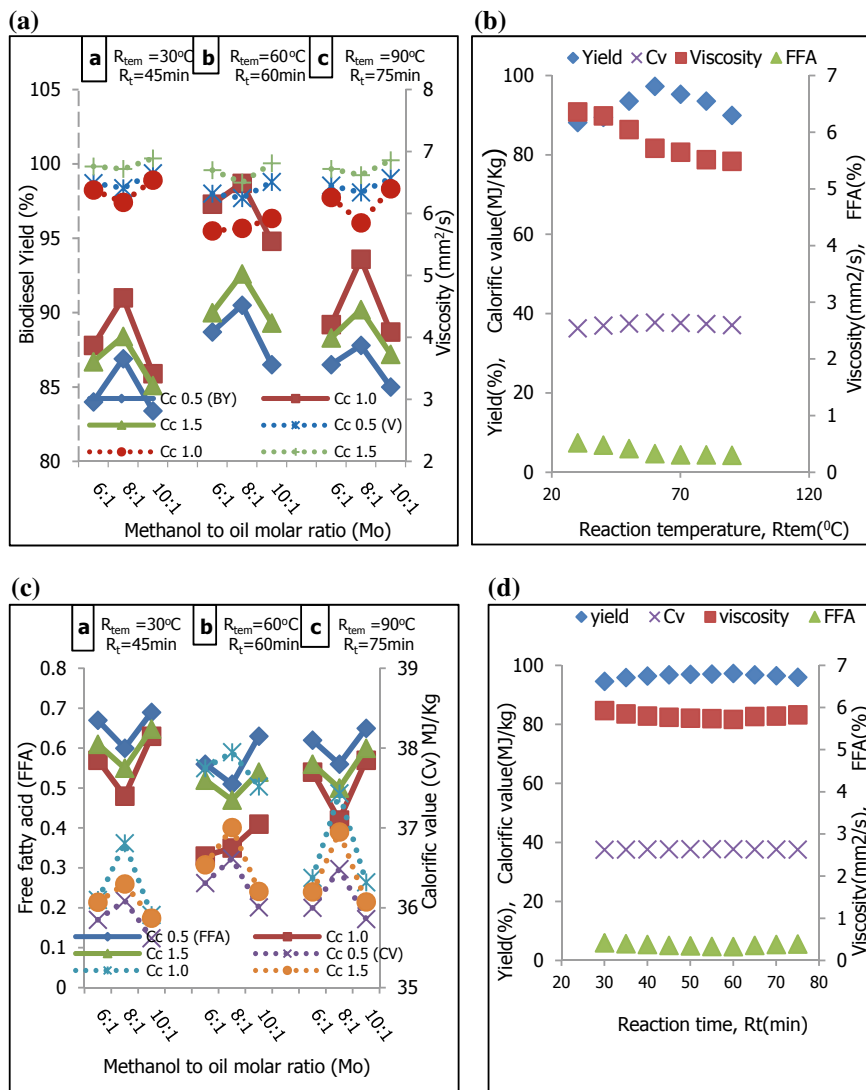


Fig. 1 a–d The variation in biodiesel yield, viscosity, FFA and calorific value of biodiesel produces at different process variables (Mo, Cc, R_{tem} and R_t)

ture. Different experimental trials were performed between the temperature range of 30–90 °C. The plotted results from Fig. 1b reveal that highest product yield (98.7%) and calorific value (37,215 kJ/kg) with lowest viscosity (5.85 mm²/s) and FFA value (0.7%) was achieved at a reaction temperature of 60 °C. This increase was attributed to the enhanced solubility of *A. concinna* oil with alcohol which provides intimate mixing between them. This effect is more noticeable as the temperature reaches near the boiling point of methanol. At this condition, the enhanced solubility of esters with methanol helps in achieving maximum conversion of triglycerides, which substantially achieve better product quantity and quality. In addition, the impact of reaction time on all output responses has been evaluated by varying the reaction time from 30 to 90 min. As evident from Fig. 1d that, very high conversion rates of triglycerides to methyl esters were achieved within first few minutes of reaction duration, once the chemical system remains in equilibrium biodiesel properties were fairly constant. Further extension in reaction time results in a slightly less biodiesel yield and inferior fuel properties. This might be due to increased hydrolysis of esters which terminates the transesterification reactions. However, the effect of reaction time is less pronounced in comparison to other process variables.

3.2 TOPSIS and GRA Analysis and Optimization Results

Based on TOPSIS optimized results, it was found that experimental trail no-05 having rank no-1 with highest preference order value of 0.975442, therefore the process variables combination for this experimental trial can be considered as an optimal setting for the production process and is expressed as Mo = 6:1, Cc = 1 wt% KOH, $R_{tem} = 60$ °C, $R_t = 60$ min as optimized values. For this optimized set of variables, the output response values are yield = 97.3%, viscosity = 5.72 mm²/s, FFA = 0.33% and calorific value = 37.75 MJ/kg values which clearly establish the accurate prediction capabilities of TOPSIS model. Further, the GRA analyses for optimization of biodiesel production parameters for multiple responses showed that experimental trial 14 has the highest GRG value (0.9590), hence assigned as rank 1. At optimized process variables Mo = 8:1, Cc = 1 wt% KOH, $R_{tem} = 60$ °C, $R_t = 60$ min, results in biodiesel yield = 98.7%, viscosity = 5.85 mm²/s, FFA = 0.35% and calorific value = 37.950 MJ/kg respectively. However, the optimized results Table 3 showed percentage improvement in yield, calorific value, FFA and viscosity to be 15.7, 5.85% (enhancement) and 47.62, 9.86% (reduction) respectively having GRG value of 0.58976. From Fig. 2, GRA result indicates that catalyst concentration is the most significant parameter among all selected process variables.

Table 3 Results of optimal set of process variables their output response and desirability for both single objective and multi objective optimization of ANN-ANFIS predicted data

TOPSIS optimization results			
Initial factor setting	Optimal set of production parameter		
Level	Experimental result		
	Mo ₁ Cc ₁ R _{tem1} R _{t1}	Mo ₁ Cc ₂ R _{tem2} R _{t2}	
Methanol to oil molar ratio(Mo)	6:1	6:1	
Catalyst concentration Cc (wt% KOH)	0.5	1.0	
Reaction temperature R _{tem} (°C)	30	60	
Reaction time R _t (minute)	45	60	
Product yield (wt %)	84.0	97.3	
Viscosity (mm ² /s)	6.49	5.72	
FFA value (%)	0.67	0.33	
Calorific value (KJ/kg)	35850	37750	
Value of preferred solution	0.088312	0.975442	
Augmentation in preferred value for optimal solution = 0.88713			
GRA results			
Initial factor setting	Optimal set of production parameter		
Level	Experimental result		
	Mo ₁ Cc ₁ R _{tem1} R _{t1}	Mo ₂ Cc ₂ R _{tem2} R _{t1}	Mo ₁ Cc ₂ R _{tem2} R _{t2}
Methanol to oil molar ratio(Mo)	6:1		8:1
Catalyst concentration Cc (wt% KOH)	0.5		1.0
Reaction temperature R _{tem} (°C)	30		60
Reaction time R _t (minute)	45		60
Product yield (wt %)	84.0		98.722
Viscosity (mm ² /s)	6.49		5.854
FFA value (%)	0.67		0.35
Calorific value (KJ/kg)	35850		37.950
Grey relational grade (GRG)	0.36924	0.8368	0.95900
Augmentation in preferred value for optimal solution = 0.58976			

4 Properties of *A. concinna* Biodiesel

The fuel properties of extracted biodiesel such as density, viscosity, calorific value, free fatty acid content, flash point and cetane number, etc. play a vital role its selection for various industrial and commercial applications [7–9]. The fuel properties of *A. concinna* extracted seed oil and biodiesel evaluated at ASTM D6751, EN-14214. The transesterification of triglycerides yields maximum 97.8% of biodiesel, which

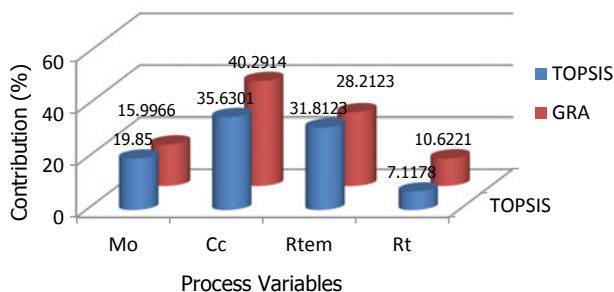


Fig. 2 Contribution (%) of selected process variables for biodiesel production based on both TOPSIS and GRA optimized results

reduces the acid value from 17.8 to 0.7 mg KOH/g, but is still higher compared to that of diesel fuel, which causes corrosion, excessive carbon and sludge deposition on various engine components during burning [10]. The density of oil decreases from 924 to 892 kg/m³, whereas viscosity values of *A. concinna* biodiesel were found to be 5.76 mm²/s, therefore conforms the ASTM standards, but was slightly higher than EN14214 specifications. The higher viscosity values of biodiesel compared to diesel fuel affects the spray pattern, atomization of injected fuel and heat release rates which affects the overall performance and combustion characteristics of a CI engine.

5 Conclusions

The present study investigates the possibility of producing biodiesel from *A. concinna* seed oil which is non-edible and still untapped. The production of *A. concinna* biodiesel was accomplished in two-step acid esterification and alkaline transesterification process. After acid esterification process, the crude oil has FFA value of 0.7% with an average yield of 85–90%. The acid esterification was found to be very effective in removing soluble fatty acids and other impurities. At optimized process variables both from TOPSIS and GRA approach showed percentage improvement in yield, calorific value, FFA and viscosity to be 15.7, 5.12% (enhancement) and 42.67, 9.35% (reduction) respectively with all physicochemical properties in accordance with ASTM standards. Hence it was concluded that the research outcomes of this work, definitely boost the Renewable Energy program of India by utilizing the waste forest feedstock *A. concinna* (seed oil) for biodiesel production. Furthermore, the optimization study proves to be an effective aid for biodiesel production industries to ascertain their product quantity and quality and make them suitable as alternative fuel, comprising fuel properties very close to that of petrodiesel fuels.

References

1. Saxena V, Kumar N, Saxena VK (2017) A comp review on com and stability aspects of metal nanoparticles and its additive effect on diesel and biodiesel fuelled C.I. engine. *Renew Sustain Energy Rev* 70:563–588
2. Kumar N, Varun, Chauhan SR (2016) Evaluation of the effects of engine parameters on performance and emissions of diesel engine operating with biodiesel blend. *J Ambient Energy* 37:121–135
3. Sahoo PK, Das LM (2009) Process optimization for biodiesel production from Jatropha, Karanja and Polanga oils. *Fuel* 88(9):1588–1594
4. Yadav RN, Sodhi S (2001) Chemical investigations of Pods of *A. concinna* DC. *Asian J Chem* 13:306–362
5. Raghuraman S, Thirrupathi K, Pannerselvam T, Santosh S (2013) Optimization of EDM parameters using Taguchi method and Grey relational analysis for mild steel IS 2026. *Int J Innov Res Sci Eng Tech* 2(7):3095–3104
6. Yuan X, Zhang Q (2017) The app res of GRA based entropy weight. *IEEE Exp*. <https://doi.org/10.1109/gsis.2017.8077681>
7. Jose DFM, Raj RE, Prasad DB, Kennedy ZR, Ibrahim AM (2011) A multi-variant app to optimize pro par for bd extraction from rubber seed oil. *Appl Energy* 88(6):2056–63
8. Kumar N, Varun, Chauhan SR (2015) Evaluation of endurance characteristics for a modified diesel engine runs on Jatropha biodiesel. *Appl Energy* 155:253–269
9. Kumar N (2017) Oxidative stability of biodiesel: causes, effects and prevention. *Fuel* 190:328–350
10. Kumar N, Varun, Chauhan SR (2014) Analysis of tribological performance of diesel engine. *J Eng Tribol* 228(7):797–807

Comparative Analysis of Wavelet Encoder and Hybrid Wavelet-Based Fractal Encoder for Image



Richa Gupta, Deepti Mehrotra and Rajesh Kumar Tyagi

Abstract This paper presents the comparative review of wavelet encoder and fractal image compression (FIC) based on DWT. Wavelet transforms, and FIC are popularly used as the domain for image compression. Encoder designed in the spatial domain cannot exploit the redundancy present in the natural image efficiently. In this paper, the image is encoded using conventional fractal encoding algorithm in both the transforms. Performance of both the encoder compared using compression ratio, encoding time and PSNR. Raw images of size 512×512 used to carry the experiment in Matlab2013a. A quick review is arranged in a tabular manner in Sect. 4.

1 Introduction

Fractal image compression is a popular technique for image encoding. Fractals multiresolution property and fast reconstruction attracted many researchers. The term fractal was coined by Barnsley [1] in 1988. Later, he extended his research and presented the idea of encoding fractal images using the iterative function system [2]. The exciting idea of compressing images using only transform codes had the massive disadvantage of non-usability for natural images. Jacquin et al. [3] overcame this drawback and presented an alternative partition iterative function system to encode natural images. This groundbreaking work had the advantage of a high compression ratio but lacking due to high computational cost. This drawback encouraged many researchers to work that reduce the computational cost of FIC. Wavelet is promising frequency domain linked to FIC. Penland and Horowitz [4] introduced the use of wavelet in the conjecture of FIC. The method introduced is similar to Jacquin's approach and used fixed vector quantizer. Davis [5] worked on the convergence problem of FIC and introduced a wavelet-based framework for the same. Andreopoulos et al. [6] used the prediction method and achieved better compression ratio from the

R. Gupta (✉) · D. Mehrotra
Amity University, Noida, Uttar Pradesh, India
e-mail: rgupta6@amity.edu

R. K. Tyagi
Krishna Institute of Engineering and Technology, Ghaziabad, Uttar Pradesh, India

© Springer Nature Singapore Pte Ltd. 2019
M. Kumar et al. (eds.), *Advances in Interdisciplinary Engineering*, Lecture Notes in Mechanical Engineering, https://doi.org/10.1007/978-981-13-6577-5_34

hybrid coder. IN article [7] Li and Kuo used partial fractal coder with prediction. Wu et al. [8] proposed searchless wavelet FIC encoder that exploited the correlation present in parent and its offspring coefficient. Similar to this, many other techniques present in the literature [9–12].

Iano et al. [13] proposed to use modified set partitioning in hierarchical tree coding to reduce the encoding and decoding time. Song et al. [14] used four fork tree structure that took advantage of energy stored in frequency sub-band. Moreno [15] proposed an algorithm in the wavelet domain for fractal image encoding based on Hilbert scanning of embedded quadtree structure. Zang and Wang [16] experimented diamond search technique with hybrid fractal wavelet coder to achieve the faster outcome. Wu [17] reduced MSE calculation by using a genetic algorithm to encode image based on fractal encoder in the wavelet domain. Another hybrid scheme [18] used variance sorting with wavelet transform for accelerated fractal image compression. In this paper, a comparative study is carried to analyze the performance of a fractal image encoding algorithm using wavelet transform. Rest of Paper is arranged as follows. Section 2 contains the theoretical framework of wavelet coding. In the next section, a hybrid wavelet fractal encoder is discussed in the following Sect. 3. Experiment and result are summarized in Sect. 4. Finally, the paper is concluded in Sect. 5.

2 Background Work Wavelet Encoding

A natural image is composed of high-frequency components such as edges and intrinsic details while smooth regions of the image correspond to low-frequency elements. An obvious workout is to consider localization of frequency in the image so that a division can be done accordingly. A wavelet gives a set of basis function that decomposes a signal in the frequency and time domain simultaneously. A wavelet can be defined as the function $\psi \in l^2(R)$ with zero mean and guarantees that it is feasible to use in multiresolution decomposition if satisfy a certain condition. Here l^2 is a square integrable real space. Equations (1.a), (1.b) defines a discrete wavelet transform as the scale and shift function of the mother wavelet.

$$\omega_\phi(J_0, K) = \frac{1}{\sqrt{M}} \sum_t f(t) \phi_{J_0, K}(t) \quad (1.a)$$

$$\omega_\psi(J, K) = \frac{1}{\sqrt{M}} \sum_t f(t) \psi_{J, K}(t) \quad (1.b)$$

In the above equation, J_0 and K are scale and translate value respectively whereas $\phi_{J_0, K}(t)$ is scaling function of the wavelet transform. Spatial domain signal f and $\frac{1}{\sqrt{M}}$ is normalization term in the expression. If scaling function satisfies the dilation equation then it can be represented as the weighted sum of translates similarly translate or wavelet function can also be represented as weighted scale function at coarse level.

$$\psi(t) = \sum_{n \in Z} \sqrt{2}h_1[n]\phi(2t - n) \quad (2.a)$$

$$\phi(t) = \sum_{n \in Z} \sqrt{2}h_0[n]\psi(2t - n) \quad (2.b)$$

Scaling function has an effect of averaging or smoothing hence called low-pass filter. These equations split the signal into sub-bands one in low-pass filter and other in high-pass filter. The signal can be divided iteratively into LPF and HPF for further analysis. In the above pair of equations, Z represents the set of an integer. Parameter h_0 and h_1 is scaling vector, and high-pass response that is used to denote the weighted sum of scale and shift function applied to express each other. The inverse of the steps is performed to reconstruct the signal back at decoder end. Decoder end is called the synthesis filter.

The 2D-scaling function $\phi(x, y)$ act as separable function $\phi(x)$, $\phi(y)$ and wavelet function act as edge descriptors in the horizontal, vertical and diagonal direction given as. Each wavelet $\psi_{k,l}^j$ has four offspring which has the same spatial location and orientation. A wavelet subtree $s_{k,l}^j$ contains the wavelet coefficient and its four children $\psi_{2k,2l}^{j+1}$, $\psi_{2k+1,2l}^{j+1}$, $\psi_{2k,2l+1}^{j+1}$ and $\psi_{2k+1,2l+1}^{j+1}$ together with three orientations. The following section discusses the hybrid the wavelet and fractal image encoder.

3 Hybrid Fractal and Wavelet Image Encoding

In fractal image encoder, a set of $2^R \times 2^R$ range blocks is mapped to $2^{R+1} \times 2^{R+1}$ domain pool. A wavelet subtree represents a set a pixel corresponding to a portion of the image that is analogous to image block in the spatial domain. An inverse 2D-Haar wavelet transform of the tree is precisely the image block without its DC coefficient.

The generalization of wavelet basis reduced the map produced by the fractal encoder into a simple set of equations in the wavelet domain. Following a set of relations used Haar Basis to obtain further wavelet-based fractal encoder. To achieve generalization Haar basis in following equations are replaced with biorthogonal and symmetric basis function:

$$\langle \tilde{\psi}_{\gamma'}^j, F \rangle \approx \frac{g_{\Gamma}}{2^{D-R}} \langle \tilde{\psi}_{\gamma'}^{j-(D-R)}, F \rangle = \frac{g_{\Gamma}}{2^{D-R}} \langle W \tilde{\psi}_{\gamma'}^j, F \rangle \quad (3.a)$$

$$\langle \tilde{\phi}_{\Gamma}^{N-R}, F \rangle \approx \frac{g_{\Gamma}}{2^{D-R}} \langle \tilde{\phi}_{\Pi(\Gamma)}^{N-D}, F \rangle + h_{\Gamma} = \frac{g_{\Gamma}}{2^{D-R}} \langle W \tilde{\phi}_{\Gamma}^{N-R}, F \rangle + h_{\Gamma} \quad (3.b)$$

Parameters $\langle \tilde{\psi}_{\gamma'}^j, F \rangle$ and $\langle \tilde{\phi}_{\Gamma}^{N-R}, F \rangle$ are coefficients of biorthogonal wavelet basis function of $\psi_{\omega,k,l}^j$ and $\phi_{k,l}^j$. An image F expressed as a linear combination of translates and scale basis functions ψ and ϕ with different orientation specified as Γ and Π . Following is the simple variance based range classification algorithm of wavelet-based fractal image coder.

4 Algorithm

- Step 1. Decompose image into four sub-image using wavelet transform defined in the equation in Sect. 2. Decomposed images LL1, LH1, HL1, HH1, formed four different range pools and coded differently. Form range blocks in LL1 go to next step.
- Step 2. Resize domain block according to the size of range block.
- Step 3. (Pool reduction). Calculate the variance of all the range blocks. Check if the variance is less than a pre-set threshold. Store average pixel value as transform code. Mark range as covered. Move to the last step. Else search the space to find the best match with minimum distance difference between the blocks.
- Step 4. Check if no range block is uncovered than stop.
- Step 5. Reconstruct image by applying all stored transform on any initial image iteratively till converge.
- Step 6. Decompose the newly created image into four sub-image LL2*, LH2*, HL2*, HH2*, using level one wavelet transform.
- Step 7. Predict range block in LH1, HL1 using sub-image LH2*, HL2*.
- Step 8. Discard HH1 image details. Store all the fractal code details.

Experiment and discussion are summarized in the following section.

5 Experimental Results

The comparative experiment analysis of fractal encoder and wavelet image encoding is carried on MATLAB2013. Three images of different complexity are used of size 512×512 . A baseline wavelet encoder is subjected to three families of wavelets Haar, Coifs and Sym. Haar is most popularly used wavelet basis function. Table 1 shows the result of encoding image using one to three level of decomposition. Performance of algorithm is analyzed by time consumed, compression ratio and quality of the reconstructed image.

It is observed from Table 1 that as the level of decomposition increases consumption of time by the encoder also increases. The result shows a high compression ratio at the first level of decomposition, but the quality of the image is very poor. Increase iteration showed a reduction in Compression ratio, but the quality of image increases drastically. While comparing the three basis function, Haar wavelet shows a better outcome. Table 2 shows the result of an experiment conducted on hybrid encoder using wavelet and fractals.

Table 2 is the observation of fractal image compression using wavelet approach. Fractal image compression is asymmetrical compression process in terms of the time consumed in encoding and decoding time. It is observed that the quality of the image is measured in terms of PSNR. Also, size of the image is compared with prior and post-compression (Fig. 1).

Table 1 Comparative analysis of wavelet encoding based on different wavelet function

Type of wave	Level of decomposition	Encoding time			Compression ratio		
		1	2	3	1	2	3
Haar	Plane	4.93499	5.971079	5.257175	100	83.33	75
Coif1		4.593766	4.625676	5.253828	100	0	0
Sym2		4.59998	4.720638	5.254262	100	0	0
Haar	Texture	4.932622	5.312642	5.268538	100	83.33	75
Coif1		4.983047	5.316588	5.307305	100	83.33	0
Sym2		4.740389	4.834185	5.1778	100	0	0
Haar	MAN	4.935161	48.78723	5.272361	100	83.33	87.5
Coif1		4.944749	4.82274	5.263452	100	0	0
Sym2		4.878236	4.808128	5.217759	100	0	0

Table 2 Comparative analysis of fractal based wavelet encoding

Image	FIC using wavelet				
	Decoding time	Encoding time	Size before compression (MB)	Size after compression (KB)	PSNR
Text	24.492	63.694	1.00	400	70.1266
Man	24.243	62.322	1.00	415	54.4047
Airport	23.51	62.197	1.00	69.4	56.1314

6 Conclusion

Hybrid wavelet fractal encoder works better than conventional fractal image encoder due to better quantization and lesser artifacts. The subtree formed due to wavelet transform saves localized feature of image efficiently in both spatial and frequency domain. An overlapping subtree of domain blocks results in faster convergence. Acceleration in encoding is observed in using wavelet-based encoder because blocks remain in the same sequence in the spatial domain as energy rearrangement characteristics of wavelet coefficient.






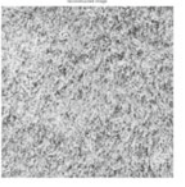
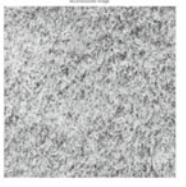
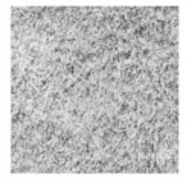
Wavelet name& Image Name	Coif Based DWT compressed Image	Haar Based DWT compressed Image	Haar Based Hybrid FIC +DWT compressed Image
			
Tribal Man	ET(5.263452)CR(0)	ET(5.272361)CR(87.5)	ET(62.322)CR(40.5)
			
Texture	ET(5.307305)CR(0)	ET(5.268538)CR(75.0)	ET(63.694)CR(39.06)

Fig. 1 Comparative visual representation along with performance measures: [compression ratio (%), encoding time (s)] using 8 bit grey-scale image of size 512 × 512

References

1. Barnsley MF (2014) *Fractals everywhere*. Academic Press
2. Barnsley MF, Sloan AD (1988) A better way to compress images. *Byte* 13(1):215–223
3. Jacquin AE (1992) Image coding based on a fractal theory of iterated contractive image transformations. *IEEE Trans Image Process* 1(1):18–30
4. Pentland A, Horowitz B (1991) A practical approach to fractal-based image compression. In: *Data compression conference, 1991. DCC'91*. IEEE
5. Davis G (1995) Self-quantized wavelet subtrees: a wavelet-based theory for fractal image compression. In: *Data compression conference, 1995. DCC'95. Proceedings*. IEEE
6. Andreopoulos I, Karayianris YA, Stouruaitis T (2000) A hybrid image compression algorithm based on fractal coding and wavelet transform. In: *The 2000 IEEE international symposium on circuits and systems, 2000. Proceedings. ISCAS 2000 Geneva, vol 3*. IEEE
7. Li J, Kuo C-CJ (1999) Image compression with a hybrid wavelet-fractal coder. *IEEE Trans Image Process* 8(6):868–874
8. Wu M (2000) A new fractal zerotree coding for wavelet image. *J Electron* 17(3):254–260
9. Xie X, Ma ZM (2000) Fractal predictive image coding based on zerotrees of wavelet coefficients. *J Image Graphics A* 5:920–924

10. Kim SH, Jang IH, Kim NC (2002) Image coding using wavelet-based fractal approximation. *IEICE Trans Inf Syst* 85(10):1723–1726
11. Xie YH, Fu DS, Ren W (2003) A fractal image coding algorithm research based on wavelet transformation. *J Image Graphics* 7(8):839–842
12. Wang DF, Jiang W (2005) Fractal image coding combined with wavelet subtree. *Syst Eng Electron* 27(6):1120–1122
13. Iano Y, da Silva FS, Mendes Cruz AL (2006) A fast and efficient hybrid fractal-wavelet image coder. *IEEE Trans Image Process* 15(1):98–105
14. Song C-L et al (2007) A novel fractal wavelet image compression approach. *J China Univ Min Technol* 17(1):121–125
15. Moreno J, Otazu X (2011) Image compression algorithm based on Hilbert scanning of embedded quadtrees: an introduction of the hi-set coder. In: 2011 IEEE international conference on multimedia and expo (ICME). IEEE
16. Zhang Y, Wang X (2012) Fractal compression coding based on wavelet transform with diamond search. *Nonlinear Anal Real World Appl* 13(1):106–112
17. Wu M-S (2014) Genetic algorithm based on discrete wavelet transformation for fractal image compression. *J Vis Commun Image Represent* 25(8):1835–1841
18. Wang X-Y, Zhang D-D (2014) Discrete wavelet transform-based simple range classification strategies for fractal image coding. *Nonlinear Dyn* 75(3):439–448

Automation of Business Cards



Shreya Srivastava, Suryanshu Sahay, Deepti Mehrotra and Vikas Deep

Abstract Business card is shared as hardcopy, the data present in business card will be highly useful if it is available in digital format. The task of manually entering the details of all business cards is laborious and time-consuming. Document image analysis is used in this paper for automating this process. This will be accomplished by performing OCR and then using the text to extract the Meta data. One more important component of business card is the logo of the organization. The text extraction OCR will be done using the Tesseract API. After conversion of the image to text, the data will be saved in the database. The raw data will be saved in the database, which will later be segregated and stored in the appropriate fields. It is generally ignored in the process of saving text information, in this paper it is extracted and stored in database. For logo detection various techniques like Gabor Filter, Harris edge detection technique, MSER, etc., are compared to determine the best technique for acquiring the most accurate logo extraction. Gabor filter gives the best result is used for the extracting logo and storing in database. Java language on NetBeans IDE platform which use the Spring MVC framework is used to implement this work.

Keywords Business card · OCR · Tesseract · Logo detection

S. Srivastava (✉) · S. Sahay · D. Mehrotra · V. Deep
Amity University Uttar Pradesh, Noida, Uttar Pradesh, India
e-mail: shreya96srivastava@gmail.com

S. Sahay
e-mail: suryanshusahay19@gmail.com

D. Mehrotra
e-mail: mehdeepti@gmail.com

V. Deep
e-mail: Vikasdeep8@gmail.com

1 Introduction

Business card is an important document which requires preservation and efficient data handling. The limitation of the card being offline and as a result it requires manual work for preserving the data digitally [1]. The greatest advantage of a business card, its tangibility has somehow also become its greatest disadvantage. These are easily accessible yet fragile. This problem has been tried to be solved by automating this process. The automation of business cards will be done by extracting all the data and saving each field into the database using different algorithms and logic using document image analysis [2–5]. This data will be saved to different fields based on the field analysis [6].

The data field extraction will be done to extract Meta data like Name, Company, Phone, Fax, Email, and Address. The rest of the information will be saved in the also be saved. The main contribution to this work was to filter the text by reducing the noise of the obtained text and then obtain the information which is necessary, i.e., categorizing the data into mapped and unmapped data. Mapped data will then be used to segregate the information and classifying it on the basis of various algorithms. Regular Expressions were used for pattern matching which will be used to extract information like email address, phone numbers, etc., which follow a certain pattern. However there will be exceptions like '@' will also be for the twitter handle which might be interpreted as an email. Core-NER-NLP (Name Entity Recognizer-Natural Language Processing) which uses Stanford Dictionary for various predefined field extraction like name of a person, organization, location, etc. The data extracted from the text will then be saved in separate fields in the data base. As the tesseract OCR is not 100% efficient, there will be a modification option where the user can manually correct the text before the data extraction takes place [7]. The home page will contain upload, modify, list, search, and delete links. Upload tab will be used to upload an image of the business card. Modify will be used to change any text which has been wrongly read by OCR. List will display all the business cards in a single page. Any query based on the business card will be done using the Search tab. For omitting/removing any uploaded business card, an option of Delete will be present.

This database will be available on the browser using the JDBC and Spring MVC framework. This will be a service available for various platforms. The database will be tried for being converted to contacts which will be directly saved in the mobile device.

2 Methodology

This work uses following APIs and software's for feature extraction: Stanford Core NLP, Tesseract, Oracle Glassfish Server, NetBeans IDE, RegEx, and MATLAB. Stanford Core NLP uses algorithms that eases the way computers are programmed in order to fulfill the humanistic requirements. Tesseract API uses optical character

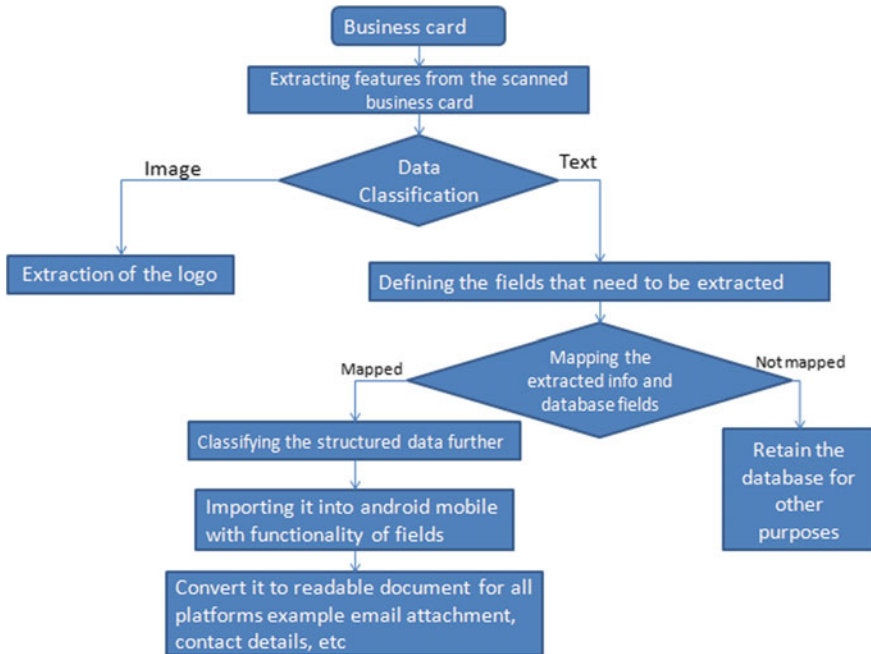


Fig. 1 Data flow diagram

recognition for extracting text from scanned images. Oracle Glassfish Server serves the purpose of handling servlets and JSP. The following diagram describe the complete work flow of the research work.

Figure 1 as shown explains how the scanned business card will be classified into two parts: image and text. The image, if detected will be extracted and the classified as the logo of the respective institution. Else the text will be mapped and classified under the respective database fields. For instance, email ids, '@' will be used for identification and 10 digit numbers will be used for mobile numbers. There are six fields in which the extracted text will be saved and classified. They are Name, Company, Phone, Fax, Email, and Address.

This work has been created on the NetBeans IDE platform using Java language. Since this is a web application, Glass Fish server was used. Glass Fish is an open-source application server built for the java platform. For the architecture, Spring Web MVC was used. The sole purpose of this is to handle all the HTTP requests as well as responses. The Maven Repository was used for this work as it helped in automatically building the dependencies for any number of times. The Tesseract OCR API was used for reading the text from the images. The acquired text was then stored in the database. It then further processed and filtered into the respective fields. This was done by using RegEx, NER, and Stanford Core NLP.

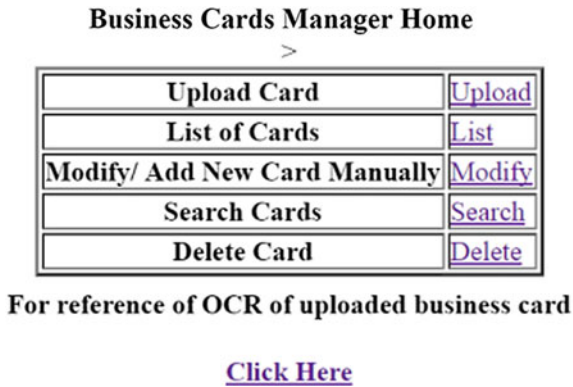


Fig. 2 Home page of the application

RegEx stands for regular expression. It is used for searching strings which follow a definite pattern. For instance an email id will always have '@' in between the string or a mobile number will have a '+' followed by ISD code and then the remaining 10 digits. There are exceptions in this as well, like for instance '@' might also be present in a twitter handle so.com was used for further classification. Phone numbers are also present in various formats like XXX-XXX-XXXX or + XX-XXXXXXXXXX, etc., which were also dealt with different user cases [8]. NER or Name Entity Recognition is generally used to extract information like names, addresses, percentages, or various quantities. Here it was used to identify the Name of the contact mentioned in the business card. Stanford Core NLP (Natural Language Processing) is an implementation of NER, it is a predefined dictionary which is used to identify and extract information having three major classes (Location, Person, and Organization) this was used to identify the address of the office or institution as duly mentioned in the business card.

The MySQL database was administered and managed by phpMyAdmin. Xampp was used to manage cross-platform operations of majorly database and php.

The class HomeController was created to manage the map the browser requests. The DAO class is used to as a logical interface between the database and the MVC model. The POJO files manage uploading of the business card as well as creating contacts in the database. Utility files include all the text extraction techniques for each field, viz., email, fax, and phone number.

Figure 2 shows the home page of the application. As mentioned, there are options to list all the uploaded cards from the database, manually edit the stored information (see Fig. 3) as the OCRed text is not 100% efficient, search for the business cards using the primary key from a database, and also delete any card.

Dependencies were built separately are done in MVC framework. The main advantage of building dependencies is to eliminate the need to the work of identifying and specifying them. These dependencies are added automatically. It is particularly useful when a large dependency tree is formed as it then becomes difficult to keep a track

Edit The Fields

Company Name:	Mukesh Motor
Name:	Mukesh Motor
Mobile:	9871886512
Email:	
Fax:	7744054755
Address:	Uphaar Cinema, New Delhi

Contact Saved !

Fig. 3 Manually editing the fields

on each one of them. The few dependencies that have been built include JAR files like tess4j for OCR extraction, jdbc for java and database connectivity, Stanford-corenlp for the predefined dictionary, spring expression which is used for querying, spring-tx which manages transactions.

For the logo part, MATLAB was used. MATLAB was preferred over Java because the scanned image requires to be processed and since Java Image processing slows down the application, therefore it is best to use the MATLAB in place of Java for image processing. Java Image Processing is useful when the image is only of a few bytes (few hundred dpis), but when larger sized images are being considered for processing, it is best to use platforms which are best suited to process the images as per the requirements. Many different techniques were used in order to identify the logo from business cards. The techniques involved were edge detection, Gabor filter, SURF and SIFT algorithms [9, 10]. All of these techniques are based on the phenomenon of feature extraction. The feature extraction is a method of extracting the important features from the image. These are useful in various fields like object recognition or identifying a particular set of textures or for image retrieval [11, 12].

Edge detection: it is a technique to identify the image boundaries. This will be useful in detecting the logos as it will extract the image present in the image itself. Boundary detection is done by comparing the image brightness and checking its discontinuities [13–15].

SIFT: Scale-Invariant Feature Transformation is one of the basic algorithms used to detect logos. It is very useful as it is invariant to mostly all types of features like scaling, translation, rotation, or even the illumination. It basically converts the image into vectors which are then used for image description.

SURF: Speeded-Up robust Features is an algorithm derived through SIFT for image detection it is better than SIFT in terms of computability and distinctiveness (Fig. 4a, b).

Harris features: This technique is used to detect the corners and identify them (Fig. 5).



Fig. 4 a Implementation of SURF. b Implementation of SURF



Fig. 5 Harris corner detection

MSER: Maximally Stable External Regions is used for image detection. It deals with the correspondences among the different image components (Fig. 6).

Gabor Filter: It is a filter used to identify the textures present. It serves the purpose of identifying the regions where a certain frequency is present. The main disadvantage of this filter is that it is over reliant on the orientation of the image Fig. 7. The following code snippet was used for implementing the Gabor filter:

Comparing all the features and results, it was Gabor Filter which was found to be most accurate and result-oriented. Others techniques like MSER and Harris corner detection identified the texts also. Thus making it difficult to extract the logo from them.



Fig. 6 Implementation of SURF



Fig. 7 Implementation of Gabor Filter

3 Results and Discussions

The business card scanned was used for text as well as logo extraction. As explained below the following results were obtained:

The OCR performed text was retrieved in the database because data other than the structured data might also be useful and hence can be of some purpose as shown in Fig. 8. Figure 9 shows how information has been mapped to the respective fields and thus the data has been retrieved in the database as well. Data has been stored in each category differently.

OCR ID	OCR Text
18	... +919423341220 Health h?? d: u in. apjadhav@gmail.com Dr. Sushma Jadhav MBBS? DNB (Medicine). IDCCM General Physician, Cardiologist, Diabetologist & Insensivist Monday to Saturday : Shop 2, Unity Commercial, Morning 10.00 am. to 01.00 pm Opp Oriental Bank of Commerce, Evening 06.00 pm. to 08.30 pm. Baner Mhalunge Road? Baner, Pune ? 45.
19	Mukesh Mob. : 9871886512 Mukesh Motor *5 H%%. 0C--7-5* S 20, Green Park, Uphav Cinema, Near Petrol Pump, New Delhi -1 10016
22	... 4-919423341220 Health Clinic drsushmapjadhav@gmail.com Dr. Sushma Jadhav MBBS. DNB (Medicine). IDCCM General Physician Cardiologist Diabetologist E insensivist Monday to Saturday : Shop 2, Unity Commercial, Morning : 10.00 am. to 01.00 pm. Opp. Oriental Bank of Commerce. Evening : 0600 pm. to 08.30 pm. Baner Mhalunge Road, Baner, Pune = 45.

Fig. 8 The OCR performed text in the database

Card ID	Company Name	Name	Mobile	Email	Fax	Address	Action
9	Cardiologist , Diabetologist & Insensivist Unity Commercial Opp Oriental Bank of Commerce	Dr. Sushma Jadhav	9194233412	apjadhav@gmail	null	Pune	Edit Delete
40	Vikas Tours & Travels	Vikas Pakhare	9975070636 9028612055		7744054755	Padmavati Pune	Edit Delete
49	CDAC	Dr. Dinesh S. Katre	91-9922992746	dinesh@cdac.in	91-20-25503386	Pune	Edit Delete

For reference of OCR of uploaded business card

[Click Here](#)

Fig. 9 Business card list

As the scanned cards may vary, they will have different formats like .jpg, .pdf, etc. Hence, ghost jar as well as imagio jar was used for different formats of the uploaded image. This application was run on the glassfish server as all the connectors and backend APIs would work properly and efficiently on this server, therefore, making user-friendly GUI. Thus, the application successfully returns the relevant extraction of data using tesseract and other APIs and techniques.

The logo extraction was done based on the comparison of different techniques; following results were obtained in the end (Fig. 10).

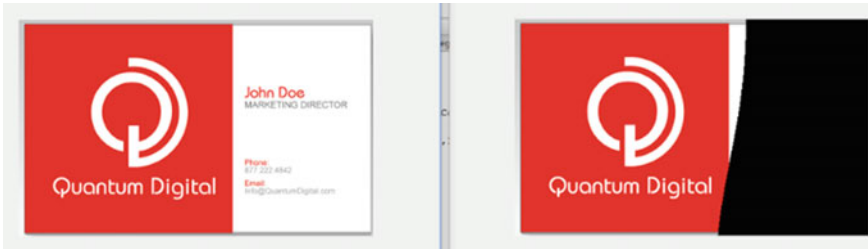


Fig. 10 Logo extraction using Gabor Filter

4 Conclusion

The work is tried and tested on business cards of different types but there was noise which was prevalent in every business card. This was reduced by specifically applying algorithms. As a result only important data was extracted in the database. Since every business card is different therefore it is difficult to extract the information from each business card with absolute efficiency. This can be improved with increase in the dictionary and refinement of algorithms of tesseract, so that the noise can be reduced and other important information can also be retrieved example some business cards may have websites as well as their designation and branches of their company. Therefore, such card's OCR text field extraction would filter out such important details as noise whereas these can also be extracted and saved under more information tab so that correct and detailed data is provided to the user. Along with the important data, the logo was also extracted which being an added feature will help in simpler and easier classification of the contacts. The Gabor Filter was the most relevant technique and as a result successful implementation was done.

References

1. LaForge L, Carlson D, Korver K, System for creating and reading digital business cards, forms, and stationery. U.S. Patent Application No. 10/055,011
2. Carton C, Lemaitre A, Coüason B (2015) Automatic and interactive rule inference without ground truth. In: 2015 13th international conference on document analysis and recognition (ICDAR). IEEE
3. Karatzas D et al (2016) Human-document interaction systems—a new frontier for document image analysis. In: 2016 12th IAPR workshop on document analysis systems (DAS). IEEE
4. Niyogi D, Srihari SN, Govindaraju V (1996) Analysis of printed forms. In: Handbook on optical character recognition and document image analysis. World Scientific Publishing Co., Singapore
5. Harvey R, Oliver G (2016) Digital curation. ALA Neal-Schuman
6. Rusinol M, Benkhelfallah T, Poulaind'Andecy V, Field extraction from administrative documents by incremental structural templates
7. Mithe R, Indalkar S, Divekar N (2013) Optical character recognition. Int J Recent Technol Eng 2.1:72–75

8. Zhu G, Bethea TJ, Krishna V (2007) Extracting relevant named entities for automated expense reimbursement. In: Proceedings of the 13th ACM SIGKDD international conference on knowledge discovery and data mining. ACM
9. Wang H, Chen Y (2009) Log detection in document images based on boundary extension of feature rectangles. IEEE
10. Park JH, Jang IH, Kim NC, Skew correction of business card images acquired in PDA
11. Aksoy S, Haralick RM (1998) Textural features for image database retrieval. Content-based access of image and video libraries. IEEE
12. Connors RW, Harlow CA (1976) Some theoretical considerations concerning texture analysis of radiographic images. In: Proceedings of IEEE conference on decision and control, pp 162–167
13. Flickner M (1993) The QBIC project: querying images by content using color texture and shape. SPIE storage and retrieval of image and video databases
14. Ma WY, Manjunath BS (1997) NETRA: a toolbox for navigating large image databases. In: Proceedings of ICIP
15. Pentland A (1994) Photobook: content-based manipulation of image databases. SPIE storage and retrieval of image and video databases II, pp 34–47, 1994 Feb

Fractional Order Sliding-Mode Controller for Quadcopter



Om Veer Dhakad and Vivek Kumar

Abstract This paper proposed the concept of fractional order sliding-mode control (FOSMC) for chattering reduction and reduced error converging time for Quadcopter. The controller is designed to control over the six degrees of freedom of the Quadcopter and enhances the stability as compared to PI-based control. In PI-based controllers the high transient overshoots deteriorate the stability of Quadcopter system. The FOSMC improves both transient and steady-state behavior of the Quadcopter motion. The FOSMC controller is highly robust controller as it rejects system uncertainties and disturbances drastically. FOSMC controller provides chattering free response as chattering is considered the main drawback in present conversational sliding-mode controls. Chattering is low amplitude noise present at high frequencies. For vertical take-off and landing (VTOL), an ERROR sliding surface is considered and then a mathematical analysis is carried out under the sliding-mode control law. The input unit step and ramp disturbances are considered to check the robustness of the controller. The Lyapunov-based stability criterion is used to check stability of the controller. The controller is tested by simulation in Simulink MATLAB. The FOSMC is not just gives better execution time with minimum control input, in addition, it shows strong, notwithstanding outer load unsettling influence and parameter varieties.

Keywords Fractional order sliding-mode control (FOSMC) · Advance control theory · Simulink MATLAB · Quadcopter (UAV)

1 Introduction

The control of Quadcopters or UAVs (unmanned aerial vehicles) has been a subject of significant intrigue over the previous decades. Be that as it may, the control out-

O. V. Dhakad (✉) · V. Kumar
Amity Institute of Aerospace Engineering, Amity University, Noida, Uttar Pradesh, India
e-mail: om.veer1995@gmail.com

V. Kumar
e-mail: Vkumar13@amity.edu

© Springer Nature Singapore Pte Ltd. 2019
M. Kumar et al. (eds.), *Advances in Interdisciplinary Engineering*, Lecture Notes in Mechanical Engineering, https://doi.org/10.1007/978-981-13-6577-5_36

line for a quadrotor UAV is not a basic assignment. Most importantly, as a turning wing flying machine and a characteristic nonlinear framework, the quadrotor is open-circle instable, which requires a quick control reaction and an expansive task go [1]. It has been broadly utilized as a part of an assortment of circumstances including reconnaissance, fire fighting, ecological observing, et cetera [2]. As a smaller scale helicopter, the quadrotor UAV pulls in extraordinary consideration from military and common applications because of its exceptional focal points, for example, straight-forward structure, vertical taking off and landing (VTOL), and quick moving [3]. Aside from the control of UAV, I&I is additionally connected in visual servoing, control of pendulum on truck, and numerous other mechatronic frameworks [4]. To control a small scale quadrotor UAV and beat the vulnerabilities related with the thrust and drag coefficients, Fujimoto et al. disentangled the dynamic model and built up a versatile controller by means of the I&I philosophy. In any case, just numerical recreation comes about are introduced in these works, and no test comes about with the I&I versatile outline are given, [5]. An I&I strategy is utilized to assess the obscure mass of a VTOL vehicle, and it ensures that the estimation focalizes to its actual esteem, [6]. This approach, not quite the same as the great versatile strategy, does not require the LP condition, nor does it summon assurance comparability. It likewise disentangles the solidness investigation by giving cross terms in the Lyapunov work [7]. As of late, another versatile control configuration utilizing the drenching and invariance (I&I) approach is the first master postured in [8] and after that further created by numerous scientists [4–7]. In any case, the exemplary versatile control strategy dependably requires a direct parameterization (LP) condition, and now and then, the controller's singularities will appear [9]. The asymptotic steadiness (AS) of the shut circle framework is demonstrated by means of a hypothesis of fell frameworks. To make up for the parametric vulnerabilities, the versatile nonlinear control technique is an appropriate decision and has been generally used [10]. The dynamic arrangement of the quadrotor is isolated into the inward circle and the external circle subsystem. Such a plan is not troublesome for usage, however, the strength of the shut circle framework cannot be effectively ensured. To defeat this downside, an inward and external circle-based flight controller is proposed in [11]. A novel vigorous back stepping-construct controller that is based with respect to an integral sliding-mode approach is proposed for an underactuated quadrotor. Despite the fact that the outline method of the back stepping plan is clear and the evidence of the strength is standardized, the control picks up are difficult for tuning [12]. In this way, lately, more nonlinear hearty control plans have been produced. With respect to the underactuated property, different control procedures have been created for the quadrotor and other under-actuated mechatronic frameworks, for example, a wheeled portable robot, a submerged vehicle, and overhead cranes [13, 14]. Second, the quadrotor UAV has six degrees of opportunity, yet it has just four control inputs accessible; this is known as an underactuated property, which additionally prompts solid couplings between the dynamic states. Third, the estimation of some parameters related to the dynamic model, for example, the inertial minutes and streamlined coefficients, cannot be estimated or gotten precisely. Besides, the quadrotor UAV is exceptionally delicate to outer aggravations, for example, twist blast because of its

little size and weight. To take care of these issues, diverse control procedures have been created. Since the dynamic model of the quadrotor can be linearized, at that point some conventional straight control can be utilized to settle the quadrotor in a little range around the balance. While considering the nonlinearity and a vast task run, the execution of the straight controller might be corrupted strategies [15, 16]. A control plot utilizing RISE input and neural system feedforward is connected on a rotorcraft-based UAV, and the semi-global asymptotic following of the disposition and elevation states is demonstrated by a Lyapunov-based dependability investigation, [17]. The RISE criticism control can make up for outside aggravations and demonstrating vulnerabilities while ensuring semi-global asymptotic outcomes in the feeling of a persistent control input, [18]. A general sliding-mode control (SMC) is produced for a class of unverifiable under-actuated frameworks and after that used to settle a quadrotor helicopter. Be that as it may, a downside of the SMC is the babbling issue, which may deteriorate the control execution for functional usage. To accomplish a nonstop control methodology, a powerful necessary of the signum of the mistake (RISE) - based controller is first exhibited in our past work in [17] and additionally created by other researchers [18, 19].

In this paper, in light of the previously mentioned control difficulties for a quadcopter, a novel nonlinear hearty following control conspire is proposed. In the first place, to comprehend the under actuation and the couplings, the control framework is separated into two sections: the inward circle (state of mind circle) controller and the external circle (position circle) controller. Second, to meet the necessities for vigorousness and quick reaction of mentality control, the RISE technique is controlled the inward circle subsystem. At long last, so as to address the obscure parameters and decrease the trouble of control outline, an I&I-based versatile control plot is used for the external circle subsystem control plan. The proposed technique yields the principal I&I, RISE, and internal and external circle-based control comes about for the underactuated quadcopter UAV within the sight of parametric vulnerabilities and obscure outer unsettling influences. Specifically, in spite of the trouble of strength examination for the internal/external circle approach, the proposed controller ensures the asymptotic following the shut circle framework through the Lyapunov-based security investigation. Besides, to approve the execution of the proposed outline, the non-straight powerful versatile control configuration is checked by the ongoing investigations on equipment on the up and up recreation (HILS) quadcopter test bed. To our best learning, a couple of past works has shown ongoing exploratory outcomes for the I&I approach on a quadcopter UAV framework.

This paper is presented in the following sections after the introduction part as covered in Sect. 1, Sect. 2 describes the Quadcopter Dynamics, mathematical Controller Designing is brought in Sect. 3, Sect. 4 explains about the sliding-mode Fractional Calculation, the Results & Discussions is placed in Sect. 5 of the paper and finally Sect. 6 Concludes the finding of the proposed controller.

2 Quadcopter Dynamics

The quadcopter schematic is shown in Fig. 1. The thrusts produced by the four rotors are signified by $q_i(t)$, $i = 1, 2, 3, 4$, individually. Let $J = \{x_J, y_J, z_J\}$ speak to one side-hand idleness outline with z_J being the vertical heading toward the sky. The body settled casing, which is signified by $S = \{x_s, y_s, z_s\}$, is situated at the focal point of gravity of the airplane. The Euclidean position and Euler point of the Quadcopter regarding the casing $\{J\}$ are described by $\epsilon(t) = [x(t), y(t), z(t)]^T \in R^3$ and $\zeta(t) = [\varphi(t), \theta(t), \psi(t)]^T \in R^3$ (Fig. 2).

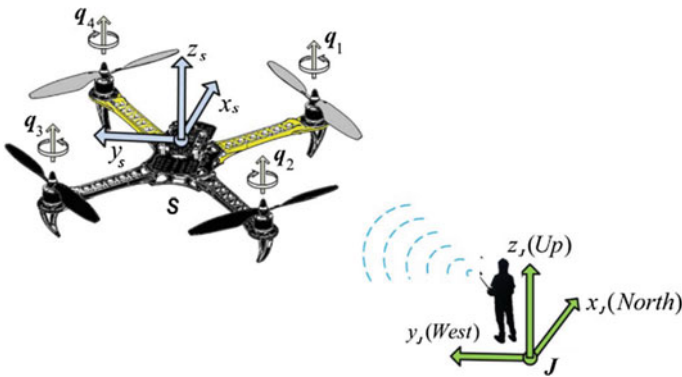


Fig. 1 Quadcopter schematic

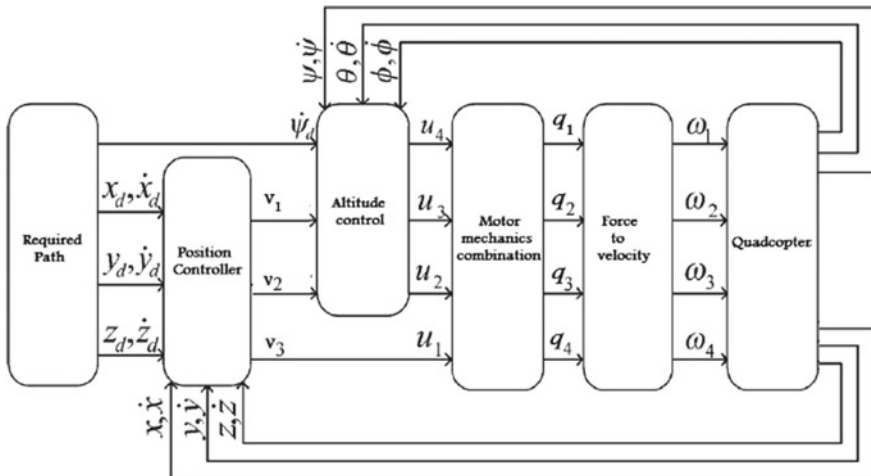


Fig. 2 Fractional controller block diagram

The dynamic model shown in $\{J\}$ is given as

$$\begin{aligned}
 J_1 \ddot{\varphi} &= -C_4 l \dot{\varphi} + b_1(t) + l \tau_1 \\
 J_2 \ddot{\theta} &= -C_5 l \dot{\theta} + b_2(t) + l \tau_2 \\
 J_3 \ddot{\psi} &= -C_6 \dot{\psi} + b_3(t) + k \tau_3 \\
 m \ddot{x} &= -C_1 \dot{x} + (\cos \psi \sin \theta \cos \varphi + \sin \psi \sin \varphi) u_t \\
 m \ddot{y} &= -C_2 \dot{y} + (\sin \psi \sin \theta \cos \varphi - \cos \psi \sin \varphi) u_t \\
 m \ddot{z} &= -C_3 \dot{z} - mg + (\cos \theta \cos \varphi) u_t
 \end{aligned} \tag{1}$$

where $m \in R^+$ signifies the mass, $J_i \in R^+$ for $i = 1, 2, 3$ are the MOI (Moments of Inertia), g is the acceleration due to gravity, $C_i \in R^+$ for $i = 1, \dots, 6$ describes the aerodynamic damping coefficient, $l \in R^+$ indicates the separation between the epicenter of the Quadcopter and the rotor pivot, and $b_i(t) \in R$ for $i = 1, 2, 3$ speaks to the obscure time-fluctuating outer unsettling influences. In(1), $\tau_1(t)$, $\tau_2(t)$, $\tau_3(t)$ and $u_t(t)$ mean the aggregate thrust and three rotational powers delivered by the four rotors, and $k \in R^+$ shows a invariant force to moment factor.

3 Controller Design

Comment 1 The general control objective is to outline the control input signs to let the quadrotor track time-changing wanted directions $[x_d(t), y_d(t), z_d(t), \psi_d(t)]^T$.

Comment 2 The framework parameters J_i (for $i = 1, 2$, and 3), C_j ($j = 1, \dots, 6$), l , and k are positive unknown constants. The rotor thrusts $[q_1, q_2, q_3, q_4]^T$ and the connection between the control input signals $[\tau_1, \tau_2, \tau_3, u_t]^T$ is given by

$$\begin{aligned}
 \tau_1 &= -q_1 - q_2 + q_3 + q_4 \quad \tau_2 = -q_1 + q_2 + q_3 - q_4 \\
 \tau_3 &= -q_1 + q_2 - q_3 + q_4 \quad u_t = q_1 + q_2 + q_3 + q_4
 \end{aligned} \tag{2}$$

The speed of rotation for each motor ω_i for $i = 1, 2, 3, 4$ can be calculated in view of the estimation of the lifting force q_i . Now simplifying the above mathematical dynamic model from Eq. (1) we get

$$\begin{aligned}
 m \ddot{\mathbf{e}} + C_{\mathbf{e}} \dot{\mathbf{e}} + mg e_3 &= u_t^J R e_3 \\
 J \ddot{\zeta} + C_{\zeta} \dot{\zeta} - b &= \tau
 \end{aligned} \tag{3}$$

where $C_{\mathbf{e}} = \text{diagonal}\{C_1, C_2, C_3\} \in R^{3 \times 3}$, $e_3 = [0, 0, 1]^T \in R^3$, $J = \text{diagonal}\{J_1/l, J_2/l, J_3/k\} \in R^{3 \times 3}$, $C_{\zeta} = \text{diagonal}\{C_4, C_5, C_6/k\} \in R^{3 \times 3}$, $b = [(b_1(t)/l), (b_2(t)/l), (b_3(t)/c)]^T \in R^3$, $\tau = [\tau_1, \tau_2, \tau_3]^T \in R^3$, ${}^J R(\eta) \in \text{SO}(3)$ signifies the rotation matrix between the inertial frame $\{J\}$ and the body-fixed-frame $\{S\}$.

4 Fractional Calculations

As specified before, considering the sliding surface as follows:

$$s_1 = \dot{\epsilon} + D^\alpha \lambda_{RL}(\text{sign}(e_1))^r \tag{4}$$

$$s_2 = \dot{\zeta} + D^\alpha \lambda_{RL}(\text{sign}(e_2))^r \tag{5}$$

Assumptions

$$\begin{aligned} \epsilon_1 &= \int \epsilon + \epsilon \\ \dot{\epsilon}_1 &= \epsilon - \dot{\epsilon} \\ \dot{\epsilon}_1 &= \dot{\epsilon} - \ddot{\epsilon} \end{aligned}$$

Similarly, $\dot{\zeta}_1 = \dot{\zeta} - \ddot{\zeta}$

Let, $\dot{s}_1 = -C_1 \text{sign}(s_1)$ and $\dot{s}_2 = -C_2 \text{sign}(s_2)$

Again $s_1 = C_J \int \dot{\epsilon} - C\dot{\epsilon}$ and $s_2 = C_J \int \dot{\zeta} - C\dot{\zeta}$

where $\text{Sign}(p) = \begin{cases} -1, & p < 0 \\ 0, & p = 0, p \text{ is variable} \\ 1, & p > 0 \end{cases}$

Now from Eqs. (4), (5) and from above expressions

$$-C_1 \text{sign}(s_1) = \dot{s}_1 = C_J \dot{\epsilon} + \ddot{\epsilon}$$

And from Eq. (3) we get

$$\begin{aligned} -C_1 \text{sign}(s_1) &= C_J \dot{\epsilon} - \frac{C\epsilon}{m} - ge_3 + \frac{u_{tS}^J Re_3}{m} \\ \text{Or, } -C_1 \text{sign}(s_1) &= \left(C_J - \frac{C\epsilon}{m} \right) \dot{\epsilon} - ge_3 + \frac{u_{tS}^J Re_3}{m} \end{aligned} \tag{6}$$

But $\dot{\epsilon} = -C_2 \text{sign}(s^1) - \epsilon$

Therefore, Eq. (6) becomes

$$-C_1 \text{sign}(s_1) = \left\{ \left(C_J - \frac{C\epsilon}{m} \right) (-C_2 \text{sign}(s^1) - \epsilon) \right\} - ge_3 + \frac{u_{tS}^J Re_3}{m}$$

Now simplifying for u_{tS}^J

$$u_{tS}^J = \frac{[-\{(C_J - \frac{C\epsilon}{m})(-C_2 \text{sign}(s^1) - \epsilon)\} + ge_3 - C_1 \text{sign}(s_1)] Re_3^T}{m} \tag{7}$$

Now calculating the values of τ_1 , τ_2 and τ_3 , and from assumptions

$$-C_2 \text{sign}(s_2) = \dot{s}_2 = C_J \dot{\zeta} + \ddot{\zeta}$$

And from Eq. (3)

$$-C_2 \text{sign}(s_2) = C_J \dot{\zeta} + \frac{\tau_1 + b_1 - C_\zeta \dot{\zeta}}{J_1}$$

Or, $-C_2 \text{sign}(s_2) = \left(\frac{C_J - C_\zeta}{J_1}\right) \dot{\zeta} + \frac{\tau_1 + b_1}{J_1}$ (8)

But $\dot{\zeta} = -C_4 \text{sign}(s^2) - \zeta$
 Therefore, Eq. (8) becomes

$$-C_2 \text{sign}(s_2) = \left(\frac{C_J - C_\zeta}{J_1}\right) (-C_4 \text{sign}(s^2) - \zeta) + \frac{\tau_1 + b_1}{J_1}$$

Now simplifying for τ_1

$$\tau_1 = J_1 \left[-C_2 \text{sign}(s_2) - \left(\frac{C_J - C_\zeta}{J_1}\right) (-C_4 \text{sign}(s^2) - \zeta) \right] - b_1$$
 (9)

Similarly,

$$\tau_2 = J_2 \left[-C_2 \text{sign}(s_2) - \left(\frac{C_J - C_\zeta}{J_2}\right) (-C_5 \text{sign}(s^2) - \zeta) \right] - b_2$$
 (10)

$$\tau_3 = J_3 \left[-C_2 \text{sign}(s_2) - \left(\frac{C_J - C_\zeta}{J_3}\right) (-C_6 \text{sign}(s^2) - \zeta) \right] - b_3$$
 (11)

4.1 Lyapunov Stability of System

Considering M as a Lyapunov Stability Function for stability analysis of sliding surface, for stable system M should be positive, i.e., $M > 0$, for error sliding surface “ s ”

$$M = \frac{1}{2} s^2$$

It means that $M > 0$, due to sliding surface (s) is a squared term it will give always positive value.

Now, according to the stability criteria \dot{M} should be negative

$$\dot{M} = s\dot{s}$$

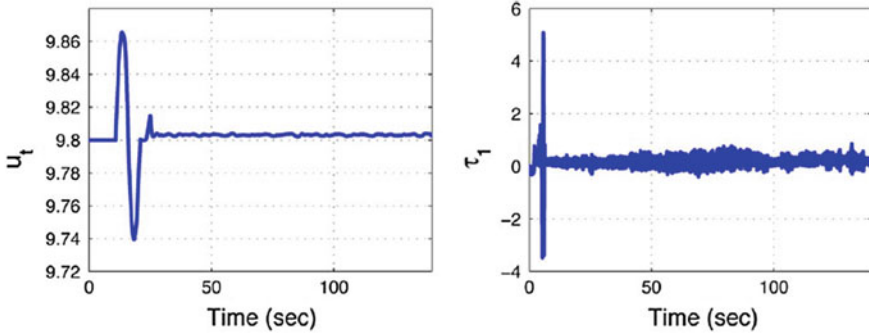


Fig. 3 Total thrust force u_t and rotational force τ_1 versus time

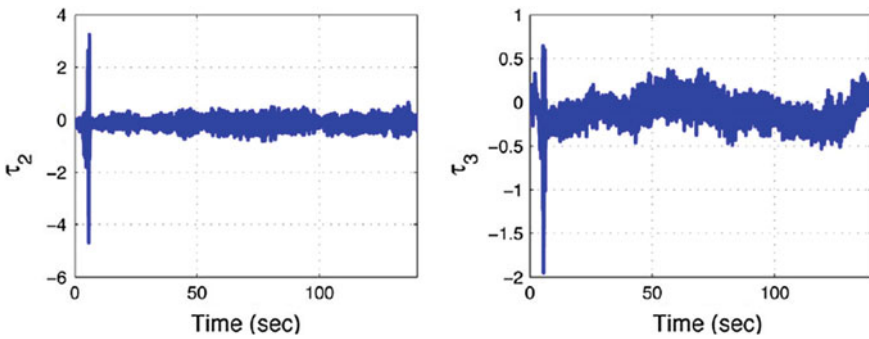


Fig. 4 Rotational forces τ_2 and τ_3 versus time

Or,

$$\dot{M} = s(-C \text{sign}(s))$$

where $C > 0$ for $t > 0$, it means that $\dot{M} < 0$.

Lyapunov Stability is satisfied.

5 Results and Discussions

The FOSMC (Error) controller is executed by Simulink MATLAB simulator. The following images show the behavior of the quadcopter to various points. In Fig. 3 the control input thrust force and rotational force parameters obtained in Eqs. (7) and (9), i.e., u_t and τ_1 by using fractional order method are shown with respect to time. The graph shows that an initial variation is more but within the finite time or very less time system attain the desired values of u_t and τ_1 .

In Fig. 4 the control input rotational forces parameters obtained in Eq. (10) and (11), i.e., τ_2 and τ_3 by using fractional order method are shown with respect to time. The graph shows that an initial variation is more but within the finite time or very less time system attain the desired values of τ_2 and τ_3 .

In Fig. 5 the variation of Euler angles φ , θ and ψ with time is shown. Initially $\varphi = 0, \theta = 0$ and $\psi = 0$ and the desired values are $\varphi = 0, \theta = 0$ and $\psi = \pi/6.28$. The graph shows that the initial variations is more but within the finite time or very less time system attain the desired values of Euler angles φ, θ and ψ . In Fig. 6 the

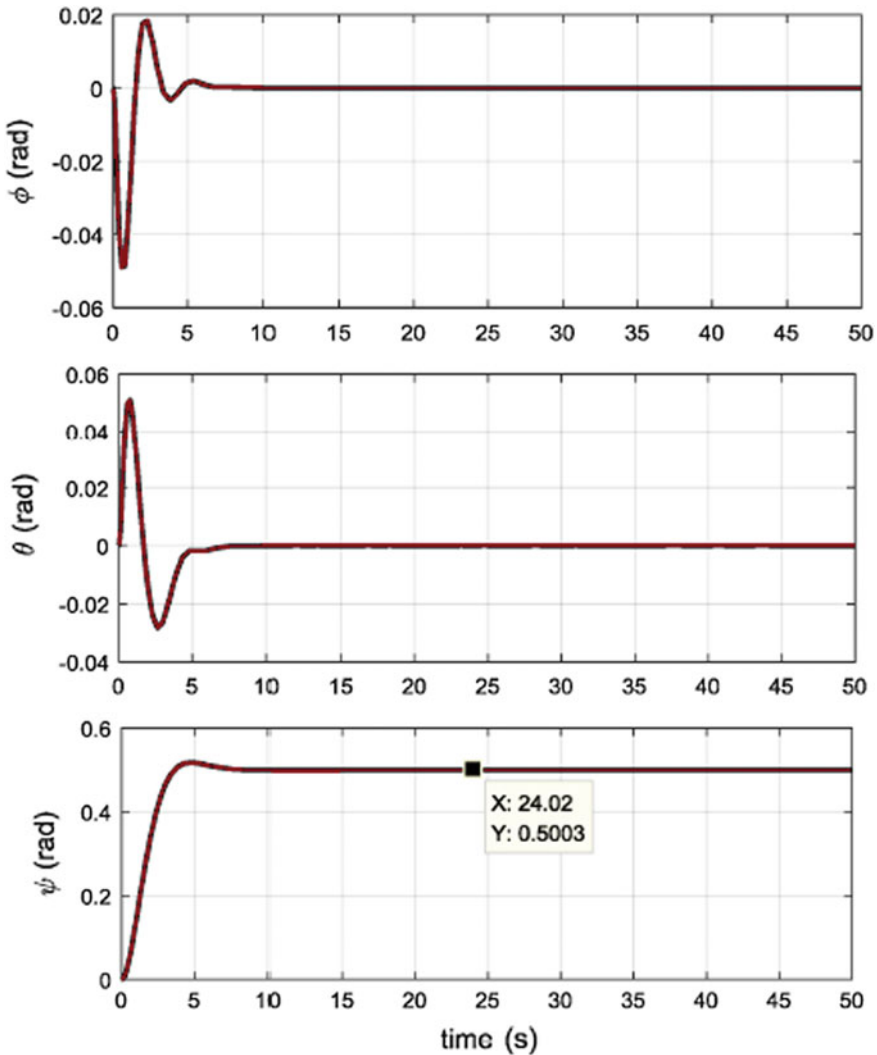


Fig. 5 Euler angles φ, θ and ψ versus time

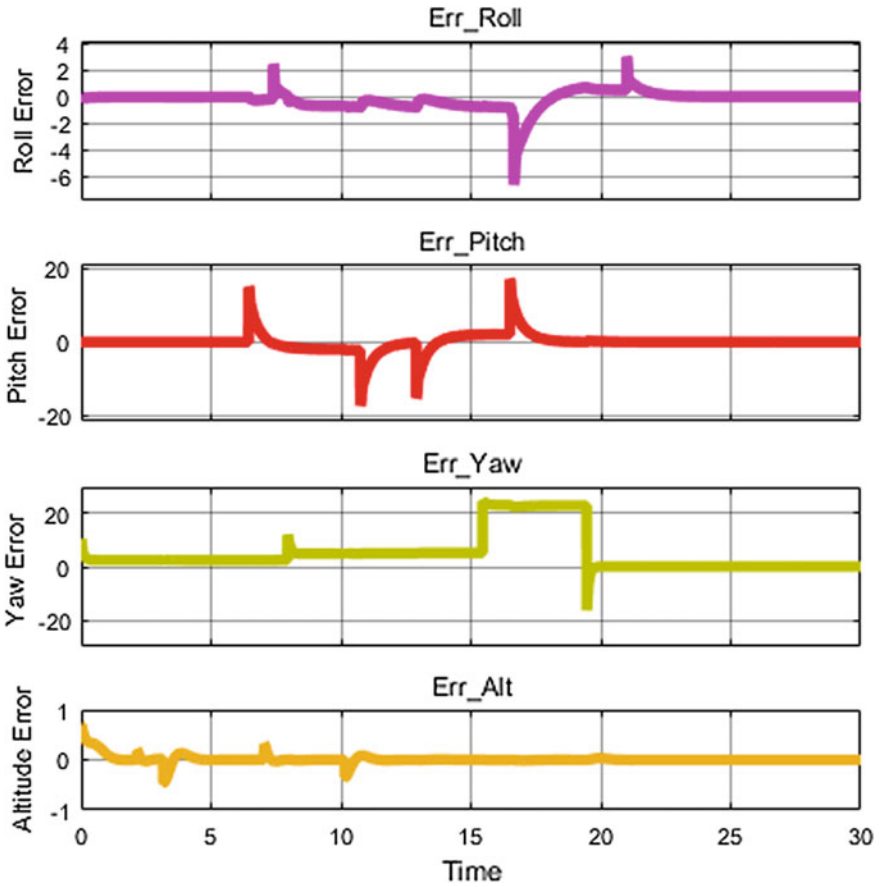


Fig. 6 Error analysis

error in roll, pitch, yaw and altitude is analyzed with time. The variation in error is very less which shows the system stability. In Fig. 7 the variation of error in chattering form is shown for the order of time is 10^{-2} s.

6 Conclusions

As per the results obtained from the simulation, it is verified that the FOSMC control is robust and chattering free. The obtained as per the Fig. 7 is of very small amplitude and can be ignored. The controller shows full control over the six degrees of freedom. It is observed from the mathematical calculations that the FOSMC control variable ‘ α ’ can be modeled to tune appropriate error amplitudes and corresponding converging

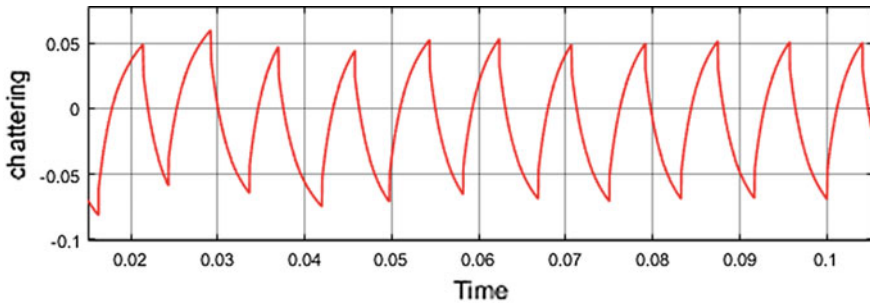


Fig. 7 Chattering

time. It is also shown by the results that the controller improves initial transients and steady-state performance of Quadcopter. The error analysis graphs show finite time converge of parametric errors as per Lyapunov Stability criterion.

References

1. Liu H, Lu G, Zhong Y (2013) Robust LQR attitude control of a 3-DOF laboratory helicopter for aggressive maneuvers. *IEEE Trans Ind Electron* 60(10):4627–4636
2. Du Y, Fang J, Miao C (2014) Frequency domain system identification of an unmanned helicopter based on adaptive genetic algorithm. *IEEE Trans Ind Electron* 61(2):870–881
3. Lugo JJ, Zell A (2014) Framework for autonomous on-board navigation with the AR. *Drone. J Intell Robot Syst* 73(1–4):401–412
4. Astolfi A, Ortega R, Venkatraman A (2010) A globally exponentially convergent immersion and invariance speed observer for mechanical systems with non-holonomic constraints. *Automatica* 46(1):182–189
5. Fujimoto K, Yokoyama M, Tanabe Y (2010) I&I-based adaptive control of a four-rotor mini helicopter. In: *Proceedings of 36th annual conference on IEEE industrial electronic society, Glendale, AZ, USA, 7–10 Nov 2010*, pp 144–149
6. Hu J, Zhang H (2013) Immersion and invariance based command-filtered adaptive backstepping control of VTOL vehicles. *Automatica* 49(7):2160–2167
7. Astolfi A, Karagiannis D, Ortega R (2008) *Nonlinear and adaptive control with applications*. Springer, Berlin, Germany
8. Astolfi A, Ortega R (2003) Immersion and invariance: a new tool for stabilization and adaptive control of nonlinear systems. *IEEE Trans Autom Control* 48(4):590–606
9. Slotine JE, Li W (1991) *Applied nonlinear control*. Prentice-Hall, Englewood Cliffs, NJ, USA
10. Dydek ZT, Annaswamy AM, Lavretsky E (2013) Adaptive control of quadrotor UAVs: a design trade study with flight evaluations. *IEEE Trans Control Syst Technol* 21(4):1400–1406
11. Kendoul F (2009) Nonlinear hierarchical flight controller for unmanned rotor-craft: design, stability, experiments. *J Guidance Control Dyn* 32(6):1954–1958
12. Ramirez-Rodriguez H, Parra-Vega V, Sanchez-Orta A, Garcia-Salazar O (2014) Robust backstepping control based on integral sliding modes for tracking of quadrotors. *J Intell Robot Syst* 73(1–4):51–66
13. Sun N, Fang Y, Zhang X (2013) Energy coupling output feedback control of 4-DOF underactuated cranes with saturated inputs. *Automatica* 49(5):1318–1325

14. Fang Y, Wang P, Sun N, Zhang Y (2014) Dynamics analysis and non-linear control of an offshore boom crane. *IEEE Trans Ind Electron* 61(1):414–427
15. Rinaldi F, Chiesa S, Quagliotti F (2013) Linear quadratic control for quadrotors UAVs dynamics and formation flight. *J Intell Robot Syst* 70(1–4):203–220
16. Mellinger D, Shomin M, Kumar V (2010) Control of quadrotors for robust perching and landing. In: *Proceedings of international powered lift conference, 2010*, pp 1–8
17. Shin J, Kim HJ, Kim Y, Dixon WE (2012) Autonomous flight of the rotorcraft-based UAV using RISE feedback and NN feedforward terms. *IEEE Trans Control Syst Technol* 20(5):1392–1399
18. Xian B, Dawson DM, de Queiroz MS, Chen J (2004) A continuous asymptotic tracking control strategy for uncertain nonlinear systems. *IEEE Trans Autom Control* 49(7):1206–1211
19. Xu R, Özgüner Ü (2008) Sliding mode control of a class of underactuated systems. *Automatica* 44(1):233–241

An Investigation of the Impact of Injection Profile Shaping on the Performance-Emission Characteristics of an Existing CI Engine: A CFD Approach



Sudharani Panda  and Rahul Banerjee

Abstract Fluid flows in an internal combustion engine play one of the most challenging fluid dynamics problems to model. It is only due to the variation of density along the flow field. So a clear understanding of the flow and combustion process is needed to enhance the engine performance and to minimize emission compromising fuel economy. An attempt is made in this paper to simulate the model of a direct injection diesel engine with the hemispherical bowl in the piston using a finite volume method. This model is used for understanding the in-cylinder gas motion with details of the combustion process to evaluate the engine performance. Combustion flow simulations were carried out at a different crank angle to analyze the distribution of temperature in the combustion chamber. In addition, swirl ratio, cylinder pressure, and kinetic energy at a different crank angle were investigated from the combustion flow simulation. However, injection rate shaping also plays a vital role in combustion and then further affect the subsequent combustion and emission performance. In this study, four different injection rate shapes (base, rectangular, sine, trapezoidal, and triangular) with constant injection duration and injected fuel mass is simulated to study the engine performance and emission rate. The emission rate includes NO_x , CO, unburnt hydrocarbon, and soot. Finally, simulation results were compared with results obtained from the experiment. The effect of different rate shapes on emission and engine performance was discussed and concluded.

Keywords Swirl ratio · Injection rate shaping · Computational fluid dynamics · Emission

1 Introduction

The diesel engine is widely used across the world because of its high efficiency, affordability, and reliability [1]. However, a significant amount of pollutants are increased in the vicinity due to the nature of the combustion process in diesel engines.

S. Panda (✉) · R. Banerjee
National Institute of Technology Agartala, Agartala 799046, India
e-mail: sanjimuni@gmail.com

© Springer Nature Singapore Pte Ltd. 2019
M. Kumar et al. (eds.), *Advances in Interdisciplinary Engineering*, Lecture Notes in Mechanical Engineering, https://doi.org/10.1007/978-981-13-6577-5_37

An automobile manufacturer is trying to explore various techniques and strategies to reduce emission without sacrificing performance and efficiency of the engine. The gas flow in the cylinder is one of the important factors which influences the performance of the engine [2]. Along with this, the fuel injection also plays an integral role in the development of the combustion in the engine cylinder. The fuel injection can be regulated by parameters like injection pressure and injection timing [3–6]. By changing the injection pressure, injection duration or both parameters at a time the engine performance and emission can be evaluated [3–7]. Depending upon the injection pressure and injection duration the injection profile also get changed which is generally known as injection rate shaping. Fuel injection shaping is a phenomenon to vary the injection rate over the course of a single fuel injection [8]. Injection rate shaping is potentially an effective technique to reduce emission characteristics and to improve the combustion process of a direct injection diesel engine [1]. It is also responsible for the distribution and mixing of fuel within the combustion chamber. The ignition delay period is the most important phase in the combustion of C.I (compression ignition) engine, because it effects the combustion rate knocking in the engine. In addition, it affects the starting ability of the engine and formation smoke in the engine [7, 9–12]. Moreover, a homogeneous air–fuel mixture is enhanced by swirl ratio. It is time-dependent of mixing. The path of motion of injected fuel into the cylinder is swirl motion. However, it enriches the complete fuel combustion in the engine cylinder [13, 14].

Model and simulation give information about how something will behave without actually testing it in real life. Here combustion model is developed and simulated using finite volume method. To carry out the process of numerical analysis FLU-ENT16.2 is used, which employs Finite volume method. Finally, simulation results are compared with that of experimental results.

2 Methodology

A combustion 3D model consists of valve, seat, cylinder head, and hemispherical piston bowl is developed using CAD software to study the effect of combustion (Fig. 1). The model with valve diameter 34 mm, seat diameter 30.6 mm, stroke 110 mm, bore 87.5 mm, hemispherical piston bowl of 26 mm is developed using CAD software. The inlet valve is closed at a crank angle of 570° , and the exhaust valve is opened at a crank angle of 833° for combustion flow simulation analysis. Whereas for combustion performance analysis, the inlet valve is closed at a crank angle of 575.5° and the exhaust valve is opened at a crank angle of 864° .

Flow through the combustion chamber is simulated using fluent (the CFD package) to study the flow field development inside the cylinder as well as to study the effect of injection rate shaping on engine performance and emission. Five different injection rate shapes such as base, rectangular, sine, trapezoidal and triangular with a variation of maximum injection pressure with constant injection duration are taken for the analysis. The injection pressure is varied between 190 and 254 bars to get

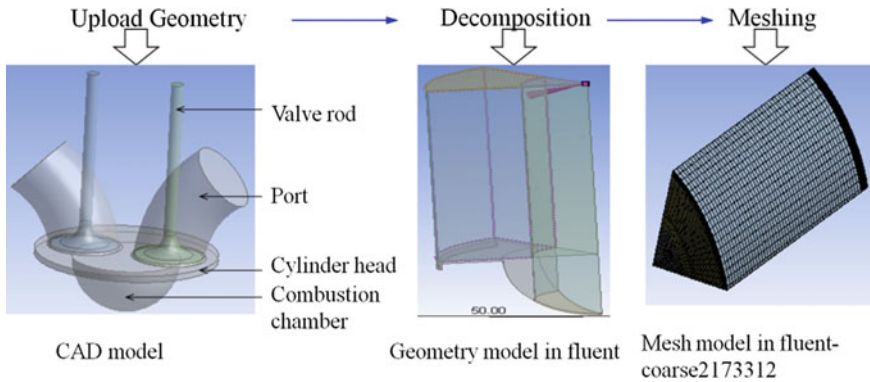


Fig. 1 Combustion flow simulation

the different injection rate shape. In this study, the mass fuel injected per cycle is 0.0208 g/cycle. Here sector combustion simulation is done to minimize the simulation time. The experimental work is carried out to validate the results obtained from simulation.

3 Results and Discussion

3.1 Combustion Simulation Results

Figure 2 shows the contour of statics temperature at crank angle 676° – 736° . From the contour, it can be observed that the maximum static temperature is at a crank angle of 734° whereas the fuel is injected at a crank angle of 734° into the hot compressed air. The combust charge expanded at a crack angle of 736° . During expansion, the temperature of the combust charge starts to fall. The temperature inside the cylinder increases during compression.

Figure 3 shows the contour of velocity magnitude at a different crank angle when piston travels from suction stroke to exhaust stroke. The velocity is varied inside the diesel engine at different step simulation.

Air swirl is required in C.I engines. Due to the swirling of air a continuous supply of fresh air to each droplet of the fuel is possible and along with this, it sweeps away the burnt product from the engine. Essentially, the heterogeneous air–fuel mixture is formed in the combustion chamber. Hence if there will be no swirling motion of air a small amount of fuel will get only oxygen due to which the combustion rate will be slower. Therefore it is necessary to cause swirling of air to supply fresh air to each droplet of fuel.

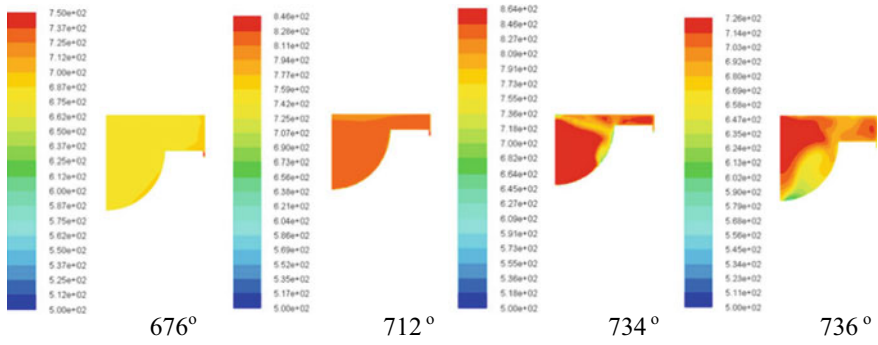


Fig. 2 Temperature contour at a different crank angle

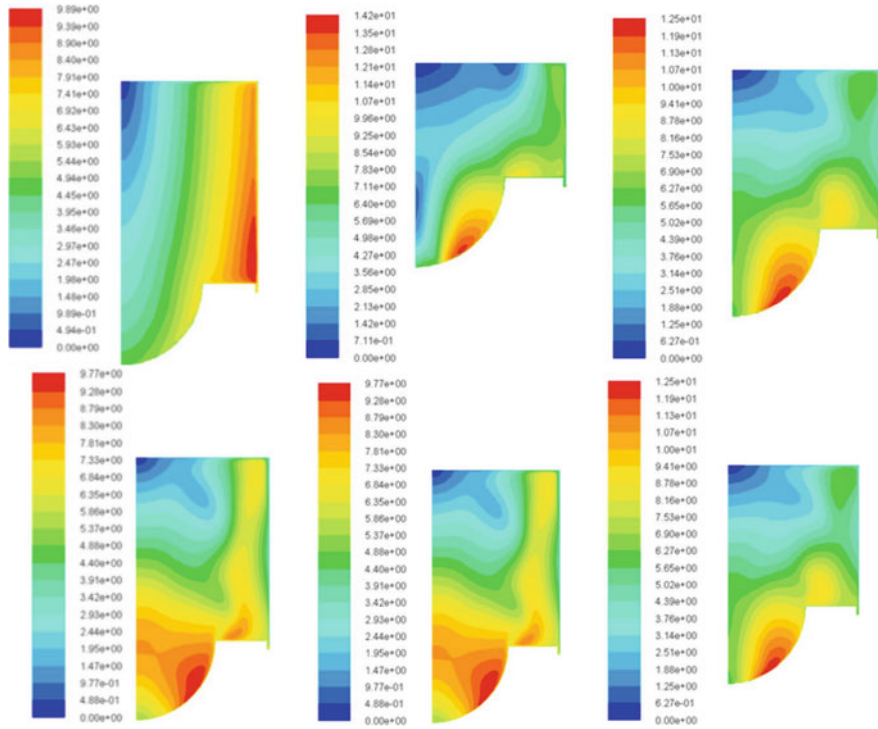


Fig. 3 Velocity contour at a different crank angle

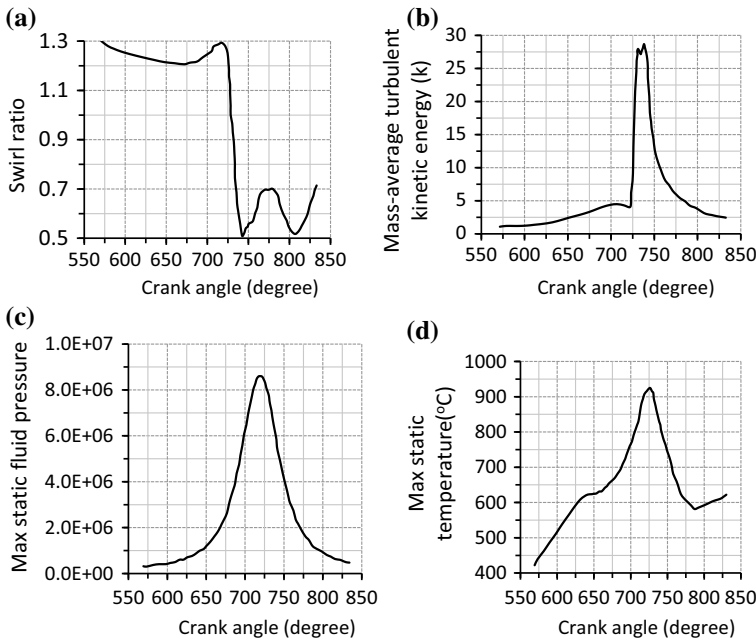


Fig. 4 a Variation of swirl ratio with crank angle, b variation of kinetic energy with crank angle, c variation of fluid pressure with the crank angle and d variation of temperature with the crank angle

From Fig. 4a, it is observed that the swirl ratio increases during the suction stroke, increases during the combustion stroke, decreases during expansion stroke and increases during the exhaust stroke. The figure shows that swirl ratio changes through a cycle of the engine. During the intake stroke, it is high, decreasing after BDC in the compression stroke as the piston approaches TDC more of air enters the cavity and air cylinder moment of inertia decreases and the angular velocity increases hence swirl increases.

During the injection of fuel, a high level of turbulence is generated by large velocity gradient near the sprays. When the gas is compressed, the internal energy of the gas starts to increase that means the temperature of the system increases. According to the kinetic theory of gases, the velocity is directly proportional to the square root of temperature hence the turbulent kinetic energy increases. From Fig. 4b, it is seen that the maximum mass average turbulent kinetic energy is obtained during combustion (at a crank angle 720°–730°).

Figure 4c shows that maximum static pressure is obtained during combustion between 700° and 730° of crank angle because the maximum in-cylinder pressure is obtained by combustion of fuel. From Fig. 4d, it is observed that maximum static temperature is obtained during combustion between 700° and 730° of crank angle due to combustion higher heat is released from the combustion product.

3.2 Engine Performance and Emission Analysis

The temperature in different rate shape

The fuel undergoes atomization, diffusion, evaporation, and then mixed with air during the period of ignition delay. Therefore, the ignition delay period plays a vital role in affecting the engine performance. The level of premixed combustion, noise and peak cylinder pressure directly affected by ignition delay period. In a word, the combustion is significantly affected by ignition delay time.

The variation of cylinder temperature with a crank angle for different injection rate shapes is shown in Fig. 5. The peak cylinder temperatures at different rate shapes are listed in Table 1. The triangular injection rate shape has a lower value of ignition delay and the sine rate shape shows the highest value of ignition delay. Highest ignition temperature was developed in the base injection rate shape; it is the fact that the higher initial injection pressure. The higher injection pressure helps in proper atomization of fuel and results required air–fuel mixture. The low injection pressure increases the period of ignition delay in sine rate shape. That means fuel droplets are too big to evaporate as well as the amount of fuel injected is less as compared to base and rectangular injection rate shape. Furthermore, less amount of fuel is burnt in the Triangular injection rate resulting in a lower value of cylinder temperature.

The rate of heat release (RoHR) in different rate shapes

The variation of RoHR with crank angle is illustrated in Fig. 6. It can be seen that the peak value of heat release rate is highest for base and rectangular rate shapes

Fig. 5 Average cylinder temperature for different shapes

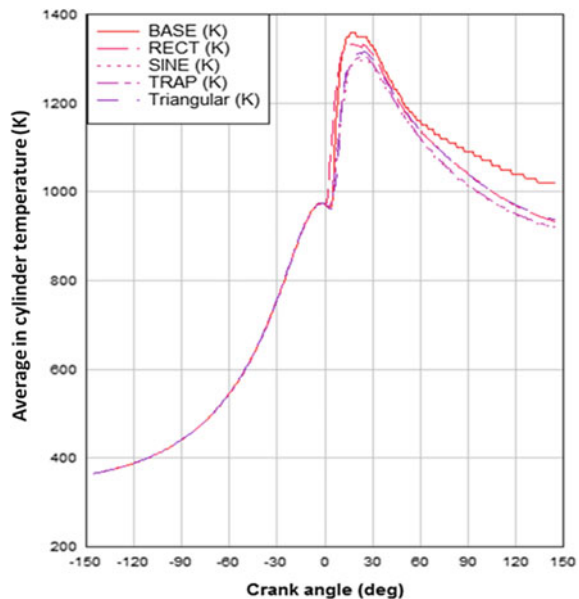


Table 1 Maximum average in-cylinder temperature

Injection rate shape	After TDC	Temperature (K)
Base	$X = 19$	1360
Rectangle	$X = 10.1$	1331.82
Sine	$X = 25$	1299.99
Trapezoidal	$X = 24$	1307.02
Triangular	$X = 8$	962.17

Fig. 6 App. RoHR for different injection rate shape

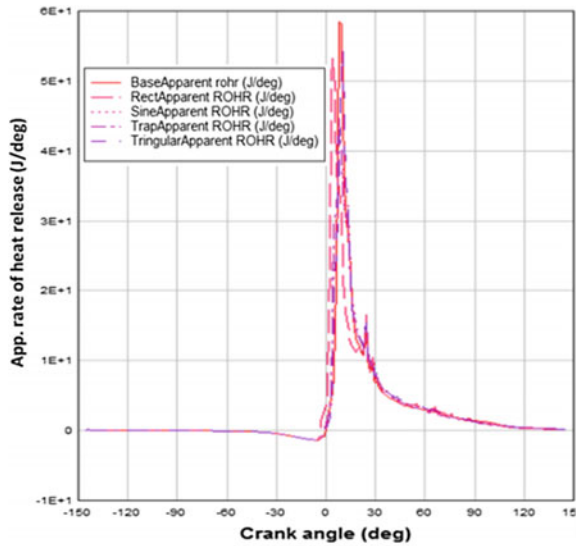


Table 2 App. ROHR values of different injection shapes

Injection rate shape	After TDC	RoHR values
Base	$X = 8$	58.4
Rectangular	$X = 4$	53.2
Triangular	$X = 10$	48.5
Trapezoidal	$X = 8$	45
Sine	$X = 8$	40.8

whereas sine rate shape has the lowest value. The heat released rate is in the order of, Base > Rectangular > *Triangular* > *Trapezoidal* > Sine. Table 2 presented the RoHR for different rate shapes.

Cylinder peak pressure in different rate shapes

The effect of different injection rate shapes on the mean pressure in the cylinder is shown in Fig. 7 and the peak pressure is presented in Table 3. Because of high injection pressure, the rectangular shape shows a higher value of the peak pressure compared to other injection rate shapes. It increases the quantity of fuel injection into

Fig. 7 Cylinder pressure for different shapes

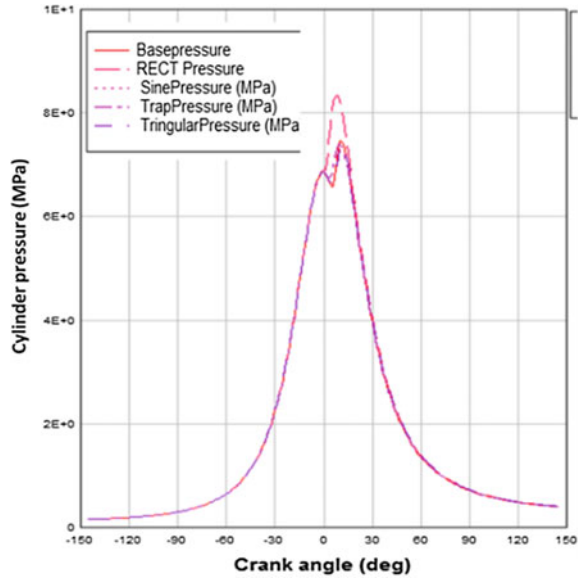


Table 3 Cylinder pressure values of different injection pressure

Injection rate shape	After TDC	In-cylinder pressure values
Base	X = 10	74.53
Rectangular	X = 8	83.41
Triangular	X = 10	73.8
Trapezoidal	X = 10	73.9
Sine	X = 10	72.9

the cylinder with a higher injected velocity. Due to high injection pressure, the spray penetration length will be higher. Hence, better air–fuel mixing, rapid evaporation of air–fuel occurs during the early stage of combustion. Due to which better combustion is carried out inside the cylinder. The in-cylinder pressure is in the following order: Rectangular > Base > Trapezoidal > Triangular > Sine.

Emission analysis

A higher value of injection pressure increases the formation of NO_x. At high injection pressure, a higher amount of fuel is combusted during the premixed combustion phase. Figure 8 shows the mass fraction of NO_x emission for different rate shapes. Table 4 presents the magnitude of NO_x in ppm for different rate shapes. The higher combustion temperature is responsible for the formation of NO_x from atomic level

shape

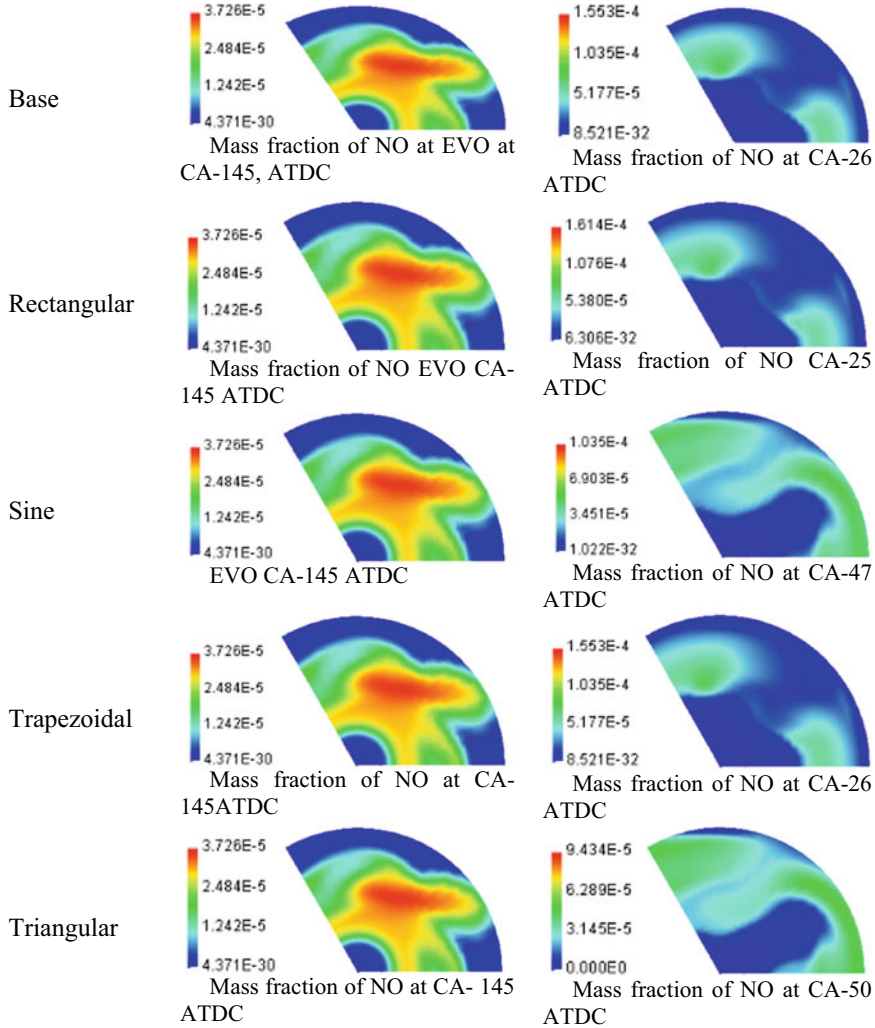


Fig. 8 Mass fraction of NO, EVO, CA after TDC for different rate shapes. EVO: exhaust valve open, CA: crank angle, ATDC: after top dead center

dissociation and series of reaction of N_2 and O_2 . Rectangular rate shape shows the highest amount of NO_x formation due to the highest temperature of burning gases during premixed burning stages. However, low RoHR and low average maximum cylinder temperature results in the lowest amount of NO_x emission in Sine injection rate shape.

Soot mass fraction at different rate shapes is shown in Fig. 9 and the values of soot are listed in Table 4. High temperature and low concentration of oxygen content

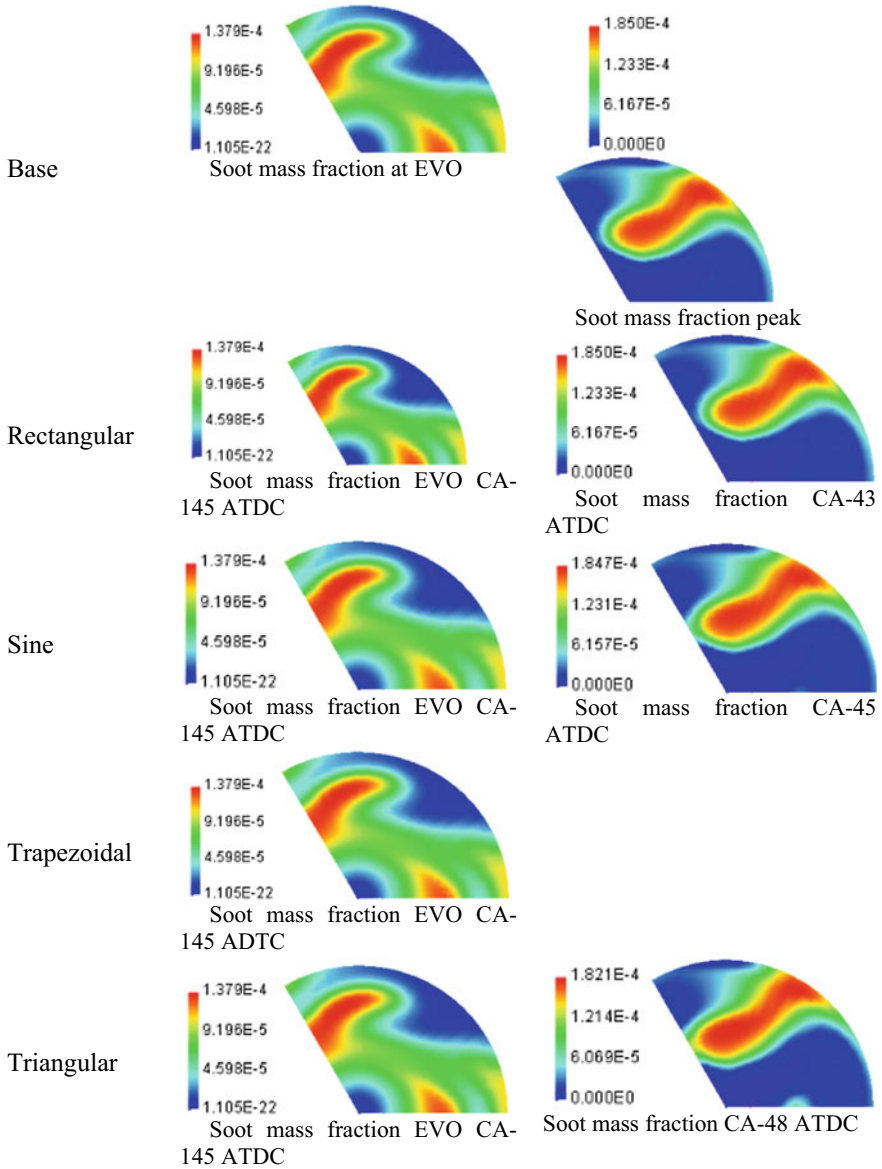


Fig. 9 Soot mass fraction of EVO, CA after TDC for different rate shapes

Table 4 Emissions and brake thermal efficiency for different injection rate shapes

Injection rate shape	NO _x (ppm)	Soot (g/kW h)	CO (%vol.)	UHC (ppm)	Brake thermal efficiency (%)
Base	957	0.246	0.046	94	32.4
Rectangular	1273	0.23	0.06	89	34.7
Sine	916	0.19	0.02	55	32.3
Trapezoidal	957	0.19	0.087	94	32.7
Triangular	922	0.18	0.042	52	33.5

is the reason for the Soot formation. In the combustion period, initially, the spray tip burns first and lead to the core of the spray with higher equivalence ratio. After that, the flame makes the surrounding with high temperature and low concentration oxygen. This induced much more soot emission.

Incomplete combustion of fuel results emission of carbon monoxide (CO). This emission is affected by air–fuel equivalence ratio, atomization rate, injection pressure. The superior air–fuel mixture resulting from an increase in injection pressure can reduce CO. From Table 4, it can be observed that the lean burning (charge contains high oxygen) produce less amount of CO emission in both sine and triangular.

Un-burn hydrocarbon (UHC) emission for different injection rate shapes is reported in Table 4. The UHC releases due to improper combustion. The UHC was found to be higher in Base injection profile.

The brake thermal efficiency (BTE) for different injection rate shapes is listed in Table 4. The BTE increases due to higher injection pressure. It may be the fact that a higher injection pressure atomizes the fuel rapidly and formed the higher air–fuel mixture during the premixed combustion phase, which improves the combustion. Hence, the increase in brake power in the cylinder increases the brake thermal efficiency. However, with the increase in pressure the temperature increases which affects the brake thermal efficiency and exhausted higher emissions. The reason is due to the increase of injection pressure the start of ignition is more advanced and combustion will be taking place before the top dead center. Due to this incomplete combustion occurs and combustion efficiency decreases.

Validation of simulation results with experiment

The simulation results as discussed previously are validated with that results obtained from the experiment as presented in Table 5. Absolute percentage error of the parameters for different rate shapes is presented in Table 6.

Table 5 Validation anchor points

Validation anchor points	Expt.	Base	Rect.	Sine	Trap.	Tri.
Average maximum cylinder pressure	75.14	74.53	83.41	72.9	73.9	73.8
Crank angle at maximum cylinder pressure (deg CA) ATDC	8	10	8	10	10	10
Averaged maximum cylinder temp (K)	1362	1360	1332	1300	1307	1320
Crank angle at averaged maximum cylinder gas temp (deg CA) ATDC	22.6	19	10.1	25	24	8
Averaged maximum heat release (J/deg)	64.34	58.4	53.2	40.8	45	48.5
Crank angle at averaged maximum rate of heat release (deg CA) ATDC	7	8	4	8	8	10
Average cumulative heat release (J) (total chem HRR)	941.64	1040	951.6	886.4	893.9	917.2
BTE	32.7	32.4	34.7	32.3	32.7	33.5
Ex NO _x (ppm)	960	957	1273	916	957	922
Ex CO% vol	0.05	0.046	0.06	0.02	0.087	0.042
Ex UHC (ppm)	94	89	55	108	94	52
Ex soot (g/kW h)	0.17	0.246	0.23	0.19	0.19	0.18

Table 6 Absolute % error

Parameters	% error				
	Base	Rect.	Sine	Trap.	Tri.
Average maximum cylinder pressure	0.81	11.00	2.98	1.65	1.78
Crank angle at maximum cylinder pressure (deg CA) ATDC	25	0	25	25	25
Averaged maximum cylinder gas temp (K)	14.68	2.20	4.55	4.03	3.08
Crank angle at averaged maximum cylinder gas temp (deg CA) ATDC	15.93	55.31	10.62	6.19	64.60
Averaged maximum heat release (J/deg)	9.23	17.31	36.58	30.05	24.61
Crank angle at averaged maximum rate heat release (deg CA) ATDC	14.28	42.85	14.28	14.28	42.85
Average cumulative heat release (J) (total chem. HRR)	10.44	1.05	5.86	5.069	2.59
BTE	0.92	6.11	1.22	0	2.44
Ex NO _x (ppm)	0.31	32.60	4.58	0.31	3.95
Ex CO% vol	8	20	60	74	16
Ex UHC (ppm)	5.31	41.48	14.89	0	44.68
Ex soot (g/kW h)	44.70	35	11.76	11.76	5.88
Total average % error	12.46	22.07	16.02	14.36	19.78

4 Conclusions

The swirl ratio is maximum during suction and it again increases when the piston moves towards TDC. The turbulent kinetic energy, static pressure, and static temperature are higher during combustion. The apparent heat release increases during combustion. The average maximum cylinder temperature of Base approaches the experimental values. The in-cylinders pressure of rectangular approaches the experimental value. The brake thermal efficiency and NO_x of trapezoidal approaches the experimental value. The UHC emission of trapezoidal injection rate shape is equal to experimental value. In the overall, injection rate shape of Base type shows the lower value of percentage error as compared to others.

Besides, it can conclude that the injection rate shape affects ignition characteristics and the temporal history of soot and NO_x formation. That implies controllability of emissions by optimization of the injection rate shape. However, this study offers a new way of looking at optimization of injection rate shape and motivates the development of advanced injection equipment in the future

References

1. Ramírez AI, Som S, Rutter TP, Longman DE, Aggarwal SK (2012) Investigation of the effects of rate of injection on combustion phasing and emission characteristics: experimental and numerical study. In: Spring technical meeting of the central states section of the combustion institute, Dayton, OH, 22–24 Apr 2012
2. Lumley JL (1999) Engines: an introduction. Cambridge University Press, Cornell University
3. Sayin C, Canakci M (2009) Effect of injection timing on the engine performance and exhaust emissions of a dual-fuel diesel engine. *Energy Convers Manag* 50(1):203–213. <https://doi.org/10.1016/j.enconman.2008.06.007>
4. Kannan GR, Anand RA (2012) Effect of injection pressure and injection timing on diesel engine fuelled with biodiesel from waste cooking oil. *Biomass Bioenerg* 46:343–352. <https://doi.org/10.1016/j.biombioe.2012.08.006>
5. Imtenan S, Rahman SA, Masjuki HH, Varman M, Kalam MA (2015) Effect of dynamic injection pressure on performance, emission and combustion characteristics of a compression ignition engine. *Renew Sustain Energy Rev* 52:1205–1211. <https://doi.org/10.1016/j.rser.2015.07.166>
6. Rao GP, Raju VRK, Rao SS (2015) Effect of fuel injection pressure and spray cone angle in DI diesel engine using CONVERGETM CFD Code. *Proc Eng* 127:295–300. <https://doi.org/10.1016/j.proeng.2015.11.372>
7. Gowthaman S, Sathiyagnanam AP (2016) Effects of charge temperature and fuel injection pressure on HCCI engine. *Alexandria Eng J* 55:119–125
8. Mohan B, Yang W, Yu W, Tay KL, Chou SK (2015) Numerical investigation on the effects of injection rate shaping on combustion and emission characteristics of biodiesel fueled C.I engine. *Appl Energy* 160:737–745. <https://doi.org/10.1016/j.apenergy.2015.08.034>
9. Ganesan V (2007) Internal combustion engine, 3rd edn. Tata McGraw Hill Companies, New Delhi
10. He X, Donovan MT, Zigler BT, Palmer TR, Walton SM, Wooldridge MS, Atreya A (2005) An experimental and modeling study of iso-octane ignition delay times under homogeneous charge compression ignition conditions. *Combust Flame* 142(3):266–275

11. Assanis DN, Filipi ZS, Fiveland SB, Syrimis M (2003) A predictive ignition delay correlation under steady-state and transient operation of a direct injection diesel engine. *J Eng Gas Turbines Power* 125(2):450–457
12. Yoon SH, Lee CS (2011) Experimental investigation on the combustion and exhaust emission characteristics of biogas–biodiesel dual-fuel combustion in a CI engine. *Fuel Process Technol* 92(5):992–1000
13. Hiroyasu H, Kadota T, Arai M (1983) Development and use of a spray combustion modeling to predict diesel engine efficiency and pollutant emissions: part 1 combustion modeling. *Bull JSME* 26(214):569–575
14. Shi Y, Reitz RD (2009) Assessment of optimization methodologies to study the effects of bowl geometry, spray targeting and swirl ratio for a heavy-duty diesel engine operated at high-load. *SAE Int J Engines* 1(1):537–557

Effect of AR Coating Properties on Diffused Reflectance and Overall Efficiency of mc-Si Silicon Solar Cells



Shivangi, A. K. Saxena and M. Shadab Siddiqui

Abstract Intensive R & D efforts are going on to increase the efficiency of the solar cells to reduce the cost. The Anti-Reflection Coating (ARC) properties play an important role on the c-Si solar cell performance. It increases the absorption of sunlight in the solar cells which leads to enhancement in current and finally cell efficiency. The ARC is done by depositing a layer of Silicon Nitride (Si_3N_4) on the top surface of the solar cell. The thickness and refractive index of the ARC layer should be such that it minimizes the diffused reflectance of the light. The thickness of the layer should be in the range of 70–90 nm so that it can help in destructive interference for the required wavelength of the light. In the present paper, we report a study of electrical characteristics of cells with different ARC film thicknesses and refractive index. The optimized cells show energy conversion efficiency up to 18.7%.

Keywords Silicon solar cells · Shallow emitters · Anti-reflection coating · Diffused reflectance · Light I-V measurement

1 Introduction

The photovoltaic (PV) power is gradually emerging as a viable source of energy. Silicon solar cells comprising mono-crystalline (c-Si) and multi-crystalline (mc-Si) varieties constitute about 90% of the world shipment in 2016. The trend would continue and crystalline silicon PV technology is poised to dominate the PV industry for the next 10–20 years [1]. Silicon solar cells with full area screen printed Al BSF currently dominates the commercial market because of low cost and process simplicity. However, cost cutting is one of the primary challenges for the PV research community throughout the world. One of the possible ways of reducing the cost of solar cell is to increase the efficiency of solar cells.

In crystalline silicon (c-Si and mc-Si) solar cell manufacturing, the p-type wafers are diffused with phosphorous to form a thin n-layer (emitter) on the surface of the

Shivangi (✉) · A. K. Saxena · M. Shadab Siddiqui
BHEL ASSCP, Gurugram Faridabad Highway, Gwalpahari, Gurugram, India
e-mail: shivangi@bhel.in

wafer and thereby a large area P-N junction, which is required for separation of photo-carriers. The majority of commercial silicon solar cells today are made by screen printed contacts on 90–100 Ω/\square sheet resistance shallow emitters to enhance blue response and junction shunting. For such lightly doped emitters, many conductor paste manufacturers have developed new type of pastes which are compatible for high sheet resistance shallow emitters: 70–100 Ω/\square . The use of newly developed front contact pastes is expected to form low resistance contacts on shallow emitters. Thus shallow emitter solar cells processed under optimized conditions using new conductor paste are expected to show improvement in efficiency due to better collection of charge carriers and low reverse saturation current density leading to improved short circuit current and open circuit voltage of solar cells without losing fill factor [2, 3]. As the generated current is directly proportional to the amount of photons absorbed by the wafer, the properties of anti-reflection coating on the front surface also plays a vital role in increasing the current. Usually, a 70–80 nm Silicon Nitride (SiN_x) layer with refractive index (RI) in the range of 2–2.2 is deposited on the front surface of solar cell. It helps in light absorption using the principle of destructive interference. In this paper, we have investigated the effect of ARC thickness and RI on the performance of solar cell through investigation of its diffused reflectance and light I-V measurements.

2 Experiment

Conventional process steps as shown in Fig. 1 are followed for the fabrication of multi-crystalline Si solar cells. P-type, 156 mm square silicon wafers are used for fabrication of solar cells. Texturing of silicon wafers is carried out in an acid mixture [4]. The textured wafers are diffused with phosphorus in an open-tube furnace using a conventional POCl_3 diffusion source. The emitter sheet resistance obtained is in the range of 80–100 Ω/\square . The phosphosilicate glass (PSG) formed during diffusion process is removed in a dilute HF solution followed by edge isolation by plasma etching. The ARC deposition is done by plasma-enhanced chemical vapour deposition (PECVD) method under three different parameters to achieve three batches of silicon wafers. Each batch had different ARC thickness and RI. The details of the batches are as per Table 1. After this process, the quality of ARC has been tested using an in-house developed Diffused Reflectance Measurement Setup (DRMS) [5]. Conventionally the diffused reflectance of a Si wafer can be measured using a spectrophotometer but the measurement technique is time-consuming and destructive. Using DRMS the diffused reflectance of the full-size Si wafer can be measured with high accuracy. The value of diffused reflectance for batch—1, 2 and 3 are in the range of ~5.7, 6.5 and 5% respectively. The thickness and RI of the samples have been evaluated using Sentech 400 Ellipometer [6]. After testing and characterization of ARC, the front and back metallization screen printing is carried out using high precision DEK printer (Eclipse model). Silver paste and aluminum paste by a renowned manufacturer are used for front contact and back contact metallization respectively.

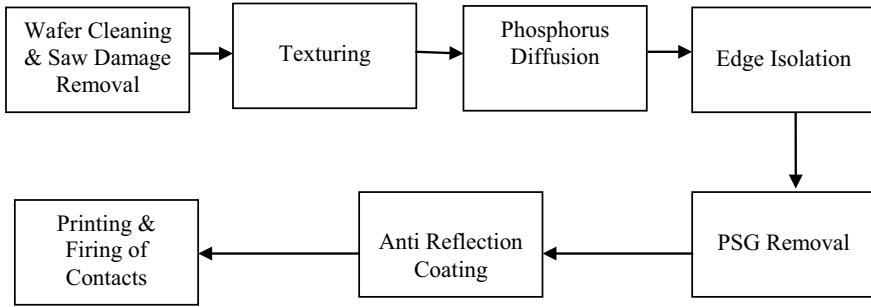


Fig. 1 Processing steps for solar cell fabrication

Table 1 Details of ARC properties of three batches

Batch details	ARC thickness range (in nm)	ARC R.I. range
Batch—1	76–78	2.02–2.06
Batch—2	80–82	2.25–2.27
Batch—3	89–91	2.10–2.12

This is followed by baking and co-firing of the contacts in a conveyer belt furnace. The furnace zone temperatures and belt speed are optimized and adjusted to get temperature profile as recommended by the paste manufacturer.

The cells are characterized by light I-V measurement. The measurement set up has a provision to hold solar cell firmly on a gold-plated, temperature controlled vacuum chuck. The measurement of current and voltage are made with four-wire arrangement (two wires for current and two separate wires for voltage). For all measurements under illumination, first, the light intensity is checked and adjusted to 100 mW/cm². Also, the temperature of the chuck is set at 25 °C with a tolerance of ±1 °C and monitored continuously using a Pt100 probe inserted horizontally inside the gold-plated chuck. Calibration of the intensity is performed with the help of the reference cell calibrated at NREL, USA (Make: PV Measurements Inc. USA, Model No.: PVM 230).

3 Results and Discussion

Three batches of solar cells are processed in a similar manner up to edge isolation and PSG removal. The emitter sheet resistance of the batches is in the range of 80–100 O/sq. The ARC deposition is done by PECVD method under three different process conditions to achieve three batches of silicon wafers with different AR coating properties. Each batch of 8 wafers has different ARC thickness and RI. Except,

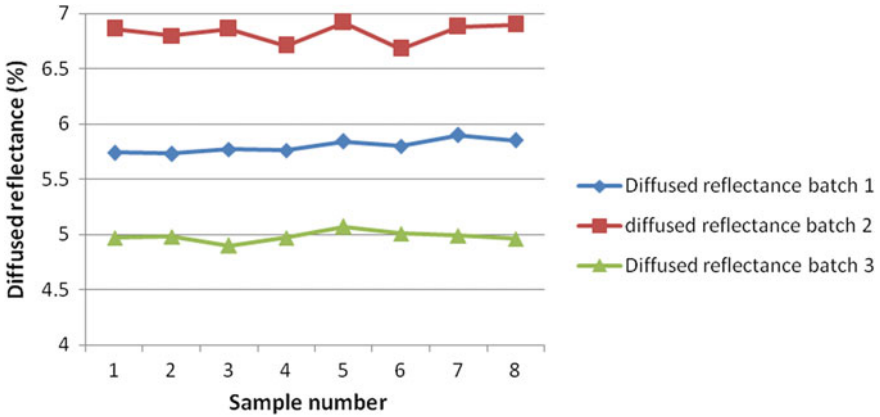


Fig. 2 Distribution of diffused reflectance over batch 1, 2 and 3

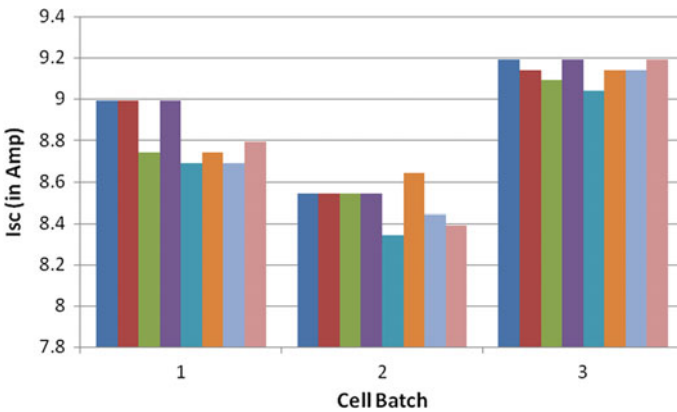


Fig. 3 Distribution of Isc in all samples over three batches

the ARC process, all the other process conditions have been kept identical for all the three batches. The value of diffused reflectance measured is shown in Fig. 2.

Lower value of diffused reflectance leads to better absorption of incident light which in turn enhances the Isc. It can be seen from Fig. 2 above that batch 3 has least D. R. (Avg 4.98).

The distribution of short circuit current over all the samples is shown in Fig. 3. The batch 3 shows the highest Isc. Figure 4 shows the cell efficiencies of three batches.

The average data of various cell electrical characteristics for the three batches are compiled in Table 2 for quick comparison:

It can be seen from the above data that the batch where the DR is least (batch 3) the Isc is highest. The cell efficiency is also the highest in batch 3 and the values of FF and Voc have not changed much. Higher Isc is the result of better absorption of

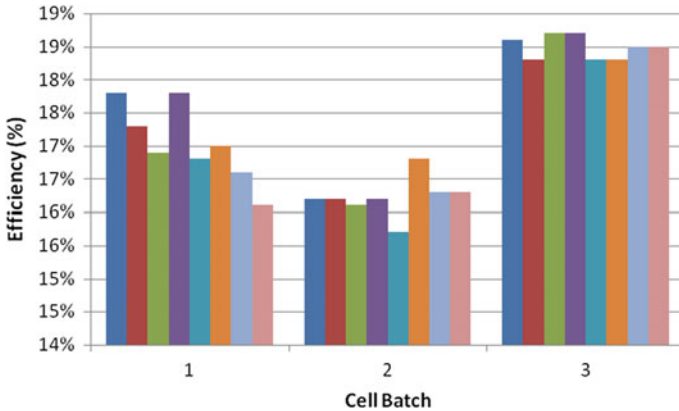


Fig. 4 Distribution of efficiency in all samples over three batches

Table 2 Electrical characteristics for three batches of solar cells for different DR

Cell batch	Avg D. R. (%)	Avg V_{oc} (mV)	Avg I_{sc} (A)	Avg (W_p)	Avg FF	Avg Rse ($\Omega\text{-cm}^2$)	Avg $\eta\%$
Batch 1	5.80	0.63	8.83	4.02	0.74	1.79	17.15
Batch 2	6.80	0.62	8.50	3.90	0.74	1.69	16.25
Batch 3	4.98	0.63	9.14	4.44	0.77	1.40	18.49

light which is clearly indicated by a very simple and accurate measurement of DR measured nondestructively in an in-house developed DR measurement setup.

The outcome of the above results has been tried on a large number of wafers ~80 number of mc-Si wafers with ARC parameters of batch 3 were taken and processed under optimized printing and firing condition. The efficiency distribution graph is shown in Fig. 5. The graph clearly shows that the recipe developed for producing 18.5% mc-Si cells is reproducible on an industrial scale.

4 Conclusion

A number of experiments have been conducted on full size (156 mm × 156 mm) mc-Si wafers for studying the effect of ARC properties using industrial-scale equipment. It is clearly seen that silicon wafer having 80–100 O/sq emitter sheet resistance and ARC layer of thickness around 90 nm and RI of around 2.12 when used with suitable printing pastes for metallization, mc-Si cells with >18.5% efficiency can be produced. Improvement in average absolute cell efficiency of ~1% is attributed to increase in I_{sc} and no significant change in FF. The DR measurement setup has a unique feature that it measures average DR under a halogen light source which has a spectrum very close to that of sun. Hence the value of DR measured gives very important information

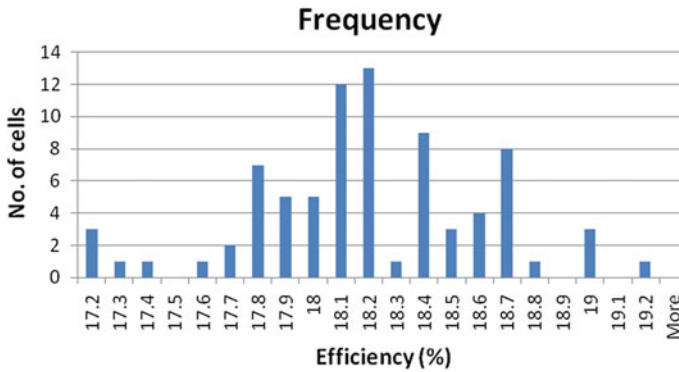


Fig. 5 Efficiency distribution of ~80 cells

about the % of light absorbed in the solar cell for the AR coating. Minimizing the DR value by varying AR deposition parameters, the optical properties can be optimized for maximizing the cells efficiency.

Acknowledgements Authors are grateful to the BHEL management and staff for providing constant support and encouragement during the course of this work and finally for permitting publication of the results of the study. We also acknowledge the Department of Science and technology (DST) Government of India for their generous support in establishing the facilities.

References

1. Solar Photovoltaic (2013) In: IEA-ETSAP and IRENA© technology brief E11
2. Shetty KD, Boreland MB, Shanmugam V, Cunnusamy J, Wu C-K, Iggo S, Antoniadis H (2012) Lightly doped emitters for high efficiency silicon wafer solar cells. In: PV Asia Pacific conference
3. Hilali MM, Rohatgi A, Asher S (2015) Development of screen-printed silicon solar cells with high fill factors on $100 \Omega/\square$ emitters. IEEE Trans Electron Dev 51(6)
4. Kumar M (2012) Acid texturization of polysilicon for solar cell applications
5. Saxena AK, Reddy SR, Bhogra RK (2007) A novel non-destructive technique for quick measurement of textured Si wafers for solar cell process. In: 22nd EUPVSEC
6. McCrackin F, Passaglia E, Stromberg RR, Steinberg HL (1963) Measurement of the thickness and refractive index of very thin films and the optical properties of surfaces by ellipsometry. J Res Nat Bur Stand-A Phys Chem 67A(4)

Comparative Study of Sheet Metal and Carbon Fibre Reinforced Composites Ceiling Fan Blade



Himanshu Garg , Joginder Singh , M. R. Tyagi , Kunal Singh ,
K. Aditya  and Himanshu Gupta 

Abstract A ceiling fan is utilized to circulate the air in the room during summer. The operation of ceiling fan must be quieter and air circulation must be even throughout the room. It should consume less amount of electricity too. The conventional ceiling fan blades are made up of sheet metal. These blades consist of substantial weight, and the whole assembly requires more electricity to run smoothly. The use of lighter materials for fan blades instead of sheet metal can provide an ample amount of weight saving. Therefore, the objective of this study is to manufacture the fan blades using Carbon Fibre Reinforced Composites (CFRC) and compare its performance with conventional ceiling fan. The industrial standard was used to fabricate the CFRC fan blades. The sheet metal blades were replaced by newly developed CFRC blades, and the data was recorded and analysed. The performance of the CFRC blades mounted fans were tested for the current requirement, power consumption, fan speed and air delivery at 180 and 230 V. The obtained outcomes were compared with the data available for the conventional ceiling fan. It was noticed that the fans mounted with CFRC blades provided higher rotational speed at lower current and consumed less power than the sheet metal blade fans. Nonetheless, the observed air delivery and peak velocity were inferior. This issue might appear due to slight variation in pitch angle or shape/size of the CFRC blades than the original sheet metal fan blades and could be resolved using stringent design and fabrication norms for CFRC fan blades.

Keywords Energy efficiency · Ceiling fan · Carbon fibre · Air delivery

1 Introduction

Ceiling fans are widely used in tropical regions and in developing countries to get relief from scorching heat. It is operational and maintenance charges are reasonably

H. Garg (✉) · J. Singh · M. R. Tyagi · K. Singh · K. Aditya · H. Gupta
Department of Mechanical Engineering, Manav Rachna University, Faridabad, Haryana, India
e-mail: garg.himanshu950@gmail.com

J. Singh
e-mail: joginder@mru.edu.in

© Springer Nature Singapore Pte Ltd. 2019
M. Kumar et al. (eds.), *Advances in Interdisciplinary Engineering*, Lecture Notes in Mechanical Engineering, https://doi.org/10.1007/978-981-13-6577-5_39

low, and it consumes less power than the air conditioning unit. It consists of a hub in which three or four blades are mounted which is usually rotated by a capacitor start induction motor. The speed of the ceiling fan is regulated by changing the voltage using a voltage regulator. Generally, the ceiling fan blades are made up of aluminium sheet, and their tip diameter is 1.2–1.6 m [1]. The selection of the fan size is usually made based on the dimensions of the room. The most effective fan blade size lies in between 24 and 99 in. The blade designs of conventional ceiling fans are aerodynamically not very well suited. So, there is an excellent opportunity to increase the efficiency of the ceiling fan by improving the aerodynamics of a fan blade [1]. Apart from aluminium, the fan blades are made up of different other materials like stainless steel, timber, plywood, plastic, composites, etc. Composite materials have excellent specific strength, good corrosion resistance, better rigidity, etc. in comparison to other sheet metals. Therefore, the use of composite material in the ceiling fan blades might reduce the power consumption and increase the overall performance of the fan by effectively reducing the weight of the ceiling fan assembly.

The objective of the present study is to design and fabricate the ceiling fan blade using carbon fibre reinforced polymer composite (CFRC). A systematic investigation of the current requirement, power consumption, fan speed, air delivery test, and peak velocity were conducted for CFRC as well as sheet metal blades mounted fans as per the industry standards. A comparison of results was performed to estimate the usefulness of newly developed CFRC fan blades.

2 Literature Review

Jain et al. [1] studied the flow characteristics of a ceiling fan utilizing smoke in a closed room. They found that only the middle portion of the fan blades was able to flow the air in downwards direction. Winglets and spikes fastened to the fan blades were seen to raise the airflow in downwards direction without any significant change in energy consumption. Mahlia et al. [2] proposed new design of the ceiling fan blade and compared its aerodynamics and efficiency with the conventional fan blade. As per their investigation, the newly introduced Gilbert Morris-15 airfoil-shaped fan blade exhibited better performance than the conventional one for similar power consumption. According to Afaq et al. [3], if the rake angle of a fan blade was changed from 5 to 6°, the rated air quality was improved from 185 to 210 m³/min. Schmidt and Patterson [4] used an axial-flux brushless DC machine (BDCM) to drive a ceiling fan fitted with newly designed fan blades. These fan blades had a variable tilt angle over the blade length. They observed that this new design achieved the rated airflow power at 140 rotation per minute (RPM) whereas the conventional fan design achieved it at 270 RPM. Adeeb et al. [5] carried out computational parametric analysis of the various geometric contours of ceiling fan blades using Reynolds-Averaged Navier–Stokes (RANS) method. They observed that the air delivery of a ceiling fan was severely impacted by the root and tip angle of attack. The best air delivery was reported when the root and tip angle of attack was 12 and 12° respectively. In

another study, Adeeb et al. [6] investigated the effect of the number of blades on the performance of the ceiling fan in terms of airflow and power consumption. It was reported that the six-blade configuration exhibited best volumetric flow rate whereas best energy efficiency was obtained with two-blade configuration. Aziz et al. [7] investigated the experimental and numerical airflow properties and thermal comfort of vortex, round, and square shaped ceiling diffuser. The vortex diffuser exhibited better performance and 1.5 times lower power consumption than its counterparts. They recommended that the vortex diffuser with 45° swirling angle is a suitable alternative of a conventional diffuser for the high-rises buildings. Momoi et al. [8] collected the air velocity data around the ceiling fan in a large air-conditioned room and compared it with the results obtained from CFD simulation. They found a close agreement between the average air velocity results obtained from experimental and CFD simulations. Shah et al. [9] reviewed various options to improve ceiling fan efficiency in terms of cost-effectiveness. They suggested that proper implementation of these options not only save 70 TWh energy per year but also reduce 25 million metric ton CO₂ emission. Chen et al. [10] found enhanced average air velocity beneath the fan blade regions for higher RPMs. Besides, the velocity profile was identical in the main jet zone for various RPMs. They also observed that the air velocity distribution was mainly affected by blade geometry, blade shape and distance from ceiling to fan. Sonne and Parker [11] developed a new twisted and tapered ceiling fan blade with airfoil cross-section. This new fan design had the highest efficiency index with respect to the conventional fan. The newly developed design was approximately two times more efficient than the conventional one. As per their investigation, larger fan blades may provide enhanced airflow coverage. Bassiouny and Korah [12] noticed that the air flow from the ceiling fan has different features. According to the numerical or mathematical results, the divergence angle of air flow was almost 150°. The local downward velocity distribution of the air inside the designated space was enhanced with the increased rotational speed of the fan. The air velocity near to the vicinity of the walls was reduced with respect to the diameter region of the ceiling fan.

3 Experimental Details

Epoxy resin and carbon fibre cloth (200 gsm) were used to fabricate the carbon fibre reinforced composite material for fan blade. The sheet metal fan blade received from Orient was utilized for die preparation. After successful die preparation, hand layup technique was employed for composite fan blade preparation. A unibody design of fan blade was fabricated using five layers of epoxy and carbon fibre cloth. This unibody design not only reduced the weight, stress concentration and power consumption but also increased the efficiency and angular speed. An original Orient fan blade and fabricated CFRC fan blade is shown in Fig. 1a, b. For the testing purpose, the blades of the fan were substituted with CFRC fan blades. The original picture of the assembly is shown in Fig. 2.

Fig. 1 **a** Conventional sheet metal fan blade (orient).
b CFRC fan blade



Fig. 2 CFRC fan blades mounted on test setup



4 Results and Discussion

Table 1 embodied the test results obtained from the fan mounted with sheet metal fan blades and CFRC fan blades at two different voltages (180 and 230 V). A comparison of the results like the current requirement, power consumption and fan speed between conventional blades and CFRC blades mounted fans is exhibited in Fig. 3. It was observed from Fig. 3 and Table 1 that the CFRC blade mounted fan required lower current, consumed less power and provided higher rotations per minute than the conventional one. The reason behind the improved performance of the CFRC mounted fan assembly is primarily the weight reduction inflicted using the composite material.

The parameters and performance of the CFRC and sheet metal fan assemblies in terms of air delivery is summarized in Table 2. A comparison of the two was also carried out and plotted in Fig. 4. It was observed that the CFRC mounted fan assembly exhibited inferior air delivery and peak velocity than its counterpart.

There are several parameters such as blade pitch, blade shape/size, rotational speed, ceiling height and fan motor which could affect the air delivery of a fan. In

Table 1 Electric current requirement, power consumption and rotational speed for sheet metal blade and CFRC blade mounted fan assemblies at 230 and 180 V

Materials	Voltage (V)	Current (A)	Power (W)	Speed (RPM)
Orient fan steel blade	230	0.302	68	338
	180	0.270	48	311
CFRC fan blade	230	0.275	60	357
	180	0.222	38	352

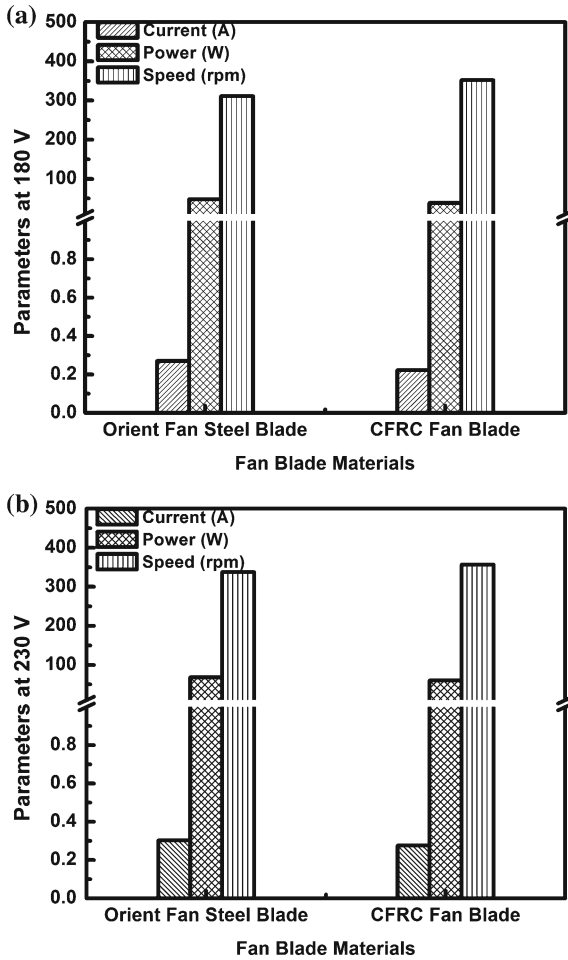
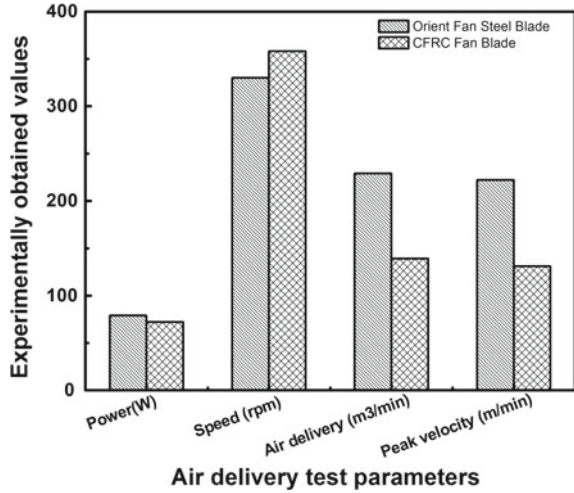


Fig. 3 Comparison of current, power and speed of conventional orient fan blade and CFRC fan blade at **a** 180 V and **b** 230 V

Table 2 Air delivery test performance of sheet metal and CFRC blade mounted fan assemblies

Parameters	Carbon fibre blade	Orient fan steel blade
Power (W)	72	79
Speed (RPM)	358	330
Air delivery (m ³ /min)	139	229
Peak velocity (m/min)	131	222

Fig. 4 Comparison of air delivery test parameters of conventional orient fan blade and CFRC fan blade



the present case, the ceiling height and fan motor are the same for both the assemblies. Therefore, the possible factors behind the lower air delivery of the CFRC fan assembly are the slight variation in pitch angle or shape/size of CFRC blade than the original one. A sophisticated and accurate manufacturing process of the CFRC fan blade might overcome this problem.

5 Conclusion

In this study, ceiling fan blades were designed and fabricated using carbon fibre reinforced composites. The CFRC fan blades were mounted on the test assembly and tested for the current requirement, power consumption, rotational speed and air delivery at 180 and 230 V. The similar tests were also conducted on conventional Orient fan. The results obtained in both cases were compared. As per the comparison, the CFRC blade mounted fan required lower current, consumed less power and provided higher rotations per minute than the conventional one. On the contrary,

the CFRC mounted fan exhibited inferior air delivery and peak velocity than its counterpart. Although the CFRC blades were light in weight, a slight variation in pitch angle or shape/size might alter the air delivery or peak velocity of a ceiling fan. The air delivery and peak velocity can be increased following a stringent design and fabrication procedure of fan blade.

Acknowledgements We would like express our sincere gratitude to Dr. Anil and Dr. Ashish from Accendere KMS for their unconditional support during manuscript preparation.

References

1. Jain A, Upadhyay RR, Chandra S, Saini M, Kale S (2004) Experimental investigation of the flow field of a ceiling fan. In: ASME 2004 heat transfer/fluids engineering summer conference. American society of mechanical engineers pp 93–99
2. Mahlia TMI, Moradalizadeh H, Zubir MNM, Olofsson T (2013) Theoretical and experimental investigation of energy efficiency improvement of the ceiling fan by using aerodynamic blade profile. *J Energy Environ* 3
3. Afaq MA, Maqsood A, Parvez K, Mushtaq A (2014) Study on the design improvement of an indoor ceiling fan. In: 2014 11th international Bhurban conference on applied sciences and technology (IBCAST), IEEE, pp 279–283
4. Schmidt K, Patterson DJ (2001) Performance results for a high efficiency tropical ceiling fan and comparisons with conventional fans: demand side management via small appliance efficiency. *Renew Energy* 22:169–176
5. Adeeb E, Maqsood A, Mushtaq A, Hussain Z (2015) Shape optimization of non-linear swept ceiling fan blades through RANS simulations and response surface methods. In: 2015 12th international Bhurban conference on applied sciences and technology (IBCAST), IEEE, pp 385–390
6. Adeeb E, Maqsood A, Mushtaq A (2015) Effect of number of blades on performance of ceiling fans. In: MATEC web of conferences. EDP Sciences, p 02002
7. Aziz MA, Gad IA, El Shahat FA, Mohammed RH (2012) Experimental and numerical study of influence of air ceiling diffusers on room air flow characteristics. *Energy Build* 55:738–746
8. Momoi Y, Sagara K, Yamanaka T, Kotani H (2004) Modeling of ceiling fan based on velocity measurement for CFD simulation of airflow in large room. In: Proceedings of 9th international conference on air distribution in rooms, Coimbra, Portugal, p 145e50
9. Shah N, Sathaye N, Phadke A, Letschert V (2015) Efficiency improvement opportunities for ceiling fans. *Energy Eff* 8:37–50
10. Chen W, Liu S, Gao Y, Zhang H, Arens E, Zhao L, Liu J (2018) Experimental and numerical investigations of indoor air movement distribution with an office ceiling fan. *Build Environ* 130:14–26
11. Sonne J, Parker D (1998) Measured ceiling fan performance and usage patterns: implications for efficiency and comfort improvement. In: ACEEE summer study on energy efficiency in buildings. Citeseer, pp 335–341
12. Bassiouny R, Korah NS (2011) Studying the features of air flow induced by a room ceiling-fan. *Energy Build* 43:1913–1918

Kinematics of Sit-to-Stand Task for Knee Osteoarthritis Patients



Siddharth Bhardwaj, Abid Ali Khan and Mohammad Muzammil

Abstract With the increase in life expectancy, the population of older people is on the rise worldwide. The health of the elderly has become a socioeconomic problem, burdening the existing health care system. Knee Osteoarthritis (KOA) is a prevalent degenerative knee joint disorder in elderly people posing significant functional disability, degrading the muscular strength and restricting the range of motion of the knee. Understanding the abnormalities in daily life activities of KOA patients are essential for the management of this degenerative joint disorder. In the present study, the basic daily-life activity sit-to-stand (STS) task has been studied with the objective to understand the kinematics of knee and trunk with spatiotemporal factors in patients diagnosed with KOA. Knee and trunk flexion/extension angles were evaluated for three different feet distances (participant normal sitting feet distance, 20% greater, and 20% lesser than the normal sitting feet distance). Seat height was kept equivalent to the participants' knee height. Ground and seat reaction forces were also measured to determine the phases of STS task. The kinematics data gathered will help in understanding the KOA patients' tactics for accomplishing the STS task, thus providing an impetus for designing a powered exoskeleton for patients with KOA.

Keywords Osteoarthritis · Assistive device · Sit to stand

1 Introduction

Knee Osteoarthritis (KOA) has emerged as a common musculoskeletal ailment and a major cause of disability in the elderly population. KOA marked a prevalence rate of 70% in the population aged 65 years and above [1]. The condition is marked by pain and stiffness in knees, causing activity limitation and thus reducing the quality of life [2]. Repetitive loading, age, and sedentariness have been found to aggravate the KOA condition in patients [3].

S. Bhardwaj (✉) · A. A. Khan · M. Muzammil
Department of Mechanical Engineering, Aligarh Muslim University, Aligarh, UP, India
e-mail: siddharth.bhardwaj@live.com

© Springer Nature Singapore Pte Ltd. 2019
M. Kumar et al. (eds.), *Advances in Interdisciplinary Engineering*, Lecture Notes in Mechanical Engineering, https://doi.org/10.1007/978-981-13-6577-5_40

421

Currently, management of KOA includes pharmacological, non-pharmacological and surgical techniques and their combinations [4]. Apparently, non-pharmacological modalities including physical therapies for rehabilitation have found to significantly improve the KOA condition. Furthermore, exercise and physical therapies have been suggested before going for multidisciplinary care and knee replacement surgeries [5]. Weakness in quadriceps femoris muscle group has shown to be susceptible towards the development of KOA [6]. The aim of these therapies is to improve the muscle strength, which is shown earlier to alleviate pain and improve KOA symptoms [7].

In recent time's emphasis have been given on the robotic system for rehabilitation and assistive needs. The notion is providing a more optimized, patient motivated and objective evaluation strategy rather than subjective exercise modules by physiotherapist [8–10]. Past researches in the domain of robotic rehabilitation and orthosis have followed the pathology owing to neurological disorders compared to musculoskeletal disorders [11, 12]. However, as of now no robotic rehabilitation system have been developed specifically for KOA patients.

Such robotic systems require the knowledge of motion biomechanics to successfully augment and provide assistance cum rehabilitation to the patients. In the present cohort study, biomechanics of the knee and trunk for KOA patients have been studied in relation to the sit-to-stand (STS) task, i.e., standing from a sitting posture. STS activity demands significant effort from the lower extremities, involving quadriceps femoris muscle group [13, 14]. Moreover, being a daily life activity the task does not require special motor learning. Hence, a robotic aid can be designed assisting the sit-stand task as well as promoting wellness in KOA patients. The results from the study can be used as a foremost step to formulate control schemes of such assistive devices for the KOA patients.

2 Materials and Methods

2.1 Participants

Three patients (females, 42–50 years of age) were recruited for the study who were previously diagnosed with KOA. As diagnosed by radiographs, the more symptomatic knee had at least grade-II on Kellgren and Lawrence (KL) rating [15]. All the participants were able to walk without any support and had no previous injury relating to the knee. Also, the right leg was the dominating leg of all the participants. Patients with severe OA (grade-IV on KL rating) were excluded from the study. All the participants signed the consent form approved by the Ethical Review Committee.

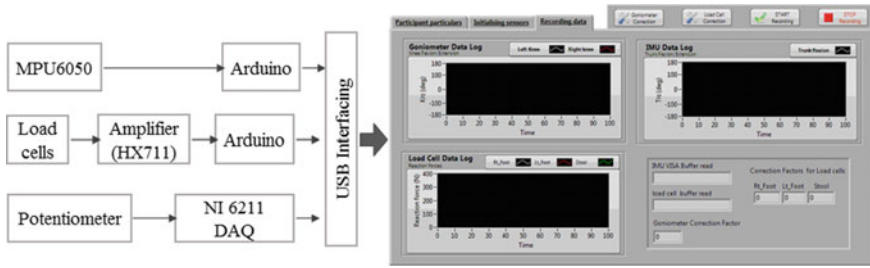


Fig. 1 Instrumentation and interfacing

2.2 Instrumentation and Data Acquisition

Time synchronized recordings of trunk flexion/extension (T_{FE}), knee flexion/extension (K_{FE}), vertical ground reaction force at the feet (R_{lf} , R_{rf} for right and left feet reaction forces respectively) and vertical seat reaction force (R_s) were logged during STS task in a custom build LabVIEW program (Version 12, National Instruments, USA). Figure 1 shows the sensor interfacing and front panel of the developed LabVIEW program.

Reaction forces were measured with load cells (rated 200 kg each). Two load cells were mounted on separate foot plates (left foot and right foot), while one load cell was mounted on the seat. The load cells were amplified with a 24-bit analog to digital converter (HX711), interfaced with Arduino Uno (ATmega328) and sampled at 90 Hz.

T_{FE} was measured with the aid of an inertial measurement unit (IMU, MPU 6050) running an onboard complimentary filter to evaluate quaternion from accelerometer and gyroscope data. Quaternion was then used to estimate the pitch angle of IMU, which reflects the T_{FE} . The IMU was interfaced with Arduino Uno (ATmega328) and sampled at 50 Hz.

K_{FE} of both the knees were measured with the aid of rotating potentiometers. The potentiometer was mounted on the metal trips, which were then tied around the knee. The potentiometers were powered and calibrated through the NI myDAQ data acquisition unit.

2.3 Design of Experiment

The STS task was conducted for three different feet positions viz. participant normal feet position while STS (N_0), 20% greater than the normal feet position (N_a) and 20% lesser than the normal feet position (N_b). The trials were randomized among participants and each participant repeated the three trials twice. The STS movement speed was not controlled, rather the participants were asked to perform the task at

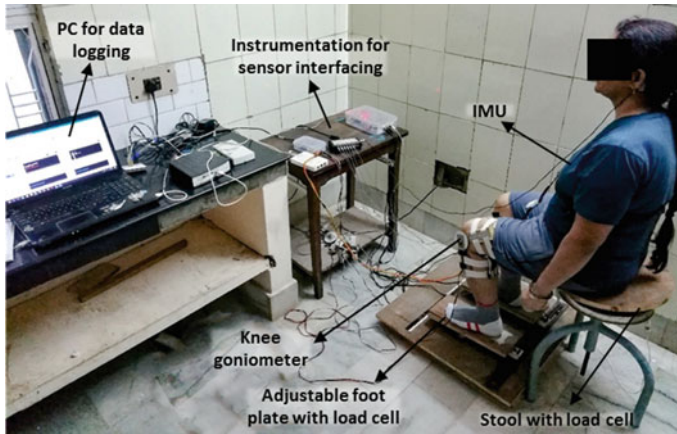


Fig. 2 Experimental setup

self-pace. The sitting height was maintained at the knee height of the participant throughout the trials. During the experiment three sensor modalities were measured: trunk flexion/extension, knee flexion/extension, and reaction forces from the seat and ground.

2.4 Procedure

Before the start of the experiment, the participants were explained about the purpose and procedure of the experiment. Tibia and femur length for the participant was measured in a sitting posture. The subject was then asked to sit on an armless and backless stool adjusted at knee height for performing the trial of STS task, during which the normal feet distance (N_0) was measured. All the sensors were then secured with the participant: potentiometer was secured at the knees using Velcro tape at the lower and upper leg, while the IMU unit was placed around the chest of the participant using a chest belt. Next, the participant was asked to perform the STS task without any support while sensor modalities were recorded using the LabVIEW program. Subsequently randomized and repeated trials of STS task for different feet positions (N_0 , N_a , and N_b) were made. Figure 2 shows the experimental setup.

3 Results and Discussions

The variation of reaction forces during STS task as performed by a participant in normal feet position is shown in Fig. 3. The figure also shows the four distinctive phases

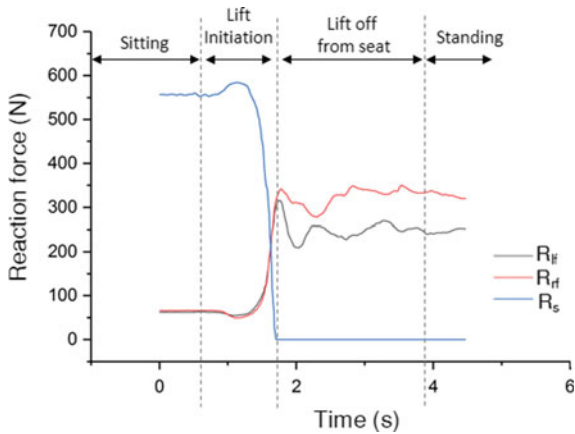


Fig. 3 Reaction forces during STS task

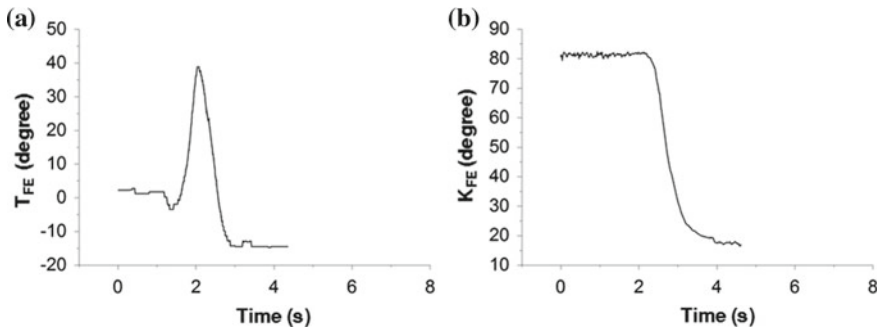


Fig. 4 Trunk (a) and left knee (b) flexion and extension in STS task for a participant in normal feet position

of STS task based upon the reaction forces. The initiation of lift in STS task is marked by a slight increase in the reaction forces at the seat as the participant performed trunk extension (Fig. 4a) while slightly taking the feet off the footplates (slight decrease in the feet reaction force). This helped the participants to gain momentum to rise from the seat and reduce the effort in terms of torque requirement at the knees.

With lift off from the seat both T_{FE} and K_{FE} begin to lower while both the feet struggle to maintain the balance during STS transition as evident from the variation of R_{if} and R_{rf} in Fig. 3.

Figure 4b shows the knee deviation in the task. The previous study has shown T_{FE} being the first step followed by a healthy individual during initiation of STS task [13]. A similar observation is found in the present study in the case of KOA patients.

Feet distance during STS task was found to be affecting the trunk movement (T_{FE}) during lift initiation phase. Feet distance greater than 20% of normal feet distance accompanied with the largest trunk flexion compared to N_0 and N_b . Furthermore, N_0

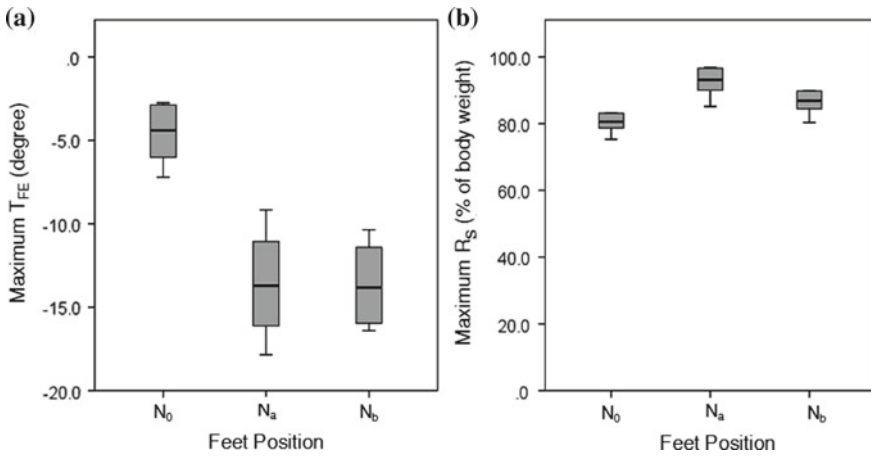


Fig. 5 Maximum trunk extension (a) and maximum reaction force (b) at stool (computed as percentage of body weight) during lift initiation phase

was accompanied with the least trunk extension (Fig. 5a). Trunk extension prior to lift off helps in achieving greater momentum by increasing the hip flexion velocity and reducing the torque requirement at the knees [16]. A 3.28% increase was shown in R_s during lift off from seat for normal feet positioning.

Figure 5b shows the maximum reaction force on stool as percentage of body weight during STS task. Maximum R_s was found for N_a showing greater effort required by KOA patients in performing STS task for greater than normal feet positioning. It was also noted that for all the participants the reaction force at the right feet was greater compared to left feet which might be attributed to their dominating leg.

It was earlier shown that seat height also influence the ease of STS task. For seat height lesser than the knee height reduces peak hip flexion velocity and hence more torque is required at the knees for accomplishing the task [16]. Hence normal seat height (knee height) combined with normal feet distance may significantly ease the STS task in KOA patients.

The deviation in the reaction forces at the feet and seat surface during lift initiation may be used as an indication of intention to perform STS task. For the realization of a user intended robotic device combination of reaction force, trunk/knee deviation, and electromyography may prove beneficial in the classification of STS task [17].

4 Conclusions

This study focused on the measurement of different modalities in the STS task for KOA patients. The aim of this study was to use these modalities for the development of

robotic aids in such STS transfer for promoting wellbeing in KOA patients. Deviation in R_s and T_{FE} was among the first indicator of the STS task. It was found that the maximum T_{FE} was in case of feet distance being 20% greater than the normal which may pose an excessive burden on the knees of KOA patients.

Acknowledgements The study protocol and the participant consent form were approved by the Department Ethical Review Committee, Department of Mechanical Engineering, Aligarh Muslim University. This work was supported by the Council of Scientific and Industrial Research (CSIR), New Delhi under Senior Research Fellow (SRF) scheme. File no. 09/112(0554)2K17.

References

1. Guilak F (2011) Biomechanical factors in osteoarthritis. *Best Pract Res Clin Rheumatol* 25(6):815–823
2. Jamtvedt G, Dahm KT, Christie A, Moe RH, Haavardsholm E, Holm I, Hagen KB (2008) Physical therapy interventions for patients with osteoarthritis of the knee: an overview of systematic reviews. *Phys Ther* 88(1):123–136
3. Carvalho NA, Bittar ST, Pinto FR, Ferreira M, Sitta RR (2010) Manual for guided home exercises for osteoarthritis of the knee. *Clinics* 65(8):775–780
4. Bhatia D, Bejarano T, Novo M (2013) Current interventions in the management of knee osteoarthritis. *J Pharm Bioallied Sci* 5(1):30
5. Smink AJ, Van Den Ende CHM, Vliet Vlieland TPM, Swierstra BA, Kortland JH, Bijlsma JWJ, Voorn TB, Schers HJ, Bierma-Zeinstra SMA, Dekker J (2011) Beating osteoarthritis: development of a stepped care strategy to optimize utilization and timing of non-surgical treatment modalities for patients with hip or knee osteoarthritis. *Clin Rheumatol* 30(12):1623–1629
6. Liikavainio T, Lyytinen T, Tyrväinen E, Sipilä S, Arokoski JP (2008) Physical function and properties of quadriceps femoris muscle in men with knee osteoarthritis. *Arch Phys Med Rehabil* 89(11):2185–2194
7. Bennell K, Hinman R (2005) Exercise as a treatment for osteoarthritis. *Curr Opin Rheumatol* 17(5):634–640
8. Bhardwaj S, Khan AA, Muzammil M (2016) Electromyography in physical rehabilitation: a review. In: National Conference on mechanical engineering—ideas, innovations & initiatives. Excel India Publisher, Aligarh, pp 64–69
9. Tsukahara A, Kawanishi R, Hasegawa Y, Sankai Y (2010) Sit-to-stand and stand-to-sit transfer support for complete paraplegic patients with robot suit HAL. *Adv Robot* 24(11):1615–1638
10. Zoss AB, Kazerooni H, Chu A (2006) Biomechanical design of the Berkeley lower extremity exoskeleton (BLEEX). *IEEE/ASME Trans Mechatron* 11(2):128–138
11. Kim JH, Han JW, Kim DY, Baek YS (2013) Design of a walking assistance lower limb exoskeleton for paraplegic patients and hardware validation using CoP. *Int J Adv Rob Syst* 10
12. Hassani W, Mohammed S, Rifai H, Amirat Y (2014) Powered orthosis for lower limb movements assistance and rehabilitation. *Control Eng Pract* 26(1):245–253
13. Bhardwaj S, Khan AA, Muzammil M, Alam MM (2016) Knee musculoskeletal biomechanics in sit-to-stand and stand-to-sit task. In: 14th international conference on humanizing work and work environment, Jalandhar, pp 57–60
14. Whitney SL, Wrisley DM, Marchetti GF, Gee MA, Redfern MS, Furman JM (2005) Clinical measurement of sit-to-stand performance in people with balance disorders: validity of data for the five-times-sit-to-stand test. *Phys Ther* 85(10):1034–1045
15. Kohn MD, Sassoon AA, Fernando ND (2016) Classifications in brief: Kellgren-Lawrence classification of osteoarthritis. *Clin Orthop Relat Res* 474(8):1886–1893

16. Hughes MA, Schenkman ML (1996) Chair rise strategy in the functionally impaired elderly. *J Rehabil Res and Dev* 33(4):409–412
17. Shen B, Li J, Bai F, Chew CM (2013) Motion intent recognition for control of a lower extremity assistive device (LEAD). In: 2013 IEEE international conference on mechatronics and automation, IEEE ICMA 2013, Takamatsu, Japan, pp 926–931

A Critical Assessment of J-Integral and CTOD as Fracture Parameters



R. Harihara Subramanian, Subbaiah Arunkumar, Sreekumar Jithin and Ravi Kiran Bollineni

Abstract Elastic-Plastic Fracture Mechanics (EPFM) is often used for the integrity assessment of components made from ductile materials. It offers two fracture criteria viz., the J-integral and Crack Tip Opening Displacement (CTOD) which predicts the onset of unstable crack growth in ductile materials or materials undergoing significant plastic deformation. Hence the measurement of these parameters is vital. After presenting a brief introduction to the J-integral, CTOD and the relationship between these two parameters, the basic technique for measuring the J-integral for mode I problem through numerical simulation for is illustrated. The objective of this work is to critically assess the viability of the aforementioned fracture parameters in the integrity assessment of structures. A number of differences and similarities that exists between these two parameters in terms of quality and measurement methods as given in the standards (such as American Society for Testing and Materials and British Standards Institution) is brought out in this work. In addition, the misconceptions detained about the elastic-plastic fracture parameters is discussed.

Keywords J-integral · Crack tip opening displacement · Fracture toughness · Stress intensity factor · Energy release rate · Crack driving force

1 Introduction

Fracture is the fragmentation of a body into two or more parts. The margin of error in the present century is higher compared to previous centuries due to the recent technological advances and its complexity. However, such complexities have been taken care by the advancements in fracture mechanics. Fracture mechanics helps in understanding failure of materials and its prevention when applied aptly. The causes of most catastrophic failures are negligence during design, construction and operation of the component and the use of an exotic material which might produce undesired results. In addition, this approach attempts to protect the component from the catastrophic

R. H. Subramanian · S. Arunkumar (✉) · S. Jithin · R. K. Bollineni
Department of Mechanical Engineering, Amrita Vishwa Vidyapeetham, Amritapuri, India
e-mail: arunkumars@am.amrita.edu

© Springer Nature Singapore Pte Ltd. 2019
M. Kumar et al. (eds.), *Advances in Interdisciplinary Engineering*, Lecture Notes in Mechanical Engineering, https://doi.org/10.1007/978-981-13-6577-5_41

429

failure by providing a margin of safety on the stress. Fracture mechanics quantifies the severity of crack situation in terms of stress, flaw size and fracture toughness. Thus, fracture mechanics assumes the presence of crack or flaw in a body in priori as opposed to continuum mechanics. The mode of loading in flawed components can be classified into three modes: Opening mode (Mode I), Sliding mode (Mode II) and Tearing mode (Mode III). In reality, most of the materials undergo mixed mode of fracture. Often, Mode I is preferred for estimating the fracture toughness of materials, since most materials are prone to fracture by tensile stresses (than shear stresses).

After the Second World War, a historical boundary occurred in the field of fracture mechanics. Researchers begun to focus on the plasticity at the crack tip as the Linear Elastic Fracture Mechanics (LEFM) is no more significant when the failure is due to excessive plastic strain at the tip of the crack [1]. Several researchers like Irwin [2], Dugdale [3], Wells [4], Barenblatt [5] have developed analysis methods to correct for yielding at the crack tip. For the case of plasticity at the crack tip, Wells [4] suggested an alternative criterion for fracture. He proposed that the new criterion be the displacement of crack faces. Wells [4] conducted experiments (at the British Welding Research Association) on low- and medium-strength structural steels. He found that these materials were too ductile for LEFM to be applied. This finding later motivated him to float a new parameter known as Crack Tip Opening Displacement (CTOD). Around the same time in US, J. R. Rice (1968) developed a parameter to characterize elastic-plastic stress field in the wake of the crack tip. He stated that the nonlinear energy release rate can be expressed as a line integral, which he called as J-integral. This line integral is evaluated along a contour around the crack. J-integral was applied to nuclear power plants in the U.S.A, where it was shown that most nuclear pressure vessel steels were too tough to be characterized using LEFM. Later, at Westinghouse Electrical Corporation, J-integral equation was used to measure the fracture toughness of steels. The objective of this work is to critically review these elastic-plastic parameters as possible fracture criterions both qualitatively and quantitatively.

1.1 Crack Tip Opening Displacement (CTOD)

CTOD is an elastic-plastic fracture parameter based on the physical movement of the surfaces of a crack. Indeed, it is a measure of plastic strain around the crack tip. Fracture of the specimen occurs when CTOD reaches a critical value. CTOD is estimated using the plastic hinge model or double clip gauge technique [6]. The British Standard Institution (BS) first published the standard for measuring the CTOD (BS 5762) in 1979 [7]. This standard demonstrates that by evaluating critical values of crack tip opening displacements (δ_c), it is possible to characterize the onset of crack growth. Work by Shih et al. [8] supported the observation on crack initiation.

Under the small-scale theory of yielding around the crack tip, the crack driving force and CTOD are related as follows [9]:

$$\delta = K_I^2 / m\sigma_{ys}E \quad (1)$$

where δ = CTOD, K_I = Mode I Stress Intensity Factor, σ_{ys} = Yield strength and E = modulus of elasticity and m = dimensionless constant.

1.2 J-Integral

It is known that a large plastic zone around the crack tip makes the material tough. In the early development of fracture mechanics, the so-called plastic zone was completely ignored in analyses. This was due to the nonavailability of practical methods to account for the elastic-plastic behaviour within the plastic zone. Various researchers after understanding the real material behaviour came to a conclusion that by supposing material responses as linear and nonlinear elastic behaviour, the plasticity at the tip of the crack can be included in the stress-strain analysis. This led to the development of several line integrals, of which the one developed by J. R. Rice become more popular [9]. This line integral is called as J-integral and is defined as follows:

$$J = \int_{\Gamma} \left(W dy - \bar{T} \cdot \frac{\partial \bar{u}}{\partial x} ds \right) \quad (2)$$

where W = strain energy per unit volume, Γ = path around the tip of the crack, ds = element of Γ , \bar{T} = traction vector on ds , \bar{u} = displacement vector and x, y = rectangular coordinates [10]. The J-integral is measured along Γ surrounding the tip of the crack, which starts from one face of the crack and ends up on the other face of the crack. From this, it can be proved that J-integral is path independent for both linear and nonlinear elastic materials. The ASTM E1290 describes the basic procedure for estimating the J-integral.

Shih [11] related CTOD and J-integral per the following equation:

$$\delta = J / m\sigma_{ys} \quad (3)$$

where m = Plastic constraint factor that depends on the strain hardening exponent of the material. This relationship is valid for both large-scale and small-scale yielding. Research based on analytical, numerical and experimental studies reveals that the value of m generally lies between 1.0 and 2.0.

2 Comparison of ASTM and BS Standards for CTOD Measurement

Both CTOD and J have their own merits and demerits. For example, J-Integral is a robust fracture parameter due to its rigorous mathematical definition. This parameter can be easily determined through finite element procedures. However, this parameter breaks down when there is excessive plasticity at the tip of the crack or the plastic zone size is comparable to the ligament length. On the other hand, CTOD is the displacement of crack surfaces at the crack tip. This parameter is easy to visualize, understand and free of mathematical limitations. In fact, CTOD is a simple physical parameter which is a measure of material's toughness. The value of CTOD increases proportionately with the toughness of the material. However, in the measurement of CTOD, the plastic hinge model assumes straight crack faces permitting the use of similar triangles to estimate CTOD. In addition, CTOD is applicable for materials with low hardening, high levels of plastic displacements and deep cracks [6].

In 1979, the British Standards Institution (BS) introduced a standard for CTOD measurement based on plastic hinge model for brittle fracture as BS 5762:1979. In the revised standard BS7448:1991, the same plastic hinge model remained as the basis for CTOD measurement. The ASTM also introduced a standard for the CTOD measurement based on the geometric displacement as ASTM E1290. This standard was revised in 2002 by evaluating the critical CTOD using critical J . Conceptually both CTOD and J are similar elastic-plastic fracture parameters and hence one can be derived from the other. Since CTOD is estimated from J in ASTM E1290, its value could be different from that estimated using BS7448. Thus, the fitness of using CTOD obtained from ASTM standard becomes questionable [12].

The CTOD based on BS7448, δ_{BS} is estimated from the following equation:

$$\delta_{BS} = \delta_{el} + \delta_{pl} = \delta = \frac{(1 - \nu^2)K^2}{2E\sigma_{ys}} + \frac{(W - a_0)v_p r_p}{a_0 + z + (W - a_0)r_p} \quad (4)$$

In the above equation, δ_{el} and δ_{pl} are elastic and plastic component of CTOD, ν is the Poisson's ratio, K is the Stress Intensity Factor, W is the width of the specimen, a_0 is the length of the crack, r_p is the rotational centre of plastic hinge model, z is specimen size obtained from plastic hinge model.

Similarly, ASTM δ_{ASTM} (which is calculated using J) is estimated from the following equation:

$$\delta = \frac{1}{\sigma_Y m} (J_{el} + J_{pl}) = \frac{1}{\sigma_Y m} \left[\frac{(1 - \nu^2)K^2}{E} + \frac{A_{pl}\eta}{(W - a_0)B\{z/(0.8a_0 + 0.2W) + 1\}} \right] \quad (5)$$

where J_{el} and J_{pl} are the elastic and plastic components of J , σ_Y is the effective yield strength (average of yield and ultimate tensile strengths), η is the plastic factor calculated using specimen dimensions, A_{pl} is the plastic area under the load versus

displacement curve and B is the thickness of the specimen. J is estimated from the load versus displacement curve.

On comparing the elastic parts of δ_{BS} and δ_{ASTM} , it is apparent that the difference may arise due to $2\sigma_{ys}$ and $m\sigma Y$. Due to this, δ_{ASTM} tend to give lower values of critical CTOD in comparison to that estimated from BS. This has been confirmed by experiments on nine different materials. On the other hand, the plastic parts of the CTOD estimated using ASTM the standard was affected by the load level and the amount of plastic strain at the tip of the crack. It is due to the fact that the J is not valid under large-scale yielding and CTOD represents a displacement parameter which can accommodate both small-scale and large-scale yielding. Thus, the plastic component that estimated from BS was slightly higher than that estimated using ASTM. Nevertheless, the difference in the critical values of CTOD estimated from both BS and ASTM are comparable [12].

3 Numerical Procedure

Finite element method which started as an extension of matrix methods to analyse structural problems is now being applied to solve various multidisciplinary problems. It is an indispensable tool in fracture mechanics and is easy to implement finite element code to estimate the fracture parameters like stress intensity factor, J-integral, etc. compared to experimental methods. A large number of samples is required to estimate these parameters through experiments, which is laborious, time-consuming and costly. It is in these situations finite element method becomes a promising tool [13–15]. In order to appreciate the advantage of the finite element method in the context of fracture mechanics, the basic technique for estimating J-integral is described in this section. Various commercial finite element packages are available in the market, for example, ANSYS, ABAQUS, etc. to name a few. All of them are well suited in estimating the fracture parameters. In this work, ABAQUS finite element code is implemented for estimating the J-integral [16–19].

The various types of standard specimens employed in the estimation of fracture parameters are Compact Tension (CT), Single Edge Notch Bend (SENB), Disc-shaped Compact Tension (DCT) and Arc-shaped Tension (AT) are used depending the type of component geometry in service. The most commonly used ones are CT and SENB. In this paper, SENB specimen is used. The geometry and dimensions of SENB specimen are shown in Fig. 1 [20]. A 2D model was developed in the aforementioned finite element software. The geometry was discretized using 8-node isoparametric quadrilateral elements (and collapsed into wedge elements at the crack tip) and a fine mesh was used due to high gradients in the deformations. The analysis was performed under plane strain conditions [21–23]. The SENB specimen after meshing is shown in Fig. 2. The material properties used in this analysis are Modulus of elasticity $E = 206.85$ GPa, $\nu = 0.3$ and the plastic stress–plastic strain data as shown in Fig. 3a. A quasi-static concentrated load is applied on the specimen. The contour domain integral method was used for calculating the J-integral around the tip of the

Fig. 1 Geometry of standard SENB specimen ($W = 50.8$ mm, $R = 12.7$ mm, $a = 2.54$ mm) [20]

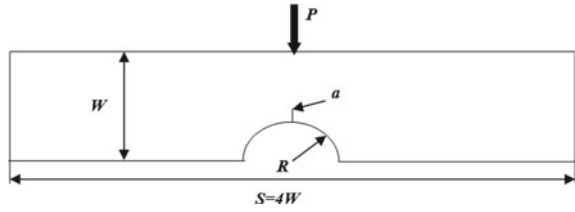


Fig. 2 Meshed SENB geometry

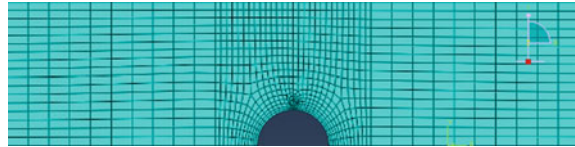


Fig. 3 a Plastic stress—strain data [20]

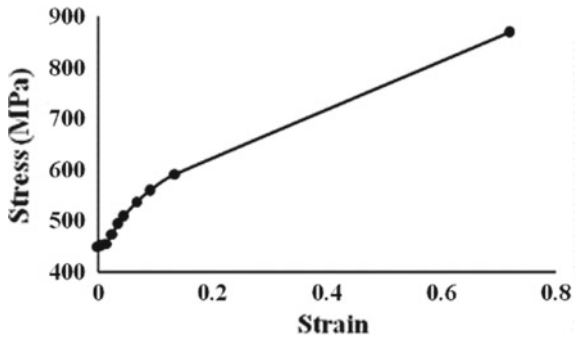
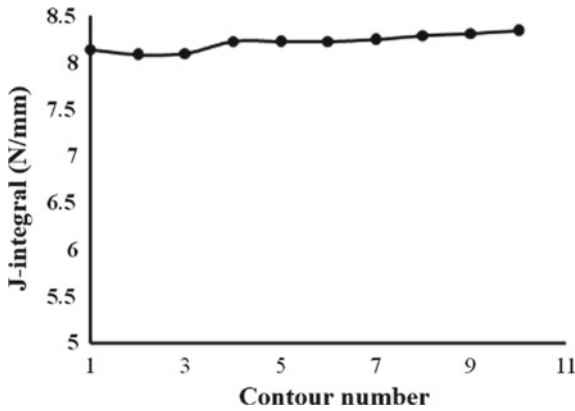


Fig. 4 J values at the crack tip for 10 domains



crack. In order for the J-integral to be path independent, its values along different contours defined around crack tip must be the same or nearly close enough. Otherwise, the estimated values of J-integral values are inaccurate. The J-integral obtained on 10 domains at the tip of the crack is shown in Fig. 4. J-integral values obtained from the simulation indicate good contour independence.

4 Comparison of J-Integral and CTOD

A parameter that precisely predicts the failure of a cracked component is always a valuable tool in engineering, as it helps in the selection of appropriate material and in the structural integrity assessment. In LEFM, the energy release rate (G) and stress intensity factor (K) are used as fracture criteria to predict the failure of cracked bodies. The limitation with these parameters is that it can handle components subjected to linear elastic stresses with small-scale yielding. Thus, LEFM parameters cannot be applied to materials with high toughness [24]. The concepts of fracture mechanics were then extended to accommodate elastic-plastic behaviour. The most commonly used elastic-plastic fracture parameters are CTOD and J-integral. Wells [1] in 1961, first proposed the CTOD parameter. In his experiments with ductile materials, Wells noticed the blunting of the crack tip with the crack faces moving apart. Based on these observations, he reached the conclusion that fracture occurs when CTOD reaches a critical value. British Standards Institution, in 1979, published a standard method for determining the Crack Tip Opening Displacement testing (BS 5762: 1979) and is predominantly in used in the United Kingdom.

On the other hand, Rice [25] developed a contour integral in 1968 and named it as J-integral as an elastic-plastic fracture parameter. J-integral characterizes the stress field near the crack tip, particularly for linear and nonlinear elastic materials. In 1981, ASTM published the standard test method for determining J (E 813-81). J is mainly used in the United States. Landes and Begley [24] recommended to use J as fracture toughness parameter. However, there was difficulty in it. As it is not possible to carry out line integration on the test specimen, J estimation procedure was modified. The new procedure makes use of the load-displacement data to calculate the value of J . Researchers with theoretical background, prefer to use J-integral over CTOD as the former can be obtained from the theory of nonlinear elasticity. In addition, J can be easily evaluated through finite element method. On the other hand, the experimentalists favor CTOD, as it can be visualized and understood easily. Numerical estimation of CTOD is little complicated as it is difficult to model the rounded tip of the crack. The other misconception is that J has been bestowed a high rank due to the intricate mathematical equation. While CTOD is a simple measure of material's toughness analogous to Izod or Charpy impact tests. It is mentioned earlier that J and CTOD are closely related. Hence, it is deceiving to ascertain one parameter as better than the other [9].

The advantage of J is that it can be applied to both elastic and plastic behaviour of materials. Within the elastic region, it is identical to G or K . One of the limitation of J is that, it can be applied to plane strain or plane stress problems only as it is defined in two dimensions. In addition, during testing, a standard specimen unloading is not permitted. On the other hand, conceptually CTOD seems to be a simple fracture parameter to visualize, it has no unique definition about crack tip opening displacement. In fact, the plastic hinge model which assumes straightness of the crack faces. This permits to use similar triangles to estimate CTOD, which is not valid for materials with high strain hardening exponent [26].

Within the acceptable limits, the elastic-plastic fracture parameters, J and CTOD are comparable through Eq. (3) linked using the plastic constraint factor, m . In fact, the elastic-plastic fracture parameters are termed as ‘crack driving forces’. While assessing the integrity of structures, J-integral is used due to its robust definition and ease of calculation using numerical methods. However, for CTOD, a detailed meshing is needed at the crack tip and a clear definition of CTOD needs to be established.

Experimental calculation of the crack driving force is easier said than done. The J-integral method is unreliable and difficult in this regard. The CTOD method, which gets inference from Crack Mouth Opening Displacement (CMOD), is widely used in the evaluation of crack driving force. The experimental procedures for evaluating J-integral and CTOD are of a different nature. Although the CTOD parameter can be easily realized visually, the relation between CTOD and CMOD is not well defined. For the case of J-integral, the experimental techniques are difficult. It can be made easier using the Moire Method. But with post-processing process, Moire Method can be numerically intensive. The solutions of crack driving force using codes for CTOD parameter (nonconservative Dugdale’s Strip Yield Model) is semi-empirical (as a virtue of CTOD design curve). Crack driving forces for the J-integral parameter, however, are directly dependent on J-integral solutions [27].

5 Conclusions

The elastic-plastic parameters J and CTOD were compared qualitatively and quantitatively. Qualitatively though both J and CTOD are similar, their measure of fracture toughness is not identical. In the case of J , the fracture toughness is proportionate to the area below the load-deflection curve. While CTOD is proportional to the crack mouth opening displacement. It is due to this, CTOD values are conservative in nature than J . The numerical simulation of CTOD is quite difficult, since a detailed meshing is needed at the crack tip and the clear definition of CTOD is not established. J-integral cannot be used for the case where there is excessive plastic deformation at the crack tip.

References

1. Anderson TL (2005) Fracture mechanics—fundamentals and applications, 3rd edn. Taylor and Francis Group, Florida
2. Gdoutos EE (2003) Crack tip plastic zone according to Irwin’s model. In: Gdoutos EE, Rodopoulos CA, Yates JR (eds) Problems of fracture mechanics and fatigue. Springer, Dordrecht, pp 95–97
3. Dugdale S (1960) Yielding of steel sheets containing slits. *J Mech Phys Solids* 8:100–104
4. Broek D (1982) Elementary engineering fracture mechanics, 3rd edn. Kluwer Academic Publisher, The Netherlands
5. Barenblatt GJ (1962) The mathematical theory of equilibrium cracks in brittle fracture. *Adv Appl Mech* 7:55–129

6. Sarsoza DFB, Ruggieri C (2015) Experimental validation of relationship between fracture parameters J and CTOD for SE(B) and SE(T) specimens during ductile crack growth. *Mar Syst Ocean Technol* 10:60–70
7. Lu ML, Chiou KC, Chang FC (1996) Elastic-plastic fracture toughness of PC/ABS blend based on CTOD and J-Integral methods. *Polymer* 7(19):4289–4297
8. Shih CF, deLorenzi HG, Andrews WR (1979) Studies on crack initiation and stable crack growth. In: Landes JD, Begley JA, Clarke GA (eds) *Elastic-plastic fracture*, ASTM STP 668, American Society for Testing and Materials, pp 65–120
9. Dawes MG (1979) Elastic-plastic fracture toughness based on the COD and J-contour integral concepts. In: Landes JD, Begley JA, Clarke GA (eds), *Elastic-plastic fracture*, ASTM STP 668, American Society for Testing and Materials, pp 307–333
10. ASTM E1820-01 Standard test method for measurement of fracture toughness, ASTM International
11. Shih CH (1981) Relationships between the J-Integral and the Crack opening displacement for stationary and extending cracks. *J Mech Phys Solids* 29(4):305–326
12. Tagawa T, Kayamori Y, Ohata M, Handa T, Kawabata T, Yamashita Y, Tsutsumi K, Yoshinari H, Aihara S, Hagihara Y (2010) Comparison of CTOD standards: BS7448-Part I and revised ASTM E1290. *Eng Fract Mech* 77:327–336
13. Bathe KJ (2014) *Finite element procedures*, 2nd edn. Prentice Hall, Pearson Education, New Jersey
14. Mohammadi S (2008) *Extended finite element method for fracture analysis of structures*. Blackwell Publishing Ltd., Singapore
15. Rao SS (2004) *The Finite element method in engineering* 4th Edn. Elsevier Sci Technol Books
16. Hrnjica B, Islamović F, Gačo D, Bajramović E (2016) Numerical calculation of J-integral using finite elements method. In: 7th international scientific conference on defensive technologies, 6–7 Oct. 2016, Belgrade, Serbia
17. Moon DH, Lee JS, Lee JM, Kim MH (2014) Validation on the relationship between J integral and CTOD for offshore structural steel weldments by experimental and numerical analyses. In: *Proceedings of the ASME 2014 international mechanical engineering congress and exposition IMECE2014*, November 14–20, 2014, Montreal, Quebec, Canada
18. Shi Y, Sun S, Murakawa H, Ueda Y (1998) Finite element analysis on relationships between the J-integral and CTOD for stationary cracks in welded tensile specimens. *Int J Press Vessels Pip* 75:197–202
19. Bomidi JAR, Sadeghi F (2014) Three-dimensional finite element elastic-plastic model for subsurface initiated spalling in rolling contacts. *J Tribol* 136:1–14
20. Validation of contour integral functions (J and C(t)) in ABAQUS v6.11-v6.14 for combined mechanical and residual
21. ABAQUS (2014) *Version 6.14 User's Manual*, DassaultSystèmesSimulia Corp.; Providence, RI, USA
22. Dodds RH Jr, Carpenter WC, Sorensen WA (1988) Numerical evaluation of A 3-D J-integral and comparison with experimental results for a 3-point bend specimen. *Eng Fract Mech* 29(3):275–285
23. Graba M (2017) Proposal of the hybrid solution to determining the selected fracture parameters for SEN(B) specimens dominated by plane strain. *Bull Pol Acad Sci Tech Sci* 65(4):523–532
24. Begley JA, Landes JD (1972) The J integral as a fracture criterion fracture toughness. In: *Proceedings of the 1971 national symposium on fracture mechanics, Part 11*, ASTM STP 514, American Society for Testing and Materials, pp 1–20

25. Rice JR (1968) A path independent integral and the approximate analysis of strain concentration by notches and cracks. *J Appl Mech* 35:379–386
26. Sorensen WA, Dodds RH, Jr, Rolfe ST (1991) A comparison of the J-integral and CTOD parameters for short crack specimen testing. In: Joyce JA (ed), *Elastic-plastic fracture test methods: the user's experience (Second Volume)*, ASTM STP 1114, American Society for Testing and Materials, Philadelphia, pp 19–41
27. DRAFT NOTE—*J.T. Martin—OGBM/3, R.W.J. Koers—OGBM/3*, CTOD versus J-Integral as a fracture parameter, 25042001—SINTAP, April 8 (1998)

Financial Performance Evaluation Using MADM Approaches in Indian Banks



Neeraj Saini and Dinesh Khanduja

Abstract Performance evaluation is critically important as it helps in the identification of weak areas and to plan or replan more effective actions for a better performance. Banking sector plays a pivotal role in economic development of any country and in a fast-developing economy like India, this sector has a major role to play. Performance appraisal of banks is very significant to boost economic planning. This study aims to utilize the multi-criteria decision model to evaluate the performance of banks during the financial year 2017–18. Total 14 banks were selected for the evaluation process in terms of financial parameters defined by Reserve Bank of India. AHP and TOPSIS methodologies of Multi-Attribute Decision Making have been utilized for the evaluation. In AHP, priority weights of three parameters were determined. These weights act as input for the TOPSIS method and final rank of various banks are obtained.

Keywords MADM · AHP · TOPSIS · Performance evaluation · Bank

1 Introduction and Literature Review

A strong banking structure in a country is highly significant and critically affects economic development by offering effective and customer friendly financial services. Banks are playing an important role in growing and developing economy like India. After recent demonetization in India, the banking system is under heavy pressure to adopt some major changes as it has brought in a major shift in public opinion on the banking sector in India. Stable and efficient banking is the backbone of economic system in a country. Recent banking frauds have also exposed important loopholes in our banking system. Indubitably, for sustainable growth of economy, performance of banks needs a continuous and comprehensive evaluation. The present

N. Saini (✉)

M. Tech, National Institute of Technology, Kurukshetra, India
e-mail: neerajsaini463@gmail.com

D. Khanduja

MED, National Institute of Technology Kurukshetra, Kurukshetra, India

© Springer Nature Singapore Pte Ltd. 2019

M. Kumar et al. (eds.), *Advances in Interdisciplinary Engineering*, Lecture Notes in Mechanical Engineering, https://doi.org/10.1007/978-981-13-6577-5_42

study tries to explore certain MADM approaches to see if the banks are performing well and are using the assigned resources optimally. A MADM approach dwells on many approaches like TOPSIS [1], VIKOR [2], graph theory and matrix approach (GTMA) [3], AHP [4], simple additive weighting (SAW), etc. Among these, TOPSIS is a widely used decision-making approach for the evaluation process. This method has been used in various case studies involving plant layout selection [5], material selection [6, 7], decision-making problems [8], supplier selection problems [9–11]. TOPSIS has also been effectively used for evaluating performance in the service sector like Turkish banks [12], Serbian banks [13], etc. In the present study, TOPSIS approach has been incorporated with AHP method to evaluate, prioritize and analyze different banks in India in terms of financial parameters identified by RBI.

2 Economic Parameters for Evaluation

RBI in India has identified eight parameters to evaluate economic performance of a bank. These are Interest Earned, Total Income, Net Profit/Loss, Total Expenditure, Capital Adequacy Ratio, Return On Assets, Gross NPA and Net NPA. Based on their impact, inputs from ‘National Reports’ of various banks, RBI guidelines and discussion with financial experts; only three parameters have been finally shortlisted for an in-depth analysis of the performance of banks. These are:

2.1 *Total Income (P1)*

This parameter includes a net sum of various incomes and spending by a bank. This may include total sum of money received from an individual or organization, interest earned/paid, profit from various sources like ATM sharing fees, securities, commissions earned through different guarantees and letters of credit, transactions, fees received from giving useful service to needy customers and sale of products involving third party.

2.2 *Net Profit/Loss (P2)*

Net Profit is also called as net earnings, and this is a measure of the profitability after account costs and taxes. It is the actual profit and includes the operating expenses. Net loss occurs when expenses exceed the income produced for a given period of time.

2.3 Gross NPA (P3)

An asset will become a non-performing one if it stops to create additional income for the concerned bank. This may also include the leased asset. Gross non-performing asset is basically the amount being shown in borrower account; it is not just an interest income loss to the bank, but a principal loss as well.

3 Methodology

For performance evaluation of banks on the basis of three financial parameters, first weightage to these parameters is given by AHP and then ranking of various selected banks is done by using TOPSIS (refer Fig. 1).

3.1 AHP

AHP was developed by T. Saaty in the 1970s for multi-criteria decision making. Complex decisions can be made with this and AHP can also be tried on prioritizing alternatives and to determine optimal alternative by using pairwise comparison method.

The AHP consists of a given procedure

1. Define the problem and then determine the criteria.
2. Structure the decision hierarchy taking into account the goal of the decision.
3. Construct a set of all judgments in a square comparison matrix in which the set of elements is compared with itself (size $m \times m$) by using the fundamental scale

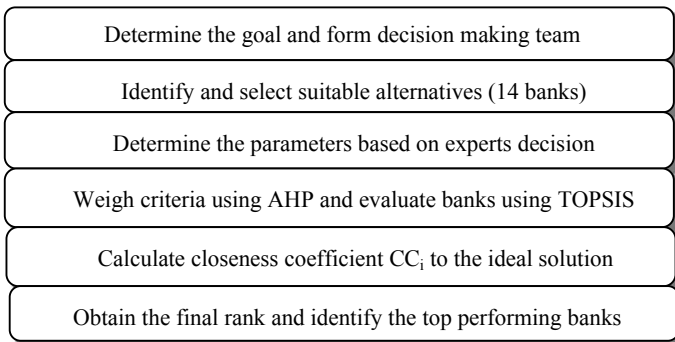


Fig. 1 Methodology used

Table 1 Fundamental Scale of Pairwise Comparison Matrix in AHP

Intensity of importance	Definition
1	Equally important
3	Highly important
5	Strongly important
2,4	Intermediate comparison

Table 2 Average RI values

m	1	2	3	4	5	6	7	8	9	10
RI	0	0	0.52	0.89	1.11	1.25	1.35	1.40	1.45	1.49

of pairwise comparison shown in Table 1. Then assign the reciprocal value in the matrix.

- Use overall priorities obtained from weighted values and for the synthesis of priorities; ensure to obtain the principal right eigenvector and largest eigenvalue.

$$Aw = \begin{bmatrix} 1 & w1/w2 & w1/w3 \\ w2/w1 & 1 & w2/w3 \\ w3/w1 & w3/w2 & 1 \end{bmatrix} \begin{bmatrix} w1 \\ w2 \\ w3 \end{bmatrix} = mw \tag{1}$$

$$a_{ij} = w_i/w_j \quad , \quad i, j = 1, 2, \dots, m \tag{2}$$

$$Aw = \lambda_{\max} w \tag{3}$$

For measuring the consistency index (CI); value to be adopted is as

$$CI = (\lambda_{\max} - m)/(m - 1) \tag{4}$$

Accept the estimate of w if the consistency ratio (CR) of CI is significant small. If CR value is too high, then it means that experts' answers are not consistent. When CR value is less than 0.10; then the consistency of the comparisons is appropriate. The CR is obtained by comparing the CI with an average random consistency index (RI).

$$CR = CI/RI \tag{5}$$

The following gives the average RI: (Table 2).

3.2 Topsis

TOPSIS stands for “Technique for Order Preference by Similarity to Ideal Solution” and it classifies the alternatives as per the distance from the NIS (negative ideal solution) and PIS (positive ideal solution). TOPSIS is conducted as follows:

Step 1: Prepare the required decision matrix. The structure of decision matrix is shown by $X = (x_{ij})_{n \times m}$ and it can be shown as

$$X = \begin{bmatrix} x_{11} & x_{12} & \cdots & x_{1j} & \cdots & x_{1m} \\ x_{21} & x_{22} & \cdots & x_{2j} & \cdots & x_{2m} \\ \vdots & \vdots & \dots & \vdots & \dots & \vdots \\ x_{i1} & x_{i2} & \cdots & x_{ij} & \cdots & x_{im} \\ \vdots & \vdots & \dots & \vdots & \dots & \vdots \\ x_{n1} & x_{n2} & \cdots & x_{nj} & \cdots & x_{nm} \end{bmatrix}$$

x_{ij} is the result of i th alternative with respect to j th criteria.
 Criteria = 1, 2... j ... m ; Alternative = 1, 2... i ... n

Step 2: Normalize the decision matrix using equation

$$r_{ij} = \frac{x_{ij}}{\sqrt{\sum_{i=1}^n x_{ij}^2}}, \quad i = 1, 2 \dots n \quad j = 1, 2 \dots m \tag{6}$$

Step 3:Weighted normalized decision matrix is computed by multiplying the normalized decision matrix by its associated weights as

$$v_{ij} = w_j r_{ij}, \quad i = 1, 2 \dots n \quad j = 1, 2 \dots m \tag{7}$$

Step 4: Segregate the PIS (positive ideal solution) and NIS (negative ideal solution).

$$PIS = A^+ = \{v_1^+, v_2^+ \dots \dots v_m^+\} = \{(\max v_{ij} | j \in \Omega_b), (\min v_{ij} | j \in \Omega_c)\} \tag{8}$$

$$NIS = A^- = \{v_1^-, v_2^- \dots \dots v_m^-\} = \{(\min v_{ij} | j \in \Omega_b), (\max v_{ij} | j \in \Omega_c)\} \tag{9}$$

Step 5: Calculate the separation measures (Euclidean distance) of every alternative from the Negative ideal solution and Positive ideal solution as shown below:

$$d_i^+ = \sqrt{\sum_{j=1}^m (v_{ij} - v_j^+)^2}, \quad i = 1, 2 \dots n \tag{10}$$

$$d_i^- = \sqrt{\sum_{j=1}^m (v_{ij} - v_j^-)^2}, \quad i = 1, 2 \dots n \tag{11}$$

Step 6: Calculate the relative closeness of the *i*th alternative to ideal solution by

$$CC_i = \frac{d_i^-}{d_i^+ + d_i^-}, \quad i = 1, 2 \dots n \quad CC_i \in [0, 1] \tag{12}$$

Step 7: The ranking of alternatives can be calculated by comparing the *CC_i* values, the higher is the *CC_i* value, and it means that the rank is better. Rank the alternatives beginning from the value that is closest to 1 and is in descending order.

4 Discussion and Result

In Fig. 2, level 0 indicates objective which is the performance evaluation of Indian banks. Three selected performance evaluation parameters are shown on level 1 and level 2 shows the selected banks for the evaluation. Interdependency of banks on these criteria shows the complexity of the problem. Once the prime factors are identified, the next question was to prioritize these.

Axis bank	A1	Corporation bank	A6	IndusInd bank	A11
Bank of India	A2	Dena bank	A7	Punjab national bank	A12
Canara bank	A3	HDFC bank	A8	Syndicate bank	A13
Central bank of India	A4	ICICI bank	A9	Yes bank	A14
City union bank	A5	Indian bank	A10		

It is important to note that all these parameters have a different impact on various banks. Hence, in order to prioritize these, pairwise comparison method was used.

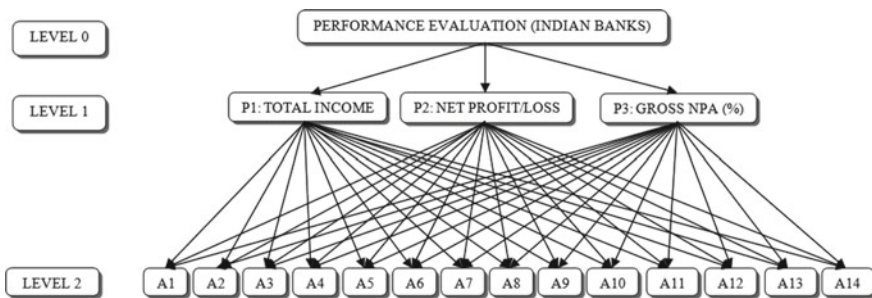


Fig. 2 Schematic hierarchy for performance evaluation of Indian banks

Table 3 AHP result for parameters

Parameter	Weights	Δ_{max} , CI, RI	CR
Total income (P1)	0.110	$\Delta_{max} = 3.0049$ CI = 0.00246 RI = 0.52	0.00473
Net profit/loss (P2)	0.309		
Gross NPA (P3)	0.581		

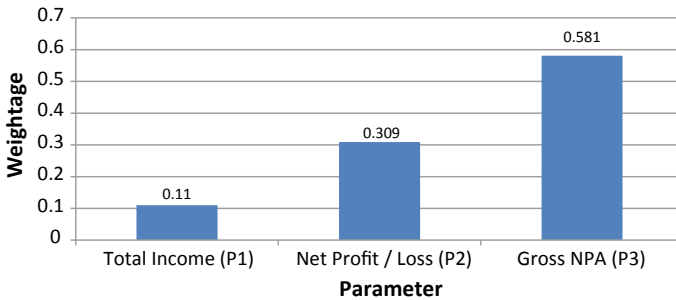


Fig. 3 Weightage of performance parameters (using AHP)

The relative decision matrix based on AHP approach and the calculated weights are summarized in Table 3. Contributions of criteria are illuminated with a bar in Fig. 3.

Tables 4, 5 6 show the TOPSIS analysis of the financial performance based on selected parameters for different banks for the three quarters of 2017. In the first quarter (April to June) HDFC Bank, Yes bank and IndusInd bank are appearing to be the best three performers and the same trend continues in the next two quarters also. Incidentally, the three worst performers (Canara bank, Bank of India and Punjab National Bank) are also the same in all the three quarters. It is also observed that banks like HDFC Bank, Yes bank, IndusInd bank, and City Union Bank show consistent performance.

5 Conclusion

This study shows that MADM approaches like AHP and TOPSIS are highly versatile in nature and can be effectively used to evaluate the performance of banks. In the study, 14 banks were selected from both public and private sectors. Three factors were finally identified, having a huge influence on their economic performance. ‘Gross NPA’ was found to be the most influencing factor for the financial performance of the banks. This result was incorporated in the TOPSIS analysis of performance analysis of the last three quarters of 2017. In all the three quarters, HDFC Bank, Yes bank, and IndusInd bank appear to be the best three performers, while three worst performers (Canara bank, Bank of India, and Punjab National Bank) are also the same.

Table 4 TOPSIS analysis of June, 2017 report

Bank	Total income (P1)	Net profit/loss (P2)	Gross NPA (P3)	d ⁺	d ⁻	CC _i	Rank
Axis bank	1405230	130,560	2,203,087	0.20	0.21	0.51	6
Bank of India	1,110,661	8771	5,101,911	0.36	0.05	0.11	13
Canara bank	1,230,410	25,160	3,765,776	0.31	0.11	0.27	12
Central bank of India	687,078	57,676	3,139,847	0.27	0.14	0.35	11
City union bank	96,086.54	14,032.41	73,495.78	0.25	0.30	0.55	4
Corporation bank	511,299.6	6014.55	2,171,267	0.27	0.19	0.41	9
Dena bank	262,028	13,265	1,299,416	0.25	0.24	0.48	7
HDFC bank	2,218,538	389,384	724,293	0.03	0.37	0.91	1
ICICI bank	1,684,704	204,900	4,314,764	0.26	0.15	0.38	10
Indian bank	478,804.1	37,240.54	965,301.7	0.23	0.26	0.52	5
IndusInd bank	530,277	83,655	127,168	0.20	0.31	0.60	3
Punjab national bank	1,446,814	34,340	5,772,070	0.38	0.04	0.10	14
Syndicate bank	617,149	26,319	2,018,385	0.26	0.20	0.44	8
Yes bank	578,596	96,552	136,438	0.19	0.31	0.61	2

Table 5 TOPSIS analysis of Sept, 2017 report

Bank	Total income (P1)	Net profit/loss (P2)	Gross NPA (P3)	d ⁺	d ⁻	CC _i	Rank
Axis bank	1,382,062	43,238	2,740,232	0.27	0.16	0.38	9
Bank of India	1,160,047	17,907	4,930,690	0.35	0.05	0.13	13
Canara bank	1,199,464	26,018	3,916,408	0.31	0.10	0.25	12
Central bank of India	689,626	75,041	3,164,115	0.27	0.14	0.35	11
City union bank	99,612.25	14,475.63	78,039.09	0.25	0.30	0.54	4
Corporation bank	534,459.1	103,520.1	2,068,488	0.22	0.20	0.48	6
Dena bank	260,883	18,502	1,320,127	0.26	0.23	0.48	7
HDFC bank	2,327,618	415,103	770,284	0.04	0.36	0.91	1
ICICI bank	1,876,329	205,819	4,448,854	0.26	0.15	0.36	10
Indian bank	487,416.4	45,154.3	962,394.9	0.23	0.25	0.52	5
IndusInd bank	539,592	88,010	134,528	0.20	0.30	0.59	3
Punjab national bank	1,420,531	56,058	5,763,011	0.37	0.04	0.11	14
Syndicate bank	641,921	10,524	2,017,664	0.27	0.20	0.42	8
Yes bank	604,878	100,273	272,034	0.20	0.29	0.60	2

Table 6 TOPSIS analysis of Dec, 2017 report

Bank	Total income (P1)	Net profit/loss (P2)	Gross NPA (P3)	d ⁺	d ⁻	CC _i	Rank
Axis bank	1,431,463	72,644	2,500,051	0.23	0.20	0.46	9
Bank of India	1,037,603	234,120	6,424,858	0.33	0.11	0.26	13
Canara bank	1,234,109	12,575	4,031,198	0.30	0.12	0.29	12
Central bank of India	658,932	166,422	3,249,035	0.22	0.17	0.44	10
City union bank	12,169,24	15,479.17	85,979.32	0.23	0.31	0.57	4
Corporation bank	484,137.2	124,049.1	2,181,796	0.21	0.22	0.51	7
Dena bank	277,596	38,007	1,416,878	0.23	0.24	0.51	6
HDFC bank	2,445,044	464,260	823,488	0.04	0.36	0.91	1
ICICI bank	1,683,222	165,024	4,603,870	0.27	0.13	0.32	11
Indian bank	490,307.4	30,306.36	959,515.3	0.23	0.27	0.54	5
IndusInd bank	547,354	93,625	149,870	0.19	0.31	0.62	3
Punjab national bank	1,525,750	23,011	5,751,941	0.36	0.05	0.13	14
Syndicate bank	594,515	86,977	2,110,295	0.22	0.21	0.49	8
Yes bank	649,256	107,687	297,434	0.19	0.30	0.62	2

References

1. Deng HYC, Willis RJ (2000) Inter-company comparison using TOPSIS with objective weights. *Comput Oper Res* 27:963–973
2. Azimi M, Taghizadeh H, Farahmand N, Pourmahmoud J (2014) Selection of industrial robots using the Polygons area method. *Int J Ind Eng Comput* 5(4):631–646
3. Rao RV (2006) A material selection model using graph theory and matrix approach. *Mater Sci Eng A* 431(1):248–255
4. Saaty TL (1990) How to make a decision: the analytic hierarchy process. *Eur J Oper Res* 48(1):9–26
5. Besbes M, Affonso RC, Zolghadri M, Masmoudi F, Haddar M (2017) Multi-criteria decision making for the selection of a performant manual workshop layout: a case study. *Int Fed Autom Control* 50(1):12404–12409
6. Kumar R, Singal SK (2015) Penstock material selection in small hydropower plants using MADM methods. *Renew Sustain Energy Rev* 52:240–255
7. Seyed Hadi Mousavi-Nasab, Alireza Sotoudeh-Anvari (2017) A comprehensive MCDM-based approach using TOPSIS, COPRAS and DEA as an auxiliary tool for material selection problems. *Mater Des* 121:237–253
8. Sabaghi M, Mascle C, Baptiste P (2015) Application of DOE-TOPSIS technique in decision-making problems. *IFAC Papers* 48(3):773–777
9. Boran FE, Genç S, Kurt M, Akay D (2009) A multi-criteria intuitionistic fuzzy group decision making for supplier selection with TOPSIS method. *Expert Syst with Appl* 36:11363–11368
10. Gurung S, Phipon R (2016) Multi-criteria decision making for supplier selection using AHP and TOPSIS method. *Int J Eng Inventions* 6(2):13–17
11. Jain V, Kumar A, Sakhuja S, Thoduka N, Aggarwal R (2016) Supplier selection using fuzzy AHP and TOPSIS: a case study in the Indian automotive industry. *Neural Comput Appl*
12. Önder E, Taş N, Hepşen A (2013) Performance evaluation of Turkish banks using analytical hierarchy process and TOPSIS methods. *J Int Sci Publ: Econ Bus* 7(1):470–503
13. Mandic K, Delibasic B, Knezevic S, Benkovic S (2014) Analysis of the financial parameters of Serbian banks through the application of the fuzzy AHP and TOPSIS methods. *Econ Model* 43:30–47
14. Dehghan-Manshadi B, Mahmudi H, Abedian A, Mahmudi R (2007) A novel method for materials selection in mechanical design: Combination of non-linear normalization and a modified digital logic method. *Mater Des* 28(1):8–15
15. Saket S, Singh A, Khanduja D (2015) Fuzzy-VIKOR analysis for customer performance index of civil domestic airline industry in India. *Manage Sci Lett* 5:301–310

Performance Analysis of Free Air Cooling Conditioning Chamber (FACCC) to Develop Improved Cold Chain During Transportation of Agricultural Crops in India



Vardan Parashar, Abid Haleem and J. A. Usmani

Abstract Need to improve the shelf life of agricultural crops, during short transportation using low-cost technology. The objective of this paper is to develop a household technology using the concept of free air cooling conditioning chamber (FACCC). Observed that, after harvesting the fruits and vegetables are directly transported to market without having the recommended ambient condition, thereby losing potency and lower shelf life. Designed an experimental setup on the concept of 'free cooling technique, towards the storage and transportation (logistics) of the crops at the prudent temperature. Examined and analysed the result of FACCC model, to observe a drop in the cabin temperature. Results show a productive use in increasing the shelf life of the crop. Optimization helped to improve the cold chain performance of the crop, within a recommended temperature range of FACCC.

Keywords Agricultural crop · Free cooling technique · Cold chain · Improved shelf life · Temperature monitoring

1 Introduction

Agriculture crops are sent directly to the market after harvesting without maintaining their appropriate temperature conditions. As they are not adequately orientated and not stored at their predetermined temperature conditions, these crops lose their potency and even the shelf life. Some fruits, vegetables bear wide variations of temperature during the process from the initial to the final consumable stage. Necessitating, preserving all these crops in their fresh form towards maintaining their chemical, biochemical and physiological changes to an acceptable level of standard of product. Towards sustain of the shelf life and maintain the potency, we store crops at the desired temperature and relative humidity. The main reasons for an improper cold chain for these crops are the cost of operating the desired atmospheric conditions and a scarcity of trained human resources; thus, there is a utility of the low-cost alter-

V. Parashar (✉) · A. Haleem · J. A. Usmani
Jamia Millia Islamia, New Delhi, India
e-mail: vardan.parashar@gmail.com

© Springer Nature Singapore Pte Ltd. 2019
M. Kumar et al. (eds.), *Advances in Interdisciplinary Engineering*, Lecture Notes in Mechanical Engineering, https://doi.org/10.1007/978-981-13-6577-5_43

native refrigeration technique. This technology should consume less power, towards the maintenance of the temperature range and relative humidity and usable in rural part.

Shelf life and post-harvesting parameter in the cold chain and quality assurance with safety by monitoring, evaluating, recording and controlling parameter during the entire shelf life of the product, includes the post-processing phase as used by the final consumer [1–3]. The fundamental principle of cooling mechanism is evaporation, when water evaporates and releases energy from the porous material, thereby producing a desirable effect of cooling, thus increase in the rate of evaporation, results in higher cooling effect [4].

The preferable temperature for many vegetables/fruits ranges between 0 °C and 12 °C. The Zero energy cooling chamber is a specially designed chamber, where the said unit is kept, and low-cost brick can maintain an inside chamber temperature of 15–18 °C and respective relative humidity 95% when outside temperature more than 30 °C [5]. Lower temperature and higher humidity create the conditioner atmosphere inside the cooling chamber. Lowering of metabolic process happens at the attained ‘atmosphere’ enabling the maintenance of crops [6].

The most important phenomenon is to maintain the shelf life of agriculture crops through temperature stabilisation, individually as per the predefined temperature range for the different crops. The temperature will change as per the transportation depending on the vehicle itself as well as the time along with the variation of the temperature range and exploitation condition during the transport. During the research, initially, the outer and inner temperature of FACCC were considered as same and assumed the heat generation inside the FACCC as negligible. Transporting the agriculture crops is a big challenge apart from distribution of food and food production [7]. Transportation is also an essential factor in the cold chain for enhancing safety, improving the shelf life, as well as the temperature. Fresh vegetables and fruits are the food type most commonly spoiled where around 50% of fruits are spoiled uneaten after harvesting [8]. For rising product temperatures in subzero weather conditions, estimated the energy requirement at 2% of the total world energy consumption [9]. Literature [10] reported that 40% of all the crops have refrigeration requirements.

The primary advantage of cold chamber storage was the maintenance of fruit firmness by lowering the physiological loss in weight (PLW) and other metabolic processes [11]. Temperature has been pointed out as one of the most influential factors affecting the quality of chilled food [12]. For determining the improvement in the shelf life condition parameter and having the range for temperature achieved by the experiment, so we have to consider such parameters as an original load of orientation for carrying the crops during transport, the cooling efficiency of the unit and thermal insulation of body and ambient settings while operating the experiment. These factors have to consider for choosing a vehicle refrigeration unit

- The vehicle, cold storage unit, has sound insulation and a suitable capacity for storage.
- Should maintain the appropriate temperature according to the crops and had to store at the supporting temperature condition to keep the shelf life. Suggested a

combination of models of 'Food supply chain temperature monitoring' and 'shelf life prediction' towards the maintenance of the crop shelf life [13].

Developed a framework suitable for the following parameters such as to develop a sustainable cold chain for agriculture crops by free cooling based ventilation technology for enhances the shelf life of agriculture foods. Maintains the desired temperature for agriculture crops and improve the shelf life of the product, by producing the cooling effect from the free cooling technique. The primary benefit of the free cooling technology is that farmers and small business entrepreneurs can efficiently use this unit and that too during transportation. The setup is beneficial for users those who cannot afford the traditional cooling system.

The technique can also provide the effect of air conditioning is called free cooling with the help of circulating the coolant from a cold source and then removed energy from cooled space. Free cooling is a cost competitive approach to lowering the air temperature in a building or data centre by using chillers naturally by circulating cold air or water instead of the mechanical unit of refrigeration. An economical technique of using cooled external air temperatures for the chilling medium and used for air conditioning unit. The cooled water is either used directly or stored as per the need. When ambient temperatures are lower relative to indoor chamber temperatures, this system utilises cooled air of the atmosphere as a free cooling source. Free cooling is a process of the production of chilled water with the help of chillers and used where the less drop in the temperature, and thus reduces the temperature up to the sustainable condition. Free cooling is not entirely a free technique; the chillers are transferring the heat continuously.

2 Materials and Methods

This experiment was carried out in the workshop of a College of Dr. Abdul Kalam Technical University, India during April 2017. The setup unit is named FACCC and stationed at RDEC, Department of Mechanical Engineering, AKTU University.

2.1 Construction of FACCC

The small-sized FACCC unit maintains sustainable low temperature compared with an ambient parameter, provides approximately a temperature difference of 30–40 °C. Figure. 1 shows the conduct of the first trial in a complete random block (FACCC). The dimension of the block is 100 cm length, 50 cm height, and 50 cm width. In the design of the setup, the following components were assembled as a unit to prepare the complete open flow conditioning unit. A fan, A pump (as required power to pump water up to the height of top coil), Tube of Copper coil (2/6" outside diameter and

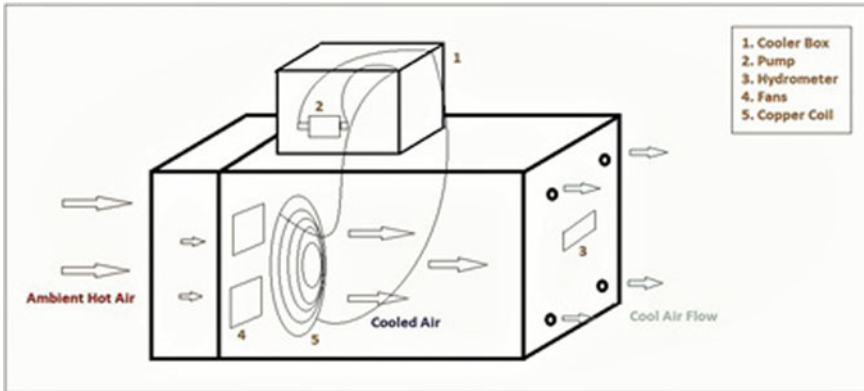


Fig. 1 Free air cooling conditioning chamber

20 feet long), Vinyl tubing (1/2" Inner Diameter tubing about 10 feet worth). These components are assembled by couplers and hose clamp to firm it.

2.2 Experimental Process

Free cooling can also provide the cooling effect so in FACCC system a pump is used to circulate a coolant that is solid ice (or chillier water) taken from a cold source. The chiller water distributes to the unit of FACCC that is an open flow chamber and acts as a heat sink also for the hot source removed from the cooled space. The conventional storage media is the copper coil having the cluster of small diameter tubes works as a heat exchanger. Cold water is circulating in the copper tubes, and the fan is used to flow the air through the unit of FACCC. So the temperature is maintained at lower than the ambient temperature and has the cooling effect which is suitable for increasing the shelf life. FACCC is also affected by some external parameter like solar radiation, excess humidity locations. The observed data was a sample of the temperature variation with time for the shading conditions and shown in Table 1. Table 2 is showing the temperature variation with time under direct sunlight. So by finding this data, we plot on a time-temperature scale, 30 points over a period of 4 hours.

2.3 Temperature Changes Inside the FACCC

Illustration 1:

The data is collected for the FACCC unit, under the shading surface to have the cooling effect by the use of chiller ice for 4 h time between 11 AM TO 3 PM as

Table 1 Temperature variation under shading surface

S. No.	Time (Ist)	Temperature measure (in degree celsius)	S. No.	Time (Ist)	Temperature measure (in degree celsius)
1	11.00	37.50	16	11.30	30.65
2	11.02	37.09	17	11.32	30.32
3	11.04	36.68	18	11.34	29.99
4	11.06	36.26	19	11.36	29.66
5	11.08	35.85	20	11.38	29.33
6	11.10	35.44	21	11.40	29.00
7	11.12	35.03	22	11.45	28.67
8	11.14	34.62	23	11.50	28.00
9	11.16	34.20	24	11.55	28.00
10	11.18	33.25	25	12.00	28.00
11	11.20	32.30	26	12.30	28.00
12	11.22	31.97	27	13.00	28.10
13	11.24	31.64	28	13.50	28.40
14	11.26	31.31	29	14.00	28.10
15	11.28	30.98	30	15.00	28.20

Table 2 Temperature variation under direct sunlight

S. No	Time (IST)	Temperature measure (in degree celsius)	S. No	Time (IST)	Temperature measure (in degree celsius)
1	11.00	38.80	16	11.30	32.80
2	11.02	38.34	17	11.32	32.20
3	11.04	37.89	18	11.34	31.80
4	11.06	37.43	19	11.36	31.30
5	11.08	36.97	20	11.38	31.00
6	11.10	36.52	21	11.40	30.80
7	11.12	36.06	22	11.45	30.70
8	11.14	35.60	23	11.50	30.80
9	11.16	35.25	24	11.55	30.80
10	11.18	34.90	25	12.00	30.90
11	11.20	34.55	26	12.30	30.90
12	11.22	34.20	27	13.00	30.80
13	11.24	33.85	28	13.50	31.00
14	11.26	33.50	29	14.00	31.10
15	11.28	33.15	30	15.00	30.80

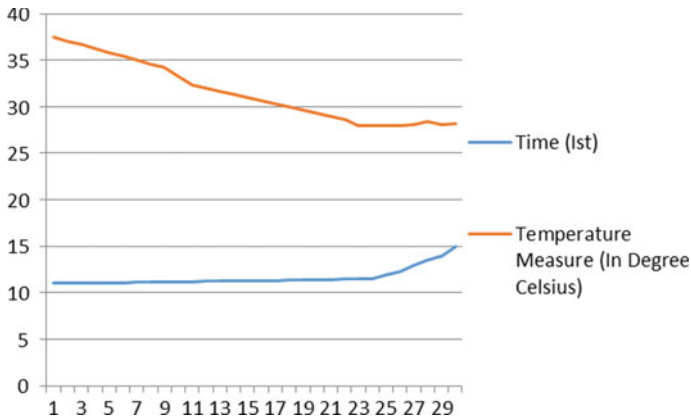


Fig. 2 Line diagram for temperature variation with time under shading condition

per Indian standard time and Table 1 shows the temperature drop. As we can see a significant temperature drop in first 30–40 min, then it will fluctuate up and down, also just because efficient heat rejection sink is not produced in the initial experiment. When the setup was slandered at that time, the ambient temperature was 37.5 °C, and maximum reduction in temperature measure is 9.5 °C during the experimental duration of 4 hours. Hence it can affect efficiently if some additional changes are made for desired output variables. This little bit temperature drop can be most useful to enhance the shelf life of agriculture crops like fruits and vegetables. Suitable application of the FACCC is for the crops having not so much high chill temperature, to sustain their original shelf life because just due to the high-temperature they are losing their original shelf life during transportation. So this FACCC unit can be helpful for maintaining their potency and improving the shelf life economically and efficiently (Figs. 2 and 3).

Illustration 2

Generally, agriculture crops after harvesting are transported to the final customer in trucks and vans, in the process, they have to bear high-temperature variation and lose their original shelf life. So during the transportation under direct sunlight, an experiment was conducted to read the temperature drop during a 4 h time duration, and maximum temperature drop is read 8 °C. Initial reading of thermometer under the direct sunlight conditions was 38.8 °C, and this will reduce to 30.8 °C (Figs. 4 and 5).

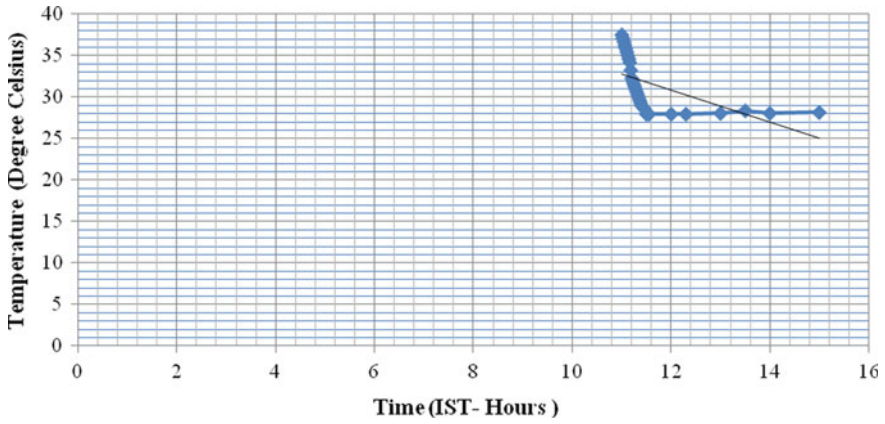


Fig. 3 Variation of temperature concerning the time at X-Y coordinate

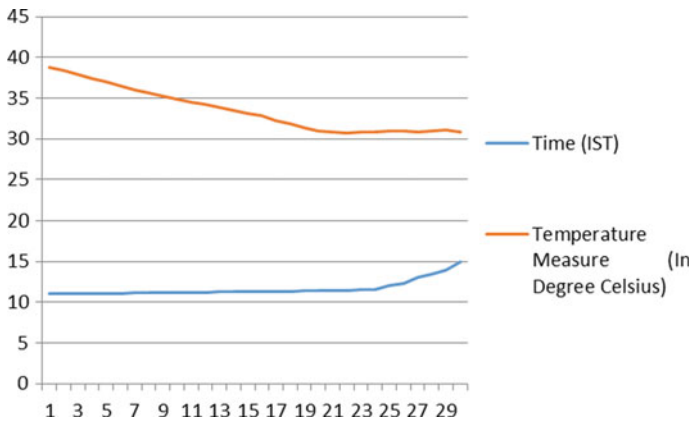


Fig. 4 Line diagram of temperature variation with time under direct sunlight

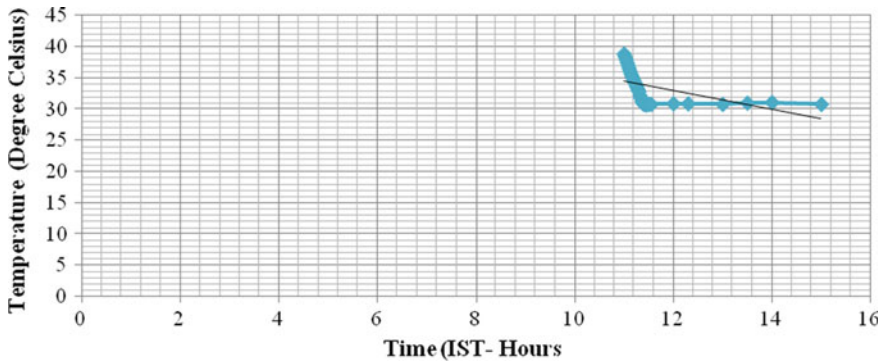


Fig. 5 Variation of temperature with respect to time

3 Conclusion

The free cooling technique as used inside the FACCC unit has a complex system. Moreover, depending on those characteristics, cooling varies with time and is also affected by the surrounding environmental conditions such as air velocity, humidity, outside air temperature, and solar radiations, these all affect the heat transfer rate of FACCC. Under these, all variable conditions such as heat drop are up to 8 °C–9.5 °C under shading and direct sunlight condition. So it will affect the shelf life of crops like fruits and vegetable and those products which do not require to be stored in such a high cold environment as mango, papaya, potato, etc. In future this FACCC can be designed and developed with better chiller medium; PCM-based evaporative technique, cooling by Peltier-effect, to maintain the cooling effect economically and not so costly as compared to traditional refrigeration units.

References

1. Koutsoumanis K, Giannakourou MC, Taoukis PS, Nychas GJE (2002) Application of shelf life decision system (SLDS) to marine cultured fish quality. *Int J Food Microbiol* 73 (2–3):375–382
2. Koutsoumanis K, Taoukis PS, Nychas GJE (2005) Development of a safety monitoring and assurance system (SMAS) for chilled food products. *Int J Food Microbiol* 100:253–260
3. Kennedy J, Jackson V, Blair IS, McDowell DA, Cowan C, Bolton DJ (2005) Food safety knowledge of consumers and the microbiological and temperature status of their refrigerators. *J Food Prot* 68(7):1421–1430
4. (Report online sources) Evaporative cooling, practical action, The Schumacher centre for technology and development, Bourton Hall, Bourton-on-Dunsmore, Rugby, Warwickshire CV239QZ, UK., 2011, pp 1–5. Available: <http://www.fao.org/climatechange/17850-0c63507f250b5a65147b7364492c4144d.pdf>
5. USAID (2009) Empowering agriculture: energy options for horticulture USAID economic growth and trade (Report style), USAID Office of infrastructure and engineering, pp. 1–79. Available: http://pdf.usaid.gov/pdf_docs/PNADO634.pdf
6. Quddus MA, Mia MMU 2010 Agricultural research priority: Vision-2030 and beyond (Report style), Bangladesh agricultural research council, pp 1–48
7. Daou K, Wang RZ, Xia ZZ (2006) Desiccant cooling air conditioning: a review. *Renew Sustain Energy Rev* 10(2):55–77
8. Hundy GF, Trott AR, Welch TC (2016) Chapter 17—The Cold Chain—Transport, Storage, Retail. Refrigeration, air conditioning and heat pumps (Fifth Edition). Butterworth-Heinemann
9. Lal Basediya A, Samuel D, Beera V (2013) Evaporative cooling system for storage of fruits and vegetables—a review. *J Food Sci Technol* 50:429–442
10. Meneghetti A, Monti L (2015) Greening the food supply chain: an optimization model for sustainable design of refrigerated automated warehouses. *Int J Prod Res* 53:6567–6587
11. Roy SK, Pal RK (1991) A low cost zero energy cool chamber for short-term storage of mango. *Acta Hort* 291:519–524
12. Jol S, Kassianenko A, Wszol K, Oggel J (2006) Issues in time and temperature abuse of refrigerated foods. *Food Saf* 11(6):30–35
13. Kuo J-C, Chen M-C (2010) Developing an advanced Multi-temperature joint distribution system. *Food Control* 21(4):559–566

Nanoparticles Reinforcement Effect on the MMC's Characteristics



Siddhartha Kosti, Jitender Kundu and Chandra S. Malvi

Abstract Nanoparticles reinforcement in the base material is called MMC's (metal matrix composites) and they possess enriched mechanical properties compared to the base material. Present work models the effect of nanoparticles reinforcement on the MMC's characteristics like mechanical properties and time-temperature history curve during solidification. Materials considered in the present work are SiC (silicon carbide), Al₂O₃ (aluminum oxide) B₄C (boron carbide) and Al6061. Thermal conductivity, specific heat and density are analyzed for nanoparticles weight percentage reinforcement varying from 0 to 30 while time-temperature history curve is analyzed by modeling the well-known energy equation using finite different (FD) technique. Individual and collective influence of the reinforcement on the mechanical properties and time-temperature history curve is also analyzed. The results from the present work are validated with the experimental results and found in good agreement. Results reveal that SiC nanoparticle gives the steeper time-temperature history curve compared to the Al₂O₃ and B₄C nanoparticles for same reinforcement. Results also reveal that cumulative reinforcement shows less steep time-temperature history curve compared to the individual reinforcement.

Keywords Mathematical modeling · Nanoparticles · Nano-manufacturing

List of Abbreviation

MMC's Metal matrix composites

CFL Courant–Friedrichs–Lewy

S. Kosti (✉)

Department of Mechanical Engineering, Rajkiya Engineering College, Banda, Atarra, Uttar Pradesh, India

e-mail: siddharth.kosti@gmail.com

J. Kundu

Department of Mechanical Engineering, Jorhat Engineering College, Jorhat, Assam, India

C. S. Malvi

Department of Mechanical Engineering, Madhav Institute of Technology and Science, Gwalior, Madhya Pradesh, India

© Springer Nature Singapore Pte Ltd. 2019

M. Kumar et al. (eds.), *Advances in Interdisciplinary Engineering*, Lecture Notes in Mechanical Engineering, https://doi.org/10.1007/978-981-13-6577-5_44

2D	Two-dimensional
FD	Finite difference
FEA	Finite element analysis

1 Introduction

Nanoparticles are smart and possess superior properties compared to the base materials. Their reinforcement in the base materials enriched the mechanical properties. Different nanoparticles give different mechanical properties based on the amount added in the base material. Larger wt% addition creates the problem of agglomeration and clogging. An efficient plan can give very good results. A lot of research work is going on this field. Many researchers like Li M et al. [8], Shorowordi et al. [19] and Cetin and Kalkanli [2], conduct microstructure studies of nanoparticles. They used a mathematical technique to conduct the microstructure study of nanoparticles and find good agreement. Some researcher (Venkatesan et al. [22], Jagadeesh et al. [4] Rajeshwari and Dey [13], Zhang and Nastac [24], Hohe et al. [3]) used FEA (Finite element analysis) technique to study the behavior of nanoparticles.

Lelito et al. [7], Barekar et al. [1], Saheb [16], Weiss et al. [23], Shabani and Mazahery [17, 18] studied the MMC's to analyze different nanoparticles behaviors and properties. Other researcher conducted the experimental study [9, 10, 13, 14, 20, 21]. Rahman and Rashed [12], Radhika et al. [11] and Zhang et al. [25] also conducted experimental analysis to examine the nanoparticles performance.

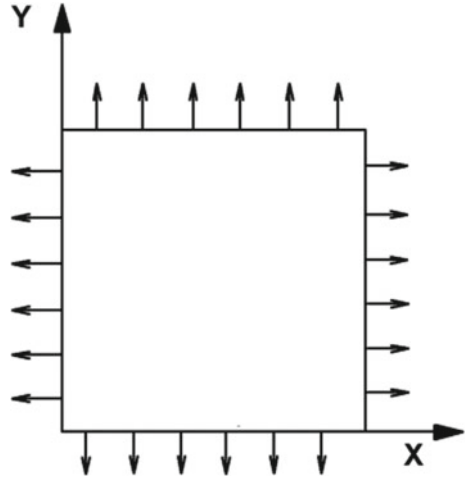
Above literature reveals that nanoparticle reinforcement is an area where a large amount of research is going on. Literature also reveals that most of the studies are being conducted using experimentation or commercial available software, and very few studies have been devoted to study the time-temperature history curve using mathematical modeling. Present work discusses the modeling of the time-temperature history curve using finite difference (FD) technique. FD technique advantage over FEA is that it works on the Taylor series expansion and is very easy to develop.

2 Mathematical Formulation

2.1 Governing Equation

Energy equation governs the present problem as no change in mass and momentum occurs during solidification. The above equation is taken from Kosti and Pathak [5, 6].

Fig. 1 2D geometry



$$\frac{\partial T}{\partial t} = \alpha \left(\frac{\partial^2 T}{\partial x^2} + \frac{\partial^2 T}{\partial y^2} \right) \tag{1}$$

where $\alpha = k/\rho C_p$ is thermal diffusivity in m^2/s , k is thermal conductivity in $W/m-K$, ρ is density in kg/m^3 , C_p is specific heat in $J/kg K$, T is the temperature in Kelvin (K), t is the time in seconds.

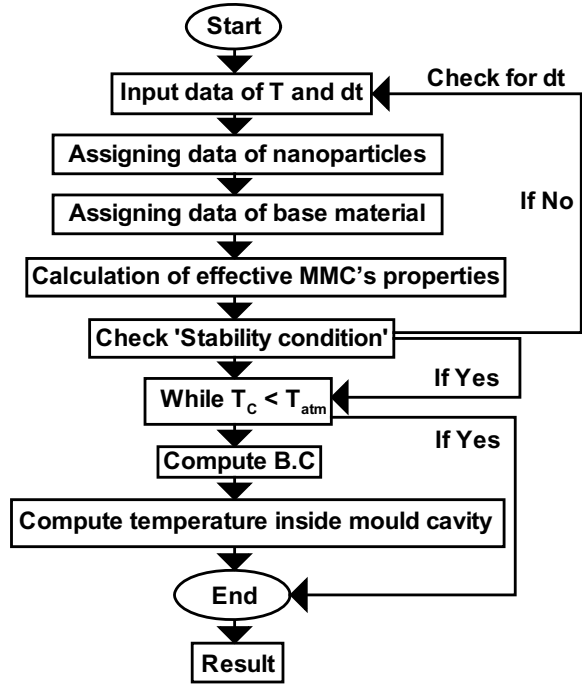
2.2 Geometry

Figure 1 shows the schematic of the two-dimensional assembly. Convective boundary conditions are considered at the walls, which mean that heat is transferred to the atmosphere by convection. A symmetric geometry is considered in the present work. Arrow direction represents the heat is losing to the atmosphere from the walls of the casting.

2.3 FD (Finite Difference) Technique

Finite difference technique is based on the Taylor series expansion that is used to calculate the dependent variable value at the nodes. Location of these nodes may be in the forward direction or in backward direction. FD technique converts the partial differential equation into algebraic form, and this method is called discretization. Equation 2 below shows the discretization of Eq. 1 into algebraic form

Fig. 2 Flow chart



$$T_{t+1,i,j} = T_{t,i,j} + \alpha \Delta t \left(\frac{T_{t,i+1,j} + T_{t,i-1,j} - 2T_{t,i,j}}{(\Delta x)^2} + \frac{T_{t,i,j+1} + T_{t,i,j-1} - 2T_{t,i,j}}{(\Delta y)^2} \right) \tag{2}$$

2.4 Stability Analysis

It is necessary to check whether the technique used in the present work is stable or not. For verification of this, a stability test is conducted using Courant–Friedrichs–Lewy (CFL) condition shown in Eq. 3. CFL condition helps in the selection of time-step size. Figure 2 shows the flow chart of the code developed in the present work.

$$\alpha \times \left(\frac{dt}{(dx)^2} + \frac{dt}{(dy)^2} \right) \leq \frac{1}{2} \tag{3}$$

Table 1 Thermal properties of base material and nanoparticles

Material	Thermal conductivity (W/m K)	Specific heat (J/kg K)	Density (kg/m ³)
Al6061	167	896	2700
SiC	100	1300	3200
Al ₂ O ₃	36	773	3880
B ₄ C	42	1288	2550

2.5 Initial and Boundary Conditions

It is considered that during the start of solidification process all the point are at molten metal temperature (750 °C). Atmospheric temperature considered is around 30 °C.

$$\begin{aligned} \text{At } x = 0, q'' &= k \frac{\partial T}{\partial x} = h_f(T - T_\infty) & \text{At } x = L, q'' &= k \frac{\partial T}{\partial x} = -h_f(T - T_\infty) \\ \text{At } y = 0, q'' &= k \frac{\partial T}{\partial y} = h_f(T - T_\infty) & \text{At } y = H, q'' &= k \frac{\partial T}{\partial y} = -h_f(T - T_\infty) \end{aligned}$$

where q'' = heat flux, h_f = heat transfer coefficient and T_∞ = Ambient temperature.

3 Materials

Materials considered in the present work are Al6061, Al₂O₃ (Aluminum oxide), SiC (Silicon carbide) and B₄C (Boron carbide). Table 1 shows the properties of these materials considered in the present work. Effective properties of the MMC's are calculated using physical mixture rule (Rohtagi).

$$\varnothing_{\text{eff}} = \varnothing_{\text{bm}}(1 - \lambda) + \varnothing_{\text{np}}\lambda$$

where \varnothing and λ are dependent variable and nanoparticles wt% reinforced. Subscript 'eff', 'bm' and 'np' represent the effective property of MMC's, base material and nanoparticles respectively.

4 Validation

Code developed in the present work is validated with the experimental work of Ramesh et al. [14] for the same physical scenario and is shown in Fig. 3. Deviation in the results may be due to the effect of surrounding conditions, as it is impossible to incorporate the effect of all physical variables of the experiments in mathematical modeling. Grid validation is also conducted for different grid sizes. Small grid size

Fig. 3 Experimental validation

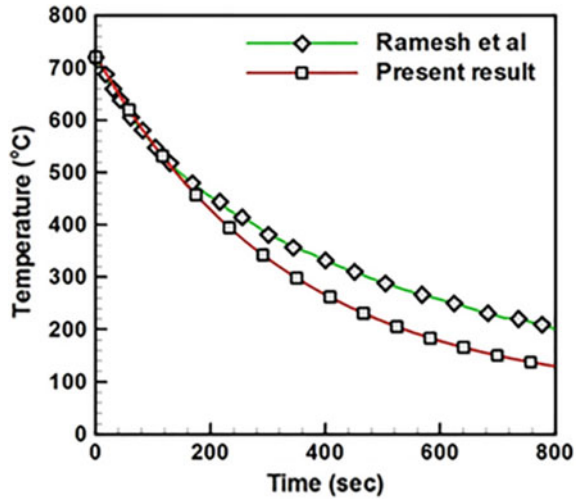
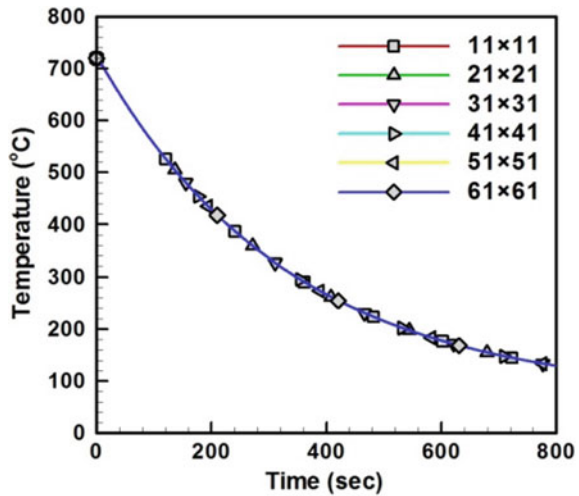


Fig. 4 Grid validation



results in coarse meshing while larger grid-size results in fine meshing. Fine meshing takes larger computation time compared to coarse meshing. Grid validation test reveals that grid size does not affect the time-temperature history curve. So for saving the computation time small grid size is selected for analysis (Figs. 4, 5, 6, 7, 8, and 9).

Fig. 5 Time-temperature history curves for Al₂O₃ reinforcement

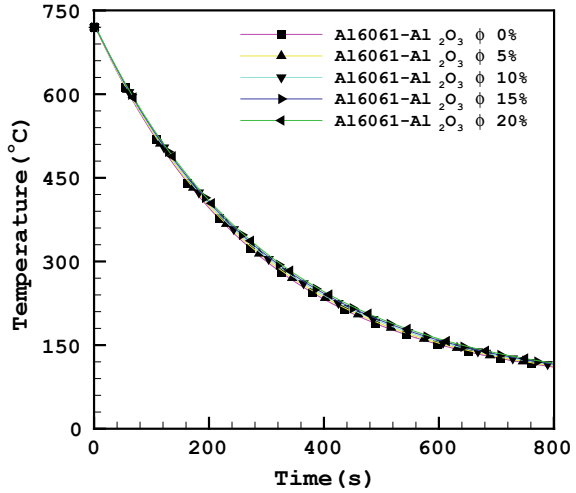
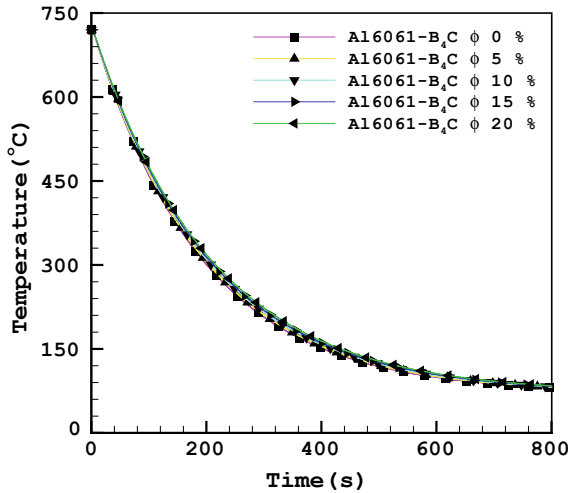


Fig. 6 Time-temperature history curves for B₄C reinforcement



5 Result and Discussion

Figures 5, 6 and 7 shows the time-temperature history curve for Al₂O₃, B₄C, and SiC nanoparticle reinforcement in the Al6061. Reinforcement of the nanoparticle weight percentage is varied from 0 to 20. From the figures it can be noticed that reinforcement of Al₂O₃ and B₄C nanoparticle reinforcement does not affect the time-temperature history curve of MMC's, this can be because of the very low thermal conductivity values of Al₂O₃ and B₄C compared to the Al6061. While reinforcement of SiC nanoparticle decreases the time-temperature history curve of MMC's, this decrement

Fig. 7 Time-temperature history curve for SiC reinforcement

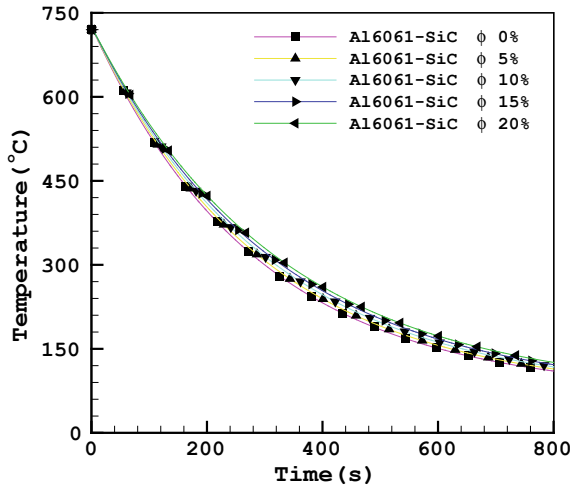
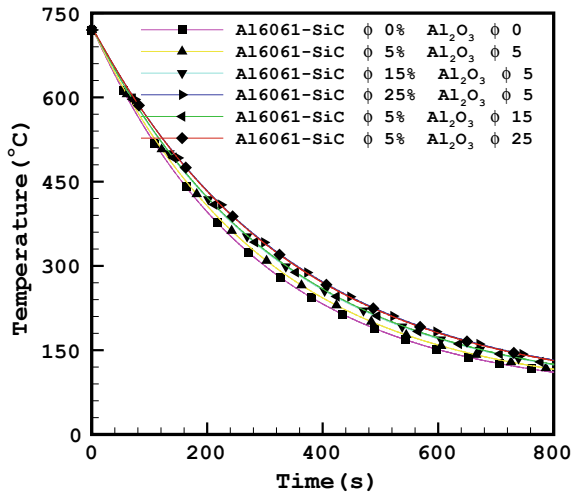


Fig. 8 Cumulative influence of nanoparticle reinforcement



indicates the decrement in solidification rate of the MMC's compared to the base material.

Table 2 represents thermal properties variation of MMC's for the cumulative addition of SiC and Al₂O₃ in the Al6061. Mixture rule is considered for the calculation of effective thermal properties of MMC's. Maximum nanoparticle wt% considered for the cumulative effect of reinforcement is 30%.

Figures 8 and 9 shows cumulative influence of the nanoparticle reinforcement on the time-temperature history curve. From the figure, it can be noticed that higher the percentage of reinforcement, higher the decrement in the time-temperature history curve. This is due to the less thermal conductivity which reduces the heat transfer

Fig. 9 Effect of nanoparticle reinforcement type on the time-temperature history curve

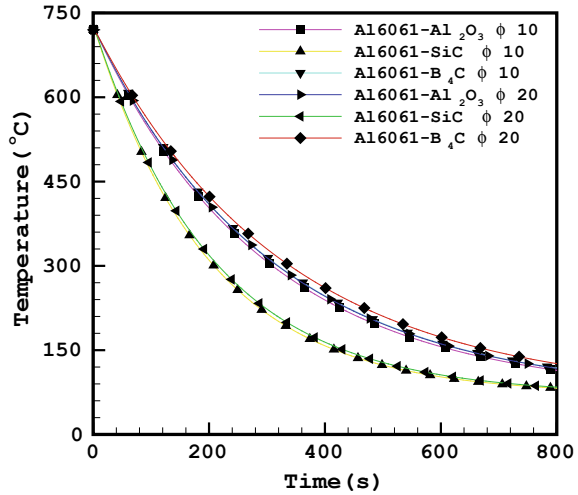


Table 2 Thermal properties of Al6061-SiC-Al₂O₃ MMC's

Wt%			Al6061-SiC-Al ₂ O ₃		
Al6061	SiC	Al ₂ O ₃	C _p (J/kg K)	ρ (kg/m ³)	k (W/m K)
Mixture					
100.00	0.00	0.00	896.00	2700.00	167.00
90.00	5.00	5.00	910.05	2784.00	157.10
80.00	15.00	5.00	950.45	2834.00	150.40
70.00	25.00	5.00	990.85	2884.00	143.70
80.00	5.00	15.00	897.75	3020.00	144.00
70.00	5.00	25.00	885.45	3200.00	130.90

rate. From Fig. 9 it can be noticed that the lowest time-temperature history curve is for SiC reinforcement in the base material. This indicates the steeper time-temperature history curve.

6 Conclusion

The present work deals with the modeling of MMC's time-temperature history curve for three different nanoparticles reinforcement on Al6061. The weight percentage of the reinforcement is varied from 0 to 30. Mixture rule to calculate the effective properties is utilized. From the result, it is concluded that SiC nanoparticle reinforcement gives the steeper time-temperature history curve for same reinforcement weight percentage addition compared to the Al₂O₃ and B₄C nanoparticles. From the result, it is observed that cumulative reinforcement shows less steep time-temperature history curve compared to the individual reinforcement.

References

1. Barekar N, Tzamtzis S, Dhindaw BK, Patel J, HariBabu N, Fan Z (2009) Processing of aluminum-graphite particulate metal matrix composites by advanced shear technology. *J Mater Eng Perform* 18(9):1230–1240
2. Cetin A, Kalkanli A (2009) Numerical simulation of solidification kinetics in A356/SiCp composites for assessment of as-cast particle distribution. *J Mater Process Technol* 209:4795–4801
3. Hohe J, Fliegenger S, Findeisen C, Reiser J, Widak V, Rieth M (2016) Numerical exploration into the potential of tungsten reinforced CuCrZr matrix composites. *J Nucl Mater* 470:13–29
4. Jagadeesh SK, Ramesh CS, Mallikarjuna JM, Keshavamurthy R (2010) Prediction of cooling curves during solidification of Al 6061–SiCp based metal matrix composites using finite element analysis. *J Mater Process Technol* 210:618–623
5. Kosti S, Pathak P (2018) Genetic algorithm based finite difference simulation of solidification process for MMC's. *Mater Today Proc* 5:8271–8291
6. Kosti S, Malvi CS (2018) Cumulative influence of nanoparticles on MMCs' time-temperature history curve. *Nanomaterials Energy* 7(1):1–10
7. Lelito J, Zak PL, Shirzadi AA, Greer AL, Krajewski WK, Suchy JS, Haberl K, Schumacher P (2012) Effect of SiC reinforcement particles on the grain density in a magnesium-based metal-matrix composite: modelling and experiment. *Acta Materialia* 60:2950–2958
8. Li M, Ghosh S, Richmond O, Weiland H and Rouns TN (1999) Three dimensional characterizations and modelling of particle reinforced metal matrix composites: Part I Quantitative description of microstructural morphology. *Mater Sci Eng A* 265:153–173
9. Muthazhagan C, Babu AG, Bhaskar GB and Rajkumar K (2013) Influence of graphite reinforcement on mechanical properties of aluminium-boron carbide composites. *Adv Mater Res* 845:398–402
10. Nagaral M, Bharath V, Auradi V (2013) Effect of Al₂O₃ particles on mechanical and wear properties of 6061Al alloy metal matrix composites. *J Mater Sci Eng* 2(1):1–4
11. Radhika N, Subramanian R, Prasat SV (2011) Tribological behaviour of aluminium/alumina/graphite hybrid metal matrix composite using Taguchi's techniques. *J Min Mater Charact Eng* 10(5):427–443
12. Rahman MH, Rashed HMMA (2014) Characterization of silicon carbide reinforced aluminium matrix composites. *Procedia Eng* 90:103–109
13. Rajeshwari P, Dey TK (2016) Finite element modelling and experimental investigation on effective thermal conductivity of AlN (nano) particles reinforced HDPE polymer nanocomposites. *Thermochim Acta* 638:103–112
14. Ramesh CS, Jagadeesh SK, Keshavamurthy R (2011) Solidification studies on sand cast Al 6061–SiCp composites. *J Alloys Compd* 509S:S371–S374
15. Rohatagi PK (1993) Metal matrix composites. *Def Sci J* 43(4):323–349
16. Saheb DA (2011) Aluminium silicon carbide and aluminium graphite particulate composites. *ARNP J Eng Appl Sci* 6(10):41–46
17. Shabani MO, Mazahery A (2012) Artificial intelligence in numerical modelling of nano sized ceramic particulates reinforced metal matrix composites. *Appl Math Model* 36:5455–5465
18. Shabani MO, Mazahery A (2013) Application of GA to optimize the process conditions of Al matrix nano-composites. *Composites Part B: Eng* 45:185–191
19. Shorowordi KM, Laoui T, Haseeb ASMA, Celis JP, Froyen L (2003) Microstructure and interface characteristics of B₄C, SiC and Al₂O₃ reinforced Al matrix composites: a comparative study. *J Mater Process Tech* 142:738–743
20. Sudindra S, Kumar AC (2013) Studies on Al6061/Al₂O₃ and graphite hybrid metal matrix composites. *Inter J Metall Mater Sci Eng* 3(3):35–42
21. Tao Y, Yeckel A, Derby JJ (2016) Steady-state and dynamic models for particle engulfment during solidification. *J Comput Phys* 315:238–263
22. Venkatesan A, Gopinath VM, Rajadurai A (2005) Simulation of casting solidification and its grain structure prediction using FEM. *J Mater Process Tech* 168:10–15

23. Weiss D, Grassi J, Schultz B, Rohatagi P (2011) Ablation of hybrid metal matrix composites. American foundry society proceeding, pp 1–7
24. Zhang D, Nastac L (2014) Numerical modelling of the dispersion of ceramic nano-particles during ultrasonic processing of aluminium-based nanocomposites. *J Mater Res Tech* 3(4):296–302
25. Zhang P, Xiao X, Ma ZW (2016) A review of the composite phase change materials: fabrication, characterization, mathematical modelling and application to performance enhancement. *Appl Energy* 165:472–510

Nonlinear Finite Element Analysis of a Gecko Spatula Adhesion on a Rigid Substrate



Saipraneeth Gouravaraju and Sachin S. Gautam

Abstract Geckos utilize the fibrillar structures on their feet for generating strong adhesive forces as well as for rapid locomotion on a variety of surfaces. Each toe pad of gecko foot contains arrays of fine hair-like structures called setae, which at their tips, further branch into hundreds of nanoscale spatula-shaped structures. These spatulae adhere to substrates through van der Waals interactions. In the present work, numerical simulation of the adhesion mechanism of a gecko spatula on a rigid substrate is carried out using a two-dimensional finite element model. To account for the geometrical and material nonlinearities in the interaction between the spatula and substrate, a nonlinear computational contact formulation is employed. For the material modelling of the spatula, a Neo-Hookean hyperelastic model is used under the plane strain assumption. The van der Waals adhesion between the bodies is described using the Lennard-Jones potential. The spatula is gradually peeled off from the substrate by applying rotation and then a vertical pull. The variation in pull-off forces with the angle from which it is peeled off is studied. It has been observed that the pull-off force decreases with increasing peeling angle and has the lowest value at $\theta = 90^\circ$ and is equal to 4.82 nN. It has also been found that the pull-off forces increase with an increase in adhesion strength (or range of adhesion) or decrease in stiffness (or spatula size).

Keywords Gecko adhesion · Finite element analysis · Computational contact mechanics

1 Introduction

Geckos can adhere to and run on a variety of surfaces by taking advantage of the hierarchical structure on their feet. Each toe on a gecko foot has rows of fine hairs called setae. Each seta on a Tokay gecko is 30–130 μm long and 5 μm in diameter

S. Gouravaraju · S. S. Gautam (✉)
Indian Institute of Technology Guwahati, Guwahati 781039, India
e-mail: ssg@iitg.ernet.in

[1]. Each seta, at its tip, further branches into hundreds of nanometer-sized spatula-type structures. Many studies, analytical, experimental, and numerical have been performed to better understand different aspects of gecko adhesion [2, 3].

Autumn et al. [1] made the first direct measurements of the adhesive force of a single gecko foot hair. They measured a maximum frictional force of $200 \mu\text{N}$ per seta. Through experiments, they found that the gecko adhesion is due to the molecular van der Waals forces [4]. The measurements of Huber et al. [5] showed that humidity significantly affects the gecko adhesion behaviour on the nanoscale level. Gao et al. [6] used finite element analysis with cohesive zone models to analyse a single gecko seta adhesion. It was observed that the seta detached from the substrate when pulled at angles $>30^\circ$. Tian et al. [7] proposed a theoretical model based on the tape peeling model for estimating the adhesion and friction forces between a single spatula and a substrate. It was observed that the lateral frictional forces and normal adhesion forces of a seta change more than three orders of magnitude with different peeling angles. Chen et al. [8] modelled the spatula as an elastic tape and showed that the peeling force of the spatula varies significantly with the peeling angle. Peng et al. [9] studied the influence of peeling angle, Young's modulus, and spatula thickness on the peel zone length and the peeling force.

In 2007 Sauer and Li [10] developed a computational quasi-continua model for nanoscale adhesion. The contact model is derived from coarse-graining of molecular dynamic simulations of individual atoms and is called Coarse-Grained Contact Model (CGCM). Sauer [11] using this method, presented a mechanical seta model that uses multi-scale framework combining three different models: an overall seta model, a spatula submodel and a molecular interaction submodel. The model was later improved by Sauer and Holl [12], in which the authors presented a detailed three-dimensional (3D) parametric model. They examined the effects of variation in the spatula shape, stiffness, strength, and range of adhesion on the pull-off behaviour. Gautam and Sauer [13] presented a new time integration scheme for solving the dynamic adhesion peeling problem. They applied the methodology to peeling of gecko spatula.

The analytical models in the literature although help in understanding the behaviour of gecko adhesion, they use approximations to arrive at the calculations of quantities like peeling forces and hence do not provide accurate predictions. On the other hand, the full-scale 3D computational model by Sauer and Holl [12] although provides great insights into peeling behaviour, is computationally expensive. Hence, in the current contribution the simplicity of analytical models in representing the spatula by a thin strip and the merit of a computational model in accurately capturing the adhesive forces are combined to analyse the adhesion characteristics of a gecko spatula on a flat, smooth, rigid substrate.

2 Formulation of the Adhesive Contact

The computational formulation within the framework of continuum mechanics to describe the adhesive contact between two bodies is presented in this section. This formulation is based on the CGC model proposed by Sauer and Li [10]. According to this model, the weak form of the governing equation of motion of dynamic adhesive contact system involving two bodies $B_k (k = 1, 2)$ in the current configuration is given as

$$\sum_{k=1}^2 \left[\int_{\Omega_k} \delta \boldsymbol{\varphi}_k \cdot \rho_k \ddot{\mathbf{u}}_k \, dv_k + \int_{\Omega_k} \text{grad}(\delta \boldsymbol{\varphi}_k) : \boldsymbol{\sigma}_k \, dv_k - \int_{\partial_c \Omega_k} \delta \boldsymbol{\varphi}_k \cdot \mathbf{t}_{c,k} \, da_k - \delta \Pi_{\text{ext},k} \right] = 0 \tag{1}$$

where $\delta \Pi_{\text{ext},k}$ represents the external forces on the c in the current work. The above equation holds true $\forall \boldsymbol{\varphi}_k \in U_k$ and $\forall \delta \boldsymbol{\varphi}_k \in V_k$. Here, U_k and V_k are the space of kinematically admissible deformation field $\boldsymbol{\varphi}$ and the space of its corresponding variations $\delta \boldsymbol{\varphi}$, respectively. Here, $\boldsymbol{\varphi}$ is defined as the motion mapping any arbitrary points \mathbf{X}_k in the reference configuration Ω_{0k} of body B_k to the current locations $\mathbf{x}_k \in \Omega_k$ and is given as: $\mathbf{x}_k = \boldsymbol{\varphi}(\mathbf{X}_k, t)$. Here, dv_k and da_k represent the volume and area differentials in current configuration.

The first term in Eq. (1) denotes the inertial contribution with $\ddot{\mathbf{u}}_k$ and ρ_k representing the acceleration and mass density of the system. The second term denotes the contribution of the internal virtual work of the Cauchy stress tensor $\boldsymbol{\sigma}_k$. In this work, a nonlinear Neo-Hookean material is considered for which $\boldsymbol{\sigma}$ is given as [14]

$$\boldsymbol{\sigma} = \frac{\lambda}{J} (\ln J) \mathbf{I} + \frac{\mu}{J} (\mathbf{F}\mathbf{F}^T - \mathbf{I}) \tag{2}$$

where $\mathbf{F} = \text{Grad}(\boldsymbol{\varphi})$ is a deformation gradient taken with respect to reference configuration corresponding to the motion mapping $\boldsymbol{\varphi}$. μ and λ are the Lamé constants, and $J = \det(\mathbf{F})$. The third term in Eq. (1) corresponds to the contribution due to the adhesion potential between the two bodies. Here, this adhesion is assumed to be originated from the van der Waals interactions between the molecules of the interacting surfaces. It is described using Lennard-Jones potential. In general, for any two particles separated by a distance r_s , the Lennard-Jones potential Φ_l is given as [15].

$$\Phi_l(r_s) := \varepsilon \left[\left(\frac{r_0}{r_s} \right)^{12} - 2 \left(\frac{r_0}{r_s} \right)^6 \right] \tag{3}$$

where ε and r_0 are the energy and length scales, respectively. Here, the first term in Eq. (3) represents the repelling part and has a large contribution at small distances and the second term is the attractive part that is prominent for large distances. Then the contact traction $\mathbf{t}_{c,k}$ can be obtained from the variation of the contact potential as (see [10] for a detailed derivation):

$$\mathbf{t}_{c,k} = \frac{A_H}{2\pi r_0^3 J_k J_l} \left[\frac{f_1 \left(\frac{r_0}{r_s}\right)^9}{45} - \frac{f_2 \left(\frac{r_0}{r_s}\right)^3}{3} \right] \mathbf{n}_p \tag{4}$$

where A_H denotes the Hamaker’s constant, f_1 and f_2 are the curvature-dependent parameters of the interacting body. Also J_k and J_l ($k \neq l$) represent the Jacobian of the neighbouring bodies. Here r_s is defined as the minimum distance between the neighbouring bodies and is defined as

$$r_s(\mathbf{x}_k) = (\mathbf{x}_k - \mathbf{x}_p) \cdot \mathbf{n}_p \tag{5}$$

where $\mathbf{x}_p \in \partial\Omega_l$, ($l \neq k$) and \mathbf{n}_p are the projection point and the normal vector over $\partial\Omega_l$, ($l \neq k$), which are computed by the closest point projection of $\mathbf{x}_k \in \partial\Omega_k$.

In CGC model, Sauer and Li [16] defined the following two material parameters (for each body in the system) that govern the weak form in Eq. (1) which are obtained by normalizing it:

$$\gamma_W = \frac{W_0}{w_0}, \gamma_L = \frac{R_0}{r_0} \tag{6}$$

Here, the first term γ_W is the ratio of two energy densities W_0 and w_0 which represent elastic deformation and adhesion, respectively. These densities are defined as

$$W_0 = E, w_0 = \frac{A_H}{2\pi^2 r_0^3} \tag{7}$$

where E is the reference Young’s Modulus chosen for the system. The second term in Eq. (6) γ_L is the ratio of global length scale R_0 used to normalize the geometry and the length scale r_0 used to define the adhesion potential Φ_l . From the definitions, it can be seen that, γ_W characterizes the strength of adhesion with respect to the strip stiffness whereas, γ_L characterizes the overall size of the geometry with respect to the range of adhesion.

The weak form given in Eq. (1) is then discretized using finite element method for which each body B_k is discretized into number of volume and surface elements containing n_{no} nodes. The displacement field and its variation $\delta\boldsymbol{\varphi}$ in each element is then approximated by interpolating functions as

$$\mathbf{u}(\mathbf{x}) \approx \mathbf{N}_e(\mathbf{x})\mathbf{u}^e, \delta\boldsymbol{\varphi}(\mathbf{x}) \approx \mathbf{N}_e(\mathbf{x})\mathbf{v}^e \tag{8}$$

where \mathbf{u}^e and \mathbf{v}^e are the nodal displacement and variations in element e and the matrix N_e is a matrix formed by n_{no} of shape functions the element and is given as

$$N = [N_1\mathbf{I} \quad N_2\mathbf{I} \quad \dots \quad N_{n_{no}}\mathbf{I}] \tag{9}$$

where $n_{no} = n_{ve}$ and $n_{no} = n_{se}$ for a given volume element and a surface element, respectively. The weak form in Eq. (1) can then be rewritten, using the relations in Eq. (8) and performing an assembly over all the volume and surface elements, as

$$\mathbf{v}^T [\mathbf{M}\ddot{\mathbf{u}} + \mathbf{f}_{int} + \mathbf{f}_C - \mathbf{f}_{ext}] = 0, \quad \forall \mathbf{v} \in V_k. \tag{10}$$

where \mathbf{M} is the mass matrix of the discretized system and \mathbf{f}_{int} , \mathbf{f}_C , and \mathbf{f}_{ext} denote the global nodal force vectors. As mentioned before, in the current paper $\mathbf{f}_{ext} = 0$.

To capture the highly nonlinear nature of the van der Waals forces [as described by Eq. (4)] using finite element analysis, in this work surface enrichment technique proposed by Sauer [17] is employed. The contact surface is enriched using a fourth-order Lagrangian polynomial and is denoted as Q1C4 whereas, the bulk of the domain is discretized using the standard four-noded quadrilateral elements denoted as Q1C1.

Since the variation of \mathbf{v} are arbitrary, the governing weak form of the equation of motion at time $t = t_{n+1}$ Eq. (10) is written as

$$\mathbf{M}\ddot{\mathbf{u}}^{n+1} + \mathbf{f}_{int}^{n+1} + \mathbf{f}_C^{n+1} - \mathbf{f}_{ext}^{n+1} = \mathbf{0} \tag{11}$$

For the given displacement \mathbf{u}^n , velocity $\dot{\mathbf{u}}^n$ and acceleration $\ddot{\mathbf{u}}^n$ at time $t = t_n$, the objective is to determine the \mathbf{u}^{n+1} , $\dot{\mathbf{u}}^{n+1}$ and $\ddot{\mathbf{u}}^{n+1}$ at time $t = t_{n+1}$. For this, in the present work, an implicit integration method, Newmark method [18] is used.

3 Numerical Problem Set-Up

A deformable strip, initially, is kept at an equilibrium distance from the rigid substrate, as shown in Fig. 1, so that there are no adhesive forces are acting on it.

The dimensions of the strip are $L \times h$, where length $L = 200L_0$, and height $h = 10L_0$ with $L_0 = 1$ nm. Adhesion is assumed to be present for 75% of the bottom surface of the strip (from $x = 0$ to $x = 150L_0$) with $r_0 = 0.4$ nm and $A_H = 10^{-19}$ J. The material parameters characterizing the adhesion behaviour are taken as $\gamma_W = 25.3$ and $\gamma_L = 2.5$ [12]. The material of the strip is taken to be an isotropic nonlinear Neo-Hookean material with $E = 2$ GPa and $\nu = 0.2$. Plain stain conditions are considered. The strip is discretized with 240×12 number of elements

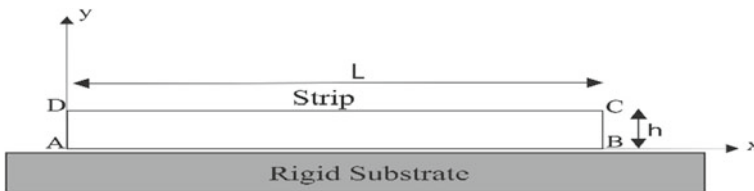


Fig. 1 Initial configuration of deformable strip on a rigid substrate

along the x and y directions [17]. While the elements in contact are Q1C4 enriched elements, the rest of the bulk domain is described by standard linear quadrilateral elements. Including the extra nodes for Q1C4 enriched elements, there are in total 3673 nodes in the mesh. Area of the gecko spatula pad is given as $49,524R_0^2$, where $R_0 = 1\text{ nm}$ [12]. As the length in which the adhesion is active in the current problem is considered to be equal to $150L_0$, the average width is calculated as 330.2 nm . All the material, geometrical and adhesion parameters considered are chosen so as to represent gecko spatula material and the associated adhesion energy.

3.1 Description of Peeling Process

The strip, initially lying on the substrate in the equilibrium position is peeled off from the substrate in two steps

1. First, an external rotation angle θ is applied to the right end of the strip (BC) ($x = L$) with the left end of the strip (AD) constrained in the x -direction and the point $x = 0, y = 0$ is constrained in both x and y directions. The rotation angle θ is applied such that the rate of change of angle $\dot{\theta} = 0.1$ and in such a manner that it yields a constant bending moment during the peeling of the strip.
2. After achieving the desired angle of rotation, a time-varying displacement $\bar{u} = \bar{u}(t)$ is applied in the vertical direction (i.e. positive y -direction) to the right end (BC) of the strip such that the velocity of pull is $\dot{u} = 0.1\text{ m/s}$. The right end of the strip (BC) is constrained to move only the y -direction in this step.

The finite element-based system of equations are solved using the Newmark time integration scheme with Newton–Raphson iterative scheme and resultant reaction forces are determined.

4 Results and Discussion

Figure 2 shows the variation of the pull-off force P that is required to apply the displacement u from different pre-rotated configurations (i.e. for different angles θ). Here the displacement u corresponds to the displacement of the centre of the right side end. It can be observed that for a particular angle, the pull-off force increases up to a certain point and then decreases. The fluctuation in the pull-off force at the end of each plot is a result of the snapping off of the strip from the substrate. The pull-off force is observed to be decreasing with increasing angle θ . The maximum pull-off force ranges from 4.82 to 7.11 nN . This is in agreement with the values obtained by Sauer and Holl [12] in their 3D spatula simulations. Also, the maximum pull-off force at $\theta = 90^\circ$ is equal to 4.82 nN which is in the range of $2\text{--}16\text{ nN}$ as reported by Sun et al. [19] in their experiments where the gecko spatulae were pulled-off at close

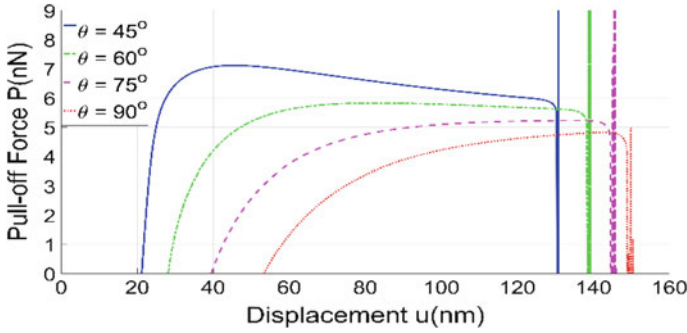


Fig. 2 Variation of pull-off force P with displacement u for different angles θ

to 90° . The low value of maximum pull-off force of 4.82 nN at $\theta = 90^\circ$ explains the swift detachment capability of Gecko toes which is ≈ 20 ms.

As mentioned in Sect. 2, the motion of the current system is characterized by the material parameters γ_W and γ_L . Hence, changing these parameters changes the adhesion behaviour of the strip. Variations in γ_W corresponds to the variations in either strip stiffness or the strength of adhesion. Similarly, variations in γ_L represents the variations in either the spatula size or range of adhesion. In this work, first, the parameter γ_W is varied while keeping $\gamma_L = 2.5$ as constant. Then, γ_L is varied keeping $\gamma_W = 25.3$. In Fig. 3a, the variation of pull-off force P with displacement u for $\gamma_{WR} = \gamma_W/\gamma_{W_0} = 1.5^{-1}, 1, 1.5, 1.5^2$ with constant $\gamma_L/\gamma_{L_0} = 1$ is shown. Here, γ_{W_0} and γ_{L_0} corresponds to the values 25.3 and 2.5, which were considered initially (see Sect. 3.1). It can be seen that, as γ_W is increased the pull-off forces decrease. This is due to the fact that by increasing γ_W the strength of adhesion decreases. This can also be understood in terms of stiffness of the material, i.e. as γ_W decreases the stiffness of the material decreases and it more readily adheres to the strip and more force is required to peel it off from the substrate. Next, the variation of pull-off force with displacement for $\gamma_{LR} = \gamma_L/\gamma_{L_0} = 1.5^{-1}, 1, 1.5, 1.5^2$ with constant $\gamma_W/\gamma_{W_0} = 1$ is plotted in Fig. 3b. The pull-off force is observed to be increasing with a decrease in γ_L which corresponds to the increase in the range of adhesion. It can also be understood that as the strip size increases the pull-off force decreases. From these results, it can be stated that as γ_L and γ_W decrease the pull-off forces increase due to either increase in adhesion strength (or range) or decrease in stiffness (or spatula size). These results can be useful for designing of the Gecko-inspired synthetic adhesives. For example, choosing a too large of a spatula size or too stiff a material results in poor adhesion capabilities. All these results are in agreement with the results obtained by Sauer and Holl [12] in their analysis of a full-scale 3D model of the spatula.

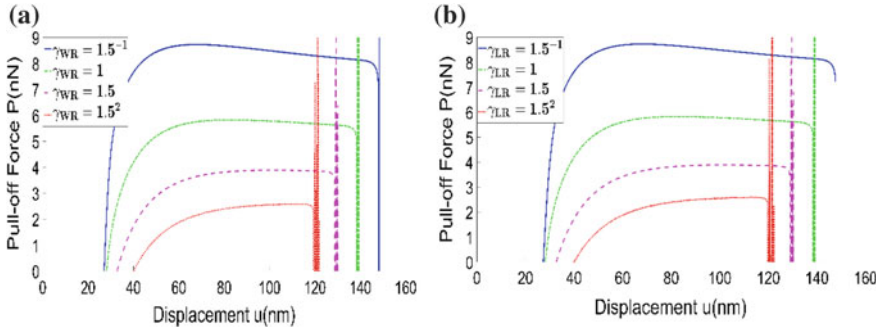


Fig. 3 Variation of pull-forces with displacement for **a** different adhesion parameters γ_W and **b** different length scales γ_L

5 Conclusions

Peeling behaviour of a gecko spatula is studied using a two-dimensional strip. Non-linear finite element analysis with surface enrichment is used to solve the numerical problem. It has been observed that the pull-off force decreases with increasing peeling angle. The value of the pull-off force at $\theta = 90^\circ$ has been found to be equal to 4.82 nN which is in agreement with the experimentally observed values of 2–16 nN. It has also been found that the pull-off forces increase with an increase in adhesion strength (or range) or decrease in stiffness (or spatula size). These observations have been used to understand the ability of gecko's swift detachment forces as well as the optimum design of their fibrillary structures.

Acknowledgements The authors are grateful to the SERB, DST for supporting this research under the project SR/FTP/ETA-0008/2014.

References

1. Autumn K, Liang YA, Hsieh ST, Zesch W, Chan WP, Kenny TW, Fearing R, Full RJ (2000) Adhesive force of a single gecko foot-hair. *Nature* 405(6787):681–685
2. Kwak JS, Kim TW (2010) A review of adhesion and friction models for gecko feet. *Int J Precis Eng Manuf* 11(1):171–186
3. Zhou M, Pesika N, Zeng H, Tian Y, Israelachvili J (2013) Recent advances in gecko adhesion and friction mechanisms and development of gecko-inspired dry adhesive surfaces. *Friction* 1(2):114–129
4. Autumn K, Sitti M, Liang YA, Peattie AM, Hansen WR, Sponberg S, Kenny TW, Fearing R, Israelachvili JN, Full RJ (2002) Evidence for van der waals adhesion in gecko setae. *Proc Natl Acad Sci USA* 99(19):12252–12256
5. Huber G, Mantz H, Spolenak R, Mecke K, Jacobs K, Gorb SN, Arzt E (2005) Evidence for capillarity contributions to gecko adhesion from single spatula nanomechanical measurements. *Proc Natl Acad Sci USA* 102(45):16293–16296

6. Gao H, Wang X, Yao H, Gorb S, Arzt E (2005) Mechanics of hierarchical adhesion structures of geckos. *Mech Mater* 37(2–3):275–285
7. Tian Y, Pesika N, Zeng H, Rosenberg K, Zhao B, McGuiggan P, Autumn K, Israelachvili J (2006) Adhesion and friction in gecko toe attachment and detachment. *Proc Natl Acad Sci* 103(51):19320–19325
8. Chen B, Wu P, Gao H (2009) Pre-tension generates strongly reversible adhesion of a spatula pad on substrate. *J R Soc Interface* 6(35):529–537
9. Peng ZL, Chen SH, Soh AK (2010) Peeling behavior of a bio-inspired nano-film on a substrate. *Int J Solids Struct* 47(14):1952–1960
10. Sauer RA, Li S (2007) A contact mechanics model for quasi-continua. *Int J Numer Methods Eng* 71(8):931–962
11. Sauer RA (2009) Multiscale modelling and simulation of the deformation and adhesion of a single gecko seta. *Comput Methods Biomech Biomed Eng* 12(6):627–640
12. Sauer RA, Holl M (2013) A detailed 3D finite element analysis of the peeling behaviour of a gecko spatula. *Comput Methods Biomech Biomed Eng* 16(6):577–591
13. Gautam SS, Sauer RA (2014) A composite time integration scheme for dynamic adhesion and its application to gecko spatula peeling. *Int J Comput Methods* 11(5):135014-1–1350104-28
14. Bonet J, Wood RD (1997) *Nonlinear Continuum mechanics for finite element analysis*. Cambridge University Press, London
15. Israelachvili JN (1991) *Intermolecular and surface forces*. Academic Press, London
16. Sauer RA, Li S (2008) An atomistically enriched continuum model for nanoscale contact mechanics and its application to contact scaling. *J Nanosci Nanotechnol* 8(7):3757–3773
17. Sauer RA (2011) Enriched contact finite elements for stable peeling computations. *Int J Numer Methods Eng* 87(6):593–616
18. Newmark NM (1959) A method of computation for structural dynamics. *J Eng Mech Div* 85(3):67–94
19. Sun W, Neuzil PT, Kustandi S, Oh S, Samper VD (2005) The nature of the gecko lizard adhesive force. *Biophys J* 89(2):L14–L17

Effect of Oxygen Enrichment on the Performance of a Rotary Furnace: A Harbinger to Ecological Sustenance and Pollution-Free Castings



Dilip Kumar, Ranjit Singh and Ashok Yadav

Abstract The iron foundries have been playing a vital role in the industrial development of India. The major problems being faced by iron foundries are restrictions on energy consumption by TERI and emission levels due to which majority of coal fired ferrous foundries in Agra have been closed by an order of the Hon'ble Supreme Court of India. The present state of foundries in Agra reveals that extensive research is necessary to develop an ecofriendly and energy efficient furnace. Therefore, A 200 kg capacity rotary furnace, have been designed and developed in DEI and studied for its technical feasibility, economic efficiency, energy consumption and emission levels. Lot of Experiments were conducted by earlier researcher with heat recovery unit, different fuels and their combination improved the energy requirements and reduced the emission levels but the levels obtained were not as per the required limits of TERI and CPCB. Looking so, a modified heat recovery unit, compact heat exchanger has been designed. Till now researcher has used circular nozzle with central holes but in our case we have used Reillo burners of the type RL/M70-190. Experiments are conducted with new heat exchanger and nozzle using LDO blended with jatropa. The furnace parameters are optimized experimentally and found that using Reillo burners of the type RL/M70-190, modified heat exchanger, rotating furnace at 1 RPM using 10–20% excess air and 400° air preheat, using 7.5–8.5% oxygen enrichment, emission levels are significantly reduced than CPCB limits and energy consumption is also reduced than permissible TERI limits. The operating cost is reduced by a significant amount and quality of the casting is also found excellent. Hence, use of rotary furnace with the above modifications will be a boon for the foundry industry of Agra and India at large.

Keywords Bio-fuel · Heat losses · Iron foundries · Rotary furnace

D. Kumar (✉) · R. Singh · A. Yadav

Department of Mechanical Engineering, Faculty of Engineering, Dayalbagh Educational Institute, Agra, India

e-mail: dilipkumar.er@gmail.com

R. Singh

e-mail: rsingh_dei@gmail.com

A. Yadav

e-mail: ashokyadavaca@gmail.com

© Springer Nature Singapore Pte Ltd. 2019

M. Kumar et al. (eds.), *Advances in Interdisciplinary Engineering*, Lecture Notes in Mechanical Engineering, https://doi.org/10.1007/978-981-13-6577-5_46

1 Introduction

The iron foundries have been playing a vital role in the industrial development of India. It is a core industry manufacturing castings which is basic raw material to almost all industrial sectors. The major problems being faced by iron foundries are restrictions on emission levels laid down by CPCB (Central Pollution Control Board) due to which majority of ferrous foundries using coal-fired cupola furnace have been closed by an order of the Hon'ble Supreme Court of India, and limits of energy consumption laid down by TERI. Bandopadhyaya [1] provided a set of strategies and necessary gas cleaning system required for bringing down the level of pollution to the desired level and recommended urgent anti-pollution measures in Cupolas. He suggested that a suitable scrubber, cyclone or bag filter may be put along with a dry/wet arrester to reduce the particulate emission level.

Bandopadhyaya [2] also emphasized the problems and strategies of environmental pollution in CI foundries. Bandopadhyaya et al. [3]. emphasized energy, environment and resource management in Indian mineral industries. Banerjee [4] emphasized that besides gasses and fumes, noise also poses serious problems. Datta et al. [5] advocated the installation of medium frequency coreless induction melting furnace. Landge [6] recommended the use of high energy venturi scrubbing system.

Maiti [7] suggested that the deletion and monitoring techniques on the basis of fundamental principles involved, mode of operation, accuracy of measurement, etc. for environmental pollution from foundries.

Mohammad et al. [8] emphasized the installation of Induction furnace for melting as they have lower emission values.

Panigrahi [9] suggested the use of dry spark arrester, wet spark arrester, cyclones, bag filter, tower wet dust catcher with venture pipe and waste water treatment.

Parthasarathy et al. [10] recommended the use of ESP (Electrostatic Precipitators), bag filters, wet collectors and cyclones for the control of air pollution in the foundries. Raizada [11] suggested a water cooling system for induction furnace. Selby [12] discussed the advantages of rotary furnace. Tiwari [13] stressed the need to install electric furnace to get rid of cupola emission.

Kumar [14] emphasized on using a rotary furnace to avoid the additional cost of pollution control equipment for producing castings in pollution-free environment using different fuels and combustion equipment. The results indicated that present combustion equipment gives improvement in pollution contents almost to the level of CPCB norms but energy requirements are still high as per the TERI norms.

The literature surveyed and present state of foundries in India reveals that extensive research work is necessary to develop an ecofriendly and energy efficient furnace for Ferrous Foundries. A 200 kg rotary furnace with a heat exchanger was designed, fabricated and used for investigations by the Faculty of Engineering, DEI, Dayalbagh. Rotary furnace made of 7 mm thick MS plates lined with mortar and refractory bricks have been used to study the emission level and energy consumption.

Under existing conditions of operation, existing combustion equipment using L. D. O. (light diesel oil) as fuel, the total energy consumption was 4172.00 kwh/tonne

Table 1 Comparison of compact and multipass counter flow heat exchanger

S. No.	Compact heat exchanger	Multipass counter flow heat exchanger
1	The maximum temperature of air from exit of exchanger is 500 °C	The maximum temperature of air from exit of exchanger is 350 °C
2	The efficiency is 46.11%	The efficiency is 30.11%
3	The area density β is 753.87 m ² /m ³ . The rate of heat transfer is better with 533 fins	The area density β is 100.14 m ² /m ³ . The rate of heat transfer is poor
4	Suitable for heat transfer between air to gas	Suitable for heat transfer between liquid to liquid (or a liquid and gas)
5	The refractory brick lining is better leading to reduced heat losses	The refractory brick lining is poor leading to more heat losses

which is very high as compared to the energy consumption as per TERI norms which is only 2084 kwh/tonne. Experiments conducted by Purshottam Kumar with heat exchanger and different fuels and their combination (LDO with 10%bio-fuel) improved the energy consumption and pollutants but still not within the limits of TERI and CPCB. So, a Modified heat exchanger is designed and new lining of the furnace is used for further experiments. Blends of LDO and bio-fuels in varying percentage are used for reducing the pollution levels below the CPCB norms. The effect of rotational speed of furnace, percentage of excess air, preheat air and different types of burners using optimal blend of LDO with bio-fuel, are considered for evaluating the performance of the furnace. Energy requirement and emission level for the castings using modified compact heat exchangers, have been experimentally investigated.

2 Design of a Modified Compact Heat Exchanger

It was observed during experimental investigations that reducing (excess air), i.e. combustion volume and supplying oxygen additionally the specific fuel consumption is reduced. In view of this development, design of compact cross-flow heat exchanger is carried out. The following data are considered for designing of Compact and Multipass counter flow heat exchangers.

Approximate volume of air = 450.0 m³, approximate time of one heat = 40.0 min, oxygen consumption in one heat = 38.5 m³, Atmospheric air temperature at inlet of exchanger = 27.0 °C, Air temperature at exit from exchanger = 500.0 °C (Table 1).

By modifying the heat exchanger the area density is increased to a very high value and efficiency is also increased from 45.36 to 46.11% and number of fins is increased from 500 to 533. 45.36% was the efficiency and 500 fins were used in the heat exchanger used by Purshottam Kumar. Modified Compact Heat Exchanger is used for further experimental evaluations.

3 Experimental Evaluations

The experimental Investigations have been carried out:

- (1) To reduce the energy consumption of furnace by
 - (a) Improving the heat transfer mechanism
 - (b) Reducing heat losses
- (2) To reduce the emission levels of SPM, SO₂, CO₂, CO, etc. and make furnace more ecofriendly.
- (3) To optimize the input parameters to achieve the above.

3.1 *Equipment for Further Experimental Investigations*

Burners: Till now the burners used were self-proportionating type or circular with number of holes on the periphery. These burners were having increased energy consumption and fuel consumption. So for reducing fuel consumption and energy consumption, the burner is changed and the experiments are conducted with the new burner.

It has been seen that at 1 RPM rotation of the furnace with 10% blending of LDO with bio-fuel, Reillo burners of the type RL/M70-190 gives the minimum fuel consumption. This burner in comparison to the other two is also having sturdy structure, easy to operate and maintain, ensures study performance and long life and is suitable for furnaces for ferrous casting.

Hence, for reducing the fuel consumption the prevailing circular ring burners and SPT types of burners are replaced by the burner of series RL/M70-190 manufactured by Riello burners. Experimental evaluations by Purshottam Kumar also reveal that minimum fuel consumption was obtained at 1 RPM with blending of 10% bio-fuel with LDO. Hence, in the further evaluations 1 RPM rotational speed and 10% blending is used.

3.2 *For Present Experimental Evaluation*

Instead of installing a ceramic fiber blanket, brick lining of alumina bricks and ramming mass consisting of quartz and fire clay for the refractory lining of furnace as used by Purshottam Kumar in his experiments, following changes in refractory brick lining are carried out to reduce the heat losses from furnace shell and increase furnace life.

- a. **Aluminium paint coating:** The outer surface of furnace shell which remains exposed to atmosphere is painted with metallic aluminium paint of thickness

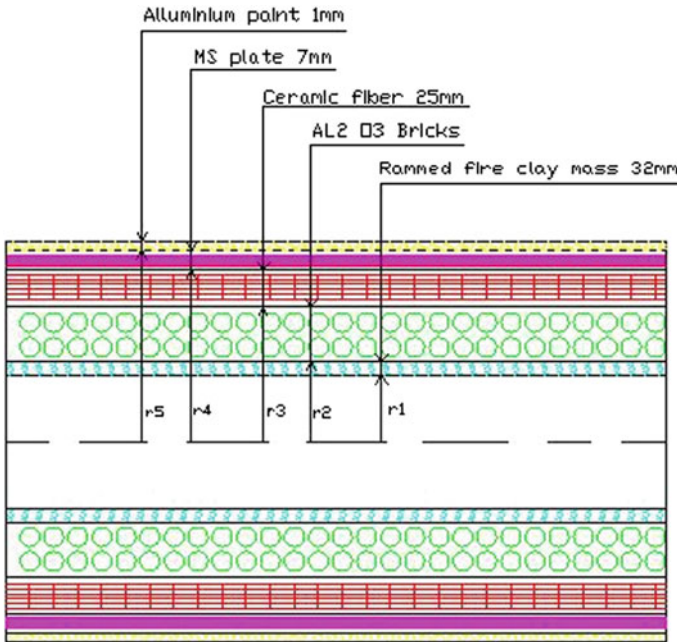


Fig. 1 Front view of layout of lining 2

1 mm. As aluminium paint has lowest emissivity among all available paints which drastically reduces the heat losses from furnace shell, and increases the utilization of heat inside the furnace and thus reduces the energy consumption.

- b. **Blanket of Ceramic fiber:** These blankets have excellent thermal stability, high resistance to burning, low thermal conductivity. (0.09w/m0 k), low heat storage, low shrinkage, and convenience in installing.
- c. **High alumina brick lining:** Instead of rammed monolithic silica brick lining, the high alumina brick lining (70% Al₂O₃ + 2.5%Fe₂O₃) which gives an excellent operational life is used with the following technical specifications.
- d. **Special ramming mass:** After few heats the ramming mass is repaired and patching is done. The special ramming mass consists of 70% Al₂O₃ + 1.0%Fe₂O₃ and balance fire clay.

For this new lining (2) the heat losses occur from inner surface to outermost surface as shown in Fig. 1.

3.2.1 Heat Losses from Furnace Shell with Lining

The heat losses from furnace shell depends upon resistance to heat flow. The comparison of heat losses from furnace shell with two different linings: (1) Without

aluminium paint, monolithic silica brick lining and rammed silica mass, and (2) With aluminium paint, ceramic fiber blanket, high alumina brick lining, and rammed fire clay mass, with proper installation, the average percentage reduction in heat losses is found to be 42.20%.

3.3 Further Experimental Investigations

After replacing the combustion equipment and refractory brick linings as explained in preceding the sections, the following experimental investigations are carried out to see the effect of the identified parameters on the performance of rotary furnace.

3.3.1 Effect of Rotational Speed on Energy Consumption and Performance of Furnace

Initially the furnace was rotated at 2 RPM. To study the effect of rotational speed the investigations have been made between 0.8 and 2.0 RPM (Table 2).

During the operation of furnace under existing conditions it was observed that

- (i) the atmospheric air is directly being supplied to burner (without preheating) for combustion of oil which leads to its incomplete combustion.
- (ii) The 30% excess air was supplied which leads to higher combustion volume and increases the air fuel ratio. These both factors increase the oil consumption, resulting into more energy consumption.

3.4 Effect of Excess Air on Performance of Furnace

The role of excess air is more dominating as explained in the following section. For maximum flame temperature and melting rate the optimization of excess air and preheat is required. To maintain the optimum flame temperature, the supply of excess air and its preheating is to be adjusted. An optimum excess air has to be used because more excess air will increase the combustion volume and reduce the flame temperature and exact amount of air will exceed the temperature beyond safe metallurgical limits which will reduce the life of refractory and furnace shell.

Table 2 Improvement in performance of furnace by changing RPM from 2.0 to 1.0

S. No.	Parameters	Absolute reduction		Percentage reductions/improvements
		2.0 RPM	1.0 RPM	
1	(a) Melting time (minutes)	46	35	23.91%
	(b) Minimum Fuel consumption (litres)	85	76	10.58%
	(c) Specific fuel consumption (lit/kg)	0.425	0.380	10.58%
	(d) Energy consumption in melting (kwh/tonne)	4110.45	3763.78	8.43%
	(e) Melting losses	6%	4%	2%
	(f) Emission levels (mg/m ³)			
	1. SO _x	90	88	0.02%
	2. SPM	40	35	2.22%
	3. CO ₂	4.00	3.90	12.50%
	4. CO	4.00	3.90	12.50%
2	(a) Melting rate (kg/hr)	260.86	342	31.10%
	(b) No. of heats per day (200 kg)	5	6	20%
3	Annual savings			
	(a) Annual energy consumption			1.6 × 10 ⁵ kwh
	(b) Annual fuel (litres)			16.2 k litres
	(c) Annual fuel cost			Rs.8.10 lakhs
4	Annual production (tonnes)	300	360	20%

3.4.1 Experimental Investigations—Effect of 20.0% Excess Air on Flame Temperature, Time, Fuel, Melting Rate, and Specific Fuel Consumption

Again experiments were repeated by reducing excess air to 20%, with compact heat exchanger, rotating furnace at optimal rotational speed 1.0 RPM, preheating LDO and bio-fuel blending up till 70.0 °C.

From the experimental evaluations it is clear that using compact heat exchanger and gradually reducing excess air, not only increases the flame temperature from 1510.0–1695.0 °C, and melting rate from 285.70 to 387.50 kg/h but also reduces the fuel consumption of molten metal to 0.280 liter/kg.

Table 3 Melting rate and fuel consumption under different conditions of excess air

S. No.	Parameter	20.0%-excess air with compact heat exchanger, rotational speed of 1.0 RPM	10.0%-excess air with compact heat exchanger, rotational speed of 1.0 RPM
1	Melting rate kg/h	285.70	387.50
2	Fuel used in melting (Litres/tonne)	290.0	280.0

Table 4 Energy consumption under different conditions of excess air

S. No.	Parameters	20.0%-excess air	10.0%-excess air
1	Melting only	2872.36	2773.31
2	Fuel combustion unit (Reillo burner)	5.128	4.818
3	Plant and Equipment	22.566	21.199
4	Pollution control equipment	12.309	11.563
5	Shot blasting m/c	7.460	7.460
	Total energy consumption kwh	2919.81 (2920.00)	2818.348 (2819.00)

3.4.2 Energy Consumption

The effect of reducing excess air initially to 20.0% and then to 10.0%, rotating furnace at optimal rotational speed 1.0 RPM on melting rate and fuel consumption are shown in Table 3.

And on energy consumptions (kwh/tonne) is shown in Table 4.

3.4.3 Comparison of Energy Consumptions

When furnace was rotated at optimal rotational speed 1.0 RPM, with excess air 10.0%, preheated up to 412.0 °C, using compact heat exchanger, in melting only, the energy consumption is reduced to 2773.31 kwh/tonne and total energy consumption to 2819.00 kwh/tonne.

4 Effect of Oxygen Enrichment: Effect of Reducing Combustion Volume

Time and fuel requirement will be more for reaching to a certain temperature if the combustion volume is more. Hence combustion volume may be optimized to certain extent by reducing the amount of air entering into the furnace and supplying oxygen externally. Number of experiments are conducted by gradually reducing air to its theoretical requirement in steps of 5.0–10.0% and supplying oxygen externally in steps of 1.0–2.0%. The effect of these variations was studied on flame temperature, time, fuel, melting rate, and fuel consumption. The effect was significant only when air was reduced to 75.0 of its theoretical requirement and approximately 7.0% oxygen was supplied externally.

Experimental investigations—Effect of 6.9% oxygen enrichment of 75.3–75.5% of theoretically required air preheated up to 460.00° C.

The effect on various parameters is shown in Table 5.

The above experimental investigations reveal that reducing combustion volume to 75.3–75.5% and supplying approximately 6.9% oxygen externally there was significant reduction in specific fuel consumption. Effect of oxygen enrichment on various parameters is shown in Figs. 2, 3, 4 and 5.

To further reduce the specific fuel consumption, it is proper to increase the oxygen enrichment and reduce the quantity of theoretically required air. The oxygen enrichment was increased in steps of 0.4–0.6% and theoretically required air was reduced

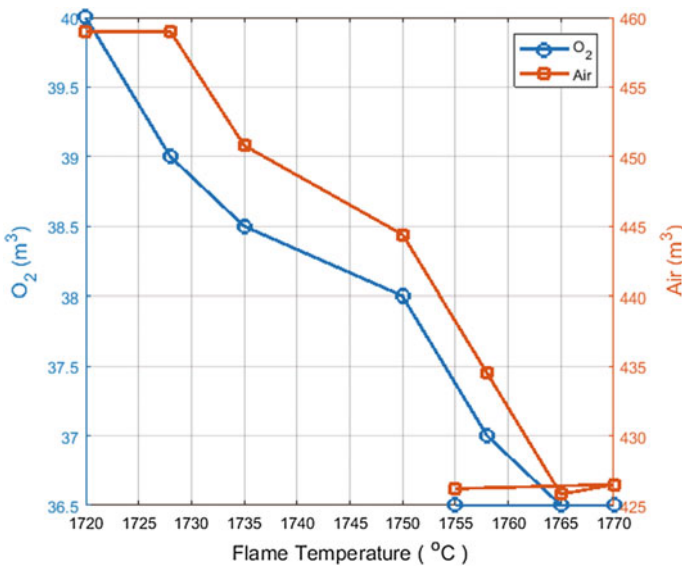


Fig. 2 Effect of 6.9% oxygen enrichment of 75.3–75.5% of theoretically required preheated air on flame temperature

Table 5 Effect of oxygen enrichment

Heat No.	RPM	Preheated air temp, °C	Flame temp, °C	Time, min	Fuel, litre	Melting rate, kg/hr	Specific fuel cons, lit/kg	Oxygen cons, m ³	Oxygen cons, %	Preheated air cons, m ³	Preheated air cons, %
1	1.0	415.0	1720.0	34.00	58.0	353.35	0.290	40.0	6.9	459.0	75.3
2	1.0	418.0	1728.0	32.50	57.0	370.37	0.285	39.0	6.9	459.0	75.4
3	1.0	430.0	1735.0	32.50	55.0	375.23	0.275	38.5	6.9	450.8	75.4
4	1.0	445.0	1750.0	32.00	54.0	380.95	0.270	38.0	6.9	444.4	75.4
5	1.0	455.0	1758.0	31.50	53.0	387.59	0.265	37.0	6.9	434.5	75.3
6	1.0	458.0	1765.0	31.00	53.0	393.70	0.265	36.5	6.9	425.8	75.3
7	1.0	460.0	1770.0	30.50	52.0	387.59	0.260	36.5	6.9	426.5	75.4
8	1.0	460.0	1755.0	30.20	52.0	397.35	0.260	36.5	6.9	426.2	75.5

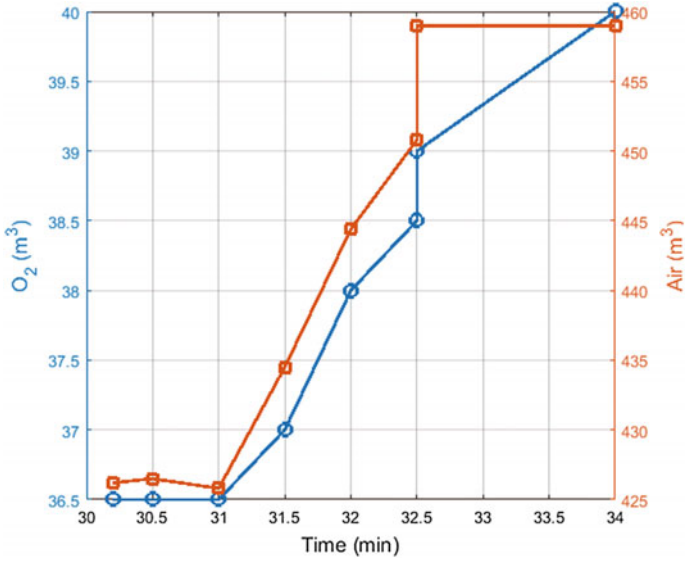


Fig. 3 Effect of 6.9% oxygen enrichment of 75.3–75.5% of theoretically required preheated air on time

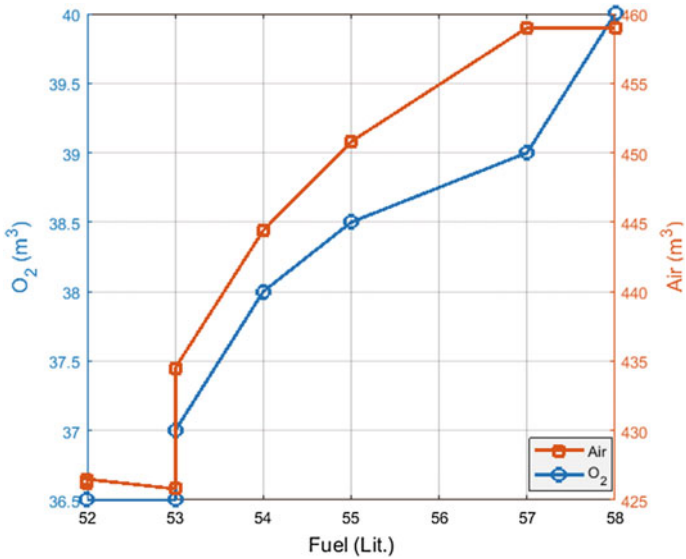


Fig. 4 Effect of 6.9% oxygen enrichment of 75.3–75.5% of theoretically required preheated air on fuel consumption

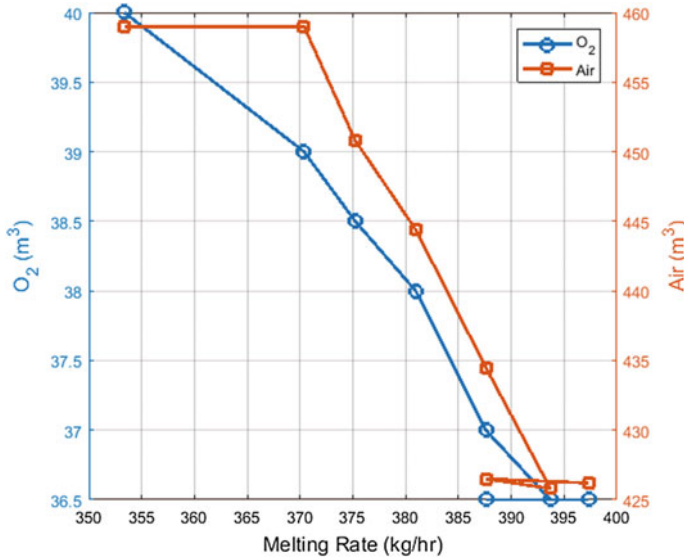


Fig. 5 Effect of 6.9% oxygen enrichment of 75.3–75.5% of theoretically required preheated air on melting rate

in steps of 3.0–4.0%. The effect was more significant when oxygen enrichment was increased to 7.58.5% and theoretically required air was reduced to 61–65%.

Several experiments were conducted by further reducing volume of air to (61–65)% of its theoretical requirement and increasing additional oxygen supply to 7.6–8.5%, maintaining the same RPM of 1.0, using combination of 10% bio-fuel and LDO. Ten heats were taken and found that in later heats the flame temperature, preheated air temperature increases whereas the time and fuel consumption decreases. The observations taken during experiment are given in Table 6.

Effect of oxygen enrichment on various parameters is shown in Figs. 6, 7, 8 and 9 (Table 7).

4.1 The Overall Comparison of Operating Cost

The overall comparison of operating cost, operating furnace under all conditions of experimental investigations (Rs/tonne) is shown in Table 8.

Table 6 Effect of 6,9% oxygen enrichment of theoretically required air

Heat No.	RPM	Preheated Temp, °C	Flame Temp, °C	Time, min	Fuel, Lit	Melting Rate, kg/hr	Specific fuel Con., lit/kg	Oxygen Cons, m ³	Oxygen Cons., %	Preheated air Cons, m ³	Preheated air Cons, %
1	1	425.0	1747.0	33.0	47.0	363.63	0.235	49.2	8.3	317.0	61.3
2	1	432.0	1753.0	32.0	47.0	375.00	0.235	48.8	8.4	319.0	62.4
3	1	437.0	1755.0	32.0	46.0	375.00	0.230	48.0	8.3	317.0	62.6
4	1	446.0	1760.0	31.0	45.8	387.00	0.229	46.2	8.2	313.0	62.8
5	1	465.0	1770.0	31.0	45.0	387.00	0.225	46.0	8.1	310.0	63.3
6	1	469.0	1772.0	30.0	44.3	399.00	0.221	45.6	8.1	309.0	63.3
7	1	472.0	1773.0	30.0	43.8	399.00	0.219	45.0	8.3	302.0	63.4
8	1	473.0	1775.0	30.0	42.9	399.00	0.214	43.6	8.1	297.0	63.6
9	1	475.0	1778.0	29.6	42.0	405.00	0.210	41.5	8.0	295.0	64.5
10	1	478.0	1780.0	29.1	41.0	412.00	0.205	40.0	7.7	294.0	64.9

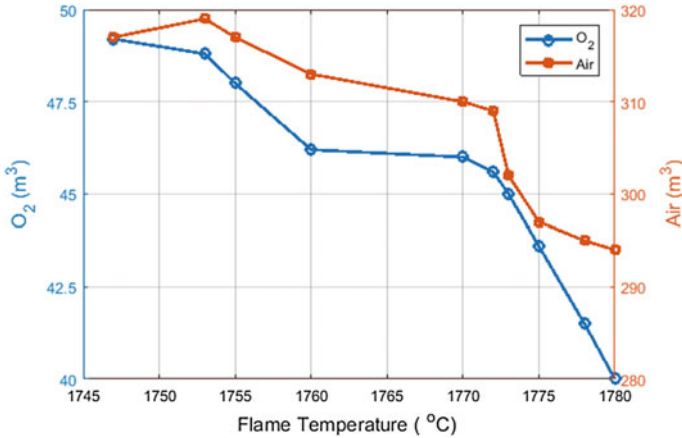


Fig. 6 Effect of 7.7–8.4% oxygen enrichment of 61.1–64.9% of theoretically required, preheated air on flame temperature

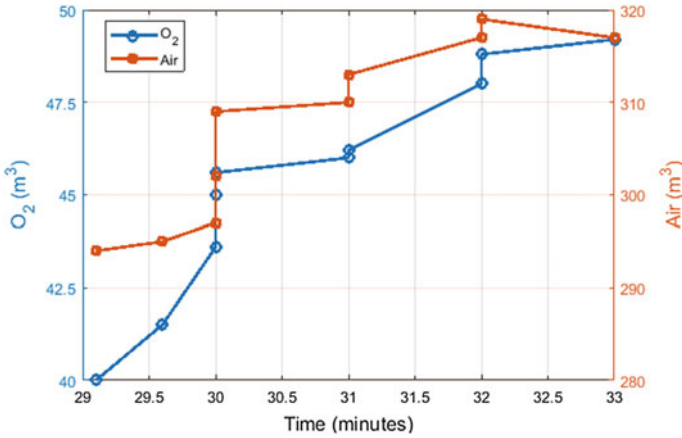


Fig. 7 Effect of 7.7–8.4% oxygen enrichment of 61.1–64.9% of theoretically required, preheated air on time

4.2 Effect of Oxygen Enrichment on Emission Level

When furnace is operated with 7.7–8.4% oxygen enrichment of 61.3–64.9% of the-oretically required air preheated up to 478.0 °C, using compact heat exchanger, rotating furnace at optimal rotational speed 1.0 RPM, the effect on emission levels has been experimentally investigated.

The comparison of emission levels (mg/m³) without preheating, and oxygen enrichment of air with 7.7–8.4% oxygen enrichment of 61.3–64.9% of theoretically

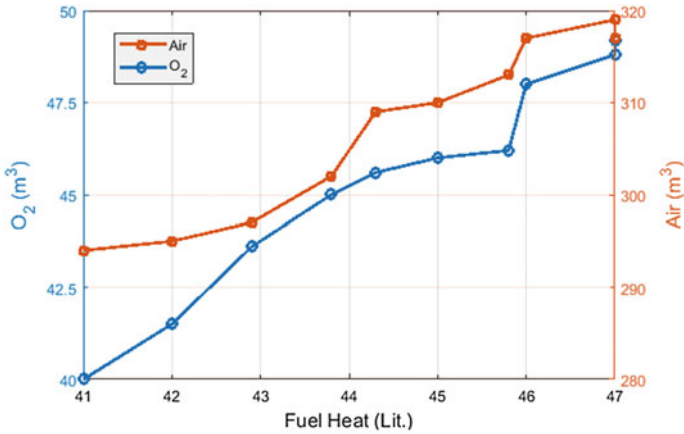


Fig. 8 Effect of 7.7–8.4% oxygen enrichment of 61.1–64.9% of theoretically required, preheated air on fuel

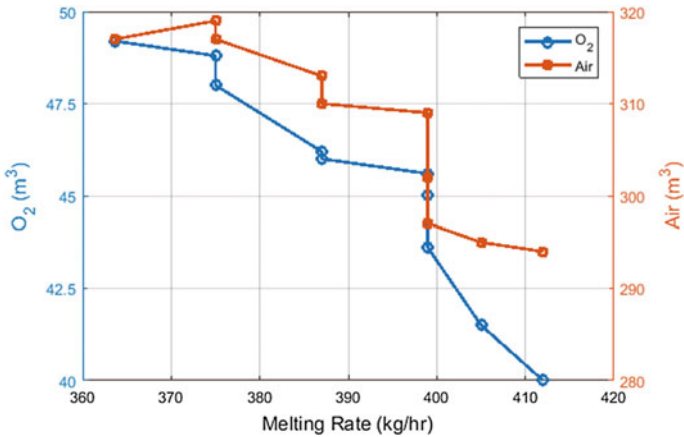


Fig. 9 Effect of 7.7–8.4% oxygen enrichment of 61.1–64.9% of theoretically required, preheated air on melting rate

required air preheated up to 478.0 °C, using compact heat exchanger, and rotating furnace at optimal rotational speed 1.0 RPM is shown in Table 9.

Table 7 Comparison of overall energy consumption based on experimental evaluations

Parameters	Operating furnace at 2.0 RPM without preheating air	Operating furnace at optimal rotational speed of 1.0 RPM using compact heat exchanger.		Operating furnace with 6.9% oxygen enrichment of 75.3%–75.4% of theoretically required air preheated up to 460 °C	Operating furnace 7.7–8.4% oxygen enrichment of 61.3–64.9% of theoretically required air preheated up to 478 °C
		Air 20%	Air 10%		
Fuel LDO + 10% bio-fuel (liter/tonne) Melting only	415.00	290.00	280.00	260 + 182.5 m ³ O ₂	(208 + 200.9 m ³ O ₂
(1) Energy consumption in Melting Only Kwh/tonne)	4110.45	2872.36	2773.31	(2575.2 + 91.25) = 2666.47	2060.1776 + 100.45 = 2160.62
(2) Plant & Equip.kwh	26.648	22.566	21.199	20.857	20.618
(3) Fuel combustion equipment	10.323	5.128	4.818	4.740	4.685 kwh
(3) Pollution equip.kwh/tonne	16.827	12.309	11.563	11.376	11.227
(4) Shot blasting kwh	7.46	7.46	7.46	7.46	7.46
Total energy consumption	4171.70 = 4172.00	2919.81 = 2920.0	2818.34 = 2819.0	2710.90 = 2711.0	2204.625 = 2205.0

5 Conclusion

- (1) The new refractory brick lining used in modified rotary furnace is found significant in reducing the energy consumption, reducing heat losses, and increasing life of furnace. Also heat utilization inside the furnace is found maximum.
- (2) It is concluded from this experimental investigation that the furnace using modified heat exchanger with changed refractory lining and using LDO with 10% bio-fuel, and rotating the furnace at 1 RPM affect the melting rate, energy consumption and pollutants. During operation of furnace under above existing conditions it is observed that.
 - (a) All the pollutants are within the range of CPCB norms.
 - (b) Only 10.0% excess air, preheated up to 410 °C, is to be supplied for complete combustion of fuel.

Table 8 The overall comparison of operating cost

S. No.	Parameters	Total operating cost	Percentage reduction/increment
1	With 20.0% excess air, without preheating or oxygen enrichment of air rotating furnace at 1.0 RPM	42,045.45	
2	With 10.0%, excess air using compact heat exchanger, air preheated up to 402.0 °C rotating furnace at optimal rotational speed of 1.0 RPM	44,499.40	-10.36
3	With 6.9% oxygen enrichment of 75.3–75.4% of theoretically required air preheated up to 460.0 °C, using compact heat exchanger, rotating furnace at optimal rotational speed of 1.0 RPM	49,376.19	+0.003
4	with 7.7–8.4% oxygen enrichment of 61.1–64.9% of theoretically required air preheated up to 476.0 °C, using compact heat exchanger, rotating furnace at optimal rotational speed of 1.0 RPM	40,056.9	-2.54

Table 9 The comparison of emission level without preheating and oxygen enrichment of air at 1.0 RPM

Heat No.	RPM	Without oxygen enrichment				With oxygen enrichment			
		SO _x	SPM	CO ₂	CO	SO _x	SPM	CO ₂	CO
1	1	91	58	3.90	4.3	90	34	3.8	3.7
2	1	91	56	3.95	4.2	92	34	3.8	3.7
3	1	88	56	3.90	4.0	87	34	3.7	3.6
4	1	88	54	3.85	4.0	86	33	3.6	3.6
5	1	86	50	3.80	4.0	84	33	3.5	3.6
6	1	85	48	3.80	4.1	83	33	3.5	3.6
7	1	84	46	3.80	4.0	81	33	3.5	3.6

- (c) With above input parameters the energy consumption in melting is reduced to 2774.00 Kwh/tonne whereas total energy consumption to 2819.00 Kwh/tonne.
- (3) The performance of LDO-fired rotary furnace has been significantly improved with 7.7–8.4% oxygen enrichment of 61.3–64.9% of theoretically required air preheated up to 478 °C, using compact heat exchanger, and rotating furnace at optimal rotational speed 1.0 RPM.
- (a) Energy consumption of the presently used rotary furnace is found much lower than the other furnaces having higher consumption than TERI norms. In our case energy consumption is found approximately 2.82% lower than the TERI norms.
 - (b) Emission levels are found significantly lower than the permitted values of CPCB. The Emission level obtained are having values SPM by 40.0%, SO₂ by 71%, CO by 30.0% and CO₂ by 10.0% lower than the normal range prescribed by CPCB.
 - (c) The operating cost of the furnace with existing modifications is reduced by 2.54% than the operating cost of ordinary rotary furnace without preheat and oxygen enrichment and 20% excess air used.

Hence, it can be concluded that a rotary furnace with the suggested modifications can be used as an energy efficient furnace for melting iron in an ecofriendly environment. Hence, rotary furnace with the above modifications will be a boon for the foundry industry of Agra and India at large.

Acknowledgements We gratefully acknowledge Most Revered Prof. P. S. Satsangi, Emeritus Chairman, Advisory Committee on Education, Dayalbagh Educational Institute, Agra for His constant support and inspiration.

References

1. Bandopadhaya A, Ramchandra PR (1994) Environmental pollution from cast iron foundries, The problems and strategies for their migration. A paper presented at workshop on, Iron foundry energy scenario in raw material and technology, Organized by development commissioner for iron and steel Calcutta
2. Bndopadhaya A, Mishra KK, Rao RC (1995) Pollution control in Foundries related problems and strategies for an economically viable solution. *Indian Foundry J*, 11–18
3. Bandopadhaya A, Dutta A, Gupta KN (1996) Energy environment and resource management. In: *Proceedings of seminar on Indian mineral industries*, pp 51–63
4. Banerjee SN (1995) Clean Air and control of pollution is a national requirement. *Indian Foundry J*
5. Datta SK, Cele AB (1995) Induction melting practices: basic aspects and recent trends. *Indian Foundry J*, 17–22
6. Landge KA, Kolhatkar (1995) Gas cleaning system in foundry industries. *Indian Foundry J*
7. Maiti BR (1995) Detection and monitoring techniques for environmental pollution from foundries. *Indian Foundry J*, 25–29

8. Mohammad NS, Sunder M, Angelo PC, Krishnan SR (1998) Pollution control in electric furnaces and oil fired furnaces. *Indian Foundry J*, 37–40
9. Panigrahi SC (1995) Some aspects of pollution in foundries. *Indian Foundry J*, 1–9
10. Parthasarthy TC, Kumar TSV (1998) Air pollution control in foundries. *Indian Foundry J*, 115–121
11. Raizada RK (1993) The role of induction furnaces in development of casting in pollution free atmosphere. National Seminar on Pollution Control Measures, Calcutta
12. Selby TR (1974) Foundry management and technology. *Indian Foundry J*, p 102
13. Tiwari SN (1998) On status of Indian foundry industry. *Indian Foundry J*, 17–20
14. Kumar P (2014) An Eco-friendly and affordable melting technique for CI foundries, A Ph.D thesis submitted to Dayalbagh Educational Institute
15. Kumar D, Singh R, Yadav A (2017) Performance enhancement of a rotary furnace: a harbinger to pollution free castings. *Int J Adv Res Sci Eng* 06(11):1862–1879

Modeling and Analysis for Barriers in Healthcare Services by ISM and MICMAC Analysis



Kanishka Kumar, Vardeep S. Dhillon, Punj Lata Singh and Rahul Sindhvani

Abstract Modern hospitals offer a panoply of services—diagnostic, curative, preventive and rehabilitative—as per the specific needs of a patient. Since the patient is no more a passive recipient of care, but an enlightened consumer, the provision of high-quality services become indispensable for earning goodwill, improve patient satisfaction and also to garner better online ratings. However, the path to providing quality services is not smooth—there are hurdles galore. The primary purpose of this study is to identify and analyze the barriers to the provision of quality care. To address this purpose, the paper first reviews systematically the introduction on healthcare services; second, it provides the barriers in achieving the quality level in healthcare services; third it uses an Interpretive Structural Modelling (ISM) and MICMAC analysis for modeling and analysis purpose. Finally, this paper concludes with managerial implications and further research directions for achieving quality services in the healthcare system.

Keywords Health care · Quality services · Barriers · Interpretative structure modelling (ISM) · MICMAC analysis

K. Kumar · V. S. Dhillon
Amity Institute of Hospital Administration, Amity University Uttar Pradesh,
Noida 201313, Uttar Pradesh, India

P. L. Singh
Civil Engineering Department, Amity School of Engineering and Technology,
Amity University Uttar Pradesh, Noida 201313, Uttar Pradesh, India
e-mail: plsingh@amity.edu

R. Sindhvani (✉)
Department of Mechanical Engineering, Amity School of Engineering and Technology, Amity
University Uttar Pradesh, Noida 201301, Uttar Pradesh, India
e-mail: rsindhvani@amity.edu

1 Introduction

Quality in health care is very important. Quality is determined by achieving certain benchmarks set by the healthcare organization or the hospital itself or any external body. The care provided in a hospital should be efficient, timely, safe, and as per the requirements of the patients. The high-quality healthcare should meet the patients' needs irrespective of the illness, race, ethnicity, culture. The communication should be very good between the treating physician and the patients; also, a trust should be developed in their relationship [1].

Quality of healthcare services have certain dimensions, reliability (e.g. the diagnosis proves to be accurate, the doctor keeps the appointment on schedule), responsiveness (e.g. the doctor listens to the patient), assurance (physician's knowledge and courtesy and their ability to build trust and confidence through their reputation), empathy (acknowledging patient as a person, have patience in dealing with patients), tangibles (cleanliness of the patient waiting room, washrooms, wards, OPDs).

2 Review of Literature

The hospital serves the purpose of promoting, restoring to the normal function or maintaining the health of the people. It includes services like curative, restorative, palliative and rehabilitative. There are highly skilled, dedicated people working at all levels of the hospital whether healthcare personnel or management staff is concerned. There are many vital functions carried out in hospitals like healthcare service provision, resource generation, and allocation as per requirement, financial requirements and stewardship [2]. Healthcare has a larger share in the service industry all over the world. The quality of healthcare services should serve two functions, i.e., enhanced clinical outcomes and improved patient and staff satisfaction along with diminishing costs which adds better and greater value to the healthcare services. The second is the technological advancement which increases the accuracy of the procedures [3].

The effectiveness of quality services in the hospital also depend on cultural and linguistic differences. When a consultant or any health care worker does not understand what the patient is saying and also vice versa when the patient doesn't understand the doctor's language, there is a compromise in the quality of healthcare services. For this purpose, the staff should be trained in variable cultures and interpreter can be used in case of language differences [4]. Accreditation is a voluntary program, where the auditors evaluate the compliance of hospital's services with the previously set benchmarks [5]. Accreditation is the quality assurance process of "self-assessment and external peer assessment used by healthcare organizations to accurately assess their level of performance in relation to established standards and to implement ways to improve continuously." Although the terms accreditation and certification are often used interchangeably, accreditation usually applies only to organizations, while certification may apply to individuals, as well as to organizations. Chassin and Galvin

in 1998 conducted a study with an objective to identify the quality related issues of health care in the US. Various discussions and community meetings were held. It was found out that there were many problems related to quality across various parts of America. They classified those problems as underuse, overuse or misuse. This requires proper planning in delivering proper care, proper education and training for the healthcare professionals as well as non-healthcare workers to improve healthcare quality [6].

Another research was carried out by Batalden and Davidoff in 2007 on Quality Improvement and how can it transform health care? According to the research, Quality improvement is a vital tool in increasing the standards of care delivered to the patients. It is the combined effort of all the staff of the hospital whether doctors, nurses, nonclinical staff, research workers, management staff, students (if it's a medical college), get together and act in a way which utilizes the full potential of everyone which lead to better patient outcome (patient's health), better system performance (Quality of care) and better professional learning as well as development [7]. A study in America revealed some facts regarding the quality of health care despite being the recognition of achievements of American medicine and American healthcare. Many things were focused upon like underuse, misuse, and overuse of drugs, medical equipment, and technology as well as processes and procedures. It stated that there is a lack of guidelines for providing care to patients according to their needs. There is lack of documentation or evidence despite being making efforts to improve all the clinical decision-making in the hospitals in the US. With the introduction of technology in the fields of healthcare, there is a rise in costs of care which leads to underuse of these devices. It also emphasized on the increased professionalism and effect of financial incentives on the quality of care being delivered. Evidence-based care and pooling of resources was suggested [8]. Gap analysis or analyzing barriers is the initial step in the review of the available service delivery system. It is an efficient base to implement a modern management system [9]. It can be measured against pre-set standards. It reveals the areas of improvement in the existing service system.

3 Barriers Analyzed

The barriers were identified and analyzed based on the observations in the multispecialty hospital.

3.1 *Waiting Time (F1)*

Waiting time for patients who require admissions. The main reason was the non-availability of beds in the wards. The waiting time in case of emergency to Inpatient department is defined in the hospital policy as 4 h (maximum time), but due to non-availability of beds in the IPD is the major reason of increased waiting time. In case of

any critical case or urgency needs, the patients are upgraded as per their requirements and availability.

Waiting time refers to, in this case, to the time a patient's request for bed is sent to IPD till the patient gets admitted. Waiting time is an important indicator of the quality of services offered by hospitals. The amount of time a patient waits is one of the factors affecting the utilization of healthcare services. Patients perceive long waiting times as a barrier to actually obtaining the services [10]. Keeping patients waiting can be a cause of stress for both patient as well as doctor and can deteriorate the condition of the patient. Waiting time is a tangible aspect of practice that patients use to judge health personnel, even more than their knowledge and skill.

3.2 Patients Leaving Against Medical Advice (F2)

In this case the patients leave the hospital against the advice given by doctor due to many reasons like non-affordability of services, the expenses are not in their panel (insurance plans), patient is at last stage of any disease, not satisfied with the care delivered by the hospital, wants to reconsider the decision of admission (if any), take an opinion from another specialist [11].

In this case, the department maintains the records of the reason of leaving against medical advice (LAMA) patients in an emergency, OPD, and IPD. Later the data is analyzed and improvements are done accordingly. [mostly occurs from emergency]

3.3 Training (F3)

Training is a major barrier in the delivery of healthcare services so proper training should be provided to the staff (e.g., the staff should be trained to do the preoperative medical assessment includes the patient's medical, physical, psychological, social, economic, and discharge needs'. After preparation, medications not immediately administered are labeled with the name of the medication, the dosage/concentration, the date prepared, the expiration date, and two patient identifiers [12].

3.4 Behavioral Barriers (F4)

There is a culture in every organization. Data from adverse events resulting from handover communications are tracked and used to identify ways in which handovers can be improved, and improvements should be implemented [13].

3.5 Cultural Barriers (F5)

Cultural and lingual differences serve as barriers in patient care, to overcome this translator and special training among the staff is provided [14].

3.6 Documentation (F6)

Documentation and maintaining healthcare records in the public or private sector is essential. Hospital statistics help in improving healthcare services [15]. It helps in providing cost-effective treatment, continuity of care, handover communication, patient safety and improvement of quality care, also helpful in education, research, auditing, medicolegal cases, monitoring, and evaluation.

3.7 Patient and Family Education (F7)

Nowadays, patient participation in treatment is very important. Patient and family education in the language and the way they understand is one of the ways to improve the quality of patient care, is done at every step of care [16].

4 ISM Approach and Methodology

After observing the gaps in the implementation of quality standards and services, the barriers were identified and analyzed. Seven barriers were identified and ISM (a multi-criteria decision-making approach) tool was used to establish the interrelationship between the barriers which were identified. MICMAC Analysis was used to analyze the dependence power and driving power of the barriers identified [17].

Step 1 Development of Structural Self-Interactive matrix (SSIM) after the identification of barriers. It is developed to show interrelationship between the barriers (I and j). Values are assigned as V , A , X , and O (Table 1).

V = Barrier i influence barrier j

A = Barrier j influence barrier i

X = Barrier i and j influence each other

O = Barrier i and j are unrelated.

Step 2 Development of Reachability Matrix

It is the interrelationship between barriers in the binary form obtained from SSIM. Initial reachability matrix is depicted in Table 2. For the Final Reachability Matrix, transitivity is incorporated. If barrier A and B are interrelated and barrier B and C are

Table 1 Structural Self-Interactive Matrix (SSIM)

	7	6	5	4	3	2
1	X	A	O	O	O	O
2	X	A	V	V	V	
3	A	A	A	A		
4	X	O				
5	X	O				
6	O					

Table 2 Initial reachability matrix

	1	2	3	4	5	6	7
1	1	0	0	0	0	0	1
2	0	1	1	1	1	0	1
3	0	0	1	1	0	0	0
4	0	0	0	1	0	0	1
5	0	0	1	0	1	0	1
6	1	1	1	0	0	1	0
7	1	1	1	1	1	0	1

Table 3 Final reachability matrix

	1	2	3	4	5	6	7
1	1	0	0	0	0	0	1
2	0	1	1	1	1	0	1
3	0	0	1	1	0	0	1*
4	0	0	0	1	0	0	1
5	1*	1*	1	1*	1	0	1
6	1	1	1	1*	1*	1	1*
7	1	1	1	1	1	0	1

*The values are upgraded due to transitivity

interrelated, then barrier A and C are automatically interrelated to each other. Final Reachability Matrix is shown in Tables 2 and 3 where transitivity is marked as 1*.

Step 3 Partitioning the reachability matrix

The reachability set (horizontal barriers) and the antecedent set (vertical barriers) is obtained by final Reachability Matrix. The intersection of these sets is derived for all barriers. The barriers for which the reachability set and the antecedent set are same, occupy the top level in the hierarchy of ISM as shown in Tables 4, 5, 6, 7.

Step 4 Development of Conical Matrix

It is developed by clubbing together all the barriers on the same level, across rows and columns of the final reachability matrix as shown in Table 8.

Table 4 Iteration 1

Factors	Reachability set	Antecedent set	Intersection	Level
1	1,7	1,5,6,7	1,7	I
2	2,3,4,5,7	2,5,6,7	2,5,7	
3	3,4,7	2,3,5,6,7	3, 7	
4	4,7	2,4,3,5,6,7	4, 7	I
5	1,2,3,4,5,7	2,5,6,7	2,5,7	
6	1,2,3,4,5,6,7	6	6	
7	1,2,3,4,5,7	1,3,4,5,6,7	1,2,3,4,5,7	

Table 5 Iteration 2

Factors	Reachability set	Antecedent set	Intersection	Level
2	2,3,5,7	2,5,6,7	2,5,7	
3	3, 7	2,3,5,6,7	3,7	II
5	2,3,5,7	2,5,6,7	2,5,7	
6	2,3,5,6,7	6	6	
7	2,3,5,7	1,2,3,4,5,6,7	2,3,5,7	

Table 6 Iteration 3

Factors	Reachability set	Antecedent set	Intersection	Level
2	2,5,7	2,5,6,7	2,5,7	III
5	2,5,7	2,5,6,7	2,5,7	III
6	2,5,6,7	6	6	
7	2, 5, 7	1,2,3,4,5,6,7	2,5,7	III

Table 7 Iteration 4

Factors	Reachability set	Antecedent set	Intersection	Level
6	2,5,6,7	6	6	IV

Table 8 Development of conical matrix

	1	4	3	2	5	7	6	Drive power
1	1	0	0	0	0	1	0	2
4	0	1	0	0	0	1	0	2
3	1	1	1	0	0	1	0	4
2	1	1	1	1	1	1	0	6
5	1	1	1	1	1	1	0	6
7	1	1	1	1	1	1	0	6
6	1	1	1	1	1	1	1	7
Dependence power	6	6	5	4	4	7	1	33\33

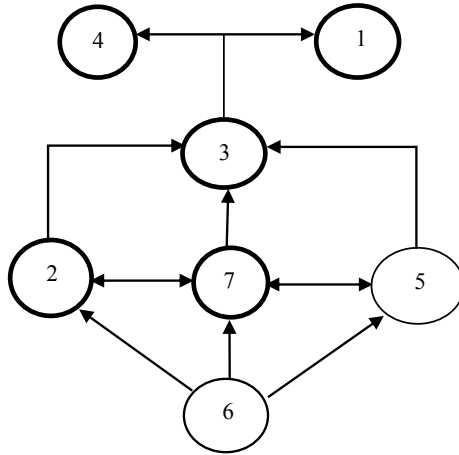


Fig. 1 Diagraph

Driving power	7	Driving barriers						7
	6	2		4	5		+	
	5		3		Linkage barriers			
	4							
	3							
	2	1	Autonomous barriers		Dependent barriers			
	1					6		
	1	2	3	4	5	6	7	

Dependence power →

Fig. 2 MICMAC analysis

Step 5 Development of Diagraph

The top-level barriers are placed at the top and second level barriers are placed at the second position and so on as shown in Fig. 1.

Step 6 MICMAC Analysis

It is done to analyze the driving force and dependence force of the barriers as shown in Fig. 2.

5 Conclusion

The contribution of this paper is to present the barriers in healthcare services using the ISM approach and MICMAC analysis. After identifying the gaps, the barriers were analyzed. These barriers affect the quality of patient care being provided in hospitals and healthcare centers. The ISM tool represents the interrelationship among the seven barriers and establishes a hierarchy among them, which will further help in root cause analysis and research in the healthcare industry.

Based on the results obtained from this study, the contributions are as follows:

This research identified the barriers to the quality of patient care and used the ISM approach and MICMAC analysis to analyze these barriers.

The barriers to the highest driving power are the training of the staff and the behavioral barriers need to be taken into account on the priority basis.

The results of this research may prove helpful to the hospital operations manager and the quality managers in the hospitals and the healthcare facilities.

The area of research is quite vast and has a number of areas for further research to make the functioning of hospital smoother and the quality of patient care cost-effective.

References

1. Davis K, Schoenbaum SC, Collins KS, Tenney K, Hughes DL, Audet AMJ (2002) Room for improvement: patients report on the quality of their health care
2. Ollila Eeva, Koivusalo Meri (2002) The world health report 2000: World Health Organization health policy steering off course- changed values, poor evidence, and lack of accountability. *Int J Health Serv* 32(3):503–514
3. Kenagy J, Berwick D, Shore F (1999) Service quality in healthcare. *JAMA* 281(7):661–665
4. Sindhvani R, Malhotra V (2015) Lean and agile manufacturing system barriers. *Int J Adv Res Innovation* 3(1):110–112
5. Anderson M (2003) Laurie: culturally competent healthcare systems: a systematic review 24(3): 68–79
6. Alkhenizan A, Shaw C (2012) The attitude of healthcare professionals towards accreditation: a systematic review of literature. *Family Community Med* 19(2):74–80
7. Chassin MR (1998) Galvin RW and the national roundtable on healthcare quality: the urgent need to improve healthcare quality. *JAMA* 280(11):1000–1005
8. Batalden PB, Davidoff F (2007) What is “Quality Improvement” and how can it transform healthcare? *Qual Saf Healthcare* 16(1):2–3
9. Mittal VK, Sindhvani R, Kalsariya V, Salroo F, Sangwan KS, Singh PL (2017) Adoption of integrated Lean-Green-Agile strategies for modern manufacturing systems. *Procedia CIRP* 61:463–468
10. McNeil B (2001) Hidden barriers to improvement in the quality of care. *N Engl J Med* 345:1612–1620
11. Sindhvani R, Malhotra V (2016) Modelling the attributes affecting design and implementation of agile manufacturing system. *Int J Proc Manag Benchmarking* 6(2):216–234
12. Institute of Medicine (2007) Advancing quality improvement research: challenges and opportunities: workshop summary. Chapter 3. The National Academics Press, Washington DC

13. Sindhwani R, Malhotra V (2017) A framework to enhance agile manufacturing system: a Total Interpretive Structural Modelling (TISM) approach. *Benchmarking Int J* 24(4):467–487
14. Sindhwani R, Malhotra V (2013) Overview and drivers of agile manufacturing system: a review. *Int J Marketing Technol* 3(12):144
15. Carayon P et al (2014) Human factors system approach to healthcare safety and patient safety. *Appl Ergonomics* 45(1):14–25
16. Sindhwani R, Malhotra V (2017) Modelling and analysis of agile manufacturing system by ISM and MICMAC analysis. *Int J Syst Assurance Eng Manag* 8(2):253–263
17. Sindhwani R, Malhotra V (2016) Barriers evaluation for agile manufacturing system with fuzzy performance importance index approach. *Int J Agile Syst Manag* 9(4):292–301

Pothole Detection and Warning System for Indian Roads



Sunil Kumar Sharma and Rakesh Chandmal Sharma

Abstract This paper is based on an application of mobile sensing: sensing and gathering the surface condition of roads. We will fabricate a system and mention the required algorithms to sense the road anomalies by making a portable sensor that can be equipped in any car or public transport. We will call this system pothole detection system (PDS), it will use the mobility of the particular vehicle on which the system will be fitted, and side by side gather data from the vibrations and the GPS sensors, and further process and filter the data to monitor road surface condition. At first, we will deploy the PDS on our own vehicle and test it out in a particular sector of Noida. Using the machine learning approach, we were able to identify and classify the potholes and other road anomalies from the accelerometer data. From the continuous testing and gathering data on a particular stretch of road, we were able to put an algorithm that will successfully detect a pothole with 4.3% chance of failure or if the pothole is too small to be detected. It was further conducted a manual inspection of the reported potholes and found that 80% of the road anomalies reported are in need of serious repair.

Keywords Pothole detection · Intelligent vehicular systems · Wi-Fi · Sensors

1 Introduction

Our project is based on the detection of potholes so as to safeguard people about the road conditions of the area. It will use the mobility of the particular vehicle on which the system will be fitted, and side by side gather data from the vibrations and the GPS sensors, and further process and filter the data to monitor road surface condition. We will use the application of accelerometer and the GPS to detect potholes and gather

S. K. Sharma (✉)

Department of Mechanical Engineering, Amity School of Engineering and Technology, Amity University Uttar Pradesh, Noida, India
e-mail: sunilsharmaitr@gmail.com

R. C. Sharma

Maharishi Markandeshwar (Deemed to be University), Mullana, Ambala 133207, India

© Springer Nature Singapore Pte Ltd. 2019

M. Kumar et al. (eds.), *Advances in Interdisciplinary Engineering*, Lecture Notes in Mechanical Engineering, https://doi.org/10.1007/978-981-13-6577-5_48

the exact location of the pothole. Accelerometer readings can be taken in Excel format as a .csv file format. We are using 3-axis accelerometer in our system and Aurdino board for the computation of the readings. It portrays a system and the algorithms linked to it so that the road conditions can be monitored using the pothole detection system. Our pothole detection system uses the data collected by the moving vehicle and gathering the data in the form of acceleration and change in vibration on x and z axis [1–15].

Our aim is to make a pothole detection system, which acts as a guide to the driver in avoiding the potholes on the road by giving a proper warning about the potholes. Interest in Intelligent Vehicle Systems comes from the problems caused by traffic congestion worldwide and synergy of new information technologies for simulation, real-time control and communications networks [16–29]. There are many problems that this system must solve in order to function properly. First, there are many events that yield high acceleration signatures such as braking, sudden swerves, doors being slammed Second, it gets difficult even manually to know whether it is a pothole or a mere bump in the road.

2 Pothole Detection System

The accelerometer which we are using is a three axis accelerometer which take accelerations on x , y , and z axis. GPS systems which are used with accelerometer provides us with coordinates of the pothole detected. This data is amalgamated using interpolation with GPS. When the network is available cars upload their data to central server. The central server clusters detections based on location, and applies a minimum cluster size given in Fig. 1.

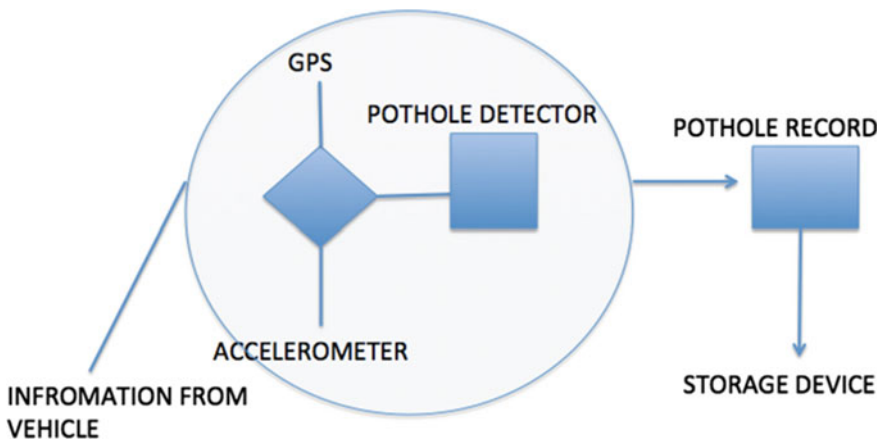


Fig. 1 Block diagram of pothole detection

The information collected by the GPS and accelerometer is collected in a cluster and then stored in a central server where we can collect data for different roads and store the potholes information for different purposes. The advantage of this system is it provides the condition of the roads along a particular area and different areas. The data can be provided to the local authorities so that they can take respective measures to fix the potholes [5–9].

2.1 Algorithm

The high pass filter eradicates frequency which is lower than the threshold value of x and z axis. A general pothole with evident z axis acceleration should evidently produce acceleration on z axis. At high speeds, even small road anomalies can create high peak acceleration readings. This filter rejects windows where the peak z acceleration.

2.2 Location of Accelerometer

We need to decide the location of the accelerometer in the vehicle so that we could get the optimum quality of the signal. We basically choose three locations to place the accelerometer. We placed accelerometers in three locations inside the cabin of a single car. The accelerometer signal for a fixed stretch of pavement from three different mounting positions: attached to the dashboard, attached to the right side of the windshield, and attached to the embedded PC, which was not firmly attached to the vehicle. The signals which we got from dashboard and windshield appeared to be quite small and computer produced unfeasible results. We finally decided that we should attach the accelerometer in dashboard which the best location out of the three which are being discussed it also keeps the sensor out of the passenger's cabin.

2.3 GPS Accuracy

GPS accuracy in our deployment is important if potholes are too located and multiple detections combined to report a single pothole. To measure accuracy, we placed a thick metal bar across a road and repeatedly drove over it. For each drive, we first calculated the peak of the accelerometer reading and the estimated the location where the peak occurred for the GPS location.

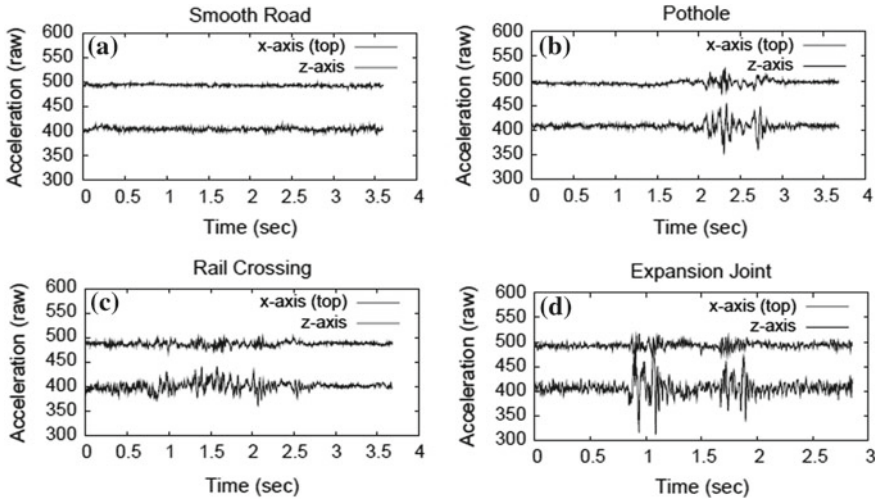


Fig. 2 a Acceleration response for smooth road b Acceleration response for the pothole. c Acceleration response for rail crossing d Acceleration response for expansion joint

2.4 Training Data

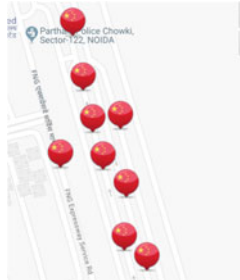
We recorded the data by driving down various areas of NCR region and continuously and continuously recording the readings of accelerometer traces. We collected a different set of data including the following event classes. Smooth roads. Pot Holes: these are the missing chunks of the pavement of the road and anomalies in the surface of the road. Manhole: it covers other equipment on the road which nearly flush with the road. Turning corner: sometimes while taking turn accelerometer shows anomalies acceleration.

Data defined as Noida Sector 122: it is a single-lane road which has heavy type of potholes in it. Noida–Greater Noida Expressway: it is a four-lane road highway which comes under smooth types of roads. Shankar road Delhi: it is a two-way lane road with moderate potholes on the road and moderate traffic. Shadipur–Kirti Nagar Bridge: it is two-way lane with heavy potholes on the road with expansion joints on the bridge shown in Fig. 2a, d.

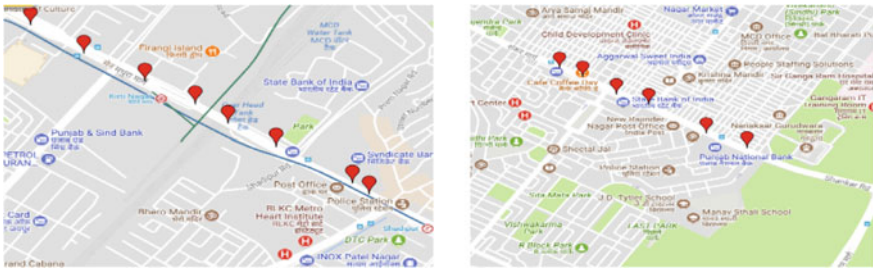
3 Potholes Detected

For Noida Sector 122, the red marks present on the map represents the potholes in that particular stretch. In Sector 122 Noida, the density of potholes is more and therefore this road is considered having a large density of potholes in the particular area Kirti Nagar. In Kirti Nagar, the density of potholes is somewhat similar as in

Sector-122 Noida stretch. Shankar road. In Shankar road, the density of potholes is limited as compared to Sector 122 Noida and Kirti Nagar it is fairly moderate. In Noida expressway stretch, there are hardly any potholes found in our observation and this can be termed as the smoothest road which we have taken for the work.



For Kirti Nagar bridge and Shankar road.



For Noida Expressway

3.1 Blacklisting

Certain types of road anomalies may produce high-energy output signals pothole like events but it is not necessary that they represent a road surface in disrepair. These include speed bumps, bridges with expansion joints and other equipment like paints, markings on the road. For this error we use blacklist contains these type of locations of these kind of anomalies and automatically remove detections in the final report submission. Blacklists are made for railroad crossings, speed breakers, paints, and markings [30–41].

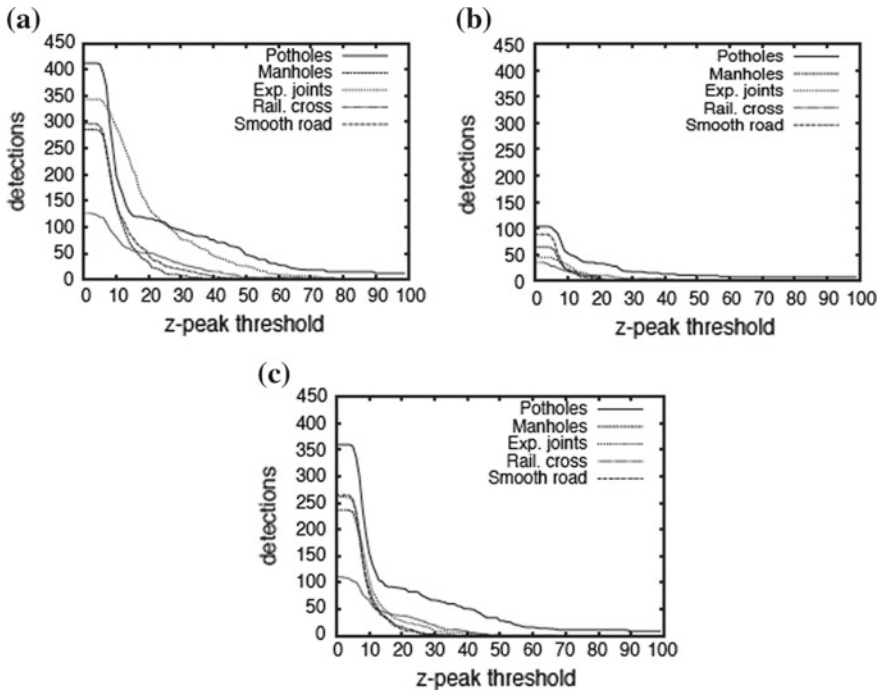


Fig. 3 **a** Up to and including z -peak filter, **b** up to and including xy -ratio filter with, **c** up to and including speed versus z ratio filter

3.2 False Negatives

There are many reasons sometimes potholes cannot be detected at a particular location may not be indicative on the smooth road. First is the error in the reading of the GPS, sometimes the pothole size is smaller than the typical size of pothole which is taken as a datum. Second, the drivers have the tendency to drive safely thereby avoiding potholes so chances of hitting a pothole is less than expected from an unbiased distribution based on road area [42–47]. The data which is collected by the pothole detection system eventually can be made a database for different people to access the data (Fig. 3).

4 Conclusion

Our system aims to provide the users with better information about the roads near their surroundings and their route of transportation. Despite hardware differences in terms of GPS accuracy, accelerometer sampling rate, and noise, we postulate that

accurate pothole detection is possible. Our system will help and safeguard people about the potholes and avoid fatal accidents which are caused by the potholes at high speed. We have explained the PDS system and associated methods to check the conditions of roads using a collection of sensor-equipped vehicles. SD uses the inherent mobility of the participating vehicles, opportunistically gathering data from vibration and GPS sensors, and processing the data and assesses the road conditions. We implemented the PDS system on taxis running across the NCR region. By the help of the output signals, we are able to detect the diverse road conditions. We collected data from different roads and by the help of the blacklisting process we were able to segregate between the potholes and other anomalies on the road.

References

1. Kumar R, Garg MP, Sharma RC (2012) Vibration analysis of radial drilling machine structure using finite element method. *Adv Mater Res* 472:2717–2721
2. Palli S, Koona R, Sharma RC, Muddada V (2015) Dynamic analysis of indian railway integral coach factory bogie. *Int J Vehicle Struct Syst* 7(1):16–20. <https://doi.org/10.4273/ijvss.7.1.03>
3. Sharma RC (2011) Ride analysis of an Indian railway coach using Lagrangian dynamics. *Int J Vehicle Struct Syst* 3(4): 219–224. <http://dx.doi.org/> <https://doi.org/10.4273/ijvss.3.4.02>
4. Sharma RC (2012) Recent advances in railway vehicle dynamics. *Int J Vehicle Struct Syst* 4(2):52–63. <https://doi.org/10.4273/ijvss.4.2.04>
5. Sharma RC (2013) Sensitivity Analysis of ride behaviour of Indian railway Rajdhani coach using Lagrangian dynamics. *Int J Vehicle Struct Syst* 5(3–4):84–89
6. Sharma RC (2013) Stability and eigenvalue analysis of an Indian railway general sleeper coach using Lagrangian dynamics. *Int J Vehicle Struct Syst* 5(1):9–14
7. Sharma RC (2016) Evaluation of passenger ride comfort of indian rail and road vehicles with ISO 2631-1 standards: part 1 - mathematical modeling. *Int J Vehicle Struct Syst* 8(1):1–6
8. Sharma RC (2016) Evaluation of passenger ride comfort of indian rail and road vehicles with ISO 2631-1 standards: part 2 – simulation. *Int J Vehicle Struct Syst* 8(1):7–10
9. Sharma RC, Palli S (2016) Analysis of creep force and its sensitivity on stability and vertical-lateral ride for railway vehicle. *Int J Veh Noise Vib* 12(1):60–76
10. Sharma RC, Palli S, Koona R (2017) Stress and vibrational analysis of an Indian railway RCF bogie. *Int J Vehicle Struct Syst* 9(5):296–302
11. Sharma SK, Sharma RC, Kumar A, Palli S (2015) Challenges in rail vehicle-track modeling and simulation. *Int J Vehicle Struct Syst* 7(1):1–9
12. Sharma SK, Kumar A (2016) Dynamics analysis of wheel rail contact using FEA. *Proc Eng* 144:1119–1128. <https://doi.org/10.1016/j.proeng.2016.05.076>
13. Sharma RC, Palli S, Sharma SK, Roy M (2017) Modernization of railway track with composite sleepers. *Int J Vehicle Struct Syst* 9(5):321–329
14. Sharma SK, Kumar A (2017) Impact of electric locomotive traction of the passenger vehicle Ride quality in longitudinal train dynamics in the context of Indian railways. *Mech Ind* 18(2):222. <https://doi.org/10.1051/meca/2016047>
15. Sharma SK, Kumar A (2017) Ride performance of a high speed rail vehicle using controlled semi active suspension system. *Smart Mater Struct* 26(5):55026. <https://doi.org/10.1088/1361-665X/aa68f7>
16. Sharma SK, Kumar A (2018) Ride comfort of a higher speed rail vehicle using a magnetorheological suspension system. *Proc Inst Mech Eng Part K: J Multi-body Dyn* 232(1):32–48. <https://doi.org/10.1177/1464419317706873>

17. Sharma SK, Kumar A (2018) Disturbance rejection and force-tracking controller of nonlinear lateral vibrations in passenger rail vehicle using magnetorheological fluid damper. *J Intell Mater Syst Struct* 29(2):279–297. <https://doi.org/10.1177/1045389X17721051>
18. Palli S, Koonar R, Sharma SK, Sharma RC (2018) A review on dynamic analysis of rail vehicle coach. *Int J Vehicle Struct Syst* 10(3):204–211
19. Sharma RC, Sharma SK, Palli S (2018) Rail vehicle modeling and simulation using lagrangian method. *Int J Vehicle Struct Syst* 10(3):188–194
20. Sharma SK, Sharma RC (2018) Simulation of quarter-car model with magnetorheological dampers for ride quality improvement. *Int J Veh Struct Syst* 10(3):169–173
21. Sharma SK, Kumar A (2016) The impact of a rigid-flexible system on the ride quality of passenger bogies using a flexible carbody In: Pombo J (ed) *Proceedings of the third international conference on railway technology: research development and maintenance stirlingshire UK 5–8 Apr 2016 Cagliari Sardinia Italy*. Civil-Comp Press 2016 87, Stirlingshire UK. <https://doi.org/10.4203/ccp.110.87>
22. Sharma SK, Chaturvedi S (2016) Jerk analysis in rail vehicle dynamics. *Perspect Sci* 8:648–650. <https://doi.org/10.1016/j.pisc.2016.06.047>
23. Sharma SK, Kumar A (2014) A comparative study of Indian and worldwide railways. *Int J Mech Eng Robotics Res* 1(1):114–120
24. Sharma SK (2013) Zero energy building envelope components: a review. *Int J Eng Res Appl* 3(2):662–675
25. Kumar P, Kumar A, Racic V, Erlicher S (2018) Modelling vertical human walking forces using self-sustained oscillator. *Mech Syst Signal Proc* 99:345–363
26. Kumar, P., Kumar, A., Erlicher, S (2018) A nonlinear oscillator model to generate lateral walking force on a rigid flat surface. *Int J Struct Stability Dyn* 18 (2): 1850020
27. Kumar P, Kumar A (2016) Modelling of lateral human walking force by self-sustained oscillator. *Proc Eng* 144:945–952
28. Kumar P, Kumar A, Erlicher S (2017) A modified hybrid Van der Pol-Duffing-Rayleigh oscillator for modelling the lateral walking force on a rigid floor. *Phys D* 358:1–14
29. Kumar P, Kumar A, Racic V (2018) Modelling of longitudinal human walking force using self-sustained oscillator. *Int J Struct Stability Dyn* 18 (6): 1850080
30. Mohanty D, Jena R, Choudhury PK, Pattnaik R, Mohapatra S, Saini MR (2016) Milk derived antimicrobial bioactive peptides: a review. *Int J Food Prop* 19(4):837–846
31. Samantaray D, Mohapatra S, Mishra BB (2014) Microbial bioremediation of industrial effluents. In: *Microbial biodegradation and bioremediation*. Elsevier, pp 325–339
32. Mohapatra S, Rath SN, Pradhan SK, Samantaray DP, Rath CC (2016) Secondary structural models (16S rRNA) of polyhydroxyalkanoates producing bacillus species isolated from different rhizospheric soil: phylogenetics and chemical analysis. *Int J Bioautom* 20(3):329–338
33. Mohapatra S, Samantaray DP, Samantaray SM, Mishra BB, Das S, Majumdar S, Pradhan SK, Rath SN, Rath CC, Akthar J, Achary KG (2016) Structural and thermal characterization of PHAs produced by *Lysinibacillus* sp. through submerged fermentation process. *Int J Biol Macromol* 93:1161–1167
34. Mohapatra S, Mishra R, Roy P, Yadav KL, Satapathi S (2017) Systematic investigation and in vitro biocompatibility studies on implantable magnetic nanocomposites for hyperthermia treatment of osteoarthritic knee joints. *J Mater Sci* 52(16):9262–9268
35. Bandekar D, Chouhan OP, Mohapatra S, Hazra M, Hazra S, Biswas S (2017) Putative protein VC0395_0300 from *Vibrio cholerae* is a diguanylate cyclase with a role in biofilm formation. *Microbiol Res* 202:61–70
36. Bandhu S, Khot MB, Sharma T, Sharma OP, Dasgupta D, Mohapatra S, Hazra S, Khatri OP, Ghosh D (2018) Single cell oil from oleaginous yeast grown on sugarcane bagasse-derived xylose: an approach toward novel biolubricant for low friction and wear. *ACS Sust Chem Eng* 6(1):275–283
37. Mohapatra S, Mohanta PR, Sarkar B, Daware A, Kumar C, Samantaray DP (2017) Production of Polyhydroxyalkanoates (PHAs) by *Bacillus* Strain isolated from waste water and its biochemical characterization. *Proc Natl Acad Sci India Sect B—Biol Sci* 87(2): 459–466

38. Sarkar MS, Segu H, Bhaskar JV, Jakher R, Mohapatra S, Shalini K, Shivaji S, Reddy PA (2018) Ecological preferences of large carnivores in remote, high-altitude protected areas: insights from Buxa Tiger Reserve. *India ORYX* 52(1):66–77
39. Mohapatra S, Sarkar B, Samantaray DP, Daware A, Maity S, Pattnaik S, Bhattacharjee S (2017) Bioconversion of fish solid waste into PHB using *Bacillus subtilis* based submerged fermentation process. *Environ Technol (United Kingdom)* 38(24):3201–3208
40. Mohanty DP, Mohapatra S, Misra S, Sahu PS (2016) Milk derived bioactive peptides and their impact on human health—a review. *Saudi J Biol Sci* 23(5):577–583
41. Sharma SK, Kumar A (2018) Multibody analysis of longitudinal train dynamics on the passenger ride performance due to brake application. In: Proceedings of the institution of mechanical engineers part K: journal of multi-body dynamics. <https://doi.org/10.1177/1464419318788775>
42. Sharma SK, Sharma RC (2018) An investigation of a locomotive structural crashworthiness using finite element simulation. *SAE Int J Commer Veh* 11(4):235–44. <https://doi.org/10.4271/02-11-04-0019>
43. Sharma RC, Sharma SK (2018) Sensitivity analysis of three-wheel vehicle's suspension parameters influencing ride behavior. *Noise Vib Worldw* 49(7–8): 272–280. <https://doi.org/10.1177/0957456518796846>
44. Sharma SK, Kumar A (2018) Impact of longitudinal train dynamics on train operations: a simulation-based study. *J Vib Eng Technol* 6(3):197–203. <https://doi.org/10.1007/s42417-018-0033-4>
45. Sharma SK, Saini U, Kumar A (2019) Semi-active control to reduce lateral vibration of passenger rail vehicle by using disturbance rejection and continuous state damper controller. *J Vib Eng Technol* 7(2). <https://doi.org/10.1007/s42417-019-00088-2>
46. Sharma RC, Goyal KK (2017) Improved suspension design of Indian railway general sleeper ICF coach for optimum ride comfort. *J Vib Eng Technol* 5(6):547–556
47. Sharma RC (2017) Ride, eigenvalue and stability analysis of three-wheel vehicle using Lagrangian dynamics. *Int J Veh Noise Vib* (1):13–25

Self-Driving Car Using Artificial Intelligence



Sahil Gupta, Divya Upadhyay and Ashwani Kumar Dubey

Abstract Self-driving autonomous vehicles are the solution for enhancing mobility intelligence related to driving. This project presents effective ways for implementation of a self-driving car. Proposed work is based on Artificial Intelligence, Computer Vision and Neural Networks. The proposed technology is implemented on a mini-robot car that was built from scratch, which uses Raspberry Pi and a camera as its core. The system built runs a script for complex task handling and sending appropriate commands to the vehicle. Image Processing techniques are also issued in the proposed system to identify various objects and traffic lights on the way. The system learns to autonomously navigate through reinforcement learning. Tensor Board is used to keep track of the working and efficiency of the trained Neural Network. The efficiency of the system is recorded at 96% as of now.

Keywords Autonomous driving · H-Bridges L239D · Neural networks

1 Introduction

In the past 50–60 years, the World of Technology; be it Information Technology, Software Engineering, Automation and Computation, Data Structures and Algorithms, Big Data Analytics, or Artificial Intelligence, it has emerged out tremendously and also is improving day by day at a very rapid pace. Automation is the topic that is of broad and current interest. It is a subject that is going under intense study and receiving close reviews worldwide.

S. Gupta · D. Upadhyay (✉)
Computer Science and Engineering, Amity University, Noida, India
e-mail: upadhyay.divya@gmail.com

S. Gupta
e-mail: guptasahilonweb2@gmail.com

A. K. Dubey
Electronics and Communication Engineering, Amity University, Noida, India
e-mail: dubey1ak@gmail.com

Automation is simply the technique and method of making a system or a subject control itself automatically without any interference or help provided by the human. Automation makes our lives easier and comfortable as it helps us by performing the task at hand repeatedly.

One area of automation that is under extreme popularity nowadays is “Autonomous Vehicle”. Autonomous vehicle refers to the vehicle that can control itself to drive and navigate efficiently on the road avoiding obstacles and collisions, giving the user a safe traveling experience without any interference, input or help provided by the human. Many reputed organizations like Google, Tesla, Volvo, etc., are doing the necessary research and have started significant work to this dream of fully automated vehicles into reality.

As Autonomous Vehicles are much more complex and difficult than other simple jobs of automation such as home automation, auto-surveillance for security purpose or automation systems used in manufacturing industries for manufacturing and production of goods, it has always been a dream of driving autonomously with the help of a computer. But with the help of advancement and development of various technologies, work on this field of autonomous driving is now at a considerable level.

Also, the number of vehicles has now arrived at a population of more than a billion. According to a recent survey, there are approximately 1.37 billion vehicles around the world that are on road.

With no doubt, these many vehicles will only produce an enormous and devastating amount of pollutants that are dangerous to every living species present on this planet. A most recent example is pollution levels of India especially in Delhi, present winter (2017), where pollution levels reached 10 times the alert value. Not only this, but such a huge amount of vehicle population would require a huge amount of fuel and oil that may reach extinction levels if we continue harassing the resources that nature has provided us. According to a seminar at UC Davis Institute of Transportation, 2.0 billion vehicles would require at least 120 million barrels of oil per day which is 87 million more than the present requirements.

Hence, there is a desperate need for a solution which are autonomous vehicles that will not only control these variables but also will make our lives simpler and easier. With autonomous vehicles on the road, there will be less need for individual cars which could be replaced by autonomous cabs; saving time, money, and resources.

The autonomous vehicle uses a diverse range of equipment and software to work in a most efficient manner. Use of sensors, radar, lasers, GPS, cameras, microcomputers such as Arduino, Raspberry Pi, etc. is frequent when talking about autonomous vehicles (Figs. 1 and 2).

The main obstacle to autonomous driving is to detect the surrounding environment of the vehicle. In technical terms, this is called object detection and tracking. Object detection can be done using sensors as well as cameras. A sensor is a device that detects variations that take place at different intervals of time; whether in terms of physical, electrical or any other quantity. It then generates an output as a response to the change in that quantity. This response is mainly in the form of an electrical or optical signal. Thereby, sensors are ideal equipment for autonomous vehicles as they would help in detection of the objects around it like vehicles, people, etc. In

Fig. 1 Different components used for vehicles

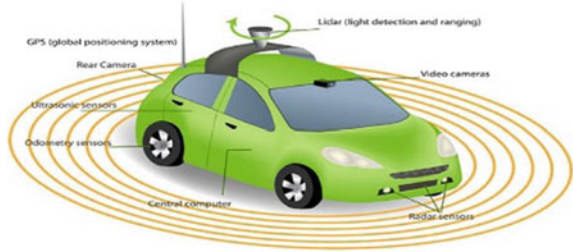
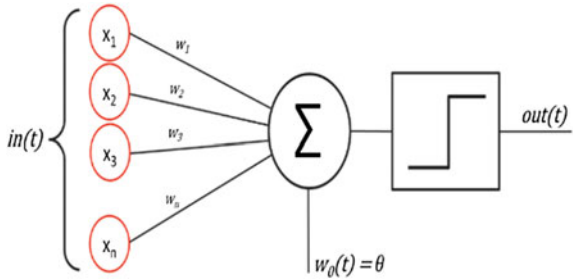


Fig. 2 Neural network layer



fact, the sensible use of these sensors is all one autonomous vehicle needs. Some of the sensors also collect relevant critical information from past input and output so that improvement can be made accordingly. Also, the implemented decision-making logic can never generate desired output against all the possible complex scenarios that an autonomous vehicle may encounter with. This is where we need to implement an independent thinking system to the system and this is done using Artificial Intelligence and Machine Learning. AI enables the system to think rationally, differentiate and recognize patterns, perform complex computations and predict the output independently based on the data relayed to the system. Neural Networks are what makes Autonomous vehicles possible and efficient.

2 Literature Review

An ANN [1, 2] can recognize various patterns in data and learn from them. They are often used for purposes like Classification, Regression, and Segmentation. The conversion of data into a numerical form is required before feeding it to the Neural Network. ANN [3] consists of layers which are categorized as Input Layer, Hidden layer, and Output Layer. Each layer consists of several independent neurons which we often call as Nodes in general. Each Neuron is connected or linked to the Neurons in the adjacent layer with a unique weight. In an Artificial Neural Network, everything starts from raw input data. This data in which each subset of data has unique weights.

Basically, it is the first layer of the Neural Network, i.e., Input Layer. Each original input value times the weight attached to it is passed further for the summation.

Self-driven cars are expected to obey traffic rules [4]. A good example [5] of self-driven car is “love bug”, an “knight riders” in TV series. The machine should also be able to differentiate between the expression and facial expressions [6]. As highlighted in a recent workshop on conversational agents [7], the new wave of mobile and ubiquitous virtual assistants is connected to the ongoing shift from touch to speech-based interfaces (i.e., conversational interfaces) and to the incorporation of these agents in “smart” devices such as smart watches, smart televisions and, of course, smart cars (not necessarily self-driving ones). In relation to the CES edition 2017, BBC News reported that “car makers choose virtual assistants” [8].

Thermal sensors, on the other hand, uses heat detection to distinguish between objects. A thermal camera is the best example of it as it generates a map of heat signatures and separates one object from another. While Thermal sensors being of great use in military intelligence, they are not suitable for autonomous [9–12] vehicles because of inaccuracy and longer delay for processing the thermal images and analyzing them. Chemical sensors are used to fetch information about the chemical composition of the environment.

Most sensors become inaccurate in changing weather conditions also. Appropriate mechanisms are still under work for handling the change in weather and relaying appropriate instructions to the vehicles. These sensors work in collaboration with the Electronic Control Unit of the vehicle, that in turn is associated with the actuators of the system. Basically, it consists of all the controls of the vehicle like a braking system, steering, acceleration, and deceleration.

On the other hand, big names like Google, Tesla, Uber are currently using LIDAR sensor for implementing Self-Driving Vehicles. Basically, it is a light pulse sensor. Light pulse sensors are almost the same as ultrasonic sensors but they use light pulses instead of sound waves. These light pulses are emitted by the emitter which is extremely powerful and are reflected to the receiver after they hit any object in the path (Figs. 3 and 4).

LIDAR stands for Light Detection and Ranging which is based on the concept of measuring the time it takes for the small burst of the light pulse to reach back to the receiver after being hit by any obstacle in the way of the vehicle. It consists of a light/laser gun which is also called a LIDAR gun that emits a short burst of concentrated light.

Now, how this interface is set up is also important. We can use minicomputer like Arduino, Raspberry Pi, etc., for processing of the data received sent by the sensors and also interfacing the sensors to the actuators which control the vehicle. We can implement GPS in the vehicle to route it and navigate to the desired location. GPS modules can be connected to the mentioned minicomputers to fetch the current location of the vehicle and destination can be input by the user to route a navigational path.

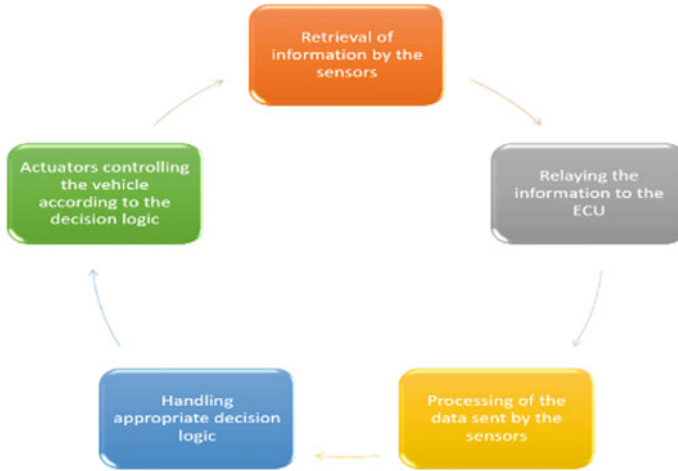
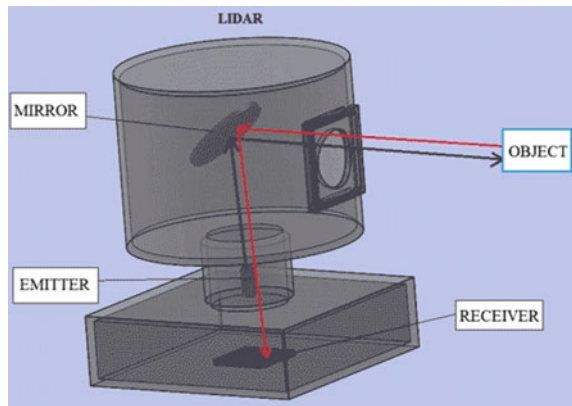


Fig. 3 Flow of information

Fig. 4 LIDAR sensor



3 Methodology

A robot car was designed which consisted of capacitors, potentiometers, 4 DC Motors connected to each of the four wheels. H-Bridge L239D was used for controlling the motors. Following is the diagram of connections of H-Bridge (Fig. 5).

The robot car built from scratch was integrated with Raspberry-Pi, Pi Camera, and Ultrasonic Sensor. In order to keep the weight of the vehicle as low as possible, we used two metallic sheets interconnected to form a robot chassis. We glued Ultrasonic sensor to the front of the robot and mounted the Pi Camera at some height with the help of some standoffs. Direct Power of 5 V to the Raspberry Pi was given through a power bank whereas the power required for the motors to work was given separately with a 8 V 1.5 mAh battery.

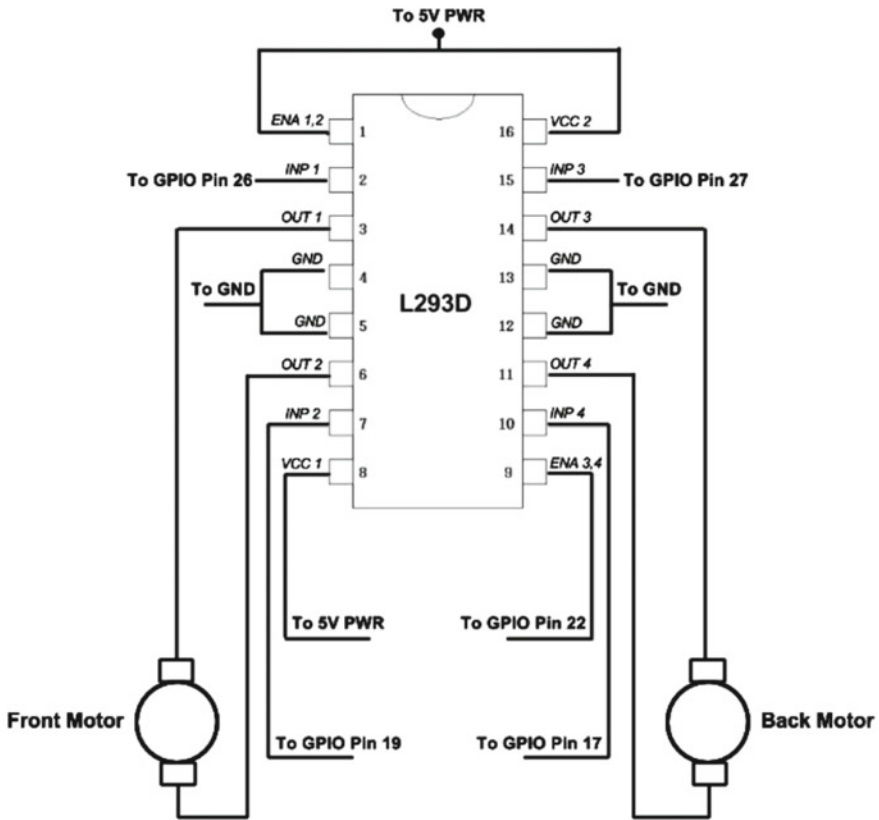


Fig. 5 H-Bridge L293D

All the controlling is done by Raspberry Pi. All the commands that the robot is performing are output to the terminal. The Circuit is made on General Purpose PCB (Figs. 6 and 7).

First, we set up the Raspberry-Pi. Now to do so, the first step is to burn the Raspbian OS to the SD Card. We used Win32DiskImager for this. We formatted SD Card in FAT and then burned Raspbian OS on SD Card. After writing the OS, two partitions are made, i.e., /boot directory and empty space. Now to access Pi, we have used DHCP(Dynamic Host Configuration Protocol) for setting up the connection between PC and Pi. For this, we used a number of software available on the internet like Putty, Advanced IP Scanner, VNCViewer. We created an empty file called SSH in the /boot directory. Then after inserting the card to the Raspberry Pi, we connected the Pi with a router having active internet connection for downloading various libraries and modules like OpenCV, NumPy, pandas which will be used throughout the project. We used Advanced IP Scanner to retrieve the IP address of the Pi. Then this IP was passed to Putty for logging into the Pi and change the configurations according to the

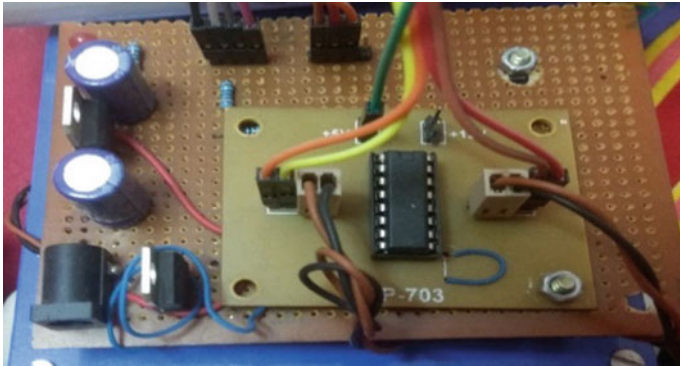


Fig. 6 Circuit for H-Bridge

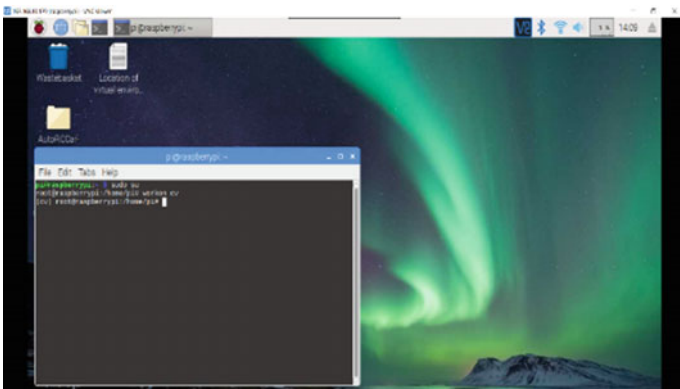


Fig. 7 Virtual environment

needs. For example: enabling the camera, enabling VNC, etc. Once all the settings are made, we are now ready to access Pi through VNCViewer. We then created a Virtual Environment for the coding purpose and decided to work on it only.

The programming languages and libraries used for the project are Python [13, 14], OpenCV, NumPy, Pandas, PiCamera, PyGame, PIL, Scipy, Sigmoid.

The H-Bridge controls the wheels; two motors on left and two motors on the right side are controlled by L293D using IN1 and IN2 pins. The robot can move in any direction just like a tank. Though there are six defined values for the robot namely Forward, Backward, Left, Right, Idle, and Reverse but the project currently does not use Reverse functionality.

The Neural Network used is CNN (Convolutional Neural Network). The collection of data for the training of the Neural Network was done by controlling the robot with keyboard keys and simultaneously capturing the video frames. Separate folders of each unique hit key were made and the video frames were added to the particular labeled key.

4 Implemented Work

Robot Car as discussed above was made from scratch. The data which has to be fed to the Neural Network for training purpose was done through controlling the robot car using keyboard arrow keys. A separate python script handled this task, which basically made use of PyGame module. The picture frame and corresponding key hit were recorded in separate folders. An arbitrary path was laid down using sheets of paper that acted in a way similar to road lanes.

The collected data was used and the neural network was trained with a training script which uses 50 hidden layers. The network was trained for a considerable amount of time, and then the trained model was obtained. The model was tested through a testing script, the robot car successfully navigated on the path with varying degree of turns and cuts (Figs. 8 and 9).

Along with this, we implemented Obstacle Detection, Traffic Light Detection, and Road Sign Detection techniques also. For Obstacle detection, proximity sensors

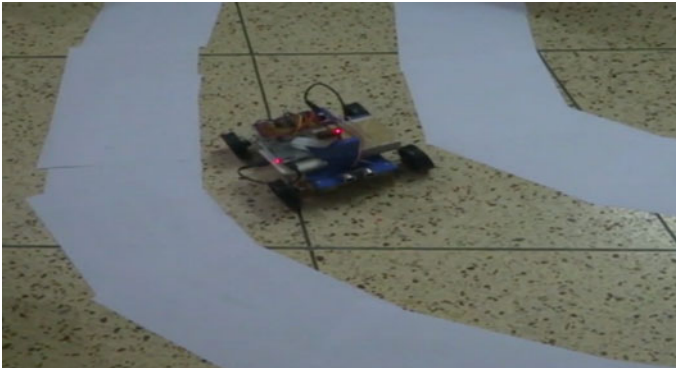


Fig. 8 Autonomous mode

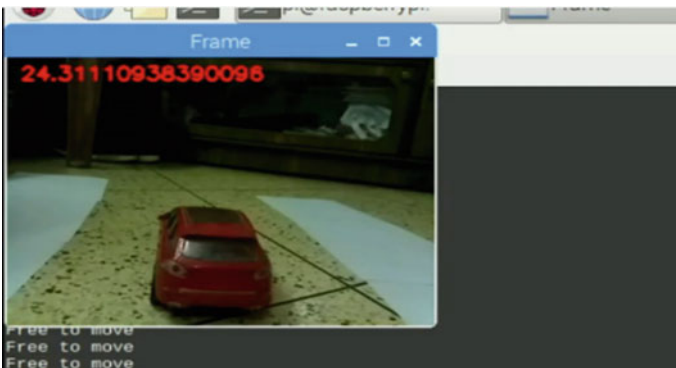


Fig. 9 Obstacle detection

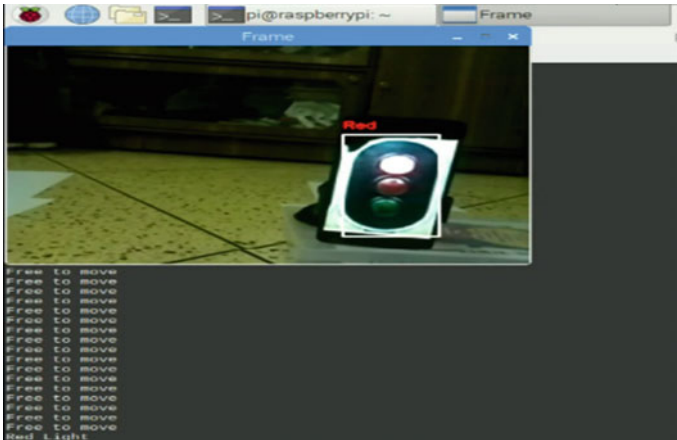


Fig. 10 Red light detection

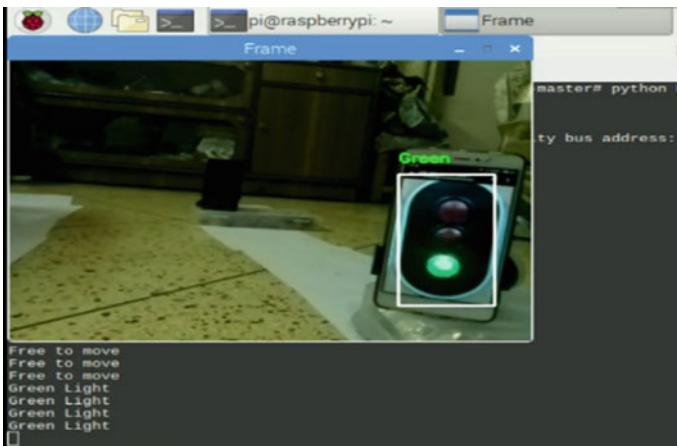


Fig. 11 Green light detection

are best and Traffic Light Detection and Road Sign Detection are also quite possible using different Image Processing Techniques.

For detecting obstacles, we installed an Ultrasonic Sensor on the front of the vehicle. The sensor continuously emits sound waves which get reflected back to its receiver side if an object is detected in its front. We programmed the robot to maintain a distance of 25 cm with the vehicle in front of it. In this way, there is no chance of collision of the vehicle. The robot will immediately stop if the read value from the sensor reaches any less than 25 cm. Also, this particularly can help tremendously in traffic jam scenarios as the vehicles will maintain a particular gap with each other leading to a smoother flow of traffic.

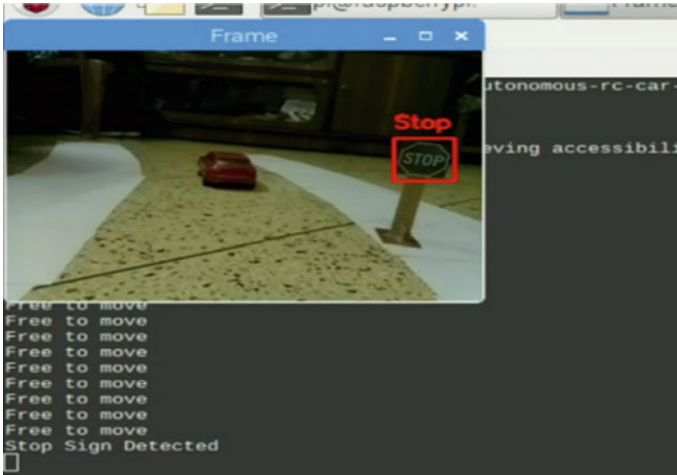


Fig. 12 Road sign detection

For traffic light detection and road sign detection, I used “Haar Cascade Classifier”. We used OpenCV for this. We collected different positive and negative samples of the traffic light and stop sign. Positive samples are the pictures of the object you want to detect and negative samples are the ones which might appear to be same as the object you want to detect but in reality, it is something else. We put the positive samples of both separately and formed a vector file for both. The samples have to be of equal size, apparently small and should contain only the object and nothing else for effective detection. After the training is done, we get an XML file which contains the numeric data for detecting the particular object (Figs. 10, 11 and 12).

5 Results and Discussion

Robot car was completely made from scratch allowing to implement and use the hardware to best suitable way. We kept the log files for keeping track of the efficiency of the neural network. TensorBoard was used for doing this. The neural network trained reached an accuracy of 96% which can be improved further. The analysis of loss for the neural network reached almost vanishing zero. (Figs. 13 and 14).

The model presented is also scalable to real-world vehicles with minimum changes to its core. We just have to change the input data that is passed to the neural network. The controls of an actual vehicle can be easily integrated with the system to fetch the different driving actions performed by the driver in the vehicle. These sets of data can then be fed to the network and trained. Also, high-quality cameras can be used for better performance of the system.

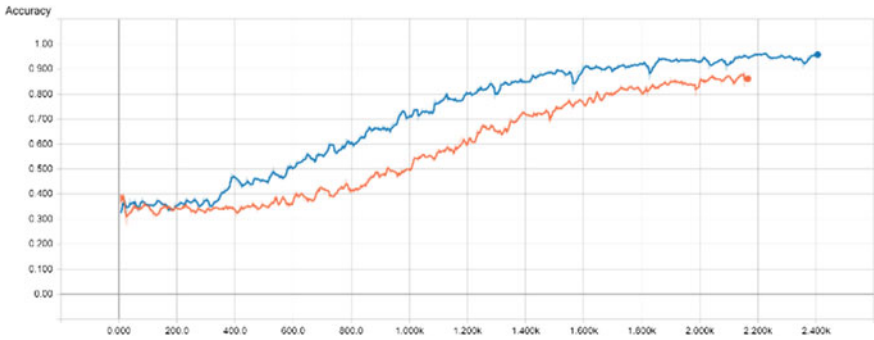


Fig. 13 Analysis of the accuracy of the neural network

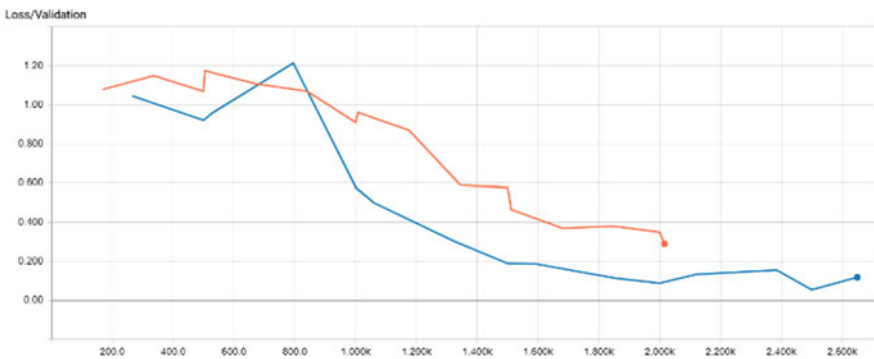


Fig. 14 Analysis of loss of neural network

6 Conclusion

Autonomous vehicles are a major milestone to the evolution of mankind. Despite having some of the drawbacks, they have more advantages which lead to a better future. This technology is still under research and organizations are still working on it but is very much possible. Reliability of decision-making and safety of vehicles strongly depends upon the quality of the sensors and the self-localization and mapping process. Also, real-time abstraction processes are needed to be developed quickly to recognize environmental situations for decision-making.

There are various advantages of implementing this which are as follows:

- **Better Safety:** The Main reason for accident leading to deaths and injuries is simply human error, be it in terms of delayed reflex time, distractions, aggressive driving, etc. All of this can be reduced to a significant amount by replacing the human driver with a computer that has faster reflex time and no distracted or aggressive driving scopes.

- Welfare of the society: Autonomous vehicles can reduce labor costs, can free the commuters from driving and traffic chaos resulting in the availability of more time for other important work. The vehicular and traffic authorities would face less difficulties in managing the traffic flow because of the data provided by the vehicles. There will be a reduced need for traffic police and road signage.
- Lesser traffic: It would include higher speed limits, smoother travel experience, increased roadway capacity and decreased traffic congestion, due to decreased need for safety gaps and higher speeds.
- Better economy and resources: Fuel consumption would be significantly reduced thereby saving our natural resources. Also, low consumption of fuel would result in decreased expenses on it. Maintenance of vehicles would require less time, effort and money.
- Reduced space for parking: Autonomous vehicles could decrease the number of vehicles owned individually and replace them by cabs and other pooling services. This would significantly reduce the need for parking space of vehicles, freeing the space for various other purposes. This would, in turn, have a positive impact on the environment and decreasing pollution levels as the number of vehicles would be decreased.

References

1. Cunningham M, Regan M A (2015) Autonomous vehicles: human factors issues and future research. In: Proceedings of the 2015 Australasian Road Safety Conference (ARSC 2015) Gold Costs, Australia, pp 14–16, Oct 2015
2. Brown B (2016) The social life of autonomous cars. *Computer* 50 (2): 92–96, Feb 2017. In: W Knight, New self-driving car tells pedestrians when it's safe to cross the street, MIT Technology Review, Aug 2016
3. Mishra M, Srivastava M (2014) A view of artificial neural network. In: 2014 International Conference on Advances in Engineering & Technology Research (ICAETR - 2014), Unnao, 2014, pp 1–3
4. Johnson BD (2016) Science-fiction and the coming age of sentient tools. *Computer* 49(6):95–97
5. Kröger F (2016) Automated driving in its social historical and cultural contexts autonomous driving. Springer, Berlin, pp 41–68
6. Greenemeier L (2017) When your self-driving car wants to be your friend too. *Sci Amer*
7. Porcheron M, Fischer JE, McGregor M, Brown B, Luger E, Candello H, O'Hara K (2017) Talking with conversational agents in collaborative action. In: Companion of the 2017 ACM conference on computer supported cooperative work and social computing, pp. 431–436
8. Baraniuk C (2017) CES 2017 car-makers choose virtual assistants. BBC News, Jan 2017, [online] Available <http://www.bbc.com/news/technology-38526807>
9. Cunningham M, Regan MA (2015) Autonomous vehicles: human factors issues and future research. Proceedings of the 2015 Australasian Road Safety Conference (ARSC 2015) gold costs (Australia), Oct 2015, pp 14–16
10. Brown B (2016) The social life of autonomous cars. *Computer* 50 (2): 92–96, Feb 2017. In: Knight W (ed) New self-driving car tells pedestrians when it's safe to cross the street, MIT Technology Review, Aug 2016
11. Porcheron M, Fischer JE, McGregor M, Brown B, Luger E, Candello H, O'Hara K (2017) Talking with conversational agents in collaborative action. In: companion of the 2017 ACM

- conference on computer supported cooperative work and social computing, Feb 2017, pp 431–436
12. Baraniuk C (2017) CES 2017: car-makers choose virtual assistants. BBC News, Jan 2017, [online] Available <http://www.bbc.com/news/technology-38526807>
 13. JAN ERIK SOLEM (2012) Programming computer vision with python
 14. Downey AB (2015) Think Python: how to think like a computer scientist. Green Tea Press, Needham
 15. How Tesla's Autonomous Car Work (2016–10). Retrieved from <http://www.xataka.com/vehiculos/para-pasar-del-autopilot-a-la-conduccion-autonoma-en-los-coches-de-tesla-hace-falta-hardware>

Mitigation of Risk in CNG Station Using Fuzzy-Integrated Technique



Priyank Srivastava, Mohit Agarwal, Aditya Narayanan, Manik Tandon and Mridul Tulsian

Abstract In a CNG refueling station, identification of the risks associated with the complex operating systems and its prioritization is essential. This identification and prioritization will result in a proper understanding of the system by reliability analyst and maintenance engineer so as to frame appropriate maintenance planning. A fuzzy rule-based inference model taking into account the failure modes for risk ranking in FMEA to manage risks and make maintenance decisions is applied to a CNG station in this paper. One of the methods used for risk analysis is FMEA (Failure Mode and Effect Analysis) where we determine an RPN (Risk Priority Number) by multiplying the feature scores that are obtained from the degree of probability of occurrence (*O*), severity (*S*) and detection (*D*) without taking into consideration the relative importance of the factors. In the fuzzy approach, we use a linguistic variable for calculation of RPN. This method is so preferred because it provides us with unbiased judgment. The results obtained from this study show that the ambiguity in the conventional FMEA can be solved with a fuzzy approach, and conveniently discover potential failure modes and help in risk and reliability analysis of the system.

Keywords Risk · Fuzzy · CNG · FMEA

1 Introduction

With a growing population of over 7.6 billion, the world is facing new challenges every day like environmental pollution and its preservation. They have implemented stern norms and policies for emission of gas, through the burning of fuels. As a result, a need for using fuels with less Carbon Dioxide (CO₂), Sulfur Dioxide (SO₂), and particulate matter (PM) are necessitated. The best alternative fuel that has low gas emissions and PM is Compressed Natural Gas (CNG). Using CNG reduces

P. Srivastava (✉)
National Institute of Technology, Kurukshetra, India
e-mail: psrivastava5@amity.edu

P. Srivastava · M. Agarwal · A. Narayanan · M. Tandon · M. Tulsian
Amity University, Noida, India

© Springer Nature Singapore Pte Ltd. 2019
M. Kumar et al. (eds.), *Advances in Interdisciplinary Engineering*, Lecture Notes in Mechanical Engineering, https://doi.org/10.1007/978-981-13-6577-5_50

greenhouse effect significantly as almost 26% CO₂ emission is reduced as compared to that by using gasoline. As a result, there is a reduction in environmental pollution. CNG being lighter than air, poses a threat of leakage through faulty subcomponents of dispensing station. Since CNG is highly inflammable, its leakage can lead to explosion hazard at the station. This can affect the process, system components, personals, people, and monitory functions. Therefore, a CNG dispensing station requires proper maintenance layout. A risk is a condition of exposure to danger that is initiated by a failure event. Risk analysis is essential to enhance the safety of operating systems, to find the probability of failure of a component and to implement maintenance planning. There are various methods of risk analysis and prioritization of risks. FMEA is a technique which uses a proactive approach to reduce facility, human life, and economical loss in case of a failure. Since it is based on different opinions by different experts, there is a chance of ambiguity or biases in judgment which leads to uncertainty. The fuzzy methodology is used to overcome this uncertainty. A case of CNG dispensing system has been taken under application of Failure Mode and Effect Analysis and Fuzzy FMEA for exemplifying the projected framework.

2 Literature Review

FMEA is one of the most popularly used tools to diagnose the probable possible failure in process or products. In 1963, NASA formulated a formal system for the reliability needs later in 1977, Ford Motors took this technique into use. FMEA has been used to improve the quality of products in the Iranian Oil Company [1]. The conventional FMEA is prone to the uncertainties and biases, this is due to the imprecise and vague judgments given by the experts in the cross-functional team. In order to reduce these drawbacks, various researches are under process to increase the efficiency of FMEA. The use of the fuzzy methodology in FMEA helps in reducing some the limitations of FMEA, i.e., the RPN number was not able to exactly depict the severity of the failure modes due to the various judgmental skills and knowledge of the operators. Fuzzy methodology helps to remove uncertainty from the analysis. It uses the minimum and maximum inference, fuzzification and then defuzzification of risk analysis of failure modes and then prioritizing them according to fuzzy RPN number is used for removing uncertainty [2]. Fuzzy integrated FMEA has been used in various application, e.g., FMEA assessment of engine system [3], improving purchasing process in public hospital [4], the risk of water treatment plant [5], risk assessment of water treatment plant [6], and failure analysis of transmission system [7]. The major advantage of Fuzzy FMEA over traditional FMEA are as follows:

- Fuzzy FMEA is comparatively faster and more reliable with less ambiguity.
- Data are recorded in natural language, as fuzzy logic is based on human communication.

3 Research Methodology

The research methodology for the current study is shown in Fig. 1.

Fig. 1 Research methodology

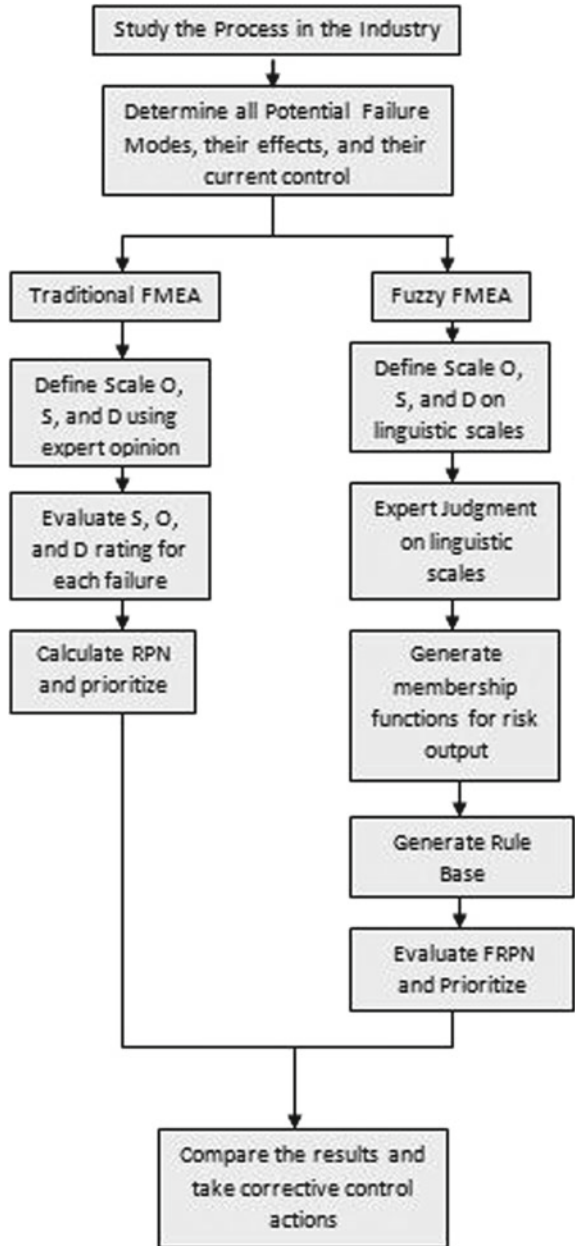


Table 1 Fuzzy linguistic scale for variable

Rating	Meaning	Severity (<i>S</i>)	Occurrence (<i>O</i>)	Not Detection (<i>D</i>)
1	Almost none	No breakdown of any component	Failure is very unlikely to happen	Detected 9/10 time
2, 3	Low	Minor breakdown of the component which can be fixed with some adjustments	These failures are relatively rare	Detected 7/10 times
4, 5, 6	Medium	Breakdown of components which can be replaced without any harm for the whole machine	Very occasional	Detected 5/10 times
7, 8	High	Permanent damage of component but n harmful for the machine but not people	More frequent failures	Detected 2/10 times
9, 10	Very high	Hazardous/permanent damage of the component which may cause harm to people	These are common failures	Detected 0/10 times

We used two quality tools in our research methodology where the first one is Failure Mode and Effect Analysis (FMEA). In FMEA, each failure is denoted in mode points with reference to Table 1. The integral values of Occurrence, Severity and Not Detection helps in calculating the Risk Priority Number (RPN) which is;

$$RPN = O \times S \times D \tag{1}$$

To evaluate the *O*, *S*, and *D* ratings, the opinions of three experts were considered and a scale was drafted. The experts gave individual ratings based on their experience and knowledge. Average of all these ratings were evaluated and charted as shown in Table 1. Risk prioritization of each is done by calculating the RPN values of different failure modes. However, there lies a certain ambiguity which poses a threat in prioritization as FMEA does not consider the interrelation between the factors for determining the RPN. Thus, fuzzy logic is used to remove the ambiguity in the system.

After FMEA, the second tool used is Fuzzy FMEA. In Fuzzy FMEA, a linguistic variable is used to mark failure modes on the basis of three parameters. A triangular membership function is used to define the *O*, *S*, and *D* ratings. This step is called fuzzification (Fig. 2).

The “Min-Max” method is used to evaluate our research which is also known by the term called “Mamdani” method. A FIS (Fuzzy Inference System) was created

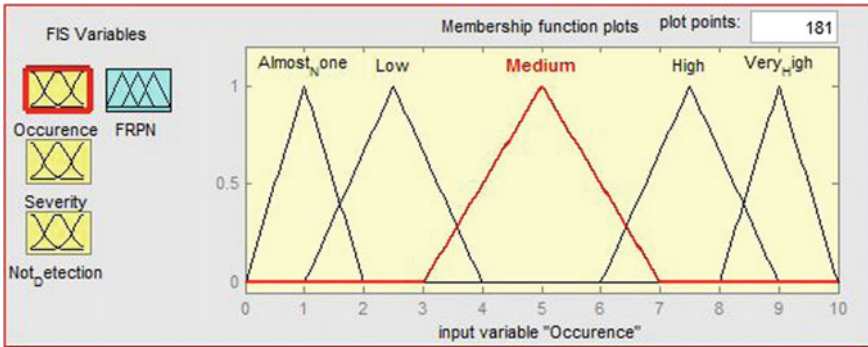


Fig. 2 Membership values for input variables

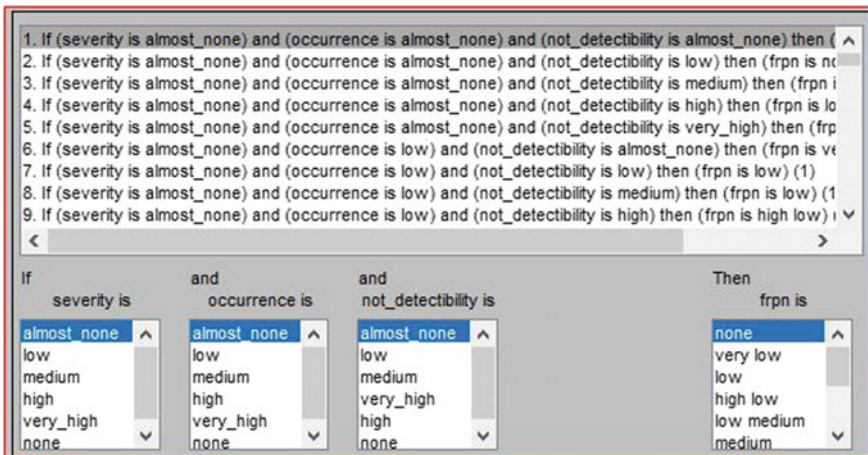


Fig. 3 Fuzzy rule base

using MATLAB R2013a, which was used in the fuzzy FMEA. A rule base was formed with the help of an expert’s review which relates the linguistic variables and input from the operators. This increased the accuracy of the investigation. Out of the 125 rules in the rule base, only 68 were used for the final evaluation. The rest of the rules were eliminated because they produced the same result for different combinations of *O*, *S* and *D* values. The figure (Fig. 3) containing the rule bases is shown.

Centroid method is used to defuzzify and restore the linguistic terms to values which are used to calculate the Fuzzy Risk Priority Number (FRPN). Prioritization of the individual failure modes is done using the FRPN values. The software used is MATLAB-2013a for both the processes (Fuzzification and Defuzzification) by integrating the membership functions. The comparison between RPN and FRPN is shown in Table 2 and also illustrated using a graph in Fig. 4.

Table 2 Comparative table for FRPN and RPN

S. No.	Subcomponents	Cause of failures	RPN	Rank	FRPN	Rank
MS1	Metering skid	Suction line filter choke	48	3	3	4
MS2		Slam shut of valve not opening	8	7	5	2
MS3		Flow sensor fail	4	8	5	2
MS4		Display error	3	9	0.75	5
MS5		Display hang	32	4	3	4
MS6		Transmitter failure	20	5	5	2
MS7		NRV valve failure	50	2	5	2
MS8		Temperature gauge failure	8	7	3	4
MS9		Pressure gauge failure	9	6	4	3
MS10		Regulator malfunction	90	1	6	1
CS1	Compressor	Inlet filter choke	80	7	5	2
CS2		Internal pipe leakage	630	1	5	2
CS3		Internal valve failure	504	2	8	1
CS4		Insufficient coolant	7	11	0.75	5
CS5		Pressure gauge failure	3	12	2	4
CS6		Tank leakage	108	4	5	2
CS7		Tank corrosion	90	5	5	2
CS8		Cable wornout	54	8	4	3
CS9		Display problem	8	10	4	3
CS10		PLC Failure	84	6	5	2
CS11		Gasket damage in engine	180	3	5	2
CS12		Insufficient engine oil	16	9	5	2
DS1	Dispenser	Nozzle failure	100	3	5	2
DS2		Fill and vent hoses leakage	126	2	6	1
DS3		Failure of motherboard	60	5	6	1
DS4		Pressure regulator valve failure	150	1	5	2
DS5		Flow sensor failure	60	5	6	1
DS6		Pressure safety valve failure	20	8	5	2
DS7		Outlet block failure	18	9	5	2
DS8		Display error	40	6	5	2
DS9		Safety check error	25	7	5	2

(continued)

Table 2 (continued)

S. No.	Subcomponents	Cause of failures	RPN	Rank	FRPN	Rank
DS10		Probe spring failure	72	4	5	2
PP1	Priority panel	Internal pipe leakage	560	1	5	1
PP2		Air filter choke	48	3	5	1
PP3		Isolation valve leakage	42	4	5	1
PP4		PLC failure	8	6	0.75	3
PP5		SOV valve failure	72	2	5	1
PP6		Pipe choke	18	5	3	2
PP7		Actuator failure	48	3	5	1
CA1	Cascade	Plug leakage	120	1	5	1
CA2		Cylinder wall failure	81	3	5	1
CA3		Tank leakage/tank corrosion	90	2	5	1
CA4		Burst disc failure	90	2	5	1

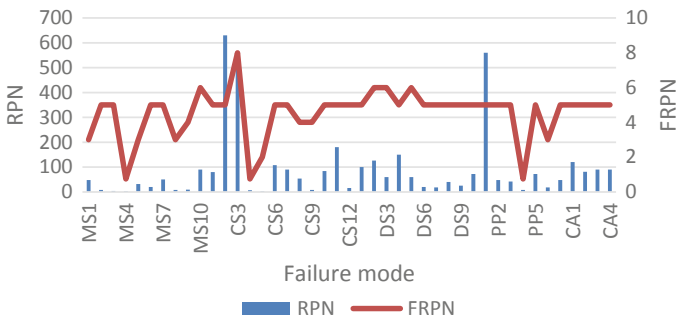


Fig. 4 Comparison graph for RPN and FRPN

4 Results and Discussion

Various failure modes have been studied and the Risk Priority Number has been elucidated by using both traditional FMEA as well as the Fuzzy FMEA. At this point, the issue is to reduce/prevent the risk conditions in CNG filling stations where the subcomponents are metering skid, compressor, dispenser, priority panel, and cascade.

A total of 43 failures are recorded for analysis of risk and the results are as follows:

1. In metering skid 4 failure modes are above the average RPN value i.e. 27.2 when referred by traditional FMEA and 6 failure modes are above the average FRPN value, i.e., 3.975 when referred by the Fuzzy FMEA.

2. In compressor 3 failure modes are above the average RPN value, i.e., 147 when referred by traditional FMEA and 8 failure modes are above the average FRPN value, i.e., 4.479 when referred by the Fuzzy FMEA.
3. In dispenser 4 failure modes are above the average RPN value, i.e., 67.1 when referred by traditional FMEA and 3 failure modes are above the average FRPN value, i.e., 5.3 when referred by the Fuzzy FMEA.
4. In priority panel 1 failure modes are above the average RPN value, i.e., 113.714 when referred by traditional FMEA and 5 failure modes are above the average FRPN value, i.e., 4.107 when referred by the Fuzzy FMEA.
5. In cascade 1 failure modes are above the average RPN value, i.e., 95.25 when referred by traditional FMEA and 4 failure modes are above the average FRPN value, i.e., 5 when referred by the Fuzzy FMEA.

5 Conclusion

Traditional FMEA and Fuzzy FMEA approach have been applied to a CNG dispensing station in this work. The failure modes have been found out and analyzed for their root causes, effects and detection methods. The RPN and FRPN number have been calculated, with the input analyzed and discussed from the experts. The use of linguistic terms allows experts to provide significant value for the risk factors that is considered. Thus, the identified failure modes are not omitted (owing to a low RPN) when taken into account. In accordance with the traditional FMEA 13 failures and 26 failures through fuzzy FMEA are found above the average value of RPN.

References

1. Hekmatpanah M, Shahin A, Ravichandran N (2011) The application of FMEA in the oil industry in Iran: the case of four litre oil canning process of Sepahan Oil Company. *Afr J Bus Manage* 5(7):3019
2. Bowles JB, Pelaez CE (1995) Fuzzy logic prioritization of failures in a system failure modes, effects and criticality analysis. *Reliab Eng Syst Saf* 50(1):203–213
3. Xu K, Tang LC (2001) Fuzzy assessment of FMEA for engine systems. *Reliab Eng Saf Syst* 2(1):1–4
4. Srivastava P, Agarwal M, Narayanan A, Tandon M, Tulsian M (2018) Risk analysis of water treatment plant using fuzzy integrated approach. Springer, Gurgaon
5. Agarwal M, Narayanan A, Tandon M, Tulsian M (2018) Risk prioritization in a gas power plant using Fuzzy inference system. IEEE, Noida
6. Kumru M, Kumuru PY (2013) Fuzzy FMEA application to improve purchasing process in a public hospital. *Appl Soft Comput* 12(1):721–733
7. Dilbagh P, Jamwal U, Srivastava P, Kamboj K, Sharma R (2018) Fuzzy methodology application for failure analysis of transmission system. *Int J Math Oper Res* 12(2):220–237

Role of Additives in Enhancing the Performance Characteristics and Stability of Biodiesel—A Review



Akshay Rasal, Sarthak Saxena, Naveen Nair, Mohit Vikal, Khushbu Yadav and Gaurav Dwivedi

Abstract Biodiesel is a renewable, nontoxic environment-friendly fuel produced by biological processes, derived directly or indirectly from plants, animals, agricultural, domestic, or industrial wastes. It has lower carbon emissions and higher cetane number. Although biodiesel is a clean renewable source of energy, due to its chemical instability, there are a few drawbacks related to its performance and storage like poor heat generation capacity, poor efficiency, high viscosity, high cloud point and pour point, high NO_x emissions due to excess nitrogen and oxygen, gel formation at low temperatures due to poor cold flow properties, etc. To optimize the quality of biodiesel and to increase stability, additives are added to the blend to improve the performance characteristics of biodiesel and to control emissions. The objectives of this review paper are to provide an insight into the need of additives to enhance the performance characteristics like brake thermal efficiency and brake specific fuel consumption of biodiesel, present a literature review of the use of additives on biodiesel, compare the results and investigate the impact of additives on performance parameters and stability. Pyrogallol, diethyl ether, butylhydroxyanisole (BHA), butylhydroxytoluene (BHT) and tert-butyl hydroquinone (TBHQ) are the predominant additives under this review. It is clear from research that additives have a significant impact on the performance of biodiesel and there is scope for further research into additives to optimize the performance of biodiesel.

A. Rasal (✉) · S. Saxena · N. Nair · M. Vikal · K. Yadav
Mechanical and Automation Department, Amity School of Engineering
and Technology, Amity University, Noida, Uttar Pradesh, India
e-mail: asrasal47@gmail.com

S. Saxena
e-mail: sarthaksaxena.drummer@gmail.com

N. Nair
e-mail: Naveen.nair35@gmail.com

M. Vikal
e-mail: mohitvikal9@gmail.com

G. Dwivedi
School of Mechanical Engineering, VIT University, Vellore, Tamil Nadu, India

Keywords Biodiesel · Performance · Additives · Stability · Diethyl ether · Pyrogallol

1 Introduction

1.1 Diesel and Its Drawbacks

Diesel is one of the most commonly used automobile fuels in the world. It is derived from crude oil or mineral oil and is being produced on a large scale with abundance in the present. However, diesel burns with the release of harmful and poisonous gases like carbon monoxide, carbon dioxide, HCs, and NO_x . These gases increase the greenhouse effect and are continuously affecting the environment adversely in a negative way. Also, diesel being obtained in the form of fossil fuels, it is a nonrenewable source of fuel and is fast depleting. With the increasing need for fuel in the market to meet the demands of technological development, researchers are working on alternative clean sources of fuel.

1.2 Biodiesel

Biodiesel is a renewable and clean source of energy obtained by the esterification process of natural oils. Unlike diesel, it is free of aromatics and is completely biodegradable. The current scenario suggests that the future availability of biodiesel is quite high as compared to petrodiesel. Biodiesel consists of long-chain alkyl esters, as a result of esterification. It is produced by combining or chemically reacting of natural oil with alcohol thus producing fatty acid esters. Biodiesel can be readily used in CI engines with very little modifications without causing any problem or damage to the engine. This is because of the similarities of the functioning of diesel and biodiesel. Although the burning characteristics of diesel are better than that of biodiesel, certain additives can be added to achieve as much efficiency as possible. Biodiesel can be obtained from lipids like oils, animal fats, and recycled grease or from algae by transesterification process using alcohol. It has lower carbon emissions compared to diesel and can also be blended with diesel. It has a higher cetane number and higher lubricity. Most importantly, biodiesel is a clean, nontoxic and biodegradable source of fuel. Researchers have predicted that fossil fuels will soon get replaced by the renewable sources without choice and hence it will encourage the production of biodiesel, thus enhancing its future availability. Although the availability of biodiesel is very less compared to other fuels right now, there is a lot of scope for the development of new methods and technology to obtain cheaper and more efficient biofuel. There are plenty of sources of biodiesel that are abundant in the world and can be cultivated on a commercial scale.

2 Biodiesel Production

2.1 Source of Biodiesel

Based on the sources, biofuels can be divided into 4 categories:

First-generation biofuels. First-generation biofuels are obtained from food crops or edible sources like vegetable oils, sugar, starch, etc., by transesterification.

Second-generation biofuels. Second-generation biofuels are obtained from non-edible sources of natural oil like plants and animals in the form of biomass.

Third-generation biofuels. Third generation biofuels are synthesized from oil-rich algae.

Fourth-generation biofuels. Fourth generation biofuels include electro-fuels and photo-biological solar fuels and they do not require destruction of any biomass.

It is important to consider the mass producing potential of biofuels before choosing the source. Since first-generation biofuels require landmass for the cultivation of the crops to be further utilized for biofuel production, it takes up too many resources and creates a shortage of both land mass and food crops. Hence focus needs to be diverted to nonedible sources of biofuel like palm oil as it can be produced on a large scale and it will only add to the environmental benefits with increased plantation of trees.

2.2 Manufacturing Biodiesel

The biodiesel manufacturing process involves the conversion of oils and fats into long chains of monoalkyl esters. These chemicals are manufactured by a process called esterification and are also referred to as fatty acid methyl esters (FAME). Transesterification or alcoholysis is a process similar to hydrolysis, except while water is used in hydrolysis, alcohol is used in this reaction [1]. It involves displacement of alcohol from an ester by another. This process is also implied for reduction of the high viscosity of triglycerides [2].

This is the general equation of the trans-esterification process (Fig. 1).

Transesterification is a reversible reaction, but the presence of a catalyst in the form of a strong base or acid speeds up the conversion. The mechanism of transesterification is described below:

- Alkoxide ion attacks the carbonyl carbon of the triglyceride molecule to produce a tetrahedral intermediate.
- This intermediate reacts with an alcohol to produce the alkoxide ion.
- In the last step, the tetrahedral intermediate is rearranged resulting in the formation of a diglyceride along with an ester. The same process is repeated for diglyceride and then for monoglyceride.

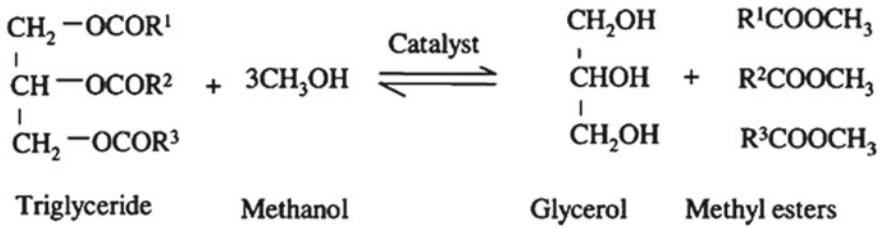


Fig. 1 Transesterification general equation

2.3 Biodiesel Quality

The final product is analyzed to make sure it satisfies the specifications and requirements of ASTM (American Society for Testing and Materials). The most significant aspects to ensure that the biodiesel manufactured can be used for the smooth operation of CI engines are:

- Trouble free completion of the chemical reaction.
- Effective separation of the glyceride and alcohol.
- Effective retrieval of the catalyst.
- No presence of free fatty acids.
- Low sulfur content.
- Low water content.

The registration for the United States Environmental Protection Agency (EPA) recognition depends upon the factors related to feedstock and the process, and it includes all biofuels that satisfy the requirements of the ASTM standards. The fuel prepared is tested for ASTM standards. The requirements and specifications of D6751

Table 1 ASTM D6751 standard requirements

Property	Test method	Unit	Requirement
Flash point (min)	D93	°C	93
Water and sediment (max)	D2709	% vol	0.050
Kinetic viscosity at 40 °C	D445	mm ² /s	1.9–6
Cetane number (min)	D613	–	46
Carbon residue (max)	D4530	% mass	0.050
Acid number (max)	D664	mg of KOH/gm	0.50
Free glycerin (max)	D6584	% mass	0.02
Total glycerin (max)	D6584	% mass	0.240
Oxidation stability (min)	EN15751	h	3

are intended to ensure that the combustion of fuel takes place effectively and efficiently and without causing any damage to the engine or any other operating machine. The standard keeps a check on the physiochemical properties of the fuel and not on the manufacturing process or the materials used for manufacturing. It is the final blend that is checked for specifications as follows (Table 1).

3 Additives

It is clear that pure biodiesel is not the most efficient fuel. In order to overcome the above drawbacks of biodiesel, we use blends of diesel and biodiesel with a certain additive to obtain the most efficient biodiesel (B10, B20, B30, etc.). B100 is the term used for pure biodiesel. The most commonly found blends are B20 (20% biofuel + 80% diesel) and B15 (15% biofuel + 85% diesel) with 5–15% additive substitution depending upon the oil and additive composition. Additives can help biodiesels achieve the required quality standards.

3.1 *Types of Additives*

There are different types of additives depending upon the applications and requirements:

Oxygenated additives. E.g., alcohols like butanol ethanol, propanol, methanol, ethers like diethyl ether, diisopropyl ether, ethyl tertiary butyl ether, and esters like dicarboxylic acid ester, dimethyl carbonate ester, etc.

Metal based additives. E.g., copper (II) chloride, iron (III) chloride, copper (II) oxide, cobalt (II) chloride, etc.

Antioxidant additives. E.g., Pyrogallol (PL), butylated hydroxyl anisole (BHA), propyl gallate, butylated hydroxyl toluene (BHT), tert-butyl hydroxyquinone (TBHQ).

Cetane number improver additives. E.g., nitrates, hexyl nitrates, peroxide nitrates, tetra azoles, aldehydes, and 2-ethyl hexyl nitrate.

3.2 *Impact of Additives on Performance and Stability Parameters Biodiesel*

Additives help the biodiesel to achieve efficient and better performance and also control emissions. They act as antioxidants to increase the oxidation stability of biodiesel by chemically reacting with the abundant oxygen. They also help to increase the power output and calorific value of the blend as they have a lower flash point and

very high calorific value. Additives can help to decrease the density and viscosity of the biodiesel to some extent and improve cold flow property [3] as well.

- **Impact on oxidation stability.** Due to the high amount of oxygen in the biodiesel and presence of unsaturated $C = C$ double bonds, biodiesel has low oxidation stability [4]. This results in autoxidation in biodiesel which changes the characteristics of the fuel when it comes in contact with air or water. It may cause severe problems like a change in viscosity of fuel, corrosion of container/tank, clogging of valves, etc.

Fernandes et al. [4] studied the use of *Moringa oleifera* oil and leaves to produce both biodiesel and antioxidant additives, respectively. The antioxidant additive was formed using ethanol extracts from the leaves of the same plant and is found to be effective with soybean biodiesel, indicated by the increase in the IP values. Das et al. [5] investigated the storage capacity of Karanja oil biodiesel for long periods of time by using antioxidants butylhydroxyanisole (BHA), butylhydroxytoluene (BHT) and *tert*-butyl hydroquinone (TBHQ), pyrogallol and propyl gallate. Results indicate improvements in peroxide value and viscosity of the biodiesel thus improving its oxidation stability. Zhou et al [6] used the PetroOXY method to investigate the oxidation stability of biodiesel, stabilized with five synthesized antioxidants. The differences in the antioxidant activity of these compounds could be clearly identified using this method. Pyrogallol (PY) and propyl gallate (PG) proved to be more efficient in inhibiting biodiesel oxidative degradation than butylated hydroxyanisole (BHA) and butylated hydroxytoluene (BHT). Sorate et al. [7] investigated the impact of antioxidants on the oxidation stability of biodiesel synthesized from high free fatty acid oil. It was found that the biodiesel dosed with antioxidants showed reduced acid value, kinematic viscosity, and peroxide value. Karavalakis et al. [8] investigated the effect of different artificial phenolic antioxidant additives on the oxidation stability of various biodiesels, with special emphasis on the stability of the blends by using the modified Rancimat method (EN 15751). The performance of antioxidants was analyzed by blending five different types of biodiesel with low sulfur diesel. The results revealed that while the efficiency of the antioxidants varied depending upon the different types and quality of biodiesel, an improvement in oxidation stability could be achieved by the addition of antioxidants. Butylated hydroxytoluene (BHT) and butylated hydroxyanisole (BHA) showed the lowest effectiveness in neat biodiesel, whereas their use in biodiesel blends showed a greater stabilizing potential. Sathiyamoorthi et al. [9] studied the impact of antioxidant additives butylated hydroxyanisole (BHA) and butylated hydroxytoluene (BHT), dissolved in lemongrass biodiesel (LGO) in different proportions. The results showed that LGO25 with the above antioxidant additives produced an increase in brake thermal efficiency (BTE) and a decrease in exhaust gas temperature (EGT) and brake specific fuel consumption (BSFC). BHA antioxidant additive exhibits a better stability than BHT in lemongrass biodiesel.

Impact on cold flow property. Cloud point and pour point are the parameters used to define the cold flow properties of any fuel. The pour point and cloud point of biodiesel are higher as compared to that of petrodiesel especially in biodiesels

with high saturated fatty acid content [10]. As a result, biodiesel has poor cold flow property. This means that in cold regions, where the temperatures are quite low, the fatty acids will start solidifying to develop gel-like material and will slowly turn semi-solid. When the temperature reaches the pour point, it will cease to flow. Hence biodiesel cannot be used as a fuel in cold regions.

Dwivedi et al. [10] studied the chemical stability of biodiesel and conducted a comparative study of different blends with different additives and derived various correlations to analyze the effects of these additives. It was found that the oxidation stability of biofuel has a major role to play in its performance, combustion, emissions, and storage. Better stability of biodiesel also improves cold flow properties. The study concluded with findings that pyrogallol is the best additive to increase the oxidation stability of biofuels and aluminum and cast iron containers are best suitable for the storage or transportation of biofuels. Ali et al. [3] conducted research on improving cold flow properties of palm oil methyl ester using diethyl ether as an additive. The addition of diethyl ether improved the density and acid value of palm oil methyl ester and hence improved its cold flow properties. Abe et al. [11] studied the impact of tert-butyl alcohol, 2 butanol, and oleyl alcohol on cold flow properties of canola biodiesel and compared the results to find out that the molar mass of the additive has a significant influence upon the ability of the additive to improve the cold flow properties of the biodiesel. Misra et al. [12] conducted a review to identify the various additives used to improve the cold flow properties of biodiesel blends using additives and improve the performance parameters of a compression ignition engine and its emissions characteristics. It was concluded that additives are vital for biodiesel production, its storage, its transportation in variable climatic conditions, and its application in a diesel ignition engine with a quality performance. Kannan et al. [13] investigated low temperature properties of biodiesel using ethanol, kerosene, and diesel as liquid additives. Biodiesel used was obtained from waste cooking palm oil by transesterification using potassium hydroxide as a catalyst. It was found that the addition of 25% kerosene and diesel reduced the cloud point value of biodiesel. Pour point of ethanol, kerosene and diesel blended biodiesel decreased by 6 °C at 35% of additive concentration. Biodiesel blended with 15% ethanol and 45% kerosene showed the reduction in cetane index value from 66.93 to 47.8 and 47.6, respectively.

Impact on performance parameters. Many physiochemical properties of the fuel like kinematic viscosity, density, brake thermal efficiency (BTE), brake specific fuel consumption (BSFC), calorific value, cetane number, flash point, fire point, etc., are considered to analyze the performance of an engine [14]. BSFC is concerned with the rate of heat conversion. BTE is highly dependent on the manner of heat conversion. These properties are different for biodiesel and diesel and hence affect the performance of the engine when using biodiesel instead of diesel. Biodiesel generates low power compared to diesel due to low calorific value and incomplete or poor burning of fuel. Thus efficiency is slightly decreased. Biofuel also has higher density and viscosity due to the presence of long chain fatty acids which may cause problems as the fuel is required to flow through the system. Some of these problems are large droplet size, clogging of injection, nozzle and poor vaporization etc.

Madiwale et al. [15] analyzed rice bran oil biodiesel with ethanol as additive (2.5%) and tests were performed to find out the effect of the additive on performance parameters. The results indicated a 9% increase in braking power and 6% decrease in BSFC. Imtenan et al. [16] conducted an analysis of palm biodiesel DP20 blends with additives (diethyl ether, n-butanol, and ethanol) and compared the results with diesel and DP20. It was found that the additives substantially improved the density and viscosity and also led to better atomization and thereby improving the combusting qualities of DP20. Diethyl ether was found to be the most effective additive due to high calorific value, while n-butanol fared pretty good. Ethanol, on the other hand, fared poor due to low calorific values. It was concluded that 5% of these additives proved to be effective to improve the performance parameters significantly with lower emissions as well. Senthil et al. [17] studied the impact of injection pressure on the operation and performance of the CI engine using different blends of annona methyl ester biodiesel. Tests were conducted and the results found out that IP 240 bar is the most optimized pressure for 20% annona methyl ester with 80% diesel, as it shows improvement in performance characteristics like brake thermal efficiency, exhaust temperature and brake specific fuel consumption with lesser exhaust and emissions like smoke and un-burnt hydrocarbons, compared to that of diesel. Nayak et al. [18] studied the biodiesel blends of different volumes produced from mahua oil by transesterification and mixed with additive (dimethyl carbonate) through multiple tests. Results found that the use of the additive in the biodiesel blends led to improvement in performance characteristics. The BSFC values lowered and BTE values were found to increase with the use of additives. The exhaust gas temperature also decreased with an increase in the additive in the blend. Kiran Kumar et al. [19] studied methods for improving the efficiency and the emission characteristics of biofuel by ensuring better combustion of the fuel. The biodiesel used for experimental analysis was obtained from fish oil and it was mixed with diesel in varying proportions and then isobutanol was added to the blends in fixed and small quantities as an additive, and the blends were tested for performance parameters on a 4 stroke single cylinder IC engine. It was observed that the BTE of the fuel increased with an increase in the additive and the blend with 5 and 10% additive was found to be most effective. Meanwhile, there was a slight negative effect observed on BSFC as it increased with increase in isobutanol. Domingos et al. [14] studied the impact of butylhydroxyanisole (BHA), butylhydroxytoluene (BHT) and tert-butyl hydroquinone (TBHQ) on soybean biodiesel. The results indicated a significant rise in induction period for all trials when compared with the control sample.

4 Conclusion

This study has covered discussions about biodiesels obtained from various sources—neem oil, Karanja oil, soya bean oil, fish oil, castor oil, Annona oil, Mahua oil, palm oil, cooking oil, lemongrass oil etc. The effect of different additives like ethanol, methanol, n-butanol, diethyl ether, BHA, BHT, TBHQ, and pyrogallol on

performance characteristics and stability of the biodiesel was analyzed and compared. Research indicates that different additives are used as per the requirement of the biodiesel in use to enhance its characteristics like increasing brake thermal efficiency, reducing brake specific fuel consumption, reducing emissions, increasing calorific value to facilitate efficient combustion, etc., thus eventually increasing the chemical stability and performance of the biodiesel. Additive pyrogallol is found to be most effective to improve the oxidation stability, thus enabling efficient storage and transportation of biodiesel, preventing gel formation during cold weather by improving cold flow properties and also affect certain physical properties like density and viscosity that allow complete and efficient combustion. Diethyl ether was found to be most effective in enhancing performance characteristics like calorific value, brake thermal efficiency (BTE) and brake specific fuel consumption (BSFC). The additives butylhydroxyanisole (BHA), butylhydroxytoluene (BHT) and tert-butyl hydroquinone (TBHQ) are found to be good antioxidants and also the enhance performance parameters like induction period, BSFC and BTE to increase the power output. More research has to be conducted in the use of additives for second, third and fourth generation biofuels. With the development of purpose-specific additives, the performance of biodiesel can be optimized for efficient burning and it can be improved to compete with and eventually replace the fossil fuels that are in prominent use today.

References

1. Bobade SN, Khyade VB (2012) Preparation of methyl ester (biodiesel) from karanja (*Pongamia pinnata*) oil. Res J Chem Sci 2(8):43–50
2. Vivek, Gupta AK (2004) Biodiesel production from karanja oil. J Sci Industrial Res (JSIR) 63:39–47
3. Ali OM, Yusaf T, Mamat R, Abdullah RN, Abdullah AA (2014) Influence of chemical blends on palm oil methyl esters' cold flow properties and fuel characteristics. Energies 7(7):4364–4380
4. Fernandes DM, Sousa RM, de Oliveira A, Morais SA, Richter EM, Muñoz RA (2015) *Moringa oleifera*: A potential source for production of biodiesel and antioxidant additives. Fuel 146:75–80
5. Das LM, Bora KD, Pradhan S, Naik KM, Naik SN (2009) Long-term storage stability of biodiesel produced from Karanja oil. Fuel 88(11):2315–2318
6. Zhou J, Xiong Y, Shihai X (2016) Evaluation of the oxidation stability of biodiesel stabilized with antioxidants using the PetroOXY method. Fuel 184:808–814
7. Sorate KA, Bhale PV, Meena RN (2016) Oxidation stability of biodiesel derived from high free fatty acid feedstock. Energy Sources Part A Recovery Utilization Environ Effects 38(10):1410–1418
8. Karavalakis G, Stourmas S (2010) Impact of Antioxidant Additives on the Oxidation Stability of Diesel/Biodiesel Blends. Energy Fuels—Energy Fuel 24. <https://doi.org/10.1021/ef1004623>
9. Sathiyamoorthi R, Sankaranarayanan G (2016) Effect of antioxidant additives on the performance and emission characteristics of a DIC engine using neat lemongrass oil–diesel blend. Fuel 174. <https://doi.org/10.1016/j.fuel.2016.01.076>
10. Dwivedi G, Sharma MP (2014) Impact of anti-oxidants and metals on biodiesel stability—a review. J Mater Environ 5(5):1412–1425. ISSN: 2028-2508

11. Abe M, Hirata S, Komatsu H, Yamagiwa K, Tajima H (2015) Thermodynamic selection of effective additives to improve the cloud point of biodiesel fuels. *Fuel* 171:94–100
12. Misra RD, Murthy MS (2011) Blending of additives with biodiesels to improve the cold flow properties, combustion and emission performance in a compression ignition engine—a review. *Renew Sustain Energy Rev* 15:2413–2422
13. Kannan GR, Bikkavolu J, Anand R (2010) Improving the low temperature properties by blending biodiesel with different liquid additives. *Petrotech*
14. Domingos AK, Saad EB, Vechiatto WW, Wilhelm HM, Ramos LP (2007) The influence of BHA, BHT and TBHQ on the oxidation stability of soybean oil ethyl esters (biodiesel). *J Brazilian Chem Soc (JBCS)* 18(2):416–423
15. Madiwale S, Karthikeyan A, Bhojwani V (2017) A comprehensive review of effect of biodiesel additives on properties, performance, and emission. *IOP Conf Series Mater Sci Eng* 197(1):012015
16. Imtenan S, Masjuki HH, Varman M, Arbab MI, Sajjad H, Rizwanul Fattah IM, Abedin MJ, Saeed A, Hasib M (2014) Emission and performance improvement analysis of biodiesel-diesel blends with additives. In: 10th international conference on mechanical engineering, ICME, *procedia engineering*, vol. 90, pp 472–477
17. Senthil R, Silambarasan R (2015) Impact of injection pressure on the performance and emission characteristics of a diesel engine fuelled with *Annona methyl ester*. *Oxid Commun* 38(2):818–829
18. Nayak SK, Pattanaik BP (2014) Experimental investigation on performance and emission characteristics of a diesel engine fuelled with mahua biodiesel using additive. In: 4th international conference on advances in energy research (ICAER), *energy procedia*, vol. 54, pp 569–579
19. Kiran Kumar S, Apparao K, Babu RN (2012) Experimental investigation on performance, combustion characteristics of diesel engine by using fish oil. *Int J Eng Res Appl (IJERA)* 2:1258–1263
20. Chaudhary JR, Seth PC (2017) A review paper on investigation on diesel engine using smart biodiesel. *Int J Innovative Res Sci Technol (IJIRST)* 3(11):2349–6010
21. Pradhan S, Madankar CS, Mohanty P, Naik SN (2012) Optimization of reactive extraction of castor seed to produce biodiesel using response surface methodology. *Fuel* 97:848–855
22. Das D, Kumar A, Yadav A (2018) Evaluation of performance, emission and combustion characteristics of a CI engine fueled with karanja biodiesel and diethyl ether blends. *Biofuels* 9(1):89–94
23. Fattah IR, Masjuki HH, Kalam MA, Hazrat MA, Masum BM, Imtenan S, Ashraf AM (2014) Effect of antioxidants on oxidation stability of biodiesel derived from vegetable and animal based feedstocks. *Renewable Sustainable Energy Rev* 30:356–370. <https://doi.org/10.1016/j.rser.2013>

Investigation of Leakage Sources in Gasoline Muffler Using RCFA, CFD, and Experimental Validation



Mritunjay Upreti and Sumit Sharma

Abstract When the exhaust valve is open high-pressure exhaust gases are released one after the other, which combine to form a steady noise. To reduce this unwanted noise a muffler or silencer is used. Thus, quality is a major concern in the production of exhaust components. An inferior exhaust component can lead to the reduction in engine efficiency and increase in undesirable vehicle noise. The major causes of an indecent muffler may arise due to play in the sheet feeder, worn out vertical or horizontal roller set, taper in the horizontal bed or improper sheet stopper settings. This paper substantially aims to diagnose leakage in Gasoline muffler. For this purpose, various statistical tools and leakage test was incorporated. To understand ideal fluid flow inside Muffler, computational fluid dynamics was carried out using Fluent in ANSYS 12.0. Through Root Cause Failure Analysis, it was evident that indecent seaming operation was the prime source of leakage. A fishbone diagram was used to illustrate various causes of the defective seam. Which lead to problem detection in Lock Seaming Machine and respective adjustment was carried out. Finally, leakage testing was carried out in Universal Leakage Testing Machine to validate the respective result.

Keywords Muffler · Leakage · Pressure drop · Lock seaming

1 Introduction

With increased environmental concerns it is essential to produce fail-safe decent exhaust components for vehicles. Furthermore, reducing the cost of the warranty is one of the major challenges faced by manufacturers. Thus, it is necessary to investigate the root causes of failure when components runout in advance to its expected life. The muffler is a soundproofing device, designed to reduce noise emitted

M. Upreti (✉) · S. Sharma
Amity University, Sector 125, Noida, India
e-mail: mritunjayupreti@gmail.com

S. Sharma
e-mail: ssharma03@amity.edu

© Springer Nature Singapore Pte Ltd. 2019
M. Kumar et al. (eds.), *Advances in Interdisciplinary Engineering*, Lecture Notes in Mechanical Engineering, https://doi.org/10.1007/978-981-13-6577-5_52

by vehicle due to high sound pressure created by the engine. This study primarily focuses on investigating causes and sources of leakage in gasoline Muffler. Other than design inconsistencies leakage is the other cause that depletes muffler efficiency, which is explained with the significant Pressure drop and turbulence noticed across the Muffler's section length. With increased back pressure levels, the engine has to compress the exhaust gases to a higher pressure which involves additional mechanical work. Finally leading to an increase in fuel consumption, and engine load. Based on the above analysis, in order to improve production performance adjustments were made on the seaming machine to improve metal locking characteristics and initiate turbulence less flow inside Muffler.

2 Literature Review

A literature review was conducted in order to determine which previous work performed in the area of Muffler Design and Operation. The review focuses on the study done by the most pertinent journal papers, articles available as open literature. The work done by Trivedi et al. [1] gave an understanding of the CFD Analysis of Flow through Muffler to Select Optimum Exhaust Muffler Model and illustrates the same. Puneetha et al. [2] studied Back Pressure in Exhaust Muffler of a Single Cylinder Diesel Engine using CFD Analysis and Prof. Pandhare [3] presented CFD Analysis of Flow through Muffler to Select Optimum Muffler Model for CI Engine. Both studies have emphasized on the importance of Pressure Drop in optimizing the Muffler Design. Vijay et al. [4] the review reveals various factors upon which the exhaust noise depends. Muffler geometry, extension in inlet and outlet valves, number of whole perforations and its diameter are the factors which affects noise from engines helped to create wider understanding of Muffler design. Dondapati et al. [5] investigated on mechanical stresses in a muffler mounting bracket using RCFA, CFD, and experimentally validated the results. Finally, Chen et al. [6] describes physical numerical modeling of the flow field of the muffler. CFD approach is used to simulate the muffler, hence helped in determining the boundary conditions for this study.

3 Identifying Root Cause and Statistical Analysis

RCFA (Root Cause Failure Analysis) is a logically structured deductive technique, which is very useful for improving the reliability of Plant process equipment and identifying the major chronic cause behind the failure [5]. In the present work, Pareto chart is used to illustrate the Frequency of various Defects in Muffler Production with respect to their cumulative percentage and all the possible causes of the failures and its effects were listed and represented with the help of Cause and Effect Diagram. This helps the designer and process planners to improve more at listed areas to avoid the future failures. To detect the root cause of an unbecoming Muffler, the

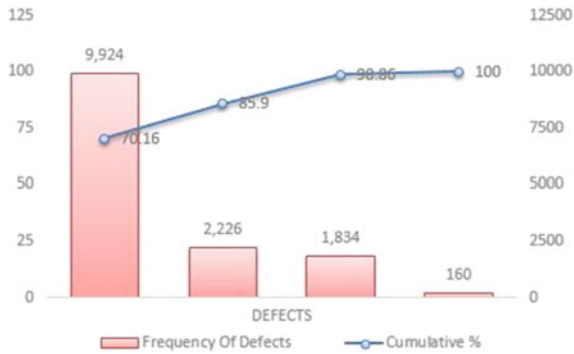


Fig. 1 Pareto chart representing the frequency of defects with respect to cumulative %

frequency of various defects was taken into account. For million parts produced 9924 had defective lock seam. Similarly, 2226 and 1834 had damaged end flanging and spinning respectively [7]. It was noted that numbers for defective lock seam were fairly high as compared to other accounted defects. Hence indecent seaming was weighted as the major source of leakage and made the muffler vulnerable (Fig. 1).

As illustrated earlier, the poor seaming operation is a primal defect and source of leakage. 4Ms (Men, Materials, Methods, and Machines) were considered in the Fishbone Diagram for failure analysis and represented in Fig. 2. Men caused human errors were due to unawareness and lack of setup knowledge. Methods accounted for poor handling as well as improper machine process setting. Similarly, causes related

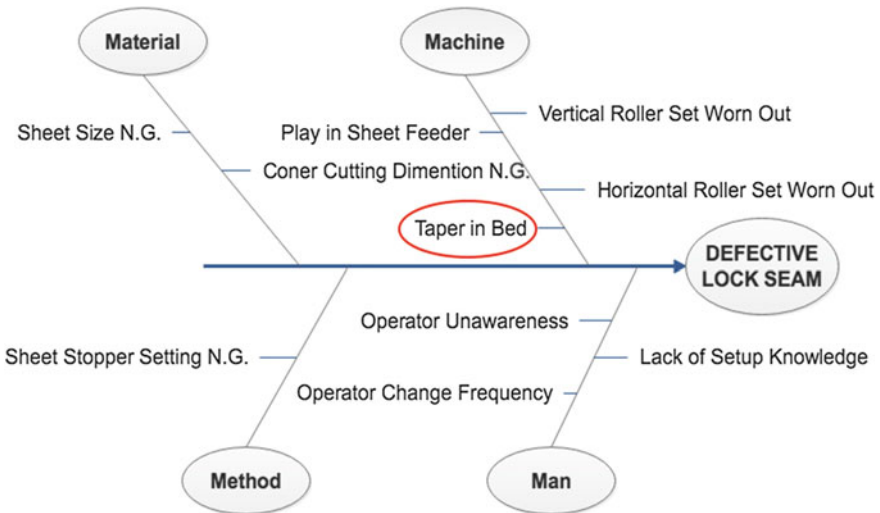


Fig. 2 Cause and defect diagram for defective lock seam

to materials were mostly due to dimensional inconsistencies. Further, Machine was considered as one of the root causes as it produced various inaccuracies.

Each listed cause was investigated and in agreement with the statistical data, taper in the bed of Lock seaming machine was considered as root cause of failure.

4 Flow Analysis Using CFD

The Muffler is developed for 4 Cylinder 1500 cc Gasoline Engine to assess fluid flow inside it and the following inlet boundary condition were defined: Inlet Gas velocity = 25.55 m/sec, Test or Gauge Pressure = 101.419 kPa, Mass Flow rate of Gas = 7.097gm/sec and Gas temperature = 633 K. Similarly, Atmospheric Pressure was defined as outlet boundary condition [3]. The meshing of the base model was done using ANSYS 12.0. After importing and repairing CAD, the cleaned-up model was meshed with a specific element size [4] (Fig. 3).

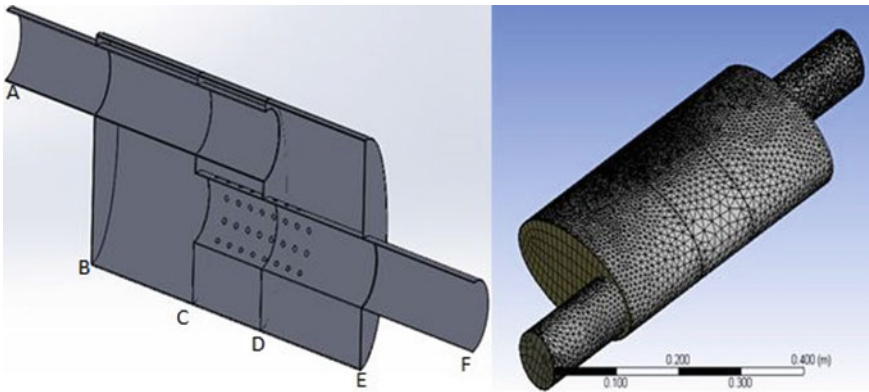


Fig. 3 Section and meshed model of exhaust muffler

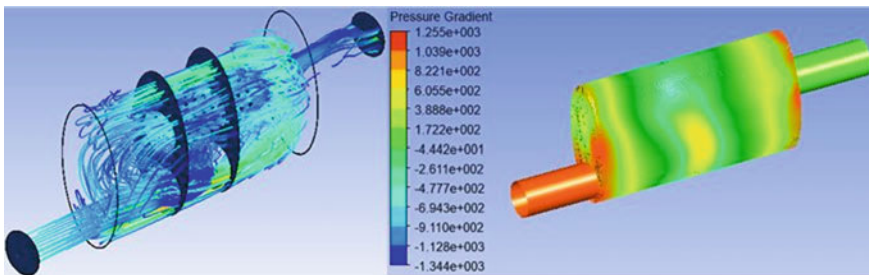


Fig. 4 Fluid flow and pressure gradient across muffler

After meshing, the study of Pressure Drop or Back Pressure across Muffler length was carried out (using preprocessing methodology in Fluent). The minimum absolute Pressure Drop calculated was 3.98 kPa. The simulated Pressure Drop Gradient and optimum Fluid flow across Muffler under the Real Gas condition is represented in Fig. 4.

5 Adjustment in Lock Seaming Machine

A Special Purpose Lock, Seamer, is a machine used to seal the lid to the Muffler body. The seam is made by mechanically overlapping the two layers to form a hook. Any damage or problems to the seamer or seamer tools can cause severe problems such as seam bumps, wrinkles, sharp seams, and open seams. In this study, poor seaming operation prompted leakage in operational Muffler. And Taper in the bed of Lock seaming machine was accounted for a major cause. Thus, various sections of the bed were inspected, which included a roller set, hydraulic cylinder, and lock pin. It was observed that every time machine is operated, Lock Pin forces mandrel to shift up (about 2 mm) as depicted in Fig. 5. Thus, leading to various imperfections such as seam crack, shifted seam and seam open from one side.

To adjust the misalignment, mandrel was shifted down and the pin was changed from adjustable nut and bolt to fixed bar. Such that height between front and rear stand same during operation. And the gap between upper and lower bed was fastened at 575 mm.

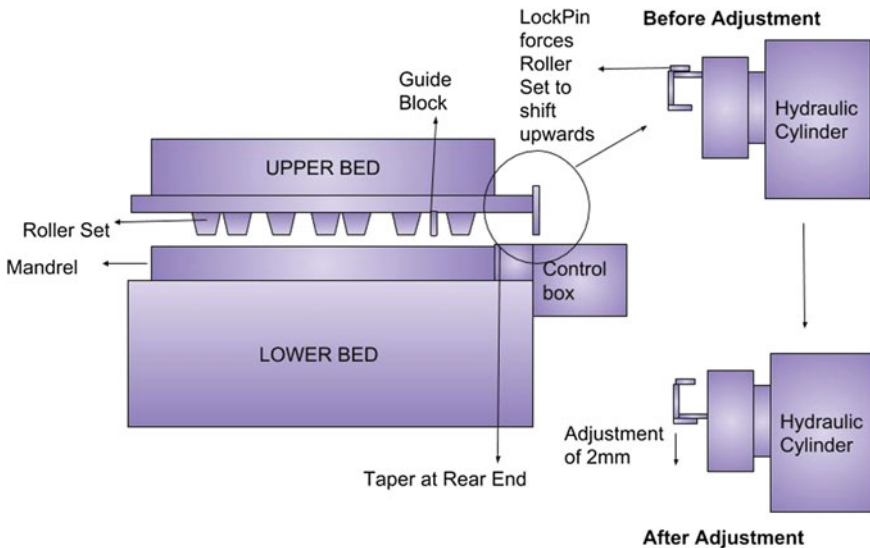


Fig. 5 Block diagram representing adjustments in lock seaming machine

6 Result and Validation

After adjustments, a newly and previously seamed Muffler were tested in ULTM (Universal Leakage Testing Machine). And a comparative diagnostic was generated to analyze Pressure Drop, between simulation and Experimental data (before and after adjustment) represented in Fig. 6. The calculated Leakage for the respective absolute Pressure Drop across the Muffler is represented in Table 1.

Before the necessary Taper adjustment, the experimentally measured Pressure drop (4.55 kPa) is more significant between section (B-F) as compared to computer-generated simulation (3.98 kPa for optimum Fluid flow across Muffler under Real Gas condition). After the adjustment of the misalignment, the experimentally measured Pressure drop (4.06 kPa) was substantially in agreement with the simulated optimum Fluid flow across Muffler.

Table 1 clearly indicates that the measured leakage (9.85 L/min) in Muffler after adjustment was less as compared to the leakage measured in Muffler before adjustment (11.16 L/min). Thus, was considerably in agreement with the simulated ideal Muffler model.

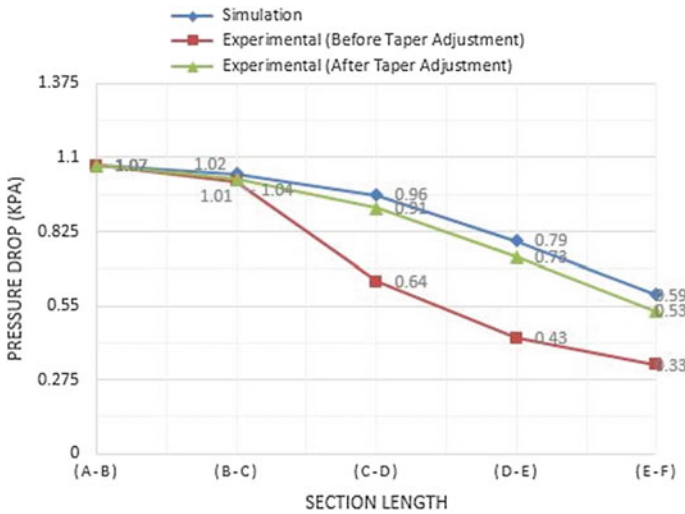


Fig. 6 Comparison between simulation and experimental drop in Pressure (before and after adjustment)

Table 1 Respective leakage for absolute pressure drop

	Pressure Drop (KPa)	Leakage (L/min)
Simulation	3.98	9.622
Experimental: before taper adjustment	4.55	11.16
Experimental: after taper adjustment	4.06	9.85

7 Conclusion

In present work, investigation on a gasoline Muffler has been carried out, which satisfy the design and flow condition of an exhaust system. After investigating and analyzing primal cause and sources of leakage, adjustments were made on lock seaming machine. Which led to the following conclusion:

1. After root cause failure analysis, it was evident that indecent seam operation was the prime source of leakage.
2. Fluent was very helpful in terms of analyzing pressure drop and studying exhaust flow dynamics inside Muffler.
3. In contrast to simulated data experiment shows significant Pressure drop in section (B–E) before adjustment. From which it is evident that some emissions from the engine were escaping from Muffler's seam.
4. After Adjustment, the experimental drop was in agreement with the simulated results.
5. There was a substantial drop in Leakage after taper adjustments were made in Lock seaming machine. The calculated Percentage Leakage reduction: 11.739%.

References

1. Trivedi S, Bansode S, P Pawar (2017) CFD flow analysis and optimization of exhaust muffler. *Int J Res App Sci Eng Technol*
2. Puneetha G, Manjunath H (2015) Back pressure study in exhaust muffler of single cylinder diesel engine using CFD analysis. *Altair Technology Conference*
3. Pandhare A (2014) CFD analysis of flow through muffler select optimum muffler model for CI engine. *Int J Latest Trends Eng Technol*
4. Vijay M, Eknath D (2015) Design and analysis of perforated muffler in automobile exhaust system. *Int J Multidisciplinary Res Devel*
5. Dondapati S, Trivedi M (2017) Investigation on mechanical stresses in a muffler mounting bracket using RCFA, CFD and experimental validation. *Elsevier*
6. Chen J, Shi X (2010) CFD numerical simulation of exhaust muffler. In: *Seventh international conference on computational intelligence and security, IEEE*
7. *Employee handbook: cold end gasoline muffler line. SKH Magneti Marelli, Manesar (2016–2017)*
8. Jigar H, Bharat S (2014) Muffler design for automotive exhaust noise attenuation. *J Eng Res Appl*
9. Mohd I, Shukari H (2005) Experimental study of noise and back pressure for silencer design characteristics. *J App Sci*

Technology Entrepreneurship Capability Development in Indian Automotive Industry



Mohd Talha Khan  and Niraj Kumar

Abstract Technology entrepreneurship comprises of technical aspects and ability of entrepreneurship skills and competency. The four interrelated and complementary factors of entrepreneurship technology are: context, firm, technology, and entrepreneur. The merging of these four factors is necessary to create a competitive edge in the present scenario. The Indian automobile industries are well equipped with local firms having natural design and development capabilities. These local firms are not only well established global brands but also have a good marketing presence in India and other emerging markets. This study focuses primarily on technology entrepreneurship capability development in the Indian automobile industry and reveals the key attributes that shaped the innovative capabilities developments.

Keywords Entrepreneurship capability development · Indian automotive industry

1 Introduction

Entrepreneurs are the drivers of the economy in almost all of the nations. It is the effort of entrepreneurs that create job opportunities for the people of the nation [1]. Defined entrepreneur as one who moves economic resources from an area of lower productivity into an area of higher productivity with greater yield. When this term becomes entrepreneurship, it is the globalization and liberalization phenomena that are running the economy of the world towards rising competitiveness. Today, the major focus is on technology-based industries such as information technology, biotechnology, automobile industries, and the electrical & electronics industries [2]. The global trend is, therefore, moving toward entrepreneurial activities that are technology-oriented, also termed as ‘technology entrepreneurship’. In the last 10 years, the

M. T. Khan (✉)
MIT, Moradabad, UP, India
e-mail: talha2207@gmail.com

N. Kumar
Amity University, Noida, UP, India

© Springer Nature Singapore Pte Ltd. 2019
M. Kumar et al. (eds.), *Advances in Interdisciplinary Engineering*, Lecture Notes in Mechanical Engineering, https://doi.org/10.1007/978-981-13-6577-5_53

Indian automotive industry is one of the fastest growing industries with increasing levels of technological understanding amongst various other emerging countries.

It provides employment in mass for local populations in the country. Also, its export revenues help to increase foreign trade [3]. It is quite clear that the Indian automotive industry also followed the same track of development followed by other emerging countries such as Brazil, Mexico, and Thailand [4]. It started with an assembly of automotive components, after that gradual increase in local content to full-scale manufacturing and after that finally to export promotion phase [5]. In 2006, the Government of India declared Automotive Mission Plan of 10 years from 2006 to 2016 for supporting strongly to the automobile industry, thus, aiming to boost production and increase export of vehicles [6]. As a result of this, in 2008 the Indian firm Tata Motors designed and developed the world's cheapest car named 'Tata Nano' which is against all the expectations of global car makers. Similarly, in the same year, Mahindra and Mahindra launched a sports utility vehicle, named 'Scorpio', which is against the product of the indigenous design and development effort. In 2010, Maruti Suzuki's car named 'Alto' became the world's largest car sold by volume [3]. In Indian car export, Hyundai and Maruti Suzuki share more than 90% of the total sales. Hyundai has located its production sites in Chennai and shipped to 95 countries in the year 2009 [7]. For Hyundai, India is a global automobile hub for production and sales both in India as well as the global market. These developments of the Indian automotive industry surprised other auto firms as their expectation of Indian success in the global market were low due to a perceived disorder between the scale of the challenges and existing capabilities of the Indian automobile companies [8].

2 Technological Capability in Indian Automobile Industry

Technological capability is defined as the ability to make trained manpower for

- Carrying out initial research work.
- Testing general facilities available in the industry.
- Acquire and accept new technologies.
- Provide information, supportive and networking system [9].

Technological capability in general can be best described in terms of three levels:

- Basic level means the ability to operate and maintain a new production plant which is based on imported technology i.e. production capability.
- Intermediate level means the ability to copy and accept the design and technique of an imported plant anywhere else in the country or abroad, i.e., investment capability.
- Advanced level means a capability to adopt new designs and develop new production systems and components, i.e., innovation capability (Table 1).

Table 1 Elements of technology capability

Level	Components
Basic level, i.e., production capability	Production engineering, production management, maintenance of capital equipment, and marketing of output produced
Intermediate level, i.e., investment capability	Project engineering, project management, capabilities to procure and training of manpower
Advanced level, i.e., innovation capability	Generates new technical possibilities for the purpose of profit making

Source Author

Most of the Indian manufacturing firms like food processing, metal forming and forging, steel, machine tools, pharmaceuticals, etc. appear to be at the basic or intermediate level of technological capability, whereas Indian automobile industry is at an advanced level [2, 10]. The industrial policy of the Indian government leads to the development of basic capabilities but on the other side, it restricts technology capability development in Indian automobile manufacturing. The key attributes of firm ownership, such as managerial vision and diversified nature of the business, helped Indian firms in the development of technological capabilities [3].

3 Salient Features of Indian Automobile Industry

The performance of Indian Automobile Industry is measured in three contexts: Automobile Production Trends, Automobile Domestic Sales Trends and Automobile Exports Trends.

3.1 Automobile Production Trends

A growth of 5.41% has been registered in industrial production in the year from April–March 2016 to 24,016,599 over April–March 2017 to 25,316,044 of vehicles which includes two wheelers, passenger vehicles, three wheelers, and commercial vehicles. [11]. The industrial production growth in the past 6 years is shown in Fig. 1.

3.2 Automobile Domestic Sales Trends

In the same time frame of last year, i. e., from April–March 2016 to April–March 2017, sales of passenger vehicles increased by 9.23% during April–March 2017.

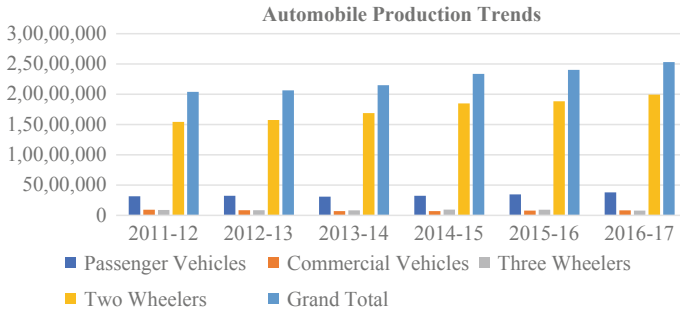


Fig. 1 Automobile production trends in the past 6 years. *Source* [12]

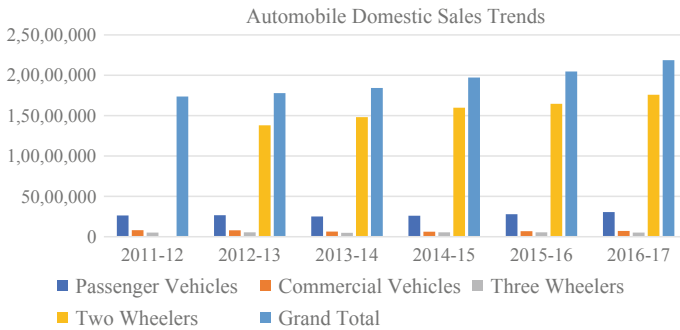


Fig. 2 Automobile Domestic Sales Trends in the past 6 years. *Source* [13]

Similarly, in this time period amongst all passenger vehicles, around 3.85% rise was in passenger cars, a 2.37% rise was in vans and 29.91% rise was in utility vehicles. In April–March 2017 net commercial vehicle segment represented 4.16% growth over the past 1-year period. Light commercial vehicles rise by 7.41% and M & HCVs (Medium and Heavy Commercial Vehicles) grown up by 0.04% in April–March 2017 over the past 1-year span. There is a decline of -4.93% in three wheelers during April–March 2017 over the last 1-year period. Sales of goods carrier increase by 12.75%, while sales of passenger carrier reduce by -8.83% during April–March 2017 over the last 1-year span. A rise of 6.89% has been registered in the sales of two wheelers during April–March 2017 over April–March 2016 which includes a 23.02% increase in mopeds, an 11.39% rise in scooters and 3.68% hike in motorcycles within two wheelers segment has been registered in April–March 2017 over April–March 2016 [11]. The industry domestic sales trend of the last six years is shown in Fig. 2.

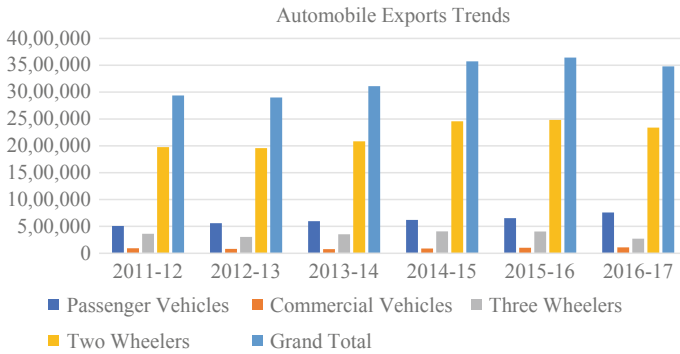


Fig. 3 Automobile Exports Trends in the past 6 years. Source [14]

3.3 Automobile Exports Trends

There is a reduction of -4.50% of overall automobile exports in April–March 2017 over April–March 2016. The rise of 4.99% in commercial vehicles and 16.20% in passenger vehicles has been registered within the same time period. Exports of two wheelers dropped by -5.78% and three wheelers dropped by -32.77% in April–March 2017 over April–March 2016 [11]. The industry exports trend for the past 6 years is shown in Fig. 3.

4 Analysis of Technology Entrepreneurship Capability Development in the Indian Automobile Industry

The analysis found that factors for Technology Entrepreneurship Capability Development in Indian Automobile Industry are growing demand, policy support and support infrastructure and high investments [15] (Table 2).

5 Indian Automotive Market 2020

India is a key pillar of the world’s automotive market. Strategies, policies, and actions of India automotive market will have core impact on the worldwide auto landscape. It is thus expected that India automotive sales lead the US market around the mid-2030s. The global automotive game will be pretty much decided by the twin forces for China and India. With global economic shift, automotive sales are resonating towards the India market in the Asian region [16]. Passenger vehicle sales distribution

Table 2 Factors of technology entrepreneurship capability development

<p>Growing demand</p>	<ul style="list-style-type: none"> • Key driver of technology entrepreneurship capability development due to the rise in income of the individual and a large youth population • Enough availability of credit and finance related support • Rise in demand for commercial vehicles which results due to the high level of activity work in the infrastructure sector
<p>Policy support</p>	<ul style="list-style-type: none"> • Indian government adopted the Public Private Partnership model with Maruti Udyog Limited and Suzuki to make India as an automobile manufacturing hub • Missions like Make in India, Automotive Mission Plan 2026, NEMMP 2020 etc. all are going to improve the automobile sector to triple, i.e., 9.4 million units of passenger vehicles by 2026
<p>Support in infrastructure and high investments</p>	<ul style="list-style-type: none"> • Developing road infrastructure is one of the key segments of technology entrepreneurship capability development and India at present has the second largest road network in the world • Recognized firm ownership and managerial vision of Indian Automobile Industry thus providing necessary support to encourage the growth of the sector • 5% of total Foreign Direct Investment inflowing to India went into Indian Automobile sector which resulted in higher supplier productivity, better and cheaper products

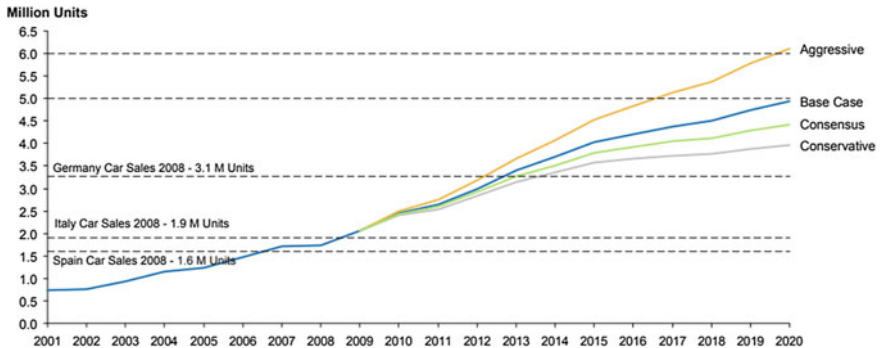


Fig. 4 Growth of passenger vehicles sales in India from 2001 to 2020. *Source* [16]

is represented in Fig. 4 shown below thus indicating the potential for rapid growth of the Indian car market to 6+ millions of units annually by 2020.

Self-governing cars are expected by 2020 to be on the roads. Amongst consumers efficiently performing hybrid cars will be most populous [17]. As India is moving towards Smart Cities Mission smart transportation is its key element.

6 Conclusion

In India, the automotive industry has a prominent future. Technology Entrepreneurship Capability Development in Indian Automobile Industry is presented in this paper. The three levels of Technology Capability, i.e., basic level (production capability), intermediate level (investment capability), and advanced level (innovation capability) are described. The performance of Indian Automobile Industry for the past 6 years is analyzed. Important growth factors of the automobile industry, i.e., growing demand, policy support and support infrastructure and high investments are identified. India's automobile market is penetrating the International automobile market and apart from this also meeting the advancing national automobile demands. Technology Entrepreneurship Capability development in the Indian Automobile Industry is also emphasized with the future scope of Indian Automotive Market by 2020.

References

1. Say JB (1803) *Treatise on political economy: on the production, distribution and consumption of wealth* (trans: 1964). Kelly, New York
2. Abdullah S (2008) *Technology entrepreneurship development in Malaysia. A case study of the national automotive industry*, Faculty of Science University of Malaysia, Kuala Lumpur. Ph.D. Thesis, pp 19
3. Kale D (2012) Sources of innovation and technology capability development in the Indian automobile industry. *Institutions Economies* 4(2):121–150
4. Bhattacharya S (2014) Supply chain management in Indian automotive industry: complexities, challenges and way ahead. *Int J Manag Value Supply Chains (IJMVSC)* 5(2)
5. Jenkins R (1995) The political economy of industrial policy. *Automobile manufacture in the newly industrializing countries*. Cambridge J Economics 19(5):625–645
6. *Automotive Mission Plan 2006–2016 A Mission for Development of Indian Automotive Industry*, Ministry of Heavy Industries & Public Enterprises, Government of India. <http://dhi.nic.in>
7. Rizvi SNA, Mukherji D (2011) *A comparative study of global competitiveness of Indian and Chinese auto components industry*. Lambert Academic Publishing, Saarbrücken
8. Katsuhiko S (2011) The impact of the rise of Chinese and Indian automobile industries. In the scale of globalization. *Think Globally, Act Locally, Change Individually in the 21st Century*. University of Ostrava, Ostrava, pp 286–291. ISBN 978-80-7368-963-6, pp 286–291
9. UNIDO (1986) *Capability building in biotechnology and genetic engineering in developing countries*. UNIDO/IS 608, UNIDO, Vienna
10. *Indian Manufacturing Industry Technology Status and Prospects*. https://www.unido.org/sites/default/files/200904/Indian_manufacturing_industry_technology_status_and_prospects_0.pdf
11. SIAM. <http://www.siamindia.com/statistics.aspx?mpgid=8&pgidtrail=9>
12. SIAM. <http://www.siamindia.com/statistics.aspx?mpgid=8&pgidtrail=13>
13. SIAM. <http://www.siamindia.com/statistics.aspx?mpgid=8&pgidtrail=14>
14. SIAM. <http://www.siamindia.com/statistics.aspx?mpgid=8&pgidtrail=15>
15. IBEF. <https://www.ibef.org/download/Automobiles-January-2018.pdf>
16. *Indian Automotive Market 2020*. <https://www.strategyand.pwc.com/media/file/Strategyand-India-Automotive-Market-2020.pdf>
17. Shoeb A, Maqbool A (2017) Growth of Indian automobile industry. *Int J Emerging Res Manage Technol* 6(5):26–29

Green Energy: A Building Block for Smart City in India



Mugdha Mishra , Mohd. Talha Khan  and Niraj Kumar

Abstract India by 2022 would be ranked as number one in densely populated nation by overtaking the China, due to population explosion in this century. That yields to acceleration in the urbanization, 30 people per minute moving from village regions to cities takes place for better living standard. Hence, stress is imposed over the existing system. For such critical issue Indian Government already initiated sustainable remedy Smart City Mission. Smart city includes following main features: uninterrupted power supply, clean environment, transportation, waste recycling, etc. Electrical power is its key domain so this paper focuses on the power challenges and region-wise power potential for green energy for the smart city mission of India.

Keywords Green energy · Solar power · Smart city · Wind power

1 Introduction

Inculcating various technologies in the existing system the quality of livelihood and efficiency of services can be enhanced along with urban development that yields to inculcating various technologies in the existing system livelihood quality and efficiency of services can be enhanced along with urban development that yields to smart city. The objective of the smart city is to upgrade the urban flows management and real-time responses allowed for the challenges. Electricity is the major factor in the smart city concept and renewable energy is its basic building block. The Renewable sources (such as Solar Energy, Wind Energy, etc.) are not extinguishing resource of energy, this energy always accessible and will not run out hence named

M. Mishra (✉) · Mohd. Talha Khan
MIT, Moradabad, UP, India
e-mail: mugdha1990@gmail.com

N. Kumar
Amity University, Noida, UP, India

Green Energy with a lot of power potential if properly utilized. Heat generated and light radiated by Sun utilized by various technologies as photovoltaic, solar thermal, artificial photosynthesis, solar architecture, and solar heating constitute to Solar Power [1].

70% of carbon emissions are due to cities as per the UN calculation. Electricity demands of Indian cities are growing every year and still, reliable energy wait is going on by 400 million people of our nation. By 2035, there will be 132% hike in electricity demand that takes place with only 112% rise in power generation as stated by British Petroleum's Energy Outlook. (ISA) between France and India for the purpose to boost Solar Energy generation in developing nations is signed. The aim of this solar alliance is proper utilization of solar power and to reduce dominion over the conventional resources. There is an extensive need of India to become the smart nation by articulating techniques such as energy-efficient city, low-carbon emitting and power-secure cities. Numerous opportunities are available with multiple cleaner options such as rooftop solar and bio-methane from sewage, the demand integrated action by all the governing bodies of private and government sector. "International Solar Alliance fossil fuels (primary objective of ISA). High capital is also invested in the renewable energy sector in India and Africa [2].

Green Energy Sources use local sources to generate electricity with negligible greenhouse gases emissions and negligible air pollutants emissions. By green technology, natural sources are converted into electricity, i.e., marketable energy future substitute to conventional power [3]. In India the calculated green energy potential is around 900 GW with Solar energy 750GW, small hydro energy 20 GW, Wind energy 102 GW (80 m height) and Bio-energy 25 GW. This paper clearly demonstrates the current and future scope of Indian states in Green Power, which is the main building block of smart city mission. Smart cities need smart electricity which is a sustainable one and at low cost. Under the smart city mission of India 100 cities were selected from various regions. In the proposed infrastructure of smart cities approved by the Indian Government, the key integrators of this project are Smart House, Environment-Friendly buildings, Intelligent Transportation System, Electric Vehicles, etc. Each of these integrators requiring energy for which needs to install solar, biofuels, windmills and other green power plants. Green clean resources of power (such as wind, solar) are smart solutions for smart cities. The shift toward distributed energy and implications for the entire electricity value chain is something that to understood and implemented [4]. In India's primary energy consumptions renewable have percentage share and initiating major steps for clean air, reducing carbon emission and adding renewable power technologies all these leads towards sustainable tomorrow [5]. The smart solution for smart city, i.e., Solar Rooftop plant for Bhopal has been presented and the Solar rooftop potential of the city has been estimated [6]. The business market history, how entrepreneurial opportunities are created for Solar Power from the time before World War II to modern era has been highlighted [7]. The rapidly decreasing carbon footprints is the target of our nation by adopting Nuclear, Wind and Solar power green resources use government have signed various agreements [8]. By 2020, 40 GW 50 Solar Parks have been approved and budget is sanctioned for 60 Solar Cities, also off-shore Wind Power and Hybrid

Table 1 MW-installed capacity region wise.

Region	Northern	Western	Southern	Eastern	Northeastern	Islands	Total
Hydro	19753.77	7447.50	11808.03	4942.12	1342.00	0.00	45293.42
Nuclear	1620.00	1840.00	3320.00	0.00	0.00	0.00	6780.00
Renewable	12873.22	20446.38	34369.28	1038.40	282.56	12.56	69022.39
Coal plant	52939.20	70608.62	45782.02	27321.64	520.02	0.00	197171.50
Gas plant	5781.26	10806.49	6473.66	100.00	1736.05	0.00	24897.46
Diesel	0.00	0.00	761.58	0.00	36.00	40.05	837.63
Total MW	92967.45	111148.99	102514.57	33402.16	3916.63	52.61	344002.39

Source [12]

Solar-Wind National scheme has been launched by the government to enhance the GDP [9]. For the promotion of Green Resources, the Government of India under MNRE (Ministry of New and Renewable Energy) initiated steps such as Incentives (Generation, Subsidies, funding) and government welcomes foreign investments in this domain. To make solar power capable of replacing fossil fuels, National Solar Mission has been started. To accomplish all these targets and promote such activities, a separate Solar Energy Corporation of India (SECI) has been set up [10]. The design and performance of solar devices and all solar power applications such as distillation of water, biogas, air and water heating systems, drying of crops with cost analysis has been comprehended [11].

2 Current Energy Scenario of India

As per diversification of power resources, the electricity production varies from region to region. Table 1 indicates the current energy scenario of various regions of our country. The western region of our country has the highest thermal power as well as the largest nuclear power generation while Northern regions are leading in Hydropower generation and the Southern region has strength in Renewable Energy generation. It is clearly seen that India's major power production contribution is from thermal plants as compared to other resources.

In the past decade, the power share of renewable resources is increased, MW-installed capacity of renewable energy in India is 69022.39 MW with the description given in Fig. 1.

3 Green Energy Potential of India Region Wise

India’s population is rapidly increasing since there is a scarcity of coal, diesel, and other fossil fuel. In the upcoming decade, Electricity shortage problem will arise in India due to power insecurity and energy cost. Conventional fuel use causes environmental problems. India is moving toward smart city mission that leads to smart country so this problem can be rectified. The solution which nature itself provided is green energy, Fig. 2 represents the MW Green Energy Prospective of Indian States.

Green power resources available in India are Solar, Wind, Small Hydro and Bio-energy (biomass, biogas cogeneration, and waste to energy), as per the data compiled by MNRE MW green power potential of Indian states and union territories are listed below in Table 2 [3].

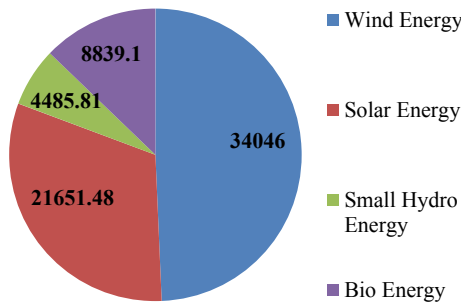


Fig. 1 MW-installed capacity of renewable energy in India. Source [12]

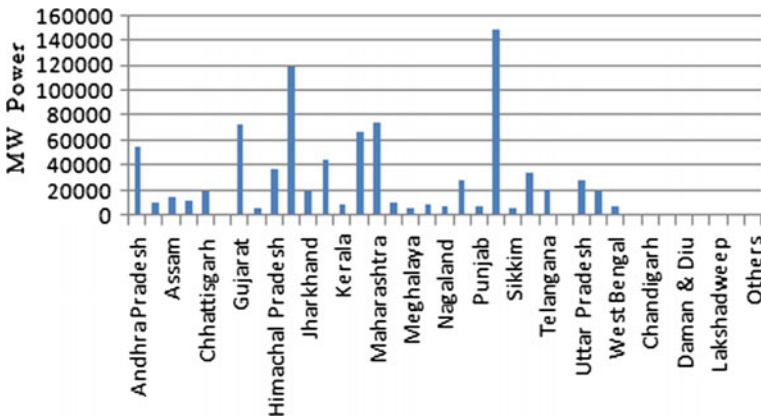


Fig. 2 MW green energy prospective of Indian states. Source [3]

Table 2 MW power potential of India's States and Union Territories

S.No.	Indian States	Bio-Energy	Small Hydro	Solar Power	Wind Power	Total MW
1	Andhra Pradesh	1001	978	38,440	4497	54,916
2	Arunachal Pradesh	8	1341	8650	236	10,236
3	Assam	520	239	13,760	112	14,330
4	Bihar	692	223	11,200	144	12,559
5	Chhattisgarh	260	1107	18,270	314	19,951
6	Goa	376	7	880	0	912
7	Gujarat	1683	202	35,770	35,071	72,726
8	Haryana	1357	110	4560	93	6470
9	Himachal Pradesh	144	2398	33,840	64	36,446
10	Jammu & Kashmir	43	1431	111,050	5685	118,208
11	Jharkhand	550	209	18,180	91	18,580
12	Karnataka	1131	4141	24,700	13,593	44,015
13	Kerala	1080	704	6110	837	8732
14	Madhya Pradesh	2692	820	61,660	2931	66,853
15	Maharashtra	2174	794	64,320	5961	74,500
16	Manipur	15	109	10,630	56	10,811
17	Meghalaya	13	230	5860	82	6185
18	Mizoram	3	169	9090	0	9261
19	Nagaland	10	197	7290	16	7513
20	Orissa	268	295	25,780	1384	27,728
21	Punjab	3517	441	2810	0	6768
22	Rajasthan	1101	57	142,310	5050	148,518
23	Sikkim	2	267	4940	98	5307
24	Tamil Nadu	1671	660	17,670	14,152	34,152
25	Telangana	0	47	20,410	0	20,410
26	Tripura	5	1260	2080	0	2131
27	Uttar Pradesh	3043	61	22,830	1260	27,593
28	Uttarakhand	29	1708	16,800	534	19,071
29	West Bengal	544	396	6260	22	7222
30	Andaman & Nicobar	0	8	0	365	373

(continued)

Table 2 (continued)

S.No.	Indian States	Bio-Energy	Small Hydro	Solar Power	Wind Power	Total MW
31	Chandigarh	6	0	0	0	6
32	Dadra and Nagar Haveli	0	0	0	0	0
33	Daman and Diu	0	0	0	4	4
34	Delhi	131	0	2050	0	2181
35	Lakshadweep	1001	0	0	0	0
36	Pondicherry	8	0	0	120	123
37	Others	520	0	790	0	1812
Total		692	19,749	748,990	102,772	896,602

Source [3]

3.1 Wind Power Potential in India

Most of the Indian regions are having low wind velocity while the regions of Jammu & Kashmir, Himachal Pradesh, Rajasthan, Gujarat, Madhya Pradesh, Maharashtra, Telangana, Andhra Pradesh, Karnataka, Tamil Nadu, and West Bengal have wind velocity which is capable of power production. MW wind power potential of Indian states and Union territories listed in Table 2, the highest wind power potential is of Gujarat state of 35071 MW.

3.2 Solar Power Potential of India

India has around 300 sunny clear days per year, 5 EWh/yr (5000 trillion kWh) amounts of solar power strikes on the Indian land. Energy output from conventional fossil fuel power reserves in a year led by available Solar Power in our country. 1500–2000 maximum rated capacity operating hours in a year is the daily average generation capacity of the solar plant in India which is approximately 0.25 kWh per meter of used earth's surface with existing proved technologies [1].

Indian government approved schemes for increasing solar power capacity by the development of Ultra Mega Solar Energy Projects and approval for installing solar parks. It is planned that the setting of around 50 solar parks of capacity greater than equal to 500 MW. In the hilly states like Himalayan region, where difficult terrain, contiguous land smaller solar parks will be incorporated under this scheme. As per the report 2016–17 given by Ministry of New and Renewable Energy the solar energy

potential of Indian states and Union Territories given in Table 2, Rajasthan is leading in this perspective with the generation of 142,310 MW.

3.3 Small Hydro Power Potential

Apart from conventional hydro plants, the hydro plants are subclassified on the basis of electrical capacity as

- Micro Hydro Power plant has power capacity less than 100 kW
- Mini Hydro Power plant has the power capacity of 100–1000 kW
- Small Hydro Power plant has the power capacity of 1–50 MW

In the smart city concept, these small projects also sanctioned MW Small Hydro Power Potential of India's States and Union Territories as per MNRE's report for regions of India. Karnataka state is having maximum small hydropower potential of 4141 MW.

3.4 Bio-Energy Potential

India is an agriculture-based country and with an abundance of crop waste, bio-energy is also adopted as a green resource of power. Urban and rural energy markets grow exponentially in India for green energy systems and the bio energy is the prominent one in this regard. It is found from the data given in Table 2 that the Punjab state is having highest bio-energy potential of around 3517 MW.

4 Government Initiatives for Green Energy

The Indian government has started multiple projects to promote green power and collaborated with Industries also to take part in the smart city project.

Rooftop solar panel over the government building is started by Azure Industry to solve the energy problem. To meet carbon footprint reduction targets and to reduce the electricity bills of industrial and commercial customers Azure roof power is providing its solution by solar power. Customers of Azure projects include DMRC(Delhi Metro Rail Corporation), Indian Railways, warehouses, commercial real estate companies, the chain of premium hotels, government ministries, the water utility company in Delhi and Distribution Companies in smart cities [13, 14]. Also the implementation of Grid-Connected Rooftop Solar Projects for 152 Schools by the company Azure Power [15].

Indian Smart city project has the following building pillars:

- Smart Power System: Smart Power system includes Smart Power Storage units, Smart Grid, and Smart Metering. Creating Smart grids and electrification of all houses, Smart grid pilot projects of US\$ 10 million investment. 130 million smart meters installation until 2021 has been planned. Investment of US\$ 26 billion planned by the Power Grid Corporation of India in the energy sector.
- Sustainable development incorporated by the growth of Renewable Power, Government focus toward setting up public transport for the growing population by promoting the Green Transport. US \$ 4.13 billion sanctioned by the Indian government for investment in 2020 electric and hybrid vehicles (with 6 million targets of such vehicles) and Electric Vehicle Charging Stations. US\$20 billion sanctioned on the metro rail projects, 534 km Mumbai–Ahmedabad high-speed rail project of approx. US\$10.5 billion and Monorail.
- In Smart Governance around US\$1.2 trillion investment required for the next 20 years in the domains such as energy, public security, and transportation to design smart city.
- Infrastructure is the next key element, Smart Buildings which save up to 40% of energy usage, reduction of building maintenance costs by 10–30% and decreases 30% of water usage [16].

World's biggest Solar Parks is shaping up in India in the place Pavagada of Karnataka under Solar Power Development Corporation which managed to acquire 12,000 acres of the 13,000 acres [17]. Solution to the extra power supply for sustainable and smart city small-scale distributed generation systems is incorporated with Renewable Energy Sources (RES) [18].

5 Conclusion

Indian government provided many opportunities by initiating smart cities mission. The objective of this mission is decreasing the carbon footprint and energy intensity of the economy. India is now at the stage to transform into the smart nation with optimized power supplies, maximum recycling, and efficient transportation. Smart cities with world-class facilities: 24 h electricity, smart grid system, smart metering system, and manageable energy consumption system. In this paper, region-wise green energy potential of India is presented, the government initiatives and schemes to promote green energy started also mentioned. Green energy is the main building block for the smart city. The green energy capacity of Indian regions/states is identified.

References

1. Jain A Aniket, Bajpai M (2016) Use of green energy for smart city: a review. SSRG Int J Civil Eng (SSRG-IJCE) 3(5):136–139

2. Balaji Hayagrish (2017) The journey in making 'smart cities' smarter with solar energy. *Int J New Technol Res (IJNTR)* 3(3):90–92
3. MNRE. <https://mnre.gov.in/file-manager/annual-report/2016-2017/EN/pdf/1.pdf>
4. Smart cities need smart electricity. <https://elecrama.com/newsletters/smart-cities-need-smart-electricity/>
5. Kumar Ashwani, Kumar Kapil, Kaushik Naresh, Sharma Satyawati, Mishra Saroj (2010) Renewable energy in India: current status and future potentials. *Renewable Sustain Energy Rev Sci Direct* 14(8):2434–2442
6. Kakoli S (20174) A remote sensing approach to smart city development in India: case of Bhopal city, Madhya Pradesh. *ICEGOV' 17 SCII*
7. Geoffrey J, Loubna B (2012) Power from sunshine: a business history of solar energy, 12–105, 1–88
8. Solar energy. <http://www.saurenergy.com/solar-energy-articles>
9. Renewable Energy. <https://www.investindia.gov.in/sector/renewable-energy>
10. Envecologic (2017) Renewable energy in India. Potential, growth and policies. *Clean Energy Green Growth Renewable Energy*
11. Tiwari GN (2002) *Solar energy: fundamentals, design, modelling and applications*. CRC Press
12. CEA report. http://www.cea.nic.in/reports/monthly/installedcapacity/2018/installed_capacity-03.pdf
13. Smart city project Azure power to install rooftop solar projects on government buildings. <https://energy.economictimes.indiatimes.com/news/renewable/smart-city-project-azure-power-to-install-rooftop-solar-projects-on-govt-buildings/62646623>
14. Azure power. <https://www.azurepower.com/commercial/>
15. Azure power rooftop solar schools. <https://mercomindia.com/azure-power-rooftop-solar-schools/>
16. Internet of things. <http://www.makeinindia.com/article/-/v/internet-of-things>
17. World largest solar park is shaping up in Karnataka. <https://www.livemint.com/Industry/UEJYwZQT5m3wNvGupBShZJ/How-the-worlds-largest-solar-park-is-shaping-up-in-Karnatak.html>
18. Sanchez-Miralles A, Calvillo CF, Francisco M, Martín-Martínez R, Jose V (2014) Use of renewable energy systems in smart cities. *Green Energy Technol* 341–370

Modification of Two-Load Method for Measuring Acoustic Properties with Mean Flow



Deepankar Das, Utkarsh Chhibber and R. N. Hota

Abstract The Two-Load method is one of the most commonly used methods to obtain the acoustic properties of a test element. It is based on ASTM standard E 26-11, which uses two microphones each on upstream and downstream section of impedance tube to decompose the wave, and then uses transfer matrix to characterize the test element. However, works in the published literature does not consider the effect of mean flow. Therefore, in this paper, the existing two-load method is modified to include the convective effect of mean flow to make applicable in more practical applications. Several experimental measurements have been done in this work on an acoustical element (Simple Expansion Chamber) at different mean flow conditions. Results show that the modified two-load method agrees more closely with analytical results than the original ASTM standard. This modified method presented gives better results at conditions closer to the real-world applications and can be used to obtain acoustic properties of any acoustical element with mean flow.

Keywords Acoustic · Flow · ASTM

1 Introduction

Reflection coefficient is a property typically used to assess the acoustic performance of acoustical elements. It is defined as the ratio of acoustic pressure incident on a material to the acoustic pressure reflected by its surface. The reflection coefficient of such elements is a strong function of frequency characterized by tailpipe resonances.

Often, the reflection coefficient is roughly measured by the use of a makeshift anechoic termination. However, its establishment which would give accuracy over a full range of frequency under consideration is difficult in practice. Another measurement technique for absorption coefficient is by the usage of a very long downstream duct. Absorption coefficient is also an acoustic property, and for precise determination of the property, measurement of the test element must be taken under two different

D. Das (✉) · U. Chhibber · R. N. Hota
Indian Institute of Technology (ISM), Dhanbad 826004, India
e-mail: deepankardas12@gmail.com

conditions. The most commonly used techniques are two-load [1–3] and two-source methods [4]. In this work, two-load method is exclusively examined. Some of the conclusions of the paper could be obtained as a result of the two-source method also. The two-load method has been standardized in ASTM E2611-09 [5]. According to this standard, two different loads are taken into consideration and determination of acoustic properties is carried out through a sound absorbing material. In this study, the methodology and algorithm are extended to the measurement of reflection coefficient only.

Munjal [4] and Abom [6] have mentioned the difficulty in finding the two different loads which would fulfill the requirement of all the frequencies of interest. The determined transmission loss becomes more prone to error when the two loads are too close to each other. Recommendation of the standard is the usage of one absorptive load out of the two. It would result in minimal reflection. The other of the two loads could be preferred as an open or closed termination. At this termination, a significant reflection of sound can be anticipated.

However, none of the present literature has investigated the effect of mean flow in the two-load method, which is done here. In this paper, two-load method is modified for mean flow conditions by taking the convective effect of flow in the modeling. Results of modified method are also compared with the original Two-Load method for a better understanding of the effect.

The following paper is organized as, in Sect. 2 analytical modeling for the existing two-load method is given, in Sect. 3 a modified model of two-load method is presented and in Sect. 4 experimental results and discussion is presented.

2 Analytical Modeling

2.1 Two-Load Method

As the name signifies, the two-load method requires two different terminations (loads) for obtaining the absorption coefficient. In this method also, like all other methods, an impedance tube is used, but here we use four microphones, two on either side of the test sample. Here also, we use a loudspeaker on one end and test sample is mounted inside the tube. All the four microphones are flush mounted inside the tube. A broadband signal generator is used to generate plane waves inside the tube which results in a standing wave pattern, which is further decomposed into forward and backward traveling waves A, B, C, D as shown in Fig. 1.

This wave decomposition is done by measuring the complex, sound pressure amplitude at four locations simultaneously and examining their relative amplitude and phase. From these, the pressure and particle velocity is obtained, which is further used to obtain transfer matrix elements. And these transfer matrix elements can yield us, the absorption coefficient, acoustic impedance, and other important properties as shown in Fig. 1 [5].

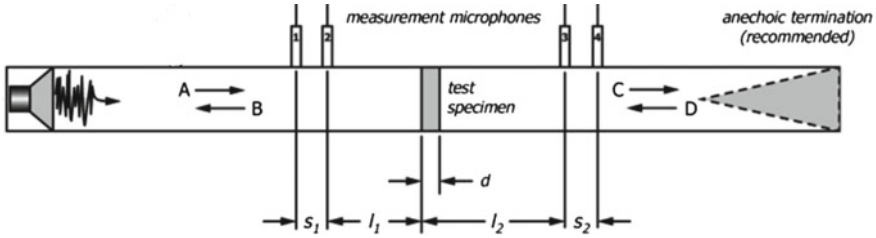


Fig. 1 Schematic of experimental setup

In this method Collection of microphone data for two loads (in the form of complex acoustic transfer functions between the reference and the remaining microphones) is the first step. For each load case, decompose the acoustic wave field inside the tube into forward and backwards traveling waves on either side of the specimen, indicated in Fig. 1 using Equations (Using microphone 1 as reference microphone).

$$A = i * \frac{[H_{11} * e^{-ikL_1} - H_{21} * e^{-ik(L_1+s_1)}]}{2 * \sin(ks_1)} \tag{1}$$

$$B = i * \frac{[H_{21} * e^{ik(L_1+s_1)} - H_{11} * e^{ikL_1}]}{2 * \sin(ks_1)} \tag{2}$$

$$C = i * \frac{[H_{31} * e^{ik(L_2+s_2)} - H_{41} * e^{ikL_2}]}{2 * \sin(ks_2)} \tag{3}$$

$$D = i * \frac{[H_{41} * e^{-ikL_2} - H_{31} * e^{-ik(L_2+s_2)}]}{(2 * \sin(ks_2))} \tag{4}$$

Calculating the pressure and velocity at each side of the specimen, we will get

$$p_0 = A + B \tag{5}$$

$$u_0 = \frac{(A - B)}{\rho * c} \tag{6}$$

$$p_d = C * e^{-ikd} + D * e^{ikd} \tag{7}$$

$$u_d = \frac{C * e^{-ikd} - D * e^{ikd}}{\rho * c} \tag{8}$$

From the pressure and particle velocity values in each load case, calculate the transfer matrix for the specimen:

$$\begin{bmatrix} p_0 \\ u_0 \end{bmatrix}_{loada,b} = \begin{bmatrix} T11 & T12 \\ T21 & T22 \end{bmatrix} \cdot \begin{bmatrix} p_d \\ u_d \end{bmatrix}_{loada,b} \quad (9)$$

Determination of Transfer matrix elements:

Relation to find transfer matrix as per ASTM 2611-09 [5] using pressure and velocity is

$$\begin{bmatrix} p_0 \\ u_0 \end{bmatrix}_{loada,b} = \begin{bmatrix} T11 & T12 \\ T21 & T22 \end{bmatrix} \cdot \begin{bmatrix} p_d \\ u_d \end{bmatrix}_{loada,b} \quad (10)$$

From Eq. (35) we have four unknowns and four equations. By solving this we will get:

$$T11 = \frac{(p_0a * u_db - p_0b * u_da)}{(p_da * u_db - p_db * u_da)} \quad (11)$$

$$T12 = \frac{(p_0a * p_db - p_0b * p_da)}{(p_da * u_db - p_db * u_da)} \quad (12)$$

$$T21 = \frac{(u_0a * u_db - u_0b * u_da)}{(p_da * u_db - p_db * u_da)} \quad (13)$$

$$T22 = \frac{(p_da * u_0b - p_db * u_0a)}{(p_da * u_db - p_db * u_da)} \quad (14)$$

After calculating transfer matrix, using elements of transfer matrix (T11, T12, T21, T22) we can calculate all the acoustic properties of an acoustic material, an example of reflection coefficient is given.

2.2 Modified Two-Load Method

For the modification of the Two-Load method given above, assuming that there is a mean flow M_u at the upstream section in Fig. 1. Axial flow at upstream section, M_u , is given by,

$$M_u = M_g \quad (15)$$

where M_g is applied grazing flow.

For a test element with porosity σ , lateral surface area A_l , cross-sectional area A_x subjected to bias flow $M - b$, axial flow velocity at downstream section, M_d is given by

$$M_d = M_g + \frac{A_l}{A_x} \sigma M_b \quad (16)$$

The effect of axial flow on wave numbers of forward and backward traveling waves can be written as

$$k_u^\pm = \frac{k}{1 \pm M_u} \tag{17}$$

$$k_d^\pm = \frac{k}{1 \pm M_d} \tag{18}$$

Using Eqs. (17) and (18) pressure perturbation at a point can be written in terms of wave components as

$$p = p^+ e^{-ik^+x} + p^- e^{ik^-x} \tag{19}$$

Velocity perturbation can be written as

$$u = \frac{p^+}{\rho c} e^{-ik^+x} - \frac{p^-}{\rho c} e^{ik^-x} \tag{20}$$

The forward A and C and backward wave components B and D can be found by

$$W = \begin{bmatrix} e^{-ik_u^+x_1} & e^{ik_u^-x_1} & 0 & 0 \\ e^{-ik_u^+x_2} & e^{ik_u^-x_2} & 0 & 0 \\ 0 & 0 & e^{-ik_d^+x_3} & e^{ik_d^-x_3} \\ 0 & 0 & e^{-ik_d^+x_4} & e^{ik_d^-x_4} \end{bmatrix} \tag{21}$$

$$\begin{bmatrix} A \\ B \\ C \\ D \end{bmatrix} = W^{-1} \begin{bmatrix} H_{11} \\ H_{21} \\ H_{31} \\ H_{41} \end{bmatrix} \tag{22}$$

Pressure and velocity at upstream and downstream end of the element for load ‘a’ and ‘b’, respectively,

$$\begin{bmatrix} p_{0,a} \\ u_{0,a} \\ p_{d,a} \\ u_{d,a} \end{bmatrix} = \begin{bmatrix} 1 & 1 & 0 & 0 \\ \frac{1}{\rho c} & -\frac{1}{\rho c} & 0 & 0 \\ 0 & 0 & 1 & 1 \\ 0 & 0 & \frac{1}{\rho c} & -\frac{1}{\rho c} \end{bmatrix} \begin{bmatrix} A_a \\ B_a \\ C_a \\ D_a \end{bmatrix} \tag{23}$$

$$\begin{bmatrix} p_{0,b} \\ u_{0,b} \\ p_{d,b} \\ u_{d,b} \end{bmatrix} = \begin{bmatrix} 1 & 1 & 0 & 0 \\ \frac{1}{\rho c} & -\frac{1}{\rho c} & 0 & 0 \\ 0 & 0 & 1 & 1 \\ 0 & 0 & \frac{1}{\rho c} & -\frac{1}{\rho c} \end{bmatrix} \begin{bmatrix} A_b \\ B_b \\ C_b \\ D_b \end{bmatrix} \tag{24}$$

The two sections can be related through transfer matrix

$$\begin{bmatrix} p_0 \\ u_0 \end{bmatrix} = \begin{bmatrix} T_{11} & T_{12} \\ T_{21} & T_{22} \end{bmatrix} \begin{bmatrix} p_d \\ u_d \end{bmatrix} \quad (25)$$

For Load 'a'

$$\begin{bmatrix} p_{0,a} \\ u_{0,a} \end{bmatrix} = \begin{bmatrix} T_{11} & T_{12} \\ T_{21} & T_{22} \end{bmatrix} \begin{bmatrix} p_{d,a} \\ u_{d,a} \end{bmatrix} \quad (26)$$

For Load 'b'

$$\begin{bmatrix} p_{0,b} \\ u_{0,b} \end{bmatrix} = \begin{bmatrix} T_{11} & T_{12} \\ T_{21} & T_{22} \end{bmatrix} \begin{bmatrix} p_{d,b} \\ u_{d,b} \end{bmatrix} \quad (27)$$

Using Eqs. (26) and (27), the transfer matrix of the elements can be found as

$$\begin{bmatrix} T_{11} & T_{12} \\ T_{21} & T_{22} \end{bmatrix} = \begin{bmatrix} p_{0,a} & p_{0,b} \\ u_{0,a} & u_{0,b} \end{bmatrix} \begin{bmatrix} p_{d,a} & p_{d,b} \\ u_{d,a} & p_{d,b} \end{bmatrix}^{-1} \quad (28)$$

2.3 Calculation of Reflection Coefficient

For calculating absorption coefficient downstream reflection coefficient is defined as

$$R_d = \frac{D}{C} \quad (29)$$

the pressure wave components are assumed as

$$A = 1 \quad (30)$$

$$B = R \quad (31)$$

$$C = T \quad (32)$$

$$D = T \cdot R_d \quad (33)$$

where R and T are reflection coefficient and transmission of the element. Substituting A, B, C, D in transfer matrix relation R can be found.

$$R = \frac{\Delta_R}{\Delta} \quad (34)$$

where:

$$\Delta = \left| \begin{matrix} -1 (T_{11}(1 + R_d) + \frac{T_{12}}{\rho c}(1 - R_d)) \\ \frac{1}{\rho c} (T_{21}(1 + R_d) + \frac{T_{22}}{\rho c}(1 - R_d)) \end{matrix} \right| \tag{35}$$

$$\Delta_R = \left| \begin{matrix} 1 (T_{11}(1 + R_d) + \frac{T_{12}}{\rho c}(1 - R_d)) \\ \frac{1}{\rho c} (T_{21}(1 + R_d) + \frac{T_{22}}{\rho c}(1 - R_d)) \end{matrix} \right| \tag{36}$$

3 Experimental Results and Validation

For validation of our modified theory, experiments were conducted on a simple expansion chamber at different Mach numbers. To conduct the experiments an 80 mm diameter impedance tube was used with the cutoff frequency of 2500 Hz, the sensors and the data acquisition system (DAS) are all B and K make. A random white noise was generated and measurements were taken upto 2 kHz.

The Transfer Matrix was obtained by both original two-load method and the modified one. In the modified two-load method, downstream reflection coefficient given in Eq. (29) was determined for a third load, to be used as reference, using direct measurements. Reflection coefficient of the element was directly measured for this load as shown by Song and Bolton [7].

This Transfer Matrix obtained was used to find reflection coefficient given in Eq. (34) for the element using reference downstream load. Below shown are the plots of reflection coefficients at random Mach numbers. These results obtained by modified theory were compared with old ASTM Method and Direct Methods.

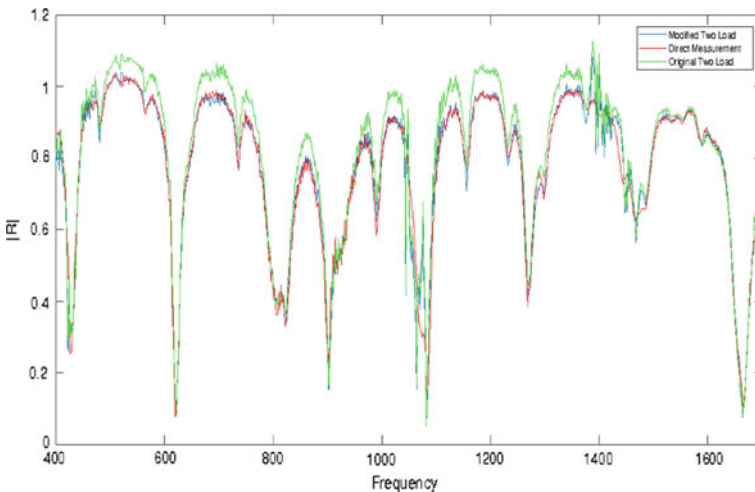


Fig. 2 Mean Flow = 0.0393M

Figures 2, 3 and 4 show the results of comparison between modified and original two-load method. It can be clearly observed that the modified transfer matrix method is closest to the direct measurements. Also, it is to be noted that original two-load method deviate by large amount in case of higher flows because of absence of inclusion of convective effect in its modelling.

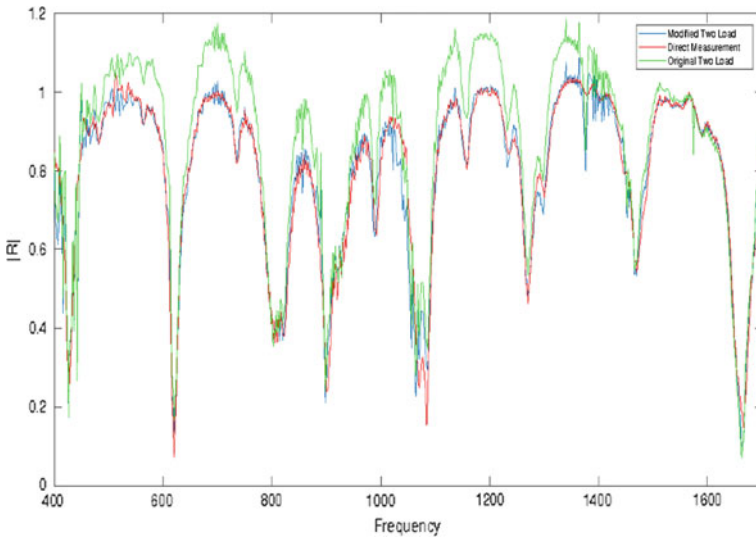


Fig. 3 Mean Flow = 0.0701M

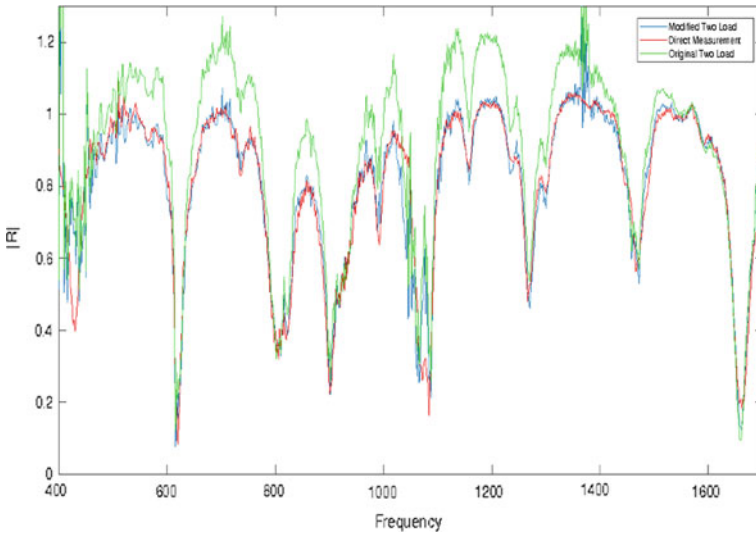


Fig. 4 Mean Flow = 0.0880M

4 Conclusions

The two-load method is modified for the cases of mean flow by including the convective effect in it and experiments are conducted to validate and compare the results obtained by both the methods. During the process of this study, the following points were observed:

1. The modified transfer matrix method is closest to the direct measurements.
2. Original two-load method is deviated by large amount in case of higher flows.
3. In Fig. 2, both methods give similar results with low variation due to low mean flow value.
4. In Figs. 3 and 4, large improvements can be seen in lower freq. due to higher Mach number.

This modified method is effective in higher mean flows and lower frequencies ranges and may be used as a guideline to conduct experiments in cases of mean flow.

References

1. To CWS, Doige AG (2016) A transient testing technique for the determination of matrix parameters of acoustic systems, 2: experimental procedures and results. *J Sound Vib* 62
2. To CWS, Doige AG (2016) A transient testing technique for the determination of matrix parameters of acoustic systems 1: theory and principles. *J Sound Vib* 62
3. Lung TY, Doige AG (1983) A time-averaging transient testing method for acoustic properties of piping system and mufflers. *J Acoust Soc Am* 73
4. Munjal ML, Doige AG (1990) Theory of a two source-location method for direct experimental evaluation of the four-pole parameters of an aeroacoustic element. *J Sound Vib* 141(2)
5. ASTM E2611-09 (2009) Standard test method for measurement of normal incidence sound transmission of acoustical materials based on the transfer matrix method
6. Abom M (1992) A note on the experimental determination of acoustical two-port matrices. *J Sound Vib* 155(1)
7. Song HB, Bolton JS (2000) A transfer-matrix approach for estimating the characteristic impedance and wave numbers of limp and rigid porous materials. *J Acoust Soc Am* 107(3)

BSA Detection on Polymeric Nanocantilever



Aviru Kumar Basu , Amar Nath Sah, Asima Pradhan
and Shantanu Bhattacharya 

Abstract MEMS-based microcantilevers have become an indispensable technique for mass sensing in the last decade. Presently, the need has come to scale down to nanoscale cantilevers for better and faster sensing. Previously, metallic cantilevers were mostly used for biochemical/analyte detection which is more expensive compared to the polymeric ones. Arrays of sensors can be fabricated easily as SU-8 is highly resistant to chemicals. In addition, SU-8 is also biocompatible, making it the most suitable material for biochemical sensors. Furthermore, due to its low Young's modulus, high sensitivity can be achieved. Polymeric nanocantilevers have been used in this study for detection of BSA (Bovine Serum Albumin) in a short time and low amount of concentration. Deflection was measured and observed through optical beam deflection technique and optical diffraction-based approach using high-speed camera.

Keywords Cantilever · High-speed camera · Response · Optical diffraction · BSA

A. K. Basu · S. Bhattacharya (✉)
Design Program, Indian Institute of Technology, Kanpur, U.P 208016, India
e-mail: bhattacs@iitk.ac.in

Microsystems Fabrication Laboratory, Department of Mechanical Engineering, Indian Institute of Technology, Kanpur, U.P 208016, India

A. K. Basu · A. N. Sah · A. Pradhan
Biophotonics Laboratory, Department of Physics, Indian Institute of Technology, Kanpur, U.P 208016, India

A. N. Sah
Department of Biological Sciences and Bioengineering, Indian Institute of Technology, Kanpur, U.P 208016, India

A. Pradhan
Department of Physics, Indian Institute of Technology, Kanpur, U.P 208016, India

1 Introduction

MEMS-based cantilevers are of great interest for small size and higher sensitivity. Microcantilevers have been used to detect various analytes, chemicals, gases [1, 2]. Silicon cantilevers [3] or mostly silicon nitride [4] or metallic cantilevers [5] were reported for sensing or AFM application. SU-8 cantilevers are comparatively easy to fabricate also much more biocompatible. Presently, piezo-resistive SU-8 cantilevers have already been used widely [6]. SU-8, cantilevers for detection using the optical detection principle has been not much utilized. Optical detection principle can give maximum accuracy compared to the other techniques used. Previously, the silicon or other metal cantilevers reported were much more thickness [7]. The thickness of the cantilevers mostly in the micron range. As a result, the deflections recorded were mostly less or less sensitive with respect to the frame per second and the sensitivity of the camera. Scaling down to NEMS from MEMS has driven the need for high-speed cameras. Polymeric cantilevers have come into role nowadays due to cheaper cost, easy to fabricate and similar young modulus like silicon [8, 9]. Most of the SU-8 cantilevers used nowadays, the thickness of the cantilevers for sensing is greater than 500 nm thickness. Scaling down the cantilevers up to 250 nm thickness gave us an additional advantage for faster response. Additionally, other than optical beam deflection technique a diffraction-based approach is shown here. This approach made much easier with lesser optics complication, to observe deflection of the cantilever due to changes in fringes leading to shifting and changes in intensity peaks.

2 Experimental Method

2.1 Fabrication of SU-8 Polymeric Cantilever

A simple two processes were used for fabricating this cantilever. SU-8 2000.5 spin-coated prebaked at 95 °C and patterned using lithography. A lift-off process was done on one of the cantilevers of the array with a thin gold layer patterned. A second body layer of 25 μm thickness was placed at the back side using SU-8 2035. Cantilevers were peeled off from the glass substrate shown in Figs. 1 and 2.

2.2 Fabrication of Channel

The chamber was fabricated using 2 mm black acrylic sheets using a laser machining process. Intentionally, black acrylic sheets were used for fabricating the chamber, so that any additional light reflection from the chamber to the CCD camera can be avoided. The volume of the chamber was made 80 μl . A small chamber with a small amount of analyte gave much faster response.

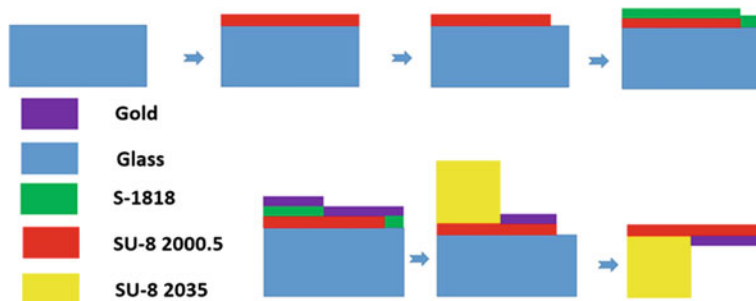


Fig. 1 Schematic of Fabrication of SU-8 Cantilever

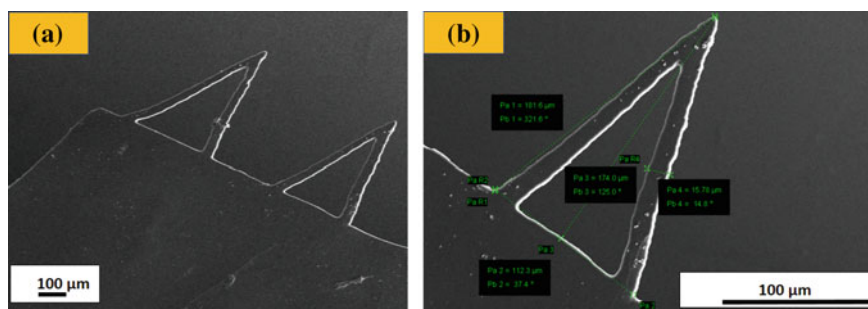


Fig. 2 **a** Fesem Image of an array of V-shaped SU-8 Nanocantilever. **b** V-shaped single cantilever of length = 181.6 μm and width = 114 μm

2.3 Optical Detection Method

He-Ne laser beam of 632 nm wavelength was collimated using spatial filter and lenses. Top surface of both the beams was sputter coated using a thin gold layer for good reflection from the surface to the CCD. A high-speed camera EMCCD was used for recording the deflection. Compared to the other CCD, EMCCD (iXon Andor Ltd.) has a higher fps rate and good sensitivity which easily enables to capture the nanomechanical deflections in high speed shown in Fig. 3.

3 Results and Discussion

3.1 BSA Detection Based on Optical Beam Deflection Technique

BSA adhesion with gold patterned cantilever occurred at a lower flow rate much easier. BSA detection was done in both micromolar and nanomolar concentration.

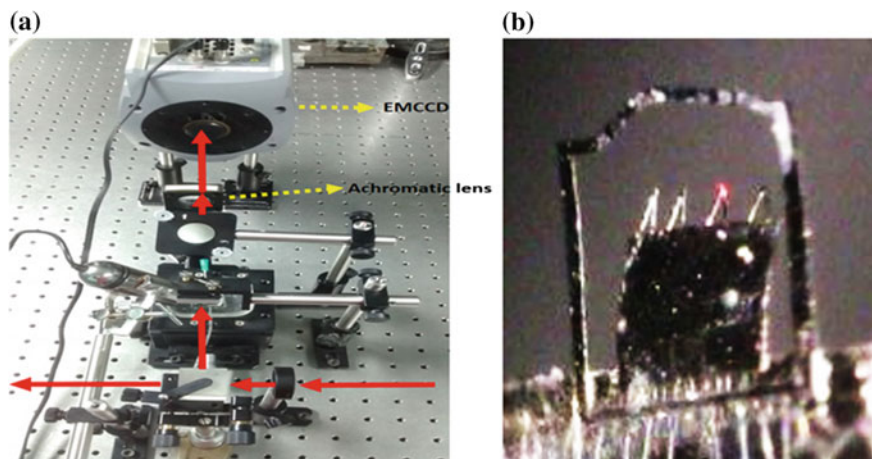


Fig. 3 a Optical Setup for Nanomechanical deflection measurement. b Single spot of the laser on a V-shaped cantilever

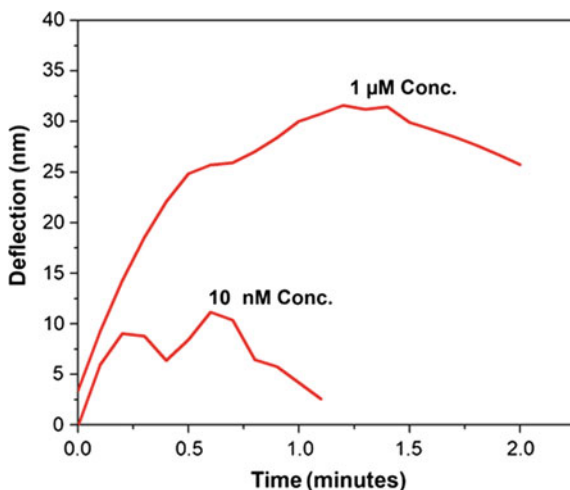


Fig. 4 Deflection curves of BSA detection at 10 nM concentration and 1 μ M concentration

Nanocantilevers showed a good response in both the cases specially in the lower concentration. Recovery of the cantilevers was better in the lower concentration compared to the higher concentration. The fast response of the cantilevers was possible to capture using high-speed camera as shown in Fig. 4.

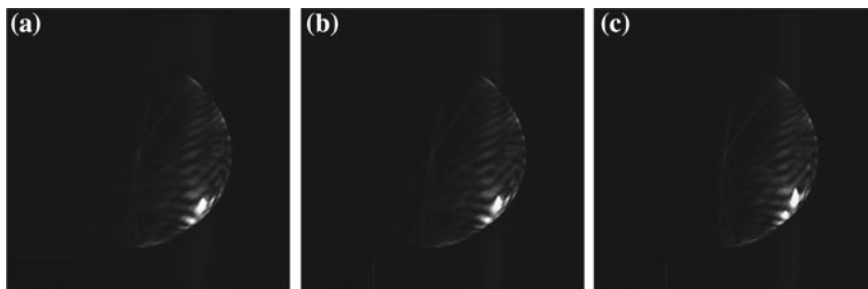
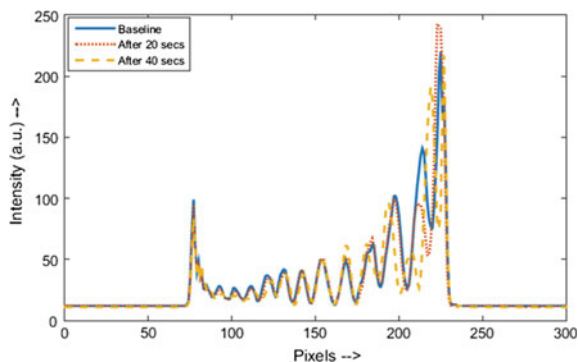


Fig. 5 Images of the fringes obtained by diffraction from reflection by illuminating the cantilever **a** baseline **b** after 20 secs and **c** after 40 secs

Fig. 6 Intensity versus pixel curves obtained from the fringes **a** Baseline **b** after 20 secs and **c** after 40 secs



3.2 *BSA Detection Based on Optical Diffraction-Based Approach*

OBDT is a long existing technique developed almost 30 years ago, and used mostly in atomic force microscopy. This technique is much more expensive compared to the diffraction-based technique shown below. OBDT technique generally requires precise alignment of the laser beam on the cantilever. In optical diffraction technique, the size of the laser beam is larger than the size of the cantilever. Precise alignment of the laser beam on the cantilever is not required [10]. Detection of BSA done with this technique is described below.

An optical diffraction approach was also followed, by fully illuminating the cantilever with the laser. Fringes were captured using the CCD camera and appropriate lenses. Images were taken of the baseline without flowing the BSA, and flowing at a constant flow rate of $2 \mu\text{l}/\text{min}$ of 100 nM concentration. Below images for diffraction patterns obtained by diffraction by reflection from the cantilever for different time intervals are shown in Fig. 5. The plot of intensity versus pixel from the images is shown in Fig. 6. Due to the bending of the cantilever changes or shift in fringes occurred as a result shift of intensity peaks can be clearly observed from the plot.

4 Conclusion

Nanocantilevers were successfully fabricated up to 250 nm of SU-8. Optical detection setup has been successfully developed using high-speed camera for deflection measurement. Microfluidic channel fabricated using laser machining with a volume of 80 μl for faster detection in lower concentration. Also, with the requirement of a lower amount of analyte on the channel. Concentrations up to nanomolar level reached for detection without any additional surface chemistry. Other than optical beam deflection technique, a diffraction-based approach has been shown which can be further utilized to observe and calculate nanomechanical deformation from the shifting in intensity peaks with minimizing the complex optics requirement.

Acknowledgements I sincerely like to acknowledge Dr. Shraddha Singh, BSBE, IITK, Sayma Ayaz, Nanoscience, IITK, Dr. Prabhat Dwivedi, Nanoscience, Dr. Seema Sharma, Nanoscience, IITK for fabrication and SEM Facilities. I will also like to acknowledge Dr. Rodolfo I. Hermans and Dr. Benjamin Dueck from the London Centre for Nanotechnology, UCL for all communications.

References

1. Wu G, Datar RH, Hansen KM, Thundat T, Cote RJ, Majumdar A (2001) Bioassay of prostate-specific antigen (PSA) using microcantilevers. *Nat Biotechnol* 19:856–860
2. Lang H, Hegner M, Gerber C (2005) Cantilever array sensors. *Mater Today* 8:30–36
3. Nakagawa K, Hashiguchi G, Kawakatsu, H (2009) Small single-crystal silicon cantilevers formed by crystal facets for atomic force microscopy. *Rev Sci Instrum* 80(9):095104. 8 Sep 2009
4. Nam HJ, Kim YS, Lee CS, Jin WH, Jang SS, Cho IJ, Bu JU, Choi WB, Choi SW (2007) Silicon nitride cantilever array integrated with silicon heaters and piezoelectric detectors for probe-based data storage. *Sens Actuators A Phys* 134:329–333
5. Basu AK, Sarkar H, Bhattacharya S (2016) Fabrication and resilience measurement of thin aluminium cantilevers using scanning probe microscopy. In: Foundations and frontiers in computer, communication and electrical engineering—Proceedings of the 3rd international conference on foundations and frontiers in computer, communication and electrical engineering, C2E2-2016
6. Reddy CVB, Khaderbad MA, Gandhi S, Kandpal M, Patil S, Chetty KN, Rajulu KG, Chary PCK, Ravikanth M, Rao VR (2012) Piezoresistive SU-8 cantilever with Fe(III)porphyrin coating for CO sensing. *IEEE Trans Nanotechnol* 11:701–706. <https://doi.org/10.1109/TNANO.2012.2190619>
7. Pandya HJ, Kim HT, Roy R, Desai JP (2014) MEMS based low cost piezoresistive microcantilever force sensor and sensor module. *Mater Sci Semicond Process* 19:163–173. <https://doi.org/10.1016/j.mssp.2013.12.016>
8. Basu AK, Sah AN, Pradhan A, Bhattacharya S (2019) Poly-L-Lysine functionalised MWCNT-rGO nanosheets based 3-d hybrid structure for femtomolar level cholesterol detection using cantilever based sensing platform. *Sci Rep* 9(1):3686. 6 Mar 2019
9. Basu AK, Tatiya S, Bhatt G, Bhattacharya S (2019) Fabrication Processes for Sensors for Automotive Applications: a Review. In: *Sensors for automotive and aerospace applications 2019*, Springer, Singapore, pp 123–142
10. Hermans RI, Dueck B, Ndieyira JW, McKendry RA, Aeppli G (2016) Optical diffraction for measurements of nano-mechanical bending. *Sci Rep* 6:26690. 3 Jun 2016

Modeling and Control of Underactuated System Using LQR Controller Based on GA



Vishal Dhiman, Gurminder Singh and Munish Kumar

Abstract Cart-pole system is the benchmark for the study of controls. Literature ensures the availability of various controllers to control an underactuated system at an unstable position. Due to its simplicity, LQR optimal control is mostly used to cart-pole system despite challenges in the selection of LQR parameters. The dynamic model of the cart-pole system is derived using the Euler–Lagrangian method and controllability analysis is considered. According to optimal determination problem of the weighting matrix Q and R in LQR, the genetic algorithm (GA) is adopted and the optimal parameter values are used to stable the system at the unstable equilibrium position. From the results, it has been found that the system is stable, robust than the unoptimized LQR controller. This algorithm can avoid heavy and complicated work, improve work efficiency, and has strong practicability.

Keywords Inverted cart-pole system · LQR · Genetic algorithm

1 Introduction

Underactuated mechanical systems have fewer control inputs than the degree of freedom due to which the system is not accelerated in every direction by the control system. These systems have broad applications in several fields including Robotics, Flexible Systems, Marine Units, Aerospace Units, etc. Cost reduction is one of the various reasons including low power utilization, enhanced dexterity, safety, and minimum environmental impact.

Cart-pole equipment is recognized as the typical experiment device of automatic control theory. The effective use of an inverted pendulum to check various control theories and approaches has attracted the focus of various researchers and scholars. This control method has an extensive range of applications in the field of defense,

V. Dhiman (✉) · M. Kumar
Chandigarh University, Mohali Punjab 140413, India
e-mail: vishal.mech@cumail.in

G. Singh
Indian Institute of Technology, Delhi, New Delhi 110016, India

© Springer Nature Singapore Pte Ltd. 2019
M. Kumar et al. (eds.), *Advances in Interdisciplinary Engineering*, Lecture Notes in Mechanical Engineering, https://doi.org/10.1007/978-981-13-6577-5_57

aerospace science and technology, robot and general industrial applications. In recent years, many scholars have used the classical control theory, modern control theory and a variety of intelligent control methods [1–3] in this system and successfully achieved stability control of inverted cart-pendulum system.

LQR controller is the optimal controller to stabilize the system. It has good robustness in the cart-pole system, so it has been widely used in the design of control system [4]. A key problem of LQR controller design is the adjustment of matrix Q and R. However, quadratic weighting matrix Q and R are chosen by trial and error method in most of the literature. There is no rule to follow for Q and R option and it usually depends on the designer's experience. Complex trial and error not only affects the design efficiency, but also cannot guarantee the system meets specific performance indicators. To solve these problems, the article uses improved algorithm optimization design [5–7] to find the optimal linear quadratic control weighting matrix Q and R for the cart inverted pendulum system.

This paper is divided into 5 sections. Introduction regarding the underactuated system, LQR controller and the genetic algorithm has been discussed in Sect. 1. Dynamic modeling of the cart-pole system is elaborated in Sect. 2 using the Euler–Lagrangian technique. LQR controller and the genetic algorithm are discussed in Sect. 3. GA-based LQR controller is used to stabilize the cart-pole system. The results and discussion for such controller are presented in Sect. 4. Finally, the conclusion of this paper is described in Sect. 5.

2 Dynamic Modeling of the System

Design, analysis, and control of the underactuated system begin with correct dynamic mathematical modeling. The mathematical equations of the system are derived by the Euler–Lagrangian method and further, the equations formulated to state-space representation. The description of the cart-pole system is considered, as shown in Fig. 1a. This is two degree of the system having inverted pendulum on moving cart. Here, M represents the mass of cart and m the mass of the pendulum, distance from the rod cart joint to the rod mass center is given by l , the friction coefficient of the cart is given by b and F force acting on the cart. The generalized coordinates of the system are x and ϕ .

The kinematics of the system is given by

$$X = \begin{bmatrix} x_p \\ y_p \end{bmatrix} = \begin{bmatrix} x - l \sin \phi \\ l \cos \phi \end{bmatrix} \quad (1)$$

$$\dot{X} = \begin{bmatrix} \dot{x}_p \\ \dot{y}_p \end{bmatrix} = \begin{bmatrix} \dot{x} - l\dot{\phi} \cos \phi \\ -l\dot{\phi} \sin \phi \end{bmatrix} \quad (2)$$

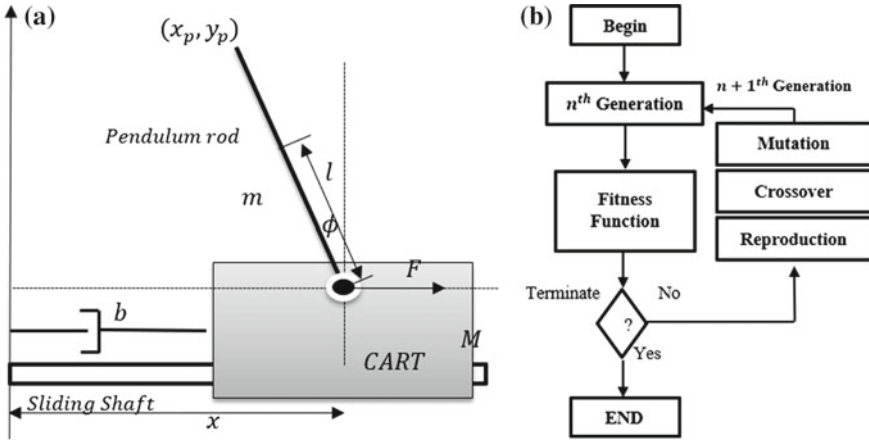


Fig. 1 a Cart-pole system, b flowchart of genetic algorithm

Total sum of kinetic energy is given as

$$KE = KE_{cart} + KE_{Pend} \tag{3}$$

$$= \frac{1}{2}(M + m)\dot{x}_p^2 + \frac{1}{2}ml^2\dot{\phi}^2 - ml \cos \phi \dot{\phi} \dot{x}_p \tag{4}$$

In this system, only pendulum possess potential energy. The total sum of potential energy of the system is given as

$$PE = PE_{cart} + PE_{Pend} \tag{5}$$

$$= 0 + (-mg(l - l \cos \phi)) \tag{6}$$

Lagrangian \mathcal{L} of the system is calculated in the terms of system KE and PE, given as

$$\mathcal{L} = KE - PE \tag{7}$$

$$= \frac{1}{2}(M + m)\dot{x}_p^2 + \frac{1}{2}ml^2\dot{\phi}^2 - ml \cos \phi \dot{\phi} \dot{x}_p - mg(l - l \cos \phi) \tag{8}$$

To drive damping force of the system Rayleigh’s dissipation function is used, which is given as

$$R = \frac{1}{2}b\dot{x}^2 \tag{9}$$

Lagrange's equations are given as

$$\frac{d}{dt} \left(\frac{\partial \mathcal{L}}{\partial \dot{x}} \right) - \frac{\partial \mathcal{L}}{\partial x} + \frac{\partial R}{\partial \dot{x}} = F \tag{10}$$

$$\frac{d}{dt} \left(\frac{\partial \mathcal{L}}{\partial \dot{\phi}} \right) - \frac{\partial \mathcal{L}}{\partial \phi} + \frac{\partial R}{\partial \dot{\phi}} = 0 \tag{11}$$

By putting the values of \mathcal{L} and R in the above equations, the equations can be written as

$$(M + m)\ddot{x} - ml \cos \phi \ddot{\phi} + ml \sin \phi \dot{\phi}^2 + b\dot{x} = F \tag{12}$$

$$(I + ml^2)\ddot{\phi} - mgl \sin \phi - ml \cos \phi \ddot{x} = 0 \tag{13}$$

These equations are nonlinear in nature. To linearize the system, take $\sin \phi = \phi$, $\cos \phi = 1$ and neglect square terms, then two equations will become as given below.

$$(M + m)\ddot{x} - ml\ddot{\phi} + b\dot{x} = F \tag{15}$$

$$(I + ml^2)\ddot{\phi} - mgl\phi = ml\ddot{x} \tag{16}$$

State-space representation of the system is written as

$$\dot{\mathbf{x}} = \mathbf{Ax} + \mathbf{Bu} \tag{17}$$

$$\mathbf{y} = \mathbf{Cx} + \mathbf{Du} \tag{18}$$

where $\mathbf{x} = [x \dot{x} \phi \dot{\phi}]$, is the state-vector, the input vector \mathbf{u} and state-weighing coefficient matrices are \mathbf{A} , \mathbf{B} , \mathbf{C} , and \mathbf{D} .

To stabilize the inverted pendulum of the cart-pole system state-space representation of Eq. 13 is considered.

$$\mathbf{A} = \begin{bmatrix} 0 & 1 & 0 & 0 \\ 0 & \frac{-(I+ml^2)b}{I(M+m)+Mml^2} & \frac{m^2gl^2}{I(M+m)+Mml^2} & 0 \\ 0 & 0 & 0 & 1 \\ 0 & \frac{-mlb}{I(M+m)+Mml^2} & \frac{mgl(M+m)}{I(M+m)+Mml^2} & 0 \end{bmatrix} \tag{19}$$

$$\mathbf{B} = \begin{bmatrix} 0 \\ \frac{I+ml^2}{I(M+m)+Mml^2} \\ 0 \\ \frac{ml}{I(M+m)+Mml^2} \end{bmatrix}, \mathbf{C} = \begin{bmatrix} 1 & 0 & 0 & 0 \\ 0 & 0 & 1 & 0 \end{bmatrix}, \mathbf{D} = \begin{bmatrix} 0 \\ 0 \end{bmatrix} \tag{20}$$

Here, the rod is of even quality. So system moment of inertia is

$$I = \frac{1}{3}ml^2 \tag{21}$$

$$\ddot{\phi} = \frac{3g}{4l}\dot{\phi} + \frac{3}{4l}\ddot{x} \tag{22}$$

The A and B matrices for the state-space representation are given as

$$A = \begin{bmatrix} 0 & 1 & 0 & 0 \\ 0 & 0 & 0 & 0 \\ 0 & 0 & 0 & 1 \\ 0 & 0 & \frac{3g}{4l} & 0 \end{bmatrix}, B = \begin{bmatrix} 0 \\ 1 \\ 0 \\ \frac{3}{4l} \end{bmatrix} \tag{23}$$

To control any system in the world, first of all, the system is an analysis that the system is controllable or not. The property of a system when an input vector can change the state of a system from initial to final in a finite time is known as controllability. The controllability of the system can be easily defined from the state-space representation.

The theorem for controllability states that, “A linear, time-invariant system described by the matrix state-equation, $\dot{x} = Ax + Bu$ is controllable if and only if the controllability test matrix

$$P = [B; AB; A^2B; A^{n-1}B] \tag{24}$$

is of rank n , the order of the system”.

3 Controller Design

The section deals with the design of the controller of the cart-pole system. The objective of the controller is to stable the inverted pendulum at an unstable point, i.e., upward position. In the present section, first LQR controller is discussed which will use to stabilize the pendulum. Then, the Genetic algorithm is discussed which is used to calculate gains for LQR controller.

3.1 Linear Quadratic Regulator Controller

Linear Quadratic Regulator (LQR) is the ideal controller used to limit the cost related to producing control inputs. The costing work comprises of two matrices, Q (weighting matrix) and R (control cost matrix). For a linearized plant, the purpose of the

LQR controller is to maintain the integration of sum of Q and R matrices from beginning to endpoint to the minimum value with the help of feedback regulator. For this cart-pole system with u input and x variable vector, the feedback regulator is given as

$$u = -Kx \quad (25)$$

And cost function, i.e., the objective function is given as

$$J_o = \int_0^{\infty} (x^T Qx + u^T Ru) dt \quad (26)$$

where K is the final optimal state feedback control matrix, which is given as

$$K = R^{-1} B^T P \quad (27)$$

Here, P is the following algebra symmetric positive definite solution of the equation:

$$PA + A^T P - PBR^{-1}B^T P + Q = 0 \quad (28)$$

It can be seen, matrix depends on A , B , Q , and R matrix, A and B , are determined by the structure and parameters of the system, respectively, so it really depends on the weight matrices Q and R . These matrices can also be located by tuning the system manually but for optimal weight matrices special types of algorithms can be used.

3.2 Genetic Algorithm

The basic idea is the solution to the optimization problem which is searched from a representative initial group, this set of solutions is called population. The population consists of a number of genes codes for individual components, and each individual is called a chromosome. Through the different chromosome copy it crossover or mutation to generate new individuals. According to the principle of survival of the fittest, the selection and elimination of the problem domain of individuals is based on individual fitness in size in each generation. Each generation evolves and computes the optimal approximate solution. Compared with the traditional, the genetic algorithm, optimization method takes biological evolution as the prototype, has very good convergence. It has the advantages of less computing time, higher robustness in calculating the accuracy. Flowchart of the genetic algorithm is shown in Fig. 1b. First, choose a coding to define problem parameters, a generation administrator, a crossover, and mutation probability. Then, pick population measure, n , hybrid likelihood, and transformation likelihood. Introduce an arbitrary populace of the strings of

Table 1 Parameters used for calculations

M	Cart Mass	1.096 kg
m	Rod Mass	0.109 kg
b	Friction coefficient of the cart	0.1 N/m/s
I	Rod inertia	0.0034 gm ²
l	Distance from the rod axis rotation center to the rod mass center	0.25 m

size l . Pick the most extreme suitable age number $[[t]]$ max. Set $t = 0$. Then, evaluate each string in the population. If $t > t_{max}$ or other termination criteria is fulfilled, the end. In the next step, perform reproduction on the population and perform crossover on arbitrary sets of strings. Further, the mutation on each string will be carried out and strings will evaluate in the new population. For the next cycle, set $t = t + 1$ and go to the termination step.

4 Results and Discussions

In this section, first of all, the controllability of the system is checked. Then genetic algorithm results are discussed for the selection of Q and R matrices. Later on, LQR controller is applied on the cart-pole system to stabilize the system.

Parameters used for this cart-pole system are given in Table 1.

By putting values of the real system, the state-space representation is given as

$$\begin{bmatrix} \dot{x} \\ \ddot{x} \\ \dot{\phi} \\ \ddot{\phi} \end{bmatrix} = \begin{bmatrix} 0 & 1 & 0 & 0 \\ 0 & -0.0883167 & 0.629317 & 0 \\ 0 & 0 & 0 & 1 \\ 0 & -0.2356 & 27.82 & 0 \end{bmatrix} \begin{bmatrix} x \\ \dot{x} \\ \phi \\ \dot{\phi} \end{bmatrix} + \begin{bmatrix} 0 \\ 0.883167 \\ 0 \\ 2.35655 \end{bmatrix} F \quad (29)$$

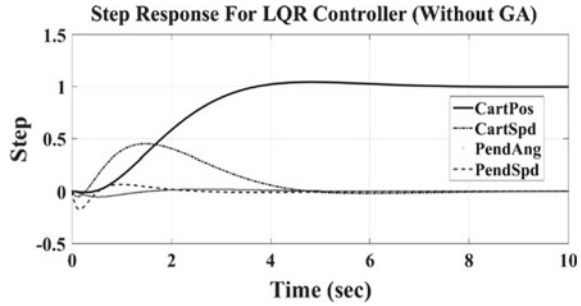
$$\begin{bmatrix} x \\ \phi \end{bmatrix} = \begin{bmatrix} 1 & 0 & 0 & 0 \\ 0 & 0 & 1 & 0 \end{bmatrix} \begin{bmatrix} x \\ \dot{x} \\ \phi \\ \dot{\phi} \end{bmatrix} + \begin{bmatrix} 0 \\ 0 \end{bmatrix} F \quad (30)$$

The system has four static variables so, here, $n = 4$, the controllability matrix is given as

$$P = [B; AB; A^2B; A^3B] \quad (31)$$

By using the rank command of MATLAB, the rank of the controllability matrix can be determined, which comes to be 4. So, the cart-pole system is controllable.

Fig. 2 Step response of LQR controller without GA



In LQR controller generally, the Q matrix is calculated by multiplication of transpose of C matrix and C matrix. The order of the Q matrix is 4×4 and of R is 1×1 , which is calculated as

$$Q = \begin{bmatrix} 1 & 0 & 0 & 0 \\ 0 & 0 & 0 & 0 \\ 0 & 0 & 1 & 0 \\ 0 & 0 & 0 & 0 \end{bmatrix}, R = 1 \tag{32}$$

So here, only Q_{11} , Q_{33} and R_{11} has to be tuned so that the system can control the desired objective. These are considered as a variable for the genetic algorithm.

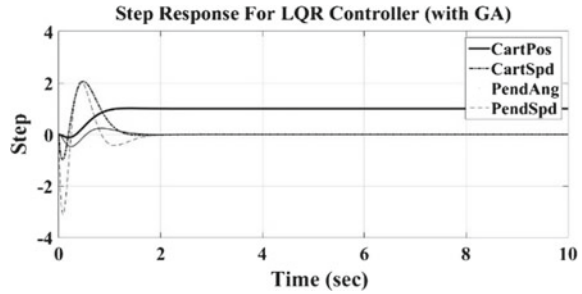
Assume population size 20, mutation probability 0.2 and crossover probability 0.4 for the genetic algorithm. For the first variable Q_{11} , let the bounds are [700 1200] and [100 600], [1 5] for Q_{33} and R_{11} . After a number of iterations on the objective function for minimizing by genetic algorithms, Q and R matrices are calculated, which is given as

$$Q = \begin{bmatrix} 915.5142 & 0 & 0 & 0 \\ 0 & 0 & 0 & 0 \\ 0 & 0 & 154.8876 & 0 \\ 0 & 0 & 0 & 0 \end{bmatrix}, R = 1.0179 \tag{33}$$

Using these weighing matrices LQR controller is designed for the cart-pole system. The controller is feedback-type controller, which stabilizes the system by minimizing the error. The gains of LQR controller by using GA-based weighting matrices are [-29.99, -19.22, 70.18, 12.74]. Step response of the system is calculated for both with and without genetic algorithms results.

Figures 2 and 3 represents the step response of the LQR controller on cart-pole system without and with a genetic algorithm. From both figures, it can be concluded that GA based LQR controller stabilize the system much earlier than general LQR controller. The system gets stabilize in 1.5 s with GA LQR, which is very much less than simple LQR controller, i.e., 7 s.

Fig. 3 Step response of LQR controller with GA



5 Conclusions

Aiming at the characteristics of difficulty to determine the weight matrix Q and R in LQR, this paper presented a genetic algorithm based approach for LQR controller design. The selection of the weight matrix is expressed as a multiobjective optimization problem, and chosen the genetic algorithm to optimize weight matrix parameters. GA-based LQR control is applied to the cart-pole system. From the results, it is found that the system is stabilized much earlier than the simple LQR controller. This algorithm can avoid heavy and complicated work, improve work efficiency, and has strong practicability.

References

1. Zeng L (2014) The robust LQR optimal control of inverted pendulum. Sichuan Southwest Jiao Tong University
2. Prasad LB, Tyagi B, Gupta HO (2011) Optimal control of nonlinear inverted pendulum dynamical system with disturbance input using PID controller & LQR. In: IEEE International conference on IEEE, Malaysia. Control system, computing and engineering (ICCSCE), pp 540–54
3. Song Z, Song X, Liu C, Zhao Y (2013) Research on real-time simulation and control of linear 1-stage inverted pendulum. *J Comput* 8(4):896–903
4. Low K, Wong T (2004) Optimization of a hard drive servo system using multiobjective genetic algorithm. In: Proceedings of the IEEE conference on cybernetics and intelligent systems. Singapore, pp 706–711
5. Onnen C, Babuška R, Kaymak U, Sousa JM, Verbruggen HB, Isermann R (1997) Genetic algorithms for optimization in predictive control. *Control Eng Pract* 5(10):1363–1372
6. Solihin M, Akmeliawati R (2010) Particle swam optimization for stabilizing controller of a self-erecting linear inverted pendulum. *Int J Electr Electron Syst Res* 3:410–415
7. Wang H, Zhou H, Wang D, Wen S (2013) Optimization of LQR controller for inverted pendulum System with artificial bee colony algorithm. In: Proceedings of the 2013 international conference on advanced mechatronic systems. Luoyang, China, pp 158–162

Analysis of Higher Alcohol Fuel Blends for IC Engine—A Review



Rahul Sharma, Dilip Kumar, Mayank Chhabra and Gaurav Dwivedi

Abstract Higher alcohols like propanol and butanol have some significant advantages over lower alcohols like Methanol and Ethanol. Higher alcohols in engine resting better engine performance due to their lower heating value. The blending of Propanol and butanol is between the ratio of 5–20% with petrol and diesel in SI and CI engines also reduces the various emissions which effect the environment and improves spray characteristics. Butanol is thus not only a promising alternative fuel for gasoline but also a possible replacement for bioethanol as a fuel for internal combustion engines for transportation. There is a lack of literature review study on using higher alcohols like propanol and butanol with different blend ratios with diesel and petrol. The main objective of this paper is to analyze the performance of an IC engine using higher alcohols and its blend as a fuel. The study in this review papers to find out effect on engine parameters and various exhaust emission at different blends ratio. This review paper will help in critical areas to address research gaps on higher alcohols as a fuel in the IC engine.

Keywords Alternative fuel · Higher alcohols · Diesel engine · Petrol engine

1 Introduction

Due to the increase in demand on a daily basis in an automotive industry, the quantity of gasoline and diesel decreases. Nowadays almost all the vehicles are run on diesel and petrol and also due to the use of these fuels various emissions takes place, which affects the environment as well as the health of the living organism. Thus, this problem raises an interest in alternative fuels like alcohol as a fuel in IC engines. The two major fuels that had been developed and widely used along with the development of

R. Sharma · D. Kumar · M. Chhabra
Department of Mechanical and Automation Engineering, Amity University, Noida, India
e-mail: dilip5feb96@gmail.com

G. Dwivedi (✉)
School of Mechanical Engineering, Vellore Institute of Technology, Vellore, India
e-mail: gdiitr2005@gmail.com

© Springer Nature Singapore Pte Ltd. 2019
M. Kumar et al. (eds.), *Advances in Interdisciplinary Engineering*, Lecture Notes in Mechanical Engineering, https://doi.org/10.1007/978-981-13-6577-5_58

the IC engines and the automotive industries over the past century are gasoline and diesel [1–4]. Higher alcohols like propanol and butanol due to their different properties are used as an alternative fuel in the current engine. Also, increase in a longer chain of carbon improves the ignition quality of alcohol molecules as compared to lower alcohols like ethanol and methanol. In SI engines, the blends of petrol and alcohols reduce the unburned hydrocarbon, emissions like carbon monoxide (CO) and knock tendency which is the main problem mainly in all vehicles. Table 1 shows the comparison of propanol and butanol with diesel.

Table 1 shows various parameters which distinguish the higher alcohols like propanol and butanol with the diesel.

According to previous investigations the use of lower alcohols like methanol and ethanol as blend in different ratio with diesel results certain complications due to their low cetane number, high latent heat of vaporization. The use of higher alcohols like propanol and butanol as blend in different ratio with diesel gives a good performance as compared to lower alcohols due to their high cetane number, better blend stability, and less hygroscopic nature. The previous papers revealed that addition of alcohols with gasoline/diesel improves the efficiency and reduces the emission gases.

This review paper aims to investigate improvements on engine performance, combustion and emission characteristics when higher alcohols like propanol and butanol blends with gasoline in SI engine and with diesel in CI engines in different ratios. The collection of literature study was collected in this review paper from the papers within the recent years of 2005–2017. There are 2 sections provided in this current

Table 1 Comparison of propanol and butanol with diesel [5–8]

Properties	Diesel	Propanol	Butanol
Molecular formula	C _x H _y	C ₃ H ₇ OH	C ₄ H ₉ OH
Molecular weight	190–211.7	60.09	74.12
C(%wt)	86.13	59.96	64.82
H(%wt)	13.87	13.31	13.49
O(%wt)	0	26.62	21.59
Solubility (g/l)	Immiscible	Miscible	77
Lubricity (μm corrected wear scar)	315	922	591
Cetane number	52	12	17
Self-ignition temperature (°C)	254–300	350	345
Density (kg/m ³)	835	803.7	809.7
Viscosity	2.72	1.74	2.22
Lower heating value (MJ/kg)	42.49	30.63	33.09
Latent heat of evaporation (kJ/kg)	270–375	727.88	581.4
Vapour pressure (mm hg)	0.4	20	7
Boiling point (°C)	180–360	97.1	117.5
Flash point (°C)	>55	11.7	35–37

review paper blends of diesel/petrol in different ratios with propanol and butanol. A brief detail of literature survey on higher alcohols like butanol and propanol blends with diesel/gasoline in different ratio summarized in terms of comprehensive discussion and tables. This review paper will help in several critical areas to address the research gaps on higher alcohols as a fuel in IC engine. This review paper will help in future studies in all areas of higher alcohols used as alternative fuels.

2 Propanol as a Fuel in I.C. Engine

Propanol is a 3-carbon structure, straight chain alcohol with higher molecular weight, C(%wt), H(%wt), cetane number, high energy density, viscosity, and lower heating value, which makes it a good alternative fuel for IC engines [5].

2.1 Propanol as Fuel in SI Engine

Zhang [5] studied on the variation in emission characteristics when gasoline blends with isopropanol in SI engine. In his study, he analyzed the blending of isopropanol with gasoline, the result of that review paper revealed that there would be less emission of HC and CO when isopropanol blend with gasoline. Nehare et al. [6] investigated on exhaust emission characteristics of SI engine, in which isopropanol blends with unleaded gasoline, the test was carried out in SI engine, the result revealed that when isopropanol blends with unleaded gasoline, the emission of carbon oxide is minimum. Table 2 shows the effect of propanol as fuel.

The different blend ratio of propanol with gasoline, engine type and the result of the various research shown in Table 2.

2.2 Propanol as Fuel in CI Engine

There are very few literatures and studies on using propanol as fuel in diesel engines. Today, most of the study is focused on the use of propanol as a solvent in the diesel blends to improve the quality of blends. The isomer of propanol now used in added with ethanol–diesel blend for increasing the cetane number which is reduced by ethanol because of its low cetane number. Banugopan et al. [10] used blends of ethanol and diesel, to increase the homogeneity and phase stability of blends he used 1% isopropanol as an additive.

Deep et al. [11] analyzed the effect of used propanol, orange peel oil methyl ester(O) as a fuel in different ratio with diesel as (D75–O20–Pr5, (D90–O5–Pr5), (D85–O10–Pr5), (D80–O15–Pr5), the result revealed that HC and CO emissions

Table 2 Result of different propanol blending ratio with gasoline in SI engine [7–9]

Fuel	Engine type	Result
Pr(5%) + Gasoline(95%)	1 cylinder, 4 s—SI engine	BSFC decreases BTE increases
Longer Chain Alcohols (<i>n</i> -propanol) + Gasoline	1 cylinder, 4 s—SI engine	Faster Flame Speed Higher Knock Resistance
Pr(20%) + Gasoline(80%)	4 cylinders, 4 s—SI engine	BSFC increases BTE increases Brake Torque increases CO ₂ increases
Pure and Higher Alcohols(<i>n</i> -propanol) + Gasoline	1 cylinder, 4 s—SI engine	HC decreases CO decreases
Pr(3.5%) + Gasoline(96.5%)	1 cylinder, 4 s—SI engine	CO decreases CO ₂ decreases HC decreases
Pr(10%) + Gasoline(90%) Pr(20%) + Gasoline(80%) Pr(40%) + Gasoline(60%)	3 cylinders, 4 s—SI engine with EGR	Brake Torque increases HC and NO _x decreases

reduced with increased in the ratio of blended fuel and also BTE increased as compared to pure diesel as a fuel.

Table 3 summarizes some of the impacts when propanol blends with diesel in different ratios to check variation on performance and emission of the diesel engine.

3 Butanol

Butanol, straight chain alcohol with 4-carbon atoms, can be prepared using same feedstocks as that of ethanol but need less energy. Production capability from both petroleum and non-petroleum resources, inferior lower heating value, superior cetane number and flash point, and higher calorific value as compared to lower alcohol have made butanol as an alternative to diesel fuel [13]. All these butanol isomers can be created from the fossil in addition from biomass. 1-butanol, better known as *n*-butanol, has a straight chain structure with the OH at the terminal carbon and presents the best qualities to be utilized as fluid fuel [14]. While butanol has higher energy density than ethanol, it has brought down octane number, being advisable to utilize it in engines with lower compression ratios and consequently, less efficiency [15–18].

Table 4 shows variation in various parameters in relation to pure diesel when butanol is blended with diesel in different ratios in CI engine. The study shows that various alcohol and biodiesel can be used as fuel of future [19, 20].

Table 3 Results of different propanol blending ratio with Diesel in CI engine [12]

Fuel	Engine	Test conditions	Result
Pr(10%) + D(90%) Pr(20%) + D(80%)	Single cylinder CFR (Cooperative Fuel Research)	Variable loads	NO _x increases Soot decreases
D(80%) + M(10%) + Pr(10%) D(70%) + M(20%) + Pr(10%) D(60%) + M(20%) + Pr(20%) D(50%) + M(30%) + Pr(20%)	Single cylinder, 4 stroke diesel engine	Variable loads 1500 rpm	PP increases No change in NO _x No change in soot HC increases CO-N/A
Pr(4%) + D(96%) Pr(8%) + D(92%)	Single cylinder, 4 stroke diesel engine	Variable loads	BSFC increases BTE decreases NO _x decreases
D(98%) + Pr(2%) D(92%) + Pr(8%) D(88%) + Pr(12%) D(84%) + Pr(16%)	Three cylinders, 4 stroke diesel engine	Variable loads 1500 rpm	PP-N/A NO _x increases Soot decreases HC decreases CO decreases
Pr(5%) + D(95%) Pr(10%) + D(90%) Pr(15%) + D(85%)	Single cylinder, 4 stroke diesel engine	Variable loads	BTE increases NO _x decreases CO decreases HC decreases
D(95%) + Pr(5%) D(90%) + Pr(10%) D(88%) + Pr(12%) D(80%) + Pr(20%)	Single cylinder, stroke diesel engine	Variable loads 1500 rpm	BTE increases at Pr15 and Pr20 BSFC increases at low loads and there will be no change in high loads HC increases CO decreases at high loads Soot decreases at high loads (Pr20%)
Pr(10%) + D(90%) Pr(15%) + D(85%) Pr(20%) + D(80%) Pr(25%) + D(75%)	Single cylinder, stroke diesel engine	Variable loads 1500 rpm	Longer ignition delay than pure diesel fuel HLV of propanol produces cooling effect NO _x decreases CO decreases Smoke emission Decreases (due to Presence of oxygen in propanol)

(continued)

Table 3 (continued)

Fuel	Engine	Test conditions	Result
Pr(5%) + D(95%) Pr(10%) + D(90%) Pr(15%) + D(85%) Pr(20%) + D(80%)	Single cylinder, stroke diesel engine	Variable loads	BTE increases HC increases NO _x decreases
D(92%) + Pr(8%) D(96%) + Pr(4%)	Single cylinder, 4 stroke diesel engines	Variable loads 1500 rpm	BTE increases 1.579% For Pr(4%) and also Increases 7.635% for Pr(8%) at medium and high loads NO _x decreases Soot decreases HC increases CO decreases
Pr(10%) + D(90%) Pr(20%) + D(80%)	Single cylinder, 4 Stroke diesel engine	Variable loads	BTE decreases NO _x N/A Smoke emission-N/A

Table 4 Diesel-*n*-butanol blends versus Diesel engines [17]

Parameter	In relation to pure diesel
Fuel consumption	About 2% high
Efficiency	About 1–2% more efficient
Soot emissions	Less than pure diesel
NO _x emissions	Less than pure diesel
CO emissions	Less than pure diesel
HC emissions	Not affected or slightly higher

4 Conclusion

Many studies reported that propanol is mainly used as a solvent to improve the quality of the blend. According to some researcher's propanol can be used up to 20–30% v/v as a blending component with diesel. NO_x and CO emissions decrease with increasing content of propanol in the blend. There is a slight increase in the ignition delay period with the increasing content of Propanol in the blend. In CI engines, most of the researchers reported that using alcohol fuel like propanol in diesel engines reduces the PM, Soot, emissions due to low aromatics in the blend. In SI engines, most of the researchers reported that using alcohol fuel like propanol in petrol engines due to chemical properties of alcohols NO_x, CO, CO₂, and HC is much lower than gasoline fuel. So nowadays Propanol is used as a solvent to improve the engine performance due to the high percentage of premixed combustion as a result of low cetane number. Propanol is mainly used as a cleaning compound, which clears

the car's fuel lines of water. At the present time, there is no substantial push to use propanol as a fuel in I.C engines.

References

1. Dwivedi G, Sharma MP, Verma P (2015) Operational and environmental impact of biodiesel on engine performance: a review of literature. *Int J Renew Energy Res (Scopus)* 5(3):961–970
2. Chhabra M, Sharma A, Dwivedi MP (2017) Performance evaluation of diesel engine using rice bran biodiesel. *Egypt J Pet* 26(2):511–518
3. Dwivedi G, Sharma MP, Verma P (2016) Impact of oil and biodiesel on engine operation in cold climatic condition. *J Mater Environ Sci (Scopus)* 7(12):4540–4555
4. Dwivedi G, Sharma MP, Verma P (2017) Experimental investigation of metals and antioxidants on oxidation stability and cold flow properties of pongamia biodiesel and its blends. *Int J Renew Energy Res (Scopus)* 7(1):26–33
5. Zhang Y (2014) Emission characteristics of iso-propanol gasoline blends in a spark ignition engine combined with EGR. *Therm Sci* 18(1):269–277
6. Nehare SU, Raizada KS, Kothare CB (2015) A review on propanol as an alternative fuel in SI engine. 1(5)
7. Liu X, Wang H, Zheng Z, Liu J, Reitz RD, Yao M (2016) Development of a combined reduced primary reference fuel-alcohols (methanol/ethanol/propanols/butanols/n-pentanol) mechanism for engine applications. *Energy*. 1 Aug 2016
8. Gravalos I, Moshou D, Gialamas T, Xyradakis P, Kateris D, Tsiropoulos Z (2013) Emissions characteristics of spark ignition engine operating on lower-higher molecular mass alcohol blended gasoline fuels. *Renew Energy* 50:27–32
9. Kothare CB, Kongre S, Bhoje DV (2016) Experimental investigation of effect of Gasoline-higher alcohol blend on performance characteristics of four stroke spark ignition engine at variable compression ratio. In: 2016 International conference on electrical, electronics, and optimization techniques (ICEEOT) 2016, pp 27–33
10. Banugopan V, Prabhakar S, Annamalai K, Jayaraj S, Sentilkumar P (2010) Experimental investigation on DI diesel engine fuelled by ethanol diesel blend with varying inlet air temperature. In: *Front Automob Mech Eng (FAME) 2010*. IEEE, pp 128–134
11. Deep A, Kumar N, Gupta D, Sharma A, Patel JS, Karnwal A (2014) Potential Utilization of the blend of orange peel oil methyl ester and isopropyl alcohol in CI Engine. *SAE Technical Paper*
12. Laza T, Bereczky A (2009) Influence of higher alcohols on the combustion pressure of diesel engine operated with Rape seed oil. *Acta Mech Slov* 13:54–61
13. Karabektas M, Hosoz M (2009) Performance and emission characteristics of a diesel engine using isobutanol–diesel fuel blends. *Renew Energy* 34(6):1554–1559
14. Brassat A, Thewes M, Muther M, Pischinger S (2011) Tailor-made fuels from biomass for gasoline combustion engines. *MTZ – Mot Z* 72(12):56–63
15. Sarathy SM, Obwald P, Hansen N, Kohse-Hoinghaus K (2014) Alcohol combustion chemistry. *Prog Energy Combust Sci* 44:40–102
16. Alasfour F (1997) Butanol, a single cylinder engine study: availability analysis. *Appl Therm Eng* 17:537–549
17. da Silva Trindade WR, dos santos RG (2017) Review on the characteristics of butanol, its production and use as fuel in internal combustion engine. *Renew Sustain Energy Rev* 69:642–651
18. Chotwichien A, Luengnaruemitchai A, Jai-In S (2009) Utilization of palm oil alkyl esters as an additive in ethanol-diesel and butanol-diesel blends. *Fuel* 88:1618–1624

19. Dwivedi G, Sharma MP (2016) Investigation of oxidation stability of pongamia biodiesel and its blends with diesel. *Egypt J Pet* 25(1):15–20
20. Dwivedi G, Sharma MP (2016) Investigation of cold flow properties of waste cooking biodiesel. *J Clean Energy Technol* 3(4):205–208

Hydrogen Vehicle—Opportunities and Challenges



Prabhakar Alok Ravi, Verma Vivek and A. K. Jouhari

Abstract Hydrogen is likely to be the fuel of the future. It is probably the cleanest possible fuel. It can be made out of the water by electrolysis and the product of combustion is also water. On large scale, the hydrogen is produced from natural gas. One of the issues which need consideration is the onboard storage of hydrogen. As hydrogen has low density and the volume required is high, the vessel will be very bulky and heavy. Hydrogen can be used as a fuel in IC engines. Both, the spark ignition and compression ignition engines are suitable for using hydrogen as a fuel. An attempt has been made to study the use of hydrogen in IC engines and modifications of the engine to get similar power compared to a gasoline engine. The problem with the combustion of hydrogen is that the reaction is highly explosive. The paper discusses all these aspects in detail. Another route for using hydrogen in an automobile is through the fuel cell.

Keywords Hydrogen energy · Onboard storage of hydrogen · Hydrogen IC engine efficiency

1 Introduction

A vehicle which uses hydrogen as an onboard fuel is designated as hydrogen vehicle. The chemical energy of hydrogen is converted to mechanical energy. This conversion may be carried out either by combustion of hydrogen in an internal combustion engine or by reaction of hydrogen and oxygen in a fuel cell to drive an electric motor. As of 2016 [1], three hydrogen cars are available; the Toyota Mirai, the Hyundai ix35 FCEV, and the Honda Clarity. Currently, 95% of hydrogen is produced from natural gas, which is mainly methane. It can also be produced from water, however, the electrical energy required for generation is more than the energy available in the

P. A. Ravi (✉) · V. Vivek · A. K. Jouhari
Department of Mechanical Engineering,
Amity School of Engineering and Technology, Amity University Uttar Pradesh, Lucknow
Campus, Lucknow 226028, India
e-mail: alok.prabhakar@gmail.com

hydrogen produced. When produced from natural gas, greenhouse gas emissions are very high. The energy density of hydrogen is three times more with respect to gasoline on a mass basis, and on a volume basis, the volumetric efficiency is almost three times less when compared with gasoline. There are three major issues while using hydrogen as a fuel, viz. onboard storage, hydrogen combustion, and modification and maintenance of hydrogen internal combustion engine. In this paper, an effort has been made to study all these aspects and their possible solutions.

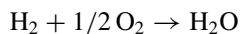
2 Onboard Storage

Probably, the most suited method to store hydrogen in a vehicle is as compressed gas in a high-pressure vessel. These vessels are made of aluminum and covered with fiberglass. Specialized hydrogen systems are ordinarily at a pressure of 20 MPa. In any case, to decrease the volume we have to increase the pressure. At higher pressure, both cost and safety aspects are associated. Two hydrogen tanks weighing about 45 kg each will be required for a vehicle with 160 km range [2]. Hydrogen has the highest energy of all the common fuels by weight. Onboard hydrogen should be available in small lightweight systems. This is particularly challenging, because it has the lowest energy density of common fuels by volume. This requires the development of compact, safer, reliable, inexpensive, and energy-efficient method of hydrogen storage. Other than mechanical compression, storage of chemical hydrates and carbon substrates are the possible solutions [3].

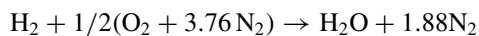
Hydrogen has a wide flammability range and requires low ignition energy. It has a high burning velocity. Hydrogen has the highest diffusion velocity and the highest buoyant velocity. Hydrogen should be handled outdoors in open spaces and in confined areas with adequate ventilation. Since hydrogen has wider combustion and detonation range, it has a greater chance of detonating. Dealing with liquid hydrogen, frostbite at 20 K (−253 °C) is a major problem, and therefore, all pipes must be insulated and operators should also insulate body parts.

3 Hydrogen Combustion

For hydrogen combustion, the stoichiometric equation with oxygen is



And with Air



The stoichiometric ratio of air/fuel is 34.3.

The combustion of hydrogen is a complex phenomenon. Very fast reactions are termed as explosions. In order for flames to propagate, the reaction kinetics must be fast, i.e., the mixture must be explosive. The explosive limits are not flammability limits. Explosion limits are the pressure–temperature boundaries for a specific mixture ratio of fuel and oxidizer and separate the regions of slow and fast reaction [4]. Consider a mixture of hydrogen and oxygen, stored in a vessel in the stoichiometric ratio at 1 atmospheric pressure. The vessel is immersed in a thermal bath kept at 500 °C (Fig. 1).

For H₂ and O₂ reaction the chain propagation steps can be written as

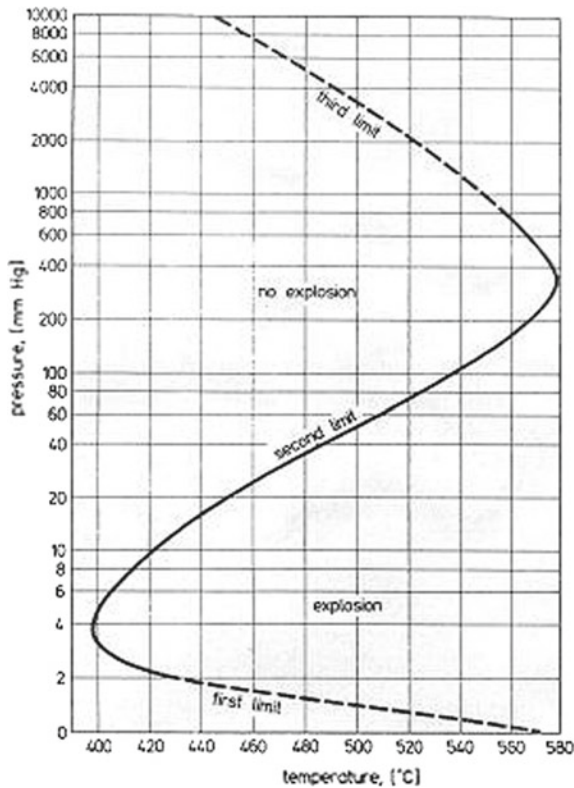
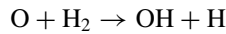
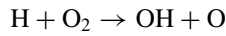
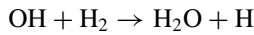
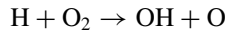
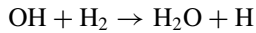
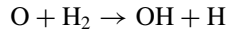


Fig. 1 Explosion limits of Stoichiometric hydrogen–oxygen mixture [4]

And the chain branching step is



This leads to a further chain branching system



The first of the above two stages are branching, in which two radicals are formed for each one consumed. An explosion happens only at a higher temperature when the first step proceeds more rapidly.

The most important chain destruction mechanism is



Or



Both of which clarifies the lower limit of the explosion. A third limit is because of density consideration and the first or lower limit is identified with wall effects and its effects in chain destruction. The explosion is in itself a branch chain reaction phenomenon. The second limit can be explained by gas phase production and gas phase destruction of radicals.

4 Use of Hydrogen in I.C. Engine

The stoichiometric requirement of air is 34.3 kg per kg of hydrogen. At this fuel–air ratio, 29% of cylinder volume will be occupied by hydrogen and only 71% will be available for air. As the adiabatic flame temperature for hydrogen is high, hydrogen is mostly burned with 100% excess air to keep the NO_x formation at the low level. Therefore, the volumetric efficiency of hydrogen IC engine goes down further. Also, the power output is reduced to half. This is why, for the same power output the size of hydrogen engine will be double and such engines are equipped with superchargers and turbochargers to increase the power output. For hydrogen engine the valves, valve seats, connecting rods are of much higher grade materials and therefore, the modifications result in 50% more cost for all these, with respect to a conventional gasoline engine. The hydrogen engine was developed as early as in 1820 by W. Cecil. His engine worked on a vacuum principle, in which atmospheric pressure drove a cylinder back against a vacuum to deliver power. The vacuum engine never became practical. Even Nicholas A. Otto during 1870s had used producer gas as fuel in his Otto cycle. The producer gas contains about 50% hydrogen. The development of a

Fig. 2 Carburetted Hydrogen Engine [2]

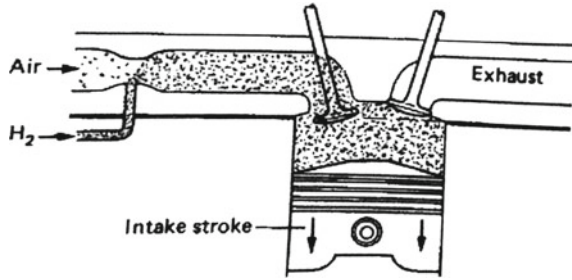
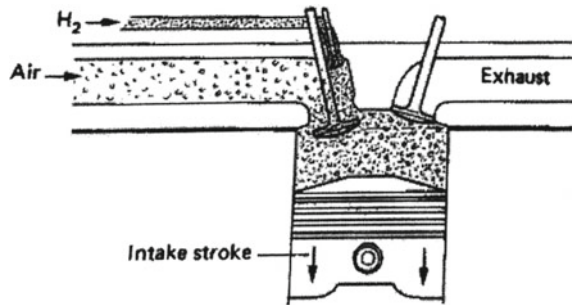


Fig. 3 Port Injection Induction System [2]



carburetor resulted in the wide use of gasoline in spark ignition engines. It was found that gasoline was a safer fuel than hydrogen [5–7].

Hydrogen requires very low energy for an ignition and has a wide range of flammability. Even a lean mixture can easily burn. At leaner mixtures, the flame velocity decreases significantly. Since unburned hydrocarbons are not a concern in hydrogen engines, a large bore to stroke ratio can be used. As the flame speeds have a wider range, two spark plugs are needed. The cooling system should also be designed to provide uniform flow to all locations that need cooling. The high autoignition temperature of hydrogen allows larger compression ratios in a hydrogen engine than in a hydrocarbon engine. Therefore, both SI and CI engines can be used for hydrogen with some modifications. A lean hydrogen mixture is less susceptible to knock than gasoline and, therefore, can tolerate higher compression ratio.

Hydrogen delivery can be of three types: control ignition (carburetor), port ignition, and direct injection. Direct injection is more technologically sophisticated. Figures 2 and 3 give the schematic diagrams of a carburetted hydrogen engine and port injection induction system.

5 Conclusions

- (i) There will be need for enough infrastructure for refueling and trained personnel's to repair and maintain the vehicles. Safety issues and infrastructure development for hydrogen filling station may take a few decades.
- (ii) More pure hydrogen is required for fuel cell than when used in an internal combustion engine. In view of this, IC engine vehicle may have an edge over fuel cell vehicle. Also, the cost of the fuel cell is very high.
- (iii) Hydrogen is an explosive gas which can be ignited easily by a spark. People may not like to house a potential bomb in their garage. There is a risk of the possibility of a major hydrogen explosion in case the automobile crashes.

Acknowledgements The authors would like to thank Wg. Cdr. (Dr.) Anil Kumar, Director, Amity School of Engineering and Technology, Amity University Uttar Pradesh, Lucknow Campus, for his kind permission to present in FLAME 2018 at Noida and publish this paper.

References

1. http://en.wikipedia.org/hydrogen_vehicle (2018)
2. Thipse SS (2015) Alternate fuels. Jaico Publishing House, Delhi
3. Durbin DJ, Malardier-Jugrot C (2013) Review of hydrogen storage techniques for onboard vehicle applications. *Int J Hydrogen Energy* 38(34):14595–14617
4. Glassman I, Yetter RA (2008) *Combustion*, 4th edn. Elsevier, New York
5. Hydrogen used in internal combustion engines, College of Desert (December 2001)
6. Feldman BJ (2005) Hydrogen fuel cell automobiles. *Phys Teach* 34:492–495
7. Gillingham K (2007) Hydrogen internal combustion engine vehicles: a prudent intermediate step or a step in the wrong direction? Stanford University

A Neural Network-Based Comparative Analysis of BR, LM, and SCG Algorithms for the Detection of Particulate Matter



Monika Arora, Farhan Ashraf, Vipul Saxena, Garima Mahendru,
Monica Kaushik and Pritish Shubham

Abstract Air pollution is one of the most common concerns for human health. Air contamination has many pollutants like NO_2 , $\text{PM}_{2.5}$, PM_{10} , and other harmful gases, which are harmful to the living system on the earth. The quality of air gets affected by these particulate matters. This paper proposes a neural network-based prediction model for detection and prediction of air pollution. Performance measurement of Bayesian Regularization (BR) algorithm, Levenberg–Marquardt (LM) algorithm, and Scaled Conjugate Gradient (SCG) algorithm has been analyzed.

Keywords Air pollutants · Bayesian regularization (BR) · Levenberg–Marquardt (LM) · Neural network (NN) · Scaled conjugate gradient (SCG)

1 Introduction

Air pollution is increasing very drastically these days and these are very harmful for all the living beings. Air is one basic amenity that almost every living being need to sustain life. Oxides of Sulfur (SO_x), oxides of nitrogen (NO_x) $\text{PM}_{2.5}$, and PM_{10} are the main air pollutant. Dispersion of these particles in the solid or liquid form is termed as aerosols. PM is not basically one pollutant but a combination or mixture of many pollutants. Industrialization and automotive vehicles have led to increase in these air

M. Arora · F. Ashraf · V. Saxena (✉) · G. Mahendru · M. Kaushik · P. Shubham
Amity University, Noida, India
e-mail: vipulsaxena95@gmail.com

M. Arora
e-mail: monika4dec@gmail.com

F. Ashraf
e-mail: farhan.ashraf56@gmail.com

G. Mahendru
e-mail: gmahendru@amity.edu

M. Kaushik
e-mail: monicakaushik2@gmail.com

pollutants. We are breathing foul and polluted air and our lungs are equivalent to that of a chain smoker. Air pollution is one of the worst forms of pollution which needs to be controlled at the earliest. Because of the unfavorable effects of pollution, a model was required to predict and control pollution of New Delhi. A model was designed alike for NO₂ gas and particulate matters for Auckland, New Zealand, and Salamanca, Mexico for the prediction and analysis of NO₂ emission and particulate matters proving vehicles and industries to be the major source of polluting gases [1].

In this paper, PM_{2.5}, PM₁₀, and NO₂ pollutants have been considered from Anand Vihar, New Delhi. It is one of the most polluted places in India which has increased the ratio of pollutants at anytime of the year. The statistical data of PM_{2.5}, PM₁₀, and NO₂ for the year (2016–2017) in micrograms/m³ have been acquired from the Central Pollution Control Board website an government organization and have been used to compare algorithms of the neural network. On the basis of these, a neural network predictive analysis is performed.

The rest of the paper is divided into various sections. Section 2 describes the data and methodology adopted. Section 3 describes the results and discussions. Section 4 describes the Conclusion and future scope. Final section includes the references.

2 Data and Methodology

The dataset has been acquired from Central Pollution Control Board. These data has been collected of Anand Vihar locality located in New Delhi starting from 2016 to 2017. Analysis of the data has been performed using 15 hidden layers. It has been observed that with 15 number of hidden layers, the feature extraction process would best fit. Hence, the afore-said hidden layers are used. On the basis of the methodology adopted, BR, LM, and SC algorithms have been used for analysis of the data and designing its prediction model using Neural Network Technique. Neural network tool of MATLAB 2017B has been used for the calculation and obtaining the result.

In the proposed research work, comparative analysis of the Bayesian Regularization (BR) algorithm, Levenberg–Marquardt (LM) algorithm, and Scaled Conjugate Gradient (SCG) algorithm has been done. Different numbers of hidden layers in the neural network is use for getting the best fit. Bayesian statistical technique builds a classifier that generates a model which allocates the class labels to problem instance. By finding the local minimum, generic curve fitting have been solved using Levenberg–Marquardt; also termed as Damped Least Square (DLS) [2]. Scaled Conjugate Gradient is forward feed and supervision algorithm for neural network. Forward feed means that there exists no loop between units [3].

Bayesian Regularization (BR):

$$x = \arg \max_{b \in \{1, \dots, B\}} p(C_b) \prod_{i=1}^n p(y_i | C_b) \tag{1}$$

Levenberg–Marquardt (LM):

$$H(\beta) = \sum_{j=1}^m [x_j - (y_j, \beta)]^2 \tag{2}$$

Scaled Conjugate (SC):

$$S_k = (\dot{E}(W_k + \sigma k Pk) - \dot{E}(W_k)) / \sigma k \tag{3}$$

2.1 Importance of Neural Network in Feature Extraction

It is inspired by the way human brain functions. Neurons (a single neuron as shown in Fig. 1) are placed in layers a multilayer neuron network [4]. The first layer is input layer receiving information and it transfers the information in the form of input signals to the intermediate layers. Neuron weight is the communication capability of each neuron with others. The number of neurons in each layer depends on the weight of neuron and the previous layers neurons. In addition, the neural network also contains the hidden layers and the output layers. Figure 2 shows the basic view of the neural network consisting of the different layers such as inputs, hidden layers and the output.

2.2 Justification of Neural Network in Prediction and Detection

Counterfeit neural system is a vigorous technique which gives record-breaking exactness on a wide assortment scope of issues, less necessity of formal factual preparing, offers different various preparing calculations and has understood the capacity of

Fig. 1 Single neuron

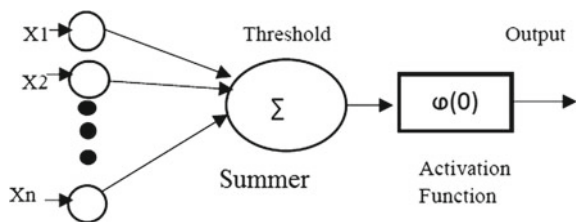
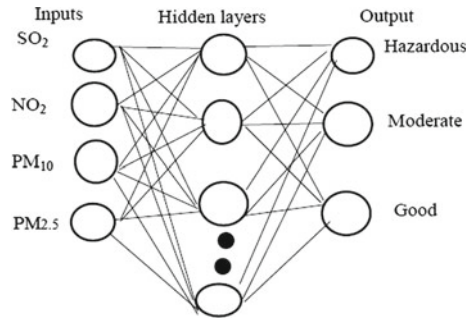


Fig. 2 Neural network



recognizing nonlinear complex connections amongst autonomous and subordinate factors [3]. Neuron is a processor and increasing the number of neurons in hidden layers will lessen the calculation error but will increase the time that is consumed for calculation [2]. Thus, it is an important aspect for choosing numbers of hidden layers in a neural network.

3 Result and Discussion

The following images show the error histogram, performance curve and the regression plots, respectively, for the different algorithms of neural network tool.

A. Bayesian regularization (BR)

See Fig. 3.

Error histogram shows error against instance with the zero error corresponds to 2.47. The training performance curve which is epochs against Mean Squared Errors (MSE) shows the best training performance values is at $7.9542e-09$ at epoch 1000.

See Fig. 4.

Error histogram shows error against instance with the zero error corresponds to -0.04243 . The training performance curve which is epochs against Mean Squared Errors (MSE) shows the best training performance values is at $3.1279e-08$ at epoch 658.

See Fig. 5.

Error histogram shows error against instance with the zero error corresponds to -0.04243 . The training performance curve which is epochs against Mean Squared Errors (MSE) shows the best training performance values is at $2.314e-08$ at epoch 1000.

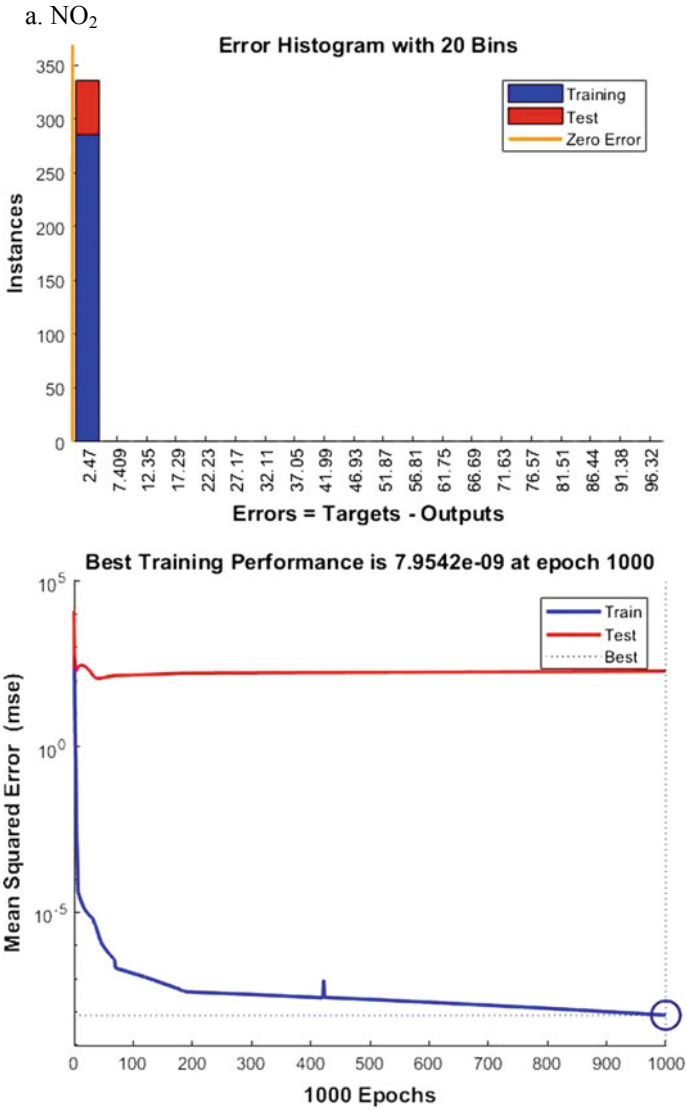


Fig. 3 Performance measurement of NO₂ using BR algorithm

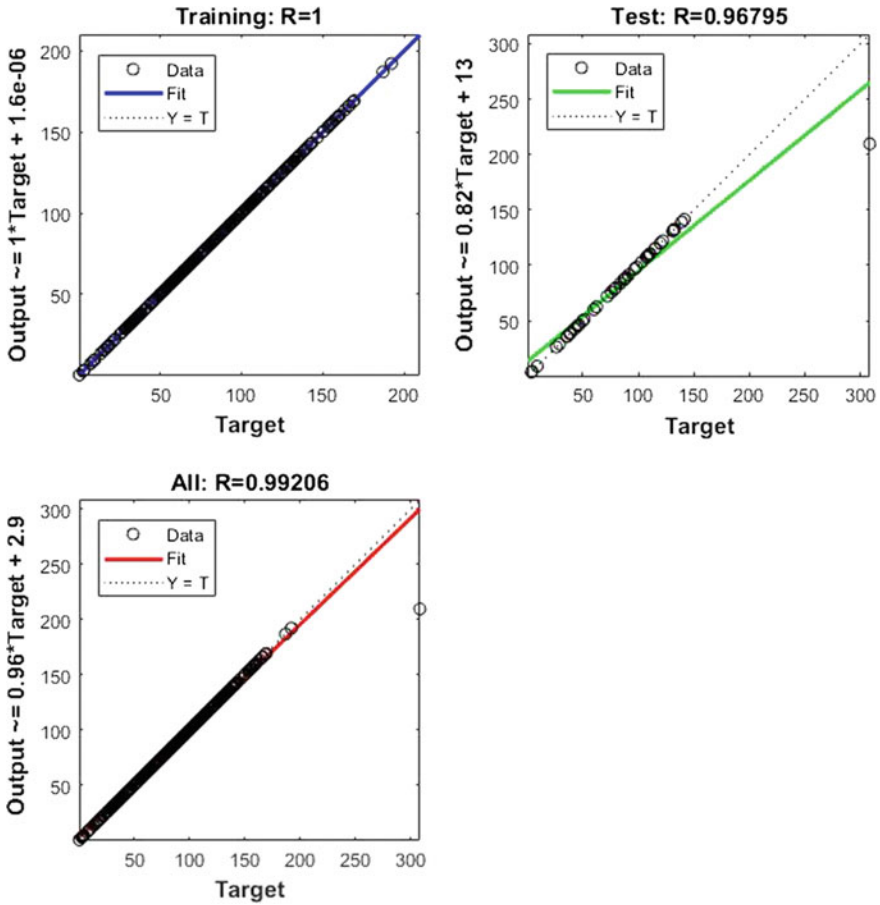


Fig. 3 (continued)

B. *Levenberg–Marquardt (LM)*

See Fig. 6.

Error histogram shows error against instance with the zero error corresponds to 0.07015. The training performance curve which is epochs against Mean Squared Errors (MSE) shows the best training performance values is at $2.1783e-06$ at epoch 2.

b. PM_{2.5}

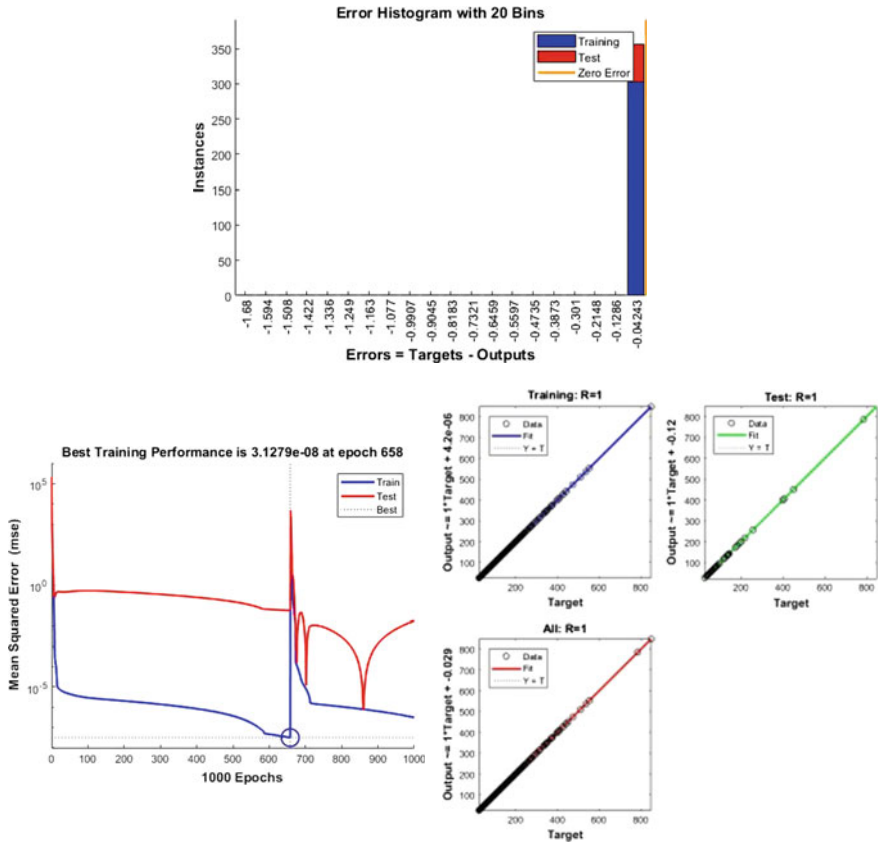


Fig. 4 Performance measurement of PM_{2.5} using BR algorithm

See Fig. 7.

Error histogram shows error against instance with the zero error corresponds to 1.389. The training performance curve which is epochs against Mean Squared Errors (MSE) shows the best training performance values is at 202.3904 at epoch 3.

See Fig. 8.

Error histogram shows error against instance with the zero error corresponds to - 25.62. The training performance curve which is epochs against Mean Squared Errors (MSE) shows the best training performance values is at 0.054846 at epoch 68.

c. PM₁₀

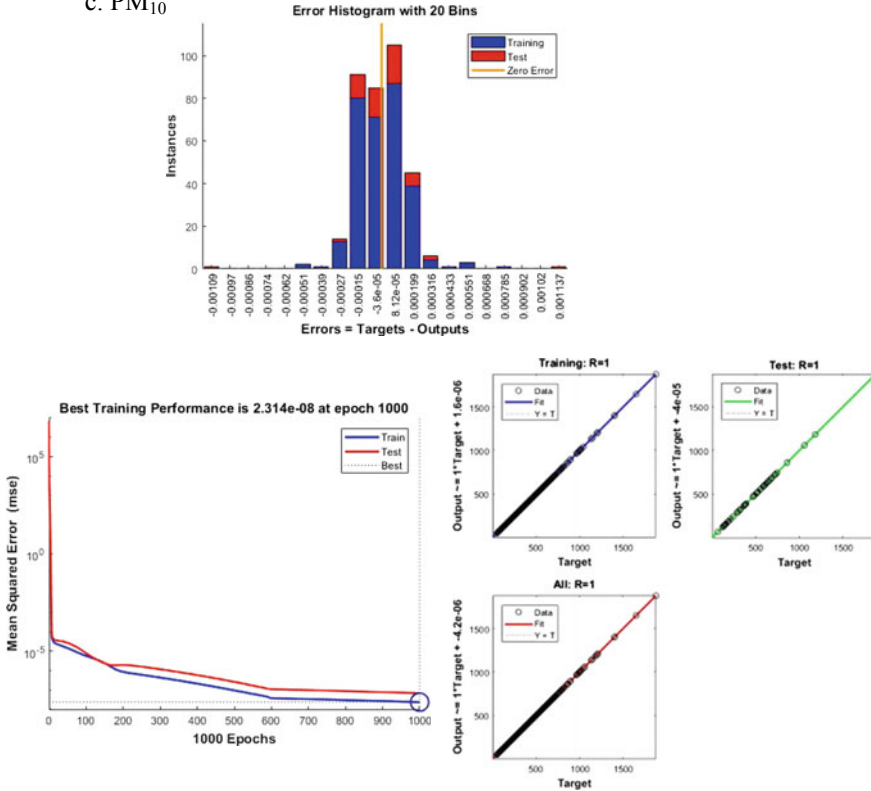


Fig. 5 Performance measurement of PM₁₀ using BR algorithm

C. Scaled Conjugate Gradient (SCG)

See Fig. 9.

Error histogram shows error against instances with the zero error corresponds to 0.0554. The training performance curve which is epochs against Mean Squared Errors (MSE) shows the best training performance values is at 1.4567 at epoch 44.

See Fig. 10.

Error histogram shows error against instance with the zero error corresponds to -1.802. The training performance curve which is epochs against Mean Squared Errors (MSE) shows the best training performance values is at 28.3045 at epoch 43.

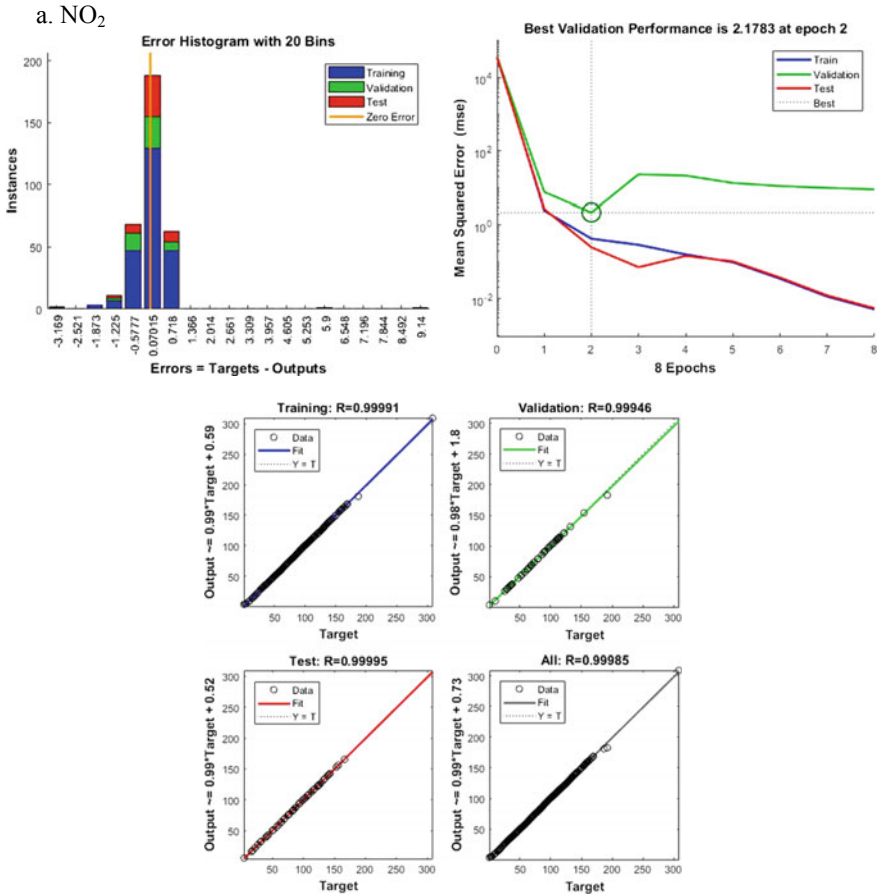


Fig. 6 Performance measurement of NO₂ using LM algorithm

See Fig. 11.

Error histogram shows error against instance with the zero error corresponds to -20.13 . The training performance curve which is epochs against Mean Squared Errors (MSE) shows the best training performance values is at 144437.8252 at epoch 12.

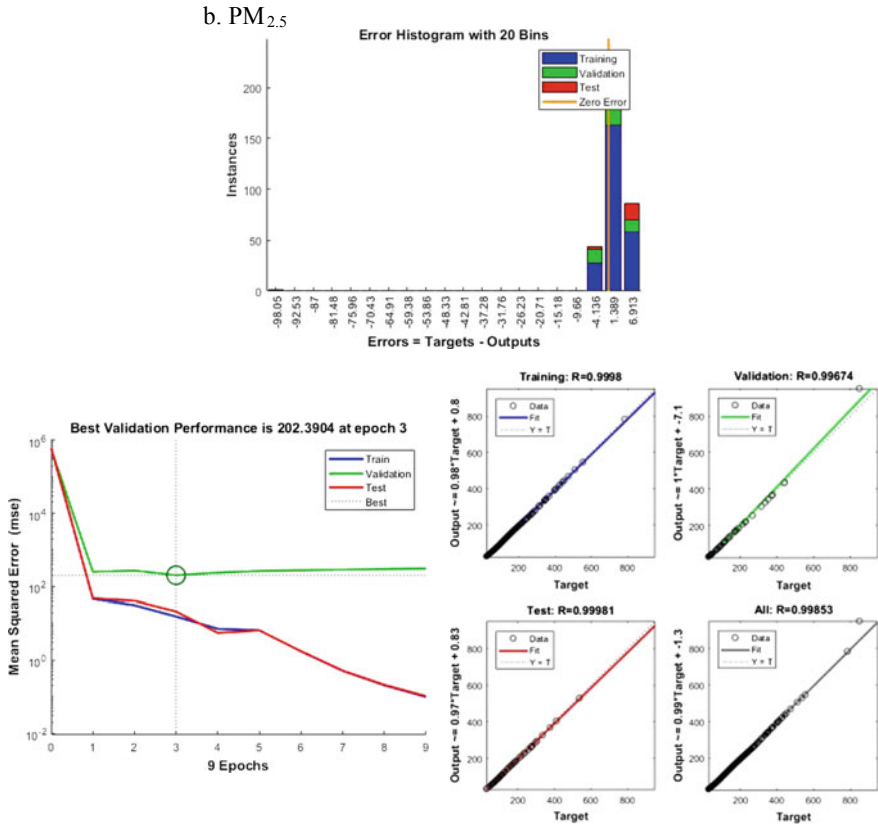


Fig. 7 Performance measurement of PM_{2.5} using LM algorithm

Table 1 represents the comparative analysis of Bayesian Regularization, Levenberg–Marquardt, and Scaled Conjugate Gradient algorithms with different particulate matter. It has been observed from the table that the calculation of mean square error is least with Scaled Conjugate Gradient algorithm. For NO₂, PM_{2.5}, and PM₁₀ is 0.0554, −0.6673, and 0.5132, respectively.

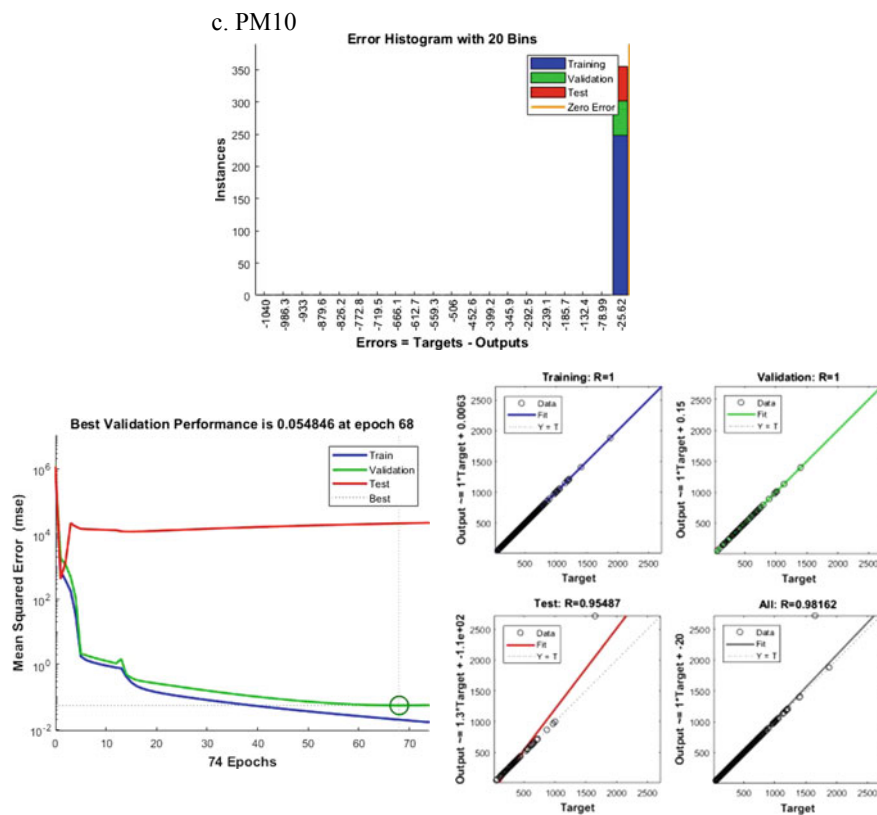


Fig. 8 Performance measurement of PM₁₀ using LM algorithm

Table 1 Comparative analysis of BR, LM, and SCG algorithm

Sr. No.	Pollutant	Algorithm	Mean square error (MSE)
1	NO ₂	Bayesian Regularization (BR)	2.47
2	NO ₂	Levenberg–Marquardt (LM)	0.07015
3	NO ₂	Scaled conjugate Gradient (SCG)	0.0554
4	PM _{2.5}	Bayesian Regularization (BR)	-1.458
5	PM _{2.5}	Levenberg–Marquardt (LM)	-1.708
6	PM _{2.5}	Scaled conjugate Gradient (SCG)	-0.6673
7	PM ₁₀	Bayesian Regularization (BR)	-0.5198
8	PM ₁₀	Levenberg–Marquardt (LM)	0.9045
9	PM ₁₀	Scaled conjugate Gradient (SCG)	0.5132

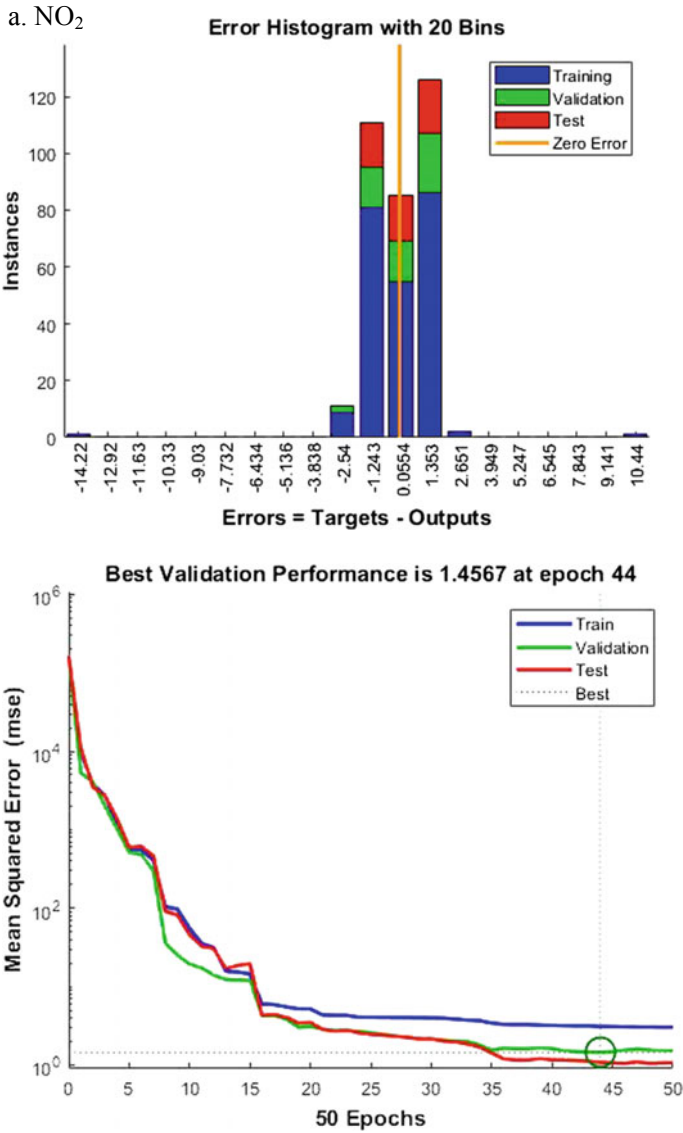


Fig. 9 Performance measurement of NO₂ using SCG algorithm

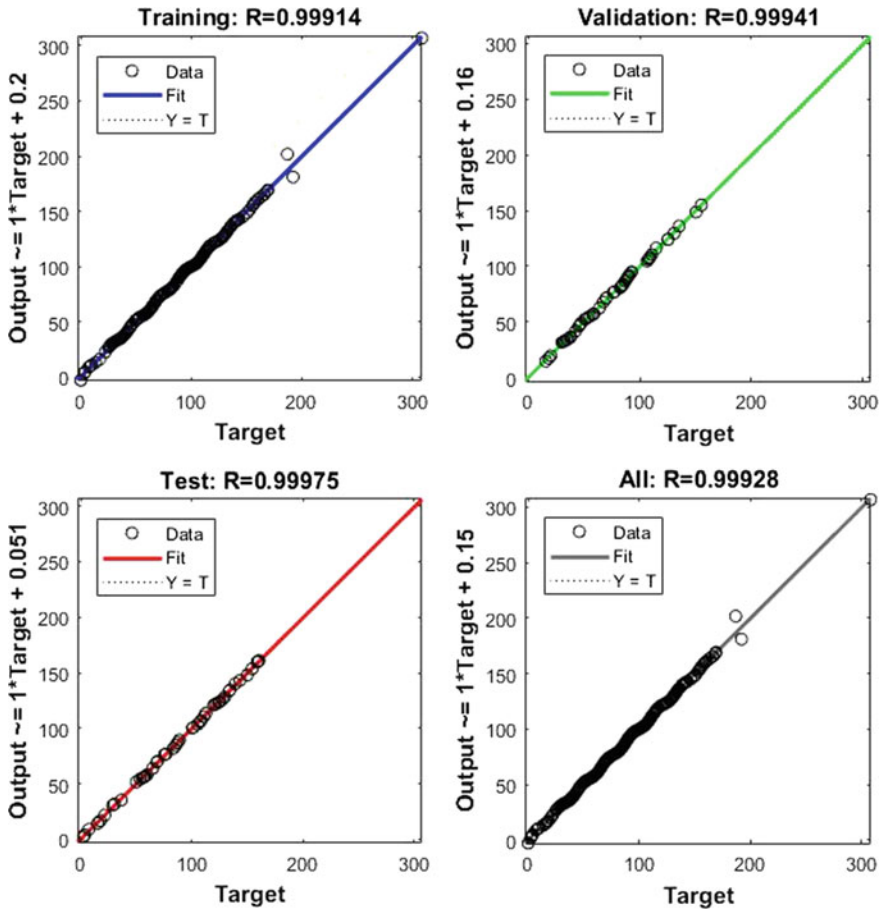


Fig. 9 (continued)

4 Conclusion

In this work, the comparative analysis between the three algorithms of neural network, namely Bayesian Regularization (BR), Levenberg–Marquardt (LM), and Scaled conjugate gradient (SCG) taking NO₂, PM_{2.5}. and PM₁₀ pollutants from Anand Vihar in New Delhi has been done through neural networks and found that Scaled Conjugate Gradient (SCG) was best suited for the detection of particulate matter. The neural networks of different parameters have been used to get the accurate results. The exposure of particulate matter in the atmosphere is slowly and gradually deteriorating and affecting the standards of ecological imbalance, which is producing a direct impact on the human health. In the recent days, the capital of India, New Delhi has experienced a major smoke-laden air full of such

b. PM_{2.5}

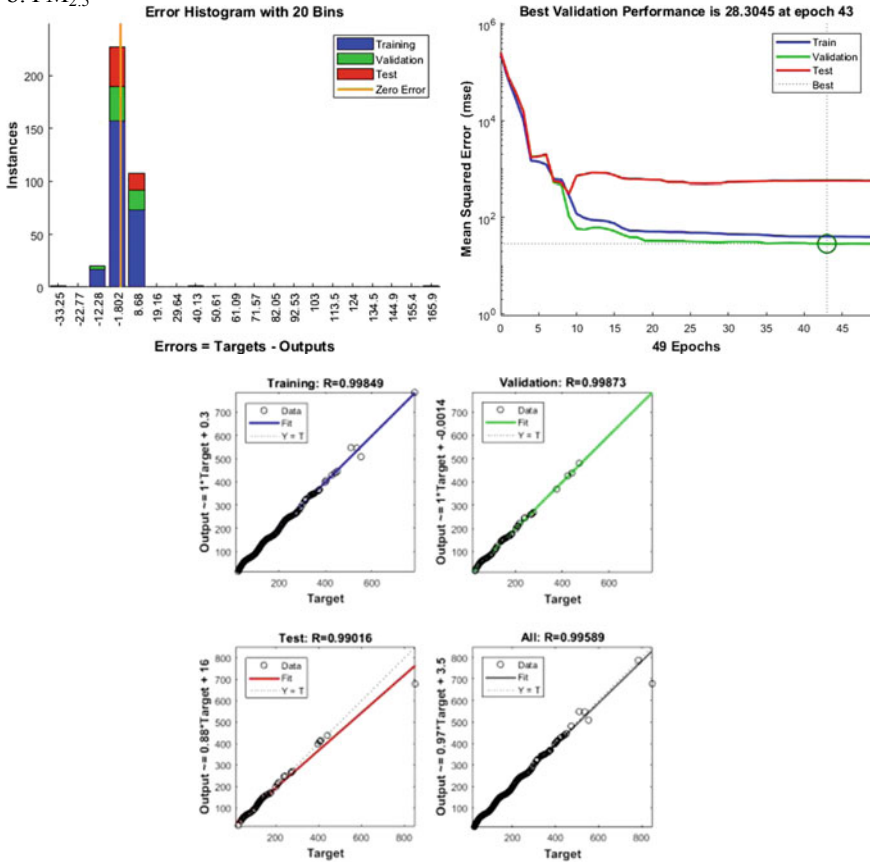


Fig. 10 Performance measurement of PM_{2.5} using SCG algorithm

particulate matters as discussed in this paper which is a matter of serious concern. A Neural network-based method has been developed using MATLAB nftool, which automatically predicts the levels of air pollutants of a particular place and various risks involved in it. This paper discusses the predictions of air pollutants using the three algorithms in the nftool in the surroundings of AnandVihar, New Delhi and its adverse effects on climate, human health and ecological balance. Therefore, there is a need of formulating steps and methodology for analyzing such harmful pollutants and particulate matters in the atmosphere. This neural network-based prediction model for the air pollution analysis would prove to be a boon to the mankind.

c. PM₁₀

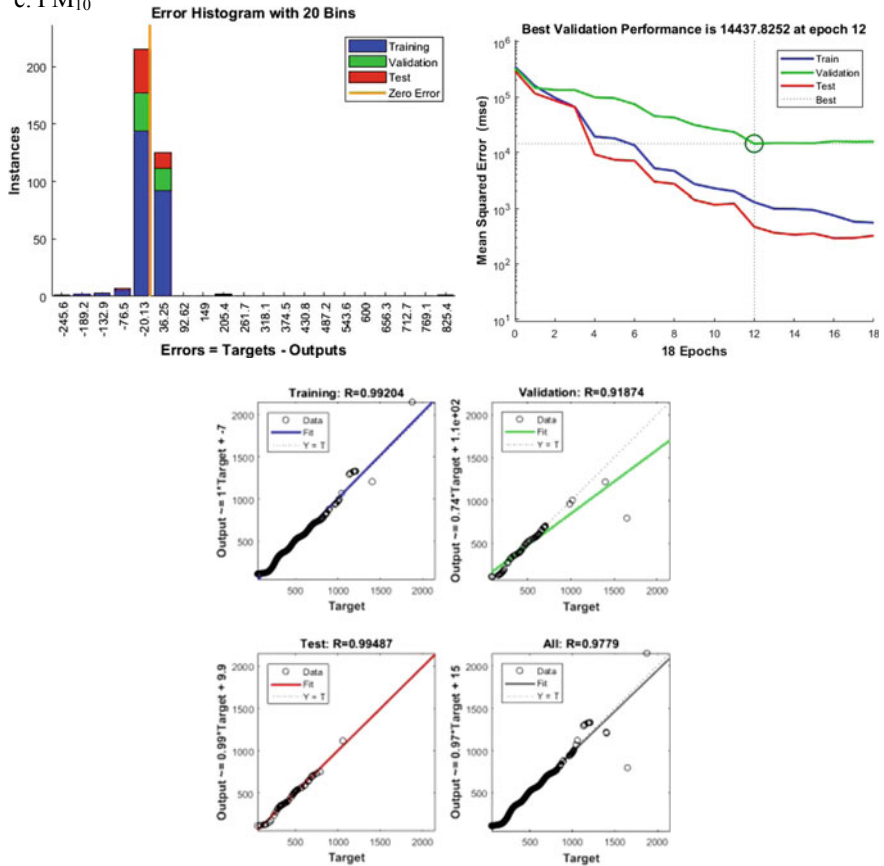


Fig. 11 Performance measurement of PM₁₀ using SCG algorithm

References

1. Elangasinghe MA, Singhal N, Dirks KN, Jennifer A (2014) Salmond development of an ANN—based air pollution forecasting system with explicit knowledge through sensitivity analysis. *Atmos Pollut Res* 5:696–708
2. Moller FM (1993) A scaled conjugate gradient algorithm for fast supervised learning. *Neural Network* 6:525–533
3. Gianola D, Okut H, Weigel KA, Rosa GJM (2011) Predicting complex quantitative traits with Bayesian neural networks. A Case Study with Jersey Cows and Wheat-BMC Genetics 12:1–37
4. Lourakis MIA (2005) A brief description of the Levenberg-Marquardt algorithm implemented by Levmar. Technical Report, Institute of Computer Science, Foundation for Research and Technology—Hellas
5. http://cpcb.nic.in/National_Ambient_Air_Quality_Standards.php
6. Younger M, Morrow-Almeida HR, Vindigni SM, Dannenberg AL (2008) The built environment, climate change, and health: opportunities for co-benefits. *Am J Prev Med* 35(5):517–526

7. Tiwari S, Srivastava AK, Bisht DS, Bano T, Singh S, Behura S, Srivastava MK, Chate DM, Padmanabhamurty B (2010) Black carbon and chemical characteristics of PM10 and PM2.5 at an urban site of North India. *J Atmos Chem* 62(3):193–209
8. Cortina-Januchs MG, Quintanilla-Dominguez J, Vega-Corona A, Andina D (2015) Development of a model for forecasting of PM10 concentrations in Salamanca, Mexico. *Atmos Pollut Res* 6:626–634

Performance Testing of Biodiesel in CI Engine



Kunal Bhatt, Om Prakash Chaudhary, Fahad Khan
and Dev Kumar Gautam

Abstract Current situation of the world demands an alternative fuel. Biofuel has several advantages over fossil fuel like they produce fewer greenhouse gases compared to fossil fuel, allowing for greater fuel security for countries, where fossil fuel is not easily available. Waste cooking oil is an alternative. Single-step transesterification process is used for converting waste cooking oil into biodiesel. Certain variables are fixed. Variables fixed are the molar ratio that is 6:1, catalyst concentration is taken as 1.25% of the weight of the oil sample, and the reaction temperature is taken 60 °C. Different blends were prepared using a splash blending technique. Different blends of biodiesel prepared such as—B10, B20, B30, B40. Then the experiment conducted on 3.5 KW single-cylinder air-cooled diesel engine widely used for the agriculture sector and for domestic purposes. Performance parameters like brake power, specific fuel consumption, and brake thermal efficiency are used with respect to the load of the engine. Then the test results were compared with conventional diesel fuel and the experiment result conveys that B20 blend biodiesel can act as alternating fuel without any modification in the current setup of the engine.

Keywords Biofuel · Single-step transesterification · Waste cooking oil · Testing · CI engine

1 Introduction

The expanding industrialization and mechanization of the world have prompted soak ascend for the request of oil-based energies. In addition, the limited stores of unrefined petroleum are amassed in specific areas of the world and the vast majority of the creating countries are the net merchants of raw petroleum. A huge outpouring of remote trade and vulnerability in its accessibility involves incredible worry for creating nations like India [1]. The road division diesel fuel utilization in India was 31,378 kT in 2009, as indicated by World Bank Indicators, listed in 2010 [2]. According to

K. Bhatt · O. P. Chaudhary (✉) · F. Khan · D. K. Gautam
Department of Mechanical Engineering, Amity University, Uttar-Pradesh Noida 201301, India
e-mail: 143opjat@gmail.com; mchhabra@amity.edu

© Springer Nature Singapore Pte Ltd. 2019
M. Kumar et al. (eds.), *Advances in Interdisciplinary Engineering*, Lecture Notes in
Mechanical Engineering, https://doi.org/10.1007/978-981-13-6577-5_61

one of the examinations in 40 years, the present stores of oil fuel including diesel will exhaust at an expanded utilization rate evaluated to be the request of 3% for each annum [3].

Unnecessary utilization of petroleum products has prompted worldwide natural corruption impacts, for example, nursery impact, corrosive rain, ozone layer exhaustion, environmental change, and so on. The primary explanation behind expanded contamination level regardless of stringent emission standards that have been implemented is the expanded interest for vitality in all parts and most essentially the vehicle segment. Exhausting stores of rough oil, vulnerability in accessibility, ecological debasement and quick climb in oil costs have prompted inquiry of substitute energies [4].

Biofuels produced using agrarian items (oxygenated by nature) diminish the reliance on oil imports, bolster neighborhood horticultural businesses and improve cultivating earnings. In addition, they additionally benefit regarding decreased smokiness or particulate issue in motor debilitates. There are a few factors that should be taken care of previously prescribing any substitute fuel to be utilized as a part of existing advances on an extensive scale. These elements are the degree of change required in existing hard products, i.e., if any other fuel needs broad alteration in the current equipment including gigantic capital then it might be hard to actualize; venture cost for creating foundation to fabricate and supply these substitute fills, i.e., over the top foundation cost may go about as a limitation for improvement of the elective vitality assets; natural similarity when contrasted with ordinary fills, i.e., in the event that another fuel is all the more dirtying then it will be unacceptable as a fuel; extra cost to the client as far as normal upkeep, hardware wear and greasing up oil life, i.e., excessive extra cost will adversely affect the broad acknowledgment of this fuel [5].

Biodiesel can be created from triglycerides display in naturally happening fats and oils by transesterification with alcohol, generally methanol, within the sight of an impetus. The sustained stocks are utilized for biodiesel creation right now are for the most part excellent sustenance review vegetable oils, for example, soya bean oil in the U.S.A, rapeseed oil in Europe, palm oil in Malaysia [6]. Lower cost sustains stocks, for example, squander cooking oil, oil, cleanser stocks are favored on account of their monetary feasibility, since feedstock costs are about over 85% of the aggregate cost of biodiesel creation [7, 8]. The non-palatable oils like Jatropa, Kaner, Karanja, Mahua, and so on are to a great extent used to create biodiesel in India.

The oxygen content in the fuel encourages total combustion of the fuel even in fuel-rich zones amid ignition in motor chamber and along these lines lessening carbon monoxide (CO) and hydrocarbon (HC) outflows. The higher cetane number of biodiesel lessens the ignition deferrals and hence the prob-capacity of fuel-rich zone development. This prompted diminishment in HC and CO emanations [9–11]. Biodiesel particle oxygen content, creates bring down stoichiometric necessity of air in the event of biodiesel burning [12, 13], which diminishes the likelihood of fuel-rich districts and the nonappearance of aromatics in biodiesel fuel, those being considered ash forerunners [14], brings about decrease of particulate issue (PM) discharges. Nitrogen Oxides (NO_x) development in motor fumes is an immediate capacity of ignition temperature. Lower temperature exists in the combustion chamber with

biodiesel because of general less fatty ignition and its lower LHV. However, the higher NO_x esteems, with respect to petroleum diesel fuel case, propose that nearby oxygen accessibility has a predominant impact [15]. Carbon stores on the barrel head, cylinder and injector tip for biodiesel-fueled motors were 40% less contrasted with diesel-fueled motors. Carbonization of biodiesel injector after 512 h of activity was far not as much as the diesel injector after 200 h of the motor task [16].

By and large, diesel motors work with superior fuel productivity and deliver a higher power torque than a regular start ignition (gas) motor diesel motors. This focal point helps to make the inner ignition diesel motor perfect for use in the overwhelming pull industry and car industry. In any case, a few discharges and waste items are discharged when diesel fills specifically nitrogen oxides (NO_x), suspended particulates matter (PM), sulfur dioxide (SO_2), and hydrocarbons. These undesirable discharges not effortlessly vanish and they can hurt the earth, for example, by adding to an Earth-wide temperature boost, worldwide darkening and corrosive rain [17].

The levels of NO_x , PM, SO_2 , and ash increments over the timeframe. The World Health Organization has announced air contamination has ascended by 8% all around in the previous 7 years (2007–2014) and condition specialists have cautioned that this situation is just going to deteriorate later on. The constant emission of poison gases into the climate will affect general well-being [18].

Biodiesel is an elective fuel which can be incorporated from vegetable oils or creature fats, including the waste cooking oils from eateries. It is to be noticed that current vehicle motors can be changed and changed over to consume unadulterated biodiesel (100%), however, it is not considered in this examination. Additionally, biodiesel can be mixed with oil diesel (0–20%) and utilized as a part of standard diesel motors with no motor change [19].

The vitality needs are increasingly elevated each year because of the request from mechanical and transportation division particularly from some high populace part of the world [20, 21]. Most transportation energizes are hydrocarbon based. These fills are gotten from oil, which is a unsustainable asset. This suggests some time or another petroleum having high potential will be exhausted [22, 23] and this will make vitality emergency the world [24]. At present, there is a developing advancement slant for electric vehicles. Notwithstanding, with the present battery innovation, the mileage of such vehicle is poor in contrast with inner ignition motor. The most developed battery has a vitality thickness of 180 Wh/kg. This is minuscule when contrasting it with fuel, which could give vitality thickness of 1800 Wh/kg subsequent to considering the effectiveness and misfortunes of the framework [25]. Given time and cash for innovative work, battery innovation will be propelled enough to rival inner burning motor in terms of vitality thickness. In any case, at that given time there will be a change period when gas will be too costly to be in any way utilized as fuel and electric auto with worthy mileage will be excessively costly, making it impossible to buy.

This paper centers around execution qualities of a four-stroke motor attribute when it keeps running on biodiesel and contrasting its outcome and ordinary diesel fuel. For this procedure, different mixes like B10, B20, B25, B30, B40 are taken into consideration.

2 Materials and Methods

2.1 Methodology for the FFA Check

Free fatty acids of the biofuel, at $\text{pH} < 7$, react with a chromogenic chemical and decrease its color. The disappearance of color, read at 628 nm, is equal to the acid concentration of the sample, expressed as % of oleic acid (Fig. 1).

- FFA calculated by titration is 1.14 which is less than 2%. So, we will do transesterification by a single step.

2.2 Methodology for the Formation of Biofuel

- First mix catalyst (KOH) 15 g (1.25% of oil) with methanol (20% of oil) 240 g making sure to cover the mixture while stirring.

Fig. 1 Titration for FFA



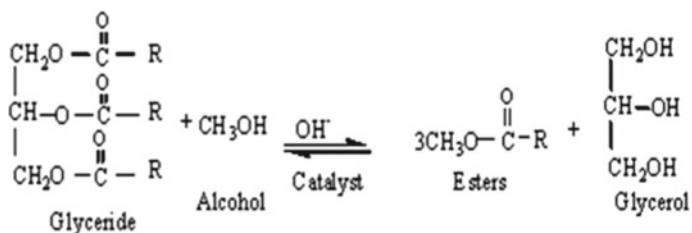


Fig. 2 Reaction between glyceride and alcohol



Fig. 3 Biofuel

- Once the mixture is ready pour it into oil 1200 g and making sure to maintain the oil temperature at 60 °C while pouring it.
- Now put the resultant mixture on magnetic stirrer hot plate for 60 min maintaining the temp at 60 °C.
- After 60 min put the mixture in the separating flask and leave it for separating glycerine from the biodiesel for 24 h. (Figs. 2 and 3)
- Biodiesel formed—176 g
- Glycerine formed—38 g
- Yield—Total biodiesel formed

divided by total oil taken for the process, i.e., $1140/1200 = 96\%$

Fig. 4 Diesel engine testing



2.3 Methodology for Testing Engine

- Checking up the experimental setup and maintenance and servicing it for testing.
- electricity consumption for different parameters like brake-specific fuel consumption, etc.
- Testing of diesel on the CI engine.
- Applying different loads by increasing the resistance (switching on the bulbs of rated).

Set up the electrical circuit and loads making connections of ammeter (Fig. 4).

2.4 Methodology of Emission Testing

Following steps are involved:

- **Preheating**
Heating of the engine before test.
- **Leak test**
Finding of leakages if any.
- **Residual test**
Residual gases must be removed if any.
- **R zero test**
Infrared test (Fig. 5).



Fig. 5 Gas emission tester

3 Performance Result

See Figs. 6, 7 and Tables 1, 2, 3 and 4.

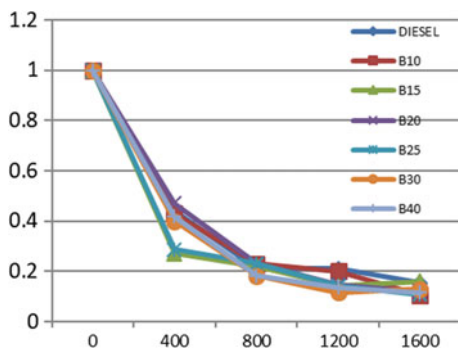


Fig. 6 BSFC with respect to load (W) curve

Fig. 7 BSFC with respect to load (W) curve

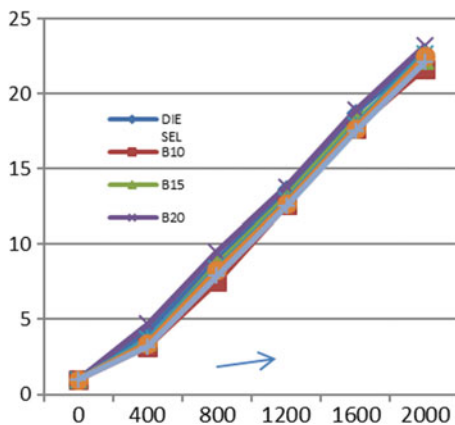


Table 1 Results of chemical process

Test/operation	Results	Methods
1. Biofuel	1140 g	By transesterification
2. Glycerine	190 g	By transesterification
3. Yield	95%	(By calculation, 1140/1200 = 95%)
4. Fire point	76.0 °C	ASTM D92
5. Flashpoint	30.5 °C.	ASTM D93
6. Pour pint	−6	ASTM D97
7. Cloud point	−2	ASTM D2500
6. K. Viscosity	4.2 cSt at 40 °C	ASTM D445
7. Gross calorific value	9688 k.cals/kg	ASTM D240
8. Density	0.8772 ay 15 °C	ASTM D1298

Table 2 BSFC at different loads of different blends

Load (W)	DIESEL	B10	B15	B20	B25	B30	B40
0	1	1	1	1	1	1	1
400	0.44	0.535	0.27	0.375	0.287	0.4	0.418
800	0.21	0.229	0.23	0.23	0.229	0.182	0.182
1200	0.2104	0.21	0.142	0.147	0.142	0.116	0.136
1600	0.153	0.105	0.159	0.12	0.106	0.129	0.116
2000	0.126	0.126	0.127	0.131	0.133	0.137	0.104

Table 3 Brake thermal eff. at different loads

Load (W)	Diesel	B10	B15	B20	B25	B30	B40
0	1	1	1	1	1	1	1
400	4.2	3.2	3.5	4.7	3.7	3.4	3.2
800	10.8	9.8	10.5	11.2	10.2	10.1	9.7
1200	13.6	12.6	13.1	13.8	12.9	12.7	12.5
1600	18.7	17.7	18.2	18.9	17.9	17.7	17.5
2000	22.7	21.7	22.2	23.2	22.7	22.5	22.1

Table 4 Emission gases at different loads

Gases	Load = idle	Load = 1200	Load = 2400
CO	0.1% volume	0.1% volume	0.1% volume
HC	34 ppm Hex	17 ppm Hex	15 ppm Hex
CO ₂	0.60% volume	1.20% volume	1.70% volume
NO	39 ppm volume	160 ppm volume	275 ppm volume

4 Conclusion

- Yield of biofuel (waste soya bean cooking oil) is very high in comparison to others.
- BTE values were higher for biodiesel blends B20 as compared to neat diesel for compression ratio equal to 14.
- Brake-specific fuel consumption of blend B20 was lower as compared to other blends in spite of an increase to BTE.

References

1. World Bank Indicators-India-transportation. Available from www.tradingeconomics.com/india/road-sector-diesel-fuel-consumption-kt-of-oilequivalent-wb-data
2. Nabi MN, Rahman MM, Akhtar MS (2009) *Appl Therm Eng* 29:2265–2270
3. Lin L, Cunshan Z, Vittayapadung S, Xiangqian S, Minutesgdong D (2011) *Appl Energy* 88:1020–1031
4. Hansen AC, Kyritsis DC, Lee CF (2009) In: Vertes AA et al (eds) *Biomass to biofuels—strategies for global industries*. Wiley, New York
5. Azam NM, Waris A, Nahar NM (2005) *Biomass bioenergy* 29:293–302
6. Haas MJ, McAloon AJ, Yee WC, Foglia TA (2006) *Bioresour Technol* 97:671–678
7. Abas N, Kalair A, Khan N (2015) Review of fossil fuels and future energy technologies. *Futures* 69:31–49
8. Miller RG (2011) Future oil supply: the changing stance of the International Energy Agency. *Energy Policy* 39:1569–1574
9. Seng LG, Itam OJA, Bangi KI (2009) An analysis of NGV market in Asia Pacific. In: The joint international conference on china natural gas vehicle technology innovation and industry development forum 13–14th May 2009, Chongqing, China
10. Ramasamy D, Zainal ZA, Kadirgama K, Walker-Gitano Briggs H (2016) Effect of dissimilar valve lift on a bi-fuel CNG engine operation. *Energy* 112:509–519
11. Pinto AC, Guarieriro LLN, Rezende JC, Ribereiro NM, Torres EA, Lopes EA et al (2005) *J Braz Chem Soc* 16(6B):1313–1330
12. Shi X, Yu Y, He H, Shuai S, Wang J, Li R (2005) *Fuel* 84:1543–1549
13. Armas O, Rodriguez J, Cardenas MD, Agudelo AF (2004) Efecto del biodiesel procedente de aceites vegetales usados sobre las emisiones y prestaciones de un motor diesel, *Anales del 16 Congreso Nacional de Ingenieria Mecanica*. Leon, Spain
14. Lapuerta M, Armas O, Ballesteros R (2002) Diesel particulate emissions from biofuels derived from Spanish vegetable oils, *SAE paper 2002-01-1657*
15. Rakopoulos CD, Dimartos AM, Giakoumis EG, Rakopoulos DC (2011) *Appl Energy* 88:3905–3916
16. Agarwal AK, Bijwe J, Das LM (2003) *J. Eng. Gas Turbine Power (ASME J.)* 125(3):820–826
17. Kassaby MEL, Nemit allah MA (2013) *Alexandria Eng J* 52:1–11
18. Ting WJ, Huang CM, Giridhar N, Wu WT (2008) *J Chin Inst Chem Eng*, 39(39):203–210
19. Omolara OO, Samuel AI (2007) *Afr J Biotechnol* 6(18):2166–2170
20. Dilip Kumar Bora (2009) *J Sci Ind Res* 68:960–963
21. Muralidharan K, Vasudevan D, Sheeba KN (2011) *Energy* 36:5385–5393
22. Murayama T, Fujiwara Y, Noto T (2000) *Inst Mech Eng* 141–148
23. Hirkude Jagannath B, Padalkar Atul S (2014) *Fuel* 119:266–273
24. Ma L, Geng J, Li W, Liu P, Li Z (2013) The development of natural gas as an automotive fuel in China. *Energy Policy* 62:531–539
25. Ismail MM, Zulkifli FH, Fawzi M, Osman SA (2006) Conversion method of a diesel engine to a Cng-diesel dual fuel engine and its financial savings

Modelling of Photovoltaic Losses from Available Meteorological Data



Rachit Gada, Ishan Doshi and Kashinath Patil

Abstract Solar photovoltaic power plants are most popular these days. The power production is limited by various parameters such as solar radiation, location, type of solar cells, demography, atmospheric conditions, losses, etc. Out of which, one of the prominent factor is losses. They occur due to shading and unclean panels. The dust settling depends on the location and atmospheric conditions. Thus, it is difficult to quantify shading percentage and therefore variable cleaning cycle time for panels. Current practice for the estimation of power loss is an experimental evaluation for the specific location. The present article discusses the effect of dust settling and shading on the solar PV system, effect of the temperature and wind speed on the power loss. The present study proposes the model for dust settling based on the standard meteorological data available for the location. The probability analysis is used to evaluate the time taken to cover 5% solar cell area for various input conditions. This helps to decide the cleaning cycle time. Further, the rise in temperature effect is evaluated. It is observed that with 10% probability for PM 2.5 particle settling and 0% probability of PM 10 settling, the time taken to cover 5% area is 7.09 h. It is observed that for 1 m² area with 317 Watts input solar radiation, the maximum temperature observed is 77 °C at noon.

Keywords Solar soiling · Dust · Particulate matter · Power loss · Temperature dependence · Shading effect

1 Introduction

Soiling is a phenomenon of deposition of dust on the surface of the solar PV module. The power obtained from a photovoltaic module basically depends on the amount

R. Gada · I. Doshi · K. Patil (✉)
Department of Mechanical Engineering, K. J. Somaiya College of Engineering, Vidyanagar,
Vidyavihar, Mumbai 400077, India
e-mail: Kashinath@somaiya.edu

I. Doshi
e-mail: ISHAN.DOSHI@SOMAIYA.EDU

© Springer Nature Singapore Pte Ltd. 2019
M. Kumar et al. (eds.), *Advances in Interdisciplinary Engineering*, Lecture Notes in
Mechanical Engineering, https://doi.org/10.1007/978-981-13-6577-5_62

of irradiance reaching the panels. The environment is the primary factor affecting the efficiency of these solar panels. Settling of dust, shadowing, the temperature of solar panels, wind velocity, etc. are some of the unavoidable factors that cause a decline in the efficiency of the solar panels. Individually, the affected output may look insignificant, but since the power output of the solar farms is in the range of megawatts and gigawatts, the slightest decrease in the efficiency of the arrays leads to a very significant overall loss in the output power. These losses can be majorly reduced by setting the optimum tilt angle and orientation of the plates and by planning cleaning cycles.

Typical dust particles are less than 10 mm in diameter, but the type of these particles depends on the location and its environment. Dust is generated from many sources such as pollution by wind, volcanic eruptions, vehicular movements, site construction and fires amongst many others. The accumulated dust overtime aggravates the soiling effect and affects the efficiency even more [1]. The data for these dust particles are easily available with the meteorological station across the country. Soiling is majorly caused by settling of PM 2.5 and PM 10 particles. These particles include various aerosols, salts, soot, fire ash, concrete dust, pollen, etc.

In a study conducted by Olivares [2] “characterization of soiling on PV modules in the Atacama Desert”, dust samples were collected and analysed from four different locations which were exhibiting different climatic characteristics, these were collected from the module surface and analysed using methods like LDS, SEM, XRD and XDS to compare the dust from the module to the ground. The relative transmission loss was found. In a study by Pedersen et al. [3] “Effects of Soiling on Photovoltaic Module in Norway” as the name suggests, the study was done for Norwegian climate and the dust accumulation was found out with respect to transmission loss, the dust accumulated in an area of $7 \times 7 \text{ cm}^2$ was directly weighed using precision balance and it was observed as the soil density or accumulation increases, transmission capacity decreases. In a study by Javed [4] and others “Modeling of Photovoltaic Soiling Loss as a Function of Environmental Variables”, this study was applied at Doha, Qatar for daily change in cleanness index with respect to the various environmental parameters like wind direction, wind velocity, PM 10, which were measured using wind direction transmitter, wind speed transmitter and aerosol transmitter, respectively. A multilinear regression model using basic statistical techniques was developed to show the relation between these parameters and daily values of cleanness index were determined. It also showed PM 10 had a high effect on the cleanness index. It used ANN model which are highly complex and also require frequent data inputs, whereas the change in the environmental variables was not significant in 24-h period.

When the PV panel is irradiated, around 20% of the total radiation that reaches the panel; after reflection, refraction and diffusion through the atmosphere; is converted to electric power, but the remaining energy is absorbed by the panel as thermal energy which raises the temperature of the panel [5] and thus of the diode junction. The diode junction has maximum conversion efficiency at 25 °C generally. With every degree rise or drop in the temperature of the panel from the optimum temperature, there is an efficiency drop in the power output of the panel corresponding to the temperature

coefficient of that panel. Wind velocity also leads to variation in the temperature of the panels. As the wind velocity increases, the amount of heat carried away by air due to convection increases and temperature of the panel decreases again affecting the panel's efficiency.

Another study by Byrakci [5] and others "Temperature Dependent Power Modeling of Photovoltaics" studies the relationship between the level of energy production with varying temperatures. In this study, two models of power generation across the United States are developed: one considers temperature and the other ignores it. The study concludes that there is a difference in the power output if the operating temperature of the panel deviates from its optimum temperature. But there is no development of any generic model by combining the effects of panel temperature, wind velocity and soiling of panels.

Thus, most of the studies conducted are location specific and require a large amount of apparatus and physical presence as data collection is one of the most important parameters. The efficiency of a solar PV module mainly decreases due to natural parameters like the quality of air (AQI), the wind density, the wind velocity, ambient temperature, the temperature of the plate, etc. The objective of this study is to develop a model which is generic and can be used with the help of meteorological data and the loss in the efficiency of the solar plant can be calculated.

2 Model and Analysis

2.1 Settling Probability due to PM 2.5 and PM 10

PM 2.5 is also known as particulate matter 2.5 and it basically consists of particles ranging from 1 to 2.5 μm in diameter and PM 10 also known as particulate matter 10 basically consists of particles ranging from 2.5 to 10 μm in diameter.

PM 2.5 basically consists of aerosols, with their densities ranging from $\rho = 1.6 \pm 0.5 \text{ gm/cm}^3$. PM 10 basically consists of fly ash ($\rho = 540\text{--}860 \text{ kg/m}^3$), cement dust ($\rho = 1600 \text{ kg/m}^3$), solid pollen ($\rho = 1435 \text{ kg/m}^3$), soot ($\rho = 1200 \text{ kg/m}^3$) and ammonium salts like ammonium sulphate ($\rho = 1770 \text{ kg/m}^3$) and ammonium chloride ($\rho = 1530 \text{ kg/m}^3$). Assuming the salts are present in equal proportion and the other pollutants as well, therefore, the relative density will be approximately $\rho = 1.317 \text{ kg/m}^3$.

Assuming the particulate matter is uniformly spread or dense throughout its diameter. Therefore, the equivalent diameter of PM 2.5 will be equal to 1.75 μm and that of PM 10 will be equal to 6.125 μm . These particles will be spherical in shape and hence their volume can be calculated as

$$V = \frac{4\pi r^3}{3} \quad (1)$$

Volume and equivalent density can be used to find out the average mass of each particle of PM 2.5 and PM 10 and co-relating with the AQI, which is available from the meteorological data and for different probabilities of settling of PM 10 and PM 2.5, the time required to cover a specific area can be calculated. This AQI can be calculated for a 24-h average period and plotted to find out the required time.

2.2 Temperature Rise of the Solar Panel

Assuming the solar panels, the sun and the wind as a system, the type of heat transfer that takes place between the solar panel and the atmospheric air is forced convection. The solar radiation reaches the solar panels of which 20% is absorbed and the remaining is used to heat up the panel which raises the temperature of the panel above the average atmospheric temperature and hence heat transfer takes place from the solar panel to the surrounding air by forced convection. The assumptions used for simplifying the problem are: (a) Type of convection is forced convection. (b) No radiation takes place from the solar panel (c) Solar panel is assumed to be a thin plate. (d) Wind flows parallel to the plate surface and plate is horizontally placed. The amount of heat absorbed by the solar panel can thus be calculated as

$$Q_u = I * A - h * A * (T_p - T_a) \quad (2)$$

where

Q_u = Heat absorbed by the solar plate (W), I = Solar Irradiance (W/m^2), A = Area of the Solar Panel (m^2) = 1, T_p = Temperature of Solar Panel (K), T_a = Ambient Temperature (K).

The temperature of the solar panel can be calculated as

$$\frac{T_p - T_a - (I/h)}{T_i - T_a - (I/h)} = e^{-\frac{A * h * Fr}{m * C_p}} \quad (3)$$

where

I = Solar Irradiance (W/m^2), A = Area of the Solar Panel (m^2), T_p = Temperature of Solar Panel (K), T_a = Ambient Temperature (K), T_i = Initial Temperature of Solar Panel (K) = 293 K, h = Convective heat transfer coefficient of Air (W/m^2K), m = mass flow rate of air (kg/s) = 0.01, C_p = Specific heat capacity at constant pressure ($J/kg-K$) = 1004, Fr = Heat removal factor = 1.

Thus, the efficiency of the solar panel at any location can be calculated using this mathematical model given that the meteorological data such as air quality index, solar irradiance and wind velocity are available.

2.3 Shading Effect

Shading has a pronounced effect on the amount of power produced by PV modules. The power produced is reduced significantly due to a reduction in current and voltage of the PV module. For analysis, 20-W solar panel was used and predefined shading was carried out. This shading test was carried out at a different time of day on a clean 20 W PV module. Partial as well as complete shading of four-string panel having a total 36 cells was carried at different shading source heights from the panel viz., 25, 50, 75 and 100 cm. Parameters like the module voltage (closed and open), current, irradiance, time, ambient temperature were noted and the following analysis was further carried out. Using this data, the power, normalized power, efficiency, normalized efficiency, drop in power, etc. were evaluated. The module is a four-string module with a total of 36 cells, i.e. 4×9 cells, the shading were carried by increasing the shading area systematically and the different cell parameters and ambient parameters were recorded. The area of this panel was 0.196 m^2 . It was observed that there was a drastic loss after the first cell was shaded in all the cases, and then the loss was incremental after the first cell being covered. Further, the maximum efficiency was observed at the no-load condition when the solar irradiance was 422 W/m^2 and the efficiency was 14.28%. The power drop can be given by

$$\text{Percent Power Drop} = \frac{(\text{Power})_{\text{No Shade}} - (\text{Power})_{\text{Observed}}}{(\text{Power})_{\text{No Shade}}} * 100 \quad (4)$$

3 Results and Discussions

3.1 The Probability of Settling of Dust Particles

The value of PM 2.5 and PM 10 are considered for 24-h average in Mumbai during the month of September. $\text{PM 2.5} = 73 \mu\text{g/m}^3$ and $\text{PM 10} = 35 \mu\text{g/m}^3$.

In the Fig. 1a–c, the curves indicate the different probability of PM 2.5 settling from 0 to 10% and on the x-axis, there are different probabilities of PM 10 settling and on y-axis is the time required in hours. The maximum time with 0.1% probability of PM 2.5 and 0% of PM 10 settling which is approximately 142 h (Fig. 1a) and minimum time required for the same line will be 8.049 h, the least minimum time will occur when probability of PM 2.5 is 10% and PM 10 is 10% and it is 1.21 h. For the PM 2.5 with probability 2%, the time ranges from 3.38 to 7.10 h. These lines and axes are same for the same graphs, and they just show change to cover different fractions of the total area of 1 m^2 and the total time required for covering these just varies as the probability of settling changes.

In Fig. 1b, the maximum time with 0.1% probability of PM 2.5 and 0% of PM 10 settling which is approximately 710 h and minimum time required for the same line will be 40.2 h, the least minimum time will occur when probability of PM 2.5

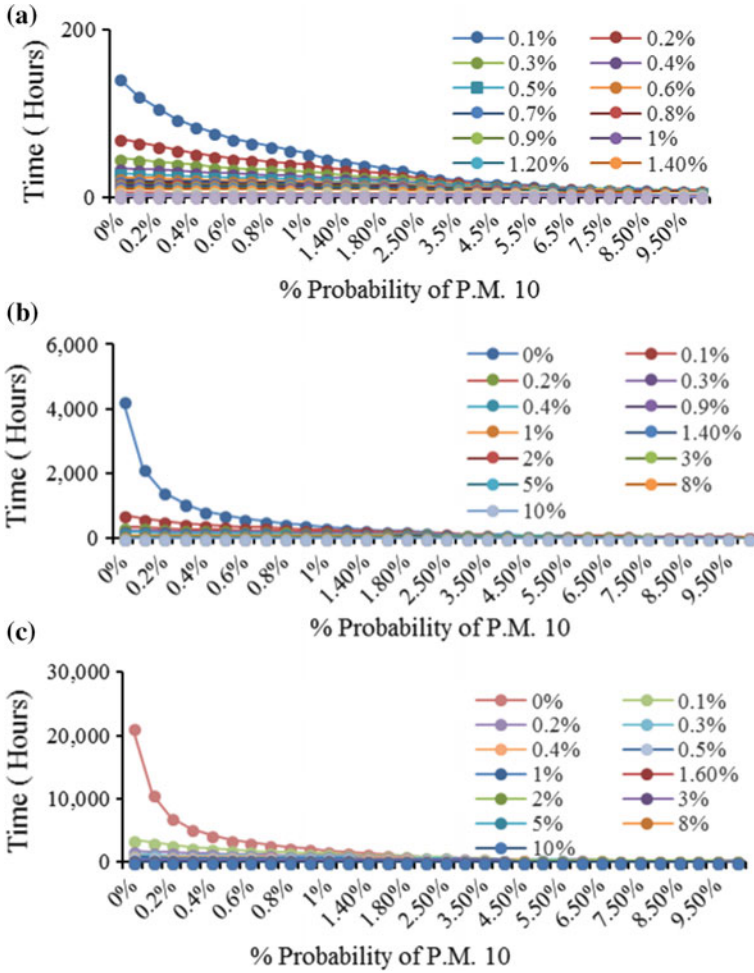


Fig. 1 a Time required to cover 1% area in 1 m² (0.01 m²). b Time required to cover 5% area (0.05 m²). c Time required to cover 25% area (0.25 m²)

is 10% and PM 10 is 10% is 6.078 h. For the PM 2.5 with probability 2%, the time ranges from 19.4 to 35.5 h.

In Fig. 1c, the maximum time with 0.1% probability of PM 2.5 and 0% of PM 10 settling which is approximately 21,300 h and minimum time required for the same line will be 213 h, the least minimum time will occur when probability of PM 2.5 is 10% and PM 10 is 10% is 30.4 h. For the PM 2.5 with probability 2%, the time ranges from 96.9 to 178 h.

3.2 Solar Panel Temperature Plots

Figure 2a indicates the rise in the solar panel temperature during the span of one entire day in summer season. The x-axis represents the time in hours and the y-axis represents the temperature of the solar panel in Kelvins. From Fig. 2a, it is evident that ample amount of solar energy is available from 9.00 a.m. to 5.00 pm but the heat absorbed by the solar panel is the maximum around 12.00 pm as the sun is overhead. There is a 9.42% variation in the panel temperature during the solar time. Figure 2b is a plot of the useful energy available to the solar panel during a summer day. The x-axis represents the time in hours and the y-axis represents the available useful energy to the solar panel in Watts. In Fig. 2b, as expected, the amount of useful energy available is maximum at noon and the solar time is 9.00 a.m.–5.00 pm. A variation of 58.7% is seen in the useful available energy during the day.

Figure 3a indicates the variation in the average temperature of the solar panel for an entire year. The x-axis denotes the months of a year (1 January–12 December) and the y-axis denotes the temperature of the solar panel in Kelvins. As can be seen from Fig. 3a, the temperature of the solar panel is maximum during the months of the summer season (March–April–May) and lowest during monsoon and winter as the clouds cover the sky and prevent the radiation from reaching the solar panel. A variation of 6% is seen in solar panel temperature during the span of an entire year. Figure 3b is a plot of the useful energy available to the solar panel during a complete year. The x-axis denotes the months of a year (1 January–12 December) and the y-axis denotes the available useful energy to the solar panel in Watts. The trend in Fig. 3b, as expected remains the same as Fig. 3a (month vs. temperature plot) but a variation of 45.83% is observed in the amount of useful energy during the year.

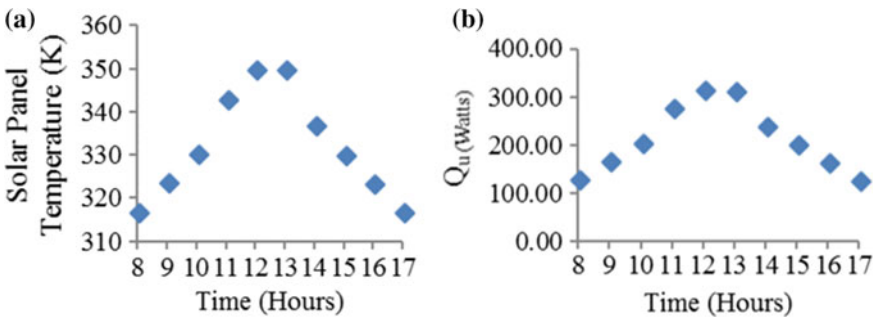


Fig. 2 a Rise in temperature of solar panel during day. b Q_u (useful energy) available throughout the day

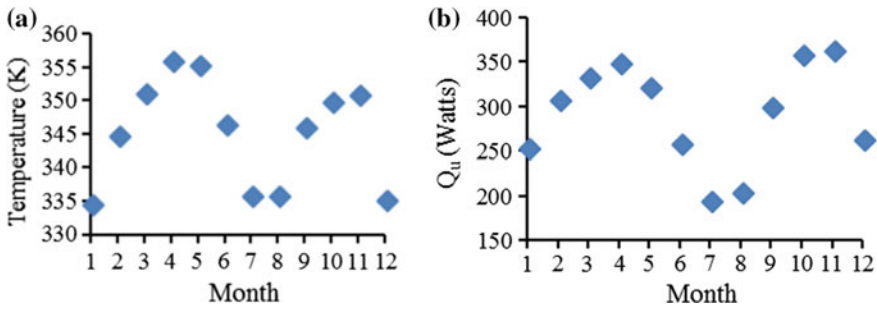


Fig. 3 a Average solar plate temperature variation for an entire year. b Q_u (average useful energy) available throughout the year

3.3 Shading Effect

In Fig. 4, the actual efficiency of solar PV module is plotted against the percentage area covered with the different distance of shading source. The maximum efficiency of the cell is at no-shade condition for the module when the irradiance was 422 W/m^2 and that efficiency is 14.28%, whereas the minimum efficiency for the same condition occurs when all 36 cells or strings are covered, and the efficiency is 2.34%. The overall minimum efficiency occurs when the obstacle stands 25 cm away covering the entire panel and the value is 0.647% when the irradiance is 735 W/m^2 . It was observed that as the distance of the shading source is closer to the solar PV module, then the actual efficiency decreases significantly due to reduction all kinds of solar radiation received by the PV modules. It is observed that as the area covered by shadow increases, the actual and normal efficiency reduces due to shading of a greater number of cells. Also, as the number of cells shaded increases, the effect of the distance of shading source on the output power becomes almost negligible.

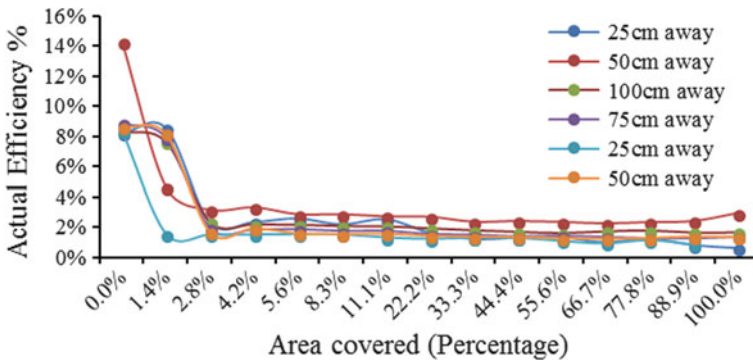


Fig. 4 Actual efficiency of the solar panel for different areas shaded when the shade source is at different distances from the panel

Figure 5 shows the actual power out from the solar PV module at various shading areas. The maximum power generated was 13.86 W and the minimum power generated was when the shade occurred at 25 cm away from the module and the entire module was shaded when the power obtained was 0.73 W. The power reduction was significantly reduced at around 4.2% of shading area and thereafter, the total output power was constant.

Figure 6 shows a scatter plot, on the x-axis, there is irradiance in W/m^2 and on the y-axis, the actual efficiency of solar PV module, the different curves indicate different distances of the obstacle from the PV module for a different number of cells and area covered. The overall minimum efficiency occurs when the obstacle stands 25 cm away covering the entire panel and the value is 0.647% when the irradiance is $735 W/m^2$ and the maximum efficiency.

Figure 7 shows a scatter plot, on the x-axis the irradiance in W/m^2 and on the y-axis, the power/area in W/m^2 , the lines show the distances of the obstacle from the solar PV module for different number of cells and area covered. The maximum

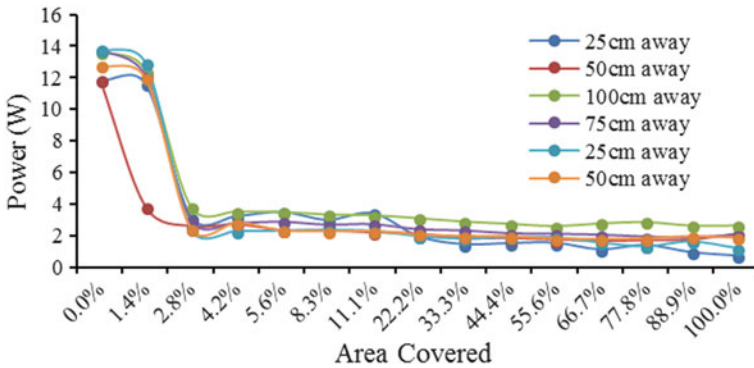


Fig. 5 Actual power of the solar panel for different areas shaded when the shade source is at different distances from the panel

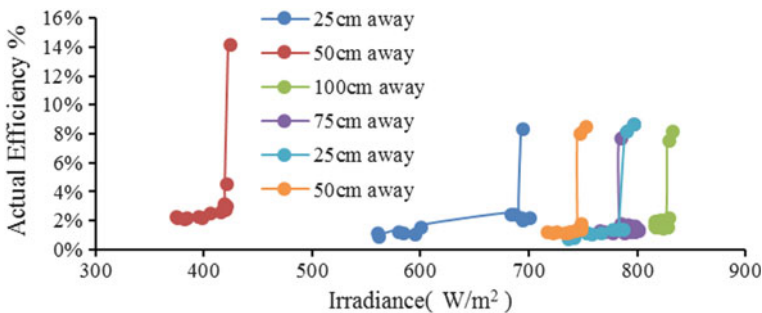


Fig. 6 Actual efficiency of the solar panel with the corresponding irradiance for different areas shaded when the shade source is at different distances from the panel

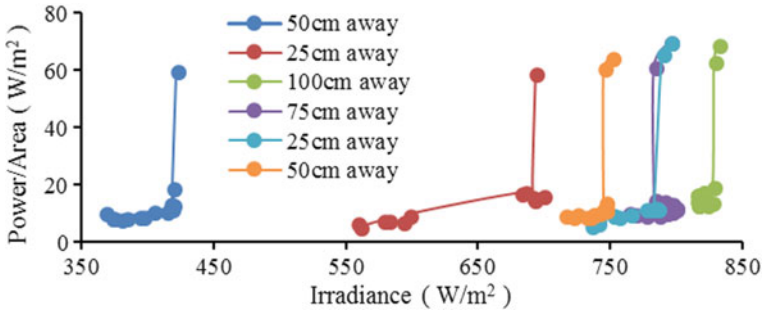


Fig. 7 Power-to-area ratio of the solar panel with the corresponding irradiance for different areas shaded when the shade source is at different distances from the panel

power/area is 70.28 W/m² at irradiance 795 W/m² at the no-shade condition and the minimum power/area is 3.72 W/m² at an irradiance of 575 W/m².

Figure 8 shows the normalized efficiency in different areas covered with shading source at different distances from the PV module. Normalized efficiency is correlated with a particular irradiance for shading source at each distance to normalize the effect of the different area covered while having different irradiance. The maximum normalized efficiency of the cell is at no-shade condition when the normalized irradiance was 422 W/m² and the corresponding efficiency is 14.28%, whereas the minimum efficiency for the same condition occurs when all 36 cells or 9 lines are covered and the efficiency is 2.514%. The overall normalized minimum efficiency occurs when the obstacle stands 25 cm away covering the entire panel and the value is 0.827%.

Figure 9 shows the power drop of the PV module at various shaded areas for the shading source at different distances from the module. It is observed that the drop in power is almost 70% as a single cell is covered, and then it increases slowly with the increase in the area shaded. The power drop is the highest when the shade is cast 25 cm away and the entire panel is shaded; the power drop is 93.81%. The losses

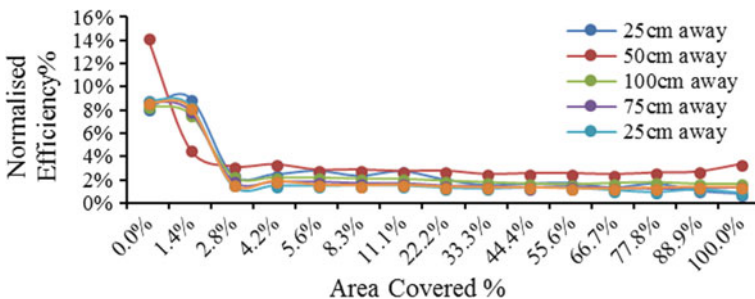


Fig. 8 Normalized efficiency of the solar panel for different areas shaded when the shade source is at different distances from the panel

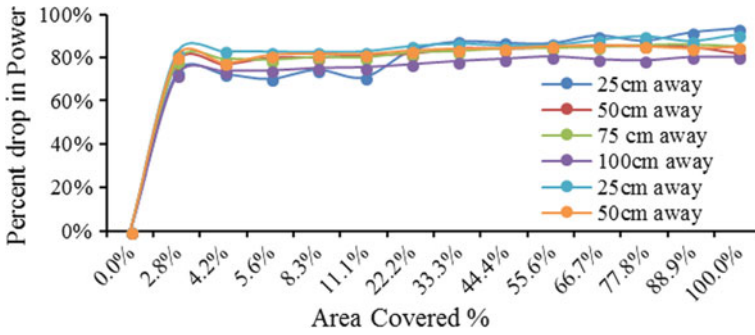


Fig. 9 Per cent drop in power of the solar panel for different areas shaded when the shade source is at different distances from the panel

or the least power was generated when the shade or the obstacle was at the distance of 25 cm away from the module. Similarly, the maximum power was obtained at no-shade condition as well as the least power loss occurred when an obstacle was at the distance of 100 cm away from the module.

Figure 10 gives the normalized power output from the PV module for different shaded areas. As it is observed, the maximum normalized power was generated at no-load condition and as a shaded region increased the power generated kept reducing with a drastic reduction when the first cell was covered. The maximum power generated was 13.83 W and the minimum power generated was when shade occurred at 25 cm away from the module and the entire module was shaded the power obtained was 0.94 W.

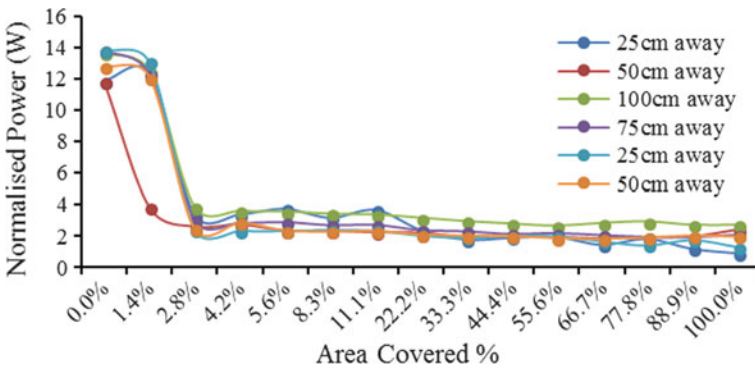


Fig. 10 Normalized power of the solar panel for different areas shaded when the shade source is at different distances from the panel

4 Conclusion

It is observed that as the probability of particulate matter's settling increases, the time required for covering a specific percentage of area decreases, but after a point, the settling density stabilizes. For 0.1% settling probability of PM 2.5 and 0% settling probability of PM 10, the time required for the same is 710 h. For 0.1% settling probability of PM 2.5 and 10% settling probability of PM 10, the time required for covering 5% area is 40.2 h. The amount of solar irradiance absorbed by the solar panels is maximum during the noontime; as a result, it provides the maximum output around 12.00 pm, but the temperature of solar panels reaches a peak and is around 350 K at the same time. This increase in solar panel's temperature causes a significant loss in the rated power output of the panel, corresponding to 0.5% loss in power with every degree rise in temperature above 298 K, which varies according to the temperature coefficient of the solar panel. Also, with the increase in shading, the efficiency significantly decreases. The maximum efficiency of the 20-W solar panel as observed was 14.28% when there was no shading. As the shading source moves away from the PV module, the output power increases, i.e. the efficiency increases. The power drop is drastic even when a single cell from the entire panel is covered and the power drop is more than 70% because of the series connection of solar cells. Thus, the meteorological data can be used to calculate the average power loss that will occur due to environmental factors at any given location.

References

1. Maghami MR, Hizam H (2016) Power loss due to soiling on solar panel: a review. *Renew Sustain Energy Rev* 59:1307–1316
2. Olivares D, Ferradaa P, de Matosb C, Marzo A (2017) Characterization of soiling on PV modules in the Atacama Desert. *Energy Procedia* 124:547–553
3. Pedersen H, Strauss J, Sleij J (2016) Effects of Soiling on photovoltaic module in Norway. *Energy Procedia* 92:585–589
4. Javed W, Guo B, Figgis B (2017) Modelling of photovoltaic soiling loss as a function of environmental variables. *Solar Energy* 157:397–407
5. Bayrakcia M, Choib Y, Brownsona JRS (2014) Temperature dependent power modeling of photovoltaics. *Energy Procedia* 57:745–754

Bio-Tribological Study of Synovial Fluid in the Orthopedic Implants



Shariq Ahmad Bhat and M. S. Charoo

Abstract The paper focuses on the influence of various constituents of synovial fluid in the lubrication mechanism of artificial implant joints. The performance of synovial fluid varies from individual to individual of different age groups, and depends on various parameters such as concentration, composition, surface characteristics, wetting degree, temperature, and pressure. The incorporation of minerals such as calcium, proteins, and lipids are found fruitful in accelerating the performance of synovial fluid. The condition that favors boundary lubrication in synovial joints is that the contact pressure should be high or sliding speed should be low. The generation of reactive oxygen species (ROS) by neutrophils leads to degradation of hyaluronic acid, and this degradation can be prevented by using antioxidants such as mannitol, thiourea, and vinpocetine. This review article aims to present an overview of the role of synovial fluid constituents on tribological behavior of orthopedic tribo pairs.

Keywords Synovial fluid · Friction · Wear · Lubrication · Hyaluronic acid

1 Introduction

The major components of synovial fluid that control the friction coefficient, film thickness in orthopedic tribo pairs are hyaluronic acid (9.4%), globulin (33%), lubricin (1%), and albumin (56.6%). Synovial fluid with non-Newtonian flow properties plays a pivotal role in orthopedic implants in deciding their permanence [1, 2]. Body joints are enclosed with cartilage, which allows smooth movement of bones and thereby friction is reduced and also the weight during walking or running is supported by it. The molecules of synovial fluid are responsible for imparting desirable friction and wear properties to articulating surfaces. SF is the best lubricant present in synovial joints such as elbow joint, knee joint, hip joint, etc., performs a number of functions such as it absorb shocks, provides a smooth movement [3, 4]. The properties of synovial fluid are unique that enables it to safeguard bone sur-

S. A. Bhat (✉) · M. S. Charoo
Mechanical Engineering Department, NIT Srinagar, Srinagar, Jammu and Kashmir, India
e-mail: bhatshariq6@gmail.com

© Springer Nature Singapore Pte Ltd. 2019
M. Kumar et al. (eds.), *Advances in Interdisciplinary Engineering*, Lecture Notes in Mechanical Engineering, https://doi.org/10.1007/978-981-13-6577-5_63

657

faces. It is present in small amount in the moveable joints and irrespective of this, it provides lubrication to the joint and nutrition to articular cartilage. In boundary lubrication of synovial joints, articular cartilage and components of synovial fluid both play a crucial role [5–8]. The lubrication process of joints is dependent on the properties of synovial fluid. A direct relationship exists between hyaluronic acid concentration and synovial fluid viscosity at lesser shear rate. The albumin increases the wear strength of articular cartilage and thus protects orthopedic implants from severe wear [9, 10]. Lubricin, a glycoprotein commonly known as superficial zone protein decreases shear strength at the point of contact, and is also responsible for boundary lubrication in movable joints. Globulin plays a pivotal performance in the lubrication mechanism of orthopedic implants, i.e., in the boundary lubrication. Variation in film thickness occurs with change in fluid content [11]. In vitro tests carried are outside the body of an organism in controlled environment, and synovial fluid is replaced with pure bovine serum or with diluted one [12–15]. After 10–15 years of implantation, the failure of artificial joints is seen in vivo and it has become mandatory that the effect of synovial components in implanted joints can be studied. In metal—on-metal joints with change in fluid concentration variation in thickness of film takes place. The friction and wear that develops in tribo pairs is greatly influenced by protein concentration present in the synovial fluid. The proteins get adsorbed on the scrubbing surfaces forming a thin film that separates surfaces from each other resulting in reducing friction and wear. The protein adsorption rate depends on the nature of surfaces whether it is hydrophobic or hydrophilic. The protein adsorption rate is high when the surface possesses high degree of hydrophobicity and low when the surface is hydrophilic. The addition of albumin to bovine serum results in decrease in coefficient of friction when used as a lubricant in orthopedic implants [16]. The coefficient of friction between two interacting surfaces decreases when bovine serum added to Hanks balanced salt solution was practiced as lubricant [16]. The friction coefficient changes with change in pH value of lubricant as it is found to be dependent on the lubricants pH value, and it increases when pH value goes beyond 7.43 as amplification of negative charge of protein takes place. The effect of change in pH value on the viscosity of lubricant is also studied at different shear rates and it is concluded that at lower shear rate, there exists an inverse relationship between pH value of lubricant and its viscosity, i.e., with increase in the pH, viscosity decreases.

2 Synovial Fluid Components

2.1 Albumin

The concentration of proteins in the synovial fluid is about 89.6%. Albumin is the most dominant protein. It performs an outstanding role in boundary lubrication and enhances wear resistance of articulating surfaces [17]. The lubricating effect of albumin is dependent on material properties as it gets easily adsorbed on hydrophobic

surfaces in comparison to hydrophilic surfaces. Its lubricating effect is also found to be dependent on pH value of the synovial fluid. The parameters that govern the formation of protective layer on frictional mating pairs include low sliding velocity and high load as these accelerate the adsorption rate of the protein.

2.2 Globulin

The percentage of globulin in the synovial fluid is about 33% and plays a vital role in the boundary lubrication. Among various components of synovial fluid, thicker films are produced by globulin. In orthopedic implants, wear is reduced by preventing the removal of metallic ions from surface layers [11, 18]. The lubricating effect of globulin at low speed is independent on the pH value of the lubricant but at high speed, the same is not true resulting in hydrodynamic mode of lubrication [19].

2.3 Hyaluronic Acid

The percentage of HA (Hyaluron) in the synovial fluid is about 9.4%. It consists of b-D-(1, 4)-*N*-acetyl glucosamine and b-D-(1-3)-*N*-glucuronic acid. The association of hyaluronic molecules occurs in solution and at higher concentrations, the formation of viscoelastic gel takes place. It exhibits elastic as well as viscous properties that make it suitable for cartilage lubrication. It is reported that 15 g of hyaluronic acid is present in a man weighing 70 kg. In arthritic joints, the concentration of hyaluronic acid is less and that of proteins is more when compared with normal synovial joints. It gets degraded by reactive oxygen species generated by neutrophils and it has been found that its degradation can be prevented by using antioxidants such as thiol compounds.

2.4 Lubricin

The concentration of lubricin (Superficial Zone Protein) in synovial fluid is about 1% and plays a vital role in cartilage coherence. Cartilage surfaces are coated with lubricin resulting in boundary lubrication and reducing shear strength at the point of contact of two surfaces. The transportation of phospholipids to the cartilage surface is facilitated by it [8]. A crucial role is played by lubricin in cartilage integrity, protection of chondrocytes. It assists in stopping cell fitment to articular surfaces.

3 Tribological Role of Synovial Fluid Components in Orthopedic Implants

In the boundary lubrication of orthopedic implants, the ingredients of synovial fluid (globulin, lubricin, hyaluronic acid, and albumin) play a vital role. The outcome of lubricant concentration on friction and wear was first studied experimentally by Coveret et al. [13]. They used bovine serum in saline solution as a lubricant and polyvinyl alcohol as a specimen, and came to the conclusion that the effect of bovine serum on coefficient of friction was negligible. Wang et al. [12] performed a wear test on Ultra-high-molecular weight polyethylene (UHMWPE) and Polytetrafluoroethylene (PTFE) using calf serum and alpha-calf serum as lubricants, and found that the wear rate for ultra-high-molecular-weight polyethylene decreased with boosting total protein percentage of both lubricants and for PTFE, the wear rate increases with the addition of proteins to both lubricants. Anil et al. [20] performed a test on Ti-6Al-4V coated with diamond-like carbon coating using bovine serum and water as lubricants, and they found that the coefficient of friction came out high when water was used as a lubricant. The coefficient of friction reduced when bovine serum was used as a lubricant in place of water. Myant et al. [11] showed that variation of film thickness takes place with change in concentration of synovial fluid components. It has been found that rate of protein adsorption is good when the surfaces are hydrophobic in nature [21]. Bovine serum when added to hyaluronic acid results in lubrication mechanism change [22]. Incorporation of lipids to a mixture of hyaluronic acid and serum albumin resulted in higher coefficient of friction than the lubricants without lipids [8] (Table 1).

4 Conclusion

The review presented the tribological role of synovial fluid components in orthopedic implants. The individual role is played by various components of synovial fluid in controlling the coefficient of friction and wear in orthopedic implants. The viscosity of synovial fluid has a direct relationship with the concentration of hyaluronic acid. A significant role is played by proteins in boundary lubrication and is found dependent on pH value of lubricant, as well on the nature of surfaces in contact. The performance of synovial fluid can be enhanced by the addition of minerals, proteins to it. The effect of proteins lipids hyaluronic acid on friction wear film thickness has been seen.

Table 1 Summary of tribological role of synovial fluid components in orthopedic implants

Lubricants used	Specimens	Key results	Reference
1. Bovine calf serum 2. Albumin 3. Globulin	Femoral head of cobalt Chromium-molybdenum Chromium-coated glass	The fluids containing globulin results in thicker films Thinner films are formed when albumin is added to the fluids	[11]
1. Human serum 2. Hyaluronic acid	UHMWPE CoCrMo	It is observed that when hyaluronic acid was added to serum, the lubrication mechanism changed to hydrodynamic from boundary and the coefficient of friction decreased	[22]
1. Synovial fluid 2. Lipids	Glass borosilicate glass	It is found that the coefficient of friction came out to be lower in reciprocating sliding contact of glass-on-borosilicate glass when lipid concentration in synovial fluid was increased	[23]
1. Phosphate buffer solution	Bovine osteochondral explant	The coefficient of friction has been found to decrease with increase in contact pressure and decrease in equilibrium time	[24]
1. Phosphate buffer solution 2. Synovial fluid of cow obtained from knee joints 3. Bovine serum albumin 4. AGP	CoCrMo pins Latex versus glass lubrication Ethanol-cleaned glass(hydrophobic) Piranha-cleaned glass(hydrophilic)	The coefficient of friction came out to be very high when PBS was used as lubricant and with the addition of bovine synovial fluid to phosphate buffer solution reduction in coefficient of friction occurred PBS in combination with AGP as a lubricant decreases the coefficient of friction. BSA in combination with AGP as a lubricant resulted in increase in the coefficient of friction	[25]
1. Water 2. Bovine serum	Ti-6Al-4V material Oxygen plasma-treated Si-diamond-like carbon	The coefficient of friction came out high when water was used as a lubricant The frictional coefficient decreased with bovine serum when used as a lubricant in place of water	[20]

(continued)

Table 1 (continued)

Lubricants used	Specimens	Key results	Reference
<ol style="list-style-type: none"> Hanks balanced salt solution Hanks balanced salt solution and human albumin HBSS+BSA HBSS+BSA+HA 	UHMWPE CoCrM	In case of metallic surfaces, the addition of bovine serum albumin to other lubricants results in lower coefficient of friction as no film transfer occurs in such surfaces but the coefficient of friction in case of aluminum increases as intense film transfer takes place	[16]
<ol style="list-style-type: none"> Human serum albumin 	Pin material UHMWPE disc material ceramic	The coefficient of friction increases when hydrophobic surfaces are used as they easily adsorb denatured proteins Using hydrophilic surfaces, the coefficient of friction came out to be lower as they have high potential of absorbing native proteins	[14]
<ol style="list-style-type: none"> BCS Alpha-calf serum 	UHMWPE PTFE	The wear rate for UHMWPE decreased when protein content of both bovine calf serum and alpha-calf serum was increased but for PTFE with the increase in protein content of both lubricants wear rate increases as a function of time. The reason is that UHMWPE is hydrophilic in nature and PTFE is hydrophobic one	[12]
<ol style="list-style-type: none"> BSF PBS 	Pure DLC coating Osteochondral core	Measurement of friction has been done and is found steady with respect to phosphate buffer solution and BSF. The friction came out lower when BSF was used	[26]
<ol style="list-style-type: none"> SF 	Three subgroups; displaced disc groups with reduction (DDR), displaced groups without reduction (DDNR), osteoarthritis	The effect of lubricin concentration on friction was studied and no significant correlation was found	[27]

References

1. Furey MJ, Burkhardt BM (1997) Biotribology: friction, wear, and lubrication of natural synovial joints. *Lubr Sci* 9(3):255–271
2. Furey MJ (1997) Exploring possible connections between tribology and osteoarthritis. *Lubr Sci* 9(3):273–281
3. Radin EL, Paul IL (1970) Does cartilage compliance reduce skeletal impact loads? The relative force-attenuating properties of articular cartilage, synovial fluid, periarticular soft tissues and bone. *Arthritis Rheumatol* 13(2):139–144
4. Widmer MR, Heuberger M, Vörös J, Spencer ND (2001) Influence of polymer surface chemistry on frictional properties under protein-lubrication conditions: implications for hip-implant design. *Tribol Lett* 10(1–2):111–116
5. Spikes H (1997) Mixed lubrication—an overview. *Lubr Sci* 9(3):221–253
6. Dowson D (1996) Paper 12: modes of lubrication in human joints. In: Proceedings of the institution of mechanical engineers, conference proceedings, vol 181, no 10. SAGE Publications Sage UK, London, England, pp 45–54
7. Unsworth A, Percy M, White E, White G (1988) Soft layer lubrication of artificial hip joints. *Lubr Sci* 5(1):55–72
8. Trunfio-Sfarghiu A-M, Berthier Y, Meurisse M-H, Rieu J-P (2007) Multiscale analysis of the tribological role of the molecular assemblies of synovial fluid. Case of a healthy joint and implants. *Tribol Int* 40(10–12):1500–1515
9. Wimmer M, Sprecher C, Hauer R, Täger G, Fischer A (2003) Tribochemical reaction on metal-on-metal hip joint bearings: a comparison between in-vitro and in-vivo results. *Wear* 255(7–12):1007–1014
10. Trunfio A, Berthier Y, Meurisse M, Rieu J (2007) Analysis of the tribological role of molecular assemblies of synovial fluid in the operation of healthy joints and articular joint prostheses. *Comput Methods Biomech Biomed Eng* 10(Sup1):173–174
11. Myant C, Underwood R, Fan J, Cann P (2012) Lubrication of metal-on-metal hip joints: the effect of protein content and load on film formation and wear. *J Mech Behav Biomed Mater* 6:30–40
12. Wang A, Essner A, Schmidig G (2004) The effects of lubricant composition on in vitro wear testing of polymeric acetabular components. *J Biomed Mater Res B Appl Biomater* 68(1):45–52
13. Covert RJ, Ott R, Ku DN (2003) Friction characteristics of a potential articular cartilage biomaterial. *Wear* 255(7–12):1064–1068
14. Heuberger M, Widmer M, Zobeley E, Glockshuber R, Spencer N (2005) Protein-mediated boundary lubrication in arthroplasty. *Biomaterials* 26(10):1165–1173
15. McCann L, Udofia I, Graindorge S, Ingham E, Jin Z, Fisher J (2008) Tribological testing of articular cartilage of the medial compartment of the knee using a friction simulator. *Tribol Int* 41(11):1126–1133
16. Gispert M, Serro A, Colaco R, Saramago B (2006) Friction and wear mechanisms in hip prosthesis: comparison of joint materials behaviour in several lubricants. *Wear* 260(1–2):149–158
17. Cooke A, Dowson D, Wright V (1978) The rheology of synovial fluid and some potential synthetic lubricants for degenerate synovial joints. *Eng Med* 7(2):66–72
18. Fan J, Myant C, Underwood R, Cann P, Hart A (2011) Inlet protein aggregation: a new mechanism for lubricating film formation with model synovial fluids. *Proc Inst Mech Eng [H]: J Eng Med* 225(7):696–709
19. Kitano T, Ateshian GA, Mow VC, Kadoya Y, Yamano Y (2001) Constituents and pH changes in protein rich hyaluronan solution affect the biotribological properties of artificial articular joints. *J Biomech* 34(8):1031–1037
20. Anil M et al (2010) Tribological performance of hydrophilic diamond-like carbon coatings on Ti–6Al–4V in biological environment. *Diam Relat Mater* 19(4):300–304
21. Vrbka M, Křupka I, Hartl M, Návrát T, Gallo J, Galandáková A (2014) In situ measurements of thin films in bovine serum lubricated contacts using optical interferometry. *Proc Inst Mech Eng [H]: J Eng Med* 228(2):149–158

22. McKellop H, Clarke I, Markolf K, Amstutz H (1981) Friction and wear properties of polymer, metal, and ceramic prosthetic joint materials evaluated on a multichannel screening device. *J Biomed Mater Res, Part A* 15(5):619–653
23. Williams P III, Powell G, LaBerge M (1993) Sliding friction analysis of phosphatidylcholine as a boundary lubricant for articular cartilage. *Proc Inst Mech Eng [H]: J Eng Med* 207(1):59–66
24. Chan S, Neu C, Komvopoulos K, Reddi A (2011) The role of lubricant entrapment at biological interfaces: reduction of friction and adhesion in articular cartilage. *J Biomech* 44(11):2015–2020
25. Roba M, Bruhin C, Ebnetter U, Ehrbar R, Crockett R, Spencer ND (2010) Latex on glass: an appropriate model for cartilage-lubrication studies? *Tribol Lett* 38(3):267–273
26. Schmidt T, Sah R (2007) Effect of synovial fluid on boundary lubrication of articular cartilage. *Osteoarthritis Cartilage* 15(1):35–47
27. Wei L, Xiong H, Li B, Cheng Y, Long X (2010) Boundary-lubricating ability and lubricin in synovial fluid of patients with temporomandibular joint disorders. *J Oral Maxillofac Surg* 68(10):2478–2483

Design and Implementation of Obfuscating Tool for Software Code Protection



Akshay Kumar and Seema Sharma

Abstract Code obfuscation is a technique to protect the raw source code by making different transformations like changing layout and control flow of the code. This is primarily done by the developers/programmers to obstruct code, understanding, and delay malicious code change such that reversing of coding becomes uneconomical by the man at the end (i.e., end user). This technique is adopted in such a fashion that it does not affect the functionalities of the program. The aim of the paper is to make an obfuscator tool, which will provide a graphical utility to the programmers to obfuscate their code. This tool can be used for protecting many high-level languages like Python, JavaScript, Java, and C and C++. It will use cryptographic algorithm to hide the program logic by encrypting and renaming identifier. This paper also aims at introducing a new cryptographic algorithm, which encrypts text to unicode by applying base64 and Devanagari encoding.

Keywords Obfuscator · Devanagari · Base64 · Unicode · Layout transformation

1 Introduction

IT ventures burning billions of dollars every year for keeping from security assaults, for example, altering and vindictive reverse engineering. On account of tremendous application and advancement on web innovations and sight and sound, the immense need to look into on security and insurance has been framed [1]. Each association is having its own licensed innovation and it's a major test for them to ensure their information, i.e., programming theft or infusion of vindictive code and so on. And furthermore, their information handling through the application is private, so its revealing may harm the product buyer's business straightforwardly. There are two general ways to protect the intellectual property, legitimately or technically. Lawfully

A. Kumar (✉) · S. Sharma
Amity School of Engineering and Technology, Amity University, Noida, India
e-mail: akshay7924@gmail.com

S. Sharma
e-mail: ssharma26@amity.edu

© Springer Nature Singapore Pte Ltd. 2019
M. Kumar et al. (eds.), *Advances in Interdisciplinary Engineering*, Lecture Notes in Mechanical Engineering, https://doi.org/10.1007/978-981-13-6577-5_64

implies getting copyrights or marking legitimate contracts against making copies and so forth [1, 2]. What's more, actually implies the proprietors of the product will give the answer for security with that specific programming. Beforehand, securing information implies the utilization of firewalls and portals in the working framework itself or on the system. In any case, for protecting from outcasts, the better thought is to utilize these instruments or techniques inside the application programming. One of those sorts of strategies is obfuscation, which is a novel range of research in the field of programming assurance and increasing more significance in this present computerized period. A code obfuscator is an automated tool used for obfuscating the source code in order to protect it from tampering and hiding its logic so that it cannot be used for malicious activities, which may result in reverse engineering of the complete software [1, 2].

Encryption and firewalls can be utilized again to secure the code a typical answer for limit the risk of programmer who tries to break the application programming for evil purposes. Be that as it may, these techniques don't help in securing when the aggressor is him/herself the end client. Therefore, code obfuscation comes up as the well-known method to shield the code from every single conceivable danger [1, 3].

2 Software Protection Techniques

2.1 Client–Server Model

Client–Server model is one of the possible ways to protect reverse engineering by storing the core logic of the program in the server side and client can only communicate using an application interface with a limited set of services. Using this model, programs logic is protected from being tampered from the client machine. Unfortunately, this causes poor performance because of the limitation on client–server bandwidth and latency.

2.2 Code Encryption

Encryption code is another way to protect code but unless the encryption/decryption is done by specialized hardware in the client machine, there is a possibility of tampering the code by the user. Unfortunately, the use of specialized hardware will limit the portability of the program.

2.3 Object Code Transformation

Programs can be transmitted in a way that makes them less vulnerable to decompilation seems like a good idea. The object code the program can be released instead of its native bytecode, which makes the reverse engineering even more complex and thus reduces the possibilities of tampering code. However, the only problem here is that different version of programs are needed for different system architecture, hence the software maintenance becomes difficult for the developers.

2.4 Code Obfuscation

Code obfuscation process involves the transformation of the code that make a program more difficult to understand by modifying its structure, though the original functionalities of the code are still preserved in the same manner as the original source code but not suitable for reverse engineering.

3 Code Obfuscation Techniques

Generally, software code is portable and distributed through networks & channels which cannot be trusted. Their protection must be done independent of the hardware and architecture of the system. Code obfuscation is a technique which ensures software code security independent of the device hardware. However, there are very few researchers focused in this technique. It is a new area of research and development in the field of software protection. There are few tools popular among developers, which includes ProGuard (for Android apps), Javaguard, DashO, and Jode. A summary of techniques and methods used for obfuscating code are discussed here.

3.1 Structured Obfuscation

The information and parts of code which are not of much importance for the program execution such as identifiers names and comments are modified in less meaningful ones. This is a common technique of obfuscation applied for many other languages. The C shroud system is an application which uses this technique for C programming language [4, 5].

3.2 Data Obfuscation

These methods alter the data structures used by a program [4, 5].

Data Storage Obfuscation affects how the program data is to be stored in the memory. For example, a local variable used in a function can be converted into global.

Data Encoding Obfuscation affects the interpretation of the stored data. For example, a variable x can be replaced with $5 * x/5$ such the effective value remains same. We can see the effect below:

Data aggregation Obfuscation changes the grouping of the stored data. For example, a 2D array can be converted into 1D array or vice versa.

Data ordering Obfuscation alters the order of how the stored data is accessed. For example, an array function (i) can be formed to determine the value of the array at index i.

Before	After
AR[2][2]={{1,2},{	AR[]={1,2,3,4}
3,4}};	;
AR[0][0]=10;	AR[0]=10;
AR[1][1]=20;	AR[4]=20;

3.3 Control Obfuscation

The main idea here is to camouflage the actual control flow of the code in a program [4, 5].

Control aggregation obfuscation changes the approach in which the statements of the program are grouped together. For example, making methods inline in a program. That is, replacing a method call with the definition from the called method itself.

Control ordering obfuscation follows the approach to change the order of the execution of statements in a program. For example, a loop can be made to iterate backward instead of incrementing forward.

Control computation obfuscation affects the control flow in a program. These can be divided up further:

- ‘Smoke and mirrors’ obfuscation uses an approach to hide the real control flow of the program behind unnecessary chunks of code. For example, code that will never execute can be appended (dead code).
- High-level language breaking obfuscation uses the approach to alter the program at the object code level that has no direct source code equivalent. For example, using go-to instruction in Java bytecode to jump out from the middle of while loop, thus control flow of the program will be difficult to reduce.
- Control-flow abstraction is essentially the inverse of the task that a compiler performs. An example of altering control-flow abstraction would be to find a sequence

of low-level instructions that are equivalent to a `wh` and then add redundant termination conditions to the loop. The loops both terminate when `i` equals 1000. `i` is not divisible by 1000 for all values that `i` takes on in the loop, namely for $1 \leq i < 1000$.

Before

```
i = 1; while (i < 1000) { ... i++; }
```

After

```
i = 1; while ((i < 1000) || (i % 1000 == 0)) { ... i++; }
```

Preventative Transformations These attempt to stop decompilers from operating, by exploiting their weaknesses. *HoseMocha* [11] is a utility which appends extra instructions after a return instruction. The execution of the program is unaffected but the obfuscation causes the Java decompiler *Mocha* [17] to crash.

4 Related Work

Mariano Ceccato et al. experimentally assesses the impact of code obfuscation on the capability of human subjects to understand and change source code. In particular, it considers code protected with two well-known code obfuscation techniques, i.e., identifier renaming and opaque predicates. *Method:* We have conducted a family of five controlled experiments, involving undergraduate and graduate students from four universities. During the experiments, subjects had to perform comprehension or attack tasks on decompiled clients of two Java network-based applications, either obfuscated using one of the two techniques, or not [6].

Levent Ertaul et al. has discussed software protection techniques in general and provide a broad overview of known obfuscation algorithms. They also addressed the issues related to implementation of obfuscation algorithms. Finally, they have proposed *JHide*, an obfuscation tool kit for protection of Java code [1].

Douglas Low describes the obfuscation techniques which can be used for software code protection. Obfuscation transformations can be classified into three main classes layout obfuscations, control-flow obfuscations, and data obfuscations [6, 3, 7].

Aman Kishore Aggarwal describes ancient *Katyapadi* encryption algorithm using Sanskrit script. Their algorithm encrypts the text, which later can be used for data transmission over the network without the threat of loss or theft [2].

Schulz, Patrick describes the methodologies for obfuscating and de-obfuscating android applications. It also throws light on the tools available to protect Android apps, which includes *ProGuard* and *Allatori* [8, 9].

5 Methodology

Previous studies throw light on algorithms which can only be used for obfuscating a particular type of a programming language. There's no such implementation which can be used to obfuscate multiple types of languages by using a single algorithm. This paper focuses on implementing such a tool in java programming language by using regular expressions that provides the functionality to obfuscate many languages like python, Java, C++14, go and Javascript. Today, most of the HLLs supports unicode which broadens the amount characters that can be used in a program thus we propose a new text-encrypting algorithm which maps the text to Unicode by applying Devanagari and base64 mapping. The primary algorithm used in this tool is shown in Fig. 1.

This algorithm takes the raw code as input and passes it to the parser which fetches all the variables from the raw code. The next step involves converting the variables into their base64 representation following with conversion into Devanagari string using Devanagari hash map. After getting the Devanagari representation of the string, the text is then converted into unicode which then is finally replaced in the original code.

The Devanagari mapping to English is made according to the phonetic sound of the words like 'a' is mapped to 'अ' and 'b' to 'ब'. The mapping of all the alphabets and numeric characters are shown in Figs. 2, 3, and 4.

```

start:
variables
raw_code,parsed_vars,base_64,encrypted_text
parsed_vars:= parser(raw_code)

foreach var in parsed_vars:
  base_64.next:=Base_64(var)
foreach b64 in base_64:
  encrypted_text.next:=toDevnagari(b64)
  var etext:= encrypted_text.at
  encrypted_text.at:=toUnicode(etext)
foreach e_text in encrypted_text:
  raw_code.replaceAll(e_text)
end

```

Fig. 1 Algorithm for generating obfuscated code

English	Hindi	Hexadecimal
a	अ	0905
b	ब	0902C
c	स	0938
d	ड	0921
e	ई	0908
f	फ	092B
g	झ	091D
h	च	091A
i	ऐ	0910
j	ज	091C
k	क	0915
l	ल	0932
m	म	092E
n	न	0928
o	ओ	0912
p	प	092A
q	क	0941
r	र	0930
s	श	0936
t	ट	091F
u	उ	0909
v	व	0935
w	भ	092D
x	ष	0937
y	य	092F
z	ऋ	090B

Fig. 2 Devanagari mapping lower case

Matra Code: 0945
 For Upper Case (A-Z): LowerDevCode + Matra Code ex. अँ
 For Symbol underscore (_): 0952

Fig. 3 Devanagari mapping upper case

NUMERIC	HINDI	HEX
00	०	0966
01	१	0967
02	२	0968
03	३	0969
04	४	096A
05	५	096B
06	६	096C
07	७	096D
08	८	096E
09	९	096F

Fig. 4 Devanagari mapping numeric characters

6 Results

We tested this graphical tool shown in Fig. 5 by providing Javascript and Python hll as input code and in result it generated the obfuscated code by using layout transformation. Layout transformation involves encrypting the variables defined in the program so that it becomes difficult to read and understand the flow of the code. The algorithm shown in Fig. 1 fetches all the variables used in the raw code by equating each line of code with the regular expression which test (shown in Figs. 6, 7, 8, and 9) whether it satisfies the regex or not, for example, in Figs. 8 and 9, line array = [2, 3, 4, 10, 40] is tested against the regex '(*) (=) (*)' and separates the variable name 'array' which then obfuscated by using Devanagari unicode mapping to

```
'\u092F\u0945\u0937\u0945\u091C\u0945\u092F
  \u092F\u0945\u0937\u0945\u0915'.
```

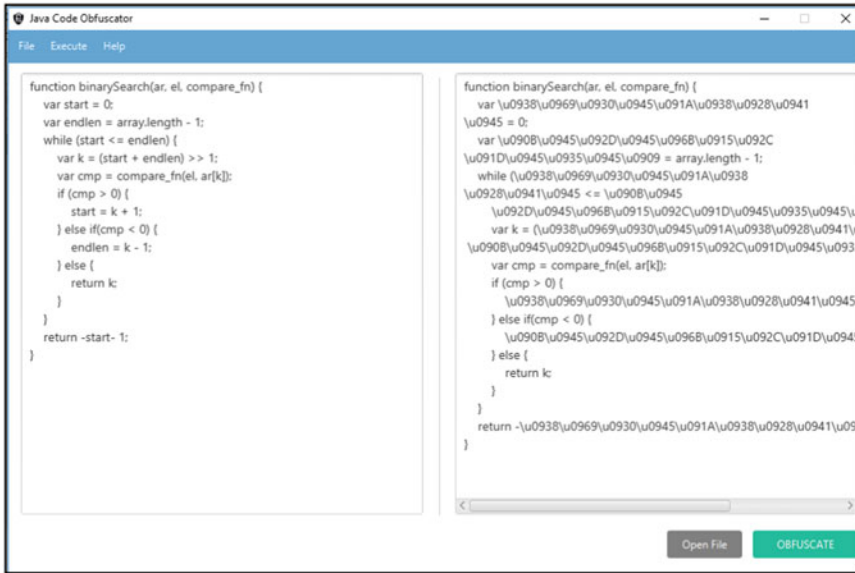


Fig. 5 Obfuscator graphical interface

Fig. 6 Js original code

```
function binarySearch(ar, el, compare_fn) {
  var start = 0;
  var end = array.length - 1;
  while (start <= end) {
    var k = (start + end) >> 1;
    var cmp = compare_fn(el, ar[k]);
    if (cmp > 0) {
      start = k + 1;
    } else if(cmp < 0) {
      end = k - 1;
    } else {
      return k;
    }
  }
  return -start- 1;
}
```

```

function binarySearch(ar, el, compare_fn) {
  var \u0938\u0969\u0930\u0945\u091A\u0938\u0928\u0941\u0945 =
  var end = array.length - 1;
  while (
\u0938\u0969\u0930\u0945\u091A\u0938\u0928\u0941\u0945
  <= end) {
    var k = (
\u0938\u0969\u0930\u0945\u091A\u0938\u0928\u0941\u0945
+ end) >> 1;
    var cmp = compare_fn(el, ar[k]);
    if (cmp > 0) {
\u0938\u0969\u0930\u0945\u091A\u0938\u0928\u0941\u0945 = k + 1
    } else if(cmp < 0) {
      end = k - 1;
    } else {
      return k;
    }
  }
  return
-\u0938\u0969\u0930\u0945\u091A\u0938\u0928\u0941\u0945- 1;
}

```

Fig. 7 Js obfuscated code

Fig. 8 Python original code

```

def binarySearch(arr, l, r, x):
  while l <= r:
    mid = l + (r - l)/2;
    if arr[mid] == x:
      return mid
    elif arr[mid] < x:
      l = mid + 1
    else:
      r = mid - 1
  array = [ 2, 3, 4, 10, 40 ]
  x = 10
  reslt = binarySearch(arr, 0, len(arr)-1, x)

```



```

def binarySearch(arr, l, r, x):
    while l <= r:
        mid = l + (r - l)/2:
        if arr[mid] == x:
            return mid
        elif arr[mid] < x:
            l = mid + 1
        else:
            r = mid - 1
arr = [ 2, 3, 4, 10, 40 ]
x = 10
binarySearch(arr, 0, len(arr)-1, x)

```

Fig. 9 Python obfuscated code

7 Conclusion

Obfuscating code does not guarantee to prevent the application code for reverse engineering. However, it makes the task difficult to decode the source code by the malicious user and it is the economical way to protect the code from tampering. The algorithm proposed in this paper increases the usability of this tool for wide range of languages and has been proved successful in obfuscating most of the high-level programming languages by using layout transformation technique and applying Devanagari unicode mapping.

References

1. Ertaul L, Venkatesh S (2004) JHide-A tool kit for code obfuscation. IASTED conference on Software Engineering and Applications
2. Agarwal AK, Srivastava DK (2014) Ancient Kalapayidi system sanskrit encryption technique unified. In: IEEE international conference on signal propagation and computer technology (ICSPCT)
3. Low Douglas (1998) Protecting Java code via code obfuscation. Crossroads 4(3):21–23
4. Granger MJ, Smith CE, Hoffman MI (2003) Use of code obfuscation to inhibit generation of non-use-restricted versions of copy protected software applications. U.S. Patent No. 6643775. 4 Nov 2003
5. Popa Marius (2011) Techniques of program code obfuscation for secure software. J Mob Embed Distrib Syst 3(4):205–219

6. Ceccato M et al (2014) A family of experiments to assess the effectiveness and efficiency of source code obfuscation techniques. *Empirical Softw Eng* 19(4):1040–1074
7. Wroblewski G (2002) General method of program code obfuscation (draft). Citeseer
8. Schulz P (2012) Code protection in android, vol 110. Insititute of Computer Science, Rheinische Friedrich-Wilhelms-Universitgt Bonn, Germany
9. Linn C, Debray S (2003) “Obfuscation of executable code to improve resistance to static disassembly. Proceedings of the 10th ACM conference on computer and communications security. ACM

A Critical Review on Calibration of Robots



Tanvi Verma and Nathi Ram Chauhan

Abstract This paper presents a state-of-the-art review of the literature on the calibration of robots. The existing studies related to this field are critically analysed and examined to ascertain the trends in the field and to possibly identify one of the best techniques of doing the calibration of robots. Since robots are similar to the mechanical system, which can be influenced by changes caused by wear, manufacturing error, backlash error, assembly of parts. As calibration plays a very important role in increasing robot positioning accuracy, repeatability and resolution. Hence, this study provides an overview on the techniques for calibration of robots, types of calibration approaches, impact on different kinds of accuracy and importance of calibration in operating the robots. So, traditional and nontraditional approaches are confined here to calibrate serial and parallel robots. The cost-effective way of choosing technique is determined to provide absolute accuracy of the robot. Calibration of parallel robots is quite complicated as compared to serial robots. So, there is always a need to determine the best method of calibration which is less costly and reasonable.

Keywords Robot calibration · Accuracy · Off-line programming calibration · Online programming calibration

1 Introduction

The foremost automation barrier in machine intelligence is the subtraction of miscalculation between end-effectors coordinate system and workpiece coordinate system. So, it is important to improve the accuracy of robots through calibration. Many researchers described robot adjustment as an assimilation formation of modelling, computation, numeral recognition of authentic substantial characteristics of robot and utilization of model. In other words, many researchers defined robot calibration

T. Verma (✉)

M.Tech (Robotics and Automation), IGDTUW, New Delhi, India
e-mail: vtanvi13@gmail.com

N. R. Chauhan

Department of Mechanical and Automation Engineering, IGDTUW, New Delhi, India

© Springer Nature Singapore Pte Ltd. 2019

M. Kumar et al. (eds.), *Advances in Interdisciplinary Engineering*, Lecture Notes in Mechanical Engineering, https://doi.org/10.1007/978-981-13-6577-5_65

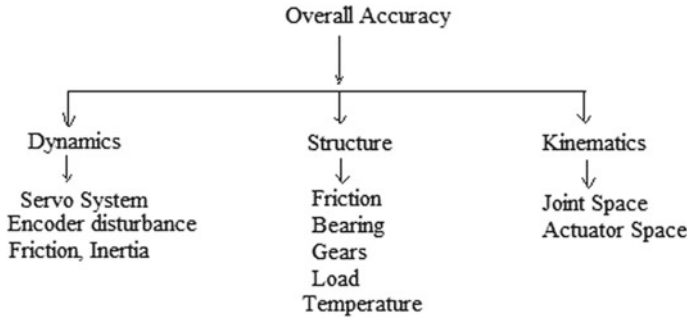


Fig. 1 Classification of error that affects the accuracy of robot

as the mechanism of enhancing the robot accuracy by transmuting its regulation software. They have worked on the calibration of robot. However, calibration of robots is the most cost-effective way of improving the absolute accuracy of robot either improving joint space accuracy or task space accuracy. Different methods and techniques are used to calibrate serial and parallel robots.

The need of calibration has been increased manifold to improve the accuracy up to 0.001 mm. Since the main sources of error are modelling difference between controller and robot, error between workpiece frame and tool frame, inaccurate fixturing and manufacturing process. Researchers improve the manufacturing error that is accounted for the maximum contribution of error while calibration.

Many researchers explained the causes of generation of error, impact on the important parameters of robots and categorization of calibration. Researchers find out the dependency of the overall accuracy of robot on various aspects of robot, which is described in Fig. 1. So, enhancing the accuracy of robot, there is a need to understand the reason behind the error and cause of error. Researchers described the error tree to understand the diversity of errors generating aspect [1].

Some important parameters that have been affected by the robotics calibration are accuracy (absolute and dynamic), repeatability and resolution [2]. In simple words, researchers described the resoluteness as the inconsequential cumulative move that this robot can materialistic yield. Recapitulation is defined as the allotment of competence of robot to rotate back to the same ground and familiarization. Definite is explained as the ability of the bionic to precisely move to the desired position in 3D plane [2]. Accuracy is further classified into two ways. One is absolute accuracy which describes the ability of a bionic person to turn to a desiderate position without any modification. Another one is effectual closeness which describes the ability of bionic to precede an adorable orbit with short or no divergent. Since full the parameters including kinematic and dynamic parameters are improved magnificently if we choose the right method of calibration.

2 Robot Calibration Procedure

The procedure of calibrating a robot is divided into main four steps, namely kinematic modelling, measurement, parameter identification and compensation. Many scientists and researchers described kinematic modelling as the explanation of calculus and kinetics of robot. A numeral of various propositions prevails for promoting the mechanic's illustration of a bionic person. This model can be done through inverse kinematics and direct kinematics. Researchers used different techniques like D-H representation, graphical analysis and vector analysis.

Measurement is the second step of this calibration procedure. It is very important in the calibration process, since it needs a collection of data that will be used for identification of parameters errors. It requires sensitivity analysis based on different roles of kinematic parameters. Choosing of the measurement tool is very complex since it should be more precise than the robots' expected accuracy. It needs knowledge of workspace volume considering the locations of confine follow-up or/mechanism of the bionic person. The calibration course should show the personalized framework of the miniature/robotic system in different ways and the evaluation entity should be accurate to payback the influences of those specifications. Many new analysis mechanism and quantum instruments are already used for bionic precision. It involves the use of auditory detectors; see able detectors; coordinate measure machines (CMM), etc. Parameter identification is the most important step of the calibration procedure. It requires numerical analysis to find the cause of the error. Here, kinematic parameters are diagnosed by diminishing the group workstation. Some techniques like meanest square method and Jacobian method are used to find the change in parameters.

Compensation is the final step of this calibration procedure. Researchers described compensation as the performance of the modern dummy with changed parameters in the locality control software [3]. It is also termed as correction step. Because of the trouble in improving the classical mechanism specification in the golem administrator correctly, intersection corrections mostly needed for the encoder readings acquired by the antithetical mechanics of corrected golem [4].

3 Classification of Robot Calibration

The calibration of robot is classified in terms of static, dynamic and off-line and online calibration.

3.1 *Static Calibration and Dynamic Calibration*

Researchers described static calibration as the recognition of those specifications which impact mainly constant attributes of golem, i.e. surroundings and situation of

after-effect or/tool. It focuses on the amendment of algorithmic and kinematic benchmark such as intersection axes and junction effects. Non-geometrical specification involves joint and interconnection flexibility, cog inappropriately and tolerances, etc. Both kinds of parameters are used for static calibration.

However, dynamic calibration involves identification of specification impacting primary moving symptomatic, i.e. speed and effects. This needs significance specifically in enormous robots subjected to big momentum and acceleration. It requires large hectic experimental procedure to investigate the reasons behind the change in dynamic parameters of robot.

3.2 Off-Line Programming and online Programming

Researchers described another way of defining calibration as off-line and online programming calibration. Off-line calibration is defined as the mechanism of developing a robot schedule unaccompanied utilizing the actual robot and recommend many leads over the online programming mechanism.

In off-line programming, there is still lack of achieving accuracy of that much extent. Hence, there is a need of introducing a method to ameliorate robot precision by software as a substitute by modifying machine-like formation or blueprint of the robot/golem. This new method is termed as online programming method for calibration. The advantages of this calibration technique is to reduce the threat of having the interchange in requisition strategy due to very less change in kinematic parameters, i.e. wearing of parts, tolerances, offsets during assembling of many parts [5] (Fig. 2).

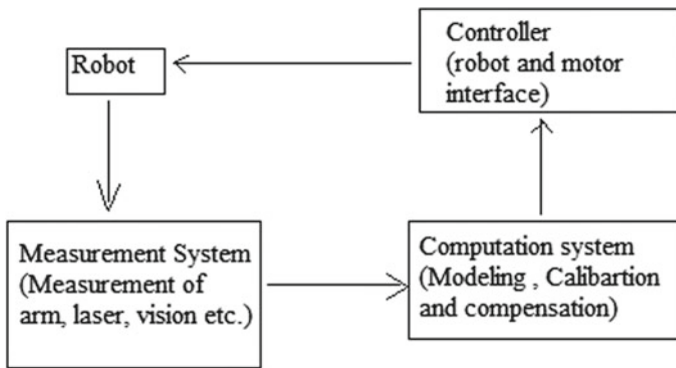


Fig. 2 Procedure of robot calibration

4 Different Approaches of Robot Calibration

Various approaches are used to calibrate the robots.

4.1 *Off-Line Programming Calibration*

1. **Common calibration technique:**

In this technique, localizing the robot to its home/ground position is the most common robot calibration technique. This technique is classified into three categories—relative, optimal and levelling-based method. Researchers described a position called home position of robot, which is termed to be a situation where all its intersections have a predefined efficacy which can change into Cartesian space as per robot kinematics.

In relative calibration, locating each robot link in a predefined location correlative to the preceding link in the kinematic formation. It needs hugely precise robot fragments and it is an exorbitant for large workspace robot. It gives an accuracy of 0.2 mm in Cartesian space.

In optimal calibration, it needs a computation formation to measure a set of robot cause with the help of mathematical and kinematic model to determine and improves kinematic parameters of robot. The repercussion home location is sensitized to the chosen adjusted postulate and geometric parametric values, leading problems in maintaining a quotable calibration.

In Levelling established calibration, it utilizes inclinometers to locus each association parallel and right angles to the profundity vector and provide effortless, faultless and quotable calibration of the robot home topography. It is a expensive process but gives an accuracy of about 100 microns [5].

2. **Calibration through Teach Pendant:**

Generally, measurements related to the end effector of robot by 3D measuring devices is being compared with teach pendant positions of robot. It is the easiest method of off-line programming calibration. It lacks in improving accuracy to that extent which is required to robots, applying in precision work. It improves accuracy up to 2 mm [1].

3. **Calibration by updating the robot:**

In this method, updating the robot imitation in the software to meet the framework recorded from calibre the golem. It is actually a way of second stage calibration. It improves the accuracy by 1 mm. It can be used for multi-work cells without recalibration.

4. **Contact and Non-contact probing method:**

Robot calibration is done with the help of contact and non-contact probing method. Non-contact probe involves devices like proximity sensors, beam breakers, high-resolution camera and visual servicing.

Contact probe method used for calibration includes the use of manikin fragment, complaisant instrument and exactness stylus.

However, non-contact probing method provides better accuracy, and these devices are more expensive as compared to calibration and the moment demand for set up and integrating with golem controller is more as compared to contact probe method.

5. **Metrology:**

It is especially much alike to adjustment. It requires that a genuine computation is taken to estimate golem presentation. Here, different calibration approaches are listed below which is already mentioned in an ISO scientific record. They are like set of circumstances list quest method, path differentiation method, surveying method, polar correlative measuring method, triangulation method, discernible tracking method, inaction quantum method, analytical interrelate quantifying method [6] and route representation method [7]

4.2 *Online Programming Method*

1. **Closed Loop calibration method:**

In this method, we need to first evaluate the frontier of approximation within workspace of end effector/tool considering quantification fallacy due to improper aspiration, non-lastingness and commotion of sensors, mathematical method handed down and sensitiveness of end plate emplacement. Collection of the specification to be calculated is a concern. But it would be archetypal to assume all kinematic specifications first, the element of safety and device effects. Least square method and convergence method are used.

2. **3D Robotics hand/eye calibration:**

Researchers described this method as a new proficiency for enumerating 3D locus and emplacement of a camera correlative to the rearmost conjoint of the golem in an eye/palm calibration. It is an easier and faster method than any other techniques. Camera is enduringly full of admiration to the grapple. To do automated measurement with robot vision, sensing planning is significant to determine optimum position. Global non-linear optimization is done over the robot kinematic model parameters [8].

5 Conclusion

This study was initiated to explain the different techniques and review the situation of art in automated progressive method. It was concluded that off-line programming is quite expensive as compared to online calibration. The accuracy of off-line programming calibration is less achieved due to increased tendency of errors. Hence, this is the high time to develop online programming method such that roboticists can attain maximum accuracy without disturbing the mechanical design of robot.

References

1. Robertson AP, Willoughby PJ, Slocu A (2002) Precision robot calibration using kinematically placed inclinometers. ABB Robotics, Vasteras, Sweden, Massachusetts Institute of Technology, Cambridge, MA
2. Robotic calibration issues: accuracy, repeatability and calibration. Proceedings of the 8th mediterranean conference on control and automation (MED 2000), Rio, Greece, July 2000, pp 17–19
3. Hsu TW, Everett LJ (1985). Identification of the kinematic parameters of a robot manipulator for positional accuracy improvement, vol 1. Proceedings of 1985, computer in engineering conference and exhibition, pp 263–267
4. Elatta AY, Gen LP, Zhi FL, Daoyuan Y, Fei L (2004) An overview of robot calibration. Inf Technol J 3:74–78. Wuhan, China
5. https://en.wikipedia.org/wiki/Robot_calibration
6. Driels MR, Swayze LW, Potter LS (1993) Full pose calibration of robot manipulator using a coordinate measuring machine. Int J Adv Manuf Technol 8:34–41
7. Kihlman H, Loser R, Cooke A (2004) Metrology—integrated industrial robots—calibration, implementation and testing. Proceedings of the 35th ISR (international symposium on robotics), pp 23–26
8. Tsai RY, Lenz RK (1986) A new technique for fully autonomous and efficient 3D robotics Hand/Eye calibration. IEEE Trans Robot Autom 5:345–358

Castor Biofuel a Renewable Energy Source in India—Status and Overview



Satyam Vatsa and Madhuranjan Vatsa

Abstract Renewable energy sources help to alleviate greenhouse gas emission and increase the rate of global warming. Energy production from renewable energy sources is increasing drastically. Due to the enhancement of pollution in the world, there is a need to give attention on the development of projects, policy framing, and operations in renewable energy technologies and their implementations. Biofuel is seen as pollution-free energy source and optimum use of these resources helps to reduce the environmental impact and to develop suitability in accordance with the current social needs of the society. Biofuel technologies provide a huge opportunity to reduce greenhouse gas emissions and reduce global warming by replacing conventional energy. Biofuel will play a significant role to create the pollution free environment throughout the globe, and it is a reagent that can be used to generate energy. Biodiesel from castor oil generates huge energy with zero emission of pollution, and by proper implementation, it can reduce the pollution like PM_{2.5}, PM₁₀, etc., which are main sources of air pollution. The paper focuses on castor oil as biofuel and its scope as fuel in Indian scenario.

1 Introduction

The rising demand of the energy and the fossil fuel prices (conventional fuel) along with the concern of the environs prompted the scientist to look after the alternative fuel. Their ignition doesn't show any increase in the carbon dioxide emissions, particulate matter (PM), carbon monoxide as well as unburnt hydrocarbon. Along with these, the emission of the sulfur is also very less and has an excellent quality of the lubricity. Biodiesel can be manufactured from both edible as well as nonedible feedstock via transesterification in the presence of alcohol and catalyst. During transesterification, methanol is commonly used due to its less cost, but the biodiesel

S. Vatsa (✉)

Mechanical Engineering Department, Gautam Buddha University, Greater Noida, India
e-mail: satymvatsa@gmail.com

M. Vatsa

Management Department, Sharda University, Greater Noida, India

© Springer Nature Singapore Pte Ltd. 2019

M. Kumar et al. (eds.), *Advances in Interdisciplinary Engineering*, Lecture Notes in Mechanical Engineering, https://doi.org/10.1007/978-981-13-6577-5_66

Table 1 Various feedstock for biodiesel production [1–10]

S. No.	Domain	Crops
1	Oil crop	Soybeans; Rapseed; Canola; Mustard; Camelina; Castor bean; Safflower; Sunflower; Jatropha; Coffee beans; Rubber; Karanja oil; Pongamia; Communis; Riccinus
2	Waste oil	Used Vegetable oil; Grease; Used castor oil
3	Animal fat	Tallow; Lard; Yellow grease; Chicken fat; Omega-3 fatty acid from fish
4	Algae	Growing on waste material, sewage, etc.
5	Oil from halophytes	Salicornia bigelovii; Penycress; Lesquerella; Hazelnuts

prepared from methanol cannot be completely termed as renewable [1–4]. So as to make it completely renewable, we need alcohols from bio-based source like ethanol. There are four types of feedstocks—vegetable oil, animal fats, algae, and different low-quality oil (waste cooking oil, etc.). Biodiesel produced at industrial scale—soybean oil, canola oil, etc. The use of food crops for the production of biofuels will adversely affect the cost of food. The large scale commercialization is the major hurdle for the production of biodiesel because of its high cost. From a study, it has been analyzed that 90% of the production cost of biodiesel can be altered by the feedstock cost. Nonedible oils such as—Jatropha, Castor, Pongamia pinnata, Rubber oil, etc., are available as nonfood-based feedstock. The various feedstocks are tabulated in Table 1. Castor is an important nonedible oil crop that can tolerate various weather conditions.

2 Literature Review

The literature reveals that various researchers have worked on different biofuels production technique using castor oil. Some of the observations are as follows: Gui et al. [11] reported his work on the crude castor oil at 300 °C using supercritical methanol transesterification after a reaction of 90 min at 43:1 molar ratio, the yield was recorded at around 96.5%. Along with this, no thermal decomposition of FAMES is noted. Dias et al. [10] worked with the raw castor oil and produced a statistical design estimating product yield, acid value, kinematic viscosity, and methyl ester content as a function of time and temperature. The experimental result estimated the best reaction time and temperature for the raw castor oil is 8 h and 65 °C, respectively, and a yield of about 73.62% is recorded. Mahmudul et al. [12] reported in his paper about the biofuel development, feedstock around the world, oil extraction technique biodiesel production technique, etc., and summarized the study in the following manner: Feedstock selection is the key role for the biodiesel production because it bears around two-third of the biodiesel production cost. Thalles et al. [13] mentioned

in his paper about the maximum yield obtained from a set of reaction is 94%. To achieve such a high yield, the molar ratio should be 6, reaction time of 8 h the enzyme should be around 5 wt% of enzymes, and an addition of 5 wt% of water by the weight of oil. Table 2 represents the various process parameters for biofuel production which include reaction time, molar ratio, type of alcohol, and feedstock chosen. It also shows the properties of the different biodiesel prepared under different conditions.

3 Biodiesel Production Methodology

3.1 Feedstock Used

Figure 1 shows the castor plant.

Fatty acid present in the castor oil is tabulated in Table 3.

3.2 Availability of the Feedstock in India

Gujarat, Rajasthan, and Andhra Pradesh contribute 96% of the total castor seed production in India. Figure 2 represents the production trend of castor in India.

Figure 3 represents major states producing castor plant.

Fig. 1 Shows the castor plant [13]



Table 2 Different fuel properties under different reaction conditions [1-13]

S. No.	Oil	Alcohol	Temp.	Catalyst	Time	Kinematic viscosity	Density	Flashpoint	Pour point	Cloud point	Cetane number
1	Rubber oil	Methanol	45	H ₂ So ₄	75	@40 °C,39,20	0.937	0129	-7	5	-
2	Rubber oil	Methanol	50	Na ₂ So ₄	23	-	-	-	-	-	-
3	Waste fish oil	Methanol	90	-	60	-	-	-	-	-	-
4	Date pits	Methanol	70	-	-	3.97	970 kg/m ³	0137	-01	4	59.23
5	Rubber seed oil	Ethanol	69-70	NaOH	-	4.5	953 kg/m ³	0120	-5	3	-
6	Caster oil	Methanol	47-0120	Super acidic sulphonomated modified mica catalyst	300	7.35	9019 kg/m ³	0179	-015	-6	50
7	Rubber seed oil	Methanol	-	NaOH	-	3.7-9.02	970-997	01010-0164	-2 to +4.9	-6 to +3.2	43-66.2
9	Karanja oil	-	-	-	-	4.37	976	0163	-3 to 5.01	013-015	39-52
9	Polanga	-	-	-	-	4-5.34	999-9010	01501-0170	4.3	013.2-014	57.3
10	Mohua	-	-	-	-	3.9-5.9	904-9016	0127-0129	01-6	3-5	501-52
11	Rubber seed oil	-	-	-	-	3.7-9.02	960-992	01010-0154.6	-9 to 4.9	-6 to 5	37-66.2
12	Jatropha	-	-	-	-	3.7-5.9	964-990	0163-239	5-6	010	46-55
13	Cotton seed	-	-	-	-	2.2-4.9	974-90,101	0120-243	-010 to -015	01.7	401.2-59.5
14	Jojoba oil	-	-	-	-	019.2-25.4	963-966	601-75	-6 to 6	6-016	63.5
15	Tobacoo oil	-	-	-	-	3.5-34.3	960-995	0152-0164.4	-012	-	49
16	Neem oil	-	-	-	-	5.2	960	34-0165	4	9	55.301

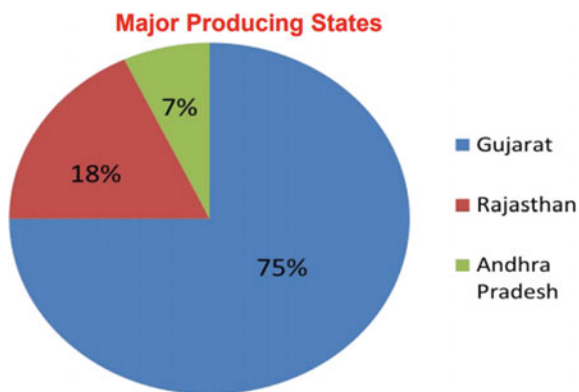
Table 3 Composition of castor oil [13]

Acid type	wt%
Ricinoleic acid	89.5
Linoleic acid	4.2
Oleic acid	3
Stearic acid	1
Palmitic acid	1
Dihydroxystearic acid	0.7
Linolenic acid	0.3
Eicosanoic acid	0.3



Fig. 2 Shows the graphical view of the production of castor in India [13]

Fig. 3 Major states producing castor [13]



3.3 *Screening of Alcohol*

There are certain alcohols that can be utilized as a part of transesterification response as reactants which include ethanol and methanol. Methanol is known as methyl liquor and its substance recipe is CH_3OH . It's regularly shortened as MeOH. Mechanical methanol is delivered in a reactant procedure specifically from carbon monoxide and carbon dioxide and hydrogen. It is the most straightforward liquor being just a methyl assembles connected to a hydroxyl gathering. It is light, unpredictable, dreary, and combustible fluids with particular request are fundamentally the same as ethanol. It is very lethal and unfit for utilization. It is utilized as a liquid catalyst, dissolvable, fuel and as a denaturant for ethanol. Methanol is delivered normally in the anaerobic digestion of numerous assortments of microorganisms and it is ordinarily present in little sum in the earth. Accordingly, air contains little measure of methanol vapor. Methanol is additionally found in bounteous amounts in star framing areas of room and is utilized as a part of stargazing as a marker for such locales.

3.4 *Catalyst*

These are required to speedup the process of reaction. They can be both acidic and basic in nature. In the transesterification reaction, they do not act as reactants because they are not consumed during the reaction. Commonly used catalysts are sodium hydroxide (NaOH), potassium hydroxide (KOH).

3.5 *Transesterification*

Evaluation of FFA: A free fatty acid is a carboxylic acid with a long aliphatic chain which is neither saturated nor unsaturated. Most naturally fatty acid consist of unbranched chain of even number of carbon item from 4 to 29. It is usually derived from the triglycerides and phospholipids. It is of two types and they are listed as follows:

Saturated: Fatty acid with carbon without double bond resaturated.

Unsaturated: Fatty acid with carbon-carbon double bond is unsaturated.

For the evaluation of FFA value in the production of biodiesel is the most important part as it will decide whether we need acid esterification or only base esterification or both. For our present work, we have opted 0.01 normality NaOH and ethanol to determine FFA value using the formula given below:

$$\text{FFA} = \frac{29.2 \times \text{volume of NaOH used}}{10}$$

Transesterification reactions are conventionally catalyzed by acids or bases. Alkaline catalysis is attractive for biodiesel production, since it is cheaper than other processes and provides high conversion of try glycerides within a relatively short reaction time. Homogeneous catalysts such as sodium hydroxide and potassium hydroxide are generally preferred. For the production of biodiesel from castor oil, first, take a suitable amount of castor oil in a beaker as per the requirement of biodiesel wanted to be produced. Then, preheat the oil till it temperature reaches up to 60 °C Maintain this temperature of the oil. Now in another flask, take 20% of methanol by weight of oil and 1.25% of KOH pallet by weight of oil in the flask. Stir the solution till the KOH pallet is completely dissolved in methanol and a solution is prepared. Now, put this mixture of methanol and KOH into the preheated oil which is maintained at 60 °C. Put this complete solution onto a well-functioning magnetic stirrer. Stirrer this solution for 1–2 h on magnetic stirrer by constantly maintaining the temperature with the help of thermometer and covered the opening of the beaker to avoid the evaporation of the methanol. During stirring, observe the formation of glycerine in the solution. After stirring, pour this solution into a separating flask. Leave this solution for 24–48 h so that the amount of glycerin and oil present in the solution can be separated. Figure 4 shows the flowchart of the whole production technique of the biodiesel. The biodiesel yield of 78% is obtained by this process.

Fig. 4 Process flowchart for the biodiesel production

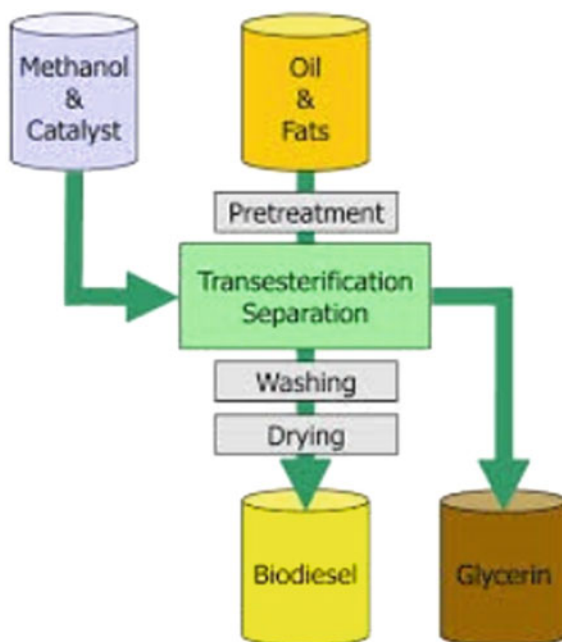


Table 4 Fuel specifications prepared from castor oil

Properties	Unit	Biodiesel from castor oil
Density (15 °C)	kg m ⁻³	950–974
Flashpoint	°C	229–260
Kinematic viscosity	mm ² s ⁻¹	240–300
Net calorific value	MJ kg ⁻¹	37.2–39.5
Flammability	–	42
Coke residues	%	0.22
Iodine number	100 g ⁻¹	82–90
Sulfur content	mg kg ⁻¹	10
Total impurities	mg kg ⁻¹	Ca. 10
Neutralization values	mg KOH g ⁻¹	1.0–4.0
Oxidation resistance	H	95
Phosphorous content	mg kg ⁻¹	<4
Total content of Mg and Ca	mg kg ⁻¹	–
Ash content	%	<0.01
Wash content	%	0.15–0.30

4 Results and Discussion

Seeds and oil yields are the most important traits which will decide castor crop as an energy fuel. Castor oil is odorless, viscous, and nondrying oil which is mild in its initial state and later become unpleasant in taste, and it appears as yellow green to yellow brown in color. The fuel-specific properties of castor oil are given in Table 4.

5 Conclusion

Castor is a nondemanding oil plant, which grows in tropical condition and provides a high yield. But requires a lot of manpower for its cultivation. It can help to improve the living conditions of small farmers as well as supply environmentally friendly energy for multiple purposes. The main problem is with the trade of the castor oil as it requires more manpower so its cost will rise up in comparison to rapeseed. The other problem with the castor oil is its extremely high viscosity and the water content. The biodiesel yield of 78% is obtained by transesterification process. To cope up with the viscosity, it requires an additive which will increase the fuel price, so castor oil is not a good option for considering as an alternate fuel.

References

1. Dwivedi G, Sharma MP (2015) Application of Box-Behnken design in optimization of biodiesel yield from Pongamia oil and its stability analysis. *Fuel* 145:256–262
2. Dwivedi G, Sharma MP (2015) Investigation and improvement in cold flow properties of Pongamia biodiesel. *Waste Biomass Valoriz* 6(1):73–79
3. Kumar P, Sharma MP, Dwivedi G (2016) Impact of ternary blends of biodiesel on diesel engine performance. *Egypt J Pet* 25(2):255–261
4. Dwivedi G, Sharma MP, Jain S (2014) Diesel engine performance and emission analysis using biodiesel from various oil sources. *J Mater Environ Sci* 4(4):434–447
5. Morshed M, Ferdous K, Maksudur RK, Mazumder MSI, Islam MI, Md TU (2011) Rubber seed oil as a potential source for biodiesel production in Bangladesh. *Fuel* 99(10):2981–2986
6. Nabel A, Negma GH, Sayed O, Habiba I, Fatma Z, Yehiaa E, Mohamed A (2017) Heterogeneous catalytic transformation of vegetable oils into biodiesel in one step reaction using super acidic sulfonated modified mica catalyst. *J Mol Liq* 237:38–45
7. Samuel E, Onoji SE, Iyuke AI, Igbafe DB, Kazi N (2016) Rubber seed oil: a potential renewable source of biodiesel for sustainable development in sub Saharan Africa. *Energy Convers Manag* 110:125–134
8. Ashraful AM, Masjuki HH, Kalam MA, Rizwanul FIM, Imtenan S, Shahir SA, Mobarak HM (2008) Production and comparison of fuel properties, engine performance, and emission characteristics of biodiesel from various non edible vegetable oil: review. *Energy Convers Manag* 80:202–228
9. Azad MG, Rasul MM, Khan K, Sharma SC, Mofijur MM, Bhuiya K (2016) Prospects, feedstocks and challenges of biodiesel production from beauty leaf oil and castor oil: a nonedible oil sources in Australia. *Renew Sustain Energy Rev* 61:302–318
10. Dias JM, Araujo JF, Costa MCM, Alvim F, Almeida MF (2013) Biodiesel production from raw castor oil. *Energy* 53:58–66
11. Gui MM, Lee KT, Bhatia S (2008) Feasibility of edible oils vs non edible oils vs waste edible oil as biofuel feedstock. *Energy* 33:1646–1653
12. Mahmudul HM, Hagos FY, Mamat R, Abdul AA, Ishak WFW, Alenezi R (2017) Production, characterization and performance of biodiesel as an alternative fuels in diesel engines—a review. *Renew Sustain Energy Rev* 72:497–509
13. Thalles AA, Massimiliano E, Knud VC (2017) Influence of the reaction conditions on the enzyme catalyzed Transesterification of castor oil: a possible step in Biodiesel production. *Bioresour Technol* 243:366–374

Renewable Energy-Based Hybrid System



Yaduvir Singh and Nitai Pal

Abstract There is energy scarcity in rural India. Energy generation and transmission is very challenging area in today's scenario energy supply in isolated rural areas by using small-scale power generation is found to be inexpensive and convenient alternative of grid utility. Under the present work, a systematic method has been established to develop a stand-alone renewable energy-based hybrid system for rural areas. In the stand-alone mode, energy supply to rural households can be achieved by single renewable energy technology or combinations of different available energy sources. Further, various criteria and parameters used for designing a hybrid energy system are discussed in detail. Different criteria include economic, technical, power reliability, social aspects, and environmental aspects related to the hybrid system. Various challenges that deviate the development of the system are also discussed in the paper.

Keywords Energy · Hybrid · Grid · Solar · Turbine · Solar · Renewable · India

1 Introduction

In the current perspective of energy scenario, renewable energy is the key substitute of conventional sources to meet out the demand of energy consumption sectors. Single renewable energy technology-based systems are suitable for villages having low energy need. Once energy requirement increases, single technology-based scheme is unable to fulfill the demand with high-power reliability due to site-specific and stochastic nature of renewable resources. However, aggregated utilization of such resources facilitates to meet the demand economically and reliably compared to single technology-based systems. Also, the hybrid system reduces the intermittency of renewable resources (solar radiation, wind speed, etc. [1–9]).

Y. Singh (✉) · N. Pal

Department of Electrical Engineering, Indian Institute of Technology (Indian School of Mines),
Dhanbad 826004, Jharkhand, India
e-mail: yaduvirrohilla@gmail.com

© Springer Nature Singapore Pte Ltd. 2019

M. Kumar et al. (eds.), *Advances in Interdisciplinary Engineering*, Lecture Notes in Mechanical Engineering, https://doi.org/10.1007/978-981-13-6577-5_67

695

The size optimization of different renewable energy combinations such as hybrid wind turbine/photovoltaic/fuel cell, and wind turbine/fuel cell. The number of storage tanks, swept area of wind turbine, and PV panels are considered as unknown solution vectors. They minimized the life-cycle cost (LCC) by filling the maximum allowable loss of power supply probability. They minimized the annual capital cost of a hybrid wind/SPV/battery system. They optimized the cost under the constraints of operative reserve of 10% of the load, 25% of PV output, and 50% of wind turbine output. They also observed that battery bank storage compensated the fluctuations of renewable energy sources [10].

Seven different scenarios of the hybrid energy system are used for an isolated community in Canada. They also performed a sensitivity analysis to assess the impact of various parameters on the system's design. Parameters such as wind speed, diesel price, solar radiation, CO₂ penalty cost, and project interest rate were considered. The size optimization of three schemes, viz., wind battery, photovoltaic battery, and wind-photovoltaic-battery system. They minimized the total system cost while accounting the seasonal variation of load and wind turbine force outage rate. They optimized total annual cost under the constraints of upper bound, lower bound, and battery bank storage limits. Three different resource combinations (SPV/Battery, WT/Battery, and SPV/WT/Battery) were considered, out of which, wind turbine/battery system was found as the most economical choice for the considered area.

The organization of the present paper is described as follows: Sect. 2 describes the methodology; Sect. 3 provides the various technology choices for energy access in rural areas while Sect. 4 presents the evaluation criterions of the hybrid energy system.

2 Methodology

To design a hybrid system for rural area, methodology is an important part which includes demand estimation, resource availability, constraints, modeling, and optimization. The important steps of methodology are summarized in the following steps.

2.1 Selection of Study Area

A study area may be selected based on the energy planning at the user end. Further, general information of the area is required to collect that include latitude, longitude, area code, mean sea level, rural households, population, etc.

2.2 Load Demand Estimation

Further, load demand of the study area is calculated based on the number of end users, rating of appliances, consumption sectors, etc. Peak demand and average demand of the considered area are estimated based on the hourly consumption of different appliances. Also, daily, monthly, and annual energy requirements are also calculated.

2.3 Resource Estimation

A field survey is necessary for the power potential estimation of different locally available resources (solar, wind, biomass, biogas, small hydro, etc.). It provides the details of several design parameters of the system.

2.4 Selection of Technology Option and Integration Configuration

As per the load demand and availability of resource, one option has been chosen, out of the two possible choices, i.e., single renewable energy technology-based scheme or hybrid system. Further, different system components may be interconnected through AC or DC buses.

2.5 System Modeling

System modeling is carried out as it gives the necessary details about the behavior of components under different conditions.

2.6 Size Optimization

Finally, the developed model of hybrid system has been simulated in HOMER software to find the optimal model of the considered system.

A flowchart for methodology of the present study has been prepared covering all the steps involved and presented in Fig. 1.

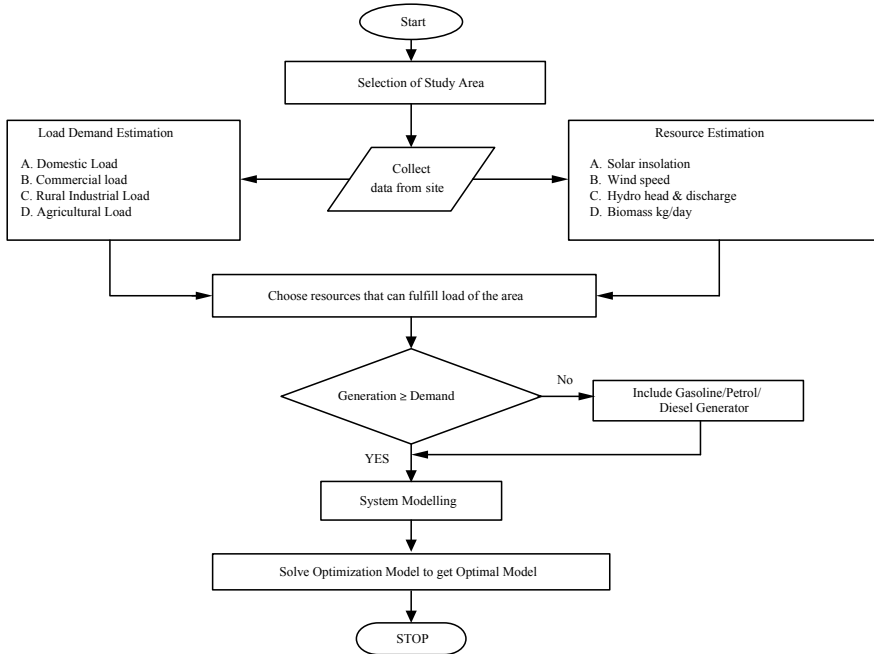


Fig. 1 Flowchart for methodology adopted

3 Technology Options

Most of the rural areas are remotely located where grid extension is not economical. However, such areas are rich in natural resources such as biomass, biogas solar radiation, etc. These resources can be utilized in off-grid mode to meet the energy requirement of villages. Energy supply improves the quality of life of the rural people by providing electricity for shops, agriculture, community centers, health centers, rural industries, public places, lighting of homes, etc.

However, renewable energy-based systems have several limitations, i.e., availability is highly time-dependent, and location-dependent and requires storage that makes the system difficult and uneconomical. Hence, depending upon the resources availability and energy demand of rural areas, rural electrification in stand-alone mode can be attained either by single renewable energy technology and group of different renewable energy technologies as shown in Fig. 2.

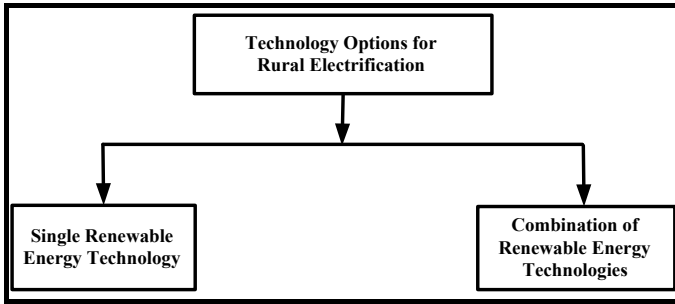


Fig. 2 Technology options for energy access in isolated rural areas

3.1 Option of Single Renewable Energy Technology

This option is suitable for villages which are located at remote and isolated areas. Generally, such area having limited energy need that can be fulfilled with the help of single energy resource. Therefore, single renewable energy technology scheme is an appropriate option for the village having low energy demand. Different schemes under this option include solar-powered centrifugal pump, small wind turbine-powered battery charging, solar lighting, solar fencing, solar spinning machines, small hydropower system, biomass/biogas operator generator, etc.

However, the availability of most of the resources of renewable energy (wind speed, solar radiation, etc.) is highly variable in nature. Some resources have surplus availability in a season and scarce in another season. Therefore, the combination of resources can be a better option for continuous energy supply in remote areas. Integrated utilization of different energy sources may also overcome the limitations of single renewable energy technology schemes.

3.2 Option of Hybrid Energy System

In hybrid energy system, electrical energy requirement of a remote rural area is met out with the resources which are nearby available in the region. This option provides better energy management, energy efficiency, and energy conservation compared to single technology. Under the condition when renewable energy sources are not sufficient in amount, other options like gasoline/petrol/diesel-operated generator can also be included along with the available resources to fulfill the demand of rural areas.

A typical schematic of an SPV/Wind/Battery-based hybrid energy system is depicted in Fig. 3. Charge controller protects the storage system by operating it between maximum and minimum capacity. Dump load such as water heater, water pump, etc., may be included to absorb the excess power.

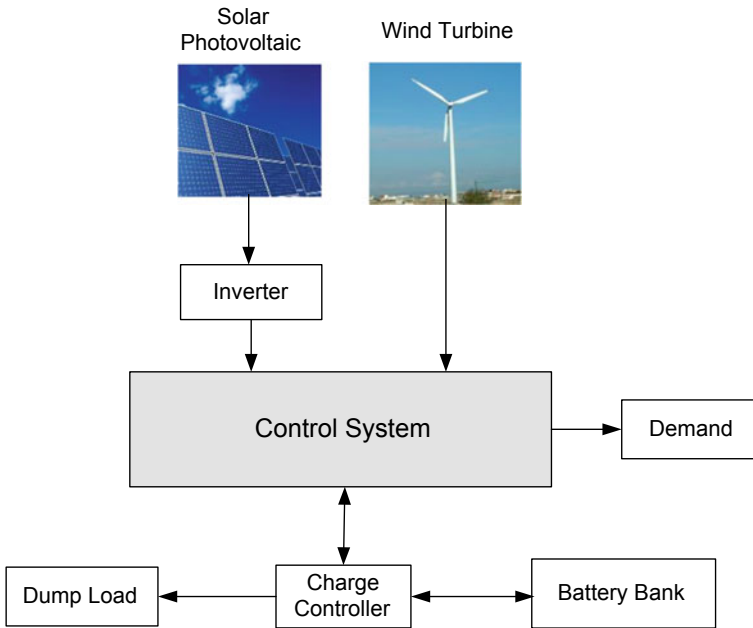


Fig. 3 Schematic of SPV/Wind/Battery-based hybrid energy system

4 Evaluation Criteria for Designing a Hybrid Energy System

Evaluation criteria play a significant role in designing a hybrid system in terms of power reliability and economics. Various criterions for the development of renewable energy-based hybrid system are shown in Fig. 4.

In economic criteria, parameters such as total annualized cost (TAC), total net present cost (TNPC), payback period (PBP), cost of energy generation (C_{av}), etc., are considered. Power reliability criteria include various system reliability parameters such as equivalent loss factor (ELF), loss of power supply probability (LPSP), level of autonomy (LA), energy index ratio (EIR), etc., are considered by various researchers.

Social criteria incorporate include different factors such as employment generation, social acceptance, etc. In technical criteria, battery bank storage limits, generators output limits, demand response, etc., are taken [11, 12]. Environmental criteria consider various issues such as land requirement, pollutant emission, etc. The mathematical expressions of different criterions are broadly discussed in the following subsection.

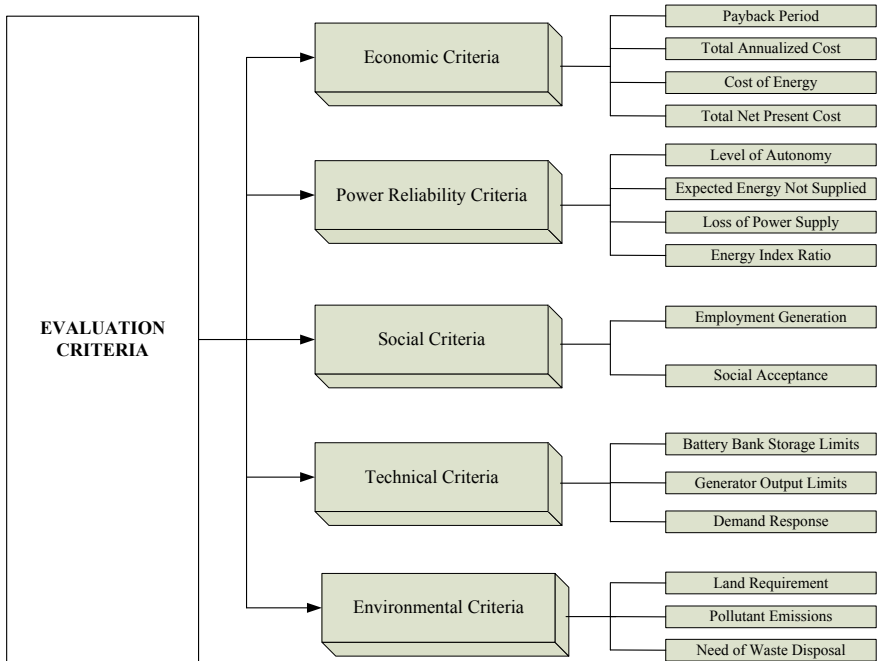


Fig. 4 Evaluation criteria for designing a renewable energy-based hybrid system

5 Conclusion

The study reveals that the utilization of renewable energy resources for energy access at user end do not pollute the environment. However, various challenges and issues are related to the design and development of hybrid energy system are described as high initial cost of PV panels, wind turbine, biomass gasifier, small hydropower, etc., compared to conventional power generation. Losses in energy conversion from AC to DC in bidirectional converter and vice versa. The life cycle of battery energy storage is low. In isolated mode, system stability is affected by step changes in generation and energy demand.

References

1. Kahraman C, Kaya I, Cebi S (2009) A comparative analysis for multiattribute selection among renewable energy alternatives using fuzzy axiomatic design and fuzzy analytic hierarchy process. *Energy* 34(10):1603–1616
2. Beccali M, Cellura M, Mistretta M (2003) Decision-making in energy planning. Application of the Electre method at regional level for the diffusion of renewable energy technology. *Renew Energy* 28(13):2063–2087

3. Li C, Ge X, Zheng Y, Xu C, Ren Y, Son C, Yang C (2013) Techno-economic feasibility study of autonomous hybrid wind/PV/battery power system for a household in Urumqi, China. *Energy* 55:263–272
4. Beccali M, Brunone S, Cellura M, Franzitta V (2008) Energy, economic and environmental analysis on RET-hydrogen systems in residential buildings. *Renew Energy* 33:366–382
5. Bakosa GC, Soursos M (2002) Techno-economic assessment of a stand-alone PV/hybrid installation for low-cost electrification of a tourist resort in Greece. *Appl Energy* 73:183–193
6. Kaviani AK, Riahy GH, Kouhsari SHM (2009) Optimal design of a reliable hydrogen-based stand-alone wind/PV generating system, considering component outages. *Renew Energy* 34(11):2380–2390
7. Colson CM, Nehrir MH, Sharma RK, Asghari B (2014) Improving sustainability of hybrid energy systems part II: managing multiple objectives with a multi-agent system. *IEEE Trans Sustain Energy* 5:46–54
8. Celik AN (2003) Techno-economic analysis of autonomous PV-wind hybrid systems using different sizing methods. *Energy Convers Manag* 44:1951–1968
9. Askarzadeh A (2014) A discrete chaotic harmony search-based simulated annealing algorithm for optimum design of PV/wind hybrid system. *Sol Energy* 97:93–101
10. Herran DS, Nakata T (2008) Renewable technologies for rural electrification in Colombia: a multiple objective approach. *Int J Energy Sect Manag* 2(1):139–154
11. Mohammad EK (2017) Rural electrification and expansion planning of off-grid microgrids. *Electr J* 30(4):68–74
12. Cook P (2011) Infrastructure, rural electrification and development. *Energy Sustain Dev* 15(3):304–313

Performance and Combustion Analysis of a PPCCI Engine with Diesel as a Premixed Fuel to Reduce Soot Emission



S. Sendilvelan, K. Bhaskar, M. Kiani Deh Kiani, Satishkumar Subendran, M. Thrinadh, P. Santheep Pandian and L. R. Sassykova

Abstract In this research work, premixed fuel (diesel) with varying premixed ratios (0.25, 0.50, and 0.75) in manifold along with traditional in-cylinder-injected diesel was used. The results were compared with conventional in-cylinder-injected CIDI engine. It was observed that unburnt hydrocarbon (UBHC) and carbon monoxide (CO) increases when compared to CIDI mode. Brake thermal efficiency was found to be slightly decreased. Soot emission decreases as the premixed ratio increases. Significant reduction in oxides of nitrogen was achieved with the partially premixed charge compression ignition (PPCCI) mode for all the premixed ratios used. Diesel premix ratio of 0.25 was observed to be optimum as the brake thermal efficiency reduction was only marginal compared to diesel mode and the soot emission was lower than that of diesel.

Keywords Diesel premix · Emission control · Oxides of nitrogen · Soot

S. Sendilvelan (✉) · S. Subendran · M. Thrinadh · P. Santheep Pandian
Department of Mechanical Engineering, Dr. M.G.R. Educational and Research Institute,
Chennai 600095, India
e-mail: sendilvelan.mech@drmgrdu.ac.in

K. Bhaskar
Department of Automobile Engineering, Rajalakshmi Engineering College, Chennai 602105,
India

M. Kiani Deh Kiani
Department of Biosystem Mechanical Engineering, Shahid Chamran University of
Ahvaz, Ahvaz, Iran

L. R. Sassykova
Faculty of Chemistry and Chemical Technology, Al-Farabi Kazakh National University,
Almaty 050040, Kazakhstan

1 Introduction

1.1 Partially Premixed Charge Compression Ignition (PPCCI)

PPCCI engine produces high thermal efficiency and simultaneous reduction of NO_x and soot emissions due to complete combustion process at lower peak combustion temperatures [1–3]. The specific advantage of using PPCCI engines are to achieve very low concentrations of pollution components, high efficiency during part and full load operating conditions, and low specific fuel consumption and also shorter combustion duration [4]. In the PPCCI engine, to get a premixed charge, fuel was injected in intake manifold along with traditional in-cylinder-injected diesel. This method has a few disadvantages like narrow operating range of automotive engine, improper combustion, and autoignition. The advantages of this PPCCI engines are that the ignition happens at multiple spots, which helps to burn the fuel mixture simultaneously [5]. PPCCI engines have extensively lower emissions as compared to the conventional compression ignition engines.

2 Methodology

In this work, premixed diesel fuel was injected into the manifold by conventional injection into the combustion chamber. The effect of different premixed ratios of 0.25, 0.50, and 0.75 was studied. This technique reduces oxides of nitrogen (NO_x) and soot [6]. With partially premixed charge, the combustion takes place rapidly compared to conventional CIDI mode. Homogeneous lean air–fuel ratio inducted during suction stroke helps in maintaining the lower peak pressure and temperature at moderate load. Table 1 shows the engine specification used in this work. To maintain the desired temperature, the fuel was heated by the thermostat electrically. The electronic fuel pump was used to inject the fuel with 30° spray angle at 4 bar. The opening and closing of the pilot injector for supplying the secondary fuel was controlled by calibrated electronic control unit. The primary fuel was supplied to the combustion chamber without heating. The secondary fuel was introduced into the chamber in the suction stroke. The secondary fuel was heated before entering the inlet manifold, an electrical heating arrangement has been used for heating.

2.1 Experimental Procedure

Diesel fuel was used to start the engine in CIDI mode. All parameters were measured at various loads after reaching the steady state condition. Then experiment was repeated at PPCCI mode at various loads with different premix ratio of 0.25, 0.50, and 0.75.

The notations used are the following:

Table 1 Test engine specifications

Engine	Four-stroke constant speed single-cylinder CIDI engine
BP and Torque (max.)	4400 W and 28 Nm at 1500 rpm
Cylinder diameter and stroke length	0.0875 m and 0.11 m
Displacement volume	0.661 L
Compression ratio	17.5:1
Standard timing of injection (bTDC)	23.4°
Dynamometer	Swinging field

CIDI Diesel-Conventional mode

D-D mode means Diesel used as premixed fuel and in-cylinder fuel

D-D mode 0.25 R_p —0.25 premix ratio

D-D mode 0.50 R_p —0.50 premix ratio

D-D mode 0.75 R_p —0.75 premix ratio

$$\text{Premix Ratio } R_p = Q_{Dp}/Q_t = (m_{Dp} \times CV_{Dp}) / [(m_{Dp} \times CV_{Dp}) + (m_d \times CV_d)] \quad (1)$$

m —Fuel mass, CV —Colorific value, Subscripts Dp —Diesel premix, d —Directly injected fuel.

3 Results

3.1 Specific Energy Consumption and Brake Thermal Efficiency

The variation of specific energy consumption and brake thermal efficiency for various values of premix ratios compared with the conventional diesel mode are shown in Figs. 1 and 2, respectively.

The premixed fuel accumulated in the premix chamber, due to the wall wetting leads to the increase in specific energy consumption also decrease in the brake thermal efficiency. Also, instantaneous complete combustion in the combustion chamber results in high rates of cylinder pressure rise and peak pressures [7]. This results in higher in-cylinder pressure and temperature which increases the heat transfer from combustion chamber to the coolant. This effect is more pronounced at higher values of the premixed ratio which increases the fuel consumption. The energy consumption varies from 13,321 to 16,542 kJ/kWh while the brake thermal efficiency varies from 26.87 to 21.01% for premixed ratios of 0.25, 0.50, and 0.75 compared to 12,661 kJ/kWh and 28.4% for diesel mode at rated power output.

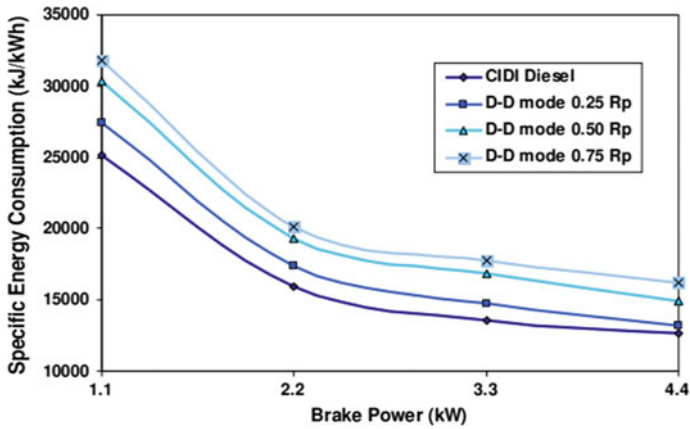


Fig. 1 Specific energy consumption with brake power

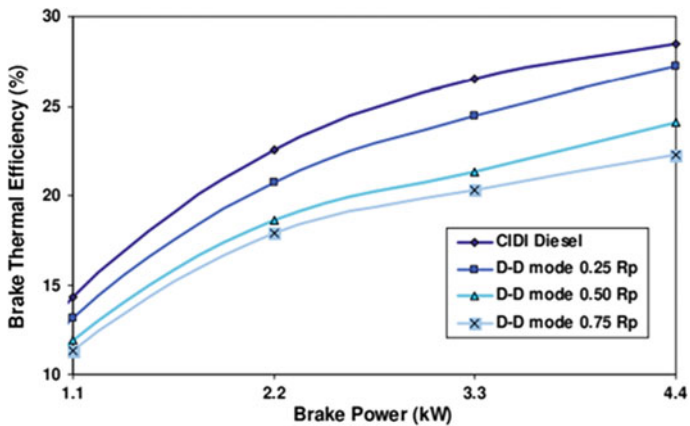


Fig. 2 Brake thermal efficiency with brake power

3.2 Unburnt Hydrocarbon Emissions

Figure 3 shows the hydrocarbon variation for various values of premix ratios compared with the conventional diesel modes with brake power. It was observed that when the premixed ratio was increased, the unburnt hydrocarbon emission increase significantly at all the power outputs as the premixed fuel injected in the manifold was higher. For a given premixed ratio, as the power output increases the equivalence ratio increases which results in an increase in fuel in the crevice volume [8]. The premixed lean air–fuel mixture is trapped in crevice volumes available in the combustion chamber during the compression. This may also increase the UBHC emissions.

The hydrocarbon emission also increases due to flame quenching, since the cylinder wall temperature is maintained at lower temperatures. Fuel vapor into oil due

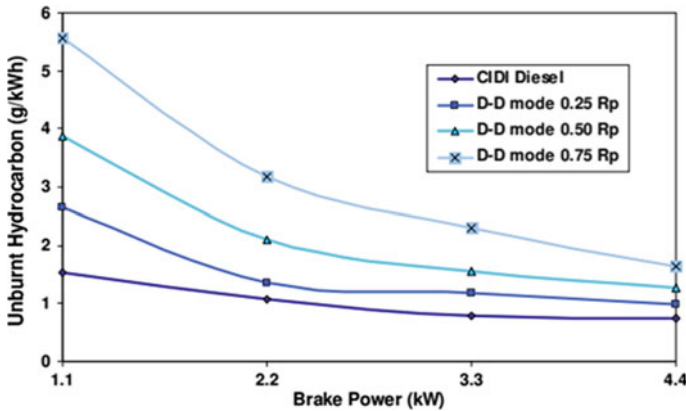


Fig. 3 Unburnt hydrocarbon with brake power

to absorption on the wall of the cylinder also gives rise to higher emission [9]. At rated power output, the unburnt hydrocarbon emission in premixed mode for premixed ratios of 0.25, 0.50, and 0.75 range from 1.123 to 1.897 g/kWh while it was 0.67 g/kWh for CIDI diesel mode.

3.3 Carbon Monoxide Emissions

The carbon monoxide emission variation for various premixed ratios compared with diesel is depicted in Fig. 4. It can be observed that carbon monoxide emission was higher at all power outputs for premixed mode compared to base mode. Higher values of premixed ratios result in higher carbon monoxide emission as the premixed fuel injected in the manifold is higher. The fuel released from the crevice volume is not fully oxidized due to low combustion chamber temperature and gives rise to higher carbon monoxide emissions. The OH radical concentration gets reduced due to incomplete combustion in intermediate temperature regions. OH radical is one of the factors for CO to CO₂ conversion [10]. Hence, carbon monoxide emission increases in premixed mode. Poor vaporization of fuel may also increase the carbon monoxide emissions. At rated power output, the carbon monoxide emission in premixed mode for premixed ratios of 0.25, 0.5, and 0.75 ranges from 20.02 to 35.68 g/kWh while it was 16.7 g/kWh for CIDI mode.

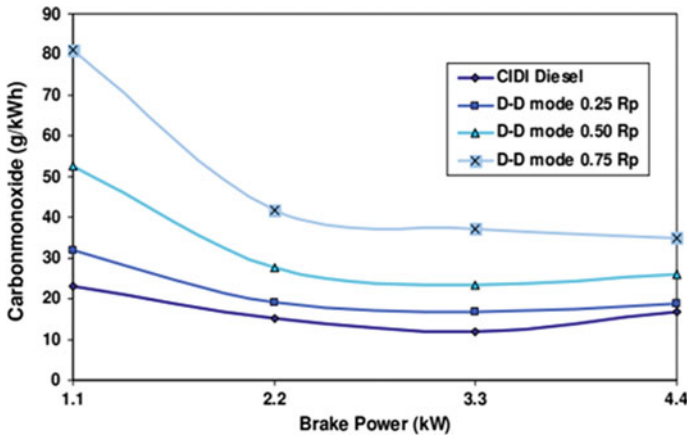


Fig. 4 Carbon monoxide with brake power

3.4 Oxide of Nitrogen Emissions

In a CI engine, premixed fuel allows a significant reduction of NO_x and particulates as homogenous mixture is formed which auto ignites due to compression heat. Due to the lean mixture, fuel-intensive zones are absent to initiate soot formation. However, the operating range of PPCCI engine was too narrow and good performance was obtained only from 25 to 75% of rated power output. Improper combustion or misfire under fuel-lean conditions was observed to limit the minimum load at which the engine can operate. Figure 5 shows the variation of oxides of nitrogen emissions with brake power. Up to 50% of rated power output, NO_x emissions decrease when the premixed ratio was increased for the premixed mode of combustion. The NO_x emission for premixed ratios of 0.25, 0.5, and 0.75 at 25% rated power (1.1 kW) output ranges from 12.5 to 10.01 g/kWh compared to 15.6 g/kWh for diesel. At 50% of rated power (2.2 kW) NO_x ranges from 11.23 to 9.22 g/kWh compared to 12.2 g/kWh for diesel. At lower power output, enough time is available for fuel and air to homogeneously. As there was no high-temperature flame front in the premixed mode of operation, the local temperatures are reduced, and the NO_x emissions were significantly decreased. It also results in lower soot formation due to lean and homogenous local air-fuel mixture.

3.5 Soot Emissions

The variation of soot emissions for premixed mode is given in Fig. 6. Soot and NO_x emissions are dependent on equivalence ratio and homogeneity of the charge in the cylinder. It can be seen that soot emissions are low at all power outputs and all

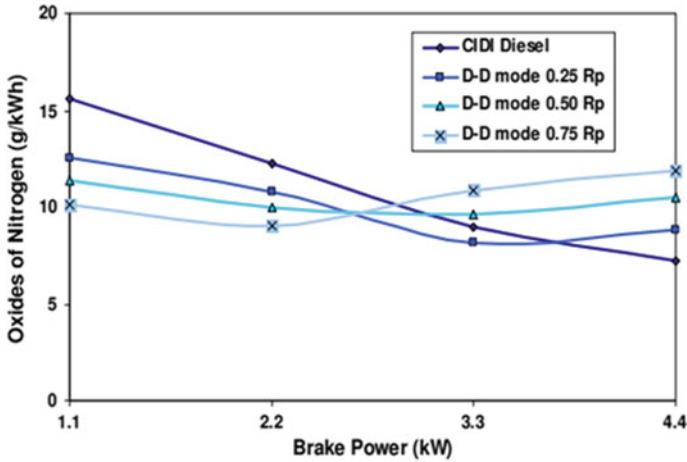


Fig. 5 Oxides of nitrogen with brake power

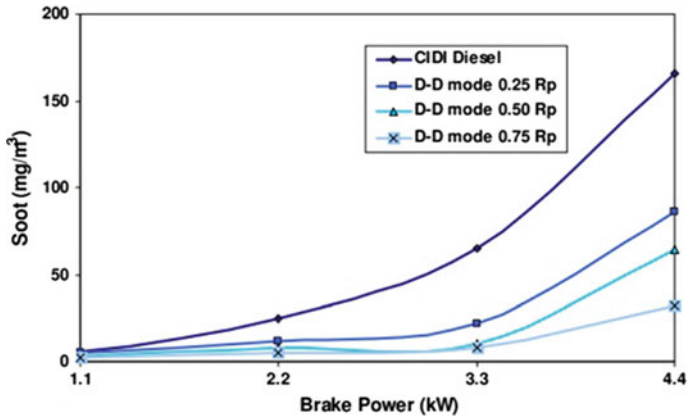


Fig. 6 Soot with brake power

premixed ratios compared to conventional mode. When the premixed ratio increases the homogeneity of fuel–air mixture increases which will reduce the soot emission. In PPCCI mode, rich mixture zones are eliminated when compared to conventional mode. At rated power, a significant decrease in soot emission is observed compared to conventional mode due to higher heat release rate [11]. Soot emission at rated power varies from 45 to 85 mg/m³ when the premixed ratio was decreased from 0.75 to 0.25 for premixed mode of operation compared to 166 mg/m³ for diesel mode.

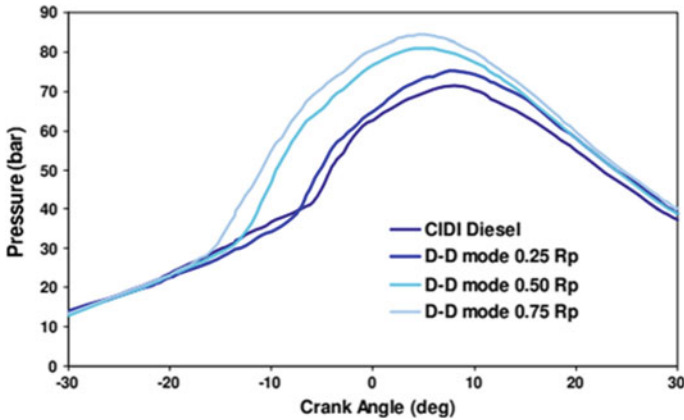


Fig. 7 In-cylinder pressure with crank angle

3.6 Pressure–Crank Angle Diagram

Figure 7 shows the in-cylinder pressure versus crank angle for various values of premixed ratios. It was observed that prior to combustion; the pressure inside the cylinder was low. At loads lower than 50%, the peak pressure was lower as well as the angle at which it occurs does not vary much from the base diesel mode. At higher loads (above 50%), the peak pressure was higher, and the start of combustion was earlier for premixed mode compared to CIDI mode. The quantity of fuel injected was more at higher power outputs while the quantity of air inducted was nearly constant. This increases the fuel–air ratio when the fuel was injected in the manifold and results in higher peak pressures and also advances the start of combustion [12]. The effect was more pronounced at higher power outputs and higher values of premixed ratio. At the rated power, the start of combustion occurs at 9, 13 and 16 °CA bTDC for premixed ratios of 0.25, 0.50, and 0.75 compared to 7 °CA bTDC for CIDI mode.

3.7 Heat Release Rate

Figure 8 shows the heat release rate at rated power output for various premixed ratios compared to CIDI mode. The first stage of heat release occurs in between 20 and 30 °CA bTDC was named as low-temperature reactions (LTR). The second stage of heat release rate was due to the in-cylinder combustion named as high-temperature reactions (HTR) occurs near TDC. The crank angle between LTR occurrence and HTR occurrence is called as negative temperature coefficient (NTC) region [13]. For fuels with lower octane number like diesel will have a predominant heat release rate

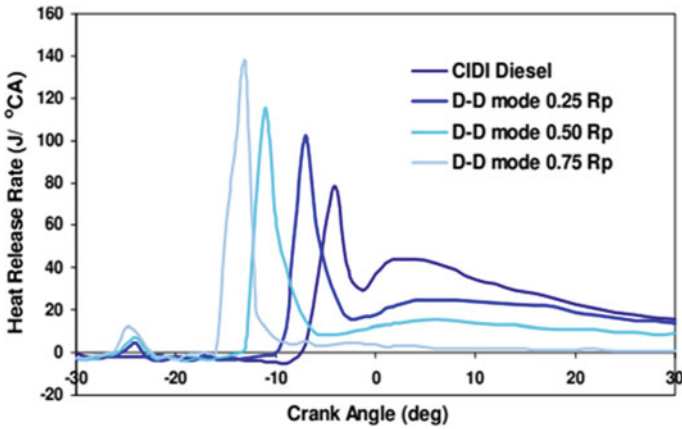


Fig. 8 Heat release rate with crank angle

at low-temperature combustion (LTC) compared to higher octane number fuels like gasoline.

Figure 9 shows the start of HTR, start of LTR, and crank angle between LTR and HTR at rated power output for various premixed ratios. It is seen that the magnitude of LTR and the timing of LTR are dependent primarily on the fuel selection and the temperature–time history. The pressure and temperature increase during low-temperature reactions (LTR), together with heat release rate (HRR) and timing of LTR control the high-temperature reactions (HTR). Hence, the control of LTR is important for increasing the operating ranges of premixed combustion. HTR peak increases in magnitude as the premixed ratio is increased and occurs earlier. LTR peak also increases and occurs nearly at the same crank angle for all premixed ratios at any given power output. LTR occurs earlier as the power output is increased due to the early start of cool flame reactions at higher power outputs. The peak heat release rates during HTR at rated power outputs were observed to be 102.5, 115.2, and 135.1 J/°CA occurring at 9, 13, and 16 °CA bTDC for premixed ratios of 0.25, 0.50, and 0.75, respectively, while the peak heat release rates during LTR were 4.8, 7.3, and 11.7 J/°CA occurring at nearly 25 °CA bTDC for all the premixed ratios. The time interval between the LTR and HTR were found to be 16, 12 and 10 °CA for premixed ratios of 0.25, 0.50, and 0.75, respectively.

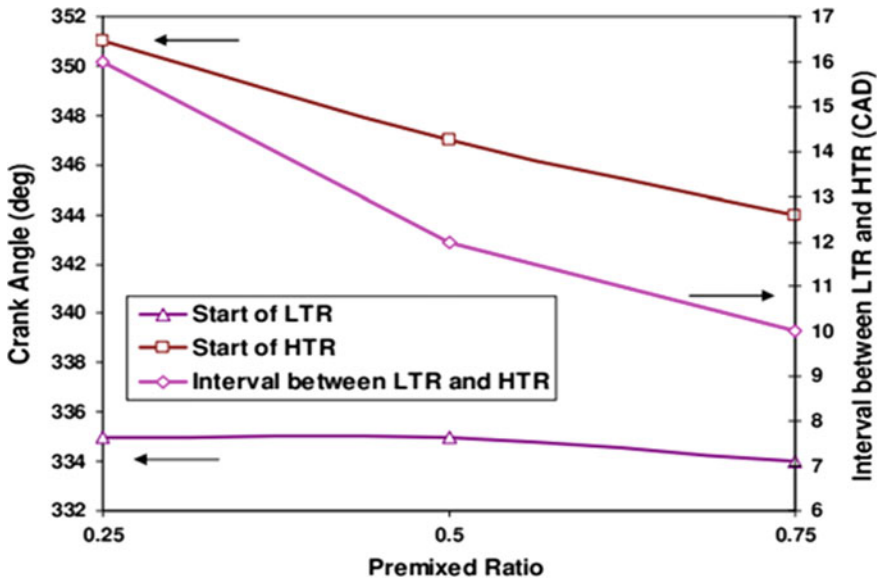


Fig. 9 LTR, HTR with various premixed ratios at rated power output

4 Conclusion

The results are summarized as follows:

- When premixed ratio increases, the brake thermal efficiency decreases significantly. The maximum percentage decrease was found to be 21.5% at premixed ratio of 0.75 and while minimum percentage decrease was 4.2% at premixed ratio of 0.25.
- UBHC and CO emissions increases with the maximum percentage increases were 123.9 and 107.1% for UBHC and CO emission, respectively, at premixed ratio of 0.75. Premixed ratio of 0.25 gives the minimum percentage increases in UBHC (34.9%) and CO (11.4%) emission. UBHC and CO emission can be controlled with oxidation catalytic converters in the exhaust manifold.
- Soot emission decreases as the premixed ratio increases in premixed mode and the maximum percentage decrease was found to be 80.7% at premixed ratio of 0.75. NO_x emission decreases up to 50% of rated power for all the premixed ratios used. Beyond 50% of rated power output, NO_x emission increases and at premixed ratio of 0.75, a percentage increase of 63.0% in NO_x emission was observed. Premixed ratio of 0.25 gives the minimum percentage increase of 20.5%.
- Increase in premixed ratio increases the peak cylinder pressure and the rate of heat release.

- Diesel premix ratio of 0.25 was observed to be optimum as the decrease in brake thermal efficiency was only marginal compared to CIDI mode and the soot emission was lesser than that of diesel-conventional mode.

References

1. Reitz RD, Duraisamy G (2015) Review of high efficiency and clean reactivity controlled compression ignition (RCCI) combustion in internal combustion engines
2. Hasan MM, Rahman MM (2016) Homogeneous charge compression ignition combustion: advantages over compression ignition combustion, challenges and solutions. *Renew Sustain Energy Rev* 57:282–291
3. Cheng X, Li S, Yang J, Liu B (2016) Investigation into partially premixed combustion fueled with N-butanol-diesel blends. *Renew Energy* 86:723–732
4. Kumar P, Rehman A (2016) Bio-diesel in homogeneous charge compression ignition (HCCI) combustion
5. Jain A, Singh AP, Agarwal AK (2017) Effect of fuel injection parameters on combustion stability and emissions of a mineral diesel fueled partially premixed charge compression ignition (PPCCI) engine. *Appl Energy* 190:658–669
6. Sun C, Kang D, Bohac SV, Boehman AL (2016) Impact of fuel and injection timing on partially premixed charge compression ignition combustion. *Energy Fuels* 30:4331–4345
7. Benajes J, García A, Domenech V, Durrett R (2013) An investigation of partially premixed compression ignition combustion using gasoline and spark assistance. *Appl Therm Eng* 52:468–477
8. Saxena S, Bedoya ID (2013) Fundamental phenomena affecting low temperature combustion and HCCI engines, high load limits and strategies for extending these limits
9. Lee J, Chu S, Cha J, Choi H, Min K (2015) Effect of the diesel injection strategy on the combustion and emissions of propane/diesel dual fuel premixed charge compression ignition engines. *Energy* 93:1041–1052
10. Mancaruso E, Vaglieco BM (2010) Optical investigation of the combustion behaviour inside the engine operating in HCCI mode and using alternative diesel fuel. *Exp Therm Fluid Sci* 34:346–351
11. Bi X, Liu H, Huo M, Shen C, Qiao X, Lee CFF (2014) Experimental and numerical study on soot formation and oxidation by using diesel fuel in constant volume chamber with various ambient oxygen concentrations. *Energy Convers Manag* 84:152–163
12. Maurya RK, Agarwal AK (2011) Experimental investigation on the effect of intake air temperature and air-fuel ratio on cycle-to-cycle variations of HCCI combustion and performance parameters. *Appl Energy* 88:1153–1163
13. El-Asrag HA, Ju Y (2014) Direct numerical simulations of NO_x effect on multistage autoignition of DME/air mixture in the negative temperature coefficient regime for stratified HCCI engine conditions. *Combust Flame* 161:256–269

Theoretical Study of Solar Air Heater Using MATLAB



Vijay Singh Bisht, Ankit Singh Bisht and Pooja Joshi

Abstract This article present a mathematical study of solar air heaters roughened with three different turbulent promoters. In this study, arc-shaped ribs, broken arc-shaped ribs, and arc shape ribs present in 'S' shape form are considered as turbulent promoters. In this research work, the numerical modeling of solar air heater is conducted in MATLAB. Thermal efficiency amplification factor (η_{th}/η_{ths}), effective efficiency amplification factor (η_{eff}/η_{effs}), and exergetic efficiency amplification factor (η_{ex}/η_{exs}) are considered as performance factors. The temperature rise parameter ($\Delta T/I$) is the only independent parameter considered in this study and it varies from 0.0001 to 0.0151. Solar air heater with arc-shaped ribs roughness has higher values of thermal efficiency amplification factor (η_{th}/η_{ths}), effective efficiency amplification factor (η_{eff}/η_{effs}), and exergetic efficiency amplification factor (η_{ex}/η_{exs}) than other two turbulent promoters. Arc-shaped ribs create high heat transfer rate with least exergetic losses of all the three turbulent promoters.

Keywords Solar air heater · Efficiency · Numerical modeling

Nomenclature

$(\Delta P)_d$	Pressure drop across duct
P_m	Pumping power
T_a	Ambient temperature
T_f	Mean bulk air temperature
T_i	Inlet air temperature
T_o	Outlet air temperature
T_p	Mean plate temperature
t_g	Thickness of glass cover

V. S. Bisht (✉) · A. S. Bisht

Faculty of Technology, Uttarakhand Technical University, Dehradun 248007, Uttarakhand, India
e-mail: vsinghbisht5@gmail.com

P. Joshi

Women Institute of Technology, Uttarakhand Technical University, Dehradun, India

© Springer Nature Singapore Pte Ltd. 2019

M. Kumar et al. (eds.), *Advances in Interdisciplinary Engineering*, Lecture Notes in Mechanical Engineering, https://doi.org/10.1007/978-981-13-6577-5_69

t_p	Thickness of absorber plate
$\Delta T/II$	Temperature rise parameter
U_b	Bottom loss coefficient
U_s, U_e	Side/Edge loss coefficient
U_l	Overall heat loss coefficient
V_w	Wind velocity
A_p	Surface area of absorber plate/collector
e/D	Relative roughness height
p/e	Relative roughness pitch
f	Friction factor
Nu	Nusselt Number
α	Angle of attack
m	Mass flow rate of air
W	Width of absorber plate
Q_u	Useful heat gain
F'	Collector efficiency factor
F_R	Heat Removal factor
η_{th}	Thermal efficiency
η_{eff}	Effective efficiency
η_{ex}	Exergetic efficiency
$\tau\alpha$	Transmittance-absorptance
ε_g	Emissivity of glass
ε_p	Emissivity of plate
t_i	Thickness of insulation
K	Insulation thermal conductivity
N	Number of covers

1 Introduction

Solar energy is an eco-friendly, plainly available, and everlasting origin of energy. Day-to-day increasing demand of energy leads to diminution of fossil fuels and for the advancement of a nation solar energy is playing a remarkable role. There are various methods by which, one can harness solar energy. Solar air heater is a primary device that directly transforms solar energy to heat energy, but the heat exchanging capability of solar air heater is low. Initiatives are made by the number of investigators to heighten the heat transfer rate of the thermal efficiency. Turbulent promoters are used by various researchers in undersurface of absorber plate to boost the thermohydraulic efficiency.

The theory of turbulent promoters was first exercised by Joule [1] to heighten the heat transfer capability of condenser tube. The researchers did plenty of investigation on distinct types of turbulent promoters, as discussed in this portion. Prasad and Saini [2] were first to incorporate small diameter wires as turbulent promoters to amplify the heat transfer capability of the solar air heater. They also discussed the effect

Table 1 Mathematical formulation of Nusselt number and Friction factor

Type of roughness	Correlation
Arc-Shaped Wire ribs [4]	$Nu = 0.001047 \left(\frac{e}{D_h}\right)^{0.3772} \left(\frac{\alpha}{90}\right)^{-0.1198} (Re)^{1.3186}$ $f = 0.14408 \left(\frac{e}{D_h}\right)^{0.1765} \left(\frac{\alpha}{90}\right)^{0.1185} (Re)^{-0.17103}$
Broken arc ribs [5]	$Nu = 0.001014 \times Re^{(1.036)} \times (p/e)^{(2.522)}$ $\times (\alpha/90)^{(-0.298)} \times (d/w)^{(-0.078)} \times (g/e)^{(-0.016)}$ $\times (e/D)^{(0.412)} \times \exp\left(-0.567\left(\ln(p/e)^2\right)\right)$ $f = 0.08192 \times Re^{(-0.147)} \times (p/e)^{(1.191)}$ $\times (\alpha/90)^{(-0.292)} \times (d/w)^{(-0.067)} \times (g/e)^{(-0.006)}$ $\times (e/D)^{(0.528)} \times \exp\left(-0.255\left(\ln(p/e)^2\right)\right)$
S shape ribs [6]	$Nu = (0.00014332) \times Re^{(1.2764)} \times (W/w)^{(0.2748)}$ $\times \exp(-0.1084 \times (\ln(W/w^2)))$ $\times (p/e)^{(0.4876)} \times \exp\left(-0.1107 \times (\log(p/e)^2)\right)$ $\times (\alpha/90)^{(-0.0468)} \times \exp\left(-0.0642 \times (\log(p/e)^2)\right)$ $\times (e/D)^{(-0.7653)} \times \exp\left(-0.1257 \times (\log(e/D))^2\right)$ $f = (0.1430) \times Re^{(-0.224)} \times (W/w)^{(0.1424)}$ $\times (p/e)^{(0.7657)} \times \exp(-0.187 \times (\log(p/e)^2))$ $\times (\alpha/90)^{(0.2129)} \times (e/D)^{(0.2159)}$

of roughness spacing and height on solar air heater performance. Taslim et al. [3] investigate the effect V-shaping on solar air heater performance. Saini and Saini [4] performed an experimental analysis of solar air heater coarsened by arc-shaped rib roughness. Hans et al. [5] performed an experimental analysis to report the effect of broken arc rib turbulent promoters on solar air heater efficiency. Kumar et al. [6] performed experimental analysis to report the impact of arc shape ribs arranged in ‘S’ shape form on the efficiency of solar air heater. Bisht et al. [7] and Patil [8] have conducted theoretical study of solar air heaters and concluded that with the incorporation of turbulent promoter’s solar air heater efficiency increases.

The mathematical formulation of heat transfer and friction characteristics developed for three different roughness elements (turbulent promoters) considered in this study are given in Table 1. The distinct roughness orientation used are arc ribs roughness, broken arc ribs roughness, and arc ribs present in ‘S’ shape form shown in Figs. 1, 2, and 3.

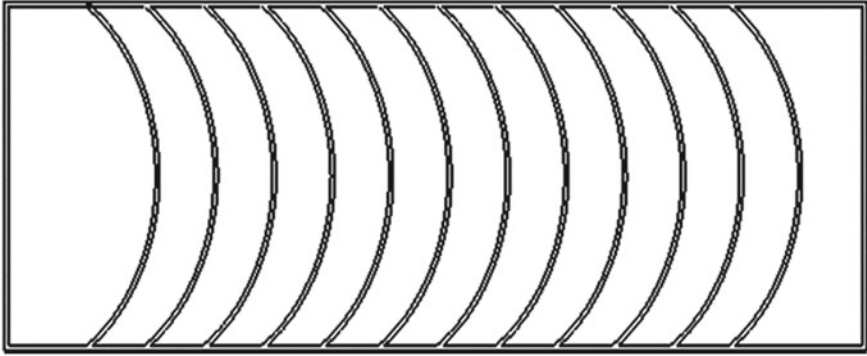


Fig. 1 Arc-shaped turbulent promoters

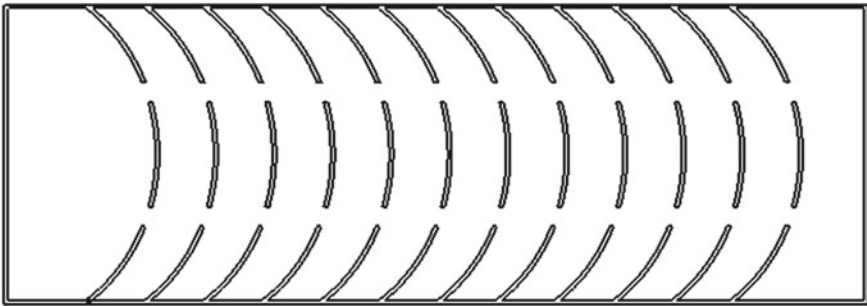


Fig. 2 Broken arc-shaped turbulent promoters

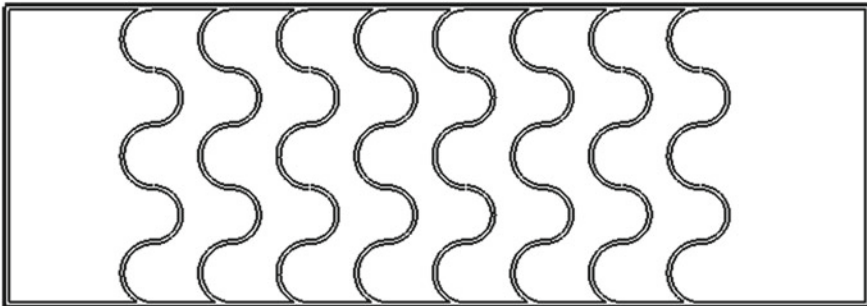


Fig. 3 Arc shape ribs present in 'S' shape form

2 Methodology

In this portion, the mathematical study of solar air heater roughened with different turbulent promoters is performed in MATLAB. The different variables used to compute the efficiency amplification factors of the solar air heater and turbulent promoters are displayed in Table 2. In Table 2, different input parameters of absorber plate and turbulent promoters are given.

These parameters are opted on the basis of previous study of Yadav and Kaushal [9] and Sahu and Prasad [10].

The valuation of all performance parameters are performed by similar step-by-step procedure mentioned by Yadav and Kaushal [9], Sahu and Prasad [10], and Kumar et al. [11]. In this work, different performance factors of solar air heaters with arc-shaped ribs, broken arc-shaped ribs, and arc shape ribs present in ‘S’ shape form roughness, respectively, are compared. The step-by-step procedure of numerical study on MATLAB is discussed in the flowchart presented in Fig. 4.

Thermal efficiency amplification factor, effective efficiency amplification factor, and exergetic efficiency amplification factors are defined below.

Thermal efficiency amplification factor (η_{th}/η_{ths}): It is the ratio of thermal efficiency of solar air heater with and without turbulent promoters.

Effective efficiency amplification factor (η_{eff}/η_{effs}): It is the ratio of effective efficiency of solar air heater with turbulent promoters to effective efficiency of smooth one.

Exergetic efficiency amplification factor (η_{ex}/η_{exs}): It is the ratio of exergetic efficiency of solar air heater with turbulent promoters to exergetic efficiency of smooth duct.

All these important factors show how much the roughened solar air heater is better than the smooth duct.

Table 2 Different parameters used in numerical study

Parameters	Value/range
$\tau\alpha$	0.8
ε_g	0.87
ε_p	0.9
t_g	0.04
N	1
t_i	0.05 m
K	$0.037 \text{ W m}^{-1} \text{ K}^{-1}$
Pl_e	10
T_a	300 K
V_w	1 m s^{-1}
I	1000 W m^{-2}
$\Delta T/I$	0.001–0.016

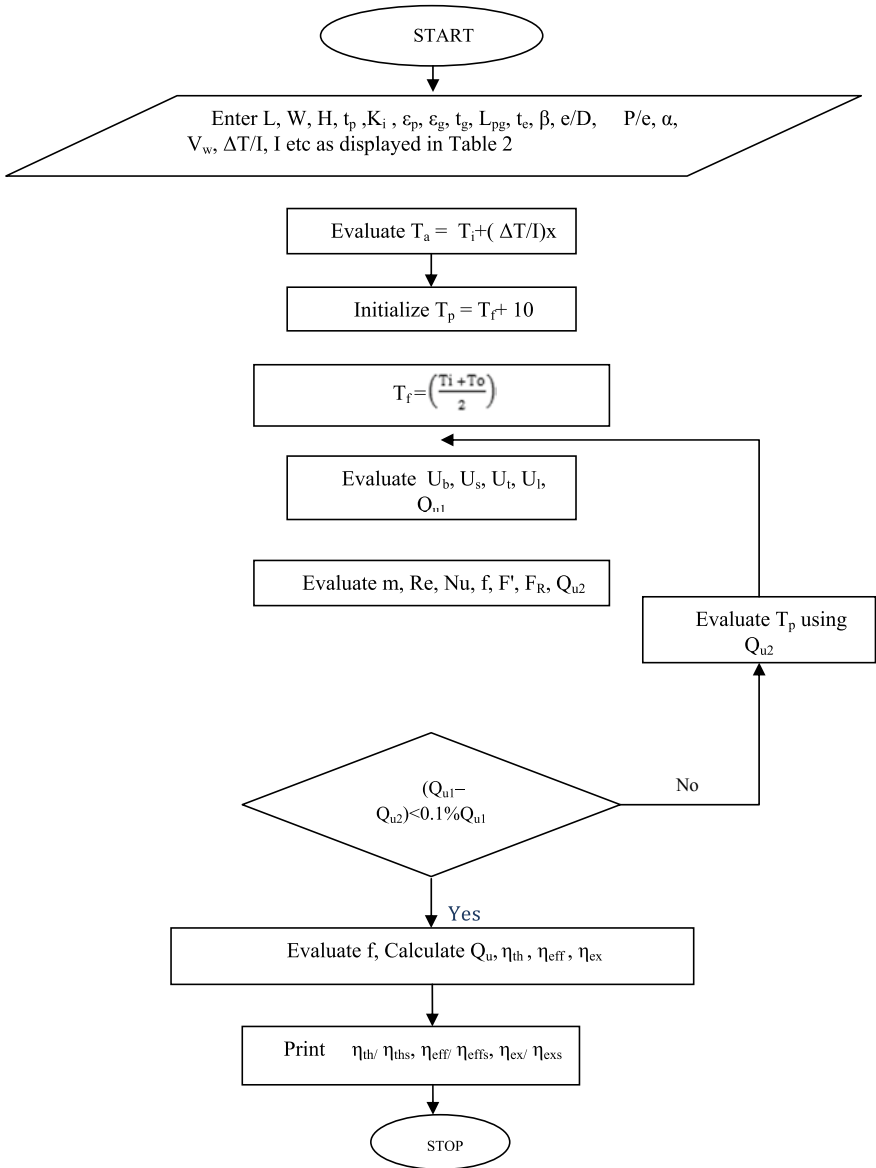
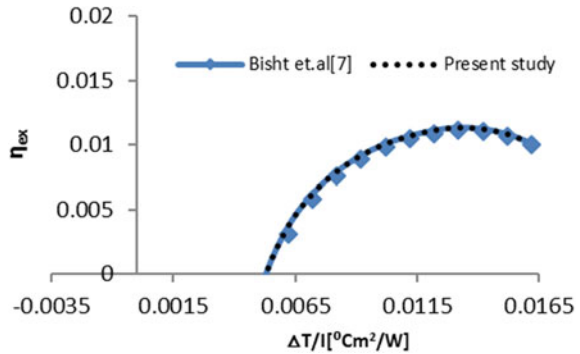


Fig. 4 Flowchart of mathematical model

Fig. 5 Effect of $\Delta T/I$ on exergetic efficiency



First of all, the numerical model is validated with previous work [7], Fig. 5 shows the comparison of exergetic efficiency of arc-shaped ribs of previous work [7] and present work considering the same input parameters and both the plots almost overlap each other.

3 Results and Discussion

3.1 Thermal Efficiency Amplification Factor (η_{th}/η_{ths})

Figure 6 shows the response of thermal efficiency amplification factor (η_{th}/η_{ths}) of solar air heaters roughened with three distinct turbulent promoters with variation in $\Delta T/I$.

Arc-shaped ribs are performed better than broken arc-shaped ribs and arc shape ribs present in ‘S’ shape form. For all three roughness geometries, thermal efficiency amplification factor increases within $\Delta T/I$ and achieves maxima and then decreases.

3.2 Effective Efficiency Amplification Factor (η_{eff}/η_{effs})

The trend of effective efficiency amplification factor (η_{eff}/η_{effs}) of solar air heaters roughened with three distinct ribs with $\Delta T/I$ is displayed in Fig. 7. For all three turbulent promoters (roughness geometries), effective efficiency amplification factor (η_{eff}/η_{effs}) increases with increase in and achieves maxima and then decreases. At lesser value of $\Delta T/I$, broken arc-shaped did better but after that, its performance has been declined. Arc-shaped ribs outperformed other two turbulent promoters.

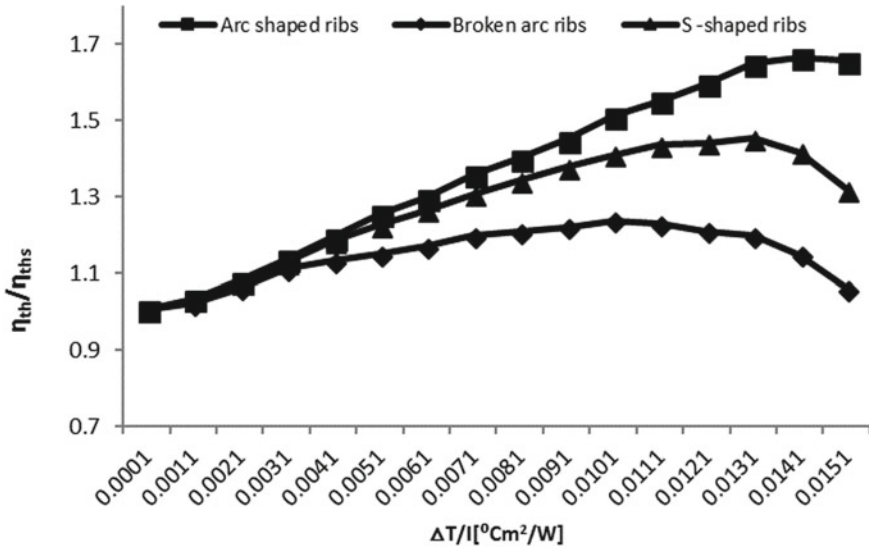


Fig. 6 Variation of thermal efficiency amplification factor (η_{th}/η_{ths}) with $\Delta T/I$

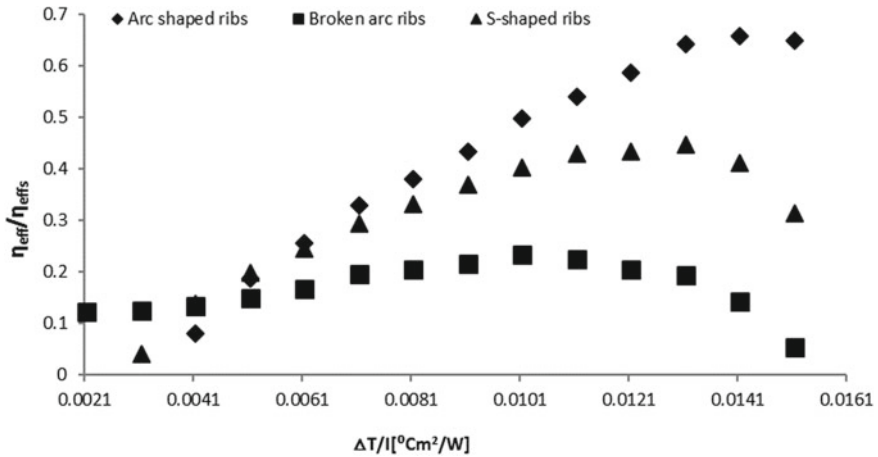


Fig. 7 Variation of effective efficiency amplification factor (η_{eff}/η_{effs}) with $\Delta T/I$

3.3 Exergetic Efficiency Amplification Factor (η_{ex}/η_{exs})

Figure 8 shows the response of exergetic efficiency amplification factor (η_{ex}/η_{exs}) of solar air heaters coarsened with three distinct turbulent promoters with change in $\Delta T/I$. For all three roughness geometries, exergetic efficiency amplification factor (η_{ex}/η_{exs}) increases with increase in $\Delta T/I$ and achieves maxima and then decreases. At lesser value, temperature rise parameters broken arc-shaped and arc shape ribs

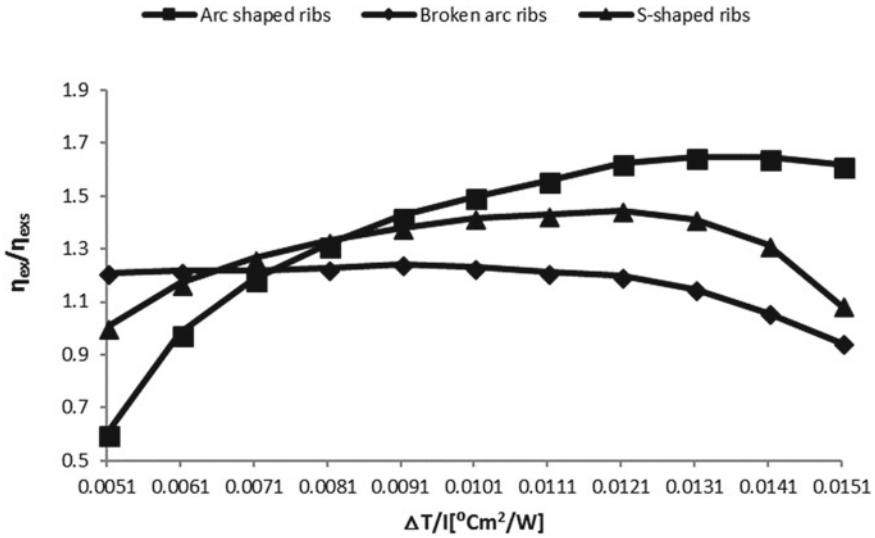


Fig. 8 Variation of exergetic efficiency amplification factor (η_{ex}/η_{exs}) with $\Delta T/I$

present in ‘S’ shape form did better than arc-shaped but at bigger value of $\Delta T/I$ that arc-shaped ribs outperformed broken arc-shaped ribs and arc shape ribs organized in ‘S’ shape form.

Exergetic efficiency amplification factor (η_{ex}/η_{exs}) cover both available energy and exergetic losses, so arc-shaped have highest available energy with minimum exergetic losses.

4 Conclusions

In this research work, the numerical investigation of solar air heater roughened by three distinct roughness arc-shaped ribs, broken arc-shaped ribs, and arc shape ribs present in ‘S’ shape form, respectively, has been performed by coding in MATLAB. The major conclusions outlined from this numerical investigation are as follows:

1. Thermal efficiency amplification factor, effective efficiency amplification factor, and exergetic efficiency amplification factor are the robust functions $\Delta T/I$.
2. For all three roughness geometries (Turbulent promoters), all three performance factors, i.e., thermal efficiency amplification factor (η_{th}/η_{ths}), effective efficiency amplification factor (η_{eff}/η_{effs}), and exergetic efficiency amplification factor (η_{ex}/η_{exs}) are increased with increase in $\Delta T/I$ achieved maxima and then decreases.
3. Arc-shaped roughness geometry has higher value of thermal efficiency amplification factor (η_{th}/η_{ths}), effective efficiency amplification factor (η_{eff}/η_{effs}), and

exergetic efficiency amplification factor (η_{ex}/η_{exs}) than other two turbulent promoters.

4. At the lesser value of $\Delta T/l$, broken arc-shaped ribs performance is better than other two turbulent promoters, but its performance decline at higher value of $\Delta T/l$.
5. Arc-shaped roughness geometry is the most suitable turbulent promoter of all the three turbulent promoters for better performance of solar air heater.

References

1. Joule JP (1861) On the surface condensation of steam. *Philos Trans R Soc Lond* 151:133–160
2. Prasad BN, Saini JS (1988) Effect of artificial roughness on heat transfer and friction factor in a solar air heater. *Sol Energy* 41:555–560
3. Taslim ME, Li T, Kercher DM (1996) Experimental heat transfer and friction in channels roughened with angled, V-shaped and discrete ribs on two opposite walls. *ASME J Turbomach* 118:20–28
4. Saini SK, Saini RP (2008) Development of correlations for Nusselt number and friction factor for solar air heater with roughened duct having arc-shaped wire as artificial roughness. *Sol Energy* 82:1118–1130
5. Hans VS, Gill RS, Singh S (2017) Heat transfer and friction factor correlations for a solar air heater duct roughened artificially with broken arc ribs. *Exp Thermal Fluid Sci* 80:77–89
6. Kumar K, Prajapati DR, Samir S (2017) Heat transfer and friction factor correlations development for solar air heater duct artificially roughened with ‘S’ shape ribs. *Exp Thermal Fluid Sci* 82:249–261
7. Bisht VS, Patil AK, Gupta A (2018) Review and performance evaluation of roughened solar air heaters. *Renew Sustain Energy Rev* 81(1):954–977
8. Patil AK (2015) Heat transfer mechanism and energy efficiency of artificially roughened solar air heaters—a review. *Renew Sustain Energy Rev* 42:681–689
9. Yadav S, Kaushal M (2014) Exergetic performance evaluation of solar air heater having arc shape oriented protrusions as roughness element. *Sol Energy* 105:181–189
10. Sahu MK, Prasad RK (2016) Exergy based performance evaluation of solar air heater with arc-shaped wire roughened absorber plate. *Renew Energy* 96:233–243
11. Kumar A, Bisht VS, Khatri M, Kumar S (2017) Numerical study of a roughened solar air heater using Matlab. *Int J ICT-Aided Arch Civ Eng* 4(1):17–26

Path Planning of Multiple Unmanned Aerial Vehicles Based on RRT Algorithm



Arleen Kaur and Mani Shankar Prasad

Abstract An optimal path planning method for multiple autonomous UAVs have been based on the modification of Rapidly-exploring Random Tree (RRT) algorithm by using the Rapidly-exploring Random Tree (RRT). The proposed method improves the path of RRT algorithm in 2D configuration space. The improved RRT algorithm is used to form the same path for each iteration and generate the minimum distance between the nodes. Moreover, the path reconstruction strategy has been put further to handle the problem of multiple UAVs. The effectiveness of the proposed method has been demonstrated through simulation using MATLAB.

Keywords Path planning · RRT algorithm · Multiple UAVs · Tree graph method · 2D configuration space

1 Introduction

Autonomous Unmanned Aerial Vehicles (UAVs) are being used for multiple missions like aerial surveillance, transport, in the military for an attack, and reconnaissance regularly. So, designing a path planner for a UAV has been a great challenging problem. Either standalone UAV or swarm of UAVs.

The RRT algorithm has been generated as the new tool for path planning where the new concept for designed a randomized data structure for a board class of path planning [1]. The RRT algorithm specifically includes the path planning problems of the nonhomlic and kinodynamic, where RRT is a data construction and its algorithm is well organized for a nonconvex in a high-dimensional space. The RRT algorithm path planner has been commonly used in the robotics field to deal with the kinodynamic

A. Kaur (✉) · M. S. Prasad
Institute of Space Science and Technology, Amity University
Uttar Pradesh, Noida, Uttar Pradesh, India
e-mail: arleenkaur95@gmail.com

M. S. Prasad
e-mail: msprasad@amity.edu

problem but Kothari [3] described the multiple path planning by using the RRT algorithm in a real time with conditions of kinematic constraints.

Kala [4] presented a path planning of multiple vehicles by using RRT algorithm where it increased the overall efficiency and safe driving of vehicles. The paper [5] generated a path planning for robotic by using the RRT algorithm. Then in the paper Zhen and Alejo [6, 7] proposed a cooperative path planning for multiple UAVs formation by using online path planning method. Furthermore, Yang [8] proposed 3D path planning of RRT algorithm and did a comparison with other algorithms. The RRT algorithm selected for a single query forms a path planning.

In this work, improvement has been done in the RRT algorithm and formed a multiple path planning for multiple UAVs based on RRT algorithm because it is faster than other algorithms, and can be used for nonconvex geometry and worked in a high-dimensional space. For autonomous operation, path planning is of most importance and in the case of multiple UAVs flying in the same area, path planning, avoiding a collision, is a challenging problem. A number of path planning algorithms for single UAV have been reported in the literature and one of the algorithms is based on RRT. The basic concept of path planning is to join a starting point and target point in a 2D configuration space, denoted by C and parameters used (x, y) . The path planning method is classified into two categories: local and global approach. Local planning method is faster, but due to lack of information about replanning, the path and fail in the trap. Global can ignore these problems but computationally costly [2].

The paper is organized as: Sect. 2 deals with RRT algorithm and its modification. Section 3 presents the simulation results, where improve RRT Path planning and multiple path formations for a UAVs tested result shown. Section 4 Conclusion.

2 Path Planning with RRT Algorithm

2.1 Basic RRT Algorithm

There are number of ways to approach path planning either go through graph search like A^* , RRT, D^* , Dijkstra algorithm, Probabilistic Road Map (PRM), cell decomposition, potential field method, or directly approach through evolutionary algorithms [6]. The study focuses in RRT algorithm because it is very fast in formatting route, there is no complex calculation required, path continuous plan in configuration space (RRT algorithm work in a high-dimensional space), capable to handle large and randomly in search space, work for nonconvex geometry, and have kinodynamic planning. The basic principle of RRT algorithm depends on the tree structure, tree generated randomly, or deterministic in a given specific area. An incremental sampling is based on single query planer form an RRT, where it allows to build a tree of a feasible path by extending the branches toward a randomly approaching target node without any parameter tuning [4]. The standard RRT algorithm tree construction or node extension for path planning is given in Fig. 1.

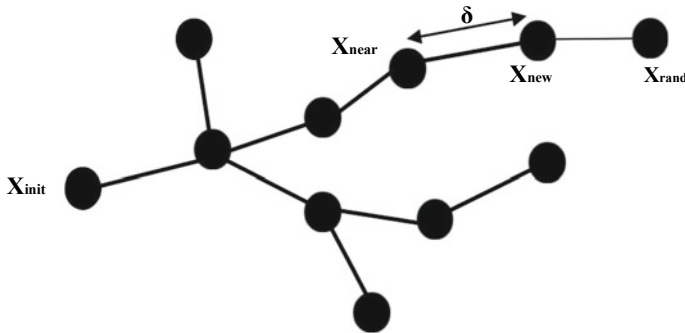


Fig. 1 RRT algorithm node extension

The tree begins with the initial state, X_{init} as the root node of the UAV. A node is randomly approaching in space, denoted by state X_{rand} , in which choices the possibility of the target node, represented by X_{target} , and the nearest point (X_{near}) in the RRT to the random node has choices. From a node nearest neighbor (X_{near}), the tree moves one footstep forward (with predefined length δ), move toward the existing random node X_{rand} and after that added new nodes and new arc, represented by X_{new} . The extending nearest-neighbor point moves toward X_{rand} , and a collision test is performed so that X_{new} is not added to RRT. The above procedure is repeated until the branches reach a target point X_{target} or maximum nodes achieve. A feasible path planning has been done by RRT algorithm (pseudocode is given below) to generate a path from starting node to target node [2].

Select initial starting node X_{init}
 Generation of free in a loop

for $i: k$
 generate random number X_{rand}
 set a distance δ

Select the point nearest X_{near} to X_{init} and X_{rand} by δ distance δ is a length to select the input between X_{rand} and X_{near}

X_{new} generated a new state with the help of parameter X_{near} and δ Vertex point generated
 Joined the initial and final nodes
 end the loop

find the completed node from X_{init} to X_{target}

2.2 Modification in RRT Algorithm Based on Path Planning

To use the RRT algorithm for multiple UAVs path planning, a modification has been done by using the RRT algorithm where for each path, it chooses different δ and a vertex index array is generated for the path. Further, these vertexes are deleted when using RRT algorithm for another UAV path planning. This leads to nonavailability of nodes (vertex) for the path generation for multiple UAVs.

The problem has solved for multiple path planning of UAVs without colliding with each other and optimal trajectory formation in the 2D configuration space. Here, from the initial point the tree vertex continues searching for a target node and once the target node finds out by tree vertex, path gets generated by a UAV 1, after that the tree vertex of UAV 1 gets deleted, so that it is no longer available for other UAV path and then go to initial point of UAV 2, from initial point of UAV 2 again the tree vertex generates and continues searching for the target node, once the target node finds out, path gets generated and vertex gets deleted. Similarly, the path planning has been done for UAV 3, UAV 4, and UAV 5, without colliding with each other in 2D configuration space (Fig. 2).

3 Simulation of the Modified Algorithm Has Been Done in MATLAB

The effective and validity of the algorithm is tested under a MATLAB software in 2D configuration space. It represents an improvement in path generated as shown in Fig. 5. The black and green node represents the starting and target position, respectively. The curve denoted the path planned in 5000 iterations, and each dot represents a single iteration. The maximum or minimum time required to complete a single iteration is about, 0.2 and 0.03 s (Figs. 3 and 4).

The second problem is to approach the path planning for a multiple UAVs with the help of RRT algorithm, where the multiple path planning of multiple UAVs is done in 2D configuration space (with a high-dimensional formation, in a kinodynamic environment). Path forming by a multiple UAVs are different in color, moving symmetrically without colliding with each other. There are around five path planning has been done between UAVs, with 5000 in iterations.

4 Conclusion

In this paper, RRT algorithm has been modified to solve the problem for multiple path planning of UAVs in 2D configuration space, where it got an appropriate result for an optimal path planning for multiple autonomous. UAVs have been based on RRT by using RRT algorithm, which helps to form path planning for multiple UAVs

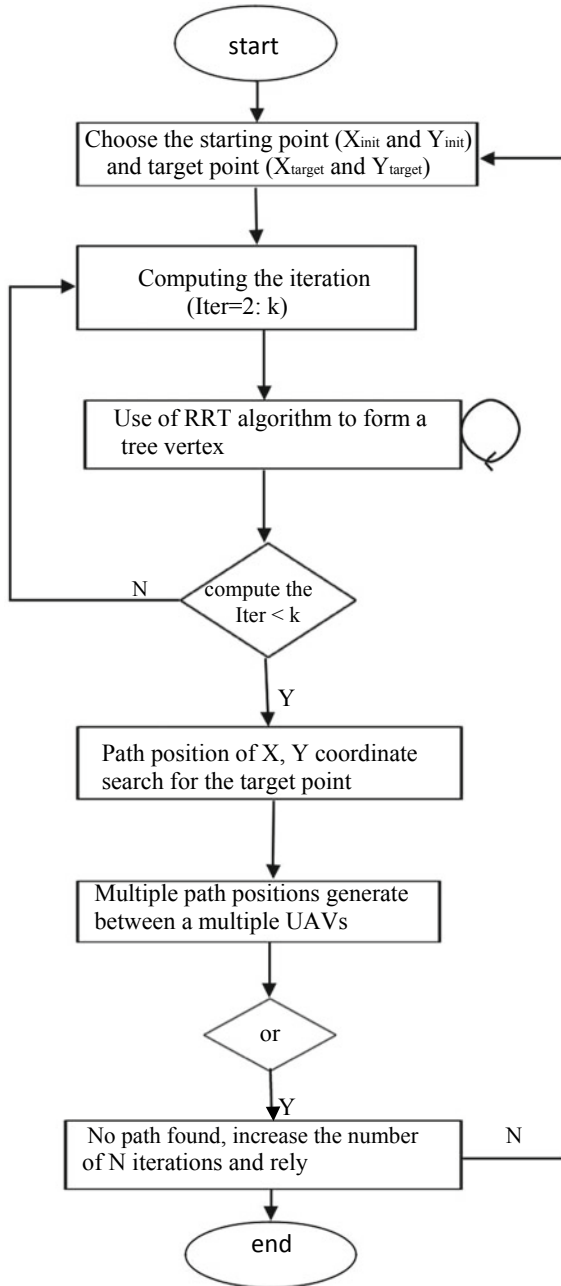


Fig. 2 Flowchart of multiple path planning for UAVs

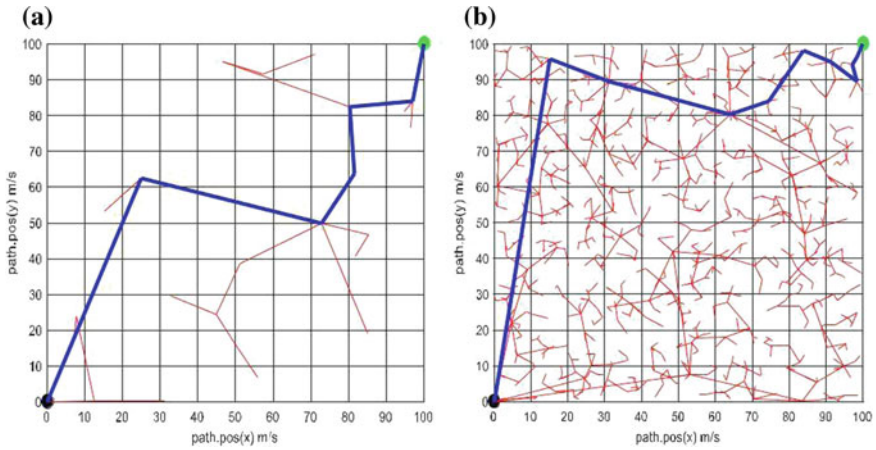


Fig. 3 a, b Represents a path planning of RRT algorithm where the black node is the starting point and the green node is the target point, as shown in the figure every time, the path change in every iteration because nodes help in generating the path planning

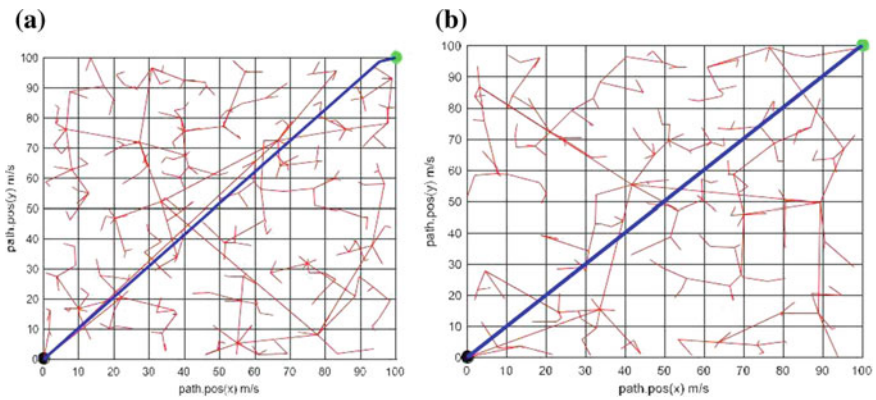


Fig. 4 a, b Represents an improvement in RRT algorithm, as shown that there is no change in the path planning of a UAV, the starting and target nodes are same and configuration space is the same and same path with optimal formation of path take place because reduces the length of tree vertex and the convergence of tree vertex take place

without colliding with each other, generate the minimum distance between the nodes, and also help to give an optimal path trajectory. The improvement has been done in the RRT algorithm to generate a path with minimum distance and the same path for each iteration. In future scope, the obstacle has been formed in the RRT algorithm for 2D configuration space, where to avoid the obstacles of multiple path planning for multiple UAVs by using RRT algorithm.

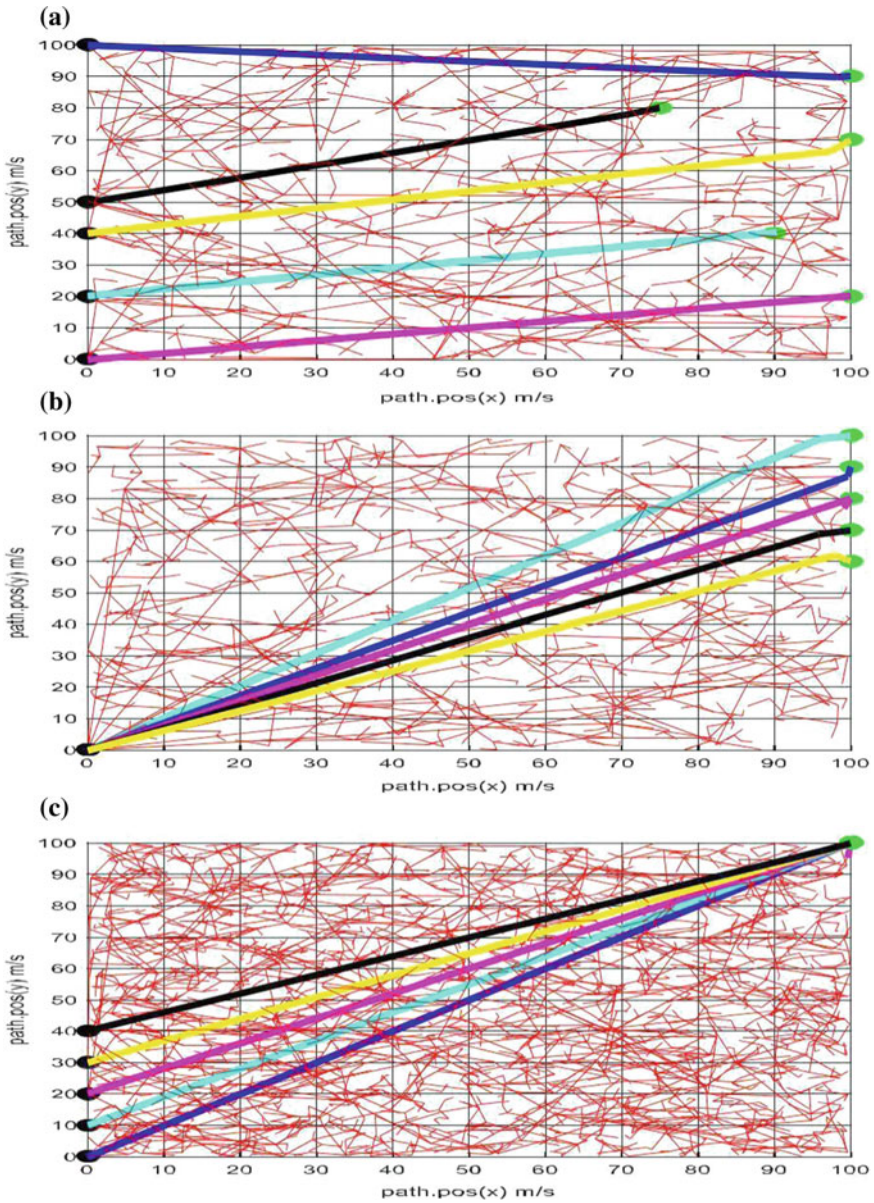


Fig. 5 a–c Represents multiple path planning of UAVs Here, the black color is the starting node and the green color is the destination nodes for a UAVs in a 2D configuration space. The multiple path formations with differences in color, these all path are not colliding from each other (if there are less or more distances) or allowed the UAVs to move from the same point and move to the different destinations or allowed the UAVs to move from the different starting point to the same destination. In each case, the path generated by multiple UAVs is not colliding with each other and form the optimal trajectory

References

1. LaValle SM (1998) Rapidly-exploring random trees: a new tool for path planning. *J Article(In)* 129
2. Peng H, Su F, Bu YL, Zhanga GZ, Shen LC (2009) Cooperative area search for multiple UAVs based on RRT and decentralized receding horizon optimization. In: *Proceedings of 7th Asian control conference, Hong Kong, China, 27–29 Aug 2009*, pp 298–303
3. Kothari M, Postlethwaite I, Gu DW (2009) Multi-UAV path planning in obstacle rich environment using rapidly-exploring random trees. In: *Joint 48th IEEE conference in decision and control and 28th Chinese control conference, Shanghai, P. R. China, 16–18 Dec 2009*, pp 3069–3074
4. Kala R, Warwick K (2011) Planning of multiple autonomous vehicles using RRT. In: *The 10th IEEE international conference on cybernetic intelligent systems (CIS), London, UK, 1–2 Sept 2011*
5. Lee HC, Yaniss T, Lee BH (2012) Grafting: a path replanning technique for rapidly-exploring random trees in dynamic environments. *Adv Robot* 26:123–141
6. Zhen Z, Gao C, Zhao Q, Ding R (2014) Cooperative path planning for Multiple UAVs Formation. In: *The 4th annual IEEE international conference on cyber technology in automation, control and intelligent systems, Hong Kong, China, 4–7 June 2014*
7. Alejo D, Cobano JA, Heredia G, Ollero A (2015) Collision-free trajectory planning based on maneuver selection-particle swarm optimization. In: *International conference on unmanned aircraft systems (ICUAS), Denver Marriott Tech Center, Denver, Colorado, USA, 9–12 June 2015*
8. Yang L, Qi J, Song D, Xiao J, Han J, Xia Y (2016) Survey of robot 3D path planning algorithms. *J Control Sci Eng* 2016 (Article ID 7426913)

Coal Mine Rescue Robot Simulation Using V-Rep and Python



Preeti Rani and Nathi Ram Chauhan

Abstract Coal mines are very dangerous working places for human beings let it be the workers or rescue team personnel. It is very urgent but risky also to enter the mine tunnels in case of disaster for the rescue team personnel due to lack of information about the environmental conditions of the disaster sites and a large number of rescue operations have resulted in numerous fatalities in coal mines. Rescue robots can be designed to navigate the rescue personnel around the disaster site and at the same time monitor/update the environmental data on real-time basis to command center. This paper introduces a coal mine surveillance robot, which is designed in such a way that it can navigate around the mine/sites and keep updating the information to the command center/rescue team using the sensors deployed on the robot on real-time basis. Smoke detection along with gas detection is done with high precision and can activate alarm after breaching safe/preset level.

Keywords Coal mine robots · V-rep · Python · Robot sensor · Security detection

1 Introduction

Coal mines are basically of two types—underground and opencast. Underground tunnels outnumber open cast but they are more prone to disasters. Gas (carbon dioxide, carbon mono oxide, methane, and poisonous gases) leakage and explosions are the two biggest threat to workers engaged in mining. They are the biggest threat even to the rescue team personnel as situation changes instantaneously inside the tunnel. The recent fatality statistics, for both underground as well as opencast mining operations worldwide, point out that the most serious risk to the personnel is from different environmental mining conditions, especially that from the inaccessible areas of the mines where regular systematic monitoring and maintenance operations are difficult. These situations can be tackled effectively if the surveillance task is accomplished

P. Rani (✉) · N. R. Chauhan
Department of Mechanical and Automation Engineering, Indira Gandhi Delhi Technical University for Women, New Delhi, Delhi, India
e-mail: preetiarya.1120@gmail.com

by a robot, which can monitor the environmental conditions on real-time basis and keep updating the command center/rescue team through continuous exchange of information.

2 Related Work

Gao et al. [1] presented coal mine detection robot, fully or partially, replacing emergency workers from entering mine shaft disaster site, and detect several sorts of hazardous gases and monitor environmental conditions. Tenreiro Machado et al. [2] presented the progress and state of the art in the field of legged locomotion system in three phases where the first phase was about mobile robot, second phase considered history of the legged robot, and the third phase compared the performance of legged robot. Jianhua [3] presented a paper for developing a hexapod robot with 42 degrees of freedom giving omnidirectional movement after understanding the gaits mechanism of the hexapod robot with six degrees of freedom of an articulated leg model in uneven terrain and aspects of adapting different obstacles. In this paper, the simulation is done for tripod gait of hexapod robot while kinematic analysis is done for angular displacement, velocity, and acceleration of each joint of each leg. Gulati et al. [4] found several issues faced by rescue teams and addressed them using how Bluetooth or Wi-Fi-controlled robot can be used for saving people after natural disasters. The paper put forward the benefits of using Bluetooth or Wireless-controlled robots over the presently used remote-controlled robots. The proposed robot with some advancement can be used where exploration and navigation is hazardous for human life, like in coal mines and nuclear plants, etc. Zhigang et al. [5] presented coal mine detection robot, which can be used in the place of emergency workers to enter the mine tunnel disaster site to avoid endangering lives of the rescue team and also detect several sorts of hazardous gases and survey environmental conditions. Manoiu-Olaru et al. [6] explored thoroughly in order to determine the locomotion of a hexapod robot for different obstacles in various applications and presented a sequence of simulations done on MATLAB. Denavit–Hartenberg algorithm is used to do the direct and inverse geometrical model of the leg and the structure of the robot. He et al. [7] presented a control technique, which is able to control robot motion and transmit live video feed, temperature data, humidity, and gas concentration using multiple sensors mounted on robot. The paper also explained exchange of information on real-time basis. Kulkarni et al. [8] designed a reliable four-wheeled monitoring robot based on Android operating system, using an Android UNO microcontroller and smartphone. Monitoring robot needs features of a video camera, a GPS module, and GSM radios. Android smartphone comes up with all features required for the surveillance. This paper also describes the control method of robot and captures the live data from the robot. Zak et al. [9] demonstrated the design, construction, and control technique of a hexapod walking robot with six legs. Introduction part of the paper elaborated the main features of legged robots, along with pros and cons of the existing robots. Basic gaits used by legged robots for their locomotion are also mentioned.

3 Methodology and Implementation

The complete simulation and the results are obtained on the V-rep software with Python programming integration with the V-rep software. We are utilizing the V-rep simulation environment and the logical coding is done on the Python. There is a module of Python named V-rep, which is to be installed and imported as a module in the Python script to start coding for the simulation.

The wheeled robot which is called a bot is taken from the module. Various sensors along with camera and control units are integrated with the bot and simulated using the V-Rep environment as shown in Fig. 1. An environment is created in V-rep where we place the bot and start coding for the simulation, after which bot enters into the tunnel and navigate and detect several gases and smoke. The robot working in terms of sensing the dangerous conditions like gases and smoke is described in the diagram in Fig. 1. The robot housing is designed in a way to protect all sensitive equipments like microcontroller and sensors.

Figure 2 shows the block diagram of the working of robot. The primary motive of the simulated robot is to keep on sensing the physical environment of its nearby areas using the sensors embedded in it and as soon as any dangerous situation comes up, as per the sensor reading, it should trigger the alarm and send the data to the appropriate place. The sensor placement on the robot is done in a protected manner so that any environmental condition should not affect its functioning and sensors should operate in an effective manner to update the present condition of the place. The controller is responsive enough to respond to the sensor input and generate the alarm within seconds.

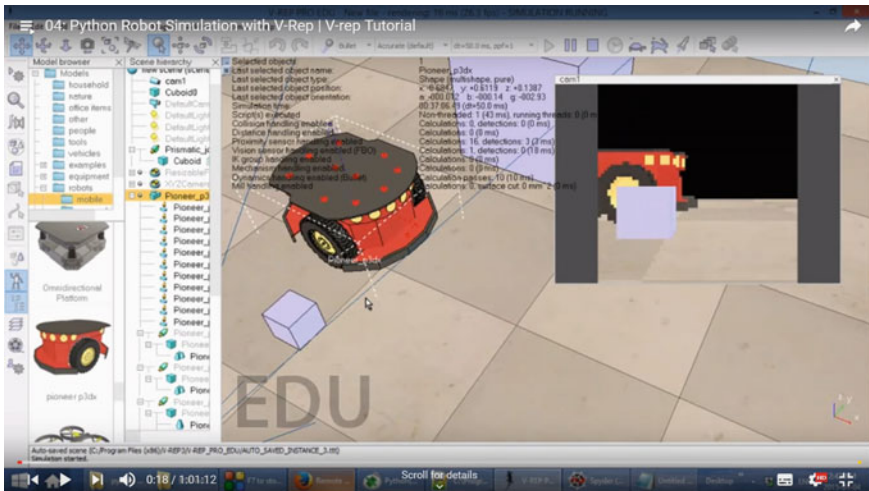
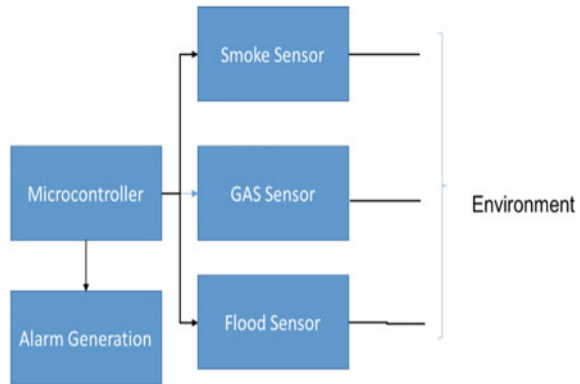


Fig. 1 Wheeled mine detector robot

Fig. 2 Block diagram of working of robot



4 Results and Experimentation

All the results and experimentation is done on the V-rep software with Python programming interfacing using Python (x, y) module. The simulation environment is created in the V-rep with the wheeled robot and incorporating sensors on the robot for detection of the various gases and smoke.

Figure 3 illustrates the complete simulation environment of the field where in the smoke and the various other possibilities of the hazardous conditions are generated on a timely basis. The field is simulated with some terrain and some water portions and some of the smoky areas. This environment is created in V-rep software to illustrate the robot robustness, and all type of hazardous conditions is manually generated in different areas of the field. The robot strolls through the complete area of the field and as soon as any preset condition comes in front of the robot, the respective sensor gets activated and triggers the alarm condition.

Figure 4 shows the Python interface where in all the logical coding part is done in the V-rep simulating environment. The coding of the robot movement and sensor value reading along with alarm activation is done in Python. All the coding of robot microcontroller is done in Python x, y environment. The Python code is certainly acting as a core part of the robot control.

Figures 5 and 6 displays the variation of the intensity. As the intensity of smoke increases the variation in the sensor reading changes and the alarm generation gets activated as per the threshold set. Robot movement in the complete field of the V-rep environment is controlled by the Python code and during the movement, the robot comes across various dangerous situations. In Fig. 6, the robot experiences the smoky environment and the smoke sensor triggers the controller with the presence of severe smoke and the microcontroller generates the alarm which, in turn, displays the red pop-up on the screen with the severity level of the smoke given by the smoke sensor.

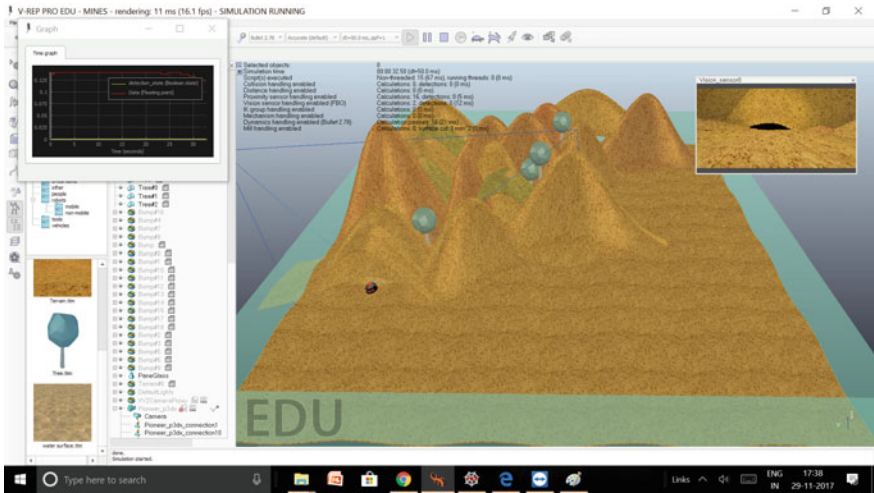


Fig. 3 V-rep simulation environment

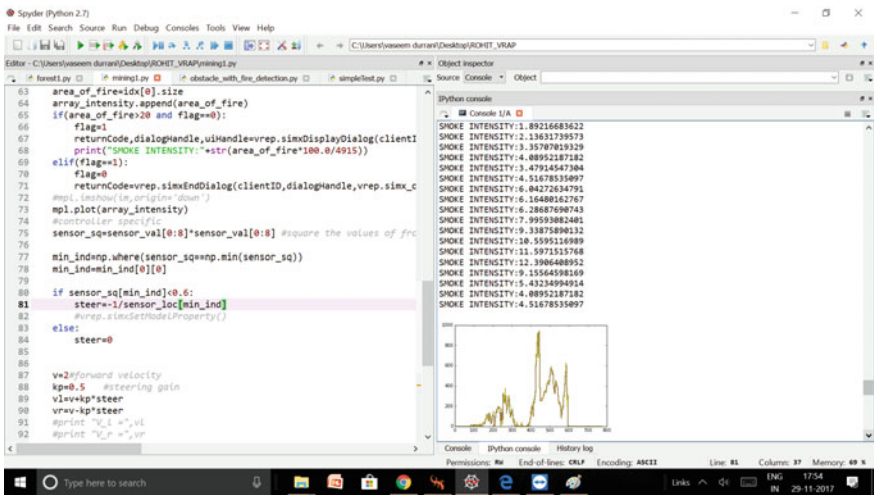


Fig. 4 Python environment

5 Conclusions

The mine detection robot is successfully simulated in the V-rep simulating environment and the Python coding environment. The triggering of the alarm generation on the increasing intensity level of the measuring condition like smoke, gas, etc., is displayed with reasonable accuracy. The work is done on the wheeled robot and till now, all the simulations have been done on wheeled robot. Sometimes, the condition

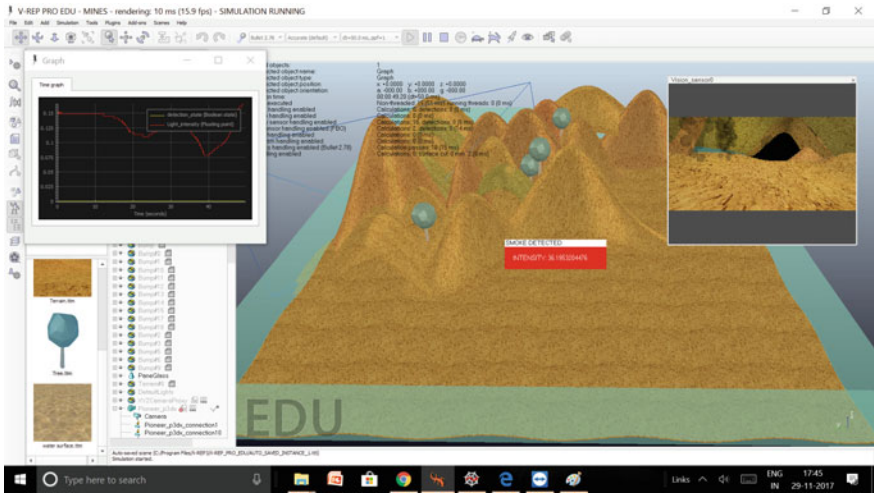


Fig. 5 Smoke detection alarm generation 1 with run time intensity

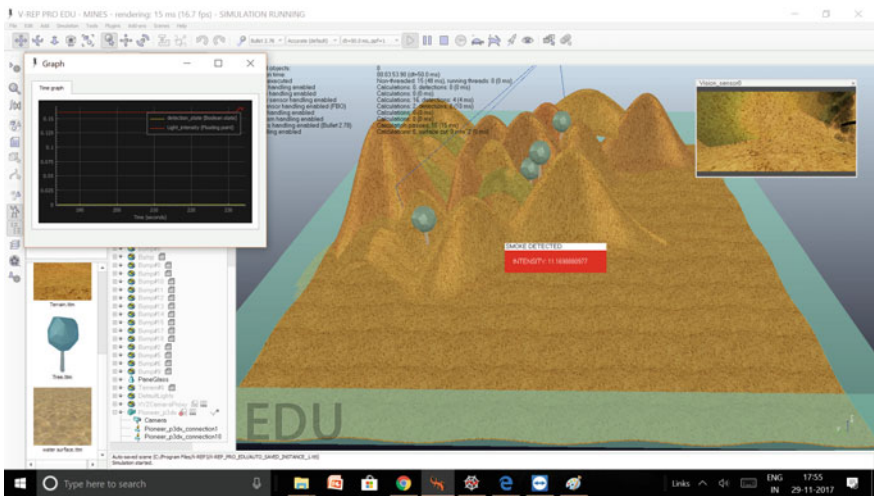


Fig. 6 Smoke detection alarm generation 2 with run time intensity

of the surface restricts the movement of wheeled robot. So, to avoid the restrictions imposed by surface conditions on wheeled robot, we can incorporate legged robot using all the sensors on it. Second, we can connect our wheeled robot with the cloud server so that the monitoring can be done on any device like the PC, phones, or the tablets.

References

1. Gao J, Gao X, Zhu J, Zhu W, Wei B, Wang S (2009) Coal mine detect and rescue robot technique research. In: Proceedings of the 2009 IEEE international conference on information and automation, Zhuhai/Macau, China, pp 1068–1073
2. Tenreiro Machado JA, Silva MF (2013) An overview of legged robots. Research Gate. <https://www.researchgate.net/publication/258972509>
3. Jianhua G (2006) Design and kinematic simulation for Six-DOF leg mechanism of hexapod robot. In: Proceedings of the 2006 IEEE international conference on robotics and biomimetic, Kunming, China, pp 625–629
4. Gulati H, Vaishya S, Veeramachaneni S (2011) Bluetooth and Wi-Fi controlled rescue robots. In: 2011 annual IEEE on India conference
5. Zhigang N, Lu W (2011) Hazardous gas detecting method applied in coal mine detection robot. In: Third international conference on measuring technology and mechatronics automation, Taiyuan, China, pp 308–311
6. Manoiu-Olaru S, Nitulescu M (2012) Hexapod robot locomotion over typical obstacles. In: 2012 IEEE international conference on automation quality and testing robotics, Craiova, Romania
7. He Zhenjun, Zhang Jiang, Peng Xu, Qin Jiaheng, Zhu Yunkai (2013) Mine detecting robot based on wireless communication with multi-sensor. IEEE, China
8. Kulkarni C, Grama S, Suresh PG, Krishna C, Antony J (2014) Surveillance robot using arduino microcontroller, android APIs and the internet. In: 2014 first international conference on systems informatics, modelling and simulation. IEEE, Manglore, India, pp 83–87. <https://doi.org/10.1109/sims.2014.25>
9. Zak M, Rozman J (2015) Design, construction and control of hexapod walking robot. In: IEEE 13th international scientific conference on informatics 2015, Poprad, Slovakia, pp 302–307

Characterisation and Zeta Potential Measurements of CuO–Water Nanofluids



Vinay Singh and Munish Gupta

Abstract Nanofluids have emerged as a potential new-generation heat transfer fluids comprising of solid nanoparticles having typical sizes (1–100 nm) suspended in base fluids. The heat transfer characteristics of nanofluids are significantly influenced by thermophysical properties. In this work, CuO–H₂O nanofluids were synthesized characterized and zeta potential was measured using Malvern zetasizer. Different weight concentrations (0.02, 0.05, 0.1, 0.2, and 0.5 wt%) of nanofluids were synthesized and their effect of concentration on thermal conductivity was examined. Cetyl trimethyl ammonium bromide (CTAB) was used as a surfactant. Characterization of the nanopowder samples were performed using XRD and HRTEM. Results showed that CuO–H₂O nanofluids showed noticeable increment in the thermal conductivity when compared with water. Zeta potential results also showed that nanofluids are quite stable except the 0.5 wt%.

Keywords Nanofluids · CuO nanoparticles · Characterization · HRTEM · Zeta potential

1 Introduction

In recent times, because of the developments in the field of nanotechnology and surface science, the researches on nanofluids have been carried out in a active manner. Particles with nanometre size dispersed in base fluids (engine oil, water, ethylene glycol, kerosene oil, and propylene glycol) are termed as nanofluids [1]. These nanometric-sized particles showed great potential in several applications because of long-term stability, high thermal conductivity, and sedimentation reduction [2–4]. The researchers [5–12] have used different types of metals, ceramics, oxides, and nitrides (Ag, CuO, Al₂O₃, ZnO, CNT, TiO₂, SiO₂, ND, Ni, AlN, Fe₂O₃, etc.) for the preparation of nanofluids.

V. Singh (✉) · M. Gupta
Guru Jambheshwar University of Science & Technology, Hisar 125001, Haryana, India
e-mail: theahlawat89@gmail.com

© Springer Nature Singapore Pte Ltd. 2019
M. Kumar et al. (eds.), *Advances in Interdisciplinary Engineering*, Lecture Notes in Mechanical Engineering, https://doi.org/10.1007/978-981-13-6577-5_72

741

2 Materials and Methods

2.1 Materials

Nanoparticles used in the study were copper oxide purchased from High Purity Chemicals Limited (HPCL), India and were used as such without any purification. Mean particle size was <80 nm and specific surface area was >13 m²/g as per the information provided by the supplier.

2.2 Methods

2.2.1 Characterization of Nanoparticles

The crystallinity of the CuO nanoparticles was studied using X-ray diffractometer (make Rigaku MiniFlex X-ray diffractometer) at GJUS&T, Hisar to obtain the X-ray diffraction pattern of nanoparticles samples. The analysis was performed at 30 kV and 15 mA having scanning range -2 to 140° (2θ), scanning speed 0.01–1000/min (2θ), and minimum step width of 0.01° (2θ). High-Resolution Transmission Electron Microscopy of CuO nanoparticles were carried out using a FEI, Technai G2 instrument operating at an accelerating voltage of 200 kV at NIPER, Mohali.

2.2.2 Nanofluids Formulation

CuO–water nanofluids were synthesized by using two-step method with the help of bath ultrasonication and probe sonicator at Department of Bio and Nanotechnology, GJUS&T, Hisar. Predetermined amount of CuO was taken as per weight concentration. This amount was mixed with the surfactant solution using ultrasonic probe. For CuO/water nanofluid, samples of five different concentrations ranging from 0.02, 0.05, 0.1, 0.2, and 0.5 wt% were prepared using distilled water and surfactant Cetyl trimethyl ammonium bromide (CTAB). Samples were also magnetically stirred for about 2 h and subsequent ultrasonication for about 3 hours was done to ensure proper mixing of the nanofluids. In order to measure the thermal conductivity of the nanofluids, KD2 Pro was used. Measurements were conducted in the temperature range of 30–80 °C.

3 Stability of Nanofluids

Stability factor is utmost crucial in nanofluids as it can change the thermophysical properties of the nanofluid for several applications. They lose their heat transfer ability because of their proneness to agglomeration. Zeta potential is one of the best methods used for stability evaluation and enhancement for nanofluids. Zeta potential of CuO–water nanofluids was measured in the Department Of Bio and Nanotechnology at GJUS&T, Hisar using Zetasizer (Nano ZS, Malvern Instruments, 7.1) that works upon the principle of dynamic light scattering (DLS). Zeta Potential was measured at a temperature of 25 °C.

3.1 Zeta Potential

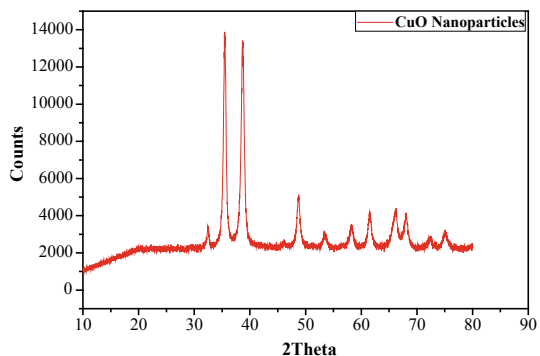
As per the electrophoresis theory, the repulsive force between the two particles is measured by zeta potential (ζ). It can be increased or decreased by controlling the pH value of the fluid. For excellent stability, the value of ζ must exceed 60 mV. For physically stable, the value must be above 30 mV. Limited stability is observed in the fluids having values below 20 mV, whereas below 5 mV undergoes agglomeration.

4 Results and Discussions

4.1 Complete Morphology and Crystalline Structure of Nanoparticles

Figure 1 shows the X-ray diffractogram of CuO nanopowder samples. Sharp peaks show the high crystalline nature of these nanoparticles. Figure 2a–d shows the HRTEM images of CuO nanopowder samples at various magnifications. Thermal

Fig. 1 XRD patterns of CuO nanopowder sample



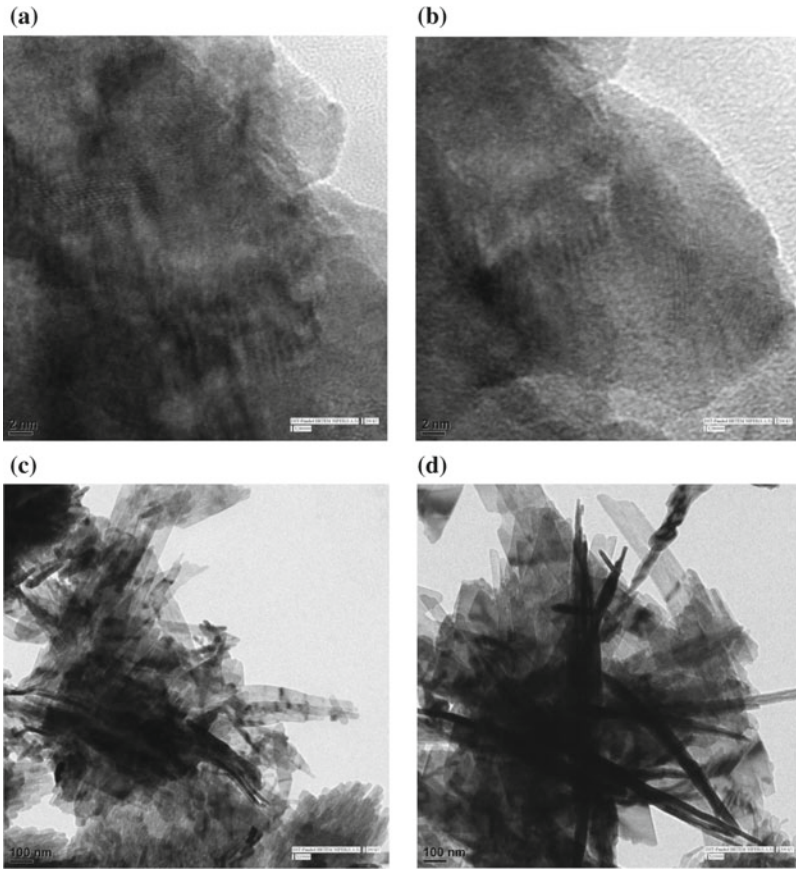


Fig. 2 a–b HRTEM images of CuO nanopowder sample at 2 nm magnifications and c–d images at 100 nm magnifications

Fig. 3 Thermal conductivity enhancement using CuO nanofluids

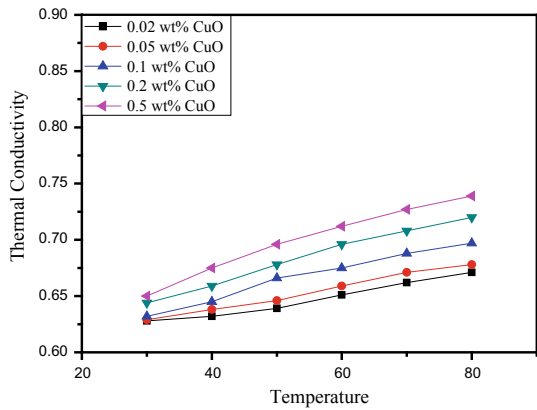
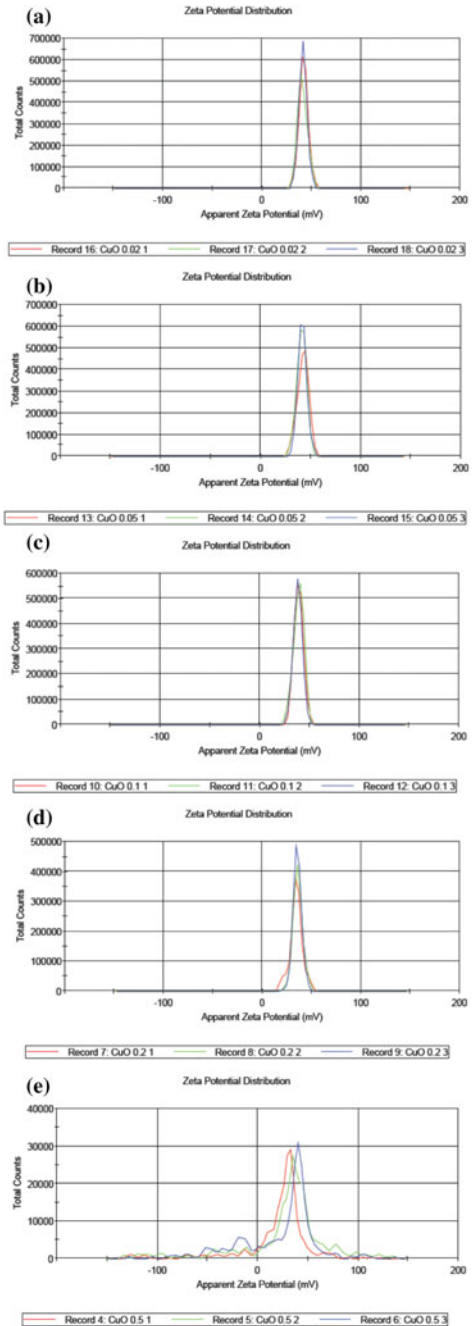


Fig. 4 **a** Zeta potential values of nanofluids at 0.02 weight concentration. **b** Zeta potential values of nanofluids at 0.05 weight concentration. **c** Zeta potential values of nanofluids at 0.1 weight concentration. **d** Zeta potential values of nanofluids at 0.2 weight concentration. **e** Zeta potential values of nanofluids at 0.5 weight concentration



conductivity enhancement of nanofluid with different weight concentrations is shown in Fig. 3. Zeta potential is shown in Fig. 4a–e for different weight concentrations. Nanofluids with particle loading of 0.02, 0.05, 0.1, 0.2, and 0.5 wt% shows the values of zeta potential equal to 42, 42.1, 38.9, 34.3, and 15.5, respectively.

5 Conclusions

In this study, CuO–water nanofluids were prepared at different concentrations and were characterized using different techniques. The experimental methods used in present investigations show good crystal structure and high purity.

The key conclusions are:

- XRD graphs show good crystalline nature of nanopowder samples.
- Thermal conductivity enhances on increasing the weight concentration of nanofluids.
- Zeta potential forms an important basis for selecting the conditions of dispersing particles. 0.02 wt% nanofluids shows best zeta potential, whereas 0.5 wt% nanofluids show the least zeta potential.

Acknowledgements The author Munish Gupta, Associate Professor, Department of Mechanical Engineering, GJUS&T, Hisar is highly thankful for the grant by University Grant Commission (UGC), Government of India, under Major Research Project wise Sanction letter no. 43-445/2014/(SR) dated 30.09.2015. The author also acknowledges the grant received under DST PURSE wise letter no. CIL/2017/364 dated 22.06.2017.

References

1. Choi SUS, Eastman JA (1995) Enhancing thermal conductivity of fluids with nanoparticles. No. ANL/MSD/CP–84938; CONF-951135–29. Argonne National Lab., IL (United States)
2. Kulkarni DP, Das DK, Vajjha RS (2009) Application of nanofluids in heating buildings and reducing pollution. *Appl Energy* 86(12):2566–2573
3. Akhavan-Behabadi MA, Shahidi M, Aligoodarz MR, Fakoor-Pakdaman M (2016) An experimental investigation on rheological properties and heat transfer performance of MWCNT-water nanofluid flow inside vertical tubes. *Appl Therm Eng* 106:916–924
4. Manasrah AD, Al-Mubaiyedh UA, Laui T, Ben-Mansour R, Al-Marri MJ, Almanassra IW, ..., Atieh MA (2016) Heat transfer enhancement of nanofluids using iron nanoparticles decorated carbon nanotubes. *Appl Therm Eng* 107:1008–1018
5. Xuan Y, Li Q (2003) Investigation on convective heat transfer and flow features of nanofluids. *J Heat Transfer* 125(1):151–155
6. Pak BC, Cho YI (1998) Hydrodynamic and heat transfer study of dispersed fluids with submicron metallic oxide particles. *Exp Heat Transf Int J* 11(2):151–170
7. Azmi WH, Sharma KV, Sarma PK, Mamat R, Anuar S, Sundar LS (2014) Numerical validation of experimental heat transfer coefficient with SiO₂ nanofluid flowing in a tube with twisted tape inserts. *Appl Therm Eng* 73(1):296–306

8. Duangthongsuk W, Wongwises S (2010) An experimental study on the heat transfer performance and pressure drop of TiO₂-water nanofluids flowing under a turbulent flow regime. *Int J Heat Mass Transf* 53(1–3):334–344
9. Sundar LS, Singh MK, Bidkin I, Sousa AC (2014) Experimental investigations in heat transfer and friction factor of magnetic Ni nanofluid flowing in a tube. *Int J Heat Mass Transf* 70:224–234
10. Sundar LS et al (2012) Experimental investigation of forced convection heat transfer and friction factor in a tube with Fe₃O₄ magnetic nanofluid. *Exp Therm Fluid Sci* (37):65–71
11. Singh V, Gupta M (2016) Heat transfer augmentation in a tube using nanofluids under constant heat flux boundary condition: a review. *Energy Convers Manag* 123:290–307
12. Gupta M, Singh V, Kumar R, Said Z (2017) A review on thermophysical properties of nanofluids and heat transfer applications. *Renew Sustain Energy Rev* 74:638–670

Analytical Model to Predict the Dislocation at Different Interfaces in Thin-Film Multilayer: Application to LED Multi-quantum Well (MQW)



Mishra Dhaneshwar, Seo Youjeong and Pak Y. Eugene

Abstract The analytical model to predict the density of misfit dislocations at different interfaces in a piezoelectric multilayer with two thin-film layers deposited on a thick substrate has been formulated considering the two-stage relaxation with the aim to generalize further for the multilayer system in future. Different lattice parameters of the film layers and the substrate give rise to high misfit strain. Misfit dislocation formation at the interface releases excessive misfit strain. The internal energy of the piezoelectric thin film at the critical thickness and after relaxation through ‘ n ’ number of misfit dislocations together with the energy of the misfit edge dislocation have been utilized to develop the formulation. This formulation has been used to estimate dislocation density at the interface of the gallium nitride film layer with various cases of misfit strains. It has rightly predicted higher dislocation density for higher misfit strain cases as well as for greater film thickness. It will be used to predict the dislocation densities at the gallium nitride–indium gallium nitride interface and the sapphire–gallium nitride interface of the LED device in future. The theoretical model developed in this work can be beneficial in estimating the optoelectronic performance of the LED devices correctly in the presence of defects. The model can also be helpful in developing strategies to reduce the dislocation density by accurately predicting them for the given misfit strain in the film.

Keywords Thin-film multilayer · Lattice misfit strain · Misfit dislocation · Dislocation density · LED multi-quantum well (MQW) · Optoelectronic performance

M. Dhaneshwar
Department of Mechanical Engineering, Manipal University Jaipur, Rajasthan 303007, India

M. Dhaneshwar · S. Youjeong · P. Y. Eugene (✉)
Advanced Institutes of Convergence Technology, Seoul National University, Suwon 443-270,
South Korea
e-mail: genepak@snu.ac.kr

1 Introduction

Gallium nitride (GaN)-based LEDs are popular due to their optoelectronic performances. These devices are fabricated by depositing multilayers of thin films on thick foreign substrates such as sapphire/silicon. High lattice mismatch between the multi-quantum well thin-film layers and the substrate material generates high misfit strain. The high magnitude of the in-plane strains in the multi-quantum well films is released by the formation of defects such as dislocations. These devices have threading and misfit dislocations in the order of 10^8 – 10^{10} cm^{-2} [1, 2]. It is essential to understand the strain relaxation mechanisms and thereby quantify the defect density in these devices to correctly predict the device performance, as well as to take necessary measures to reduce the defects. There are some works available in the literature to estimate the dislocation density for a film layer deposited on a thick substrate [3, 4]. The authors also developed the dislocation density model at the interface of indium gallium nitride film grown on gallium nitride substrate [5]. These models are the single film layer model, therefore, do not consider multistage relaxation, which occurs when more than one thin-film layers are deposited on a substrate. There are some works strain relaxation mechanisms in the thin-film multilayers [6–8], but they do not provide any theoretical formulation to estimate dislocation density. Holec [3] has discussed a very preliminary analytical model to predict the critical thicknesses for different percentage of indium nitride in the quantum well layer of the multi-quantum well in his Master's thesis. In his model, different layers of the multi-quantum well have been considered isotropic, and only Poisson's ratio has been used as the material property. Moreover, Holec [3] has not discussed the dislocation densities at different interfaces of the multi-quantum well.

Considering the importance of correctly predicting dislocation density for the optoelectronic devices, such as LED multi-quantum wells and absence of such model in the literature, we have developed a theoretical model to predict the dislocation density in a piezoelectric multilayer of two film layers with hexagonal crystal lattice deposited on a thick sapphire substrate. The c -axis of the hexagonal crystal is considered in the thin-film growth direction. The source of the misfit strain in the thin-film layers is the lattice mismatch between the following layers has been taken into account in the formulation. The concept of multistage relaxation of misfit strain has been considered. The theoretical formulation will further be developed and utilized to predict the misfit dislocation densities in a layer model in future.

2 Piezoelectric Multilayer Thin Film

We consider the piezoelectric film layers each having thickness, t_i ($i = 0, 1, 2, \dots, n$), are bonded together as shown in Fig. 1 [10]. The coordinate system is defined such that the bottom surface of the first layer is located at $z = 0$, the top surface of the top layer is at $z = h_n + 1$, and the interface between layers i and $i + 1$ is located at $z = h_i + 1$. The relationship between h_i and t_i can be expressed as [10]

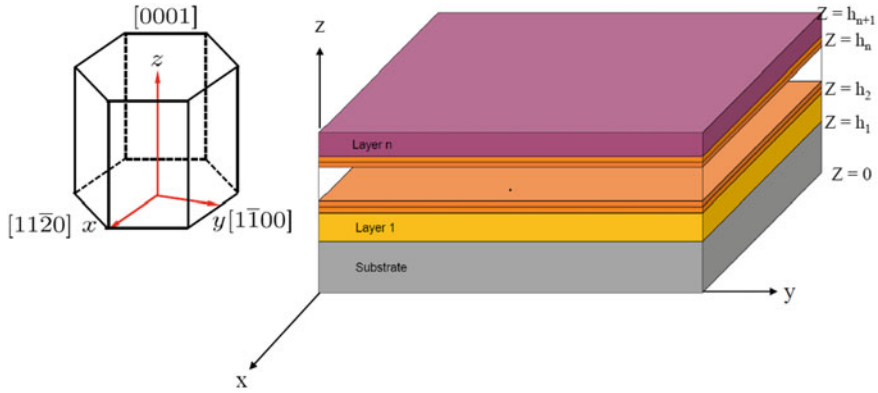


Fig. 1 Schematic representation of hexagonal crystal and ‘n’ layers of film deposited on a substrate

$$h_i = \sum_{j=0}^{i-1} t_j \quad (i = 1 \text{ to } n + 1). \tag{1}$$

The LED multi-quantum wells (MQWs) are fabricated by nitride-based gallium nitride and indium gallium nitride materials. The constitutive relations are expressed for the piezoelectric materials with *z*-direction as *c*-axis exhibiting transversely isotropic behavior (hexagonal symmetry) [11]. The LED multi-quantum well has the structure of translational symmetry. Therefore, the shear components of the stresses and strains are vanished [3]. Zero shear stresses and strains lead to vanishing the electric field and the electric displacement components, E_x, E_y and D_x, D_y , respectively. After discarding these stresses, strains, electric fields, and electric displacement components, the constitutive relations relating the normal stresses and the electric displacement along *z*-direction with normal strains and electric field along *z*-direction in the *i*th layer of the hexagonal piezoelectric multilayer can be expressed as [12]

$$\begin{Bmatrix} \sigma_{xx}^i \\ \sigma_{yy}^i \\ \sigma_{zz}^i \\ D_z^i \end{Bmatrix} = \begin{bmatrix} c_{11}^i & c_{12}^i & c_{13}^i & -e_{31}^i \\ c_{12}^i & c_{11}^i & c_{13}^i & -e_{31}^i \\ c_{13}^i & c_{13}^i & c_{33}^i & -e_{33}^i \\ e_{31}^i & e_{31}^i & e_{33}^i & \kappa_{33}^i \end{bmatrix} \begin{Bmatrix} \varepsilon_{xx}^i \\ \varepsilon_{yy}^i \\ \varepsilon_{zz}^i \\ E_z^i \end{Bmatrix} + \begin{Bmatrix} 0 \\ 0 \\ 0 \\ P_{sp}^i \end{Bmatrix}. \tag{2}$$

Here, σ_{xx}, σ_{yy} , and σ_{zz} , are the normal stress components while $\varepsilon_{xx}, \varepsilon_{yy}$, and ε_{zz} are the normal strain components in *x*-, *y*-, and *z*-directions, respectively. D_z and E_z are the electric displacement and the electric field components along *z*-direction, whereas c_{11}, c_{12}, c_{13} , and c_{33} are the elastic constants, e_{31} and e_{33} are piezoelectric constants while κ_{33} is the dielectric constant and P_{sp} is the spontaneous polarization along the *c*-axis of the crystal.

3 Misfit Dislocation Density Prediction Model

We would like to consider a piezoelectric multilayer thin film made up of consecutive layers of gallium nitride, and indium gallium nitride deposited on a thick sapphire substrate. The sapphire substrate and the gallium nitride and indium gallium nitride films have transversely isotropic material properties (hexagonal symmetry). The multilayer is supposed to be grown in c -growth orientation, i.e., the plane of growth is isotropic. The lattice mismatch between the substrate and the film layers give rise to the misfit strain in the film layers. The excessive misfit strain in the film layer is released by the formation of the misfit dislocation at the interfaces. These misfit dislocations at the interfaces are the anisotropic edge dislocations with Burger's vector in $[11\bar{2}0]$ crystal direction only for the simplicity of the analysis purpose.

3.1 Misfit Dislocation Density at the Interface of the Two-Layer System

The internal energy of the c -plane piezoelectric thin film deposited on a thick substrate can be calculated by [13]

$$E_f = \frac{1}{2}(\sigma_{ij}\varepsilon_{ij} + D_i E_i). \quad (1)$$

The plane stress condition will prevail as the thickness is very small in comparison to the in-plane directions. Therefore, the normal stress, σ_{zz} becomes zero in the absence of the externally applied load in the growth direction. Similarly, the electric displacement, D_z in the growth direction becomes zero because of the charge-free condition at the free surface. These two conditions have been utilized to evaluate the strain due to the Poisson's effect, ε_{zz} and E_z . As explained in Sect. 2, the in-plane electric displacement and electric field components, D_x, D_y and E_x, E_y , respectively, become zero in the absence of the shear stresses and shear strains. The in-plane strains $\varepsilon_{xx} = \varepsilon_{yy}$ for this growth orientation. After substitution of the stresses, strains, electric displacements and the electric field components, the internal energy of the c -plane piezoelectric film grown on a thick substrate can be calculated as [14]

$$E_f = \varepsilon_{xx}^2 A_x + \varepsilon_{xx} B_x \quad (4)$$

where

$$A_x = \frac{1}{(e_{33}^2 + c_{33}\kappa_{33})} [(c_{11} + c_{12})(e_{33}^2 + c_{33}\kappa_{33}) + 2(e_{31}^2 c_{33} - c_{13}^2 \kappa_{33}) - 4c_{13}e_{31}e_{33}]$$

$$B_x = \frac{P_{sp}(c_{33}e_{31} - c_{13}e_{33})}{(e_{33}^2 + c_{33}\kappa_{33})}.$$

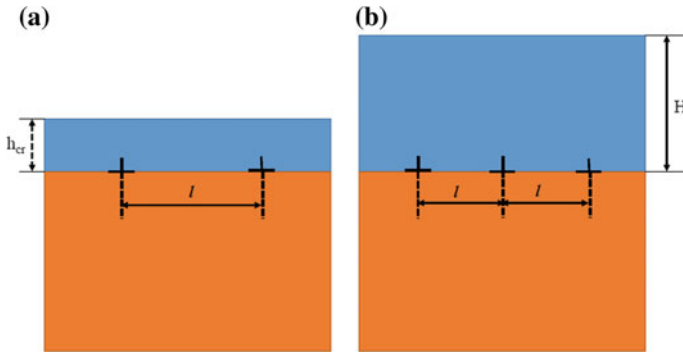


Fig. 2 Schematic representation of **a** thin-film layer of thickness ‘*h*’ deposited on a thick substrate with an array of two edge dislocations ‘*l*’ distance **b** thin-film layer of thickness ‘*H*’ deposited on a thick substrate with ‘*n*’ number of dislocations in an array

The energy of an array of two noninteracting piezoelectric dislocations with Burger’s vector b_y at a distance ‘ l ’ (Fig. 2a) lying at the interface of a film layer of thickness ‘ h ’ made up of material with a hexagonal crystal symmetry can be given as [5]

$$E_d = (\epsilon_m - \epsilon_{xx})(\alpha_x b_x^2 + \beta_x b_x q + \gamma_x q^2) \left(1 + \ln \frac{h}{b_x} \right), \tag{5}$$

where α_x , β_x , and γ_x are the numerical factors generated from the elastic, piezoelectric, and dielectric constants of the anisotropic piezoelectric dislocation [3] and q is the line charge associated with the dangling bonds. The total energy of the film of thickness h with an array of two noninteracting dislocations at the interface can be expressed as $E_T = E_f \cdot h + E_d$. The critical thickness of the film deposited on a thick substrate can be calculated by

$$\frac{\partial E_T}{\partial \epsilon_{xx}} = \frac{\partial (E_f h)}{\partial \epsilon_{xx}} + \frac{\partial E_d}{\partial \epsilon_{xx}} = 0. \tag{6}$$

When the relaxation strain, ϵ_{xx} becomes equal to the lattice misfit strain, ϵ_m ($\epsilon_{xx} = \epsilon_m$), the film thickness, h becomes the critical thickness, h_{cr} , at which the misfit dislocation forms. From Eq. 6, we can write $(\alpha_x b_x^2 + \beta_x b_x q + \gamma_x q^2)$ as

$$\alpha_x b_x^2 + \beta_x b_x q + \gamma_x q^2 = \frac{[2\epsilon_m A_x + B_x] h_{cr}}{\left(1 + \ln \frac{h_{cr}}{b_x} \right)}. \tag{7}$$

When the film has thickness $H \gg h_{cr}$ (Fig. 2b), an array of n dislocations is required to release the excessive strain in the film. The total energy of the film misfit dislocation, in this case, can be written as

$$E_T = \left[A_x (\varepsilon_m - \varepsilon_{\text{relax}})^2 + B_x (\varepsilon_m - \varepsilon_{\text{relax}}) \right] H + \varepsilon_{\text{relax}} \left(\alpha_x b_x^2 + \beta_x b_x q + \gamma_x q^2 \right) \left(1 + \ln \frac{H}{b_x} \right). \quad (8)$$

Here, $\varepsilon_{\text{relax}}$ is the strain relaxation in the film due to the formation of an array of n misfit dislocations at the interface. After minimization of the total energy with respect to the relaxation strain, $\varepsilon_{\text{relax}}$ and substitution of $(\alpha_x b_x^2 + \beta_x b_x q + \gamma_x q^2)$ from Eq. (7), the relaxation strain can be written as

$$\varepsilon_{\text{relax}} = \left(\varepsilon_m + \frac{B_x}{2A_x} \right) \left(1 - \frac{h_{\text{cr}}}{H} \left[\frac{1 + \ln \frac{H}{b_x}}{1 + \ln \frac{h_{\text{cr}}}{b_x}} \right] \right), \quad (9)$$

where $\varepsilon_{\text{relax}} = b_x/l$ and ' l ' is the spacing between the dislocations. The misfit dislocation density at the interface of the film of thickness, H can be expressed as

$$n = \frac{1}{l}. \quad (10)$$

The derived formulation herein Eqs. (9) and (10) are new to the extent have been derived the first time for the piezoelectric film deposited on a piezoelectric substrate. The dislocation density for a gallium nitride film deposited on a thick foreign substrate was estimated using the formulation, and it rightly predicts higher density for the case of higher misfit strain as well as for the greater film thickness. The detailed results of dislocation densities utilizing the formulation developed here at different interfaces of LED devices along with the appropriate comparisons with an elastic film layer deposited on an elastic substrate are part of another work and will be presented elsewhere.

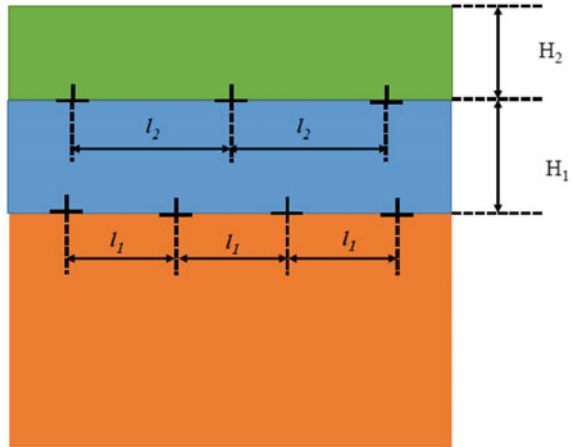
3.2 Misfit Dislocation Densities Prediction in a Three-Layer System

In this subsection, we would like to include the stage-wise relaxation in the multilayer system. Therefore, we have considered two thin-film layers deposited on a thick substrate having different densities of dislocations at two different interfaces. Here, we would like to predict the density of misfit dislocations at the interface of the second film layer with the thickness, H_2 , and the first film layer. In this case, the substrate and the first film layer can be treated as the substrate for the second film layer. The array of noninteracting dislocations is at l_2 distance apart from each other (Fig. 3).

The total energy of the film with the array of dislocations, in this case, can be expressed as

$$E_{T_2} = \left[A_{x_2} (\varepsilon_{m_2} - \varepsilon_{\text{relax}_2})^2 + B_{x_2} (\varepsilon_{m_2} - \varepsilon_{\text{relax}_2}) \right] H_2$$

Fig. 3 Schematic representation of the arrays of dislocations at different interfaces in a three-layer system



$$+ \varepsilon_{\text{relax}_2} (\alpha_{x_2} b_{x_2}^2 + \beta_{x_2} b_{x_2} q + \gamma_{x_2} q^2) \left(1 + \ln \frac{H_2}{b_{x_2}} \right). \quad (11)$$

Here, ‘2’ stands for the second layer. All other notations have the same meaning as defined previously. The minimization of Eq. (11) with respect to the relaxation strain in the second film layer can give

$$\varepsilon_{\text{relax}_2} = \frac{b_{x_2}}{l_2} = \left(\varepsilon_{m_2} + \frac{B_{x_2}}{2A_{x_2}} \right) \left(1 - \frac{h_{\text{cr}_2}}{H_2} \left[\frac{1 + \ln \frac{H_2}{b_{x_2}}}{1 + \ln \frac{h_{\text{cr}_2}}{b_{x_2}}} \right] \right). \quad (12)$$

The density of dislocation at the interface of the second and first film layer can be expressed as

$$n_2 = \frac{1}{l_2} \quad (13)$$

The relaxation required in the three-layer system considered now is the residual strain in the second film layer and the misfit strain in the first film layer. Relaxation of the remaining strain is supposed to be occurred by the formation of the array of misfit dislocations at the interface of the first film layer and the substrate. The total energy of the film and the array of misfit dislocations at the interface of the first film layer and the substrate can be expressed as

$$\begin{aligned} E_{T_1} = & \left\{ A_{x_2} [(\varepsilon_{m_2} - \varepsilon_{\text{relax}_2}) - \varepsilon_{\text{relax}_1}]^2 + B_{x_2} [(\varepsilon_{m_2} - \varepsilon_{\text{relax}_2}) - \varepsilon_{\text{relax}_1}] \right\} H_2 \\ & + \left\{ A_{x_1} (\varepsilon_{m_1} - \varepsilon_{\text{relax}_1})^2 + B_{x_1} (\varepsilon_{m_1} - \varepsilon_{\text{relax}_1}) \right\} H_1 \\ & + \varepsilon_{\text{relax}_1} (\alpha_x b_{x_1}^2 + \beta_{x_1} b_{x_1} q + \gamma_{x_1} q^2) \left(1 + \ln \frac{H_1}{b_{x_1}} \right). \end{aligned} \quad (14)$$

The minimization of the total energy given in Eq. (14) with respect to the relaxation strain, $\varepsilon_{\text{relax}_1}$ will provide the total strain relaxation at this stage which can be used to determine the dislocation density at the interface of the first film layer and the substrate.

The formulation and prediction of the dislocation density in the piezoelectric multilayer system are still in progress. The improved formulation and the dislocation density prediction studies at the different interface of the multilayer will be presented in the conference.

4 Conclusion

The density of misfit dislocations prediction model for a three-layer system has been developed as a first step in the direction of improving the dislocation density prediction model at the interfaces of the piezoelectric multilayer with ‘ n ’ number of layers having transversely isotropic material properties. A single piezoelectric multilayer grown on a thick substrate with lattice mismatch has been considered first which has further been generalized for the three-layer system and the relaxation at different stages has been adequately studied. This model will be utilized to predict the dislocation densities in LED multi-quantum well (MQW) layers in future.

Acknowledgements The Korea National Research Foundation supported this work with the grants NRF-2014M1A3A3A02034928, NRF-2016R1D1A1B03932553, and NRF-2017R1D1A1B03033267.

References

1. Mathis SK, Romanov AE, Chen LF, Beltz GE, Pompe W, Speck JS (2000) Modeling of threading dislocation reduction in growing GaN layers. *Phys Status Solidi (a)* 179:125e145
2. Tapajna M, Kaun SW, Wong MH, Gao F, Palacios T, Mishra UK, Speck JS, Kuball M (2011) Influence of threading dislocation density on early degradation in AlGaIn/GaN high mobility transistors. *Appl Phys Lett* 99:021113
3. Holec D (2006) Critical thickness calculations for $\text{In}_x\text{Ga}_{1-x}\text{N}/\text{GaN}$ Systems. Master's thesis, Selwyn College, Cambridge University
4. Romanov AE, Young EC, Wu F, Tyagi A, Gallinat CS, Nakamura S, DenBaars SP, Speck JS (2011) Basal plane misfit dislocations and stress relaxation in III-nitride semipolar heteroepitaxy. *J Appl Phys* 109:103522
5. Mishra D, Seo Y, Pak YE (2017) Dislocation density prediction model for GaN-based electronic devices. Presentation in: MRS Fall Meeting 2017
6. Dunstan DJ (1991) Geometrical theory of critical thickness and relaxation in strained-layer growth. *J Appl Phys* 70(6):3038–3045
7. Tersoff J (1993) Dislocations and strain relief in compositionally graded layers. *Appl Phys Lett* 62(7):393–695
8. Vawter GA, Myers DR (1989) Useful design relationships for the engineering of thermodynamically strained-layer structures. *J Appl Phys* 65(12):4769–4773

9. Mishra D, Pak YE (2017) Electroelastic fields for piezoelectric threading dislocation in various growth orientations of gallium nitride. *Eur J Mech A/Solids* 61:279–292
10. Gao C, Zhao Z, Li X (2015) Modeling of thermal stresses in elastic multilayer coating systems. *J Appl Phys* 117:055305
11. Berlincourt DA, Curran DR, Jaffe H (1964) Piezoelectric and piezomagnetic materials and their function in transducers. In: Mason WP (ed) *Physical Acoustic 1A*. Academic Press, New York, p 177
12. Mishra D, Lee SH, Seo Y, Pak YE (2017) Modeling of stresses and electric fields in piezoelectric multilayer: application to multi-quantum wells. *AIP Adv* 7:075306
13. Barnett DM, Lothe J (1975) Dislocations and line charges in anisotropic piezoelectric insulators. *Phys Status Solidi (b)* 67:105–111
14. Mishra D, Cho Y-H, Shim M-B, Hwang S, Kim S, Park CY, Seo SY, Yoo S-H, Park S-H, Pak YE (2015) Effect of piezoelectricity on critical thickness for misfit dislocation formation at InGaN/GaN interface. *Comput Mater Sci* 97:254–262

Surface Modified Carbon Fibre Reinforced PA6 and its Blend-Based Composites



Anurag R. Patil, S. Aparna and D. Purnima

Abstract Polyamide 6 (PA6) matrix-based composite system are widely used in automotive sector. PA6 can be directly used as matrix material, but for avoiding the moisture intake by PA6, Polypropylene (PP) has been used as a secondary polymer and PP grafted with maleic anhydride (PP-g-MA) has been used as compatibilizer. The use of carbon fibre as reinforcement increases the strength and stiffness of the composite. Laminate composites have been studied for automotive and wind turbine blade application. But, commercially injection moulding is used for making automobile components. In that case, short carbon fibre (SCF) can be used as reinforcement. In this study, the effect of surface treatment of SCF on mechanical properties of PA6 and its blend-based composites has been studied. Two types of modification have been compared viz., sizing and coupling agent. To investigate the effect of sizing and coupling agent, commercially available SCF was desized by thermal etching and then modified with suitable amount of epoxy and silane as sizing and coupling agent, respectively, and its effect on PA6 and modified PA6 matrix was studied. Mechanical properties and thermal properties of the composites were studied using tensile testing and DSC analysis. It was found that epoxy-based sizing is suitable for PA6 and silane-based coupling agent is suitable for blend-based PA6 matrix.

Keywords Polyamide 6 · Polypropylene · Short carbon fibre · Mechanical properties · Surface modification

1 Introduction

Polyamide 6 (PA6) composites are widely used for varied applications including automotive and aerospace application, due to its high toughness, strength and wear resistance in comparison to other thermoplastic matrices [1–3]. The drawback limiting the use of PA6 in higher end application is water/moisture absorption. Due

A. R. Patil · S. Aparna · D. Purnima (✉)

Department of Chemical Engineering, Birla Institute of Technology and Science-Pilani,
Hyderabad Campus, Hyderabad 500078, India
e-mail: dpurnima@hyderabad.bits-pilani.ac.in

© Springer Nature Singapore Pte Ltd. 2019

M. Kumar et al. (eds.), *Advances in Interdisciplinary Engineering*, Lecture Notes in Mechanical Engineering, https://doi.org/10.1007/978-981-13-6577-5_74

759

Table 1 Composition of blend and composite

Blend/composite	PA6	PP	PP-g-MA	SCF
PA6	100	–	–	–
PA6/CD	100	–	–	5
PA6/CS	100	–	–	–
PA6M	80	20	4	–
PA6M/CD	80	20	4	5
PA6M/CS	80	20	4	5

to the amide bonds present in PA6, it tends to form a bond with water leading to amide bond weakening which reduces the tensile properties of the PA6. To reduce the water/moisture intake, Polypropylene (PP) has been added to PA6. PA6/PP matrix is modified using Polypropylene-grafted-Maleic anhydride (PP-g-MA) to improve the compatibility between PA6 and PP [4, 5]. The modified matrix has been used for the preparation of composites and compared with the PA6 composites.

In recent times, various studies aim at using thermoplastic matrix in place of thermosetting matrix for composite application with balanced stiffness and toughness [6, 7]. For achieving higher strength and stiffness carbon fibres are used as reinforcement. Commercially available SCF are coated with low concentration sizing agent as SCF are very fragile in nature. Also, this sizing facilitates the handling and transportation of SCF. Generally, 1–3% epoxy-coated SCF are commercially available. The sizing agent applied on the fibre plays a major role in determining the interfacial adhesion between the fibre and the matrix [8]. Even though the effect of surface modification of fibre has been studied for PA6 composites, literature on the effect of surface modification of fibre on blend-based composite is very scarce. Hence to understand the effect of coating of fibre on matrix three systems were chosen; 10% epoxy-coated fibre (sizing agent), 10% silane-coated fibre (coupling agent) and 4 phr PP-g-MA (compatibilizer) modified PA6/PP blend to compare the effect of sizing agent, coupling agent and compatibilizer, respectively, on the SCF reinforced PA6 and PA6/PP blend-based composite. The compositions studied are elaborated in Table 1. The nomenclature followed here is as follows: PA6 represents pure PA6; CD represents epoxy-treated SCF; CS represents silane-treated SCF; PA6M represents PA6/PP/PP-g-MA blend. In this study along with the individual effect of sizing and coupling agent, the combined effect of compatibilizer and sizing and compatibilizer and coupling agent could be found as PA6/PP/PP-g-MA blend has been used as matrix. Also, the effect of compatibilizer is also studied.

2 Experimental Details

2.1 Materials

PA6 of grade GUJLON M28RC (Melt flow index: 35 g/10 min at 230 °C, 2.16 kg load) was obtained from Gujarat State Fertilizer and Chemicals Ltd., India and PP of grade H030SG (Melt flow index: 3.4 g/10 min at 230 °C, 2.16 kg load; tensile strength: 34 MPa) was obtained from Reliance Industries Ltd., India. Short Carbon Fibre (SCF) of 1 mm length and average diameter of 7 μm, was obtained from Sun Young Industry, South Korea and PP-g-MA of grade OPTIM-408 (Melt flow index: 50 g/10 min at 190 °C, 2.16 kg load) was obtained from Pluss Polymers Limited, India. Laboratory grade acetone and ethanol was obtained from SD Fine Chemicals Limited, India; diglycidyl ether of bisphenol-A (DGEBA/epoxy) and (3-glycidylxypropyl)trimethoxysilane (silane) was procured from Sigma-Aldrich.

2.2 Method

Samples of PA6 and composites were prepared by direct injection moulding using laboratory injection moulding machine at 245 °C whereas PA6M containing PA6/PP/PP-g-MA was twin screw extruded using Berstorff Maschinenban (ZE-25 GmbH, Germany) at a temperature range of 170 to 235 °C, and then tensile samples of PA6M and its composites were injection moulded in the laboratory. Tensile specimens were tested using microcontrol systems universal testing machine at 5 mm/min cross head speed. DSC was carried out using Shimadzu DSC 60 at the rate of 10 °C/min, nitrogen atmosphere for three cycles of heating, cooling and reheating to obtain the crystallization and melting enthalpy. FTIR of fibres was analysed using Jasco FTIR-4200 equipment.

2.3 Desizing the Fibres

SCF fibres contained 1% oligomeric epoxy coating which was desized by thermal etching of SCF surface. Initially, the fibres were heated from 450 to 550 °C for a time period of 30 min to 3 h and FTIR was done for every sample to understand the extent of sizing removal. After optimization, it was found that fibres should be thermally treated for 3 h at 550 °C in a muffle furnace for complete removal of sizing agent. The desized fibres were analysed using FTIR to check the absence of sizing agent and the obtained graph was similar to that of the FTIR of desized fibre by Feng et al. [9].

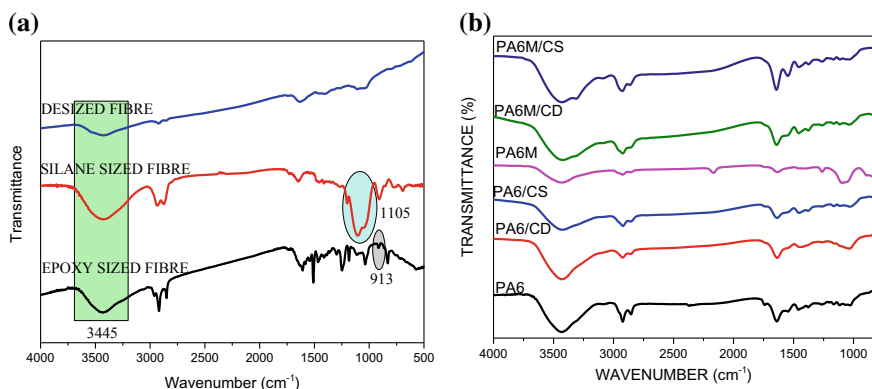


Fig. 1 FTIR of **a** desized and sized fibres, **b** blends and composites

2.4 Surface Modification of Fibre

The desized fibres were then soaked in 10 wt% DGEBA dissolved in a suitable amount of acetone for 16 h, and then dried in vacuum oven at 90 °C for 2 h [9]. Similarly, fibres were soaked in (3-glycidylxypropyl)trimethoxysilane dissolved in ethanol/water 95/5 vol/vol for 16 h followed by vacuum drying at 90 °C for 2 h. Figure 1a shows the FTIR result of desized and sized SCF [10].

3 Result and Discussion

3.1 FTIR

From Fig. 1a desized fibre showed lower intensity peaks at 3445 cm^{-1} representing lower $-\text{OH}-$ group from cured epoxy groups representing reduction in sizing coating as also proved by Feng et al. [9]. The increase in $-\text{OH}-$ group in silane sized fibre represents the ring opening of epoxy present in (3-glycidylxypropyl)trimethoxysilane and the 1105 cm^{-1} represents $\text{Si}-\text{CH}_3$ bonds proving the presence of silane on fibres [10]. In epoxy coated fibres $-\text{OH}$ group and peak at 913 cm^{-1} represents the presence of epoxy on fibres. Considering the possibility of reaction between PA6 and epoxy, where $-\text{NH}_2$ groups of PA6 react with epoxy group to form $-\text{OH}$ group, the intensity increase substantiates the formation of bonds between the fibre and the matrix [9]. However, the reaction of silane with PA6 has not been widely discussed. While treating fibres with silane, water is added to convert $-\text{OCH}_3$ group of silane to $-\text{OH}$. From Fig. 1a, it is seen that both $-\text{OH}$ group and $-\text{OCH}_3$ groups were present in silane. Considering the composites, the FTIR in Fig. 1b, it can be seen that the $-\text{OCH}_3$ peak is absent in composites and $-\text{OH}$ peaks are predominantly visible.

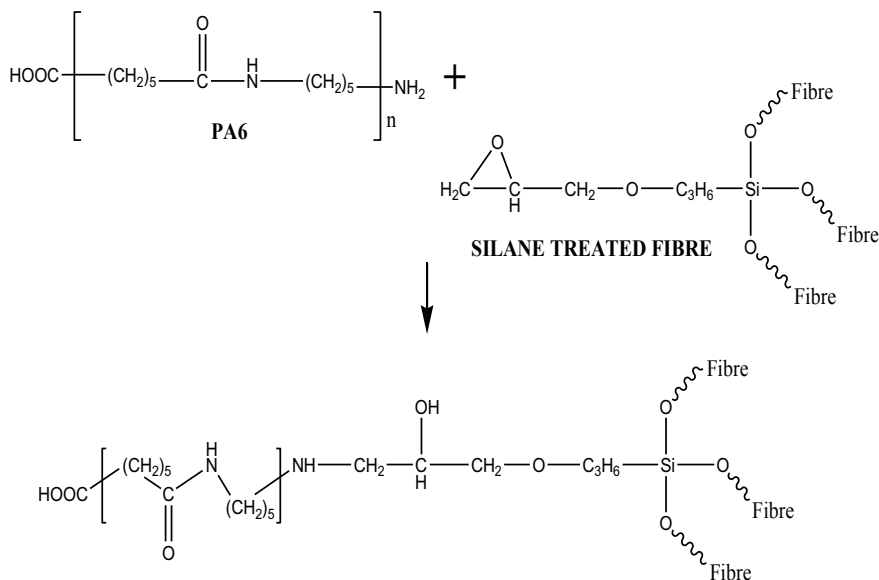


Fig. 2 Schematic diagram explaining the reaction between PA6 and silane

The possibility of reaction is shown in Fig. 2. Since the silane used contains both silane and epoxy group, it could be suggested that silane groups will anchor on the fibre surface and epoxy group will react with PA6 as well as PP-g-MA [11, 12]. Hence for PA6M/CS, the possibility of reaction between PA6 and epoxy group, PA6 and PP-g-MA, PP-g-MA and epoxy group, led to higher peak intensity at 3445 cm^{-1} and PA6M/CS had better property for blend-based composite.

3.2 Tensile Properties

Tensile strength of the blends and composites are illustrated in Fig. 3a. From the test, it was observed that PA6 had higher tensile strength than PA6/CD and PA6/CS due to agglomeration of SCF during processing. But comparing CD and CS; CD gave higher tensile strength due to better interfacial adhesion between the fibre and the matrix. Comparing PA6M with PA6M/CD and PA6M/CS, it was evident that PA6M showed higher tensile strength than PA6M/CD but equivalent tensile strength than PA6M/CS. Comparing the effect of CS and CD for blends, CS showed higher tensile strength than PA6M/CD which may be due to the better interaction of PA6, PP and PP-g-MA with silane-based coupling agent. Also, in the case of silane coupling, it contains silane and epoxy group which helps in retaining the mechanical properties of the blend. It can be concluded that silane has better effect on PA6M than epoxy. Considering modified matrix, silane proves to be a better option.

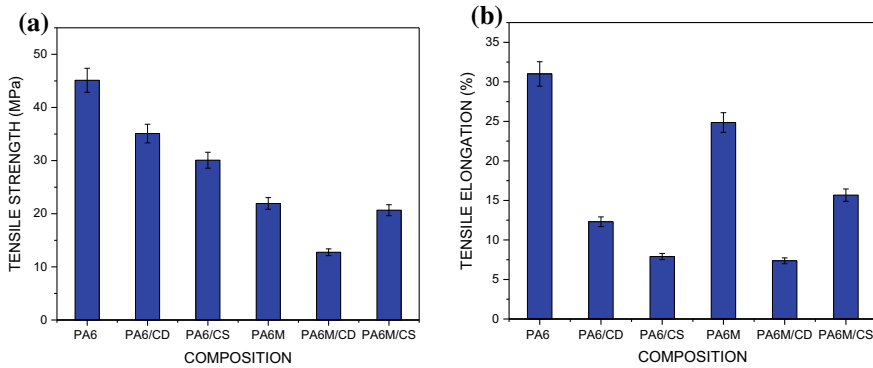


Fig. 3 Tensile properties of blends and composites **a** tensile strength **b** tensile elongation

Tensile elongation of blends and composites are illustrated in Fig. 3b. PA6 had the highest elongation followed by the modified matrix. Tensile elongation showed a similar trend as that of strength. Epoxy sizing proved better for PA6 and silane coupling proved better for PA6 blend.

3.3 DSC

DSC of PA6 and composites are shown in Fig. 4a, b. Five parameter model was applied for the crystallization peaks of samples to understand the effect of SCF and surface modification on crystallization of samples. This includes the onset temperature (T_o), peak temperature (T_p), width at half height (Δw), area of the peak (ΔH_c) and the angle (α) at the peak initiation (S_i) for PA6 [13].

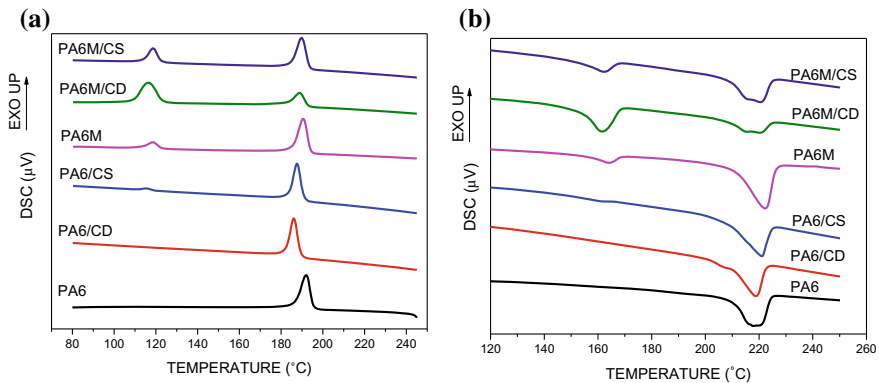


Fig. 4 DSC thermogram of PA6 and composites **a** crystallization enthalpy **b** melting enthalpy

Table 2 Variation of crystallization parameters for blends and composites

Blend/composite	T_o (°C)	T_p (°C)	Δw (°C)	ΔH_c (J/g)	$S_i = \tan \alpha$ (°)
PA6	198.5	192	5.22	64	3.49
PA6/CD	188.6	186	4.09	78	3.08
PA6/CS	190.1	187.5	3.99	67	2.25
PA6M	195.4	189.7	4.68	48	4.33
PA6M/CD	196.6	188.8	6.05	26	1.96
PA6M/CS	195.4	189.8	5.09	44	3.27

The parameters of crystallization have been given in Table 2. From the T_p value, it is evident that PA6/CD is showing cold crystallization which is caused due to better compatibility between PA6 and SCF due to the formation of bond between PA6 and epoxy. Also, the higher ΔH_c value of PA6/CD shows that the SCF acts as nucleating agent for crystallization of PA6. Whereas PA6/CS shows lower nucleation and lower crystallinity compared to PA6/CD. Yet PA6/CS also shows cold crystallization. Comparing PA6, PA6/CD and PA6/CS it could be concluded that both epoxy and silane can efficiently help in nucleation of PA6 but epoxy shows better properties in comparison to silane. Δw and ΔH_c of PA6/CD is higher than that of PA6 and PA6/CS because of which it had higher strength. Δw can be related to tensile strength of the blends and composites [14]. Here in case of PA6/SCF, with decrease in Δw , the tensile strength decreases. The Δw parameters refer to the formation of multiple crystallite sites which with increased crystallinity aids in improving the tensile strength of the composite.

Comparing modified matrix and composites data it is evident that PA6M, PA6M/CD and PA6M/CS had reduced enthalpy of crystallization showing lower crystallinity of PA6 because of which it had lower tensile strength. The crystallization enthalpy of PA6 is 64 J/g whereas it is 26 J/g and 44 J/g for PA6M/CD and PA6M/CS, respectively. Comparing the ΔH_c values with PA6M it could be said that PA6M/CS shows better crystallinity. It can be understood that SCF is not acting as a nucleating agent and the presence of sizing/coupling agent is further hindering the crystallization of PA6. Conversely, crystallization enthalpy of PP in PA6M/CS (46 J/g) was higher than PA6M/CD (26 J/g). This could be due to the reaction of PP-g-MA with silane leading to the formation of macromolecule which cannot crystallize easily due to chain cross-linking. Considering the Δw for PA6M composites, epoxy had higher Δw than silane as in case of PA6 composites but was unable to enhance the crystallinity as in case of PA6 composite which could be the reason for lower tensile strength. Since silane supported the crystallinity, it showed higher tensile strength than PA6M/CD. Melting enthalpy showed twin peak of PA6 showing the presence of α and γ phases of PA6 in PA6M/CD and PA6M/CS showing the restriction in chain mobility causing the formation of thermodynamically unstable γ phase of PA6 at 212 °C. For modified matrix silane proves to be a better surface modifier for SCF than epoxy.

4 Conclusion

PA6 and modified PA6-based composites with short carbon fibre as reinforcement were studied. The effect of modification of fibre and matrix were studied. From the study, it could be concluded that desizing of fibre was possible by thermal etching method and fibres were coated with requisite epoxy and silane successfully which was verified using FTIR. The reinforcing effect of fibres was not seen as the fibres agglomerated and poor dispersion was seen due to direct injection moulding method. Hence for better distribution and dispersion of fibres extrusion followed by injection moulding could be used. Elongation decreased with reinforcement as it acts as a barrier for extension of molecules. The presence of SCF hindered the crystallinity of PA6. Also, the crystallinity was affected by the reaction of the coating and the end groups of PA6. Epoxy is suitable for PA6 as it enhances the strength and crystallinity of the composite, whereas in the case of blend, epoxy decreased the crystallinity. Overall, it is understood that epoxy sizing agent is suitable for PA6 matrix and silane coupling agent is suitable for PA6/PP blend-based matrix. But, further research is required to optimize the coating concentration and to study the effect of processing method.

References

1. Luo H, Xiong G, Ma C, Li D, Wan Y (2014) Preparation and performance of long carbon fiber reinforced polyamide 6 composites injection-molded from core/shell structured pellets. *Mater Des* 64:294–300
2. Karsli NG, Aytac A (2013) Tensile and thermomechanical properties of short carbon fiber reinforced polyamide 6 composites. *Compos B Eng* 51:270–275
3. Botelho EC, Rezende MC, Lauke B (2003) Mechanical behavior of carbon fiber reinforced polyamide composites. *Compos Sci Technol* 63:1843–1855
4. Aparna S, Purnima D, Adusumalli RB (2017) Review on various compatibilizers and its effect on mechanical properties of compatibilized nylon blends. *Polym-Plast Technology Eng* 56(6):617–634
5. Ide F, Hasegawa A (1974) Studies on polymer blend of nylon 6 and polypropylene or nylon 6 and polystyrene using the reaction of polymer. *J Appl Polym Sci* 18(4):963–974
6. Do V-T, Nguyen-Tran H-D, Chun D-M (2016) Effect of polypropylene on the mechanical properties and water absorption of carbon-fiber-reinforced-polyamide-6/polypropylene composite. *Compos Struct* 150:240–245
7. Arhant M, Le Gac PY, Le Gall M, Burtin C, Briançon C, Davies P (2016) *Compos A Appl Sci Manuf* 91:250–261
8. Sharma M, Gao S, Mäder E, Sharma H, Wei LY, Bijwe J (2014) Carbon fiber surfaces and composite interphases. *Compos Sci Technol* 6:35–50
9. Feng N, Wang X, Wu D (2013) Surface modification of recycled carbon fiber and its reinforcement effect on nylon 6 composites: mechanical properties, morphology and crystallization behaviors. *Curr Appl Phys* 13(9):2038–2050
10. Yu B, Jiang Z, Tang XZ, Yue CY, Yang J (2014) Enhanced interphase between epoxy matrix and carbon fiber with carbon nanotube-modified silane coating. *Compos Sci Technol* 99:131–140
11. Chen JJ (2000) Moisture curable balloon materials US7182906B2

12. Arun Prakash VR, Rajadurai A (2017) Inter laminar shear strength behavior of acid, base and silane treated E-glass fibre epoxy resin composites on drilling process. *Defence Technology* 13(1):40–46
13. Purnima D, Maiti SN, Gupta AK (2006) Interfacial adhesion through maleic anhydride grafting of EPDM in PP/EPDM blend. *J Appl Polym Sci* 102(6):5528–5532
14. Gupta AK, Purwar SN (1984) Crystallization of PP in PP/SEBS blends and its correlation with tensile properties. *J Appl Polym Sci* 29(5):1595–1609

Study of Bubble Dynamics and Free Liquid Surface Mixing in a Rectangular Container Having Ullage Area with Double Gas Inlets



Sarath Raj and J. S. Jayakumar

Abstract In this work, the Volume of Fluid (VOF) [1] method is used to study bubble dynamics and collapse of bubbles on free surface in a rectangular domain with double gas inlets. The simulation is done by using open-source CFD software OpenFOAM-3.0.1. The conservation equations for mass and momentum, which incorporates the influence of surface tension and gravity, are solved by using PIMPLE algorithm. The physical model for the simulation process is a 2D rectangular domain with a width of 50 mm and height of 100 mm. In order to study the collapsing of the bubble on the surface and free liquid surface mixing, an ullage area of 15% was considered within the domain. The numerical computation was performed with multiphase solver *interFoam*. Modeling of the geometry, meshing and setting the boundary conditions were done, using the OpenFOAM software. The simulation results were compared with the available literature results and found that the bubble formation and dynamics are in good agreement. The behaviors of gas bubbles emanating from two adjacent orifices at different gas velocities are studied. Mixing behavior in the bulk liquid due to bubble formation under different inlet gas velocities was also numerically investigated. The impact of surface tension and density of bulk liquid on collapsing of the bubble on the free liquid surface is investigated numerically.

Keywords Bubble dynamics · *interFoam* · OpenFOAM · VOF · CFD

1 Introduction

Gas–liquid bubble columns are extensively used as reactors and multiphase contactors in chemical, biochemical, petrochemical industries, and in various other engineering applications. It has numerous advantages, which can be explained in terms

S. Raj · J. S. Jayakumar (✉)

Department of Mechanical Engineering, Amrita Vishwa Vidyapeetham, Amritapuri, India
e-mail: jsjayan@gmail.com

S. Raj

e-mail: srsnit2013@gmail.com

© Springer Nature Singapore Pte Ltd. 2019

M. Kumar et al. (eds.), *Advances in Interdisciplinary Engineering*, Lecture Notes in Mechanical Engineering, https://doi.org/10.1007/978-981-13-6577-5_75

of higher heat–mass transfer rates, efficient interphase interaction, compactness, low operating and maintenance cost, etc. Even though a large number of studies prevail in the literature, bubble column studies are still not well established because the majority of these studies were often carried out on only one phase, i.e., either gas or liquid. However, in bubble columns, the primary focus should be given to the interaction between the different phases, which are in fact mutually linked. Bubble performance is crucial in defining the fluid characteristics in bubble columns.

In bubble columns, due to high density and viscosity ratios, the motion of bubbles can be very intricate and also is very problematic so as to estimate an accurate mathematical model that can be used to compute the bubble rise velocity in various transport properties. In the past, numerous periods and numerous techniques were developed to simulate complex two-phase flow problem. Denoij et al. [2] studied the time-dependent behavior of the large gas bubble by using volume tracking method. The volume tracking method is based on Volume of Fluid concept. With the help of volume tracking model, the authors studied the formation and rising behavior of skirted bubble, spherical cap bubble. Shimizu et al. [3] carried out experimental analysis in bubble column reactor and based on that model for bubble break up and agglomeration, they studied the gas holdup and gas–liquid mass transfer phenomena. Arsam et al. [4] measured the mass transfer coefficient and bubble size distribution in large-scale industrial bubble column reactor for CO, N₂, H₂, and CH₄ in two organic mixtures solids in a wide pressure range, superficial gas velocities, and solid concentration. From the experimental analysis, the authors found that the values of mass transfer coefficient depend on bubble size distribution. Andrzej et al. [5] studied bubble dynamics using Computational Fluid Dynamics (CFD) software. For tracking the liquid interface in 2D and 3D domain, the authors used momentum balance equation coupled with Volume of Fluid algorithm. Ammar et al. [6] investigated the behavior of bubbles in a bubble column by using the VOF model. The authors compared the results of both commercial and Open-Source Solver with experimental results. From the analysis, it was found out that the numerical results showed a better prediction of the gas bubble hold up in bubble column, compared with experimental results. Han et al. [7] numerically studied the impact of surface tension on bubble behavior of a spherical bubble rising in a stationary liquid using VOF method. For the simulation for bubble dynamics, the authors used the gas–liquid density ratio as 0.001 and found out that there exist four critical Webber numbers which differentiate five different kinds of bubble behaviors. Ma et al. [8] carried out a numerical simulation to study the bubble dynamics by using Fluent 6.3. For the simulation, the authors used Volume of Fluid method and Continuum Surface Force model. The authors studied the effect of physical properties such as surface tension, liquid viscosity, density, and orifice size on various bubble behaviors. Peyman et al. [9] carried out a numerical simulation to examine the formation and motion of bubbles in bulk liquid by using VOF method. For the numerical investigation, the authors used FLUENT 6.3. For simulating gas–liquid interface, the pattern in VOF method conservation of mass and momentum equations were used. The authors studied the effect of fluid physical properties and orifice diameter in bubble behavior, detachment time and found out bubble detachment time is linear function of surface tension. Tariqul et al.

[10] investigated the effect of inlet gas velocity and Reynolds number on bubble formation in viscous liquid using VOF-CSF method in CFD. The study has verified the capability of CFD to predict the bubble velocity, bubble shape, and detachment time was in good agreement compared to experimental analysis. Kang et al. [11] carried out an experimental analysis in pressurized bubble column of diameter 0.152 and height of 2.0 m and they investigated the bubble distribution and its effects on the gas–liquid mass transfer. Wang et al. [13] numerically investigated the phenomenon of bubble agglomeration, considering two droplets with different temperature. For the simulations, the authors used VOF method and for describing the effects of interfacial tension force the Continuum Surface Stress model was used.

In the present work, the VOF [1] technique is applied in the simulation of bubbling characteristics and collapse at free liquid surface. The simulation dealt with bubble behavior in a 2D rectangular domain with double orifice of small diameters in contrast to the single orifice simulations carried out earlier using other CFD tools. So far, no studies have been reported on bubble dynamics and collapse at free surface in a rectangular container with double orifices using OpenFOAM. The time for bubble detachment, average bubble diameter, and the agglomeration and mixing rates of bubbles are deliberately scrutinized by utilizing computer simulations.

2 Governing Equations

The continuity and momentum equations for two-phase flow fluid problems are written as follows:

$$\frac{\partial \rho}{\partial t} + \nabla \cdot (\rho \vec{v}) = 0 \quad (1)$$

$$\frac{\partial(\rho \vec{v})}{\partial t} + \nabla(\rho \vec{v} \vec{v}) = -\nabla p + \nabla[\mu(\nabla \vec{v} + \vec{v})] + F_s + \rho \vec{g} \quad (2)$$

2.1 VOF Model

In the VOF scheme, the fluids share a solitary set of momentum and volume fraction equations. Hence, each computational grid is traced along the entire domain. VOF methodology depends on the assumption that the fluid phases do not interpenetrate each other and uses the function $F(x, y, t)$, whose value is 1 at any point occupied by pure liquid, 0 for pure gas and the value ranges between 0 and 1 for gas–liquid composition.

$$F = \frac{\text{Volume of fluid in unit}}{\text{Volume of unit}} \quad (3)$$

$$F = \begin{cases} 0 & \text{In bubble} \\ 0 < F < 1 & \text{Interface} \\ 1 & \text{In liquid fluid} \end{cases} \quad (4)$$

The transport equation of fluid volume function is

$$\frac{DF}{Dt} = \frac{\partial F}{\partial t} + (\vec{v}\nabla)F = 0 \quad (5)$$

2.2 Interface Reconstruction Techniques

Various methods are available for solving fluid volume functions like the donor–acceptor, FLAIR, SLIC, and PLIC methods [7, 8]. In Piecewise Linear Interface Calculation (PLIC) method, the interface fluid transport is incorporated in detail and reconstruction details are moderately accurate. Therefore, the PLIC method is applied here for the reconstruction of fluid interface [7, 8].

2.3 Continuum Surface Force (CSF) Model

The CSF model is utilized for calculating the surface tension force in the liquid–gas interface by combining the volumetric force equation and momentum equation [7, 8].

$$F_S = \sigma \frac{\alpha_l \rho_l k_v \nabla \alpha_v + \alpha_v \rho_v k_l \nabla l}{0.5(\delta_v + \delta_l)}$$

where $k_l = \frac{\nabla \alpha_l}{|\nabla \alpha_l|}$ $k_v = \frac{\nabla \alpha_v}{|\nabla \alpha_v|}$

3 Validation

For validating the methodology used in the present study, the work of Ma et al. [8] was considered. The comparison of bubble diameter with inlet gas velocity was investigated. It was observed that with an increase in inlet gas velocity, the bubble average diameter increases, as shown in Fig. 1. The results of the present study are in good agreement with Ma et al. [8] and the relative error was within 5%.

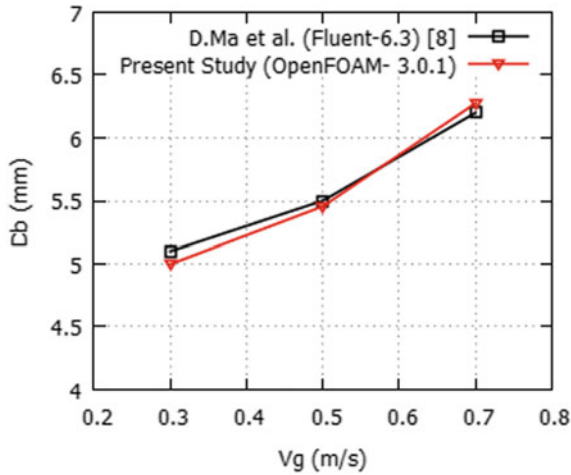


Fig. 1 Bubble diameter versus inlet gas velocity, orifice diameter $D_o = 0.5$ mm

4 Analysis

In the present study, a rectangular domain of 50 mm width and 100 mm height is considered. Figure 2a shows the geometry depiction and dimensional details of a rectangular container with 15% ullage area. The grid is shown in Fig. 2b. An enlarged view of the rectangular region near the orifice is shown in Fig. 2c. Finite

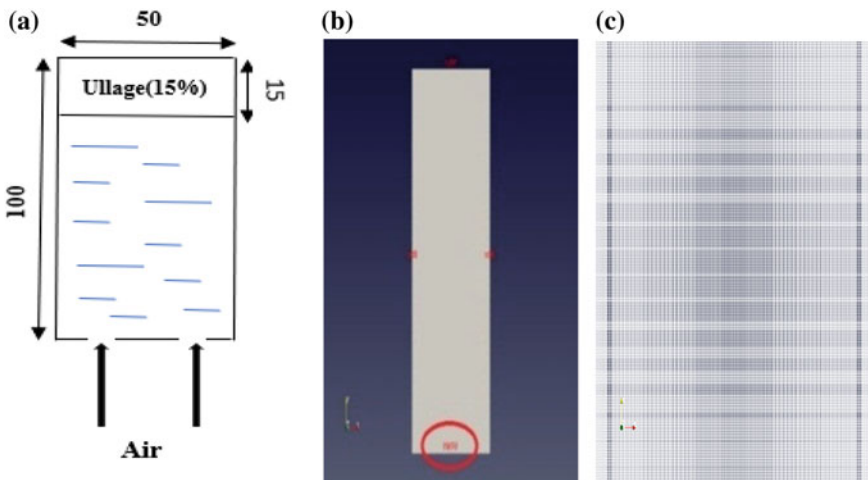


Fig. 2 a Rectangular domain with double inlets and 15% ullage area. b Computational model of rectangular domain. c Enlarged view near the inlet orifice

Volume Method (FVM) is used for the discretization of continuity and momentum equation. PIMPLE algorithm is employed to convert PDE to a system of algebraic equations and is solved concurrently. The Piecewise Linear Interface Calculation (PLIC) method is applied here for the reconstruction of fluid interface [7, 8].

Numerical computations are performed with well-known multiphase solver `interFoam`. For these simulations, a small time step of the order 0.1 ms is considered. The gas inlets are defined as velocity inlets. The walls are defined as no-slip. For checking the dependency of a number of cells on the analysis, five ranges of cell numbers are used. The results show that a representative accuracy can be attained in bubble behavior simulation with cell number $9.00e+05$ and the precision did not improve even if a higher cell number used [12].

5 Results and Discussion

5.1 Influence of Inlet Gas Velocity on Bubble Behavior and Free Liquid Surface Mixing

The influence of inlet gas velocity on bubble detachment time, diameter of bubble, and free liquid surface mixing are numerically simulated and the results are shown in this section. The phase contours (Fig. 3) show the influence of inlet gas velocity in free liquid surface collapsing and bursting. In which the blue part shows the liquid phase and the red portion shows the air bubble. The liquid surface gets more deformed with the increase in inlet gas velocity and is clearly shown in Fig. 3e–h. At the initial stage, the bubble develops and grows but the gas bubble neck still remains in contact with the orifice mouth. The surface tension force plays an important part at this moment. When the buoyancy force on the bubble overrules the liquid drag force, bubble gets detached from the orifice and finally gets deformed. The process is repeated for the consecutive bubbles. Figure 4 shows the void fraction contours for bubble coalescence and the position changes of bubbles along the vertical direction of the rectangular domain during agglomeration at inlet gas velocity of 0.5 m/s. It is clear that velocity of the first bubble is lower than that of the trailing bubbles. This means that the trailing bubbles accelerates more under the wakening effect of the first bubble and thus the distance between the first leading and second trailing bubble get reduced and ultimately with the increment in time the bubbles get agglomerated to form a single larger bubble. Streamline contours are plotted to study the disturbance pattern of the wakes behind the leading bubble. Figure 5 shows the streamlines around the bubble when orifice diameter is 0.5 mm and inlet gas velocity is 0.5 m/s. The vortices created at either end sides of the rising bubble are also shown in Fig. 5. Figure 6a shows the position changes of bubbles along the vertical direction of the rectangular domain during agglomeration. It can be observed that the upper first bubble gets deformed at a much faster rate than the lower rising bubble. This is because of the

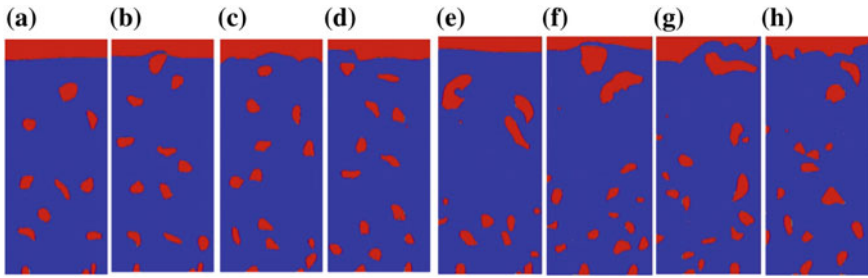


Fig. 3 Bubble behavior for various inlet gas velocities when $D_o = 0.5$ mm, **a** $t = 0.62$ s, **b** $t = 0.72$ s, **c** $t = 0.82$ s, **d** $t = 0.92$ s, **a-d** $V_g = 0.5$ m/s, **e** $t = 0.62$ s, **f** $t = 0.72$ s, **g** $t = 0.82$ s and **h** $t = 0.92$ s, **e-h** $V_g = 0.7$ m/s

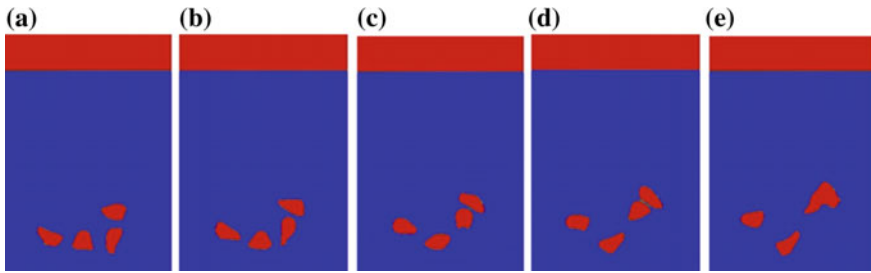


Fig. 4 Bubble agglomeration process of two bubbles in the bubble column when $D_o = 0.5$ mm, **a** $t = 0.40$ s, **b** $t = 0.41$ s, **c** $t = 0.42$ s, **d** $t = 0.43$ s, **e** $t = 0.44$ s, **a-e** $V_g = 0.5$ m/s

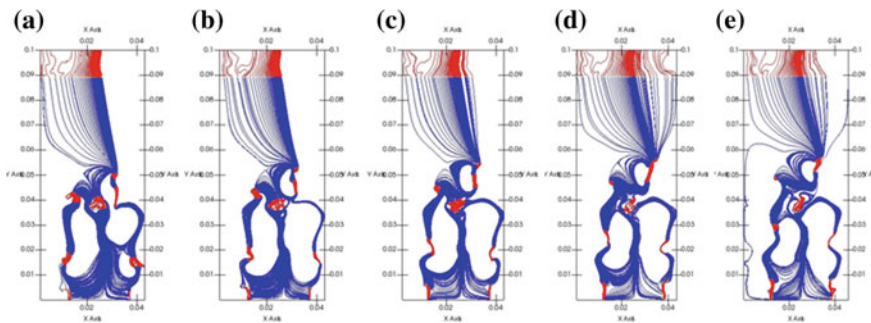


Fig. 5 Comparison of the streamlines around the bubble during bubble coalescence, when $D_o = 0.5$ mm, **a** $t = 0.40$ s, **b** $t = 0.41$ s, **c** $t = 0.42$ s, **d** $t = 0.43$ s, **e** $t = 0.44$ s, **a-e** $V_g = 0.5$ m/s

fact that the upper first bubble flows through the dormant liquid, while the lower travels through the wake region left behind the upper leading bubble.

A lower drag force is created for the lower bubble due to the wake left behind the upper bubble. Hence, the relative distance between two bubbles gets decreased with

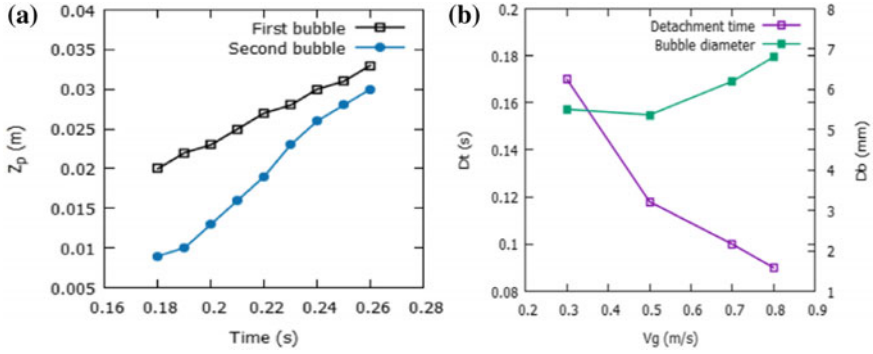


Fig. 6 **a** Vertical position change of bubbles during agglomeration. **b** Variation in bubble detachment time and diameter with respect to different inlet gas velocity

Table 1 Transport properties of bulk liquid used for the study of the effect of surface tension on bubble behavior [8]

σ_1 (N/m)	μ_1 (Pa s)	ρ_l (kg/m ³)
4.82×10^{-2}	1.005×10^{-3}	1003.8
5.38×10^{-2}	1.005×10^{-3}	1006.2
6.93×10^{-2}	1.005×10^{-3}	1002.2
7.28×10^{-2}	1.005×10^{-3}	998.2

time and is clearly shown in Fig. 6a. The bubble agglomeration causes turbulence in the bulk liquid and microbubbles are formed in the vicinities of bubble fusion.

Free liquid surface collapsing depends on bubble detachment time as well as the bubble diameter. Figure 6b shows the variation in time of detachment and bubble diameter with different inlet gas velocity. It is clear from the figure that bubble diameter increases with increase in inlet gas velocity. But detachment time shows a downward trend with the increment in gas velocity hence bigger and more number of bubbles was formed and bubble rises near to the ullage area which causes the free liquid surface to be deformed more.

5.2 Influence of Surface Tension on Bubble Behavior and Free Liquid Surface Mixing

The impact of surface tension force of bulk liquid on free liquid surface deformation due to bubbling is shown in Fig. 7. Figure 8 shows the void fraction contours for bubble coalescence and the position changes of bubbles along the vertical direction of the rectangular domain during agglomeration at a surface tension value of 0.0538 N/m. The transport properties used to scrutinize the surface tension effects in bubble behavior are enumerated in Table 1.

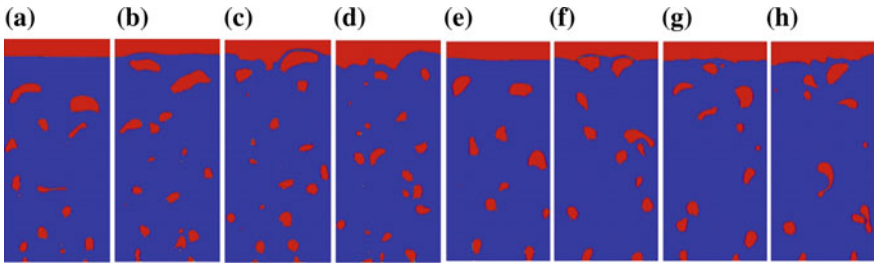


Fig. 7 Effect of surface tension on free liquid surface collapsing when $D_o = 0.5$ mm, **a** $t = 0.68$ s, **b** $t = 0.78$ s, **c** $t = 0.88$ s, **d** $t = 0.98$ s, **a-d** $V_g = 0.9$ m/s, $\sigma_1 = 0.0538$ N/m, **e** $t = 0.68$ s, **f** $t = 0.78$ s, **g** $t = 0.88$ s, **h** $t = 0.98$ s, **e-h** $V_g = 0.9$ m/s, $\sigma_1 = 0.0728$ N/m

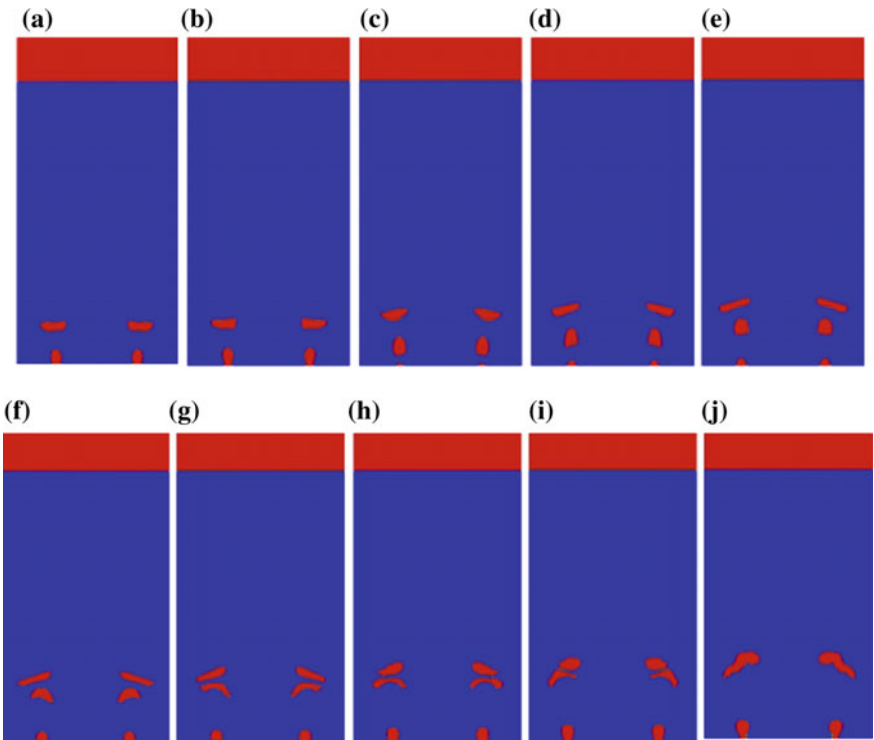


Fig. 8 Bubble agglomeration process of two bubbles in the bubble column when $D_o = 0.5$ mm, **a** $t = 0.14$ s, **b** $t = 0.15$ s, **c** $t = 0.16$ s, **d** $t = 0.17$ s, **e** $t = 0.18$ s, **f** $t = 0.19$ s, **g** $t = 0.20$ s, **h** $t = 0.21$ s, **i** $t = 0.22$ s, **j** $t = 0.23$ s, **a-j** $V_g = 0.9$ m/s, $\sigma_1 = 0.0538$ N/m

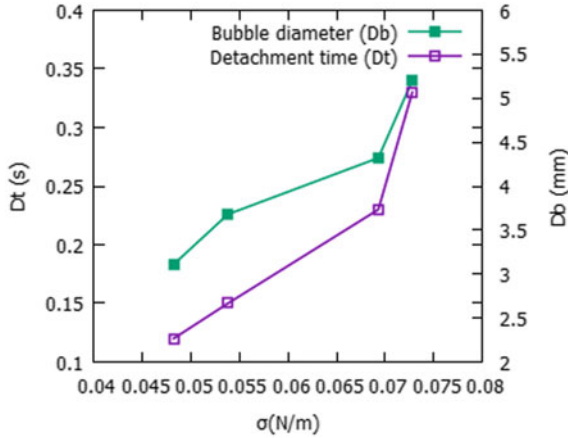


Fig. 9 Variation in bubble diameter and detachment time with respect to different surface tension forces

From Fig. 8, it is clear that the velocity of the first bubble is lower than that of the trailing bubbles. This means that the trailing bubbles accelerates more under the wakening effect of the first bubble and thus the distance between the first leading and second trailing bubble get reduced and ultimately the bubbles get agglomerated to form a single larger bubble. The free liquid surface deformation rate depends on bubble detachment time and bubble diameter which is shown in Fig. 9. As the surface tension value is increased, the detachment time increases and bubbles get detached from the orifice mouth at slower rate hence more amount of air is entrapped within the gas bubbles. Therefore, average bubble diameter increases with increase in surface tension of the bulk liquid. At higher values of surface tension, due to the increment in the detachment, timeless number of the bubble are available at the top end near to the ullage area which is clear from Fig. 7. This leads to less turbulence effect and hence collapsing rate of free liquid decreases with increase in surface tension.

5.3 Influence of Density of Bulk Liquid on Bubble Behavior and Free Liquid Surface Mixing

Formation of a single bubble was numerically simulated in a rectangular 2D bubble column with 15% ullage area in which air is bubbled into liquid water through two inlets. Variation of bulk liquid density has a substantial impact on bubble behavior. The transport properties used in order to scrutinize the density effects in bubble behavior and liquid surface mixing are enumerated in Table 2. The numerical results of bubbling behavior at two different liquid density values equal to 998.2 and 1500 kg/m³ are shown in Fig. 10. From the contours, it is observed that bub-

Table 2 Transport properties of bulk liquid used for the study of the effect of density on bubble behavior [8]

ρ_l (kg/m ³)	μ_l (Pa s)	σ_1 (N/m)
998.2	1.005×10^{-3}	7.28×10^{-2}
1500	1.005×10^{-3}	7.28×10^{-2}
2000	1.005×10^{-3}	7.28×10^{-2}
2500	1.005×10^{-3}	7.28×10^{-2}

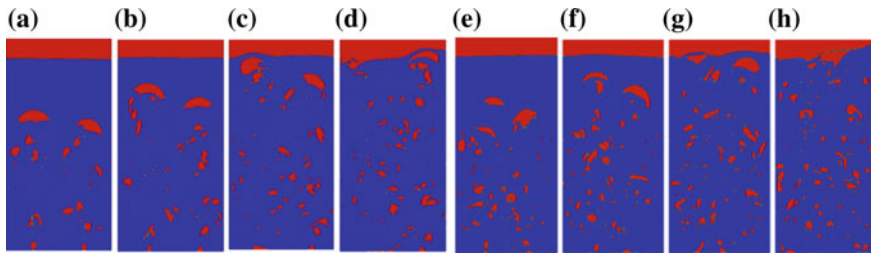


Fig. 10 Effect of density on free liquid surface collapsing when $D_o = 0.5$ mm, **a** $t = 0.65$ s, **b** $t = 0.75$ s, **c** $t = 0.85$ s, **d** $t = 0.95$ s. **a–d** $V_g = 0.25$ m/s, $\rho_l = 998.2$ kg/m³, **e** $t = 0.65$ s, **f** $t = 0.75$ s, **g** $t = 0.85$ s, **h** $t = 0.95$ s, **e–h** $V_g = 0.25$ m/s, $\rho_l = 1500$ kg/m³

ble behavior is influenced by bulk liquid density to a greater extent. Comparing Fig. 10a–d with 10e–h, it can be concluded that increase in liquid density augments the bubbling frequency because a number of bubbles are formed with density value 1500 kg/m³, i.e., increase in liquid density increases the frequency of bubbling. The bubble agglomeration causes turbulence in the bulk liquid and microbubbles are

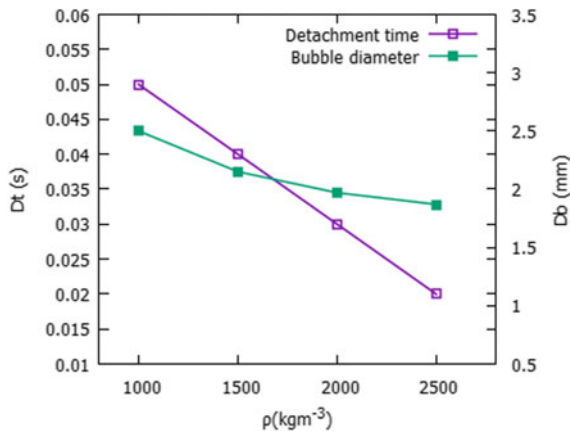


Fig. 11 Variation in bubble diameter and detachment time with respect to different density values of bulk liquid

formed in the localities of bubble fusion. The influence of bulk liquid density on diameter and detachment time of bubble is shown in Fig. 11.

From Fig. 11, it is clear that the bubble diameter and detachment times are getting reduced considerably with the upturn of liquid density at constant inlet gas velocity. This is because high liquid density increases bubble buoyant force, which makes the bubble to detach early. The coalescence rate and free liquid surface mixing rate also increases because more number of bubbles was formed at high values of liquid density.

6 Conclusions

The Volume of Fluid (VOF) method was used to numerically investigate the bubble formation, dynamics and free liquid surface mixing in a rectangular domain with double inlets. The numerical investigation was carried out by using the software `OpenFOAM-3.0.1`. Compared to other methods the VOF method has less computational intricacy, higher accuracy, and is easier to understand. In order to validate the problem, the works of Ma et al. [8] were used and the results were in good agreement related to the present study. The relative error was less than 5%. Therefore, `OpenFOAM` proves to be a proficient and ingenious CFD tool. The use of commercial CFD codes for the analysis of these problems is not a good choice, because of the fact that they are very expensive. Using Open-Source Software (OSS) is an alternative, which is economical for analyzing these problems. The current study involves the investigation of bubble behavior by varying the different transport properties and physical properties. These properties include liquid density surface tension and inlet gas velocity. The variations in bubble diameter, bubble detachment time, bubble agglomeration rates, and liquid surface mixing rates were numerically investigated and different contours and graphs are plotted regarding this matter.

From the investigation, the following conclusions are drawn. With the increment in liquid density, the average bubble diameter, and bubble detachment time reduce considerably but it augments the bubble formation and bubble coalescence frequency. The density variation has a significant impact on free liquid surface mixing rate, i.e., mixing rate increases with increase in bulk liquid density. Surface tension studies show that the bubble diameter and the time of bubble detachment increase with the increment in surface tension, whereas the bubble formation frequency, bubble coalescence rate, and free liquid surface mixing rate shows an inverse proportion relation with surface tension. However, the numerical analysis results indicate that the average bubble diameter increases with increase in inlet gas velocity, whereas the bubble detachment time reduces with the increment in inlet gas velocity. The liquid surface deformation rate increases with increase in inlet gas velocity.

References

1. Hirt CW, Nichols BD (1981) Volume of fluid (VOF) method for the dynamics of free boundaries. *J Comput Phys* 39:201–225
2. Delnoij E, Kuipers JAM, van Swaaij WPM (1998) Computational fluid dynamics applied to gas-liquid contactors. *Chem Eng Sci* 52:3623–3638 (Elsevier Science Ltd)
3. Shimizu K, Takada S, Minekawa K, Kawase Y (2000) Phenomenological model for bubble column reactors: prediction of gas hold-ups and volumetric transfer coefficients. *Chem Eng J* 21–28 (Elsevier Science Ltd.)
4. Behkish A, Men Z, Inga JR, Badie I (2002) Mass transfer characteristics in a large-scale slurry bubble column reactor with organic liquid mixtures. *Chem Eng Sci* 3307–3324
5. Andrzej Bin K, Machniewski P, Rundniak L (2002) Modeling of bubble formation with the aid of CFD. Polish Scientific Committee, pp 17–26
6. Ammar AT, Amano RS (2009) Factors affecting fine bubble creation and bubble size for activated sludge. *Water Environ J*, 21–30
7. Wang H, Zhen-Yu Z (2010) Surface tension effects on the behavior of a rising bubble driven by buoyancy force. *J Phys B* 19:1–9
8. Ma D, Liu M, Zu Y, Tang C (2012) The two-dimensional volume of fluid simulation studies on single bubble formation and dynamics in bubble columns. *Chem Eng Sci* 72:61–77 (Elsevier Science Ltd.)
9. Zahedi P, Saleh R, Moreno-Atanasio R, Yousefi K (2014) Influence of fluid properties on bubble formation, detachment, rising and collapse; investigation using volume of fluid method. *Korean J Chem Eng*, 1349–1361
10. Islam T, Ganesan P, Sahu JN, Hamad FA (2015) Numerical study to investigate the effect of inlet gas velocity and Reynolds number on bubble formation in a viscous liquid. *Thermal Sci* 2127–2138
11. Kang C, Zhang W, Gu Y, Mao N (2017) Bubble size and flow characteristics of bubbly flow downstream of a ventilated cylinder. *Chem Eng Res and Des* 263–272 (Elsevier Science Ltd.)
12. Raj S, Jayakumar JS (2017) Investigation of bubble dynamics with single and double gas inlet(s) in a rectangular container using OpenFOAM. In: Proceedings of the 24th national and 2nd International Ishmt-Astfe Heat and mass transfer conference, December 27–30, Bits Pilani, Hyderabad, India. IHMTTC, pp 1–8
13. Wang Z, Chen R, Zhu X, Liao Q, Ye D, Zhang B, He X, Jiao L (2018) Dynamic behaviors of the coalescence between two droplets with different temperatures simulated by the VOF method. *Appl Therm Eng* 132–140 (Elsevier Science Ltd)

Performance Enhancement of Induction Motor Using PID Controller with PID Tuner



Megha Yadav and Vijay Kumar Tayal

Abstract The real-time industrial systems are continuously subjected to time-varying load and other disturbances. The induction motors are extensively used in numerous applications due to rugged construction and need for low maintenance. However, the induction motors are categorized by intricate, extremely nonlinear, and time-varying dynamics and henceforth maintaining their speed is a stimulating problematic in engineering. This paper is grounded on the performance improvement of induction motor subjected to disturbances by means of proportional–integral–derivative (PID) controller. The PID controller parameters are optimized using PID tuner software available in MATLAB. The simulation results show the efficacy of the proposed scheme.

Keywords Induction motor (IM) · Proportional–integral–derivate controller (PID controller) · Genetic algorithms (GA) · Perturbed system · Particle swarm optimization (PSO)

1 Introduction

The largest machine which man has ever made is certainly an electric power grid. This is composed of various electrical machines such as synchronous machines, generators, transmission line, switches, transformers, and relays, etc. Moreover, the solution of optimization problems requires several control objectives as well as design decisions. Aimed at such a nonlinear nonstationary system by conceivable din and qualms, by way of numerous design/operational limitations, the key to the optimization unruly is by no means insignificant. In an induction motor the speed control can be found via fluctuating its limits from rotor or stator cross. Here, stay portion of advantages in stator side control and that is why they are ideal and subsequently

M. Yadav (✉) · V. K. Tayal
Amity University Uttar Pradesh, Noida, India
e-mail: Meghayadav14@yahoo.com

V. K. Tayal
e-mail: vktayal@amity.edu

© Springer Nature Singapore Pte Ltd. 2019
M. Kumar et al. (eds.), *Advances in Interdisciplinary Engineering*, Lecture Notes in Mechanical Engineering, https://doi.org/10.1007/978-981-13-6577-5_76

leads to improved efficiency, improved control approaches, inexpensive technique, etc. [1–3]. There are many approaches for speed control of IM such as voltage control, on–off control method, and phase angle control method. Stator voltage control is favored in local requests as speed difference is in smaller amount and intended for domestic requests low power rating is vital [4, 5].

Through consuming vector control performance, PID controller can be castoff in the direction to govern an induction motor. Owing this advantage of vector control technique takes develop commerce normal control for AC drives and ejecting the scaler control method [6, 7]. These existences of PID controllers are broadly castoff in numerous productions to control diverse plants and they have rational recital.

Intended for growing order of the system, the conventional proportional-integral controller is castoff [8, 9]. It similarly advances damping by dipping maximum overshoot and reduction bandwidth and surge rise time. Nonetheless, faultless control cannot be attained through PI controllers and henceforth, we require an improved control system, Due to several advantages, the PID controllers are commonly used in various industrial applications [10]. However, the tuning of PID controller gains for optimum results in a highly difficult task. In the literature, a number of optimization techniques such as genetic algorithm, ant colony optimization, particle swarm optimization, and teaching learning algorithm, etc., have been presented in the literature. In this paper, the PID controller design using PID tuner is proposed for performance enhancement of an IM in the presence of loading uncertainty. This paper is organized as follows: Sect. 2 details about induction motor modeling, Sect. 3 discusses about PID Controller design, simulation results are detailed in Sect. 4, and conclusion is presented in Sect. 5.

2 Induction Motor

2.1 Induction Motor

In an **induction motor**, torque is produced through electromagnetic **induction** by the magnetic field at stator winding. An **induction motor** can be therefore finished deprived of electrical networks to the rotor [11, 12].

2.2 Induction Motor Model

The succeeding Fig. 1 determines the corresponding circuit model of the IM. The block here, characterizing both electrical and torque characteristics:

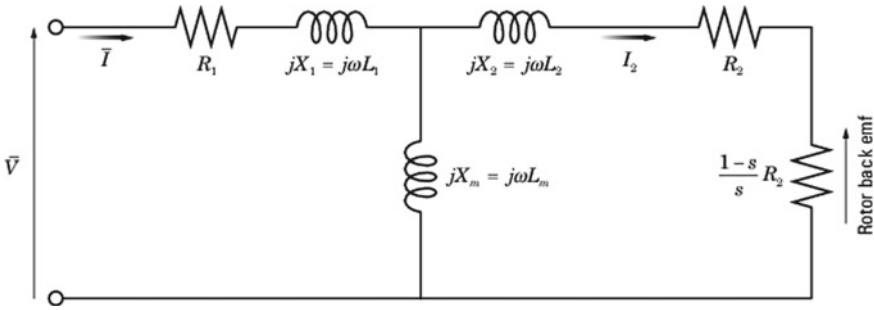


Fig. 1 Equivalent circuit of single-phase induction motor

The variance among slip and frequency is given as

$$S = 1 - \frac{p\omega_m}{\omega_s} \tag{1}$$

For an n -phase induction motor, the torque–speed relationship is given by

$$T = \frac{npR_2}{s\omega} \frac{V_{rms}^2}{(X_1 + X_2)^2 + (R_1 + R_2 + \frac{1-s}{s}R_2)^2} \tag{2}$$

3 PID Controllers

Many industrial applications require using suitable system control such as PI, PD, P, or I controller. The derivative controllers are sensitive to measurement noise and the absence of an integral control action may prevent the system from reaching its target value due to the control action. However, the PI controllers are quite common. The PI controller alone is not able to improve the transient performance of the system, therefore, a PID controller is needed. Proportional–integral–derivative (PID) control is the utmost common control procedure used in engineering and has been unanimously acknowledged in industrial control design. The acceptance of PID controllers can be credited moderately to their robust performance in an extensive variety of functioning settings and partially to their useful effortlessness, which permits control engineers to function them in an effective manner [13, 14].

The dynamic equation governing the PID control is given by

$$u(t) = K_p \left[\frac{1}{T_i} \int_0^t e(\tau) d\tau + T_d \frac{de(t)}{dt} + e(t) \right] \quad (3)$$

Here, $u(t)$ is the control error, $e(t)$ is the error signal. T_i , T_d , and K_p are the constants to be modified.

The constant T_F will be

$$K(s) = K_p \left(\frac{1}{T_i s} + T_d s + 1 \right) \quad (4)$$

4 PID Tuning

The proportional–integral–derivative (PID) controllers have remained extensively used for speed and location control for numerous applications. Amongst the conformist PID tuning approaches, the Ziegler–Nichols technique might be the utmost familiar procedure. For an extensive variety of applied procedures, this modification method proceeds fairly glowing. Though, occasionally, it does not offer fair tuning and inclines to provide an immense overshoot. Therefore, this method usually needs retuning before useful to govern manufacturing courses. To develop the competences of outmoded PID restriction tuning performances, numerous intellectual techniques have been recommended to advance the PID tuning, such as individual usage via genetic algorithms (GA) and the particle swarm optimization (PSO), etc. Due to the development of computational approaches in the current period, optimization processes are frequently anticipated to tune the control constraints in demand to discover an ideal performance. The proportional portion of the PID controller decreases fault comebacks to instabilities. The integral span of the error eliminates steady-state error and the derivative span of fault diminishes the active comeback and thus recovers constancy of the structure. The limit settings of a PID controller for ideal control of a plant (procedure) hang on the plant's characteristics. To project the PID controller, the person duty is to select the fine-tuning way of strategy limits to recover the transient response as well as the steady-state error.

The PID tuning algorithm by PID Tuner mainly includes the following factors:

Closed-loop stability—The closed-loop structure feedback remains restricted for limited input.

Acceptable performance—The pathways in closed-loop structure position variations and overpowers conflicts as speedily as conceivable. The greater the bandwidth of the loop (the frequency of unison open-loop increase), the sooner the controller retorts in variations on the locus and instabilities in the loop.

Table 1 PID controller parameters

S. No.	PID controller parameters	With PID tuner	Without PID tuner
1	P	0.001683	1
2	I	1.4788e-005	1
3	D	-0.00079278	0
4	N	2.1229	100

Acceptable robustness—Gain margin and phase margin in the loop plan has sufficient to permit for modeling faults and disparities in plant undercurrents.

The system for tuning PID controllers encounters these purposes by tuning the PID gains to attain a decent stability among performance and robustness. Through evasion, the procedure selects a crossover frequency founded on the station subtleties, and projects for a mark phase margin of 60° . When an operator interactively modifies the bandwidth, phase margin, transient response, or response time using the PID tuner interface, the procedure calculates original PID advances.

In a specified strength, the modification in the procedure selects a controller project that equilibrums the two events of presentation, position following, and uproar refusal. The operator can alter the project effort to indulge in one of these presentation events. For this, the usage of design focus option of PID tune at the grasp streak or the choices discourse case in PID tuner [15].

When operator modifies the design focus, the procedure efforts to regulate the improvements to service whichever position tracing or uproar refusal, though attaining the similar least phase margin. In additional tunable limits, there are in the scheme, and the additional possibility is that the PID procedure can accomplish the anticipated design focus deprived of forgoing heftiness. For instance, locating the design focus is added to attain active power for PID controllers than for P or PI controllers. In every situation, tuning the action of the structure hinge on sturdily on the belongings of operator plant. In few plants, varying the DF has slight or not at all consequence [22] (Table 1).

5 Simulation Results

To judge the efficacy of proposed scheme, the single-phase induction motor is simulated in MATLAB/Simulink without/with any controller as shown in Figs. 2 and 3, respectively. The induction motor speed is taken as input of the PID controller (Fig. 3).

The disturbance is created in mechanical load torque at $t = 2$ s.

The speed as a function of time in two cases is shown in Figs. 4 and 5, respectively. From these curves, it has been observed that the speed is rising and does not settle to any final value. Thus, the system speed is unstable when no controller is connected

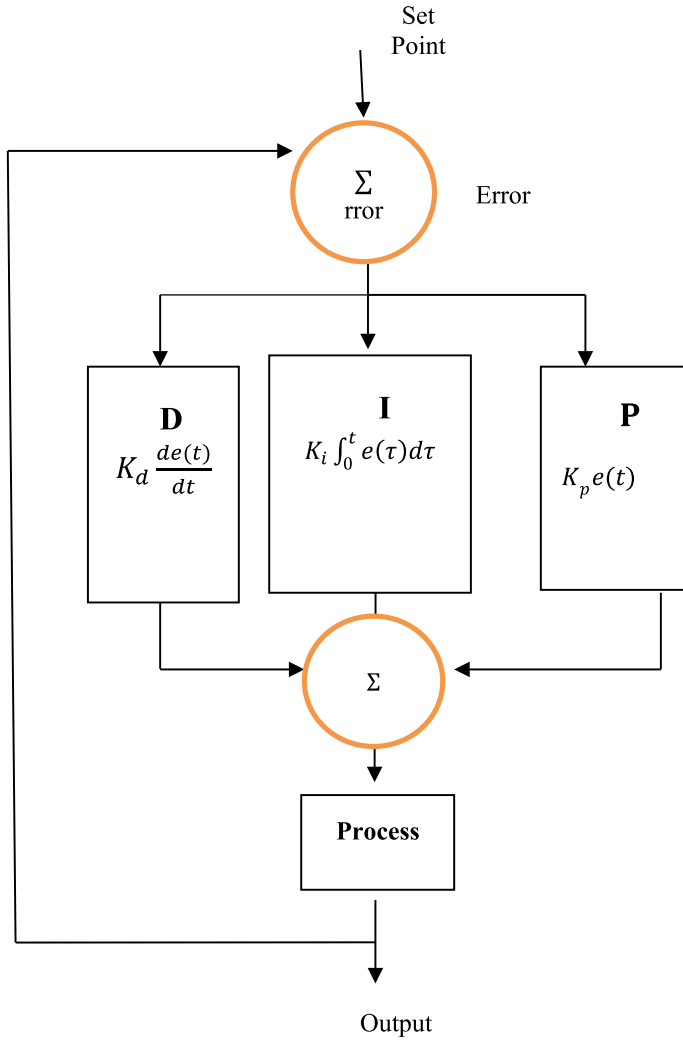


Fig. 2 Basic PID control scheme

(Fig. 4). However, in the presence of tuned PID controller, the induction motor speed becomes stable (Fig. 5) with good performance. The various performance parameters, viz., rise time, overshoot, peak value, gain margin, and phase margin are quantitatively shown in Table 2 (Fig. 6).

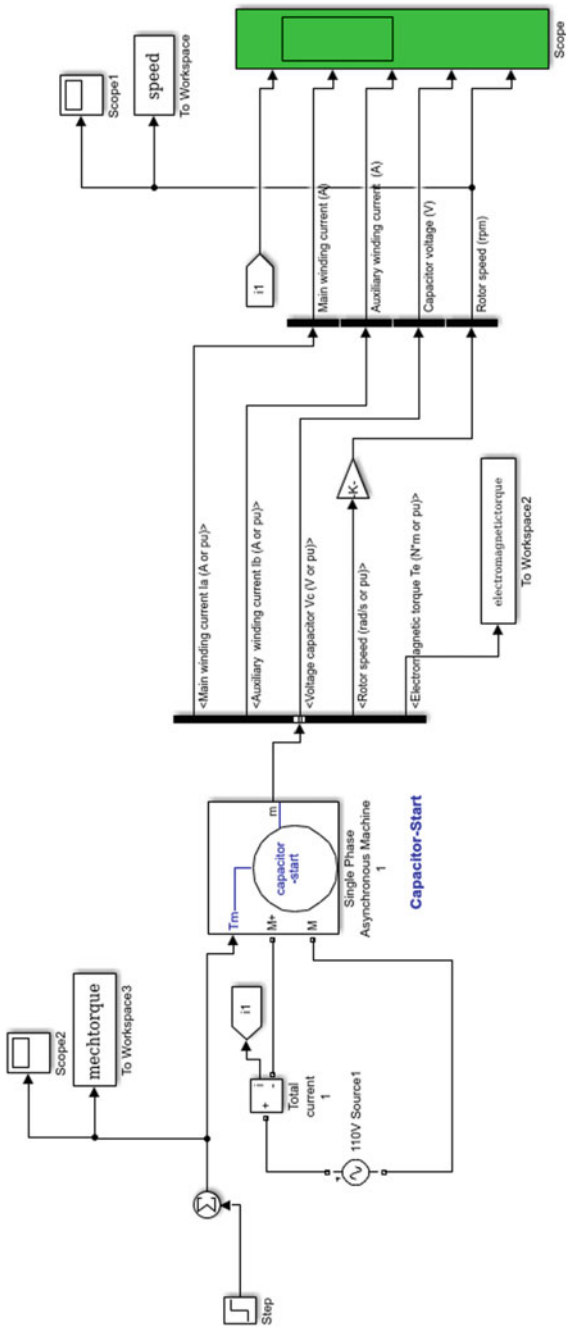


Fig. 3 Induction motor simulink model without any controller

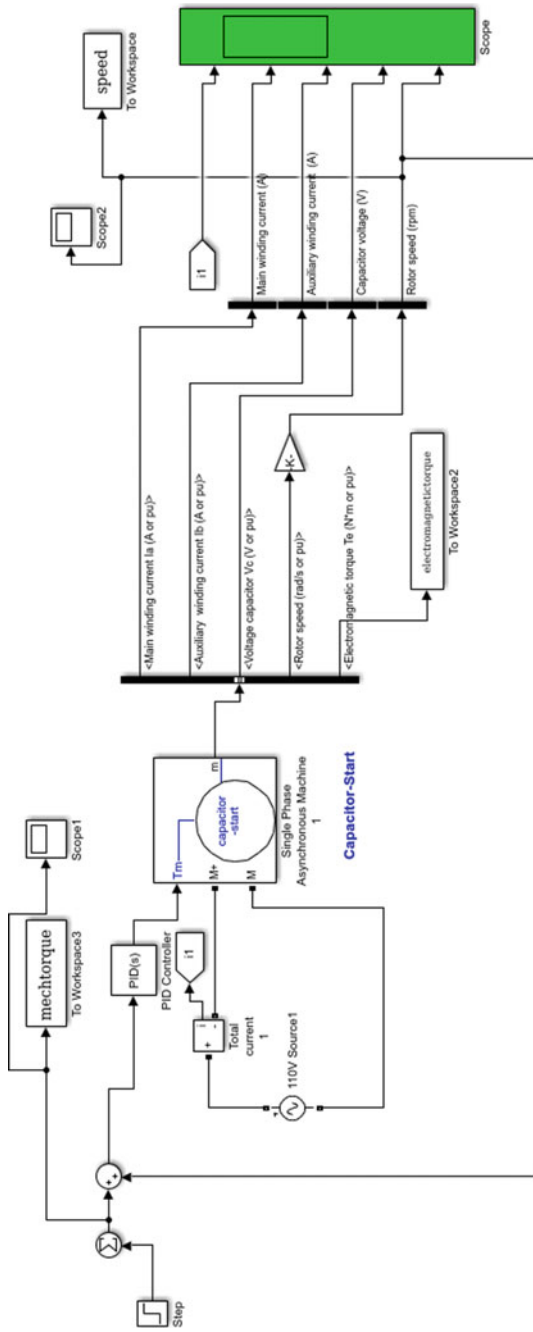


Fig. 4 Induction motor simulink model with PID controller

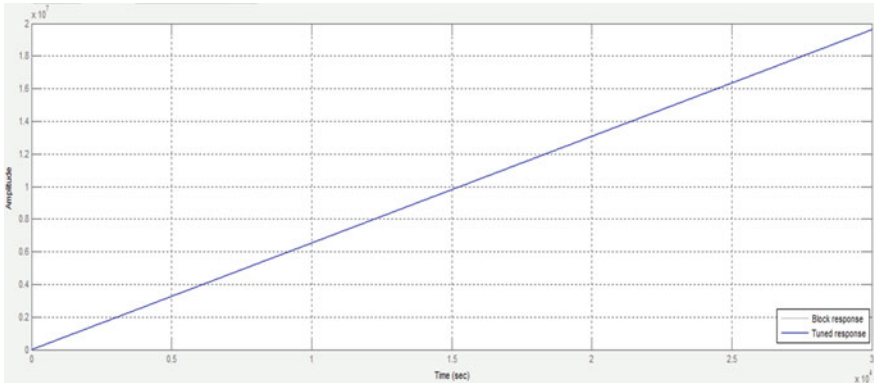


Fig. 5 Induction motor speed versus time (without any controller)

Table 2 Performance and robustness

S. No.	Performance and robustness	With PID controller
1	Rise time (s)	1.36
2	Settling Time (s)	4.21
3	Overshoot (%)	5.71
4	Peak	1.06
5	Gain margin (db @ rad/s)	0
6	Phase margin (deg @ rad/s)	64.3
7	Closed-loop stability	Stable

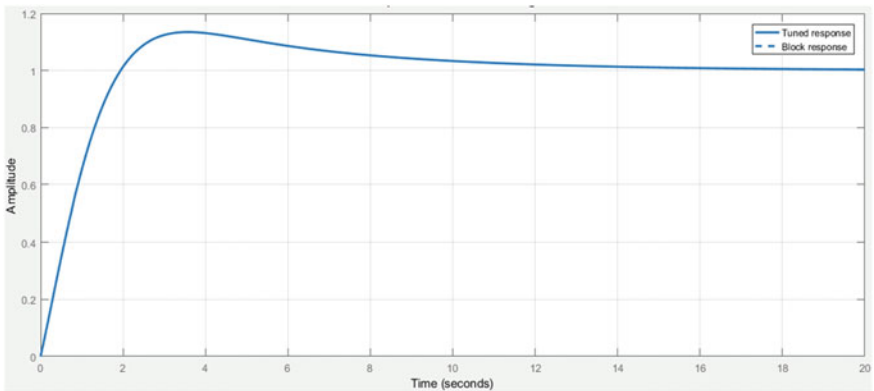


Fig. 6 Induction motor speed versus time (with PID controller)

6 Conclusion

The PID controllers are conventionally used in the industrial systems to achieve the improvement in dynamic stability and performance of electric drives. In this work, the PID controller parameters have been optimized using PID tuner software in MATLAB/Simulink. The computer simulation results show the remarkable improvement in stability and performance of the single-phase induction motor speed in the presence of loading uncertainties.

References

1. Padma S, Bhuvanewari R, Subramanian S (2007) Application of soft computing techniques to induction motor design. *Comput Math Elec Electron Eng* 26(5):1324–1345
2. Kim JW et al (2005) Optimal stator slot design of inverter-fed induction motor in consideration of harmonic losses. *IEEE Trans. Magn* 41(5):2012–2015
3. Paice Derek A (1968) Induction motor speed control by stator voltage control. *IEEE Trans Power Appar Syst* 87(4):585–590
4. Lyshevski SE (1999) *Electromechanical Systems, Electric Machines, and Applied Mechatronics*. CRC
5. Wiczeorek JP, Gol O, Michalewicz Z (1998) An evolutionary algorithm for the “optimal design of induction motors”. *IEEE Trans Magn* 34(6)
6. Madhavi LM (2001) *Int J Technol Eng Sci* 1:11–1
7. Bharadwaj DG, Venkatesan K, Saxena RB (1979) Induction motor design optimization using constrained rosenbrock method (Hill Algorithm). *Comput Electr Eng* 41–46
8. Erickson CJ (1988) Motor design features for adjustable-frequency drives. *IEEE Trans Ind Appl* 24(2)
9. Goutam KP (2012) PID controller based closed loop control of L-matrix based induction motor using V/f constant method. *J Sci Theory Meth* 1–21
10. Rajamani HS, Mcmohan RA (1997) Induction motor drive for domestic application. *IEEE Ind Appl Mag* 3(3)
11. Boglietti A et al (2005) No tooling cost process for induction motors energy efficiency improvements. *IEEE Trans Ind Appl* 41(3):808–816
12. Uddin MN, Wen H (2002) Development of a self-tuned neuro-fuzzy controller for induction motor drives. *IEEE Trans Ind Appl* 43(4):1108–1116
13. Singh C, Sarkar D (2009) Practical considerations in the optimization of induction motor design. *Int J Comput Electr Eng* 1(1):1793–8198
14. Yaohua L, Jinqi R (2008) *Electrical Machines and Systems*. Drive system of single side linear induction motors. In: ICE EEE conference, 2008
15. Rodriguez J, Pontt J, Silva C, Huerta R, Miranda H (2009) Simple direct torque control of induction machine using space vector modulation. *IEEE Electr* 23(4):412–413
16. Ustun SV, Demirtas M (2008) Optimal tuning of PI coefficients by using fuzzy-genetic for V/f controlled induction motor. *Exp Syst Appl* 2007:2714–2720
17. Cunkas M, Akkaya R (2006) Design optimization of induction motor by genetic algorithm and comparison with existiong motor. *Math Comput Appl* 11(3):193–203
18. Ying X (2009) , Characteristic performance analysis of squirrel cage induction motor. *IEEE Trans Magnet* (2) (1)
19. Dazhi WR, Hui J, Jie Y (2004) Sensorless speed control strategy of induction motor based on artificial neural networks. In: *Proceeding of 5th world congress on intelligent control and automation (WCICA)* 5(2):4467–4471

20. Lashok K, Kodad SF, Sankar Ram BV: Modelling of induction motor and control of speed using hybrid controller technology
21. Kale B, Ozdemir M (2004) A novel technique for optimal efficiency control of induction motor fed by AC chopper Saracoglu. In: IEEE 35th annual power electronics specialists conference PESC 04, vol 5, no 2

IoT (Internet of Things) Based Emergency Push-Button System



Jasmeen Kaur Ahluwalia and Misha Kakkar

Abstract This paper aims at aiding the security industry by enhancing the security of people anywhere and everywhere by creating and analysing a system that makes use of an emergency push-button service. The proposed system involves notifying the family members or close relatives of the user around the globe as soon as the button is pressed (for instance, during emergency situations). The system involves making use of the microcontroller ESP8266 chip, which is a Wi-Fi compatible chip, and the If This Then That (IFTTT) web service. The underlying concept used for making the system is Internet of Things, which allows machine-to-machine communication. The system makes use of email and SMS notifications that are sent to the recipients who are well known to the user along with the user's current location. The proposed system also finds a wide variety of uses in the mechanical industry. It can be used in factories to pinpoint the exact location of dysfunctional machine parts, or in automobile vehicles during emergency situations. This system is extremely cost-effective, handy to carry, sturdy and reliable, and if implemented on a larger scale, can be a huge boon to the security industry in the near future.

Keywords Push button · IFTTT · Location tracking · Security · ESP8266

1 Introduction

In the present world, due to increasing crimes such as abductions, murders, assaults etc., the personal security of individuals is constantly being threatened. Despite such advancements in technology, there has not been much improvement in the security of individuals. The project proposed in this work aims to make a revolutionary advancement in this field and thus enhance the security of each and every person. The proposed system is capable of notifying the family members of the user as soon

J. K. Ahluwalia (✉) · M. Kakkar
Amity University Uttar Pradesh, Noida, Uttar Pradesh, India
e-mail: jasmeenkaurahluwalia@gmail.com

M. Kakkar
e-mail: mkakkar@amity.edu

© Springer Nature Singapore Pte Ltd. 2019
M. Kumar et al. (eds.), *Advances in Interdisciplinary Engineering*, Lecture Notes in Mechanical Engineering, https://doi.org/10.1007/978-981-13-6577-5_77

as he/she presses the button. The family members of the user will then receive an email and SMS notification that contains the emergency message along with the current location URL of the user. This system is not only portable, but is also very reliable and cost-effective. The system is also relatively less prone to damage, thus making it ideal for daily use.

Similar works exist that make use of the emergency panic button and various types of location-tracking services. However, the existing systems usually contain too many components, thus making them heavier and less portable, or do not possess Wi-Fi capability, thus rendering them unreliable in various situations [1, 2]. On the contrary, our proposed system aims to work on these shortcomings and thus create a system that consists of lesser components, supports Wi-Fi capability and is much more reliable, sturdy and cost-effective.

This proposed system allows us to carry out machine-to-machine communication. Here, the button and microcontroller set, which is a machine, is successfully able to use the If This Then That (IFTTT) [3, 4] applet to send emails and SMSs to the recipients' devices, which are also machines. Machine-to-machine communication is the principle concept of Internet of Things (IoT) [5]. The Internet of Things is the concept of connecting any device to the internet and to other connected devices. The IoT is a giant network of connected things and people—all of which collect and share data about the way they are used and about the environment around them. It makes use of the ability to transfer data over a network without requiring human-to-human or human-to-computer interaction. This includes an extraordinary number of objects of all shapes and sizes—from smart microwaves, which automatically cook your food for the right length of time, to self-driving cars, whose complex sensors detect objects in their path.

1.1 Usage in Industry

The system proposed in this work is also extremely useful in the industrial sector. Similar systems can be modified and built to aid the mechanical industry by providing locations of damaged parts/components in the factories, etc. A few such examples are mentioned below:

1. This system can easily be attached to automobile vehicles. Since the system is miniature, it can easily be incorporated into vehicles and can be used by the drivers to send emergency messages with their locations to their loved ones, mechanics, or any other intended recipients. Since the system is extremely sturdy and reliable, it would be ideal in helping the users during emergencies. Thus, such an inbuilt system in vehicles would provide extra security to the users.
2. Such systems can also be attached to the various machines in a large factory. The system could be programmed to initiate a trigger as soon as a machine part stops functioning properly. This would allow an alarm to be triggered to notify the factory's workers/caretakers/owners and pinpoint the exact location of the

damaged machine part. Such systems could also be incorporated with separate GPS modules, and a common Wi-Fi connection in the factory to cut on the costs of the system.

Thus, the above-mentioned modifications would render this system extremely useful in various industries such as the power, railway, aerospace industry, construction and building sites etc., in addition to being useful in the security industry.

A detailed description of the working of the system and the various components involved shall be explained in the subsequent sections of this paper. Section 2 of this work contains a detailed description of the materials and methods involved in building the system, followed by Sect. 3, which contains a discussion about the various advantages, disadvantages of the system and its comparison with various other similar existing technologies. The observed working of the project and the various findings are elaborated in Sect. 4, followed by Sect. 5, which concludes this work and gives an insight into the future scope of this system.

2 Materials and Methods

The materials required to build the system are as follows:

1. Push Button (Digital): The push button is a digital button that can easily be used with microcontrollers like ESP8266, Arduino, etc. The button sends digital signals to the microcontroller, and it sends the value '0' whenever it is pressed.
2. ESP8266 Node MCU Development Board [6] with NodeMCU Firmware installed. The microcontroller ESP8266 is a very low-cost Wi-Fi chip with full TCP/IP stack and microcontroller capabilities. The chip is compatible with various sensors and buttons and can hence easily be integrated with our digital button.
3. IFTTT web service, which is a freely available web service that allows its users to make use of simple conditional statements to create applets. These applets are capable of receiving trigger messages and then executing certain tasks.
4. Location-Tracking Services: For this project, any freely available location-tracking service or application can be used which makes use of GPS modules of our smartphones. Since this system will require constant Internet connection, which can be provided via the mobile devices that the users own, it is better and more affordable to use the GPS capabilities of the users' smartphone itself. In this project, we shall be making use of the 'Real-Time Location Tracking' application.
5. An Integrated Development Environment (ESPlorer IDE): This IDE will allow us to type our code in Lua language, transfer it to the microcontroller, debug and check for any errors, etc.
6. Mobile Device: The proposed system will require constant Internet connection which can only be provided by mobile devices. Hence, a mobile device is ideal for this system. Moreover, this will also allow us to use the GPS capabilities of

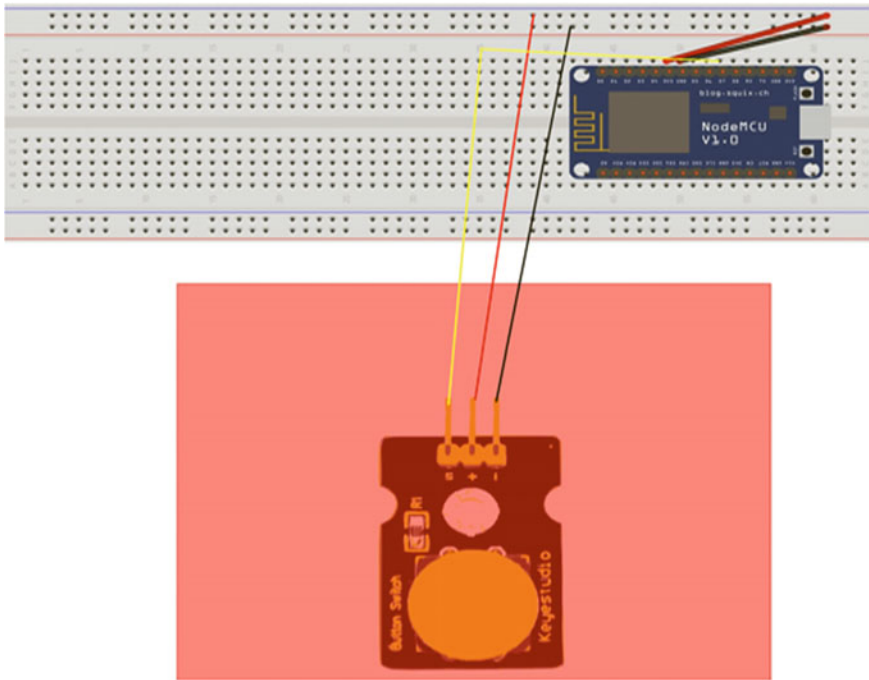


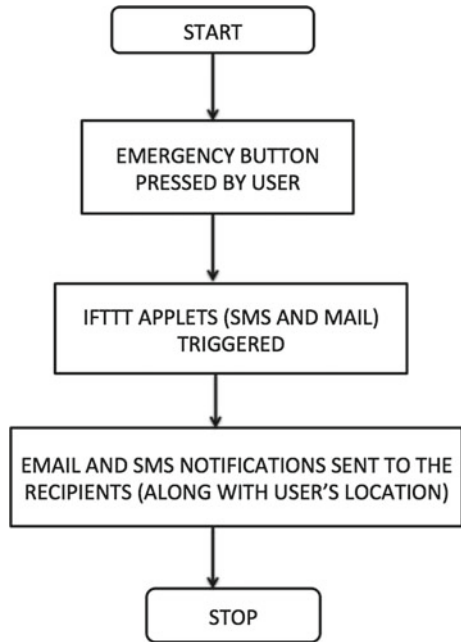
Fig. 1 Circuit of the push-button system

the mobile device. It is also essential for the users' family members to possess mobile devices such as smartphones, tablets, etc. so that the family members can receive the emergency messages sent by the user on pressing the button during emergencies.

The proposed methodology to be adopted to build the system is as follows:

1. Initially, the ESP8266 NodeMCU Development Board, the digital button, breadboard, jumper wires etc., were connected as depicted in the circuit shown in Fig. 1.
2. The next step was to create two applets on IFTTT, one for email notification, and one for SMS notification. For this, a trigger event was created using the webhook service of the 'if this' condition of IFTTT. It was then integrated with the Gmail and SMS service via the 'then that' condition. The applet was configured according to our needs and was then checked for any errors or issues.
3. The next step involved writing the Lua [7] code to be pushed onto the ESP8266 NodeMCU Development Board. ESPlorer IDE was used to successfully write, and check the code for any errors. The configuration details of the IFTTT applets were also put into the code so that the chip could access the trigger event when the button was pressed.

Fig. 2 Flowchart depicting the working of the emergency push-button system



4. After this, location-tracking services were setup. The application real-time location-tracking was installed into the smartphone (that would be used to provide Internet connection to the microcontroller). The public URL of the location-tracking service was written within the Lua code, and then the Lua code was pushed onto the ESP8266 chip.
5. The button was then pressed. The moment the button was pressed, an SMS and email was received on the devices of the intended recipients with the location URL that would provide the exact location of the push-button system.

A flowchart depicting the working of how this system works is given in Fig. 2.

3 Discussion

The emergency push-button system proposed in this work possesses a number of advantages that make it extremely feasible for everyday use. A few of these advantages are highlighted in this section which make this system commercially viable:

- The proposed system requires a minimal budget. This would make this system within the purchasing capacity of the lower income households as well. Hence, this system can cater to a large audience when implemented commercially.
- The system has an accuracy of nearly 98% and is hence extremely reliable. This can hence assure the user that the system would provide a huge benefit in emergency

situations. The factors leading to this accuracy are: the durability and reliability of the ESP8266 chip, and the current advancements in technology leading to better Internet connectivity all over the globe. The ESP8266 chip is extremely sturdy and works very well for a period of at least a year when operated on the ideal voltage of 3.3 V. Thus, this ensures that the chip is durable and thus reliable.

- The system is also extremely sturdy. This would allow less money to be spent on repairing the system as it would not require much maintenance.
- The system is a miniature and hence, it is easy to carry. This system would be much easier to carry as compared to other modes of self defence, and would also be much more reliable as it would aid in calling the necessary help well in time.
- With the increase in Internet services all over the globe, the range in which the system can be used is ever expanding. This would soon allow the system to be useful in even the most remote locations.

As compared to the various location-tracking technologies that currently exist, this proposed emergency panic button system poses a great number of advantages over them. It is essential to compare and contrast these available technologies with the system proposed in this work. Let us take for instance, the currently available popular Android, iOS etc., applications that allow sending emergency buttons (Table 1).

Hence, it can be observed that the push-button system would be more reliable as compared to the currently available Emergency mobile applications. More such panic button systems are currently being made as well, which makes use of GSM and GPS Modules, such as the one proposed by Nivedita Majumdar et al. in their work titled 'Emergency Panic Button using Microcontrollers' [1]. A comparison of the emergency push button with these types of systems is provided in Table 2.

Hence, it is observed that the advantages of the system proposed in this work outweigh those of the existing systems that require making use of the GSM and GPS modules. It is because of these advantages that the emergency system proposed in this work would be much more cost-efficient, reliable, sturdy and useful to the public.

4 Observations

The system was successfully implemented and it was observed that as soon as the button was pressed, an email and an SMS were received on the recipients' devices as shown in Fig. 3.

The message received on the recipients' devices contained the details of when the button was pressed, the name of the event, an emergency message, as well as the URL of the user's location, as depicted in Fig. 4. The same message was sent to all the family members of the user. On clicking the provided URL, it was possible to get the exact coordinates of the user's location, which would be redirected onto Google maps. This allowed the family members of the user to track the exact location and easily reach their loved ones during emergencies. It was also observed that every time the button was pressed, the messages '0 Emergency' and '200 Congratulations!

Table 1 Comparison of the proposed emergency push-button system with various emergency mobile applications

	Emergency applications	Emergency panic button system
Reliability	Most free applications (like ‘Self Defense for women’, ‘iHollaback’, ‘Eyewatch’, etc.) are not very reliable, and the comparatively more reliable ones need to be purchased	Extremely reliable with an efficiency of nearly 98%
Need of handset	The user needs to access the application on the mobile handset to be able to avail the emergency services	The user only needs to press the digital push button in order to send emergency notifications to loved ones
Wearable	The mobile application is contained within the mobile device, and thus cannot be utilised as a wearable	The emergency button can be made into a wearable that the user can wear on his/her wrist just like a watch. This makes the button easily accessible to the user
Battery drainage	The mobile applications when used constantly lead to battery drainage of the smartphone thus rendering it useless	The emergency button system makes use of a separate long lasting battery that is solely meant for it, thus not having any effect on the smartphone
Instant attacks	During instant attacks, it will be difficult for the user to open the smartphone, locate the app, and then use its services. Thus, rendering them impractical	During emergency situations, it is easier for the user to immediately press the panic button attached to their wrists. This is a more practical solution
Internet connectivity	Required	Required
Storage space	The application takes up extra storage space in the smartphone	The button is a separate module. It has no correlation with the mobile device’s storage space
Updates	Application may need to be updated regularly for better service	No updates needed
Sturdy	Mobile applications are prone to frequent crashes, or inefficient working	This system is extremely sturdy and rugged, thus making it more reliable
Device’s operating system	The functioning of the mobile application being used would depend on the operating system of the mobile device (such as Android, iOS, etc.)	The system is independent of the operating system of the mobile device.

Table 2 Comparison of the emergency push-button system with various push-button systems involving GSM and GPS modules

	Panic button with GSM and GPS modules	Emergency panic button system
Reliability	Depends on the reliability and quality of the GSM and GPS modules	Depends on the ESP8266 chip, which is extremely reliable
Wi-Fi compatible	No	Yes
Size of system	System is large since more modules are needed (e.g. GPS module, GSM module, microcontroller, push button, etc.)	Miniature, since only microcontroller and push button are needed
Sturdy	Not so sturdy due to the requirement of many delicate components	Sturdy and robust
Portability	Not very portable due to its large size.	Extremely portable and handy due to its small size.
Wearable	Cannot be incorporated into a wearable. Thus it is not very handy during emergency attacks	Can be made into a wearable (similar to a wrist watch) that can make it more accessible and handy for the user during emergency attacks
Cost	This system requires a minimum budget of approximately Rs. 3000 to be built. However, this budget would only allow a low quality system to be built	Can be built within a budget of Rs. 1500 with excellent quality components
SIM card requirement	This system would require a separate SIM card to be put into the GSM module	No additional SIM card is needed since the Wi-Fi chip ESP8266 makes use of the mobile device's Internet connectivity

You've fired the button event' (for instance, here 'button' is the event name) were received on the ESPlorer IDE, the default message being '1 Relax' when the button was not pressed. This indicated that our code was functioning properly as per our given commands. It was also observed that the messages (both email and SMS) were received as soon as the button was pressed. The delay observed was that of a mere 2 s. Moreover, the URL provided in the message redirected the recipient to the real-time location-tracking website that showed the real-time location of the user. It auto refreshed after every 15 s as shown in Fig. 5.

On clicking on the coordinates, it was possible to get redirected onto the Google maps website thus providing the family members with the exact location, as well as the directions towards the coordinates of the user (who pressed the button) as shown in Fig. 6.

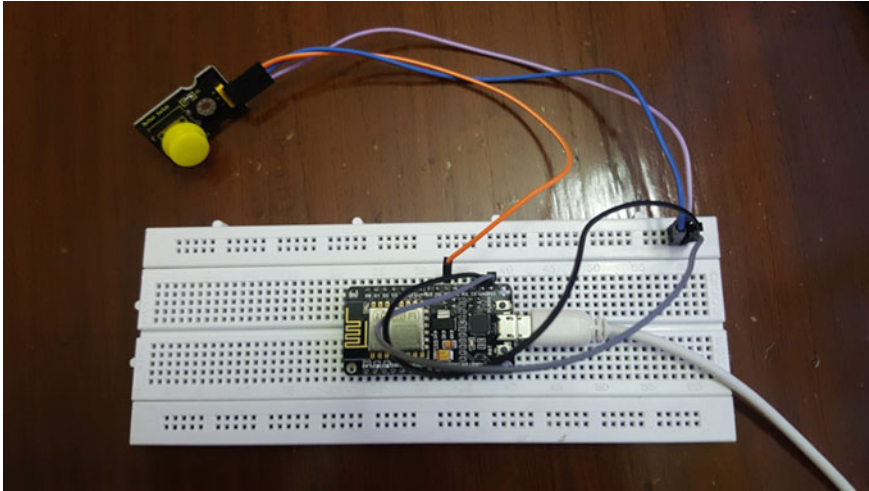


Fig. 3 Emergency push-button system

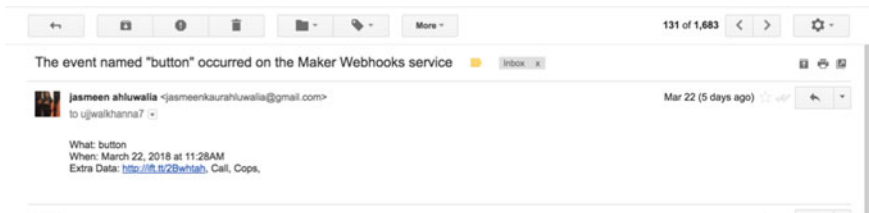


Fig. 4 Screenshot showing the email message received by the user’s family members with a URL indicating the user’s location

5 Conclusion

Through the technique proposed in this work, it was possible to successfully create an emergency push-button system that would notify the family members of the user as soon as the user presses it. This would allow an email and SMS message to be sent to the recipients along with the location details of the user facing an emergency. The proposed system is extremely sturdy, reliable and cost-effective. The system makes use of the IFTTT web service and the ESP8266 NodeMCU Development Board. The system is simple to build and implement, easy to carry, and very accurate. These factors make it well suited for nearly every household. Moreover, the low budget within which it can be built makes it economical and commercially viable. In addition, considering the increasing rates of crime in today’s world, a system like this would prove to be a huge boon to every individual as it would allow family members to keep track of their loved ones and act efficiently during untoward happenings. Moreover, with the current advancements taking place in the field of technology, the

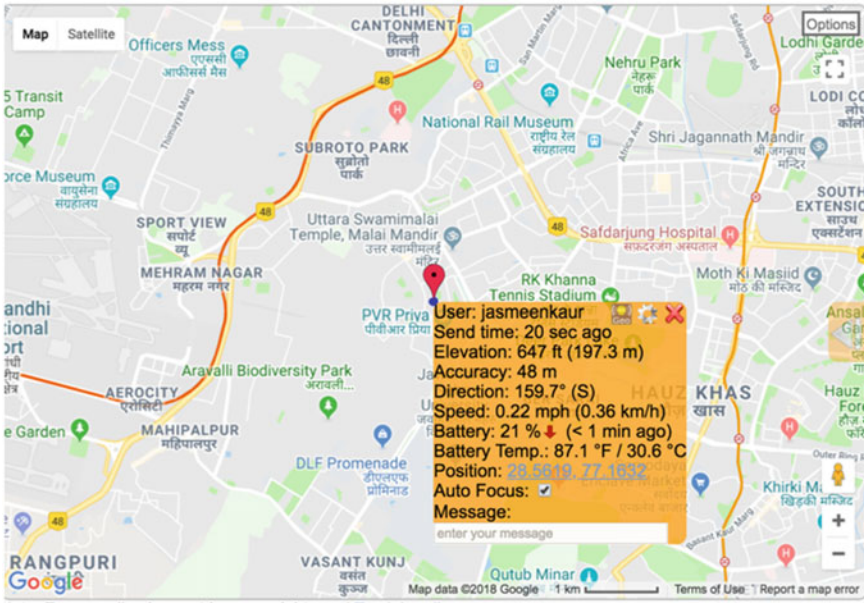


Fig. 5 Real-time location of the user, obtained by clicking the link in the email and SMS notification

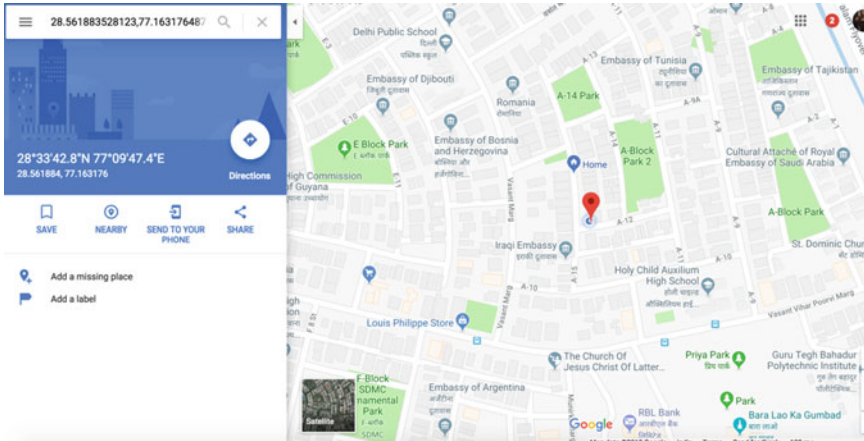


Fig. 6 Google maps website showing exact location of the user

reliability and efficiency of this system is expected to be enhanced even further, thus increasing the scope of this system in the future by manifolds.

References

1. Majumdar N, Bhargava P, Shirin RK (2014) Emergency panic button using microcontrollers. *Int J Comput Appl* 99(9):1–3
2. Near real-time tracking of IoT device users—IEEE conference publication (2017). [Ieeexplore.ieee.org](http://ieeexplore.ieee.org) [Online]. Available: <http://ieeexplore.ieee.org/document/7529985/>
3. IFTTT (2017). [En.wikipedia.org](https://en.wikipedia.org/wiki/IFTTT) [Online]. Available: <https://en.wikipedia.org/wiki/IFTTT> [Online]. Available: 1. <https://ifttt.com>
4. IFTTT (2017). [Ifttt.com](https://ifttt.com) [Online]. Available: <https://ifttt.com/email>
5. Internet of Things (2017). [En.wikipedia.org](https://en.wikipedia.org/wiki/Internet_of_things) [Online]. Available: https://en.wikipedia.org/wiki/Internet_of_things
6. ESP8266 (2017). [En.wikipedia.org](https://en.wikipedia.org/wiki/ESP8266) [Online]. Available: <https://en.wikipedia.org/wiki/ESP8266>
7. Lua: getting started (2017). [Lua.org](https://www.lua.org) [Online]. Available: <https://www.lua.org/start.html>

Investigative Analysis of Thumba Biodiesel Blends in a Single Cylinder Four Stroke IDI CI Engine at Varying Loads



Rabisankar Debnath , G. R. K. Sastry, R. N. Rai
and Jibitesh Kumar Panda

Abstract The present study investigates the performance (BThE) and emission (UHC, NO_x) of Thumba biodiesel at varying load percentages with respect to diesel. The experiment was conducted in an IDI CI engine at 34, 67, and 100% load conditions at constant 1500 rpm. Totally, three blends were used for the experiment. The first blend was 100% diesel (PD), the second blend was Thumba biodiesel 10% diesel 90% (Blend 1), and the third blend was Thumba biodiesel 20% and diesel 80% (Blend 2). The experimental result of both biodiesel blends was compared with diesel. From the experimental result, it was found that both the biodiesel blends showed comparable results of BThE, But UHC was lower for the blends whereas NO_x was higher for both the blends compared to diesel. From the experimental work, it was also found that the Blend 1 (Biodiesel containing Thumba biodiesel 10% and Diesel 90%) had better results than Blend 2. Also, Blend 1 showed comparable results to diesel.

Keywords Biodiesel · Diesel · BThE · UHC · NO_x

Nomenclature

BThE	Brake Thermal Efficiency
UHC	Unburned Hydrocarbon
NO_x	Oxides of Nitrogen
PD	Diesel 100%
Blend 1	Thumba Bio Diesel 10% Diesel 90%
Blend 2	Thumba Biodiesel 20% Diesel 80%

R. Debnath (✉) · R. N. Rai · J. K. Panda
Department of Production Engineering, National Institute of Technology Agartala,
Tripura 799055, India
e-mail: rabi101991@gmail.com

G. R. K. Sastry
Department of Mechanical Engineering, National Institute of Technology Andhra Pradesh,
Tadepalligudem 534101, India

1 Introduction

There is a greater influence of fossil fuels in various fields of development like industrial field, transportation, automobiles, and power generation. But uses on a larger scale is causing depletion of the level of these fuels day by day [1]. Also, the price of the fuels is rising due to mass utilization which is causing the depletion of the fuels [1, 2]. Addition to that, the emission from these fossil fuels is affecting the environment as well as human health directly or indirectly [3–6]. Therefore nowadays, various researches are going on for finding alternative sources that can be replaced partially or fully for these fossil fuels. Among them, biodiesels are in the center of attraction due to the similar properties of these fuels to the fossil fuels [5–7]. Biodiesels are oxygenated fuels [8] due to which it provides better combustion in the cylinder providing better performance as well as reducing the emission parameters. But the viscosity and density of the biodiesels are higher than diesel advancing towards poor atomization and engine carbon deposits leading to improper combustion. Due to these reasons, many papers have stated that biodiesel can be practiced in the engine with 80% diesel [9]. But this problem can be minimized by preheating of biodiesel [10] or transesterification of biodiesels [11, 12]. Various works expressed that biodiesel can reduce UHC, CO, and PM while NO_x is increased [13]. In the present work, blending of Thumba was done with diesel which was used as a biodiesel for the experimental work.

2 Materials and Methods

In the study, Thumba biodiesel blends were tested in a four stroke single cylinder IDI CI engine at varying load percentages. The blends taken for the experiment were of Thumba biodiesel 10 and 20% by volume with diesel fuel. Third fuel was 100% diesel. The experiment was conducted at 34% (2 kg load), 67% (4 kg load), and 100% (6 kg Load) conditions at constant 1500 rpm.

The fuel property of diesel and Thumba biodiesel is shown in Table 1.

The experiments were performed in an air-cooled indirectly injected (IDI) engine. The engine setup was connected with data acquisition system for calculating the

Table 1 Fuel properties of diesel and Thumba biodiesel used in the experiment

Fuel property	Diesel	Thumba bio diesel
Density (Kg/m^3)	830	880
Viscosity (mm^2/s)	2.7	5
Lower heating value (kJ/kg)	42	39
Cetane number	47	55
Flash point ($^{\circ}\text{C}$)	63	91

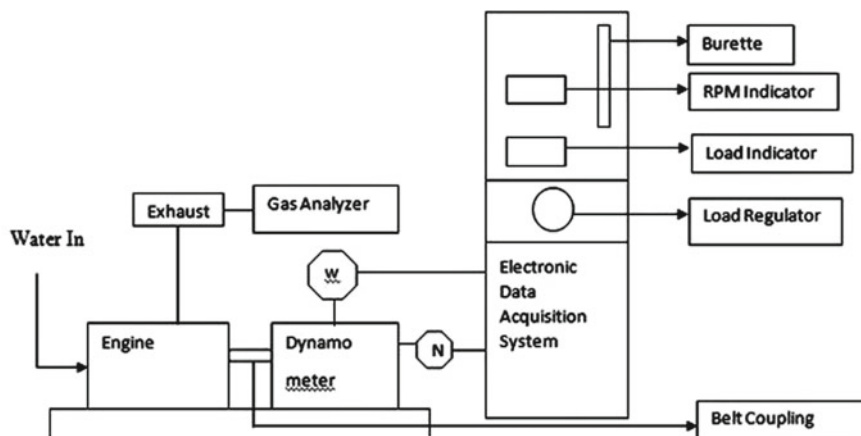


Fig. 1 Schematic layout of test setup

Table 2 Engine specifications

Make/Model	Kirloskar Varsha
Type	Horizontal 4 stroke/single cylinder diesel cylinder
Combustion type	Pre-combustion chamber type
Cooling	Air
Displacement (swept volume)	0.381 L
Fuel	Diesel

performance characteristics. The emission parameters were calculated by the AVL DI Gas analyzer. The schematic layout of the engine is given in Fig. 1.

The specification of the IDI engine used for the experiment is given in Table 2.

The full experiment was organized with varying loads from 34% (2 kg Load) to 100% (6 kg load) at constant 1500 rpm. The performance was calculated by measuring the data acquisition system and the emission was calculated from AVL DI gas analyzer. The result after the experiment was gathered and compared with diesel.

3 Results and Discussion

3.1 Change of Brake Thermal Efficiency with Load

Figure 2 shows the BThE with respect to load. From the figure, it was found that blends showed higher or equal brake thermal efficiency compared to diesel at 100% load conditions, which resulted from the cetane number of biodiesel which is higher than diesel. Also higher oxygen content resulted in better combustion and heat release

Fig. 2 Change of brake thermal efficiency with load

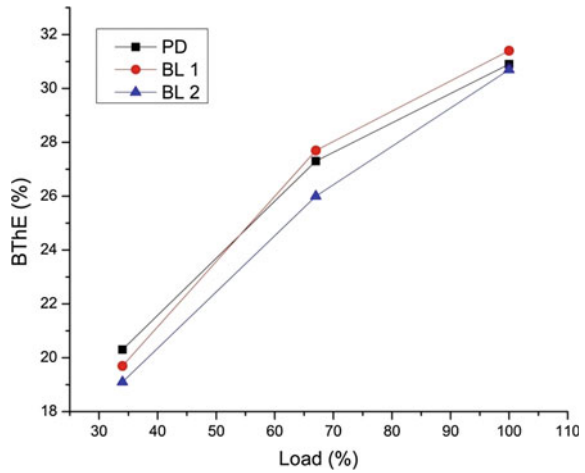
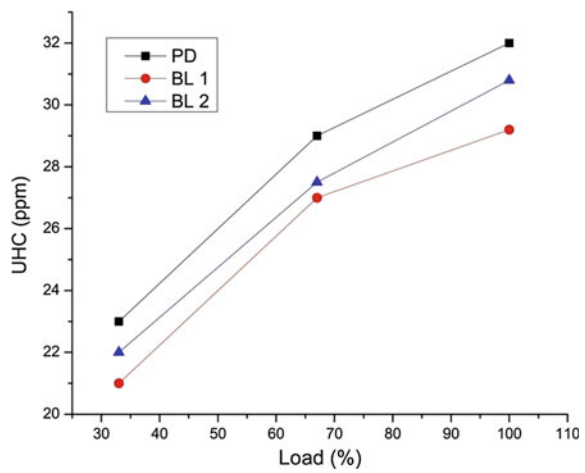


Fig. 3 Change of UHC with load

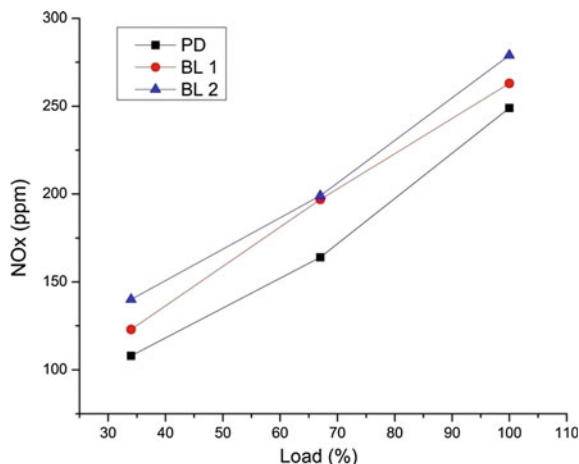


rate for the biodiesel blends. At lower load percentages, the BThE was lower for the blends due to lesser rate of complete combustion for lower heating values.

3.2 Change of UHC with Load

Figure 3 represents the change of UHC with load. It is clear that blends resulted in less UHC emission due to the better fuel burning inside the cylinder. Also, the biodiesel blends are more oxygenated fuels which helps in proper burning of mixtures at all load conditions for the blends compared to diesel. Many papers showed similar findings of UHC compared to diesel [14–16].

Fig. 4 Change of NO_x with load



3.3 Change of NO_x with Load

Figure 4 shows the NO_x emission with various load conditions of the fuels. From the figure, it was found that the blends resulted in higher NO_x than diesel at all load conditions. It was found that with biodiesel blends, the oxygen content as well as combustion temperature was higher which lead to higher NO_x emissions. The NO_x found to be on the higher side for the blends, which was mentioned in many papers [17, 18].

4 Conclusion

In this study, the various blends of Thumba biodiesel, i.e., 10% Thumba biodiesel with 90% diesel and 20% Thumba biodiesel with 80% diesel, were compared with diesel. The experiment was conducted in an IDI CI engine at varying loads of 34–100% at constant 1500 rpm. The BThE, UHC, and NO_x were calculated from the experiment and it was found that the biodiesel blends showed better or comparable results for BThE and better results for UHC. Whereas blends resulted in higher NO_x emission compared to diesel. From the experimental results, it can be concluded that the Blend 1, i.e., Thumba 10% and diesel 90% showed overall better results among the used blends.

References

1. Rinaldini CA, Mattarelli E, Savioli T, Cantore G, Garbero M, Bologna A (2016) Performance, emission and combustion characteristics of a IDI engine running on waste plastic oil. *Fuel* 183:292–303
2. Murugesan A, Umarani C, Subramanian R, Nedunchezian N (2009) Bio-diesel as an alternative fuel for diesel engines—a review. *Renew Sustain Energy Rev* 33:653–662
3. Ramkumar S, Kirubakaran V (2016) Biodiesel from vegetable oil as alternate fuel for C.I engine and feasibility study of thermal cracking: a critical review. *Energy Convers Manage* 118:155–169
4. Lau LC, Lee KT, Mohamed AR (2012) Global warming mitigation and renewable energy policy development from the Kyoto Protocol to the Copenhagen Accord—a comment. *Renew Sustain Energy Rev* 16:5280–5284
5. Lee ZH, Lee KT, Bhatia S, Mohamed AR (2012) Post-combustion carbon dioxide capture: evolution towards utilization of nanomaterials. *Renew Sustain Energy Rev* 16:2599–2609
6. Rai MP, Gupta S (2016) Effect of media composition and light supply on biomass, lipid content and FAME profile for quality biofuel production from *Scenedesmus abundans*. *Energy Convers Manage*. <http://dx.doi.org/10.1016/j.enconman.2016.05.018> (in press)
7. Shahid EM, Jamal Y (2008) A review of biodiesel as vehicular fuel. *Renew Sustain Energy Rev* 12:2484–2494
8. Ramadhas AS, Jayaraj S, Muraleedharan C (2004) Use of vegetable oils as IC engine fuels—a review. *Renew Energy* 29:727–742
9. Yilmaz N, Morton B (2011) Effects of preheating vegetable oils on performance and emission characteristics of two diesel engines. *Biomass Bio energy* 35(5):2028–2033
10. No S-Y (2011) Inedible vegetable oils and their derivatives for alternative diesel fuels in CI engines: a review. *Renew Sust Energy Rev* 15(1):131–149
11. Lapuerta M, Armas O, Rodriguez-Fernandez J (2008) Effect of biodiesel fuels on diesel engine emissions. *Progr Energy Combust* 34:198–223
12. Sharma YC, Singh B, Upadhyay SN (2008) Advancements in development and characterization of biodiesel: a review. *Fuel* 87:2355–2373
13. Yilmaz N, Donaldson AB, Johns A (2005) Some perspectives on alcohol utilization in a compression ignition engine. *SAE Trans J Fuels Lubricants* 114:1198–1203
14. Leevijit T, Prateepchaikul G (2011) Comparative performance and emissions of IDITurbo automotive diesel engine operated using degummed, deacidified mixed crude palm oil-diesel blends. *Fuel* 90:1487–1491
15. Ndayishimiye P, Tazerrouf M (2011) Use of palm oil-based biofuel in the internal combustion engines: performance and emissions characteristics. *Energy* 36:1790–1796
16. Aziz AA, Said MF, Awang MA (2005) Performance of palm oil-based biodiesel fuels in a single cylinder direct injection. *Palm Oil Develop* 42:15–27
17. Tuccar G, Ozgur T, Aydın K (2014) Effect of diesel–microalgae biodiesel–butanol blends on performance and emissions of diesel engine. *Fuel* 132:47–52
18. Atmanlı A, Yuksel B, Ileri E (2013) Experimental investigation of the effect of diesel–cotton oil–n-butanol ternary blends on phase stability, engine performance and exhaust emission parameters in a diesel engine. *Fuel* 109:503–511

Breast Cancer Detection Using Image Processing Techniques



Poorti Sahni and Neetu Mittal

Abstract Image processing is a widely used methodology in various medical sectors. Image processing involves performing some operations on images to extract some useful information. Image analysis is very helpful in the early detection of various cancers in which time factor is very crucial. The number of cases of breast cancer has increased worldwide. In this paper, breast cancer disease detection and its subsequent treatment has been discussed. In the proposed work, mammogram and MRI, the two important modalities, have been used to detect the tumorous portion more accurately. The tumorous part from the resultant image has been separated by different segmentation method such as edge detection and threshold method. Further different operators have been applied on resultant image and its quantitatively verified by performance measuring parameter entropy. The early detection of breast cancer can save life and make treatment less complex for medical practitioners.

Keywords Breast cancer · Image preprocessing · Image segmentation · Histogram analysis · Entropy · Mammogram · MRI

1 Introduction

Image processing is a technique to perform relevant operations on an image to extract significant data from it. It is a sort of signal process in which input is a picture and output could also be image or characteristics/features related to that image [1]. The purpose of medical imaging is to reveal internal structures additionally on diagnose and treat diseases [2]. Basic image processing includes—Image acquisition, image enhancement, and image segmentation [3]. To improve the characteristics of the image, or to provide a better representation for further image processing such as

P. Sahni (✉) · N. Mittal
Amity Institute of Information Technology, Amity University Uttar Pradesh,
Noida, Uttar Pradesh, India
e-mail: poortisahni@gmail.com

N. Mittal
e-mail: savini09@gmail.com

segmentation, detection analysis, and diagnosis, image enhancement is performed. Image enhancement is an important step in medical image processing. Due to low visibility and contrast, different segments or parts from the complete image cannot be distinct from the dark background. The primary goal of image enhancement is to reorient attributes of a picture to make it acceptable for a given task and a particular observer—human or machine. Throughout this method, one or a lot of attributes of the image matrix are reconstructed [4]. Image segmentation is the process of classifying or identifying sub-patterns in a given image. The purpose of image segmentation is to apportion a picture into many parts/segments having attributes almost like each other. There are two basic classifications of image segmentation: local segmentation (concerned with specific region of image) and global segmentation (concerned with segmenting the total image, consisting of enormous range of pixels). Based on the properties of image, the approaches towards image segmentation can be subdivided into two categories:

1.1 Detection Based on Discontinuity

It is the one in which an image is partitioned into parts based on discontinuity. Under this category, the edge detection based segmentation falls in which edges are built based on discontinuity in intensity levels and coupled to form the image borders.

1.2 Detection-Based on Similarity

It is based on the idea to divide the pixels of the image based on some similarity. Thresholding, clustering, region growing, merging, and splitting come under this category. The idea is to segment the images based on some criteria.

Breast cancer is the collection of abnormal cells which starts to grow in the breast cells. A major cause of death amongst women is breast cancer [5]. In 2016, the new cases of cancer in India were approximately 14.5 lakhs and this figure will likely be reaching 17.3 lakhs in 2020 as suggested by The Indian Council of Medical Research [6]. It is important for any research to understand the signs and symptoms of the problem. Having the signs and symptoms does not reflect that person has breast cancer but these signs should not be ignored and medical advice should be consulted if they are found. The indicators of the breast cancer involve—modification in the shape or size of the breast, i.e., unexplained swelling or shrinking of the size of the breast (especially on one side only), lump in the breast, nipples inverted or slightly inwards, skin of the breast becomes scaly or red, swollen or having ridges, thickening of the breast area, or the underarm area and milky discharge [7]. Breast pain is not a common sign of breast cancer. But if the breast pain persists along with signs and symptoms of the breast cancer, then a physician should be consulted [4]. If a lump is present in any of body part that may be the symptom of breast cancer. Lump can be

either benign or cancerous tumor. Benign tumors are harmless. Lump that appears soft, round, moveable is more suspected to be benign tumor or cysts and lumps that are hard, oddly shaped and feels as if attached with the breasts firmly are more likely to be cancerous. A mammogram is an X-ray in which a little dosage of ionizing radiation is used to create an image of the breast tissue. Mammograms can often show a breast lump before it can be felt. If the mammograms show an abnormal area of breast, then further test is performed that provides clearer and refined image of the suspicious area. The tests may include ultrasound and MRI. If the mass is found to be solid, then doctors recommend biopsy. Biopsy is the procedure in which some cells from the suspicious areas are taken for examination for the presence of cancer. The only diagnostic procedure that definitely determines the presence of cancer is biopsy. Diagnostic procedure for breast cancer—It involves a series of examinations and tests under proper guidance based on the symptoms and signs. If the biopsy results determine that the tumor detected is cancerous, then further tests (hormone receptor test and the HER2/neu test) are suggested to determine the stage of cancer and the type of treatment.

2 Proposed Methodology

To obtain more accurate results, the following procedure has been used.

2.1 Image Conversion

Grayscale conversion is also a vital part of image processing. Colored images make signal processing heavy as they have three dimensional properties (RGB information). This makes grayscale conversion necessary. Therefore, grayscale images do not carry any color information as all the color information is converted.

2.2 Image Filtering

The purpose of image filtering to remove noise and enhance the visual property of the image. This makes many useful tasks possible since a clearer and better version of image is obtained after filtration. There are many types of filtration techniques used for achieving different results. In this research, Gaussian smoothing filters have been used. Gaussian smoothing filters are a result of blurring of image using Gaussian function. Applying Gaussian filter includes three steps:

- Converting images to matrices of numbers
- Using Gaussian function
- Get blurred images.

2.3 Histogram Analysis

An image bar chart is the graphical illustration of the tonal distribution during a digital image within the type of histograms. It plots the number of pixels for every tonal value. Histogram can provide complete tonal distribution for an image because of its graphical representation. The x-axis is the gray level (intensity, brightness) of the image. The y-axis is the count of how many pixels in the image have the gray level.

2.4 Edge Detection Based Segmentation

The assumption behind the edge detection methodology is that edge is present when there is an abrupt change in intensity or change in intensity function. There are various edge detection methodologies and operators that implement these methods.

Steps for edge detection method.

Input: An image under consideration (MRI or mammogram)

Output: Magnitude of the slope of the image

- Step 1: Enter the input image
- Step 2: Application of mask to the input image
 - Horizontal mask (G_x)
 - Vertical mask (G_y)
- Step 3: To find the gradients, apply edge detection theorems
- Step 4: Construction of separate images for horizontal mask and vertical mask.
- Step 5: The magnitude of the gradient is found by combining the results.
- Step 6: Magnitude of the slope of the image is obtained as an output.

2.5 Thresholding-Based Segmentation

One of the simplest methods for segmentation is thresholding. Thresholding works on the principle to cluster the image pixels in accordance with their intensity values. Considering the threshold, T , the pixel located at position (i, j) , having grayscale value P_{ij} , is allocated to category 1.

If $P_{ij} \leq T$, Otherwise, the pixel is allocated to category 2 (Table 1).

3 Performance Assessment

To characterize the quality of the image under consideration, a statistical measure of randomness called entropy is used. Measurement of uncertainty before and after

Table 1 Comparison between thresholding- and edge-based techniques

Segmentation method	Explanation	Strength	Weakness
Thresholding technique	Threshold values can be computed on the basis of histogram peaks	No prior information is required	Spatial details missing
Edge-based technique	Based on detection of discontinuity	Images displaying difference among different objects have good results	Not preferable for images with high number of edges



(a) Original



(b) Grayscale

Fig. 1 Mammogram image

imaging is calculated to record the deduction in the uncertainty, i.e., information entropy provides the quantitative measure of the information transmitted by the image.

4 Simulation and Results

In the proposed work, image filtering is applied by using Gaussian filter on mammogram and MRI images to eliminate the noise shown in Figs. 1, 2, 3, 4, 5, and 6.

Figure 1 shows the original mammogram and its grayscale images and Fig. 2 shows original MRI and its conversion to grayscale images respectively.

Histogram analysis of the original mammogram and MRI images shown in Figs. 3 and 5 respectively.

Further, image segmentation process is done by thresholding and edge detection method to extract the tumorous portion from the rest of the mammogram and MRI images. To find out the best out of the thresholding and edge detection methods,

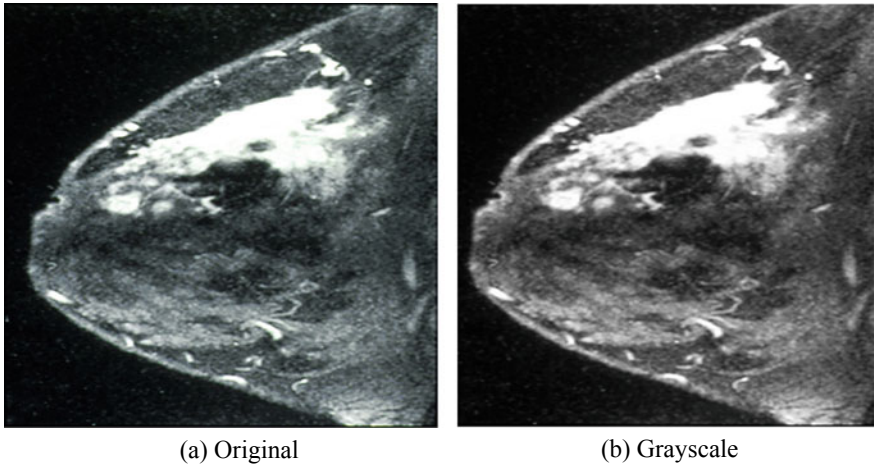
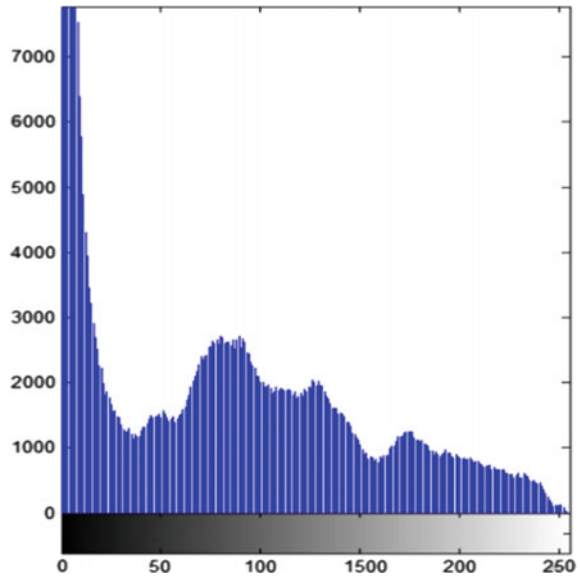


Fig. 2 MRI image

Fig. 3 Histogram of original mammogram



comparative analysis has been done by measuring the entropy of output images (Figs. 7, 8, 9, 10, and 11).

From Table 2, the entropy value of edge detection method and thresholding value of MRI are 0.0987 and 0.0763, respectively, and the values of edge detection method and thresholding value of MRI are 0.1002 and 0.040. The analysis proves that the edge detection method gives better results for MRI and mammogram images.

Fig. 4 Filtered image of mammogram

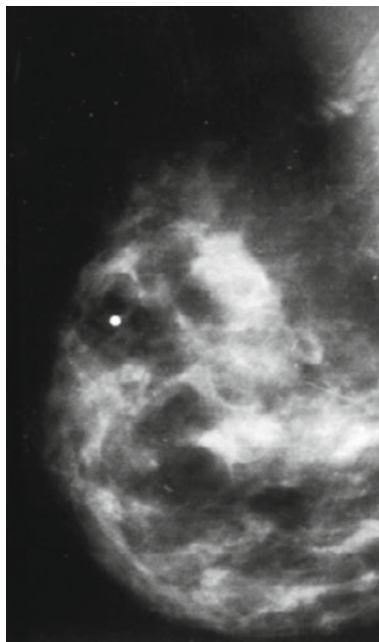


Fig. 5 Histogram of original MRI

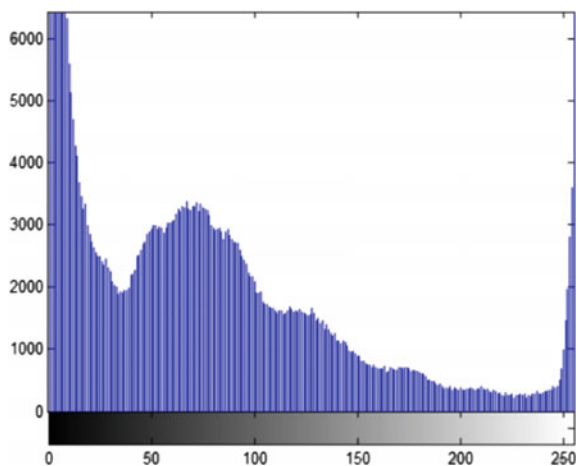


Table 2 Comparative analysis of entropy among mammogram and MRI images

Measuring parameter	Technique	Mammogram	MRI
Entropy	Edge detection	0.1002	0.0987
	Thresholding	0.0401	0.0763

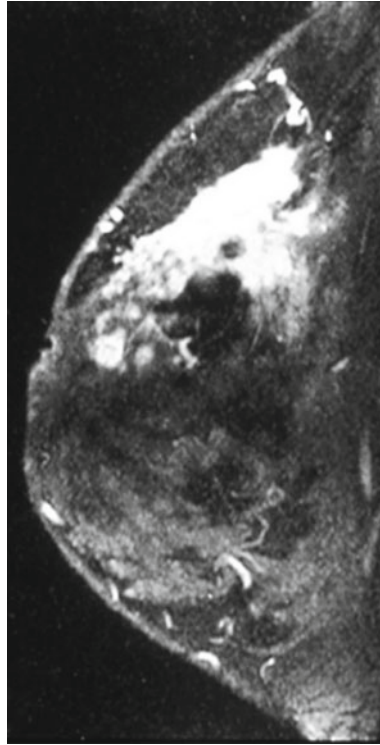
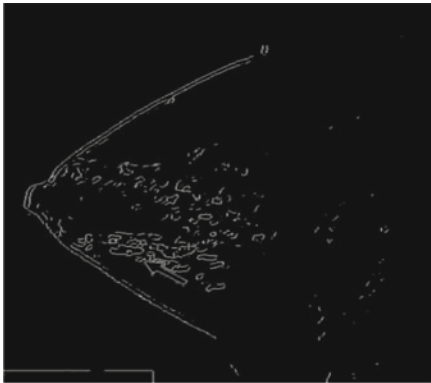
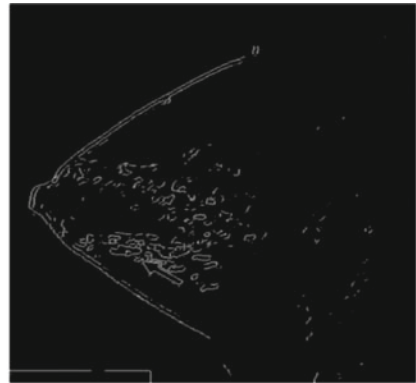


Fig. 6 Filtered image of MRI



(a) Edge detection for MRI



(b) Edge detection for Mammogram

Fig. 7 a, b Edge detection segmentation of MRI and mammogram

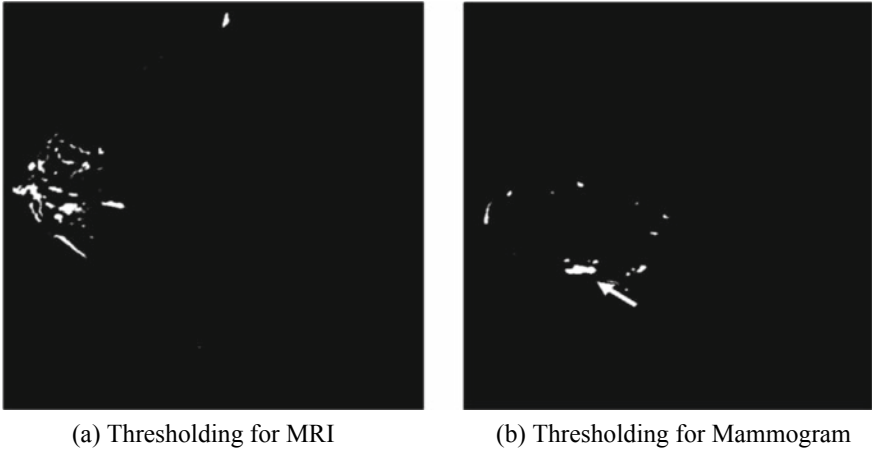


Fig. 8 a, b Thresholding segmentation of MRI and Mammogram

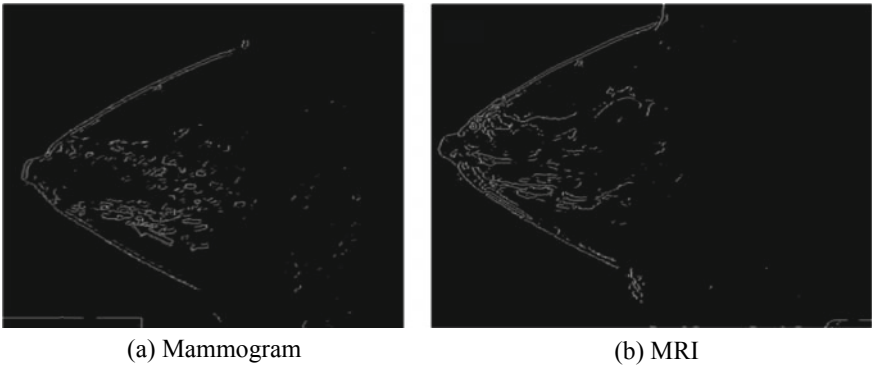


Fig. 9 a, b Sobel operator for Mammogram and MRI

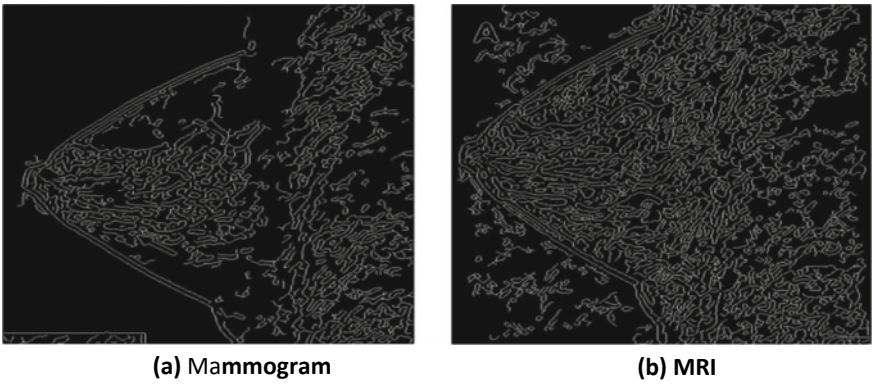


Fig. 10 a, b Canny operator on Mammogram and MRI

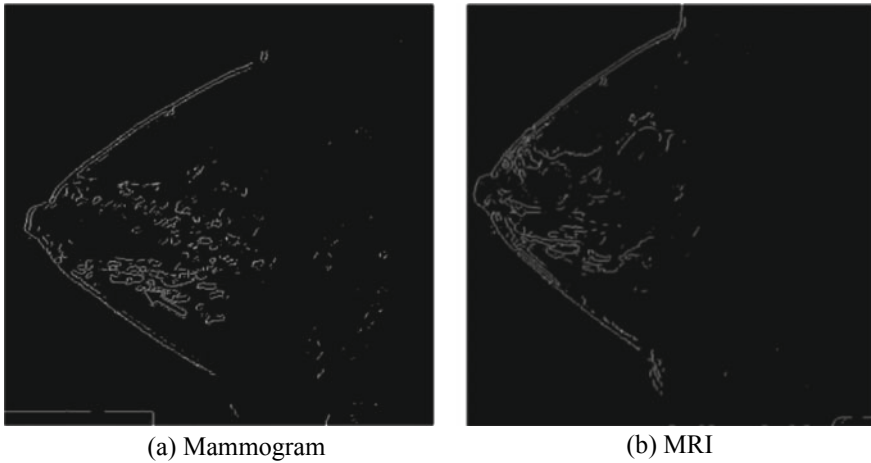


Fig. 11 a, b Prewitt operator on Mammogram and MRI

Table 3 Comparative analysis of edge detection operators among mammogram and MRI images

Edge detection operator	Mammogram	MRI
Sobel	0.1024	0.1010
Canny	0.3707	0.5334
Prewitt	0.1031	0.1012

Further, the work has been extended and finds out the best operator among the Sobel, Canny, and Prewitt for edge detection method on MRI and mammogram images.

Edge detection operators and its resultant images shown in Figs. 9, 10, and 11.

Table 3 shows the comparative analysis of edge detection operators among mammogram and MRI images. From the analysis, Canny edge detector gives the best value for entropy.

5 Conclusions

The gist of this research is to enhance image quality and provide accurate tumorous portion with better visibility of disease. Edge detection algorithms have shown better results for mammogram and MRI in comparison to thresholding which are compared using the quantitative measure called entropy. Further, edge detection operators are being analyzed for both mammogram and MRI. Results show that Canny operator shows better results than Sobel and Prewitt. Canny edge detection can help to segment the tumors in breast cancer for both the major modalities.

References

1. Gubern-Merida A, Kallenberg M, Mann RM, Marti R, Karssemeijer N (2015) Breast segmentation and density estimation in breast MRI: a fully automatic framework. *IEEE J Biomed Health Inform* 19(1):349
2. Ramani R, Vanitha NS (2013) The pre-processing techniques for breast cancer detection in mammography images. *Int J Image, Graph Signal Process* 5:47–54
3. Al-Tarawneh MS (2012) Lung cancer detection using image processing techniques. *Leonardo Electron J Pract Tech* (20). Issn 1583-1078, January–June 2012
4. Mageswarim SU, Sridevic M (2013) An experimental study and analysis of different image segmentation techniques. *Proced Eng* 64:36
5. Kaymaka S, Helwan A, Uzuna D (2017) Breast cancer image classification using artificial neural networks. In: 9th international conference on theory and application of soft computing, computing with 24–25 August 2017, Budapest, Hungary
6. Breast Cancer Cases in India (2016) Indian Council For Medical Research, New Delhi. https://icmr.nic.in/guide/cancer/Breast_Cancer.pdf
7. Singh AK, Gupta B (2015) A novel approach for breast cancer detection and segmentation in a mammogram. In: Eleventh international multi-conference on information processing-2015 (Imcip-2015)

Reduction of Noise of Cloud Medical Images Using Image Enhancement Technique



Ayushi Chauhan, Neetu Mittal and Sunil Kumar Khatri

Abstract The medical images are commonly available on cloud by researchers and doctors for better diagnosis and find new cures to diseases. However, due to blurriness and noises presented in such images, the intended purpose is not served. This paper presents stationary wavelet transform based two techniques i.e. Daubechies (DB) and HAAR wavelets for Gaussian noise removal from medical images. The computer simulations are carried out on a set of 20 medical images. The remarkable rise in entropy value of every image is noticed. The comparative analysis of MATLAB results suggest that DB is better than HAAR wavelet transform based method to improve the medical images and make them much more useful.

Keywords Image processing · Image enhancement · Image restoration · Peak signal-to-noise ratio · Denoising · Stationary wavelet transform · Image entropy

1 Introduction

Images describe a lot of knowledge. Any works can be explained better if it has an image with it but for that to happen, it is important for these images to be perfectly clear and understandable for a person to know what actually is that image depicting. Cloud contains a lot of images, which are used in different studies so it is necessary for these images to reflect properly.

The images of almost everything, every dimension, color and angle are available. There are images, which are not very clear because of the noise present in them and are difficult to understand, as we are not able to recognize each and every part of the image. There are a few techniques proposed by the researchers to enhance

A. Chauhan · N. Mittal (✉) · S. K. Khatri
Amity Institute of Information Technology (AIIT), Amity University,
Noida, UP, India
e-mail: nmittal1@amity.edu; savini09@gmail.com

A. Chauhan
e-mail: Ayushichauhan0110@gmail.com

S. K. Khatri
e-mail: skkhatri@amity.edu

the visibility of images available on cloud but not much research has been done on techniques of reducing the noise in them.

This research paper shows a comparative analysis between two wavelets of stationary wavelet transform and, depending on the results, suggests the better one to remove the noise which causes blurriness in the images and makes them more apt for researchers and doctors.

Before starting the method, let us go through the basic terms and concepts which are being used in the process.

Image processing is a branch of science in which computer algorithms are used to perform image processing on digital images. As a part of digital signal processing, digital image processing has many pros as compared to the analog image processing [1]. It provides a much wider range and better result of algorithms to be applied to the data that is being sent as an input. It also avoids problem like the build-up of noise and signal distortion during processing of an image. The images, which are defined over two dimensions digital image processing might be structured in the form of multidimensional systems [2].

Image enhancement is a part of image processing by which we can adjust the image in such a way that it becomes much more suitable for displaying somewhere for using them further in any process or research, etc. [3].

There are many techniques offered by image enhancement like histogram equalization, linear contrast adjustment, Wiener filter, median filtering, de-correlation stretch, etc. [4].

Image restoration can be defined as a process of taking up a corrupt or noisy image and perform simulation on it so as to obtain a clean and original image. This corruption in an image happens because of many reasons like motion blur, noise, and camera mis-focus [5]. Image restoration is performed by applying a reversing the process to the image that is blurred and is then performed by predicting a point source and using this point source image, that is known as the Point Spread Function (PSF) to restore the image information that was lost in the blurring process [6].

PSNR value stands for peak signal-to-noise ratio is a term that defines the use for the ratio of the maximum possible power of a signal to the power of corrupting noise that affects the fidelity of its representation [7]. Due to numerous signals which have a very wide dynamic range, PSNR value is normally represented in terms of the logarithmic decibel scale [8].

Denosing is a process in which any signal processing method is used to remove noise from signal [9]. The motive here is to preserve the meaningful information by removing noise from it. Denosing in image refers to the removal of blurriness from an image so as it can be used for various purposes.

Stationary wavelet transformation also known as “algorithm à trous” is the process of inserting zeros in the filters that was introduced by Holschneider et al., is a wavelet transform algorithm is prepared to outlook the lack of translation invariance of the discrete wavelet transform (DWT) [10]. Translation invariance is attained by discarding the downsamplers and upsamplers in the discrete wavelet transform and upsampling the filter coefficients by a factor of 2^{j-1} in the j th level of the algorithm [11]. SWT is an constitutionally needless scheme as the output of each level

of SWT holds the same number of samples as the input—so for the decomposition of “ n ” levels, there is a redundancy of “ n ” in the wavelet coefficients [12].

Image entropy is a unit which is used to define the “business” of an image, i.e., the amount of information that must be coded for by a compression algorithm [13]. Low entropy images, like the ones containing more of black sky, have very little contrast and large runs of pixels with the similar or sometimes exactly same DN values [14].

2 Literature Review

In the field of image processing techniques, some researchers have introduced quite a few new researches and proved that these images can be improved. In the case of the satellite image, image quality is degraded because of noises that are generally involved during capturing, transmission, and acquisition process of the image [15]. So, segmenting such noisy images does not produce an effective analysis result. Hence, we need some preprocessing techniques to remove artifacts; outliers or we can say noises from the images before going for further analysis stage. Image enhancement is such a preprocessing technique where our goal is to suppress the noise while preserving the integrity of edges and the other detailed information [16]. Actually, noises can be removed completely only when the real causes of their formation are studied and investigated. But in real fact, we cannot completely investigate them [17]. So, the only thing we can do is to introduce some mathematical equation based techniques to partially remove the noises as much as possible.

We calculate the 2-level SWT of the resampled signal using “db3” as the mother wavelet and then extricating the level 2 detail coefficients [18]. Level 2 coefficients then correspond to the [10, 20] Hz frequency band, which is well known to have maximal QRS energy and therefore is the most appropriate for QRS detection (1, 17) [19]. Note that the level-2 detail coefficients consequently procure having a sampling frequency of 80 Hz. We then resample these coefficients back to the earlier sampling frequency of the input signal for forward analysis [20].

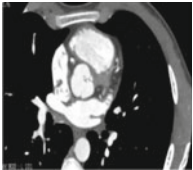

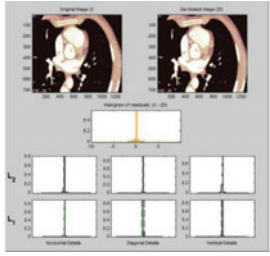
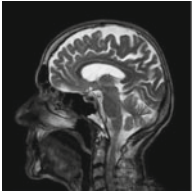

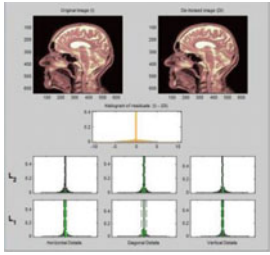


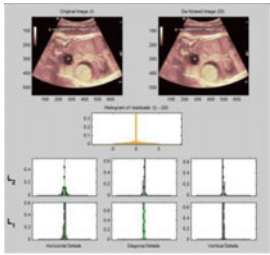
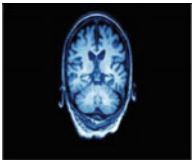
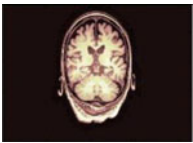
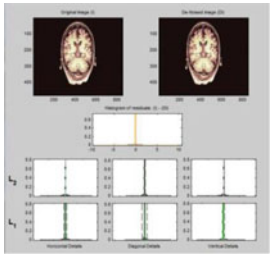
Though having quite a few techniques to reduced noise from these images which are effective and feasible in terms of quality but we still need to compare and find out the best possible solution of these images.

3 Proposed Work

For proceeding with simulation on the image, hardware requirement will be Microsoft Windows 7 (32-bit) and Image processing software like MATLAB and 3D slicer.

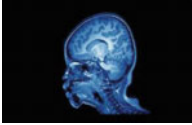
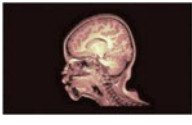
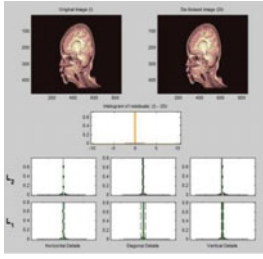


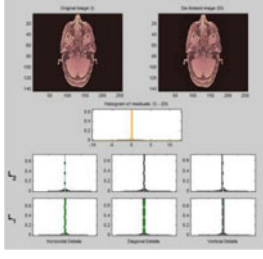


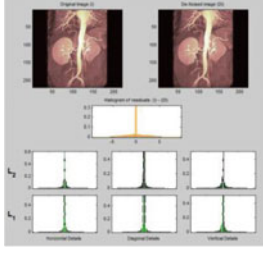
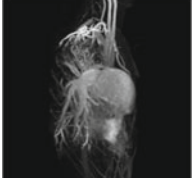
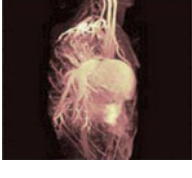
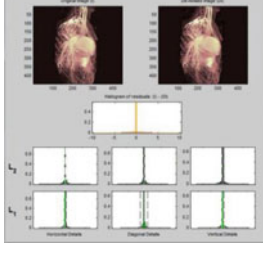
In the proposed work, 20 blur and noisy medical images have been taken and denoised under two wavelets of stationary wavelet transform. These two wavelets are HAAR and DB, keeping the same level in both, the wavelets blur medical images are simulated. After simulation of the image is completed, histograms of residuals

and the denoised image are obtained. This process is repeated on all the images and under both the wavelets so as to obtain results from a list of simulations. When all the images are simulated successfully, we need to check the entropy of the images and form a comparison table for them. This comparison gives the better wavelet type used for denoising an image.

S. No.	Input image	Final image	Graph
1			
2			
3			
4			

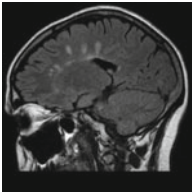
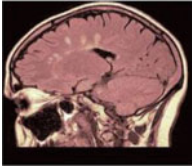
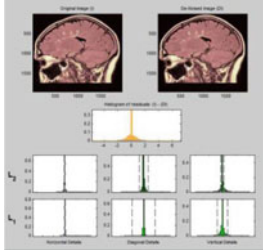

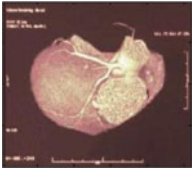
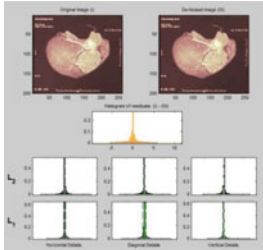
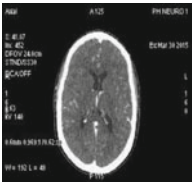
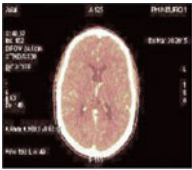
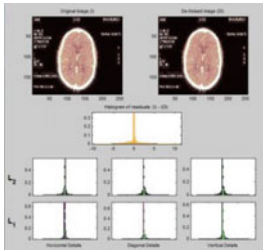
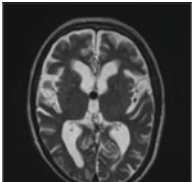
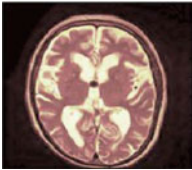
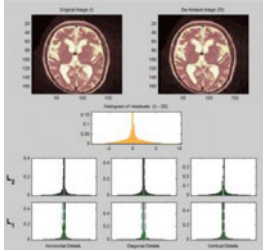
(continued)

(continued)

S. No.	Input image	Final image	Graph
5			
6			
7			
8			

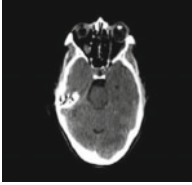
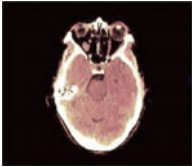
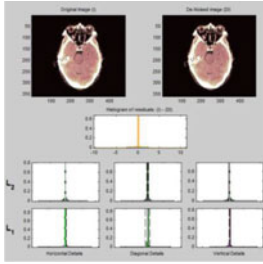
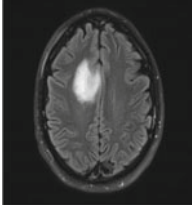
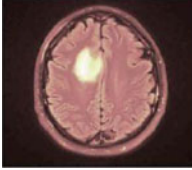
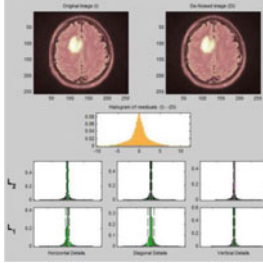

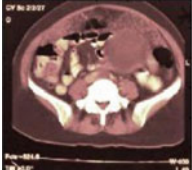
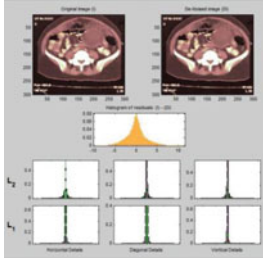
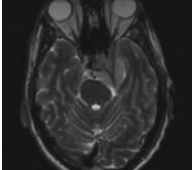
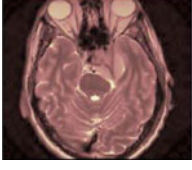
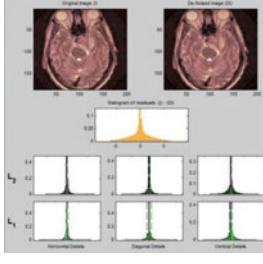
(continued)

(continued)

S. No.	Input image	Final image	Graph
9			
10			
11			
12			

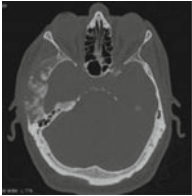
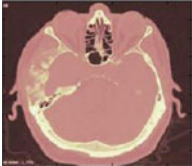
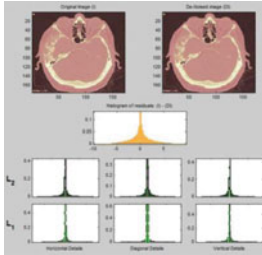
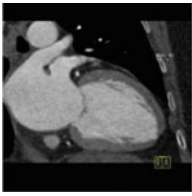

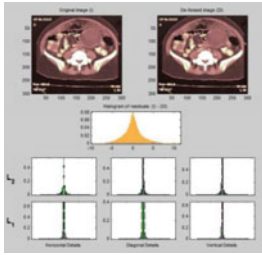


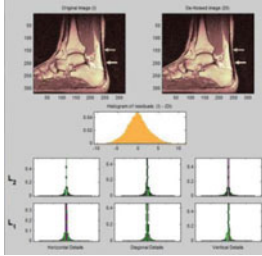
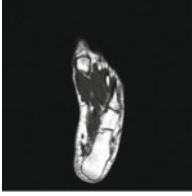

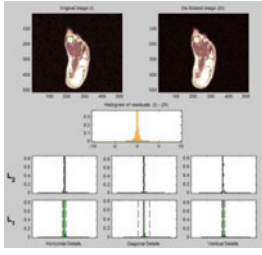
(continued)

(continued)

S. No.	Input image	Final image	Graph
13			
14			
15			
16			

(continued)

(continued)

S. No.	Input image	Final image	Graph
17			
18			
19			
20			

4 Analysis

Following is the entropy table made by the results of simulation.

S No.	Input image entropy	HAAR entropy	DB entropy
1	5.6657	6.6388	6.6906
2	4.3625	6.4324	6.6144
3	5.4146	6.6005	6.6043
4	5.7448	6.7639	6.7759
5	2.8539	4.7440	5.0147
6	3.0278	4.8669	5.1251
7	3.3118	5.4623	5.8353
8	5.8177	6.5712	6.7361
9	4.1311	5.7750	5.9349
10	5.8483	6.9569	6.9866
11	5.9028	6.9526	6.9862
12	3.9385	5.8490	5.8913
13	6.2809	7.5108	7.5455
14	3.1494	4.6381	4.6666
15	5.7883	7.1573	7.1863
16	6.5113	7.6066	7.6178
17	6.1361	7.4772	7.5147
18	5.8138	6.9973	7.0498
19.	6.6058	7.5199	7.5582
20.	3.0425	5.6628	5.7066

In the above table, results of 20 images are shown and each is denoised under both the techniques DB as well as HAAR. In the table, we can see the initial entropy values of the images referred to as Input Image Entropy (Column 1) then there is HAAR entropy (Column 2) which is the entropy value of image after denoising under HAAR technique and finally there is DB entropy (column 3) which contains the entropy of the image after getting denoised under DB technique.

5 Conclusion

The success rate of medical treatment for any disease largely depends on its diagnosis. In real time the medical images suffers with the problem of various unwanted noises. In this work, denoising of blurred medical images has been presented by using

two stationary wavelet transform techniques namely DB and HAAR wavelets, for accurate disease detection and its treatment. This has been observed that DB wavelet is showing higher entropy values than HAAR wavelet. The higher entropy indicates the greater visibility and clarity of medical image. The improved visibility with higher clarity may assist the medical professionals in accurate diagnosis and subsequent treatment of various diseases.

References

1. El Bouny L, Khalil M, Adib A (2017) ECG noise reduction based on stationary wavelet transform and zero-crossings interval thresholding. In: International conference on electrical and information technologies (ICEIT)
2. Kalidas V, Tamil L (2017) Real-time QRS detector using stationary wavelet transform for automated ECG analysis. In: IEEE 17th international conference bioinformatics and bioengineering (BIBE)
3. Patil PB, Chavan MS (2012) A wavelet based method for denoising of biomedical signal. In: International conference on pattern recognition, informatics and medical engineering (PRIME)
4. Tornekar RV, Gajre SS (2017) New improved methodology for ECG signal compression. In: Computing in cardiology (CinC)
5. Keshavamurthy TG, Eshwarappa MN (2017) Review paper on denoising of ECG signal. In: Second international conference electrical, computer and communication technologies (ICECCT)
6. Clifford GD, Azuaje F, McSharry PE (2006) Advanced methods and tools for ECG data analysis. Artech house engineering in medicine and biology series
7. Maniruzzaman M, Kazi M, Billah S, Biswas U, Gain B (2012) Least-mean-square algorithm based adaptive filters for removing power line interference from ECG signal. In: International conference on informatics, electronics and vision
8. Lai D, Zhang F, Wang C (2015) A real-time QRS complex detection algorithm based on differential threshold method. In: IEEE international conference on digital signal processing (DSP), Singapore
9. Merah M, Abdelmalik TA, Larbi BH (2016) R-peaks detection based on stationary wavelet transform. *Comput Methods Programs Biomed*
10. Sameni R et al (2007) A nonlinear bayesian filtering framework for ecg denoising. *IEEE Trans Biomed Eng*
11. Mallat S (1991) Zero-crossings of a wavelet transform. *IEEE Trans Inf Theor*
12. Sun Y, Chan KL, Krishnan SM (2005) Characteristic wave detection in ECG signal using morphological transform. *BMC Cardiovasc Dis*
13. Hussain SS, Zabit U, Bernal OD (2017) Real time Discrete Wavelet Transform architecture for self mixing interferometry signal processing. In: 14th international Bhurban conference applied sciences and technology (IBCAST)
14. Naser AM Color to grayscale image conversion based dimensionality reduction with stationary wavelet transform. In: International conference on multidisciplinary in IT and communication science and applications (AIC-MITCSA)
15. Donoho D (1995) De-noising by soft-thresholding. *IEEE Trans Inf Theory*
16. Moody GB, Mark RG (2001) The impact of the MIT-BIH arrhythmia database. *IEEE Eng Med Biol Mag*
17. Poornachandra S (2008) Wavelet-based denoising using subband dependent threshold for ECG signals. *Digital Sig Process*
18. Chopade PB, Patil PM (2015) Image super resolution scheme based on wavelet transform and its performance analysis. In: International conference on computing, communication and automation (ICCCA)

19. Wang R, Wang Y, Luo C (2015) EEG-based real-time drowsiness detection using Hilbert-Huang transform. In: 7th international conference on intelligent human-machine systems and cybernetics (IHMSC)
20. Rasti P, Lüsi I, Demirel H, Kiefer R, Anbarjafari G (2014) Wavelet transform based new interpolation technique for satellite image resolution enhancement. In: IEEE international conference on aerospace electronics and remote sensing technology (ICARES)

Segmentation of Skin Lesion Images Using Fudge Factor Based Techniques



Sudhriti Sengupta, Neetu Mittal and Megha Modi

Abstract Automatic edge detection is an important and noninvasive step in skin lesion identification. In this paper, the segmentation of skin lesion image is proposed by using edge detection operator with an adjusted threshold value. The clinical skin lesion image is first preprocessed via hair removal, contrast enhancement, and filtering techniques. After this, the skin lesion is segmented using a standard edge detection technique. The fudge factor is introduced and tuned in this detection to adjust the threshold value. For comparative study, Sobel, Prewitt, and Canny edge detection techniques are applied in the skin lesion image. The segmented outputs are compared using entropy and dice similarity index values of the segmented image.

Keywords Segmentation · Skin lesion · Threshold

1 Introduction

Segmentation is one of the most important steps in image processing. Segmentation is the process to extract objects and boundaries within an image for proper understanding of the image contents. The different computer-aided systems require some techniques for segmentation to extract region of interest in images. There are many types of segmentation methods based on edge or region of the images. A segmentation technique suitable for one type of image may not be applicable in other type of image. So, it is challenging to find an optimum segmentation process in terms of accuracy, speed, and computational efficiency [1].

Skin lesion image segmentation in CAD is used for the diagnosis of diseases related to skin. There are different types of skin lesion due to the effect of various diseases and other factors. Variation in the skin lesion image can be due to change

S. Sengupta (✉) · N. Mittal
Amity Institute of Information Technology, Amity University Uttar Pradesh, Noida, Uttar Pradesh, India
e-mail: ssgupta@amity.edu

M. Modi
Vaishali Speciality Hospital, Ghaziabad, Uttar Pradesh, India

© Springer Nature Singapore Pte Ltd. 2019
M. Kumar et al. (eds.), *Advances in Interdisciplinary Engineering*, Lecture Notes in Mechanical Engineering, https://doi.org/10.1007/978-981-13-6577-5_81

837

in color, shape, size dimensions, etc. Due to the presence of different skin lesions, image automated segmentation is challenging.

In this paper, a novel process of segmentation is introduced for extracting edges or boundary from skin lesion image. In the first step, the skin lesion image is pre-processed to remove any noise and enhance the quality of the image. After this, a segmentation method is applied with tuning of the fudge factor. The organization of this paper is as follows: Sect. 2 describes the work previously done. Section 3 describes the proposed methodology. The implementation and the analysis of the result are given on Sects. 4 and 6 discusses the conclusion.

2 Literature Review

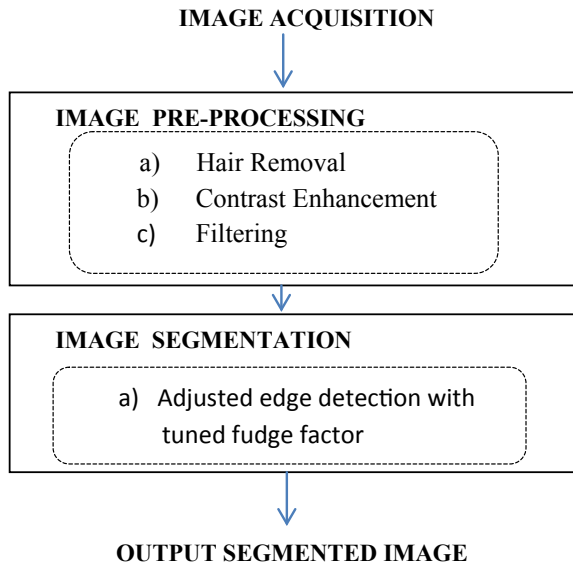
Skin lesion segmentation for detection of lesion type is an important step in automatic dermoscopic image analysis. However, skin lesion is very challenging because of variation of lesion color, texture, size or shape [2]. Some skin lesion has irregular edges while in some cases, there is a smooth change between lesion area and healthy skin area. There are many different approaches proposed for detecting the edge of skin lesion. They are generally categorized into three types: edge-based segmentation, region-based segmentation and threshold-based segmentation. In edge-based and region-based segmentation, edge pixels are searched and connected to form image contours [3]. Two most common edge detection methods are Laplacian of Gaussian and Canny Edge Segmentation [4]. The Laplacian filter is a derivative filter applied to find the regions of rapid intensity change in an image to detect the edges. Canny edge detector is very popular technique which is used as a standard for measuring other techniques [5]. The performance of edge based technique is poor when the edges are not clearly defined. Region-based segmentation partitions an image into regions based on some properties. The main concept applied in this technique is that neighboring pixels within the same regions have similar values. Threshold-based segmentation is also called pixel-based or point-based segmentation. It is a simple process where segmentation depends on gray level value of the image. The issue in this technique is to find the optimum level for threshold to get the best result.

3 Proposed Methodology

Figure 1 describes the workflow of the proposed model.

The proposed methodology consists of two main steps, as shown in Fig. 1. The first step is the preprocessing stage which is followed by image segmentation. Image preprocessing is an important step to enhance the image quality before proceeding to the next phase. In the proposed method preprocessing is done by three steps. First dull razor algorithm is applied to remove any hair from the skin lesion, and then the contrast of the image is enhanced to have better perception. Lastly, filtering

Fig. 1 Flow chart of the proposed technology



technique is applied to emphasise the region of interest. After these three steps of preprocessing, segmentation process is applied for edge detection in the skin lesion image. Four different edge detection operators are applied by tuning the threshold value with the help of the adjusted threshold value. The value of the threshold is adjusted using a fudge factor. In this paper fudge, we have taken two values of fudge factor, i.e., 0.5 and 1. The result of the proposed method is technique is measured quantitatively by using entropy and dice similarity index.

3.1 Preprocessing

The main goal of image preprocessing is improving the image data by enhancing the quality of the image and removing any kind of noise or distortion. Image features are also enhanced in this step. There are many different techniques of image processing such as contrast enhancement, wavelet function, DWT (Discrete Wavelet Function), filtering, etc. [6]. In skin lesion images, hair is one of the most common types of noise present. In this method, we have applied the well-known dull razor algorithm for removal of hair in skin lesion image. After this, the contrast enhancement method is applied. Contrast enhancement is used to improve the interpretability or perception of data in the image. It focuses on improving the contrast of an image to make various features more easily perceived. There are many different contrast enhancement methods like histogram equalization, morphological enhancement, grayscale modification, thresholding, interpolation, etc. For experimenting two contrasts, enhancement methods are applied separately to the test image. The image having a better

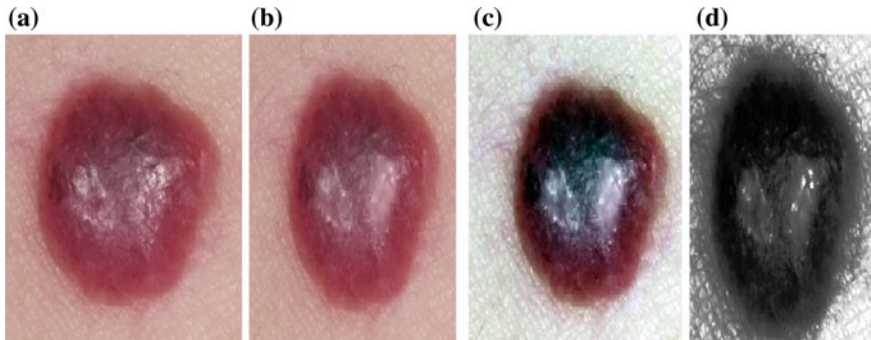


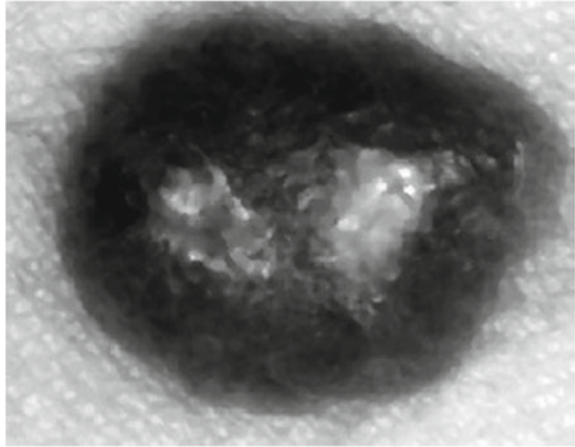
Fig. 2 **a** Original image; **b** result of dull razor hair removal; **c** result of morphological enhancement; **d** result of histogram equalization

level of enhancement is taken as the input in further stages of processing. Contrast enhancement is done by adjusting the intensity value of the pixels in first case. In the second case, histogram equalization is done for contrast enhancement of the image. The result is shown in Fig. 2.

The original images, i.e., Fig. 2a is obtained <https://www.gponline.com/clinical-images-nodular-skin-Lesions/dermatology/article/1228962>.

It is observed from Fig. 2c, d that contrast enhancement provides a better result if contrast enhancement is done by adjusting the pixel values on the image. Further for quantitative analysis of the better image contrast enhancement technique, the entropy of the images in Fig. 2c, d are taken. The entropy of image in Fig. 2c is 6.8815 where the entropy of image in Fig. 2d is 5.1437. So it is clear that contrast enhancement technique by adjusting pixel value yields a better result than contrast enhancement by histogram equalization. Hence the image from Fig. 2c is taken as input in further processing steps. After this, filtering technique is applied to further enhance and modify the image. We apply filters to emphasize certain features or remove some particular feature. In filtering, the value of any given pixel is calculated by applying some kind of algorithm to the neighborhood pixel. We have used median filtering which is a state-of-the-art filtering technique. In this approach, each pixel value is replaced with the median of the gray value in local neighborhood. This type of filtering technique is very useful in removing salt and pepper noise while preserving the details of the image. As discussed in the previous section, we have taken image from Fig. 2c and applied median filtering to this image. The output image will be taken for further processing in the segmentation stage.

Figure 3 is the resultant image after the preprocessing steps. This image is obtained by applying dull razor algorithm, morphological contrast enhancement and median filtering. This image is used in segmentation, which is the next phase in the proposed methodology.

Fig. 3 Image after filtering

3.2 Segmentation

Segmentation is basically used to find some pattern in the image in terms of shape, texture, or color. This pattern can be further analyzed to infer knowledge. Segmentation is the process of analysis image with the aim of extracting significant information that represents various classes of objects [7]. Gradient of image and threshold value are applied to create a binary mask that contains the segmented image. Threshold value is calculated by using the different edge detection method. Also, a fudge factor is introduced into the calculation of binary mask to make it fit for observation error [8]. There are several edge detection method defined like Sobel edge detection, Prewitt edge detection, Canny edge detection, Roberts edge detection, etc. The stages in segmentation of images in this proposed method are mentioned below.

- (1) By using edge detection methods, we calculate the threshold value in the image.
- (2) Introduce the fudge factor in determining the sensitivity of the threshold value.
- (3) Use the threshold value along with the different edge detection method to return all the edges in the image stronger than the threshold value.

The result of the proposed edge detection method is depicted in Fig. 4. We have used the popular edge detection methods, i.e., Canny, Sobel, Prewitt, and Roberts in the test image. The test image is obtained as an output of the preprocessing step as mentioned in Sect. 3.1. We have considered the fudge factor to have value of 0.5 and 1. The value is selected one as a fractional number and other as whole number.

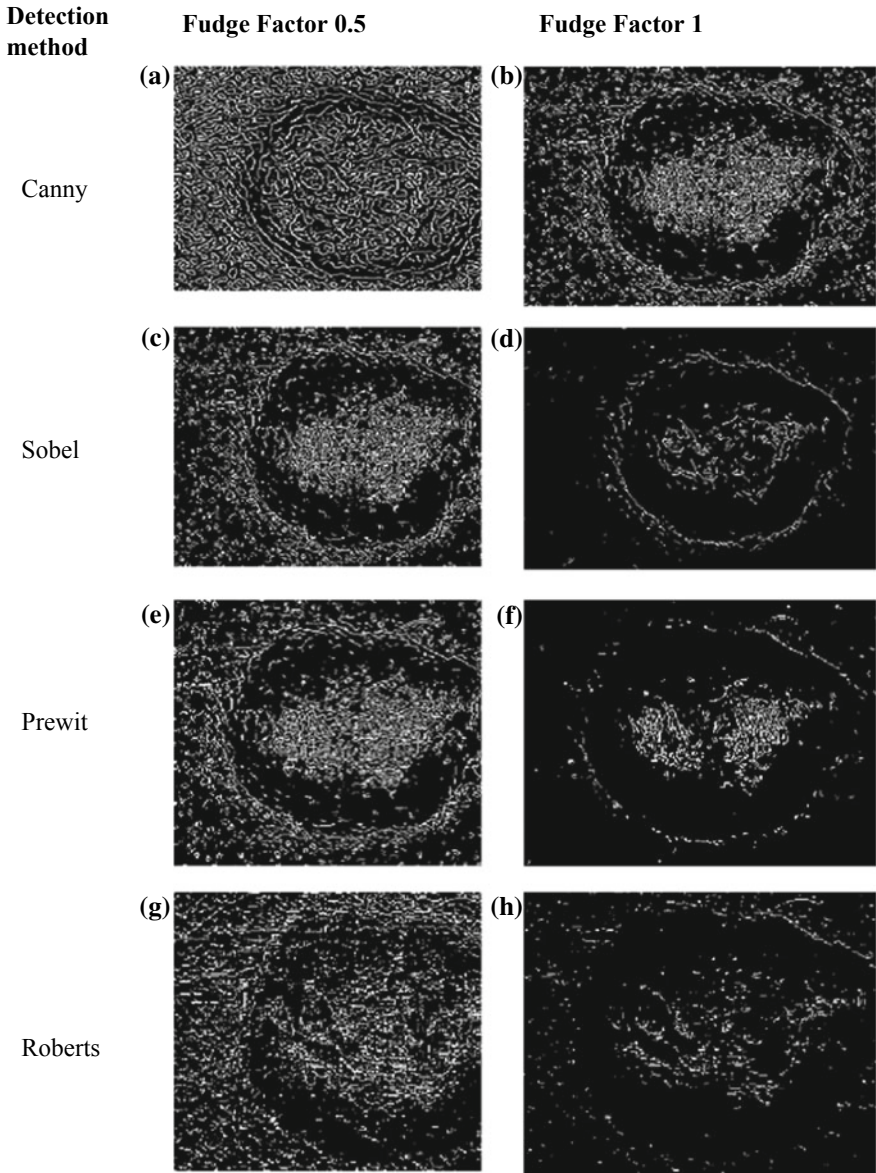


Fig. 4 a Edge detection using Canny with fudge factor 0.5, b edge detection using Canny with fudge factor 1, c edge detection using Sobel with fudge factor 0.5, d edge detection using Sobel with fudge factor 1, e edge detection using Prewitt with fudge factor 0.5, f edge detection using Prewitt with fudge factor 1, g edge detection using Roberts with fudge factor 0.5, h edge detection using Roberts with fudge factor 1, Sobel, Prewitt, and Roberts edge detector fudge factor 0.5 and 1

4 Implementation

To find the effectiveness of the proposed method, a skin lesion image is taken from an open access web portal. The experiments are conducted using GNU Octave 4.2.1 on Windows 7, 64 bit OS with Intel® Core™, 1.90 Ghz CPU and 4.00 GB RAM. The image processing toolbox of GNU Octave 4.2.1 is also used to carry out the experiments [9]. In the proposed methodology, hair removal is done by using dull razor algorithm. The algorithm is implemented in the test image by using the dullrazor.exe [10].

5 Result and Discussion

The quality of the proposed methodology is measured by using two basic parameters of image processing, i.e., Entropy and Dice Similarity Index. These parameters and the corresponding result are defined below.

5.1 Entropy

Entropy is one of the most popular performance measuring parameter in image processing. It is a statistical measure which is used for evaluating the original image quality and output image quality. Entropy is used for characterization of image texture and quantifies the amount of information within the image. If the entropy of the image is high then image depicts high information. Larger entropy means a better quality of image [11]. The entropy of the segmented image obtained by various edge detection methods with fudge factor tuned to two values 0.5 and 1 is shown in Table 1.

By observing the entropy in case of image of the skin lesion segmentation, it can be derived that Sobel edge detection with fudge factor 0.5 demonstrates better result.

Table 1 Entropy of the segmented images derived by applying different parameters

Edge detection method	Fudge factor	Entropy
Sobel	0.5	4.6148
	1	2.4317
Canny	0.5	2.6583
	1	2.6462
Prewitt	0.5	2.3407
	1	0.8246
Roberts	0.5	2.3669
	1	2.0547

It also shows that Prewitt edge detection method with fudge factor 1 displays the poor quality segmentation.

Further analysis of the experimental output image reveals that Prewitt edge detection with fudge factor 1 provides better edge detection. This method removes the textural effect or patterns of the skin lesion image to some extent as compared to other result. As a result better edge boundary can be perceived. But entropy of this method is average as compared to the other methods. This happens due to the lack of textural effect or patterns which in turns reduces the randomness of information in the image. So we have taken another parameter dice similarity index for further result analysis and performance measurement of the proposed method.

5.2 Dice Similarity Index

One of the most commonly used parameters in medical image segmentation is dice similarity index. It is widely used in reporting performance of image segmentation and gives maximum weightage to instance where two image overlaps [12]. The value of dice similarity index ranges from 1, indicating complete overlap, to 0, indicating no overlap between sets of binary segmentations. The dice similarity index of the segmented image obtained by various edge detection methods with fudge factor tuned to two values 0.5 and 1 is depicted in Table 2.

From the above table, it can be inferred that Prewitt edge detection technique with fudge factor 1 shows the best segmentation result followed by Sobel edge detection technique with fudge factor 1. By analysis of the proposed image edge detection process, we can say that the techniques along with the fudge factor affect the segmentation of images. In Prewitt edge detection, if the fudge factor is 0.5 then it presents worst case of segmentation. If we change the fudge factor to 1 in the same technique, then we get a better result. This implies the importance of fudge factor in segmentation in skin lesion images.

Table 2 Dice similarity index of the segmented images derived by applying different parameters

Edge detection method	Fudge factor	Dice similarity index
Sobel	0.5	0.83601
	1	0.49346
Canny	0.5	0.87028
	1	0.86581
Prewitt	0.5	0.91737
	1	0.36309
Roberts	0.5	0.84257
	1	0.63405

A novel approach for edge detection has been proposed in this paper. Preprocessing of skin lesion image is carried out in three steps. In the first step, artifacts like hair are removed by using dull razor algorithm. Next, the contrast of the skin lesion image is adjusted by using threshold-based contrast enhancement techniques. As the third and final step in preprocessing, median filtering is applied to further improve the quality of the image. The output obtained by the preprocessing is taken as input in the segmentation stage. Segmentation is carried out by applying Sobel, Canny, Prewitt, and Roberts operator. These operators are tuned by adjusting the threshold value with the introduction of a fudge factor. The quality of the resulting segmented image is analyzed by using entropy and dice similarity index.

6 Conclusions

By this study, it is found that Prewitt operator with fudge factor 1 shows better segmentation result, followed by Sobel operator with fudge factor 1. Prewitt operator with fudge factor shows poor result of segmentation. Similarly, if the fudge factor of Sobel operator is changed then it does not show good result. From this, we can observe that the threshold value in these segmentation processes is important to obtain better result. Future work can be done to find out the best threshold value which can be applied in segmentation operator to obtain the best segmented result.

References

1. Glaister J, Wong A, Clausi D (2014) Segmentation of skin lesions from digital images using joint statistical texture distinctiveness. *IEEE Trans Biomed Eng* 61:1220–1230
2. Sumithra R, Mahamad S, Guru D (2015) Segmentation and classification of skin lesions for disease diagnosis. *Procedia Comput Sci* 45:75–86
3. Hassana G, Zou B (2009) Region-based segmentation versus edge detection. In: *Intelligent information hiding and multimedia signal processing*, pp 1217–1221
4. Tutorial: Image Segmentation. Tutorial: Image Segmentation. Last accessed 2017/12/19
5. Rafiqul Z, Noor A (2012) Survey on gesture recognition for hand image postures. *Can Cent Comput Inf Sci* 3:110–121
6. Azadeh NH, Adel AJ, Afsaneh NH (2014) Pre-processing of automatic skin cancer detection system: comparative study. *Int J Smart Sens Intell Syst* 7:1364–1370
7. Xua L, Jackowska M, Goshtasbya A, Rosemanb D, Binesb S, Yuc C, Dhawand A, Huntley A (1999) Segmentation of skin cancer images. *Image Vis Comput* 17:65–74
8. Gill R, Kaur N (2012) Indian vehicle number plate detection by image processing technique in MATLAB. *Int J Comput Sci Technol* 3:365–367
9. Hansen JS, GNU Octave. *Beginner's Guide*, 1st edn. Packt Publishing. ISBN 978-1-849-51332-6
10. Lee T, Ng V, Gallagher R, Coldman A, McLean D (1997) DullRazor: a software approach to hair removal from images. *Comput Biol Med* 27:533–543

11. Tsai D-Y, Lee Y, Matsuyama E (2008) Information entropy measure for evaluation of image quality. *J Digit Imaging* 3:338–347
12. Zou K, Simon KW, Aditya B (2004) Statistical validation of image segmentation quality based on a spatial overlap index. *Acad Radiol* 11(2):178–189

Nanomaterial in Lubricants—A Real Approach



Neha Deepak Saxena and Nathi Ram Chauhan

Abstract Nanolubricants are the advanced form of lubricants which can improve efficiency in term of both energy saving and enhancing the machinery life cycle. Nowadays, these advanced lubricants are the hot topic of great interest due to their high potential application in wide areas. Previous studies have clarified that even a minute quantity of nanoparticle, when dispersed in base fluid shows great potential to improves physical, chemical transport, thermal, and radiative properties of base engine oil. This paper focuses on the preparation of nanofluid and their properties along with the application of wide range of nanoparticles in lubricants. Buckminsterfullerene, detonation nanodiamonds, ultradispersed boric acid, and polytetrafluoroethylene (PTFE) are the considered various range of nanomaterial. Modern advancement had been done on engineering lubricants by grafting the nanoparticle in traditional lubricants or high viscous fluid like Grease. It is strongly suggested that nanomaterials have the latent for enhancing convinced lubricant property. Still, there is a time-consuming step need to be followed in order to formulate or developed nanolubricant to enhance the properties of traditional oil.

Keywords Nanoparticles · Nanolubricants · Buckminsterfullerene · Detonation · Nanodiamonds · Ultradispersed boric acid · PTFE

1 Introduction

Nanoparticles are the particles of the size 1–100 nm. These particles are very small in size but represent an object as a whole unit. The use of nanoparticles has been escalated in the past few years. Major application of nanoparticles is nanofluids. Nanofluids are engineered colloidal suspension of Nanoparticles in base fluid [1]. Nanofluids basically enhances the thermal conductivity of base oil and also reduces

N. D. Saxena
JSS Academy of Technical Education, Noida, UP, India

N. R. Chauhan (✉)
Indira Gandhi Delhi Technical University for Women, New Delhi, India
e-mail: nramchauhan@gmail.com

© Springer Nature Singapore Pte Ltd. 2019
M. Kumar et al. (eds.), *Advances in Interdisciplinary Engineering*, Lecture Notes in Mechanical Engineering, https://doi.org/10.1007/978-981-13-6577-5_82

the wear and tear between the rubbing surfaces of the machine [2]. Nanofluids are better than other commercial fluids because of their better transportation [3]. Nanofluids enhance the heat transfer property, thus increasing the life of compressor and other machine part used. Also, the use of Nanofluids improves the energy cycle of the machines. Properties like thermal conductivity, wear and tear reduction, and optical properties are some of the major properties that make them better alternatives for the traditional substances [4–7]. Nanomaterials find their application in treating diseases like HIV [8] and cancer as an efficient drug carrier. Also, nanofluids along with other classes of nanomaterials are used in the production of semiconductors, oral dentifrices, dry lubricants for metals, micromechanics, bioactive carriers, audio/videotapes, and many more uses. Advantages of using nanofluids are that it improves the lubricity of the engine oils; enhances the thermal conductivity, wear reduction properties and provides a large surface area to volume ratio, thus proving as efficient catalyst. At a broad spectrum, many researchers study the common properties of engine oil and its effect of adding nanoparticles to base engine oil [9].

1.1 Nanoparticles as Lubricant Additives

Nanoparticles unlock innovative ways to enhance the performance of lubricant [2–4]. However, nanoparticles play a vital role and show significant affect for which a number of studies have been carried out viewing that nanotechnology can definitely advance the properties of lubricant such as traditional oils and greases, In the broad scale, the industry market facing serious technical issues of nanofortified lubricants. One realistic problem is the formulation of lubricant in the evenhanded way with respect to its properties, which was the main reason to deter the entry of nanoparticle in the market. The current article reviews the recent advances in the application of nanoparticle in traditional engine oils, lubricants and thickened grease (Fig. 1 and Table 1).

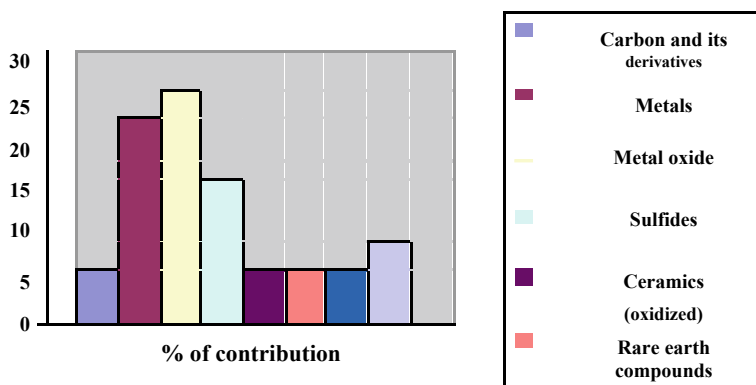
Nanofluids are prepared by dispersing nanosolid particles with base liquid. This base liquid could be water, oil, ethylene glycol, etc. Mainly, there are two techniques used to produce nanofluids.

One-step or single-step method or VEROS. This method is also termed as vacuum evaporation onto a running oil substrate. It is a direct evaporation method and was first developed by Akoh et al. [10] in 1978. Then series of researcher uses ultrasonic equipment in order to separate the fluid particles and thus produce Al_2O_3 nanofluids. This equipment also reduces the problem of agglomeration of particles.

Two-step method. Patil et al. [11] discussed the two-step method to produce TiO_2 suspension in low viscosity fluid which is being developed by Murshed in 2005. Current method is good for oxide nanoparticles whereas for metallic particles single step method is preferred [12]. Many researcher produces number of nanofluids like—fullerene, copper oxide, MWCNT, and silicon dioxide; base fluid; DI water, ethylene glycol, and oil. Stability of these nanofluids was examined by UV–vis spectral ana-

Table 1 Summary of nanoparticles as lubricant additives

Types	% of contribution	Nanoparticles
Carbon and its derivatives	7	Graphene, diamond, SWCNT, MWCNTs
Metals	23	Sn, Fe, Bi, Cu, Ag, Ti, Ni, Co, Pd, Au
Metal oxide	26	ZrO ₂ , TiO ₂ , Fe ₃ O ₄ , Al ₂ O ₃ , ZnO, CuO
Sulfides	16	WS ₂ , CuS, MoS ₂ , NiMoO ₂ S ₂
Ceramics (oxidized)	6	Al ₂ O ₃ , CuO
Rare earth compounds	7	LaF ₃ , CeO ₂ , La(OH) ₃ , Y ₂ O ₃ , CeBO ₃
Nanocomposites	6	Cu/SiO ₂ , Cu/graphene oxide, Al ₂ O ₃ /SiO ₂ , serpentine/La(OH) ₃ , Al ₂ O ₃ /TiO ₂
Others	9	CaCO ₃ , ZnAl ₂ O ₄ , zeolite, ZrP, SiO ₂ , PTFE, hydroxide, BN, serpentine

**Fig. 1** Percentage of contribution of nanomaterials

lyzer. Results of this examination proved that the stability of nanofluid strongly depends on the chemical structure of both particles and base oil. Furthermore,

- Stability of suspension can be improved by adding surfactant.
- Surface properties of suspended particles can be changed by ultrasonic vibration.
- PH value can be altered by adding dispersant. However, heat transfer performance at high temperature of nanofluid is highly effected by adding dispersant.

2 Effect of Nanoparticles on Properties of Lubricants

Nanoparticles can act as nanorolling substance in between the rubbing surfaces. A series of experiments shows that nanoparticles that get deposited on the rubbing surface show first-rate friction and thus reduces the wear characteristics even at very

Table 2 Examples of nanoparticles

S. No.	Nanoparticles	Examples
1	Nitrides	SiN, AlN
2	Metal carbides	SiC
3	Ceramics (oxidized)	Al ₂ O ₃ , CuO
4	Layered particles	Al + Al ₂ O ₃ , Cu + C, PCM-S/S
5	Metals	Al, Cu
6	Nanometals	Graphite, carbon nanotubes

low concentrations. Nanolubricants are relatively insensitive to heat and temperature and in comparison to traditional additives they show limited tribochemical reactions.

Addition of nanoparticles basically reduces the wear and friction of lubricants. These properties highly depend on the size, shape, and concentration of nanoparticles. The size range of nanoparticles is about 20–120 nm. Experimentally, it has been proved that nanoparticles are extremely reactive because of their high surface area. Nowadays Nitrides, metal carbides, ceramics (oxidized), layered particles, metals, and nanometals are commonly used as nanoparticles. Examples of these nanoparticles are as follows (Table 2).

Lubricating oil with nanoparticles basically improves the properties like anti-wear, EP, and reduces friction. And therefore service life of the machine was also improved. From various studies, it was concluded that Cu and CuO when mixed with base oil shows lower friction coefficient and minimum wear on tribo-surfaces.

Also, it is being observed from experiments that nanoparticles display good characteristics such as reduction in friction and wear properties, for the concentrations lower than 2 wt%. However, it is evident from range of case study that nanoparticles reveal the detrimental effect, enhancing either wear or friction.

3 Classes of Nanomaterials

3.1 Buckminsterfullerene

Buckminsterfullerene (C₆₀) is solely made up of 60 carbon atoms and has cage-like molecules, which actually resembles the shape of Football [13]. Some chemistry scientist invented buckminsterfullerene in 1985, and later it got to know that carbon is also exit in the form of C₆₀ in the space. Around 0.1–0.9% of carbon is in the form of fullerene in the universe.

Preparation of Fullerene Nanoparticles: Size of nanoparticles is less than 100 nm, and these nanoparticles are building blocks for nanotechnology and fabrication of these particles needs intensive study. There are various fabrication methods, among those methods Hand grinding C₆₀ solids by agate mortar and pestle is widely used

because this novel method can only obtain particles of size 20 nm [4]. This method is also termed as MARS (Mechano Assisted Reduction of size).

MARS: If the specimen is crushed routinely and milled to fine particles by using mortar and pestle. By this facile method, the size of the particles is around one micrometer. But by Simple Hand grinding bulk solids method, the size of C60 can be reached to 20 nm [5]. If fullerene is obtained by the method termed as MARS then it can stably disperse in water, alcohol, silicon oil, acetonitrile, acetone, and fluorinated oil [7]. During the preparation, no organic solvent was used therefore np is free from residues and toxic testing can easily be done on this fullerene particles. It is highly recommended for biological application.

3.2 Synthesis Methods for Nanodiamonds

Nanodiamonds are basically characterized on the basis of their structural formula, their physical and chemical properties, method of processing and forming the composites had been discussed. There are various synthesis methods like—(1) Ion and Laser bombarding, (2) CVD, (3) Hydrothermal, (4) Ultrasonic, (5) Electrochemical, and (6) Detonation techniques for fabricating the various forms of Nanodiamonds (NDs). Furthermore, the application of nanodiamond also possesses the extensive interest. Such as—medicine, electrochemistry, materials science, and technology.

Biological Activities of Nanoparticles. Various novel properties were found in fullerene np which opens the way for many medical and biotechnological applications. Buckminsterfullerene has an inhibiting effect for protease from HIV (Human Immunodeficiency Virus), which makes it more interesting for biological activities. But Buckminsterfullerene is the purest form of carbon and therefore cannot be soluble in water, and hence need to be modified the chemical structure of fullerene which makes it soluble in water. Another interesting property is the dispersibility in water, i.e., the dispersion remains the same for the years without forming any precipitates [8].

3.3 Nanodiamonds

Nanodiamonds are much smaller in size in comparison to the diamonds used in jewelry. But nanodiamonds have all positive and wide range of applications.

Application of Nanodiamonds. Currently, nanodiamonds are considered being the most interesting area for research in the field of nanotechnology. As research on nanodiamond with same vigor could attain certain breakthroughs in the subsequent few years. Because in the future, nanodiamond is going to become energy saving affect and consequently a great life saver.

In current decades, from the chain of experiments, it was concluded that nanodiamonds could be wonderful resources to fight cancer, which is being possible

because of their small size, and ability to enter into the cells in the body. So adding the nanodiamonds with medical drugs could affect the cancer cells by entering into it and remain there in the cells and releases the drug for a longer period of time. Such treatment method has never come into existence which reaches so close to the cells of the disease.

Furthermore, nanodiamonds are broadly applied as reinforcement additives in order to coat the metal which enhances the mechanical, chemical, and frictional characteristics. Dispersing the nanodiamond to engine oil enhances the life of oil and reduces the wear and friction which in turn reduces the fuel consumption, and detrimental emissions while exhaust, and thus enhances the torque and power of the system [9].

3.4 Ultradispersed Boric Acid

Boron a semimetallic substance with planar hexagonal structure was first discovered by Sir Humphrey Davy in the year 1808. Boron Nitride is termed to be best existing technology because of the following wonderful properties like improves the lubricity of diesel fuel, particles dispersion, substantial reduction in friction, behaves like a solid lubricant, ceramic, excellent thermal stability, and stable in acids [14].

But it consists of some issues too, and they are suspension is quite a difficult task, does not tolerate water, no antioxidant effect, and not compatible with various lubricant additives. But some of these issues can be resolved by using borate nanoparticles. These nanoparticles are produced by using unique manufacturing process. These compounds are having

- Planar structures on metal surfaces
- Stable suspension
- Tolerate water.

Boric acid has excellent EP/AW properties therefore it can be used as metal working fluid [13]. From the recent studies, it is also preferred to use lubricant which has boron based Nanoparticles because it has low friction and wear in various applications. It can be used in windmill, industrial and transportation applications by making slight modification.

3.5 PTFE (Polytetrafluoroethylene)

PTFE or Teflon were discovered by Roy Plunkett in 1938. PTFE is fortified oils and grease and has shown very impressive performance in the field of lubrication engineering [13]. It can hold higher welding loads, reduced stick slip, reduce friction, wear, etc. Though PTFE was recognized to have high potential ten also, it has limited

use in engine oil because of its inherent stability, clogging of oil filter, cannot be recycled.

Following properties make PTFE very attractive and they have high melting point, stable at low temperature, corrosion resistive, very slick and slippery, low electrical conductivity, and good insulator [15].

Applications:

- PTFE is an excellent material and widely used for coating purpose especially those parts which are subjected to heat, wear, and friction and can also resist corrosive chemicals.
- PTFE is also termed as stain resistor that works very quickly to remove stains from carpets, wall coverings, and as weatherproofing on outdoor walls.
- PTFE is used to insulate communication cable as it is a good insulator and therefore it is used to manufacture semiconductors.
- PTFE is also found a wide application in the field of medical such as vascular grafts.
- If fiberglass is coated with PTFE, then it can be used to protect airports and stadium roofs.
- If fiberglass is coated with PTFE, then it can be used to protect airports and stadium roofs.
- PTFE has low friction and therefore can be used in weaving socks because it makes socks smooth and thus protects feet from blisters.
- In short, PTFE can be used in cable insulation, hose and tubing, solid lubricants, small electrical motors and pumps, nonstick domestic utensils, solid lubricants, lining of reactor and plant equipment, permeable membranes for clothing and shoes.

4 Conclusion

A nanoparticle in lubricants shows great potential for enhancing the properties of lubricant. Still, to develop a stable and balanced formulation is a typical task. With the dawn of nanotechnology, follow a line of investigation into lubricants and nanolubricants qualified an archetype move. As a substitute of traditional lubricants, new nanolubricants have been freshly developed under deep extensive research as it possesses unusual properties. In addition, the two vital engineering components like friction and wear in various systems fails, such as pumps, gears, compressors, and turbines. The cost for the repair related to frictional and wear damage throws the giant trouble on any countrywide financial system. It is also being suggested that further investigations can also be done on the structural analysis and amalgamation of nanolubricant. Furthermore, focusing on clean and green environment with their unique application.

References

1. Chang L, Friedrich K (2010) Enhancement effect of nanoparticles on the sliding wear of short fiber-reinforced polymer composites. *Tribol Int* 43:2355–2364
2. Wu YY, Tsui WC (2006) Experimental analysis of tribological properties of lubricating oils with nanoparticles additives. *Wear* 262(2007):819–825
3. Wang X-Q, Mujumdar AS (2008) A review on nanofluids—part II: experiments and applications. *Braz J Chem Eng* 25(04):631–648. ISSN 0104-6632
4. Deguchi S, Mukai S, Yamazaki T, Tsudome M, Horikoshi K (2011) Correction to “nanoparticles of fullerene C60 from engineering of antiquity”. *J Phys Chem C* 115(21):10929
5. Deguchi S, Mukai S, Yamazaki T, Tsudome M, Horikoshi K, (2010) Nanoparticles of fullerene C60 from engineering of antiquity. *J Phys Chem C* 114(2):849–856
6. Deguchi S, Mukai S, Tsudome M, Horikoshi K (2006) Facile generation of fullerene nanoparticles by hand-grinding. *Adv Mater* 18(6):729–732
7. Deguchi S, Mukai S (2006) Top-down preparation of dispersions of C60 nanoparticles in organic solvents. *Chem Lett* 35(4):396–397
8. Deguchi S, Yamazaki T, Mukai S, Usami R, Horikoshi K (2007) Stabilization of C60 nanoparticles by protein adsorption and its implications for toxicity studies. *Chem Res Toxicol* 20(6):854–858
9. Koppula S, Sudheer N V V V S (2016) A review on effect of adding additives and nano additives on thermal properties of gear box lubricants. *Int J Appl Eng Res* 11(5):3509–3526. ISSN 0973-4562
10. Akoh H, Tsukasaki Y, Yatsuya S et al (1978) Magnetic properties of ferromagnetic ultrafine particles prepared by vacuum evaporation on running oil substrate. *J Cryst Growth* 45(2):495–500
11. Patil SJ, Patil DP, Shrotri AP, Patil VP (2014) A review on effect of addition of nanoparticles on tribological properties of lubricants. *Int J Mech Eng Technol (IJMET)* 5(11):120–129
12. Canter N (2009) Boron nanotechnology-based lubricant additive. *Tribol Lubr Technol* 65:12–13
13. Ebnesaajad S (2012) Fluoropolymer additives, Chapter 6. Elsevier, Amsterdam, The Netherlands
14. Greco A, Mistry K, Sista V, Eryilmaz O, Erdemir A (2011) Friction and wear behaviour of boron based surface treatment and nano-particle lubricant additives for wind turbine gearbox applications. *Wear* 271:1754–1760
15. Heatwole O (1991) Presenting PTFE: a potent resin, a well-kept secret; QMI/Ever-Wear, Inc., Lakeland, FL, USA. Canter N (2009) Boron nanotechnology-based lubricant additive. *Tribol Lubr Technol* 65:12–13

Emission Control System Using Lambda Sensors and Application in Soil Respiration



Sharad Chandra and Sheelam Misra

Abstract Most vehicles since 1986 Lambda sensors have no less than one oxygen sensor and now vehicles frequently have at least two oxygen sensors. An oxygen sensor's work has changed minimal from/into the most recent 30 years from when they were first utilized as a part of European fuel infused autos yet their significance of motor activity has expanded altogether oxygen sensors are currently basic to present day vehicles engine management and emission control systems. An oxygen sensor screens the measure of oxygen in fumes gas. The measure of oxygen in the fumes gas is a decent pointer to/towards motor ignition proficiency and is likewise the best place to screen the air to fuel proportion, things being what they are there is a specific proportion of air and fuel that is immaculate and that proportion is 14.7:1, otherwise called the stoichiometric proportion (diverse energizes have distinctive impeccable proportions, the proportion relies upon the measure of hydrogen and carbon found in a given measure of fuel). An excessive amount of oxygen in debilitate gases shows a lean blend. A lean blend tends to create more nitrogen oxide contaminations NO_x , and now and again, it can cause poor execution including to fizzle and even motor harm to/in the motor running excessively hot. Too little oxygen shows a rich blend, which squanders fuel and decreases economy, and the unburned fuel brings about overabundance outflows. Either condition can abbreviate the life of the costly exhaust system. The oxygen sensor is situated in the ventilation system downpipes before the exhaust system or between the ventilation systems and the exhaust systems.

Keywords Lambda sensors · Oxygen sensors · Catalytic converter

S. Chandra
Amity University, Noida, India
e-mail: sharad.chandra350@gmail.com

S. Misra (✉)
Amity University, Sector-125, Noida, India
e-mail: smisra1@amity.edu

1 Introduction

Checking and control of productivity and one of the major issues society faces due to the petroleum derivatives utilize poisons outflows in the field of modern ignition and environmental change. The car division and the huge scale ventures in a certain way have conditions to handle such issues while the little scale enterprises have constraints to settle it due to the generally high speculation they need to do obtaining or leasing burning analyzers or administrations.

There are different methodologies of controlling burning. One of them is to decide previously the heat capacity and chemical composition of a fuel and pre-set the air–fuel proportion. Other is to monitor the combustion in situ utilizing optical sensors and in due time make the modification of the air to fuel proportion. Another approach is to quantify the concentration of gases, for example, oxygen, carbon monoxide, or carbon dioxide in the fumes and to make the changes. Among these gases, the estimation of oxygen concentration is more qualified for the proficiency trial of a burning procedure since oxygen and overabundance air are relatively free of the fuel compose. Strategy for controlling ignition by the estimation of the convergence of gases in the fumes is possible for the most part because of the advancement of the cutting edge strong state sensors different sorts of strong state sensors have been initially created for the burning effectiveness control in the car business. For recognition of oxygen, the most widely recognized sensor utilized is a zirconium oxide element, known as zirconia cell or electrochemical sensor that builds up a voltage distinction crosswise over two platinum cathodes isolated by a permeable earthenware layer if there is a distinction in oxygen fixation, this procedure for the most part in vehicle is made by an oxygen sensor known as Lambda sensor. In the trade, there are different kinds of Lambda sensor.

2 Objective

1. To study the emission control system with the use of Lambda Sensors.
2. To implement the application of Lambda in Hypoxic fire extinguishers (In Air-crafts).
3. To implement the application of Lambda sensors in Soil Respiration.

3 Scope

All IC engines produce undesirable emissions as a result of combustion, including hydrogen-fueled engines. The emissions of concern are: unburned hydrocarbons (HC), carbon monoxide (CO), nitric oxide and nitrogen dioxide (NO_x), sulfur dioxide (SO), and solid carbon particulates (particulate matter).

These emissions pollute the environment (smog, acid rain) that contributes to respiratory and other health problems. HC emissions from gasoline-powered vehicles include a number of toxic substances such as benzene, polycyclic aromatic hydrocarbons (PAHs), 1,3-butadiene, and three aldehydes (formaldehyde, acetaldehyde, acrolein). Carbon dioxide (CO) is an emission that is not regulated but is one of the primary greenhouse gases, water vapor, and methane are the others, believed to be responsible for global warming.

1. To control the global warming by controlling the emissions from automobiles.
2. To Measure respiration or production of oxygen content.
3. Can be used in oxygen analyzers like anesthesia monitors, respirators, and oxygen concentrators.
4. Can be used in Hypoxic Fire Extinguisher systems (In Aircraft and various industries).
5. Can be used in big fish tanks and aquariums to control oxygen contents.

4 Evaporative Emissions

4.1 Diurnal Emissions

Take place from fuel tanks and carburetor float bowls (in engines fitted with carburetors) of parked vehicles.

1. It draws in air at night as it cools down.
2. Expels air and gasoline vapor as it heats up during the day.
3. These could be up to 50 g per day on hot days.

4.2 Hot Soak Emissions

1. This occurs after an engine is shut down.
2. The residual thermal energy of the engine heats up the fuel system leading to release of fuel vapors.

4.3 Running Losses

Gasoline vapors are expelled from the tank (or float) the car is driven and the fuel tank becomes hot, this can be high if the ambient temperature is high.

4.4 *Filling Losses (Refueling Losses)*

Gasoline vapors can escape when the vehicle is being refueled in the service station.

4.5 *Exhaust Emission*

1. CO
2. NO
3. HC

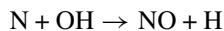
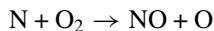
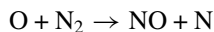
CO Formation

1. Primarily dependent on the equivalence ratio.
2. Levels of CO observed are lower than the most extreme values measured inside the burning chamber.
3. In any case, are fundamentally higher than balance esteems for the fumes conditions.
4. The procedures which govern Co debilitate levels are dynamically controlled. The rate of reversion from Co to Co is slower than the rate of cooling.
5. This explains why CO is formed even with stoichiometric and lean mixtures.

NO Formation

1. There is a temperature appropriation over the chamber due to the passage of flame.
2. Blend that burns early is compacted to higher temperatures after combustion, as cylinder pressure keeps on rising.
3. Blend that burns later is compacted primarily as unburned blend and winds up after combustion at a lower burned gas temperature.
4. Using the NO formation kinetic model based on the extended.

Zeldovich mechanism



1. The measure of decay from crest NO levels happens amid extension relies upon motor conditions and whether the blend component burned early or late.
2. Earlier burning parts of the charge contribute substantially more to Exhausted NO than do later burning portions of the charge.

- 3. Frozen NO concentrations in these early-consuming components can be a request of magnitude higher than concentrations in late consuming components.
- 4. Without fiery mass gas movement, the most astounding NO concentrations happen closest to the start plug (Fig. 1).

- 1. Equivalence Ratio
- 2. Burned gas fraction (Residual gas plus EGR if any)
- 3. Excess air
- 4. Spark Timing.

HC Formation

- 1. Storage
- 2. In-cylinder post-flame oxidation
- 3. Residual gas retention
- 4. Exhaust oxidation.

HC Sources

- 1. Quench Layers
- 2. Crevices
- 3. Lubricant Oil Layer
- 4. Deposits
- 5. Liquid Fuel and mixture preparation
- 6. Poor Combustion Quality.

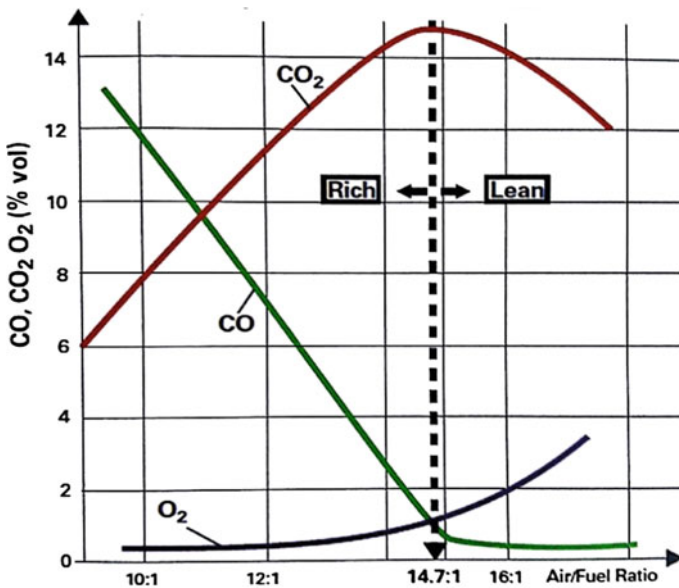


Fig. 1 Carbon monoxide, carbon dioxide, and oxygen levels compared with air/fuel ratio

5 Lambda Sensor

LAMBDA SENSOR is a device fitted to cars, light commercials and even some motorcycles that are equipped with a petrol engine. Located in the exhaust system and its purpose is to monitor the concentration of residual oxygen within the exhaust gases produced by the engine. A more descriptive name for this device is the exhaust gas oxygen sensor, although oxygen sensors have many applications for industry, medicine, and science the most common use is in the automotive sector.

6 Operation

The Lambda sensor introduced to/into the motor's exhaust gas framework of a point which all through the engine's entire working extent and gives the temperature which is vital for effective sensor working. The sensor distends into the exhaust gas, plan to be with the end goal that one terminal surface is encompassed by the exhaust gas and the other is associated with the air. The utilization of permeable platinum terminals implies that at the cathode surface, reactant transformation of this lingering oxygen can occur with the carbon monoxide (CO), hydrocarbons (HC), and the hydrogen display in the fumes gas. The leftover oxygen staying after total change is a component of the fumes gas Lambda esteem and is estimated by the Lambda (oxygen) sensor. Amid progress of a lean blend (high remaining oxygen content) to a rich blend (low leftover oxygen content), the lingering oxygen content decreases unexpectedly by a few forces of 10 in the stoichiometric area $\lambda = 1$ of air–fuel blend.

7 Design

The Lambda sensor works as per the standard of a galvanic oxygen concentration cell with strong electrolyte (Nernst rule). The solid-state electrolyte contains a gas impermeable ceramic component of zirconium dioxide which is balanced out with yttrium oxide and shut down toward one side. The Ceramic component inside and outside surfaces are furnished with electrodes made out of a thin gas—penetrable, permeable layer of platinum which on the one side has an impact on the sensor characteristic because of its synergist impacts, and on alternate serves for electrical reaching. Outwardly surface of the sensor clay which distends into the fumes gas stream, the platinum layer are itself covered with an exceedingly permeable fired layer. This powerful layer keeps the synergist platinum layer being attacked by the corrosive and erosive impacts of the deposits in the exhaust gas and guarantees long-term sensor stability (Fig. 2).

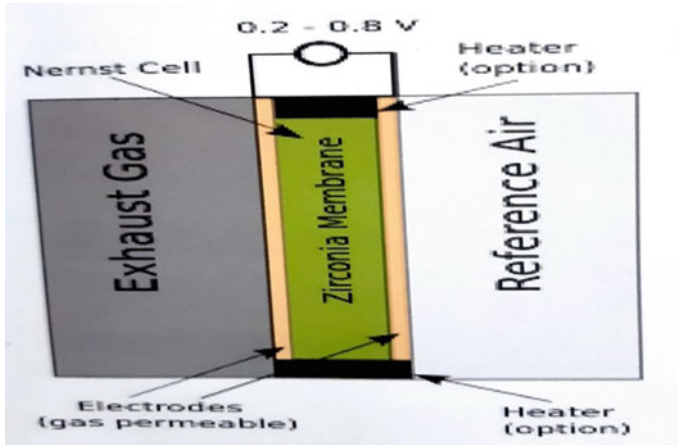


Fig. 2 Galvanic oxygen concentration cell with solid electrolyte (Nernst principle)

8 Monitoring the Oxygen Concentration

In an oxygen reduction system, the monitoring process is carried out by directly measuring the oxygen concentration in the protected area. The measurement must always be taken by at least two independent oxygen sensors per protected volume.

Volume in ft (m ²)	Number of measuring sensors
From to	Minimum
>017,657 (500)	2
>17,657 (500) 141,258 (4,000)	4
>141,258 (4,000) 353,146 (10,000)	6
>353,146 (10,000) 882,866 (25,000)	8
>882,866 (25,000) 1,765,733 (50,000)	10
>1,765,733 (50,000) 3,531,466 (100,000)	12
>3,531,466 (100,000) 7,062,933 (200,000)	14
>7,062,933 (200,000) 10,594,400 (300,000)	16
>10,594,400 (300,000) 14,125,866 (400,000)	18

9 Soil Respiration

Soil respiration is the whole of root respiration and the decay of soil natural issue, plant litter, and root exudates by soil small scale creatures. Soil respiration speaks to a critical wellspring of carbon transition to the environment and hence is a noteworthy

part in the worldwide carbon cycle. The comprehension of biological system carbon cycling reactions to worldwide environmental change depends on exact estimations of soil respiration. Progressively, estimations of soil respiration rate included as contributions to worldwide carbon cycling models used to anticipate an earth-wide temperature boost consequence of soil carbon stockpiling. Dispersion along focus angles is the essential instrument for vaporous transport in soils, and from soil to the air, and is depicted by Fick's law:

$$J = D * (dC/dz)$$

where J is gas motion [$\text{mol m}^{-2} \text{s}^{-1}$], D is the dirt gas dissemination coefficient [$\text{m}^2 \text{s}^{-1}$] which is reliant on soil porosity and water content, C is gas fixation [mol m^{-3}], z is soil profundity [m], and dC/dz is the focus inclination driving gas transition (Fig. 3).

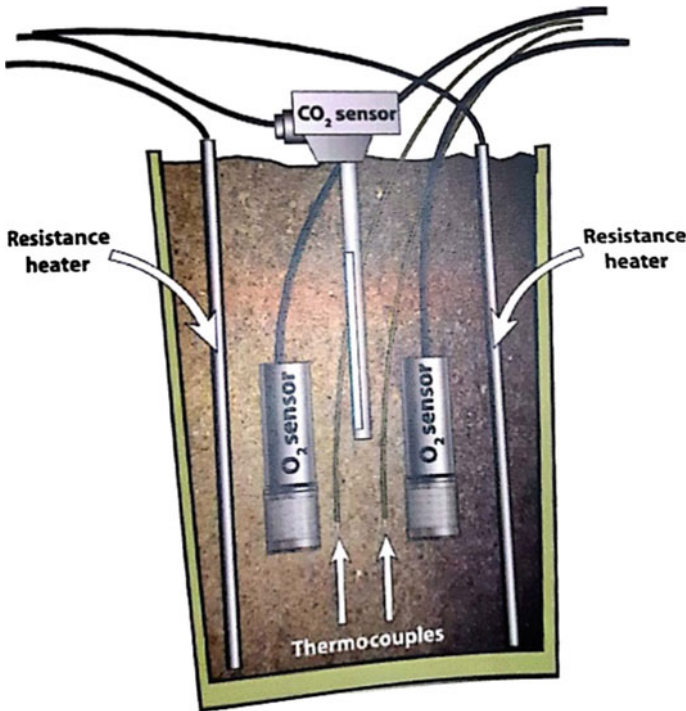


Fig. 3 Soil respiration

9.1 Application to Soil Respiration Estimation

Changes in temperature offer ascent to non-metabolic transitions to CO₂. On the off chance that the CO₂ fixations estimated at the wet sand as a component of temperature was utilized to decide CO₂ angles the inclination, and along these lines motion, would increment by roughly 13% as the temperature expanded on/upon 25–30 °C. The impact on CO₂ solvency increments as soil waters/watered content increments in light of the fact that there is a bigger CO₂ source/sink. Matched O₂ and CO₂ transition estimations in soil can possibly enhance estimation of soil respiration since one mole of O₂ expended measures up to one mole of CO₂ developed. So as to utilize gas transition estimations to appraise soil respiration, the essential rectifications to gas fixation estimations must be connected. Barometric weight, temperature, dampness, and solvency changes should all be represented. Moistness and dissolubility changes are interceded by temperature.

10 Conclusion

1. Estimations of CO₂ fixation in wet ($V = 0.2$) autoclaved sand affirmed hypothetical expectations of CO₂ focus change emerging from CO₂ dissolvability as a component of temperature.
2. The temperature impact on CO₂ solvency must be represented when utilizing CO₂ motion.
3. The estimations to appraise soil breath, generally temperature changes creating CO₂ transition changes might be deciphered as soil breath changes, not CO₂ solvency impacts.
4. Estimations of O₂ are considerably less touchy to the CO₂ solvency impact on the grounds that the grouping of O₂, 20.95% under surrounding conditions, is around two requests of size more noteworthy than common CO₂ focus in the dirt.
5. Notwithstanding the insignificant impact of CO₂ solvency on relative O₂ focus, the impacts of O₂ dissolvability are immaterial in light of the fact that O₂ is around 30 times less solvent than CO₂.
6. Combined O₂ and CO₂ estimations in soil can possibly enhance portrayal of soil breath.
7. The two estimations require numerous redresses, which represent physical impacts that change supreme gas focuses, so as to yield precise estimations of relative gas fixation, in light of the fact that O₂ and CO₂ are by and large announced in relative terms.
8. The important adjustments for exact gas estimation are barometric weight, temperature, and dampness.
9. The important adjustments for exact CO₂ estimations are the same with the expansion of a remedy to represent CO₂ dissolvability impacts as an element of temperature.

References

1. Gupta AK, Thakur H Engineering research department for conducting the experiments
2. Twigg MV (2007) Progress and future challenges in controlling automotive exhaust gas emissions. *Appl Catal B Environ* 70:2–15
3. Kotliar IGK, Currin JD (2003) Fire pass—a new technology for total flooding application. In: HOTWC proceedings
4. Ramalingam KK (2005) *Automobile engineering*, 2nd edn. SciTech Publications (India) PVT. LTD, Chennai
5. NGK: Some sensors “breathe” through their leads, so are susceptible to contamination of the leads
6. Lang MA (2001) DAN Nitrox workshop proceedings. Divers Alert Network, Durham, NC, p 197. Retrieved 2009-03-20
7. Goble S (2003) Rebreathers. *South Pacific Underwater Med Soc J* 33(2):98–102. Retrieved 2009-03-20

Renewable Energy Sources and Development in Their Use



Mohit Misra, Vijay Kumar Tayal and H. P. Singh

Abstract The continuous depletion of availability of existing fossil fuels with exponential increase in energy demand, the gap between demand and supply has been increased exponentially. The possible way to bridge this gap is by use of nonconventional energy resources for production of energy, often termed as green power. These sources also help in reducing the greenhouse gasses effect, which has direct impact on the average temperature of earth. Further, these sources are everlasting sustainable energy sources. This paper presents review on various renewable energy systems, their optimizing and modeling techniques, interfacing mechanism with different mathematical models, algorithms used like HOMER, GA, PSO, etc.

Keywords Hybrid energy system (HES) · Distributed energy systems (DES) · Global sensitivity analysis (GSA) · Automatic generation control · Multi-pulse width modulation (M-PWM) · Distribution company (DisCo) · Modular multilevel converter (MMC) · Renewable/alternative energy (RE/AE) · Integrated renewable energy systems (IRES) · Unscented transformation based fast scheduling optimization method (UTFSO)

1 Introduction

Renewable energy sources have various industrial and domestic applications. They are highly useful in remote locations. In such areas, the installation of conventional grid supply and fuel cost increases drastically. Conventional power generation is supplemented greatly by renewable energy sources as depicted by recent research and developments, as it shows excellent potential. Integration of different renewable sources and convertors is a need of hour, so that alternative energy can be used fully, despite varying natural conditions.

The grid power quality is maintained by the controller and power conditioning units. Concept of HES is represented in Fig. 1 depicts generator or grid (conventional

M. Misra (✉) · V. K. Tayal · H. P. Singh
Amity University Uttar Pradesh, Noida, Uttar Pradesh, India
e-mail: misra.mohit85@gmail.com

© Springer Nature Singapore Pte Ltd. 2019
M. Kumar et al. (eds.), *Advances in Interdisciplinary Engineering*, Lecture Notes in Mechanical Engineering, https://doi.org/10.1007/978-981-13-6577-5_84

865

system) are utilized for assistance only. During the last decade, many countries has shown their keen interest in various hybrid energy systems, which results in massive development of system that may fully complete fuel-based energy system in remote area and the power supplies for numerous applications. Researchers focused primarily on developing efficient power converters like bidirection inverters and continuously monitoring and improving their performance indices which includes maximum power point trackers also. Numbers of simulation software are used, which shows the most favorable sizing of such systems (HES). Research shows the upcoming technical advancements in the hybrid energy system, such as use of power electronic semiconductor for electrical power conversion which results in better efficiency, better quality, and more reliability of a system.

2 Motivation and Objective

With the growth of population, accordingly growth in demand for energy and depletion in fossil fuel resource, alternate energies become favorites for researchers. Also the sustainability, it provides to the environment is the measured feature which motivates researchers to build a long term sustainable development plans for future.

3 Chronological Review and Related Scientific Developments

A novel framework for the finding uncertainty in the context of distributed energy systems design, which is also methodological, has been presented by Mavromatidis et al. [1]. The proposed method combines optimization based distributed energy systems models and methods of uncertainty analysis and global sensitivity analysis.

A new approach on evaluating the promising nature of solar energy is having Two-phase [2], which is based on robust optimization and envelopment analysis of data and models to design a framework of solar supply chain in an unpredictable environment. In automatic generation control (AGC) along with RES is controlled using proportional–integral–derivative (PID) controller developed using the whale optimization algorithm (WOA) [3]. The experimental results depicting effective behavior of transmission system under variable speed wind energy, variable consumer load and with various faults in the system is obtained with use of STATCOM [4]. To overcome inherent uncertainty in solar generation microgrids [5] are proposed, the effectiveness of which is shown by various numerical simulations. This paper proposes three stage models for an UTFSO [6] to solve the high unit delivery problem considering solar and wind energies forming a hybrid power systems. Reduction in operating cost of the system may be obtained using electric vehicles with certain travel path along with increase in the utilization rate of renewable energy effectively [7]. The

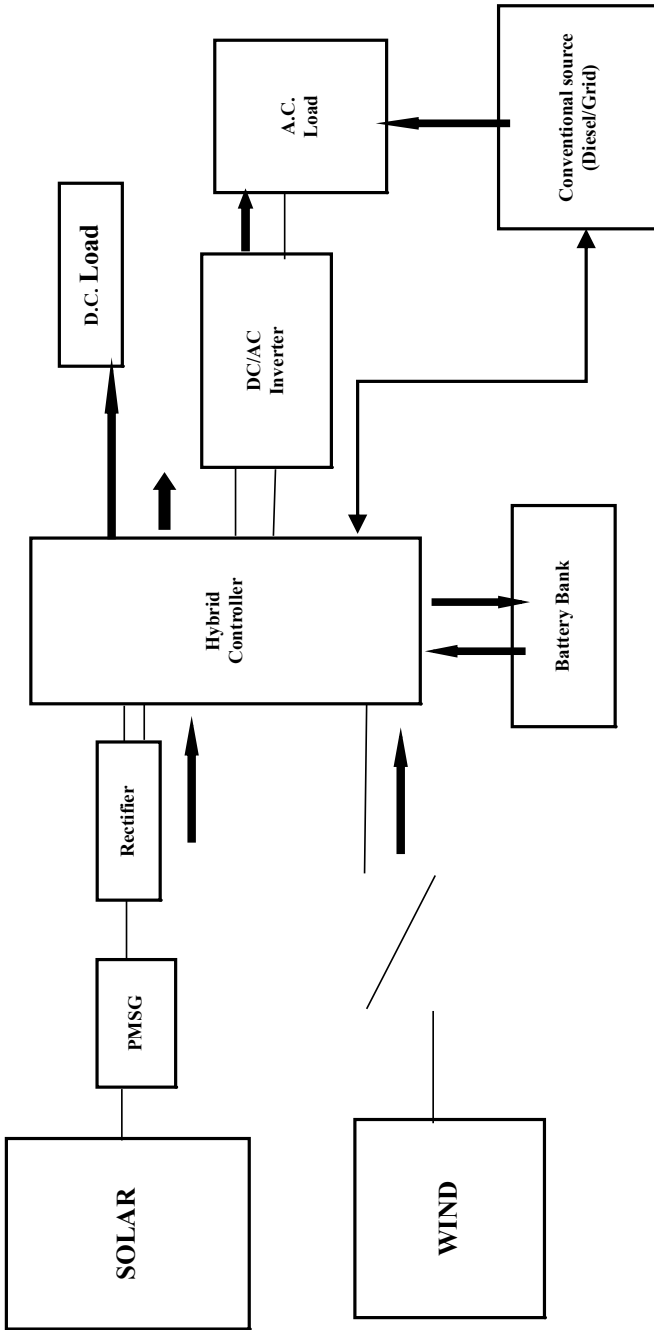


Fig. 1 Concept of HES

optimization model with genetic algorithm method using Monte Carlo simulation is proposed which increases the DisCo [8] benefit by effective utilization of charging stations (CSs), increases the benefit up to maximum, and reduces the power losses to zero. Distributed intelligence [9] is another prominent prospects which was illustrated along with adjustment in energy mixing rates (by PSO algorithm) of multi-pulse width modulation (M-PWM), so that cost-effective and energy balanced management is achieved. Using Iterated solution of a finite-horizon optimal control for developing a robust model predictive control and including economic and operational constraints is also proposed [10]. The author defines the effective and competitive power supply system which is based on RES and which also includes disturbances from harsh climate conditions [11] and discuss the methodology and software with the example of WDPF vil. Amderma. Design of Shunt/Parallel Active power filter (SAPF) [12] with Proportional Integral (PI) controller is proposed to increase quality of power in the grid connected solar system. In the THD, simulation results show 0.49% effectiveness of grid integrated solar PV (inverter Voltage) using MPTT [13]. MATLAB/SIMULINK environment is established to test the effectiveness. In case of weather report data only, the PV systems, estimated CV-RMSE the hourly power consumed prediction varies in range of 3–2 and with 8.6% accuracy in measurement [14]. Author depicted that implementation of microgrid is beneficial for health care and education [15], further it also ensures sustainability to combat global warming. By using HOMER and with different case studies, various configurations are analyzed. In investigating the problem comprising commitment in terms of unit [16] with stochastic PV integration, the proposed method performed better as compared from a deterministic language programming, a robust language programming, and astochastic language programming through a modified six-bus system. Solar Wind Hybrid Power System (SWHPS) [17], as a RES will enhance the qualities of each other and another. Constant voltage method is used for MPT wind solar based energy harvesting scheme [18] which is domestically relevant, isolated-grid installations suited in regions low like hilly Himalayas or coastal regions where availability is low. Author [19] gives insight to decentralized imaginary power optimization of capacitors placed in distribution energy systems with unpredictable alternate energy sources which are renewable in nature. The modified economic dispatch of multigrid, using PSO, with renewable energy source having several microgrids is simulated. Results show that operating costs with and without MG renewable energy sources is 1443.3 USD [20]. The time proportional controlled resistive load like boiler is examined for control of power flow [21] in HES along with grid. Also such load consumes the left out energy produce by the source. Similar is the case of phase angle controlled. The prototype develops Analyzer of Power Quality [22]. Remote renewable energy becomes source of acquisition for the main control central system. A Modular multi converter (MMC) integrated conversion system with microgrid is applied on power quality problems of nonconventional energy were studied [23]. Findings of MATLAB/Simulink simulation results for such microgrid system with multi level inverter, controller integrated modular multilevel inverter were discussed in this paper [24]. MATLAB simulation is used. The change in angle of incidence of sunrays throughout the day is being tracked by adjustable/movable photovoltaic

system placed on dual axis DC motor, one keep control of elevation angle while another consider Azimuth angle [25]. This sun tracked system generates electricity by self adjustment mechanism. Systems efficiency is defined using experimental results. Bootstrap confidence intervals (CIs) [26] for quantification of uncertainties use deterministic approach for hybrid smart model. A phase-locked loop algorithm [27] for swift and accurate synchronization, in the presence of harmonics and low voltage faults in a grid, uses advanced decoupling network integrated with zero displacement reference with bounded requirements imposed on processing time. This paper emphasizes electricity generation with the use of hydrogen fuel cell [28] approaches for combining hydrogen energy. Combining it with energy storing unit, methodologies for appropriate units, power management, and their related optimization algorithms with software are considered. Paper [29] presents review of utility of fuzzy logic in nonconventional energy systems namely solar, wind, and bioenergy. Fuzzy logic is extensively utilized in past few years for MPPT in solar or wind energy system, assessment of site, optimization with conflicting criteria. It is suggested that fuzzy logic model gives more realistic predictions. Solution to the problem of electricity supply in remote location is addressed via this paper [30]. Further this includes modeling of such system with the feature of improved power quality. Such alternate energies or nonconventional energy sources such as solar, wind, geothermal, hydro, etc., are integrated to achieve decentralized source of electric power. MPPT system for achieving reliable power; with photovoltaic system coupled with dc convertors. Appropriate or best fitted sizing for cost effectiveness and economic consideration as presented in literature [31] Sustainable development through energy generated using nonconventional resources are reviewed and focused [32]. The need of extensive research and development in the field of HES for modeling the techniques which more closely predict the output and able them to be integrated with other energy sources as well [33]. Proton exchange membrane fuel cell powered hybrid system is explained [34]. Its application and design issues in interfacing it with various power electronic semiconductors are detailed along with its daily utility. Stand-alone hybrid system is in demand from past few years. A study [35] reveals and evaluate the existing design and simulation methods which are needed for electricity power generation. The relatively new technique called solar (PV) array inverter assemblies implied in stand-alone systems [36]. Experimental outcomes are cross examined with obtained result verifies the utility of above mentioned technique. Futuristic approach or forecasting behavior of hybrid renewable energy system having two or more energies combined to perform the electricity generation function is being evaluated for stability in performance and economical benefits to user [37]. Various techniques to model its components, its designing capability, and their evaluation are depicted [38]. Forthcoming development in the usage of wind energy due to the healthy economies, stable political scenario, and growing cost of conventional fuels regulates the market interest [39]. This paper presents a unique approach of a 3-level [40] 3-phase common-point clamped inverter (Voltage source), which is an integral part of the interfacing system. A multiple independent component control law is enforced to regulate because of the intrinsic multiple component structure of the system. A current source, which may be considered as renewable energy source such as PV cell is connected to

the grid. The expandable simulator, supporting low cost utility, called RPM-SIM detailed here [41]. It also assists the specific detailing of dynamics of solar, wind and diesel renewable hybrid power systems. The unpredictable nature of wind that is speed, direction, humidity, particle content, etc., always disturbs the performance indices study of wind energy. Hence, calculating annual estimation using computer model which is probabilistic in nature is detailed [42]. This also gives insight the use of Markov Process of combining stochastic characteristic with its operational data. Behavior of system components is studied by the repeated test results. A 50 kVA prototype, which is scalable is implemented with the technique or model comprising of cascaded 3-level inverter [43] which permits us to control the specific parameter which in turn controls the specific utility. The unbalance voltage created in capacitors is also addressed including the run time disturbances in capacitors. Further model can work on variable load. Moreover, the model of different loads can be incorporated as well. The prototype gives satisfactory output. The fuzzy logic is implemented to form fuzzy cognitive network [44] along with PV array to detect maximum power point so that renewable energy systems become more efficient. Under variable isolation and temperature, the above technique shows increment in efficiency. This is validated by the simulated environment. The cost effectiveness can be achieved by genetic algorithm [45] applied on renewable energy system which also gives best fit configuration due to which total incurred cost becomes more reasonable which is confirmed by simulation done in lab. Output obtained from wind energy system [46] in terms of power is not solely depend upon the input, however the controller used is also plays vital role in determining characteristic and behavior of output. The technology without using mechanical sensors are also detailed. Dual functional cascaded power converter which may work as grid or may work as stand-alone is controlled with flexible strategy [47]. A customer tailored or user friendly digital signal processor which is flexible in nature is developed which is tested online for its control strategy [48]. A longitudinal conversion loss filter and involved proportional integral controller is also detailed. This paper details distributed method of control [49] which interfaces converter with renewable system of generation units using active filtering. There is an immediate need of green power that is nonconventional resources. These resources are sustainable in nature hence they are eco friendly in nature. The green power [50] includes solar, wind, hydro, geothermal, etc (Table 1).

4 Conclusion

This study presents the hybrid energy systems as an important cost-effective alternative in comparison to conventional, fuel-based grid-connected power supplies across the world. The comprehensive literature review gives the insight of benefits and cost of renewable energy which further reveals that renewable energy based low emission hybrid energy systems were not very cost competitive against conventional fossil fuel power systems. However, the use of cleaner power for sustainable development,

Table 1 Technique versus utility

S. No.	Year	Publisher	Technique	Utility
1	2018	ELSEVIER	Monte Carlo simulation	Uncertainty analysis in DES
2	2018	ELSEVIER	DEA and robust optimization model	PV supply chain
3	2017	IET	Whale optimization algorithm	Automatic generation control of interconnected modern power systems including renewable energy sources
4	2017	I-SMAC	Use of SEIG and STATCOM	Behavior of transmission system under variable speed wind energy
5	2017	IEEE	Robust optimization	Microgrid optimal scheduling (Variability and uncertainty in solar energy)
6	2017	IEEE	Fast scheduling optimization	Unit commitment for larger scale. Including lesser predictive behavior of solar and wind energy
7	2017	IEEE	Coordinate optimization	Microgrid including fluctuations of renewable energy sources
8	2017	IEEE	Genetic algorithm (GA) is combined with Monte Carlo simulation	Solar charging stations integrated with storage units. Simulating electric vehicles by including uncertainties
9	2017	IEEE	Particle swarm optimization	Multi-source energy mixing for renewable energy
10	2017	J.ENERGY	Model predictive control	Optimization of microgrid
11	2017	IEEE	Sequential decision	Optimization of power supply (wind energy)
12	2017	IEEE	Shunt Active Power Filter (SAPF) with PI controller	Improvement of power quality in a grid combined photovoltaic system
13	2017	IEEE	MPPT (Using MATLAB/SIMULINK)	Power quality evaluation and improvement of integrated version of PV with the storage

(continued)

Table 1 (continued)

S. No.	Year	Publisher	Technique	Utility
14	2017	IEEE	Power prediction model/cell temperature model	PV power output prediction accuracy
15	2017	IEEE	HOMER	HES: simulation and optimization technique
16	2017	IEEE	Two-stage stochastic programming method (MCS)	Scheduling of optimal power with solar energy
17	2017	IEEE	MPPT controller	Solar wind hybrid energy system
18	2017	IEEE	HOMER	Two winding IG based wind-PV generation control
19	2016	IET	Decentralized conic optimization/multi-scenario approach	Imaginary power minimization including fluctuations of renewable energy sources
20	2016	IEEE	PSO	Economic dispatch of multi-microgrid system
21	2016	IEEE	PWM control, phase angle control	Power flow control
22	2016	IEEE	Metric application, graphical representation of forwarding time versus average message size	Wireless renewable energy networks implemented with power quality control and command
23	2016	IEEE	Modular multilevel inverter with controller using MATLAB Simulink	Power quality challenge of a nonconventional energy sources
24	2016	IEEE	MATLAB Simulink	Optimization of renewable energy sources
25	2016	IEEE	Solar sensor	Energy measurements and uncertainty analysis of SOLAR
26	2015	IEEE	Bootstrap confidence intervals (CIs)	Quantification and estimation of uncertainties in PV power predictions
27	2015	IEEE	Phase-locked loop ALGORITHM	Power quality
28	2015	ELSEVIER	PSO, ACO, GA, SA	Integrating hydrogen fuel cell (Review)

(continued)

Table 1 (continued)

S. No.	Year	Publisher	Technique	Utility
29	2015	ELSEVIER	Fuzzy AHP, fuzzy DEA, fuzzy GA, fuzzy PSO, fuzzy honey bee optimization	Modeling of solar, wind, bioenergy applications (Review)
30	2014	IEEE	MPPT	Modeling and power quality analysis
31	2012	ELSEVIER	AISA, ACO, GA, PSO, SA	Detailed analysis of optimum sizing approaches in RES (Review)
32	2011	IEEE	System configurations, generation unit sizing, storage needs, and energy management and control	Hybrid energy system
33	2010	IEEE	Optimizing techniques	HES: solar–wind power generation systems, stand-alone system
34	2010	ELSEVIER	Proton exchange membrane (PEM)	PEMFC hybrid systems (Review)
35	2009	IEEE	Multi-objective evolutionary algorithm HOMER.HYBRID2, HOGA, TRNSYS, and HYBIRDS	Stand-alone power system. Wind/Solar renewable energy system (Review)
36	2008	IEEE	Systems with PV array–inverter assemblies, operating in the slave-and-master modes	Optimization and modeling of photovoltaic power generators
37	2008	IEEE	Conventional: MATLAB Expert: fuzzy logic, genetic algorithm	Unit sizing and optimization of PV/wind renewable system
38	2008	ELSEVIER	Mathematical model	Modeling of hybrid energy system
39	2005	IEEE	Loss of LOAD probability Multi-area reliability simulation	Wind energy delivery issues
40	2006	IEEE	Three-level inverter	Interfacing renewable energy
41	2006	IEEE	RPM-SIM simulator	Analysis of renewable energy systems
42	2006	IEEE	Markov process	Probabilistic representation of wind farms generation

(continued)

Table 1 (continued)

S. No.	Year	Publisher	Technique	Utility
43	2006	IEEE	Fuzzy cognitive network	To find the MPPT of the PV array
44	2006	IEEE	Fuzzy logic, fuzzy controller	MPPT evaluation
45	2006	IEEE	Genetic algorithm (GA)	Optimum configuration for renewable generating systems
46	2004	IEEE	Digital simulations	Maximum power estimation in a mechanical system: without sensor
47	2004	IEEE	Flexible digital signal processor (DSP)	Control technique which is flexible, examined on 11-kW wind turbine with a cascade power converters
48	2004	IEEE	Mathematical model of the hybrid scheme with variables expressed in d-q synchronous	Comparison between transients simulated and transients obtained
49	2003	IEEE	Solar, wind, geothermal	Green energy
50	2004	IEEE	Distributed control method	Renewable generation units with active filtering capability interfaced with converter

lower carbon dioxide emission, and advancements in alternative energy technologies shows good potential for worldwide use of such system.

References

1. Mavromatidis G, Orehounig K, Carmeliet J (2018) Uncertainty and global sensitivity analysis for the optimal design of distributed energy systems. *Appl Energy* 214:219–238
2. Dehghani E, Jabalameli M, Jabbarzadeh A (2018) Robust design and optimization of solar photovoltaic supply chain in an uncertain environment. *Energy* 142:139–156
3. Hasanien H (2018) Whale optimisation algorithm for automatic generation control of interconnected modern power systems including renewable energy sources. *IET Gener Trans Distrib* 12(3):607–614
4. Ghuman P, Rachna (2017) Wind energy electricity generator electricity generator system using SEIG and STATCOM. In: International conference on I-SMAC (IoT in social, mobile, analytics and cloud) (I-SMAC), pp 418–424
5. Majzoobi A, Khodaie A, Barhamirad S (2017) Capturing distribution grid-integrated solar variability and uncertainty using micro grids. In: IEEE power & energy society general meeting

6. Zheng JH, Kou YN, Li Z, Wu QH (2017) Unscented transformation-based fast scheduling optimization for large-scale unit commitment considering uncertainties of wind and solar power. In: IEEE power & energy society general meeting
7. Xiaodong Y, Youbing Z, Guofeng W, Shuaijie R, Weiwei S, Junjie L (2017) Coordinate optimization for grid-connected microgrid considering uncertainties of renewable energy sources and electric vehicles. In: 29th Chinese control and decision conference (CCDC)
8. Khanghah BY, Moghaddam A, Guerrero JM, Vasquez JC (2017) Combined solar charging stations and energy storage units allocation for electric vehicles by considering uncertainties. In: IEEE international conference on environment and electrical engineering IEEE industrial and commercial power systems Europe (EEEIC/I&CPS Europe)
9. Keles C, Alagoz BB, Kaygusuz A (2017) Multi-source energy mixing for renewable energy microgrids by particle swarm optimization. In: International artificial intelligence and data processing symposium (IDAP)
10. Guo X, Bao Z, Lai H, Yan W (2017) Model predictive control considering scenario optimisation for microgrid dispatching with wind power and electric vehicle. *J Eng* 13:2539–2543
11. Elistratov V, Konishev M, Fedorov M (2017) Optimization of power supply of the circumpolar territories on the basis of renewable energy sources. In: International conference on industrial engineering, applications and manufacturing (ICIEAM)
12. Shiva C, Bhavani R, Prabha N (2017) Power quality improvement in a grid integrated solar PV system. In: IEEE international conference on intelligent techniques in control, optimization and signal processing (INCOS)
13. Praiselin WJ, Edward JB (2017) Improvement of power quality with integration of solar PV and battery storage system based micro grid operation. In: International conference on innovations in power and advanced computing technologies [i-PACT2017], IEEE conference
14. Moslehi S, Reddy TA, Katipamula S (2017) Evaluation of data-driven models for predicting solar photovoltaics power output. *Energy* 142:1057–1065
15. Brenna M, Longo M, Yaici W, Abegaz TD (2017) Simulation and optimization of integration of hybrid renewable energy sources and storages for remote communities electrification. In: IEEE PES innovative smart grid technologies conference Europe (ISGT-Europe)
16. Hanhuawei H, Chunli W, Weiwei J, Ning S (2017) A two-stage stochastic programming method for optimal power scheduling with solar power integration. In: Chinese automation congress (CAC)
17. Vasant LG, Pawar VR (2017) Solar-wind hybrid energy system using MPPT. In: International conference on intelligent computing and control systems, international conference on intelligent computing and control systems (ICICCS)
18. Chatterjee A, Ghosh S, Chatterjee D (2017) Analysis and control of a two winding IG based wind-photovoltaic generation scheme for domestic application. In: IEEE Calcutta conference (CALCON)
19. Li J, Xin H, Wei W, Dai W (2016) Decentralised conic optimisation of reactive power considering uncertainty of renewable energy sources. *IET Renew Power Gener* 10(9):1348–1355
20. Firduas, Umar, Ontoseno (2016) Economic dispatched of multi microgrid system with renewable energy sources using PSO. In: International seminar on intelligent technology and its application (ISITIA)
21. Moravek J, Drapela J (2016) Power quality issues related to power flow control in systems with renewable energy micro sources. In: 17th international scientific conference on electric power engineering (EPE)
22. Hammouti M, El Miloud A, Ghoumid K (2016) Power quality command and control systems in wireless renewable energy networks. In: International renewable and sustainable energy conference (IRSEC)
23. Gaythri C, Dhanalakshmi R (2016) Analysis of power quality on a renewable energy micro grid conversion system with current and power controller. In: International conference on advanced communication control and computing technologies (ICACCCT), IEEE conference
24. Shaha R, Kothari OP, Chandrakar VS (2016) Optimization of renewable energy sources for hybrid power generation. In: Biennial international conference on power and energy systems: towards sustainable energy (PESTSE)

25. Jankar PA, Patil AS (2016) Maximum utilization of solar (renewable energy) by using multiple sensor technology. In: International conference on signal processing, communication, power and embedded system (SCOPEs), pp 446–451
26. AlHakeem D, Mandal P (2015) A new strategy to quantify uncertainties of wavelet-GRNN-PSO based solar PV power forecasts using bootstrap confidence intervals. In: IEEE power & energy society general meeting
27. Hadjidemetriou L, Kyriakides E (2015) A robust synchronization to enhance the power quality of renewable energy systems. *IEEE Trans Ind Electron* 62(8):4858–4868
28. Eriksson E, Gray E (2017) Optimization and integration of hybrid renewable energy hydrogen fuel cell energy systems—a critical review. *Appl Energy* 202:348–364
29. Suganthi L, Iniyan S, Samuel A (2015) Applications of fuzzy logic in renewable energy systems—a review. *Renew Sustain Energy Rev* 48:585–607
30. Mosobi RW, Chichi T, Gao S (2014) Modeling and power quality analysis of integrated renewable energy system. In: Eighteenth national power systems conference (NPSC)
31. Erdinc O, Uzunoglu M (2012) Optimum design of hybrid renewable energy systems: overview of different approaches. *Renew Sustain Energy Rev* 16(3):1412–1425
32. Nehrir M, Wang C, Strunz K, Aki H, Ramakumar R, Bing J, Miao Z, Salameh Z (2011) A review of hybrid renewable/alternative energy systems for electric power generation: configurations, control, and applications. *IEEE Trans Sustain Energy* 2(4):392–403
33. Zhou W, Lou C, Li Z, Lu L, Yang H (2010) Current status of research on optimum sizing of stand-alone hybrid solar–wind power generation systems. *Appl Energy* 87(2):380–389
34. Erdinc O, Uzunoglu M (2010) Recent trends in PEM fuel cell-powered hybrid systems: investigation of application areas, design architectures and energy management approaches. *Renew Sustain Energy Rev* 14(9):2874–2884
35. Bernal-Agustín J, Dufo-López R (2009) Simulation and optimization of stand-alone hybrid renewable energy systems. *Renew Sustain Energy Rev* 13(8):2111–2118
36. Bialasiewicz J (2008) Renewable energy systems with photovoltaic power generators: operation and modeling. *IEEE Trans Ind Electron* 55(7):2752–2758
37. Nema P, Nema R, Rangnekar S (2009) A current and future state of art development of hybrid energy system using wind and PV-solar: a review. *Renew Sustain Energy Rev* 13(8):2096–2103
38. Deshmukh M, Deshmukh S (2008) Modeling of hybrid renewable energy systems. *Renew Sustain Energy Rev* 12(1):235–249
39. Piwko R, Osborn D, Gramlich R, Jordan G, Hawkins D, Porter K (2005) Wind energy delivery issues [transmission planning and competitive electricity market operation]. *IEEE Power Energy Mag* 3(6):47–56
40. Alepuz S, Busquets-Monge S, Bordonau J, Gago J, Gonzalez D, Balcells J (2006) Interfacing renewable energy sources to the utility grid using a three-level inverter. *IEEE Trans Ind Electron* 53(5):1504–1511
41. Bialasiewicz J, Muljadi E (2006) Analysis of renewable-energy systems using RPM-SIM simulator. *IEEE Trans Ind Electron* 53(4):1137–1143
42. Leite A, Borges C, Falcao D (2006) Probabilistic wind farms generation model for reliability studies applied to Brazilian sites. *IEEE Trans Power Syst* 21(4):1493–1501
43. Portillo R, Prats M, Leon J, Sanchez J, Carrasco J, Galvan E, Franquelo L (2006) Modeling strategy for back-to-back three-level converters applied to high-power wind turbines. *IEEE Trans Ind Electron* 53(5):1483–1491
44. Kottas T, Boutalis Y, Karlis A (2006) New maximum power point tracker for PV arrays using fuzzy controller in close cooperation with fuzzy cognitive networks. *IEEE Trans Energy Convers* 21(3):793–803
45. Senjyu T, Hayashi D, Urasaki N, Funabashi T (2006) Optimum configuration for renewable generating systems in residence using genetic algorithm. *IEEE Trans Energy Convers* 21(2):459–466
46. Tan K, Islam S (2004) Optimum control strategies in energy conversion of PMSG wind turbine system without mechanical sensors. *IEEE Trans Energy Convers* 19(2):392–399

47. Teodorescu R, Blaabjerg F (2004) Flexible control of small wind turbines with grid failure detection operating in stand-alone and grid-connected mode. *IEEE Trans Power Electron* 19(5):1323–1332
48. Daniel S, AmmasaiGounden N (2004) A novel hybrid isolated generating system based on PV fed inverter-assisted wind-driven induction generators. *IEEE Trans Energy Convers* 19(2):416–422
49. Macken K, Vanthournout K, VandenKeybus J, Deconinck G, Belmans R (2004) Distributed control of renewable generation units with integrated active filter. *IEEE Trans Power Electron* 19(5):1353–1360
50. Rahman S (2003) Green power: what is it and where can we find it? *IEEE Power Energy Mag* 1(1):30–37

Performance Analysis of PV System Integrated with Boost Converter for Low Power Applications



Ruchira, R. N. Patel and Sanjay Kumar Sinha

Abstract This paper presents stand-alone PV system integrated with boost converter which can be used for low power applications. The performance of PV is affected due to changing temperature and irradiation. In this paper, the Current–Voltage ($I-V$) and Power–Voltage ($P-V$) characteristics have been obtained for a PV module for varying temperature and solar irradiation. In the present study, the boost converter design connected to a PV module has been simulated in Matlab/Simulink and its performance and the analysis of results have been discussed in this paper. It is known that there are many regions of India which are still without electricity so the focus has been done on standalone systems so that basic lighting can be provided in such areas. The present research will be helpful to implement PV systems for standalone low power applications like street lighting, small domestic load, charging of mobile phones, etc.

Keywords Photovoltaic · Boost converter · Duty cycle

1 Introduction

The present source of power generation is from hydro, thermal, nuclear, gas based plants, fossil fuel small power plants, gohar gas plants, etc. Since fossil fuels are depleting at a fast rate, it is necessary to find its replacement. To provide the solution, the emphasis is being given on renewable sources of energy like wind energy, solar energy, etc. The main advantage of use of these sources of energy is that the fuel required for generation is available free of cost and does not cause any pollution. The

Ruchira (✉) · S. K. Sinha
Amity University Uttar Pradesh, Noida, Uttar Pradesh, India
e-mail: er.ruchiragarg@gmail.com

S. K. Sinha
e-mail: sinha.sanjay66@gmail.com

R. N. Patel
National Institute of Technology Raipur, Raipur, India
e-mail: ramnpatel@gmail.com

© Springer Nature Singapore Pte Ltd. 2019
M. Kumar et al. (eds.), *Advances in Interdisciplinary Engineering*, Lecture Notes in Mechanical Engineering, https://doi.org/10.1007/978-981-13-6577-5_85

present work focuses on the use of solar energy for different applications. In case of solar power generation, the fuel cost is zero. Moreover for the standalone systems, the operational staff is also not required. Only the nominal maintenance cost will be borne by the consumer. Moreover, the consumer will be his own master of the power source.

At present, lot of research is being done to reduce the initial capital cost of the system and also to increase the efficiency. In the new era of renewable solar energy, it is sensed that the cost of solar power equipment panel, etc., and its installation cum maintenance will become cheaper. The main benefit of solar power is that it does not cause any pollution rather make the environment eco friendly green. These days efforts are being made to develop and use more and more renewable energy sources by harnessing the solar energy obtained from sun. But the only concern with this method that power we get is not constant. This happens due to the dependency on physical conditions like temperature, irradiation, etc. These variable supplies are supplemented by additional converters and batteries to provide the reliable supply. The use of DC-DC converter provides a desirable fixed voltage. There are many applications like computers, medical instrumentation, communication devices, etc., where the converters are used [1, 2]. They also find its use in DC motor speed control applications.

There are different types of converters like buck converter, boost converter, buck–boost converter and Cuk converter, etc. Switching concept is used to control the converter's output voltage. The conventional converters use SCRs (silicon-controlled rectifiers) for the switching mechanisms. However, the present-day converters use either IGBT or MOSFET and are called as switch mode power supplies (SMPS). The full form of MOSFET is metal oxide silicon field effect transistors (MOSFETs) and IGBT is insulated gate bipolar transistors (IGBTs). The present work deals with the designing of boost converter for a low power PV system.

The concept of Pulse width modulation (PWM) is generally used to control the output voltage which is a function of the pulse width, t_{on} on time of the switch, and the switching frequency f_s . With change in duty ratio (D), the output voltage can be controlled.

The term "Duty cycle" is generally expressed as a percentage of the signal period where the signal is considered on. Mathematically duty cycle can be expressed as mentioned in (1).

$$\% \text{ duty cycle} = \left(\frac{T_{on}}{T_{on} + T_{off}} \right) * 100\% \quad (1)$$

In the process of controlling the voltage constant, the switching period (switching frequency) remains constant however on time and therefore the duty ratio of the switch is changed. In the present work the switching frequency is chosen as 30 kHz. Depending on the characteristics of the output current there are two modes in which these converters operate. These modes are called as continuous conduction and discontinuous conduction.

The converter is said to operate in continuous conduction mode if over the entire switching period, the continuous output current has positive integer value, whereas the converter works in discontinuous conduction mode if the output current is null during any portion of the switching period [3, 4].

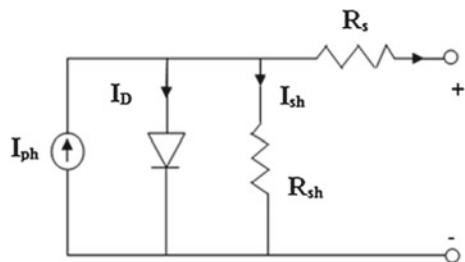
In this paper, the $P-V$ and $I-V$ characteristics of solar photovoltaic panel has been obtained for SPR 250W module under varying temperature and irradiation. The paper also explains the step-by-step procedure to design the parameters of step-up DC chopper or the boost converter. The performance analysis of the standalone system and results obtained by simulations have been discussed.

2 Characteristics of PV Cell

PV cell is an important component which is used to extract the power of sun. Electrically, any PV cell is represented by either single PN junction diode or double diode along with the series and parallel resistance in parallel with current source. When this cell is exposed to sunlight then due to electrons movement the solar power is converted into electrical power. In the equivalent circuit shown in Fig. 1, I_{ph} is the current developed in photon, I_D is the diode current, I_{sh} and R_{sh} indicate the current and resistance of shunt branch, respectively. In practice, 36 or 72 cells are used for series connection. The behavior of photovoltaic module is analyzed using $P-V$ and $I-V$ characteristics. The Simulink connection diagram for obtaining the above characteristics is shown in Fig. 2.

It is very well known that the behavior of solar cell shows a change with the change in physical conditions like temperature and irradiation. From the characteristics curve we can see that there is one point where the PV module produces maximum possible power and it is called as maximum power point (MPP). The operation of PV module(s) at the MPP (operating condition) must be guaranteed by the inverters and the same is accomplished with MPPT. The current-voltage and power-voltage characteristics of a solar cell for fixed irradiance of 1000 W/m^2 and varying temperature has been shown in Fig. 3. Figure 4 shows the $P-V$ and $I-V$ characteristics for fixed temperature and varying irradiation. Hence, if we want to obtain maximum

Fig. 1 Model of PV cell



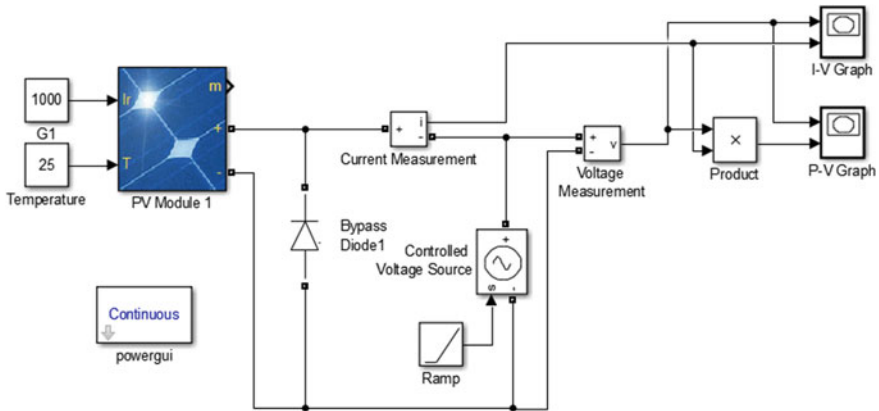


Fig. 2 Block diagram to obtain the $P-V$ and $I-V$ characteristics

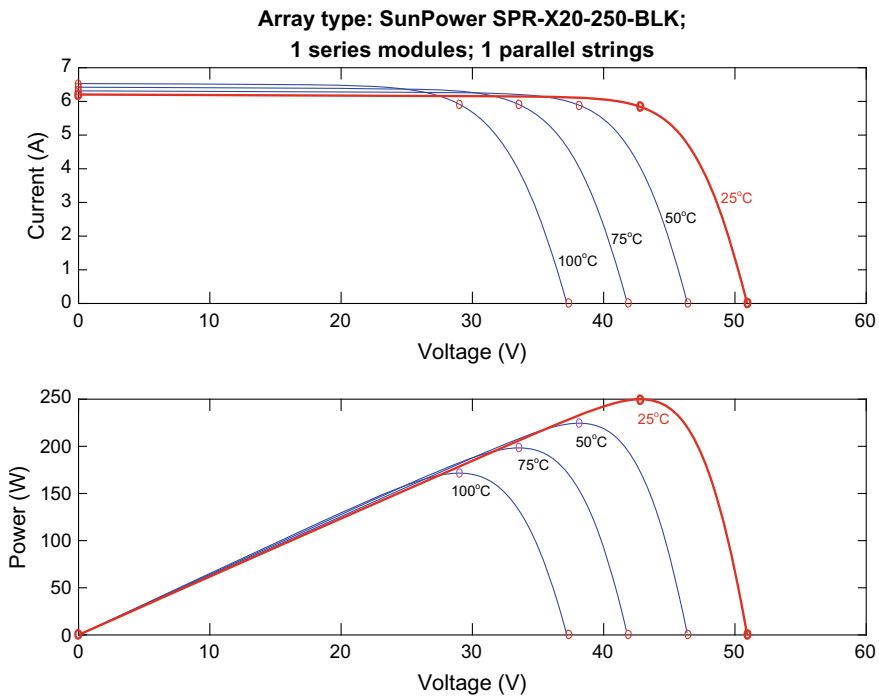


Fig. 3 $I-V$ and $P-V$ characteristics with changing temperature and fixed irradiation

output power from the cell, we have to ensure that the module always operate at the maximum operating voltage and current and it should be global maxima [5–9].

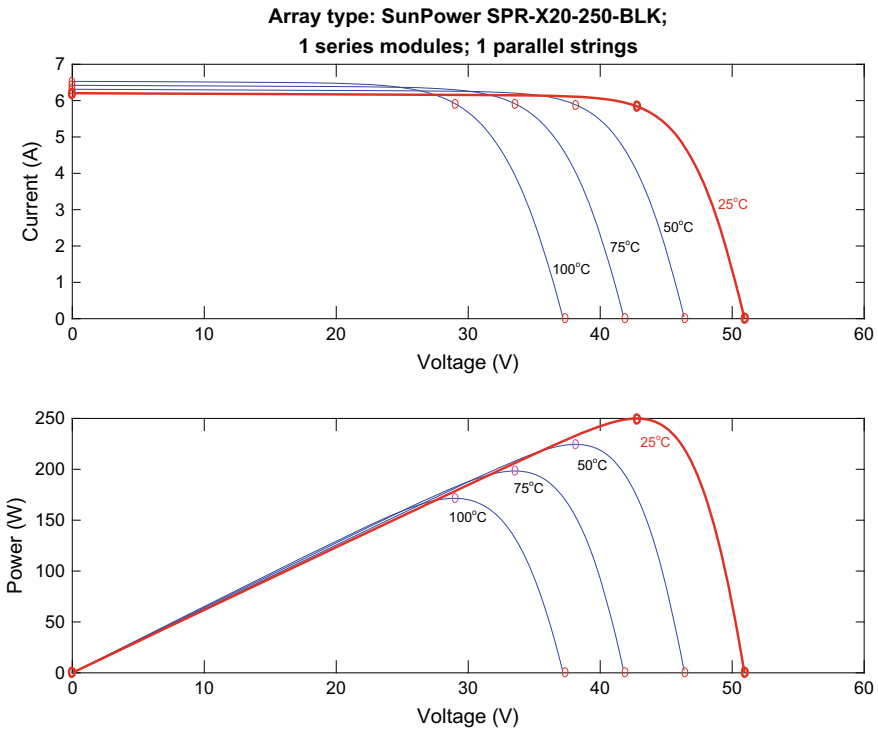
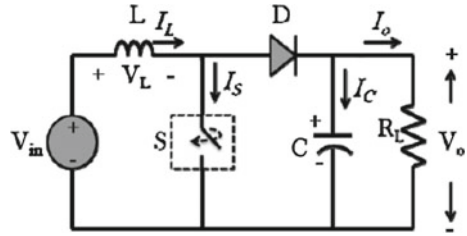


Fig. 4 I-V and P-V characteristics for fixed temperature and changing irradiation

3 Working of Boost Converter

The boost converter is also called step-up DC-DC chopper. The word “boost” means to raise. So, its function is also to raise the input voltage to a desired output voltage level. The circuit diagram of the designed converter is shown in Fig. 5. The design of the circuit consists of passive components namely inductor and capacitor, semiconductor switch and diode. The inductor stores the energy when the switch S is turned on, the diode does not conduct at this time. But when the switch is off then the energy of inductor is released through diode to the load. At this time the polarity of inductor is reversed. The input voltage and inductor voltage get added and output voltage is raised [2, 3].

Fig. 5 Schematic diagram of DC-DC step-up boost converter



4 Design Procedure of Boost Converter

The process of designing of boost converter mainly involves finding out the optimized values for the passive components namely inductor and the capacitor. The design specifications are tabulated in Table 1.

A. Selecting the Inductor Size

The value of the inductor used in the boost converter is mainly dependent on switching frequency f_s , the input current ripple ΔI_L , duty ratio D and input voltage V_{in} . The mathematical relation to find the component value is given below.

$$L = \frac{V_{in}}{f_s \Delta I_L} D \tag{2}$$

For optimum selection of inductor size, the current ripple factor CRF should bound within 30%. CRF is defined as the fraction obtained if input current ripple is divided by output current.

$$\frac{\Delta I_L}{I_o} = 30\% \tag{3}$$

It is recommended to keep the inductor rating always more than the maximum output current [3].

B. Selecting the Capacitor Size

The relation to obtain the capacitor value is given below.

Table 1 Specifications for design of boost converter

Input voltage	25 V
Switching frequency	30 kHz
Output voltage	50 V
Duty ratio	0.5
Load resistance	10 Ω

Table 2 Design formulas and calculated values for boost converter

Name of the component	Design formula	Calculated value
Inductor	$L = \frac{V_{in}}{f_s \Delta I_L} D$	277 μ H
Capacitor	$C = \frac{I_{out}}{f_s \Delta V_o} D$	33 μ F

$$C = \frac{I_{out}}{f_s \Delta V_o} D \tag{4}$$

where ΔV_o represents the output voltage ripple. The value of output voltage ripple is 0.5 times the output voltage.

$$\frac{\Delta V_o}{V_o} = 0.5 \tag{5}$$

In the present simulation work, the converter is designed for input voltage of 25 V, output voltage of 50 V, load resistor of 10 Ω , and switching frequency of 30 kHz. The component values obtained are shown in Table 2.

5 Applications of Boost Converter

The choppers are building blocks that provide control supply frameworks in which a typical direct current voltage is changed over to different voltages as indicated by necessities of specific loads. Such distributed dc frameworks are normal in space stations, boats and planes and also in PC. It is normal that advanced versatile remote correspondence and flag preparing frameworks will utilize inconsistent supply voltages to limit control utilization and to expand battery life.

Another significant application is identified with the grid utility. For basic load requirements, if the distributor framework breakdowns, there must be a support source of energy, for illustration, a battery pack. This requirement for consistent power transfer has given rise to different kinds of uninterruptable power supplies (UPSs). Consequently, dc-dc converters are utilized as a part of UPSs to modified the level of a rectified grid voltage to that of the backup source. In routine normal situations, the power flows from the utility to the backup source and amid crisis conditions, the reinforcement source must supply the load, bidirectional dc-dc converters are frequently utilized. In addition, dc-dc converters are additionally utilized as a part of devoted battery chargers. Power electronic loads, particularly those with front-end rectifiers, degrade the grid with odd harmonics. In this way, these converters are utilized as moderate stages, soon after a rectifier and before the load providing dc-dc converter, for forming the information grid current to enhance control factor and diminish the harmonics. The step-up converter is particularly prevalent in such power factor correction (PFC) applications.

Table 3 Specifications of Sunpower SPR-X20-250-BLK PV Module

Maximum power	249.95 W
Cells per module	72
Open circuit voltage	50.93 V
Short circuit current	6.2 A
Voltage at maximum power point	42.8 V
Current at maximum power point	5.84

6 Simulated Results

In this work, the PV module has been used for simulation in MATLAB/Simulink. Table 3 represents the specifications of PV module used in the present simulation. The simulation of boost converter has been performed in MATLAB/Simulink. The specifications used to design the boost converter have been mentioned in Table 1 and the designed values are shown in Table 2. Figure 6 shows the Simulink model of Boost converter fed by PV.

The Simulink model in Fig. 6 shows the connection of PV module with the design circuit of converter. There are two inputs to the PV module namely temperature and irradiation. The specifications of the PV module are set. The output is taken to the converter design and various measuring devices are placed. The measurements are shown in Fig. 7a, b. The input current is shown in Fig. 7a and input voltage to the DC chopper circuit is shown in Fig. 7b. In the figure, we can see that 25 V is the constant DC input voltage and nearly 6.16 A is the panel current. Figure 8 shows the pulse generation given to the semiconductor switch with the duty cycle $D = 0.5$. The inductor current can be seen in Fig. 9. The graph of output voltage with time is shown in Fig. 10a. Figure 10b shows the graph of output current of boost converter. From the graph, it can be noticed that both the voltage and current approaches the desired values.

7 Conclusion

In this work, first, the electrical characteristics, i.e., $I-V$ and $P-V$ curves are obtained for Sunpower SPR-X20-250-BLK PV Module for two conditions. The first condition is constant irradiation and fixed temperature and the second condition is vice versa case. Further, the paper presents the design of boost converter for a standalone PV System for low power. The results of design are shown in Table 3. Further designed values of inductor and capacitor are simulated in MATLAB and the outputs are shown in Fig. 10a, b. The converter design has been done for fixed temperature and irradiation.

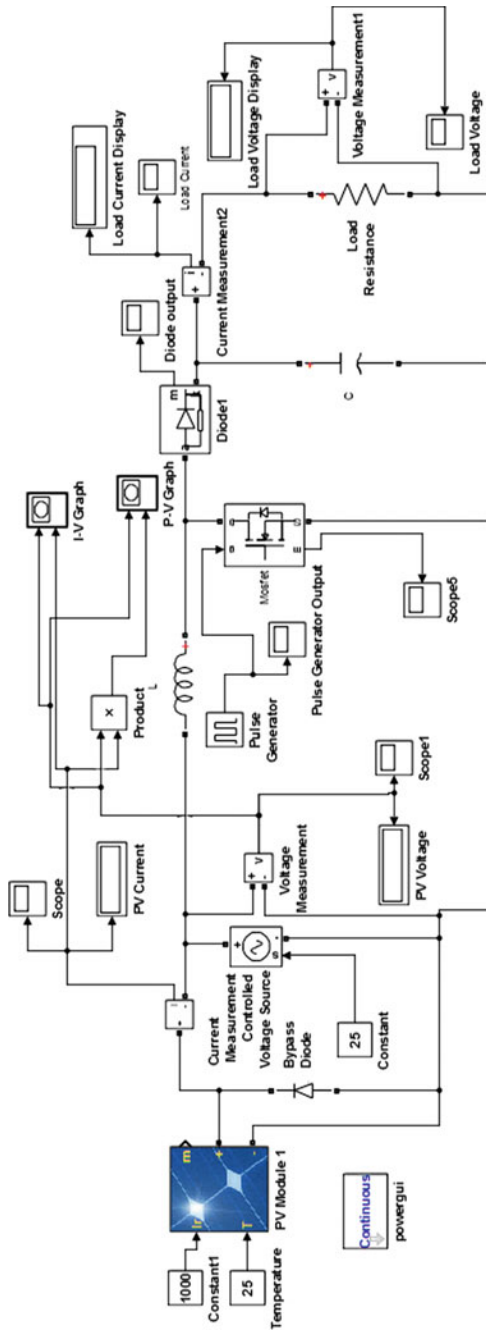


Fig. 6 PV system integrated with DC-DC boost converter

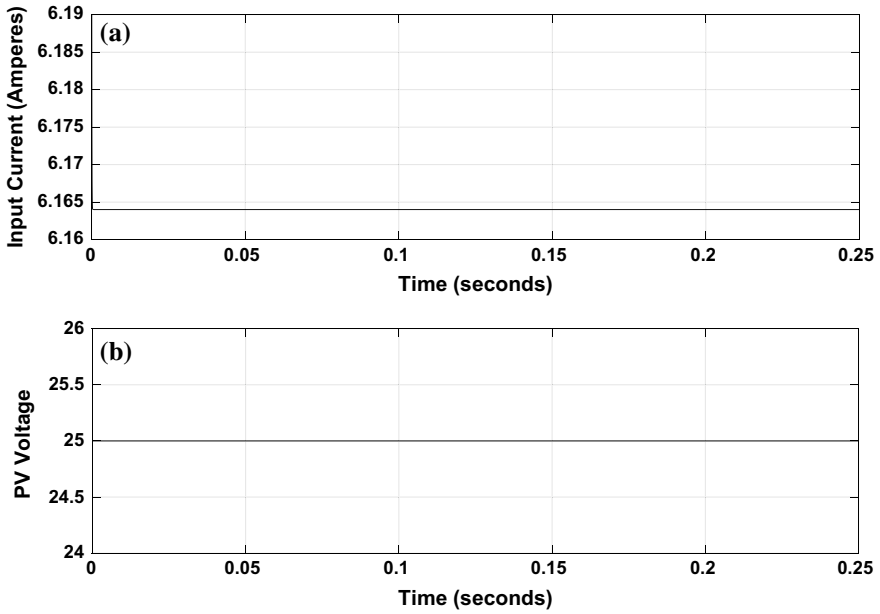


Fig. 7 a Input current of PV fed converter, b input voltage of PV fed converter

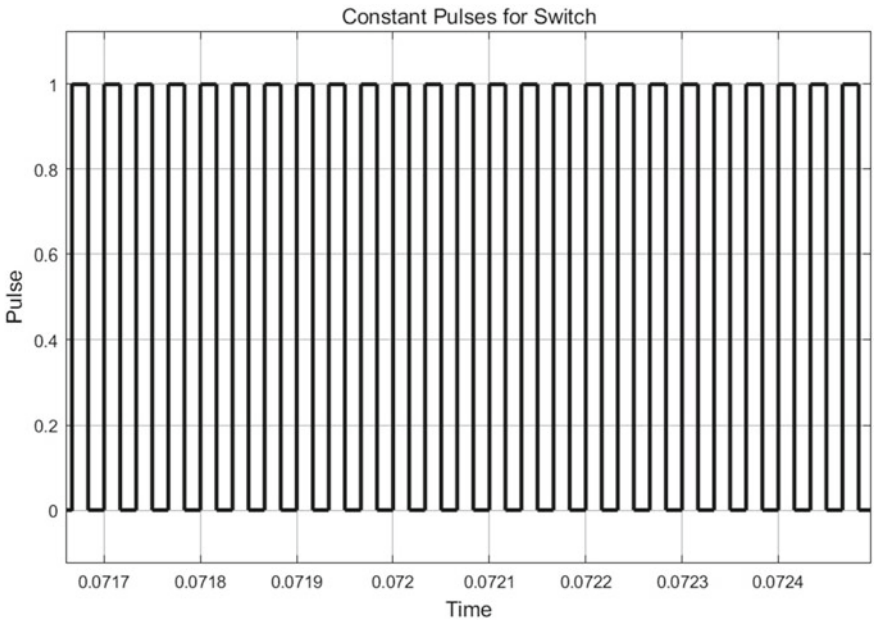


Fig. 8 PWM pulse generation

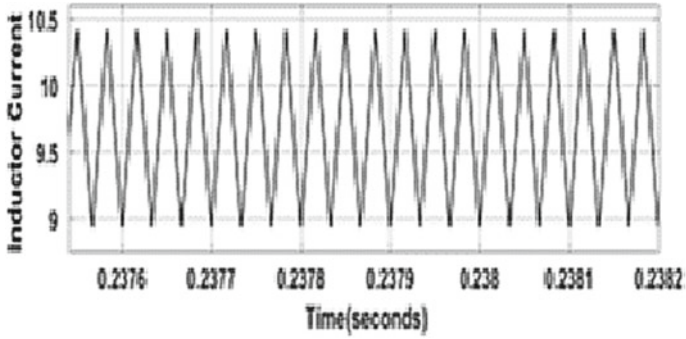


Fig. 9 Inductor current

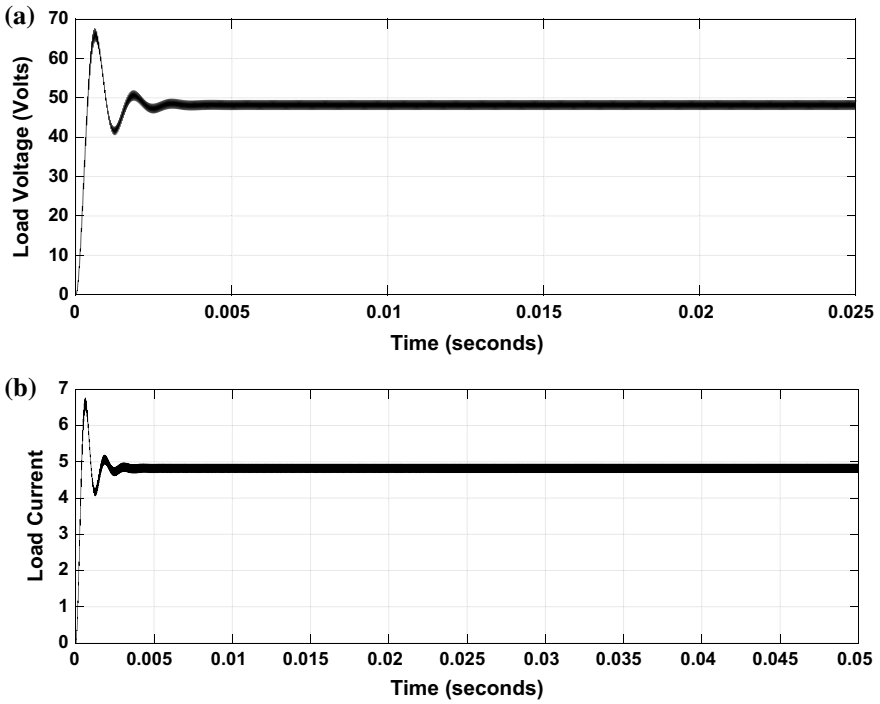


Fig. 10 a Output voltage across the load resistance, b output current across the load resistance

References

1. Rashid MH (2011) Power electronics handbook, 3rd edn. Butterworth-Heinemann, Oxford
2. Sahu P, Verma D, Nema S (2016) Physical design and modelling of boost converter for maximum power point tracking in solar PV systems. In: International conference on electrical power and energy systems (ICEPES)
3. Mohammed SS, Devaraj D (2014) Simulation and analysis of stand-alone photovoltaic system with boost converter using MATLAB/Simulink. In: International conference on circuits, power and computing technologies
4. Brey JJ et al (2007) Power conditioning of fuel cell systems in portable applications. *Int J Hydrogen Energy* 32(10–11):1559–1566
5. Wies R, Satavalekar B, Agrawal A, Mahdavi J, Agah A, Emadi A, Shortt DJ (2002) The power electronics handbook - industrial electronics series, CRC Press, ISBN 0-8493-7336-0
6. Verma D, Nema S, Shandilya AM (2016) A different approach to design non-isolated DC–DC converters for maximum power point tracking in solar photovoltaic systems. *J Circuits Syst Comput* 25(08):1630004
7. Armstrong S, Glavin ME, Hurley WG (2008) Comparison of battery charging algorithms for stand alone photovoltaic systems. In: IEEE power electronics specialists conference
8. Spertino F, Ahmad J, Di Leo P, Ciocia A (2016) A method for obtaining the I-V curve of photovoltaic arrays from module voltages and its applications for MPP tracking. *Solar Energy* 139:489–505
9. John R, Mohammed SS, Zachariah R (2017) Variable step size perturb and observe MPPT algorithm for standalone solar photovoltaic system. In: IEEE international conference on intelligent techniques in control, optimization and signal processing (INCOS)

Modal Analysis of 132 kV Double Circuit Electric Power Transmission Tower Made up with Composite Material Thermoplastic Long Carbon Fiber Nylon 66



Chiranjit Bhowmik, Prasun Chakraborti, Shankar Swarup Das and Ram Singh

Abstract In recent days, the tendency of composite materials uses in tower structural member material is increasing tremendously over conventional zinc galvanized steel materials because of their special advantages. Using the composite materials over conventional materials in the field of large structure construction like tower in mass scale, it is important to study the dynamic behavior of these structures made up with composite materials in detail. Modal analysis of tower structure made up with composite materials has been reported few or all most nil in the literature. This study has taken up the challenge for the modal analysis of the present design approach of 132 kV double circuit tower made up with composite material like Thermoplastic Long Carbon Fiber Nylon-66. The results found for the first six modes of vibration using subspace iteration method. The results are compared with the results obtained by typical conventional method, still followed by the industry for erection of such high tower made up of conventional material like zinc galvanized steel.

Keywords Dynamic analysis · Modal analysis · Double circuit · Transmission tower

1 Introduction

Electricity transmission network is a basic need of infrastructure of civilization, which assumes a critical part in improvement of economy and society for any country. A large transmission line system is required to provide electricity to every house. Transmission line system is again required due to uneven disposition of resources. Extra-High-Voltage (EHV) tower is the essential part of the transmission line system which is constructed by steel L section members. Guiding of power carrying lines, steel lattice towers represent approximately 40% in aggregate of gross investment in the electricity transmission network. Also their wellbeing and reliability precisely

C. Bhowmik (✉) · P. Chakraborti · S. S. Das · R. Singh
National Institute of Technology, Agartala 799035, India
e-mail: chiranjit040291@gmail.com

© Springer Nature Singapore Pte Ltd. 2019

M. Kumar et al. (eds.), *Advances in Interdisciplinary Engineering*, Lecture Notes in Mechanical Engineering, https://doi.org/10.1007/978-981-13-6577-5_86

impact the regular function of the entire transmission network including the development of the society [1].

Most vibration studies on transmission line systems are conducted on transmission towers under wind loads [2, 3]. Displacements and internal forces in transmission lines are substantial underground vibrations, and the dynamic effects may exceed those caused by the wind loads [4]. Transmission towers subjected to spatially incoherent seismic ground motions had significant effects on lateral displacements of transmission lines. The complexity caused by the coupling between cables and supporting structures increases the difficulty in studying dynamic responses of transmission systems [5]. The behavior of transmission lines under severe winds had significant effects on dynamic behaviors of cables [6, 7]. Cable behaviors for galloping may be initiated in a purely vertical mode, purely torsional mode or a combination of both. It is challenging to simulate coupled conductor/tower behaviors using full solid FE models: Cable vibration alone is difficult to model using finite element method [8, 9]. Hence, simplified models, which take into account the coupling characteristics, have been developed for transmission tower-line systems. Studies of the free vibration of transmission pole structures are limited: modal tests on several concrete pole structures under free-free boundary conditions and developed distributed mass models using ANSYS [10]. Identified vibration modes of pre-stressed concrete poles using both modal testing and FE simulation is one of the ways for dynamic analysis through natural frequency of composite poles [11].

Nowadays, using composite materials as a transmission tower structural member material is rapidly increased last few decades over conventional zinc galvanized steel materials because of their special advantages over conventional steel materials. These special advantages are durability, light in weight, less corrosiveness, less maintenance, etc. So before using the composite materials over conventional materials in the field of large structure construction like lattice transmission tower in mass scale, it is important to study the dynamic behavior of these structures made up with composite materials in detail. Modal analysis of lattice transmission tower structure made up with composite materials has been reported few or all most nil in the literature. Hence, this study has taken up the challenge for the modal analysis of the present design approach of 132 kV double circuit transmission tower made up with composite material like Thermoplastic Long Carbon Fiber Nylon-66. The results found for the first six modes of vibration using subspace iteration method. The results are compared with the results obtained by typical conventional method, still followed by the power line industry for erection of such high power transmission line tower made up with conventional material like zinc galvanized steel.

2 Importance of Dynamic Properties

Natural frequency, damping proportion, and mode shape are the three fundamental segment used to characterize the dynamic properties in basic building. To foresee their conduct and outline them successfully, it is important to offer regard for the

dynamic properties of the structure [3]. Mean and fluctuating breeze stack are the fundamental two sort of twist stack on any ecological uncovered structure. Wind speed gives the mean breeze stacks though mean breeze stack increase by the factor of wind weight direction gives fluctuating breeze stack [2]. Wind weight direction factor is as per the following:

$$\beta = 1 + (v\gamma\varepsilon/\mu) \tag{1}$$

Here, β is the wind pressure regulation factor, v is fluctuation influence coefficient, ε is oscillating coefficient, γ is fluctuating amplifying coefficient, and μ is wind pressure height coefficient.

3 Theoretical Base of Modal Analysis

Free vibration motion equation with no damping of multi-degree of freedom system

$$[M]\{\ddot{X}\} + [S]\{X\} = \{0\} \tag{2}$$

Here $[M]$ is system mass matrix, $[S]$ is system stiffness matrix, $\{X\}$ is nodal acceleration vector, and $\{X\}$ is nodal displacement vector [4].

For harmonic oscillations, $\{X\} = \{X0\}\sin\omega t$, characteristic equation of Eq. (2) is as follows

$$([S] - \omega^2[M])\{X0\} = \{0\} \tag{3}$$

Here ω is the natural frequency. The condition that Eq. (3) has a nonzero solution:

$$|[S] - \omega^2[M]| = 0 \tag{4}$$

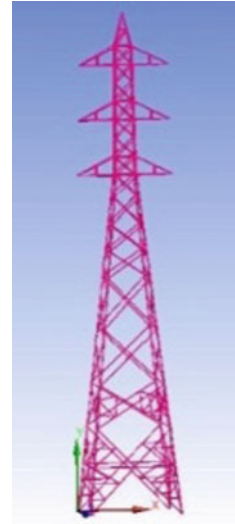
Frequencies of the system are obtained by solving Eq. (4). Eigenvalues and Eigenvectors of the characteristic equation are the free vibration frequencies and the corresponding vibration modes [4].

4 Modal Analysis Simulation by ANSYS

The FE numerical methodology is utilized to describe and check the utility of composite material for the lattice steel tower structure. Thermoplastic long carbon fiber nylon-66 is used as a suitable structural member material, specifications of the composite materials are given in Table 1. The steel angled members mostly carry axial

Table 1 Suitable composite materials for transmission tower available in market

Composite materials	Glass fiber polyamide 6 (thermoplastic)	Carbon fiber epoxy (thermoset)	Carbon fiber rigid polyurethane (thermoplastic)	Long carbon fiber, nylon 66 (thermoplastic)
Young modulus (GPa)	29	109	28	36
Breaking stress (MPa)	450	1200	427	507

Fig. 1 The FE model of the structure

force and members are connected by weld or bolt. Also, the FE model depends on the accompanying fundamental suppositions as stated below:

- The individual members are straight, and cross sections stay unaltered in length of the members;
- The steel angled member material is isotropic in nature and retains required mechanical properties even during stressed and other conditions;
- The strain of the individual members remains unaltered throughout all sections;
- All the individual members are subjected to two forces either tension or compression and the individual members fixed by hinged joints at both ends;

Following these presumptions, a 3-D FE model of the lattice steel tower is created utilizing software ANSYS. The model of a solitary tower comprises of 294 truss components and 170 nodes, appeared in Fig. 1. The lattice steel tower in its working conditions has to bear the load exerted by the power distribution cables and wires. The load impact of the power carrying wires effecting natural frequencies is also an important phenomenon and not going to be avoided during the study. The steel-cored

Table 2 Parameters of steel-cored aluminum strand wire “ACSR PANTHER”

Parameters	Conductor wire	Ground wire
Name of the conductor	“ACSR PANTHER” 30/3.00+7/3.00	GSW 7/3.15
Area (m ²)	2.615*E-4	5.455*E-5
Diameter (m)	0.021	0.00945
Weight of the conductor (kg/m)	0.974	0.428
Ultimate tensile strength (kg)	9144	5710
Modulus of elasticity (kg/m ²)	8.154*E9	1.933*E10
Maximum working span (m)	335	335
Minimum temperature (°C)	4	4
Every day temperature (°C)	32	32
Maximum temperature (°C)	75	53
Coefficient of linear expansion (°C)	1.78E-05	1.15E-05
Sag (m)	NA	4.438
Factor of safety	4	NA
Initial temperature (°C)	32	4
Initial wind pressure (kg/m ²)	0	0
Radial ice formation (m)	0	0

aluminum strand wire “ACSR PANTHER 30/3.00+7/3.00” is picked as the appropriated power cables as customarily used in this sector, and the wire specifications are given in Table 2. Since the length to diameter of the wire is too long, the flexural rigidity related factors of the wires are kept aside.

Finite element model of transmission tower is marched modal analysis by using ANSYS finite element software. It gives us the six steps of modes. It completely restricted 6 (Six) degrees of freedom. Relationship between frequency (f) and time period (T) is as follows:

$$T = 1/f \tag{5}$$

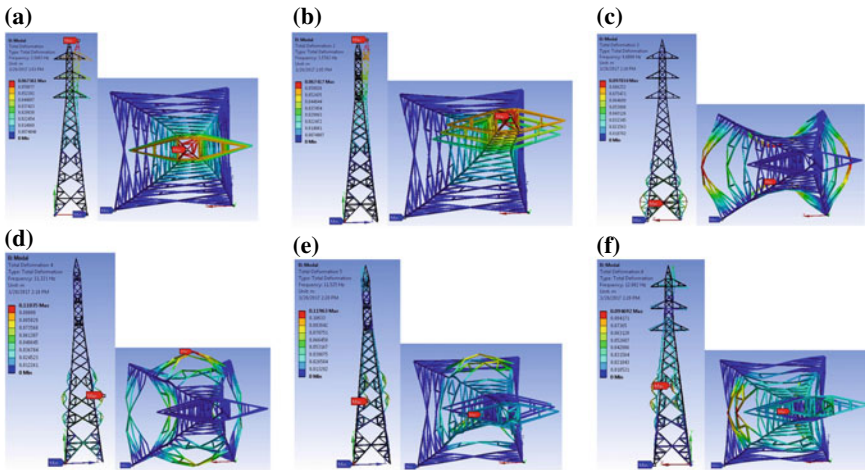


Fig. 2 Modes of vibration for tower structure obtained from Ansys. **a** 1st mode of vibration, **b** 2nd mode of vibration, **c** 3rd mode of vibration, **d** 4th mode of vibration, **e** 5th mode of vibration, **f** 6th mode of vibration

Using Eq. (5), we can easily get the six steps of vibration period of the transmission tower model [4]. Modal analysis using ANSYS finite element software obtains the six free modes of vibration frequency and time period.

It is found that both first and second modes of vibration are twisting in nature about z -axis and x -axis with frequencies of 3.5603 and 3.5762 Hz separately as shown in Fig. 2a, b. Additionally, it is seen that the third method of vibration is pressure in nature at the lower some portion of frequency 8.6808 Hz while the fourth mode of vibration demonstrates the development of a few individuals from the lower some portion of the structure, as appeared in Fig. 2c, d separately. The bending mode of vibration of transmission tower about z -axis with frequency 11.525 Hz appears in Fig. 2f. From this investigation, it is found that the twisting impact of vibration about x -axis is most risky when contrasted with every single other modes of vibration as appeared in Fig. 2e.

Figure 3 gives the mode versus frequency curve for the transmission tower. It can be seen from Fig. 3 that frequency followed increasing with modes of the transmission tower made up with composite material with minimum frequency 3.5603 Hz. Figure 4 illustrates the frequency versus maximum displacement curve for the composite tower structure. It indicates the maximum displacement occurred at 11.525 Hz in the amount of 0.11963 m.

Fig. 3 Variation of frequency with different vibration modes for the structure

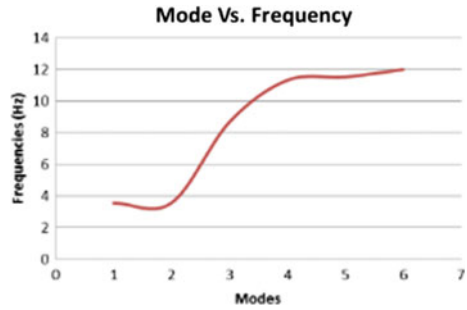
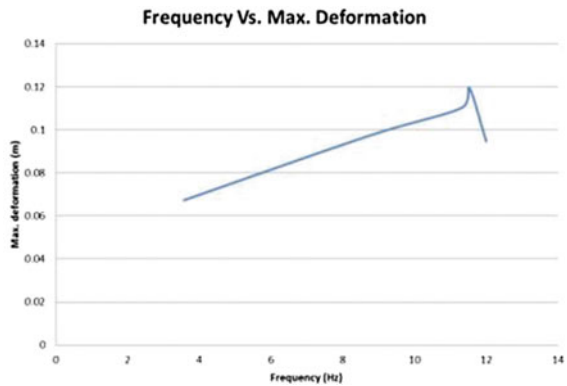


Fig. 4 Max. displacement versus frequency curve for the structure



5 Analysis of the Results

Electric power sector of India generally uses the formula to nearly estimate the free vibration period (T) of the tower structure as follows:

$$T = 0.034 H / (B + b)^{1/2} \tag{6}$$

Here H is the height of the tower, B is the top width of the tower, and b is the width of the root opening [2].

The first free vibration period of the composite tower structure from modal analysis is 0.2808 s, but calculated by the formula (6), it is 0.4357 s. Therefore, the difference between the two periods is 35.55%. Thus, it can be seen that the modal analysis results of the tower correspond well with the formula results of the electric power sector. The free vibration period of transmission tower is in between (0.007–0.013) H according to the design code. The free vibration period of the 132 kV double circuit transmission tower, which is made up with composite material, is in between (0.005–0.011) H according to the modal analysis by the standard software.

6 Conclusions

This paper uses FE software to establish the model of the 132 kV double circuit which is made up with composite material like thermoplastic long carbon polymer nylon 66, studies the dynamic properties the tower structure, and compares the results with the results obtaining from the experienced formula. From the above study, the following can be concluded

- The first free vibration period obtained from ANSYS is 35.55% more than that of the period which is calculated by the experienced formula.
- The bending mode of vibration of transmission tower about transverse direction with frequency 11.321 Hz is found most hazard situation among all the vibration modes.
- The free vibration period of the 132 kV double circuit transmission tower, which is made up of conventional steel material is in between (0.007–0.013) *H* according to the design code, but according to the modal analysis of the same tower structure which is made up with composite material by ANSYS software is in between (0.005–0.011) *H*.

This research only manages one typical lattice tower structure made up with composite material nylon 66; the investigating technique displayed in this research can be promptly reached out to different kinds of lattice steel tower structures with other composite type of materials. Also, the accuracy and legitimacy of the numerical technique ought to be further endorsed and changed by modal testing to apply in real application.

References

1. Xiaofeng L (2011) The study on modal analysis theory and measurement method for transmission towers. IEEE. <https://doi.org/10.1109/mace.2011.5987317>
2. Li MH, Yang JB, Li Z (2011) Latest developments of materials used in transmission tower structure. *Adv Mater Res* 3:4038–4041
3. Yeh HY, Yang SC (1997) Building of a composite transmission tower. *J Reinf Plast Compos* 16(5):414–424
4. Zhang LL, Sun Q, Zhang L (2011) Experimental study on the durability of glass fiber reinforced polymer pole and tower for power transmission. *Adv Mater Res* 12:1717–1724
5. Hollaway LC, Cadei J (2002) Progress in the technique of upgrading metallic structures with advanced polymer. *Prog Struct Eng Mater* 4(2):131–148
6. Rovira J, Ivorra S, Rovira J (2004) Construction of a tower with pultruded FRP composites. *J Int Assoc Shell Spatial Struct* 45(2):109–117
7. Feng P, Bekey S, Zhang Y, Bai Y (2012) Experimental study on buckling resistance technique of steel members strengthened using FRP. *Int J Struct Stab Dyn* 12:153–178
8. Momomura Y, Marukawa H, Okamura T, Hongo E, Ohkuma T (1997) Full-scale measurements of wind-induced vibration of a transmission line system in a mountainous area. *J Wind Eng Ind Aerodyn* 72:241–252
9. Khalili SMR, Saboori B (2010) Transient dynamic analysis of tapered FRP composite transmission poles using finite element method. *Compos Struct* 92(2):275–283

10. Li HM, Deng SC, Wei QH, Wu YN, Xiang QQ (2010) Research on composite material towers used in 110 kV overhead transmission lines. In: Proceedings of 2010 international conference on high voltage engineering and application (ICHVE), IEEE Computer Society, New York, pp 572–575
11. Polyzois DJ, Raftoyiannis IG, Ochonski A (2013) Experimental and analytical study of latticed structures made from FRP composite materials. *Compos Struct* 97:165–175

Decision-Making for Selection of Most Suitable Materials for Biomedical Applications



Shankar Swarup Das, Prasun Chakraborti, Chiranjit Bhowmik and Ram Singh

Abstract The selection of an optimal material needed for the design and development of various biomedical implants is very complex and challenging task today. Such implants are necessary for orthopedic applications as substitutes of various human joints like hip, knee, ankle, shoulder, etc. Hence, a simple mathematical and logical tool is needed to enable the decision-makers to take correct decisions in selecting the most suitable materials in spite of many selection attributes. This paper presents the applications of some novel Multi-attribute Decision-Making (MADM) techniques like AHP (Analytical Hierarchy Process), WPM (Weighted Product Method), and TOPSIS (Techniques of Order Preference by Similarity to Ideal Solution), etc., to accelerate the selection process of biomaterials for hip joint implants and enhance selection confidence and objectivity. The material selection is mainly based on their preferential ranking in all the methods. It is found that the Metal on Metal (MoM) pair is the best candidate for the hip joint implants among all other pairs such as Ceramic on Ceramic (CoC), Ceramic on Polyethylene (CoP), and Metal on Polyethylene (MoP) because it is at the top rank in all the methods.

Keywords Multi-attribute decision-making · Hip implants · Femoral · Acetabular cup · Wear debris

1 Introduction

The materials commonly used for biomedical applications are characterized as biomaterials for artificial organs or implants for rehabilitation to replace the tissues in the human body [1]. Development of novel or better biomaterial for implant in conjunction with manufacturing constraints is a complex and challenging task for the design engineers to meet up the market demand [2]. At present, there are a number of biomaterials having their own properties, applications, advantages, and disadvantages. So it is essential to choose a suitable material for a known biomedical application con-

S. S. Das (✉) · P. Chakraborti · C. Bhowmik · R. Singh
Department of Mechanical Engineering, National Institute of Technology, Agartala, India
e-mail: shankarswarup@gmail.com

© Springer Nature Singapore Pte Ltd. 2019
M. Kumar et al. (eds.), *Advances in Interdisciplinary Engineering*, Lecture Notes in Mechanical Engineering, https://doi.org/10.1007/978-981-13-6577-5_87

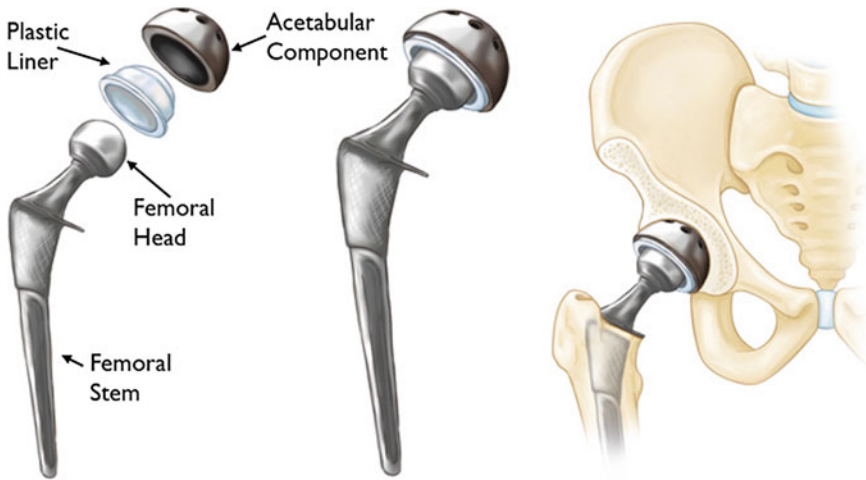


Fig. 1 Hip joint implant with its components fitted inside human body (web MD collection)

sidering its medical, technological, and economical aspects for decision-making [3]. The decision-makers should consider many issues in relation with the material such as mechanical, physical, chemical, biological, and economical properties that affect the quality and applicability of a biomedical product [4]. The decision expert has to understand the product requirements and selection criteria for a given biomedical application [5].

Therefore, both design engineer and the orthopedic surgeon should identify and select the most suitable material required for making hip joint implants with much better performance and minimum cost as shown in Fig. 1. The objectives in the material selection process should involve important factor such as preferred property, production process, in-service situation, product performance, cost and availability with a systematic and structured mathematical approach [5]. Using the multi-criteria decision (MCD) making methods, the material selection problems can be easily solved with many commensurable and contradictory criteria. The MCDM problems may broadly be classified as multi-objectives and multi-attribute decision-making methods depending on the kind of problem, i.e., design problem or a selection problem [6]. The MADM techniques create decision system considering the importance of chosen criteria leading which the whole ranking of alternatives is determined [7]. The material selection is mainly based on their preferential ranking in all the methods. Sometimes the decision-maker is not satisfied with the solutions obtained from one ranking in a particular method. Therefore, it is suggested to apply two or more methods to compare the rankings obtained from each method and select the material which is in top rank in most of the methods as the best solution [7].

In this paper, all the above three decision-making techniques are applied for selecting the most suitable material for making the so-called hip joint implants. Some of the materials are considered with necessary mechanical and physical properties as mul-

multiple criteria and then these three MADM methods such as WPM (Weighted Product Method), AHP (Analytic Hierarchy Method), and Technique for Order Preference by Similarity to Ideal Solution (TOPSIS) are applied one by one for ranking the list of alternative materials, and then the most appropriate material was selected. It is found that the Metal on Metal (MoM) pair is the best candidate for the hip joint implants among all other pairs such as Ceramic on Ceramic (CoC), Ceramic on Polyethylene (CoP), Metal on Polyethylene (MoP) since it is at the top rank in all the methods.

2 Methods for Materials Selection

A range of approaches are already reported by the past researchers to resolve the problem of material selection. The MADM methods are adopted in this study because they are simple and logical tools useful for the decision experts for considering many selection criteria and their inter-relations. Some of the commonly used MADM methods can be listed as Weighted Product Method (WPM) [6], Analytic Hierarchy Process (AHP) [7], TOPSIS (Technique for Order Preference by Similarity to an Ideal Solution) [8]. Each method is important for the material engineers working on biomechanical behavior of hip joints.

2.1 Weighted Product Method (WPM)

In this method, each attribute is assigned with a weight, where the sum of all weights must be one. All the attributes (n_{ij}) are multiplied with each other after powering them with the assigned weights (w_j). The overall performance score of an alternative is given by Eq. (1) as follows [6]:

$$Q_i = \prod_{j=1}^N [(n_{ij})_{\text{normal}}]^{w_j} \quad (1)$$

Finally, the highest value alternative is considered to be the best one from the ranking.

2.2 Analytic Hierarchy Process (AHP)

This is a popular technique useful for decision-makers as reported by Saaty in 1980 [5]. In this method, any such problem is divided into a hierarchical system of objectives, alternatives, and criteria or attributes. The method deals with tangible and intangible attributes where intangible decisions of dissimilar persons form a sig-

nificant component of the process [9]. The AHP procedure using geometric mean method (also called radial root method) is given in the following steps [6].

Step I. The attributes and objectives are found by developing a structural hierarchical objective at the high level, the middle-level attributes, and the alternatives at the bottom level.

Step II. Then the relative importance of various attributes w.r.t. the objectives are to be determined. A property contrasted and it is constantly relegated the esteem 1, so every one of the components of the corner to corner in the lattice are one. Now using the numbers 3, 5, 7, 9 to represent the informal decisions like ‘moderate’, ‘strong’, ‘very strong’ and ‘absolute strong’ compromising with 2, 4, 6, 8 in between. The pair wise comparison between i and j gives a square matrix $A_{M \times M}$ where a_{ij} indicates the relative importance of attribute i w.r.t. attribute j considering M attribute. This matrix represents, $a_{ij} = 1$ when $a_{ji} = 1/a_{ij}$ and $i = j$

$$A_{M \times M} = \begin{matrix} & \text{Attributes} & \begin{bmatrix} A_1 & A_2 & A_3 & \dots & A_M \end{bmatrix} \\ \begin{matrix} A_1 \\ A_2 \\ A_3 \\ \dots \\ A_M \end{matrix} & & \begin{bmatrix} 1 & a_{12} & a_{13} & \dots & a_{1m} \\ a_{21} & 1 & a_{23} & \dots & a_{2m} \\ a_{31} & a_{32} & 1 & \dots & a_{3m} \\ \dots & \dots & \dots & \dots & \dots \\ a_{m1} & a_{m2} & a_{m3} & \dots & 1 \end{bmatrix} \end{matrix} \tag{2}$$

AHP mainly uses the geometric mean (GM) method for determining the relative normalized weights (W_j) of the attributes as follows [7]:

$$GM_j = \left[\prod_1^N (a_{ij}) \right]^{1/N} \tag{3}$$

$$W_j = GM_j / \sum_{j=1}^n GM_j \tag{4}$$

where a_{ij} represents the relative importance of i w.r.t. j .

In this method it is easy to determine the maximum λ_{\max} (max Eigen value) and reduce the inconsistency of decision. Calculations from the matrices $A3$ and $A4$ gives $A3 = A1 * A2$ and $A4 = A3/A2$, considering $A2 = [w_1 \ w_2 \ \dots \ w_j]^T$. Then the maximum Eigen value λ_{\max} can be determined by taking the average of matrix $A4$.

The consistency index is calculated by $CI = (\lambda_{\max} - M)/(M - 1)$. The smaller value of CI indicates the smaller deviation from the consistency. Then the random index (RI) for the number of attributes used in decision-making is given in Table 1. The consistency ratio $CR = CR/RI$ should be less than 0.1 for acceptability since it reflects an informed judgment attributable to the knowledge of the analysts of the problem.

Step III. In this step the pair wise alternatives are compared with each other to see how the attributes are better or stronger. If there are M number of alternatives

Table 1 Random index values

Attribute	3	4	5	6	7	8	9	10
RI	0.52	0.89	1.11	1.25	1.35	1.4	1.45	1.49

Table 2 Table for multi-attribute decision method [10]

Alternatives	Attributes					
	$B_1 (w_1)$	$B_2 (w_2)$	$B_3 (w_3)$	–	–	$B_m (w_m)$
A_1	m_{11}	m_{12}	m_{13}	–	–	m_{1m}
A_2	m_{21}	m_{22}	m_{23}	–	–	m_{2m}
A_3	m_{31}	m_{32}	m_{33}	–	–	m_{3m}
–	–	–	–	–	–	–
–	–	–	–	–	–	–
A_N	m_{n1}	m_{n2}	m_{n3}	–	–	m_{nm}

then there will be $N \times N$ choice matrices, since there are M attributes. A pair wise comparison matrix is to be constructed [6].

Step IV. This step is similar to the Simple Addition of Weights (SAW) method. In this step the overall performance scores for the alternatives are to be obtained by multiplying the relative normalized weight (w_j) of each attribute as per step II, with its corresponding normalized weight values for each alternative as per step III and summing the attributes for each alternative.

2.3 Technique for Order Preference by Similarity to Ideal Solution (TOPSIS) Method

The TOPSIS strategy created by Hwang and Yoon [9] depends on the idea that the option chose the most brief Euclidean separation from the positive perfect arrangement, and most distant from the negative perfect arrangement. Decision-making for the best option by utilizing TOPSIS technique is explained in the following steps:

Step I. In the first step the objective is to be determined and identified for the pertinent evaluation attributes.

Step II. In this step, a matrix is prepared considering the available information of attributes as shown in Table 2. In this matrix each row represents the alternatives, and each column represents the attributes.

Hence an element of the decision table m_{ij} represents the value of j th attribute in real values, which is not in normalized form and units for the i th alternative. But in case of a subjective attribute a ranked value judgment is taken. Once the subjective attributes are represented in a scale then the normalized values of the assigned attribute are calculated for different alternatives in the same way as that of the objective attributes (Table 3).

Table 3 Values of the subjective attribute [10]

Measures of attribute	Exceptionally low	Extremely low	Very low	Low	Below average	Average	Above average	High	Very high	Extremely high	Exceptionally high
Values assigned	0.0	0.1	0.2	0.3	0.4	0.5	0.6	0.7	0.8	0.9	1.0

Step III. The normalized decision matrix (K_{ij}) is to be obtained and represented as

$$K_{ij} = m_{ij} / \left[\sum_{j=1}^M m_{ij}^2 \right]^{1/2} \tag{5}$$

Step IV. In this step the relative importance (in weights) of different attributes with respect to the objective is to be decided. Also the weights in set w_j (for $j = 1, 2, 3, 4, \dots, m$) are assigned such that $\sum w_j = 1$ can be decided.

Step V. The normalized weighted matrix V_{ij} is obtained by multiplying each element of the column matrix K_{ij} with the assigned weights w_j . Now, expressing the elements of the weighted normalized matrix V_{ij} as Eq. (6).

$$V_{ij} = w_j K_{ij} \tag{6}$$

Step VI. In this step the positive (best) and negative (worst) solutions are obtained as follows [8]:

$$V^+ = \left[\left(\max_i \left(\sum_j V_{ij}/j \in J \right), \left(\min_i \left(\sum_j V_{ij}/j \in J' \right) \right) / \{i = 1, 2, \dots, n\} \right] \right. \\ \left. = \langle V_1^+, V_2^+, V_3^+, \dots, V_M^+ \rangle \tag{7}$$

$$V^- = \left[\left(\min_i \left(\sum_j V_{ij}/j \in J \right), \left(\max_i \left(\sum_j V_{ij}/j \in J' \right) \right) / \{i = 1, 2, \dots, n\} \right] \right. \\ \left. = \langle V_1^-, V_2^-, V_3^-, \dots, V_M^- \rangle \tag{8}$$

where $J = (j = 1, 2, \dots, M)/j$ is related to profitable attributes, and $J' = (j = 1, 2, \dots, M)/j$ is related to nonprofitable attributes V_j^+ represents best value of the attribute among different alternatives. For profitable attributes (higher values desirable), V_j^+ represents the higher value attribute. For nonprofitable attributes (lower values desirable), V_j^+ indicates lower value of the attribute. V_j^- shows the worst value of the attribute considered among the values of the attribute for different alternatives.

Step VII. In this step, the separation measures are obtained by considering the Euclidean distance in the following equations [8]:

$$S_i^+ = \left\{ \sum_{j=1}^M (V_{ij} - V_j^+)^2 \right\}^{0.5}, \quad i = 1, 2, 3, \dots, N \tag{9}$$

$$S_i^- = \left\{ \sum_{j=1}^M (V_{ij} - V_j^-)^2 \right\}^{0.5}, \quad i = 1, 2, \dots, N \tag{10}$$

Step VIII. The relative closeness of a particular alternative to the ideal solution, P_i can be expressed as follows:

$$P_i = S_i^- / (S_i^+ + S_i^-) \quad (11)$$

Step IX. In this step, the value of a set of alternatives is generated by descending order according to P_i indicating the most preferred and least preferred feasible solutions. P_i may also be called as overall or composite performance score of alternative. Apart from the above three methods there are many method.

All the above three methods contribute the following common steps [10]:

- To resolve the associated goals and to find out the alternative to be evaluated
- To recognize the applicable attributes to establish the values over the range of all attributes
- To rank and acquire weights (already normalized) for the attributes as per their relative importance
- To calculate the multi-attribute characters of the different options by using three score method
- To carry out an analysis after evaluation, and then come to a decision for selecting the best alternative.

An excellent example related to the selection of most suitable material for biomedical applications has been solved by using the above three MADM methods in the following context.

3 Material Combination for Hip Joint Prosthesis

Usually an orthopedic surgeon carefully selects the type of hip joint prosthesis considering a number of factors such as patient's age, life style, and level of activity before starting the replacement surgery. The material combination used in the replacement of femoral and acetabular components has different friction coefficients and wear rates. Therefore different combinations of materials are available as follows:

3.1 Metal on Polymer (MoP)

UHMWPE (Ultrahigh Molecular Weight Polyethylene) is a commonly used material in hip joint prostheses as acetabular cup with a metallic femoral head [11, 12]. This has higher wear rate as compared to all other combinations of materials. Table 4 shows the values of wear rates of the different combination of materials and the corresponding size of particles. The wear particles generated from the UHMWPE element may cause severe adverse reactions inside the human body, which is called osteolysis (damage of tissue bone) in the neighboring tissues [13, 14]. Usually, the

Table 4 Wear rates and average wear particle sizes of different combination of materials (a case study)

S. No.	Alternatives	Linear wear ($\mu\text{m}/\text{million}$ cycle)	Debris size ($\mu\text{m}/\text{million}$ cycle)	Mechanical loosening (%)
1	MoP	200	0.5	0.24
2	CoP	100	0.2	0.22
3	MoM	5	0.05	0.20
4	CoC	4	0.2	0.39

harder metallic material offers greater resistance to abrasive wear, due to which the softer material suffers from greater wear [15].

3.2 *Metal on Metal (MoM)*

This type of hip prostheses (MoM) evokes more interest since the problems raised by the pair MoP [16], mainly by showing lower wear rates than that of the MoP type of prostheses [17]. Some of the studies reported that the wear rate of MoM hip prosthesis as $1\text{--}6\text{ mm}^3$ per year, as compared to $3\text{--}100\text{ mm}^3$ per year for MoP hip prosthesis [18, 19].

MoM prosthesis produces lesser wear rate as compared to the MoP prosthesis with similar chemical properties and operating conditions. But the release of unwanted metallic ions from the MoM prosthesis causes severe infection due to its toxic effect in the blood. The problem can be resolved by using the Cobalt-Chromium alloys instead of stainless steel to minimize the release of worn particles inside the joint. In such case the metal ions mixed with the synovial fluid and get water soluble with metal salts and come out in the urine [15].

3.3 *Ceramic on Polymer (CoP)*

In CoP prostheses, the wear can be reduced by 50% by using a ceramic femoral ball, but it may involve a huge quantity of released particles [20]. Therefore the study about CoC materials has drawn more attention of the researchers.

3.4 Ceramic on Ceramic (CoC)

CoC prostheses generate a low quantity of wear particles ($1 \text{ mm}^3/\text{year}$) [20], which are lower than the MoP articular joint wear rate ($100 \text{ mm}^3/\text{million cycles}$) [18]. The most commonly used ceramic materials concerning the hip joint prostheses are Zirconia (ZrO_2) and Alumina (Al_2O_3) having features like good biocompatibility, corrosion and wear resistance [19]. Studies reported that the absorption of wear particles generated in the Ceramic on Ceramic ($\text{Al}_2\text{O}_3/\text{Al}_2\text{O}_3$) joint pair was about twenty times lesser than that observed in the Metal on Polymer joints [15, 21].

4 Material Selection for Hip Implants: A Case Study Under MCDM

In this study, the wear performances of some of the commonly used bio materials pairs such as MoP (Co–Cr alloy on UHMWPE), CoP (Zr–O₂ on UHMWPE), MoM (Co–Cr alloy on Co–Cr alloy), CoC (Zr–O₂ on Zr–O₂) are considered in the case of hip joint prosthesis as a case study as given in Table 4.

Majority of the materials used for the making the hip implants are available in alloy form, since commercially pure Titanium and Cobalt metals are not suitable because of the toxic effect. Alloys highly biocompatible to the human body and also they minimize the toxic effects.

In a biomedical application, following combination of materials are required in the case of hip joint prosthesis. The particle sizes and mean wear rate taken from in vitro simulator test of different material pairs with modified data in addition to the mechanical loosening are mentioned below. The question is how to select the most suitable material for making the hip joint prosthesis [10, 11].

5 Results and Discussion

The selection procedure is discussed below by using all the three MADM methods for material selection.

5.1 WPM (Weighted Product Method)

First, the given alternatives and the criteria are normalized as explained in the following steps.

Step-1 Choosing the lowest wear rate value, smallest debris particle size, and minimum value of mechanical loosening as best combination for a particular pair in the table, we can get the normalized value.

S. No.	Alternatives	Linear wear ($\mu\text{m}/\text{million}$ cycle)	Debris size ($\mu\text{m}/\text{million}$ cycle)	Mechanical loosening (%)
1	MoP	200	0.5	0.24
2	CoP	100	0.2	0.22
3	MoM	5	0.05	0.20
4	CoC	4	0.2	0.39

Step-2 Normalized values of attributes can be obtained by dividing the chosen values with other elements in the table.

Alternatives	LW	DS	ML
1. MoP	0.02	0.4	0.833
2. CoP	0.04	0.25	0.909
3. MoM	0.8	1	1
4. CoC	1	0.25	0.512

Step-3 Let us assign weights in terms of points (from 0 to 100) giving importance to the following criteria:

Wear rate as minimum as possible	50 points
Debris particle size as small as possible	20 points
Mechanical loosening as low as possible	10 points
Total	80 points

Step-4 Calculating the weights of the parameters wears rate, debris particle size, and mechanical loosening as follows:

Weight assigned to wear rate = $50/80 = 0.625$

Weight assigned to debris particle size = $20/80 = 0.25$

Weight assigned to mechanical loosening = $10/80 = 0.125$

Step-5 Assigning the above mentioned weights to the normalized attributes, the values of alternatives can be calculated by using the weighted product method, we get

Alternatives	LW	DS	ML
1	0.02	0.4	0.833
2	0.04	0.25	0.909
3	0.8	1	1
4	1	0.25	0.512
Attributed weights	0.625	0.25	0.125

Step-6 Calculating the final values of the alternatives as per Weighted Product Method as follows:

- $(0.02)^{0.625} \times (0.4)^{0.25} \times (0.833)^{0.125} = 0.0674$
- $(0.04)^{0.625} \times (0.25)^{0.25} \times (0.909)^{0.125} = 0.0934$
- $(0.8)^{0.625} \times (1)^{0.25} \times (1)^{0.125} = 0.8698$
- $(1)^{0.625} \times (0.25)^{0.25} \times (0.512)^{0.125} = 0.6503$

Now arranging the above values in the descending order, the preference ranking is 3–4–2–1.

LW DS ML	Geometric Mean (GM)	Weight = GM/ Total
LW $\begin{bmatrix} 1 & 3 & 5 \\ 1/3 & 1 & 3 \\ 1/5 & 1/3 & 1 \end{bmatrix}$	$(1 \times 3 \times 5)^{1/3} = 2.46$	0.636
DS	$(\frac{1}{3} \times 1 \times 3)^{1/3} = 1.0$	0.258
ML	$(\frac{1}{5} \times \frac{1}{3} \times 1)^{1/3} = 0.404$	0.1047

Total = 3.871

5.2 AHP (Analytic Hierarchy Process) Method

Step-1 Choosing the lowest values of the parameters as the best value similar to the WPM method, we have the following table.

Alternatives	Linear wear (µm/million cycle)	Wear debris size (µm/million cycle)	Mechanical loosening (%)
1. MoP	200	0.5	0.24
2. CoP	100	0.2	0.22
3. MoM	5	0.05	0.20
4. CoC	4	0.2	0.39

Step-2 In this case the normalized values of the attributes will be same as the WPM method provided that the assumed weights must be consistent. So the consistency of these weights is to be checked first.

Alternatives	LW	DS	ML
1. MoP	0.02	0.4	0.833
2. CoP	0.04	0.25	0.909
3. MoM	0.8	1	1
4. CoC	1	0.25	0.512

Step-3 Here the numbers 1, 3, 5, 7 and 9 correspond to the verbal judgments, such as “moderate importance”, “strong importance”, “very strong importance” and so on. Now assigning 1 for LW, 3 for DS and 5 for ML the Relative Importance Relation Matrix can be written as follows.

$$R_{ij} = \begin{bmatrix} 0.894 & 0.8671 & 0.4396 \\ 0.447 & 0.3468 & 0.4030 \\ 0.0223 & 0.0867 & 0.3663 \\ 0.0178 & 0.3468 & 0.7144 \end{bmatrix}$$

Attributed weights **0.625** **0.125** **0.25**

Step-4 For consistency check, the matrices A1, A2, A3, and A4 can be calculated as

$$A1 = \begin{bmatrix} 1 & 3 & 5 \\ \frac{1}{3} & 1 & 3 \\ \frac{1}{5} & \frac{1}{3} & 1 \end{bmatrix}, A2 = [0.636 \ 0.258 \ 0.1047]$$

$$A3 = A1 \times A2 = \begin{bmatrix} 1 & 3 & 5 \\ \frac{1}{3} & 1 & 3 \\ \frac{1}{5} & \frac{1}{3} & 1 \end{bmatrix} [0.636 \ 0.258 \ 0.1047] = \begin{bmatrix} 1.93 \\ 0.782 \\ 0.3172 \end{bmatrix}$$

$$A4 = A3/A2 = \begin{bmatrix} 1.93 \\ 0.782 \\ 0.3172 \end{bmatrix} \div \begin{bmatrix} 0.636 \\ 0.258 \\ 0.1047 \end{bmatrix} = \begin{bmatrix} 3.034 \\ 3.038 \\ 3.0 \end{bmatrix}$$

Eigen value $\lambda_{max} = 3.038$

Consistency Index $CI = \frac{\lambda_{max} - M}{M - 1} = \frac{3.038 - 3}{3 - 1} = \frac{0.038}{2} = 0.019$

Consistency Ratio $CR = CI/RI = 0.019/0.52 = 0.0365 < 0.1$

The allowed values are found to be consistent. Therefore the assumed weights are perfect in this method.

Step-5 Now using the simple addition of weights (SAW) method, the final values can be calculated as follows:

- $(0.02 \times 0.636) + (0.4 \times 0.258) + (0.833 \times 0.1047) = 0.2031$
- $(0.04 \times 0.636) + (0.25 \times 0.258) + (0.909 \times 0.1047) = 0.1851$
- $(0.8 \times 0.636) + (1 \times 0.258) + (1 \times 0.1047) = 0.8715$
- $(1 \times 0.636) + (0.25 \times 0.258) + (0.512 \times 0.1047) = 0.7541$

Now arranging the above values in the descending order, the preference ranking is 3–4–1–2.

5.3 TOPSIS (Technique for Order Preference by Similarity to the Ideal Solution) Method

Step-1 Choosing the lowest values of the parameters as the best value similar to the WPM and AHP method, we have the following table

Alternatives	Linear wear (μm/million cycle)	Wear debris size (μm/million cycle)	Mechanical loosening (%)
1. MoP	200	0.5	0.24
2. CoP	100	0.2	0.22
3. MoM	5	0.05	0.20
4. CoC	4	0.2	0.39

Step-2 The normalized decision matrix can be calculated as follows.

$$m_1 = \sqrt{(200^2 + 100^2 + 5^2 + 4^2)} = 223.69$$

$$m_2 = \sqrt{(0.5^2 + 0.2^2 + 0.05^2 + 0.2^2)} = 0.5766$$

$$m_3 = \sqrt{(0.24^2 + 0.22^2 + 0.20^2 + 0.39^2)} = 0.5459$$

Dividing each row elements of the above table by m_1, m_2, m_3 , we get the normalized weights of each attributes are calculated as follows:

Step-3 Normalized Weighted matrix can be represented as

$$W_{ij} = \begin{pmatrix} 0.5587 & 0.1083 & 0.1099 \\ 0.2793 & 0.04335 & 0.1007 \\ 0.0139 & 0.01083 & 0.0915 \\ 0.01125 & 0.04335 & 0.1786 \end{pmatrix}$$

Step-4 Now choosing the lowest values as best and highest values as worst in each column of the above matrix

Best value (V_{ij}^+)	Worst value (V_{ij}^-)
$V_1^+ = 0.01125$	$V_1^- = 0.5587$
$V_2^+ = 0.01083$	$V_2^- = 0.04335$
$V_3^+ = 0.0915$	$V_3^- = 0.1786$

Step-5 The separation measures can be calculated based on the best and worst values as follows:

$$S_1^+ = \sqrt{(0.5587 - 0.01125)^2 + ((0.1083 - 0.01803)^2) + ((0.1099 - 0.0915)^2)}$$

$$= 0.5564$$

$$S_1^- = \sqrt{(0.5587 - 0.5587)^2 + ((0.1083 - 0.04335)^2) + ((0.1099 - 0.1786)^2)}$$

$$= 0.0945$$

$$S_2^+ = \sqrt{(0.2793 - 0.01125)^2 + ((0.04335 - 0.01803)^2) + ((0.1007 - 0.0915)^2)}$$

$$= 0.2695$$

$$S_2^- = \sqrt{(0.2793 - 0.5587)^2 + ((0.04335 - 0.04335)^2) + ((0.1007 - 0.1786)^2)}$$

$$= 0.290$$

$$S_3^+ = \sqrt{(0.0139 - 0.01125)^2 + ((0.01083 - 0.01803)^2) + ((0.0915 - 0.0915)^2)}$$

$$= 0.00277$$

$$S_3^- = \sqrt{(0.0139 - 0.5587)^2 + ((0.01083 - 0.04335)^2) + ((0.0915 - 0.1786)^2)}$$

$$= 0.5526$$

$$S_4^+ = \sqrt{(0.01125 - 0.01125)^2 + ((0.04335 - 0.01803)^2) + ((0.1786 - 0.0915)^2)}$$

$$= 0.5543$$

$$S_4^- = \sqrt{(0.01125 - 0.5587)^2 + ((0.04335 - 0.04335)^2) + ((0.1786 - 0.1786)^2)}$$

$$= 0.5474$$

Rearranging again as follows, we have

$S_1^+ = 0.5564$	$S_1^- = 0.0945$
$S_2^+ = 0.2695$	$S_2^- = 0.290$
$S_3^+ = 0.00277$	$S_3^- = 0.5526$
$S_4^+ = 0.5543$	$S_4^- = 0.5474$
Total $S^+ = 1.3829$	Total $S^- = 1.4835$

Step-6 Now the Index values of preferences (Pi) are given by

Index values	Ranking
$P_1 = \frac{S_1^-}{S_1^+ + S_1^-} = \frac{0.0945}{0.5564 + 0.0945} = 0.1451$	4
$P_2 = \frac{S_2^-}{S_2^+ + S_2^-} = \frac{0.290}{0.2695 + 0.290} = 0.5183$	2
$P_3 = \frac{S_3^-}{S_3^+ + S_3^-} = \frac{0.5526}{0.00277 + 0.5526} = 0.995$	1
$P_4 = \frac{S_4^-}{S_4^+ + S_4^-} = \frac{0.5474}{0.5543 + 0.5474} = 0.4968$	3

Therefore the ranking obtained from the above values according to their descending order is 3–2–4–1.

It is found that the rankings are slightly different from each other in all the above three methods. However the alternative-3 is the first choice in all the methods, which is Metal on Metal (MoM) hip joint implant. Similarly the alternative-4 is the second choice in WAP and AHP methods whereas alternative-2 is the second choice in TOPSIS method. Considering the majority for selection the alternative-2 i.e., Ceramic on Ceramic (CoC) should be given second priority.

6 Conclusion

Selection of proper combination of materials for developing the hip joint implants is often remains a challenging task for the biomedical engineers. But proper selection always tends to better stability and longer life of the prosthesis. Hence it is recommended to use the decision-making techniques like WPM, AHP and TOPSIS to select the best combination of materials. In this study, it is found that the Metal on Metal (MoM) combination is considered to be the best choice because of their strength and rigidity which yields lesser wear during the bio-motion and action during the walking cycles. Out of all the three methods, the TOPSIS method should be preferred because its preferential ranking system using the unique concept of separation measures of best and worst values.

References

1. Petkovic D, Radenkovic G, Mitkovic M (2012) Fractographic investigation of failure in stainless steel orthopedic plates. *Facta Univ Ser Mech Eng* 10(1):7–14
2. Aherwar A, Singh A, Patnaik A (2016) Cobalt based alloy: a better choice biomaterial for hip implants. *Trends Biomater Artif Organs* 30(1):50–55
3. Suhendra N, Stachowiak G (2007) Computational model of asperity contact for the prediction of UHMWPE mechanical and wear behaviour in total hip joint replacements. *Tribol Lett* 25:9–22. <https://doi.org/10.1007/s11249-006-9128-2>
4. Chatterjee P, Chakraborty S (2012) Material selection using preferential ranking methods. *Mater Des* 35:384–393
5. Saaty TL (2000) Fundamentals of decision making and priority theory with the AHP. RWS Publications, Pittsburg
6. Ashby MF, Brechet YJM, Cebon D, Salvoc L (2004) Selection strategies for materials and processes. *Mater Des* 25:51–67
7. Jee DH, Kang KJ (2000) A method for optimal material selection aided with decision making theory. *Mater Des* 21:199–206
8. Kwiesielewicz M, Uden EV (2004) Inconsistent and contradictory judgments in pair wise comparison method in the AHP in software selection. *Eur J Oper Res* 137:134–144
9. Hwang CI, Yoon KP (1981) Multiple attribute decision making: methods and applications. Springer, New York
10. Azar FS (2001) Multi-attribute decision-making: use of three scoring methods to compare the performance of imaging techniques for breast cancer detection. Technical report available at scholarly commons: http://repository.upenn.edu/cis_reports/119
11. Windler M, Klabunde R (2001) Titanium for hip and knee prostheses. Material science, surface science, engineering, biological responses and medical applications. Springer, Berlin, pp 703–746
12. Dumbleton JH, Manley MT (2005) Metal-on-metal total hip replacement: what does the literature say. *J Arthroplasty* 20(2):174–188
13. Wang FC, Brockett C, Williams S, Udofia I, Fisher J, Jin ZM (2008) Lubrication and friction prediction in metal-on-metal hip implants. *Phys Med Biol* 53:1277
14. Park J, Lakes R (2007) Biomaterials, 3rd edn (Springer Journal)
15. Briggs TWR, Hanna SA, Kayani B, Tai S, Pollock RC, Cannon SR, Blunn GW, Carrington RWJ (2015) Metal-on-polyethylene versus metal-on-metal bearing surfaces in total hip arthroplasty a prospective randomised study investigating metal ion levels and chromosomal aberrations in peripheral lymphocytes. *Bone Joint J* 97-B(9):1183–1191
16. Ollivere B, Wimhurst JA, Clark IM, Donell ST (2012) Current concepts in osteolysis. *J Bone Joint Surg Br* 94:10–15
17. Delaunay C, Petit I, Learmonth ID, Oger P, Vendittoli PA (2010) Metal-on-metal bearings total hip arthroplasty: the cobalt and chromium ions release concern. *Orthop Traumatol Surg Res* 96:894
18. Yen SK, Guo MJ, Zan HZ (2001) Characterization of electrolytic ZrO₂ coating on Co–Cr–Mo implant alloys of hip prosthesis. *Biomaterials* 22:125
19. Carvalho I, Polcar T, Henriques M, Carvalho S (2015) Materials incompatibility as a major cause of hip prostheses rejection. *Rev Adv Mater Sci* 42:36–49
20. Das SS, Chakraborti (2018) Development of biomaterials for total hip joint replacement. *IOP Conf Series Mater Sci Eng* 377:012177. <https://doi.org/10.1088/1757-899X/377/1/012177>
21. Arun S, Kanagaraj S (2015) Mechanical characterization and validation of poly-methyl methacrylate/multi walled carbon nano-tube composite for the polycentric knee joint. *J Mech Behav Biomed Mater* 50:33–45